VII | **Gruppo Nazionale di Bioingegneria**

SEVENTH NATIONAL CONGRESS OF BIOENGINEERING
Proceedings

Organizers
Agostino Accardo
Francesco Brun
Sara Marceglia
Gianni Pedrizzetti

Pàtron editore

9 - 11 June 2021 | Trieste, Italy

GNB 2020

VII Congress of the National Group of Bioengineering (GNB)

UNIVERSITÀ
DEGLI STUDI DI TRIESTE

Gruppo Nazionale
di Bioingegneria

comune di trieste

AIIC
associazione
italiana
ingegneri clinici

REGIONE AUTONOMA
FRIULI VENEZIA GIULIA

60TH
1959-2019
ANNIVERSARY

biovalley
investments

sihta
SOCIETÀ ITALIANA DI HEALTH TECHNOLOGY ASSESSMENT

GNB 2020

Conference Chairs

Agostino Accardo, *Università di Trieste*
Francesco Brun, *Università di Trieste*
Sara Marceglia, *Università di Trieste*
Gianni Pedrizzetti, *Università di Trieste*

Scientific Committee

Agostino Accardo, *University of Trieste*
Valentina Agostini, *Polytechnic of Turin*
Francesco Amato, *University of Catanzaro "Magna Graecia"*
Vitoantonio Bevilacqua, *Polytechnic of Bari*
Luigi Bianchi, *University of Roma "Tor Vergata" (Roma2)*
Silvio Bicciato, *University of Modena and Reggio Emilia*
Leonardo Bocchi, *University of Firenze*
Laura Burattini, *Polytechnic University of Marche*
Emanuele Luigi Carniel, *University of Padova*
Federico Carpi, *University of Firenze*
Federica Caselli, *University of Roma "Tor Vergata" (Roma2)*
Mario Cesarelli, *University of Napoli "Federico II"*
Silvia Conforto, *University of Roma Tre (Roma3)*
Michele Conti, *University of Pavia*
Luca Crisofolini, *University of Bologna*
Marco Deriu, *Polytechnic of Turin*
Stefano Diciotti, *University of Bologna*
Gabriele Angelo Dubini, *Polytechnic of Milano*
Andrea Facchinetti, *University of Padova*
Luca Faes, *University of Palermo*
Giancarlo Ferrigno, *Polytechnic of Milano*
Gionata Fragomeni, *University of Catanzaro "Magna Graecia"*
Giordano Franceschini, *University of Perugia*
Simone Furini, *University of Siena*
Eugenio Guglielmelli, *University Campus Bio-Medico - Roma*
Nicola Lopomo, *University of Brescia*
Paolo Massobrio, *University of Genova*
Arianna Menciassi, *Sant'Anna School of Advanced Studies*
Silvestro Micera, *Sant'Anna School of Advanced Studies*
Antonella Motta, *University of Trento*
Giandomenico Nollo, *University of Trento*
Danilo Pani, *University of Cagliari*
Paolo Pascolo, *University of Udine*
Laura Pastorino, *University of Genova*
Gianni Pedrizzetti, *University of Trieste*
Stefano Ramat, *University of Pavia*
Andrea Remuzzi, *University of Bergamo*
Alessandro Tognetti, *University of Pisa*

Review Committee

Valentina Agostini, *Polytechnic of Turin*
Francesco Amato, *University of Catanzaro "Magna Graecia"*
Riccardo Barbieri, *Polytechnic of Milano*
Vitoantonio Bevilacqua, *Polytechnic of Bari*
Luigi Bianchi, *University of Roma "Tor Vergata" (Roma2)*
Silvio Bicciato, *University of Modena & Reggio Emilia*
Leonardo Bocchi, *University of Firenze*
Francesco Brun, *University of Trieste*
Laura Burattini, *Polytechnic University of Marche*
Emanuele Luigi Carniel, *University of Padova*
Federico Carpi, *University of Firenze*
Federica Caselli, *University of Roma "Tor Vergata" (Roma2)*
Mario Cesarelli, *University of Napoli "Federico II"*
Michele Conti, *University of Pavia*
Luca Crisofolini, *University of Bologna*
Cristiano De Marchis, *University of Roma Tre (Roma3)*
Marco Deriu, *Polytechnic of Turin*
Stefano Diciotti, *University of Bologna*
Andrea Facchinetti, *University of Padova*
Luca Faes, *University of Palermo*
Gionata Fragomeni, *University of Catanzaro "Magna Graecia"*
Giordano Franceschini, *University of Perugia*
Simone Furini, *University of Siena*
Eugenio Guglielmelli, *University Campus Bio-Medico - Roma*
Stefano Lai, *University of Cagliari*
Cecilia Laschi, *Sant'Anna School of Advanced Studies*
Nicola Lopomo, *University of Brescia*
Sara Marceglia, *University of Trieste*
Paolo Massobrio, *University of Genova*
Antonella Motta, *University of Trento*
Giandomenico Nollo, *University of Trento*
Danilo Pani, *University of Cagliari*
Paolo Pascolo, *University of Udine*
Laura Pastorino, *University of Genova*
Gianni Pedrizzetti, *University of Trieste*
Stefano Ramat, *University of Pavia*
Andrea Remuzzi, *University of Bergamo*
Leonardo Ricotti, *Sant'Anna School of Advanced Studies*
Silvia Storti, *University of Verona*
Alessandro Tognetti, *University of Pisa*
Pasquale Vena, *Polytechnic of Milano*
Christian Vergara, *Polytechnic of Milano*
Loredana Zollo, *University Campus Bio-Medico - Roma*

Tracks & Chairs

Theme 1 - Informatics and Electronics

1.1 - E-Health and clinical engineering

Mario Cesarelli, *Università di Napoli*
Giovanni D'Addio, *Istituti Clinici Scientifici Maugeri Spa*

1.2 - Biomedical signals, images, and Bioinformatics

Giuseppe Baselli, *Politecnico di Milano*
Maria Gabriella Signorini, *Politecnico di Milano*

Theme 2 - Clinical Biomechanics

2.1 - Biomechanics and mechanobiology

Francesco Migliavacca, *Politecnico di Milano*
Umberto Morbiducci, *Politecnico di Torino*

2.2 - Biomaterials, tissue engineering and regenerative medicine

Luca Cristofolini, *Università di Bologna*
Alberto Audenino, *Politecnico di Torino*

Theme 3 - Applied Bioengineering

3.1 - Artificial Organs, Medical and assistive robotics

Cecilia Laschi, *Scuola Superiore Sant'Anna di Pisa*
Leonardo Ricotti, *Scuola Superiore Sant'Anna di Pisa*

3.2 - Neural and rehabilitation engineering

Eugenio Guglielmelli, *Università Campus Bio-Medico di Roma*
Loredana Zollo, *Università Campus Bio-Medico di Roma*

Day 1: Informatics and electronics

Podium session:

A Stochastic Language Model of Italian Applied to Functional MRI during Narrative Listening
Andrea Gerardo Russo, Maria De Martino, Azzurra Mancuso, Francesco Di Salle, Alessandro Laudanna and Fabrizio Esposito

Automated Detection and Counting of Acne Lesions for Evaluation of Acne Severity
Antonella Melina, Pietro Salvagnini, Carlo Cosentino, Francesco Amato and Andrea Cherubini

3D Printing open source non-critical spare parts of medical devices: the oxygen concentrator as a case study
Licia Di Pietro, Carmelo De Maria, Giuseppe Gallone and Arti Devi Ahluwalia

Towards classification of ovarian cancer via micro-arrays data analysis
Diego Liberati

Radiomics-based prediction of head and neck cancer recurrence: a multi-centric MRI study
Marco Bologna, Valentina Corino, Giuseppina Calareso, Salvatore Alfieri, Rebecca Romanò, Laura Locati, Lisa Licitra and Luca Mainardi

Does a medical device nomenclature suitable for all purposes exist? Twenty years of Italian experience with the CND and its adoption in EUDAMED at European level
Michela Franzo', Federico D'Agostino, Catello Chierchia, Katiuscia Cucchiara, Eugenio Carrani, Letizia Sampaolo, Elisabetta Stella, Marina Torre and Mauro Asaro

Resting State Networks spatio-spectral fingerprints: the Default Mode Network case study
Ilaria Mazzonetto, Ettore Ambrosini, Antonino Vallesi and Alessandra Bertoldo

Comparison of different CNNs for breast tumor classification from ultrasound images
Jorge Lazo, Elena De Momi and Sara Moccia

Predicting the Onset of Chronic Obstructive Pulmonary Disease in the English Longitudinal Study of Ageing
Martina Vettoretti, Andrea Facchinetti and Barbara Di Camillo

Poster session:

Human exposure to electromagnetic fields generated in smart vehicle communications
Gabriella Tognola, Silvia Gallucci, Marta Bonato, Serena Fiocchi, Emma Chiaramello, Laura Dossi, Marta Parazzini and Paolo Ravazzani

CT-based FFR: paving the way to future hearts
Clarissa Bargellini, Quan Long and Tarun Mittal

A 3D CNN for preterm-infants' movement detection in NICUs from depth streams
Lucia Migliorelli, Sara Moccia, Giuseppe Pio Cannata, Alessia Galli, Ilaria Ercoli, Luigi Mandolini, Virgilio Carnielli and Emanuele Frontoni

Modelling the Meal Variability of Individuals with Type 1 Diabetes under Free-Living Conditions

Nunzio Camerlingo, Martina Vettoretti, Simone Del Favero, Andrea Facchinetti, Giorgio Maria Di Nunzio and Giovanni Sparacino

Performance of Dual-Augmented Lagrangian Method and Common Spatial Patterns applied in classification of Motor-Imagery BCI

Aleksandar Miladinovic, Milos Ajcevic, Giulia Silveri and Agostino Accardo

Human Activity Recognition through Wearable Sensors: a Deep Learning Approach

Daniele Fortunato, Marco Ghislieri, Samanta Rosati, Gabriella Balestra, Marco Knaflitz and Valentina Agostini

An Augmented-Reality App to communicate through the eye-gaze

Mirko Rossi, Giuseppe D'Avenio, Febo Cincotti and Mauro Grigioni

An application of DMAIC methodology for reducing voluntary departures from an Emergency Department

Giovanni Improta, Maria Romano, Carlo Ricciardi, Carlo Cosentino and Francesco Amato

Unobtrusive monitoring of stress indicators: a preliminary evaluation at rest

Veronica Chiara Zuccalà, Riccardo Favilla and Giuseppe Coppini

No-reference evaluation of the reconstructed images in single-shot K-Edge Subtraction X-ray Computed Tomography

Giulia Saccomano, Vittorio Di Trapani, Pasquale Delogu and Francesco Brun

Detecting low-to-moderate isometric muscle activity through a generalized CWT-based technique

Tiwana Varrecchia, Carmen D'Anna, Daniele Bibbo, Maurizio Schmid and Silvia Conforto

Preventive Healthcare through Air Pollution Exposure Modeling: the example of PULSE in Pavia

Daniele Pala, Luigi Zurlo, Marica Franzini, Riccardo Bellazzi, Vittorio Casella, Domenico Vito and Cristiana Larizza

Harmonisation of medical devices classification systems: development of a generalised approach starting from hip prostheses. A first example of an international and standardised nomenclature to be integrated within the European Medical Device Nomenclature

Michela Franzo', Eugenio Carrani, Mauro Asaro, Edward Caton, John keith Tucker, Richard Armstrong, Elaine Young, Letizia Sampaolo, Fabiano Bini, Franco Marinozzi and Marina Torre

Deep learning for improving in room imaging in radiotherapy: CBCT to synthetic CT conversion

Paolo Zaffino, Roberta Raso, Maria Chiara Angiocchi, Monica Merola, Sergio Canino, Matteo Nonnis, Antonella Bavasso, Caterina Mezzotero, Rosa Antonella Anoja, Elvira Mazzei and Maria Francesca Spadea

Five years of Lean Six Sigma in the healthcare: an overview of main tools and results

Giovanni Improta, Alfonso Maria Ponsiglione, Arianna Scala, Danilo Di Laura, Lucia Sara D'Angiolella and Giuseppe Cesarelli

Play-Draw-Write: usability and acceptance of a tablet app for the early screening of handwriting difficulties in kindergartners

Linda Greta Dui, Francesca Lunardini, Cristiano Termine, Matteo Matteucci and Simona Ferrante

Geometric alterations of capillary network in hypertension: preliminary results

Virginia Altamore, Francesco Giardini, Camilla Olianti, Irene Costantini, Leonardo Sacconi and Leonardo Bocchi

Linear Regression Models to Improve the Estimation of Insulin Boluses in Type 1 Diabetes Therapy
Giulia Noaro, Giacomo Cappon, Simone Del Favero, Giovanni Sparacino and Andrea Facchinetti

A Heuristic-Sliding-Window-based RRT Path Planning for Endovascular Catheterization
Zhen Li, Alice Segato, Alberto Favaro, Jenny Dankelman and Elena De Momi

Correlation between hyper-acute EEG alterations and 7-Day NIHSS score in thrombolysis treated ischemic stroke patients
Milos Ajcevic, Giovanni Furlanis, Aleksandar Miladinovic, Lara Stragapede, Giulia Silveri, Paola Caruso, Marcello Naccarato, Paolo Manganotti and Agostino Accardo

Assessment of Indoor Exposure Scenario by an 8x8 Planar Array Antenna at 3.7 GHz
Marta Bonato, Laura Dossi, Emma Chiaramello, Serena Fiocchi, Silvia Gallucci, Gabriella Tognola, Paolo Ravazzani and Marta Parazzini

Blood glucose prediction from Flash Glucose Monitoring and Fitbit data: a deep learning approach
Pietro Bosoni, Marco Meccariello, Valeria Calcaterra, Cristiana Larizza, Lucia Sacchi and Riccardo Bellazzi

IoT ink pen for the ecological study of age-related changes in handwriting
Davide Di Febbo, Francesca Lunardini, Milad Malavolti, Alessandra Pedrocchi, Alberto Borghese and Simona Ferrante

Comparison of Parametric Linear Techniques for Glucose Prediction in Type-1 Diabetes
Simone Faccioli, Andrea Facchinetti, Giovanni Sparacino and Simone Del Favero

A markerless gait analysis protocol based on a single RGB-Depth camera: sensitivity to background changes
Diletta Balta, Massimo Salvi, Filippo Molinari, Giulio Figari, Gabriele Paolini, Ugo Della Croce and Andrea Cereatti

Quantification and reduction of crosstalk in surface electromyogram by inverse modelling
Luca Mesin

Combining autoencoder and artificial neural network for classifying colorectal cancer stages
Antonio Brunetti, Maria Pia Caputo, Tommaso Maria Marvulli, Giacomo Donato Cascarano, Nicola Altini, Simona De Summa and Vitoantonio Bevilacqua

Correlation analysis of PRSA-based parameters during labor: a simulation study
Moira Barbieri, Tamara Stampalija, Massimo Walter Rivolta and Roberto Sassi

Analysis of heart rate variability as evaluation method for the risk of sepsis in the low-weight preterm infant
Fabio Tarricone, Viviana Bernocco, Domenico Buongiorno, Antonio Brunetti, Antonella D'Orazio, Antonio Del Vecchio, Vitoantonio Bevilacqua and Flavia Petrillo

Connectivity in Parkinson's disease patients with cognitive impairment: a simultaneous PET/MRI study
Erica Silvestri, Angelo Antonini, Marco Castellaro, Roberta Biundo, Diego Cecchin and Alessandra Bertoldo

Improving the assessment of vascular complexity in peripheral artery occlusive disease
Pierangela Bruno, Paolo Zaffino, Francesco Calimeri, Salvatore Scaramuzzino, Ciro Indolfi, Salvatore De Rosa and Maria Francesca Spadea

Modeling Intraperitoneal Insulin Kinetics in Patients with Type 1 Diabetes
Filippo Moret, Michele Schiavon, Claudio Cobelli and Chiara Dalla Man

Human papillomavirus early promoter: Sensitivity analysis and biological behaviour
Alberto Giaretta

Experimental Validation of an E-Textile T-Shirt for ECG Monitoring
Federica Amitrano, Armando Coccia, Leandro Donisi, Arcangelo Biancardi, Gaetano Pagano and Gianni D'Addio

Benchmarking between a Sensorized E-textile Sock for Remote Monitoring and a Stereophotogrammetric System
Leandro Donisi, Armando Coccia, Federica Amitrano, Carlo Ricciardi, Giuseppe Cesarelli and Gianni D'Addio

Day 2: Clinical Biomechanics

Podium session:

Cardiac fluid dynamics of patient-specific geometries in Pre and Post Mitral Valve Repair by Direct Numerical Simulation
Dario Collia and Gianni Pedrizzetti

Biomechanical implications of leg bending in popliteal stenting
Michele Conti, Alice Finotello, Anna Ferrarini, Giancarlo Salsano, Auricchio, Palombo, Spinella and Pane

Computational investigation of the male lower urinary tract in health and disease
Chiara Giulia Fontanella, Ilaria Toniolo, Alessandro Arduino, Joseph Vannel Fotso Fogang, Arturo Natali and Emanuele Luigi Carniel

Eulerian-based wall shear stress topological skeleton analysis and near-wall transport in aortic flow
Giuseppe De Nisco, Valentina Mazzi, Karol Calò, Raffaele Ponzini, Giovanna Rizzo, David A. Steinman, Diego Gallo and Umberto Morbiducci

3D nichoid substrates affect mesenchymal stem cell morphology and euchromatin organization
Emanuela Jacchetti, Emanuele Colombo, Tommaso Zandrini, Roberto Osellame, Giulio Cerullo, Davide Mazza and Manuela Raimondi

Advanced Firmware and Hardware for Multiscale and Multimaterial Bioprinting
Amedeo Franco Bonatti, Gabriele Maria Fortunato, Anna Lapomarda, Aurora De Acutis, Carmelo De Maria, Chiara Vitale Brovarone and Giovanni Vozzi

Are your cells alive?
Adele De Ninno, Riccardo Reale, Alessandro Giovinazzo, Francesca Romana Bertani, Luca Businaro, Paolo Bisegna, Claudia Matteucci and Federica Caselli

Ultrasound-triggered permeabilization of polyelectrolyte microcapsules
Marietta Pisano, Marta Clerici, Donatella Di Lisa, Roberto Raiteri and Laura Pastorino

Development of a compliance-matching biohybrid vascular graft through an integrated approach.
Elia Pederzani, Alessandro Caimi, Marco Pezzotta, Alice Caldiroli, Mattia Lupacchini, Matteo Tironi, Fabio Sangalli, Marina Figliuzzi, Nadia Azzollini, Sonia Fiori, Francesco G. Greco, Emiliano Votta, Gianfranco B. Fiore, Andrea Remuzzi, Stefania A. Riboldi, Monica Soncini and Alberto Redaelli

Poster session:

Abdominal visceral and subcutaneous adipose tissues in obese patients: mechanical behaviour
Chiara Giulia Fontanella, Mirto Foletto, Livio Corain and Emanuele Luigi Carniel

Computational tools for the evaluation of surgical parameters after LSG
Ilaria Toniolo, Chiara Giulia Fontanella, Mirto Foletto and Emanuele Luigi Carniel

A novel step counting algorithm using a head-mounted sensor
Alessia Cristiano, Alberto Sanna and Diana Trojaniello

Hybrid membranes for blood-contacting surfaces: preliminary characterization
Martina Todesco, Giorgia Merigliano, Valentina Candela, Laura Iop, Tiziana Palmosi, Gino Gerosa and Andrea Bagno

Single cell fluid dynamics: a VOF model of a red blood cell vs a leukocyte
Monica Piergiovanni, Elena Bianchi, Paola De Stefano and Gabriele Dubini

Mechanical properties of oxidized polyvinyl alcohol hydrogel scaffolds for tissue engineering
Silvia Todros, Silvia Barbon, Martina Favaron, Elena Stocco, Daniele Dalzoppo, Rafael Boscolo-Berto, Veronica Macchi, Claudio Grandi, Andrea Porzionato, Raffaele De Caro and Piero Pavan

Biofabrication and characterization of a biphasic construct to study osteochondral tissue in vitro
Irene Chiesa, Carmelo De Maria, Anna Lapomarda, Gabriele Maria Fortunato, Francesca Montemurro, Roberto Di Gesù, Rocky S Tuan, Giovanni Vozzi and Riccardo Gottardi

Electrospun ultrathin scaffold for Bruch's membrane regeneration in retinal tissue engineering
Beatrice Belgio, Gabriele Dubini, Federica Boschetti and Sara Mantero

Surface coated chitosan microbeads for the sustained release of drugs
Pietro Arnaldi, Orietta Monticelli and Laura Pastorino

Balance control after tripping: Margin of Stability and Limb Support Quotient
Alberto Finazzi, Adele Panarese Macrì, Paolo Gallina, Silvestro Micera and Vito Monaco

Impact of the shear stress on cultured human gut microbiota
Francesco Biagini, Marco Calvigioni, Ermes Botte, Alessandra Vecchione, Carmelo De Maria, Francesca Montemurro, Chiara Magliaro, Francesco Celandroni, Emilia Ghelardi and Giovanni Vozzi

Pectin-based biomaterial ink for Green Tissue Engineering applications
Anna Lapomarda, Aurora De Acutis, Irene Chiesa, Gabriele Maria Fortunato, Francesca Montemurro, Carmelo De Maria, Monica Mattioli Belmonte, Riccardo Gottardi and Giovanni Vozzi

Polymeric microchambers arrays for cargo protection
Stefania Boi, Valeriya Kudryavtseva, Jiaxin Zhang, Andrey Udalov, Evgeniy Shesterikov, Sergei Tverdokhlebov, Laura Pastorino and Gleb Sukhorukov

A hydrogel channel-based system to model the blood flow dynamic stimuli
Chiara Vitale, Arianna Fedi, Gabriele Varani, Alessandra Marrella, Marco Fato and Silvia Scaglione

Rapid and affordable prototyping of bioinspired microfluidic networks for Tissue Engineering
Guglielmo Pacetta, Aurora De Acutis, Francesca Montemurro, Carmelo De Maria and Giovanni Vozzi

Tensile properties of porcine retina
Beatrice Belgio, Sara Ragazzini, Paolo Arpa, Vito De Molfetta, Sara Mantero and Federica Boschetti

SensRing, a wearable ring-shaped device for measuring kinematics in reach-to-grasp tasks
Guenda Galperti, Erika Rovini, Laura Fiorini, Gianmaria Mancioppi, Radia Zeghari, Auriane Gros, Valeria Manera and Filippo Cavallo

Driving neuronal network connectivity with a modular alginate mask
Martina Brofiga, Elena Dellacasa, Enrica Vitali, Donatella Di Lisa, Paolo Massobrio and Laura Pastorino

Bioactive silica-based glass nanoparticles containing boron and copper
Elisa Piatti, Marta Miola and Enrica Vernè

Strategies to speed up the standardized bone plates mechanical testing for regulatory purposes
Mara Terzini, Gianpaolo Serino, Andrea Tancredi Lugas, Giancarlo Dichio, Piero Costa and Alberto L. Audenino

DXA-based Finite Element models to improve hip fracture risk prediction: a comparison with CT-based models
Alessandra Aldieri, Mara Terzini, Cristina Bignardi and Alberto Audenino

A Multibody Model for Ligament Balancing Assessment in Total Knee Arthroplasty
Giovanni Putame, Mara Terzini, Simone Borrelli, Cristina Bignardi and Alberto Audenino

Influence of cartilage thickness on Human Femur Neck: a 3D Stress-Strain Analysis
Andrada Pica, Fabiano Bini, Andrea Marinozzi and Franco Marinozzi

Image processing for rheological characterization of blood under flow
Giuseppe D'Avenio, Patrizia Caprari, Carla Daniele and Mauro Grigioni

Fontan Computational Hemodynamics: Impact of Inlet Velocity Profile Features with Implications on Clinically Relevant Parameters
Maurizio Lodi Rizzini, Paola Tasso, Diego Gallo, Giuseppe D'Avenio, Antonio Amodeo, Umberto Morbiducci and Mauro Grigioni

From Mocap data to inertial data through a biomechanical model to classify countermeasure exercises performed on ISS
Martina Ravizza, Alessandra Pedrocchi, John DeWitt and Giancarlo Ferrigno

Thermosensitive hydrogels for the encapsulation of primary and human derived neuronal cells
Donatella Di Lisa, Elena Dellacasa, Lorenzo Muzzi, Alberto Lagazzo, Monica Frega, Sergio Martinoia and Laura Pastorino

Transcatheter Aortic Valve with Embolic Filter: Experiments and Simulations
Dario Carbonaro, Claudio Chiastra, Umberto Morbiducci and Alberto Audenino

Use of an optimized automatic procedure for measuring the hydraulic permeability of articular cartilage
Naomi Giuliani, Arianna B Lovati, Marco Ferroni, Laura Ferrari, Laura Mangiavini, Giuseppe M Peretti and Federica Boschetti

Design and validation of a novel low cost-bicompartmental platform for cell and tissue cultures
Lorenzo Coppadoro, Chiara Foglieni, Gianfranco Fiore and Monica Soncini

The eccentric phase of countermovement jump: comparing motion capture and inertial sensors
Luigi Truppa, Michelangelo Guaitolini, Carlo Castagna and Andrea Mannini

Development of a novel bioreactor for the generation of controlled hydrodynamic stimuli on vascular planar tissue samples
Elia Pederzani, Lorenzo Pietro Coppadoro, Aldo Josè Suria Roldan, Chiara Foglieni, Monica Soncini and Gianfranco Beniamino Fiore

Versatile perfusion and electrical stimulation bioreactor for bone tissue engineering

Diana Massai, Stefano Gabetti, Giovanni Putame, Ileana Armando, Elisa Fiume, Alessandro Sanginario, Dario Carbonaro, Francesco Baino, Alberto Audenino, Enrica Vernè and Cristina Bignardi

Application of deer hearts for ex-vivo modelling of mitral valve pathology – preliminary results

Michal Jaworek, Edoardo Maroncelli, Federico Lucherini, Guido Gelpi, Claudia Romagnoni, Rubina Rosa, Cristina Manenti, Carlo Antona, Gianfranco Beniamino Fiore and Riccardo Vismara

Thrombogenicity of cardiovascular devices: mutual and relative effect of biomaterial and shear stress

Silvia Bozzi, Federica Vercellino, Filippo Consolo, Yana Roka Moiia, Tatiana Mencarini, Marvin Slepian and Alberto Redaelli

Gellan gum-based hydrogels as injectable materials for cartilage tissue engineering

Laura Riacci, Lorenzo Vannozzi, Lorena Garcia Hevia and Leonardo Ricotti

The influence of turbulence modelling on thrombosis in cardiovascular devices

Giuseppe Passoni, Silvia Bozzi, Alberto Redaelli and Davide Dominissini

Internal fixation of femour fractures: a new wireless electromechanical dynamization system

Giancarlo Dichio, Giovanni Putame, Mara Terzini, Sergio Cannata, Piero Costa, Eros Gian Alessandro Pasero and Alberto Audenino

Day 3: Applied Bioengineering

Podium session:

Somatotopical feedback restoration in the lower limb through TENS: a feasibility study
Andrea Demofonti, Alessia Scarpelli, Valentina Iannelli, Anna Lisa Ciancio, Francesca Cordella and Loredana Zollo

An Innovative High-Fidelity Neonatal Pneumothorax Simulator
Sabina Maglio, Selene Tognarelli , Arianna Menciassi

An innovative High-Fidelity simulator of cervical changes during labour
Carlotta Luchini, Selene Tognarelli , Arianna Menciassi

Preliminary Design and Validation of an Implantable Artificial Bladder
Stefano Pane, Veronica Iacovacci, Tommaso Mazzocchi, Arianna Menciassi , Leonardo Ricotti

A new motor-driven smart prosthetic socket
Linda Paternò, Claudio Quaglia, Michele Ibrahimi, Emanuele Gruppioni, Leonardo Ricotti , Arianna Menciassi

A Dual-Branched Convolutional Neural Network for P300 detection and feature interpretation
Davide Borra, Silvia Fantozzi and Elisa Magosso

A neuromorphic haptic feedback for lower limb sensory substitution
Jessica D'Abbraccio, Sahana Prasanna, Ilaria Cesini, Filippo Dell'Agnello, Simona Crea, Nicola Vitiello, Alberto Mazzoni and Calogero Maria Oddo

Estimation of the base of support during gait with an unobtrusive wearable system
Rachele Rossanigo, Stefano Bertuletti, Marco Caruso, Marco Knaflitz, Ugo Della Croce and Andrea Cereatti

Poster session:

Portable Normothermic Perfusion System for Laboratory test of Microwave Devices
Mattia Dimitri, Lucrezia Mazzantini, Sara Aquino, Fabio Staderini, Fabio Cianchi , Andrea Corvi

Ultrasonic neural stimulation of zebrafish larvae reveals region-specific calcium imaging activation patterns
Nicolò Meneghetti, Francesca Dedola, Vladislav Gavryusev, Giuseppe Sancataldo, Lapo Turrini, Giuseppe de Vito, Francesco Vanzi, Jacopo Carpaneto, Annarita Cutrone, Francesco Saverio Pavone, Alberto Mazzoni and Silvestro Micera

Biomarkers of Impulse Control Disorder in firing patterns of parkinsonian subthalamic nucleus
Federico Micheli, Matteo Vissani, Guido Pecchioli, Federica Terenzi, Silvia Ramat and Alberto Mazzoni

Muscle forces and activations in Parkinson's disease: a model-based approach
Marco Romanato, Daniele Volpe, Massimo Sartori and Zimi Sawacha

A neural electrode for closed-loop vagus nerve recording and stimulation to control autonomic reflexes
Alice Giannotti, Ivo Strauss and Silvestro Micera

Assessing Transfer Entropy as a functional connectivity measure via a Neural Mass Model
Giulia Ricci, Elisa Magosso and Mauro Ursino

A Dataset of DMPs for robot motion planning
Christian Tamantini, Clemente Lauretti, Francesca Cordella and Loredana Zollo

MVAR estimation of source-level EEG connectivity in Parkinson's disease
Emanuela Formaggio, Maria Rubega, Jessica Rupil, Stefano Masiero, Alessandra Del Felice and Gianna Maria Toffolo

Design of novel ventricular chambers: comparison of three different models
Valentina Candela, Martina Todesco, Giovanni Meneghetti, Gino Gerosa , Andrea Bagno

Neural response to acoustic stimulation mediated by piezoelectric nanoparticles
Marietta Pisano, Mariateresa Tedesco, Martina Brofiga, Paolo Massobrio, Attilio Marino, Gianni Ciofani and Roberto Raiteri

The suitability of Gait Variable Scores for Myotonic Dystrophy types classification
Margherita Lofrumento, Elda Judica, Barbara Fossati, Massimo Corbo and Peppino Tropea

Neuroimaging biomarkers toward an optimized and personalized AOT
Marco Ottaviani, Paola Romano, Sanaz Pournajaf, Michela Goffredo, Fabiano Bini, Franco Marinozzi, Marco Franceschini and Francesco Infarinato

Design and development of an origami-based pump for soft robotics wearable applications
Giorgio Bondì, Debora Zrinscak , Matteo Cianchetti

Stereo-PIV study of the flow across an axial pump for circulatory support
Giuseppe D'Avenio, Umberto Morbiducci, Costantino Del Gaudio , Mauro Grigioni

Clinical and technology-based assessment of an innovative integrated rehabilitation programme for persons affected by Parkinson's disease
Gian Pietro Salvi, Annamaria Quarenghi, Eleonora Sigismondi, Emanuele Mion, Marcello Simonini and Stefano Mazzoleni

Development of a capnometer for extracorporeal life support devices: compensation of the temperature effect on the mid-IR LED
Michele Bellancini, Laura Cercenelli, Stefano Severi , Emanuela Marcelli

Unassisted in-vitro simulation of superior cavo pulmonary shunt for evaluation of pathophysiological issue
Francesco De Gaetano, Massimo Griselli , Maria Laura Costantino

Comparison of the performances of six magneto-inertial sensor fusion filters for orientation estimation in movement analysis
Marco Caruso, Daniel Laidig, Angelo Maria Sabatini, Marco Knaflitz, Ugo Della Croce, Thomas Seel and Andrea Cereatti

A novel multi-sensor system for gait assessment in real-world conditions: preliminary results
Francesca Salis, Stefano Bertuletti, Marco Caruso, Tecla Bonci, Kirsty Scott, Rachele Rossanigo, Ugo Della Croce, Claudia Mazzà and Andrea Cereatti

A patient-specific approach for the IDH risk evaluation in the early stage of Haemodialysis
Giustina Casagrande , Maria Laura Costantino

A simulation study on safety and efficacy of tFUS
Mattia Stefano, Alessia Scarpelli, Francesca Cordella and Loredana Zollo

Falls and prostheses in patients with transfemoral amputation
Pierpaolo Palumbo, Serena Moscato, Francesca Caterini, Antonella Miccio, Luca Casagli, Angelo Davalli, Pericle Randi and Lorenzo Chiari

Evaluation of robotic endoscopic neurosurgery through kinematic analysis of surgical gesture
Salih Ertug Ovur, Elena De Momi, Enrico Karim Siena, Amy Wynn, Leandro Lucangeli, Alessandro De Benedictis, Carlo Efisio Marras, Giancarlo Ferrigno , Valentina Camomilla

Integration of 3D Action Observation Therapy and Rehabilitation Exercises in Mixed Reality: A Feasibility Study on Post-Stroke Patients
Stefano Elio Lenzi, Paolo Mosna, Stefano Lazzarini, Massimiliano Gobbo, Monica Angelini, Riccardo Buraschi, Stefano Negrini, Maddalena Fabbri Destro, Pietro Avanzini, Giacomo Rizzolatti and Nicola Francesco Lopomo

Stretchable polymer-based biopotential electrodes for unobtrusive EMG detection
Andrea Spanu, Annalisa Bonfiglio and Danilo Pani

DoMoMEA: a home neuromotor telerehabilitation system for stroke patients
Andrea Zedda, Elisa Gusai, Marco Caruso, Stefano Bertuletti, Salvatore Spanu, Giulia Baldazzi, Krizia Masciavé, Andrea Pibiri, Marco Monticone, Andrea Cereatti, Luigi Raffo and Danilo Pani

Author Index

Accardo Agostino	Smoking effect on the circadian rhythm of blood pressure in hypertensive subjects
–	Performance of Dual-Augmented Lagrangian Method and Common Spatial Patterns applied in classification of Motor-Imagery BCI
–	Correlation between hyper-acute EEG alterations and 7-Day NIHSS score in thrombolysis treated ischemic stroke patients
Agostini Valentina	A Machine Learning Approach for Muscle Activity Detection
–	Human Activity Recognition through Wearable Sensors: a Deep Learning Approach
Ajcevic Milos	Smoking effect on the circadian rhythm of blood pressure in hypertensive subjects
–	Performance of Dual-Augmented Lagrangian Method and Common Spatial Patterns applied in classification of Motor-Imagery BCI
–	Correlation between hyper-acute EEG alterations and 7-Day NIHSS score in thrombolysis treated ischemic stroke patients
Aldieri Alessandra	DXA-based Finite Element models to improve hip fracture risk prediction: a comparison with CT-based models
Alfieri Salvatore	Radiomics-based prediction of head and neck cancer recurrence: a multi-centric MRI study
Altamore Virginia	Geometric alterations of capillary network in hypertension: preliminary results
Altini Nicola	Quantification and reduction of crosstalk in surface electromyogram by inverse modelling
Amato Francesco	Automated Detection and Counting of Acne Lesions for Evaluation of Acne Severity
–	An application of DMAIC methodology for reducing voluntary departures from an Emergency Department
Ambrosini Ettore	Resting State Networks spatio-spectral fingerprints: the Default Mode Network case study
Amitrano Federica	Experimental Validation of an E-Textile T-Shirt for ECG Monitoring
–	Benchmarking between a Sensorized E-textile Sock for Remote Monitoring and a Stereophotogrammetric System

–	Does a medical device nomenclature suitable for all purposes exist? Twenty years of Italian experience with the CND and its adoption in EUDAMED at European level
Audenino Alberto	Strategies to speed up the standardized bone plates mechanical testing for regulatory purposes
–	DXA-based Finite Element models to improve hip fracture risk prediction: a comparison with CT-based models
–	A Multibody Model for Ligament Balancing Assessment in Total Knee Arthroplasty
–	Transcatheter Aortic Valve with Embolic Filter: Experiments and Simulations
–	Versatile perfusion and electrical stimulation bioreactor for bone tissue engineering
–	Internal fixation of femour fractures: a new wireless electromechanical dynamization system
Auricchio Ferdinando	Biomechanical implications of leg bending in popliteal stenting
Avanzini Pietro	Integration of 3D Action Observation Therapy and Rehabilitation Exercises in Mixed Reality: A Feasibility Study on Post-Stroke Patients
Azzollini Nadia	Development of a compliance-matching biohybrid vascular graft through an integrated approach.
Bagno Andrea	Hybrid membranes for blood-contacting surfaces: preliminary characterization
–	Design of novel ventricular chambers: comparison of three different models
Baino Francesco	Versatile perfusion and electrical stimulation bioreactor for bone tissue engineering
Baldazzi Giulia	DoMoMEA: a home neuromotor telerehabilitation system for stroke patients
Balestra Gabriella	A Machine Learning Approach for Muscle Activity Detection
–	Human Activity Recognition through Wearable Sensors: a Deep Learning Approach
Balta Diletta	A markerless gait analysis protocol based on a single RGB-Depth camera: sensitivity to background changes

Barbieri Moira	Correlation analysis of PRSA-based parameters during labor: a simulation study
Barbon Silvia	Mechanical properties of oxidized polyvinyl alcohol hydrogel scaffolds for tissue engineering
Bardozzo Francesco	Detecting the neural processes of lie generation with low-cost EEG: a preliminary study
Bargellini Clarissa	CT-based FFR: paving the way to future hearts
Bavasso Antonella	Deep learning for improving in room imaging in radiotherapy: CBCT to synthetic CT conversion
Belgio Beatrice	Electrospun ultrathin scaffold for Bruch's membrane regeneration in retinal tissue engineering
–	Tensile properties of porcine retina
Bellancini Michele	Development of a capnometer for extracorporeal life support devices: compensation of the temperature effect on the mid-IR LED
Bellazzi Riccardo	Preventive Healthcare through Air Pollution Exposure Modeling: the example of PULSE in Pavia
–	Blood glucose prediction from Flash Glucose Monitoring and Fitbit data: a deep learning approach
Bernocco Viviana	Analysis of heart rate variability as evaluation method for the risk of sepsis in the low-weight preterm infant
Bertani Romana Francesca	Are your cells alive?
Bertoldo Alessandra	Connectivity in Parkinson's disease patients with cognitive impairment: a simultaneous PET/MRI study
–	Resting State Networks spatio-spectral fingerprints: the Default Mode Network case study
Bertuletti Stefano	Estimation of the base of support during gait with an unobtrusive wearable system
–	A novel multi-sensor system for gait assessment in real-world conditions: preliminary results
–	DoMoMEA: a home neuromotor telerehabilitation system for stroke patients
Bevilacqua Vitoantonio	Combining autoencoder and artificial neural network for classifying colorectal cancer stages

–	Analysis of heart rate variability as evaluation method for the risk of sepsis in the low-weight preterm infant
Biagini Francesco	Impact of the shear stress on cultured human gut microbiota
Biancardi Arcangelo	Experimental Validation of an E-Textile T-Shirt for ECG Monitoring
Bianchi Elena	Single cell fluid dynamics: a VOF model of a red blood cell vs a leukocyte
Bibbo Daniele	Detecting low-to-moderate isometric muscle activity through a generalized CWT-based technique
Bignardi Cristina	DXA-based Finite Element models to improve hip fracture risk prediction: a comparison with CT-based models
–	A Multibody Model for Ligament Balancing Assessment in Total Knee Arthroplasty
–	Versatile perfusion and electrical stimulation bioreactor for bone tissue engineering
Bini Fabiano	Neuroimaging biomarkers toward an optimized and personalized AOT
–	Influence of cartilage thickness on Human Femur Neck: a 3D Stress-Strain Analysis
–	Harmonisation of medical devices classification systems: development of a generalised approach starting from hip prostheses. A first example of an international and standardised nomenclature to be integrated within the European Medical Device Nomenclature
Bisegna Paolo	Boosting automated palynology via microfluidics and machine learning
–	Are your cells alive?
Biundo Roberta	Connectivity in Parkinson's disease patients with cognitive impairment: a simultaneous PET/MRI study
Bocchi Leonardo	Geometric alterations of capillary network in hypertension: preliminary results
Boi Stefania	Polymeric microchambers arrays for cargo protection
Bologna Marco	Radiomics-based prediction of head and neck cancer recurrence: a multi-centric MRI study

Bonato Marta	Human exposure to electromagnetic fields generated in smart vehicle communications
–	Assessment of Indoor Exposure Scenario by an 8x8 Planar Array Antenna at 3.7 GHz
Bonatti Franco Amedeo	Advanced Firmware and Hardware for Multiscale and Multimaterial Bioprinting
Bonci Tecla	A novel multi-sensor system for gait assessment in real-world conditions: preliminary results
Bondì Giorgio	Design and development of an origami-based pump for soft robotics wearable applications
Bonfiglio Annalisa	Stretchable polymer-based biopotential electrodes for unobtrusive EMG detection
Borghese Alberto	A patient-specific approach for the IDH risk evaluation in the early stage of Haemodialysis
Borra Davide	A Dual-Branched Convolutional Neural Network for P300 detection and feature interpretation
Borrelli Simone	A Multibody Model for Ligament Balancing Assessment in Total Knee Arthroplasty
Boschetti Federica	Electrospun ultrathin scaffold for Bruch's membrane regeneration in retinal tissue engineering
–	Tensile properties of porcine retina
–	Use of an optimized automatic procedure for measuring the hydraulic permeability of articular cartilage
Boscolo-Berto Rafael	Mechanical properties of oxidized polyvinyl alcohol hydrogel scaffolds for tissue engineering
Bosoni Pietro	Blood glucose prediction from Flash Glucose Monitoring and Fitbit data: a deep learning approach
Botta Fabio	Filtering techniques for whole body vibration artefact removal from low-SNR sEMG signals
Botte Ermes	Impact of the shear stress on cultured human gut microbiota
Botter Alberto	Mapping the sEMG distribution over the forearm for grip myotonia characterization: methodological aspects
Bozzi Silvia	Thrombogenicity of cardiovascular devices: mutual and relative effect of biomaterial and shear stress

–	The influence of turbulence modelling on thrombosis in cardiovascular devices
Brigadoi Sabrina	Detection of the N2/N2pc event-related potential (ERP) components buried in the EEG using phase angle distribution across sweeps
Brighetti Antonia Maria	Boosting automated palynology via microfluidics and machine learning
Brofiga Martina	Neural response to acoustic stimulation mediated by piezoelectric nanoparticles
–	Driving neuronal network connectivity with a modular alginate mask
Brovarone Vitale Chiara	Advanced Firmware and Hardware for Multiscale and Multimaterial Bioprinting
Brun Francesco	No-reference evaluation of the reconstructed images in single-shot K-Edge Subtraction X-ray Computed Tomography
Brunetti Antonio	Combining autoencoder and artificial neural network for classifying colorectal cancer stages
–	Analysis of heart rate variability as evaluation method for the risk of sepsis in the low-weight preterm infant
Bruno Pierangela	Improving the assessment of vascular complexity in peripheral artery occlusive disease
Buongiorno Domenico	Analysis of heart rate variability as evaluation method for the risk of sepsis in the low-weight preterm infant
Buraschi Riccardo	Integration of 3D Action Observation Therapy and Rehabilitation Exercises in Mixed Reality: A Feasibility Study on Post-Stroke Patients
Burattini Laura	Model-based assessment of incretin effect from OGTT data in healthy subjects
–	Electrocardiographic Alternans in Hemodialysis: A Case Report
–	Novel recurrence features for prefall and fall detection in backward and forward fall types
Businaro Luca	Boosting automated palynology via microfluidics and machine learning
–	Are your cells alive?

Caimi Alessandro	Development of a compliance-matching biohybrid vascular graft through an integrated approach.
Calareso Giuseppina	Radiomics-based prediction of head and neck cancer recurrence: a multi-centric MRI study
Calcaterra Valeria	Blood glucose prediction from Flash Glucose Monitoring and Fitbit data: a deep learning approach
Caldiroli Alice	Development of a compliance-matching biohybrid vascular graft through an integrated approach.
Calimeri Francesco	Improving the assessment of vascular complexity in peripheral artery occlusive disease
Calò Karol	Eulerian-based wall shear stress topological skeleton analysis and near-wall transport in aortic flow
Calvigioni Marco	Impact of the shear stress on cultured human gut microbiota
Camerlingo Nunzio	Modelling the Meal Variability of Individuals with Type 1 Diabetes under Free-Living Conditions
Camomilla Valentina	Evaluation of robotic endoscopic neurosurgery through kinematic analysis of surgical gesture
Candela Valentina	Hybrid membranes for blood-contacting surfaces: preliminary characterization
–	Design of novel ventricular chambers: comparison of three different models
Canino Sergio	Deep learning for improving in room imaging in radiotherapy: CBCT to synthetic CT conversion
Cannata Pio Giuseppe	A 3D CNN for preterm-infants' movement detection in NICUs from depth streams
Cannata Sergio	Internal fixation of femour fractures: a new wireless electromechanical dynamization system
Cappon Giacomo	Linear Regression Models to Improve the Estimation of Insulin Boluses in Type 1 Diabetes Therapy
Caprari Patrizia	Image processing for rheological characterization of blood under flow
Caputo Pia Maria	Combining autoencoder and artificial neural network for classifying colorectal cancer stages

Carbonaro Dario	Transcatheter Aortic Valve with Embolic Filter: Experiments and Simulations
–	Versatile perfusion and electrical stimulation bioreactor for bone tissue engineering
Carniel Luigi Emanuele	Abdominal visceral and subcutaneous adipose tissues in obese patients: mechanical behaviour
–	Computational tools for the evaluation of surgical parameters after LSG
–	Computational investigation of the male lower urinary tract in health and disease
Carnielli Virgilio	A 3D CNN for preterm-infants' movement detection in NICUs from depth streams
Carpaneto Jacopo	Ultrasonic neural stimulation of zebrafish larvae reveals region-specific calcium imaging activation patterns
Carrani Eugenio	Harmonisation of medical devices classification systems: development of a generalised approach starting from hip prostheses. A first example of an international and standardised nomenclature to be integrated within the European Medical Device Nomenclature
–	Does a medical device nomenclature suitable for all purposes exist? Twenty years of Italian experience with the CND and its adoption in EUDAMED at European level
Caruso Marco	Estimation of the base of support during gait with an unobtrusive wearable system
–	Comparison of the performances of six magneto-inertial sensor fusion filters for orientation estimation in movement analysis
–	A novel multi-sensor system for gait assessment in real-world conditions: preliminary results
–	DoMoMEA: a home neuromotor telerehabilitation system for stroke patients
Caruso Paola	Correlation between hyper-acute EEG alterations and 7-Day NIHSS score in thrombolysis treated ischemic stroke patients
Casagli Luca	Falls and prostheses in patients with transfemoral amputation
Casagrande Giustina	A patient-specific approach for the IDH risk evaluation in the early stage of Haemodialysis

Cascarano Donato Giacomo	Combining autoencoder and artificial neural network for classifying colorectal cancer stages
Casella Vittorio	Preventive Healthcare through Air Pollution Exposure Modeling: the example of PULSE in Pavia
Caselli Federica	Boosting automated palynology via microfluidics and machine learning
–	Are your cells alive?
Castagna Carlo	The eccentric phase of countermovement jump: comparing motion capture and inertial sensors
Castellaro Marco	Connectivity in Parkinson's disease patients with cognitive impairment: a simultaneous PET/MRI study
Caterini Francesca	Falls and prostheses in patients with transfemoral amputation
Caton Edward	Harmonisation of medical devices classification systems: development of a generalised approach starting from hip prostheses. A first example of an international and standardised nomenclature to be integrated within the European Medical Device Nomenclature
Cavallo Filippo	SensRing, a wearable ring-shaped device for measuring kinematics in reach-to-grasp tasks
Cecchin Diego	Connectivity in Parkinson's disease patients with cognitive impairment: a simultaneous PET/MRI study
Celandroni Francesco	Impact of the shear stress on cultured human gut microbiota
Cercenelli Laura	Development of a capnometer for extracorporeal life support devices: compensation of the temperature effect on the mid-IR LED
CereattiAndrea	Estimation of the base of support during gait with an unobtrusive wearable system
–	Comparison of the performances of six magneto-inertial sensor fusion filters for orientation estimation in movement analysis
–	A novel multi-sensor system for gait assessment in real-world conditions: preliminary results
–	A markerless gait analysis protocol based on a single RGB-Depth camera: sensitivity to background changes
–	DoMoMEA: a home neuromotor telerehabilitation system for stroke patients

Cerone Luigi Giacinto	Mapping the sEMG distribution over the forearm for grip myotonia characterization: methodological aspects
Cerullo Giulio	3D nichoid substrates affect mesenchymal stem cell morphology and euchromatin organization
Cesarelli Giuseppe	Five years of Lean Six Sigma in the healthcare: an overview of main tools and results
–	Benchmarking between a Sensorized E-textile Sock for Remote Monitoring and a Stereophotogrammetric System
Cesini Ilaria	A neuromorphic haptic feedback for lower limb sensory substitution
Cherubini Andrea	Automated Detection and Counting of Acne Lesions for Evaluation of Acne Severity
Chiaramello Emma	Human exposure to electromagnetic fields generated in smart vehicle communications
–	Assessment of Indoor Exposure Scenario by an 8x8 Planar Array Antenna at 3.7 GHz
Chiari Lorenzo	Falls and prostheses in patients with transfemoral amputation
Chiastra Claudio	Transcatheter Aortic Valve with Embolic Filter: Experiments and Simulations
Chierchia Catello	Does a medical device nomenclature suitable for all purposes exist? Twenty years of Italian experience with the CND and its adoption in EUDAMED at European level
Chiesa Irene	Biofabrication and characterization of a biphasic construct to study osteochondral tissue in vitro
–	Pectin-based biomaterial ink for Green Tissue Engineering applications
Cianchetti Matteo	Design and development of an origami-based pump for soft robotics wearable applications
Cianchi Fabio	Portable Normothermic Perfusion System for Laboratory test of Microwave Devices
Ciancio Lisa Anna	Somatotopical feedback restoration in the lower limb through TENS: a feasibility study
Cincotti Febo	An Augmented-Reality App to communicate through the eye-gaze
Ciofani Gianni	Neural response to acoustic stimulation mediated by piezoelectric nanoparticles

Clerici Marta	Ultrasound-triggered permeabilization of polyelectrolyte microcapsules
Cobelli Claudio	Modeling Intraperitoneal Insulin Kinetics in Patients with Type 1 Diabetes
Coccia Armando	Experimental Validation of an E-Textile T-Shirt for ECG Monitoring
–	Benchmarking between a Sensorized E-textile Sock for Remote Monitoring and a Stereophotogrammetric System
Collia Dario	Cardiac fluid dynamics of patient-specific geometries in Pre and Post Mitral Valve Repair by Direct Numerical Simulation
Colombo Emanuele	3D nichoid substrates affect mesenchymal stem cell morphology and euchromatin organization
Colonna Alessia	Automatic estimation of nerve tortuosity in corneal images
Conforto Silvia	Filtering techniques for whole body vibration artefact removal from low-SNR sEMG signals
–	Detecting low-to-moderate isometric muscle activity through a generalized CWT-based technique
Consolo Filippo	Thrombogenicity of cardiovascular devices: mutual and relative effect of biomaterial and shear stress
Conti Michele	Biomechanical implications of leg bending in popliteal stenting
Coppadoro Lorenzo	Design and validation of a novel low cost-bicompartmental platform for cell and tissue cultures
Coppadoro Pietro Lorenzo	Development of a novel bioreactor for the generation of controlled hydrodynamic stimuli on vascular planar tissue samples
Coppini Giuseppe	Unobtrusive monitoring of stress indicators: a preliminary evaluation at rest
Corain Livio	Abdominal visceral and subcutaneous adipose tissues in obese patients: mechanical behaviour
Corbo Massimo	The suitability of Gait Variable Scores for Myotonic Dystrophy types classification
–	Mapping the sEMG distribution over the forearm for grip myotonia characterization: methodological aspects
Cordella Francesca	Somatotopical feedback restoration in the lower limb through TENS: a feasibility study
–	A Dataset of DMPs for robot motion planning

–	A simulation study on safety and efficacy of tFUS
Corino Valentina	Radiomics-based prediction of head and neck cancer recurrence: a multi-centric MRI study
–	Poincaré Image-Based Atrial Fibrillation Detection for Photoplethysmography Signals
Corvi Andrea	Portable Normothermic Perfusion System for Laboratory test of Microwave Devices
Cosentino Carlo	Automated Detection and Counting of Acne Lesions for Evaluation of Acne Severity
–	An application of DMAIC methodology for reducing voluntary departures from an Emergency Department
Costa Piero	Strategies to speed up the standardized bone plates mechanical testing for regulatory purposes
–	Internal fixation of femour fractures: a new wireless electromechanical dynamization system
Costantini Irene	Geometric alterations of capillary network in hypertension: preliminary results
Costantino Maria Laura	Unassisted in-vitro simulation of superior cavo pulmonary shunt for evaluation of pathophysiological issue
–	A patient-specific approach for the IDH risk evaluation in the early stage of Haemodialysis
Crea Simona	A neuromorphic haptic feedback for lower limb sensory substitution
Creato Elisea	Model-based assessment of incretin effect from OGTT data in healthy subjects
Cristiano Alessia	A novel step counting algorithm using a head-mounted sensor
Cucchiara Katiuscia	Does a medical device nomenclature suitable for all purposes exist? Twenty years of Italian experience with the CND and its adoption in EUDAMED at European level
Cutrone Annarita	Ultrasonic neural stimulation of zebrafish larvae reveals region-specific calcium imaging activation patterns
D'Abbraccio Jessica	A neuromorphic haptic feedback for lower limb sensory substitution
D'Addio Gianni	Experimental Validation of an E-Textile T-Shirt for ECG Monitoring
–	Benchmarking between a Sensorized E-textile Sock for Remote Monitoring and a Stereophotogrammetric System

D'Agostino Federico	Does a medical device nomenclature suitable for all purposes exist? Twenty years of Italian experience with the CND and its adoption in EUDAMED at European level
Dalla Man Chiara	Modeling Intraperitoneal Insulin Kinetics in Patients with Type 1 Diabetes
Dalzoppo Daniele	Mechanical properties of oxidized polyvinyl alcohol hydrogel scaffolds for tissue engineering
D'Angiolella Sara Lucia	Five years of Lean Six Sigma in the healthcare: an overview of main tools and results
Daniele Carla	Image processing for rheological characterization of blood under flow
Dankelman Jenny	A Heuristic-Sliding-Window-based RRT Path Planning for Endovascular Catheterization
D'AnnaCarmen	Filtering techniques for whole body vibration artefact removal from low-SNR sEMG signals
–	Detecting low-to-moderate isometric muscle activity through a generalized CWT-based technique
Davalli Angelo	Falls and prostheses in patients with transfemoral amputation
D'Avenio Giuseppe	Stereo-PIV study of the flow across an axial pump for circulatory support
–	Image processing for rheological characterization of blood under flow
–	An Augmented-Reality App to communicate through the eye-gaze
–	Fontan Computational Hemodynamics: Impact of Inlet Velocity Profile Features with Implications on Clinically Relevant Parameters
De Acutis Aurora	Pectin-based biomaterial ink for Green Tissue Engineering applications
–	Advanced Firmware and Hardware for Multiscale and Multimaterial Bioprinting
–	Rapid and affordable prototyping of bioinspired microfluidic networks for Tissue Engineering
De Gaetano Francesco	Unassisted in-vitro simulation of superior cavo pulmonary shunt for evaluation of pathophysiological issue

De Maria Carmelo	Biofabrication and characterization of a biphasic construct to study osteochondral tissue in vitro
–	Impact of the shear stress on cultured human gut microbiota
–	Pectin-based biomaterial ink for Green Tissue Engineering applications
–	3D Printing open source non-critical spare parts of medical devices: the oxygen concentrator as a case study
–	Advanced Firmware and Hardware for Multiscale and Multimaterial Bioprinting
–	Rapid and affordable prototyping of bioinspired microfluidic networks for Tissue Engineering
De Martino Maria	A Stochastic Language Model of Italian Applied to Functional MRI during Narrative Listening
De Molfetta Vito	Tensile properties of porcine retina
De Momi Elena	A Heuristic-Sliding-Window-based RRT Path Planning for Endovascular Catheterization
–	Evaluation of robotic endoscopic neurosurgery through kinematic analysis of surgical gesture
–	Comparison of different CNNs for breast tumor classification from ultrasound images
De Ninno Adele	Boosting automated palynology via microfluidics and machine learning
–	Are your cells alive?
De Nisco Giuseppe	Eulerian-based wall shear stress topological skeleton analysis and near-wall transport in aortic flow
De Rosa Salvatore	Improving the assessment of vascular complexity in peripheral artery occlusive disease
De Stefano Paola	Single cell fluid dynamics: a VOF model of a red blood cell vs a leukocyte
De Summa Simona	Combining autoencoder and artificial neural network for classifying colorectal cancer stages
De Vito Giuseppe	Ultrasonic neural stimulation of zebrafish larvae reveals region-specific calcium imaging activation patterns

DeBenedictis Alessandro	Evaluation of robotic endoscopic neurosurgery through kinematic analysis of surgical gesture
DeCaro Raffaele	Mechanical properties of oxidized polyvinyl alcohol hydrogel scaffolds for tissue engineering
Dedola Francesca	Ultrasonic neural stimulation of zebrafish larvae reveals region-specific calcium imaging activation patterns
Del Favero Simone	Personalized Linear Data-Driven Algorithms for Real-Time Glucose Forecasting in Type 1 Diabetes
–	Sensitivity to carb-counting error in T1D management
–	Modelling the Meal Variability of Individuals with Type 1 Diabetes under Free-Living Conditions
–	Linear Regression Models to Improve the Estimation of Insulin Boluses in Type 1 Diabetes Therapy
–	Comparison of Parametric Linear Techniques for Glucose Prediction in Type-1 Diabetes
Del Felice Alessandra	MVAR estimation of source-level EEG connectivity in Parkinson's disease
Del Gaudio Costantino	Stereo-PIV study of the flow across an axial pump for circulatory support
Del Vecchio Antonio	Analysis of heart rate variability as evaluation method for the risk of sepsis in the low-weight preterm infant
Dellacasa Elena	Driving neuronal network connectivity with a modular alginate mask
–	Thermosensitive hydrogels for the encapsulation of primary and human derived neuronal cells
DellAcqua Roberto	Detection of the N2/N2pc event-related potential (ERP) components buried in the EEG using phase angle distribution across sweeps
DellaCroce Ugo	Estimation of the base of support during gait with an unobtrusive wearable system
–	Comparison of the performances of six magneto-inertial sensor fusion filters for orientation estimation in movement analysis
–	A novel multi-sensor system for gait assessment in real-world conditions: preliminary results

–	A markerless gait analysis protocol based on a single RGB-Depth camera: sensitivity to background changes
DellAgnello Filippo	A neuromorphic haptic feedback for lower limb sensory substitution
Delli Priscoli Mattia	Detecting the neural processes of lie generation with low-cost EEG: a preliminary study
Delogu Pasquale	No-reference evaluation of the reconstructed images in single-shot K-Edge Subtraction X-ray Computed Tomography
Demofonti Andrea	Somatotopical feedback restoration in the lower limb through TENS: a feasibility study
DeWitt John	From Mocap data to inertial data through a biomechanical model to classify countermeasure exercises performed on ISS
Di Febbo Davide	IoT ink pen for the ecological study of age-related changes in handwriting
Di Gesù Roberto	Biofabrication and characterization of a biphasic construct to study osteochondral tissue in vitro
Di Laura Danilo	Five years of Lean Six Sigma in the healthcare: an overview of main tools and results
Di Lisa Donatella	Driving neuronal network connectivity with a modular alginate mask
–	Ultrasound-triggered permeabilization of polyelectrolyte microcapsules
–	Thermosensitive hydrogels for the encapsulation of primary and human derived neuronal cells
Di Monte Jessica	Model-based assessment of incretin effect from OGTT data in healthy subjects
–	Electrocardiographic Alternans in Hemodialysis: A Case Report
Di Nunzio Giorgio Maria	Modelling the Meal Variability of Individuals with Type 1 Diabetes under Free-Living Conditions
Di Pietro Licia	3D Printing open source non-critical spare parts of medical devices: the oxygen concentrator as a case study
Di Salle Francesco	A Stochastic Language Model of Italian Applied to Functional MRI during Narrative Listening
Di Trapani Vittorio	No-reference evaluation of the reconstructed images in single-shot K-Edge Subtraction X-ray Computed Tomography

DiCamillo Barbara	Predicting the Onset of Chronic Obstructive Pulmonary Disease in the English Longitudinal Study of Ageing
Dichio Giancarlo	Strategies to speed up the standardized bone plates mechanical testing for regulatory purposes
–	Internal fixation of femour fractures: a new wireless electromechanical dynamization system
Dimitri Mattia	Portable Normothermic Perfusion System for Laboratory test of Microwave Devices
Dominissini Davide	The influence of turbulence modelling on thrombosis in cardiovascular devices
Donisi Leandro	Experimental Validation of an E-Textile T-Shirt for ECG Monitoring
–	Benchmarking between a Sensorized E-textile Sock for Remote Monitoring and a Stereophotogrammetric System
D'Orazio Antonella	Analysis of heart rate variability as evaluation method for the risk of sepsis in the low-weight preterm infant
D'Orazio Michele	Boosting automated palynology via microfluidics and machine learning
Doro Mattia	Detection of the N2/N2pc event-related potential (ERP) components buried in the EEG using phase angle distribution across sweeps
Dossi Laura	Human exposure to electromagnetic fields generated in smart vehicle communications
–	Assessment of Indoor Exposure Scenario by an 8x8 Planar Array Antenna at 3.7 GHz
Dubini Gabriele	Single cell fluid dynamics: a VOF model of a red blood cell vs a leukocyte
–	Electrospun ultrathin scaffold for Bruch's membrane regeneration in retinal tissue engineering
Dui Linda Greta	Play-Draw-Write: usability and acceptance of a tablet app for the early screening of handwriting difficulties in kindergartners
Ercoli Ilaria	A 3D CNN for preterm-infants' movement detection in NICUs from depth streams
Esposito Fabrizio	A Stochastic Language Model of Italian Applied to Functional MRI during Narrative Listening

–	Detecting the neural processes of lie generation with low-cost EEG: a preliminary study
Fabbri Destro Maddalena	Integration of 3D Action Observation Therapy and Rehabilitation Exercises in Mixed Reality: A Feasibility Study on Post-Stroke Patients
Facchinetti Andrea	Personalized Linear Data-Driven Algorithms for Real-Time Glucose Forecasting in Type 1 Diabetes
–	Sensitivity to carb-counting error in T1D management
–	Modelling the Meal Variability of Individuals with Type 1 Diabetes under Free-Living Conditions
–	Linear Regression Models to Improve the Estimation of Insulin Boluses in Type 1 Diabetes Therapy
–	Comparison of Parametric Linear Techniques for Glucose Prediction in Type-1 Diabetes
–	Predicting the Onset of Chronic Obstructive Pulmonary Disease in the English Longitudinal Study of Ageing
Faccioli Simone	Comparison of Parametric Linear Techniques for Glucose Prediction in Type-1 Diabetes
Fantozzi Silvia	A Dual-Branched Convolutional Neural Network for P300 detection and feature interpretation
Faraci Stefano	Filtering techniques for whole body vibration artefact removal from low-SNR sEMG signals
Fato Marco	A hydrogel channel-based system to model the blood flow dynamic stimuli
Favaro Alberto	A Heuristic-Sliding-Window-based RRT Path Planning for Endovascular Catheterization
Favaron Martina	Mechanical properties of oxidized polyvinyl alcohol hydrogel scaffolds for tissue engineering
Favilla Riccardo	Unobtrusive monitoring of stress indicators: a preliminary evaluation at rest
Fedi Arianna	A hydrogel channel-based system to model the blood flow dynamic stimuli
Ferrante Simona	Play-Draw-Write: usability and acceptance of a tablet app for the early screening of handwriting difficulties in kindergartners

–	IoT ink pen for the ecological study of age-related changes in handwriting
Ferrari Laura	Use of an optimized automatic procedure for measuring the hydraulic permeability of articular cartilage
Ferrarini Anna	Biomechanical implications of leg bending in popliteal stenting
Ferrigno Giancarlo	From Mocap data to inertial data through a biomechanical model to classify countermeasure exercises performed on ISS
–	Evaluation of robotic endoscopic neurosurgery through kinematic analysis of surgical gesture
Ferroni Marco	Use of an optimized automatic procedure for measuring the hydraulic permeability of articular cartilage
Figari Giulio	A markerless gait analysis protocol based on a single RGB-Depth camera: sensitivity to background changes
Figliuzzi Marina	Development of a compliance-matching biohybrid vascular graft through an integrated approach.
Finazzi Alberto	Balance control after tripping: Margin of Stability and Limb Support Quotient
Finotello Alice	Biomechanical implications of leg bending in popliteal stenting
Fiocchi Serena	Human exposure to electromagnetic fields generated in smart vehicle communications
–	Assessment of Indoor Exposure Scenario by an 8x8 Planar Array Antenna at 3.7 GHz
Fiore GianfrancoBeniamino	Development of a compliance-matching biohybrid vascular graft through an integrated approach.
–	Design and validation of a novel low cost-bicompartmental platform for cell and tissue cultures
–	Development of a novel bioreactor for the generation of controlled hydrodynamic stimuli on vascular planar tissue samples
–	Application of deer hearts for ex-vivo modelling of mitral valve pathology – preliminary results
Fiori Sonia	Development of a compliance-matching biohybrid vascular graft through an integrated approach.
Fiorini Laura	SensRing, a wearable ring-shaped device for measuring kinematics in reach-to-grasp tasks

Fiume Elisa	Versatile perfusion and electrical stimulation bioreactor for bone tissue engineering
Foglieni Chiara	Design and validation of a novel low cost-bicompartmental platform for cell and tissue cultures
–	Development of a novel bioreactor for the generation of controlled hydrodynamic stimuli on vascular planar tissue samples
Foletto Mirto	Abdominal visceral and subcutaneous adipose tissues in obese patients: mechanical behaviour
–	Computational tools for the evaluation of surgical parameters after LSG
Fontanella Chiara Giulia	Abdominal visceral and subcutaneous adipose tissues in obese patients: mechanical behaviour
–	Computational tools for the evaluation of surgical parameters after LSG
–	Computational investigation of the male lower urinary tract in health and disease
Formaggio Emanuela	MVAR estimation of source-level EEG connectivity in Parkinson's disease
Fortunato Daniele	Human Activity Recognition through Wearable Sensors: a Deep Learning Approach
Fortunato Gabriele Maria	Biofabrication and characterization of a biphasic construct to study osteochondral tissue in vitro
–	Pectin-based biomaterial ink for Green Tissue Engineering applications
–	Advanced Firmware and Hardware for Multiscale and Multimaterial Bioprinting
Fossati Barbara	The suitability of Gait Variable Scores for Myotonic Dystrophy types classification
–	Mapping the sEMG distribution over the forearm for grip myotonia characterization: methodological aspects
Foti Calogero	Filtering techniques for whole body vibration artefact removal from low-SNR sEMG signals
Fotso Fogang Joseph Vannel	Computational investigation of the male lower urinary tract in health and disease

Franceschini Marco	Neuroimaging biomarkers toward an optimized and personalized AOT
Franzini Marica	Preventive Healthcare through Air Pollution Exposure Modeling: the example of PULSE in Pavia
Franzo Michela	Harmonisation of medical devices classification systems: development of a generalised approach starting from hip prostheses. A first example of an international and standardised nomenclature to be integrated within the European Medical Device Nomenclature
–	Does a medical device nomenclature suitable for all purposes exist? Twenty years of Italian experience with the CND and its adoption in EUDAMED at European level
Frega Monica	Thermosensitive hydrogels for the encapsulation of primary and human derived neuronal cells
Frontoni Emanuele	A 3D CNN for preterm-infants' movement detection in NICUs from depth streams
Furlanis Giovanni	Correlation between hyper-acute EEG alterations and 7-Day NIHSS score in thrombolysis treated ischemic stroke patients
Gabetti Stefano	Versatile perfusion and electrical stimulation bioreactor for bone tissue engineering
Galli Alessia	A 3D CNN for preterm-infants' movement detection in NICUs from depth streams
Gallina Paolo	Balance control after tripping: Margin of Stability and Limb Support Quotient
Gallo Diego	Eulerian-based wall shear stress topological skeleton analysis and near-wall transport in aortic flow
–	Fontan Computational Hemodynamics: Impact of Inlet Velocity Profile Features with Implications on Clinically Relevant Parameters
Gallone Giuseppe	3D Printing open source non-critical spare parts of medical devices: the oxygen concentrator as a case study
Gallucci Silvia	Human exposure to electromagnetic fields generated in smart vehicle communications
–	Assessment of Indoor Exposure Scenario by an 8x8 Planar Array Antenna at 3.7 GHz

Galperti Guenda	SensRing, a wearable ring-shaped device for measuring kinematics in reach-to-grasp tasks
Garofalo Davide	Detecting the neural processes of lie generation with low-cost EEG: a preliminary study
Gavryusev Vladislav	Ultrasonic neural stimulation of zebrafish larvae reveals region-specific calcium imaging activation patterns
Gazzoni Marco	Mapping the sEMG distribution over the forearm for grip myotonia characterization: methodological aspects
Gelpi Guido	Application of deer hearts for ex-vivo modelling of mitral valve pathology – preliminary results
Gerosa Gino	Hybrid membranes for blood-contacting surfaces: preliminary characterization
–	Design of novel ventricular chambers: comparison of three different models
Ghelardi Emilia	Impact of the shear stress on cultured human gut microbiota
Ghislieri Marco	A Machine Learning Approach for Muscle Activity Detection
–	Human Activity Recognition through Wearable Sensors: a Deep Learning Approach
Giannotti Alice	A neural electrode for closed-loop vagus nerve recording and stimulation to control autonomic reflexes
Giardini Francesco	Geometric alterations of capillary network in hypertension: preliminary results
Giaretta Alberto	Human papillomavirus early promoter: Sensitivity analysis and biological behaviour
Giordano Noemi	Single-subject analysis of the variability of the latency of heart sounds over 25-day period
Giovinazzo Alessandro	Are your cells alive?
Giuliani Naomi	Use of an optimized automatic procedure for measuring the hydraulic permeability of articular cartilage
Gobbo Massimiliano	Integration of 3D Action Observation Therapy and Rehabilitation Exercises in Mixed Reality: A Feasibility Study on Post-Stroke Patients
Goffredo Michela	Neuroimaging biomarkers toward an optimized and personalized AOT

Gottardi Riccardo	Biofabrication and characterization of a biphasic construct to study osteochondral tissue in vitro
–	Pectin-based biomaterial ink for Green Tissue Engineering applications
Grandi Claudio	Mechanical properties of oxidized polyvinyl alcohol hydrogel scaffolds for tissue engineering
Greco Francesco	Development of a compliance-matching biohybrid vascular graft through an integrated approach.
Grigioni Mauro	Stereo-PIV study of the flow across an axial pump for circulatory support
–	Image processing for rheological characterization of blood under flow
–	An Augmented-Reality App to communicate through the eye-gaze
–	Fontan Computational Hemodynamics: Impact of Inlet Velocity Profile Features with Implications on Clinically Relevant Parameters
Griselli Massimo	Unassisted in-vitro simulation of superior cavo pulmonary shunt for evaluation of pathophysiological issue
Gros Auriane	SensRing, a wearable ring-shaped device for measuring kinematics in reach-to-grasp tasks
Gruppioni Emanuele	A new motor-driven smart prosthetic socket
Guaitolini Michelangelo	The eccentric phase of countermovement jump: comparing motion capture and inertial sensors
Gusai Elisa	DoMoMEA: a home neuromotor telerehabilitation system for stroke patients
Hevia Lorena Garcia	Gellan gum-based hydrogels as injectable materials for cartilage tissue engineering
Iacovacci Veronica	Preliminary Design and Validation of an Implantable Artificial Bladder
Iannelli Valentina	Somatotopical feedback restoration in the lower limb through TENS: a feasibility study
Ibrahimi Michele	A new motor-driven smart prosthetic socket
Ilari Ludovica	Model-based assessment of incretin effect from OGTT data in healthy subjects

Improta Giovanni	An application of DMAIC methodology for reducing voluntary departures from an Emergency Department
–	Five years of Lean Six Sigma in the healthcare: an overview of main tools and results
Indolfi Ciro	Improving the assessment of vascular complexity in peripheral artery occlusive disease
Infarinato Francesco	Neuroimaging biomarkers toward an optimized and personalized AOT
Iop Laura	Hybrid membranes for blood-contacting surfaces: preliminary characterization
Isla García Guadalupe	Poincaré Image-Based Atrial Fibrillation Detection for Photoplethysmography Signals
Jacchetti Emanuela	3D nichoid substrates affect mesenchymal stem cell morphology and euchromatin organization
Jaworek Michal	Application of deer hearts for ex-vivo modelling of mitral valve pathology – preliminary results
Judica Elda	The suitability of Gait Variable Scores for Myotonic Dystrophy types classification
–	Mapping the sEMG distribution over the forearm for grip myotonia characterization: methodological aspects
Khorasani Elnaz	Novel recurrence features for prefall and fall detection in backward and forward fall types
Knaflitz Marco	Single-subject analysis of the variability of the latency of heart sounds over 25-day period
–	A Machine Learning Approach for Muscle Activity Detection
–	Human Activity Recognition through Wearable Sensors: a Deep Learning Approach
–	Estimation of the base of support during gait with an unobtrusive wearable system
–	Comparison of the performances of six magneto-inertial sensor fusion filters for orientation estimation in movement analysis
Kudryavtseva Valeriya	Polymeric microchambers arrays for cargo protection
Lagazzo Alberto	Thermosensitive hydrogels for the encapsulation of primary and human derived neuronal cells

Laidig Daniel	Comparison of the performances of six magneto-inertial sensor fusion filters for orientation estimation in movement analysis
Lapomarda Anna	Biofabrication and characterization of a biphasic construct to study osteochondral tissue in vitro
–	Pectin-based biomaterial ink for Green Tissue Engineering applications
–	Advanced Firmware and Hardware for Multiscale and Multimaterial Bioprinting
Larizza Cristiana	Preventive Healthcare through Air Pollution Exposure Modeling: the example of PULSE in Pavia
–	Blood glucose prediction from Flash Glucose Monitoring and Fitbit data: a deep learning approach
Laudanna Alessandro	A Stochastic Language Model of Italian Applied to Functional MRI during Narrative Listening
Lauretti Clemente	A Dataset of DMPs for robot motion planning
Lazo Jorge	Comparison of different CNNs for breast tumor classification from ultrasound images
Lazzarini Stefano	Integration of 3D Action Observation Therapy and Rehabilitation Exercises in Mixed Reality: A Feasibility Study on Post-Stroke Patients
Lenzi Stefano Elio	Integration of 3D Action Observation Therapy and Rehabilitation Exercises in Mixed Reality: A Feasibility Study on Post-Stroke Patients
Leoni Chiara	Electrocardiographic Alternans in Hemodialysis: A Case Report
Li Zhen	A Heuristic-Sliding-Window-based RRT Path Planning for Endovascular Catheterization
Liberati Diego	Towards classification of ovarian cancer via micro-arrays data analysis
Licitra Lisa	Radiomics-based prediction of head and neck cancer recurrence: a multi-centric MRI study
Locati Laura	Radiomics-based prediction of head and neck cancer recurrence: a multi-centric MRI study
Lodi Rizzini Maurizio	Fontan Computational Hemodynamics: Impact of Inlet Velocity Profile Features with Implications on Clinically Relevant Parameters

Lofrumento Margherita	The suitability of Gait Variable Scores for Myotonic Dystrophy types classification
Long Quan	CT-based FFR: paving the way to future hearts
Lopomo Nicola Francesco	Integration of 3D Action Observation Therapy and Rehabilitation Exercises in Mixed Reality: A Feasibility Study on Post-Stroke Patients
Lovati AriannaB	Use of an optimized automatic procedure for measuring the hydraulic permeability of articular cartilage
Lucangeli Leandro	Evaluation of robotic endoscopic neurosurgery through kinematic analysis of surgical gesture
Lucherini Federico	Application of deer hearts for ex-vivo modelling of mitral valve pathology – preliminary results
Luchini Carlotta	An innovative High-Fidelity simulator of cervical changes during labour
Lugas Tancredi Andrea	Strategies to speed up the standardized bone plates mechanical testing for regulatory purposes
Lunardini Francesca	Play-Draw-Write: usability and acceptance of a tablet app for the early screening of handwriting difficulties in kindergartners
–	IoT ink pen for the ecological study of age-related changes in handwriting
Lupacchini Mattia	Development of a compliance-matching biohybrid vascular graft through an integrated approach.
Macchi Veronica	Mechanical properties of oxidized polyvinyl alcohol hydrogel scaffolds for tissue engineering
Magliaro Chiara	Impact of the shear stress on cultured human gut microbiota
Maglio Sabina	An Innovative High-Fidelity Neonatal Pneumothorax Simulator
Magosso Elisa	Assessing Transfer Entropy as a functional connectivity measure via a Neural Mass Model
–	A Dual-Branched Convolutional Neural Network for P300 detection and feature interpretation
Mainardi Luca	Radiomics-based prediction of head and neck cancer recurrence: a multi-centric MRI study
–	Poincaré Image-Based Atrial Fibrillation Detection for Photoplethysmography Signals

Malavolti Milad	IoT ink pen for the ecological study of age-related changes in handwriting
Mancioppi Gianmaria	SensRing, a wearable ring-shaped device for measuring kinematics in reach-to-grasp tasks
Mancuso Azzurra	A Stochastic Language Model of Italian Applied to Functional MRI during Narrative Listening
Mandolini Luigi	A 3D CNN for preterm-infants' movement detection in NICUs from depth streams
Manenti Cristina	Application of deer hearts for ex-vivo modelling of mitral valve pathology – preliminary results
Manera Valeria	SensRing, a wearable ring-shaped device for measuring kinematics in reach-to-grasp tasks
Manganotti Paolo	Correlation between hyper-acute EEG alterations and 7-Day NIHSS score in thrombolysis treated ischemic stroke patients
Mangiavini Laura	Use of an optimized automatic procedure for measuring the hydraulic permeability of articular cartilage
Mannini Andrea	The eccentric phase of countermovement jump: comparing motion capture and inertial sensors
Mansour Zahara	Electrocardiographic Alternans in Hemodialysis: A Case Report
Mantero Sara	Electrospun ultrathin scaffold for Bruch's membrane regeneration in retinal tissue engineering
–	Tensile properties of porcine retina
Marcantoni Ilaria	Electrocardiographic Alternans in Hemodialysis: A Case Report
Marcelli Emanuela	Development of a capnometer for extracorporeal life support devices: compensation of the temperature effect on the mid-IR LED
MarinoAttilio	Neural response to acoustic stimulation mediated by piezoelectric nanoparticles
Marinozzi Andrea	Influence of cartilage thickness on Human Femur Neck: a 3D Stress-Strain Analysis
Marinozzi Franco	Neuroimaging biomarkers toward an optimized and personalized AOT
–	Influence of cartilage thickness on Human Femur Neck: a 3D Stress-Strain Analysis

–	Harmonisation of medical devices classification systems: development of a generalised approach starting from hip prostheses. A first example of an international and standardised nomenclature to be integrated within the European Medical Device Nomenclature
Maroncelli Edoardo	Application of deer hearts for ex-vivo modelling of mitral valve pathology – preliminary results
Marras Carlo Efisio	Evaluation of robotic endoscopic neurosurgery through kinematic analysis of surgical gesture
Marrella Alessandra	A hydrogel channel-based system to model the blood flow dynamic stimuli
Martinelli Eugenio	Boosting automated palynology via microfluidics and machine learning
Martinoia Sergio	Thermosensitive hydrogels for the encapsulation of primary and human derived neuronal cells
Marturano Francesca	Detection of the N2/N2pc event-related potential (ERP) components buried in the EEG using phase angle distribution across sweeps
Marvulli Tommaso Maria	Combining autoencoder and artificial neural network for classifying colorectal cancer stages
Masciavé Krizia	DoMoMEA: a home neuromotor telerehabilitation system for stroke patients
Masiero Stefano	MVAR estimation of source-level EEG connectivity in Parkinson's disease
Massai Diana	Versatile perfusion and electrical stimulation bioreactor for bone tissue engineering
Massobrio Paolo	Neural response to acoustic stimulation mediated by piezoelectric nanoparticles
–	Driving neuronal network connectivity with a modular alginate mask
Matteucci Claudia	Are your cells alive?
Matteucci Matteo	Play-Draw-Write: usability and acceptance of a tablet app for the early screening of handwriting difficulties in kindergartners
Mattioli Belmonte Monica	Pectin-based biomaterial ink for Green Tissue Engineering applications

Mazza Davide	3D nichoid substrates affect mesenchymal stem cell morphology and euchromatin organization
MazzàClaudia	A novel multi-sensor system for gait assessment in real-world conditions: preliminary results
Mazzantini Lucrezia	Portable Normothermic Perfusion System for Laboratory test of Microwave Devices
Mazzei Elvira	Deep learning for improving in room imaging in radiotherapy: CBCT to synthetic CT conversion
Mazzi Valentina	Eulerian-based wall shear stress topological skeleton analysis and near-wall transport in aortic flow
Mazzocchi Tommaso	Preliminary Design and Validation of an Implantable Artificial Bladder
Mazzoleni Stefano	Clinical and technology-based assessment of an innovative integrated rehabilitation programme for persons affected by Parkinson's disease
Mazzonetto Ilaria	Resting State Networks spatio-spectral fingerprints: the Default Mode Network case study
Mazzoni Alberto	Ultrasonic neural stimulation of zebrafish larvae reveals region-specific calcium imaging activation patterns
−	Biomarkers of Impulse Control Disorder in firing patterns of parkinsonian subthalamic nucleus
−	A neuromorphic haptic feedback for lower limb sensory substitution
Meccariello Marco	Blood glucose prediction from Flash Glucose Monitoring and Fitbit data: a deep learning approach
MelinaAntonella	Automated Detection and Counting of Acne Lesions for Evaluation of Acne Severity
Mencarini Tatiana	Thrombogenicity of cardiovascular devices: mutual and relative effect of biomaterial and shear stress
Mencattini Arianna	Boosting automated palynology via microfluidics and machine learning
Menciassi Arianna	An Innovative High-Fidelity Neonatal Pneumothorax Simulator
−	An innovative High-Fidelity simulator of cervical changes during labour

–	Preliminary Design and Validation of an Implantable Artificial Bladder
–	A new motor-driven smart prosthetic socket
Meneghetti Giovanni	Design of novel ventricular chambers: comparison of three different models
Meneghetti Nicolò	Ultrasonic neural stimulation of zebrafish larvae reveals region-specific calcium imaging activation patterns
Merigliano Giorgia	Hybrid membranes for blood-contacting surfaces: preliminary characterization
Merola Monica	Deep learning for improving in room imaging in radiotherapy: CBCT to synthetic CT conversion
Mesin Luca	Quantification and reduction of crosstalk in surface electromyogram by inverse modelling
Mezzotero Caterina	Deep learning for improving in room imaging in radiotherapy: CBCT to synthetic CT conversion
Miccio Antonella	Falls and prostheses in patients with transfemoral amputation
Micera Silvestro	Ultrasonic neural stimulation of zebrafish larvae reveals region-specific calcium imaging activation patterns
–	A neural electrode for closed-loop vagus nerve recording and stimulation to control autonomic reflexes
–	Balance control after tripping: Margin of Stability and Limb Support Quotient
Micheli Federico	Biomarkers of Impulse Control Disorder in firing patterns of parkinsonian subthalamic nucleus
Migliorelli Lucia	A 3D CNN for preterm-infants' movement detection in NICUs from depth streams
Miladinovic Aleksandar	Smoking effect on the circadian rhythm of blood pressure in hypertensive subjects
–	Performance of Dual-Augmented Lagrangian Method and Common Spatial Patterns applied in classification of Motor-Imagery BCI
–	Correlation between hyper-acute EEG alterations and 7-Day NIHSS score in thrombolysis treated ischemic stroke patients
Miola Marta	Bioactive silica-based glass nanoparticles containing boron and copper

Mion Emanuele	Clinical and technology-based assessment of an innovative integrated rehabilitation programme for persons affected by Parkinson's disease
Mittal Tarun	CT-based FFR: paving the way to future hearts
Moccia Sara	A 3D CNN for preterm-infants' movement detection in NICUs from depth streams
–	Comparison of different CNNs for breast tumor classification from ultrasound images
Moiia Roka Yana	Thrombogenicity of cardiovascular devices: mutual and relative effect of biomaterial and shear stress
Molinari Filippo	A markerless gait analysis protocol based on a single RGB-Depth camera: sensitivity to background changes
Monaco Vito	Balance control after tripping: Margin of Stability and Limb Support Quotient
Montemurro Francesca	Biofabrication and characterization of a biphasic construct to study osteochondral tissue in vitro
–	Impact of the shear stress on cultured human gut microbiota
–	Pectin-based biomaterial ink for Green Tissue Engineering applications
–	Rapid and affordable prototyping of bioinspired microfluidic networks for Tissue Engineering
Monticelli Orietta	Surface coated chitosan microbeads for the sustained release of drugs
Monticone Marco	DoMoMEA: a home neuromotor telerehabilitation system for stroke patients
Morbiducci Umberto	Eulerian-based wall shear stress topological skeleton analysis and near-wall transport in aortic flow
–	Stereo-PIV study of the flow across an axial pump for circulatory support
–	Fontan Computational Hemodynamics: Impact of Inlet Velocity Profile Features with Implications on Clinically Relevant Parameters
–	Transcatheter Aortic Valve with Embolic Filter: Experiments and Simulations

Moret Filippo	Modeling Intraperitoneal Insulin Kinetics in Patients with Type 1 Diabetes
Morettini Micaela	Model-based assessment of incretin effect from OGTT data in healthy subjects
–	Electrocardiographic Alternans in Hemodialysis: A Case Report
–	Novel recurrence features for prefall and fall detection in backward and forward fall types
Moscato Serena	Falls and prostheses in patients with transfemoral amputation
Mosna Paolo	Integration of 3D Action Observation Therapy and Rehabilitation Exercises in Mixed Reality: A Feasibility Study on Post-Stroke Patients
Muzzi Lorenzo	Thermosensitive hydrogels for the encapsulation of primary and human derived neuronal cells
Naccarato Marcello	Correlation between hyper-acute EEG alterations and 7-Day NIHSS score in thrombolysis treated ischemic stroke patients
Nasim Amnah	Novel recurrence features for prefall and fall detection in backward and forward fall types
Natali Arturo	Computational investigation of the male lower urinary tract in health and disease
Nchekwube David Chukwudi	Novel recurrence features for prefall and fall detection in backward and forward fall types
Negrini Stefano	Integration of 3D Action Observation Therapy and Rehabilitation Exercises in Mixed Reality: A Feasibility Study on Post-Stroke Patients
Noaro Giulia	Linear Regression Models to Improve the Estimation of Insulin Boluses in Type 1 Diabetes Therapy
Nonnis Matteo	Deep learning for improving in room imaging in radiotherapy: CBCT to synthetic CT conversion
Nota Francesco David	Detecting the neural processes of lie generation with low-cost EEG: a preliminary study
Oddo Calogero Maria	A neuromorphic haptic feedback for lower limb sensory substitution
Olianti Camilla	Geometric alterations of capillary network in hypertension: preliminary results

Osellame Roberto	3D nichoid substrates affect mesenchymal stem cell morphology and euchromatin organization
Ottaviani Marco	Neuroimaging biomarkers toward an optimized and personalized AOT
Ovur Ertug Salih	Evaluation of robotic endoscopic neurosurgery through kinematic analysis of surgical gesture
Pacetta Guglielmo	Rapid and affordable prototyping of bioinspired microfluidic networks for Tissue Engineering
Pagano Gaetano	Experimental Validation of an E-Textile T-Shirt for ECG Monitoring
Pala Daniele	Preventive Healthcare through Air Pollution Exposure Modeling: the example of PULSE in Pavia
Palmosi Tiziana	Hybrid membranes for blood-contacting surfaces: preliminary characterization
Palombo Domenico	Biomechanical implications of leg bending in popliteal stenting
Palumbo Pierpaolo	Falls and prostheses in patients with transfemoral amputation
Panarese MacrìAdele	Balance control after tripping: Margin of Stability and Limb Support Quotient
Pane Bianca	Biomechanical implications of leg bending in popliteal stenting
Pane Stefano	Preliminary Design and Validation of an Implantable Artificial Bladder
Pani Danilo	Stretchable polymer-based biopotential electrodes for unobtrusive EMG detection
–	DoMoMEA: a home neuromotor telerehabilitation system for stroke patients
Paolini Gabriele	A markerless gait analysis protocol based on a single RGB-Depth camera: sensitivity to background changes
Parazzini Marta	Human exposure to electromagnetic fields generated in smart vehicle communications
–	Assessment of Indoor Exposure Scenario by an 8x8 Planar Array Antenna at 3.7 GHz
Pascazio Lorenzo	Smoking effect on the circadian rhythm of blood pressure in hypertensive subjects
Pasero Eros GianAlessandro	Internal fixation of femour fractures: a new wireless electromechanical dynamization system

Passoni Giuseppe	The influence of turbulence modelling on thrombosis in cardiovascular devices
Pastorino Laura	Surface coated chitosan microbeads for the sustained release of drugs
–	Polymeric microchambers arrays for cargo protection
–	Driving neuronal network connectivity with a modular alginate mask
–	Ultrasound-triggered permeabilization of polyelectrolyte microcapsules
–	Thermosensitive hydrogels for the encapsulation of primary and human derived neuronal cells
Paternò Linda	A new motor-driven smart prosthetic socket
Pavan Piero	Mechanical properties of oxidized polyvinyl alcohol hydrogel scaffolds for tissue engineering
Pavanelli Elisa	A Machine Learning Approach for Muscle Activity Detection
Pavone Francesco Saverio	Ultrasonic neural stimulation of zebrafish larvae reveals region-specific calcium imaging activation patterns
Pecchioli Guido	Biomarkers of Impulse Control Disorder in firing patterns of parkinsonian subthalamic nucleus
Pederzani Elia	Development of a compliance-matching biohybrid vascular graft through an integrated approach.
–	Development of a novel bioreactor for the generation of controlled hydrodynamic stimuli on vascular planar tissue samples
Pedrizzetti Gianni	Cardiac fluid dynamics of patient-specific geometries in Pre and Post Mitral Valve Repair by Direct Numerical Simulation
Pedrocchi Alessandra	From Mocap data to inertial data through a biomechanical model to classify countermeasure exercises performed on ISS
–	IoT ink pen for the ecological study of age-related changes in handwriting
Peretti Giuseppe M	Use of an optimized automatic procedure for measuring the hydraulic permeability of articular cartilage
Petrillo Flavia	Analysis of heart rate variability as evaluation method for the risk of sepsis in the low-weight preterm infant

Pezzotta Marco	Development of a compliance-matching biohybrid vascular graft through an integrated approach.
Piatti Elisa	Bioactive silica-based glass nanoparticles containing boron and copper
Pibiri Andrea	DoMoMEA: a home neuromotor telerehabilitation system for stroke patients
Pica Andrada	Influence of cartilage thickness on Human Femur Neck: a 3D Stress-Strain Analysis
Piergiovanni Monica	Single cell fluid dynamics: a VOF model of a red blood cell vs a leukocyte
Pisano Marietta	Neural response to acoustic stimulation mediated by piezoelectric nanoparticles
–	Ultrasound-triggered permeabilization of polyelectrolyte microcapsules
Ponsiglione Maria Alfonso	Five years of Lean Six Sigma in the healthcare: an overview of main tools and results
Ponzini Raffaele	Eulerian-based wall shear stress topological skeleton analysis and near-wall transport in aortic flow
Porzionato Andrea	Mechanical properties of oxidized polyvinyl alcohol hydrogel scaffolds for tissue engineering
Pournajaf Sanaz	Neuroimaging biomarkers toward an optimized and personalized AOT
Prasanna Sahana	A neuromorphic haptic feedback for lower limb sensory substitution
Prendin Francesco	Personalized Linear Data-Driven Algorithms for Real-Time Glucose Forecasting in Type 1 Diabetes
Putame Giovanni	A Multibody Model for Ligament Balancing Assessment in Total Knee Arthroplasty
–	Versatile perfusion and electrical stimulation bioreactor for bone tissue engineering
–	Internal fixation of femour fractures: a new wireless electromechanical dynamization system
Quaglia Claudio	A new motor-driven smart prosthetic socket

Quarenghi Annamaria	Clinical and technology-based assessment of an innovative integrated rehabilitation programme for persons affected by Parkinson's disease
Raffo Luigi	DoMoMEA: a home neuromotor telerehabilitation system for stroke patients
Ragazzini Sara	Tensile properties of porcine retina
Raimondi Manuela	3D nichoid substrates affect mesenchymal stem cell morphology and euchromatin organization
Raiteri Roberto	Neural response to acoustic stimulation mediated by piezoelectric nanoparticles
–	Ultrasound-triggered permeabilization of polyelectrolyte microcapsules
Ramat Silvia	Biomarkers of Impulse Control Disorder in firing patterns of parkinsonian subthalamic nucleus
Ranaldi Simone	Filtering techniques for whole body vibration artefact removal from low-SNR sEMG signals
Randi Pericle	Falls and prostheses in patients with transfemoral amputation
Raso Roberta	Deep learning for improving in room imaging in radiotherapy: CBCT to synthetic CT conversion
Ravazzani Paolo	Human exposure to electromagnetic fields generated in smart vehicle communications
–	Assessment of Indoor Exposure Scenario by an 8x8 Planar Array Antenna at 3.7 GHz
Ravizza Martina	From Mocap data to inertial data through a biomechanical model to classify countermeasure exercises performed on ISS
Reale Riccardo	Boosting automated palynology via microfluidics and machine learning
–	Are your cells alive?
Redaelli Alberto	Development of a compliance-matching biohybrid vascular graft through an integrated approach.
–	Thrombogenicity of cardiovascular devices: mutual and relative effect of biomaterial and shear stress
–	The influence of turbulence modelling on thrombosis in cardiovascular devices

Remuzzi Andrea	Development of a compliance-matching biohybrid vascular graft through an integrated approach.
Riacci Laura	Gellan gum-based hydrogels as injectable materials for cartilage tissue engineering
Riboldi Stefania	Development of a compliance-matching biohybrid vascular graft through an integrated approach.
Ricci Giulia	Assessing Transfer Entropy as a functional connectivity measure via a Neural Mass Model
Ricciardi Carlo	An application of DMAIC methodology for reducing voluntary departures from an Emergency Department
–	Benchmarking between a Sensorized E-textile Sock for Remote Monitoring and a Stereophotogrammetric System
Ricotti Leonardo	Preliminary Design and Validation of an Implantable Artificial Bladder
–	A new motor-driven smart prosthetic socket
–	Gellan gum-based hydrogels as injectable materials for cartilage tissue engineering
Rivolta Massimo Walter	Correlation analysis of PRSA-based parameters during labor: a simulation study
Rizzo Giovanna	Eulerian-based wall shear stress topological skeleton analysis and near-wall transport in aortic flow
Rizzolatti Giacomo	Integration of 3D Action Observation Therapy and Rehabilitation Exercises in Mixed Reality: A Feasibility Study on Post-Stroke Patients
Romagnoni Claudia	Application of deer hearts for ex-vivo modelling of mitral valve pathology – preliminary results
Romanato Marco	Muscle forces and activations in Parkinson's disease: a model-based approach
Romano Maria	An application of DMAIC methodology for reducing voluntary departures from an Emergency Department
Romano Paola	Neuroimaging biomarkers toward an optimized and personalized AOT
Romanò Rebecca	Radiomics-based prediction of head and neck cancer recurrence: a multi-centric MRI study

Rosa Rubina	Application of deer hearts for ex-vivo modelling of mitral valve pathology – preliminary results
Rosati Samanta	A Machine Learning Approach for Muscle Activity Detection
–	Human Activity Recognition through Wearable Sensors: a Deep Learning Approach
Rossanigo Rachele	Estimation of the base of support during gait with an unobtrusive wearable system
–	A novel multi-sensor system for gait assessment in real-world conditions: preliminary results
Rossi Andrea	Filtering techniques for whole body vibration artefact removal from low-SNR sEMG signals
Rossi Mirko	An Augmented-Reality App to communicate through the eye-gaze
Roversi Chiara	Sensitivity to carb-counting error in T1D management
Rovini Erika	SensRing, a wearable ring-shaped device for measuring kinematics in reach-to-grasp tasks
Rubega Maria	MVAR estimation of source-level EEG connectivity in Parkinson's disease
Ruggeri Alfredo	Automatic estimation of nerve tortuosity in corneal images
Rupil Jessica	MVAR estimation of source-level EEG connectivity in Parkinson's disease
RussoAndrea Gerardo	A Stochastic Language Model of Italian Applied to Functional MRI during Narrative Listening
Sabatini Angelo Maria	Comparison of the performances of six magneto-inertial sensor fusion filters for orientation estimation in movement analysis
Sacchi Lucia	Blood glucose prediction from Flash Glucose Monitoring and Fitbit data: a deep learning approach
Saccomano Giulia	No-reference evaluation of the reconstructed images in single-shot K-Edge Subtraction X-ray Computed Tomography
Sacconi Leonardo	Geometric alterations of capillary network in hypertension: preliminary results
Salis Francesca	A novel multi-sensor system for gait assessment in real-world conditions: preliminary results
Salsano Giancarlo	Biomechanical implications of leg bending in popliteal stenting

Salvagnini Pietro	Automated Detection and Counting of Acne Lesions for Evaluation of Acne Severity
Salvi Gian Pietro	Clinical and technology-based assessment of an innovative integrated rehabilitation programme for persons affected by Parkinson's disease
Salvi Massimo	A markerless gait analysis protocol based on a single RGB-Depth camera: sensitivity to background changes
Sampaolo Letizia	Harmonisation of medical devices classification systems: development of a generalised approach starting from hip prostheses. A first example of an international and standardised nomenclature to be integrated within the European Medical Device Nomenclature
–	Does a medical device nomenclature suitable for all purposes exist? Twenty years of Italian experience with the CND and its adoption in EUDAMED at European level
Sancataldo Giuseppe	Ultrasonic neural stimulation of zebrafish larvae reveals region-specific calcium imaging activation patterns
Sangalli Fabio	Development of a compliance-matching biohybrid vascular graft through an integrated approach.
Sanginario Alessandro	Versatile perfusion and electrical stimulation bioreactor for bone tissue engineering
Sanna Alberto	A novel step counting algorithm using a head-mounted sensor
Sartori Massimo	Muscle forces and activations in Parkinson's disease: a model-based approach
Sassi Roberto	Correlation analysis of PRSA-based parameters during labor: a simulation study
Sawacha Zimi	Muscle forces and activations in Parkinson's disease: a model-based approach
Sbrollini Agnese	Electrocardiographic Alternans in Hemodialysis: A Case Report
Scaglione Silvia	A hydrogel channel-based system to model the blood flow dynamic stimuli
Scala Arianna	Five years of Lean Six Sigma in the healthcare: an overview of main tools and results
Scaramuzzino Salvatore	Improving the assessment of vascular complexity in peripheral artery occlusive disease

Scarpa Fabio	Automatic estimation of nerve tortuosity in corneal images
Scarpelli Alessia	Somatotopical feedback restoration in the lower limb through TENS: a feasibility study
–	A simulation study on safety and efficacy of tFUS
Schiavon Michele	Modeling Intraperitoneal Insulin Kinetics in Patients with Type 1 Diabetes
Schmid Maurizio	Filtering techniques for whole body vibration artefact removal from low-SNR sEMG signals
–	Detecting low-to-moderate isometric muscle activity through a generalized CWT-based technique
Sciuto Salvatore Andrea	Filtering techniques for whole body vibration artefact removal from low-SNR sEMG signals
Scorza Andrea	Filtering techniques for whole body vibration artefact removal from low-SNR sEMG signals
Scott Kirsty	A novel multi-sensor system for gait assessment in real-world conditions: preliminary results
Seel Thomas	Comparison of the performances of six magneto-inertial sensor fusion filters for orientation estimation in movement analysis
Segato Alice	A Heuristic-Sliding-Window-based RRT Path Planning for Endovascular Catheterization
Serino Gianpaolo	Strategies to speed up the standardized bone plates mechanical testing for regulatory purposes
Severi Stefano	Development of a capnometer for extracorporeal life support devices: compensation of the temperature effect on the mid-IR LED
Shesterikov Evgeniy	Polymeric microchambers arrays for cargo protection
Siena Enrico Karim	Evaluation of robotic endoscopic neurosurgery through kinematic analysis of surgical gesture
Sigismondi Eleonora	Clinical and technology-based assessment of an innovative integrated rehabilitation programme for persons affected by Parkinson's disease
Silveri Giulia	Smoking effect on the circadian rhythm of blood pressure in hypertensive subjects
–	Performance of Dual-Augmented Lagrangian Method and Common Spatial Patterns applied in classification of Motor-Imagery BCI

–	Correlation between hyper-acute EEG alterations and 7-Day NIHSS score in thrombolysis treated ischemic stroke patients
Silvestri Erica	Connectivity in Parkinson's disease patients with cognitive impairment: a simultaneous PET/MRI study
Simonini Marcello	Clinical and technology-based assessment of an innovative integrated rehabilitation programme for persons affected by Parkinson's disease
Slepian Marvin	Thrombogenicity of cardiovascular devices: mutual and relative effect of biomaterial and shear stress
Soncini Monica	Development of a compliance-matching biohybrid vascular graft through an integrated approach.
–	Design and validation of a novel low cost-bicompartmental platform for cell and tissue cultures
–	Development of a novel bioreactor for the generation of controlled hydrodynamic stimuli on vascular planar tissue samples
Spadea Maria Francesca	Deep learning for improving in room imaging in radiotherapy: CBCT to synthetic CT conversion
–	Improving the assessment of vascular complexity in peripheral artery occlusive disease
Spanu Andrea	Stretchable polymer-based biopotential electrodes for unobtrusive EMG detection
Spanu Salvatore	DoMoMEA: a home neuromotor telerehabilitation system for stroke patients
Sparacino Giovanni	Detection of the N2/N2pc event-related potential (ERP) components buried in the EEG using phase angle distribution across sweeps
–	Personalized Linear Data-Driven Algorithms for Real-Time Glucose Forecasting in Type 1 Diabetes
–	Sensitivity to carb-counting error in T1D management
–	Modelling the Meal Variability of Individuals with Type 1 Diabetes under Free-Living Conditions
–	Linear Regression Models to Improve the Estimation of Insulin Boluses in Type 1 Diabetes Therapy
–	Comparison of Parametric Linear Techniques for Glucose Prediction in Type-1 Diabetes

Spinella Giovanni	Biomechanical implications of leg bending in popliteal stenting
Staderini Fabio	Portable Normothermic Perfusion System for Laboratory test of Microwave Devices
Stampalija Tamara	Correlation analysis of PRSA-based parameters during labor: a simulation study
Stefano Mattia	A simulation study on safety and efficacy of tFUS
Steinman DavidA	Eulerian-based wall shear stress topological skeleton analysis and near-wall transport in aortic flow
Stella Elisabetta	Does a medical device nomenclature suitable for all purposes exist? Twenty years of Italian experience with the CND and its adoption in EUDAMED at European level
Stocco Elena	Mechanical properties of oxidized polyvinyl alcohol hydrogel scaffolds for tissue engineering
Stragapede Lara	Correlation between hyper-acute EEG alterations and 7-Day NIHSS score in thrombolysis treated ischemic stroke patients
Strauss Ivo	A neural electrode for closed-loop vagus nerve recording and stimulation to control autonomic reflexes
Sukhorukov Gleb	Polymeric microchambers arrays for cargo protection
Suria Roldan Aldo Josè	Development of a novel bioreactor for the generation of controlled hydrodynamic stimuli on vascular planar tissue samples
Tagliaferri Roberto	Detecting the neural processes of lie generation with low-cost EEG: a preliminary study
Tamantini Christian	A Dataset of DMPs for robot motion planning
Tarricone Fabio	Analysis of heart rate variability as evaluation method for the risk of sepsis in the low-weight preterm infant
Tasso Paola	Fontan Computational Hemodynamics: Impact of Inlet Velocity Profile Features with Implications on Clinically Relevant Parameters
Tedesco Mariateresa	Neural response to acoustic stimulation mediated by piezoelectric nanoparticles
Terenzi Federica	Biomarkers of Impulse Control Disorder in firing patterns of parkinsonian subthalamic nucleus
Termine Cristiano	Play-Draw-Write: usability and acceptance of a tablet app for the early screening of handwriting difficulties in kindergartners

Terzini Mara	Strategies to speed up the standardized bone plates mechanical testing for regulatory purposes
–	DXA-based Finite Element models to improve hip fracture risk prediction: a comparison with CT-based models
–	A Multibody Model for Ligament Balancing Assessment in Total Knee Arthroplasty
–	Internal fixation of femour fractures: a new wireless electromechanical dynamization system
Tironi Matteo	Development of a compliance-matching biohybrid vascular graft through an integrated approach.
Todesco Martina	Hybrid membranes for blood-contacting surfaces: preliminary characterization
–	Design of novel ventricular chambers: comparison of three different models
Todros Silvia	Mechanical properties of oxidized polyvinyl alcohol hydrogel scaffolds for tissue engineering
Toffolo Maria Gianna	MVAR estimation of source-level EEG connectivity in Parkinson's disease
Tognarelli Selene	An Innovative High-Fidelity Neonatal Pneumothorax Simulator
–	An innovative High-Fidelity simulator of cervical changes during labour
Tognola Gabriella	Human exposure to electromagnetic fields generated in smart vehicle communications
–	Assessment of Indoor Exposure Scenario by an 8x8 Planar Array Antenna at 3.7 GHz
Toniolo Ilaria	Computational tools for the evaluation of surgical parameters after LSG
–	Computational investigation of the male lower urinary tract in health and disease
Torre Marina	Harmonisation of medical devices classification systems: development of a generalised approach starting from hip prostheses. A first example of an international and standardised nomenclature to be integrated within the European Medical Device Nomenclature

–	Does a medical device nomenclature suitable for all purposes exist? Twenty years of Italian experience with the CND and its adoption in EUDAMED at European level
Travaglini Alessandro	Boosting automated palynology via microfluidics and machine learning
Tricomi Enrica	Mapping the sEMG distribution over the forearm for grip myotonia characterization: methodological aspects
Trojaniello Diana	A novel step counting algorithm using a head-mounted sensor
Tropea Peppino	The suitability of Gait Variable Scores for Myotonic Dystrophy types classification
–	Mapping the sEMG distribution over the forearm for grip myotonia characterization: methodological aspects
Truppa Luigi	The eccentric phase of countermovement jump: comparing motion capture and inertial sensors
Tuan Rocky S	Biofabrication and characterization of a biphasic construct to study osteochondral tissue in vitro
Tucker John keith	Harmonisation of medical devices classification systems: development of a generalised approach starting from hip prostheses. A first example of an international and standardised nomenclature to be integrated within the European Medical Device Nomenclature
Turrini Lapo	Ultrasonic neural stimulation of zebrafish larvae reveals region-specific calcium imaging activation patterns
Tverdokhlebov Sergei	Polymeric microchambers arrays for cargo protection
Udalov Andrey	Polymeric microchambers arrays for cargo protection
Ursino Mauro	Assessing Transfer Entropy as a functional connectivity measure via a Neural Mass Model
Vallesi Antonino	Resting State Networks spatio-spectral fingerprints: the Default Mode Network case study
Van der Maaden Nina E	Novel recurrence features for prefall and fall detection in backward and forward fall types
Vannozzi Lorenzo	Gellan gum-based hydrogels as injectable materials for cartilage tissue engineering
Vanzi Francesco	Ultrasonic neural stimulation of zebrafish larvae reveals region-specific calcium imaging activation patterns

Varani Gabriele	A hydrogel channel-based system to model the blood flow dynamic stimuli
Varrecchia Tiwana	Detecting low-to-moderate isometric muscle activity through a generalized CWT-based technique
Vecchione Alessandra	Impact of the shear stress on cultured human gut microbiota
Vercellino Federica	Thrombogenicity of cardiovascular devices: mutual and relative effect of biomaterial and shear stress
Vernè Enrica	Bioactive silica-based glass nanoparticles containing boron and copper
–	Versatile perfusion and electrical stimulation bioreactor for bone tissue engineering
Vettoretti Martina	Sensitivity to carb-counting error in T1D management
–	Modelling the Meal Variability of Individuals with Type 1 Diabetes under Free-Living Conditions
–	Predicting the Onset of Chronic Obstructive Pulmonary Disease in the English Longitudinal Study of Ageing
Vismara Riccardo	Application of deer hearts for ex-vivo modelling of mitral valve pathology – preliminary results
Vissani Matteo	Biomarkers of Impulse Control Disorder in firing patterns of parkinsonian subthalamic nucleus
Vitale Chiara	A hydrogel channel-based system to model the blood flow dynamic stimuli
Vitali Enrica	Driving neuronal network connectivity with a modular alginate mask
Vitiello Nicola	A neuromorphic haptic feedback for lower limb sensory substitution
Vito Domenico	Preventive Healthcare through Air Pollution Exposure Modeling: the example of PULSE in Pavia
Volpe Daniele	Muscle forces and activations in Parkinson's disease: a model-based approach
Votta Emiliano	Development of a compliance-matching biohybrid vascular graft through an integrated approach.
Vozzi Giovanni	Biofabrication and characterization of a biphasic construct to study osteochondral tissue in vitro
–	Impact of the shear stress on cultured human gut microbiota

–	Pectin-based biomaterial ink for Green Tissue Engineering applications
–	Advanced Firmware and Hardware for Multiscale and Multimaterial Bioprinting
–	Rapid and affordable prototyping of bioinspired microfluidic networks for Tissue Engineering
Wynn Amy	Evaluation of robotic endoscopic neurosurgery through kinematic analysis of surgical gesture
Young Elaine	Harmonisation of medical devices classification systems: development of a generalised approach starting from hip prostheses. A first example of an international and standardised nomenclature to be integrated within the European Medical Device Nomenclature
Zaffino Paolo	Deep learning for improving in room imaging in radiotherapy: CBCT to synthetic CT conversion
–	Improving the assessment of vascular complexity in peripheral artery occlusive disease
Zandrini Tommaso	3D nichoid substrates affect mesenchymal stem cell morphology and euchromatin organization
Zedda Andrea	DoMoMEA: a home neuromotor telerehabilitation system for stroke patients
Zeghari Radia	SensRing, a wearable ring-shaped device for measuring kinematics in reach-to-grasp tasks
Zhang Jiaxin	Polymeric microchambers arrays for cargo protection
Zoleo Fabrizio	Detecting the neural processes of lie generation with low-cost EEG: a preliminary study
Zollo Loredana	Somatotopical feedback restoration in the lower limb through TENS: a feasibility study
–	A Dataset of DMPs for robot motion planning
–	A simulation study on safety and efficacy of tFUS
Zrinscak Debora	Design and development of an origami-based pump for soft robotics wearable applications
Zuccalà Veronica Chiara	Unobtrusive monitoring of stress indicators: a preliminary evaluation at rest

Zurlo Luigi

Preventive Healthcare through Air Pollution Exposure Modeling: the example of PULSE in Pavia

Stochastic Language Model of Italian Applied to Functional MRI during Narrative Listening

A.G. Russo[1], M. De Martino[1], A. Mancuso[1], F. Di Salle[1], A. Laudanna[1], F. Esposito[1]
[1] University of Salerno, Italy

Abstract—**Stochastic language models are increasingly used to encode linguistic processes in neural data, to objectively quantify the cognitive engagement or effort during narrative listening.**

A stochastic language model based on the surprisal function was built from a publicly available Italian corpus and applied to the off-line analysis of functional MRI data in an Italian narrative listening experiment.

Preliminary results show that the spatial and temporal patterns obtained via this kind of data modelling are in line with previous results from two different languages motivating the use of the surprisal model in the assessment of Italian language comprehension from neural data over a larger cohort of subjects.

Keywords—**fMRI, Natural Language Processing, Naturalistic stimulus, Surprisal.**

I. Introduction

During normal functioning, the brain acts as a prediction machine as it is constantly engaged in inferring the next input based on the current data [1]. For instance, it has been shown that the neural processes underlying the language comprehension are synchronized with the expectation and prediction of linguistic units (such as words, letters and phonemes) when these are embedded in naturalistic streams (e.g. speech) [2]. A viable approach to the encoding of prediction processes in speech comprehension is the use of a stochastic language model that provides a possibly language-independent mathematical formalization of the problem for creating informative neural predictors to map cognitive processes in human brain [2]. For example, an information-theoretic measure known as surprisal [3] has been proposed to quantify the relative unexpectedness of the actual word given the current context (i.e. the previous words). It has been shown that the surprisal is linked to the cognitive effort associated with the linguistic processing difficulty [4]. Therefore, the more unexpected is the incoming word (i.e. high surprisal) the higher is the amount of neural resource needed to process it.

In previous functional magnetic resonance imaging (fMRI) studies, different surprisal models have been correlated with the neural signals during active reading and passive listening tasks [5]–[7]. For example, Willems et al. (2016) have used a word surprisal model of the Dutch language in an fMRI listening experiment and reported significant activations within a broad network including the temporal poles bilaterally [6]. In 2017, Willems and Frank applied the surprisal and the semantic distance to both fMRI and electroencephalography (EEG) data to encode the neural responses during passive listening of spoken narratives in Dutch and English [8].

The aim of this work is to present pilot experiments to validate the use of surprisal models in explaining neural activation patterns, as measured by single-subject fMRI, in healthy participants listening to Italian spoken narratives. Italian language differs from the languages used in previous studies [5], [6], [8] in several aspects such as the inflectional system, the word order within the sentence, the higher orthographic transparency and the lower syllabic complexity [11]. Therefore, the implementation of a dedicated surprisal model, and its application to the analysis of fMRI time series during natural language processing, may improve our knowledge about the neural network supporting the linguistic prediction by either confirming previous findings (from different languages) or, eventually, revealing the involvement of additional brain areas specifically recruited to handle the peculiarities of the Italian language.

For this purpose, fMRI data were acquired on a 3 Tesla scanner while Italian healthy volunteers listened to an Italian audiobook (12 minutes) in both the original (task condition) and the reversed (control condition) version. The word-by-word surprisal, for both the original and the reversed story, was estimated using a second-order Markov model built on a large Italian written corpus [12].

In the light of previous findings [6], as far as the surprisal model is a good proxy of the prediction processes underlying the language comprehension, also for the Italian language, neural patterns activating key areas for the speech comprehension processes are expected, such as the secondary auditory areas within the temporal lobe, the ventral inferior-temporal cortex and the inferior frontal areas.

II. Materials and methods

A. Participants

Four healthy Italian proficient native speakers (2 males: M1, M2 respectively 22 and 29 years old; 2 females: F1, F2 respectively 21 and 23 years old) without known psychiatric or neurological problems, with normal or corrected-to-normal vision and without hearing, developmental and language-related problems, were enrolled in this study. All participants were right-handed by self-report and naive with respect to the purpose of the experiment. Written informed consent was obtained in accordance with the Declaration of Helsinki, and the study was approved by the local ethics committee.

B. Stimuli

The stimulus used in the present study is "Storia di Gianna e delle sue chiavi" ("Story of Gianna and her keys") written by Carlo Santulli and read by Silvia Cecchini (https://www.progettobabele.it/AUDIOFILES/ascolta.php?ID=841). Stimulus duration was 11:50 min (1856 spoken words). Reversed speech version of the stimulus was obtained with Audacity 2.03 (https://www.audacityteam.org/) and used as

control condition. Specifically, the original audio track was imported in Audacity and then a transformation was applied so that the end of the audio could have been heard first and the beginning last. This technique makes the audio track intelligible without altering the sound power [13].

C. Surprisal model

The surprisal associated with a word at time (or position) t is defined as the negative logarithm of its conditional occurrence probability:

$$surprisal(t) = -log_{10} P(W_t|W_{t-1}, W_{t-2}, ..., W_1) \ (1)$$

The higher the probability of the observed word the lower will be this value. Therefore, when the appearance of the word W_t is certain the probability is 1 and the surprisal is zero. Whereas, when the appearance of the word W_t is highly unlikely the probability is 0 and the surprisal values goes to infinite.

The conditional probability can be calculated from a stochastic language model trained on a large linguistic corpus [6], [7]. In this work, a stable and widely used stochastic model was used: the second-order Markov model, also known as trigram [2], [6]. It is based on the idea that given a sentence formed by N words $\{W_1, W_2 ...., W_N\}$, the probability of observing the word W_t given the whole left-side context $P(W_t|W_1,..., W_{t-1})$ can be approximated to $P(W_t|W_{t-2}, W_{t-1})$ (i.e. the probability of observing the word W_t given only the two preceding words). Surprisal values calculated using a trigram model have been used successfully in previous neuroimaging studies [5], [6], [8] showing brain activations in cortical areas involved in speech.

D. Model estimation

The trigram probabilities assigned to the word series of the story used as stimuli have been estimated on a large written linguistic corpus. In this study, the PAISÀ corpus [12] that is a Creative Commons licensed large web corpus of contemporary Italian was used. Briefly, it is composed of 388,000 documents from 1,067 different websites, for a total of about 250M tokens.

Before the estimation of the probabilities, the corpus was pre-processed to obtain better performances, more robust estimates and to reduce the computational cost. Thereby, residuals and spurious HTML tags, typos and obsolete words (mostly tokens with a total frequency of less than fifty) were removed from the whole corpus using custom scripts in Python (Software Foundation. Python Language Reference, version 3.5. available at http://www.python.org). Finally, the corpus was split into sentences (one sentence per line), all words were lowered, and the punctuation marks were removed.

The surprisal values were estimated using the software SRILM [14] and Kneser-Ney smoothing was used to control for possible unknown words (i.e. words not present in the corpus) that would otherwise lead to infinite surprisal values. A scheme of the workflow followed to implement the model is reported in Fig. 1.
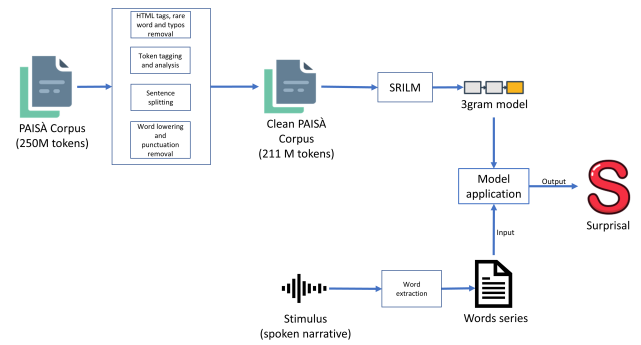
Fig. 1: Summary of the workflow followed to obtain the word surprisal values. The PAISÀ was cleaned and formatted in one sentence per line, then it was given as input to the SRILM package to train a trigram model. This model was applied to the series of words extracted from the audio narrative.

E. Experimental procedure and image acquisition

Participants listened to a story, as well as to its reversed version, while lying in the MRI scanner. Half of the participants started with the non-reversed stimulus and half with the reversed speech stimulus. Before entering the scanner, the participant was instructed to listen as carefully as possible and to maintain the eyes gaze on a white cross superimposed on a black screen. Stimuli were presented by means of custom scripts written in Python 2.7 with the use of the PsychoPy2 module [15] via MRI compatible earphones (Serene Sound, Resonance Technology, USA).

At the end of the scanning session, participants' overall comprehension was tested with a multiple-choice questionnaire (8 questions, 4 possible options per question).

MRI was performed on a 3T scanner (Magnetom Skyra, Siemens Healthcare, Germany) equipped with a 20-channel parallel head coil. The fMRI scan consisted of 750 volumes of a multi-band [16], [17] repeated gradient-echo echo-planar imaging (EPI) sequence (repetition time (TR) = 1000 ms, echo time (TE) = 30 ms, number of axial slices = 60, matrix = 96 x 96, field of view (FOV) = 240 mm, thickness= 2.5 mm, interslice gap = 0 mm, multi-band factor = 4). Two more multi-band gradient echo EPI sequences (5 volumes each) were acquired. The first was identical to the sequence of 750 volumes, whereas the second was acquired with an opposite phase encoding. Three-dimensional T1w Magnetization Prepared Rapid Gradient-Echo (MPRAGE) sequence (TR =2400 ms, TE= 2.26 ms, TI = 950 ms, flip angle =8°, slice thickness = 1.0 mm, matrix size = 256x256, number of slices = 192 and voxel size = 1.0 x 1.0 x 1.0 mm3) was acquired in the same session.

F. FMRI Data Preprocessing

First, using BrainVoyager (BrainInnovation, Maastricht, The Netherlands), slice scan time correction followed by motion correction and high-pass filtering (cut-off to 0.008 Hz) was applied to all three fMRI time-series after DICOM file import. Then, the data was converted to NIfTI format, and the image series was corrected for EPI geometrical distortions with the FSL tool TOPUP [18] using the two short series acquired with opposite phase encoding to estimate the warps. The corrected series were then further pre-processed in Matlab

using the Data Processing Assistant for Resting-State fMRI toolkit (DPARSF; http://www.rfmri.org) [19]. In particular, the anatomical and functional scans were spatially normalized to the standard Montreal Neurological Institute (MNI) template, functional images were resampled to 2x2x2 mm voxel sizes and then, white matter (WM), cerebrospinal fluid (CSF) signals and the Friston-24 movement parameters [20] were regressed out from fMRI time series. Finally, functional images were spatially smoothed using an isotropic 4-mm full-width at half maximum Gaussian kernel.

After these steps, all individual fMRI series were imported back in BrainVoyager and further transformed to the Talairach space to allow the statistical analysis and presentation of subject-level activation maps in a standard space and on the cortical surface meshes.

G. FMRI Data Modeling and Statistical Analysis

A whole-brain voxel-based statistical analysis of the fMRI time-courses for each subject was performed in BrainVoyager using a general linear model (GLM), in which the correlation between surprisal estimates and fMRI time-courses was estimated as a fixed effect in both narrative conditions (original and reversed speech).

In addition to the predictor of interest (i.e. the surprisal) the lexical frequency (LF), the word duration (WD) and the root mean square (RMS) of the word sound were added as confound predictors in the GLM. Particularly, the inclusion of the LF ensures that no extra effects result from the correlation of fMRI responses with the main predictor due to the absolute (context-independent) uncommonness of a word in the considered corpus, whereas the inclusion of the WD and of the RMS excludes additional effects resulting from purely acoustic sources of variance (e.g. sound volume and the speaker's prosody)

All four predictors were then convolved with the hemodynamic response (to account for the hemodynamic delay) at the sampling rate of 100Hz. Finally, the convolved predictors were down-sampled to the time resolution of fMRI (1 Hz). This procedure was identically followed for the original and reversed speech stimuli. Because each subject performed two runs (in random order), the modelled time courses from both runs (original and reversed speech) were concatenated along time.

For each subject, the contrast between the "original" and the "reversed" speech was evaluated, resulting in a statistical map of the difference (t statistics). The resulting maps were corrected for multiple comparisons with False Discovery Rate (FDR) [21] and the threshold of p=0.05 was applied.

All the maps were overlaid in pseudo-colour, and, for visualization purposes, only clusters with more than 10 voxels, were projected on an inflated cortical mesh of a Talairach-normalized T1-weighted scan of a single subject.

III. RESULTS

Participants showed a satisfactory level of comprehension with a 0.94±0.25 of correct responses in the questionnaire (p<0.05, binomial distribution, chance level: 0.25).

The application of the surprisal model to encode the neural activity in the fMRI time-series, observed in the contrast between the original and the reversed version of the story, resulted in single-subject patterns involving temporal, parietal and frontal areas.

Significant bilateral activations of the temporal poles were observed consistently in subjects M1, M2 and F1 (p<0.05, FDR-corrected). Subject F2 exhibited a significant activation only in the left temporal pole (p<0.05, FDR-corrected).

Frontal areas were found significantly activated in subject M1 (superior frontal gyrus bilaterally), F1 (left inferior and middle frontal gyrus) and F2 (left inferior frontal gyrus) (p<0.05, FDR-corrected).

Activations in the ventral inferior-temporal cortex were detected in F1 and F2 (bilaterally) (p<0.05, FDR-corrected).

Areas in the parietal cortex were found activated in subject M1 (left hemisphere), and bilaterally in M2 and F1 (p<0.05, FDR-corrected).

Clusters of significantly higher neural response in the original compared to the reversed speech were observed also in the precentral gyrus in subjects M2, F1 and F2 (bilaterally) and in the orbitofrontal cortex for subjects M1, F1 and F2 (right hemisphere) (p<0.05, FDR-corrected).
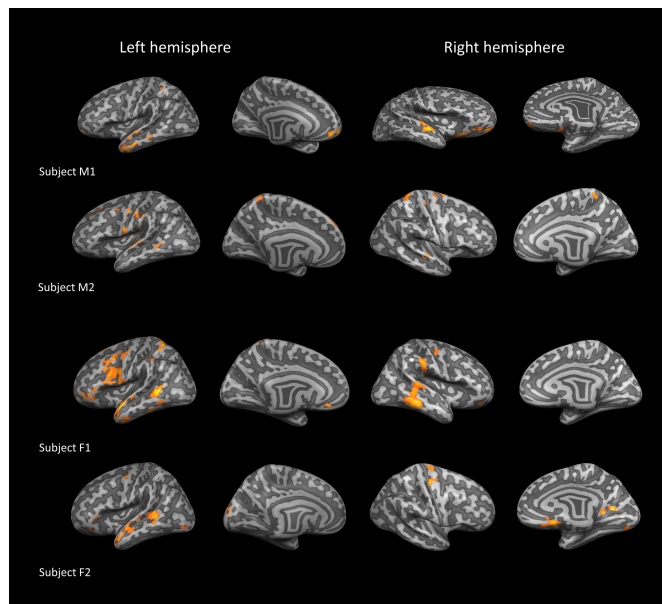
Fig. 2: Surprisal brain response for all the four subjects.
Subject M1 elicited activations bilaterally in the temporal poles, in the frontal cortex in the right orbitofrontal cortex. A cluster of activation was observed also in the left parietal cortex.
Subject M2 showed significant activations bilaterally in the temporal pole, in the left precentral gyrus and in the superior parietal cortex bilaterally.
Subject F1 yielded significant bilateral activations in the temporal pole, in the parietal cortex, in the precentral gyrus and in the left inferior frontal cortex.
Subject F2 presented significant activations in the left temporal pole, in the right orbitofrontal cortex and bilaterally in the inferior temporal cortex. A small cluster of significant activation was observed in the left inferior frontal cortex and in the calcarine cortex.
All the activations were FDR-corrected at a threshold of p=0.05.

IV. Conclusion

A stochastic language model, previously used in combination with fMRI for English and Dutch languages, has

been trained on a large Italian written corpus and, for the first time, applied to fMRI data acquired in a naturalistic experiment (narrative listening). The results, albeit preliminary, seem to be in line with previous findings in similar experimental frameworks operating in other languages. For instance, for all the subjects, the contrast between original and reversed speech activated key brain areas in the language comprehension such as the temporal poles, the parietal cortex and the frontal regions.

Particularly, the clusters of activations observed consistently across the subjects in the temporal lobes are in line with the findings of Willems et al. [6] that used an identical implementation of surprisal and a similar naturalistic framework on the Dutch language. For instance, the activations in the superior temporal gyri confirm the idea that these regions host a prediction mechanism by being sensitive to how well the incoming word is predictable from the context [6]. Furthermore, the activations detected in the most anterior part of the left temporal lobe corroborate the idea that in this region the new input is unified with the available information during the speech processing [6].

The clusters of activation observed in two subjects (F1 and F2) in the left inferior frontal cortex are supported by previous studies as this area has been extensively associated with language-related processing tasks such as syntax computation, lexical-semantic selection and phonological tasks [22].

The activation of the ventral inferior-cortex is in line with previous results as this region has been already linked with the lexical-semantic expectation processing during language comprehension [5].

The results presented in this work showed that it is possible to use a stochastic language model, like the surprisal, to encode at subject-level the expectation processes, and the related cognitive efforts, underlying the language processing in a naturalistic scenario, such as the listening to an audiobook. Furthermore, the paradigm used in this study could have clinical applications. In fact, while the use of language models yields informative neural predictors that can target several linguistic aspects from the fMRI signal changes for both healthy and pathological populations, the use of naturalistic stimuli provides robust and ecologically valid data by simulating real-life experiences [23].

Although the presented findings are promising, future studies are warranted to increase the sample size and to perform a random-effects statistical group analysis in order to validate the use of the surprisal model in the Italian language.

REFERENCES

[1] A. Clark, "Whatever next? Predictive brains, situated agents, and the future of cognitive science," *Behav. Brain Sci.*, vol. 36, no. 3, pp. 181–204, 2013, doi: 10.1017/S0140525X12000477.

[2] K. Armeni, R. M. Willems, and S. L. Frank, "Probabilistic language models in cognitive neuroscience: Promises and pitfalls," *Neurosci. Biobehav. Rev.*, vol. 83, no. July, pp. 579–588, 2017, doi: 10.1016/j.neubiorev.2017.09.001.

[3] J. Hale, "A probabilistic earley parser as a psycholinguistic model," 2001, pp. 1–8, doi: 10.3115/1073336.1073357.

[4] R. Levy, "Expectation-based syntactic comprehension," *Cognition*, vol. 106, no. 3, pp. 1126–1177, 2008, doi: 10.1016/j.cognition.2007.05.006.

[5] A. Lopopolo, S. L. Frank, A. Van Den Bosch, and R. M. Willems, "Using stochastic language models (SLM) to map lexical, syntactic, and phonological information processing in the brain," *PLoS One*, vol. 12, no. 5, pp. 1–18, 2017, doi: 10.1371/journal.pone.0177794.

[6] R. M. Willems, S. L. Frank, A. D. Nijhof, P. Hagoort, and A. Van Den Bosch, "Prediction during Natural Language Comprehension," *Cereb. Cortex*, vol. 26, no. 6, pp. 2506–2516, 2016, doi: 10.1093/cercor/bhv075.

[7] J. M. Henderson, W. Choi, M. W. Lowder, and F. Ferreira, "Language structure in the brain: A fixation-related fMRI study of syntactic surprisal in reading," *Neuroimage*, vol. 132, pp. 293–300, 2016, doi: 10.1016/j.neuroimage.2016.02.050.

[8] S. L. Frank and R. M. Willems, "Word predictability and semantic similarity show distinct patterns of brain activity during language comprehension," *Lang. Cogn. Neurosci.*, vol. 32, no. 9, pp. 1192–1203, 2017, doi: 10.1080/23273798.2017.1323109.

[9] G. Berardi, A. Esuli, and D. Marcheggiani, "Word embeddings go to Italy: A comparison of models and training datasets," *CEUR Workshop Proc.*, vol. 1404, 2015.

[10] M. Baroni, G. Dinu, and G. Kruszewski, "Don't count, predict! A systematic comparison of context-counting vs. context-predicting semantic vectors," *Proc. 52nd Annu. Meet. Assoc. Comput. Linguist. (Volume 1 Long Pap.*, pp. 238–247, 2014, doi: 10.3115/v1/P14-1023.

[11] E. Borleffs, B. A. M. Maassen, H. Lyytinen, and F. Zwarts, "Measuring orthographic transparency and morphological-syllabic complexity in alphabetic orthographies: a narrative review," *Reading and Writing*. 2017, doi: 10.1007/s11145-017-9741-5.

[12] V. Lyding *et al.*, "The PAISÀ Corpus of Italian Web Texts," *Proc. 9th Web as Corpus Work.*, pp. 36–43, 2014, doi: 10.1109/ICIEV.2016.7760164.

[13] E. C. Brown *et al.*, "Evaluating reverse speech as a control task with language-related gamma activity on electrocorticography," *Neuroimage*, vol. 60, no. 4, pp. 2335–2345, 2012, doi: 10.1016/j.neuroimage.2012.02.040.

[14] A. Stolcke, J. Zheng, W. Wang, and V. Abrash, "SRILM at Sixteen : Update and Outlook," *Proc. IEEE Autom. Speech Recognit. Underst. Work.*, pp. 5–9, 2011.

[15] J. Peirce, "PsychoPy - Psychology software for Python," 2017.

[16] D. A. Feinberg *et al.*, "Multiplexed echo planar imaging for sub-second whole brain fmri and fast diffusion imaging," *PLoS One*, vol. 5, no. 12, 2010, doi: 10.1371/journal.pone.0015710.

[17] S. Moeller *et al.*, "Multiband Multislice GE-EPI at 7 Tesla, With 16-Fold Acceleration Using Partial Parallel Imaging With Application to High Spatial and Temporal Whole-Brain FMRI," *Magn. Reson. Med.*, vol. 63, no. 5, pp. 1144–1153, 2010, doi: 10.1002/mrm.22361.Multiband.

[18] J. L. R. Andersson, S. Skare, and J. Ashburner, "How to correct susceptibility distortions in spin-echo echo-planar images: Application to diffusion tensor imaging," *Neuroimage*, vol. 20, no. 2, pp. 870–888, 2003, doi: 10.1016/S1053-8119(03)00336-7.

[19] Y. Chao-Gan and Z. Yu-Feng, "DPARSF: A MATLAB toolbox for 'pipeline' data analysis of resting-state fMRI," *Front. Syst. Neurosci.*, vol. 4, 2010, doi: 10.3389/fnsys.2010.00013.

[20] K. J. Friston, S. Williams, R. Howard, R. S. J. Frackowiak, and R. Turner, "Movement-Related effects in fMRI time-series," *Magn. Reson. Med.*, vol. 35, no. 3, pp. 346–355, Mar. 1996, doi: 10.1002/mrm.1910350312.

[21] C. R. Genovese, N. A. Lazar, and T. Nichols, "Thresholding of statistical maps in functional neuroimaging using the false discovery rate," *Neuroimage*, vol. 15, no. 4, pp. 870–878, 2002, doi: 10.1006/nimg.2001.1037.

[22] J. R. Binder, J. A. Frost, T. A. Hammeke, R. W. Cox, S. M. Rao, and T. Prieto, "Human Brain Language Areas Identified by Functional Magnetic Resonance Imaging," vol. 17, no. 1, pp. 353–362, 1997.

[23] G. Chen *et al.*, "Untangling the relatedness among correlations, part III: Inter-subject correlation analysis through Bayesian multilevel modeling for naturalistic scanning," *Neuroimage*, p. 116474, Dec. 2019, doi: 10.1016/j.neuroimage.2019.116474.

Human exposure to electromagnetic fields generated in smart vehicle communications

G. Tognola[1], S. Gallucci[1], M. Bonato[1,2], S. Fiocchi[1], E. Chiaramello[1], L. Dossi[1], M. Parazzini[1], and P. Ravazzani[1]

[1] *CNR IEIIT–Ist Elettronica, Ingegneria dell'Informazione e delle Telecomunicazioni, Milano; gabriella.tognola@ieiit.cnr.it*
[2] *Dipartimento di Elettronica, Informazione e Bioingegneria DEIB, Politecnico di Milano, Milano*

Abstract—**This paper evaluates the dose of exposure to radiofrequency electromagnetic fields (EMF) of people inside a car during vehicle-to-vehicle (V2V) communication operated at 5.9 GHz. The exposure dose is estimated with numerical simulations that make use of detailed and realistic 3D models of the geometry and material of the car and V2V antennas and of the organs and different tissues of an adult phantom at the driver position. The dose of EMF exposure was expressed in terms of the power absorbed by the tissues and organs of the driver and was quantified with the Specific Absorption Rate (SAR). The simulations revealed that SAR was higher in the body regions closer to the emitting antennas (the limbs) and very rapidly decreased with the distance from the antennas. Also, SAR values were observed only in the very superficial tissues, i.e., in the skin and were negligible elsewhere, such as in the muscles, bones and other more profound tissues. SAR values for both the whole-body- and local-body-exposure were well below the ICNIRP general public exposure limit in the 100 kHz-6 GHz frequency range and were equal to 1% and 7% of the limits of exposure for the whole-body and local body regions, respectively.**

Keywords—**EMF exposure, vehicle communication, specific absorption rate, human model.**

I. INTRODUCTION

CARS are rapidly evolving into smart connected objects that can communicate not only with the infrastructure (i.e., for mobile communication) but also with other cars in vehicle-to vehicle (V2V) communication, Internet of Things devices and with people (i.e., passengers and pedestrians). Within the framework of V2V communications, the 5GAA organization – the 5G Automotive Association of companies from the automotive, technology and IT fields for the development of future mobility solutions – estimates that by the end of 2023 there will be sold more than 72 million vehicles in the world equipped with devices and technologies that enable them to exchange data and communicate with other cars. Examples of V2V communication include broadcasting of information for safe mobility (e.g., for detection of car accidents, detection of obstacles, etc.), traffic management, and environment sensing.

V2V communication is a new scenario that has an impact not only in the IT field for the management of channels and protocols for communication but also in the biomedical field for what concerns the exposure of people (driver, passengers and pedestrians) to the EMF generated by these new technologies.

Assessment of human exposure in the V2V communication context has never been approached before. This new exposure scenario generated by V2V communications has a number of peculiarities, ranging from the different frequency band of the radiating field to the different exposure environment which is strongly affected by the 'EMF-shield' effect of the metallic parts of the car and its dimensions. All these peculiarities make impossible to assess EMF exposure in V2V scenarios from a simple re-analysis of results already existing from other types of scenarios. In the recent literature, it is possible to find studies that estimated EMF generated in V2V scenarios by simulating realistic V2V antennas operated at the correct V2V frequency (5.9 GHz) and mounted on realistic car models [1-8]. Although these studies used realistic models of the antennas and the car and realistic operating frequency for V2V communication, they didn't assess the exposure on humans because they aimed to investigate the effects of antenna characteristics and placement on the efficacy of the propagation of antenna signals only. Other recent studies, instead, evaluated human exposure to EMF generated inside cars from the use of mobile infotainment sources, e.g., UMTS, WiMax, Bluetooth [9-11]. Although these latter studies used realistic human phantoms and realistic sources, their results cannot be used to infer human exposure in V2V scenarios because the EMF sources they investigated were operated at frequencies different and lower than those used in V2V communication.

Differently from the past studies, the present study investigates for the first time human exposure in realistic V2V communication scenarios that take into account realistic frequency band at which EMF sources were operated, realistic model of the exposure setup (car, V2V antennas) and realistic model of a passenger (driver) in the car.

II. MATERIAL AND METHODS

A. Exposure setup

The exposure setup is illustrated in Fig. 1. It consisted of a 3D model of a car, four V2V antennas and a human phantom sit at the driver position. The shape and dimension of the car model were the same of a typical city car. The body of the car was modelled as a PEC (perfectly electric conductor); the windows (six) of the car were modelled as glass (density ρ=2500 kg/m³; conductivity σ=0.0043 S/m; relative permittivity ε_r=4.82) of 6 mm thickness. The inside of the car was modelled as air as it was demonstrated that typical materials used in car interiors (i.e., plastics and foam) do not affect the distribution of the electric field E generated by the antennas [12]. Four V2V antennas were placed outside the car, close to the car outer surface, at the front/back and left/right side of the car. The antennas were modelled as quarter-wave monopoles and were operated at 5.9 GHz, according to the

current IEEE 802.11p standard for V2V communications [13]. To simulate the worst case exposure scenario, each antenna was operated at the maximum power allowed by the IEEE 802.11p standard, i.e., at 30 W. The 'Duke' human phantom (adult male) of the ViP v.1.0 family was placed inside the car at the driver position. The dielectric properties of the nearly 80 different tissues of the phantom were assigned according to literature data [14].
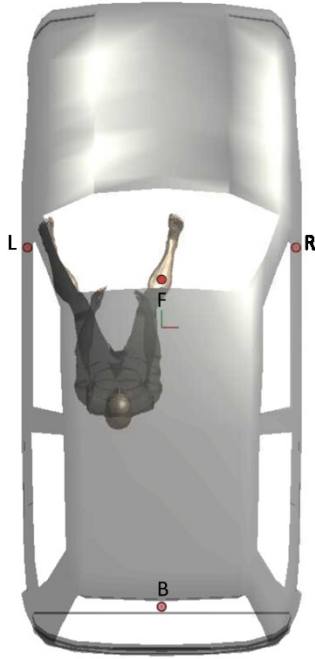

Fig. 1: Exposure setup. Top view of the realistic 3D models of the car, the human phantom at the driver position and four V2V antennas at the left (L), right (R), front (F), and back side (B) of the car. The dimensions of the car model are 3.8 (length) x 1.6 (width) x 1.3 m (height).

B. Exposure simulation and analysis

The finite-difference time-domain (FDTD) solver of the simulation platform SIM4life (ZMT Zurich Med Tech AG, Zurich, Switzerland, www.zurichmedtech.co) was used to calculate EMF generated by the antennas in the computational domain, which consisted of the car, the human phantom and the four antennas. The computational domain was discretized with a non-uniform grid with a maximum step of 2 mm, resulting in a total number of about 10^9 cells; the boundaries of the computational domain were modelled as perfectly matched layers (PML).

EMF exposure was analysed in terms of the electric field E generated in the computational domain and the specific absorption rate (SAR), which is the rate of the absorption of the energy in the human body when exposed radio frequencies. Following the ICNIRP guidelines on EMF exposure [15], SAR was calculated in the whole body of Duke, in local body regions (head, torso, arms, legs), and in single tissues. The whole body average SAR was calculated as the ratio of the total power absorbed by the body to the total mass of the body. EMF exposure in local body region and tissues was analyzed by considering the distribution within a given body region or tissue of the 10g average SAR, which is the SAR averaged over any 10 g of body region or tissues.

III. RESULTS

Fig. 2 shows as an example the distribution of the electric field E generated when the four V2V antennas were operated simultaneously. It is possible to note that E decreased rapidly with the distance from the antennas. As a result, only body regions closer to the antenna, that is forearms and legs, were characterized by significant E values. Other body regions such as the head and torso, which were more distant from the antennas were characterized by negligible E fields.
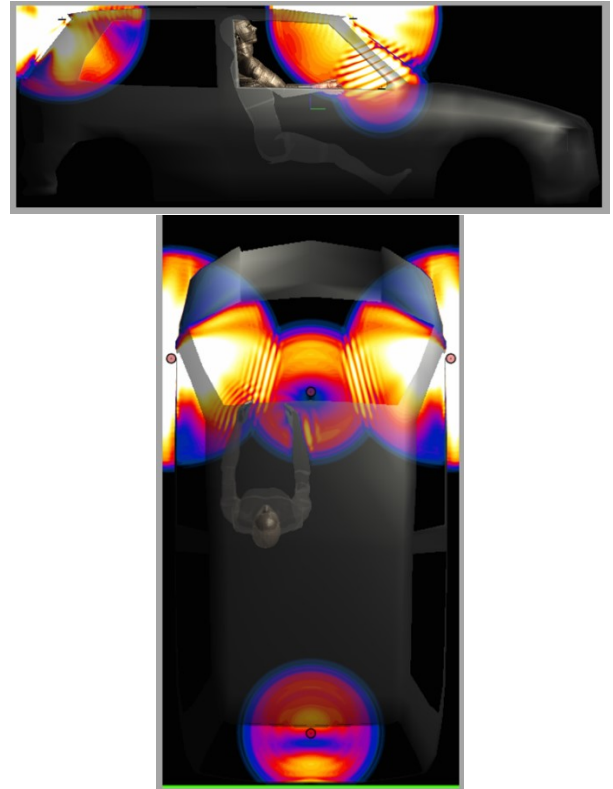
Fig. 2: Distribution of E field generated simultaneously by the four antennas on the sagittal (top panel) and horizontal plane (bottom panel). The sagittal plane is located at the midline of the human phantom. The horizontal plane is located at the same height of the left and right antennas. The colormap ranges from 70 (bright yellow) to 0 V/m (black). E values are expressed on a linear scale.

As a results of this particular distribution of E, SAR was found to be significant only in the left and right arms and in the left leg. The peak (i.e., maximum) value of SAR in these latter body regions was 267 mW/kg in the left arm, 249 mW/kg in the right arm, and 32 mW/kg in the left leg. All these values were well below the 4 W/kg general public ICNIRP limit of exposure for the limbs in the 100 kHz-6 GHz range. The whole body average SAR was 0.78 mW/kg and was, again, lower than the ICNIRP limit of 0.08 W/kg for the average whole body exposure.

As to the exposure in the single tissues, we found that SAR was not negligible only in the most superficial tissues, i.e., mainly in the skin and to a lower degree in the subcutaneous fat tissue, whereas more profound tissues, such as muscles, bones, and blood had negligible values of SAR. Fig. 3 displays the distribution of SAR over the skin: it is possible to clearly see how SAR was localized only in the limbs and how it

rapidly decreased when proceeding towards the trunk and the head of the phantom.

Lastly, Fig. 4 illustrates in detail the distribution of SAR values in the skin of the body regions where exposure was not negligible, i.e., the arms and the left leg. It is noticed that the SAR in the left forearm was on average higher than in the right arm. Also, the distribution of SAR in the left forearm was broader than in the left forearm.
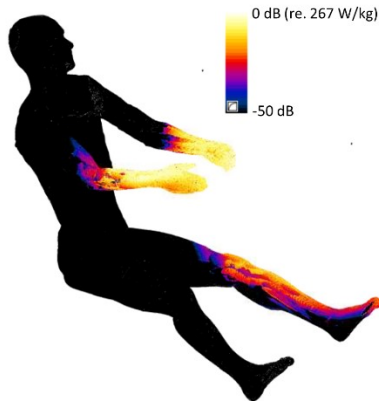

Fig. 3: Distribution of 10 g average SAR induced simultaneously by the four antennas on the skin of the human phantom.
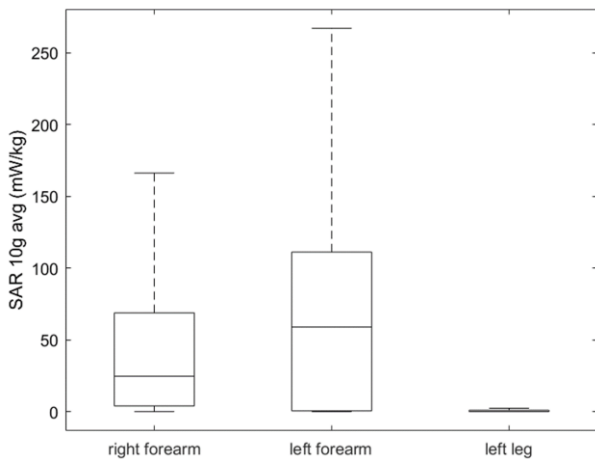
Fig. 4: Boxplot of SAR induced simultaneously by the four antennas in the skin of the right and left forearms and the left leg. The center lines in the boxes indicate the median; the bottom and top edges indicate the 25th and 75th percentiles. The whiskers extend to 1.5 times the height of the box and correspond to approximately 99.3% of the data.

IV. CONCLUSION

This paper presents the first results available in the literature on the estimation of EMF exposure generated by the new communication technologies used in V2V communications in smart vehicles. Numerical dosimetry was performed by using a state-of-the-art human phantom whose different tissues were accurately modelled in terms of shape, dimensions and electromagnetic characteristics. The novelty of the analysis presented in the current study was in the study of the exposure in a frequency band (5.9 GHz) which has never been studied before and whose effect on SAR could not be inferred by a simple re-use of the results available in the literature for other frequency bands and different exposure setup. As to the exposure setup, the novelty is in the simulation of a realistic exposure scenario for vehicular communications using realistic models of the car and the antennas; models that allowed to accurately evaluate the effect of the 'EMF-shield' of the body of the car. The results evidenced that exposure was mainly limited to the very superficial tissues of the body, i.e., the skin and that was located only in those body parts closer to the emitting antennas, i.e., the limbs. Other body parts more critical for what concerns the possible effect of the exposure, i.e., the head and torso, were characterized by negligible SAR. The simulations revealed that the position of the body inside the car, the position of the antennas and the shape of the car were parameters that have an impact on the exposure. As such, it would be interesting in future studies to further explore EMF exposure in V2V scenarios with non-deterministic dosimetric approaches, based e.g., on Machine Learning or stochastic algorithms [16-17], to assess the exposure in different scenarios and with people of different ages (e.g., adults, children, neonates, foetuses, etc.).

REFERENCES

[1] D. Kornek, M. Schack, E. Slottke, O. Klemp, I. Rolfes and T. Kürner, "Effects of antenna characteristics and placements on a Vehicle-to-Vehicle channel scenario," in *Proc. 2010 IEEE International Conference on Communications Workshops*, Capetown, 2010, pp. 1-5.

[2] M.B. Diez, P. Plitt, W. Pascher, and S. Lindenmeier, "Antenna placement and wave propagation for Car-to-Car communication," in *Proc. 2015 European Microwave Conference (EuMC)*, Paris, 2015, pp. 207-210.

[3] G. Gavilanes, M. Reineri, D. Brevi, R. Scopigno, M. Gallo, M. Pannozzo, S. Bruni, and D. Zamberlan, "Comparative characterization of four antennas for VANETs by on-field measurements," in *Proc. 2013 IEEE International Conference on Microwaves, Communications, Antennas and Electronic Systems (COMCAS 2013)*, Tel Aviv, 2013, pp. 1-5.

[4] E. Condo Neira, U. Carlberg, J. Carlsson, K. Karlsson and E.G. Ström, "Evaluation of V2X antenna performance using a multipath simulation tool," in *Proc. The 8th European Conference on Antennas and Propagation (EuCAP 2014)*, The Hague, 2014, pp. 2534-2538.

[5] E. Condo Neira, J. Carlsson, K. Karlsson and E.G. Ström, "Combined LTE and IEEE 802.11p antenna for vehicular applications," in Proc. *2015 9th European Conference on Antennas and Propagation (EuCAP)*, Lisbon, 2015, pp. 1-5.

[6] E. Whalen, A. Elfrgani, C. Reddy and R. Rajan, "Antenna placement optimization for Vehicle-to-Vehicle communications," in *Proc. 2018 IEEE International Symposium on Antennas and Propagation & USNC/URSI National Radio Science Meeting*, Boston, MA, 2018, pp. 1673-1674.

[7] D. Eckhoff, A. Brummer and C. Sommer, "On the impact of antenna patterns on VANET simulation," in P*roc. 2016 IEEE Vehicular Networking Conference (VNC)*, Columbus, OH, 2016, pp. 1-4.

[8] G. Artner, W. Kotterman, G. Del Galdo and M.A. Hein, "Automotive Antenna Roof for Cooperative Connected Driving," IEEE Access, vol. 7, pp. 20083-20090, 2019.

[9] E. Aguirre, PL. Iturri, L. Azpilicueta, S. De Miguel-Bilbao, V. Ramos, U. Gárate, and F. Falcone, "Analysis of estimation of electromagnetic dosimetric values from non-ionizing radiofrequency fields in conventional road vehicle environments," *Electromagn Biol Med*, vol. 34, pp. 19–28, 2015.

[10] S-W. Leung, Y. Diao, K-H. Chan, Y-M. Siu, and Y. Wu, "Specific Absorption Rate evaluation for passengers using wireless communication devices inside vehicles with different handedness, passenger counts, and seating locations," *IEEE T Bio Med Eng*, vol. 59, pp. 2905-2912, 2012.

[11] L.-R. Harris, M. Zhadobov, N. Chahat, and R. Sauleau, "Electromagnetic dosimetry for adult and child models within a car: multi-exposure scenarios," *Int J Microw Wirel T*, vol. 3, no. 6, pp. 707–715, 2011.

[12] A. Ruddle, "Influence of dielectric materials on in-vehicle electromagnetic fields," in *Proc. IET Seminar on EM Propagation in Buildings and Large Structures*, London, 2008.

[13] IEEE Standard for Information technology-- Local and metropolitan area networks-- Specific requirements-- Part 11: Wireless LAN Medium Access Control (MAC) and Physical Layer (PHY) Specifications Amendment 6: Wireless Access in Vehicular Environments," in IEEE Std 802.11p-2010, pp.1-51, 2010.

[14] S. Gabriel, RW. Lau, and C. Gabriel, "The dielectric properties of biological tissues: II. Measurements in the frequency range 10 Hz to 20 GHz", *Phys Med Biol*, vol. 41, pp. 2251-2269, 1996.

[15] International Commission on Non-Ionizing Radiation Protection, "ICNIRP guidelines for limiting exposure to time-varying electric, magnetic and electromagnetic fields (up to 300 GHz)", *Health Phys*, vol. 74, pp. 494–522, 1998.

[16] M. Bonato, E. Chiaramello, S. Fiocchi, G. Tognola, P. Ravazzani and M. Parazzini, "Influence of low frequency near-field sources position on the assessment of children exposure variability using Stochastic Dosimetry," *IEEE J Electromag RF and Microw Med Biol,* 2019 (Early Access).

[17] G. Tognola, M. Bonato, E. Chiaramello, S. Fiocchi, I. Magne, M. Souques, M. Parazzini, and P. Ravazzani, Use of Machine Learning in the analysis of indoor ELF MF exposure in children", *Int J Environ Res Public Health*, vol. 16, p. 1230-1243, 2019.

Abdominal visceral and subcutaneous adipose tissues in obese patients: mechanical behaviour

C.G. Fontanella[1,2], M. Foletto[2,3], L. Corain[4] and E.L. Carniel[1,2]

[1] *Department of Industrial Engineering, University of Padova, Italy*
[2] *Centre for mechanics of biological materials, Department of Industrial Engineering, University of Padova, Italy*
[3] *Department of Surgery, Oncology and Gastroenterology, University of Padova, Italy*
[4] *Department of Management and Engineering, University of Padova, Italy*

Abstract - **Obesity is an epidemic disease associated with multiple co-morbidities, whose prevalence in developed countries is increasing. In particular, central obesity carries greater risk of developing diabetes and future cardiovascular events. Abdominal adipose tissue is composed of two distinct anatomical components: subcutaneous adipose tissue (SAT) and visceral adipose tissue (VAT). Nowadays, VAT, SAT and their characteristics are studied in relation with metabolic risk factors and subject characteristics considering clinical aspects. In order to identify new correlations between SAT/VAT mechanics and pathologies, mechanical tests are here reported. Mechanical tests have been performed on SAT and VAT specimens, obtained from patients with obesity during standard laparoscopic sleeve gastrectomy surgery. A specific indentation setup and procedure have been designed. Experiments allowed to assess the typical features of the mechanical response, such as non linear stress-strain behaviour and time-dependent effects. The statistical analysis of results provided a unique set of data, accounting also for the influence of subject characteristics, such as sex, BMI and age. Results showed that the increment of BMI plays an important role in the variation of the mechanical response, resulting in a decrease of stiffness for both VAT and SAT.**

Keywords - **Abdominal adipose tissue, indentation tests, obesity, mechanical response.**

I. INTRODUCTION

ABDOMINAL visceral adipose (VAT) and subcutaneous adipose (SAT) tissues (Fig. 1), two distinct abdominal adipose compartments, have been shown to confer different metabolic risks. Excess of both VAT and SAT contributes to obesity. Abdominal obesity is a major risk factor for diabetes and cardiovascular disease. Although both SAT and VAT are correlated with metabolic risk factors, they differ in structural composition, metabolic activity and functional significance [1]-[3]. VAT remains more strongly associated with an adverse metabolic risk profile.

The here reported activities aim at providing information about VAT and SAT properties, with a specific focus on mechanical behaviour. More in details, experimentations on tissues samples from subjects with obesity made it possible to discriminate between VAT and SAT mechanics and to evaluate the influence of subject characteristics, such as sex, BMI and age. Such data are fundamental to identify correlations between SAT/VAT mechanics and pathologies.

II. MATERIALS AND METHODS

A. Specimen collection

Abdominal and subcutaneous adipose samples (Fig. 2a) have been collected from bariatric patients at Padova University Hospital. The investigations enrolled 16 patients with obesity (M: 4, F: 12; age 45 ± 12 years; BMI 45 ± 5 Kg/m^2) who were scheduled for Laparoscopic Sleeve Gastrectomy (LSG) and gave specific informed consent [4],[5].

Samples were carefully cleaned with cold saline solution to eliminate tissues debris and blood residuals. A 20 mm punch was used to cut cylindrical samples. The mean thickness of the samples ranged between 5 and 12 mm. Samples were stored frozen at -20°C in sealed vials and thawed prior to testing. All the subsequent mechanical tests were performed within three hours after defrosting at room temperature [6].
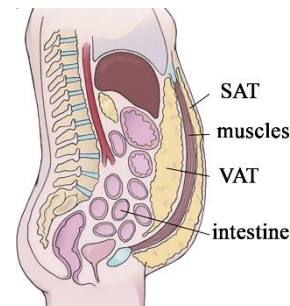
Fig. 1: Identification of abdominal subcutaneous and visceral adipose tissue.

B. Experimental tests

A Galdabini material testing machine was equipped with a specifically designed spherical indenter (10 mm diameter), which allowed performing confined compression tests (Fig. 2b). During preparation and testing, samples were continuously moistened with saline solution at room temperature.
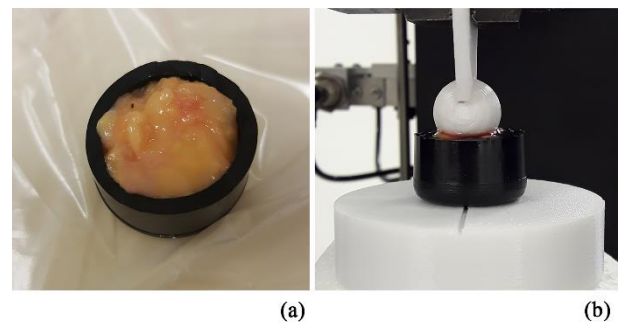

(a)   (b)

Fig. 2: Cylindrical specimen (a) and indentation tests (b) performed using a spherical indenter.

Mechanical testing was performed via a multi-step procedure. Each sample was preconditioned by applying 10

loading-unloading cycles with strain ranging between 0 and 20% at 10%/s strain rate. Subsequently, each step was composed of 15% strain at 3000%/s strain rate, and subsequent 300 s of resting to allow the almost complete development of relaxation phenomena [6],[7]. The step was repeated up to 75% strain. Finally, the sample was completely unstrained at 10%/s strain rate.

C. Data elaboration

Experimental activities allowed achieving force-time data, depending on strain-time setting (Fig. 3). For each confined compression test, force and strain data at the end of the rest stages led to force-strain almost equilibrium curves. The equilibrium force-strain curve define the samples behavior when all the time-dependent micro-structural rearrangement phenomena completely develop during testing, such as either at the end of the relaxation stages or during continuous straining test developed at a sufficiently low strain rate [8],[9]. On the other side, the analysis of force-time results during the constant strain stages led to force relaxation curves [10]. Force-relaxation data were processed to identify the drop of normalized force with time. The normalized force was defined as the ratio of the force at the current time and the peak force at the beginning of the relaxation stage.
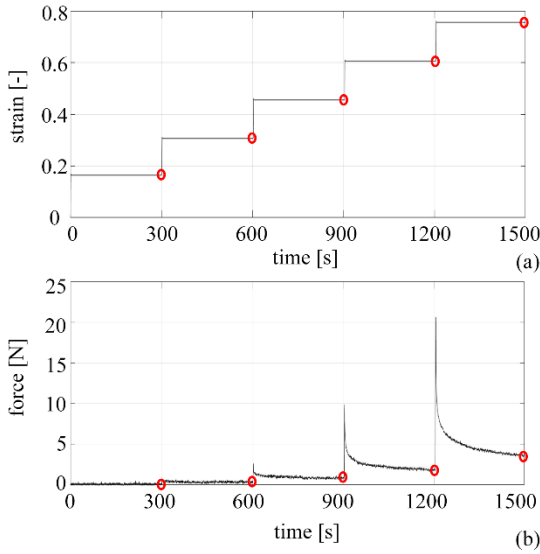
Fig. 3: Loading protocol: the imposed strain history vs time (a) and the measure force vs time data (b).

D. In silico analysis

To provide an effective and rational characterization of VAT and SAT mechanical behaviour, tissue mechanics must be defined in the framework of a constitutive formulation. Results from the performed experimentations highlighted the non-linearity and the time-dependence of VAT and SAT mechanics, and suggested to develop the constitutive model in the framework of visco-hyperelasticity [8]. The Helmholtz free energy ψ was defined as a function of the right Cauchy-Green strain tensor $\mathbf{C}$, which defines the instantaneous strain condition, and viscous variables $\mathbf{q}^i$, which define viscous dissipation phenomena [11],[12]:

$$\psi\left(\mathbf{C},\mathbf{q}^i\right) = W^\infty\left(\mathbf{C}\right) + \sum_{i=1}^{n}\int_0^t \frac{1}{2}\mathbf{q}^i\left(s\right):\dot{\mathbf{C}}\,ds \qquad (1)$$

where W^∞ is the hyperelastic potential that describes the tissues equilibrium mechanical response, while the integral terms define viscous contributions. An Ogden formulation [8] was assumed to interpret the equilibrium response of VAT and SAT tissues:

$$W^\infty\left(\lambda_1,\lambda_2,\lambda_3\right) = \frac{2\mu}{\alpha^2}\left[\tilde{\lambda}_1^\alpha + \tilde{\lambda}_2^\alpha + \tilde{\lambda}_3^\alpha - 3\right] + \frac{1}{D}\left(J-1\right)^2 \qquad (2)$$

where $\tilde{\lambda}_i = J^{-1/3}\lambda_i$ are the deviatoric principal stretches and μ,α,D are hyperelastic parameters. The parameters μ and D specify the initial shear and bulk moduli, as $G_0 = \mu$ and $B_0 = 2/D$. The parameter α describes the non-linearity of tissue elasticity, as the increase of elastic stiffness with stretching phenomena. The evolution of viscous variables is defined according to convolution integral formulations, depending on stress-strain history and viscous parameters, as relative stiffnesses γ^∞, γ^i and relaxation times τ^i:

$$\mathbf{q}^i\left(t\right) = \frac{\gamma^i}{\gamma^\infty\tau^i}\int_0^t \exp\left(-\frac{t-s}{\tau^i}\right)\left(\frac{2\partial W^\infty\left(\mathbf{C}\right)}{\partial\mathbf{C}}\right)ds \qquad (3)$$

Inverse analyses techniques of experimental activities were necessary to identify the constitutive parameters. To interpret the testing procedures, the computational model of the compressive indentation tests accounted for the average geometrical configurations of VAT and SAT samples was developed. A rigid body formulation was assumed for the indenter, while a frictionless contact strategy characterized interaction phenomena between the indenter and the biological tissues. The computational model was exploited to simulate both equilibrium force-strain and force relaxation conditions, leading to the identification of sets of constitutive parameters that interpreted the average behavior of VAT and SAT samples (table I).

TABLE I
CONSTITUTIVE PARAMETERS

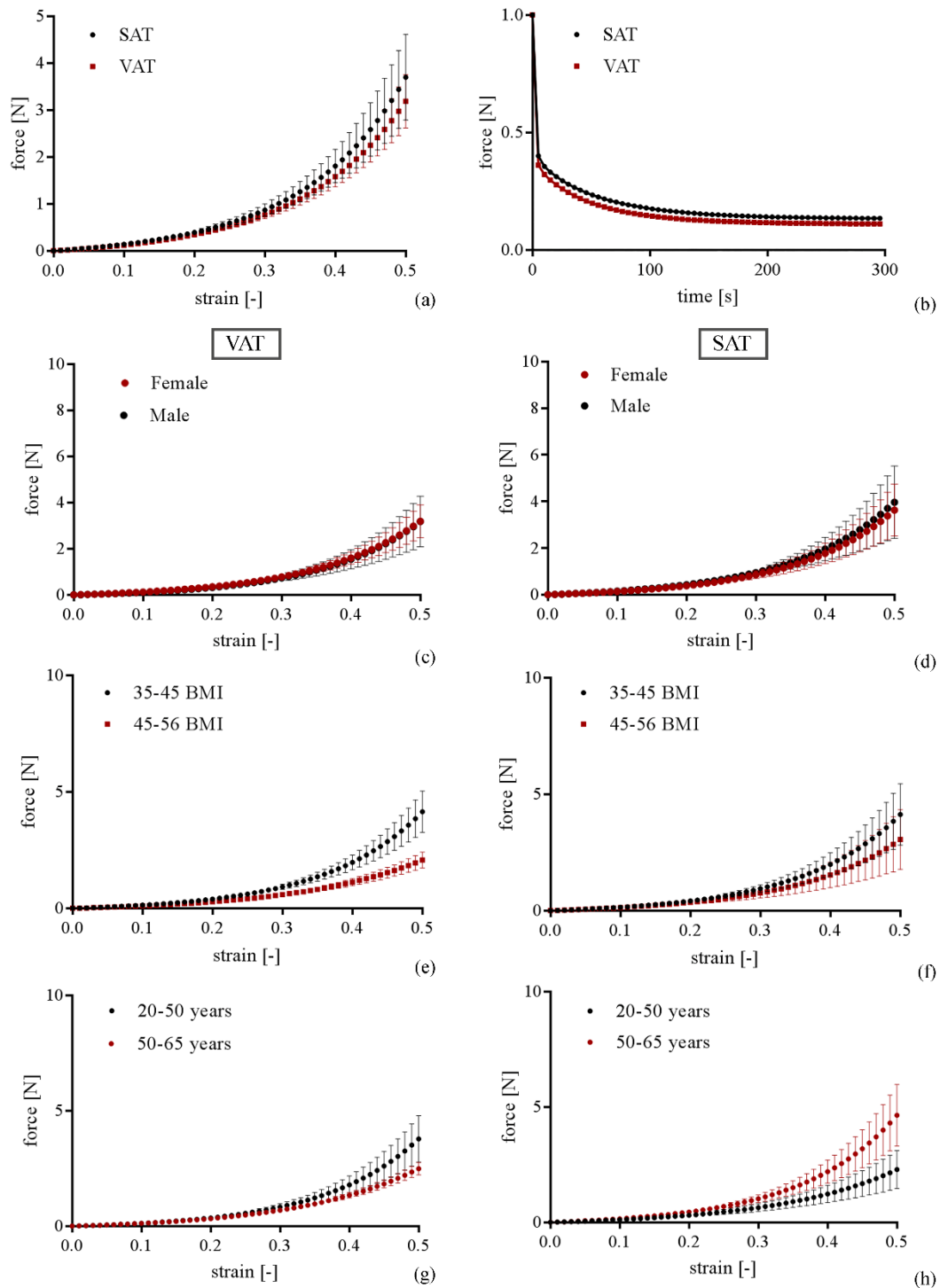| Samples	μ (MPA)	α	D (MPa^{-1})	γ_1	γ_2	τ_1 (s)	τ_2 (s)
VAT	0.01255	7.23	64.66	0.6306	0.2576	1.212	47.48
SAT	0.01988	6.455	67.30	0.6006	0.2643	1.409	52.63

Constitutive parameters for abdominal SAT and VAT.

Fig. 4: Elaboration of experimental data: equilibrium force-strain data (a) and normalized force-time (b) from tests performed on VAT and SAT specimens. Equilibrium force vs strain data from tests performed on VAT (c-e-g) and SAT (d-f-h) specimens, divided in male and female subjects (a-b), subjects with different BMI (c-d), subjects with different ages (e-f) (mean±SEM).

III.   RESULTS AND DISCUSSION

A.   Experimental tests

Results from mechanical tests showed the typical features of adipose tissues mechanics, such as isotropic behavior, non-linear stiffening with strain and time-dependent response. Processing of experimental data led to statistical distributions of the equilibrium force-strain and the normalized force-time curves, by mean and standard error of mean (Fig. 4), aiming to highlight the non-linear viscoelastic behavior of SAT and VAT. During the resting period assumed of 300 s, the micro-structural rearrangement phenomena almost completely developed. The equilibrium force-strain curves were reported in relation with BMI, age and sex (Fig. 4), showing differences between the groups analyzed.

B.   In silico tests

The visco-hyperelastic constitutive model, with the associated constitutive parameters, was able to interpret the mechanical response of abdominal VAT and SAT, in terms of non linear elastic response and time-dependent behavior (Fig. 5). The contour of minimum principal stress was reported for the force relaxation analysis of VAT samples, showing the

capability of the tissue to relax stresses during time by means of micro-structural rearrangement phenomena.
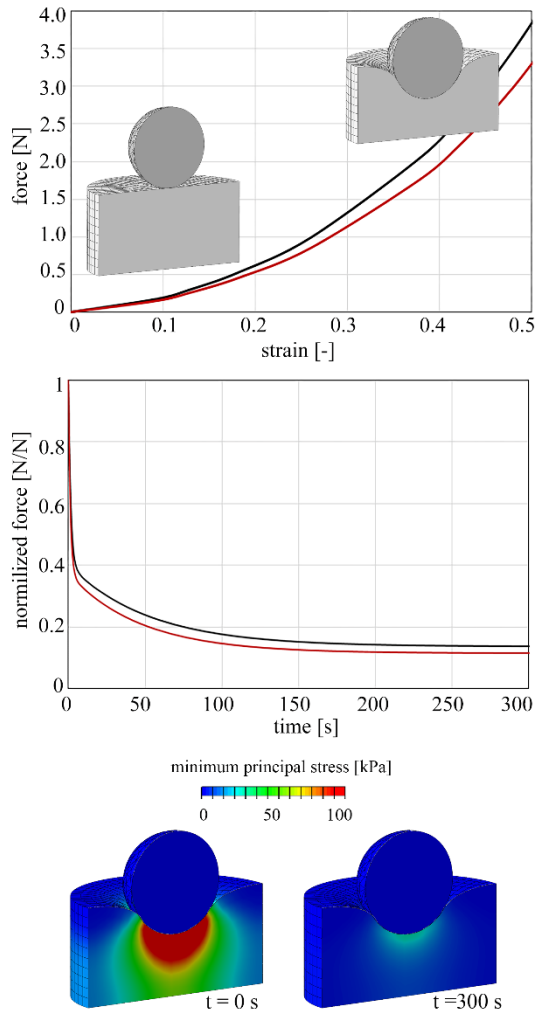
Fig. 5: Results from the numerical analysis of compression test: equilibrium stress-strain data (a) and normalized stress-time results (b). Contours of minimum principal stress in the deformed configuration: viscous recovery time t=0 s and t = 300 s (c).

IV. CONCLUSION

Visceral and abdominal subcutaneous adipose tissues contribute to obesity but may have different metabolic and atherosclerosis risk profiles. Previous experiments did not characterize SAT and VAT mechanics, with particular regard to overweight and obesity conditions.

The reported experiments provide an original set of data about SAT and VAT mechanics. Results highlight that there is little difference in stiffness between SAT and VAT specimens. Computational investigations and the identified parameters confirm such similarity. Finite element modeling provides a feasible method to quantitatively evaluate the mechanical response of adipose tissues. These models can be used to explore the large-scale response of tissues and organs in clinical and pato-physiological research.

A similar mechanical response is reported for both abdominal adipose tissues in male and female subjects, while the influence of ageing determines different mechanical response for SAT and VAT. On the contrary, the increase of BMI causes a decrease of stiffness in both visceral and subcutaneous adipose tissues. Additional studies are in progress to identify the influence of SAT and VAT mechanical properties on obesity and on the risk of developing other pathologies.

REFERENCES

[1]   L. Tang, F. Zhang, N. Tong, "The Association of Visceral Adipose Tissue and Subcutaneous Adipose Tissue with Metabolic Risk Factors in a Large Population of Chinese Adults", *Clin Endocrinol (Oxf)* 2016, vol. 85(1), pp. 46–53.

[2]   W. Ahrens, I. Pigeot, H. Pohlabeln, S. De Henauw, L. Lissner, D. Molnár, L.A. Moreno, M. Tornaritis, T. Veidebaum, A. Siani, "IDEFICS consortium. Prevalence of overweight and obesity in European children below the age of 10", *Int J Obes (Lond)*. 2014 Sep; vol.38 Suppl 2, pp.S99-107.

[3]   L. Bahia, E.S. Coutinho, L.A. Barufaldi, A. Abreu Gde, T.A. Malhão, C.P. de Souza, D.V. Araujo, "The costs of overweight and obesity-related diseases in the Brazilian public health system: cross-sectional study", *BMC Public Health*. 2012 Jun 18, pp.12:440.

[4]   M.A. Kueper, K. M. Kramer, A. Kirschniak, A. Königsrainer, R. Pointner, and F. A. Granderath, "Laparoscopic sleeve gastrectomy: Standardized technique of a potential stand-alone bariatric procedure in morbidly obese patients", *World J. Surg*. 2008, vol 32, pp. 1462–1465.

[5]   K. Hayes, G. Eid, "Laparoscopic Sleeve Gastrectomy: Surgical Technique and Perioperative Care", *Surg. Clin. North Am*, 2016, vol. 96, pp. 763–771.

[6]   C.G. Fontanella, C. Salmaso, I. Toniolo, N. de Cesare, A. Rubini, G.M. De Benedictis, E.L. Carniel, "Computational Models for the Mechanical Investigation of Stomach Tissues and Structure", *Ann Biomed Eng,* 2019, vol. 47, pp. 1237–1249.

[7]   W. Yang, T.C. Fung, K.S. Chian, C.K. Chong, "Viscoelasticity of esophageal tissue and application of a QLV model", J Biomech Eng, 2006, vol. 128, pp. 909-916.

[8]   G.A. Holzapfel, "Nonlinear Solid Mechanics: A Continuum Approach for Engineering", J. Wiley & Sons Ltd, 2000, New York.

[9]   A. Fallah, M.T. Ahmadian, K. Firozbakhsh, M.M. Aghdam, "Micromechanical modeling of rate-dependent behavior of connective tissues", *J Theor Biol*, 2017, vol. 416:, pp. 119-128.

[10]   E.L. Carniel, A. Frigo, C.G. Fontanella, G.M. De Benedictis, A. Rubini, L. Barp, G. Pluchino, B. Sabbadini, L. Polese, "A biomechanical approach to the analysis of methods and procedures of bariatric surgery", *J Biomech*, 2017, vol. 56, pp. 32-41.

[11]   A.N. Natali, C.G. Fontanella, E.L. Carniel, "Constitutive formulation and numerical analysis of the heel pad region", *Comput Methods Biomech Biomed Engin*, 2012, vol. 15, pp. 401-9.

[12]   Y.C. Fung. "Biomechanics: mechanical properties of living tissues", 2nd ed. Springer-Verlag, 1993, New York.

Computational tools for the evaluation of surgical parameters after LSG

I. Toniolo[1,2], C.G. Fontanella[1,2], M. Foletto[1,3], E.L. Carniel[1,2]

[1] Centre for Mechanics of Biological Materials, University of Padova, Padova, Italy
[2] Department of Industrial Engineering, University of Padova, Padova, Italy
[3] Department of Surgery, Oncology and Gastroenterology, University of Padova, Padova, Italy

Abstract—Bariatric surgery is the most effective intervention for severe obesity, one of the most serious health problems of our time. Nonetheless, major complications are frequent, and weight-loss is not always successful. A bioengineering approach can provide outcomes allowing the identification of a more rational approach of intervention. Laparoscopic Sleeve Gastrectomy is one of the principal bariatric techniques. The aim of the here reported activities consists on the evaluation of how bougie size influences stomach functionality after LSG. Computational tools can help medical staff in improving LSG applicability and reliability, and in individualizing the optimal post-surgical stomach configuration, without an invasive approach.

Keywords—Bariatric Surgery, FEM, Effectiveness Prediction

I. INTRODUCTION

N OWADAYS, obesity is a global health problem and its spread is increasing. It is associated with high BMI value (>30) and multiple co-morbidities. Approximately, 4 million deaths worldwide are attributable to obesity, most due to cardiovascular diseases [1]. The most effective treatment consists in bariatric surgery, leading to a higher weight loss than pharmacological or life-style interventions. Moreover, bariatric surgery has shown to induce remission of type 2 diabetes [2]. However, surgical procedures are not without risk and complications are frequent. Non-optimal intervention design and surgery invasiveness can compromise treatment success.

Some bariatric operations aim at reducing the volumetric stomach capacity (restrictive operations), others at decreasing the absorbing capacity (malabsorption operations) [3]. In case of restrictive operations, the lower dimension of the stomach leads to a greater stiffness. This effect has great consequences on the mechanical stimulation of mechano-receptors belonging to the gastric tissue, which are involved in the satiety response [4]. During and after food ingestion, mechanical and chemo-physical stimulation, biological transduction, neurological signal transmission, hormones levels and brain activations take part in complex phenomena which vehicles satiety and satiation [5].

Among the bariatric procedures, Laparoscopic Sleeve Gastrectomy (LSG) is the most performed bariatric surgery operation in the world [6] (Fig. 1a), accounting for 46% of all bariatric procedures [7]. LSG is a restrictive operation involving the removal of part the stomach, whose capacity is reduced from about 1500 ml to about 100 ml [8]. LSG is a primary and effective intervention, in fact about 82% of the patients lose more than 50% of the excessive weight [9] but complications, side effects, like bleeding and leaks, and weight regain phenomena suggest that improvements should be done [10].
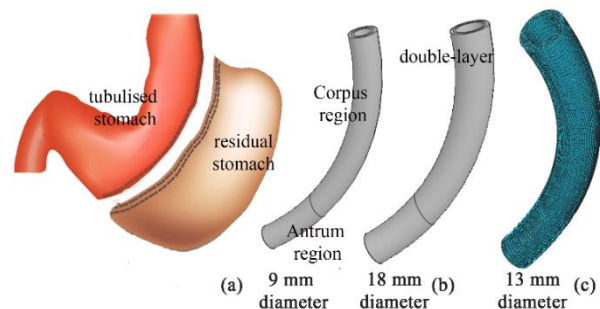
Fig. 1: A schematic view of the surgical operation results (a), examples of two virtual solid models of the tubulised stomach after LSG (9 and 18 mm bougie sizes) and the discretisation to finite elements of the 13mm-diameter stomach (c).

With regard to the LSG surgical planning and intervention, the decision of the tubulised stomach size falls on surgeon preference. In clinical practise, the bougie (i.e.: the tubular guide which is inserted within the stomach during the surgical dissection) size ranges from 9 to 18 mm [11], but the most common guides vary from 10.6 to 12.6 mm [12] .

The aim of this work is to rationally analyse how post-surgical parameters, as endoluminal pressure/volume and mechanical stimulation of stomach wall, change depending on the tubulised stomach size. Such post-surgical parameters deeply affect the effectiveness and the outcomes of the intervention.

II. METHODS

A. Virtual solid model generation and material assignment

Ten computational models of sleeve stomachs were developed simulating the use of different guide tubes to dimension the bougie size. The simulated inner diameters varied from 9 mm to 18 mm, while the length of the greater curvature was kept fixed at 15 cm (Fig. 1b). The geometries were simplified as hollow cylinders, but in future studies the sleeve stomach shape and dimension will be derived by the processing of clinical images, as MRI scan.

The models were divided in Antrum and Corpus regions, because most of the Fundus region is removed during LSG. According to the structural configuration of stomach wall, a

double-layer model describing both the submucosa-mucosa stratum and the muscular layers was chosen. The mechanical behaviour of the wall tissues was defined by means of an anisotropic visco-hyperelastic formulation, which allowed accounting for the fibre-reinforced configuration of the tissues, the non-linear elastic response and the time-dependent behaviour, as fully reported by Fontanella et al. [13]. The stress-strain relationship is reported in Eq. (1), where C is the right Cauchy-Green strain tensor, W is the strain energy function (Eq. 2), which specifies the instantaneous mechanical response of the tissue, and q^i are viscous variables (Eq. 3).

$$S(C,t) = 2\frac{\partial W(C)}{\partial C} - \sum_i q^i(C,t) \qquad (1)$$

$$W(C) = W_m(C) + W_f(C,a_0,b_0) \qquad (2)$$

$$q^i(C,t) = \frac{\gamma^i}{\tau^i}\int_0^t 2\frac{\partial W(C)}{\partial C}exp\left[-\frac{t-s}{\tau^i}\right]ds \qquad (3)$$

The composite configuration of gastric wall tissues suggested to define the strain energy function by means of different terms: the ground matrix contribution (Eq. 4) and the fibers term, which is further divided in contributions from longitudinal (Eq. 5) and circumferential (Eq. 6) fibers families:

$$W_m(C) = -p(J-1) + \left[\frac{c_1}{\alpha_1}\right]\{exp[\alpha_1(\tilde{I}_1 - 3)] - 1\} \qquad (4)$$

$$W_{fL}(I_4) = \left[\frac{c_4}{\alpha_4{}^2}\right]\{exp[\alpha_4(I_4 - 1)] - \alpha_4(I_4 - 1) - 1\} \qquad (5)$$

$$W_{fC}(I_6) = \left[\frac{c_6}{\alpha_6{}^2}\right]\{exp[\alpha_6(I_6 - 1)] - \alpha_6(I_6 - 1) - 1\} \qquad (6)$$

$\tilde{I}_1$ is the first invariant of the iso-volumetric part of the right Cauchy-Green strain tensor, as $\tilde{C} = J^{-2/3}C$, while J is the deformation Jacobian and p is the hydrostatic pressure, which is introduced to enforce tissue incompressibility condition. The parameter C_1 is related to the tissue initial shear stiffness, while α_1 specifies the stiffness increase with stretch. I_4 and I_6 are structural invariants that specify the square of tissue stretch along fibers directions a_0 and b_0, longitudinal and circumferential directions, respectively. The constitutive parameters C_4 and C_6 are constants that define the fibers initial stiffness, while α_4 and α_6 depend on fibers stiffening with stretch.

The inverse analysis of experimental tests on human and swine stomach samples led to the identification of constitutive parameters. In literature, most studies adopted an animal model to extract the mechanical properties of gastric tissues, as in Zhao et al. [14], but more reliable results can be obtained adopting human samples, as in Yehoshua et al. 2008 [8].

Experimentations have been performed on both stomach samples from swine animal models and surgical residuals from LSG bariatric interventions. Aiming to a reliable and effective identification of parameters, different experimental activities have been performed, accounting for different loading conditions [13], [15]. The preliminary action pertained to uni-axial tensile tests (Fig. 2a), which have been performed on tissue samples harvested along both longitudinal and circumferential directions. Such experimentations led to a

preliminary identification of model parameters. Subsequently, the development and the computational simulation of bi-axial flexural tests (Fig. 2b) made it possible to validate the parameters. Finally, insufflation tests have been performed to evaluate the structural behavior of the overall stomach structure. The computational analysis of such insufflation conditions allowed assessing the reliability of both the constitutive formulation and the developed computational models.
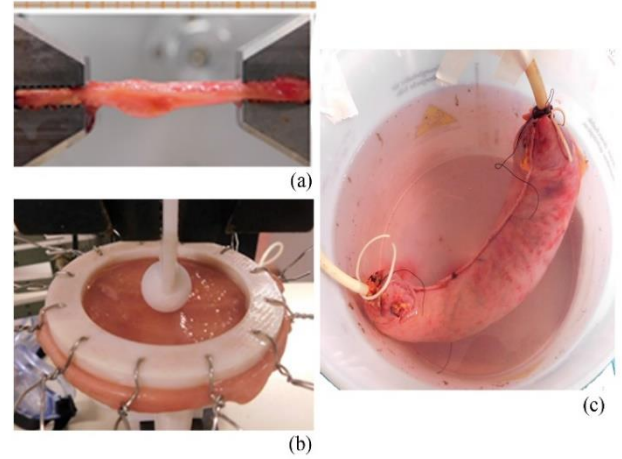
Fig. 2: Examples of experimental tests on human stomach samples. Tensile test (a), indentation test (b) and inflation test (c).

The identified parameters are reported in Table I, with regard to the fibres contributions. Different values have been identified for the different tissues form the different regions of the stomach.

With regard to ground matrix parameters, C_1 and α_1, they were assumed to be the same for all the parts and the layers. The identification led to 1.58 kPa and 1.05 values, respectively.

TABLE I
CONSTITUTIVE PARAMETERS

Part, Layer	C_4 [kPa], α_4 [-]	C_6 [kPa], α_6 [-]
Co, mu	2.04, 1.10	1.03, 1.10
Co, sm	2.14, 1.90	1.00, 1.90
An, mu	1.00, 1.30	1.00, 1.50
An, sm	1.02, 1.17	1.35, 1.32

Table I: Constitutive parameters of the anisotropic visco-hyperelastic formulation (Co: Corpus, An: Antrum, mu: muscolaris layer, sm: submucosa-mucosa layer).

B. Mesh operation and boundary conditions

The cylindric-shape virtual solid models of the post-surgical stomachs were imported in the general-purpose finite element code Abaqus Standard 2018 (Dassault Systèmes, Simulia Corp., Providence, RI) and hexahedral elements were adopted to mesh the models. The size of the elements was the same for all the models and was set at 1 mm along longitudinal and

circumferential directions, and 0.3 mm along radial direction. The total number of nodes varied from 80,000 to 150,000 (Fig. 1c). The gastroesophageal and gastroduodenal junctions were kept fixed, while to simulate the inflation process, a fluid filled-cavity was defined and a fluid cavity pressure reaching 5 kPa was imposed.

All the simulations were performed by means of a High-Performance Computing Server Fujitsu Primergy RX4770 equipped with two Intel Xeon E7 8890 v4 processors, 256 GB RAM and SSD HD. The mean time of execution of a simulation was about 4 hours running on 15 threads.

III. RESULTS

Since the research activity would lead to a computational tool usable by clinicians, the results highlighted how bougie size influence other surgical parameters, as basal volume, stomach stiffness and mechanical stimulation of gastric wall. At an inner pressure of 2 kPa, the basal volume varied from 7.5 to 49.2 ml according with the increase in sleeve stomach size (Fig 3).

Another relevant result consisted in the relationships between pressure and volume, reported in Figure 4. The pressure-volume trend remained almost exponential in all the configurations, but the slope decreased with higher sizes, showing the great influence of bougie size on stomach stiffness.

Computational analyses further allowed analyzing the influence of stomach conformation on wall tissues mechanical stimulation, as reported in Figure 5 for two tubulized stomachs (10 mm and 16 mm of inner diameter). Both the internal and the external layers were considered, in order to evaluate how mechanical solicitation varied. The distribution of maximum principal strain revealed higher values in the submucosa-mucosa stratum than in muscular layer for all the configurations analyzed.

The stress and strain belong to mechanical field and are not usually considered as surgical parameters. However, their magnitude and distribution influence the mechano-receptors response and the following influence on satiety and satiation [4], [16].
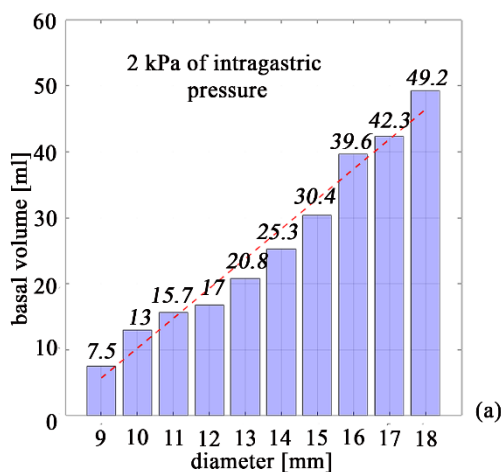
Fig. 3: Basal volumes calculated at 2 kPa of intragastric pressure for the different bougie sizes.
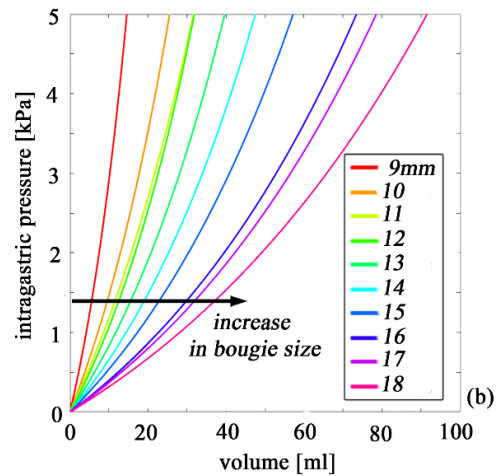
Fig. 4: Pressure-volume behavior for different bougie sizes (b).
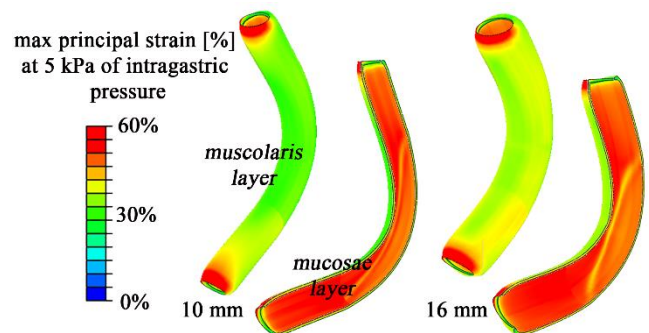
Fig. 5: Results of computational analyses: distribution of strain at 5 kPa of intragastric pressure in the outer and inner layers of two different tubulized model.

IV. DISCUSSION AND CONCLUSION

The here reported activities and results show the potentialities of bioengineering methods for the reliability assessment and the optimization of surgical procedures. With specific regard to LSG interventions, the performed investigations rationally proved the relationship between stomach functionality, as basal volume, stiffness and distribution of mechanical quantities, and the imposed tubulised configuration.

Most bariatric surgery operations aim is to reduce food and calories intake by modifying stomach capacity and stiffness and controlling meal induced satiety [17]. The mechanical stimulation of gastric wall takes part in the control of the release of satiety signals [18], but in past lot of studies were not able to give quantitative measurements.

Nowadays, computational biomechanics, coupled with experimentations, allows quantitatively analysing how loading conditions influence mechanical stimuli, and what changes bariatric procedures provide. Furthermore, computational finite element models allow investigating many different scenarios in a short time. Moreover, many quantities, which *in vivo* would be impossible to measure or would require very invasive equipment, can be recorded.

With regard to the overall activities that are under development at the University of Padova in the field of bariatric surgery, a synergic cooperation between bioengineers and clinicians has been established. The here reported activities provide a brief overview of preliminary results,

which aim to the reliability assessment of current surgical techniques.

The goals of the cooperation are wider, and focus on the implementation of a revolutionary approach to bariatric surgery, considering the maximization of surgical effectiveness and the minimization of surgical risks and complications. The action rests on a quantitative modelling approach of the gut-brain axis, and aims at providing relationships between ingested food, patient characteristics, surgical intervention and induced satiety. In this sense, it will be possible to plan the optimal intervention, as the surgical procedure that allows achieving satiety when the exactly required meal has been assumed.

ACKNOWLEDGEMENT

REFERENCES

[1] The GBD 2015 Obesity Collaborators, "Health Effects of Overweight and Obesity in 195 Countries over 25 Years.", *N Engl J Med*, vol. 377, pp. 13–27, 2017.

[2] D.E. Arterburn and A.P.Courcoulas, "Bariatric surgery for obesity and metabolic conditions in adults.", *BMJ*, vol. 349, pp. 1–11, 2014.

[3] W.J. Pories, "Bariatric surgery: risks and rewards.", *J. Clin. Endocrinol. Metab,* vol. 93, pp. 89–96, 2008.

[4] H. Piessevaux, J. Tack, A. Wilmer, B. Coulie, A. Geubel and J. Janssens, "Perception of changes in wall tension of the proximal stomach in humans.", *Gut*, vol. 49, pp. 203–8, 2001.

[5] A.H.. Sam, R.C.Troke, T.M. Tan and G.A. Bewick "The role of the gut/brain axis in modulating food intake", *Neuropharmacology,* vol. 63, pp. 46-56, 2012.

[6] L. Angrisani , A. Santonicola, P. Iovino, A. Vitiello, N. Zundel, H. Buchwald and N. Scopinaro, "Bariatric Surgery and Endoluminal Procedures: IFSO Worldwide Survey 2014.", *Obes Surg*, vol. 27, pp. 1–11, 2017.

[7] L. Angrisani, A. Santonicola, P. Iovino, G. Formisano, H. Buchwald and N. Scopinaro, "Bariatric Surgery Worldwide 2013.", *Obes Surg*, vol. 25, pp. 1822–32, 2015.

[8] R.T. Yehoshua, L.A. Eidelman, M. Stein, S. Fichman, A. Mazor, J. Chen, H. Bernstine, P. Singer, R. Dickman, N. Beglaibter, S.A. Shikora, R.J. Rosenthal and M. Rubin, "Laparoscopic Sleeve Gastrectomy—Volume and Pressure Assessment", *Obes Surg,* vol 18. pp. 1083–1088, 2008.

[9] Praxedes, A. Andre, E. Rosa, C. Trindade, J. Baptista and L. Cortez, "Analysis for the Success Rate of Patients after Laparoscopic Sleeve Gastrectomy.", *J Obes Weight Loss Ther*, vol. 7, pp. 8–11, 2017.

[10] N. Sakran, A. Raziel, O. Goitein, A. Szold and D. Goitein, "Laparoscopic Sleeve Gastrectomy for Morbid Obesity in 3003 Patients: Results at a High-Volume Bariatric Center.", *Obes Surg*, vol. 26, pp. 2045-50, 2016.

[11] A.Y.C. Tsai and A. Osborne, "Bariatric surgery", *Surg (United Kingdom)*, vol. 35, pp 658–64, 2017.

[12] R.J. Rosenthal, International Sleeve Gastrectomy Expert Panel, A.A. Diaz, D. Arvidsson, R.S. Baker, N. Basso, D. Bellanger, C. Boza, H. El Mourad, M . France, M. Gagner, M. Galvao-Neto, K.D. Higa, J. Himpens, C.M. Hutchinson, M. Jacobs, J.O. Jorgensen, G. Jossart, M. Lakdawala, N.T. Nguyen, D. Nocca, G. Prager, A. Pomp, A.C. Ramos, S. Shah, M. Vix, A. Wittgrove and N. Zundel, "International sleeve gastrectomy expert panel consensus statement: Best practice guidelines based on experience of >12,000 cases.", *Surg Obes Relat Dis*, vol. 8, pp. 8-19, 2012.

[13] C.G. Fontanella, C. Salmaso, I. Toniolo, N. de Cesare, A. Rubini, G.M. De Benedictis, E.L. Carniel, "Computational Models for the Mechanical Investigation of Stomach Tissues and Structure.", *Ann Biomed Eng*, vol. 47, pp, 1237-49, 2019.

[14] J. Zhao, D. Liao, P. Chen, P. Kunwald and H. Gregersen, "Stomach stress and strain depend on location, direction and the layered structure.", *J Biomech*, vol. 41, pp. 3441–7, 2008.

[15] E.L. Carniel, A. Frigo, C.G. Fontanella, G.M. De Benedictis, A. Rubini, L. Barp, G. Pulchino, B. Sabbadini and L. Polese, "A biomechanical approach to the analysis of methods and procedures of bariatric surgery", *J Biomech*, vol. 56, pp. 32-41, 2017.

[16] S. Delgado-Aros, F. Cremonini, J.E. Castillo, H.J. Chial, D.D. Burton, I. Ferber and M. Camilleri, "Independent Influences of Body Mass and Gastric Volumes on Satiation in Humans.", *Gastroenterology*, vol. 126, pp. 432–40, 2004.

[17] S.C. Woods, "Gastrointestinal Satiety Signals I. An overview of gastrointestinal signals that influence food intake", *Am J Physiol Gastrointest Liver Physiol*, vol. 286, pp. G7-13, 2004.

[18] H.R. Berthoud, P. Lynn and L. Blackshaw, "Vagal and spinal mechanosensors in the rat stomach and colon have multiple receptive fields." *Am J Physiol Regul Integr Comp Physiol*, vol. 280, pp. 1371-81, 2001

Portable Normothermic Perfusion System for laboratory test of Microwave Devices

Mattia Dimitri[1*], Fabio Staderini[2], Sara Aquino[1], Lucrezia Mazzantini[1], Fabio Cianchi[2] and Andrea Corvi[1]

[1]*Department of Industrial Engineering, University of Florence, via di Santa Marta 3, Florence, Italy*
[2]*Department of Experimental and Clinical Medicine, University of Florence, S. Marco Square 4, Florence, Ital*

staderini.fabio@gmail.com, { mattia.dimitri, sara.aquino, lucrezia.mazzantini, andrea.corvi, fabio.cianchi} @unifi.it

Abstract -- The need to keep livers as long as possible awaiting transplantation and to conduct laboratory tests to assess the differences between perfused and non-perfused organ using a microwave thermal ablation tool, required to implement a previous perfusion system normothermic. This required the implementation of new components necessary for the survival of the organ and for the transportability of the structure, necessarily increasing its dimensions. The new perfusion system allowed to perform thermoablation tests on ex vivo pig liver using two non-internally cooled tools (14 gauge, 17 gauge) fed at 120 W. The results showed that in the case of a perfused organ its surface temperature near the tool tends to stabilize, unlike what happens in the non-perfused organ. Moreover it is observed that the ablation area undergoes a reduction of about 30% in the radius and of about 55% in the volume passing from non-active perfusion to active perfusion.

Keywords - Perfusion System, Ex-vivo Tissues, Liver Transplant, Thermal ablation , Microwave

I. INTRODUCTION

The liver has important regenerative characteristics, such as to allow the removal of some of its parts without compromising its functioning. However, situations may arise in which the organ is so compromised as to require replacement by transplant. This procedure is based on the resection of a part of the donor's liver to be implanted in the patient to regenerate itself completely.

This intervention, a highly successful therapy for the last three decades, has become one of the main treatments for late-stage liver diseases, with over 11,000 transplants performed annually worldwide. As a result, the procedure has become the victim of its own success: more and more patients require transplantation, but the quantity of available organs has remained practically constant. The

through the combination of a continuous circulation of metabolic substrates for ATP regeneration and product removal waste [1] . As concerns the liver, over the years equipment such as Liver Assist, or perfusion systems for the maintenance of the organ while awaiting transplantation, have been designed and are currently on the market [12]. They allow a real regeneration of the hepatic tissue as they provide all the components necessary to develop their own functions, reproducing as much as possible the physiological environment, even if the organ is partially damaged [1].

With reference to the anatomy of the organ, the system

main source of organs comes from donors with heart still active, although in the presence of brain death (heart-beating donor, HBD), from which the organs can be removed with a minimum interruption of oxygenation before cooling and its conservation [1]. However, the increase in request has led to the need for additional sources: both organ transplants from living donors (elderly, obese) and marginal use of organs from cadavers have entered clinical practice (patients without a heartbeat) [2], [3], [4]. They are known to be more inclined to malfunctions [5], [6], [7], [8], causing up to 40% of them to be previously rejected as a potential cause of problems in the event of a transplant [9]. In recent years, the increasing use of these organs has been accompanied by a growing interest in strategies to optimize conditions during the storage period, allowing better results to be achieved: a prolonged graft survival, a decrease in malfunctions and a consequent lower need for second transplants. The standard procedure involves a "static cold storage" of the organ taken, according to the principle of slowing down the metabolism and reducing cellular swelling thanks to the composition of the solution used for storage. However, this method can cause various damage to the liver in the later stages of the procedure, from storage to perfusion before grafting [1], [10].

Since the mid-twentieth century, the effectiveness of normothermic perfusion has been demonstrated following tests on various organs, which has allowed them to be kept alive for several days thanks to adequate oxygenation [11]. The main difference between cold storage preservation and normothermic preservation is that the metabolism of the organ is maintained

includes two entrances through the portal vein and the hepatic artery, and two exits represent from a suprahepatic inferior vena cava and intrahepatic inferior vena cava. The circuit consists of a main tank in which the fluid temperature is kept constant at 38 ° C and from which three branches originate: the first to the venous reservoir; the second which gives the fluid the physiological characteristics towards the hepatic artery, through an oxygenator; the third towards the portal vein.

The perfusor shown is developed starting from a normothermic perfusion system born from the need to perfuse a swine liver with physiological heparinized to

conduct experimental microwave thermoablation tests without the need to access the enclosure.

II. OBJECTIVES

The objectives of a system for liver perfusion are mainly to keep the organ alive for as long as possible before transplantation, an improvement in liver function and an increase in survival of recipient patient.

In the liver it's possible to study the phenomena that involve the interactions between the cellular component of the hepatocytes and the parenchymal cell component, including the cells of the bile ducts, the connective cells and those of the capillary endothelium. Thanks to the maintenance of an adequate blood perfusion it's possible to control or study physiological parameters such as blood pressure and perfusion speed.

The main objective of the developed normothermal perfusor is to demonstrate the successful perfusion of the liver by the infrared thermal-camera (FLIR A320G) and to evaluate the effect of perfusion during microwave thermal thermoablation test [14].

Due to intrinsic limits of the previous perfusor system [13] it is also necessary to implement the device by adding a suitable heater and an oxygenation circuit to evaluate a possible future use for organ transport even if today the perfusor has a strictly research purpose. For the choice of the components, a study was carried out on the desired flow rates, pressures and temperatures and a market survey that allowed the selection of components with a high quality - price ratio.

So that, it has been necessary to introduce the following improvements:

- Integrate an organ oxygenation circuit inside the system. This requires the addition of two components, such as an oxygen concentrator and an oxygenator.
- The introduction of a heating system that does not damage the erythrocytes.
- Identify a system able to guarantee a constant flow rate in portal vein equal to the physiological value of 900 ml/min – 1200 ml/min.
- Identify a fluid with rheological characteristics like blood.
- Plan a battery to be integrated into the system to ensure perfusion during transport.

It was therefore essential to modify the configuration of the system, necessarily going to increase its size to allow the introduction of the new components and relocating the present constituent elements. In addition, the liver housing inside the device has been shifted to the upper part, for both practical and hygienic reasons.

The new structure is made entirely in aluminum and plexiglass, making it extremely light.

III. MATERIALS AND METHODS

A. Perfusor Structure

The addition of the new components required the enlargement of the structure. For practical reasons the structure has been designed on two levels: the upper part houses the organ, while in the lower part are housed the various components of the perfusion circuit, such as the oxygenation circuit, the two centrifugal pumps, a peristaltic pump and the heating system with its 5-liter capacity reservoir. The main reservoir sizes are of 200x100x150 mm and 5 mm thick with a capacity of 1.5 l, are arranged. To make the structure light and therefore more easily transportable, it is made entirely of aluminum, while the 2 mm thick plexiglass panels make the various components visually accessible. The presence of four self-locking wheels further facilitates transport.

The structure has a size of 900x500x500 mm, of which the upper part of 200x500x500 mm, and the lower part of 500x500x500 mm. The liver case consists of a plexiglass reservoir measuring 150x500x300 mm and 5 mm thick.
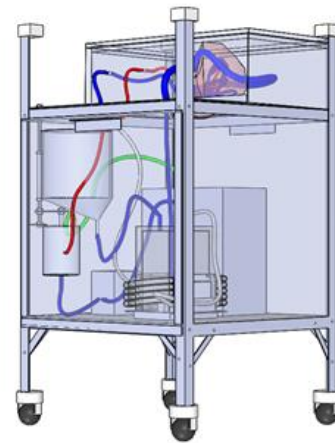
Figure 1: Perfusion Structure.

B. Oxygenation Circuit

To keep the liver alive, it is necessary to integrate a circuit for the oxygenation of the blood inlet in hepatic artery with which it is perfused into the system. This requires the addition of two components, such as an oxygen concentrator and an oxygenator. The first step was to conduct a bibliographic analysis to identify the components necessary for the realization of a normothermal perfusion device for the liver. A market analysis was therefore performed in order to select suitable components for this purpose, at a reasonable price, such as:

Oxygen concentrator: SimplyGo PHILIPS - RESPIRONICS;

Oxygenator: Affinity Pixie - MEDTRONIC.

The chosen oxygen concentrator is a portable device capable of delivering both pulsed and continuous flow oxygen (from $0.5 \, l/min$ to $2 \, l/min$), a mandatory mode

for the perfusion of taken organs. The device has the following operating characteristics:
Weight included battery 4.5 kg;
Operating temperature 5 - 40 ° C;
Battery life 3 h (pulsed flow) and 0.9 h (continuous flow at 2 l / min);
Internal antibacterial filter;
Lithium ion battery 14.4 VDC 6.600 mAh (Li-Ion), 0.7 kg;
Charging time about 2-3 h (completely discharged battery).

Figure 2: Oxygen Concentrator.

The Affinity Pixie Oxygenation System delivers performance and versatility for neonates, infants and small children requiring cardiopulmonary bypass at flow rates up to 2.0 L/min. It is composed of an oxygenator and a venous reservoir.
This pediatric hollow fiber oxygenator, which is a microporous disposable device with hollow fibers for gaseous exchange with plasmaresistent polypropylene fibers and integral PET heat exchanger. It presents the following characteristics:
Max gas / blood ratio 2: 1
Oxygenator membrane surface 0.67 m2
Recommended blood flow rate 0.1-2.0 l / min
Max water pressure 206 kPa (1550 mmHg)
Max nominal blood pressure 100 kPa (750 mmHg)

The venous reservoir is a disposable device for blood collection and storage during extracorporeal circulation. Its characteristics are:
Tank capacity 1200 ml
Recommended blood flow rate 0.1-2.0 l / min
Min operating level 20 ml
Max nominal pressure +20 mmHg / -100 mmHg.

Figure 3: Oxygenator.

To obtain a pulsed flow typical of hepatic artery flow, a peristaltic pump is used which takes the fluid from the heating circuit reservoir and sends it to the oxygenator inlet. The peristaltic pump is upstream of the oxygenator to prevent the presence of lumps and air bubbles entering the organ. Despite its location in the oxygenation circuit, fed at 5V, it is possible to reproduce the physiological values of pressure and flow rate.

C. Heating System

The fluid in the reservoir circulates in the pipes passing through the system thanks to a recirculation pump, fed at 5V. A thermostat powered by 12V 10A, detects the temperature of the fluid, through a probe immersed in the reservoir and in contact with the wall, allowing the activation of the plates to guarantee a temperature of 38-39 ° C.
The thermostat has the following characteristics:
Measuring range: -40 / 120 ° C;
Measurement accuracy: 0.1 ° C;
Measurement error: + 0.5 ° C;
Operation temperature: -20/70 ° C.
The heating system is composed of two Joule effect plates made of PTC aluminum, secured by M3 screws to milled aluminum plates to allow for the housing of 304 stainless steel, cheap and compatible (ASME Publication, 1980). The plates have been made of aluminum by virtue of their characteristics in terms of lightness, thermal conductivity, economy and ease of processing. Hemocompatible silicone tubes are mounted by interference on steel tubes of the same diameter to ensure continuity of flow.
Two Joule Effect PTC Aluminum Plates have the following characteristics:
Power: 60W;
Voltage: 12 V;
Temperature: 180 + 10 ° C.
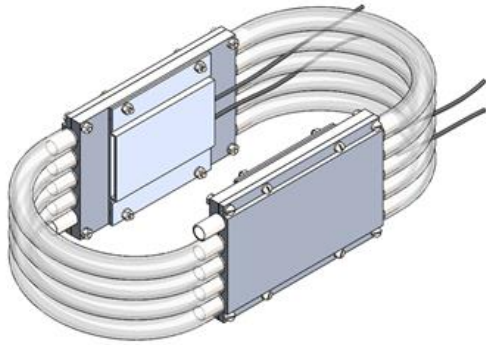
Figure 4: Heating System.

D. Constant Flow Rate in the Portal Vein

It has been adopted a centrifugal pump fed at 5V located in the heating system reservoir to guarantee a constant flow rate in the portal vein, given the presence of losses neglected in the previous configuration. Tests have been carried out to assess the most suitable voltage to guarantee values that best match the physiological values of flow and pressure (tests performed at 3V, 4.5V, 5V, 6V, 7.5V, 9V, 12V).

It is reliable, biocompatible, low cost and not re-sterilizable. Its characteristics are:

- Voltage DC: 12 V;
- Power: 4.8 W;
- Max flow rate: 240 l / h;
- Operation temperature: 0-60 ° C;
- Max lifting high: 3 m.

E. Non - Newtonian Fluid

In order to evaluate the functioning of the system avoiding the use of blood, a fluid was identified that was able to simulate its behavior. The blood has a dynamic viscosity of about 3 cP. To make a fluid capable of reproducing the rheological properties of blood in terms of viscosity and density, it is possible to use distilled water, glycerol and cornstarch. Since the blood has a physiological temperature of about 37 °C, the percentages of the constituent elements of the fluid must therefore be determined.

With a capillary viscometer, it is possible to measure the kinematic viscosity [m2∕s], from which it is possible to calculate the dynamic viscosity [cP]. It was estimated that at 37 °C the fluid with a viscosity as close as possible to the blood is composed of:

70% distilled water; 30% vegetable glycerol. Dynamic viscosity $\mu = 3.52 \pm 0.01$ cP

70% distilled water; 30% vegetable glycerol; 1% cornstarch. Dynamic viscosity $\mu = 3.52 \pm 0.15$ cP.

Therefore, since about 3.5 L of fluid is circulated in the system in question, it is possible to simulate blood using 2450 mL of distilled water and 1050 mL of glycerol (and 35 mL of cornstarch).

F. Electronic and battery components

A lithium ion battery has been designed for the perfusion system to be autonomous during the organ transport phase. The choice of these cells rather than those of nickel-cadmium or nickel-metal-hydride depends on the highest level of safety, energy density, efficiency, occupied space and costs.

A 6s-3p configuration was chosen to power all the components of the perfusor. The wiring diagram for battery management and component operation was printed on a dedicated PCB which controls: the Arduino Nano 5V 16MHz board, the five Hall effect current sensors - ACS712 20 A, the 16x2 5V LCD display to display the battery charge level, the 22 kΩ + 4.7 kΩ voltage divider, the buzzer and the 10k trimmer contrast display regulator. Each component to be powered was then connected to the PCB using the appropriate DC-DC power converter.

The batteries chosen are the Samsung INR18650 - 35E 3500mAh, with a diameter of (18,55 ± 0.1) mm, a high of (62,25 ± 0,1) mm, and a weight of (48 ± 1) g. Their features are:

- Nominal Capacity: 3500 mAh;
- Minimum Capacity: 3350 mAh;
- Nominal Tension: 3,6 – 3,7 V;
- Charging Voltage: 4,2 V;
- Discharge Current: 8 A;
- Max Discharge Current:13 A;
- Charging Current: 0,6 C 2000 mA;
- Final Discharge Voltage: 2,65 V
- Pluspol: FlatTop
- Chemistry: LiNiCoAlO2.

The system is housed in a case to allow transport even separately from the perfusion device.
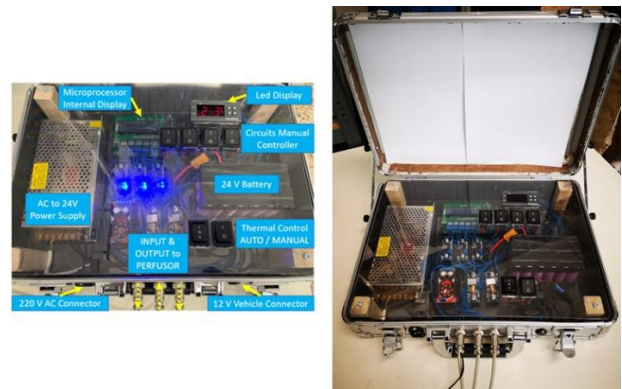
Figure 5: Electronic Components.

G. Starter Protocol

As a first step it is necessary to fill the main reservoir with the perfusion fluid to then activate centrifugal pump of the heater system. Therefore the circuit preheating phase starts. It is necessary to carry out a gradual heating of the blood to avoid the onset of too high thermal divergences in the heat exchanger, as with instantaneous ΔT too high between the wall and the adjacent layer of fluid meatus the formation of clots may arise: this it would cause a loss of efficiency of the exchanger and of the amount of blood useful for perfusion. This phase ends upon reaching the physiological temperature value (38 ° C) set and monitored through the RP Thermocouple and the RA Thermocouple and is kept constant until the completion of the cannulation and deposit phase of the explanted organ.

H. Thermal Ablation Tests

Two TATO[1] thermal ablation systems no-internally cooled 14-gauge and 17-gauge applicators (NIC) were tested. The experiment was carried out on fresh ex vivo swine livers recovered from animals in the food chain: this would make it possible to obviate important ethical implications and also reduce the economic burden compared to the most common in vivo studies.
The liver was taken and immediately connected to the perfusion apparatus by means of flexible tubes sutured to the vessels.
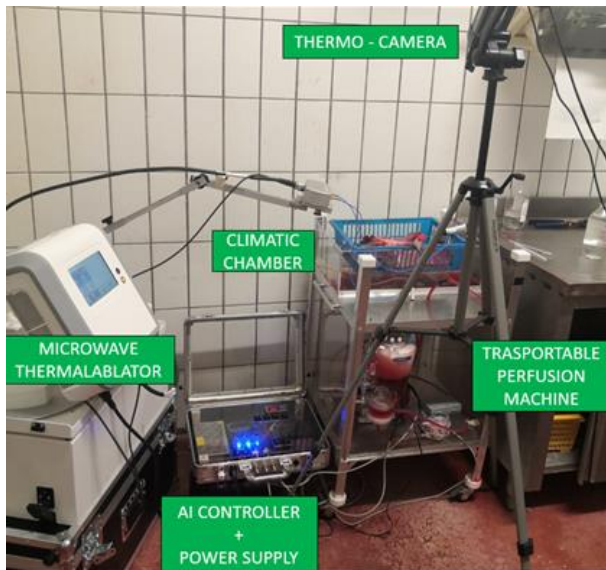
Figure 6: Setup System.

The tests were conducted on an ex vivo organ, perfused and not perfused, in order to evaluate the coagulation divergences. The tool is powered at 120 W for 10 minutes.

IV. RESULTS

Plotting on a time-temperature graph the thermal trend acquired by the thermal-camera during the tests it's clear that:
when perfusion is active, the surface temperature of the liver near the tool tends to stabilize reaching lower temperature peaks than in the case in which the perfusion does not is active;
when perfusion is not active, the temperature continues to grow over time without stabilizing itself following an almost linear trend.
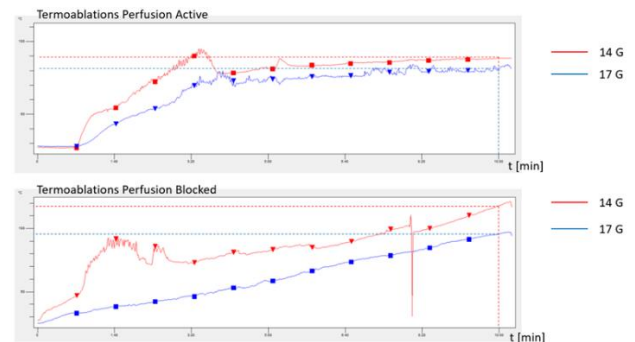
Figure 7: Tests Thermical Trend

The preliminary results obtained by comparing ablation performed in the non-perfused and perfused state show a reduction of about 30% in the radius and about 55% in the volume passing from one to the other, regardless of the size of the tool.
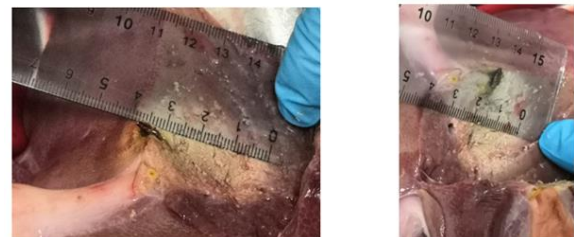
Figure 8: 14 Gauge Non-Perfused Liver.

---

[1] TATO (Thermal Ablation Treatments for Oncology) is a multi-applicator system developed from a scientific/industrial collaboration between the University of Florence and the biomedical society.
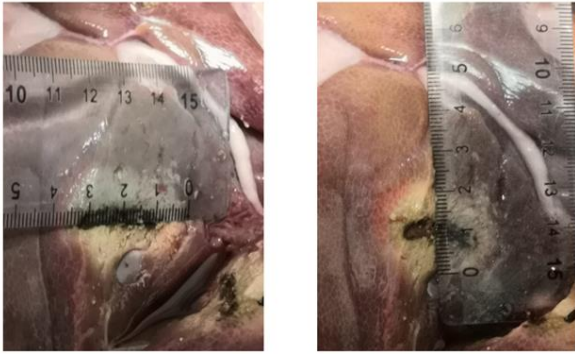
Figure 9: 14 Gauge Perfused Liver.
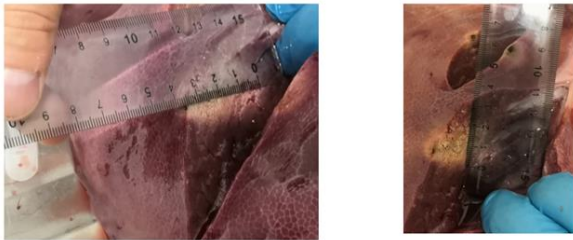
Figure 10: 17 Gauge Non-Perfused Liver.

Figure 11: 17 Gauge Perfused Liver.

The availability of a thermoablation model based on an ex vivo perfused liver could lead to a more detailed investigation into the effect of heat dissipation in peripheral and central sites of vessels. This model could also be used to emulate laparotomic surgical ablation, which is rapid and economical, allowing the surgeon to rotate the liver within its anatomical environment, manually protect the heat-sensitive organs (intestine) and easily insert grouped applicators to treat large non-spherical ablations. The perfusion device used to ensure blood flow within the explanted swine liver makes it possible to easily modify the perfusion rate of the hepatic parenchyma by emulating fibrosis, cirrhosis or steatosis in order to study the influence on volume and on ablation size. However, the preliminary results obtained with this study are too limited to obtain statistical relevance: the final validation of the proposed approach will therefore require a further and more in-depth experimental campaign.

V. DISCUSSION

The plates are designed to avoid haemolysis of red blood cells due to the effects of thermal osmosis, a phenomenon comparable to a force capable of guiding the moleculars water transport in cellular structures.

Maintaining small values of ΔT through the cell membrane can generate high values of stationary ΔP (if $\Delta T = 0.01 \,°\, C$, $\Delta P = 1.3$ atm). The extent of thermal osmosis depends on the transfer energy of the water molecules, Q^*, from the outside of the membrane inside the cell $\left(\Delta P = - \frac{Q*}{VT} \Delta T , V = Molar\ Volume \right)$. The induced ΔP can determine the swelling of the cells and causes its rupture if the ΔP is large and associated with a rapid T. For times less than 2 µs, it results:

- If $\Delta T = 0.05 \,°\, C$ → No visible damage;
- If $\Delta T = 0.5 \,°\, C$ → Hemolysis.

The designed system is such that the instantaneous ΔT between fluid and plates is less than 0.5 ° C.

Our main objective was to create a compact and transportable system able to preserve the physiological behavior of the liver once it was removed, to allow the implantation in a receiving patient.

The experimental tests performed allowed to verify the stability of the system in terms of pressure, flow rate and temperature. Experimental tests were performed using a simplified liver model made through 3D printing and with the sole function of heat exchanger.

The subdivision of the device into three distinct modules allows the possible replacement of the individual components in the event of need.

The positioning of the liver in the upper part allows better accessibility and guarantees greater sterility of the organ.

The aluminum and plexiglass structure ensure that the device is light and easily transportable even thanks to the wheels.

VI. CONCLUSION

We have designed a light and easily transportable device capable of perfusing an explanted liver with a fluid with characteristics in terms of viscosity similar to those of blood.

The tests carried out using a mockup instead of a real liver made it possible to verify, using electronic sensors, the correspondence with the physiological values in terms of pressure, exposure and temperature.

However, it was not possible to conduct in vivo validation tests on laboratory animal guinea pigs as it requires a prior analysis of reliability and criticality of the system. This would also allow an optimization of the electronic part by implementing safety devices and monitoring of the variables.

This device would also allow testing with energy surgical tools to evaluate the coagulation efficacy on perfused ex vivo tissue and could be used for cell culture processes on a 3D scaffold.

REFERENCES

[1] Ruiter S.J.S., Heerink W.J., De Jong K.P., (2019). Liver microwave ablation: a systematic review of

various FDA-approved systems. *Eur Radiology 29(8):4026-4035*

[2] Meloni M.F. et alii, (2017). Microwave ablation in primary and secondary liver tumours: technical and clinical approaches. *International Journal of Hyperthermia 33(1): 15–24.*

[3] Yung J., Liang P., (2017). Status and advancement of microwave ablation in China. *International Journal of Hyperthermia Vol. 33, 2017 - Issue 3*

[4] Kodama H., (2018). High power microwave ablation of normal swine lung: impact of duration of energy delivery on adverse event and heat sink effects. *International Journal of Hyperthermia 34(8):1186-1193.*

[5] Biffi Gentili G, Ignesti C, Tesi V. (2014). Development of a novel switched-mode 2.45 GHz microwave multi-applicator ablation system. *International Journal of Microwave Science and Technology, Article ID 973736*

[6] De Cobelli F et alii, (2017). Microwave ablation of liver malignancies: comparison of effects and early outcomes of percutaneous and intraoperative approaches with different liver conditions. *Medical Oncology 34(4)*

[7] R. Ravikumar, et alii, (2016). Liver transplantation after ex-vivo normothermic machine preservation: a phase 1 (first-in-man) clinical trial. *American Journal of Transplantation,* pp. 1779-1787.

[8] F. Romano et alii, (2012). Bleeding in hepatic surgery: sorting through methods to prevent it. *HPB Surgery, vol. 2012, 12pg, Article ID 169351.*

[9] Kalisvaart M, et alii, (2018).The impact of combined warm ischemia time on development of acute kidney injury in donation after circulatory death liver transplantation: stay within the golden hour. *P. Transplantation. 102(5):783-793.*

[10] M. Dimitri et alii, (2018). A new microwave applicator for laparoscopic and robotic liver resection. *Internal Journal of Hyperthermia, vol 36 : 75-86.*

[11] M.Bedoya et alii (2012). Microwave ablation energy delivery: Influence of power pulsing on ablation results in an ex vivo and in vivo liver model. *Medical Physics 41 (12).*

A novel step counting algorithm using a head-mounted sensor

A. Cristiano[1], A. Sanna[1], and D. Trojaniello[1]

[1]*Center for Advanced Technology in Health and Wellbeing, IRCCS San Raffaele Hospital, Milan, Italy*

Abstract — Step counters have the potential to measure activity, to provide valuable information related to the quality of life and to encourage an active and healthy lifestyle. However, to spread their usage by people of all ages, step counters require to be accurate and as much as possible unobtrusive and practical for a daily use. The validity of step counters has been verified by several study in literature; their accuracy has been found strictly related to their placement and, feet and trunk have been shown as the ideal locations for such devices able to detect the number of steps performed. Although feet-worn and trunk-worn devices can benefit from a favourable location that makes them accurate, they may reveal unpractical in everyday life. The ongoing development of virtual reality devices significantly increased the applications of head-mounted technologies laying thus the groundwork for the integration of activity tracking functions in daily used accessories (e.g. glasses). The current study presents a step counting method using a head-mounted inertial measurement unit (IMU). Data from five healthy young subjects wearing the head-mounted IMU have been acquired in controlled conditions in the presence of a tester. Participants were asked to walk up to 40 steps (i.e. *reference value*) along a straight path at their comfortable speed and to repeat the test four times at different head orientations (i.e. looking forward, looking down, looking left and looking right). The method presented in the study has been evaluated in terms of percentage error with respect to the actual steps number and then compared with three existing step counting methods (previously validated on trunk) applied to head accelerations acquired during the experimental procedure. The results showed that the proposed method detects the number of steps with an average percentage error lower than 1% and it proves to be the most robust across all examined methods. Moreover, no great disparity is observed among methods under the same testing conditions although a slight increase of error is registered when the head is down while walking. Despite some limits related to the poor number of subjects involved and the restricted variety of test conditions examined (i.e. self-selected comfortable walking speed and straight path, only), the current study confirms the feasibility of using a miniaturized head-mounted device as step counter.

Keywords — Step counting, activity monitoring, motion sensors, head-mounted device.

I. INTRODUCTION

THE monitoring of daily physical activity (PA) is a key aspect in the evaluation of peoples quality of life. A regular PA contributes to the primary and secondary prevention of several chronic diseases that start in childhood and augment with the age according to the relation between the volume of PA and the health status [1-3]. Nevertheless, physical inactivity (i.e. absence of PA) levels have been identified as a risk factor of non-communicable diseases (NCDs) which include cardiovascular and respiratory disorders [2]. The interest in daily PA monitoring in people of all ages so to promote an increase of PA levels worldwide is therefore strong.

Starting in the mid-1900s, researchers became interested in using steps to quantify PA since they are intuitive, easy to measure and objective [3] and correlations between steps per day and health variables have been demonstrated [4-6].

Step counting in free-living conditions is mostly entrusted to accelerometers embedded within wristbands, bracelets and belts [7-14] that wirelessly send data to a mobile computing device, which can use the signals to recognize the number of steps performed. Nowadays thanks to their ever-decreasing cost and ease of deployment, step counters are getting a wide acceptance. However, their abandonment after a relatively short time of usage is recurring. The main reasons of that behaviour lie in the aesthetics, ease of use, functionality and practicality of the device as well as in the accuracy perceived by users [14]. The accuracy of step counters is indeed dependent on the device location; higher accuracies have been achieved with feet-mounted and trunk-mounted sensors that however could appear uncomfortable and obtrusive in everyday routine. More common but less accurate devices are the step counters worn at wrist: indeed, they usually record extra steps because of extraneous arm movements in real life environments [3]. In that regard, other placements, i.e. head location, which could be more practical for the integration of step counting functions in daily worn accessories (i.e. glasses and headset) have been explored in only few studies [15, 16] although they could offer an interesting solution in the activity monitoring context [17]. A recent study confirmed the hypothesis that already existing step counting methods, validated on trunk, could be applied to the head acceleration in order to accurately identify steps [18].

The objective of the present study is twofold: (1) to present a new head sensor based step counting method, and (2) to compare its performances with already validated methods on trunk [19-21] applied to head accelerations [18].

The paper is structured as follows. The head-mounted accelerometer, the sample population, the acquisition protocol, the methods and data analysis procedure are described in Section 2; the gained results are reported in Section 3 while the discussions on the gained insights in Section IV and, finally, the conclusions are presented in Section V.

II. MATERIALS & METHODS

A. Equipment

An IMU (LSM6DSL, ST) featuring a tri-axial accelerometer and a tri-axial gyroscope (size: 2.5 mm x 3 mm x 0.83 mm, ±6g) enabling always-on low-power features was used. Sampling frequency (f_s) was set at 50 Hz. The IMU was attached on the left side of subject's head (Fig. 1) with X, Y

and Z axes pointing downward, backward and to the left respectively to measure the accelerations (±2g) along the three directions. During the acquisitions, the IMU raw data were collected through the mobile app Sensor Log.
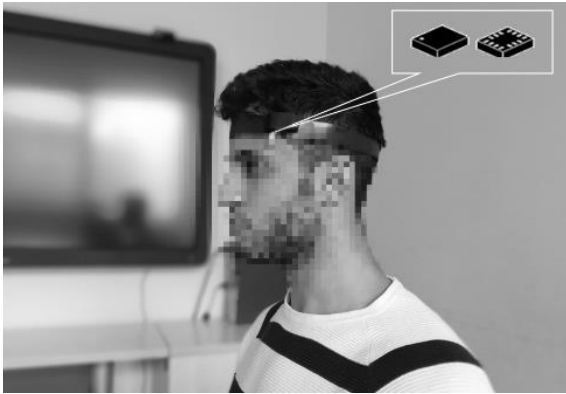

Fig. 1: IMU's placement on subjects' body

B. Sample population

Five healthy subjects took part to the study. Subjects were enrolled among students and workers of San Raffaele Hospital, in Milan. Demographic characteristics of sample population are summarized in Table 1 (m: mean, sd: standard deviation). All participants provided informed written consent edited in accordance to the Declaration of Helsinki.

TABLE I
SUBJECTS' DEMOGRAPHIC CHARACTERISTICS

Style	# Number	Age [years] ($m \pm sd$)	Height [m] ($m \pm sd$)	Weight [kg] ($m \pm sd$)
Male	2	29±6	1.81±0.04	81±4
Female	3	29±2	1.67±0.02	62±2

C. Experimental procedure

Subjects have been invited in an ad-hoc furnished room in San Raffaele Hospital to participate in the experiments. Here, in presence of a tester, subjects were asked to maintain an upright posture for 20 seconds and then to walk at their self-selected comfortable speed along a predefined walkway up to 40 steps (i.e. *reference value*). Each subject performed the walking task four times (i.e. tests):

i)   looking forward (LF)
ii) looking down (LD)
iii) looking left (LF)
iv) looking right (LR)

D. Methods

Four methods have been applied to the signals acquired from the head-mounted IMU to detect the number of steps performed by participants during the tests. As previously reported, the method proposed in the current study (head method, HM) was, indeed, compared with methods validated on trunk (trunk methods, TMs) whose feasibility to accurately count steps whether applied to head accelerations, save for some slight modifications, was verified in a recent study [18].

HM. The method aimed at determining the steps performed during overground walking using a peak detection procedure applied to head vertical acceleration, a_V. According to the proposed method, steps correspond to positive peaks, *pos Pks*, between two consecutive negative peaks, *neg Pks*, (i.e. peaks of the overturned signal) in the signal a_{V_20Hz}, that is obtained by applying a 4th order Butterworth low-pass filtering at 20 Hz to a_V (Fig. 2). Two thresholds (th_p and th_n) have been used to identify *Pks*. In particular, th_p was employed for *pos Pks* while th_n for *neg Pks* and they are defined using the mean (m_{av_20Hz}) and the standard deviation (sd_{av_20Hz}) of a_{V_20Hz}:

$$th_p = m_{av\_20Hz} + 1 \cdot sd_{av\_20Hz} \qquad (1)$$

$$th_n = m_{av\_20Hz} - 0.5 \cdot sd_{av\_20Hz} \qquad (2)$$
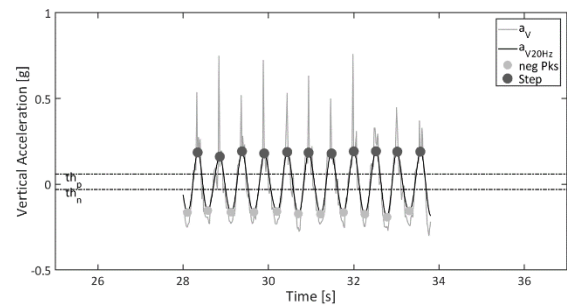
Fig. 2: Step counting according to HM

TM1. According to the authors [19], steps correspond to the zero crossing points, *ZCs*, in the signal b that is obtained by applying the sliding window summing technique (*SWS*) on acceleration norm, a_{NORM}. The values of the a_{NORM} falling within a sliding window of fixed length (N=10), less than the duration of the detected steps, were summed. The *SWS* signal was affected by walk motion and gravity. The difference of the resulting *SWS* and those obtained N samples earlier was then computed to remove the gravity. The signal b as a smooth curve crossing periodically the zero value is thus obtained and the steps identified. The detected steps are denoted by the dark grey full circles in Fig. 3.
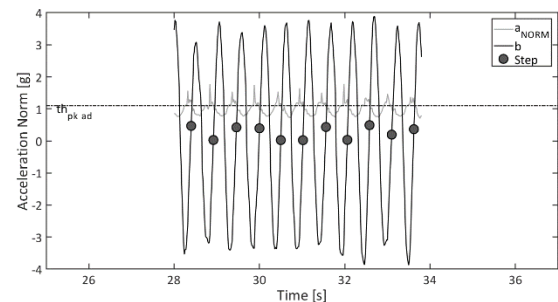

Fig. 3: Step counting according to TM1

TM2. According to the study [20], steps correspond to the *Pks* found between two consecutive *ZCs* in the signal a_{V_2Hz} obtained by a_V through a low-pass filter at 20 Hz followed by an additional low-pass filter at 2 Hz (Fig. 4). Because of the lower accelerations of the head compared with the ones of the trunk, a smaller threshold has been applied in the zero crossing procedure ($th_{ZC}=0.03$ g against the suggested value of 0.1 g).
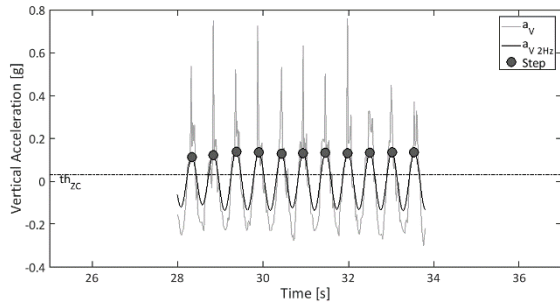
Fig. 4: Step counting according to TM2

TM3. Based on the method [21], steps correspond to the *Pks* in the signal a_{NORM_20Hz} obtained by a low-pass filtering at 20 Hz applied to a_{NORM} (Fig.5). The peak detection is entrusted to three parameters: *i*) C=0.8, a parameter chosen heuristically within the range [0.6 − 0.8] suggested by the authors, *ii*) *peakM,* the mean of values representative of a slope inversion in a_{NORM_20Hz} signal and *iii*) K=1.15 the recommended safety threshold to make step counting more insensitive to minor bumps or undesired movements. The values satisfying the following condition were considered as valid steps*:*

$$a_{NORM\_20Hz} > C \cdot peakM \ \& \ a_{NORM\_20Hz} > K \qquad (3)$$
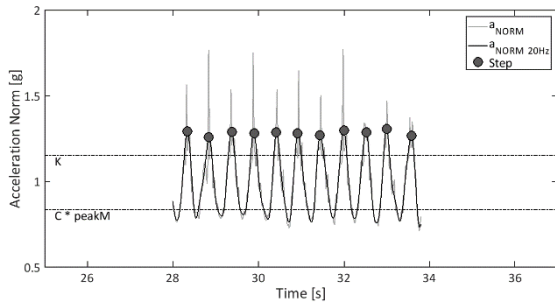
Fig. 5: Step counting according to TM3

E. Error computation

To evaluate the performances of HM, TM1, TM2 and TM3 in estimating the number of steps during overground walking, the difference in terms of percentage error, *E*, between the number of steps estimated by each method (s_e) and the relevant reference value ($s_r=40$) was calculated for all participants in every test:

$$E = \frac{|s_r - s_e|}{|s_r|} \times 100 \qquad (4)$$

The gained errors were then averaged to overall characterize methods' performances in each examined testing condition.

III. RESULTS

The following figures (Fig. 6, Fig. 7, Fig. 8 and Fig. 9) show how *E* values computed for all participants are distributed in each executed test (i.e. LF, LD, LR and LL) according to the method employed (i.e. HM, TM1, TM2 and TM3).

The mean (*m*) and the standard deviation (*sd*) of *E* for every test and method are, instead, reported in Table II.
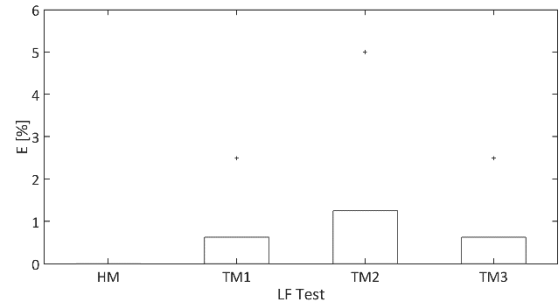
Fig. 6: Boxplot of E for all examined methods in LF test
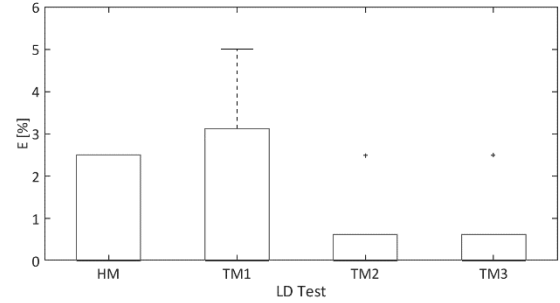
Fig. 7: Boxplot of *E* for all examined methods in LD test
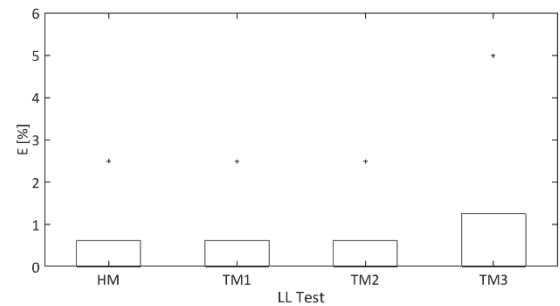
Fig. 8: Boxplot of *E* for all examined methods in LL test
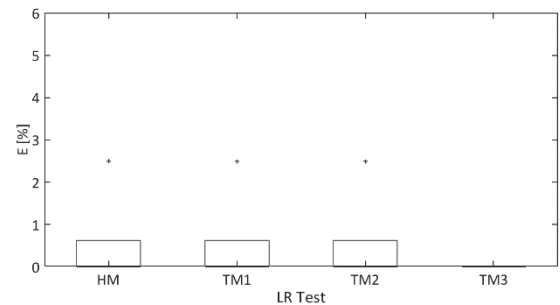
Fig. 9: Boxplot of *E* for all examined methods in LR test

TABLE II
MEAN AND STANDARD DEVIATION OF THE ERROR (E) IN ESTIMATING THE NUMBER OF STEPS

Style	TOT STEPS	HM (m±sd)	TM1 (m±sd)	TM2 (m±sd)	TM3 (m±sd)
LF	200	0±0	0.5±1.1	1.0±2.2	0.5±1.1
LD	200	1.0±1.4	1.5±2.2	0.5±1.1	0.5±1.1
LL	200	0.5±1.1	0.5±1.1	0.5±1.1	1.0±2.2
LR	200	0.5±1.1	0.5±1.1	0.5±1.1	0±0

IV. Discussions

According to the results reported in the previous section, the proposed method (i.e. HM) exhibits an average percentage error E lower than 1% across testing conditions. Besides, in step counting during walking looking forward (i.e. LF test), it results the most accurate when compared to other methods while it is in line with the latter in LD, LL and LR tests. Indeed, HM overestimates the number of steps performed by users of one step, as in the worst case, contrary to the remaining methods where a difference up to two steps is registered (particularly, in LD test for TM1, in LF test for TM2 and in LL test in TM3). The count of extra steps by HM is observed for two subjects in LD test, which therefore results as the testing condition with higher errors. This could be probably due to the fact that HM employs the only vertical component of head acceleration which, during walking condition with the head down, is affected also by the contribution of the anterior-posterior acceleration. A possible solution to overcome that issue could lie in defining adaptive thresholds for th_p and th_n according to head orientation (i.e. in terms of pitch, roll and yaw angles). No great disparity in LD test among methods has been however found. Such promising results appear even better when compared to literature [15, 16]. In [15], for instance, sixteen subjects equipped with a Google Glass device were asked to walk 40 steps in a straight line in an indoor environment looking forward (i.e. LF test) in the presence of an observer. To identify steps, the authors applied the windowed peak detection (*WPD*) technique and an higher error in the computation of steps number when compared to the current study ($E_{[15]\_LF}$=1.9±1.6% vs E_{HM_LF}=0±0%) is registered. In [16], instead, a head-mounted display and four algorithms (i. algorithm based on acceleration, ii. algorithm based on velocity, iii. algorithm based on position and iv. algorithm with a Gaussian low-pass filter) have been used to detect steps. The velocity-based step detection algorithm performed best with an accuracy of about 90% in the task "walking looking around" (i.e. a combination of tests provided in the present study) while the algorithm based on head acceleration signals reached in the considered task an accuracy of about 80% by confirming a poorer performance with respect to the presented HM.

V. Conclusion

The insights obtained in the present study showed that the proposed algorithm is able to correctly detect the number of steps performed. Moreover, it appears robust at different head orientations although a slight increase of error is observed during walking looking down that anyway remains the most challenging task across the methods using head accelerations. Ultimately, its performance can be judged in line with the examined methods, validated on trunk, and; even better than some methods based on head-mounted sensors [15, 16]. Despite the encouraging results, the suggested method can be beyond improved by both involving a larger number of participants and carrying out additional tests. Indeed, the number of subjects involved in the study was limited (i.e. only five subjects), and, in addition, only young participants (i.e. characterized by similar and healthy motor patterns) were enrolled. More numerous and varied tests, including different gait velocities and path typologies for instance, are finally desirable to find the optimal definition of th_p and th_n thresholds in order to enhance step counting and, consequently, daily PA monitoring using head-worn devices.

References

[1] D.E.R. Warburton, C.W. Nicol, S.S.D. Bredin, "Review health benefits of physical activity: the evidence", CMAJ, 2006, 174 (6): 801 – 809.

[2] J. A. Knight, "Physical inactivity: associated diseases and disorders", Ann. Clin. Lab. Sci., 2012, 42 (3): 320–337.

[3] D.R. Bassett, J. Lindsay, P.T. Samuel, R.L. Scott, "Step counting: a review of measurement considerations and health-related applications", Sport. Med., 2017, (47): 1303–1315.

[4] M.D. Schmidt, V.J. Cleland, K. Shaw, T. Dwyer, A.J. Venn, "Cardiometabolic risk in younger and older adults across an index of ambulatory activity", AMEPRE, 2009 (37): 278–284.

[5] S.B. Sisson, S.M. Camhi et al., "Accelerometer-determined steps/day and metabolic syndrome", AMEPRE, 2010 (38): 575–582.

[6] S. Inoue, Y. Ohya, C. Tudor-Locke, N. Yoshiike, "Step-defined physical activity and cardiovascular risk among middle-aged japanese: the national health and nutrition survey of Japan 2006", Journal of Physical Activity and Health, 2012, 9 (8): 1117–1124.

[7] M.J. Mathie, A.C.F. Coster, N.H. Lovell, B.G. Celler, "Accelerometry: providing an integrated, practical method for long-term, ambulatory monitoring of human movement", Physiological Measurement, 2004, (25):1–20.

[8] J.J. Kavanagh, H.B. Menz, "Accelerometry: a technique for quantifying movement patterns during walking", Gait & Posture, 2008, (28): 1–15.

[9] A. Bayat, M. Pomplun, D.A. Tran, "A study on human activity recognition using accelerometer data from smartphones", Procedia Computer Science, 2014, (34): 450–457.

[10] L. Atallah, B. Lo, R. King, G. Yang, "Sensor placement for activity detection using wearable accelerometers", IEEE Transactions on Biomedical Circuits and Systems, 2010, 5(4): 320-329.

[11] A.S. Evani, B. Sreenivasan, J.S. Sudesh, M. Prakash, "Activity recognition using wearable sensors for healthcare", SENSORCOMM, 2013, 173–177.

[12] B. Najafi, et al., "Ambulatory system for human motion analysis using a kinematic sensor: monitoring of daily physical activity in the elderly", IEEE Trans. Biomed. Eng., 2003, (50): 711–723.

[13] A. Godfrey, A.K. Bourke, G.M. Ólaighin, P. Van De Ven, J. Nelson, "Medical engineering & physics activity classification using a single chest mounted tri-axial accelerometer", Med. Eng. Phys., 2011, (33): 1127–1135.

[14] S. Hermsen, J. Moons, P. Kerkhof, C. Wiekens, "Determinants for sustained use of an activity tracker: observational study", JMIR Mhealth Uhealth, 2017, 5(10): e164.

[15] I. Apostolopoulos, D.S. Coming, E. Folmer, "Accuracy of pedometry on a head-mounted display, CHI'15, 2015.

[16] P. Caserman, P. Krabbe, J. Wojtusch, O. von Stryk, "Real-time step detection using the integrated sensors of a head-mounted display", IEEE International Conference on Systems, Man and Cybernetics, 2016, 3510-3515.

[17] J. Windau, L. Itti, "Situation awareness via sensor-equipped eyeglasses", IEEE/RSJ Int. Conf. on Intel. Robots and Systems, 2013, 5674-5679.

[18] A. Cristiano, A. Sanna and D. Trojaniello, "Step counting using a head-mounted accelerometer", EMBC, 2019.

[19] S.H. Shin, C.G. Park, "Adaptive step length estimation algorithm using optimal parameters and movement status awareness", Medical Eng. & Physics, 2011, 33: 1064-1071.

[20] W. Zijlstra, "Assessment of spatio-temporal parameters during unconstrained walking", Eur. J. Appl. Physiol., 2004, 92: 39-44.

[21] M. Mladenov, M. Mock, "A step counter service for java-enabled devices using a built-in accelerometer", CAMS, 2009.

CT-based FFR: paving the way to future hearts

C. Bargellini[1], Q. Long[1], T.K. Mittal [2,3]

[1] *Brunel Institute for Bioengineering, Brunel University, Uxbridge, Middlesex UB8 3PH, UK*
[2] *Heart Assessment, Royal Brompton and Harefield NHS Foundation Trust, London, UK*
[3] *Faculty of Medicine, NHLI, Imperial College London, London, UK*

Abstract— **FFR (Fractional Flow Reserve) is the gold standard for guiding the diagnosis and management of stable CAD by estimating the haemodynamic or functional severity of coronary stenosis. As the index is an indicator of ischemia, it was found to overcome the poor diagnostic performance of the anatomical assessments, especially in the case of intermediate stenoses. Nevertheless, the procedure is time-consuming and invasive, with poor clinical uptake rate due to high short-term costs. Several research groups have implemented their own approach for a non-invasive alternative to the standard clinical procedure. Some of the solutions have also been recently commercialised. In this paper, further testing for the virtual estimation of fractional flow reserve is provided. Patient-specific coronary arterial trees are reconstructed from high-resolution CT images and analysed with a simplified methodology consisting of multiple, steady-state computational fluid dynamics (CFD) simulations for the evaluation of a "virtual" FFR (vFFR). 3D coronary models are obtained from four different cases of documented CAD and vFFR evaluations are presented for a total of ten lesions. 20% of the lesions turned out to be significant, with an average vFFR of 0.69, much lower than the cut-off value (0.75). Significant and mild stenoses were identified by pressure drops greater than 17 mmHg and lower than 12 mmHg, respectively. The variability of vFFR was explored with respect to coronary anatomy, boundary conditions and lesion geometry. Discrepancy with the anatomical assessment was also found, in accordance with the literature.**

Keywords—**Cardiovascular Disease, Image Processing, CFD.**

I. INTRODUCTION

THE blockage of the coronary arteries due to the development of atherosclerosis may increase the blood flow resistance and reduce the blood supply to the myocardium, ultimately causing an ischemic heart attack. This condition is known as Coronary Artery Disease (CAD). Not only in Italy, but also globally, CAD is a major concern. In 2015, in Italy, 37% of deaths had CAD as its underlying cause, accounting for an average of 240.000 [1]. CAD was also reported as the leading cause of death worldwide in 2016 [2], even before cancer, dementia, and respiratory syndromes.

The disease usually presents a long asymptomatic phase, meaning that in most cases the patients will experience chest pain and burden when the atheroma is already severe [3]. Therefore, encouraging prevention is a pivotal step in CAD management, as it may minimise the risk of stroke and other major adverse cardiac events. The procedures for myocardial revascularization are invasive and associated with high short-term and hospitalisation expenses [4], [5]. Therefore, most likely only the lesions showing haemodynamically significant stenosis will be selected for treatments.

The gold clinical standard for evaluating stenoses' severity is based on the calculation of the fractional flow reserve (FFR) of the specific stenosis lesion. However, the procedure is time-consuming and invasive, with specific laboratory setting and high short-term costs. Most importantly, it is used on a small cohort of diagnostic cases. Yet, the index provides clinicians with accurate functional information on the significance of atherosclerotic lesions, which is the most important prognostic factor in the treatment of ischaemia linked to CAD.

Alternative approaches comprising image processing, 3D reconstruction and Computational Fluid Dynamics (CFD) have been presented by several research groups with promising results, as in [6], [7], and may be the solution for bringing the FFR practice available to a larger number of patients. The basic idea is to reconstruct the coronary arterial tree from the patients' CT scans and analyse the blood flow with CFD to identify the regions which present severe conditions, therefore requiring treatment. In particular, the pressure field across the whole 3D model is evaluated via computational means and the FFR ratio is calculated "virtually" by measuring the pressure drop across the stenosis. In the present paper, a simplified approach for non-invasive testing is applied to the CT data sets from four different patients with documented CAD. Pressure distributions are derived, the virtual-FFR (vFFR) is evaluated for each lesion and its variability is explored with respect to coronary anatomy, simulation settings and lesion geometry.

II. METHODOLOGY

All operations were conducted on a standard workstation (Intel Core i5 8250U 1.60 GHz, 8 GB RAM, 4 cores).

A. Data acquisition and image processing

Anatomical information was gained by CT images at diastole from four patients with documented CAD (the data was provided by Harefield Hospital, UK). ITK-SNAP was used for image visualisation in different planes (axial, sagittal and coronal views), which guided the cutting of the volume of interest for the segmentation of the coronary vessels. In Matlab, the data sets were processed with a Gaussian smoothing filter, resampled with the use of a cubic spline interpolation and segmented with an active contour method. In particular, the Distance Regularized Level Set Evolution [8] was adopted for the segmentation of the lumen contours in the axial view, which were then exported into ICEM for further analysis. Once the final axial sections were obtained, vessels surfaces were created in Rhino 3D.

B. CFD simulation

The CFD simulations are divided into two sections. The first one reports the complete procedure on the assessment of the disease on patient two (anatomical assessment and functional assessment). The second section, instead, focuses on the analysis of the vFFRs and trans-lesion pressure drops in all the clinical cases to explore the index variability.

Multiple steady-state simulations were run on Fluent®. The blood was assumed to be incompressible, with a density equal to 1060 kg/m^3, and Newtonian, with a constant value for the viscosity of 0.004 $Pa \cdot s$. The walls were assumed to have null thickness and be rigid and the flow to be laminar. A polyhedral mesh (Fluent) and a tetrahedral one (ANSYS Mechanical) were used for the simulations, with a density of 0.5mm element size. Absolute convergence and stability were controlled by ensuring that the net flux levels were below 2% as well as with the residuals being set at 1e^(-3). Mesh independency tests were conducted on the two types of meshes in order to check the sensitivity of the results to mesh type and density (element size varying between 0.5mm and 5mm). The values of the maximum pressure at the left aortic ostium were collected for each mesh refinement iteration. The test was assumed to be converging when the difference between the values obtained with different mesh sizes was below 0.1% and the net mass flux was below 2%. At the boundaries, an inlet flow condition, pressure outlets and non-slip condition at the wall (zero relative velocity) were applied. The aortic outlet was set at 88 mmHg, which is the physiological aortic pressure at diastole [9], and the coronary outlets at 37 mmHg, as the value is close to the physiological pressure of the epicardial arteries immediately before entering the coronary microcirculation [10]. A series of inflow boundary conditions were imposed at the inlet, starting from a physiological range of 20 cm/s [10] and being gradually increased up to 80 cm/s. In this way, the increasing inlets against constant pressure outlets allow finding the velocity at which the trans-stenotic pressure drop becomes critical (meaning that the vFFR has reached the cut-off value of 0.75). Only haemodynamically significant stenoses will reach the critical vFFR value within the physiological pressure range. The Navier-Stokes equations were discretised in the viscous-laminar domain both in space and time at a finite number of nodes, using the element-based finite volume method and a standard, 2nd order, upwind differencing scheme. The pressure-velocity coupling method followed the SIMPLE algorithm. Standard initialisation was set at the inlet with a reference frame relative to the cell zone.

C. Stenosis assessment

The reconstructed lesions from patient two followed both an anatomical and a functional assessment. The anatomical method consisted of calculating the ratio between the lesion cross-sectional area and the proximal segment normal to the stenosis [11]. Reduction of 50% and over were set as significant. The functional method was applied to the lesions from all patients. The vFFR index was calculated as the ratio between the pressure downstream and upstream of the stenosis, consistently with the invasive FFR definition, as in Eq. (1), [12]. The values for the up-stream and down-stream pressures were derived on Fluent on two cross-sectional planes in the up-stream and down-stream regions, respectively. Stenoses with vFFR equal to or lower than 0.75 were assessed as functionally significant. When the vFFR was between 0.75 and 0.8, the stenoses were included in the "grey-zone". Finally, stenoses with vFFR greater than 0.8 were set as mild or non-significant.

$$vFFR = \frac{P_{stenosis\_downstream}}{P_{stenosis\_upstream}} \qquad (1)$$

III. RESULTS

A. Segmentation and 3D reconstruction

The segmentation was obtained in the axial view for the aortic root, main coronary arteries [Left Main, Left Anterior Descending (LAD), ramus (if visible), CircumfleX (CX), Right Coronary Artery (RCA)] and their main collateral branches [Posterior Descending Artery (PDA), Postero-Lateral Branches (PLB), Right Marginal Artery (RMA) and diagonal branches]. All patients exhibited standard left dominance and the identified anatomies were greatly different from one another [Fig.1], allowing valuable comparison between the results of pressure distribution and vFFR.
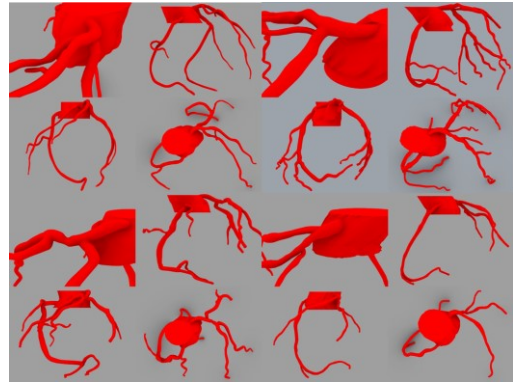

Figure 1. 3D reconstructed geometries

B. Characterisation of lesions in the second patient

Figure 2. Second patient mesh, cutting planes and close-ups on lesions

TABLE I
ANATOMICAL VS FUNCTIONAL ASSESSMENT, SECOND PATIENT

Lesion	Stenosis diameter [mm]	Mean vessel diameter [mm]	% Blockage	vFFR at 20-80 [cm/s]
L1	1.17	2.75	57%	0.68-0.70
L2	3.11	4.09	24%	0.81-0.88
L3	1.70	2.47	31%	0.85-0.87
L4	1.90	2.44	22%	0.65-0.74

Table I. Anatomical parameters, anatomical (%blockage) and functional assessment (vFFR) of the lesions in the 2nd patient

Four lesions were found in the second patient [Fig.2]. Disagreement with the anatomical assessment was shown for one lesion [Table I], confirming the discrepancy between anatomical and functional considerations from the literature

[13]. Indeed, L4 was hemodynamically significant with a vFFR of 0.65-0.74 despite a diameter reduction of 22%.

C. Overall stenosis assessment

Overall, 10 lesions were identified with an average of 2-3 lesions per patient, with no diffuse disease. The isolated stenoses were in the LM bifurcation and other main vessels (LAD, CX, RCA), with the LM as the most common site (4 lesions out of 10). Major calcifications were observed in the main arteries (especially LM and CX) for most of the cases (three out of four). On a per-vessel basis, the functional assessment of the stenoses concluded that only 20% of the stenoses were haemodynamically significant, while 40% were mild and the last 40% belonged to the "grey" region. Overall, 2 lesions were significant with a value for vFFR below 0.7 (0.65-0.7). Meanwhile, 4 lesions were set in the "grey-zone", with uncertain significance. These lesions have the potential of becoming significant at high flow rates for the vFFR becomes lower than 0.8 at high velocities or with the development of the disease, when the vFFR is between 0.75 and 0.8. Consequently, the lesions were divided into severe (yellow), mild (orange) and intermediate (grey) and the vFFR was plotted against the pressure drop. The relationship between the two parameters was observed to be well represented with polynomial (cubic) trendlines [Fig. 3]. Significant stenoses were identified by pressure drops greater than 17 mmHg, while mild stenoses did not generally have a pressure drop greater than 12 mmHg.
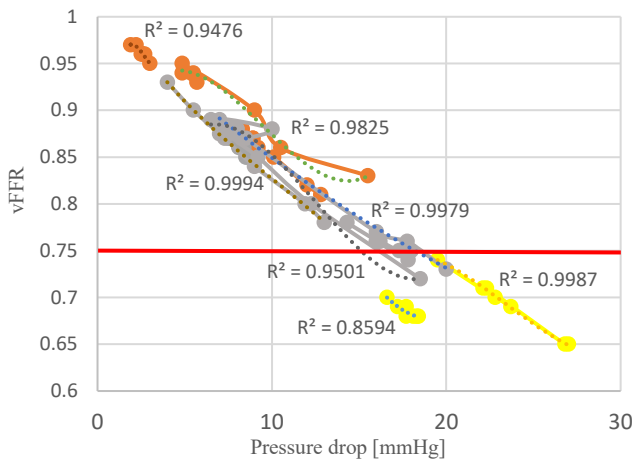
Figure 3. vFFR-pressure drop relationships, all lesions. Trendlines are reported next to their R^2 value. The red line identifies the vFFR cut-off value (0.75). *Yellow: severe; Orange: mild; Grey: intermediate*

When analysed with rising inlet velocities, vFFR values decreased for all the lesions [Table II], consistently with the increase in trans-stenotic pressure drop [Table III].

TABLE II
FUNCTIONAL ASSESSMENT, ALL LESIONS

Lesion	20 cm/s	22 cm/s	24 cm/s	30 cm/s	40 cm/s	60 cm/s	80 cm/s
L1	0.7	0.68	0.68	0.68	0.69	0.69	0.68
L2	0.88	0.87	0.87	0.86	0.85	0.82	0.81
L3	0.87	0.86	0.86	0.85	0.85	0.87	0.86
L4	0.74	0.7	0.71	0.69	0.71	0.65	0.65
L5	0.89	0.88	0.88	0.87	0.77	0.76	0.73
L6	0.94	0.93	0.94	0.95	0.9	0.86	0.83
L7	0.78	0.74	0.76	0.76	0.76	0.75	0.75
L8	0.96	0.96	0.96	0.96	0.97	0.97	0.95
L9	0.88	0.87	0.88	0.89	0.85	0.8	0.72
L10	0.93	0.9	0.875	0.87	0.84	0.8	0.78

Table II. vFFR values at different inlets. Yellow: severe; Orange: mild; Grey: intermediate

TABLE III
TRANS-STENOTIC PRESSURE DROPS, ALL LESIONS

Lesion	20 cm/s	22 cm/s	24 cm/s	30 cm/s	40 cm/s	60 cm/s	80 cm/s
L1	16.6	18.1	18.3	18.4	17.7	17.2	17.7
L2	8.3	8.9	8.9	9.2	10.1	12	12.8
L3	7.5	8.4	8.3	8.6	8.5	7.7	8.1
L4	19.5	22.8	22.1	23.7	22.3	26.8	27
L5	7	7.7	8	8.5	16	17.75	20
L6	5.5	5.7	4.85	4.85	9	10.5	15.5
L7	14.3	17.8	16	16	16.2	17.3	18
L8	2.5	2.6	2.6	2.7	2.2	1.9	3
L9	7.5	8.25	10	6.5	9.2	12.25	18.5
L10	4	5.5	7	7.3	9	11.9	13

Table III. Pressure drops [mmHg] at different inlets. Yellow: severe; Orange: mild; Grey: intermediate

IV. DISCUSSION

The strength of the model is that it provides a straightforward, stable, and simple analysis with no need for clinical pressure and velocity data. Simplified approaches for atherosclerosis assessment have been used before. Reference [14] shows the influence of different types of inflow boundary conditions and impedance characterisation on the estimation of flow patterns and virtual FFR with the use of sets of steady-state simulations. It was shown that the inclusion of pulsatile patterns does not bring additional information when evaluating virtual fractional reserve (the difference between the pulsatile and steady approaches was 2.4%, below the average practical uncertainty in the clinic). In reference [15], it results that the steady analysis had a negative and a positive predictive value of 91.3% and 88.9%, respectively as well as a diagnostic accuracy of 90.6%. In conclusion, although transient approaches should not be replaced as they provide important information for flow modelling, the use of steady-state analyses may indeed not be too restrictive when evaluating vFFR. As the invasive FFR itself is being derived using time-averaged measurements over multiple cardiac-cycles, the steady-state-based virtual index may still show good performance when implemented on a standard workstation, like the one used for this study (Intel Core i5 8250U 1.60 GHz, 8 GB RAM, 4 cores). The methodology successfully allowed the reconstruction of the patient-specific coronary trees [Fig.1] as well as the functional assessment of multiple atherosclerotic lesions [Table II]. It was also possible to show non-agreement with anatomical evaluations [Table I] as well as providing indications about the critical trans-stenotic pressure drops [Table III] and vFFR-pressure drop relationships [Fig.3]. However, there are some concerns about the accuracy of the analysis. Due to the lack of high-performance computing, it was not possible to provide a very fine mesh (typically ranging between 2-3 million elements [16]) and a net flux threshold below 2%. For the same reason, multiscale modelling for the derivation of the boundary conditions could not be implemented. 0D-3D coupling through lumped-parameter models allows the integration of the effect of the systemic circulation, microcirculation, and heart movement on the flow. In the present study, velocity and pressure values were taken

from the literature and no resistance conditions were applied. This makes the analysis far from being totally patient-specific, which is restrictive given the extensive variability of vFFR on flow rate [Table II] and simulation settings. Furthermore, simple pressure boundary conditions can lead to wrong flow distributions. Another source of inaccuracy was the lack of patient-specific data. Physiological measurements such as the brachial pressure and CT-derived myocardial mass may be useful for the determination of the inlet flow rate. In fact, a general assumption [17] is to assume the mean aortic pressure equal to the brachial pressure. The total demand for blood can then be quantified from the myocardial mass, which is indicative of the basal coronary flow. Myocardial perfusion at rest can also be determined by the size of the feeding vessel as well as the number of vessels downstream. If available in 4-phases, CT can also provide the structural deformation of the vessels, knowing that the flow rate is proportional to the organ size (allometric scaling law) [17]. Velocity and pressure measurements on multiple heart cycles can be obtained by time-resolved imaging, such as ultrasound or 4D MRI. Lumped parameter networks can be tuned in order to match clinical values such as the patient's cardiac output from echocardiography [18]. Anatomical parameters can be obtained with any high-resolution imaging techniques, such as CT, MRI or angiography. The representation of maximal hyperemia can also be gained by knowing the response of the microcirculation to adenosine from clinical data (it has been established that the resistance at hyperemia is a fraction of the basal resistance [17]). In this study, given the lack of clinical data, the anatomical measurements were approximated with software-based tools. The comparison with anatomical assessments from the cath-lab (for instance, stenosis length and invasive FFR values as well as the catheter's resolution) may provide valuable information for validation purposes. Furthermore, the segmentation approach was not fully automatic. Rather, it required significant input from the user. This significantly increases the overall procedure time, even with expert operators. The sections were obtained by segmenting on the axial plane only, which is not ideal especially for the reconstruction of bifurcations and narrowed regions. Segmentation contours in the sagittal and coronal views may be needed at least in bifurcation and stenosis regions. Finally, the algorithm did not include a way of detecting uncertainty from noise or CT artifacts. The blooming artifact alone has been reported to lead to an overestimation of about 50% calcified stenoses [19]. As most of the anatomies were affected by calcifications, it is expected that the vFFR might overestimate some of the lesions. Further analysis may be required in this regard (confidence interval estimations, inclusion of algorithms for the detection of "bloomed" zones).

V. CONCLUSIONS

The present study presented further testing for CT-based FFR with regards to segmentation procedures and boundary conditions. The proposed method is completely non-invasive and can be implemented on a standard workstation. Significant improvement to the present analysis can be obtained by running the methodology on a modest workstation with higher computational power (10-20 cores), with the use of relevant patient-specific data and multiscale-modelling, as well as by providing uncertainty quantification for both the segmentation procedure and the CFD simulations.

REFERENCES

[1] https://www.ambrosetti.eu/wp-content/uploads/MS13-def-completo.pdf [Accessed 2020, Jan 17]

[2] http://www.who.int/en/news-room/fact-sheets/detail/the-top-10-causes-of-death [Accessed 2020, Jan 17]

[3] Díaz-Zuccarini V, Di Tomaso G, Agu O, Pichardo-Almarza C. Towards personalised management of atherosclerosis via computational models in vascular clinics: technology based on patient-specific simulation approach. Healthcare technology letters. 2014 Feb 11;1(1):13-8.

[4] Wijns W, Kolh P, Danchin N, Di Mario C, Falk V, Folliguet T, et al. Guidelines on myocardial revascularization: The Task Force on Myocardial Revascularization of the European Society of Cardiology (ESC) and the European Association for Cardio-Thoracic Surgery (EACTS). European Heart Journal. 2010 Aug 29;31(20):2501–55.

[5] Tu S, Barbato E, Köszegi Z, Yang J, Sun Z, Holm NR, Tar B, Li Y, Rusinaru D, Wijns W, Reiber JH. Fractional flow reserve calculation from 3-dimensional quantitative coronary angiography and TIMI frame count: a fast computer model to quantify the functional significance of moderately obstructed coronary arteries. JACC: Cardiovascular Interventions. 2014 Jul 1;7(7):768-77.

[6] Koo BK, Erglis A, Doh JH, Daniels DV, Jegere S, Kim HS, Dunning A, DeFrance T, Lansky A, Leipsic J, Min JK. Diagnosis of ischemia-causing coronary stenoses by noninvasive fractional flow reserve computed from coronary computed tomographic angiograms: results from the prospective multicenter DISCOVER-FLOW (Diagnosis of Ischemia-Causing Stenoses Obtained Via Noninvasive Fractional Flow Reserve) study. Journal of the American College of Cardiology. 2011 Nov 1;58(19):1989-97.

[7] Morris PD, Ryan D, Morton AC, Lycett R, Lawford PV, Hose DR, Gunn JP. Virtual fractional flow reserve from coronary angiography: modeling the significance of coronary lesions: results from the VIRTU-1 (VIRTUal Fractional Flow Reserve From Coronary Angiography) study. JACC: Cardiovascular Interventions. 2013 Feb 1;6(2):149-57.

[8] Li C, Xu C, Gui C, Fox MD. Distance regularized level set evolution and its application to image segmentation. IEEE transactions on image processing. 2010 Aug 26;19(12):3243-54.

[9] DOLE WP, RICHARDS KL, HARTLEY CJ, ALEXANDER GM, CAMPBELL AB, BISHOP VS. Diastolic coronary artery pressure-flow velocity relationships in conscious man. Cardiovascular research. 1984 Sep 1;18(9):548-54.

[10] Abe M, Tomiyama H, Yoshida H, Doba N. Diastolic fractional flow reserve to assess the functional severity of moderate coronary artery stenoses: comparison with fractional flow reserve and coronary flow velocity reserve. Circulation. 2000 Nov 7;102(19):2365-70.

[11] Lee J, Smith NP. The multi-scale modelling of coronary blood flow. Annals of biomedical engineering. 2012 Nov 1;40(11):2399-413.

[12] De Bruyne B, Sarma J. Fractional flow reserve: a review. Heart. 2008 Jul 1;94(7):949-59.

[13] De Bruyne B, Sarma J. Fractional flow reserve: a review. Heart. 2008 Jul 1;94(7):949-59.

[14] Lo EW, Menezes LJ, Torii R. Impact of Inflow Boundary Conditions on the Calculation of CT-Based FFR. Fluids. 2019 Jun;4(2):60.

[15] Zhang JM, Zhong L, Luo T, Lomarda AM, Huo Y, Yap J, Lim ST, San Tan R, Wong AS, Tan JW, Yeo KK. Simplified models of non-invasive fractional flow reserve based on CT images. PloS one. 2016;11(5).

[16] Morris PD, Gunn JP. Computing Fractional Flow Reserve From Invasive Coronary Angiography: Getting Closer.

[17] Taylor CA, Fonte TA, Min JK. Computational fluid dynamics applied to cardiac computed tomography for noninvasive quantification of fractional flow reserve: scientific basis. Journal of the American College of Cardiology. 2013 Jun 4;61(22):2233-41.

[18] Marsden AL. Simulation based planning of surgical interventions in pediatric cardiology. Physics of fluids. 2013 Oct 23;25(10):101303.

[19] Li P, Xu L, Yang L, Wang R, Hsieh J, Sun Z, Fan Z, Leipsic JA. Blooming artifact reduction in coronary artery calcification by a new de-blooming algorithm: initial study. Scientific reports. 2018 May 2;8(1):6945.

Cardiac fluid dynamics of patient-specific geometries in Pre and Post Mitral Valve Repair by Direct Numerical Simulation

D. Collia[1], G. Pedrizzetti[1]

[1] *Department of Engineering and Architecture, University of Trieste, Trieste, Italy*
E-mail: dar.collia@gmail.com, giannip@dia.units.it

Abstract— **Fluid dynamics is considered an important factor that influences the myocardial adaptation during cardiovascular disease and after surgical therapy. We aim to study the fluid dynamics inside the left ventricle (LV) with healthy, prolapsed and repaired mitral valve (MV). Geometries are extracted from 4D-transesophageal echocardiography and flow analysis is performed by direct numerical simulations. Results confirm that the regurgitated volume is drastically reduced after repair. The analysis of blood wash-out demonstrates that a successful MV repair also restores a balanced flow transit in terms of physiological sub-volumes. This study shows that numerical simulation represents an integration to clinical imaging for hemodynamic assessments after MV surgery.**

Keywords— **Cardiac fluid dynamics, mitral valve repair, direct numerical simulation, biofluid mechanics.**

I. INTRODUCTION

FLUID dynamics is gaining increasing attention in cardiology for the influence it may have on the long-term outcome of several cardiac dysfunctions [1, 2]. Numerous studies in literature reported how stresses due to the interaction between flow and tissue play a primary role in the development of embryonic hearts [3–5], and flow mediated forces participate in the progression or regression of cardiac pathologies in adult hearts [6, 7]. Given its potential importance, it is foreseeable that measurements of intra cardiac fluid dynamics will soon become an integral part of the clinical evaluation process. We study the fluid dynamics inside the left ventricle (LV) in patients with normal volumetric and deformations cardiac measures before and after surgical mitral valve repair (MVR) for several degrees of mitral regurgitation. The study will focus on the analysis of the LV wash-out as well as the residence time properties of the blood that could reflect in additional risk factors [8].

II. MATERIAL AND METHODS

A. Medical imaging and geometries

Five patients undergoing conventional mitral valve repair (MVR) and one healthy control were analysed. The MV and LV geometries were extracted from 4D – transesophageal echocardiography with the use of dedicated software (4D LVA and 4D MVA, TomTec Imaging Systems GmbH, Unterschleissheim, Germany) that performs a semi-automated delineation of the LV endocardial surface during all phases of the heartbeat. The LV boundary is then described the position vector $X(\vartheta, s, t)$, where the structured parametric coordinates, (ϑ, s), run along the circumference and from base

to apex, respectively, t is time. The same LV geometry, evaluated immediately pre-implant, was used for both the pre- and post-MVR as the main volumetric properties (end-diastolic volume EDV, end-systolic volume ESV) do not vary significantly in the few days after surgery. This approach allows focusing on the differences imputable to MV surgery only.

The MV geometries (figure 1) were extracted in the fully-open (at peak diastole) and fully-closed (peak systole) positions and were reorganized in terms of another set of parametric coordinates, (ϑ, s), running along the circumference and extending from the annulus to the trailing edge, respectively.
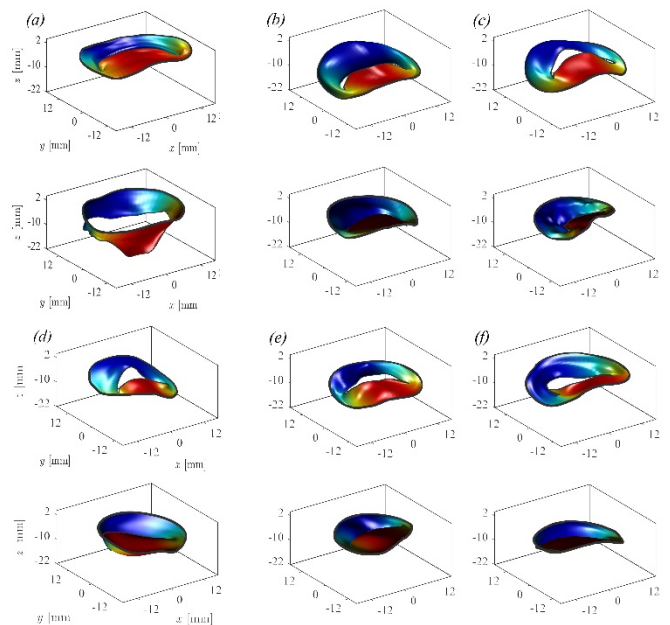

Figure 1. Healthy MV geometry in open and closed configuration, Pre and Post MVR geometries in closed position. (a) Healthy, (b) MVR 1, (c) MVR 2, (d) MVR 3, (e) MVR 4, (f) MVR 5.

B. Numerical model

The intraventricular fluid dynamics was reproduced by numerical solution of the governing equation, Navier-Stokes equation and continuity equation, for the fluid assumed as incompressible and Newtonian. The numerical solution is based on the immersed boundary method (IBM) extensively described in previous studies [8–13]. The MV geometry during all stages between the open and closed configurations is assumed to be described by two degrees of freedom corresponding to the opening angle of the anterior and

posterior leaflets, say $\varphi_1(t)$ and $\varphi_2(t)$, respectively, assumed to move independently. The valve geometry at every instant was thus described formally as $X_v(\vartheta, s, \varphi_1(t), \varphi_2(t))$, which represents a two-dimensional set of intermediate positions associated to the different degrees of leaflets' opening preliminarily estimated by interpolation between the closed $X_v(\vartheta, s, 0, 0)$, and open $X_v(\vartheta, s, \pi/2, \pi/2)$ configurations obtained from images. Then, a dynamic equation for the opening angles is obtained by imposing global mass conservation between leaflet motion and flow at the leaflet position. The leaflet movements is in interaction with the flow and assumed without elastic resistance, instead the dynamics is obtained by least-square minimization of the difference, integrated over the valvular surface A_v, between the fluid and the valve velocity component normal to the valvular surface. This results is a 2x2 linear system

$$
\begin{bmatrix} \iint_{A_v} \left(\frac{\partial X_v}{\partial \varphi_1} \cdot \boldsymbol{n}\right)^2 dA & \iint_{A_v} \left(\frac{\partial X_v}{\partial \varphi_1} \cdot \boldsymbol{n}\right)\left(\frac{\partial X_v}{\partial \varphi_2} \cdot \boldsymbol{n}\right) dA \\ \iint_{A_v} \left(\frac{\partial X_v}{\partial \varphi_1} \cdot \boldsymbol{n}\right)\left(\frac{\partial X_v}{\partial \varphi_2} \cdot \boldsymbol{n}\right) dA & \iint_{A_v} \left(\frac{\partial X_v}{\partial \varphi_2} \cdot \boldsymbol{n}\right)^2 dA \end{bmatrix} \begin{bmatrix} \frac{\partial \varphi_1}{\partial t} \\ \frac{\partial \varphi_2}{\partial t} \end{bmatrix} =
$$
$$
\begin{bmatrix} \iint_{A_v} (\boldsymbol{v} \cdot \boldsymbol{n})\left(\frac{\partial X_v}{\partial \varphi_1} \cdot \boldsymbol{n}\right) dA \\ \iint_{A_v} (\boldsymbol{v} \cdot \boldsymbol{n})\left(\frac{\partial X_v}{\partial \varphi_2} \cdot \boldsymbol{n}\right) dA \end{bmatrix}; \quad (1)
$$

for the two unknowns $\frac{\partial \varphi_1}{\partial t}$ and $\frac{\partial \varphi_2}{\partial t}$, where $\boldsymbol{v}$ is the fluid velocity and $\boldsymbol{n}$ is the local normal to the valvular surface.
This approach was extensively described in [8, 9].

C. Flow transit analysis

The evaluation of the flow transit is an important step for the identification of blood transport and mixing inside the LV in order to verify the wash-out properties that are related to the risk of the thrombus formation. Following the established literature in cardiology [14–17], this evaluation is obtained by subdividing the EDV into 4 sub-volumes

$$
EDV = V_{direct} + V_{delayed} + V_{retained} + V_{residual} \quad (2)
$$

V_{direct} is the volume of blood that entered during diastole and transits directly to the aortic outlet during systole residing less than one heartbeat in the LV, $V_{retained}$ is the part that entered during diastole that is not ejected during the following systole while the $V_{delayed}$ was already present in the LV at the beginning of diastole and is then ejected during the following systole, and $V_{residual}$ that was present in the LV before the beginning of diastole and persists in the chamber after the end of systole. Therefore, the stroke volume, $SV = EDV - ESV$, of blood entering the LV is given by $SV = V_{direct} + V_{retained}$. It must be equal to the volume ejected during systole $SV = V_{direct} + V_{delayed} + V_{reg}$, where V_{reg} is the volume regurgitated in the atrium when the MV is insufficient. The last two terms in (2) are those remaining in the LV at the end of the systolic ejection, $ESV = V_{retained} + V_{residual}$.
The analysis of blood transport is performed by solving the transport-diffusion equation for a passive scalar,

$$
\frac{\partial C}{\partial t} + \nabla \cdot (\boldsymbol{v} C) = \nu \nabla^2 C \quad (3)
$$

where $\boldsymbol{v}(\boldsymbol{x}, t)$ is the velocity vector field and ν is the kinematic viscosity. The scalar $C(\boldsymbol{x}, t)$ is a marker for selected blood particles, that allows identifying the composition of fresh and old blood that enter and exit the LV and the quality of the regurgitated blood [8].
Equation (3) is solved with initial condition $C = 1$ inside the LV at end-systole and following the mean reduction in the following beats. This method allows identification of the residual volume that is composed of the marked blood that is found in the LV chamber at the end of the next systole. Then, from the knowledge of $V_{residual}$ and V_{reg} in presence of MV insufficiency, it is possible to identify all contributions through the linear relationships.

III. RESULTS

A. Fluid dynamics analysis

The flow field at diastolic peak in healthy case (figure 2 (a)) was previously described in numerous studies [8, 9, 14, 15]; which features the formation of a typical asymmetric vortex ring (figure 2 (a)).
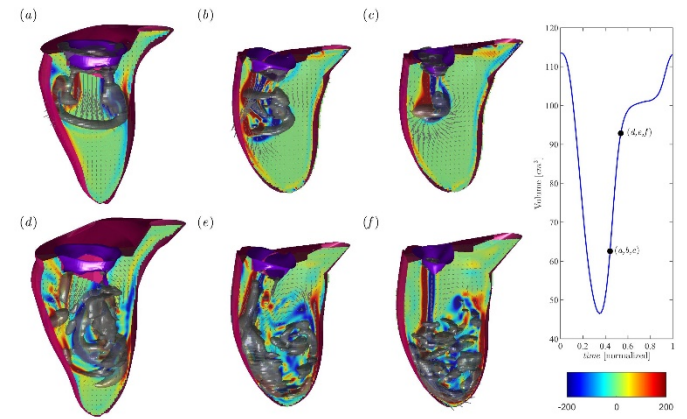

Figure 2. Flow field at healthy (a,d), Pre-MVR (b,e) and Post MVR (c,f). Diastolic flow at peak E-wave (a), (b), (c); as indicated in the volume curve inset; the normal vorticity is shown by red to blue color from -200 units to 200 units equal to the inverse of the heartbeat period and the velocity vector (ever 4 grid points) on a longitudinal plane crossing the center of MV, of aorta and LV apex; the three-dimensional grey surfaces represents one iso-surface of the λ_2 parameter. The loer side is the flow during filling phase (d), (e), (f).

The pre-repair condition (figure 2 (b)) typically displays a deviated flow that impacts the posterior wall of the LV causing the rapid dissipation of the vortex ring. After MVR (figure 2 (c)), the mitral jet is more compact and directed across the centre of LV. The vortex is smaller and more regular in comparison to the corresponding pre-surgery condition, which is probably a consequence of the MV area reduction due to repair. The flow field during the filling phase (figure 2 (d, e, f) shows that before repair (figure 2 (e)), the flow follows the deviated direction along the posterior wall, rotates about the apex to reach the opposite wall. After reparation (figure 2 (f)), the vortex associated to the strong central jet flow breaks in proximity of the apex resembling better the situation found in the healthy case.

B. *Regurgitation and washout analysis*

TABLE I

CLINICAL DATA AND GLOBAL AND TRANSIT REGURGITATION IN HEALTHY, PRE
AND POST MVR. EDV= END DIASTOLIC VOLUME, ESV= END SYSTOLIC VOLUME,
SV=EDV-ESV = STROKE VOLUME, EF=SV/EDV = EJECTION FRACTION, MVA=
MITRAL VALVE AREA, EOA= EFFECTIVE ORIFICE AREA IN MV CLOSED POSITION,
V_{REG}/SV=VOLUME OF BLOOD REGURGITATED NORMALIZED WITH SV.
$V_{REG_{OLD}}/V_{REG}$ =VOLUME OF OLD BLOOD REGURGITATED NORMALIZED WITH V_{REG}.

	EDV [cm³]	ESV [cm³]	SV [cm³]	EF [%]	$\frac{V_{reg}}{SV}$ [%]	$\frac{V_{reg_{old}}}{V_{reg}}$ [%]
	LV	LV	LV	LV	PRE POST	PRE POST
Healthy	114	47	67	59	0.06	11
MVR 1	64	17	47	74	14 0.07	24 32
MVR 2	133	50	83	63	19 0.82	49 2
MVR 3	81	32	49	61	19 0.76	23 4
MVR 4	93	41	52	56	11 1.4	52 8
MVR 5	73	36	51	51	33 3	22 12

Table 1 and figure 3 show the results of the clinical data and the regurgitated volume pre and post repair, also differentiating the percentage old blood regurgitation.
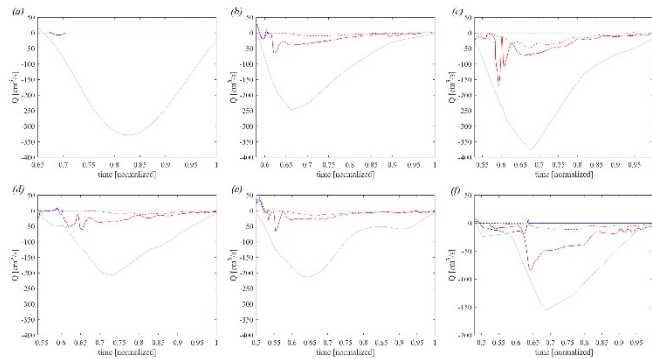
Figure 3. Flow balance in systole. Comparison between Q_{MV} and $Q_{MV_{old}}$ in healthy (a), pre and post MVR (b, c ,d ,e ,f). Continuous dark line is healthy Q_{MV}, dashed dark line is $Q_{MV_{old}}$, continuous red line is pre MVR Q_{MV}, dashed red line is pre MVR $Q_{MV_{old}}$, continuous blue line is post MVR Q_{MV} and dashed blue line is post MVR $Q_{MV_{old}}$.

Results confirm the great reduction of the regurgitation after repair and an optimal reduction of old blood regurgitated showing the efficacy of this reparation technique and its potential impact on the reduction of the risk of thrombus formation.
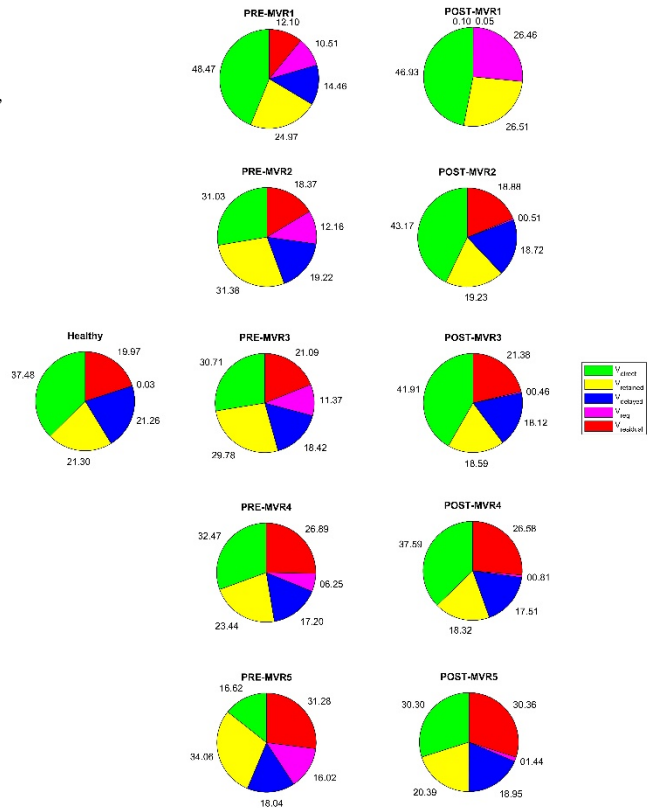
Figure 4. Pie graph of healthy, pre and post MVR cases.

Figure 4 shows that after repair V_{direct} increase and $V_{retained}$ is reduced; remarkably, the V_{reg} that was present pre-MVR is essentially transformed into V_{direct}. These results demonstrate the improvement of LV washout after surgery, thus reducing the risk of thrombus formation. A large amount of incoming blood is immediately ejected, the balance indicates that the blood regurgitated pre repair not is new, but is part of blood retained from the precedent heartbeat. In fact post repair this blood is englobed in V_{direct}. Moreover, $V_{retained}$ becomes similar to $V_{delayed}$ and this shows how V_{reg} influences the balance of the sub-volumes.

Figure 5 shows the distribution of the fresh and old blood inside the LV after one heartbeat (a, b, c) and after four heartbeat (d, e, f).
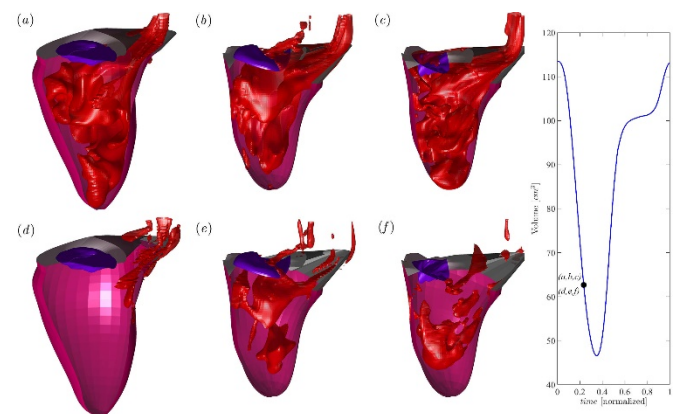
Figure 5. Three-dimensional flow field calculated with the passive scalar iso-surface method at the same instants of early systole in the first heartbeat at value C=0.6 and after four heartbeat at value C=0.3. (a, d) healthy case, (b, c) pre MVR and (c, f) post MVR; as indicated in the volume curve inset.

The healthy case (figure 5 (a)), presents a good quantity of fresh blood (transparency section), a good mixed zone (red color more transparent) and the old blood (red color) directed toward the aorta. The flow before repair (figure 5 (b)) presents the volume regurgitated and a slower wash-out of old volume with respect to the healthy case. After repair (figure 5 (c), we notice more mixed zone and a better distribution of the fresh and old blood directed toward the aorta. After four heartbeat (figure 5 (d), the healthy case has discharged a good quantity of old blood, while a significant quantity of old blood is present in the pathological case (figure 5 (e)) inside the LV and in regurgitation. After repair (figure 5 (f)), we note a reduced quantity of old blood respect pre repair case better directed toward the aorta, this is important because confirm that the LV discharges a large amount of old blood, in addition to that incorporated in $V_{retained}$.

IV. CONCLUSION

Numerical simulations allows a deeper evaluation of the effect of MV repair to the LV blood flow. Results show that the MV regurgitation before surgery presents a significant percentage of old blood volume that in most cases is close to 50%; this increases the risk of thrombus formation because the regurgitated blood takes a long time before complete washed-out. The wash-out improves after repair; besides the correction of insufficiency, it presents a better blood circulation inside the LV with a rebalancing of the mixture of old and fresh blood as well a better resynchronization of ejection.

This work shows that the clinical use of numerical simulation is increasingly feasible and provides novel information to assess the quality of surgical therapy. In perspective, this approach can also be used for reproducing the virtual flow that would realize in hypothetical therapeutic solutions and therefore introducing predictive capabilities to modern flow imaging technology.

REFERENCES

[1] A. Pasipoularides, "Mechanotransduction Mechanisms for Intraventricular Diastolic Vortex Forces and Myocardial Deformations: Part 2," *J. Cardiovasc. Transl. Res.*, 2015.

[2] G. Pedrizzetti, G. La Canna, O. Alfieri, and G. Tonti, "The vortex - An early predictor of cardiovascular outcome?," *Nature Reviews Cardiology*. 2014.

[3] L. Andrés-Delgado and N. Mercader, "Interplay between cardiac function and heart development," *Biochim. Biophys. Acta - Mol. Cell Res.*, 2016.

[4] J. C. Culver and M. E. Dickinson, "The effects of hemodynamic force on embryonic development," *Microcirculation*. 2010.

[5] J. R. Hove, R. W. Köster, A. S. Forouhar, G. Acevedo-Bolton, S. E. Fraser, and M. Gharib, "Intracardiac fluid forces are an essential epigenetic factor for embryonic cardiogenesis," *Nature*, 2003.

[6] J. Eriksson, J. Zajac, U. Alehagen, A. F. Bolger, T. Ebbers, and C. J. Carlhäll, "Left ventricular hemodynamic forces as a marker of mechanical dyssynchrony in heart failure patients with left bundle branch block," *Sci. Rep.*, 2017.

[7] G. Pedrizzetti, A. R. Martiniello, V. Bianchi, A. D'Onofrio, P. Caso, and G. Tonti, "Changes in electrical activation modify the orientation of left ventricular flow momentum: Novel observations using echocardiographic particle image velocimetry," *Eur. Heart J. Cardiovasc. Imaging*, 2016.

[8] D. Collia, L. Zovatto, and G. Pedrizzetti, "Analysis of mitral valve regurgitation by computational fluid dynamics," *APL Bioeng.*, 2019.

[9] D. Collia, M. Vukicevic, V. Meschini, L. Zovatto, and G. Pedrizzetti, "Simplified mitral valve modeling for prospective clinical application of left ventricular fluid dynamics," *J. Comput. Phys.*, vol. 398, 2019.

[10] J. O. Mangual, F. Domenichini, and G. Pedrizzetti, "Three dimensional numerical assessment of the right ventricular flow using 4D echocardiography boundary data," *Eur. J. Mech. B/Fluids*, 2012.

[11] J. O. Mangual *et al.*, "Comparative numerical study on left ventricular fluid dynamics after dilated cardiomyopathy," *J. Biomech.*, 2013.

[12] F. Domenichini and G. Pedrizzetti, "Hemodynamic forces in a model left ventricle," *Phys. Rev. Fluids*, 2016.

[13] C. Celotto, L. Zovatto, D. Collia, and G. Pedrizzetti, "Influence of mitral valve elasticity on flow development in the left ventricle," *Eur. J. Mech. B/Fluids*, 2019.

[14] A. F. Bolger *et al.*, "Transit of blood flow through the human left ventricle mapped by cardiovascular magnetic resonance," *J. Cardiovasc. Magn. Reson.*, 2007.

[15] C. J. Carlhäll and A. Bolger, "Passing strange flow in the failing ventricle," *Circulation: Heart Failure*. 2010.

[16] G. Pedrizzetti and F. Domenichini, "Left ventricular fluid mechanics: the long way from theoretical models to clinical applications.," *Ann. Biomed. Eng.*, 2015.

[17] V. M. Stoll *et al.*, "Left Ventricular Flow Analysis," *Circ. Cardiovasc. Imaging*, 2019.

[18] F. Domenichini and G. Pedrizzetti, "Asymptotic Model of Fluid–Tissue Interaction for Mitral Valve Dynamics," *Cardiovasc. Eng. Technol.*, 2015.

Hybrid membranes for blood-contacting surfaces: preliminary characterization

M. Todesco[1,2], G. Merigliano[1,2], V. Candela[1,2], L. Iop[2,3], T. Palmosi[2,3], G. Gerosa[2,3] and A. Bagno[1,2]

[1] *Department of Industrial Engineering, University of Padua, via Marzolo 9, 35131, Padova, Italy*
[2] *L.i.f.e.L.a.b. Program, Padova, Italy*
3 *Department of Cardiac, Thoracic and Vascular Sciences, University of Padova, via Giustiniani 2, 35127, Padova, Italy*

Abstract — **The hemocompatibility of any mechanical circulatory support device is mostly conditioned by the nature of the blood-contacting surface. Hybrid membranes as the inner surfaces of the artificial ventricle were produced by coupling a polymeric material (polycarbonate urethane) with decellularized biological tissues (animal pericardia). Physicochemical and mechanical characteristics of the hybrid membranes were carefully evaluated confirming satisfactory features in terms of composition and mechanical resistance.**

Keywords— **pericardium, hybrid membrane, blood contacting surface, hemocompatibility.**

I. INTRODUCTION

NOWADAYS, heart transplantation represents the optimal solution for refractory end-stage heart failure [1]. However, patients' mortality is increasing due to the prolonged waiting list time.

The quest for alternative therapeutic options resulted in the development of mechanical circulatory support devices that can replace one ventricle or the whole heart performances. These supports are respectively defined as: Ventricular-Assist Devices (VADs), which have the potential to increase patients' survival and quality of life mostly replacing the left ventricle, and Total Artificial Hearts (TAHs), which are the most sophisticated mechanical circulatory supports. These latter replace both ventricles and heart valves with a double pneumatically or electromechanically driven pump.

Over the years, several TAHs have been developed and implanted, but currently only one is still in clinical use: the CardioWest TAH [2]. At present, another implantable TAH, named Carmat, is under evaluation in clinical trials.

Several drawbacks are still limiting the extended application of TAHs: geometry, power supply, mechanical and biological factors [3]. These latter can be summarized as "blood compatibility" concerns: they can result in hemorrhages, hemolysis, thrombosis and thromboembolism. In addition, calcification and infections can cause the device failure.

Hemocompatibility involves several aspects (from platelet activation to immune system recruitment) and engineering requirements (from design to hemodynamics) [4]. The selection of appropriate biomaterials does not necessarily imply the compatibility of the whole device [5], but the progression of blood–material interactions is surely determined by blood-contacting surfaces.

The present work aims at producing and preliminarily characterizing innovative hybrid membranes for the construction of blood-contacting surfaces, which are intended for the production of the inner surfaces of novel mechanical circulatory supports. Membranes were obtained by coupling a polymeric material (commercial polycarbonate urethane, available in two different formulations with and without added silica), which is responsible for the mechanical resistance, with biological decellularized tissues (porcine and bovine pericardia), which are in direct contact with blood, to assure high hemocompatibility. The biological layer will also be prone to endothelialization by circulating cells.

The hybrid membranes were characterized from physicochemical and mechanical point of views.

II. MATERIALS AND METHODS

A. Tissue preparation

Fresh pericardia of healthy animals (calves and pigs) were supplied from local abattoirs. Pre-pericardial fat was removed and each pericardium was dissected free from its attachment at the base of the heart. Samples from the anterior left ventricular region of each pericardium were used for the fabrication of the hybrid membrane.

B. Decellularization

Tissues were treated according to the TriCol procedure [6]. The procedure was carried out under constant agitation and following 8 hour-long cycles. The inactivation of the cell proteases was followed by alternated hypo- and hypertonic solutions, combined with increasing concentrations of Triton X-100 (0.1-1%, Sigma-Aldrich). Cellular components were extracted from the tissue by 10 mM bile salt anionic surfactant sodium cholate (Sigma-Aldrich).

C. Membrane fabrication

Decellularized tissue samples were washed in deionized water and gently dried with filter paper. The samples were then placed on the serosa side and fastened into a customized metallic frame (Figure 1). On the other side (fibrosa), a thin layer of liquid polycarbonate urethane was poured (ChronoFlex AR and ChronoFlex AR-LT, AdvanSource Biomaterials, Wilmington, MA, US). Both polymers were supplied as 22% (w/v) solution in N,N-dimethylacetamide (DMAc). The membranes were dried for 24 hours at 40°C in a vacuum oven (Raypa, Barcelona, Spain).

Therefore, four different hybrid membranes were produced by coupling porcine and bovine pericardia with the two polymers.

D. Analytical techniques

The following analytical techniques were utilised to characterize biological samples, polymers themselves and hybrid membranes: Fourier Transform Infrared spectroscopy

Attenuated Total Reflection FTIR-ATR (Nicolet iS-50, Thermo Fisher Scientific, Waltham, Massachusetts, USA), Differential Scanning Calorimetry DSC (Q200, TA Instruments, New Castel, Delaware, USA), Thermo-Gravimetric Analysis TGA (SDT Q600, TA Instruments, New Castel, Delaware, USA).
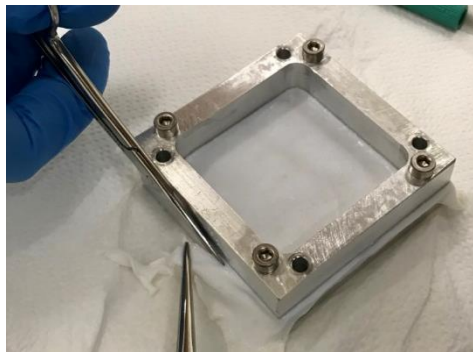

Fig. 1: Pericardium is fastened into the metallic frame (50 x 50 mm^2) before being covered with the polymeric solution

E. Mechanical characterization

For the mechanical assessment, samples were shaped into dog bone specimens by means of an in-house designed cutter. Sample thickness was measured using a Mitutoyo digital caliber (model ID-C112XB, Aurora, IL, USA) (Table I). Mechanical tests (uniaxial tensile loading tests) were performed by means of the Bose Electroforce System (Bose Corporation, Eden Prairie, Minnesota, USA). The system was equipped with two Bose linear actuators (200 N) and one loading cell (225 N). Tests were performed at room temperature; biological samples were continuously wetted with 0.9% NaCl solution to prevent dehydration. The gauge length of each sample was 5 mm.

Samples were elongated (elongation rate set at 0.5 mm/s) to rupture for measuring the Ultimate Tensile Strength (UTS) and the Failure Strain (FS); the elastic modulus was calculated as the slope of the stress-strain curves in the linear region.

III. RESULTS

A. FTIR-ATR, DSC and TGA

FTIR-ATR spectra confirmed the chemical composition of the polycarbonate urethanes. FTIR-ATR spectra were also acquired on the pericardial side of the hybrid membranes: these spectra allowed ascertaining that the polymers do not diffuse throughout the biological tissues because of the solvent casting procedure (data not shown).

DSC analysis allowed determining the glass transition temperature of both polymers: – 31.5°C for ChronoFlex AR-LT, and – 28°C for ChronoFlex AR (Figure 2).

TGA analysis confirmed the presence of a 9% inorganic residue in the ChronoFlex AR-LT (Figure 3): this is due to the microsilica added to make the polycarbonate urethane less sticky.

B. Mechanical characterization

Mechanical tensile tests were performed on polymeric membranes, on decellularized animal pericardia, and on hybrid membranes.

Table II summarizes the results obtained from the mechanical tests on native bovine (NBP) and native porcine (NPP) pericardia, on the membrane fabricated by coupling decellularized bovine pericardium with Chronoflex AR (DBP-AR) and AR-LT (DBP-ARLT), and by coupling decellularized porcine pericardium with Chronoflex AR (DPP-AR) and AR-LT (DPP-ARLT).
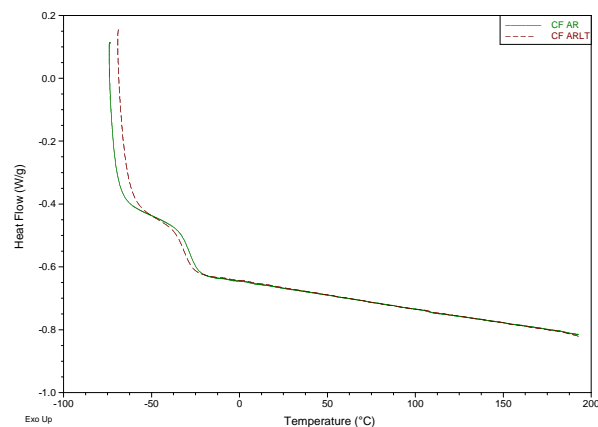
Fig. 2: DSC analysis of ChronoFlex AR and ChronoFlex AR-LT: glass transition temperatures are -28°C and -31.5°C, respectively
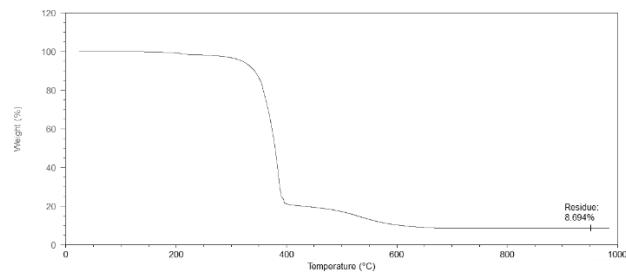
Fig. 3: TGA analysis of the ChronoFlex AR-LT identified the presence of 9% inorganic residue (silica)

TABLE I
SAMPLES THICKNESS

Sample	Thickness [mm]
NBP	0.23 ± 0.17
NPP	0.12 ± 0.07
DBP-AR	0.53 ± 0.05
DBP-ARLT	0.62 ± 0.1
DPP-AR	0.42 ± 0.02
DPP-ARLT	0.59 ± 0.04

It is worthy to mention that hybrid membrane failure is mainly influenced by pericardium mechanical resistance: the application of tensile load causes the elongation of collagen fibres within tissue matrix; therefore, collagen fibres lose their crimped configuration until they break. Since pericardium and polymer are well adhered to each other, collagen fracture results in the entire membrane failure.

Mechanical data showed a distinct decrease of stiffness when biological tissues are decellularized and coupled with

polymers, which is more evident for the ChronoFlex AR than the ChronoFlex AR-LT. Similarly, a decrease in UTS values appeared, which is larger for porcine pericardium than for bovine one. Interestingly, FS values increased up to more than 120% when both decellularized pericardia are coupled with the ChronoFlex AR. On the other hand, ChronoFlex AR-LT, which contains 9% microsilica, did not largely modify FS values of native tissues. This outcome is of particular interest in the perspective of the foreseen application: in line of principle, the hybrid membrane is required to be compliant with respect to the movements of the pulsatile chamber.

As to the membrane thickness (see Table I), different values are due to pericardia variability (considering both different species and different animals within the same specie): it is possible to control membrane thickness by adjusting the amount of polymer.

TABLE II
MECHANICAL DATA

Sample	E [MPa]	UTS [MPa]	FS [adim]
NBP	51.38 ± 13.85	17.27 ± 2.45	0.696 ± 0.1
NPP	71.59 ± 27.20	24.88 ± 7.88	0.617 ± 0.2
DBP-AR	8.64 ± 1.83	13.45 ± 5.51	1.21 ± 0.5
DBP-ARLT	10.21 ± 0.29	9.55 ± 0.26	0.74 ± 0.06
DPP-AR	6.21 ± 0.77	8.72 ± 0.66	1.29 ± 0.1
DPP-ARLT	13.65 ± 0.82	8.39 ± 2.62	0.69 ± 0.3

IV. CONCLUSION

This preliminary evaluation of the hybrid membranes fabricated by coupling decellularized biological tissues with polycarbonate urethanes allowed assessing their composition and mechanical properties. At present, morphological studies are in progress by using SEM and two-photon microscopy to investigate both the surface and the cross-section of the hybrid membranes. Moreover, further investigations are ongoing to assess fatigue resistance under cyclic loading and the capacity of the hybrid membranes to evoke (or not) platelet activation and thrombin formation. Eventually, cytocompatibility tests (in vitro) and calcification test (in vivo) will be carried out for an exhaustive characterization of the hybrid membranes.

REFERENCES

[1] E. J. Benjamin, S. S. Virani, C. W. Callaway, A. R. Chang, S. Cheng S, et al., "Heart disease and stroke statistics—2018 update: a report from the American Heart Association", *Circ. J.*, vol. 137, pp. e67–492, 2018.

[2] G. Gerosa, S. Scuri, L. Iop, G. Torregrossa, "Present and future perspectives on total artificial hearts", *Ann Cardiothorac Surg.*, vol. 3(6), pp. 595-602, 2014.

[3] E. Dal Sasso, A. Bagno, S. T. G. Scuri, G. Gerosa, L. Iop, "The Biocompatibility Challenges in the Total Artificial Heart Evolution", *Annu Rev Biomed Eng.*, vol. 4, pp. 85-110, 2019.

[4] T. G. Grasel, R.S. Wilson, M. D. Lelah, H. W. Bielich, S. L. Cooper, "Blood flow and surface-induced thrombosis", *ASAIO Trans.*, vol. 32(1), pp. 515-20, Jul-Sep 1986.

[5] B. D. Ratner, A. S. Hoffman, F. J. Schoen, J. E. Lemons, "Biomaterials Science: An Introduction to Materials in Medicine", 2nd ed. Elsevier Academic Press, 2004.

[6] M. Spina, F. Ortolani, A. El Messlemani, A. Gandaglia, J. Bujan, N. Garcia-Honduvilla, I. Vesely, G. Gerosa, D. Casarotto, L. Petrelli, M. Marchini, "Isolation of intact aortic valve scaffolds for heart-valve bioprostheses: extracellular matrix structure, prevention from calcification, and cell repopulation features", *J Biomed Mater Res A*, vol. 67(4), pp. 1338-50, Dec 2003.

Automated Detection and Counting of Acne Lesions

A. Melina[1,2], P. Salvagnini[2], C. Cosentino[1], F. Amato[1] and A. Cherubini[2]

[1] Faculty of Biomedical Engineering, University "Magna Graecia"
[2] Linkverse-CosmoAI

Abstract— In the acne severity evaluation, the quantification of inflammatory lesions on the patients' face is a fundamental step.

The aim of this work is to develop a method that automatically performs acne lesions counting. We acquired high-resolution multi-polarization images of facial skin using the visible spectrum. 1089 patients with acne grading ranging from clear to severe were imaged from one to four times at two weeks interval. Images from five different point of views were acquired from each subject and converted to a standardized planar representation.

Experts annotated these planar images creating the ground truth. Patients were subdivided into training (648), validation (111), and holdout test subsets (330).

A U-net architecture was trained for 61 epochs to output a gray-scale image where hyperintensities corresponded to predicted location of potential acne lesion. Subsequently a blob detection algorithm was used to perform the counting of predicted lesion on each patient.

Results showed that the correlation coefficient between ground truth and automatized counting was 0.65 (confidence interval (C.I.) 0.61 - 0.69). This result suggests a very good agreement between ground truth and automatized counting, indicating that it is indeed feasible to meet this clinical need using deep learning methods.

Keywords—deep learning, acne, lesion counting.

I. INTRODUCTION

A. Clinical problem

ACNE vulgaris is a chronic skin disease whose severity is characterized by multiple factors such as the type of the lesions, their quantity and the density of involvement, which constantly varies in time and space. In clinical practice the lesion counting is the standard method used by physicians for assessing the disease severity [1]; however, this task is tedious for the dermatologist, who is subjected to fatigue and can easily incur into mistakes. For these reasons the clinical evaluation of acne severity is complex and with high inter-intra-observer variability. An accurate counting of acne lesions and an objective assessment of disease severity are fundamental steps to select the right treatment and to evaluate the response to therapy.

B. State of the art

During the last years, computer vision and deep learning systems have been developed in order to automate the counting process, but, as of today, results are not satisfactory and a clinically approved system performing this task does not exist. Maroni et al. [2] created an automated system based on computer vision techniques (Haar-Cascade classifiers, random forest models and blob detection algorithms) for acne detection and lesion counting, using pictures of body parts of the patients taken with a mobile phone. Although a feature importance ranking is presented, the authors do not report quantitative results regarding counting task. Wu et al. [3] proposed a unified framework based on Label Distribution Learning (LDL). LDL instead of assigning a single label, covers a certain number of adjacent labels where each label represents different description degree to the instance. Wu et al. [3] used LDL to simultaneously classify acne severity according to Hayashi criterion and count lesions on a proprietary dataset. They report good results in terms of specificity, sensitivity and precision. However, their algorithm is highly tuned to the distribution of colour skin in the images in their dataset, which comprise only Asian ethnicity and as such it is difficult to generalize. Moreover, they use images showing only portion of patients' face, whereas a proper counting needs to be performed on the entire face. Abas et al. [4] proposed an automated acne lesion identification system based on entropy filtering and thresholding. Their method generated region-of-interest map for acne lesions as preliminary step to count the number of lesions within a specific skin area. However, they do not extend their results to the entire face and thus do not provide quantitative results about the lesion counting method. Min et al. [5] proposed an automatic acne lesions counting and characterization algorithm using image processing techniques and an artificial neural network for the whitehead comedones detection. Their dataset is very small (25 subjects) and the algorithm is highly tuned to colour parameters identified during training of the algorithm. Amini et al. [6] validated an automated facial acne assessment system, combining existing algorithms for facial recognition and landmark identification techniques based on gaussian filters. The authors build the entire pipeline on standard computer vision techniques without using learning-based approaches. Their model is then tested on a dataset of images which mostly contained artificially created digital human models. Deep learning and Image segmentation using Convolutional Neural Networks, such as U-net [7]-[9], have been studied in dermatology for problems other than acne evaluation, in particular for the identification and segmentation of malignant melanoma. However, this is a different clinical problem, where the main aim is to characterize a lesion rather than finding its location. Moreover, in this case it is not necessary to analyse the entire face simultaneously since the task can be subdivided and repeated on each single suspect skin area.

C. Proposed methodology

The aim of this study is to create an automatic system able to

perform lesion counting without any human intervention.

A peculiarity of this work consists of using a flattened bi-dimensional representation of the patients' face: this approach allows to standardize the input data by taking into account the anatomical localization of the lesions, and to gather all the lesion of each patient in a single frame. These planar images, together with manually annotated masks were used for training and validating a Deep Neural Network (DNN) for automatically detecting acne lesions. The rationale behind using a DNN for detecting lesions is that this family of learning-based approaches has shown increased robustness in lesion segmentation tasks for large datasets. Subsequently, a blob detection algorithm was run on the DNN output, in order to perform lesions counting. The dataset used in this work is not limited to one ethnic group and skin colour, as it represents the largest and most heterogeneous dataset of acne patients in the literature so far.

II. MATERIALS AND METHODS

A. Dataset

An imaging device including a remotely controlled Nikon camera, lenses and tungsten flashes with polarizing filters was used to acquire high-resolution multi-polarization images of facial skin using the visible spectrum. 1089 patients (age range 9-60 years, median 19.2 years; female 64%), with acne grading ranging from clear to severe, participated in this study. Each patient was imaged from one to four times at two weeks interval. Images from five different point of views were acquired from each subject and each session. The multiple images collected from a patient were post-processed and converted to a standardized planar representation (Fig. 1), [10].
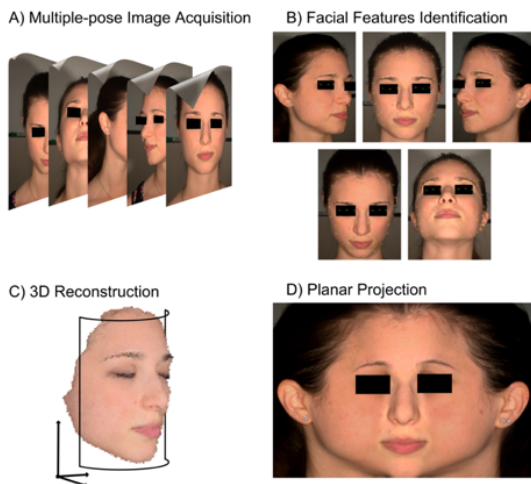
Fig. 1. The figure shows the images capture and processing workflow. The subjects seated in front of the device were asked to rotate their head in five different poses with a 30° tilt respect to the lens axis (A). For each pose, lateral flash bulbs were lighted to collect a first reference image and a second image with cross-polarized filters to reduce reflections in the images. Anatomical landmarks (B) were identified on each view and subsequently used to reconstruct the three-dimensional shape (C) of the individual face. The skin of the patient was then projected upon a cylindrical surface in order to generate a "flattened" image (D) showing the entire facial skin in a single bi-dimensional facial template.

Fig. 2. The figure shows examples of different patients with variable ethnicity, age and gender. Dataset used in this work is the largest and most heterogeneous in the literature. Represented ethnic groups are: White-Caucasian: 90,11%, Black-African: 6,03%, Asian: 2,14%, Hawaiian: 0,31%, Indian: 0,19%, Other: 1,22%.

Experts annotated these planar images by marking each lesion using an ad-hoc software tool. The software uses a graphic interface implemented in Python. The annotators visualize the RGB planar image with the ability to zoom in on details and to draw circles around the lesions that are identified. The software exports the annotations as binary images with dimensions identical to the input planar and hyperintensities corresponding to the location of the annotated circles. These annotated binary images represented the ground truth used to train the Neural Network. The ground truth for the total number of lesions in a single planar image was the number of circles drawn on the planar images by the expert during the annotation process.

B. Workflow

The whole dataset was split so that each subject was present only in one of the sub-sets. Thus, if the same patient was imaged in multiple session, all sessions of the same patient would be assigned to the same sub-set. 30% of the whole dataset was used as a holdout set used as a Testing set (330 patients, 954 images). The remaining 70% was further splitted in two subsets: 55% (648 patients, 1891 images) was used as a Train dataset and the remaining 15% (111 patients, 333 images) as Validation dataset. The planar images and the ground-truth masks were fed to an U-net neural network implemented in Keras [11]. The U-net architecture consists of two paths: contraction and expansion. The contraction path consists of 6 contraction blocks where each block takes an input applies two 3x3 convolution layers followed by a 2x2 max pooling; the expansion path consists of 6 expansion blocks; each block passes the input to two 3x3 CNN layers followed by a 2x2 up-sampling layer. At the last layer a sigmoid activation function, or logistic function, was used to calculate the binary output images. For the optimization was used an Adam adaptative learning rate optimization algorithm.
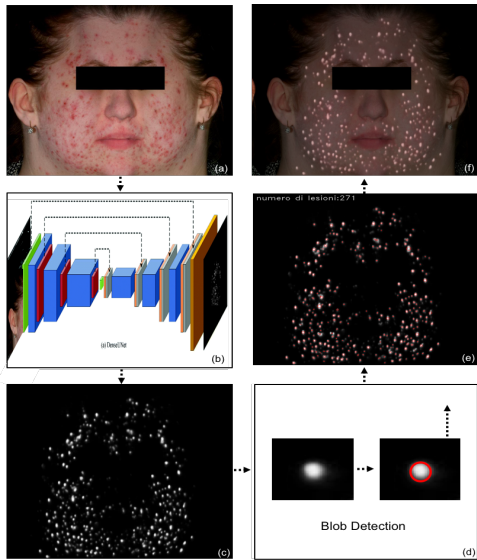
Fig. 3. The figure shows the workflow of the detection and counting system. The planar images reshaped in a squared matrix (a) were the input to a DNN algorithm, called U-net (b) [12]. A U-net neural network consisting of a contraction section with 6 contraction blocks where each block takes an input applies two 3X3 convolution layers followed by a 2x2 max pooling; an expansion section with 6 expansion blocks, each block passes the input to two 3x3 CNN layers followed by a 2x2 up-sampling layer. A grey-scale image (c) was obtained as output of this DNN. A blob detection algorithm (d) was used to detect the number of inflammatory lesions in the output of the DNN. (e) It is possible to observe the superimposition of the net result on the original image (f).

During the optimization phase, the difference between ground truth (y) and predict values ($\hat{y}$) of each pixel (N) in the image was minimized using the loss function called Binary Cross-Entropy, Eq. (1).

$$L(y, \hat{y}) = -\frac{1}{N}\sum_{i=0}^{N}(y * \log(\hat{y}_i) + (1 - y) * \log(1 - \hat{y}_i)) \quad (1)$$

During the training phase, a batch size of 16 and a learning rate of 10^{-4} was used.

After each iteration of training phase, the U-net learned the rules to determine relevant features to detect inflammatory lesions in the patient images. The network was trained for 61 epochs. The validation dataset was used at the end of each epoch to assess the quality of the training, by comparing the output of the network with the ground truth. During the validation phase, the best model was chosen at the time when the loss, calculated through binary cross entropy, stabilized around a minimum of 0,021. The output of the network consisted of gray-scale images in which not-black pixels are considered parts of probable lesions. After the training phase, the test dataset was used to verify the performances of the network. In order to perform the lesions counting, a blob detection algorithm [13] implemented in Python OpenCV library with optimized parameters (algorithm cv2.SimpleBlobDetector, threshold range 50-255; minimum area: 1-pixel, minimum convexity = 0.87; blob Color = 255) was run on each output image from the test set. In order to be considered for counting, only the detected blobs with an Intersection over Union with GT above a threshold of 0.5 were retained as valid detections. Using this threshold, we can provide an estimate of True Positives (lesions that are present

in both GT and prediction) False Positives (lesions that are present only in prediction) and False Negatives (lesions that are present only in GT but missed during detection).

III. RESULTS

A complete confusion matrix of the system could not be evaluated since we did not have a definition for True Negatives. However, we measured a sensitivity of 0.78 (TP/P; C.I. 0.71-0.85) and a precision of 0.82 (TP/(TP+FP); C.I. 0.75-0.89).

The clinical performances of the system were evaluated measuring the correlation between the number of lesions in the ground-truth for each patient and the predicted counting from the algorithm. We chose to use the correlation because this is the standard metric used in the clinical literature to compare the reliability of dermatologists in counting acne lesions [14]. The higher the correlation value the better the agreement between dermatologists, with values above 0.6 considered very good.

A Pearson's correlation coefficient of r = 0.65 (C.I. 0.61 - 0.69) was obtained (Fig. 4), (Table 1). A deeper investigation was conducted by evaluating the correlation between ground truth and automated counting on subsets of data divided for sex and age group. Correlation of the data based on sex showed a coefficient r=0.61 (C.I. 0.55 - 0.67) and r=0.65 (C.I. 0.61 - 0.70) for males and females respectively (Fig. 5a), (Table 1). For the age range, the correlation coefficients were: r = 0.62 (C.I. 0.56 - 0.67) for patients aged 0-18 years, r = 0.70 (C.I. 0.65 - 0.75) for age of 19-30 years and r = 0.47 (C.I. 0.18 - 0.68) for 31-60 years range (Fig. 5b), (Table 1). For the last class we obtained the worst results, this might be related to the low number of samples in this category, which affected the training: in the training set only 48 subjects belonged to the 31-60 years group, while we had 377 subjects for the 0-18 years group, and 223 subjects for the 19-30 years; the test set was composed of 156, 159, and 15 subjects for the 0-18 years group, the 19-30 years group and 31-60 years group respectively.

The performance of the blob detection algorithm was evaluated for both ground-truth images and predicted images. Comparing the results of the blob detection algorithm on the GT images with the number of circles annotated by experts using the software we obtained a sensitivity of 0.98. The mean absolute error and root mean squared error between the counts performed on GT images and predicted images were 0.029 and 37.42 respectively.

TABLE I

Pearson's correlation coefficient between GT counting and counting from the proposed method. Confidence intervals of Pearson's correlation computed using Fisher'z.

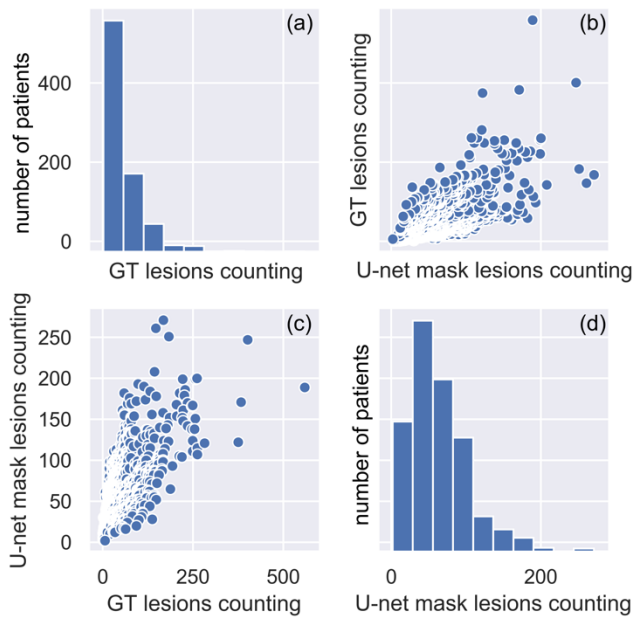|		Pearson's Correlation coefficient (r)	Confidence intervals
All		0.65	0.61-0.68
Sex	M	0.61	0.55-0.67
	F	0.65	0.61-0.70
Age (years)	0-18	0.62	0.56-0.67
	19-30	0.70	0.65-0.75
	31-60	0.47	0.18-0.68

Fig. 4. The subplots show the distribution of GT counting (a) and automatized counting (d). Subplots (b) and (c) show the scatterplots of the number of lesions on the same patients calculated with the algorithm versus the GT. Pearson correlation for the scatterplots is (r = 0.65, C.I. 0.61 - 0.69). r = Pearson correlation coefficient, C.I. = confidence interval.
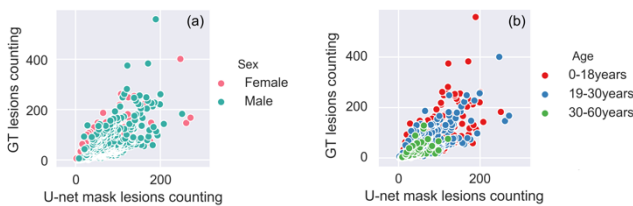

Fig. 5. Subplot (a) shows the scatterplot of the data based on sex (male: r =0.61, C.I. 0.55 - 0.67 and female: r = 0.65, C.I. 0.61 - 0.70). Subplot (b) shows the scatterplot subdivided according to age ranges (0-18 years: r = 0.62, C.I. 0.56 - 0.67, 19-30 years: r = 0.70, C.I. 0.65 - 0.75 and 31-60 years: r = 0.47, C.I. 0.18 - 0.68). r = Pearson correlation coefficient, C.I. = confidence interval.

IV. DISCUSSION

Our experiments showed promising results for the agreement between ground truth and automatized counting. It is important to note that this is results is obtained on the largest and more heterogeneous dataset of Acne patients published so far in the literature. As a consequence, the potential generalizability of the results can be considered robust.

The main innovation introduced here compared to previous works on the same topic is the use of a flattened transformation of the patient face. This pre-processing step allowed us to output a single number representing all the lesions present in a patient. Conversely, when counting algorithms are used on an image taken from a single perspective (e.g. right side of the face), there will be some lesion present in region of the face that could be present also in other perspectives, thus introducing the problem of multiple counting. Moreover, standardization of the input images means that the same anatomical region in one subject corresponds to the same region in all subjects. In other words, the DNN input would find a particular region (e.g. the right eye) always in the same input node. This characteristic allows the network to learn that

there are facial areas in which the probability to observe inflammatory lesions are higher, and region where lesions are never present. As a consequence, we allow the DNN to combine efficiently local information about skin colour/contrast with anatomical a priori knowledge.

V. CONCLUSION

In this work we obtained for the first time an automated lesion counting on a large dataset with excellent correlation with clinical ground truth. Future work will further refine the neural network, introducing the ability to output all the parameters needed for a complete evaluation of acne severity: lesion counting, global grading and binary mask with lesion location.

REFERENCES

[1] J.A. Witkowski, L.C. Pairsh, J.D. Guin. Acne grading methods. Archives of Dermatology. 1980;116(5):517-518. doi:10.1001/archderm.1980.01640290027005

[2] G. Maroni, M. Ermidoro, F. Previdi and G. Bigini, "Automated detection, extraction and counting of acne lesions for automatic evaluation and tracking of acne severity,". IEEE Symposium Series on Computational Intelligence (SSCI), Honolulu, HI, 2017, pp. 1-6, doi: 10.1109/SSCI.2017.8280925.

[3] X. Wu, N. Wen, J. Liang, Y. Lai, D. She, M. Cheng and J. Yang. "Joint acne image grading and counting via label distribution learning". EEE/CVF International Conference on Computer Vision (ICCV), Seoul, Korea (South), 2019, pp. 10641-10650, doi: 10.1109/ICCV.2019.01074.

[4] F. S. Abas, B. Kaffenberger, J. Bikowski, and M. N. Gurcan. "Acne image analysis: lesion localization and classification,". Proc. SPIE 9785, Medical Imaging 2016: Computer-Aided Diagnosis, 97850B (24 March 2016); doi: 10.1117/12.2216444.

[5] S. Min, H.J. Kong, C. Yoon, H.C. Kim, D.H. Suh. "Development and evaluation of an automatic acne lesion detection program using digital image processing". Skin Research and Technology. 2013;19(1):e423-e432. doi:10.1111/j.1600-0846.2012.00660.x

[6] M. Amini, F. Vasefi, M. Valdebran, K. Huang, H. Zhang, W. Kemp, N. MacKinnon. "Automated facial acne assessment from smartphone images,". Proc. SPIE 10497, Imaging, Manipulation, and Analysis of Biomolecules, Cells, and Tissues XVI, 104970N, 22 February 2018; doi: 10.1117/12.2292506

[7] A. Motsch, S. Motsch, T. Saguet. "Lesion segmentation using U-Net network". ISIC 2018, arXiv:1807.08844 [cs.CV]

[8] H. Jiang, R. Rong, J. Wu, X. Li, X. Dong, E.Z. Chen. "Skin lesion segmentation with improved C-UNet networks". BioRxiv, 382549 ,2018, doi: https://doi.org/10.1101/382549

[9] D. Ramani and S. Ranjani. "U-Net Based Segmentation and Multiple Feature Extraction of Dermascopic Images for Efficient Diagnosis of Melanoma". Lecture Notes in Computational Vision and Biomechanics, 2019, Vol. 31, 81-101, 2019. doi:10.1007/978-3-030-04061-1_9.

[10] A. Melina, N.N. Dinh, B. Tafuri, G. Schipani, S. Nisticò, C. Cosentino, F. Amato, D. Thiboutot, A. Cherubini. "Artificial Intelligence for the Objective Evaluation of Acne Investigator Global Assessment". Journal of Drugs in Dermatology, 2018 Sep 1;17(9):1006-1009.

[11] O. Ronneberger, P. Fischer and T. Brox. "U-Net: Convolutional Networks for Biomedical Image Segmentation". arxiv1505.04597, 2015.

[12] S. Li, Y. Chen, S. Yang, W. Luo. "Cascade Dense-Unet for Prostate Segmentation in MR Images". Lecture Notes in Computer Science, 2019, vol 11643. Springer, Cham. doi: 10.1007/978-3-030-26763-6_46.

[13] X. Xiong and B.J. Choi. "Comparative Analysis of Detection Algorithms for Corner and Blob Features in Image Processing". International Journal of Fuzzy Logic and Intelligent Systems Vol. 13, No. 4, December 2013, pp. 284-290 doi: 10.5391/IJFIS.2013.13.4.284

[14] J.K. Tan, K. Fung, L. Bulger. Reliability of dermatologists in acne lesion counts and global assessments. Journal of Cutaneous Medicine and Surgery. 2006;10(4):160-165. doi:10.2310/7750.2006.00044

A 3D CNN for preterm-infants' movement detection in NICUs from depth streams

Lucia Migliorelli[1], Sara Moccia[1,*], Giuseppe Pio Cannata[1], Alessia Galli[2], Ilaria Ercoli[3], Luigi Mandolini[4], Virgilio Carnielli[5], Emanuele Frontoni[1]

[1]Department of Information Engineering, Università Politecnica delle Marche, Ancona (Italy)
[2]Unit of Neonatology, Ospedali Riuniti di Ancona, Ancona (Italy)
[3]JEF s.r.l., Civitanova Marche, (Italy)
[4]MAC s.r.l., Porto Recanati (Italy)
[5]Department of Neonatology, Università Politecnica delle Marche, Ancona (Italy)
*Correspondence to: s.moccia@univpm.it

Abstract—Preterm-infants' movement monitoring in neonatal intensive care units (NICUs) has a strong diagnostic and prognostic role. Despite its importance, movement monitoring still relies on clinicians' visual observation at the crib side. The goal of this work is to present an automatic, deep-learning based approach to movement detection from depth-image streams. The proposed approach relies on a pre-trained 3D convolutional neural network (CNN), which we proposed in a previous work for joint-pose estimation (joint-CNN). The joint-CNN is here modified (mov-CNN) to fulfill the movement detection task by combining the encoder path of the joint-CNN with 3 fully-connected layers. When tested on a dataset acquired in the actual clinical practice, the proposed mov-CNN achieved a recall of 0.84. The achieved results prompt the possibility of translating the developed methodology into the actual clinical practice, as a valuable tool to support clinicians in NICUs.

Keywords—Preterm infants, movement detection, deep learning, fine tuning.

I. INTRODUCTION

The World Health Organization (WHO) reported that, every year, 15 millions of infants born preterm (i.e., before the 37 gestational weeks) worldwide[1], and this number is expected to grow. Cognitive dysfunctions, motor impairments and behavioural disorders are among the major adverse implications of preterm birth, and their early identification in Neonatal Intensive Care Units (NICUs) is crucial to allow proper treatments [1]. Infants' spontaneous motility is a valuable diagnostic and prognostic index of infants' cognitive and motor development [2]. However, despite its importance, infants' movement monitoring still mainly relies on clinician's observation at the crib side in NICUs. This procedure is qualitative, time consuming and prone to human fatigue. Moreover, preterm infants' movements are infrequent and often imperceptible, posing challenges in the observation task [3].

In this complex scenario, a tool to automatically and accurately detect infants' movement would provide clinicians with (i) movement statistics, (ii) meaningful video portion to be reviewed for movement analysis.

A number of approaches to quantitatively measure preterm infants' spontaneous movement has been proposed in the

[1]https://www.who.int/news-room/fact-sheets/detail/preterm-birth

Fig. 1: Acquisition set-up: the RGB-D camera (light-blue box) does not hinder the healthcare team of the Neonatal Intensive Care Unit (NICU) during the actual clinical practice. An example of acquired depth stream is showed on top left.

literature. In [4], wearable sensors, such as accelerometers and gyroscopes, are exploited to detect limb-specific movement. However, wearable sensors placed on infants' limbs hinder infants' spontaneous movements and need to be constantly re-calibrated, posing limitations in their use in the actual clinical practice.

To overcome such limitations, camera sensors can be used. These sensors can be easily integrated into the daily mon-

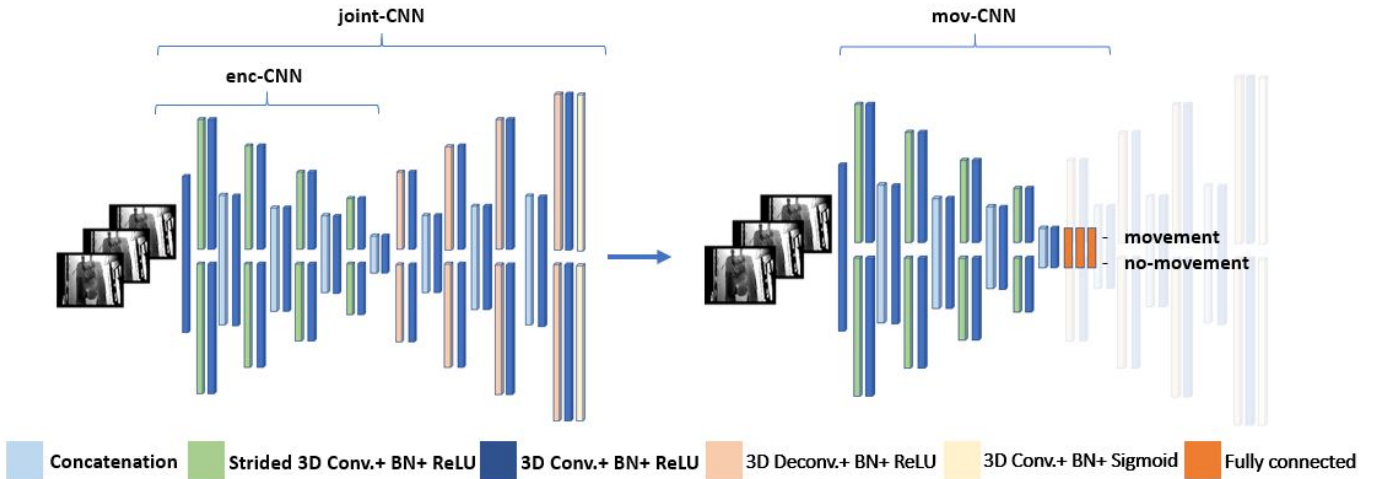**Fig. 2:** (Left) The joint-CNN model from our previous work [5] (aimed at detecting limb-joint position). The descending part (enc-CNN) of joint-CNN is highlighted. (Right) The mov-CNN aims at detecting those video portions in which the infant moves. It combines enc-CNN with 3 newly stated fully-connected layers. Batch normalization (BN) and activation with rectified linear unit activation (ReLu) are implemented after each 3D convolution (Conv).

itoring practice as they do not hamper infants' movement neither healthcare operators in their daily practice. Examples include [6] and [7], where optical flow is exploited to estimate preterm infants' spontaneous movement in RGB-image streams. However, the two approaches are semi-supervised and computational expensive, hampering their use in the clinical practice. In [8], an automatic threshold-based approach is proposed to detect infants' movement from images acquired with depth sensors, which have the advantage of preserving infants' and operators' privacy. However, the threshold value has to be manually set, resulting in high sensitivity to noise and inter-subject variability.

Besides inter-subject variability and image noise, further challenges that have to be addressed when processing depth images include homogeneous image portion, variable distance between the crib and the camera, and variability in infants' movements (both in terms of frequency and intensity). To tackle these challenges, a possible solution could be to exploit the generalization power of deep learning (DL). DL, and in particular convolutional neural networks (CNNs), have already been applied in the field of depth-image analysis for the estimation of infants' limb pose: in [5], a 3D encoder-decoder CNN (joint-CNN) is designed to detect infants' joints from depth streams. Assuming that infants' movement is mostly related to limb-joint movement, our hypothesis is that movement detection can be achieved by partially relying on the same joint-CNN.

The goal of this paper is to design a 3D CNN (mov-CNN) to detect preterm-infants' movement from depth streams. The mov-CNN exploits the encoder (enc-CNN) of the joint-CNN and adds fully-connected layers to classify depth streams where the infant moves (*movement* class) and does not (*no-movement* class). Depth streams were acquired with the setup presented in [5], [9] and showed in Fig. 1.

TABLE I: Overall architecture to preterm infants' movement detection. The architecture includes the encoder path (enc-CNN) from [5] for feature extraction, and 3 fully-connected layers for classification. Kernel size and stride, and number of channels are reported for each CNN kernel.

Name	Kernel (Size / Stride)	Channels
enc-CNN		
Input	–	3x1
Convolutional layer - Common branch	3x3 / 1x1	3x64
Block 1 - Branch 1	2x2x2 / 2x2x1	3x64
	3x3x3 / 1x1x1	3x64
Block 1 - Branch 2	2x2x2 / 2x2x1	3x64
	3x3x3 / 1x1x1	3x64
Block 1 - Common branch	1x1x1 / 1x1x1	3x128
Block 2 - Branch 1	2x2x2 / 2x2x1	3x128
	3x3x2 / 1x1x1	3x128
Block 2 - Branch 2	2x2x2 / 2x2x1	3x128
	3x3x3 / 1x1x1	3x128
Block 2 - Common branch	1x1x1 / 1x1x1	3x256
Block 3 - Branch 1	2x2x2 / 2x2x1	3x256
	3x3x3 / 1x1x1	3x256
Block 3 - Branch 2	2x2x2 / 2x2x1	3x256
	3x3x3 / 1x1x1	3x256
Block 3 - Common branch	1x1x1 / 1x1x1	3x512
Block 4 - Branch 1	2x2x2 / 2x2x2	3x512
	3x3x3 / 1x1x1	3x512
Block 4 - Branch 2	2x2x2 / 2x2x1	3x512
	3x3x3 / 1x1x1	3x512
Block 4 - Common branch	1x1x1 / 1x1x1	3x1024
Fully-connected layers		
Fully connected 1	3x512	-
Fully connected 2	3x512	-
Fully connected 3	3x2	-

This paper is organized as follows: Sec. II describes the DL-approach to preterm infant's movement detection, Sec. III presents the experimental protocol to validate the proposed approach. The experimental results are reported in Sec. IV and discussed in Sec. V, which concludes the paper.

TABLE II: Training and validation sets size.

	Training set	Validation set
movement	1028	332
no-movement	1028	332

II. Methods

The proposed mov-CNN for movement detection is fed with a depth stream (i.e., a stack of 3 consecutive depth frames or *triplet*) and consists of:

- enc-CNN: The encoder path of the joint-CNN, for joint spatio-temporal feature extraction
- 3 fully-connected layers, for the binary classification of depth streams in *movement* and *no-movement*

The overall mov-CNN architecture is described in Table I. The enc-CNN has 4 convolutional blocks. Each block has 2 branches (for processing limb joints and joint connections separately), each of which implements two consecutive 3D convolutions. Batch normalization and activation with the rectified linear unit (ReLu) are implemented after each convolution operation. The outputs of the two branches are then concatenated and given as input to the next block.

The three fully connected layers (with 512, 512 and 2 neurons, respectively) are added after the last block to fulfill the classification (right side of Fig. 2).

To train our mov-CNN, we adopted fine tuning. This allows to migrate the knowledge learned by the joint-CNN for joint detection to the mov-CNN for the movement-detection task. We initialized the enc-CNN weights with the weights of the encoder of joint-CNN, while the connection between neurons in the fully-connected layers were initialized with standard *Glorot* initialization. Then, Adam was used as optimizer to minimize the binary cross-entropy with mini-batch gradient descent.

III. Experimental Protocol

A. Dataset

The dataset used in this work consisted of 16 depth videos of 16 preterm infants spontaneously breathing. The videos were acquired in the NICU of the G. Salesi Hospital in Ancona, Italy. Each infant's legal guardian signed an informed consent.

The videos were acquired using the Astra Mini S-Orbbec ®. The camera frame rate was 30 frames per second with image size of 640x480 pixels. Video length was 180s.

Video annotation was performed in cooperation with the healthcare team of the Salesi Hospital. Considering the average preterm infants' movement rate [10], in accordance with our clinical partners, we decided to select 1 frame every 5. Then, three subsequent frames were grouped to form a *triplet*. Supported by our clinical partners, we assigned each *triplet* to the *movement* and *no-movement* class.

The final annotated dataset consisted of 333 *triplets* for each of the 16 infants. These were divided in training (183), validation (67) and testing (83) set. To solve the class-imbalance problem (1628 and 2953 *triplets* for the *movement* and *no-movement*, respectively), we decided to randomly remove samples from the majority class, both the in training and the validation set. The training and validation set size are shown in Table II.

B. Training settings

Prior feeding the network, the frames forming a *triplet* were resized to 128 x 96 pixels, for size compatibility with the joint-CNN proposed in [5].

For training purposes, the binary cross-entropy was minimized with Adam in 100 epochs, with a learning rate equal to 0.0001. The batch size was set to 32, as a trade off between memory requirement and training convergence. The best model among epochs was retrieved according to the highest macro-Recall ($macro - Rec$) on the validation set:

$$macro - Rec = \frac{\sum_{i=0}^{1} Rec_i}{2} \tag{1}$$

where:

$$Rec_i = \frac{TP_i}{TP_i + FN_i} \tag{2}$$

and with $i \in [0 = no\text{-}movement, 1 = movement]$. TP_i and FN_i are the correctly classified samples and the false negatives for the i-th class, respectively.

All our analyses were performed using the Keras[2], a Python library, on a Nvidia GeForce GTX 1050 Ti/PCIe/SSE2.

C. Ablation study

As ablation study, the performance of the proposed fine-tuned mov-CNN model was compared against the same model trained from scratch. This means that the mov-CNN kernels and neuron connections were initialized with *Glorot* initialization.

D. Performance metrics

For performance assessment, we computed, using the test set, the classification Rec_i (Eq. 2), Precision ($Prec_i$) (Eq. 3), and f1-score ($f1_i$) (Eq. 4), for $i \in [0 = no\text{-}movement, 1 = movement]$.

$$Prec_i = \frac{TP_i}{TP_i + FP_i} \tag{3}$$

$$f1_i = \frac{2 \times Prec_i \times Rec_i}{Prec_i + Rec_i} \tag{4}$$

where FP_i are the false positives samples of the i-th class.

IV. Results

Results for both the fine-tuned mov-CNN and the mov-CNN trained from scratch are shown in Table III. Both achieved similar results when predicting one class with respect to the other. Hence, the mov-CNN trained from scratch achieved a Rec of 0.72 and 0.74 for the *movement* and *no-movement* class, respectively. The fine-tuned mov-CNN achieved a Rec equal to 0.83 and 0.84 for the *movement* and *no-movement* class, respectively. Figure 3 shows the relative confusion matrices.

[2]https://keras.io/

TABLE III: Results for the mov-CNN trained from scratch and the fine-tuned mov-CNN in terms of Precision ($Prec_i$), Recall (Rec_i) and f1-score ($f1_i$) where i represents the i-th class, with $i \in [0 = no\text{-}movement, 1 = movement]$.

	$Prec$		Rec		$f1$	
	movement	no-movement	movement	no-movement	movement	no-movement
mov-CNN trained from scratch	0.70	0.75	0.72	0.74	0.71	0.74
fine-tuned mov-CNN	0.82	0.85	0.83	0.84	0.83	0.84

Fig. 3: Confusion matrices for (left) fine-tuned mov-CNN and (right) mov-CNN trained from scratch.

The fine-tuned mov-CNN overcame the training from scratch when predicting the *movement* class, with values of $Prec$, Rec, $f1$ equal to 0.82, 0.83 and 0.83, respectively.

V. DISCUSSION AND CONCLUSION

Monitoring preterm-infants' spontaneous movement is crucial to early detect the onset of long-term complications, such as: motor impairments and behavioural disorders. To support clinicians during the diagnosis, in this work we presented a DL methodology based on a 3D CNN (mov-CNN) to achieve preterm infants' movement detection. Considering the complexities of detecting such movements, which are infrequent and often imperceptible, we exploited fine-tuning relying on a pre-trained CNN designed for joint-position estimation.

The performance of the fine-tuned mov-CNN was compared against that of the mov-CNN trained from scratch. Both the fine-tuned mov-CNN and the mov-CNN trained from scratch did not outperform when predicting one class with respect to the other. The fine-tuned mov-CNN achieved better performance. Hence, it has its kernels initialized with the kernel of the enc-CNN proposed in [5], which was trained to detect joint position. This considerably improved network generalization ability, confirming our initial hypothesis for which the movement of preterm infants is highly due to joint movement.

The proposed methodology could provide clinicians with infants' movement statistics. Moreover, it could be integrated as pre-processing step of computer-assisted algorithms aimed at recognizing movement patterns. However, to offer all the possible support to clinicians in NICUs, it is acknowledged that further research is required.

Among the possible future improvements, the same architecture could be revised (i.e., modifying the output layer) to detect limb-specific movement. To have a broad overview of the infant's health status, movement statistics may be integrated with other computer-based tools for vital parameters processing (e.g., bilirubinometry data and blood samples) [11]. The outcome of these tools, which are relevant for the monitoring of infants' health status in NICUs, could be included within electronic health record software [12] as to support clinicians during the actual clinical practice.

REFERENCES

[1] C. Einspieler, A. F. Bos, M. E. Libertus, and P. B. Marschik, "The general movement assessment helps us to identify preterm infants at risk for cognitive dysfunction," *Frontiers in Psychology*, vol. 7, p. 406, 2016.

[2] F. Ferrari, C. Einspieler, H. Prechtl, A. Bos, and G. Cioni, *Prechtl's method on the qualitative assessment of general movements in preterm, term and young infants*. Mac Keith Press, 2004.

[3] C. Marcroft, A. Khan, N. D. Embleton, M. Trenell, and T. Plotz, "Movement recognition technology as a method of assessing spontaneous general movements in high risk infants," *Frontiers in Neurology*, vol. 5, p. 284, 2015.

[4] C. B. Redd, L. A. Barber, R. N. Boyd, M. Varnfield, and M. K. Karunanithi, "Development of a wearable sensor network for quantification of infant general movements for the diagnosis of cerebral palsy," in *41st Annual International Conference of the IEEE Engineering in Medicine and Biology Society*. IEEE, 2019, pp. 7134–7139.

[5] S. Moccia, L. Migliorelli, V. Carnielli, and E. Frontoni, "Preterm infants' pose estimation with spatio-temporal features," *IEEE Transactions on Biomedical Engineering*, 2019.

[6] A. Stahl, C. Schellewald, Ø. Stavdahl, O. M. Aamo, L. Adde, and H. Kirkerod, "An optical flow-based method to predict infantile cerebral palsy," *IEEE Transactions on Neural Systems and Rehabilitation Engineering*, vol. 20, no. 4, pp. 605–614, 2012.

[7] S. S. Shivakumar, H. Loeb, D. K. Bogen, F. Shofer, P. Bryant, L. Prosser, and M. J. Johnson, "Stereo 3d tracking of infants in natural play conditions," in *IEEE International Conference on Rehabilitation Robotics*. IEEE, 2017, pp. 841–846.

[8] A. Cenci, D. Liciotti, E. Frontoni, P. Zingaretti, and V. P. Carnielli, "Movements analysis of preterm infants by using depth sensor," in *International Conference on Internet of Things and Machine Learning*. ACM, 2017, pp. 1–9.

[9] S. Moccia, L. Migliorelli, R. Pietrini, and E. Frontoni, "Preterm infants' limb-pose estimation from depth images using convolutional neural networks," in *IEEE Conference on Computational Intelligence in Bioinformatics and Computational Biology*. IEEE, 2019, pp. 1–7.

[10] B. Fallang, O. D. Saugstad, J. Grøgaard, and M. Hadders-Algra, "Kinematic quality of reaching movements in preterm infants," *Pediatric research*, vol. 53, no. 5, p. 836, 2003.

[11] L. Migliorelli, A. Cenci, M. Bernardini, L. Romeo, S. Moccia, and P. Zingaretti, "A cloud-based healthcare infrastructure for neonatal intensive-care units," in *ASME 2019 International Design Engineering Technical Conferences and Computers and Information in Engineering Conference*. American Society of Mechanical Engineers Digital Collection.

[12] E. Frontoni, A. Mancini, M. Baldi, M. Paolanti, S. Moccia, P. Zingaretti, V. Landro, and P. Misericordia, "Sharing health data among general practitioners: The Nu.Sa. project," *International Journal of Medical Informatics*, 2019.

Single cell fluid dynamics: a VOF model of a red blood cell vs a leukocyte

M. Piergiovanni[1], E. Bianchi[1], P. De Stefano[1], G. Dubini[1]

[1] *Lab. of Biological Structure Mechanics, Dpt. Of Chemical, Materials and Chemical Eng. "G. Natta", Politecnico di Milano, Italy*

Abstract—**A Volume of Fluid (VoF) model, a computational approach often used to study two-phase flows, was developed to study the fluid dynamics of a single cell flowing in a confined flow, in particular in a blood capillary. The cell - either a leukocyte or a Red Blood Cell (RBC) - was represented as a fluid droplet, with physical properties derived from literature experimental measurements. The results indicated that the ratio between the cell and the plasma viscosity plays a crucial role on the deformation of the cell, providing results that range from the small to the large deformations. By post processing data from the VoF model, we estimated the fluid shear stresses and forces acting on the cell, parameters hardly available with experimental methods, providing hints on the membrane mechanics.**

Keywords—**Flow induced deformation, Cell fluid mechanics, Two-Phase flow, Microcirculation.**

I. INTRODUCTION

FROM a fluid mechanical point of view, blood can be modelled as a dense suspension of cells in plasma, a solution of proteins, glucose, salt and other solutes in water. Plasma is a Newtonian fluid with a viscosity of approximately 0.0012 Pa·s [1].

When modelling blood for applications in the large arteries, it is usually a good approximation to treat blood as a homogeneous fluid, where the cells are modelled as a change in the overall rheological parameters and can be accurately estimated for physiological and pathological conditions [2]. In microcirculation, however, the dimension of the cells is quite relevant with respect to the geometrical domain of the capillaries, thus the particulate nature of blood has to be accounted for when studying the fluid dynamics. Many experimental and computational studies were specifically focused on this dimensional range [3], [4].

The use of mechanical models of cells is quite established in the literature and it usually implies a number of simplifications due to the specific focus of the different applications. It is possible to identify two different groups: a continuous approach and a particle-based approach [5].

Continuous liquid drop models can successfully be used in large deformations caused by distributed forces, since these methods are based on a Lagrangian approach. As a comparison, this is the case of micropipette aspiration [6], electro-deformation [7] or optical tweezer [8], where cells are largely deformed with important, time-dependent deformation and shape recovery. These models can also be used when accounting for the rheology of the cells and are widely used to represent flowing cells. Immersed boundary approaches are large-scale simulations that are currently the gold standard to model whole blood, accounting for the interaction of all cells. When going down to small capillaries, where cells are flowing in a row, it is also possible to study each cell separately.

The fluid dynamic range investigated by literature works on single cell modelling is strictly limited to specific applications [9-12]. Even if the described fluid dynamics falls largely in the laminar regime, the Reynolds number remains 1-3 orders of magnitude higher than in blood microcirculation, thus the obtained results are quite far from the real deformation of a cell flowing in the capillary network. The VoF method is a tool to precisely represent single cells in various fluid dynamic regimes, including microfluidic devices design and microcirculation modelling. The application of the VoF, however, is usually limited to white blood cells in inertial microchannels with high cell/channel ratio and a quite high Re [12].

In this work, several parameters were used to completely map the fluid dynamics range of microcirculation in a representative circular microchannel. Moreover, the viscosity range of the fluid droplet was extended in order to include the two main types of circulating cells, both Red Blood Cells (RBCs) and leukocytes, thus obtaining results in both the small and large deformation regime.

II. MATERIALS AND METHODS

A coupled Volume of Fluid - Level Set method was used to investigate the motion of a generic cell inside a three-dimensional domain, representing a capillary. A single cell was modelled as a viscous drop with assigned internal viscosity μ and surface tension γ. The drop was suspended into a fluid representing plasma flowing into a channel. In this model the cell membrane is seen as a surface with infinitesimal thickness, whose properties are represented by a constant parameter, γ. All simulations were performed with ANSYS Fluent 16.0 (ANSYS Inc., Canonsburg, Pennsylvania, USA).

Generally speaking, the VoF can account for two or more immiscible fluids, defined as separate phases - a continuous, primary phase and one or more dispersed, secondary phases. For each phase, the volumetric fraction Φ_n is defined as:

- $\Phi_n = 1$, if the phase n totally occupies the computational element; $\Phi_n = 0$, if the phase n is absent in the computational element; $0 < \Phi_n < 1$, if the computational element partially contains the phase n: this identifies the elements with the interface.

The membrane is defined where the volume fraction Φ_n of the two phases is equal ($\Phi_1 = \Phi_2 = 0.5$), through the definition of an isosurface. An isosurface "cuts" the mesh at a fixed value of Φ and models the interface with a 2D linear surface. At every time step, fluid dynamic - pressure, velocities and their derivatives - and geometrical - nodes coordinates, face normal vectors, face areas - parameters were exported.

A. Deformation index and cell shift.

At each time point, the radial position of the cell mass centre and the cell deformation were calculated $B(x_B; y_B: z_B)$. The coordinates of the nodes included in the cell membrane were used to calculate cell centre of mass. The normalized final position P_{norm} is the centre of mass of the cell with respect to the capillary axis, normalized to the capillary diameter:

$$P_{norm} = \frac{\sqrt{x_B^2 + y_B^2}}{H_{channel}}$$

To quantify the deformation, Taylor index Ta was used:

$$Ta = \frac{D_{max} - D_{min}}{D_{max} + D_{min}}$$

where D_{max} and D_{min} are the maximum and minimum diameter of the cell in the deformed configuration.

The minimum bounding box algorithm was applied to the membrane nodes and used to calculate the two axes, as reported in [11]. The minimum bounding box algorithm defines the smallest enclosing box of a set of points in three dimensions. It is also possible to estimate the bounding box rotation with respect to a fixed reference system.

B. Cell stress tensor and membrane forces.

The stress distribution on the cell surface - caused by both the plasma and the cytoplasm - was calculated from the VoF data, thus estimating the forces acting on the cell membrane during its flowing. Post processing was performed with Matlab. The state of stress on an infinitesimal element in a flowing Newtonian fluid, with viscosity μ and velocities u, v and w in the x, y and z directions, respectively, can be expressed by the symmetrical stress tensor σ_{ij}.

$$\sigma_{ij} = -p\delta_{ij} + 2\mu e_{ij} + \lambda e_{kk}\delta_{ij}$$

where p is the thermodynamic pressure, δ_{ij} is the Kronecker delta and λ is the dilatational viscosity. After calculation of the magnitude of the scalar stress σ for the face with normal n, the normal and tangential stresses were derived. This calculation was repeated for both fluids - internal and external – by reversing the unit normal vector direction and considering their specific physical properties (i.e. viscosity). Of note, the velocity of the two fluids is assumed to be the same, since the the VoF model solves only one Navier-Stokes equation. The overall stress distribution on the membrane was obtained by summing all the normal and tangential stresses for every face k of the isosurface. Finally, the face area was used to determine the normal F_N and tangential F_T forces that build up to the total force on the cell membrane.

C. VoF for microcirculation

After a sensitivity analysis, a mesh of 2.5 million elements was chosen to represent the whole domain. The choice was made in the worst-case scenario, where the cell was small with respect to the microchannel – D/H = 0.3 (Figure 1). A flat velocity profile was imposed at the inlet and a zero pressure at the outlet. Walls were imposed a no-slip condition. Two fluids were used in the domain, a primary phase representing plasma (ρ_{plasma} = 1030 kg/m^3; μ_{plasma} = 0.0012 Pa·s) and a secondary phase representing the cell (ρ_{cell} = 1060 kg/m^3; μ_{cell_RBC} = 0.003 Pa·s; μ_{cell_LEUKO} = 100 Pa·s; γ_{CELL} = 60 pN/μm). The cell had an initial spherical shape, with a radius calculated according to the chosen D/H.
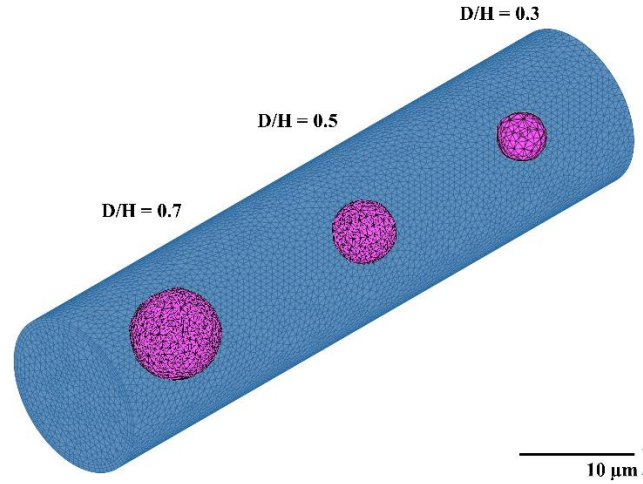
Figure 1. Mesh used for CFD simulations. At increasing D/H, more elements were assigned the secondary phase (cell). In particular, 800 elements were used for D/H = 0.3, 3400 elements for D/H = 0.5 and 9500 for D/H = 0.7.

III. RESULTS AND DISCUSSION

A number of simulations were performed, in order to better investigate the values that are characteristic of the microcirculation. In particular: microchannel with circular cross section - D = 12 μm; mean velocity: 100 ÷ 500 μm·s; cell viscosity tuned to represent both RBCs and leukocytes.

The RBC was modelled as a droplet with a viscosity of 0.0045 Pa·s, to better represent its a-nucleated shape. The velocity profile maintained a parabolic shape, with a mean velocity of 296 μm·s, uninfluenced by the cell flow. The RBC was slightly dragged by the primary phase towards the microchannel wall, reaching an equilibrium position at 1.72 μm from the capillary axis. The Taylor index nicely represented the RBC high deformability, reaching values of 0.7, typical of the RBC slippery shape. Initial, fast cell deformation occurred from spherical to parachute to slipper shape and subsequent shifting towards the channel centreline. The specific deformed shapes of RBCs under flow in microfluidic channel is well known in the literature, from the theoretical [13] and experimental [14] (Figure 2) points of view.
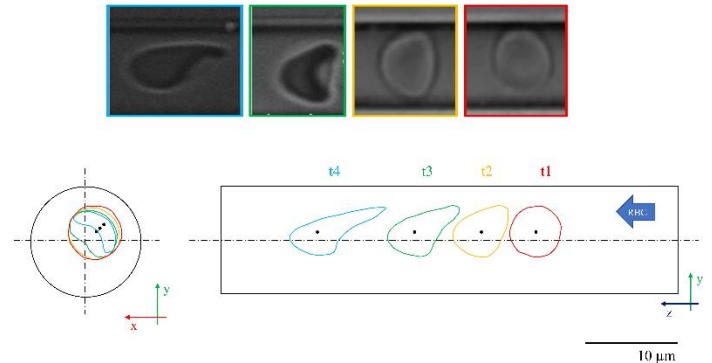

Figure 2. Results of a VoF RBC model (Re = 6.36·10^{-4}; Ca = 3·10^{-2}; viscosity ratio = 1.5; D/H = 0.5). Deformation and equilibrium position at four time steps - z = 31 - 41 - 62 – 83 μm - and comparison with literature data acquired from experimental high-speed imaging [14].

When representing the leukocyte, a high cytoplasmatic viscosity (100 Pa·s) is suggested by several literature articles on micropipette aspiration [15]. The presence of a more viscous cell highly influenced the overall fluid dynamic in the
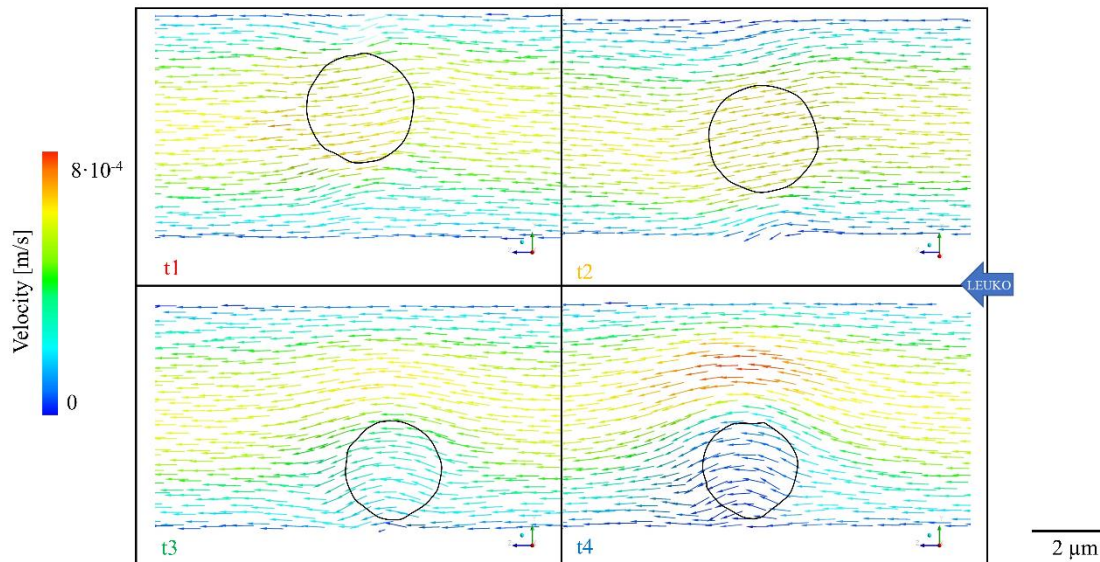
Figure 3. Results of the leukocyte model (Re = 6.36·10⁻⁴; Ca = 3·10⁻²; viscosity ratio = 3.33·10⁴; D/H = 0.5). Velocity field at time steps corresponding to z = 31 - 41 - 62 – 83 μm. Flow goes from right to left.

capillary, as shown by disturbances in the velocity field. At the end of the simulation, the leukocyte reached a position of "quasi-adhesion" near the wall of the capillary – 3.17 μm from the capillary axis. Computational models of deformable particles [16] also confirm that less deformable cells tend to shift towards the microchannel wall. Experimental literature data on leukocyte margination show a prominent shift of the cells towards the endothelial wall [17], even if this effect is also highlighted by the high haematocrit used in the setup. During the rolling phase, the capillary cross section was greatly reduced. As a consequence, the mean velocity was 412 μm·s, a third higher than the inlet value imposed as a boundary condition. The cell was not deformed by the plasma flow, thus the Taylor index remained always lower than 0.1 (Figure 3).

A. Parameter analysis

By means of the VoF model, it was possible to represent the fluid dynamics of a single cell in a range of conditions representing the microcirculation, with a Reynolds number always between 10^{-5} and 10 and the Capillary number always between 10^{-3} and 100. The effect of the main fluid dynamic and geometrical parameters on the cell deformation and its radial shift across the channel were analysed with CFD simulations.

The ratio between the cell dimension and the channel diameter (D/H), greatly affected the radial shift, as confirmed by a regression coefficient of determination R^2 of 0.66 (Figure 4). The radial shift seems to have a parabolic trend with respect to the dimensional ratio. At low D/H ratio, the cell was subject to a small velocity gradient and it tended to follow the fluid streamlines. Bigger cells tended to shift more towards the centreline, as confirmed also by [16] for D/H = 0.2. At D/H = 0.6, on the other hand, the cell shift was limited by the wall force acting on the cell membrane. The highest shift was reported when the cell dimension was about half of the channel: in this situation, the cell was subject to a velocity difference that made it rotate and shift towards the channel wall until an equilibrium position. An exception - not considered in the regression calculation - to this behaviour

occurred in a simulation of a very deformable cell. Here, the force caused by the velocity gradient mainly deformed the cell, thus reducing the radial shift.
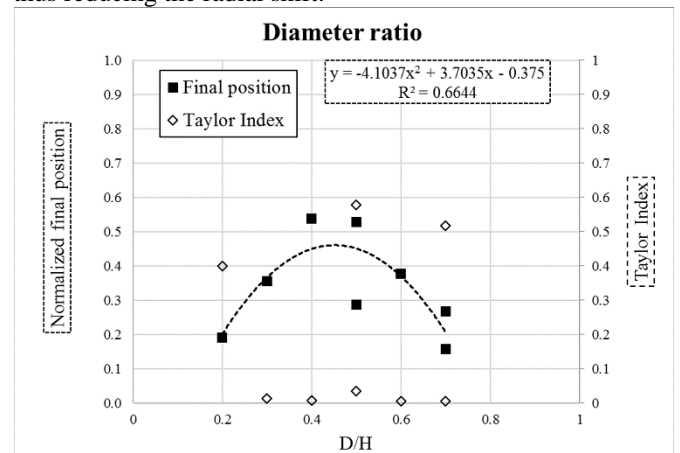
Figure 4. Summary of the simulations performed - left axis: normalized final position, right axis: Taylor index. Results are shown at varying dimension ratios D/H.

The viscosity ratio influenced the radial shift ($R^2 = 0.50$). A lower viscosity ratio determined a lower radial shift, as showed by the exception reported in Figure 4. Thus, our results nicely agree with the results of [12] - at increasing viscosity ratio, the Taylor index decreased, while the cell final position shifted towards the channel wall.

The viscosity ratio had a strong impact also on the velocity field: more viscous cells tended to move quickly towards the wall of the channel, reaching a "quasi-adhesion" position that reduced the channel cross section. In simulations with a viscosity ratio of 3.3×10^5, the cell was shifted to a normalized radial position of 0.38 at z = 42 μm, while the fluid velocity locally doubled, going from 331 to 643μm/s. Cells with a lower viscosity, on the other hand, were mainly deformed at the beginning of the simulation. Then, they followed the flow stream, slowly shifting towards the channel wall. When the viscosity ratio was set at 3.3×10^3, the cell was shifted to a normalized radial position of 0.35 at z = 43 μm, while the fluid

velocity field was not influenced by the cell presence - the mean velocity stayed stable at 300 μm/s.

B. Stress and force acting on a single cell

By postprocessing the VoF results, it was possible to evaluate the stress distribution on the cell membrane, in both the normal and tangential components, considering also the effect of the cytoplasm flow inside the cell. Figure 6 clearly shows that the RBC deformation was mainly due to the high stress acting on the cell membrane. On the right side of the cell, flowing next to the wall, the normal stress σ was of 2.5 Pa, while σ was just 1 Pa near the channel centre. Slightly higher values were calculated for the tangential component τ. These values were caused by the low viscosity ratio between the internal cytoplasmatic fluid and the surrounding plasma. Similar viscous forces arose on both sides of the membrane, with a mean net force F_N of 202 pN in the normal direction and F_T of 180 pN in the tangential direction (configuration at time step t4, taken as an example). During the time evolution of the simulation, both the normal and tangential forces remained constant, with values ranging from 111 to 203 pN. A completely different behaviour was predicted for the leukocyte, since the forces on the membrane did not act to deform the cell but only to move it. A high shear across the cell membrane was caused by the high viscosity of the internal fluid. Values as high as 35 kPa in the normal direction and 50 kPa in the tangential direction were predicted in this configuration. The stress distribution did not follow a constant pattern with time, but it changed with the axial migration of the cell towards the wall, in the direction of increasing shear stresses. Therefore, the viscous force acting across the membrane was mainly due to the viscosity of the internal fluid and to the radial shift (F_N = 797 nN and F_T = 894 nN - time step t4).

Literature values on leukocyte adhesion or shear stress on vessel walls, usually account only for blood viscosity (0.003 Pa·s) in general. Thus, predicted shear stresses on the external cell membrane are usually reported to stay in the range 0.1÷10 Pa, depending on the specific fluid dynamic problem addressed. By adequately postprocessing the results of the VoF model, it is possible to account also for the effect of the internal fluid. By breaking up the contribution of the two fluids, it is possible to isolate the contribution of plasma. In this case, the VoF model predicts a mean shear stress of 0.237 Pa for the leukocyte model and 2.1 Pa for the RBC model (time step t4).

IV. CONCLUSION

In the present work, we developed a VoF model to investigate cell flowing in a confined flow, in microcirculation conditions similar to the *in vivo* situation. By tuning the Reynolds number, the D/H ratio and the viscosity ratio γ it was possible to cover the whole fluid dynamic range, as well as to apply the model to different kinds of cells, from RBCs to leukocytes, based on their mechanical properties. VoF models provided accurate results in a wide application range, from small to large deformations. The calculation times, however, were quite long and required smart meshing strategies, especially when the viscosity ratio γ was high (larger than 10^6).

Further work will lead to the coupling of the VoF model with a capillary network in order to account also for the real conduit geometry, a goal that can hardly be achieved by using other computational methods of cell mechanics.
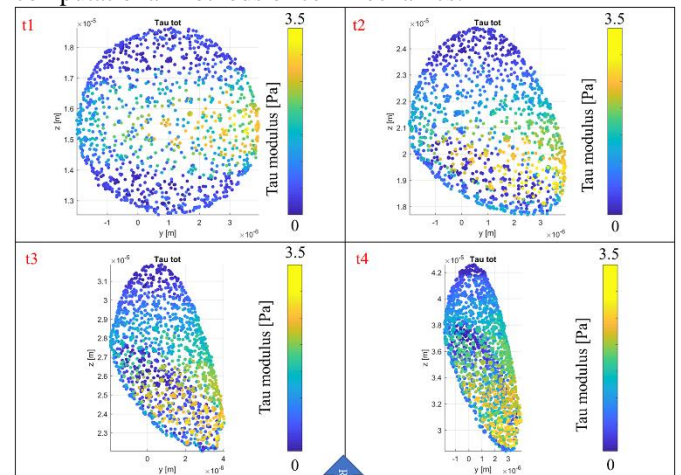

Figure 5. Distribution of τ magnitude for the RBC model at four different time steps, corresponding to z = 33 - 48 - 71 - 77 μm. Channel wall is on the right side, channel center is on the left side.

REFERENCES

[1] Y. C. Fung, *Biomechanics: Mechanical properties of living tissues.* Springer, 1993.

[2] O. K. Baskurt, M. R. Hardeman, M. W. Rampling, *Handbook of Hemorheology and Hemodynamics*. IOS Press, 2007.

[3] R. Dias, A. Martins, R. Lima, T. M. Mata, *Single and two-Phase Flows on Chemical and Biomedical Engineering*. Bentham Science, 2012.

[4] T. Omori, Y. Imai, K. Kikuchi, T. Ishikawa, T. Yamaguchi, "Hemodynamics in the microcirculation and n microfluidics", *Annals of Biomedical Engineering*, 43(1):238-257, 2014.

[5] M. Worner, "Numerical modeling of multiphase flows in microfluidics and micro process engineering: a review of methods and applications", *Microfluid Nanofluid*, 12:841-886, 2012.

[6] R. M. Hochmuth, "Micropipette aspiration of living cells", *Journal of Biomechanics*, 33(1):15-22, 2000.

[7] N. A. Nodargi, J. Kiendl, P. Bisegna, F. Caselli, L. De Lorenzis, "An isogeometric analysis formulation for red blood cell electro-deformation modelling", *Computer Methods in Applied Mechanics and Engineering*, 338:392-411, 2018.

[8] H. Zhang, K. K. Liu, "Optical tweezers for single cells", *Journal of the royal society interface*, 5:671-690, 2008.

[9] T. W. Murphy, Q. Zhang, L. B. Naler, S. Ma, C. Lu, "Recent advances in the use of microfluidic technologies for single cell analysis", *Analyst*, 143:60-80, 2018.

[10] P. Paie, F. Bragheri, D. Di Carlo, R. Osellame, "Particle focusing by 3d inertial microfluidics", *Microsystems and Nanoengineering*, 3:17027, 2017.

[11] J. O'Rourke, "Finding minimal enclosing boxes", *International Journal of Computer and Information Sciences*, 14(3):183-199, 1985.

[12] H. Lan, D. B. Khismatullin, "A numerical study of the lateral migration and deformation of drops and leukocytes in a rectangular microchannel", *International Journal of Multiphase Flow* 47:73-84, 2012.

[13] C. Pozrikidis, "Numerical simulation of cell motion in tube flow", *Annals of Biomedical Engineering,* 33(2):165-178, 2005.

[14] G. Tomaiuolo, *et al.,* "Microconfined behavior of red blood cells", *Medical engineering and physics,* 38(1):11-16, 2016.

[15] M. A. Tsai, R. S. Frank, R.E. Waugh, "Passive mechanical behavior of human neutrophils: Power-law fluid", *Biophysical journal*, 65:2078-2088, 1993.

[16] A. H. Raffee, S. Dabiri, A. M. Ardekani, "Suspension of deformable particles in newtonian and viscoelastic fluids in a microchannel", *Microfluidics and nanofluidics*, 22:23, 2019.

[17] A. Kumar, M. D. Graham, "Margination and segregation in confined flows of blood and other multicomponent suspensions", *Soft matter*, 8:10536-10548, 2012.

Biomechanical implications of leg bending in popliteal stenting

Conti Michele[1], Ferrarini Anna[1], Finotello Alice[2], Salsano Giancarlo[3], Auricchio Ferdinando[1],
Palombo Domenico[4], Spinella Giovanni[4], Pane Bianca[4]

[1] Department of Civil Engineering and Architecture, University of Pavia, Italy
[2] Department of Surgical and Integrated Diagnostic Sciences, University of Genoa, Italy
[3] Department of Radiology, Ospedale Policlinico San Martino, Genoa, Italy
[4] Vascular and Endovascular Surgery Unit, Ospedale Policlinico San Martino, University of Genoa, Italy

Abstract. Femoro-popliteal artery is exposed to a unique set of severe repetitive deformations due to the proximity of the artery with the knee joint resulting in one of the most challenging arteries in which to perform endovascular treatment. The present study aims at evaluating the morphological changes of the femoro-popliteal axis (FPA) due to limb flexion in patients with endovascularly treated popliteal artery aneurysm, using a standardized protocol for Computed tomography angiography (CTA) scan with both straight and bent limb positions. We have combined medical image analysis with structural finite element analysis (FEA) and computational fluid dynamics (CFD) in order to assess the structural loading of the implanted stent-grafts and post-operative hemodynamics, respectively. Our results support the key idea that leg bending induces dramatic biomechanical changes of femoro-popliteal artery; such changes should be taken into account during procedure planning and design of novel devices.

Keywords — popliteal artery aneurysm, peripheral stenting, medical image analysis, limb flexion, biomechanics, structural FEA, Computational Fluid Dynamics.

I. INTRODUCTION

Popliteal artery aneurysms (PAA) are the most frequently encountered peripheral aneurysms. Even if bypass surgery is considered the gold standard to treat popliteal pathologies, endovascular treatment of PAA achieved through the positioning of a covered stent could be performed in elective cases with the aim of maintaining adequate blood flow to the foot, reducing the risk of aneurysm thrombosis or distal embolization. However, the efficacy of endovascular treatment still remains controversial due to the relatively high rate of stent failure, which is often attributed to the severe repetitive deformations and loading conditions during limb flexion.

Since 1995 when the first manuscript regarding in-vivo analysis of superficial femoral kinematics was published [1], the scientific interest on this topic is still high and motivates further investigations. Up today, several studies based on the assessment of in-vivo [2] or ex-vivo arterial deformations have been conducted [3]. Moreover, biomechanical studies to investigate the mechanical response of stent(-grafts) in this vascular region has been conducted as well. However, to our current knowledge, an approach combining in-vivo medical image analysis of leg bending, patient-specific structural finite element analysis (FEA) and computational fluid dynamics (CFD) is still missing.

Given this motivation, the present study aims at evaluating the morphological changes of the femoro-popliteal axis (FPA) due to limb flexion in patients with endovascularly treated PAA using a standardized protocol for CTA acquisition with both straight and bent limb positions,

Starting from a standardized protocol of CTA acquisition with both straight and bent limb positions, the present study illustrates the in-vivo morphological changes of FPA due to flexion and the integration such analyses with the results of FEA and CFD simulations.

II. IN-VIVO GEOMETRIC ANALYSIS

A. CTAs acquisition protocol

During the follow-up, one contrast-enhanced CTA of the lower limbs was acquired for each patient. Two scans were performed a few minutes one from the other. The first scan was obtained with the treated lower limb in a standardized 90° position (bent-leg configuration) using a dedicated foam-coated leg support, while the contralateral limb remained straight (see Figure 1a). The second scan was obtained with the treated limb placed at 180° position (straight-leg configuration) (see Figure 1b). All CTA images were acquired with the same 64 multidetector-row CTA (General Electric Optima 660). A low-dose-radiation protocol, with 100 keV and automated tube current modulation was used. Low contrast material volume (50-70 ml, Iomeron 400 or Iopamiro 370) was administered, with flow rate of 4ml/s followed by saline flushing (30 ml; flow rate, 4ml/s).

Adopted scan parameters were: thickness 0.625 mm; increment 0.625 mm; collimation 64x0.625; pitch 0.915; rotation time 0.7 s; field of view 35 cm; matrix 512x512 pixel.

B. Medical image analysis

Seven patients who underwent endovascular treatment for PAA with a covered self-expandable polytetrafluoroethylene stent-graft (Viabahn, W.L. Gore and Associates Inc, Flagstaff, AZ, USA) at IRCCS San Martino hospital (Genoa, Italy) between January 2013 and December 2017 were selected.

Post-operative CTA images were anonymized and transferred to a workstation for image processing. Segmentation of the FPA from the femoral artery bifurcation to the popliteal artery bifurcation, leg bones, and the implanted stent-graft, was performed using the open source tool Vascular Modeling ToolKit (VMTK) [4] version 1.3. For each patient, rigid-

registration of bent leg structures on their corresponding straight counterparts was automatically performed by means of the Iterative Closest Point algorithm implemented in VMTK. The output is a rigid transformation matrix that is then applied to both the vessel and stents in the bent configuration (see Figure 2a).

The femoral-popliteal vessel was then divided into three zones spanning the distance between the origin of the superficial femoral artery and the proximal end of the covered stent (zone A), from the proximal to the distal end of the stent-grafted segment (zone B), and from the distal end of the covered stent to the origin of the anterior tibial artery (zone C) (see Figure 2b). 3D reconstruction of the FPA segment was performed to compute mean diameter and eccentricity of the vascular lumen, and to measure length, tortuosity, and curvature of the vessel centerline into the three arterial segments.

Segment A on average foreshortened 6% from 238.5±56.77 mm to 225.21±56.87 mm during limb flexion (p=0.001), and the curvature (p=0.05) and tortuosity (p<0.05) increased 15% and 67%, respectively. Stent-grafted segment B on average foreshortened 4%, from 236.36 mm to 226.08 mm with limb flexion (p=0.001), and when devices overlapped, the length of the overlapped segment decreased 9% with limb flexion. Similar to segment A, limb flexion produced a significant increase in mean curvature (from 0.026 to 0.033 on average; p=0.005) and tortuosity (0.06 to 0.15 on average; p<0.05). In both A and B zones mean arterial diameter and eccentricity were not significantly affected by limb flexion.

Segment C was 5-fold shorter than both segments A and B. No significant differences in length, diameter or eccentricity with limb flexion were detected in segment C.

III. FEA OF POPLITEAL STENTING

The information deriving from the medical image analysis are used to reconstruct the configuration change of the FPA and to define displacement boundary conditions in structural finite element analysis of the implanted stent. In particular, FPA kinematics during leg flexion was reconstructed by linear interpolation starting from the centerline of extended and flexed vessel using in-house Matlab scripts (MathWorks, Natick, Mass). Post-operative FPA kinematics was used as input of the simulation environment imposing the computed vessel displacement as a loading condition to a stent model. An accurate model of the stent adopted in the clinical practice was created using the commercial software Abaqus CAE v.16 (Simulia, Dassault Systemes, FR). The simulation of FPA stenting was performed through FEA with Abaqus/Explicit v.2017 as FEA solver. The results highlight that leg bending induces a different stress distribution along the stent, where the proximal part, located above the knee are exposed to the highest loading. More details are reported in [5].

IV. CFD ANALYSIS

The 3D models derived from image segmentation of straight-and bent-leg configuration are used to perform patient-specific hemodynamic analysis by CFD.

In particular, we have considered the case-study of a patient reporting a popliteal aneurysm treated with endovascular deployment of two overlapped stent-grafts, and showing intra-stent thrombosis at one-year follow-up examination. A CFD-suitable mesh was created using the VMTK tool. CFD simulations were run in Intel Xeon W-2123 computing workstation (3.6GHz, 32 GB RAM) with the commercial package Ansys Fluent (v19.2, ANSYS Academic Research [Fluent], Inc, USA). Transient simulations were performed using viscosity of 4 cP and blood density of 1060 kg/m^3. For transient simulations, a flat inflow profile was imposed according to [6]. An outflow condition enforcing the flow in the tibial artery to be 25% of the inflow and traction-free conditions in the other outlets were imposed.

No-slip conditions were prescribed on the wall. Simulations were run for four cardiac cycles.

The computational fluid-dynamics analysis (see Figure 3) showed that the overlapping zone of the stent-grafts induces a severe discontinuity of lumen, dividing the landing site in two segments: the proximal part, affected by thrombosis, is characterized by larger section diameters (7.85±0.42 mm), low centerline tortuosity (0.003 [-]), low flow velocity (0.1 m/s), low helicity (0.4 m/s^2), and low wall shear. Despite leg bending induces an overall increase of arterial tortuosity (0.006 and 0.1 in the proximal and distal stent), it reduced the flow velocity (0.09 m/s, and 0.16 m/s in the proximal and distal segment) promoting furtherly the luminal area exposed to low wall shear stress.

V. CONCLUSIONS

Our analyses ranging from medical image analysis to computational fluid dynamics support the key idea that leg bending induces dramatic biomechanical changes of femoro-popliteal artery; such changes should be taken into account during procedure planning and design of novel devices.

REFERENCES

[1] Wensing P, Scholten F, Buijs P, Hartkamp M, Mali W, Hillen B. Arterial tortuosity in the femoropopliteal region during knee flexion: a magnetic resonance angiographic study. J Anat 1995; 187(1):133–139.

[2] Cheng CP, Wilson NM, Hallett RL, Herfkens RJ, Taylor CA In vivo MR angiographic quantification of axial and twisting deformations of the superficial femoral artery resulting from maximum hip and knee flexion. J Vasc Interv Radiol 2006; 17(6):979–987.

[3] Smouse HB, Nikanorov A, LaFlash D. Biomechanical forces in the femoropopliteal arterial segment. Endovascular Today 2005; 4(6), 60-66.

[4] Antiga L, Piccinelli M, Botti L, et al. An image-based modeling framework for patient-specific computational hemodynamics. Medical & biological engineering & computing 2008; 46.11:1097-1112.

[5] Conti, M., Marconi, M., Campanile, G., Reali, A., Adami, D., Berchiolli, R., & Auricchio, F. (2017). Patient-specific finite element analysis of popliteal stenting. Meccanica, 52(3), 633-644.

[6] Desyatova, A., MacTaggart, J., Romarowski, R., Poulson, W., Conti, M., & Kamenskiy, A. (2018). Effect of aging on mechanical stresses, deformations, and hemodynamics in human femoropopliteal artery due to limb flexion. Biomechanics and modeling in mechanobiology, 17(1), 181-189.
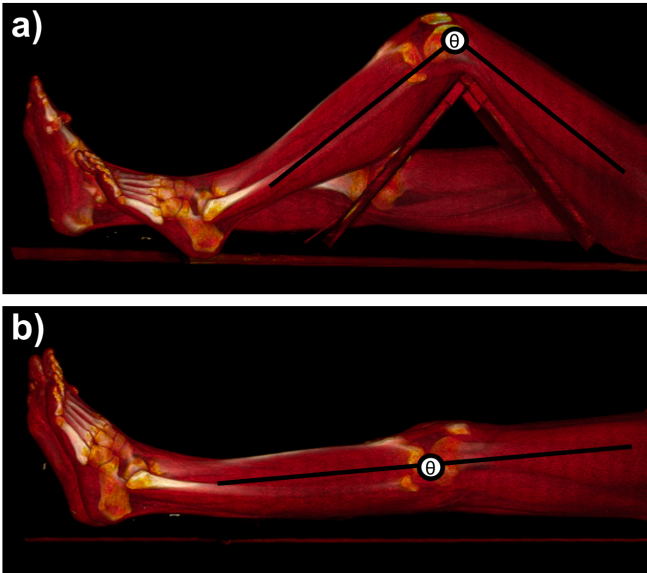
Figure 1. CTA acquisition protocol with a) bent- and b) straight-leg configuration.
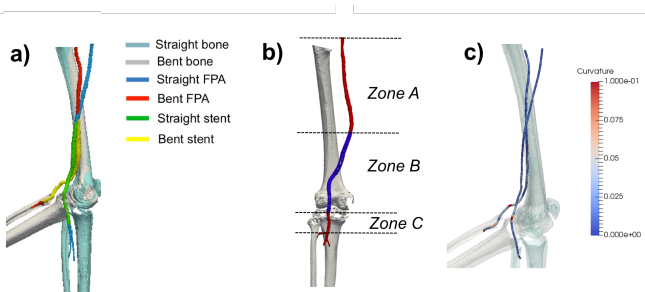

Figure 2. a) superimposition of straight- and bent-leg configuration; b) subdivision of femoral-popliteal vessel in three segments; c) computation of centerline curvature.
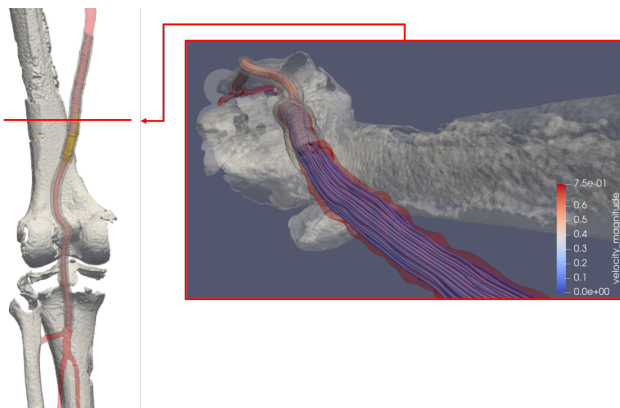

Figure 3. Streamlines of blood flow within the femoro-popliteal artery after endovascular repair of popliteal aneurysm.

Single-subject analysis of the variability of the latency of heart sounds over 25-day period

N. Giordano[1] and M. Knaflitz[1]

[1] *Dipartimento di Elettronica e Telecomunicazioni, Politecnico di Torino, Torino, Italy*

Abstract—**The digital analysis of the phonocardiogram (PCG) has opened, in the last decade, to promising diagnostic possibilities thanks to the extraction of novel features from the heart sounds. In this context, the estimation of the latency of heart sounds and their components with respect to the R-wave may have an interesting clinical impact. The aim of this work is to investigate the variability of the heart sounds latencies with respect to R-wave in a single subject, over a period of 25 days. Signals were recorded daily, in repeatable conditions, by means of a custom acquisition system. Signals were then processed through an envelope-based algorithm we previously developed for the segmentation and classification of the heart sound components and the estimation of their latencies. Analysis of Variance (ANOVA) proved that the measured latency values were significantly different on different days, whereas Run test revealed no significant trends over the observation period. Coefficients of Variation of 8%, 11%, 2% and 3% were found for, respectively, the mitral, tricuspid, aortic and pulmonary valves. The latencies of the first sound components were found to have higher variability with respect to those of the second sound. This work must be considered as a pilot study, to be followed by a wider analysis on a healthy population consisting of a sufficiently high number of healthy subjects.**

Keywords—**phonocardiography, heart sounds, variability analysis.**

I. Introduction

HEART sounds and their significance in the understanding and the diagnosis of cardiovascular diseases have been studied for decades. Being acoustic waves mainly generated by the closing of the cardiac valves [1], they are a fundamental expression of the heart mechanical behavior.

In the recent years, the availability of digital phonocardiography (PCG) has opened to a wide range of possibilities in studying the physiology of the heart, with potential clinical implications [2]. The analysis of the PCG allows for extracting from the heart sounds novel features that are impossible to perceive while performing traditional auscultation [2].

The possibility of evaluating the time of occurrence of heart sounds within the cardiac cycle is a relevant example. Timing of heart sounds is interesting because it provides indications about the status of the electromechanical coupling of the heart, which is difficult to assess otherwise [3]. In fact, the measurement of Systolic Time Intervals is an established technique for the assessment of cardiovascular performance [4].

Nevertheless, further research is necessary to fully understand the physiological meaning of the latency of heart sounds with respect to the R-wave. One aspect, which is not yet described in the literature, is the physiological variability of the latency values.

Even though there are some indications about the values expected for the timing intervals of the components of heart sounds (mitral, tricuspid, aortic, pulmonary) in the population [5]–[7], the inter-subject variability is quite wide, making the clinical interpretation of the measured values difficult. Moreover, we expect that the cardiac electromechanical timing intervals present a physiological variability.

It is known that a significant increase in the timing intervals may be correlated to a worsened electromechanical coupling of the heart and, in general, to cardiac stress [8]. However, determining if a change in the time of occurrence of heart sounds is significant or not is not a naïve issue. Gaining a better understanding of the variability of timing intervals would be a step in that direction.

The scope of this work is to study the physiological variability of the time of occurrence of the two main heart sounds and of their components in a single subject over a period of 25 days. This work is a pilot study that anticipates a wider analysis of the physiological variability of the latency of heart sounds across a larger population.

To our best knowledge, the characterization of the variability of the heart sound timing over time has never been explored in the literature.

II. Materials and Methods

A. Protocol

This study was conducted over a period lasting 25 days. The tested subject was a female volunteer, 25 years old, with no history of cardiopathy or hypertensive disease.

Recordings were repeated once a day for 25 consecutive days. Each daily recording session consisted of a 10-minute simultaneous acquisition of one ECG signal and one PCG signal, with the subject at rest, in supine position, within an hour from wake up, before breakfast and with the same experimental setup.

The aim was to ensure the highest possible repeatability of the test conditions, in both an environmental and a physiological sense.

B. Acquisition system

ECG and PCG signals were recorded by means of a 4-channel commercial acquisition system for biomedical signals (ReMotus®, IT-MeD, Italy). Signals were converted by a 24-bit A/D converter (ENOB 17.25) with a sampling frequency of 1 kHz. The system 3-dB bandwidth spans from DC to 262 Hz.

The ECG signal was acquired by means of three disposable adhesive Ag/AgCl electrodes. Electrodes were positioned in the left and right subclavian areas, whereas the reference electrode was located over the right lateral abdomen, as to

recreate a sort of I standard lead. Electrodes were connected to an active probe with 1 GΩ input impedance and 0 dB gain.

A custom microphone probe was used for the transduction of the acoustic waves on the chest surface into an electric signal. A condenser microphone transducer, electronic circuits limiting the bandwidth of the signal to 2 Hz – 250 Hz, and a 3d-printed plastic container shaped as a stethoscope head compose the probe. The probe mechanically adhered to the skin thanks to double-sided adhesive tape.

The probe positioning over the chest is a critical issue, since it was proved that the latency values measured at different positions are not equal [9]. A suitable position for this study was experimentally found by recording PCG signals from different positions of the subject chest and assessing the signal quality by computing the Signal-to-Noise Ratio for first and second heart sounds.

The point of auscultation, which was found suitable for obtaining good-quality PCG signals for both heart sounds was the second intercostal space, sternal area, left hemithorax.

Fig. 1 displays the positioning of electrodes and microphone over the subject chest.

C. Estimation of the latency of heart sound components

We were interested in estimating the latencies with reference to the corresponding R-wave peak, of the main components of the first heart sound (mitral and tricuspid) and the second heart sound (aortic and pulmonary). To estimate these latencies we applied to the signals an algorithm we previously developed
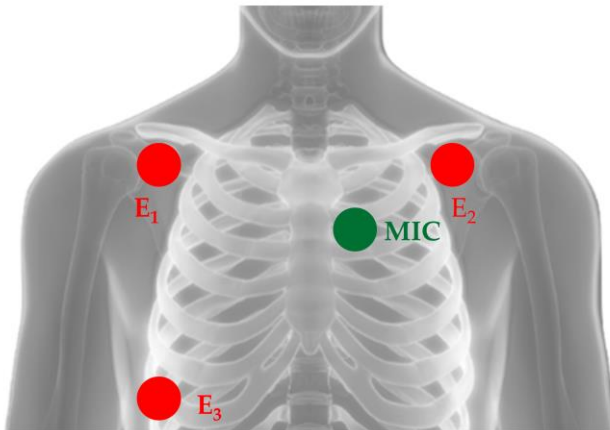
Fig. 1: Positioning of the electrodes for ECG recording (E_1, E_2, E_3) and the microphone probe for PCG recording (MIC) over the subject chest.

and validated [10].

The first step of this algorithm is the localization of R-wave peaks within the ECG recording, which is necessary for PCG segmentation. R-wave detection is performed by means of a modified version of Pan-Tompkins algorithm. The latter involves pre-filtering, which is the cascade of a 100-sample median filtering and a FIR low-pass filter with a cut-off frequency at 35 Hz, derivative filtering, point-wise squaring, moving integration, and, finally, the application of decision rules based on amplitude and time thresholding to identify the R-wave peaks within the signal.

Before applying our envelope-based method to segment the PCG signal and identify the components of heart sounds, filtering is applied to the PCG signal to reduce the contribution

of noise and interferences, which may be important in phonocardiography. We applied a bandpass IIR Chebyshev filter with cut-off frequencies at 20 Hz and 100 Hz to preserve the frequency content typical of the two main heart sounds while discarding murmurs and other artefacts (respiration noise, …).

Segmentation and classification of heart sounds are performed on the PCG signal envelope. The signal envelope is computed as the second order Shannon Energy (SE) calculated on a 20-millisecond moving window, as in Eq. 1.

$$SE = -\frac{1}{N} \sum_{i=1}^{N} x^2(i) \cdot \log x^2(i) \quad (1)$$

The window slides by one sample at each iteration, to preserve the initial resolution of 1 ms, which is required for a proper discrimination of the two components of the same heart sound.

Heart sounds are segmented by applying amplitude thresholding criteria to the SE signal. Two SE peaks are located within each heart sound segment, identifying its components (mitral and tricuspid for the first, aortic and pulmonary for the second heart sound). First and second heart sounds are classified following decision rules based on their latency with respect to the corresponding R-wave peak: 18% of the corresponding RR-interval was experimentally found to be an appropriate cut-off.

We extract four latencies, namely:
1) R-$S_{1,M}$: the latency of the mitral component of the first heart sound with respect to the corresponding R-wave peak.
2) R-$S_{1,T}$: the latency of the tricuspid component of the first heart sound with respect to the corresponding R-wave peak.
3) R-$S_{2,A}$: the latency of the aortic component of the second heart sound with respect to the corresponding R-wave peak.
4) R-$S_{2,P}$: the latency of the pulmonary component of the second heart sound with respect to the corresponding R-wave peak.

D. Analysis of the variability

Following the latency estimation phase, we have, for each recording, four arrays of values, one for each latency. They represent the latencies measured at consecutive heartbeats all along the 10-minute recording (450 – 850 heart cycles).

The analysis described below is repeated for each of the four latencies.

To study the variability of latencies over time, we first performed the Analysis of Variances (ANOVA) between arrays of latency values measured at different days. The goal was to assess whether there are statistically significant differences among latency values measured in different days. We hypothesized a difference to exist, due to the expected physiological variability.

Then, we applied the Wald-Wolfowitz run test to the daily mean values of the four latencies, to detect possible trends. Since the subject was healthy, we did not expect to detect any statistically significant trend.

Finally, we characterized the variability of the latency values. We computed mean, standard deviation, 95% confidence intervals, and the coefficient of variation (CV) of the time series for each of the four latencies.
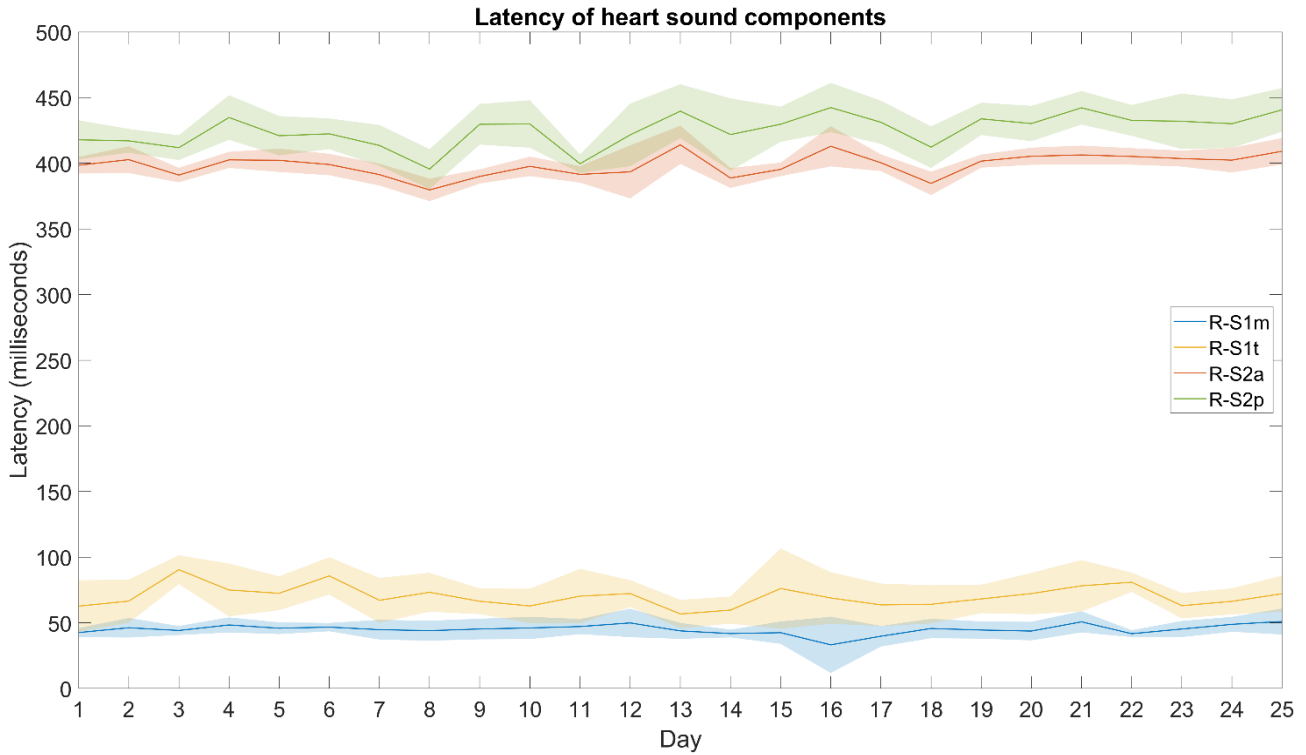
Fig. 2: Mean values of the latency of heart sounds components over time. The shaded areas represent the standard deviation band of the measurement over a 10-minute long recording.

III. RESULTS AND DISCUSSION

The next paragraphs present the results of the variability analysis over the 25-day period. First, we present plots of the measured values to allow for a qualitative analysis of their variability. The results of the statistical analysis will then provide a deeper quantitative insight in the variability of the latencies.

A. Latency values over the 25-day period

Fig. 2 shows, for every latency, the plot of the mean value (solid line) and of the standard deviation band (colored band around the solid line) of the specific latency over the 25-day period. No curves show any evident trend.

The standard deviation bands show a similar behavior for the two atrio-ventricular valves and for the two semilunar valves, whereas there is no clear correspondence between valves from the same side of the heart. To validate this point, the Pearson's Correlation Coefficient was computed for each possible pair of latencies. A Correlation Coefficient as high as 0.81 was found only for the aortic-pulmonary pair, whereas all other combinations resulted in Correlation Coefficients lower than 0.2. We can conclude that only the variations of the latencies of aortic and pulmonary components are correlated.

Fig. 3 presents the between-day variability of the latency of the components of heart sounds over the observation period. We computed each point of the between-day variability as the difference between the measured latency values in consecutive days. The plot shows that the right heart components (tricuspid and pulmonary) typically present a higher between-day variability with respect to their equivalent in the left side of the heart.

B. Analysis of variability

Table I presents the results of ANOVA applied to the four time series.

ANOVA p-values lower than 0.001 were found for each time series. This demonstrates that the latencies measured on different days are significantly different ($\alpha = 0.05$) for each of the observed valves. It should be highlighted that the low p-value also depends on the large sample of heartbeats used to obtain the daily values (averagely 600), which allows for defining a tight 95% confidence interval (approximately 8% of the standard deviation).

Table I shows that the Run test presents for all latencies a p-value considerably higher than the significance level ($\alpha = 0.05$). This confirms the hypothesis that data show no trend, as expected.

CVs of 8%, 11%, 2% and 3% were found for the latency of the mitral, tricuspid, aortic and pulmonary components, respectively. It could be hypothesized that the first sound
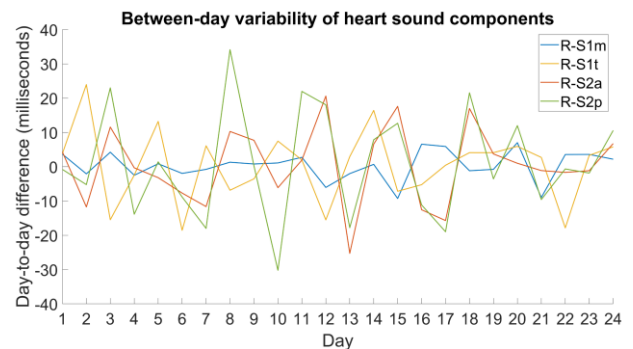

Fig. 3: Between-day variability of the latency of heart sounds components over the days.

TABLE I
STATISTICAL ANALYSIS OF THE RESULTS

Param	$R\text{-}S_{1,M}$	$R\text{-}S_{1,T}$	$R\text{-}S_{2,A}$	$R\text{-}S_{2,P}$
ANOVA p-value	< 0.001	< 0.001	< 0.001	< 0.001
RunsTest p-value	0.84	0.84	0.30	0.30
Mean (ms)	45	70	399	425
Std (ms)	8	15	9	16
CI 95 (ms)	42 - 48	64 - 76	395 - 402	419 - 432
CV (%)	8	11	2	3

components show CVs higher than those of the second sound components. Although the statistical significance of this difference has not been tested, the large ratio between the latencies of the components belonging to the same hearth side (3.7 – 4) supports this hypothesis.

The fact that results have been obtained on a single subject is the main limitation of this study. Nonetheless, due to the lack of similar data currently available in the literature, this contribution may be considered as a first attempt to describe the variability of the heart sound components over time.

IV. CONCLUSIONS

In this work, we recorded from a single subject simultaneous ECG and PCG signals in daily sessions during a period of 25 consecutive days. From each daily recording, we estimated the time of occurrence of each component of the first and second heart sounds with respect to the R-wave. Our goal was to analyze the variability of the latency values of the different components over time.

ANOVA demonstrated that statistically significant differences exist among values measured in different days. Moreover, we demonstrated that there is no trend in the series of the latency values. We computed the Coefficients of Variation for each latency and we found values equal to 8% for the mitral, 11% for the tricuspid, 2% for the aortic valve, and 3% for the pulmonary valve.

Moreover, we found evidence that, in the tested subject, the variability of the components related to the first hearth sound is higher than that related to the second heart sound.

Due to the encouraging results of this pilot study, we plan to extend a similar analysis to a wider population in the near future.

REFERENCES

[1]   A. C. Guyton and J. E. Hall, *Textbook of Medical Physiology*, 11th ed. Pennsylvania: Elsevier Health Sciences, 2015.

[2]   A.-L. Noponen, S. Lukkarinen, and R. Sepponen, "Phonocardiography," in *Multimodal Cardiovascular Imaging: Principles and Clinical Applications*, McGraw Hill Professional, 2011.

[3]   R. P. Lewis, S. E. Rittgers, W. F. Forester, and H. Boudoulas, "A Critical Review of the Systolic Time Intervals," *Circulation*, vol. 56, no. 5, pp. 146–158, 1977.

[4]   K. Tavakolian, "Systolic Time Intervals and New Measurement Methods," *Cardiovasc. Eng. Technol.*, vol. 7, no. 2, pp. 118–125, 2016.

[5]   L. Hamza Cherif and S. M. Debbal, "Algorithm for detection of the internal components of the heart sounds and their split using a Hilbert transform," *J. Med. Eng. Technol.*, vol. 37, no. 3, pp. 220–230, 2013.

[6]   S. R. Thiyagaraja, J. Vempati, R. Dantu, T. Sarma, and S. Dantu, "Smart phone monitoring of second heart sound split," *2014 36th Annu. Int. Conf. IEEE Eng. Med. Biol. Soc. EMBC 2014*, no. 1, pp. 2181–2184, 2014.

[7]   N. Brooks, G. Leech, and A. Leatham, "Factors responsible for normal splitting of first heart sound. High-speed echophonocardiographic study of valve movement," *Br. Heart J.*, vol. 42, no. 6, pp. 695–702, 1979.

[8]   J. Herzig, A. Bickel, A. Eitan, and N. Intrator, "Monitoring Cardiac Stress Using Features Extracted From S1 Heart Sounds," *IEEE Trans. Biomed. Eng.*, vol. 62, no. 4, pp. 1169–1178, 2015.

[9]   J. Fontecave-Jallon, K. Fojtik, and B. Rivet, "Is there an Optimal Localization of Cardio-microphone Sensors for Phonocardiogram Analysis?," *2019 41st Annu. Int. Conf. IEEE Eng. Med. Biol. Soc.*, pp. 3249–3252, 2019.

[10]   N. Giordano and M. Knaflitz, "A novel method for measuring the timing of heart sound components through digital phonocardiography," *Sensors (Switzerland)*, vol. 19, no. 8, 2019.

A Machine Learning Approach for Muscle Activity Detection

M. Ghislieri[1,2], E. Pavanelli[1], S. Rosati[1,2], G. Balestra[1,2], M. Knaflitz[1,2], and V. Agostini[1,2]

[1] *Department of Electronics and Telecommunications of Politecnico di Torino, 10129, Torino, Italy.*
[2] *PoliToBIOMedLab of Politecnico di Torino, 10129, Torino, Italy.*

Abstract - **The aim of this contribution is to introduce and validate a powerful approach to detect muscle activations in surface electromyography (sEMG) signals, based on feature extraction and Artificial Neural Network (ANN) classification. The proposed algorithm outperforms the traditional approach, widely used in gait analysis, that is based on a double threshold statistical detector. The new ANN-based Muscle Activity Detector (ANN-MAD) shows a smaller percentage of erroneous transitions, and a smaller bias and standard deviation with respect to the ground-truth onset detection. The advantages of using the ANN-MAD algorithm are particularly evident for signals with a low or medium signal-to-noise ratio (SNR).**

Keywords - **sEMG, onset-offset detection, ANN, machine learning.**

I. INTRODUCTION

DYNAMIC muscle activity can be non-invasively investigated by means of surface electromyography (sEMG). Determining the start (*onset*) and end (*offset*) instants of muscle activity during human movements is of great interest in different research fields including: gait analysis [1], motor rehabilitation and sport science [2], myoelectric control of prostheses [3], human-machine interaction [4], design of biofeedback systems [5] and pre-processing of muscle synergy extraction [6]–[8]. In particular, the accurate temporal analysis of muscle activation in terms of burst onset, duration of the activation interval, and burst offset, can be useful in the assessment of the altered locomotion patterns of orthopaedic and neurological patients [9].

A classical way to detect the timing of muscle activations from sEMG signals is using a double threshold detector, such as the statistical detector by Bonato et al. [10], specifically developed for gait analysis. However, this detector requires, as a necessary input parameter, to set the first (amplitude) threshold that depends on the background noise level. Furthermore, to fine-tune the second threshold, it is important to estimate the signal-to-noise ratio (SNR), e.g. through the algorithm described in Ref. [11]. Post-processing is also required.

Alternative methods, such as machine learning approaches, are being explored to perform sEMG-based pattern recognition. Our problem is somewhat easier with respect to a pattern-recognition problem. Indeed, we are not interested in classifying different movements, but simply detecting the presence or absence of muscle activations. Exploiting artificial intelligence, such as an Artificial Neural Network (ANN), has been a winning strategy in a wide variety of different applications and might be explored also for our problem. ANN is a powerful learning algorithm inspired by the biological

neural networks that constitute the human brain, and it is trained presenting to the network a large number of labelled "examples" [12].

The aim of this contribution is to assess if the application of a novel approach (based on feature extraction and ANN classification) can be used to overcome the limitations of the standard algorithms for muscle activity detection during gait. The new ANN-based Muscle Activity Detector (ANN-MAD) is compared to the double threshold statistical detector of Ref. [10] in terms of percentage of erroneous transitions, bias and standard deviation of the onset instants using simulated data.

II. MATERIALS AND METHODS

A dataset of simulated sEMG signals was built to compare the performance of the ANN-MAD algorithm with respect to the standard approach based on the double threshold statistical detector. Figure 1 represents the block diagram of the procedure followed.

A. Data Simulation

The sEMG signals acquired during cyclic movements, such as gait, can be modeled as the superimposition of two different entities: (a) the activity generated by the muscle and (b) the background noise generated by the neighbouring muscles and the electronics. Therefore, the simulated sEMG signals were generated as the superimposition of two different stationary processes [13]:

i. Background noise (n) modeled as a Gaussian process with zero-mean and variance σ_n^2:
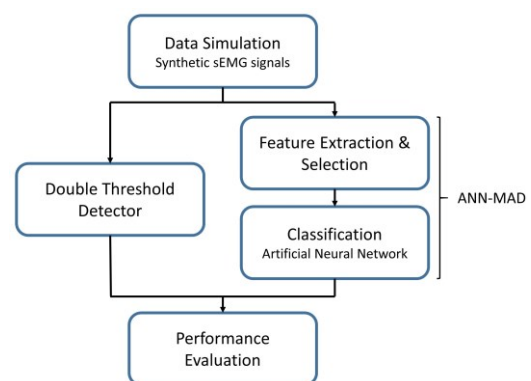

Figure 1. Block diagram of the procedure followed to assess the performance of the new algorithm ANN-MAD (ANN-based Muscle Activity Detector) with respect to the standard approach based on the double threshold statistical detector.

$$n(t) \in N(0, \sigma_n^2) \qquad (1)$$

being $\sigma_n = 1\mu V$.

ii.   Muscle activity (s) modelled as a zero-mean Gaussian process with variance σ_s^2:

$$s(t) \in N(0, \sigma_s^2) \qquad (2)$$

where $\sigma_s = 10^{(SNR/20)} \cdot 1\mu V$.

To simulate a physiological muscle activity, the Gaussian process (s) was time-windowed by means of a single truncated Gaussian function centred at 50% of the gait cycle. Then, the background noise process (n) was superimposed.

More specifically, the simulated signals were modeled with three different values of standard deviation of the truncated Gaussian function ($\sigma = 50, 100, 150$ ms), four different values of time support $\alpha\sigma$ of the truncated Gaussian function ($\alpha = 1, 1.5, 2, 2.4$), and nine different values of signal to noise ratio ($SNR = 3, 6, 10, 13, 16, 20, 23, 26, 30$ dB). For each triplet of σ, α, and SNR values, 100 different realizations (N) have been simulated assuming a gait cycle period equal to 1 s and a sampling frequency equal to 1 kHz. The simulated sEMG signals obtained were then band-pass filtered through a 4th order Butterworth digital filter with a lower cut-off frequency of 10 Hz and a higher cut-off frequency of 450 Hz. Figure 2 represents an example of a simulated sEMG signal.

B. Double Threshold Detector

A classical approach to muscle activity detection is the double threshold statistical detector proposed in Ref. [10]. The algorithm, specifically developed for gait analysis, operates on the raw sEMG signals and, hence, it does not require any pre-processing step (e.g. envelope extraction). A post-processor is then applied to the output of the detector to reject the erroneous transitions due to the stochastic nature of the sEMG signal. Since it is generally accepted that a muscle activation shorter
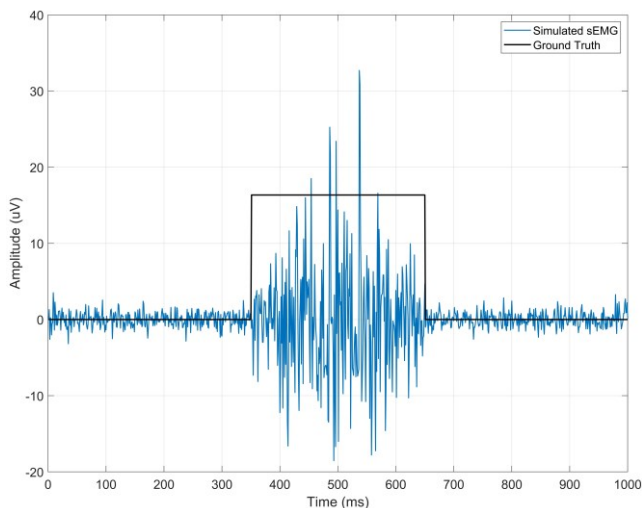
Figure 2. Example of a simulated sEMG signal with the indication of the ground truth (black line). The SNR is set equal to 20 dB, standard deviation of the truncated Gaussian functions (σ) is equal to 100 ms and α is equal to 1.5.

than 30 ms has no effect on the kinetics and the kinematics of gait [14], all the muscle activation durations lower than 30 ms were discarded.

C. ANN-based Muscle Activity Detector (ANN-MAD)

The new ANN-MAD algorithm has two main steps: (1) the feature extraction and selection, and (2) the ANN classification.

1) Feature Extraction and Selection

Reviewing the literature, 15 time-domain features were selected as the most relevant for muscle activity detection [15]–[17]. The features were extracted from each 25-ms epoch of the simulated sEMG signals considering an overlap of 96% (24 samples). After a min-max normalization step, these 15 features were used as input of the ANN classifier. A detailed description of the input features is provided in Table I.

2) ANN classification

Muscle activity detection was performed by means of a feed-forward ANN. Briefly, an ANN model is composed by an input layer, one or more hidden layers, and an output layer. Each layer is defined by means of an activation function (linear or non-linear) and it is composed of several units (or neurons).

In order to define the best ANN model for muscle activity detection, the entire dataset of simulated sEMG signals was divided into 3 different sets called training set, validation set, and test set, respectively. The training set was used to train the ANN, while the validation set (or development set) was used to evaluate the network performances and to avoid the overfitting of the training data. The truncated Gaussian functions considered for data simulation were used to compute the target (ground truth) of the ANN classifier. The final performances of the ANN (in terms of classification accuracy) were evaluated considering the test set only.

The output of the ANN classifier was then processed considering the same post-processor applied to the output of the double threshold statistical detector (muscle activation durations lower than 30 ms were discarded).

The algorithm for the definition of the best ANN model was developed in MATLAB® release R2019a (The MathWorks Inc., Natick, MA, USA).

D. Performance Evaluation

In this contribution, the performances of the two approaches are compared in terms of (*i*) percentage of the erroneous transitions, (*ii*) bias and (*iii*) standard deviation of the onset instants with respect to the ground truth.

i.   *Percentage of erroneous transitions* (ET) is defined as the number of gait cycles in which there are false positive or false negative estimates, divided by the total number of gait cycles simulated and multiplied by 100.

$$ET = \left(\frac{\#\ misclassified\ gait\ cycles}{\#\ simulated\ gait\ cycles}\right) \cdot 100$$

ii. *Bias* (b_{onset}) of the onset instants with respect to the ground truth is defined as

$$b_{onset} = \frac{1}{N}\sum_{i=1}^{N}(\hat{y}_i - y)$$

<div style="column: left">

TABLE I
FEATURES EXTRACTED FROM SIMULATED sEMG SIGNALS

Name	Definition
Mean Absolute Value (MAV)	$\dfrac{1}{N}\sum\limits_{n=1}^{N}|x_n|$
Modified Mean Absolute Value 1 (MAV1)	$\dfrac{1}{N}\sum\limits_{n=1}^{N} w_n|x_n|$ $w_n = \begin{cases} 1, if\ 0.25N \le n \le 0.75N \\ \quad 0.5, otherwise \end{cases}$
Modified Mean Absolute Value 2 (MAV2)	$\dfrac{1}{N}\sum\limits_{n=1}^{N} w_n|x_n|$ $w_n = \begin{cases} 1, if\ 0.25N \le n \le 0.75N \\ \dfrac{4n}{N}, \qquad if\ n < 0.25N \\ \dfrac{4(n-N)}{N}, if\ n > 0.75N \end{cases}$
Integrated EMG (IEMG)	$\sum\limits_{n=1}^{N}|x_n|$
Simple Square Integral (SSI)	$\sum\limits_{n=1}^{N}|x_n|^2$
Variance (VAR)	$\dfrac{1}{N-1}\sum\limits_{n=1}^{N} x_n^2$
Waveform Length (WL)	$\sum\limits_{n=1}^{N-1}|x_{n+1} - x_n|$
Log Detector (LOG)	$e^{\frac{1}{N}\sum_{n=1}^{N-1}\log(|x_n|)}$
Absolute Value for Third, Fourth and Fifth Temporal Moment (TM3, TM4, TM5)	$TM3 = \left|\dfrac{1}{N}\sum\limits_{n=1}^{N-1} x_n^3\right|$ $TM4 = \dfrac{1}{N}\sum\limits_{n=1}^{N-1} x_n^4$ $TM5 = \left|\dfrac{1}{N}\sum\limits_{n=1}^{N-1} x_n^5\right|$
Different Absolute Standard Deviation Value (DASDV)	$\sqrt{\dfrac{1}{N-1}\sum\limits_{n=1}^{N-1}(x_{n+1} - x_n)^2}$
Zero Crossing (ZC)	$\sum\limits_{n=1}^{N-1}(sgn(x_n \times x_{n+1}) \cap |x_n - x_{n+1}| \ge threshold)$ $sgn(x) = \begin{cases} 1, if\ x \ge threshold \\ \quad 0, otherwise \end{cases}$
Slope Sign Change (SSC)	$\sum\limits_{n=2}^{N-1} f(x_n - x_{n-1} \times x_n - x_{n-1})$ $f = \begin{cases} 1, if\ x \ge threshold \\ \quad 0, otherwise \end{cases}$
Root Mean Square (RMS)	$\sqrt{\dfrac{1}{N}\sum\limits_{n=1}^{N} x_n^2}$

where N is the number of estimates of y (ground truth), and $\hat{y}_i$ is the *i-th* estimate of y obtained by means of the detector.

iii. *Standard Deviation* (σ_{onset}) of the onset instants with respect to the ground truth is defined as

$$\sigma_{onset} = \sqrt{\frac{1}{N}\sum_{i=1}^{N}(\hat{y}_i - y)^2}$$

</div>

<div style="column: right">

A dataset of 10854 different simulated sEMG signals was built to define the best ANN model and to compare the performances of the two algorithms for muscle activity detection. To determine the best ANN model, the whole dataset was divided into the training set (70%), the validation set (15%), and the test set (15%). The same test set was used to assess and compare the performance of the two detectors.

A. ANN-MAD Model

Using the neural network toolbox of MATLAB®, 500 different feed-forward ANNs were tested. All the ANNs had an input layer composed of 15 units (number of features extracted from each 25-ms epoch), and a softmax output layer composed of 2 units (number of sEMG classes to be detected). Different number of hidden layers (from 1 to 3 hidden layers), number of units in each hidden layer (from 5 to 30 units), and activation functions (linear, ReLu, and sigmoid) were tested to achieve the ANN architecture with the highest classification accuracy.

The best ANN model was selected among all the tested networks as the one with the highest classification accuracy, discarding those networks with a difference between the training and validation accuracy higher than 4% (to avoid overfitting of the training data).

The highest test classification accuracy (90.6%) was achieved by the ANN model described in Table II.

B. Performance Evaluation

The performances of the two muscle activity detectors were assessed in terms of (1) percentage of the erroneous transitions, (2) bias, and (3) standard deviation of the onset instants with respect to the ground truth.

1) Erroneous Transitions

Figure 3(a) compares the percentage of erroneous transitions of the two detectors, for different values of SNR.

Results revealed that if the SNR is higher than 16 dB the percentage of erroneous transitions is always lower than 5% in both ANN-MAD and double threshold statistical detectors. Instead, considering SNR lower than 16 dB, the ANN-MAD algorithm significantly outperforms the double threshold statistical detector in terms of percentage of erroneous transition.

2) Bias of the onset of muscle activity

Figure 3(b) compares the bias affecting the estimates of the onset instants of the two detectors, at different SNR values.

TABLE II
DETAILS OF THE BEST ANN MODEL

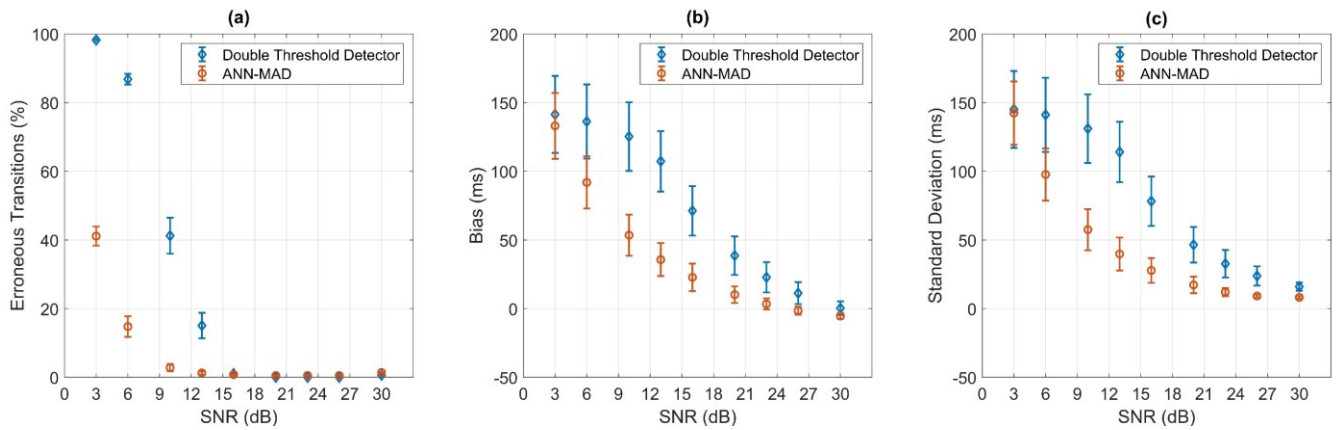| ANN Properties	Values
Number of input variables	15
Number of hidden layers	1
Number of units in hidden layer	10
Number of units in output layer	2
Activation functions	[sigmoid, sigmoid, softmax]
Training algorithm	Levenberg-Marquardt
Cost function	Mean Squared Error (MSE)

</div>

Figure 3. Comparison between the performance of the ANN-MAD and the double threshold statistical detector, in terms of: (a) percentage of erroneous transitions, (b) bias with respect to the ground-truth onset, and (c) standard deviation with respect to the ground-truth onset. Mean value ± standard error are reported.

The bias affecting the onset detection of the muscle activity is significantly lower for the ANN-MAD with respect to the double threshold statistical detector, for every SNR value. More specifically, bias lower than 30 ms is achieved at SNR ≥ 16 dB for the ANN-MAD detector, while the same is obtained only at SNR ≥ 23 dB for the double threshold statistical detector.

3) Standard Deviation of the onset of muscle activity

Figure 3(c) compares the standard deviation affecting the estimates of the onset instants of the two detectors, for different values of SNR. The standard deviation affecting the onset detection of the muscle activity is lower considering the ANN-MAD with respect to the double threshold statistical detector, for every SNR value. In particular, standard deviation values lower than 30 ms are achieved at SNR ≥ 16 dB for the ANN-MAD detector, while the same is obtained only at SNR ≥ 26 dB for the double threshold statistical detector.

IV. DISCUSSION AND CONCLUSIONS

The results presented in this contribution demonstrate that the detection of the muscle activity during gait can be successfully performed by means of the novel approach proposed (based on feature extraction and ANN classification), allowing for better performances in terms of percentage of erroneous transitions, bias and standard deviation of the onset instants. In particular, the novel approach clearly outperforms the standard one when considering simulated sEMG signals with an SNR lower than 16 dB. Finally, the ANN-based approach does not require any preliminary knowledge about the signal amplitude and the signal-to-noise ratio. Further studies are necessary to test the proposed approach also on experimental sEMG data.

REFERENCES

[1]   V. Agostini, A. Nascimbeni, A. Gaffuri, P. Imazio, M. G. Benedetti, and M. Knaflitz, "Normative EMG activation patterns of school-age children during gait," *Gait Posture*, vol. 32, no. 3, pp. 285–289, 2010.
[2]   A. D. Vigotsky, I. Halperin, G. J. Lehman, G. S. Trajano, and T. M. Vieira, "Interpreting signal amplitudes in surface electromyography studies in sport and rehabilitation sciences," *Frontiers in Physiology*. 2018.
[3]   S. Micera, J. Carpaneto, and S. Raspopovic, "Control of hand prostheses using peripheral information," *IEEE Rev. Biomed. Eng.*, 2010.
[4]   M. Simao, N. Mendes, O. Gibaru, and P. Neto, "A Review on Electromyography Decoding and Pattern Recognition for Human-Machine Interaction," *IEEE Access*, 2019.
[5]   S. Ma, M. Varley, L. K. Shark, and J. Richards, "EMG biofeedback based VR system for hand rotation and grasping rehabilitation," in *Proceedings of the International Conference on Information Visualisation*, 2010, pp. 479–484.
[6]   D. Rimini, V. Agostini, S. Rosati, C. Castagneri, G. Balestra, and M. Knaflitz, "Influence of pre-processing in the extraction of muscle synergies during human locomotion," *Proc. Annu. Int. Conf. IEEE Eng. Med. Biol. Soc. EMBS*, pp. 2502–2505, 2017.
[7]   M. Ghislieri, V. Agostini, and M. Knaflitz, "How to Improve Robustness in Muscle Synergy Extraction," in *2019 41st Annual International Conference of the IEEE Engineering in Medicine and Biology Society (EMBC)*, 2019, pp. 1525–1528.
[8]   M. Ghislieri, V. Agostini, and M. Knaflitz, "Muscle Synergies Extracted Using Principal Activations: Improvement of Robustness and Interpretability," *IEEE Trans. Neural Syst. Rehabil. Eng.*, pp. 1–1, 2020.
[9]   C. Castagneri, V. Agostini, S. Rosati, G. Balestra, and M. Knaflitz, "Asymmetry Index in Muscle Activations," *IEEE Trans. Neural Syst. Rehabil. Eng.*, vol. 27, no. 4, pp. 772–779, 2019.
[10]   P. Bonato, T. D'Alessio, and M. Knaflitz, "A statistical method for the measurement of muscle activation intervals from surface myoelectric signal during gait," *IEEE Trans. Biomed. Eng.*, 1998.
[11]   V. Agostini and M. Knaflitz, "An algorithm for the estimation of the signal-to-noise ratio in surface myoelectric signals generated during cyclic movements," *IEEE Trans. Biomed. Eng.*, vol. 59, no. 1, pp. 219–225, 2012.
[12]   I. . Basheer and M. Hajmeer, "Artificial neural networks: fundamentals, computing, design, and application," *J. Microbiol. Methods*, vol. 43, no. 1, pp. 3–31, Dec. 2000.
[13]   V. Agostini and M. Knaflitz, "An algorithm for the estimation of the signal-to-noise ratio in surface myoelectric signals generated during cyclic movements," *IEEE Trans. Biomed. Eng.*, vol. 59, no. 1, pp. 219–225, 2012.
[14]   R. a Bogey, L. a Barnes, and J. Perry, "Computer algorithms to characterize individual subject EMG profiles during gait.," *Arch. Phys. Med. Rehabil.*, vol. 73, no. 9, pp. 835–841, 1992.
[15]   A. Phinyomark, P. Phukpattaranont, and C. Limsakul, "Feature reduction and selection for EMG signal classification," *Expert Syst. Appl.*, vol. 39, no. 8, pp. 7420–7431, Jun. 2012.
[16]   D. Tkach, H. Huang, and T. A. Kuiken, "Study of stability of time-domain features for electromyographic pattern recognition," *J. Neuroeng. Rehabil.*, vol. 7, no. 1, pp. 1–13, 2010.
[17]   A. Phinyomark, S. Hirunviriya, C. Limsakul, and P. Phukpattaranont, "Evaluation of EMG feature extraction for hand movement recognition based on euclidean distance and standard deviation," *ECTI-CON 2010 - 2010 ECTI Int. Conf. Electr. Eng. Comput. Telecommun. Inf. Technol.*, no. May, pp. 856–860, 2010.

Mechanical properties of oxidized polyvinyl alcohol hydrogel scaffolds for tissue engineering

S. Todros[1], S. Barbon[2,3], M. Favaron[1], E. Stocco[2,3], D. Dalzoppo[4], R. Boscolo-Berto[2],
V. Macchi[2,3], C. Grandi[4,5], A. Porzionato[2,3], R. De Caro[2,3] and P.G. Pavan[1,6]

[1] Department of Industrial Engineering, Centre for Mechanics of Biological Materials, University of Padova, Padova, Italy
[2] Department of Neurosciences, Section of Human Anatomy, University of Padova, Padova, Italy
[3] L.i.f.e.L.a.b. Program, Consorzio per la Ricerca Sanitaria (CORIS), Veneto Region, Padova, Italy
[4] Department of Pharmaceutical and Pharmacological Sciences, University of Padova, Padova, Italy
[5] Foundation for Biology and Regenerative Medicine, Tissue Engineering and Signaling (T.E.S.) Onlus, Padova, Italy
[6] Fondazione Istituto di Ricerca Pediatrica Città della Speranza, 35121 Padova, Italy

Abstract—Due to their biocompatibility, microstructural features and high water content, polyvinyl alcohol hydrogels are synthetic polymers which can be used as scaffolds for tissue engineering.

In this field, the mechanical properties of scaffold materials are fundamental and should mimic the ones of biological tissues, in order to ensure mechanical compatibility in vivo.

In this work, the mechanical behaviour of native and partially oxidized PVA hydrogels is compared, to evaluate if the use of different oxidizing agents, such as bromine, iodine and potassium permanganate, can improve PVA scaffold biocompatibility and biodegradation, without deteriorating mechanical performances.

In detail, the different PVA hydrogels are characterized by investigating their tensile and compressive behaviour, also taking into account time-dependent mechanical response. Experimental results allow to evaluate the effect of the oxidizing treatment and to estimate short-term in-vivo performance in physiological loading conditions.

Keywords—polyvinyl alcohol, mechanical behaviour, experimental testing, tissue engineering.

I. Introduction

Recent developments in the field of tissue engineering have inspired successful strategies for the synthesis and the application of novel materials which can be used as scaffolds promoting tissue regeneration [1].

Among these materials, hydrogels consist of a three-dimensional network of cross-linked polymer chains, able to retain water [2,3]. Their unique combination of properties, including biocompatibility, permeability, hydrophilicity, and low friction coefficient, makes them suitable for the development of scaffolds for tissue engineering [4,5].

Hydrogel biomaterials have been proposed for a wide range of biomedical applications including drug delivery and substitutes for skin, tendons, ligaments, cartilage and vascular tissue [6,7]. They can be natural polymers, such as collagen or alginate, or synthetic polymers such as Polyvinyl Alcohol (PVA). However, insufficient biodegradation properties have severely limited the use of hydrogels as biosynthetic scaffolds for replacement of damaged tissues.

To overcome this limitation, partially oxidized PVA has been synthesized thorough chemical oxidation by means of potassium permanganate (Fig. 1) in perchloric acid, obtaining scaffolds with improved biocompatibility, protein-loading ability, and biodegradability in vivo [8,9].
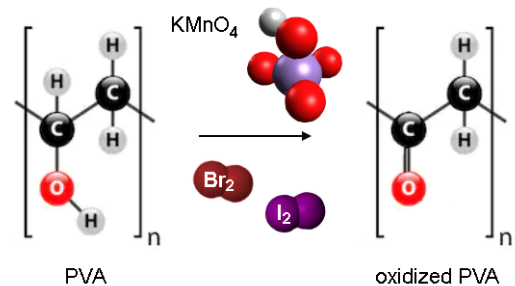

Fig. 1: Scheme of PVA oxidation by means of different oxidizing agents.

However, this specific PVA oxidation also induces a reduction of hydrogel viscosity, which could have an influence on mechanical performances.

In this work, bromine and iodine (Fig. 1) are used to perform controlled PVA oxidation as an alternative to potassium permanganate, aiming at improving scaffolds biodegradation without affecting polymer molecular weight distribution.

In fact, the possibility to control the polymeric structure of oxidized PVA could have an impact on its specific biological features, such as mechanical behaviour. In order to evaluate mechanical performances of native and oxidized PVA in different loading conditions, depending on specific tissue engineering applications, PVA hydrogels were characterized in tensile and compressive conditions, also considering time-dependent effects.

Previous characterization of hydrogels has focused on mechanical testing and dynamic mechanical analysis in compression or shear, aiming at development of cartilage substitutes [10,11]. For broadening the range of possible tissue engineering applications, it is critical to evaluate both tensile and compressive mechanical properties, since these are the primary modes of loading in vivo, and to take into account hydrogel viscoelastic properties.

II. Materials And Methods

A. Reagents

The reagents used for the synthesis of oxidized PVA are PVA [Molecular Weight 124,000-184,000 Da], 80% phosphoric acid (H_3PO_4), perchloric acid ($HClO_4$), elementary Br_2, sodium bicarbonate ($NaHCO_3$) (purchased from Sigma-Aldrich, S. Louis, MO, USA); $KMnO_4$, elementary I_2 and potassium iodide (purchased from Carlo Erba, Milan, Italy).

B. Preparation of native PVA

Native PVA solution is prepared as previously reported [8], suspending PVA powder in milliQ water and then heating for 48 h at 100°C under stirring until the polymer is completely dissolved.

C. Preparation of partially oxidized PVA

The partial (1%) oxidation of PVA with potassium permanganate is achieved as described in [8]. The obtained material will be labelled as "oxidized PVA 1" hereinafter.

The partial oxidation by means of bromine and iodine is made from PVA solution by adding $NaHCO_3$ and the oxidizing agent in stoichiometric quantity to oxidize 1% of secondary alcoholic groups to carbonyl groups.

The obtained solution is dialyzed against water using a membrane with 8000 Da cut-off (Sigma-Aldrich), frozen at –20°C and lyophilized by an under-vacuum evaporator (Speed Vac Concentrator Savant, Instruments Inc., Farmingdale, NJ, USA).

The PVA oxidized by means of bromine and iodine will be labelled as "oxidized PVA 2" and "oxidized PVA 3", respectively. Further details on oxidized PVA preparation and characterization can be found in [12].

D. Preparation of hydrogels

Hydrogels of PVA and oxidized PVA are obtained via physical cross-linking through the freeze-thaw (FT) process [13], with three cycles of freezing at –20°C for 24 h and thawing at –2.5°C for 24 h.

PVA hydrogels 2 mm-thick are cut in rectangular samples (width × free length equal to 5 mm × 20 mm) for tensile and stress-relaxation tests. The width-to-length aspect ratio is 1:4 for all samples, in accordance with other test protocols [14,15].

Cylindrical samples (diameter 24.5 mm; height 4 mm) are used for indentation tests. Samples are then stored at –20°C and unfrozen at room temperature about 1 h before any experiment by immersing them in physiologic solution.

E. Tensile tests

Bose ElectroForce® Planar Biaxial Test Bench instrument (TA Instruments, New Castle, USA) with a load cell of 22 N is used for all mechanical tests (Fig. 2a).

Uniaxial tensile tests are performed at constant strain rate of 0.5 %s^{-1}, up to 100% strain. Ten test repetitions for each material are developed. For each material, experimental data are used to calculate functional mean curves with associated standard deviation (SD).

Contactless marker tracking is used to measure local displacements in the centre of the samples by means of Allied Vision Prosilica GE680 camera (Edmund Optics Inc., Barrington, USA) [16].

(a)

(b)   (c)

Fig. 2. Experimental set-up for uniaxial tensile and stress relaxation tests (a). Detail of sample gripped for testing and hydration system (b). Detail of sample surface and indenter before testing (c).

(a)

(b)
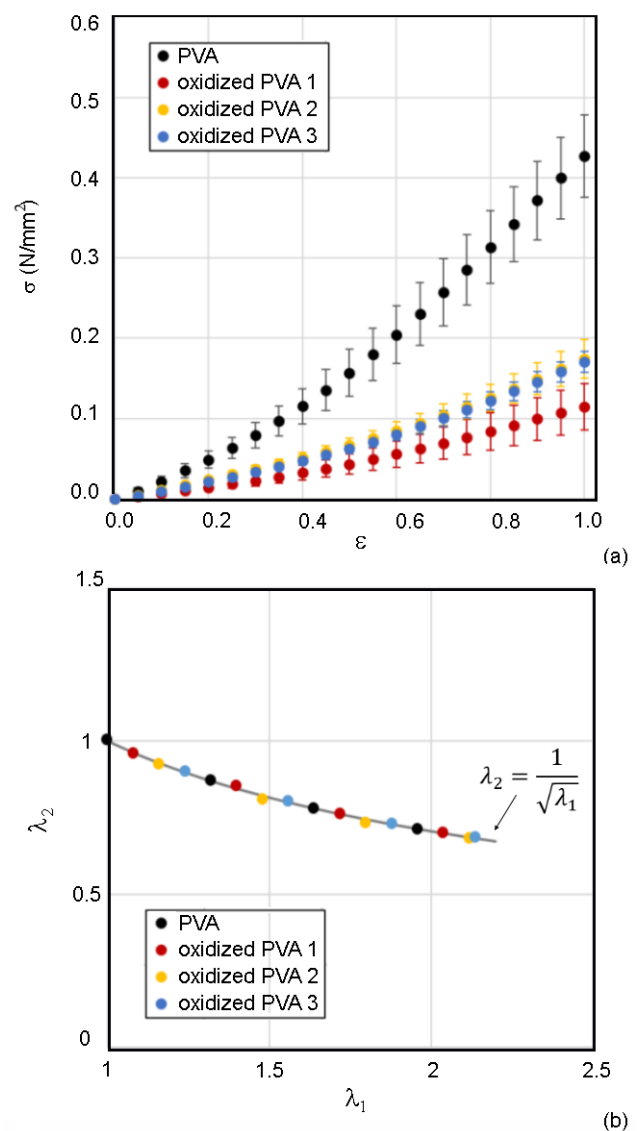
Fig. 3: Results of uniaxial tensile tests of PVA and oxidized PVA, shown as nominal stress σ vs. nominal strain ε (a). Local transverse stretch λ_2 vs. local longitudinal stretch λ_1 for PVA and oxidized PVA during tensile tests.
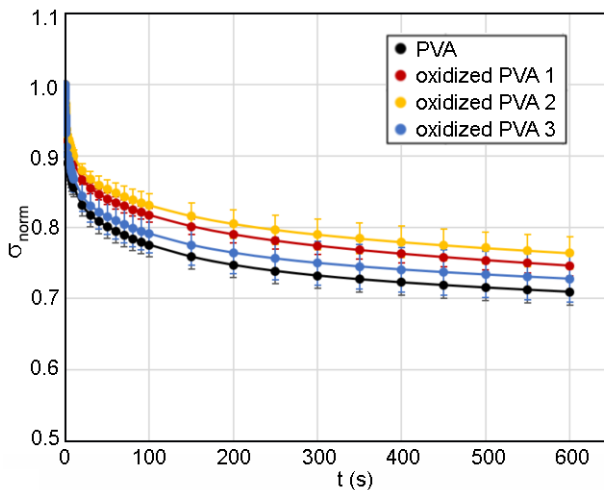
Fig. 4: Results of stress relaxation tests on PVA and oxidized PVA.

F. Stress-relaxation tests

Stress relaxation tests are carried out by elongating the sample at a strain rate of 500 %s^{-1} up to 50% strain and keeping a constant strain for 600 s.

During each test, the samples are hydrated by continuously dropping physiologic solution on the sample surface (Fig. 2b), to avoid any de-hydration effect.

Normalized stress σ_{norm} is calculated dividing stress data by the maximum value at the initial time of relaxation process. For each material, mean curves with associated SD are computed. Analysis of variance (ANOVA) is performed among normalized stress values of different materials at t = 600 s, followed by a Fisher Least Significant Difference (LSD) post-hoc test.

G. Indentation tests

Indentation tests are performed by using a rigid spherical indenter with a radius of 35 mm (Fig. 2c).

The indenter is slowly lowered onto the hydrogel surface up to contact, which is assumed when measuring a compressive force equal to −0.001 N. Tests were then performed at an indentation depth rate of 2 mm s^{-1}, up to −2 mm. Five tests are performed for each material.

In order to deduce the appropriate relation between stress and strain distribution within the sample, a numerical model that simulates test conditions is developed by using ABAQUS CAE software (SIMULIA, Dassault Systems).

III. RESULTS

The tensile behaviour of PVA and oxidized PVA is shown in Fig. 3a. Native and oxidized PVA show a nonlinear behaviour with a slight increase of the tangential stiffness with strain. None of the samples has undergone damage or break in the overall strain range of tensile testing.

The oxidation treatment largely reduces PVA stiffness: considering the secant modulus at 10% strain, a value of about 220 kPa is measured for native PVA, while the modulus of oxidized PVA is in the range between 60 and 140 kPa.

As shown by the plot of local transverse stretch as a function of local longitudinal stretch (Fig. 3b), an almost-

incompressible behaviour can be verified for each material by means of local strain measurements.

The equation reported in Fig. 3b refers to the relation between stretch in longitudinal and transverse direction (λ_1 and λ_2, respectively) for an incompressible isotropic material, subject to uniaxial stress state, corresponding to the mechanical condition of the tensile test. The experimental data for PVA and oxidized PVA are almost superimposed and show to fit the condition of incompressibility represented by the continuous line in Fig. 3b.
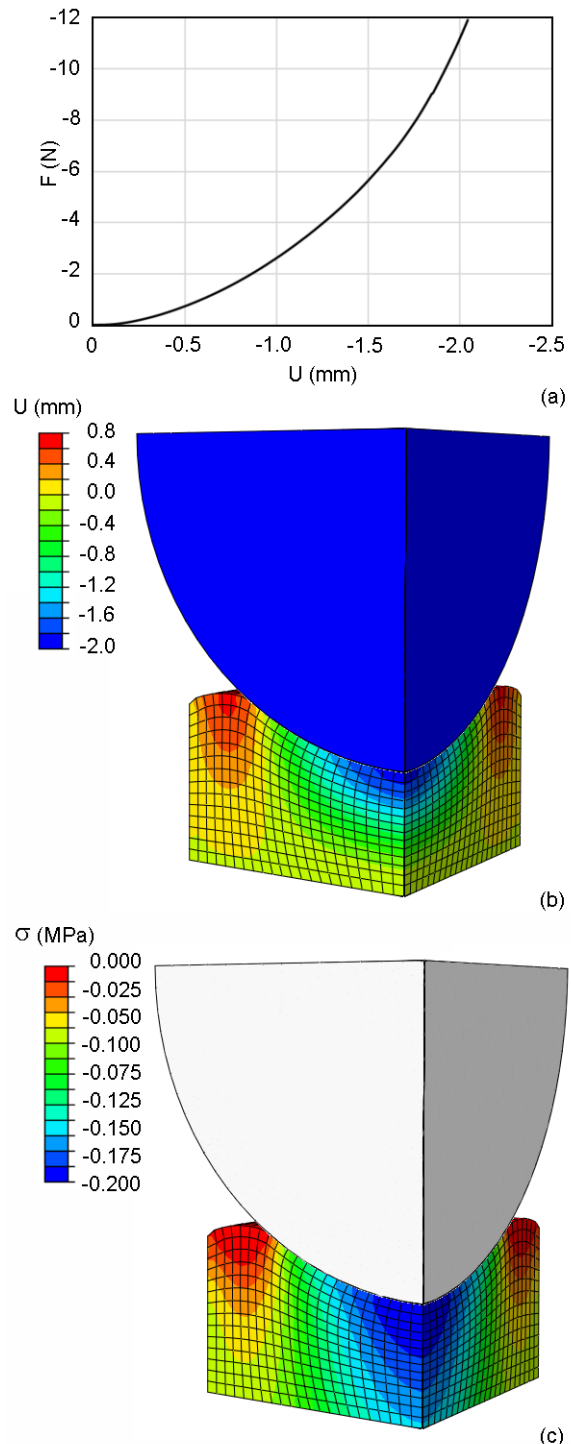
Fig. 5: Results of indentation tests of PVA, shown as indentation force F vs. indentation depth U (a). Contour of indentation depth (b) and stress (c) in the normal direction from numerical analysis of indentation test.

Stress relaxation data are shown in Fig. 4 for native and oxidized PVA, in terms of normalized stress σ_{norm} versus time t. At $t = 600$ s, the average stress decrease is of 29 %, 25 %, 24 % and 27 %, respectively for native PVA, oxidized PVA 1, 2 and 3, with SD is in the order of 2−5%. Statistical analysis highlights a significant difference between native and oxidized PVA in material relaxation processes. In detail, post-hoc test shows a significant difference in the following pairwise comparisons: native PVA vs. oxidized PVA 1; native PVA vs. oxidized PVA 2; oxidized PVA 2 vs. 3. Nonetheless, the time-dependent mechanical behaviour of native and oxidized PVA can be considered equivalent in terms of functional response from a biomechanical point of view, considering the relaxation time investigated.

The results of a typical indentation test are reported in Fig. 5a for native PVA. Since the compressive mechanical response depends on several factors, such as elastic properties and time-dependent behaviour of polymer network, as well as embedded water flow due to pressure gradients, it is necessary to develop numerical models (Fig. 5b).

This approach, combined with experimental data, allows to identify mechanical parameters related to drained or undrained conditions, considering the PVA as a poroviscoelastic material. The characterization of PVA compressive behaviour is aimed at evaluating its mechanical compatibility as substitute of tissues undergoing compressive loading in vivo, such as cartilages. For different applications, including vascular implants, heart valves and corneal substitutes, tensile mechanical behaviour is worth investigating.

Some limitations of this work, such as the lack of biaxial tensile characterization and tests oriented to point out the time-dependent in compression, will be part of a next investigation.

IV. Conclusion

The analysis of the mechanical properties of PVA hydrogels is fundamental to evaluate the possibility to use these materials for engineering tissues of different anatomical districts. Mechanical data shall be associated to biocompatibility and biodegradation data to get a comprehensive view of PVA hydrogel features for scaffold developments.

Moreover, general loading conditions, covering a very broad range, have been taken into account in this work, to get an overall description of native and oxidized PVA mechanical behaviour. According to specific tissue engineering application, the loading conditions can be tuned to simulate in vivo environment and the mechanical response of PVA scaffolds can be compared with the one of autologous tissues in physiological or pathological conditions.

References

[1] S. Ahadian, and A. Khademhosseini, "Smart scaffolds in tissue regeneration", *Regen. Biomater.*, vol. 5, pp. 125–128, 2018.

[2] S.L. Vega, M.Y. Kwon, and J.A. Burdick, "Recent advances in hydrogels for cartilage tissue engineering", *Eur Cell Mater.*, vol. 33, pp. 59–75, 2017.

[3] L. Saludas, S. Pascual-Gil, F. Prósper, E. Garbayo, and M. Blanco-Prieto, "Hydrogel based approaches for cardiac tissue engineering", Int. J. Pharm., vol. 523, pp. 454–475, 2017.

[4] Z. Gu, K. Huang, Y. Luo, L. Zhang, T. Kuang, Z. Chen, and G. Liao, "Double network hydrogel for tissue engineering", *Wiley Interdiscip. Rev. Nanomed. Nanobiotechnol.*, vol. 10, pp. 1–15, 2018.

[5] A. Vedadghavami, F. Minooei, M.H. Mohammadi, S. Khetani, A. Rezaei Kolahchi, S. Mashayekhan, and A. Sanati-Nezhad, "Manufacturing of hydrogel biomaterials with controlled mechanical properties for tissue engineering applications", *Acta Biomater.*, vol. 62, pp. 42–63, 2017.

[6] H. Yamaoka, H. Asato, T. Ogasawara, S. Nishizawa, T. Takahashi, T. Nakatsuka, I. Koshima, K. Nakamura, H. Kawaguchi, U.I. Chung, T. Takato, and K. Hoshi, "Cartilage tissue engineering using human auricular chondrocytes embedded in different hydrogel materials", *J. Biomed. Mater. Res. A.*, vol. 78, pp. 1–11, 2006.

[7] X. Hu, W. Lui, L. Cui, M. Wang, and Y. Cao, "Tissue engineering of nearly transparent corneal stroma", *Tissue Eng.*, vol. 11, pp. 1710–1707, 2005.

[8] E. Stocco, S. Barbon, F. Grandi, P.G. Gamba, L. Borgio, C. Del Gaudio, D. Dalzoppo, S. Lora, S. Rajendran, A. Porzionato, V. Macchi, A. Rambaldo, R. De Caro, P.P. Parnigotto, and C. Grandi, "Partially oxidized polyvinyl alcohol as a promising material for tissue engineering", *J. Tissue Eng. Regen. Med.*, vol. 11, pp. 2060–2070, 2017.

[9] E. Stocco, S. Barbon, L. Lora, F. Grandi, L. Sartore, C. Tiengo, L. Petrelli, D. Dalzoppo, P.P. Parnigotto, V. Macchi, R. De Caro, A. Porzionato, and C. Grandi, "Partially oxidized polyvinyl alcohol conduit for peripheral nerve regeneration", *Sci. Rep.*, vol. 8, 604, 2018.

[10] K.S. Anseth, C.N. Bowman, and L. Brannon-Peppas, "Mechanical properties of hydrogels and their experimental determination." *Biomaterials*, vol. 17, pp. 1647–1657, 1996.

[11] J.A. Stammen, S. Williams, D.N. Ku, and R.E. Guldberg, "Mechanical properties of a novel PVA hydrogel in shear and unconfined compression", *Biomaterials*, vol. 22, pp. 799–806, 2001.

[12] S. Barbon, E. Stocco, D. Dalzoppo, S. Todros, A. Canale, P. Pavan, V. Macchi, C. Grandi, R. De Caro, "Novel halogen-mediated partial oxidation of polyvinyl alcohol for tissue engineering purposes", *Int. J. Mol. Sci.*, vol. 21, pp. 801, 2020.

[13] V.I. Lozinsky, E.V. Solodova, A.I. Zubov, and I.A. Simenel, "Study of cryostructuration of polymers systems. XI. The formation of PVA cryogels by freezing-thawing the polymer aqueous solutions containing additives of some polyols", *J. Appl. Polym. Sci.*, vol. 58, pp. 171–177, 1995.

[14] S. Todros, A.N. Natali, G. Pace, and V. Di Noto, "Correlation between chemical and mechanical properties in renewable poly(ether-block-amide)s for biomedical applications", *Macromol. Chem. Phys.*, vol. 214, pp. 2061–2072, 2013.

[15] S. Todros, C. Venturato, A.N. Natali, G. Pace, and V. Di Noto, "Effect of steam on structure and mechanical properties of biomedical block copolymers", *J. Polym. Sci. Pol. Phys.*, vol. 52, pp. 1337–1346, 2014.

[16] S. Todros, S. Pianigiani, N. de Cesare, P.G. Pavan, and A.N. Natali, "Marker tracking for local strain measurement in mechanical testing of biomedical materials", *J. Med. Biol. Eng.*, vol. 39, pp. 764–772, 2019.

Detection of the N2/N2pc event-related potential (ERP) components buried in the EEG using phase angle distribution across sweeps

F. Marturano[1], S. Brigadoi[1,2], M. Doro[2], R. Dell'Acqua[2] and G. Sparacino[1]
[1] Department of Information Engineering, University of Padova, Italy
[2] Department of Developmental and Social Psychology, University of Padova, Italy

Abstract—**The visual N2/N2pc evoked responses are largely investigated in cognitive neuroscience as indices of allocation of covert visuo-spatial attention to target objects. In particular, the time-dependent variation of the N2/N2pc may reveal important aspects about how the cognitive mechanism of attention works in human subjects and many interesting applications using these components have been developed over the years. Unfortunately, detecting the N2/N2pc from noisy EEG recordings is particularly difficult and the estimation accuracy is not usually very high.**

In this work, we evaluated whether the phase angle (PA) of N2/N2pc data showed a specific pattern across trials compared to the spontaneous EEG noise that could suggest the use of PA as a reliable metric for their detection. The PA was evaluated both using simulated data and the real EEG recordings of fourteen subjects acquired during a standard visual search task evoking covert shifts in attention. N2 data, compared to noise and N2pc, showed a significant alignment of PAs around the average angle of 240° in the δ band and the time interval of the N2 component (i.e., 200-300 ms). These results highlight that, when the N2 is present, the single sweeps exhibit a specific and in phase pattern of oscillatory activity in the δ band and suggest that PA might be a reliable and informative measure to be employed in applications requiring the detection of small ERP responses buried in background EEG (e.g., brain-computer interface, BCI).

Keywords— **Visual N2/N2pc, event-related potentials, time-frequency analysis, ERP detection.**

I. INTRODUCTION

THE visual N2/N2pc are negative event-related potential (ERP) components usually arising between 200 and 300 ms after stimulus onset at the posterior sites of the scalp, more negative on the contralateral (CL) than ipsilateral (IL) to the cued target's location in the visual search array [1]. The N2pc, in particular, obtained as difference between two N2 waves, i.e., the CL minus the IL N2, is a recognized marker of the temporal allocation of covert visuo-spatial attention to the cued target [2], [3]. Therefore, the N2pc could be a useful ERP for instance in brain computer interface (BCI) applications [4], [5]. In this context, the N2pc should be reliably isolated from the background noise on a single-trial basis and some of its features converted into practical commands for the device. The N2pc is, however, a very small component (usually lower than 1-2 µV) and the detection is extremely difficult. For this reason, so far only few studies have considered the N2pc component as control signal for BCI [4], [5].

In general, all small-amplitude ERP components are difficult to isolate from background noise in the time domain, because both the ERP and the EEG activity have comparable orders of magnitude, with the latter most of the times being even larger. A time-frequency approach could therefore be more suitable in the N2/N2pc detection context. So far, the time-frequency domain has been largely explored to study the role of temporal dynamics in attention mechanisms and to investigate the contribution of frequency sub-bands, the goal being most of the time optimizing BCI classification [6], [7].

Several studies observed that the EEG rhythmic activity during an ongoing cerebral process is predominant in specific frequency bands and cerebral regions and different states of excitability may have an influence on the process as well as on the evoked response [8], [9]. These studies also demonstrated that different experimental events and subject-specific parameters, like the predictability of the stimulus timing, may modulate the phase of the ongoing activity. However, there is still a lack of a solid empirical support regarding these evidences and discrepancy of results [9]–[11]. Cognitive studies investigating EEG oscillatory activity during a task often evaluate the phase angle (PA) of the EEG trials and the inter-trial phase coherence (ITPC), an index measuring synchrony and uniformity of the PA across trials [11], [12]. These metrics quantify phase modulations of the ERP, but are also very sensitive to task-induced changes in the power of oscillations and noise content in the data [13]. Therefore, their use and stability should be carefully evaluated.

In this work, we evaluated the possibility of using PA and ITPC as features to discriminate the presence of an N2/N2pc response in individual experimental datasets and possibly in the single sweeps of the experiment. Preliminary investigations were firstly performed on synthetic data built through the use of a recently developed N2 simulator [14]. Then, methods were assessed on a real experimental dataset consisting in 14 subjects.

II. DATASETS

A. Simulated dataset

The use of a reliable simulation framework for validating or developing methods is powerful because it provides a total control of the data and a ground truth that can be employed to evaluate objective metrics on the performance of the tested techniques. Furthermore, simulation allows a simple manipulation of factors modulating the component of interest, inaccessible in the real dataset. For these purposes, it is essential that the generated synthetic data are as accurate and similar as possible to real data.

To create a reliable synthetic dataset, we resorted to the N2/N2pc simulator described in [14]. Briefly, the simulator was able to generate realistic N2 sweeps from a data-driven template of the ERP. By randomly perturbing the template in the N2 time window, the amplitude and latency variability of the N2 component observed in a real dataset was emulated. Single sweeps could be then arranged to simulate the timeline

of events of a real experiment and, hence, a complete EEG recording of an arbitrary number of trials and virtual subjects. In this work, we used the simulator to generate a noise-free dataset consisting of 50 random N2 sweeps.

Background EEG noise was taken from the resting-state (RS) EEG acquisitions of two real subjects to keep its natural features unaltered. We manipulated the RS noise sweeps by using multiplicative factors to generate many new noise sweeps. These sweeps, coupled with the synthetic N2 traces previously generated, produced noisy sweeps with controlled and different SNR. Finally, we created three noisy datasets with SNR of [0.1-0.5], [0.5-1] and [1-1.5], respectively, hereafter labelled as *low*, *middle* and *high* SNR (Fig. 1).

B. Real dataset

Data of fourteen healthy volunteers (mean age 23.2 ± 2.1 years, 5 males and 9 females) were collected whilst running an experiment based on a common visual search task eliciting the visual posterior N2 component, at a sampling frequency of 500 Hz and in a multi-channel setting with 28 scalp electrodes. Three electrodes were placed at the outer canthi and below the left eye for measuring the electrooculogram (EOG) and two on both the earlobes as reference. During the experiment, 600 visual search arrays were presented to the participant on a screen, 200 per visual hemi-field and 200 along the sagittal midline. While fixating a fixation cross in the centre of the screen, participants were presented with 12 little white circles clock-wisely positioned around the fixation cross. The stimulation consisted in a turning-blue circle with a bar (tilted or not) appearing inside. Participants had to report the orientation of the bar inside the target circle.

After being collected, data were band-pass filtered (0.1-30 Hz), divided into single trials (from 0.6 s pre-stimulus to 1 s post-stimulus each), re-referenced using the mean of the earlobe signals and baseline corrected. Sweeps with ocular artefacts were removed using EOG. Afterwards, only electrodes P7/P8 [4], both located at the posterior left/right side of the scalp, respectively, were selected. Trials from incorrect or no responses and trials associated to central stimuli were discarded. Remaining trials were partitioned into right- (RT) and left-target (LT) trials (Fig. 1).
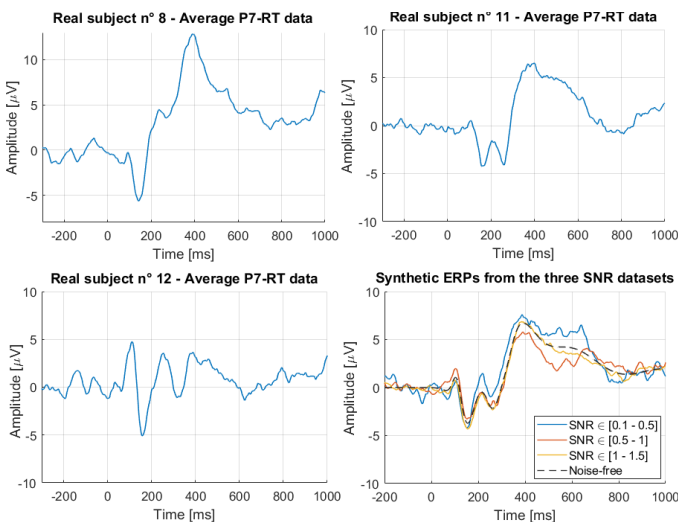
Figure 1. Noisy ERPs of some representative real subjects (for P7-RT data group only) and of the three synthetic SNR scenarios (bottom-right panel).

III. Methodology

A. Definition of PA and ITPC metrics

In EEG applications, ITPC measures the similarity of the oscillatory phase across trials and represents a global estimate of the instantaneous PA, i.e., the position along the sine wave resulting from the convolution between each EEG trial and the Morlet's wavelet at frequency *f*. If there is a dominant *f* at a certain *t*, the PA distribution across trials is concentrated around a specific angle. The proximity of the phases is summarized by the ITPC [12], [13]. ITPC values close to 0 reflect a high variability of PA across sweeps, while an ITPC close to 1 means that all sweeps have similar PAs.

In the following, we report the algorithm used to compute ITPC, at any frequency (N_f points, from *fmin* to *fmax*) and time (N_t points) of interest. In our study, *fmin* = 0.5 Hz, *fmax* = 30 Hz, N_f = 40 and N_t = 800.

Algorithm to compute ITPC

for f ∈ [fmin, fmax]
   a. Morlet's wavelet (at frequency f) convolution of EEG data
   b. Inverse Fourier transform of the result
   c. Data reshaping (dim: N_t x N_{swp})
   d. Exponential form ($e^{i\vartheta}$) of the complex values
   e. Average across the N_{swp} sweeps (dim: N_t x 1)
   f. Absolute value of the complex vector (dim: N_t x 1)
end

Obtain ITPC at each frequency and time point (dim: N_t x N_f)

Instead, the PA of each sweep is obtained by considering the phase of the complex values in the N_{swp} columns of the matrix resulting from step *d.* in the algorithm description. Then, at a certain frequency, *f*, (or frequency range [f_1, f_2]) the time instant, *t*, (or time window [t_1, t_2]) of interest can be selected to observe the PA distribution across sweeps in those ranges.

B. Implementation

Van Diepen et al. [13] observed that a difference in power (amplitude^2) of the EEG oscillation induces a different spread around the true PA (and thus a lower ITPC) even if the phase of the ongoing oscillation is the same. They demonstrated that this difference is actually caused by the SNR of the data, but even differences in the amplitude and latency of the ERP could lead to differences in the ITPC. Therefore, the use of ITPC to compare different conditions or experimental events should be carefully evaluated.

Here, because of PA and ITPC sensitivity to noise-/ERP-driven fluctuations, we investigated whether these metrics could be reliably used to discriminate individual datasets having a predominant noise content as well as a high variability of the ERP across sweeps from those where the noise content was instead favourable to an accurate detection of the ERP. To this aim, a preliminary assessment in a synthetic and controlled context was essential for a reliable use of these metrics. All the investigations were performed in MATLAB environment (version 2019b, The MathWorks, Natick, 2019).

IV. RESULTS

A. Simulated data

We used the synthetic noise-free dataset to observe the PAs in the N2/N2pc time window (i.e., 200-300 ms) across synthetic sweeps, as a function of frequency, and compared the outcomes with those of RS noise sweeps (Fig. 2, top and bottom panel, respectively). Noise and ERPs showed a very different pattern of the PA, especially at lower frequencies, suggesting that phase synchronization at these bands could be a marker of the N2 component: the average of PA distribution across trials was about -120° (that is equivalent to 240°) vs. 0° for ERPs and noise sweeps, respectively, in the δ band (0.5-4 Hz) and about 100° vs. 0° in the θ band (4-8 Hz).

These results open up a new interesting possibility to use PA distribution to discriminate individual datasets with a clear N2 response from those where noise is predominant.
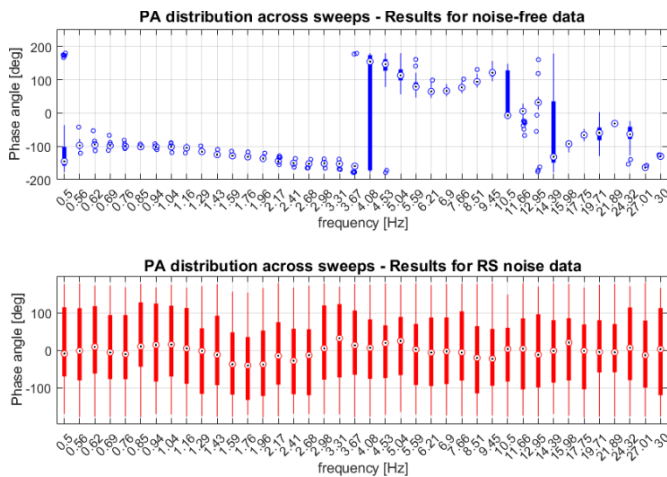
Figure 2. PA distribution across sweeps as a function of frequency, for noise-free ERPs (top panel) and resting-state (RS) noise sweeps of the *high* SNR scenario (bottom panel).

To evaluate the dependence of PA distribution on the noise level, we used the three SNR datasets previously generated and compared their average PA with that of the noise-free scenario, considering the δ band and the N2 time window only (Fig. 3).
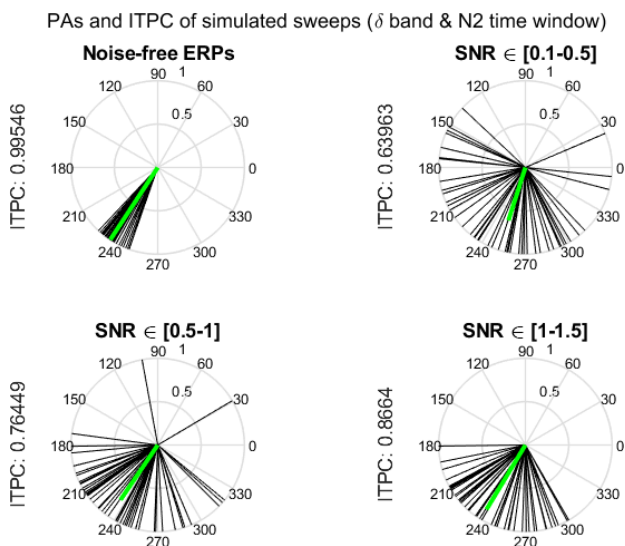
Figure 3. PAs and ITPC computed both for the noise-free synthetic dataset (top-left panel) and the three SNR scenarios. In each plot, the solid green line represents the average PA across sweeps and its length the ITPC.

Here, PA distribution resulted spread around a mean of about 240° (solid green line) in the four scenarios, with a degree of dispersion mostly dependent on the SNR. Differences in the PAs were also present across noise-free ERPs (Fig. 3, top-left panel) caused by N2 parameters' fluctuations across trials, i.e., amplitude and latency [13].

It is worth mentioning that the PA distribution in other time intervals was very different from that observed in the N2/N2pc time window: about 180° in (100-200 ms) and 300° in (300-400 ms), for example.

Considering N2pc data in each SNR scenario, the same phase analysis did not reveal any significant result, whatever the frequency considered: the PA distribution in the N2/N2pc time window was similar for N2pc data and noise and the ITPC was always lower than 0.5, even when considering the *high* SNR dataset. Only noise-free N2pcs substantially differed from noise, showing an average PA in the δ band and N2 time window of about 100° and an ITPC of 0.6.

The analysis on RS noise sweeps, instead, confirmed the absence of a relevant alignment of the PAs; indeed, the corresponding ITPC was almost nihil. This finding suggests that EEG noise could be discriminated from the ERP most of the time because of its random PA distribution across sweeps (Fig. 4).
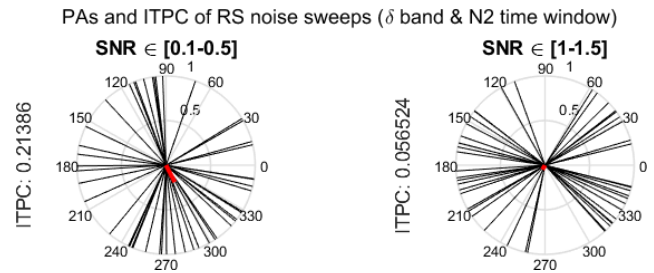

Figure 4. PAs and ITPC for the resting-state (RS) noise traces of the *low* (left panel) and *high* (right panel) SNR scenario.

B. Real experimental data

To confirm simulation results, we computed the PA of the experimental data, for each channel-target side group. Fig. 5 shows some exemplary real subjects, considering P7-RT data.
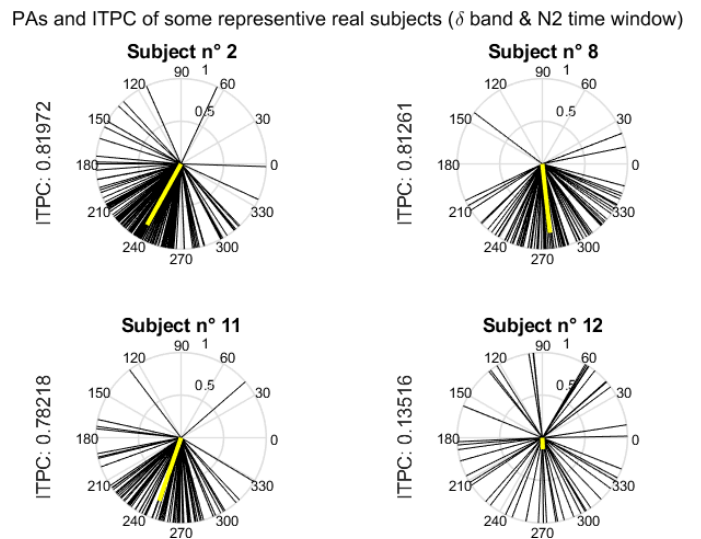

Figure 5. PAs and ITPC of four representative subjects of the real experimental dataset, considering P7-RT data group only.

Table I. Between-trials ITPC and PA distributions for each real subject.

	sbj #1	sbj #2	sbj #3	sbj #4	sbj #5	sbj #6	sbj #7	sbj #8	sbj #9	sbj #10	sbj #11	sbj #12	sbj #13	sbj #14
PA [deg]	277.7 (2.5)	252.0 (9.3)	247.3 (11.8)	284.5 (5.8)	286.0 (8.0)	229.9 (6.4)	242.9 (6.9)	271.3 (7.6)	290.3 (19.9)	243.6 (6.3)	258.3 (5.8)	295.0 (21.0)	236.8 (5.0)	226.8 (11.9)
ITPC	0.7 (0.1)	0.9 (0.0)	0.4 (0.2)	0.4 (0.1)	0.7 (0.1)	0.8 (0.1)	0.8 (0.0)	0.8 (0.0)	0.4 (0.1)	0.8 (0.0)	0.8 (0.0)	0.3 (0.1)	0.8 (0.1)	0.7 (0.0)

Subjects n° 2 and 11 showed a similar pattern of PA distribution around the average PA (solid yellow line). These results are in accordance with those of the simulated scenario (see Fig. 3). Instead, the average PA of subject n° 8 was about 270° but the corresponding ITPC was significantly greater than zero, suggesting a phase synchronization across sweeps and thus the presence of the N2 component. This increment in the PA might be due to a slightly different pattern of the N2 wave (see Fig. 1, top-left panel). On the contrary, subject n° 12 presented random PAs and a low ITPC, similarly to RS noise (see Fig. 4). One reason could be that the subject's ongoing brain activity during the task was not synchronized or, instead, this result could be representative of a context were noise prevails over the ERP. See also the average ERPs of subjects n° 8, 11 and 12 reported in Fig. 1, for a comparison.

Table I summarizes results for each real subject in terms of average PA and ITPC (± std), across channel-target side data groups. The between-subjects average PA and ITPC (± std) were 260° (± 24°) and 0.7 (± 0.2), respectively. For the N2 data, most of the subjects presented a precise alignment of the PA across sweeps that was close to the value obtained in simulation. This information might indicate the presence of a relevant ERP response and could be used in future investigation to identify a dataset with a clear evoked response, when all experimental trials are considered, and possibly to develop a new method able to discriminate in each trial whether the ERP is clearly visible or heavily buried in noise.

PA distribution of N2pc real data resulted for all subjects very similar to the RS noise one: the average ITPC (± std) was equal to 0.09 (± 0.05), confirming the results of the simulation.

V. CONCLUSION

Achieving a reliable detection of small ERP components, that are usually hidden in the EEG noise, is a common issue in cognitive neuroscience. In this work, we investigated the time-frequency domain of both synthetic and real ERP/EEG data and assessed the possibility of using PA distribution across trials and the corresponding global ITPC as useful metrics for discriminating the presence of the evoked response in individual acquisitions. The specific application of this study was to the visual N2/N2pc components.

For the N2 data, the PA distribution across trials was spread around the average value of 240° in the N2/N2pc time window and δ band, with a dispersion level summarized by the ITPC and depending mostly on the SNR of the sweeps and partly on the parameters' variation of the component. This finding suggests that the presence of a good N2 response might be distinguishable from a noise-driven context when looking at the PA distribution across trials at low frequencies and considering simultaneously the value of the resulting ITPC. Indeed, the ITPC was significantly close to 1 when the evoked response was present in the data and almost 0 when not present. The same analysis instead failed when applied to the

N2pc component, probably because of its subtractive origin, which causes a decrease in amplitude, and therefore in the SNR, so that noise and ERP become indistinct.

The present investigation, although preliminary, opens up new interesting scenarios regarding the use of phase analysis for isolating good individual datasets from those where background noise prevails over the ERP. In the future, we aim to perform new evaluations using larger synthetic and real datasets and including in the investigation other frequency bands (e.g., the θ band) to define a precise rule for classifying data according to presence or absence of the N2 component. Other ERP components could be investigated through this approach as well.

REFERENCES

[1] S. J. Luck and S. A. Hillyard, "Electrophysiological correlates of feature analysis during visual search," *Psychophysiology*, vol. 31, no. 3, pp. 291–308, May 1994.

[2] G. F. Woodman and S. J. Luck, "Serial Deployment of Attention During Visual Search," *J. Exp. Psychol. Hum. Percept. Perform.*, vol. 29, no. 1, pp. 121–138, 2003.

[3] M. Kiss, J. Van Velzen, and M. Eimer, "The N2pc component and its links to attention shifts and spatially selective visual processing," *Psychophysiology*, vol. 45, no. 2, pp. 240–249, 2008.

[4] H. Awni, J. J. S. Norton, S. Umunna, K. D. Federmeier, and T. Bretl, "Towards a brain computer interface based on the N2pc event-related potential," in *International IEEE/EMBS Conference on Neural Engineering, NER*, 2013, pp. 1021–1024.

[5] A. Matran-Fernandez and R. Poli, "Towards the automated localisation of targets in rapid image-sifting by collaborative braincomputer interfaces," *PLoS One*, vol. 12, no. 5, May 2017.

[6] L. Tonin, R. Leeb, and J. del R Millán, "Time-dependent approach for single trial classification of covert visuospatial attention," *J. Neural Eng.*, vol. 9, no. 4, p. 045011, Aug. 2012.

[7] M. S. Treder, A. Bahramisharif, N. M. Schmidt, M. A. Van Gerven, and B. Blankertz, "Brain-computer interfacing using modulations of alpha activity induced by covert shifts of attention," *J. Neuroeng. Rehabil.*, vol. 8, no. 1, 2011.

[8] G. Thut, C. Miniussi, and J. Gross, "The functional importance of rhythmic activity in the brain," *Current Biology*, vol. 22, no. 16. pp. R658–R663, 21-Aug-2012.

[9] M. Bonnefond and O. Jensen, "Alpha oscillations serve to protect working memory maintenance against anticipated distracters," *Curr. Biol.*, vol. 22, no. 20, pp. 1969–1974, Oct. 2012.

[10] R. M. Van Diepen, M. X. Cohen, D. Denys, and A. Mazaheri, "Attention and temporal expectations modulate power, not phase, of ongoing alpha oscillations," *J. Cogn. Neurosci.*, vol. 27, no. 8, pp. 1573–1586, Aug. 2015.

[11] C. Tallon-Baudry, O. Bertrand, C. Delpuech, and J. Pernier, "Stimulus specificity of phase-locked and non-phase-locked 40 Hz visual responses in human," *J. Neurosci.*, vol. 16, no. 13, pp. 4240–4249, 1996.

[12] B. J. Roach and D. H. Mathalon, "Event-Related EEG Time-Frequency Analysis: An Overview of Measures and An Analysis of Early Gamma Band Phase Locking in Schizophrenia," *Schizophr. Bull.*, vol. 34, no. 5, pp. 907–926, Jul. 2008.

[13] R. M. Van Diepen and A. Mazaheri, "The Caveats of observing Inter-Trial Phase-Coherence in Cognitive Neuroscience," *Sci. Rep.*, vol. 8, no. 1, Dec. 2018.

[14] F. Marturano, S. Brigadoi, M. Doro, R. Dell'Acqua, and G. Sparacino, "Computer Data Simulator to Assess the Accuracy of Estimates of Visual N2/N2pc Event-Related Potential Components," *J. Neural Eng.*, 2020.

Computational investigation of the male lower urinary tract in health and disease

C.G. Fontanella[1,2], I. Toniolo[1,2], A. Arduino[2,3], J.V. Fotso Fogang[2,3],
A.N. Natali[1,2] and E.L. Carniel[1,2]

[1] Department of Industrial Engineering, University of Padova, Italy
[2] Centre for mechanics of biological materials, Department of Industrial Engineering, University of Padova, Italy
[3] Department of Civil, Environmental and Architectural Engineering, University of Padova, Italy

Abstract - **In the last few years, engineering and computational methods proved their feasibility and reliability in the areas of physiology, medicine and surgery. The here reported activities show the potentialities of typical tools of bioengineering, as Computational Fluid Dynamics, Computational Structural Mechanics and Fluid Structure Interaction techniques, in the field of lower urinary tract pathophysiology. Computational models of male lower urinary tract were assumed, together with typical properties of both biological tissues and fluids, to investigate its mechano-physiology in health and disease. The reliability of these models was assessed by the mutual comparison between computational results and the investigation of data from experimental and clinical activities. Computational models allowed analyzing typical situations, as the physiological micturition and the lumen occlusion by external devices. Computational results gave information that clinical and experimental tests barely provide, as the occurrence of turbulent phenomena within urine flow, the shear stresses at the lumen wall, the external pressure that is strictly required to occlude the lumen.**

Keywords - **Lower urinary tract, Computational Fluid Dynamics, Computational Structural Mechanics, Fluid Structure Interaction.**

I. INTRODUCTION

URETHRAL mechanical functionality represents a relevant topic for the actual comprehension of lower urinary tract physiology in health and disease [1]. Such investigation pertains to biomechanics area of study and provides considerable challenges, because it couples both solid and fluid mechanics problems.

Urodynamic analyses of urine flow and pressure along the urethra allow investigating how urethral sphincters work, discovering obstructions, and diagnosing patients who have urinary incontinence or other urinary symptoms [2]. The precise knowledge of the actual pattern of urine flow and pressure from the bladder up to the external meatus should provide a reliable tool for a better comprehension and explanation of results from such uroflowmetry and urodynamic tests. The methods of Computational Fluid Dynamics (CFD) provide quantitative information about the urine flow regime, the velocity and the pressure fields, depending on many different influencing factors. Urethral wall is made of soft biological tissues, defining a considerably compliant duct. Consequently, the reliable investigation of urine flow should take into consideration the urethral wall dilatation that occurs because of urine pressure. The methods of Computational Solid Mechanics (CSM) allow the analysis

of such dilatation phenomena. In turn, the expansion of urethral wall influences the urine flow regime, leading to the coupling of fluid flow and solid mechanics problems, which is the framework of Fluid Structure Interaction (FSI) phenomena. The methods of FSI can be exploited to investigate urinary incontinence, which is one of the principal health concerns worldwide. Despite the Artificial Urinary Sphincter (AUS) is the gold standard for the treatment of male incontinence, up to 50% of patients receiving AUS requires surgical revision after initial placement [3]. The principal causes of AUS failure are infection processes, urethral atrophy, urethral erosion and device malfunction. The AUS is usually applied all around the bulbar urethra, which is a non sphincteric region, because the local tissues are not used to support occluding actions. Furthermore, the AUS device has to ensure continence up to the highest bladder pressure conditions, and consequently it constantly applies a trying occluding action. Such mechanical stimulation of urethral tissues is responsible for damage phenomena that may evolve to atrophy or erosion. CSM and FSI investigations allow analysing mechanical interaction phenomena between AUS and urethra, and provide useful information about the AUS reliability [4],[5]. Furthermore, CSM and FSI techniques can be exploited to evaluate the minimal mechanical actions that are strictly required to ensure lumen occlusion and, consequently, continence. Such investigations are mandatory for the optimal design of novel and more reliably AUS devices.

II. MATERIALS AND METHODS

A. Experimental characterization of male lower urinary tract

The investigation of the macro- and the micro-structural configuration of the biological structure and the building tissues is mandatory for the geometrical identification of the system and for the characterization of tissues mechanics. The histo-morphometrical configuration of the male lower urinary tract has been widely described in the scientific literature. Here, attention will focus on the bladder and the urethra, which define the final path of urine (Fig. 1).

The bladder is a hollow and distensible viscus that functions as a temporary reservoir for the urine. The capacity of the full male bladder ranges between 300 and 400 mL. The bladder wall is a complex structure made up of mucosa, submucosa, muscolaris and serosa layers. The mucosa is the innermost tissue and consists of transitional epithelial cells layers and loose connective tissue. The submucosa is a thick layer of dense connective tissue and it is rich in collagen fibers, nerves,

blood and lymphatic vessels. The tunica muscolaris is composed of three smooth muscular layers together with connective elements. Within the inner and the outer layers, muscular fibers predominately arrange from the apex to the bottom of the bladder, while a circumferential organization characterizes the fibers within the middle layer. Finally, the serosa layer is a visceral peritoneum.
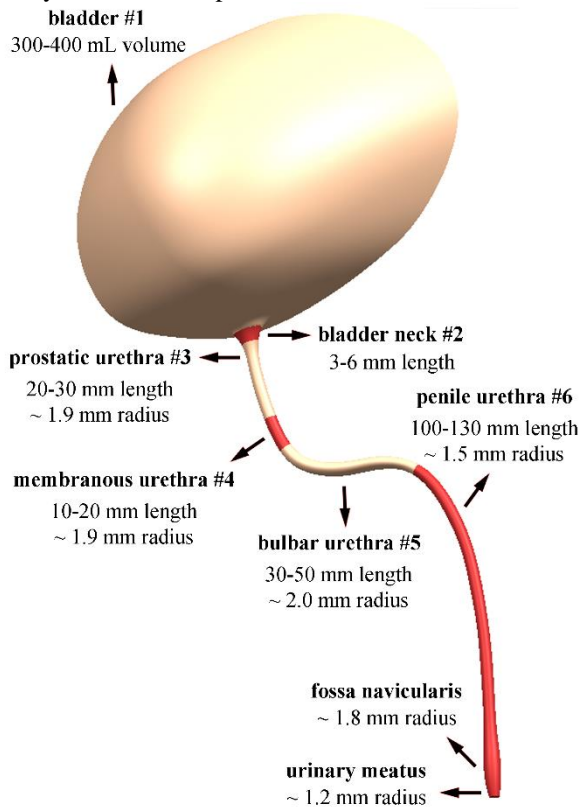

bladder #1
300-400 mL volume

bladder neck #2
3-6 mm length

prostatic urethra #3
20-30 mm length
~ 1.9 mm radius

penile urethra #6
100-130 mm length
~ 1.5 mm radius

membranous urethra #4
10-20 mm length
~ 1.9 mm radius

bulbar urethra #5
30-50 mm length
~ 2.0 mm radius

fossa navicularis
~ 1.8 mm radius

urinary meatus
~ 1.2 mm radius

Fig. 1: Morphometric characterization of male bladder and urethra.

The male urethra is a 180-200 mm long hollow tube that allows the flow of urine from the bladder neck up to the urinary meatus. In the absence of urine flow, urethral lumen shows a complex cross-sectional shape, ranging between slit- and star-like ones, while it assumes an almost circular shape during micturition. The dimension of the lumen (Fig. 1) is usually defined in a distended and circular condition of the wall. Different regions compose the urethra, as the prostatic urethra, the membranous urethra, the bulbar urethra and the penile urethra. A complex histological configuration characterizes the urethral wall, which further depends on the specific region. In general, the urethral wall assumes a multi-layered configuration. The inner layer, as the urethral mucosa, is made of an epithelium, which lines the lumen, and a lamina propria. The latter is made of fibrous-connective tissue with highly oriented collagen fibers. An outer muscular layer characterizes the prostatic and the membranous urethra, while a thick spongy layer defines the outer shell of both the bulbar and the penile urethra. The natural urethral sphincter is located all around the prostatic and the membranous urethra. The histological configuration of the building tissues suggests the complex mechanical response of both bladder and urethral walls, which must be further investigated by means of mechanical experiments [6],[7]. The mechanical behavior of both bladder and urethral tissues has been mostly investigated

by means of uni-axial and bi-axial tensile tests. Further experimental activities aimed at analyzing the mechanical behavior of the entire biological structure by means of insufflation tests. Mechanical tests have been performed on tissue samples from animal models, human cadavers and surgical residuals. The results confirm the complex mechanical behavior of the tissues, with particular regard to non-linearity of the stress-strain response. Such non-linearity occurs because of tissues microstructural changes during stretching (i.e.: collagen fibers uncramping and alignment), which induce a progressive increase of material stiffness. This is a typical phenomenon of soft biological tissues mechanics, which is usually interpreted by means of hyperelastic constitutive formulations [8].

B. CFD investigation of micturition

CFD allows to simulate and to analyze the flow of urine from the bladder up to the external meatus. The bladder and the urethra inner surfaces define the mathematical domain of urine flow. The morphometrical investigation of bladder and urethra, and the analysis of anthropometric data led to an average three-dimensional model of the urine domain: an ellipsoidal conformation was assumed for the bladder, while the urethra was defined by means of a circular tube with variable diameter (Fig. 1). The finite volume discretization of the domain was developed by assuming hexahedral elements within the boundary layer and tetrahedral elements elsewhere. Different mesh sizes were defined for bladder and urethra, aiming to provide for both a reliable discretization and a reasonable computational effort. The final mesh consisted of about 2.840.000 elements. No slip condition characterized the interaction between urine and wall domain. The classical Navier-Stokes equations defined the mathematical problem, together with the k-ε model for the description of turbulent flow mean conditions. The material characterization of urine assumed incompressible and Newtonian behavior. Density and viscosity at 37 °C were identified in the scientific literature, as 1.02 kg/m^3 and 0.83 cSt, respectively [9]. The boundary conditions of the CFD problem, as bladder pressure (inlet pressure condition) and atmospheric pressure at the end of the urinary meatus (outlet pressure condition), aimed at analyzing the typical micturition. The investigated bladder pressure ranged between 0 and 8 kPa, including the contributions from both detrusor and abdominal pressure. Transient CFD simulations were performed by means of the general-purpose code Comsol Multiphysics 5.4 (Comsol Inc., Burlington, MA, USA): the inlet bladder pressure condition was increased from 0 up to the target value in 2 seconds, subsequently bladder pressure was kept constant for 5 seconds aiming to achieve an almost steady state flow situation. Model reliability was assessed by comparing urine flow values from computational simulations and data from experimental measurements [10].

C. FSI investigation of lumen occlusion

CFD approach assumes rigid behavior of bladder and urethral walls. Actually, the reliable investigation of flow phenomena must contemplate the real compliance of bladder and urethral tissues. Indeed, urine flow depends on the geometrical configuration of bladder and urethra domains.

Urine pressure induces dilatation phenomena of bladder and urethral walls, which lead to modifications of the fluid domain. All these aspects become essential for the investigation of lumen occlusion phenomena. The methods of FSI allow contemplating the coupling of such fluid dynamics and solid mechanics problems. Because the computational effort of FSI techniques is usually relevant, the investigation was performed on a portion of the urethral duct only. The developed model concerned a 30 mm length region from the bulbar urethra (Fig. 2a). The urethral wall was assumed to be composed by a 0.15 mm thick inner layer of dense connective tissue, as the lamina propria, and a 5.00 mm thick outer layer of spongy tissue. Fully incompressible hyperelastic formulations characterized the mechanical behavior of the different biological tissues [4],[5]. A cylindrical shape (2 mm radius) characterized the fluid domain. Urine properties were defined as previously reported for CFD analyses. The geometrical configuration of both solid and fluid domains suggested to develop an axis-symmetric model. The solid domain discretization was performed by means of about 4.400 and 9.000 rectangular elements for lamina propria and spongy layer, respectively. The discretization of the fluid domain consisted of about 30.000 elements and assumed rectangular elements within the boundary layer and triangular elements elsewhere. No slip condition characterized the coupling of solid and fluid domains. The displacement along the axial direction was constrained at both the lower and the upper boundaries of the solid domain. The assumption allowed approximating the continuity of the bulbar urethra with the adjacent membranous and penile regions.
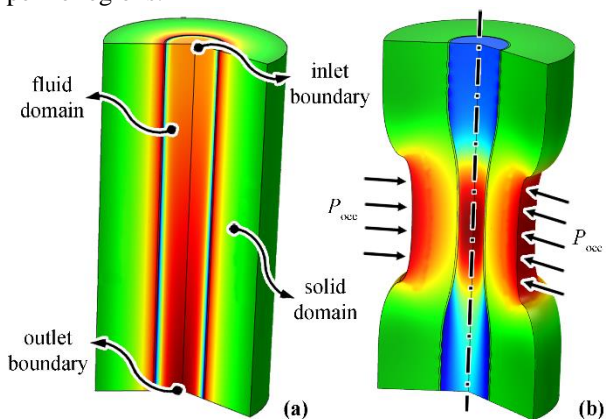
Fig. 2: FSI model of bulbar urethra (a), and schematic representation of the occluding action (b).

Aiming to investigate functionality, efficacy and reliability of AUS devices, FSI analysis of lumen occlusion and of the subsequent opening because of urine inflow is a real challenge. In fact, the complete occlusion of the lumen should require an unattainable distortion of the fluid domain. Therefore, the FSI investigation was performed by assuming an inverse approach, as the occluding action was imposed after the establishment of the urine flow. The steady state flow condition was provided by assuming a 3 kPa inlet pressure condition and a variation of at most 0.1 kPa along the 30 mm length region. Such inlet and outlet pressure conditions were defined based on results from the previously reported CFD investigations. Based on the typical configurations of AUS devices, an occlusive pressure field was applied over a 10 mm length central region of the

urethra external surface (Fig. 2b). The occlusive pressure was progressively increased up to the target value in 2 seconds, and then it was kept constant up to a new steady state condition. Different analyses were performed by assuming different target values of the occlusive pressure. FSI investigations were developed by means of the general-purpose code Comsol Multiphysics 5.4 (Comsol Inc., Burlington, MA, USA)

III. RESULTS AND DISCUSSION

CFD and FSI computational techniques have been exploited aiming to analyze the functionality of the lower urinary tract, with regard to both micturition and lumen occluding actions.

CFD analysis of urine flow during micturition was performed by assuming a fully 3D model of both bladder and urethra. The analyses reveled the actual complexity of urine flow. The non-uniformity of lumen dimension and the three-dimensional shape of the urethral duct determine irregular pressure drop from the bladder to the external meatus (Fig. 3a) and discontinuous changes of urine velocity. CFD analysis further allowed to appreciate the occurrence of turbulent phenomena (Fig. 3b).
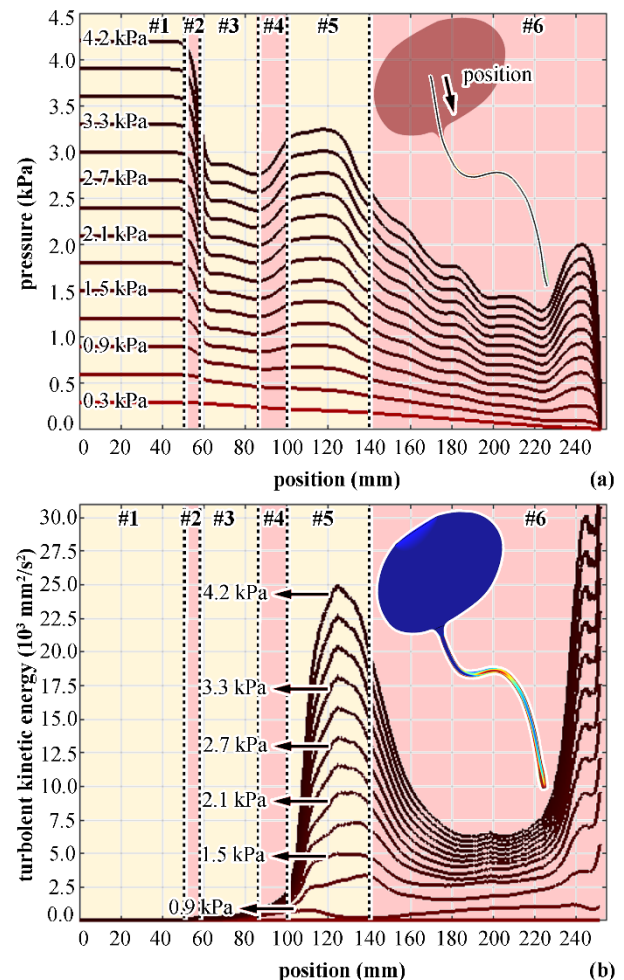

Fig. 3: CFD analysis of micturition: profile of urine pressure (a) and turbulent kinetic energy (b) from bladder to external meatus.

Aiming to a more comprehensive investigation of urethral functionality, an FSI investigation of a urethral segment from the bulbar region was performed. FSI techniques made it possible to investigate the comprehensive fluid-mechanical functionality of the urethra accounting for the influence of

external occluding actions. Given a specific bladder pressure condition, the developed analyses provided data about the actual influence of the occlusive pressure on lumen dimension, urine flow (Fig. 4a) and urine velocity profile. The investigation further allowed evaluating the effects of occluding actions on flow turbulence, actual urine pressure in the occluded region and shear stress (Fig. 4b) acting on the lumen wall.
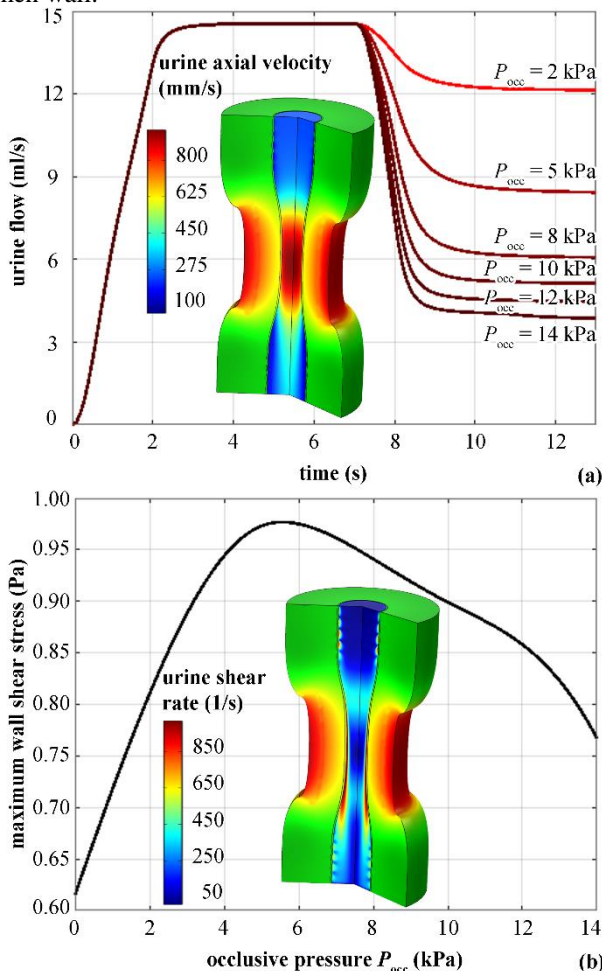

Fig. 4: FSI analysis of urethra occlusion: influence of occluding pressure on urine flow (a) and wall shear stress (b).

IV. CONCLUSION

The here reported investigations aim to prove the feasibility of computational methods for the investigation of the lower urinary tract functionality and physiology. CFD investigation of micturition allows appreciating the complexity of urine flow throughout the urethra. The complex morphometric configuration of the urethral duct entails a nonlinear drop of pressure from bladder to the urinary meatus (Fig. 3a) and a non-homogenous distribution of urine velocity. Furthermore, turbulent phenomena characterize the urine flow, with particular regard to the bulbar region and the urinary meatus (Fig. 3b). The investigation and the prediction of turbulences is a relevant topic, because turbulent urinary flow in the urethra may be a causal factor for different pathologies and diseases, as prostatic hyperplasia, reflux of urine in the prostatic ducts, prostatitis and urinary tract infections.

CFD and FSI techniques allow evaluating the shear stresses that act on the lumen wall because of urine flow. Shear stresses

provide for mechanical stimulation of the urethral epithelium, where urethral-neuroendocrine cells are located and release mediators, which via activation of adjacent sensory nerves can stimulate urethral reflexes. In the literature, it is reported that such mechano-sensitive cells may play a role in continence and sensation [11]. Furthermore, many investigations have been reported in the field of vascular fluid-dynamics about the role of shear stresses on endothelial cells physiology. Shear stresses induce morphological changes of endothelium and vessel wall, but also trigger biochemical and biological events. There is considerable evidence that physiologic stresses exert vasoprotective roles and a perturbation of the stresses can lead to remodeling and possible dysfunction. Similar phenomena may characterize the urethral epithelium. It follows the relevance of investigating the influence of occlusive pressure on wall shear. With regard to AUS patients, even though the device is deactivated during micturition, it anyway exerts mechanical actions on the urethra, which lead to a magnification of shear stresses (Fig. 4b).

The developed models provide a preliminary approach to the computational investigation of the lower urinary tract. A more refined investigation of urine flow during micturition should require a FSI model of both bladder and urethra, aiming to analyze many different diseases, as urethra strictures or prostatic obstructions. With regard to the investigation of lumen occlusion mechanisms by AUS devices, the modeling of the prosthetic device and of its interaction with the urethra is mandatory [4],[5].

REFERENCES

[1] D.J. Griffiths, "The mechanics of the urethra and of micturition", Br J Urol 1973, vol. 45(5), pp. 497-507.

[2] K.D. Clement, H. Burden, K. Warren, M.C. Lapitan, M.I. Omar, M.J. Drake, "Invasive urodynamic studies for the management of lower urinary tract symptoms (LUTS) in men with voiding dysfunction", Cochrane Database Syst Rev 2015, vol. 28(4), CD011179.

[3] A. Srivastava, G.A. Joice, H.D. Patel, M.G. Manka, N.A. Sopko, E.J. Wright, "Causes of Artificial Urinary Sphincter Failure and Strategies for Surgical Revision: Implications of Device Component Survival", Eur Urol Focus 2018, vol. 5(5), pp. 887-893.

[4] A.N. Natali, E.L. Carniel, C.G. Fontanella, "Interaction phenomena between a cuff of an artificial urinary sphincter and a urethral phantom", Artif Organs 2019, vol. 43(9), pp. 888-896.

[5] A.N. Natali, C.G. Fontanella, E.L. Carniel, "Biomechanical analysis of the interaction phenomena between artificial urinary sphincter and urethral duct", Int J Numer Meth Bio 2020, vol. 36(3), e3308.

[6] A.N. Natali, E.L. Carniel, A. Frigo, P.G. Pavan, S. Todros, P. Pachera, C.G. Fontanella, A. Rubini, L. Cavicchioli, Y. Avital, G.M. De Benedictis, "Experimental investigation of the biomechanics of urethral tissues and structures", Exp Physiol 2016, vol. 101(5), pp. 641-656.

[7] A.N. Natali, A.L. Audenino, W. Artibani, C.G. Fontanella, E.L. Carniel, E.M. Zanetti, "Bladder tissue biomechanical behavior: Experimental tests and constitutive formulation", J Biomech 2015, vol. 48(12), pp. 3088-3096.

[8] E.L. Carniel, V. Gramigna, C.G. Fontanella, A. Frigo, C. Stefanini, A. Rubini, A.N. Natali, "Characterization of the anisotropic mechanical behaviour of colonic tissues: experimental activity and constitutive formulation", Exp Physiol 2014, vol. 99(5), pp. 759-771.

[9] B.A. Inman, W. Etienne, R. Rubin, R.A. Owusu, T.R. Oliveira, D.B. Rodriques, P.F. Maccarini, P.R. Stauffer, A. Mashal, M.W. Dewhirst, "The impact of temperature and urinary constituents on urine viscosity and its relevance to bladder hyperthermia treatment", Int J Hyperthermia 2013, vol. 29(3), pp. 206-210.

[10] V.W. Nitti, "Pressure flow urodynamic studies: the gold standard for diagnosing bladder outlet obstruction", Rev Urol 2005, vol. 7, pp. S14-21.

[11] P. Khandelwal, S.N. Abraham, G. Apodaca, "Cell biology and physiology of the uroepithelium", Am J Physiol Renal Physiol 2009, vol. 297(6), pp. F1477-1501.

Automatic estimation of nerve tortuosity in corneal images

A. Colonna[1], F. Scarpa[1], and A. Ruggeri[1]

[1] Department of Information Engineering, University of Padova, Padova, Italy

Abstract— In-vivo confocal microscopy allows acquiring images of the cornea in a rapid e non-invasive way. The correlation between tortuosity of corneal nerves and a wide group of ocular and systemic diseases has been already shown. However, there is no universally accepted definition of tortuosity. As a consequence, the reproducibility of its measurement is poor and it is not used in the clinical practice. Moreover, most methods recently proposed in the literature derive a quantification of corneal nerves tortuosity from nerves tracing. This would require to consider segmentation errors (especially if tracking is performed automatically), to manage the typical bifurcations of the corneal nerves, and to combine individual segment values into an image-level tortuosity.

In this study, we developed an algorithm that automatically traced corneal nerves with a deep-learning technique. The algorithm identifies and splits the main nerve fibres from the branches and estimates three overall image values of tortuosity. These tortuosity measures are linearly combined to best differentiate images into three groups: low-, mid- high-tortuosity. An excellent agreement between manual and automated classification of tortuosity (96,6% accuracy) was obtained on 30 images from normal and pathological subjects.

Keywords—Corneal nerves, in-vivo confocal microscopy, tortuosity.

I. Introduction

ACCURATE diagnoses in ophthalmology usually depend on the recognition of typical features and of their changes in the main ocular structures, e.g., nerve fibres in the corneal nerve plexus.

Thanks to in-vivo confocal microscopy (IVCM), nerves are accessible in a fast and in a non-invasive way. Due to these attributes, IVCM becomes an indispensable tool for studying corneal physiology and diseases. Despite the importance of IVCM images of corneal nerves, they are qualitatively used in the current clinical diagnostic process because of the lack of a reliable and accurate quantitative investigation.

Cornea is one of the most densely innervated tissues in the human body [1] and the correlation between morphometric parameters of corneal nerves (density, branching, tortuosity, etc.) and a wide group of ocular (e.g., dry eye syndrome) and systemic diseases (e.g., diabetic neuropathy) has been demonstrated several times [2]-[7]. In particular, tortuosity has been shown to be an important clinical parameter and many studies [4]-[8] have found links to dry eye disease [3], keratoconus [8], and even diabetes [4], [6]. However, to the best of our knowledge, there is no universally accepted definition or standard description of tortuosity.

The current main issue with this morphological parameter is its reproducibility and generalization. A variety of methods for quantifying corneal nerves tortuosity has been recently proposed in the literature, each with a different definition of tortuosity and facing specific problems. Moreover, many methods are based on a manual or semi-automatic tracing of nerve fibres, which is a tedious, subjective (not reproducible) and time consuming process.

In this work, we used a completely automatic tracing for corneal nerve, performed by a procedure developed in our group [10]. Starting from this segmentation step, we developed an algorithm capable of identifying the main nerve fibres and splitting them from the branches. Subsequently we derived the value of the tortuosity from each single segment using three different methods: the first one based on curvature, the second one based on twists, and the last one based on fractal geometry. We investigated if these measurements of tortuosity, or a combination of them, are capable to reproduce the manual classification into three groups of increasing image-level tortuosity.

II. Material

In our study, we used the public available dataset provided in [7]. The dataset consists in 30 confocal images of sub-basal corneal nerve plexus from 30 different normal or pathological subjects (diabetes, pseudoexfoliation syndrome, keratoconus).

Images were acquired using the Heidelberg Retina Tomograph II with Rostock Corneal Module (HRTII32-RCM) confocal laser microscope (Heidelberg Engineering GmbH, Heidelberg, Germany). Image acquisition was performed at the Department of Ophthalmology, Ehime University School of Medicine, (Ehime, Japan), and each image was anonymized eliminating any patient information.

IVCM provides grayscale images of the sub-basal nerve plexus, but one downside to this imaging protocol is that it can be limited by its field of view: each image cover only an area of 400x400 μm (384x384 pixels), showing a small region of the central corneal nerves structure.

Each image was manual classify as having low-, mid- or high-tortuosity. A representative image for each group is shown in Fig 1.

III. Methods

A. Corneal Nerve Tracing

We automatically traced corneal nerves with our own algorithm [10]. Shortly, the method is based on an U-shaped convolutional neural network (CNN), which consists in a contracting-encoder part and an expanding-decoder part that allow obtaining a label classification of every single pixel. The CNN was able to provide a reliable nerves segmentation (with sensitivity higher than 95%, when compared to manual tracing).
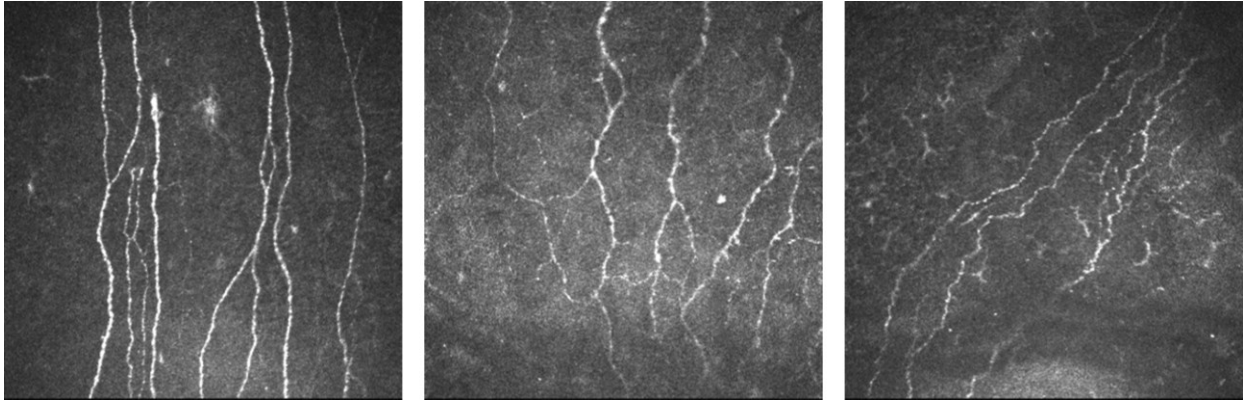
Fig. 1: Representative images for each tortuosity group: low-tortuosity (left), mid-tortuosity (centre) and high-tortuosity (right).

As the CNN provided a quite high value of false discovery rate, we decided to implement a post-processing step to provide a better nerve segmentation, which allows to estimate more precisely the clinical parameters such as tortuosity.

B. Nerve Tortuosity Metrics

Although there is no universally accepted definition of corneal nerve tortuosity, a great number of tortuosity measures has been proposed over the years. Generally, those measurements are grouped into four different categories, each one based on different morphological features (length, angles, curves and twists). There are also other metrics that are based on a combination of two or more of those mentioned above.

Common practice has outlined an evaluation of tortuosity metrics that has to conform to some properties [11].

- The tortuosity measurement must not be influenced by rigid transformations, such as translation and rotation. Indeed, these transformations are related to the topology and orientation of nerve fibre and do not alter the clinical perception of tortuosity.
- The tortuosity τ of a nerve fibre must be in the middle of the values of two single segments that compose it

$$\tau(s_1) \leq \tau(s_2) \ \Rightarrow \ \tau(s_1) \leq \tau(s_1 \oplus s_2) \leq \tau(s_2). \quad (1)$$

- For two nerve fibres having *turn curves* (segment between two consecutive twists) with the same amplitude (maximum distance of the curve from the underlying chord), the difference in tortuosity τ varies with the number of turn curves φ (property of modulation at constant amplitude)

$$\varphi(s_1) \leq \varphi(s_2) \ \Rightarrow \ \tau(s_1) \leq \tau(s_2); \quad (2)$$

and, conversely, for two nerve fibres with the same number of twists (property of modulation at constant frequency), the difference in tortuosity depends on the difference in amplitude α of the turn curves

$$\alpha(s_1) \leq \alpha(s_2) \ \Rightarrow \ \tau(s_1) \leq \tau(s_2). \quad (3)$$

We decided to investigate two of the metrics proposed in literature: the absolute squared curvature (AC) [12] and the tortuosity index (TI) [7]. They both satisfy the above

properties and are widely used in literature.

Given a nerve fibre segment (S), represented by the centreline points ($S = [(x_1, y_1), (x_2, y_2), \ldots, (x_n, y_n)]$) , the curvature k at point i is estimated as:

$$K_i = \frac{\Delta x_i^\theta \Delta^2 y_i^\theta - \Delta^2 x_i^\theta \Delta y_i^\theta}{(\Delta^2 x_i^\theta + \Delta^2 y_i^\theta)^{3/2}} \quad (4)$$

The absolute squared curvature is defined in equation (5): the integral of the squared curvature K^2 over the whole segment S is considered to be a measure of the variability of the nerve fibre direction.

$$AC = \sum_3^n |K_i^2|. \quad (5)$$

Instead, the tortuosity index is computed as

$$TI = \frac{m-1}{m} \sum_1^m \left[\frac{L_{C_{si}}}{L_{X_{si}}} - 1 \right], \quad (6)$$

where m is the number of twists of the nerve fibre, $L_{C_{si}}$ is the length of the segment between two subsequent twists and $L_{X_{si}}$ is the chord length between two subsequent twists.

The higher the TI value, the more complex is the nerve fibre.

We also implemented a method to compute the nerve fibres tortuosity based on the fractal geometry. It is a measure of the irregularity of a line or contour, which was able to achieve good results in medical imaging. To quantify the shape complexity in fractal geometry, we estimated the fractal dimension (FD) via the box-counting algorithm.

Box counting consists in dividing the segmented image (the image with the nerve fibre centrelines traced) into a grid of equal squares with size l, and counting the number of squares containing part of the nerve centrelines. This process is repeated for different square size (from $l = 1$ to $l =$ image size). The number of boxes containing nerve fibres is plotted against the corresponding box size (in a double logarithmic plot). Finally, a line is fitted to these points using the least-squares method, and the slope of this line corresponds to the FD measure. Thus, a high value of FD indicated a complex nerve fibre's structure. The tortuosity properties mentioned before are also satisfied for FD.

Each measurement allowed calculating a different value for each single segment (centreline with no branches), which means that the tortuosity is calculated locally, so that it could be interesting to analyse some normalization factors. For instance, several studies have used as normalization factors the length of the segment or its chord [6], [7]. However, there is no agreement if normalization (and which factor) is of any advantage. IVCM images of corneal nerves could contain nerve segments with large length variability. In this study, we decided to apply two different normalization factors to each metric and to choose for each metric the one that provided the best results.

Empirically, we decided to consider AC and FD normalized by 1 (no normalization) and TI normalized by $1/L_C$, where L_C is the total segment length (by applying this normalization, small segments are weighted less than large ones). Thus, TI normalized by the nerve segment length may be interpreted as a tortuosity density (TD).

C. Measurement aggregation

The goal of analysing the nerve fibres structure and tortuosity is to classify each image as high-, mid- or low-tortuous. To achieve this, the algorithm needs to manage the typical bifurcations of the corneal nerves, and to combine individual segment values into an image-level tortuosity.
As shown in Fig.2, we dealt with the bifurcations in two different ways and compared them. In the first case (Fig.2, left), as proposed in previous studies, we split the nerve fibre into different segments at each single branching. In the second case (Fig.2, right), we devised an algorithm capable to divide branches keeping the main path, which had the characteristics to be considered a continuous nerve fibre. In particular, when a nerve fibre exhibited a branching pattern, the two branches that respected some rules (similar direction, thickness, brightness and length) were joined and considered to be part of the main nerve. The other segments were considered as secondary nerve fibres and split from the main nerve.
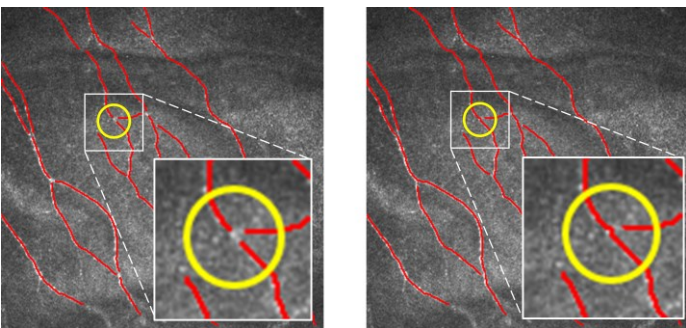
Fig. 2: Example of the two methods to deal with bifurcations: on the left, each branch corresponds to a different segment, on the right, the result of our algorithm to identify the main nerve fibres (based on direction, thickness, brightness and length).

To combine all the individual nerve tortuosity metrics into a single image-level tortuosity, there are several methods proposed in literature [13]:
1. The average value for all nerves;
2. The maximum value for all nerves;
3. The 75th percentile;
4. The average value of the (at most) 3 longest nerves;
5. The average value of all nerves whose length is within 15% of the longest nerve.

However, an expert ophthalmologist would classify an image as highly tortuous if only some nerves are twisted enough.

Based on this observation, in order to combine the individual nerve tortuosity metrics into a single image value, we identified those fibre nerves that have a sufficiently large length and twist number. Then, we calculated the average tortuosity metrics on these nerves to derive the overall image index.

IV. RESULTS

AC, TD and FD indices were computed for each of the 30 images as described before.
A Linear Discriminant Analysis (LDA) was performed to evaluate the ability of the tortuosity indices to classify each image as having low, mid or high tortuosity.
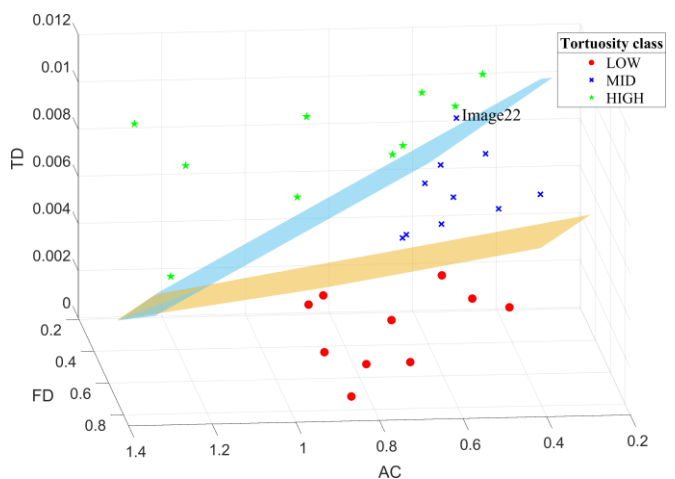

Fig. 3: Absolute squared curvature (AC), tortuosity density (TD) and fractal dimension (FD) obtained for each single image.
The different symbols indicate the manual tortuosity class: low- (red dot), mid- (blue cross) and high-tortuosity (green pentagram). The two surfaces represent the result obtained by Linear Discriminant Analysis (LDA). The only one classification error corresponds to image 22.

Dividing nerve fibres into different segments at each single branching, we obtained 8 classification errors, while considering the best path we obtained 1 classification error.
We evaluated the performance of each index considering it individually and computing the threshold for a minimal classification error. Considering only AC or only FD, we obtained an accuracy of 50.0%, while considering TD we achieved an accuracy of 83.3%.
Moreover, we also performed LDA to evaluate the performance considering combinations of two of the indices. The results definitely improved compared to the previous cases in which the indices were considered individually: considering both FD and TD we achieved an accuracy of 86.6%, while considering AC and TD or AC and FD we achieved lower accuracies, 83.3% and 76.6% respectively.
As mentioned before, the best result was obtained

considering all three metrics together: in this case, we obtained an accuracy of 96.6%.

Results are reported in Table I.

TABLE I
CLASSIFICATION ERRORS

Variable used	Number of classification errors	Accuracy
AC	15	50.0%
FD	15	50.0%
TD	5	83.3%
AC & FD	7	76.6%
FD & TD	4	86.6%
AC & TD	5	83.3%
AC, FD & TD	1	96.6%

A two-tailed paired t-test was performed to check the capability of the best method (longest path with 3 tortuosity measurements) to correctly reproduce the manual classification into the three groups. The obtained p-values show significant differences between all pairs of classes (p-value <0.05), as reported in Table II.

TABLE II
TWO-TAILED PAIRED T-TEST, P-VALUE

	P-value
Low VS Mid	0.0001
Low VS High	0.00000003
Mid VS High	0.00004

V. DISCUSSION

Over the years, many studies revealed correlations between corneal nerves tortuosity and ocular and/or systemic diseases. However, there is no universally accepted definition of this parameter, making it difficult to allow reproducibility. In addition, many methods are based on a manual or semi-automatic nerves tracing, which is time-consuming and subjective (not reproducible).

The proposed algorithm provides a completely automatic procedure to trace corneal nerves and distinguish what appears to be the main nerve fibre from its branches. This first step allows estimating parameters that quantify the tortuosity as absolute squared curvature (AC), the tortuosity density (TD) and the fractal dimension (FD). A Linear Discriminant Analysis was performed to evaluate the ability of the estimated tortuosity indices to classify each image as having low-, mid- or high-tortuosity.

We compared the obtained automatic tortuosity quantification against the manual assessment performed by a clinical expert. Considering a linear combination of the three indexes, the algorithm failed to classify only one of 30 images (Fig.3): Image22 had an automatic value of tortuosity that classified it as high-tortuosity, while manual grading assigns

this image to the mid-tortuosity class.

The algorithm failed to classify 4 or more images when considering each index individually or the combinations of two of them.

A statistical analysis revealed a good capability of the proposed tortuosity quantification (the one obtained by the linear combination of the three metrics) to correctly reproduce the manual classification: a two-tailed paired t-test was performed and a significant difference between all pairs of classes was obtained.

VI. CONCLUSION

We developed a completely automatic method capable to classify corneal nerve images into low-, mid- and high-tortuosity class with 96.6% accuracy in the 30 images of our dataset. Further developments and investigations are required to evaluate its performance on a large dataset and its ability to differentiate between healthy and pathological conditions, as well as to assess the robustness of the proposed method across different images of the same subject. It will also be interesting to investigate how the quality of the images influences the tracing of the nerve fibres and, consequently, the tortuosity metrics.

REFERENCES

[1] L.J. Müller, C.F. Marfurt, F. Kruse, T.M.T. Tervo, *Corneal nerves: structure contents and function*. Exp Eye Res., vol. 76, pp. 521-542, 2003.
[2] N. Efron, *The Glenn A. Fry Award Lecture 2010: Ophthalmic Markers of Diabetic Neuropathy*. Optom Vis Sci., vol. 88, pp. 661, 2011.
[3] J.M. Benítez del Castillo, M.A. Wasfy, C. Fernandez, J. Garcia-Sanchez: *An in vivo confocal masked study on corneal epithelium and subbasal nerves in patients with dry eye*. Invest Ophthalmol Vis Sci, 45(9):3030-5 (2004)
[4] S. De Cillà, S. Ranno, E. Carini, et al.: *Corneal subbasal nerves changes in patients with diabetic retinopathy: an in vivo confocal study*. Invest Ophthalmol Vis Sci, 50(11):5155-8 (2009).
[5] M. Dabbah, J. Graham, I. Petropoulos, M. Tavakoli, R. Malik: *Automatic analysis of diabetic peripheral neuropathy using multi-scale quantitative morphology of nerve fibres in corneal confocal microscopy imaging*. Med Image Anal. 2011;15:738–747.
[6] F. Scarpa, A. Ruggeri: *Development of Clinically Based Corneal Nerves Tortuosity Indexes*. In M. Jorge Cardoso, Tal Arbel et al. (Eds.), MICCAI 2017. LNCS, 10554, pp 219-226, Springer, Cham (2017).
[7] F. Scarpa, X. Zheng, Y. Ohashi, A. Ruggeri: *Automatic Evaluation of Corneal Nerve Tortuosity in Images from In Vivo Confocal Microscopy*. Invest Ophthalmol Vis Sci, 52(9):6404-8 (2011).
[8] M. Parissi, S. Randjelovic, E. Poletti, et al: *Corneal nerve regeneration after collagen cross-linking treatment of keratoconus: a 5-year longitudinal study*, JAMA ophthalmology, pp. 1–9, (2015).
[9] N. Lagali, E. Poletti, D.V. Patel et al.: *Focused Tortuosity Definitions Based on Expert Clinical Assessment of Corneal Subbasal Nerves*. Invest Ophthalmol Vis Sci, 56(9):5102-9 (2015).
[10] A.Colonna, F. Scarpa, A. Ruggeri: *Segmentation of Corneal Nerves Using a U-Net-Based Convolutional Neural Network*. Stoyanov D. et al. (eds) Computational Pathology and Ophthalmic Medical Image Analysis. OMIA 2018, COMPAY 2018. Lecture Notes in Computer Science, vol 11039. Springer, Cham.
[11] E. Grisan, M. Foracchia, A. Ruggeri, A novel method for the automatic grading of retinal vessel tortuosity. IEEE Transactions on Medical Imaging, vol. 27, pp 310 – 319, (2008).
[12] W. E. Hart, M. Goldbaum, B. Cˆotˆe, P. Kube, and M. R. Nelson, *Measurement and classification of retinal vascular tortuosity,*" International journal of medical informatics, vol. 53, no. 2, pp. 239–252, (1999).
[13] P. Guimaraes, J. Wigdahl, A. Ruggeri, Automatic estimation of corneal nerves focused tortuosities. 8th Annual International Conference of the IEEE Engineering in Medicine and Biology Society (EMBC), 1332-1335 (2016)

Eulerian-based wall shear stress topological skeleton analysis and near-wall transport in aortic flow

G. De Nisco[1], V. Mazzi[1], K. Calò[1], R. Ponzini[2], G. Rizzo[3], D.A. Steinman[4], D. Gallo[1], U. Morbiducci[1]

[1]PoliTo[BIO]Med Lab, Department of Mechanical and Aerospace Engineering, Politecnico di Torino, Turin, Italy;
[2]HPC Department, Cineca, Milan offices, Milan, Italy
[3]Institute of Biomedical Technologies, National Research Council, Segrate (MI), Italy;
[4]Biomedical Simulation Laboratory, Department of Mechanical & Industrial Engineering University of Toronto, Toronto, Canada

Abstract— **Personalized computational hemodynamics is a promising tool to clarify/predict the link between low density lipoproteins (LDL) transport in aorta, disturbed shear and atherogenesis. However, properly modelling mass transfer to the wall requires the use of high-resolution grids, which increase the computational costs associated to this approach. Recent studies have demonstrated that Lagrangian Wall Shear Stress (WSS) structures are able to provide a template for near-wall transport. In the present work, a recently proposed Eulerian-based method is applied to compute WSS topological skeleton in a patient-specific computational model of human aorta, and its ability to properly describe LDL wall transfer is tested. The results indicate that the Eulerian approach provides a close representation of the LDL wall uptake, with a significative reduction of computational costs with respect to classical mass transport simulations and Lagrangian-based techniques.**

Keywords— **WSS manifolds, fixed points, arterial mass transport, computational hemodynamics.**

I. Introduction

MASS transport plays a key role in vascular disease. In the past, it has been suggested that the accumulation of high molecular weight solutes in the arterial intima might promote early atherosclerosis [1], and observations have reported that high plasma levels of low-density lipoproteins (LDL) are causally related to the development of atherosclerotic lesions [2].

Among the complex and nonlinear mechanisms regulating blood-arterial wall mass transfer [3],[4], the shear forces exerted by the streaming blood on endothelial cells (ECs) have been identified to play a key role, because of their influence on the permeability of the endothelial lining [5].

The complexity of the scenario has markedly limited *in vivo* studies on the biomechanical role exerted by the wall shear stress (WSS) on blood-arterial wall mass transfer. Aiming at filling this gap of knowledge, in the last decade, computational fluid dynamics (CFD) has been proposed to study the impact that local hemodynamics has on LDL transport and on their blood-to-wall transfer in realistic models of human aorta [6]-[8], a cardiovascular district characterized by intricate local hemodynamics [9]. These studies have demonstrated that regions at the luminal surface where LDL concentration is high in general co-localize with low shear regions.

However, cardiovascular mass transport problems are characterized by high Peclet number (~ 10^8 for LDL), indicating the relative predominance of advective *vs.* diffusive transport. Therefore, highly resolved computational grids are needed to accurately solve the near-wall transport and blood-wall transfer [10]. Due to that, high computational costs are usually associated with this class of numerical simulations [11].

To overcome this limitation, a marked interest has recently emerged on using WSS Lagrangian Coherent Structures (WSS LCS) to study mass transport in cardiovascular flows. In detail, WSS LCS have been brilliantly proposed to provide a template for near-wall transport, with reduced computational costs compared to a full transport problem [12],[13]. In addition, previous studies have proved the capability of the LCS in identifying WSS topological skeleton features, i.e., WSS manifolds, which in turn have been demonstrated to be connected with near-wall mass transport [12],[13].

Here we briefly remind that the WSS topological skeleton consists in fixed points and stable/unstable manifolds connecting them. In detail, a fixed point is a point where the WSS vector field vanishes, and the WSS manifolds identify the strength and the nature of the WSS contraction/expansion imparted on the endothelium [14].

This study is based on the considerations that (1) the use of LCS might have some practical limitations, namely the poor control over the flow region of interest and the application of higher-order integration schemes [15], and (2) a Eulerian method has been recently proposed to analyse WSS topological skeleton, based on the fast calculation of the divergence of the WSS vector field to approximate manifolds avoiding numerical integration [14]. The aim of the present study is to test the ability of the proposed Eulerian method for WSS topological skeleton analysis based on WSS vector field divergence [14] to provide an affordable template of the LDL blood-wall transfer in patient-specific computational hemodynamic models of human aorta. Such endeavour would identify a methodology faster and less computationally expensive than both Lagrangian-based techniques and full 3D continuum problems to solve mass transport in cardiovascular flows.

II. Materials and Methods

An overview of the study methods is provided in Fig. 1.
The geometry of an ostensibly healthy human aorta was reconstructed from 4D flow MRI images, by applying a multiple step procedure into the Vascular Modeling Toolkit
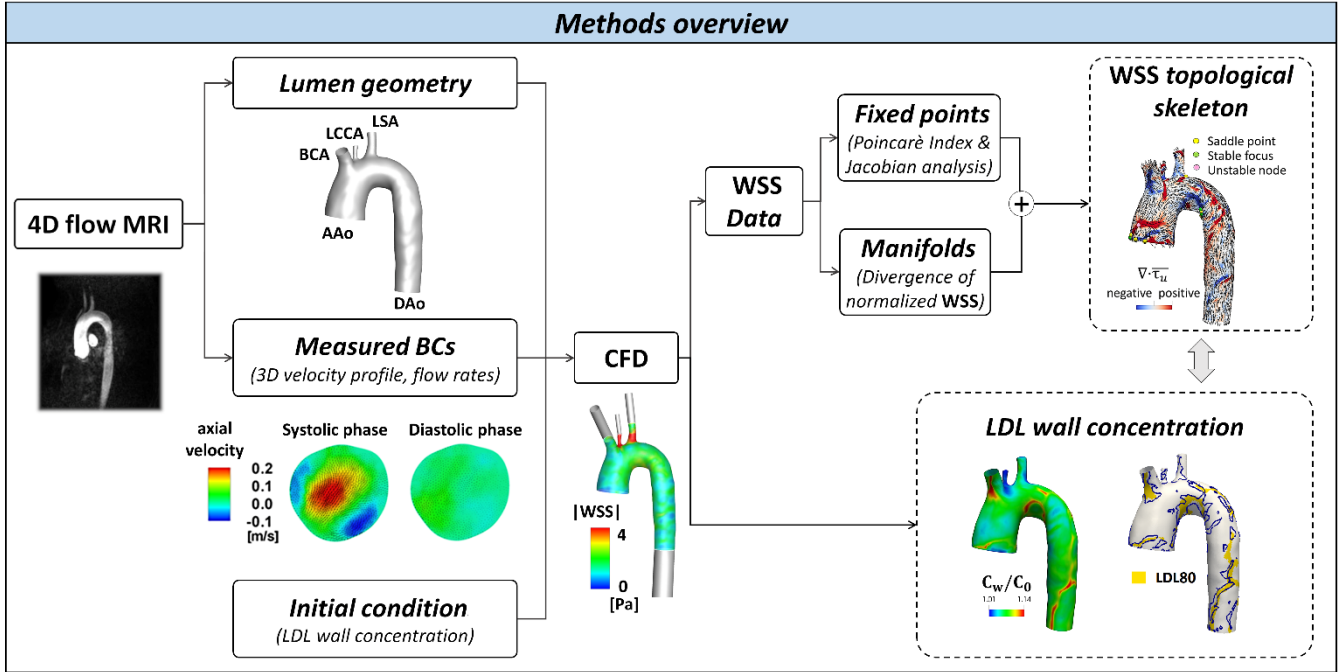
Fig. 1: Overview of the proposed approach to study near-wall LDL transport and WSS topological skeleton. Explanatory examples of contours of the 4D flow MRI-derived axial velocity component, applied as inflow BCs, averaged along systole and diastole are also displayed.

environment (VMTK). MRI image acquisition and aortic geometry reconstruction are extensively described elsewhere [16]-[19].

A. Computational hemodynamics

To model LDL transport in the streaming blood, the governing equations of fluid motion (the Navier-Stokes equations) were coupled with the advection-diffusion equation under unsteady flow conditions. In detail, LDL was modelled as a passive non-reacting scalar, transported in the flowing blood according to the advection-diffusion equation:

$$\frac{dC}{dt} + \boldsymbol{u} \cdot \nabla C - D_{LDL} \nabla^2 C = 0, \tag{1}$$

where C is the LDL concentration, $\boldsymbol{u}$ is the velocity vector, and D_{LDL} is the diffusivity of LDL in blood, set to $5.98 \cdot 10^{-12}$ m^2 s^{-1} [20]. Blood was assumed to be an isotropic, incompressible, homogeneous, Newtonian viscous fluid with density equal to 1060 kg/m^3 and dynamic viscosity equal to 0.0035 Pa s. The finite volume method was applied to solve the coupled Navier-Stokes and advection-diffusion equations in their discretized form. The general purpose CFD code Fluent (ANSYS Inc., USA) was used on a computational mesh-grid with 30 layers of high-quality prismatic cells near the wall and structured tetrahedral elements in the lumen region [11].

The instantaneous measured (with 4D flow MRI) 3D velocity profiles were prescribed as inflow boundary condition (BC) at the ascending aorta (AAo) inlet section (Fig. 1) [18]. The strategy applied at the outflow boundaries is the same as in previous studies [17],[18]. Briefly, at the outflow sections of the supra-aortic vessels (BCA - brachiocephalic artery; LCCA - left common carotid artery; LSA - left subclavian artery) and of the descending aorta (DAo) measured flow rate ratios were imposed as BCs. Arterial walls were assumed to be rigid with no-slip condition at the wall.

To solve the governing equation of mass transport (Eq. 1) a constant LDL concentration C_0 equal to $2.86 \cdot 10^{-9}$ mol/m^3 (corresponding to the physiological LDL concentration in whole blood) [21] was prescribed at the inlet section, and the stress free condition was applied at each outlet.

The LDL blood-to-wall transfer was modelled by prescribing Eq. 2 at the luminal surface [11]:

$$C_W v_W - D_{LDL} \frac{\partial C}{\partial n}\Big|_W = 0, \tag{2}$$

where C_W is the LDL concentration at the vessel wall, v_W the water filtration velocity through the wall, $\partial C/\partial n$ is the concentration gradient normal to the wall.

To be consistent with previous studies using WSS LCS to identify mass transfer to the arterial wall [12],[13], a null LDL concentration was applied as initial condition to the whole domain (with the exception of the inflow section, as detailed before).

Details on the applied numerical schemes and convergence criteria are extensively provided elsewhere [11].

B. WSS topological skeleton

A very recently proposed Eulerian method to identify and analyse the topological skeleton of the WSS vector field [14] was here considered. Briefly, based on Volume Contraction theory, it was demonstrated that the computation of the divergence of a vector field gives practical information about the associated dynamical system, quantifying the rate of separation of close trajectories. In particular, the divergence of the WSS vector field allows to encase the connections between WSS fixed points, i.e., the WSS manifolds.

Consequently, according to the method extensively described elsewhere [14], the divergence of the normalized WSS vector field was here computed:

$$DIV = \nabla \cdot \boldsymbol{\tau}_u = \nabla \cdot \left(\frac{\boldsymbol{\tau}}{\|\boldsymbol{\tau}\|_2}\right), \tag{3}$$

where $\boldsymbol{\tau}_u$ is the WSS unit vector. In detail, negative values of DIV identify contraction regions, approximating the unstable manifolds, while positive DIV values identify expansion regions, approximating the stable manifolds, on the luminal surface of a vessel. The use of the normalized WSS in Eq. (3), neglecting the vector field magnitude variation, allows the identification of the WSS spatial contraction/expansion configuration patterns, thus correctly identifying WSS manifolds [14].

To complete the WSS topological skeleton analysis, the Poincarè index was here considered to identify WSS fixed points on the luminal surface. Once identified, the Jacobian analysis was carried out to classify fixed points, distinguishing between an attractive or repelling nature of fixed points [14]. Poincarè index values and eigenvalues λ_i of the Jacobian matrix for each fixed point-type are summarized in Table I.

TABLE I

Fixed point	Eigenvalues	Poincarè index
unstable node	$\lambda_1 > \lambda_2 > \lambda_3 > 0$	1
stable node	$\lambda_1 < \lambda_2 < \lambda_3 < 0$	1
saddle point	$\lambda_1 < \lambda_2 < 0 < \lambda_3$	-1
saddle point	$\lambda_1 > \lambda_2 > 0 > \lambda_3$	-1
unstable focus	$\lambda_1 > 0, \lambda_{2,3} = \alpha \pm \beta i$	1
stable focus	$\lambda_1 < 0, \lambda_{2,3} = -\alpha \pm \beta i$	1

Identification and classification of fixed points based on Poincarè index and eigenvalues of the Jacobian matrix.

The Eulerian-based WSS topological skeleton analysis was here applied to the cycle-average WSS vector field $\overline{\boldsymbol{\tau}}(\boldsymbol{x})$ at the aortic luminal surface:

$$\overline{\boldsymbol{\tau}}(\boldsymbol{x}) = \frac{1}{T}\int_0^T \boldsymbol{\tau}(t,\boldsymbol{x})dt, \qquad (4)$$

where T is the time duration of the cardiac cycle.

C. Co-localization analysis

The analysis of the extent of the co-localization between luminal WSS contraction/expansion regions and local LDL uptake was carried out according to schemes proposed elsewhere [11],[22]. In detail, an objective threshold for the normalized LDL concentration at the aortic luminal surface (C_W/C_0) was identified as the 80th percentile value of C_W/C_0 distribution. The surface area (SA) exposed to normalized LDL concentration values higher than the defined threshold was then quantified and denoted as LDL80.

As for WSS topology, luminal contraction regions were identified by determining the 20th percentile value of normalized WSS divergence and computing the SA exposed to DIV values lower than this threshold. The latter area was denoted as DIV20. No threshold was set for identifying the luminal expansion regions, because no co-localization was observed with high LDL uptake regions, by visual inspection (as explained below).

III. RESULTS

A qualitative comparison between WSS topological skeleton and normalized LDL wall distribution at the luminal surface is provided by Fig. 2 (panel A and B, respectively). WSS contraction regions are coloured by blue, while WSS
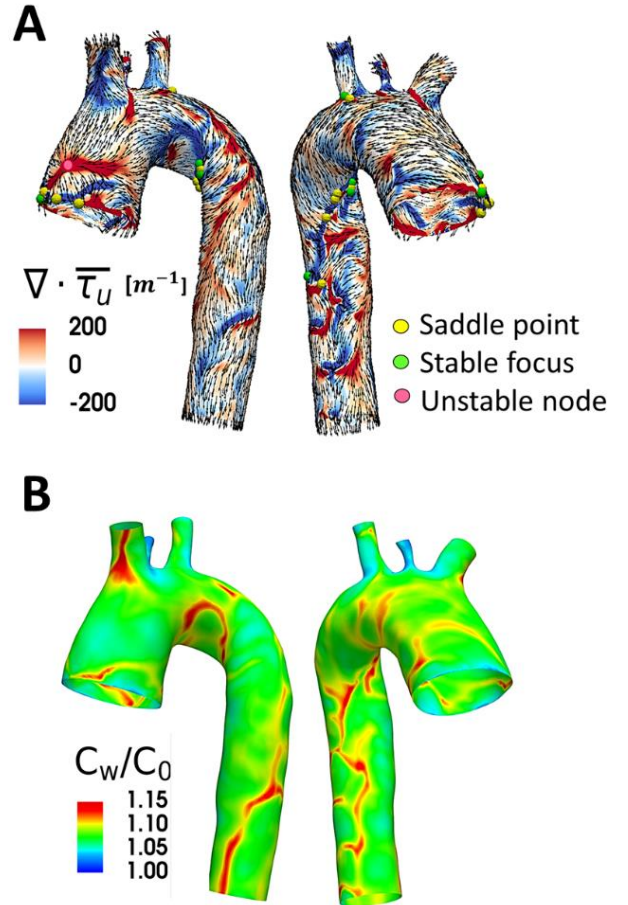
Fig. 2: A: Cycle-average WSS topological skeleton. Blue and red color define the contraction and expansion regions, respectively. Vector field is normalized for visualization. B: LDL wall concentration (two different views).

expansion regions are presented in red colour (Fig. 2-A). Interestingly, it can be observed that only one unstable node of cycle-average WSS vector is identified at the luminal surface of the investigating thoracic aorta. The unstable fixed point, repelling near-wall trajectories, is located at a point at the ascending aorta luminal surface characterized by a low value of LDL concentration. Contrarily, all the stable fixed points of cycle-average WSS vector are located in luminal regions where the normalized LDL concentration assumes high values (> 15%, Fig. 2).

As for WSS manifolds, a marked co-localization between high LDL luminal concentration and WSS contraction regions clearly emerges from Fig. 2: the regions at the luminal surface where the divergence of the normalised WSS vector is negative are characterized by LDL concentration polarization. This is particularly evident in three main regions along the aortic wall, i.e., the inner part of the BCA, the intrados of the aortic arch and the DAo segment.

A direct co-localization analysis between LDL concentration polarization and WSS contraction regions at the aortic luminal surface is provided in Fig. 3, where LDL80 (yellow-coloured regions) and DIV20 (blue contour lines) luminal SAs are displayed. The figure shows a marked spatial overlap between LDL80 and DIV20, with the contour lines of DIV20 mostly encasing luminal regions with high LDL
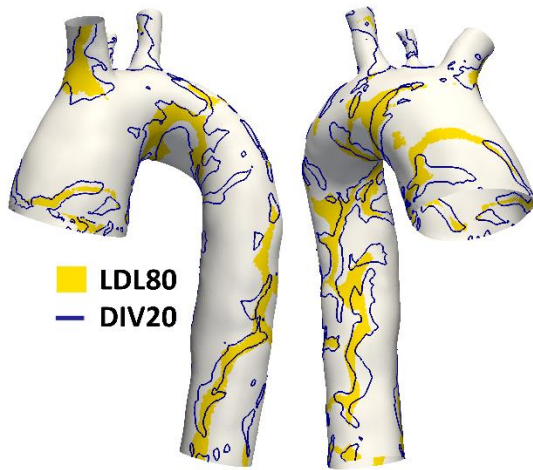
Fig. 3: Distribution of LDL80 (yellow-coloured regions) and DIV20 (blue contour lines) luminal SAs (two different views).

concentration. Their co-occurrence is less evident only locally at the AAo and at the proximal DAo.

The latter results suggest that WSS contraction regions lead to high LDL uptake in their surroundings, in accordance to previous findings linking the WSS topological skeleton to near-wall mass transport using a Lagrangian approach [13]. The maps in Fig. 2 and Fig. 3 prove the ability of the Eulerian-based WSS topological skeleton analysis to provide an affordable template of the LDL concentration polarization at the luminal surface of the aorta. The plausibility of the here reported findings finds a physical explanation in the theory of dynamical systems [23], affirming that near-wall trajectories are attracted by WSS contraction regions and they accumulate around these structures, thus producing high surface concentration.

IV. CONCLUSION

This study demonstrates that the Eulerian-based method here applied to identify WSS topological skeleton [14] efficiently provides a template of the LDL blood-to-wall transfer. The methodology, requiring less computational efforts with respect to a fully 3D simulation of mass transport in cardiovascular flows, as well as less computational efforts than LCS-based strategies, candidates as an effective tool enriching the analysis of cardiovascular flows with relatively low computational effort [11].

In addition, recent studies have demonstrated the marked impact of the prescribed LDL concentration initial conditions on the results of mass transport simulations [11]. Moving from this consideration, future studies investigating the effects of the imposed LDL initial conditions on the relation between WSS topological skeleton and LDL transfer are warranted and encouraged.

REFERENCES

[1] C.G. Caro, J.M. Fitzgerald, R.C. Schroter, "Atheroma and arterial wall shear. Observation, correlation and proposal of a shear dependent mass transfer mechanism for atherogenesis", *Proc. R. Soc. B*, vol. 177, pp. 109-159, Feb. 1971

[2] L.B. Nielsen, "Transfer of low density lipoprotein into the arterial wall and risk of atherosclerosis", *Atherosclerosis* vol. 123, pp. 1-15, Jun. 1996.

[3] J.M. Tarbell, "Mass transport in arteries and the localization of atherosclerosis", *Annu Rev Biomed Eng* vol. 5, pp. 79-118, Mar. 2003.

[4] P.E. Vincent, P.D. Weinberg, "Flow-dependent concentration polarization and the endothelial glycocalyx layer: multi-scale aspects of arterial mass transport and their implications for atherosclerosis", *Biomech Model Mechanobiol*, vol 13, pp. 313-326, Apr. 2014.

[5] C.R. Ethier, "Computational modeling of mass transfer and links to atherosclerosis", *Ann Biomed Eng*, vol. 30, pp. 461-471, Apr. 2002.

[6] J. Lantz, M. Karlsson, "Large eddy simulation of LDL surface concentration in a subject specific human aorta", *J Biomech*, vol. 45, pp. 537-542, Feb. 2012.

[7] X. Li, X. Liu, P. Zhang, C. Feng, A. Sun et al., "Numerical simulation of haemodynamics and low-density lipoprotein transport in the rabbit aorta and their correlation with atherosclerotic plaque thickness", *J. R. Soc. Interface*, vol. 14, pii20170140, Apr. 2017.

[8] X. Liu, F. Pu, Y. Fan, X. Deng, D. Li, S. Li, "A numerical study on the flow of blood and the transport of LDL in the human aorta: the physiological significance of the helical flow in the aortic arch", Am J *Physiol Heart Circ Physiol*, vol. 297, pp. H163-H170, Jul. 2009.

[9] U. Morbiducci, R. Ponzini, G. Rizzo, M. Cadioli, A. Esposito et al., "Mechanistic insight into the physiological relevance of helical blood flow in the human aorta: an in vivo study", *Biomech Model Mechanobiol,* vol. 10, pp. 339-355, Jun. 2011.

[10] S. Tada, "Numerical study of oxygen transport in a carotid bifurcation" *Phys. Med. Biol.*, vol. 55, pp. 3993-4010, 2010.

[11] G. De Nisco, P. Zhang, K. Calò, X. Liu, R. Ponzini, et al., "What is needed to make low-density lipoprotein transport in human aorta computational models suitable to explore links to atherosclerosis? Impact of initial and inflow boundary conditions", *J Biomech*, vol. 68, pp. 33-42, Feb. 2018.

[12] A. Arzani A.M. Gambaruto, G. Chen, S.C. Shadden, "Lagrangian wall shear stress structures and near-wall transport in high-Schmidt-number aneurysmal flows", *J Fluid Mech*, vol. 790, pp. 158–172, Mar. 2016.

[13] A. Arzani, A.M. Gambaruto, G. Chen, S.C. Shadden, "Wall shear stress exposure time: a Lagrangian measure of near-wall stagnation and concentration in cardiovascular flows", *Biomech Model Mechanobiol*, vol. 16(3), pp. 787–803, Jun. 2017.

[14] V. Mazzi, D. Gallo, K. Calò, M. Najafi, M.O. Khan et al., "A Eulerian method to analyze wall shear stress fixed points and manifolds in cardiovascular flows", *Biomech Model Mechanobiol,* doi:10.1007/s10237-019-01278-3, 2019.

[15] M.M.S. Reza, A. Arzani, "A critical comparison of different residence time measures in aneurysms", *J Biomech*, vol. 88, pp. 122-129, May 2019.

[16] U. Morbiducci, R. Ponzini, G. Rizzo, M. Cadioli, A. Esposito et al., "In vivo quantification of helical blood flow in human aorta by time-resolved three-dimensional cine phase contrast MRI", *Ann Biomed Eng,* vol. 37, pp. 516–531, Mar. 2009.

[17] D. Gallo, G. De Santis, F. Negri, D. Tresoldi, R. Ponzini et al., "On the use of in vivo measured flow rates as boundary conditions for image-based hemodynamic models of the human aorta: implications for indicators of abnormal flow", *Ann Biomed Eng*, vol. 40, pp. 729-741, Mar. 2012.

[18] U. Morbiducci, R. Ponzini, D. Gallo, C. Bignardi, G. Rizzo, "Inflow boundary conditions for image-based computational hemodynamics: impact of idealized versus measured velocity profiles in the human aorta", *J Biomech*, vol. 46(1), pp. 102-109, Jan. 2013.

[19] P. Volonghi, D. Tresoldi, M. Cadioli, A.M: Usuelli, R. Ponzini et al., "Automatic extraction of three-dimensional thoracic aorta geometric model from phase contrast MRI for morphometric and hemodynamic characterization", *Magn Reson Med*, vol. 75(2), pp. 873-882, Feb. 2016.

[20] S. Wada, T. Karino, "Theoretical prediction of low-density lipoproteins concentration at the luminal surface of an artery with a multiple bend", *Ann Biomed Eng*, vol. 30, pp. 778–791, Jun. 2002.

[21] N. Yang, K. Vafai, "Modeling of low-density lipoprotein (LDL) transport in the artery—effects of hypertension." *Int J Heat Mass Transfer*, vol. 49, pp. 850–867, Mar. 2006.

[22] D. Gallo, D.A. Steinman, U. Morbiducci, "Insights into the co-localization of magnitude-based versus direction-based indicators of disturbed shear at the carotid bifurcation", *J Biomech*, vol. 49, pp. 2413–2419, Aug. 2016.

[23] J.H. Argyris, G. Faust, M. Haase, R. Friedrich, *An exploration of dynamical systems and chaos*, Berlin, Springer, 2015.

3D nichoid substrates affect mesenchymal stem cell morphology and euchromatin organization

E. Jacchetti[1#], E. Colombo[1#], T. Zandrini[1,2,3], R. Osellame[1,2], G. Cerullo[1,2], D. Mazza[4] and M.T. Raimondi[1]

[1] Department of Chemistry, Materials and Chemical Engineering "Giulio Natta", Politecnico di Milano, Milano, Italy
[2]Istituto di Fotonica e Nanotecnologie (IFN)-CNR and Department of Physics, Politecnico di Milano, Milano, Italy;
[3]Institute of Material Science and Technology, Technische Univesrität Wien, Vienna, Austria
[4]Center for Experimental Imaging, IRCCS San Raffaele Scientific Institute, Milan Italy,
# Authors equally contributed to this work

Abstract — **In recent years, it has been demonstrated that the extracellular microenvironment plays a pivotal role in controlling mesenchymal stem cell fate and functionality. At the basis, there is the mechanotransduction process by which cells sense physical forces and translate them into biochemical/biological responses. In order to modulate gene expression, cell mechanotransduction involves cell-substrate interaction and cytoskeleton proteins, but also nuclear geometry and chromatin remodelling.**

We developed an innovative isotropic 3D culture substrate, nanoengineered via two-photon laser polymerization, able to control nuclear shape. In this work, we studied cell cytoskeleton and chromatin organization of rat bone marrow mesenchymal stem cells seeded into our 3D scaffold and compared to cells grown on standard flat glass substrates. Our results show that the 3D micro-lattice structure inhibits the formation of actin cup and fibers joining cell periphery to the nucleus. It affects nuclear morphology and euchromatin organization. Interesting, similar results were obtained on cells treated with a drug able to inhibit actin polymerization and cytoskeleton organization.

In order to correlate euchromatin localization and organization with cell fate and functionality, future work will be focalized investigating gene expression of MSC cultured on standard glass 2D substrate and into our 3D micro-lattice structure.

Keywords — **mechanotransduction, nuclear shape, actin fibers, chromatin remodelling.**

I. INTRODUCTION

In the last decade, stem cells have widely interested the research world due to their ability to differentiate in specialized cells and stimulate the damaged tissue regeneration. Mesenchymal stem cells (MSCs) are good candidate to use in tissue regeneration. They are easily isolated from bone marrow; they have immunosuppressive properties, are very sensitive to mechanical environmental stimuli and differentiate into mesodermal line cells [1]. Although MSCs have a good expandability in culture, their differentiation in a specific cell line is not yet easily controllable *in vitro* and the maintenance of their multipotency, *i.e.* their stemness, has not yet been achieved. Therefore, a biomimetic approach should be adopted in order to build scaffolds that replicate *in vitro* the environment in which MSCs are stored and preserved *in vivo*: this environment is called "stem cell niche" and has the purpose of preserving stem cells and acting as a reservoir if it is necessary to regenerate an injured or damaged tissue.

In the last few years a three-dimensional (3D) structure, the nichoid, has been identified as a suitable substrate for MSCs

in vitro expansion, guaranteeing their multipotency and affecting cell functionality [2]-[4]. However, the mechanism by which it maintains cell stemness has not yet been identified. The nichoid is manufactured by two-photon polymerization, a technique with spatial resolution down to 100 nm allowing to engineer stable, three-dimensional and accurate polymeric structures at the cellular scale. Here, in order to study the organization of chromatin in cells with very different nuclear morphologies (spread and roundish) we create a modified 3D geometry of the nichoid that is completely isotropic in the three-dimensional space. We observed that the new structure is able to minimize forces transmitted on the cell nucleus by the actin fibers and induce roundish nuclei in MSC grown into the 3D structure. Moreover, it produces a homogeneous distribution of active chromatin into the cell nucleus. In this work we also evaluate the effect of a drug, cytochalasin D, able to destroy actin cytoskeleton, to compare results obtained with cells grown into the 3D isotropic niche and pondering how fundamental is the role of the cytoskeleton in cell growth in 3D systems.

II. MATERIAL AND METHODS

Scaffold photopolymerization
3D structures were fabricated by two-photon polymerization, using a biocompatible hybrid organic inorganic resin called SZ2080 [2]-[4]. The size of the structure is $375 \times 375 \times 30$ µm3, and it is made of three lattice grids composing 625 pores with $15 \times 15 \times 15$ µm3 dimensions. The support to the structure is given by lateral windowed walls, made of parallel lines with 1 µm of distance. These structures were photopolymerized on glass bottom Nunc™ Lab-Tek™-8-chamber, covering an area equal to 1mm2 in in the four central wells (figure 1). Standard flat glass substrates were used as 2D control samples.
Cell culture and seeding.
MSCs were isolated from the bone marrow of adult rats provided from IRCCS-Istituto di Ricerche Farmacologiche "Mario Negri" (Bergamo, Italy) [5] and cultured in alpha-MEM medium supplemented with 20% fetal bovine serum, 1% L-glutamine (2 mM), penicillin (10 units/ml), and streptomycin (10 µg/ml) at 37 °C and in 5% CO2 (Euroclone, Italy). Culture medium was changed every 2-3 days and cells were used at passages 1-6 after thawing. For the experiments performed with fluorescence microscopy 104 MSC cells were

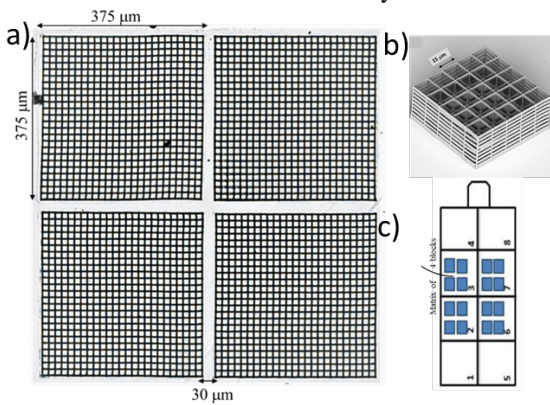seeded in each well and analyzed after 24 hours.

Figure 1. a) Phase contrast image of a photopolymerized sample inside a Lab-Tek's well: top-down view. b) Small size model of the niches SEM image. Pore dimension15x15x15 ▢m3. c) Scheme of 3D nichoid produced in the central wells of a glass bottom Lab-Tek-8-chambers cell culture.

Cytochalasin-D treatment.

Cell incubation with 1 μM cytochalasin D (Sigma Aldrich, Italy) was used to inhibit actin polymerization. After 15 minutes incubation the medium was replaced with fresh medium.

Immunofluorescence assay.

To visualize chromatin and actin localization and organization, one day after seeding, cells were fixed for 10 min in 4% paraformaldehyde, rinsed with 0.1 mM glycine solution in phosphate buffered saline, permeabilized with 0.25% Triton X-100 in PBS for 10 min at room temperature, and finally processed for indirect immunofluorescence analysis. Cells were incubated for 4 h in PBS 2% BSA (Sigma Aldrich, Italy) and then incubated overnight with anti-H3K4me3 antibody (dilution 1:750, Abcam, United Kingdom) at 4 °C.

The day after samples were wash 3 times with PBS and then incubated for 45 min at room temperature with 2 μg/ml of donkey anti-mouse IgG H&L Alexa Fluor 647 1 μg/ml phalloidin-FITC (Sigma-Aldrich, Italy). Cell nuclei were labeled by 1 μg/ml of Hoecst 33342 (Thermo Fischer Scientific, Italy). After washing 3 times in PBS, samples were mounted with Moviol-Dabco mounting medium and imaged at confocal microscope.

3D cell imaging

Samples were imaged using the Olympus FV10i confocal microscope equipped with diode lasers and a 60x water immersion objective 1.2 N.A. The pinhole was set to 1 Airy Unit. Z-stack images were acquired with 1 μm step. Image size 212.13x212.13 μm2.

Cellular parameter analysis

Cell nucleus: The z-stack rendering shows that the shape of the cell nuclei can be modelled as an ellipsoid. To evaluate the semi-axes, for each cell, a z-projection of the z-stack was performed. This solution corresponds to the identification of the biggest xy and xz nuclear sections. Fitting the two projection with ellipses, the semi-axes a, b and c were obtained (**table 2**).

Actin cytoskeleton: A maximum projection of the z-stack acquisition were performed to evaluate actin cytoskeleton organisation. On these resulting images a rectangular ROI is drawn around the nucleus; actin fibers directionality was measured using the Directionality-ImageJ plugin. Resulting histograms where fitted to obtain a single curve describing actin orientation and amount of fibers for each studied population (flatNT, flatCD, nichNT and nichCD).

Euchromatin distribution: Samples images at the cellular equatorial plane were used to define the euchromatin distribution. A linear ROI (yellow in **Figure 2**) has been drawn from the nuclear edge towards the inside of each imaged cell. The chosen ROIs has a length equal to the shorter semi-axis (b_{min}) obtained during the geometric analysis (see **table 1**): it makes possible to analyse the same nucleus portion (from the edge to the nuclear centre) for each cell population investigated. In order to calculate the "coefficient of variation (CV)" parameter, the mean intensity ($\bar{I}$) and its standard deviation (ΔI) was measured in each cell from the ROI intensity profile (**Figure 2**). The CV is a dimensionless parameter defined as

$$CV = \frac{\Delta I}{\bar{I}} \qquad (1)$$

And it is used to evaluate the homogeneity degree of the total DNA and the euchromatin in the four cases under analysis.

TABLE I
ROI LENGTH FOR EUCHROMATIN DISTRIBUTION EVALUATION

Samples	b_{min} (μm)
FlatNT	4.4
FlatCD	3.8
NichNT	3
NichCD	2
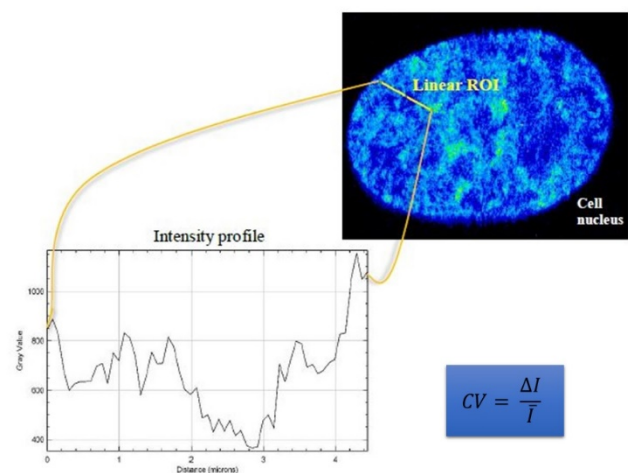
Figure 2. *Representative images of the DNA distribution in the equatorial plane of the cell nucleus (image upper right) and its intensity profile, calculated on the selected ROI (image bottom left).*
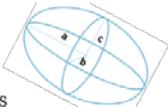
III. RESULTS AND DISCUSSION

Results on cell nuclear morphology show that nuclei can be modelled as an ellipsoid for each population studied. Results are summarized in **table 2**.

The nuclear morphology of MSCs seeded on 2D glass flat substrate is similar to a thin disk with a>b>c, while into the 3D niche the nuclear shape is roundish and it correspond to a prolate ellipsoid a>b~c. In spread cells treated with CD the nucleus of the MSC assumes a statistically similar shape to

cells grown into the niche; conversely the treatment does not affect significantly the nuclear shape respect to the non-treated cells grown in the niche (**table 2).**

TABLE II
CELL NUCLEUS SEMI AXES

Samples	a (μm)	b (μm)	c (μm)
FlatNT	9.61±1.78	6.70±1.31	2.17±0.46
FlatCD	8.04±1.99	5.24±.48	3.74±1.06
NichNT	6.63±1.63	3.69±0.94	4.71±1.37
NichCD	5.70±1.28	3.35±0.78	5.10±1.23

The number of actin filaments and their spatial organization were quantified evaluating the structures amount and their directionality. The comparison was made between the four situations in exam (flatNT, flatCD, nichNT, nichCD). The gaussian distributions (**Figure 3)** show that in the flatNT configuration there are many and extremely oriented actin filaments. In the other cases, the number of oriented filaments is smaller and the distribution is wider. It is due, in the nichNT case, to the reorganization of the actin cytoskeleton operated by the niche while, in the flatCD case, to the inhibition of actin polymerization obtained by the CD treatment.

The effect of the CD treatment is negligible on MSCs grown in the niche, which means that in the niche there are few actin filaments whose polymerization can be inhibited (**Figure 4)**. Therefore, the niche and the CD-treatment have similar effects: a reduction of the interactions between actin fibers and the nuclear envelope that consist in a decrease of tension on the nuclear envelope. It induces a rounded shape of the cell nucleus. In the nichNT sample, there seem to be even fewer actin fibers than in all the other samples, anyway this is due to the number of cells analysed for each sample (flatNT n=144, flatCD n=123, nichNT n= 55, nichCD n=60). This implies that, in this case, the goodness of the fitting is reduced from 0.9 to 0.7. In the future, the number of cells analysed in the niche samples will be increased in order to obtain a proper fitting.

Euchromatin is the DNA potion in which there is an intense transcription activity for protein synthesis: its variability in distribution allows to identify if there are differences in the amount of transcriptionally active DNA areas. The total amount of DNA and euchromatin were marked with fluorescent dye and antibody. Confocal images allow to study the localization and organization of both.

Examples of euchromatin distribution at the cell equatorial plane is shown in **figure 5**. Images show zones of the cell nucleus with different intensities are more present in the flatNT sample than in the others, where the intensity distribution is quite uniform. The variance coefficient of euchromatin (**Figure 6**), confirms the qualitative result of images: in samples flatCD, nichNT and nichCD the euchromatin distribution is very similar and significantly lower than in sample flatNT, where there is a greater heterogeneity of the genetic material that is transcriptionally active. The variance coefficient measurement was also performed on the totality of the DNA, and this difference in its spatial organization it is no significant difference among any sample (data not shown). This means that the external forces

acting on MSC spread cells, and transmitted to the nucleus by actin filaments, have as a macroscopic effect the nuclear shape modulation and as microscopic the activation of a redistribution of chromatin by creating separate areas with high packing of eu- and hetero-chromatin.
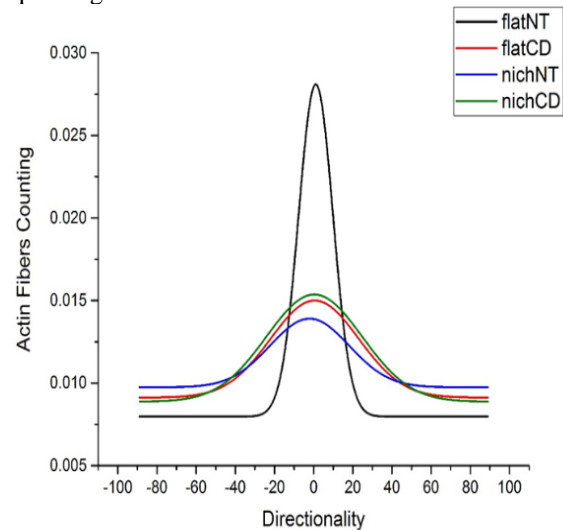
***Figure 3**. Actin fibers directionality histograms post-Gaussian fitting. The height of the Gaussian curve indicates the quantity of quantified fibers. The width their spatial distribution.*
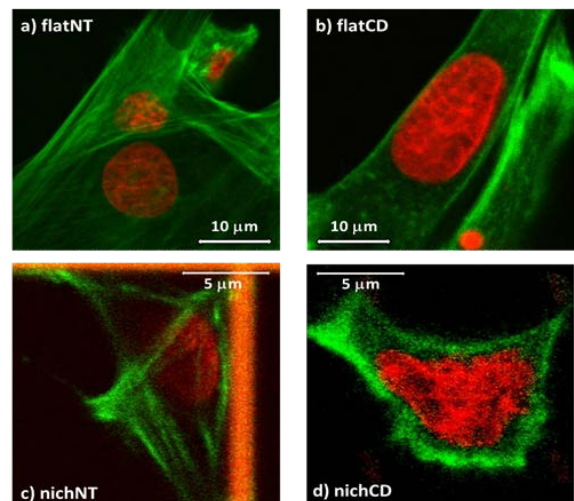

***Figure 4**. Representative confocal microscope images of MSCs seeded on 2D glass substrate and into the 3D niche, untreated or treated with CD: flatNT (a), flatCD (b), nichNT (c) and nichCD (d). in green is represented the organization of the actin cytoskeleton, the nucleus in red. In MSC treated with cytochalasin D and grown in the niche there exist just the cortical actin, there are not polymerized stress fibers from the cell edge to the nucleus.*

It is extremely interesting to observe that the treatment of MSCs with the CD simulate, also in this case, the "niche" configuration on the flat cells, confirming the fundamental role of actin cytoskeleton on nuclear morphology and chromatin organization. The latter were compared with those reported by Ricci et al. In their study the arrangement of chromatin and, in particular, the H2B2 histones nucleosomes nanodomains linked to it in different cell types was investigated. To obtain images with very high resolution they used Stochastic Optical Reconstruction Microscopy (STORM) imaging technique.
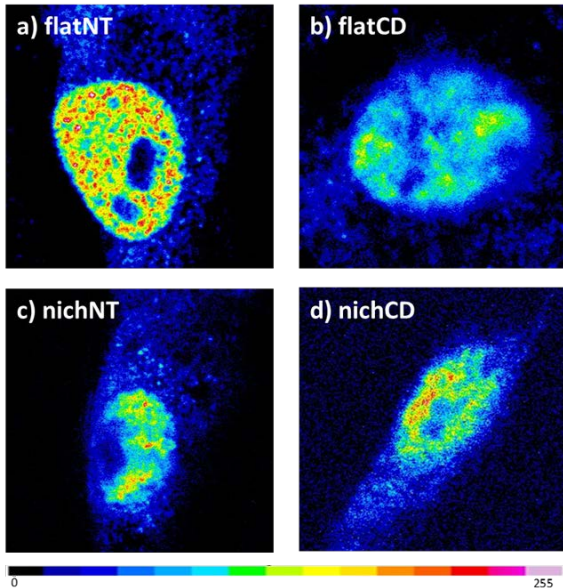
Figure 5. Intensity map of euchromatin in MSCs grown on 2D and 3D substrate and treated with CD. High intensity areas indicate a higher density of euchromatin. The intensity spans from green to red. The blue colour indicates cells autofluorescence.
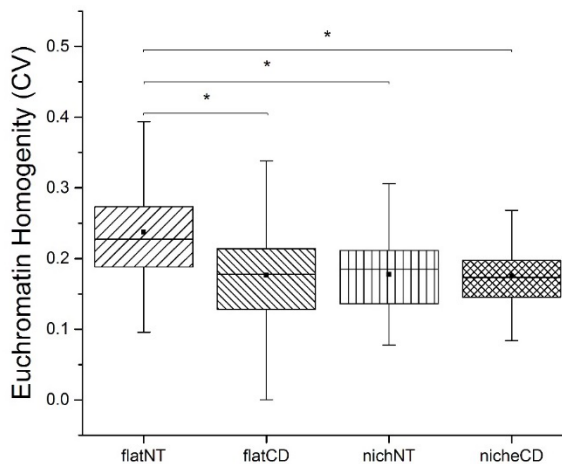

*Figure 6. Euchromatin variation coefficient (CV) boxplot in the four cases under analysis. *p-value < 0.05.*

From this study, it was found that the distribution of nucleosome nanodomains is much more dispersed and homogeneous, in mouse embryonic stem cells compared to somatic cells, in which much larger and more heterogeneously distributed nanodomains were observed [6].

This striking correlation between spatial distribution, size, and compaction of nucleosome clutches and cell pluripotency may be due to the fact that the arrangement of nucleosomes in small clutches with lower compaction could potentially facilitate the binding of transcription factors, polymerases, and other proteins to the DNA, factors that are inevitably linked to cellular pluripotency. The disposition of euchromatin detected in the flatNT case could suggest the hypothesis that the heterogeneous arrangement of the nucleosome domains can prevent the access of certain TFs for the maintenance of pluripotency and therefore favour the differentiation of MSCs with consequent loss of stemness.

IV. CONCLUSION

In the last two decades, researchers realized how important the environment is to drive cellular function. Recently they also observed that *in vitro* analysis, which are generally carried out on two-dimensional substrates, can create biases or artefacts.

In this work it has been evaluated how our innovative isotropic 3D micro-lattice substrate is able to modulate MSC nuclear morphology and actin and chromatin organization. In particular, our results show that it is able to induce:

1.   a reorganization of the actin cytoskeleton, with a loss of directed filaments around the nucleus, implicating a modulation of the nuclear morphology from a thin disk to a prolate ellipsoid;

2.   a reorganization of the active DNA: it is more homogeneously distributed in roundish cell nucleus, showing a reduction in the number and size of nucleosome clusters.

Moreover, the surprising result is that cytochalasin D, a drug able to inhibit acting cytoskeleton polymerization, in MSC cells cultured on 2D glass flat substrate is able to replicate the effect of the 3D niche scaffold not only on the MSC nuclear shape and actin fibers arrangement, but also on euchromatin organization. It would be very interesting to observe if similar results will also be obtained on the gene expression of stem markers such as sox9, oct4 and nanog. In addition, in future, to deeply investigate the pattern formed by the euchromatin clutches and their correlation with cell fate, we will focalize our attention on the evaluation of the patterns' organization and the quantification, in number and size, of the euchromatin clusters, for example, by using super resolution microscopy techniques.

REFERENCES

[1] H. A. Papadaki et al. Bone Marrow Mesenchymal Stem Cells: Biological Properties and Their Role in Hematopoiesis and Hematopoietic Stem Cell Transplantation. 2011. Stem Cell Rev and Rep; 7: 569–589.

[2] M.T. Raimondi *et al*, "3D structural niches engineered via two-photon laser polymerization promote stem cell homing". Acta Biomaterialia 9: 4579–4584, 2013

[3] M.M. Nava *et al*, "Synthetic niche substrates engineered via two-photon laser polymerization for the expansion of human mesenchymal stromal cells". Journal of tissue engineering and regenerative medicine 11: 2836–2845, 2017.

[4] A García-González, Jacchetti E *et al*,"The Effect of Cell Morphology on the Permeability of the Nuclear Envelope to Diffusive Factors". Front Physiol. 2018 Jul 13;9:925.

[5] C Zoja *et al*, "Mesenchymal stem cell therapy promotes renal repair by limiting glomerular podocyte and progenitor cell dysfunction in adriamycin-induced nephropathy". American Journal of Physiology. Renal Physiology 303: F1370–F1381, 2012.

[6] M. A. Ricci, C. Manzo, M. F. García-Parajo, M. Lakadamyali, M. P. Cosma. "Chromatin Fibers Are Formed by Heterogeneous Groups of Nucleosomes in Vivo". 2015. Cell; 160, 6: 1145-1158.

Ultrasonic neural stimulation of zebrafish larvae reveals region-specific calcium imaging activation patterns

N. Meneghetti[1,2,*], F. Dedola[1,2,*], V. Gavryusev[3,4,*], G. Sancataldo[3,4], L. Turrini[3,4], G. de Vito[4,5], F. Vanzi[4,6], J. Carpaneto[1,2], A. Cutrone[1,2], F. Saverio Pavone[3,4,7,+], S. Micera[1,2,8,9,+], and A. Mazzoni[1,2,+]

[1] The Biorobotics Institute, Scuola Superiore Sant'Anna, 56025 Pisa, Italy
[2] Department of Excellence for Robotics and AI, Scuola Superiore Sant'Anna, 56025 Pisa, Italy
[3] University of Florence, Department of Physics and Astronomy, Sesto Fiorentino, Italy
[4] European Laboratory for Non-Linear Spectroscopy (LENS), Sesto Fiorentino, Italy
[5] University of Florence, Department of Neuroscience, Psychology, Drug Research and Child Health, Florence, Italy
[6] University of Florence, Department of Biology, Florence, Italy
[7] National Institute of Optics, National Research Council, Florence, Italy
[8] Bertarelli Foundation Chair in Translational Neuroengineering, Center for Neuroprosthetics, Lausanne, Switzerland
[9] Institute of Bioengineering, School of Engineering, École Polytechnique Federale de Lausanne, Switzerland.
*these authors share same first author contribution   +these authors share same senior author contribution

Abstract— Ultrasound (US) stimulation of neural activity has gained increasing attention in the scientific community, especially thanks to its advantages, first and foremost non-invasiveness. Little is known, however, about the relationship between the properties of the target neuronal populations and their responsiveness to this form of stimulation *in vivo*. Here, we report cortex-wide US-induced activity patterns of zebrafish larvae recorded through calcium imaging microscopy. We were able to induce a reliable neuronal activation monotonically increasing with applied pressure. As expected by previous results, activation probability grows with stimulus duration. Moreover, a spatial analysis of the responsiveness showed that it was highly area-specific, indicating a role of neuronal type and architecture in US sensitivity. Control experiments finally proved that sensory perception of US-induced water movements did not account for the whole neural activation, highlighting the role of direct neuronal stimulation. These results provide a frame for US studies on zebrafishes, characterizing the relationship between stimulation parameters and local responsiveness. Future studies will focus on the link between area-specific neuronal properties and US sensitivity to shed light on the biophysics of US neuromodulation.

Keywords—Ultrasound, Neuromodulation, Zebrafish, Cerebellum, Calcium imaging

I. INTRODUCTION

THE use of ultrasound (US) for non-invasive neuromodulation of specific areas with millimeter precision has been the focus of several studies in the last decade [1]. The current literature, however, lacks a thorough study on direct cortex-wide neuronal responses to US stimulation. Many works have investigated intracranial electrical recordings [2]–[8] monitoring a limited number of central nervous system (CNS) regions. Fewer works have instead selected metabolic or hemodynamic acquisition paradigms (first and foremost PET and fMRI) [9]–[13] that only indirectly monitor neurons' activity. Calcium imaging overcomes these limitations, offering a direct readout of neuronal activity across multiple brain areas with relatively high spatiotemporal resolution[14]–[18]. Here we report the US-evoked activity patterns of zebrafish larvae encephalon gathered through wide-field calcium imaging microscopy.

II. RESULTS

US stimulations were tested on larval stages of zebrafishes at three different phases: 3,4, and 5 days post-fertilization (dpf). We used transgenic larvae expressing the calcium reporter GCaMP6s [19]–[21] in all CNS neurons to visualize whole-CNS response. To stimulate the whole encephalon we developed a setup (Fig.1A) with a 490 kHz ultrasound planar transducer immersed in a tank full of degassed deionized water and recorded fluorescence images of the induced responses (Fig. 2A). The stimulation parameters adopted (Fig. 1B) were similar to the ones tested in a previous study of our group [22].

A. Subregions of maximal and minimal sensitivity to US

We identified the spots of maximal and minimal activation in the zebrafish encephalon following US stimulation considering the pixels (with 1.6 μm side) whose summed fluorescence variation $\Delta F/F_0$ [23] after the stimulus trigger was greater/lower than the 99-/1- percentile of the global relative fluorescence. The spatial probability distribution of the spots of minimal activation was found to be always confined to the larval telencephalon for every stimulus parameter applied and animal development stage (an example of such areas for the 5 dpf group is displayed in the right columns of Fig. 2B and Fig. 2C). The time evolution of the calcium fluorescence response in these sub-regions showed a low-amplitude long-lasting reaction to US stimulation (not shown). The spatial probability distribution of the spots of maximal activation revealed, instead, the strongest sensitivity to the US to be confined to the cerebellum (as displayed for the 5 dpf group in the left columns of Fig. 2B and Fig. 2C). Maximal activation was stereotypically located near the border between the cerebellum and the upper portion of the medulla for every dpf considered. The activation probability in maximal response spots linearly correlated with both stimulus pressure amplitude (P_{RMS}) (Figure 2B, left, $R^2=0.91$, $p<0.01$,) and duration (Fig. 2C, $R^2=0.76$, $p<0.05$), suggesting that the key factor is the overall acoustic intensity I_{SPTA} (see Methods), as previously found [22].
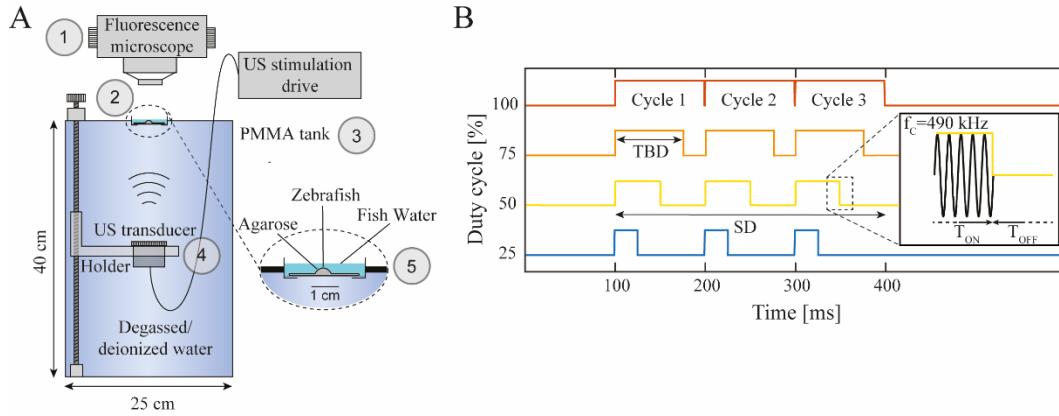
Fig. 1: Experimental setup and stimulation parameters. A) Illustrative scheme of the experimental setup composed of a polymethyl methacrylate (PMMA) tank full of degassed deionized water (3) in which the 44 mm diameter PZT (Lead Zirconate Titanate) unfocused US was immersed (4). On top of the tank a custom-made interlocking housing (2) contained a Petri Dish filled with Fish Water in which the zebrafish larvae were immobilized with Agarose (5). Above the setup, a custom-made upright fluorescence microscope in epi configuration (1) was used for imaging the encephalon of the mounted larvae. Each recording sessions lasted for 60 seconds during which 3 stimulations were triggered every 15 seconds by a waveform in series with a 50 dB gain radio frequency power amplifier. B) Temporal protocol of US stimulation: duty cycle (DC) 5% (blue) with T_{ON}=5 ms and T_{OFF}=95 ms; DC 50% (yellow) with T_{ON} =50 ms and T_{OFF}=50 ms; DC 75% (orange) with T_{ON}=75 ms and T_{OFF}=25 ms; DC 100% (red) with T_{ON}=100 ms. The tone burst duration (TBD) is equal to T_{ON} and the pulse repetition period (PRP) is equal to 100 ms; the stimulation duration (SD) is of 300 ms for the four chosen temporal protocols. Each stimulation was repeated three times during every recording session whit an inter stimulation interval of 15 s. In the inset it is shown the temporal evolution of US stimulation waves produced by a transducer with central frequency equal to 490 kHz.

We analyzed then time evolution of the fluorescence variation of the spots of maximal activation. The median time series of $\Delta F/F_0$ computed across animals showed these areas to respond to sonication with a significant increase of relative fluorescence variation that reached its apex ~1-2 seconds after stimulus onset (Fig. 2D). The maximal $\Delta F/F_0$ amplitude, moreover, was found to be linearly correlated with the US P_{RMS} (linear correlation coefficient r^2=0.97, p<0.01).

Analyzing the time intervals between the stimulation onset and the respective $\Delta F/F_0$ apex, we found that the spots of maximal activation are characterized by an early response to US compared to other brain regions such as telencephalon, optic tectum, and medulla (see Fig. 2A).

B. Direct stimulation and sensory perception

The US stimulation inevitably produced not negligible movements in the water in which the animals were immersed. Therefore, the observed response could be ascribed to both direct US stimulation on specific ionic channels [24], on the neuronal membranes [25] or on the animal sensitivity to the US-induced water movements. Control experiments were carried out to characterize the relative contribution of these two factors to the observed responses. We placed a soundproofing element in the path between the US transducer and the fishes' encephalon and recorded the calcium fluorescence signals with the same stimulation parameters adopted in the unconstrained (i.e., without the soundproofing element) experiments. In this way the brain was not directly hit by the US, but the surrounding watery media moved due to the upcoming stimulation sound waves. This allowed isolating sensory-driven neuronal activation. Since the cerebellum was the most sensitive area to US stimulation, we compared the maximal amplitude of fluorescence variation $\Delta F/F_0$ induced by the stimulus in this region for the control and the experimental groups when subject to the same intensity of water movements (see Methods). This comparison (Fig. 3) showed the cerebellar calcium fluorescence to be significantly higher in the unconstrained experiments (Wilcoxon's rank-sum test adjusted with Bonferroni correction, p<0.01), ruling out the
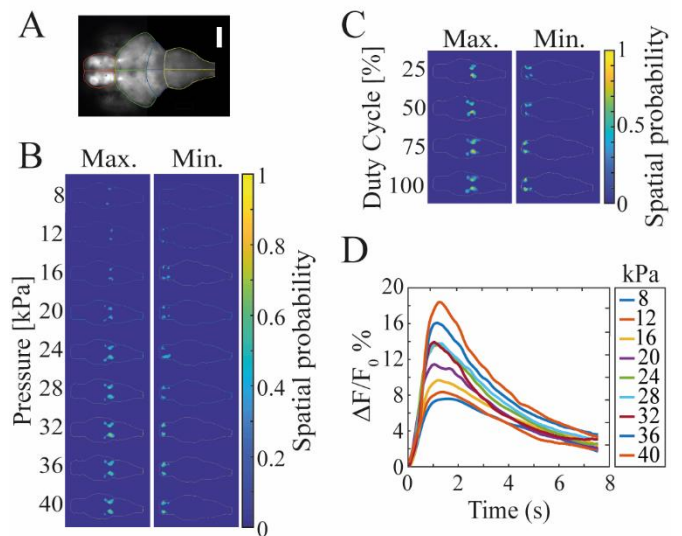

Fig. 2: Region-specific response to US stimulation in zebrafish larvae.
A) Fluorescence image of the encephalon of a representative 4 dpf larva expressing GCaMP6s. Scale bar: 100 μm. The four principal zebrafish brain regions used here for the analysis are highlighted (Telencephalon, red; Optic tectum, green; Cerebellum, blue; Medulla, yellow). B) Spatial probability distribution of the spots of maximal (> 99% overall response, left column) and minimal activation (<1% overall response, right column) as a function of US pressure amplitudes. Most of the maximal response spots are in the cerebellum, most of the minimal response spots in the telencephalon.
C) Same for B, with spatial probability distribution of the spots of maximal and minimal activation displayed as a function of the duty cycle.
D) Across animals $\Delta F/F0$ median traces of the spots of maximal activation as a function of US pressure amplitude P_{RMS}.

possibility of the water movements to be the exclusive cause of the zebrafishes' neuronal activity following stimulation.

III. MATERIALS AND METHODS

A. Sample preparation

Adult and larval zebrafish were maintained for breeding at 28°C on a 14/10 hours light/dark cycle according to standard procedure[26]. Larvae were raised up to 5 dpf in fish water
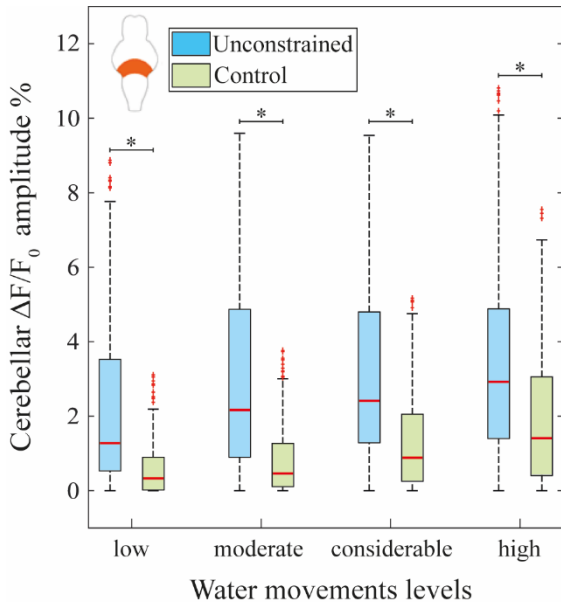
Fig. 3. Role of direct stimulation and US-induced water movements in the neuronal responses. Unconstrained (i.e., without the soundproofing element) experiments (light blue) was confronted with control experiments (green) with the same magnitude of water movements. Boxplot depicts the distribution of cerebellar $\Delta F/F_0$ amplitude. Inset schematically represents the cerebellum within the zebrafish encephalon. Statistically significant differences are represented through asterisks (Wilcoxon's rank-sum test adjusted with Bonferroni correction, hence p<0.01).

[150 mg/L Instant Ocean, 6.9 mg/L NaH2PO4, 12.5 mg/L Na2HPO4 (pH 7.2)] in a Petri dish kept at 28∘C. We used 3 to 5 dpf transgenic Tg (elavl3: GCaMP6s) zebrafish larvae [20], [21] in homozygous *albino* background to avoid the presence of skin pigments. Following [21], each larva was then transferred into an Eppendorf tube containing in 1.5% w/v low gelling temperature agarose (A9414, Sigma) dissolved in fish water kept at 38 °C, and introduced into a glass capillary tube (O.D. 1.5mm) with a pipette. After gel polymerization, the larva was extruded from the capillary, laid on the bottom of a small Petri dish (5 cm diameter) and this position was blocked with a drop of melted agarose. After polymerization the dish was filled with fish water.

B. US stimulation setup and transducer

US stimulation was applied by placing a 44 mm diameter PZT unfocused transducer (Precision Acoustics LTD, Dorchester, UK) at a distance of 165 mm from the animal samples. The transducer was driven by a waveform generator (Agilent33220A Keysight Technologies, Santa Rosa, CA, USA) in series with a 50 dB gain radio frequency power amplifier (240L, Electronics & Innovation, Rochester, NY, USA) and it was immersed in the PMMA tank. The US transducer was characterized in free field conditions both in terms of ultrasonic pressure field mapping and intensity vs. driven voltage calibration. The pressure signals were detected by a 2 mm PVDF (Polyvinylidene Fluoride) needle hydrophone (Precision Acoustics LTD, Dorchester, UK) at different locations, thereby producing maps that provide information on the geometry of the generated acoustic field. The P_{rms} and the I_{sppa} were evaluated at the experimental distance of 165 mm at different driving voltages, each measured at the output of the power amplifier. I_{spta} was defined as $I_{SPTA} = (P_{RMS}^2 * DC)/\rho c$ where ρ is the medium density and c is the wave speed through it. Finally, in order to consider

possible acoustic reflections and attenuations phenomena, additional intensity measurements were performed by positioning the hydrophone tip inside the Petri dish used during experiments.

C. Microscope

Imaging of the agarose restrained larvae was performed using a custom-made upright fluorescence microscope in epi configuration. Fluorescence was excited in wide-field approach using an LED with emission centered at 470nm (M470L3, Thorlabs), followed by an excitation band-pass filter (469/35 nm, Semrock). The fluorescence signal was collected by an air objective (Nikon, NA 0.3, WD 16). The detection path was implemented with a dichroic mirror (DC FF495-DI02, Semrock) and an emission band-pass filter (525/50nm, Semrock), and recorded with a sCMOS camera (OrcaFLASH 4.0, Hamamatsu Photonics) with 16-bit dynamic range at a frame rate of 20 Hz.

D. Stimulation protocol

Pulsed ultrasound stimulations of 490 kHz were delivered in block of three stimuli of 100 ms each, with a duty cycle of 25, 50, 75 or 100%. A stimulus duration of 300 ms with a pulse repetition frequency of 10 Hz was chosen. Pressure amplitude varied from 8 to 40 kPa in nine discrete steps. The I_{spta}, therefore, varied from 1.5 to 120 mW/cm^2. Each recording session consisted of three identical US stimulation windows delivered every 15 s. The overall acquisition time for every recording session was fixed at 60 s. We tested twelve 3-dpf fishes, ten 4-dpf fishes and eight 5-dpf fishes. Each fish has undergone two sets of nine recording sessions, one for each pressure amplitude. For each pressure amplitudes the duty cycle was first set at either 25% or 50% and then increased to 100% or 75%.

E. Control experiments

In order to verify whether the induced neuronal activity was ascribable to a direct US neuromodulation effect or to US-induced fish water movements, we performed the following control experiments. We placed in the path between the US transducer and the Petri dish a soundproofing rectangular element. We used a blue polyurethane sheet (AptFlex F28, Precision Acoustics) with density and wave speed similar to that of water, but with significant absorption (acoustic impedance equals to 1.5 MRayls). This protocol allowed us to image the fish brain fluorescence dynamics without the brain being directly hit by the US, but while still making the surrounding watery media moving due to the sound stimulation waves. As the presence of the soundproofing element decreased the magnitude of water movements in the control experiments, compared to unconstrained case, we selected four pressure level pairs that ensured comparable magnitude of water movements for the two groups, as observed in the fluorescence images. For example, we compared the post-stimulus $\Delta F/F_0$ of the control group at P_{RMS}=40 kPa with the ones of the unconstrained experiments at P_{RMS}=28 kPa. Specifically, in Fig. 3 the P_{RMS} corresponding to the water movement labels are: *low:* 16 kPa for unconstrained and 24 kPa for control; *moderate:* 20 kPa for unconstrained and 28 kPa for control; *considerate:* 24 kPa for unconstrained and 36 kPa for control; *high:* 28 kPa for unconstrained and 40 kPa for control. The control group is

made up of eight 3-dpf fishes, eight 4-dpf fishes and six 5-dpf fishes.

IV. CONCLUSION

Using an unfocused planar transducer and an *ad hoc* setup we were able to deliver ultrasonic stimulation to larval zebrafish CNS. We managed to induce a reliable neuronal response in the animals' encephalon. Control experiments were conducted to disambiguate the US direct effects on larvae CNS and the sensory perception of the stimulation-induced water movements. We proved the analyzed calcium fluorescence activity patterns to be caused not solely by the US-induced water movements, hence highlighting a direct role played by US in triggering neural activation. The compound contribution of the US stimulation and the water movements in the unconstrained experiments was however inextricable with the experimental paradigm here adopted, and further efforts should be made to completely disambiguate the role of water movements in the results reported. The strongest and quickest response was found to be highly consistent across animals and confined in a cerebellar subregion. The activation probability and the fluorescence variation of this region were observed to be positively modulated both by stimulus magnitude (i.e., pressure, P_{RMS}) and duration (i.e., duty cycle), in accordance with previous results in a different animal model [22]. This regionality of the response suggests a dependence of the adopted neuromodulation strategy on neuronal population characteristics and architecture. Further characterization of the relationship between single cells properties and sonication parameters could, therefore, shed clearer light on the basic mechanisms of US neuromodulation.

ACKNOWLEDGEMENT

REFERENCES

[1] E. Landhuis, "Ultrasound for the brain," *Nature*, vol. 551, no. 7679, pp. 257–259, Nov. 2017, doi: 10.1038/d41586-017-05479-7.

[2] J. B. Choi, S. H. Lim, K. W. Cho, D. H. Kim, D. P. Jang, and I. Y. Kim, "The effect of focused ultrasonic stimulation on the activity of hippocampal neurons in multi-channel electrode," in *2013 6th International IEEE/EMBS Conference on Neural Engineering (NER)*, San Diego, CA, USA, 2013, pp. 731–734, doi: 10.1109/NER.2013.6696038.

[3] Y. Tufail *et al.*, "Transcranial Pulsed Ultrasound Stimulates Intact Brain Circuits," *Neuron*, vol. 66, no. 5, pp. 681–694, Jun. 2010, doi: 10.1016/j.neuron.2010.05.008.

[4] N. Wattiez *et al.*, "Transcranial ultrasonic stimulation modulates single-neuron discharge in macaques performing an antisaccade task," *Brain Stimulat.*, vol. 10, no. 6, pp. 1024–1031, Nov. 2017, doi: 10.1016/j.brs.2017.07.007.

[5] R. F. Dallapiazza *et al.*, "Noninvasive neuromodulation and thalamic mapping with low-intensity focused ultrasound," *J. Neurosurg.*, vol. 128, no. 3, pp. 875–884, Mar. 2018, doi: 10.3171/2016.11.JNS16976.

[6] D. Daniels *et al.*, "Focused Ultrasound-Induced Suppression of Auditory Evoked Potentials in Vivo," *Ultrasound Med. Biol.*, vol. 44, no. 5, pp. 1022–1030, May 2018, doi: 10.1016/j.ultrasmedbio.2018.01.010.

[7] H. Guo *et al.*, "Ultrasound Produces Extensive Brain Activation via a Cochlear Pathway," *Neuron*, vol. 98, no. 5, pp. 1020-1030.e4, Jun. 2018, doi: 10.1016/j.neuron.2018.04.036.

[8] M. L. Prieto, K. Firouzi, B. T. Khuri-Yakub, and M. Maduke, "Activation of Piezo1 but Not NaV1.2 Channels by Ultrasound at 43 MHz," *Ultrasound Med. Biol.*, vol. 44, no. 6, pp. 1217–1232, Jun. 2018, doi: 10.1016/j.ultrasmedbio.2017.12.020.

[9] S.-S. Yoo *et al.*, "Focused ultrasound modulates region-specific brain activity," *NeuroImage*, vol. 56, no. 3, pp. 1267–1275, Jun. 2011, doi: 10.1016/j.neuroimage.2011.02.058.

[10] W. Legon, A. Rowlands, A. Opitz, T. F. Sato, and W. J. Tyler, "Pulsed Ultrasound Differentially Stimulates Somatosensory Circuits in Humans as Indicated by EEG and fMRI," *PLoS ONE*, vol. 7, no. 12, p. e51177, Dec. 2012, doi: 10.1371/journal.pone.0051177.

[11] W. Lee *et al.*, "Transcranial focused ultrasound stimulation of human primary visual cortex," *Sci. Rep.*, vol. 6, no. 1, p. 34026, Sep. 2016, doi: 10.1038/srep34026.

[12] L. Ai, J. K. Mueller, A. Grant, Y. Eryaman, and W. Legon, "Transcranial focused ultrasound for BOLD fMRI signal modulation in humans," in *2016 38th Annual International Conference of the IEEE Engineering in Medicine and Biology Society (EMBC)*, Orlando, FL, USA, 2016, pp. 1758–1761, doi: 10.1109/EMBC.2016.7591057.

[13] P.-F. Yang *et al.*, "Neuromodulation of sensory networks in monkey brain by focused ultrasound with MRI guidance and detection," *Sci. Rep.*, vol. 8, no. 1, p. 7993, Dec. 2018, doi: 10.1038/s41598-018-26287-7.

[14] C. Grienberger and A. Konnerth, "Imaging Calcium in Neurons," *Neuron*, vol. 73, no. 5, pp. 862–885, Mar. 2012, doi: 10.1016/j.neuron.2012.02.011.

[15] G. Sancataldo *et al.*, "Flexible Multi-Beam Light-Sheet Fluorescence Microscope for Live Imaging Without Striping Artifacts," *Front. Neuroanat.*, vol. 13, p. 7, Feb. 2019, doi: 10.3389/fnana.2019.00007.

[16] G. Sancataldo, L. Silvestri, A. L. Allegra Mascaro, L. Sacconi, and F. S. Pavone, "Advanced fluorescence microscopy for in vivo imaging of neuronal activity," *Optica*, vol. 6, no. 6, p. 758, Jun. 2019, doi: 10.1364/OPTICA.6.000758.

[17] M. C. Müllenbroich *et al.*, "Bessel Beam Illumination Reduces Random and Systematic Errors in Quantitative Functional Studies Using Light-Sheet Microscopy," *Front. Cell. Neurosci.*, vol. 12, p. 315, Sep. 2018, doi: 10.3389/fncel.2018.00315.

[18] V. Gavryusev *et al.*, "Dual-beam confocal light-sheet microscopy via flexible acousto-optic deflector," *J. Biomed. Opt.*, vol. 24, no. 10, p. 1, Oct. 2019, doi: 10.1117/1.JBO.24.10.106504.

[19] T.-W. Chen *et al.*, "Ultrasensitive fluorescent proteins for imaging neuronal activity," *Nature*, vol. 499, no. 7458, pp. 295–300, Jul. 2013, doi: 10.1038/nature12354.

[20] M. B. Ahrens, M. B. Orger, D. N. Robson, J. M. Li, and P. J. Keller, "Whole-brain functional imaging at cellular resolution using light-sheet microscopy," *Nat. Methods*, vol. 10, no. 5, pp. 413–420, May 2013, doi: 10.1038/nmeth.2434.

[21] L. Turrini *et al.*, "Optical mapping of neuronal activity during seizures in zebrafish," *Sci. Rep.*, vol. 7, no. 1, p. 3025, Dec. 2017, doi: 10.1038/s41598-017-03087-z.

[22] F. Dedola *et al.*, "Ultrasound stimulations induce prolonged depolarization and fast action potentials in leech neurons," *IEEE Open J. Eng. Med. Biol.*, pp. 1–1, 2020, doi: 10.1109/OJEMB.2019.2963474.

[23] D. A. Dombeck, A. N. Khabbaz, F. Collman, T. L. Adelman, and D. W. Tank, "Imaging Large-Scale Neural Activity with Cellular Resolution in Awake, Mobile Mice," *Neuron*, vol. 56, no. 1, pp. 43–57, Oct. 2007, doi: 10.1016/j.neuron.2007.08.003.

[24] J. Kubanek, P. Shukla, A. Das, S. A. Baccus, and M. B. Goodman, "Ultrasound Elicits Behavioral Responses through Mechanical Effects on Neurons and Ion Channels in a Simple Nervous System," *J. Neurosci.*, vol. 38, no. 12, pp. 3081–3091, Mar. 2018, doi: 10.1523/JNEUROSCI.1458-17.2018.

[25] T. Lemaire, E. Neufeld, N. Kuster, and S. Micera, "Understanding ultrasound neuromodulation using a computationally efficient and interpretable model of intramembrane cavitation," *J. Neural Eng.*, vol. 16, no. 4, p. 046007, Jul. 2019, doi: 10.1088/1741-2552/ab1685.

[26] M. Westerfield, *The Zebrafish Book: A Guide for the Laboratory Use of Zebrafish*, 4th ed. Univ. of Oregon Press, Eugene.

Biofabrication and characterization of a biphasic construct to study osteochondral tissue *in vitro*

Irene Chiesa[1,2,3,4], Carmelo De Maria[1,4], Anna Lapomarda[1,4], Gabriele Maria Fortunato[1,4], Francesca Montemurro[1], Roberto Di Gesù[2,3,5], Rocky S. Tuan[2,6], Giovanni Vozzi[1,4], Riccardo Gottardi[2,3,5]

[1]*Research Center 'E. Piaggio', University of Pisa, Pisa, Italy*
[2] *Department of Orthopedic Surgery, School of Medicine, University of Pittsburgh, Pittsburgh, USA*
[3]*Department of Pediatrics, Division of Pulmonary Medicine, The Children's Hospital of Philadelphia, Philadelphia, USA*
[4] *Dept. of Ingegneria dell'Informazione, University of Pisa, Pisa, Italy.*
[5] *Fondazione Ri.MED, Palermo, Italy*
[6] *The Chinese University of Hong Kong, Hong Kong SAR, China*

Abstract—**The osteochondral junction is a highly organized structure where the articular cartilage and the subchondral bone are intimately connected, which makes it challenging to be replicated *in vitro*. In this work, we developed and characterized an *in vitro* osteochondral construct combining a bone and a cartilage scaffold in a dual chamber bioreactor. First, a bone-mimicking gelatin-nanohydroxyapatite scaffold was 3D bioprinted by bioplotting. Then, the cartilage phase was obtained by incorporating human mesenchymal stem cells (hMSCs) in a photocrosslinkable hydrogel of methacrylated gelatin and hyaluronic acid. Live/dead and histological assays showed promising results on hMSCs vitality and differentiation into osseous and chondral linages after four weeks of culture in a dual chamber bioreactor.**

Keywords—**Osteochondral junction, biphasic scaffold, bioreactor, biofabrication.**

I. Introduction

THE osteochondral junction (OCJ) is a highly organized structure where articular cartilage and subchondral bone are intimately connected. The OCJ is a complex, graded tissue, characterized by different microstructures, properties and function throughout its volume [1], [2], thus, representing a significant challenge to be reproduced *in vitro* by tissue engineering. To meet biological requirements, an osteochondral (OC) scaffold must comprise a hard phase that mimics bone and a soft phase to mimic cartilage. Therefore, Functionally Graded Scaffolds (FGSs) are natural candidates to correctly simulate bone, cartilage and their interface, mimicking the OCJ [3], [4]. FGSs are characterized by a variation of their physical, biochemical and topological properties throughout their volume and can be classified as discrete and continuous [3], [5]. Discrete FGSs (biphasic or multiphasic) have clearly visible layers that are separated by interfaces, whereas continuous FGSs show a continuous change in their structure and no single layer can be identified [5].

Both conventional fabrication techniques and bioprinting have been employed to manufacture osteochondral FGSs. Notably, discrete FGSs can be fabricated through independent processes, where the bone and cartilage phases are produced with different fabrication techniques and then physically joined to build the graded structure [6]. For instance, Scaffaro *et al.* [7] combined melt matching, compression molding and particulate leaching to obtain biphasic scaffolds of poly-L-lactic acid and polycaprolactone for the bone and cartilage phase, respectively. Through tensile testing, the authors showed a high phases cohesion. Differently, Zhou *et al.* [8] used a table-top custom-designed stereolithography 3D bioprinter to fabricate biphasic osteochondral scaffolds. The authors used a methacrylated gelatin (gelMA) – polyethylene (glycol) diacrylate (PEGDA) – nanohydroxyapatite (nHA) mixture as photocrosslinkable bone ink and a gelMA – PEGDA – transforming growth factor β1 mixture as photocrosslinkable cartilage ink.

In this study, a biphasic OC scaffold was biofabricated combining extrusion-based 3D bioprinting for the bone phase [9] and indirect rapid prototyping (IRP) [10] for the cartilage phase. The biphasic construct was characterized for differentiation by Alcian Blue and Alizarin Red histological analyses. Osseous and chondral maturation occurred in a previously developed dual chamber bioreactor [11], [12], uniquely designed to differentially direct towards chondrogenic and osseous lineages the two phases of the OC construct.

II. Materials and Methods

A. Bone scaffold biofabrication

The biomaterial ink was composed of type A gelatin from porcine skin (Sigma-Aldrich), nHA (nanoXIMHAp, Fluidinova) and genipin as crosslinker (Challenge Bioproduct Co.). A 10% w/v solution of gelatin in deionized water (milliQ) was prepared by stirring on a heated plate at 50°C for 30 minutes. nHA was added to the gelatin solution at a concentration of 50% w/v and the mixture was sonicated for three minutes with a VC130 sonication probe (130W, Sonics and Materials Inc.). Genipin was then added to the gel-nHA solution at a final concentration of 0.2% w/v and sonicated for one minute.

A wood-pile scaffold with an interconnected pore network was designed in Solidworks® exported as a *.stl* file and sliced by Slic3r® that automatically generated the GCode for the 3D bioprinter. Then, the bone scaffolds were fabricated with a piston-driven extruder 3D bioprinter, developed at the research Center "Enrico Piaggio" of the University of Pisa. Due to the low viscosity and low yield stress of the biomaterial ink, scaffolds were bioprinted into a sacrificial support material (bioplotting technique) (Fig. 1a) [9] [13], [14], pluronic acid F-127 (Sigma-Aldrich). A solution at 20% w/v in deionized

water was prepared by the previously described "hot technique" [15]. After printing, scaffolds were kept in the support material for 48 hours, until full crosslinking was achieved (Fig. 1b). Then, they were placed at 4°C for 2 hours to liquefy the Pluronic acid and gently washed in deionized water to eliminate any support leftovers. Finally, 4 mm diameter cylinders were cored from the scaffolds (Fig 1c) and stored at 4°C until use.
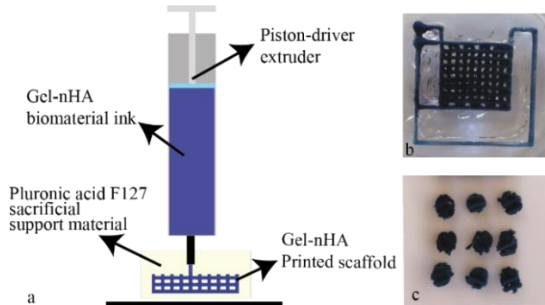

Fig. 1: (a) Schematic of the bioplotting technique. (b) Bioprinted scaffold 48 hours after the crosslinking. (c) Scaffold 4 mm diameter cylindrical cores.

B. Bone scaffold morphological analysis

Cross section images of cored scaffolds were obtained by microCT (Skyscan11®, Bruker) using 0.25 mm aluminium filter. Projection images were reconstructed into cross section images by NRecon® software and a 3D reconstruction of the cored scaffold was obtained by ITKSnap®.

Porosity, pore interconnectivity, scaffold fibers width and size of lateral and axial pores were evaluated by an in house developed script, based on the image processing toolbox of Matlab® (The Mathworks Inc.), as previously described [9].

C. Cartilage scaffold fabrication

A 10% w/v solution of gelMA (Cellink) and 0.15% w/v Lithium phenyl-2,4,6-trimethylbenzoylphosphinate (LAP, Sigma-Aldrich) in PBS 1X (Gibco) and a 3.5% w/v solution of methacrylated hyaluronic acid (meHA, Cellink) and 0.15% w/v LAP (Sigma-Aldrich) in PBS 1X (Gibco) were used. Human mesenchymal stem cells (hMSCs) were resuspended in a gelMA and meHA mixture (3:1 ratio) at a final concentration of 10^7 cell/ml.

Scaffolds were fabricated by IRP [10]. Briefly, cylindrical molds (4 mm diameter, 3.5 mm height) were fabricated by fused deposition molding in ABSplus. Then, 55 µl of hMSCs-laden hydrogel were poured in each mold and crosslinked *in situ* by 2 minutes of UV light (405 nm) exposure. Finally, cylindrical cartilage scaffolds were extracted from the molds.

Cartilage scaffolds were kept in growth medium (GM: Dulbecco's Modifies Eagle Medium, 10% v/v fetal bovine serum, 2% v/v penicillin/streptomycin/fungizone, 1% v/v sodium pyruvate, 1% v/v glutaMAX®) overnight before use.

D. Live/Dead Assay

Bone scaffolds were sterilized by 1 hour in UV oven, seeded with hMSCs (10^5 hMSCs/scaffolds) and cultured in static condition in GM for 7 days to allow proliferating cells to uniformly cover the scaffold surface. Then, GM was changed to osteogenic medium (OM: GM supplemented with 0.1 mM ascorbic acid, 10 mM beta glycerophosphate and 10 nM vitamin D3). Live cell assay was carried out 24 hours after seeding and 14 days after change to OM medium, imaging bone scaffolds after 45 minutes of incubation in calcein AM solution (4 µM, Invitrogen) in the dark.

Cartilage scaffolds were fabricated as described in sub-section C and cultured in chondrogenic medium (CM: GM without FBS, with 10ng/ml TGF-β3, 50 µM ascorbic acid, 10 nM dexamethasone and 23µM proline) in static conditions. Live/Dead assay was carried out after 24 hours and 28 days from cartilage scaffold fabrication, by imaging cartilage constructs after incubating in calcein AM/Ethidium homodimer (4 µM/8 µM, Invitrogen) for 45 minutes in the dark. For both bone and cartilage scaffolds at each time point, top and cross section surfaces were imaged with two fluorescent microscopes (Olympus SZX16, Nikon Eclipse Ts2) to assess cell viability and uniformity of scaffold colonization by cells.

The genipin present in the bone scaffolds is strongly fluorescent in the red channel [17], thus the Dead component of the Live/Dead assay was carried out only on the cartilage constructs.

E. Dual chamber bioreactor

A previously developed dual chamber bioreactor was used for the simultaneous differentiation towards an osseous and chondral linage of the hMSCs in each compartment [11], [12].

The bioreactor (Fig. 2), is composed by four removable cylindrical inserts with porous walls that can host four OC constructs. The inserts are secured inside the bioreactor body via four O-rings. The body of the bioreactor is closed by a base and four lids, one for each well. The bioreactor can accomodate a biphasic OC construct, creating two separate microenvironments for the chondral and osseous development that can be individually and separately controlled.
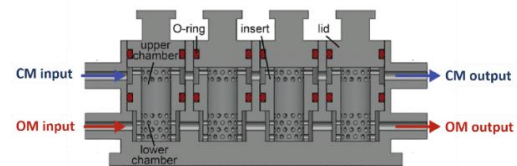

Fig. 2: Cross section of an individual bioreactor [6]. Inserts, lids, medium inputs and medium outputs are highlighted. Chondrogenic medium (CM) was perfused through the upper part of the inserts in communication with the chondral phase, whereas osteogenic medium (OM) was perfused through the lower part of the inserts in communication with the bone tissue

F. Fabrication of an in vitro osteochondral biphasic scaffold.

To minimize cell stress, the bone scaffolds described in subsection D were seeded inside the bioreactor inserts. Cartilage constructs were fabricated as described in sub-section C. Three different pools of hMSCs, comprising three donors each (9 donors total), were used to seed bone and cartilage scaffolds, each in triplicate.

After 7 days from bone scaffold seeding, bioreactor inserts, containing hMSCs-seeded bone scaffolds, were put in the bioreactor body and cartilage scaffolds were added in the upper part of the inserts. 10 µl of gelMA (prepared as described in sub-section C) was used to physically join the bone and cartilage scaffolds by *in situ* UV crosslinking (405 nm, 1

minute). No interpenetration between the bone and the cartilage constructs was introduced.

Bioreactor inlets were connected to 20 ml syringes containing differentiation media while outlets were connected to 20 ml reservoir bags. The CM was perfused through the upper part of the inserts in communication with the chondral phase, whereas the OM was perfused through the lower part of the inserts in communication with the bone tissue. Medium outflow was stored in the reservoir bags. The final assembly of a complete bioreactor (four inserts) is shown in Fig. 3.

A pump was used to continuously perfuse the construct at a flow rate of 2 ml/day. Scaffolds were cultured in the bioreactor for 4 weeks with media reservoirs changes every 5 days.

Fig. 3: Final assembly of a complete bioreactor.

G.   Histological analysis

After four weeks of culturing in the bioreactor, constructs were extracted from the inserts, fixed in 4% paraformaldehyde in PBS, embedded in paraffin and sectioned at 5 μm thickness. In both phases, Alcian Blue (Sigma-Aldrich) staining was used to detect glycosaminoglycans (GAGs) and Alizarin Red (Sigma-Aldrich) staining was used to detect calcium deposition.

III.   RESULTS

A.   Pore connectivity of bone scaffold

From the microCT images of the bone scaffolds, no collapse between layers is visible. The 3D reconstruction of the scaffold by ITKSnap® is shown in Fig. 4b. Cross section images were processed with an in house developed Matlab® script, to create a negative 3D reconstruction of the scaffolds, which represents the pore network (Fig. 4c). Analysis revealed that scaffold pore network is interconnected with an axial square pore of 0.92 ± 0.14 mm, a lateral pore size of 0.5 ± 0.15 mm, and a porosity of approximately 60%.
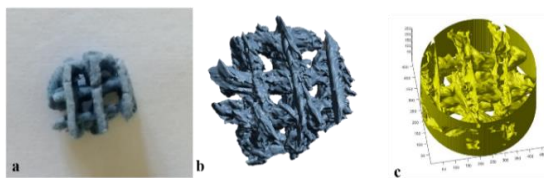
Fig. 4: (a) 4 mm cored scaffold. (b). (b): 3D reconstruction of a cored scaffold made by ITKSnap®. (c): Interconnected pore network reconstruction obtained by Matlab® script.

B.   Biofabricated bone and cartilage scaffolds retain cell viability.

Live cell assay was carried out on bone scaffold 24 hours after seeding and 14 days after the medium change. Live/Dead assay was carried out on cartilage scaffold 24 hours and 28 days after scaffold fabrication.

Images of top and cross section surfaces at each time point are shown in Fig. 5 and 6 for bone and cartilage scaffold,

respectively.

On bone scaffolds, 24 hours after seeding, cells are attached non-homogeneously and several cell aggregates could be seen (red circles). However, at the end of the experiment, scaffolds were completely and homogenously covered by cells.

On cartilage scaffolds, cells retained high viability after 28 days of chondrogenic static culture. Notably, few dead cells can be seen in the inner part of the scaffold (Fig. 6, cross section, day 28).
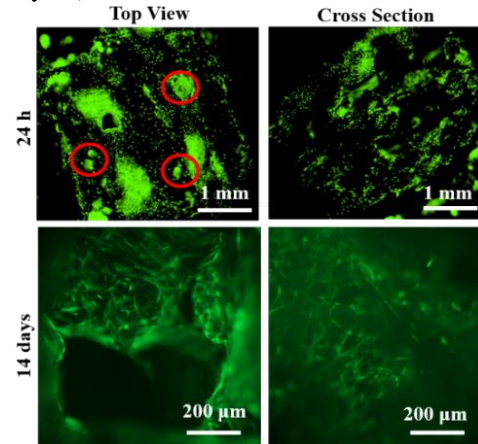

Fig. 5: Live assay of bone scaffolds at different time points for top and cross section surfaces. After 24h, cells attached to the scaffolds non-homogeneously and several cell aggregates (red circles) are visible. After 14 days since medium change, scaffolds were completely and homogeneously covered by hMSCs.
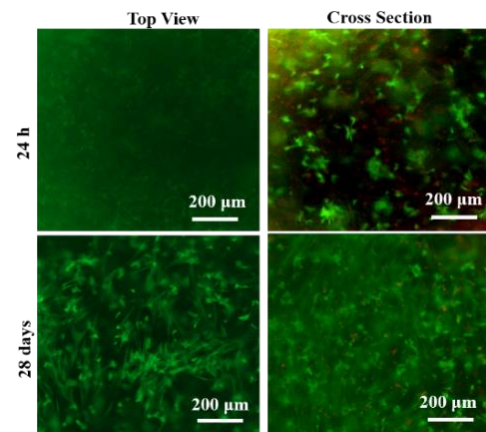

Fig. 6: Live/Dead assay of cartilage scaffolds at different time points for top and cross section surfaces. In 28 days of chondrogenic static culture cells retained a high viability and few dead cells (red spots in the picture) can be seen in the inner part of the scaffold (cross section).

C.   Osteochondral construct maturation

OC constructs were cultured for 4 weeks inside the dual chamber bioreactor. After 4 weeks, the OC constructs were removed from the inserts of the bioreactor (Fig. 7a) and resulted stable during the handling, showing a good cohesion between the cartilage and the bone phase.

Then Alcian Blue and Alizarin Red histological staining were carried out for both construct phases. Alcian Blue staining revealed GAG matrix deposition in the chondral phase (Fig. 7b, red arrows), concentrated around the lacunae-like structures around cells. No GAGs deposition can be seen in the bone phase.

Alizarin Red staining (Fig. 7c) showed no calcium deposition in the chondral phase, whereas calcium deposition

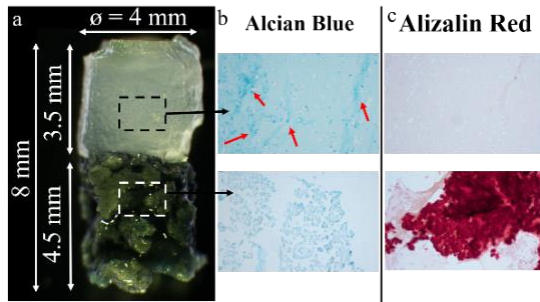in the bone phase is hardly distinguishable from the nHA present in the scaffold biomaterial.

Fig. 7: (a): developed OC construct after 4 weeks of dynamic culture inside the dual chamber bioreactor. Dimensions of construct are reported. (b) Alcian Blue staining in cartilage and bone construct, GAG deposition can be seen in the chondral phase while no deposition can be seen in the bone phase. Red arrows highlight main GAG deposition. (c) Alizarin Red staining in cartilage and bone construct. No calcium deposition in the chondral phase, whereas calcium deposition in the bone phase is hardly distinguishable from nHA in the scaffold

IV. DISCUSSION AND CONCLUSION

A highly reproducible gel-nHA scaffolds were fabricated using bioplotting. Morphological analysis highlighted the presence of an interconnected pore network with pores in the longitudinal plane. This is a crucial point in scaffolding since it facilitates nutrient and fluid circulation, waste removal and improved cells seeding and cell distribution. Then, a cell-laden hydrogel-based cartilage scaffold was fabricated by IRP.

Live assay was carried out on both bone and cartilage scaffolds, and the results indicate that the developed structures are a good support for cell growth and proliferation.

Using a previously developed dual chamber bioreactor, we were able to create two separate environments for bone and cartilage culture, maintaining the two phases of the *in vitro* OC construct in contact and able to signal to each other, mimicking what happens *in vivo*.

Histological analysis of the osteochondral constructs gave promising preliminary results suggesting that hMSCs differentiated towards a chondrogenic or osteogenic lineage, respectively, and that no mixing of media occurred in the bioreactor. Gene expression by real-time PCR has to be carried out to conclusively validate our OC model. In addition, we will deeply analyse if any interpenetration between osseous and chondral newly developed tissues occurred at the end of the culture.

Developing an OC model that truthfully and effectively mimics both cartilage and bone is essential to obtain an effective *in vitro* analogue of the OC unit, which can be used to understand osteochondral development and regeneration and as a platform to study bone and cartilage crosstalk in physiological and pathological conditions.

In addition, we will use the approach reported here with the vascularized *in vitro* bone model we previously described in [9] to develop an OC construct with vascularized bone phase. This will be extremely useful to explore the complex crosstalk occurring in the joint between cartilage, bone, and vasculature.

ACKNOWLEDGEMENT

REFERENCES

[1] Shimomura, K., Moriguchi, Y., Murawski, C. D., Yoshikawa, H., and Nakamura, N. (2014). Osteochondral tissue engineering with biphasic scaffold: current strategies and techniques. *Tissue Engineering Part B: Reviews*, 20(5), 468-476.

[2] Yousefi, A. M., Hoque, M. E., Prasad, R. G., and Uth, N. (2015). Current strategies in multiphasic scaffold design for osteochondral tissue engineering: a review. *Journal of biomedical materials research Part A*, 103(7), 2460-2481.

[3] Jeon, J. E., Vaquette, C., Klein, T. J., and Hutmacher, D. W. (2014). Perspectives in multiphasic osteochondral tissue engineering. *The Anatomical Record,* 297(1), 26-35.

[4] Lopa, S., and Madry, H. (2014). Bioinspired scaffolds for osteochondral regeneration. *Tissue engineering Part A*, 20(15-16), 2052-2076.

[5] Scaffaro, R., Lopresti, F., Maio, A., Sutera, F., and Botta, L. (2017). Development of polymeric functionally graded scaffolds: A brief review. *Journal of applied biomaterials & functional materials*, 15(2), 107-121.

[6] Zhang, X. Y., Fang, G., and Zhou, J. (2017). Additively manufactured scaffolds for bone tissue engineering and the prediction of their mechanical behavior: A review. *Materials*, 10(1), 50.

[7] Scaffaro, R., Lopresti, F., Botta, L., Rigogliuso, S., and Ghersi, G. (2016). Integration of PCL and PLA in a monolithic porous scaffold for interface tissue engineering. *Journal of the mechanical behavior of biomedical materials*, 63, 303-313.

[8] Zhou, X., Esworthy, T., Lee, S. J., Miao, S., Cui, *et al.*. (2019). 3D Printed scaffolds with hierarchical biomimetic structure for osteochondral regeneration. *Nanomedicine: Nanotechnology, Biology and Medicine*, 19, 58-70.

[9] Chiesa, I. De Maria, C. Lapomarda, A, Fortunato G. M., Montemurro, F. *et al.* (2020). Endothelial cells support osteogenesis in an *in vitro* vascularized bone model developed by 3D bioprinting. *Biofabrication.* https://doi.org/10.1088/1758-5090/ab6a1d

[10] De Maria, C., De Acutis A., and Vozzi G.. Indirect rapid prototyping for tissue engineering. *Essentials of 3D Biofabrication and Translation*. Academic Press, 2015. 153-164.

[11] Alexander, P. G., Gottardi, R., Lin, H., Lozito, T. P., and Tuan, R. S. (2014). Three-dimensional osteogenic and chondrogenic systems to model osteochondral physiology and degenerative joint diseases. *Experimental biology and medicine*, 239(9), 1080-1095.

[12] Iannetti, L., D'Urso, G., Conoscenti, G., Cutrì, E., Tuan, R. S., *et al.,*. (2016). Distributed and lumped parameter models for the characterization of high throughput bioreactors. *PloS one*, 11(9), e0162774.

[13] Moroni, L., Boland, T., Burdick, J. A., De Maria, C., Derby, B., *et al.,*. (2018). Biofabrication: a guide to technology and terminology. *Trends in biotechnology*, 36(4), 384-402.

[14] O'Bryan, C. S., Bhattacharjee, T., Niemi, S. R., Balachandar, S., Baldwin, N., *et al.,* (2017). Three-dimensional printing with sacrificial materials for soft matter manufacturing. *MRS bulletin*, 42(8), 571-577.

[15] Schmolka, I. R. (1972). Artificial skin I. Preparation and properties of pluronic F-127 gels for treatment of burns. *Journal of biomedical materials research*, 6(6), 571-582.

[16] Hwang, Y. J., Larsen, J., Krasieva, T. B., and Lyubovitsky, J. G. (2011). Effect of genipin crosslinking on the optical spectral properties and structures of collagen hydrogels. *ACS applied materials & interfaces*, 3(7), 2579-2584.

Biomarkers of Impulse Control Disorder in firing patterns of parkinsonian subthalamic nucleus

F. Micheli[1,2,*], M. Vissani[1,2,*], G. Pecchioli[3], F. Terenzi[4], S. Ramat[3], A. Mazzoni[1,2]

[1]The Biorobotics Institute, Scuola Superiore Sant'Anna, 56025 Pisa, Italy

[2]Department of Excellence in Robotics and AI, Scuola Superiore Sant'Anna, 56025 Pisa, Italy

[3]AOU Careggi, Dipartimento Neuromuscolo-Scheletrico e degli Organi di Senso, Florence, Italy

[4]Università degli Studi di Firenze, Dipartimento di Neuroscienze, Psicologia, Area del Farmaco e Salute del Bambino, Italy

* These authors share same first author contribution

Abstract—**Impulse Control Disorders (ICD) are a widespread co-morbidity of Parkinson's Disease (PD) severely affecting the quality of life of patients. The Subthalamic Nucleus (STN) is a pivotal element of the cortico-basal ganglia-thalamic network that encompasses both motor and cognitive functions, and is a common target for Deep Brain Stimulation (DBS) PD therapy. So far, the relation between STN activity and ICD in PD is not completely understood, hampering the development of specific therapies. Here, we show that the temporal structure of firing patterns of subthalamic neurons, acquired from exploratory microrecordings during DBS implant surgery, is significantly different in PD patient with and without ICD. ICD PD patients, indeed, present spontaneous firing activity far from the poissonian regime, as indicated by the shape factor of the Inter-spike Interval distribution. Poissonian firing is instead the dominant regime in non-ICD PD patients. No such difference between ICD and non-ICD PD patients is detectable in the average firing rate. These results corroborates the hypothesis that PD-related ICD is associated to altered patterns of firing in STN. The shape factor is then a candidate biomarker for the assessment of ICD in PD patients, paving the way for the development of specific treatments.**

Keywords—**Parkinson's Disease, Impulse Control Disorder, DBS, microrecordings**

I. INTRODUCTION

Parkinson's disease (PD) is a condition characterized by progressive degeneration of dopamine production in the substantia nigra (SN), particularly in the ventrolateral and caudal areas of the SN pars compacta, affecting dopaminergic projections from these areas to the dorsal striatum [1]. While the main symptoms of PD are motor dysfunctions as tremor, stiffness, bradykinesia and freezing of gait, there are also some relevant cognitive symptoms. Impulse control disorders (ICDs) are a class of psychiatric disorders, e.g. pathological gambling, compulsive shopping, compulsive sexual behavior, and binge eating, which affects a significant portion of the PD population (13% vs 5% of the general poulation) [2]. Studies involving large cohorts of PD patients found that one of the most relevant factor associated to ICD is the association with dopamine agonist and L-dopa treatment [2] [3]. The clinical efficacy

of Deep brain stimulation (DBS) treatment over Subthalamic Nucleus (STN) and Internal globus pallidus (GPi) in basal ganglia is a well-established therapy for motor symptoms of PD [4]. However, the impact of this treatment on the non-motor symptoms of PD, as ICDs, remains to be elucidated, although recent results are promising [5]. In particular, hyperactive STN behavior has been linked to deficits in inhibitory control of PD, both in motor and cognitive domains [6]. This has lead to hypothesis of a strong involvement of STN in both reactive and proactive inhibition (for a review see [7]). Several studies showed how Local Field Potentials (LFPs) in STN are able to discriminate between PD patients with and without ICD, during rest [8], and before [9], during [10] and after [11] risky choices. The organization in subregions of the STN (limbic, associative and motor) seems also to play crucial role in the outcome of non-motor neuropsychiatric symptoms after DBS implantation. Indeed, it has been shown that the inter-individual variability of non-motor outcomes after subthalamic nucleus DBS depends on the location of neurostimulation [12], which can influence also the emergence of neuropsychiatric symptoms, with disorder regarding inhibiton related to site of stimulation in the associative subregion [13]. Here, we analyze the firing pattern of single STN neurons, with an approach that was already effective in capturing temporal structure in the spike trains during STN DBS implant procedures [14], looking for possible neural markers at the single neuron level, discriminating between ICD and non-ICD PD patients.

II. MATERIALS AND METHODS

A. Patients

Patients were diagnosed with idiopathic PD by a neurologist expert in movement disorders, based on the UK Brain Bank Criteria [15]. All PD patients met standard DBS criteria (Core Assessment Program for Surgical Interventional Therapies in PD [16]) and NICE criteria (https://www.nice.org.uk/guidance/ipg19). PD related motor disability was assessed in both off- and on-drug states in all patients, using the Unified Parkinson's Disease Rating Scale

Patient 12 (non-ICD PD)   Patient 2 (ICD PD)

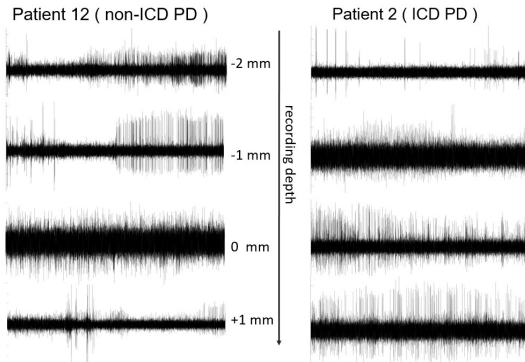-2 mm

-1 mm

0 mm

+1 mm

recording depth

Fig. 1: Intraoperative microelectrode recordings from patient 12 (non-ICD PD) on the left and patient 2 (ICD PD) on the right for depths close to the optimal clinical depth (indicated as 0 mm).

(UPDRS) and was classified according to the Hoehn & Yahr (H-Y) stage score 1 to 2 months prior to surgery.

We analyzed micro-electrode recordings from 25 PD patients (12 non-ICD PD, 13 PD; see Table I for details) undergoing STN DBS implant surgery. The study was carried out according to the Declaration of Helsinki. Informed written consent was obtained either from the patients or from their legal representative.

TABLE I: PATIENTS

	Age	PD duration	H-Y in off	group	sex	neurons
Patient 1	61	9	3	non-ICD PD	M	39
Patient 3	70	7	3	non-ICD PD	F	80
Patient 5	59	8	4	non-ICD PD	M	44
Patient 9	65	12	4	non-ICD PD	F	47
Patient 10	61	10	3	non-ICD PD	M	32
Patient 12	71	14	5	non-ICD PD	M	54
Patient 13	54	12	2.5	non-ICD PD	F	15
Patient 15	62	7	2	non-ICD PD	M	88
Patient 16	62	12	3	non-ICD PD	M	25
Patient 18	69	12	3	non-ICD PD	M	34
Patient 22	62	16	3	non-ICD PD	M	28
Patient 25	64	14	5	non-ICD PD	F	8
mean (std)	63.3 (4.9)	11.1 (2.9)	3.4 (0.9)		4F/ 8M	41.2 (23.9)
Patient 2	62	8	4	ICD PD	M	113
Patient 4	61	12	3	ICD PD	F	27
Patient 6	63	11	3	ICD PD	M	21
Patient 7	64	25	3	ICD PD	M	57
Patient 8	54	18	4	ICD PD	F	48
Patient 11	45	15	5	ICD PD	F	38
Patient 14	63	10	2	ICD PD	M	58
Patient 17	58	13	3	ICD PD	M	25
Patient 19	67	16	4	ICD PD	M	36
Patient 20	66	19	3	ICD PD	M	95
Patient 21	63	12	3	ICD PD	M	34
Patient 23	48	6	3	ICD PD	F	22
Patient 24	67	20	3	ICD PD	M	45
mean (std)	60.1 (7.1)	14.2 (5.3)	3.3 (0.75)		4F/ 9M	47.2 (28.6)

B. Surgical Procedure

STN DBS surgery was performed using the traditional stereotactic frame-based procedure with intraoperative micro-electrode recordings and macrostimulation for STN targeting. Under local anesthesia, implantation of the quadripolar DBS electrodes (model 3387; Medtronic, Minneapolis, MN, USA) was performed bilaterally. Afterwards, an implantable pulse generator was fixed to the DBS electrodes under general anesthesia.

C. Electrophysiological Recordings

Electrophysiological recordings were performed by means of a Medtronic LeadpointTM system (Medtronic Inc., Minneapolis, MN, USA) using 3 tracks : anterior, central and lateral. An exploratory trajectory was followed by extruding the microelectrode (250 lm tip, and impedance 1–1.5 MX; FHC Inc., Bowdoinham ME, USA). Microrecording tracks started at 10mm above the candidate target location identified through stereotactic imaging and were performed with 0.5 mm steps. Each recording lasted at least 10 seconds. Signals were acquired at 24kHz and high pass filtered with a hardware filter at 200 Hz to remove low frequencies and allow the visualization of firing activity during surgery.

D. Spikes Detection and Sorting

The signals were exported at 24 kHz and transformed into .mat files for off-line analysis with custom MATLAB (Mathworks) scripts. Files at the same depth and track were concatenated if were continuous in time; otherwise were treated as independent. Spike detection and sorting were performed using MATLAB ToolBox Wave_Clus [18]. Every isolated neuron was visually inspected and only the well separated ones were selected for further analysis. We used the following criteria : more than 90% of the total area of the amplitude histogram had to be above the detection threshold; the mean waveform had to have a typical action potential shape, i.e. biphasic shape either with a positive or negative most prominent peak (Fig. 2A); the percentage of spikes occurring within 3ms of each other had to be less than 3% and the number of spikes detected had to be more than 20.

E. Firing Rate and $log(\kappa)$ estimation

The firing rate of each neuron were estimated using the Gaussian Kernel bandwidth optimization method [19] (Figure 2C). The Firing regularity was quantified by fitting the inters-spike interval (ISI) distribution (Fig. 2D) with a Gamma distribution :

$$g_{\lambda,\kappa}(I) = \frac{(\lambda\kappa)^{\kappa} I^{\kappa-1} e^{-\lambda\kappa I}}{\Gamma(\kappa)} \qquad (1)$$

where I is the duration of the ISI, λ and κ are the firing rate and scale factor, and $\Gamma(\kappa)$ is the gamma function. The shape factor $log(\kappa)$ represents the firing regularity itself and it is estimated by the maximizing the likelihood, as follows :

$$log(\kappa) - \psi(\kappa) = -log(\lambda) - \frac{1}{n} log(\sum_{i=1}^{n} I_i) \qquad (2)$$

where $\psi(\kappa)$ and n are the digamma function and the number of ISIs respectively. Note that by construction $log(\kappa) = 0$ corresponds to Poissonian firing. We used $log(\kappa)$ as a criterion (as fully described in [14]) to determine three distinct patterns : burst-like for $log(\kappa) < 0.3$, regular tonic characterized by a very stable ISI for $log(\kappa) > 0.3$, and an intermediate state of irregular (poisson-like) firing (Fig.2 B-D).
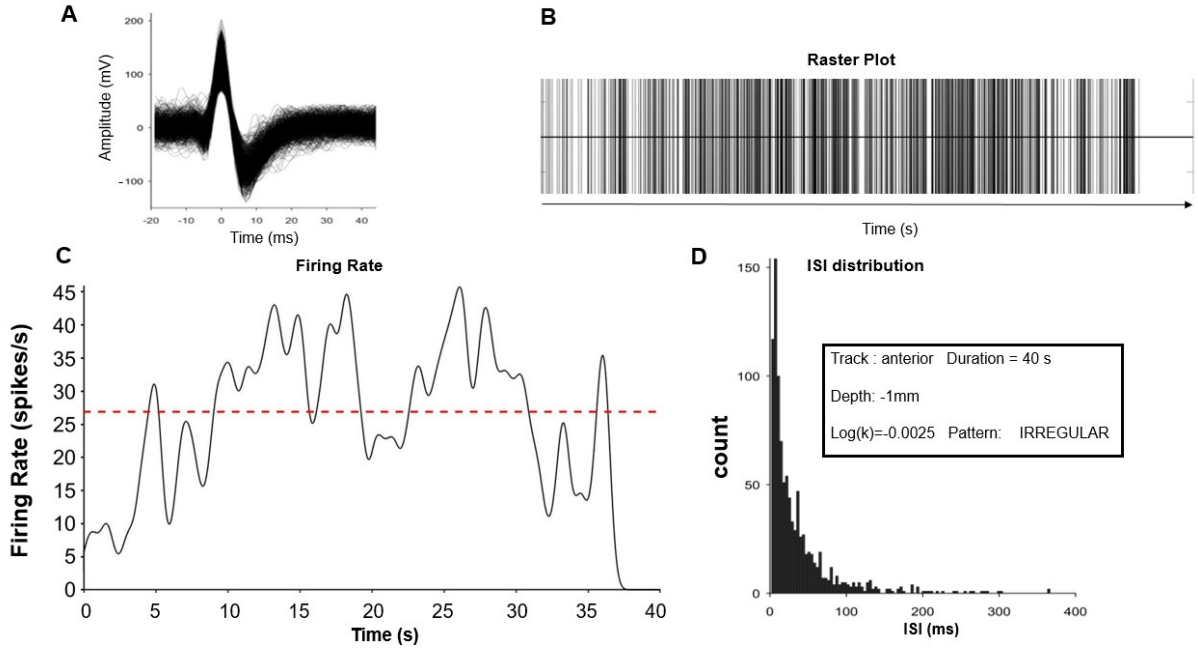
Fig. 2: Single neuron activity from registration at depth -1mm (anterior track, duration 40s). **A** Superimposition of action potential shapes **B** Neuron activity over time. Vertical lines represent spikes, **C** Firing rate estimation over time, (see Material and Methods). The horizontal red line indicates mean firing rate. **D** Inter-spike Interval (ISI) distribution. Inset reports recording details and the shape factor for the neuron.

III. RESULTS

We extracted the activity of single-units from 828 microrecordings acquired across different depths during STN DBS implant in PD patients with or without ICD. The number of neurons identified in the two groups was similar (N = 494 neurons in 12 non-ICD PD patients and N = 619 neurons in 13 ICD PD patients; 44.52 ± 8.87 neurons in each subject). We looked for neural features able to discriminate between the two groups. We did not find any significant difference in the overall firing rate between the two groups (non-ICD PD: 10.59 ± 1.05 Hz vs. ICD PD: 10.52 ± 0.95, Mann-Whitney U-test (MWW), P = 0.2, see Fig. 3A). As visual inspection of the recordings suggested differences between spiking patterns of the two groups (Fig. 1), we focused on the temporal structure of the neural activity. We quantified the level of regularity through the shape factor $\log(\kappa)$ [14], estimated by a fitting procedure of the ISI distribution with a Gamma distribution (see Methods Section D for details). Interestingly, the median shape factor of the neurons in non-ICD PD patients was significantly lower than in ICD patients (non-ICD PD: 0.05 ± 0.03 vs. ICD PD: 0.08 ± 0.04, MWW, P = 0.04, see Fig. 3B). This suggest the presence of firing pattern differences between ICD and non-ICD activity in the subthalamic nucleus of PD patients. Moreover, it suggests that the shape factor is a potentially useful neural marker to discriminate between the two groups.

We then looked for differences both in Firing Rate and shape factor $\log(\kappa)$ across depths. Inter-subjects data are aligned according to the reference depth chosen for the electrode implant, and depth is measured as difference from this depth. We did not find significant differences between the
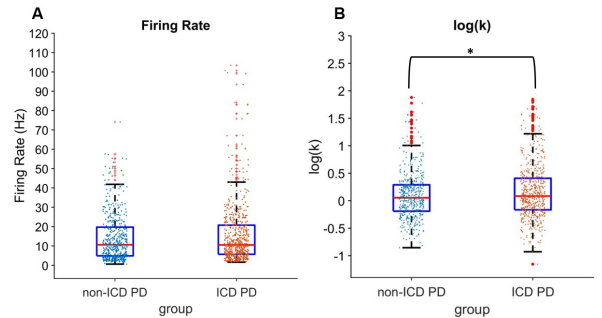
Fig. 3: Firing rate and temporal structure of the activity in non-ICD PD (left, blue) and ICD PS (right, red). Red line indicates medians, edges of the box represent 25th and 75th percentiles respectively, whiskers extend to the most extreme data points not considered outliers, and the outliers are plotted individually using the '+' red symbol **A** Distribution comparison for Firing Rate . **B** Distribution comparison for logarithm of ISI's shape factor k.

two groups for the Firing Rate at any depth (Fig. 4A, MWW at different depths, lowest P=0.1, at central bin). We found instead difference for the shape factor $\log(\kappa)$ at the central bin (between -2 and +2 mm), with median value in non-ICD patients significantly lower than in ICD (Fig. 4B, non-ICD PD: 0.034 ± 0.03 vs. ICD PD: 0.096 ± 0.04, MWW, P=0.004) but not for other bins (MMW at different depths, lowest P=0.1, at lowest bin). This shows that the cumulative shape factor difference at the global level (Fig.3) primarily reflects differences in firing patterns occurring close to the optimal target for DBS stimulation. This is then also the optimal depth at which biomarkers can be extracted. We finally explored the possibility of defining a simpler discrete neural feature related
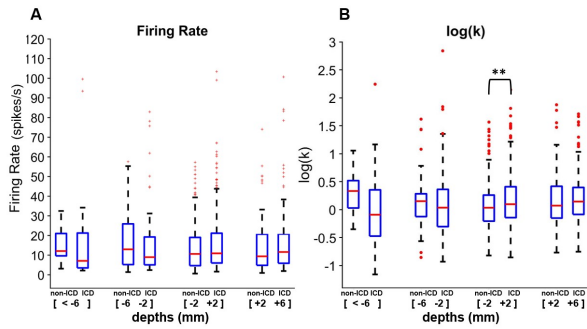
Fig. 4: Depth-wise comparison of firing rate and temporal structure of the activity in non-ICD PD and ICD PD. Red line indicates medians,edges of the box represent 25th and 75th percentiles respectively, whiskers extend to the most extreme data points not considered outliers. **A** Depth-wise distributions for Firing Rate. No depth showed significant difference between the two groups. **B** Depth-wise distributions of shape factor k. Significant difference (P=.004) between the two groups was found only in the central bin.

to the shape factor as a biomarker for ICD vs non-ICD PD patients discrimination. Each neuron was classified within three categories according to its temporal patterns of firing. The distribution of the temporal structure of spiking activity in non-ICD group showed a dominant fraction of 'Irregular' (poisson-like) neurons (217/494, 43.9 %) and a small fraction of 'Tonic' neurons (116/494, 23.5 %). The ICD PD group, instead, presented a more homogeneous distribution with a lower fraction of 'Irregular' neurons (225/619, 36.3 %) and an higher fraction of 'Tonic' neurons (196/619, 31.7%), coherently with the results derived from log(k) distribution. The interaction between different groups and amount of neurons for each category was highly significant (Table II. Chi-squared test - $\chi^2(2, N = 1113) = 10.57$, P = .0051). This suggests that this type of classification can be used as a simple biomarker for ICD in PD: the smaller/larger the fraction of irregular/tonic neurons, the more likely the presence of ICD.

TABLE II: DISCHARGE PATTERN

	Burst-like	**Irregular**	**Tonic**
non-ICD PD	32.6% (161)	43.9% (217)	23.5% (116)
ICD PD	32% (198)	36.3% (225)	31.7% (196)

Table II. Discharge pattern distribution for non-ICD PD and ICD PD patients. While the percentage of Burst-like neurons remained the same, the proportion of neurons with an Irregular (Poisson-like) firing pattern was lower in ICD PD and the proportion of neurons with a Tonic firing patter was higher.

IV. CONCLUSIONS

Thanks to the analysis of microrecordings acquired during STN DBS implant we found differences in temporal structure of subthalamic activity between PD patients with or without ICD. A depth-wise analysis suggests that this difference is spatially localized, but this result requires further analysis. We propose two measures of spiking

irregularity that could be easily computed online during the STN DBS implant as neural markers of ICD.

REFERENCES

[1] Lang, Anthony E., and Andres M. Lozano. "Parkinson's disease." New England Journal of Medicine 339.16 (1998): 1130-1143.

[2] Weintraub, Daniel, et al. "Impulse control disorders in Parkinson disease: a cross-sectional study of 3090 patients." Archives of neurology 67.5 (2010): 589-595.

[3] Voon, Valerie, et al. "Impulse control disorders in Parkinson disease: a multicenter case–control study." Annals of neurology 69.6 (2011): 986-996.

[4] Follett, Kenneth A., et al. "Pallidal versus subthalamic deep-brain stimulation for Parkinson's disease." New England Journal of Medicine 362.22 (2010): 2077-2091.

[5] Kurtis, Mónica M., et al. "The effect of deep brain stimulation on the non-motor symptoms of Parkinson's disease: a critical review of the current evidence." npj Parkinson's Disease 3.1 (2017): 1-12.

[6] Jahanshahi, Marjan, et al. "Parkinson's D isease, the S ubthalamic N ucleus, I nhibition, and I mpulsivity." Movement disorders 30.2 (2015a): 128-140.

[7] Jahanshahi, Marjan, et al. "A fronto–striato–subthalamic–pallidal network for goal-directed and habitual inhibition." Nature Reviews Neuroscience 16.12 (2015b): 719-732.

[8] Rodriguez-Oroz, Maria C., et al. "Involvement of the subthalamic nucleus in impulse control disorders associated with Parkinson's disease." Brain 134.1 (2011): 36-49.

[9] Mazzoni, Alberto, et al. "Subthalamic neural activity patterns anticipate economic risk decisions in gambling." eNeuro 5.1 (2018).

[10] Rosa, Manuela, et al. "Pathological gambling in Parkinson's disease: subthalamic oscillations during economics decisions." Movement Disorders 28.12 (2013): 1644-1652.

[11] Fumagalli, Manuela, et al. "Conflict-dependent dynamic of subthalamic nucleus oscillations during moral decisions." Social neuroscience 6.3 (2011): 243-256.

[12] Petry-Schmelzer, Jan Niklas, et al. "Non-motor outcomes depend on location of neurostimulation in Parkinson's disease." Brain 142.11 (2019): 3592-3604.

[13] Mosley, Philip E., et al. "The site of stimulation moderates neuropsychiatric symptoms after subthalamic deep brain stimulation for Parkinson's disease." NeuroImage: Clinical 18 (2018): 996-1006.

[14] Vissani, Matteo, et al. "Spatio-temporal structure of single neuron subthalamic activity identifies DBS target for anesthetized Tourette syndrome patients." Journal of neural engineering 16.6 (2019): 066011.

[15] Hughes, Andrew J., et al. "Accuracy of clinical diagnosis of idiopathic Parkinson's disease: a clinico-pathological study of 100 cases." Journal of Neurology, Neurosurgery Psychiatry 55.3 (1992): 181-184.

[16] Defer, Gilles-Louis, et al. "Core assessment program for surgical interventional therapies in Parkinson's disease (CAPSIT-PD)." Movement disorders: official journal of the Movement Disorder Society 14.4 (1999): 572-584.

[17] Anderson, William S., and Frederick A. Lenz. "Surgery insight: deep brain stimulation for movement disorders." Nature clinical practice Neurology 2.6 (2006): 310-320.

[18] Chaure, Fernando J., Hernan G. Rey, and Rodrigo Quian Quiroga. "A novel and fully automatic spike-sorting implementation with variable number of features." Journal of neurophysiology 120.4 (2018): 1859-1871.

[19] Shimazaki, Hideaki, and Shigeru Shinomoto. "Kernel bandwidth optimization in spike rate estimation." Journal of computational neuroscience 29.1-2 (2010): 171-182.

Muscle forces and activations in Parkinson's disease: a model-based approach

M. Romanato[1], D. Volpe[2], M. Sartori[3], and Z. Sawacha[1]

[1] *Department of Information Engineering, University of Padua, Italy*
[2] *Fresco Parkinson Center, Villa Margherita, S. Stefano, Vicenza, Italy*
[3] *Department of Biomechanical Engineering, University of Twente, Netherlands*

Abstract—**Parkinson's disease (PD) is a progressive pathological condition caused by a dopamine deficiency. Although gait alterations are well-known in PD patients, changes in neural strategies have recently been explored. The presented study aims to address the advantages of adopting a neuromusculoskeletal modelling approach, in order to detect alterations in PD's motor control and report differences in knee and ankle muscle forces with respect to the healthy individuals. The adopted electromyography (EMG)-informed computational model was fed by EMG signal coupled with 3D marker trajectories and ground reaction forces. Ten PD subject-specific models were developed and compared with a control group of 13 subjects matched for age and BMI. Results showed significant differences in the neuromuscular control strategy of the PD group both in terms of muscle forces and co-contraction index. The estimated variables can become a measurable outcome in order to assess the effect of physical therapy interventions thus allowing to track the disease progression. Furthermore, this technology might be adopted to plan interventions through exoskeletons, by providing an estimate of the degree of muscle forces required by the specific subject to restore a physiological gait profile.**

Keywords—**Parkinson's disease, forward dynamics, motion analysis, neuromusculoskeletal modelling.**

I. INTRODUCTION

PARKINSON'S disease (PD) is the second most common neurodegenerative disorder, affecting about 1% of adults over 60 years of age [1]. PD is a neurodegenerative pathological condition characterized by a dopamine deficiency causing tremor, rigidity, bradykinesia, postural instability and a typical flexed posture. Gait alterations have been identified as a hallmark of this pathology; indeed, PD subjects are characterized by an increment of cadence, stance and double support phases that has been interpreted as a compensatory strategy to the reduction of both stride length and lower limb joints range of motion [2]. Recently, the authors detected a further sign of motor disorder in PD patients, by identifying specific alterations in both the timing and the amplitude of electromyography (EMG) activation during the gait cycle [3], [4] in comparison with control subjects. It should be mentioned that, the routine clinical assessment of motor symptoms in PD subjects relies on the use of clinical scales, as the Movement Disorder Society – Unified PD Rating Scale [5], in some cases coupled with the instrumented gait analysis [6]. Although these are both established tools for clinical practice, they do not allow accounting for the different neural strategies derived from the neurological impairment. Combining gait analysis and a forward dynamics approach, as EMG-informed modeling [7], [8], could provide a deeper understanding of disease progression. This methodology has been successfully applied across a range of neuromuscular pathologies [9] and healthy individuals [10]. In this context a subject specific neuromusculoskeletal model is created for each individual, driven by their own EMG signals. In comparison with inverse dynamics approaches [11], that rely on a cost function which does not consider the PD subjects' neural strategies, the proposed modelling approach links in vivo neuromuscular functions to the individual, thus providing new biomarkers and reliable muscle forces estimation.

Currently, no studies investigated the possibility to quantitatively assess strength in PD subjects. This work has the goal to address the estimation of non-directly accessible biomarkers, by computing reliable muscle-tendon forces together with the muscle activations strategy, which directly relate to changes in strength over time. With this purpose the co-contraction ratio index (CCR) is computed to describe the simultaneous activity of the agonist-antagonist muscles spanning the knee and ankle joints [12], by adopting a simplified experimental setup purposely adapted for the clinical practice.

II. METHODS

A. Participants

Ten PD patients (6 males, 4 females, age=66.89±12.78 years, weight=81.33±16.17 kg, height=1.72±0.11 m, BMI=23.38±3.35 kg/m^2) were chosen from a former study cohort, approved by the Ethic Committee with protocol number CE/PROG 61/16 del 19/11/2015. The participants had a Hoen and Yahr scale of 2-3 [13] and Mini Mental State Evaluation > 24 [14]. Moreover, patients were able to walk autonomously and to perform the required tasks, on a stable treatment regimen for at least 3 months with a disease duration > 5 years, and had a good response to anti-Parkinsonian therapy.

B. Data Collection

The measures have been acquired at the Human Movement Bioengineering Laboratory (10 m walkway) of the Department of Information Engineering at the University of Padova (Italy) equipped with 6 cameras stereophotogrammetric system (60-120 Hz, BTS S.r.l., Padova), synchronized with two force plates (960 Hz, Bertec Corporation, USA) and an 8 channel EMG system (1000 Hz, BTS Free, Italy) that recorded bilaterally the activities of 4 muscles: Rectus Femoris (RF), Biceps Femoris (BF), Gastrocnemius Lateralis (GL) and Tibialis Anterior (TA), following the minimal crosstalk area guidelines introduced by Y. Blanc and U. Dimanico [15], in

order to maximize the measured selective activity per muscle. A modified version of the IOR-Gait protocol [16] was adopted for anatomical landmarks identification. Data collection included static acquisitions for anatomical calibration [17] as well as several self-selected speed gait trials.

C. Data processing and neuromusculoskeletal model

Three left and three right foot strikes were considered for the processing when the foot was naturally landing on the force plates. MOtoNMS [18] was adopted to export the motion data used in OpenSim framework and to normalize the EMG signals with the maximum value of each muscle activation during the trial. A generic musculoskeletal model (gait2392 [19]) was used to linearly scale each subjects' geometry in OpenSim, matching the virtual markers of the model with the experimental ones of the subjects acquired during the static pose trial. Inverse kinematics, inverse dynamics (ID) and muscle analysis tools were used to obtain joint angles and moments and musculotendon moments and moment arms during the recorded trials.

TABLE I
MAPPED MUSCULOTENDON UNITS

Experimental Muscle EMG	Musculotendon Unit	Knee/Ankle Ago-Antagonist Muscle
RF	Rectus femoris	Knee extensor
	Vastus Medialis	Knee extensor
	Vastus Lateralis	Knee extensor
	Vastus Intermedius	Knee extensor
BF	Biceps Femoris Long Head	Knee flexor
	Biceps Femoris Short Head	Knee flexor
	Semimembranosus	Knee flexor
	Semitendinosus	Knee flexor
GL	Gastrocnemius Lateralis	Knee flexor/Plantar flexor
	Gastrocnemius Medialis	Knee flexor/Plantar flexor
	Soleus	Plantar flexor
TA	Tibialis Anterior	Dorsi flexor

Electromyograms, musculotendon units, and ago-antagonist muscles.

CEINMS [20] was adopted as toolbox to estimate the muscle forces that best matched the experimental EMGs and joint moments. In order to take into account restrictions related to clinical applications, the experimental setup was reduced with respect to [21], and 4 bilateral EMG channels were mapped to a total of 12 musculotendon units (Table 1) [22]. Two degrees of freedom (ankle plantar-dorsi flexion and knee flexion-extension) were analyzed separately. For each subject all the dynamic trials were used both for the calibration and the execution. After calibration, the software was used to predict the knee and ankle moments, muscle forces and activations with a hybrid EMG-informed model, that combined both the forward dynamics and the static optimization procedure that minimally adjusts experimental EMG-excitations to minimize instantaneous EMG-predicted joint moment estimates [23].

The weighting factors of the hybrid function were obtained averaging the results from a previous study [23]. In order to calculate the CCR, the formula Eq. (1) was implemented [24], where an index of -1 indicates a solely contribution of the agonist excitations, 1 indicates a contribution derived just from antagonist excitations and 0 indicates a balanced contribution of both the agonist and antagonist excitations, i.e. the maximum value of co-contraction. $EMG(t)_{antagonist}$ and $EMG(t)_{agonist}$ were respectively representative for the averages of all the agonist and antagonist muscle excitation over a same time instant.

$$\begin{cases} CCR(t) = \dfrac{EMG(t)_{antagonist}}{EMG(t)_{agonist}} - 1, & if\ EMG(t)_{antagonist} \\ & < EMG(t)_{agonist} \\[2mm] CCR(t) = 1 - \dfrac{EMG(t)_{agonist}}{EMG(t)_{antagonist}}, & if\ EMG(t)_{antagonist} \\ & > EMG(t)_{agonist} \end{cases} \quad (1)$$

D. Statistical Analysis

The assessed variables were represented by the mean from six representative walking trials per subject. In order to aid in the selection of which walking trial could be included in the calculation of the mean, intra-class correlation was used for each kinematic parameter. All the trials with a coefficient greater than 0.75 (75%) were included in the statistical analysis [16]. The average kinematic data were plotted in percentage of the gait cycle and the 2 tailed Student's T-test was used, after evidence of normality to compare the data of the PD versus a control group (CG), which was extracted from a previous study [25] (7 males, 6 females, age=58.23±11.48 years, weight=77.08±16.50 kg, height=1.72±0.11 m, BMI=25.63±3.34 kg/m^2) and between the different models and experimental data.

III. RESULTS

A. Neuromusculoskeletal model validation

In order to verify the reliability of the model we both compared the envelopes peak position of the experimentally measured muscles and the models-derived ones (Fig. 1), as in [9], and the ID-generated joint moments in OpenSim versus the CEINMS-estimated torques (Fig. 2), as in [26].
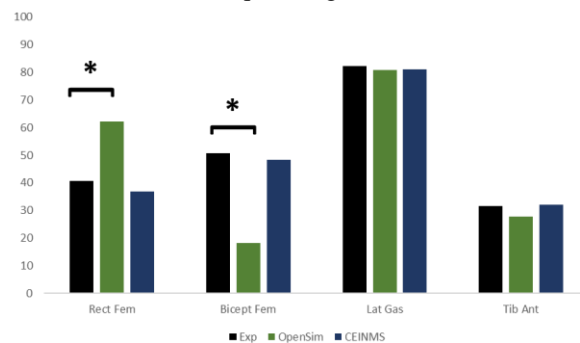

Fig. 1: Activation peaks position in percentage of the gait cycle for PD participants. Experimentally measured muscle activation (in black), OpenSim derived ones for the same muscles (in green) and CEINMS derived ones for the same muscles (in blue). * = p < 0.05.

We observed a better estimation of the simulated activations calculated with the EMG-informed model than the ones estimated with the optimization approach for the RF and BF

muscles. Furthermore, the calibrated neuromusculoskeletal model well predicted the ankle and knee flexion-extension moments, solely overestimating the final phase of the stance.

B. Internal motion variables

We reported here the results obtained with the EMG-informed modelling approach from the PD participants compared with the CG. Muscle forces (Fig. 3) showed statistically significant differences between the two populations, except for the ankle joint plantar-flexor muscles during the stance phase. Major differences were highlighted in
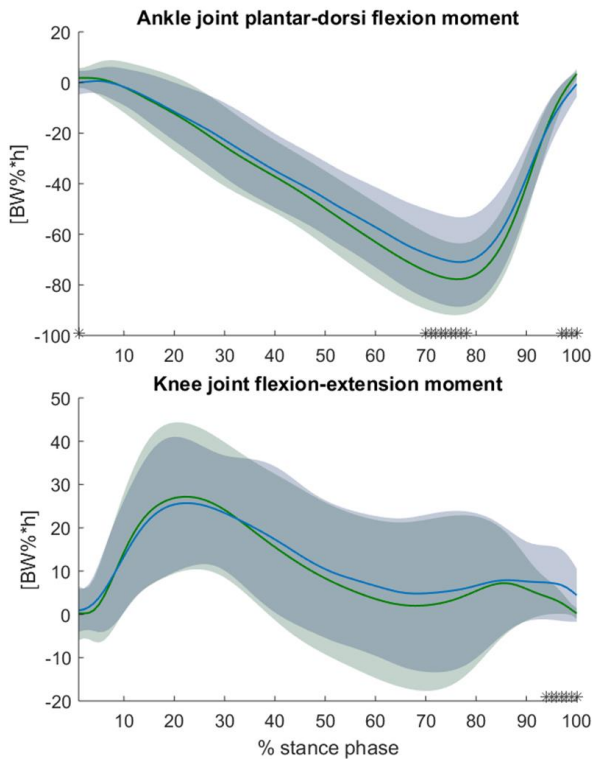
Fig. 2: Joint moments in PD subjects in percentage of the stance phase and normalized with respect to body weight × height (BW×h)% , ID-generated moments from OpenSim (mean in green, ±1 standard deviation in shaded green area), CEINMS-estimated torques (mean in blue, ±1 standard deviation in shaded blue area). Top of the figure presents the ankle joint moments, bottom of the figure knee joint moments. * = p < 0.05.

the BF long head, BF short head, semitendinosus, semimembranosus and in the second half of the gait cycle of the RF. The vasti showed similar patterns during the stance phase in both the samples. CCR (Fig.4) did not show statistically significant differences between the CG and the PD, but a greater variability in the second half of the stance

phase for the knee joint was noticed. This suggests a lower neuromuscular control involvement at the knee joint level in that phase with respect to the more distal joint, and the adoption of different motor control strategies within the PD group. The limitations of the current study should be acknowledged: first the reduced number of EMG recorded might have impacted on the estimation of internal variables, as well as the lack of gold standard available for muscle forces estimation; second the small number of subjects. However, it should be mentioned that the proposed technique allows overcoming some limitations of standard musculoskeletal modelling techniques (i.e. OpenSim static optimization [27]) which purely relies on optimization, tuned on non-altered neural pathways, by using an EMG-informed musculoskeletal model. This allows us to capture realistic patterns of PD population's muscle activation by means of EMGs, and using them in a forward dynamics approach to virtually model the movements produced by both the skeletal and muscular system as controlled by the neural system [28].

IV. CONCLUSION

This study investigates an approach to estimate internal motion variables for the first time in people with PD in a clinical environment, with a method that both considers their motor dysfunctions and neurological impairments. Even though we recorded a reduced number of EMG channels than the optimal experimental setup described in [24], results have proven to be consistent both at EMG and dynamic levels (Fig. 1-2), allowing the analysis of differences in muscle forces and co-activation strategies between the CG and the PD participants. Overall, musculotendon units in PD patients produced a lower force than the CG, underling a deficit in the neural motor control, especially for the muscles involved in the knee joint, as confirmed also from the CCR results.

To be able to quantitatively assess these variables will enable understanding the best clinical approach and treatment plan for PD patients. Moreover, this approach will allow to comprehend how assistive and wearable technologies should interact with the user in order to provide an appropriate support and to restore a more physiological neuromusculoskeletal functions profile. Limitations derived from the reduced experimental setup will be addressed comparing the proposed and the optimal setup and further discussed in a future publication.
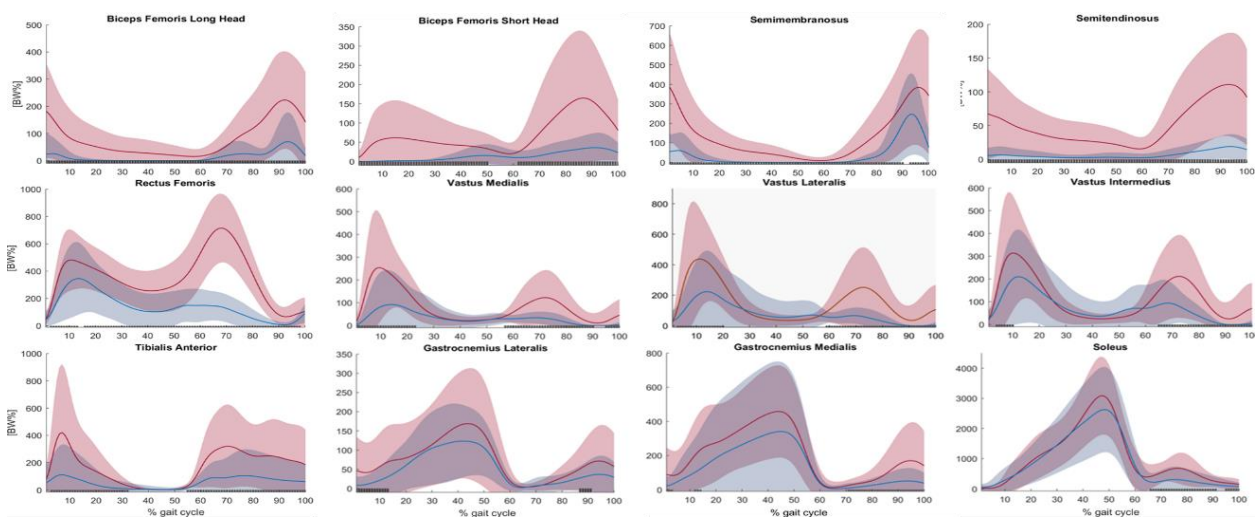
Fig. 3: Muscle forces estimated with CEINMS. CG (in red, ±1 standard deviation in shaded red area) in comparison with PD subjects (in blue, ±1 standard deviation in shaded blue area). The muscle forces are presented in percentage of the gait cycle and normalized with respect to body weight (BW)%. ■ = $p < 0.05$.
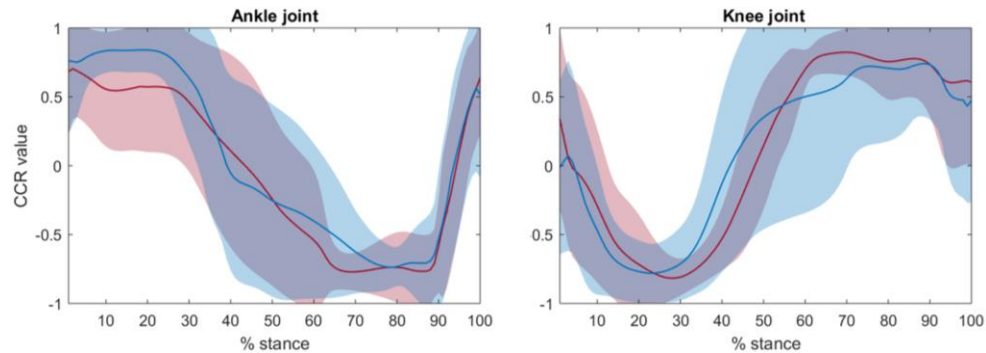

Fig. 4: CCR estimated from the activations generated via CEINMS. CG (mean in red, ±1 standard deviation in shaded red area) in comparison with PD subjects (mean in blue, ±1 standard deviation in shaded blue area). The ratio is presented in percentage of the stance phase and varies between -1 and 1.

REFERENCES

[1] D. Volpe, D. Pavan, M. Morris, A. Guiotto, R. Iansek, S. Fortuna, G. Frazzitta, Z. Sawacha, "Underwater gait analysis in Parkinson's disease", Gait Posture, 2017 Feb, vol. 52, pp. 87-94.

[2] M. E. Morris, R. Iansek, J McGinley, T. Matyas, F. Huxham, "Three-dimensional gait biomechanics in Parkinson's disease: evidence for a centrally mediated amplitude regulation disorder", Mov. Disord, 2005 Jan, vol. 1, pp. 40–50.

[3] F. Spolaor, D. Volpe, D. Pavan, A. Guiotto, F. Fichera et al, "Surface EMG analysis in Parkinson's disease patients before and after underwater gait training", Gait & Posture, 2017 Sept, vol. 57, pp. 53-54 (ESMAC Conference, 6-9 Sept 2017, Trondheim, Norway)

[4] D. Volpe, F. Spolaor, Z. Sawacha, A. Guiotto, D. Pavan et al, "Muscular activation changes in lower limbs after underwater gait training in Parkinsons's disease: a surface EMG pilot study", Gait & Posture, 2020, under review.

[5] Movement Disorder Society Task Force on Rating Scales for Parkinson's Disease; Mov Disord, 2003; Jul 18(7):738-50.

[6] D. Volpe, M. Signorini, A. Marchetto, T. Lynch, M. E. Morris, "A comparison of Irish set dancing and exercising for people with Parkinson's disease: A phase II feasibility study" BMC Geriatrics, 2013 Jun, art. 54.

[7] M. Sartori, J. W. Fernandez, L. Modenese, C. P. Carty, L. A. Barber et al, "Toward modeling locomotion using electromyography-informed 3D models: application to cerebral palsy", WIREs Syst. Biol. Med, 2017 Mar, vol 9.

[8] M. Sartori, D. G. Lloyd, D. Farina, "Neural data-driven musculoskeletal modeling for personalized neurorehabilitation technologies", IEEE Trans. Biomed. Eng., 2016; vol. 63, pp. 879–93.

[9] A. Scarton I. Jonkers, A. Guiotto, F. Spolaor, G. Guarneri et al, "Comparison of lower limb muscle strength between diabetic neuropathic and healthy subjects using OpenSim" Gait & Posture, 2017, vol. 58, pp. 194-200.

[10] C. Varotto, Z. Sawacha, L. Gizzi, D. Farina, M. Sartori, "Closed-loop EMG-informed model-based analysis of human musculoskeletal mechanics on rough terrains" IEEE Int Conf *Rehabil* Robot, Jul 2017; (2017) pp. 364-68.

[11] K. Veerkamp, W. Schallig, J. Harlaar, C. Pizzolato, C.P. Carty, D.G. Lloyd, M.M. van der Krogt, "The effects of electromyography-assisted modelling in estimating musculotendon forces during gait in children with cerebral palsy", Journal of Biomechanics, 2019 Jul, vol. 92, pp 45-53.

[12] M.E. Busse, C.M. Wiles & R. W.M. van Deursen, "Muscle coactivation in neurological conditions", Physical Therapy Reviews, 2005, vol. 10, pp 247-253.

[13] M. M. Hoehn, M. D. Yahr, Parkinsonism: onset, progression and mortality, Neurology, 1967, vol. 47.

[14] F. E. Folstein, S. E. Folstein, P. R. McHugh, "Mini-mental state. A practical method for grading the cognitive state of patients for the clinician", J Psychiatr Res, 98 1975, vol. 98, pp. 189.

[15] Y. Blanc and U. Dimanico, "Electrode placement in surface electromyography (sEMG) "Minimal Crosstalk Area" (MCA)", The Open Rehabilitation Journal, 2010, vol. 3, 110-126.

[16] S. Del Din, E. Carraro, Z. Sawacha, et al, "Impaired gait in ankylosing spondylitis", Med. Biol. Eng. Comput., 2011, vol. 49 pp. 801–809.

[17] A. Cappozzo, F. Catani, U. Della Croce, A. Leardini, "Position and orientation in space of bones during movement: anatomical frame definition and determination", Clin. Biomech. 1995, vol. 10, pp. 171–178.

[18] A. Mantoan, C. Pizzolato, M. Sartori, Z. Sawacha, C. Cobelli, M. Reggiani, "MOtoNMS: A MATLAB toolbox to process motion data for neuromusculoskeletal modeling and simulation", 2015 Nov, vol. 10.

[19] Delp, S.L., Loan, J.P., Hoy, M.G., Zajac, F.E., Topp E.L., Rosen, J.M. "An interactive graphics-based model of the lower extremity to study orthopaedic surgical procedures", IEEE Transactions on Biomedical Engineering, 1990, vol. 37, pp. 757-767.

[20] C. Pizzolato, D. G. Lloyd, M. Sartori, E. Ceseracciu, T. F. Besier et al, "CEINMS: A toolbox to investigate the influence of different neural control solutions on the prediction of muscle excitation and joint moments during dynamic motor tasks", J. Biomech., 2015 Nov, vol. 48, pp. 3929-36.

[21] Sartori,M., Reggiani, M.,Farina, D.,Lloyd, D.G., "EMG driven forward-dynamic estimation of muscle force and joint moment about multiple degrees of freedom in the human lower extremity". 2012 Dec, vol. 7.

[22] M. Romanato, M. Sartori, G. Durandau, D. Volpe, Z. Sawacha, "An EMG-informed modelling approach for the prediction of internal variables during locomotion in Parkinson's disease patients : a feasibility study", Gait and Posture, 2019 Sep, vol. 74, pp. 32-33.

[23] M. Sartori, D. Farina, D. G. Lloyd, "Hybrid neuromusculoskeletal modeling to best track joint moments using a balance between muscle excitations derived from electromyograms and optimization", J. Biomech., 2014, vol. 47, pp. 3613-21.

[24] M. Sartori, M. Maculan, C. Pizzolato, M. Reggiani, D. Farina, "Modeling and simulating the neuromuscular mechanics regulating ankle and joint stiffness during human locomotion", J Neurophysiol, 2015 Aug, vol. 114, pp. 2509-2527.

[25] Z. Sawacha, G. Guarneri, A. Avogaro, C. Cobelli, "A new classification of diabetic gait pattern based on cluster analysis of biomechanical data", Journal of Diabetes Science and Technology, 2010, vol. 4, pp. 1127-1138.

[26] G. Davico, C. Pizzolato, D. G. Lloyd, S. J. Obst, H. P. J. Walsh, C. P. Carty, "Increasing level of neuromusculoskeletal model personalisation investigate joint contact forces in cerebral palsy : a twin case study", Clinical Biomechanics, 2020, vol. 72, pp. 141-49.

[27] Delp, Scott L., Anderson, Frank C., Arnold, Allison S., Loan, Peter, et al, "OpenSim: Open-Source Software to Create and Analyze Dynamic Simulations of Movement", IEEE Transactions On Biomedical Engineering, 2007, vol. 54, pp. 1940-1950.

[28] T. S. Buchanan, D. G. Lloyd, K. Manal, T. F. Besier, "Neuromusculoskeletal modeling: estimation of muscle forces and joint movements and movements from measurements of neural command", J. Appl. Biomech., 2004 Nov, vol. 20, pp. 367-95.

A neural electrode for closed-loop vagus nerve recording and stimulation to control autonomic reflexes

A. Giannotti[1,2*], I. Strauss[1,2*], and S. Micera[1,2,3]

[1] The BioRobotics Institute, Scuola Superiore Sant'Anna, Pisa, Italy
[2] Department of Excellence in Robotics & AI, The BioRobotics Institute, Scuola Superiore Sant'Anna, Pisa, Italy
[3]Bertarelli Foundation Chair in Translational NeuroEngineering, Center for Neuroprosthetics and Institute of Bioengineering, Ecole Polytechnique Federale de Lausanne (EPFL), Lausanne, Switzerland
*Equally contributed authors

Abstract— The vagus nerve is a mixed nerve that maintains physiological homeostasis through autonomic reflexes. Nerve afferents collect information from the periphery. They transmit physiological parameters sent from the heart, guts, and so forth. Efferent fibers on the other hand control organs. Disruptions in the autonomic nervous system are responsible for pathologic conditions such as heart failure and diabetes. Pharmaceutical treatments are available, but often have side effects such as dizziness, muscular weakness, or hypotension. The electrical stimulation of vagus nerve fibers showed the successful treatment of pathologic conditions. The recording of afferent fibers can be correlated to the presence of biomarkers of various diseases. Here we adapt an existing, intrafascicular electrode to enable recording and stimulation of the vagus nerve. The hereby created diagnostic and therapeutic tool could substitute pharmaceutical treatment. Vagal nerve histology has been used to adapt the electrode model dimensions. The dimensional adaptation showed to be accurate. Electrochemical characterization showed improved electrochemical parameters. Further *in vivo* testing should confirm the electrode's capabilities.

Keywords—vagus nerve stimulation, vagus nerve recording, neural electrode.

I. INTRODUCTION

HEART failure is the leading cause of death in the United States according to estimates from 2019 involving about 6.5 million adults [1]. According to the World Health Organization [2], chronic disease prevalence is expected to rise by 57% by the end of the year 2020.

Pharmaceutical treatments have been the current solution for such diseases but they are not always effective and they are slow-acting therapies. Drug dosages are not patient-specific therapies and they can have side effects [3]. For example, beta-blockers, widely used for heart failure treatment, are associated with the increase in the risks of hypotension, dizziness, and bradycardia [4].

The autonomous nervous system maintains physiological homeostasis with the so-called 'autonomic reflex'. These reflexes are composed of a sensory afferent arc and a motor efferent arc. The first consists of nerves that transmit sensorial information from the body periphery to the homeostatic control centers [5]. These centers integrate the information and consequently a motor response is transmitted through nerves of the efferent arc to body organs. Autonomic reflexes are crucial to control several body functions that are not under voluntary control. They maintain bodily parameters in a physiological range [6].

The vagus nerve (VN) is one of the most important components of the autonomous nervous system and supervises functions such as mood, immune response, digestion,

respiratory frequency and heart rate [7], [8]. Approximately 80% of the fibers in the VN are afferent [9], so great interest is involved in developing technologies able to record signals propagating through it.

Electrical vagus nerve stimulation (VNS) of efferent nerve fibers has been successfully used to treat pathologic conditions such as epilepsy, depression, heart failure and inflammatory bowel diseases [7], [10].

Recent studies presented promising results in recording the sensory afferent arc of peripheral neural reflexes [11-13]. It was possible to decode these signals to verify the presence of biomarkers of previously mentioned diseases [9], [11], [14].

Most technologies that can record sensory fibers of nerve and relate signals to pathological biomarkers involve the use of cuff electrodes. Limitations of cuff electrodes are the low signal-to-noise-ratio (SNR) and selectivity. Cuff electrodes allow only to acquire compound action potentials (CAPs), so great efforts are necessary to decode neural signals [15]. Cuff electrodes are also able to stimulate nerve fibers but they are not sufficiently accurate because of their unprecise, superficial stimulation approach [16].

An interesting approach is the use of carbon nanotube (CNT) yarn electrodes developed by [14]. They limit nerve damage due to their axon-like dimensions. They have an excellent SNR and high selectivity thanks to their intraneural approach. CNT yarns can carry electrical signals 10 times stronger than current technologies but are still under investigation.

However, the limitation of current approaches is that not many highly selective neurostimulation has been successfully developed so far. Such technologies could enable real-time monitoring for a variety of physiological parameters under the control of the VN. This includes the heart rate, breathing rate, digestive functions and the immune response [8]. This approach could be implemented as a new strategy for disease treatment, avoiding drug side effects.

For example, autonomic reflexes involved in the homeostasis of the heart could be controlled with a closed-loop neuromodulation strategy by monitoring cardiac function through VN recording, extracting in real-time electrocardiogram parameters (ECG) and consequently stimulating the same VN to maintain the desired heart rate (Fig. 1). In addition, this would allow the patient to have a completely implanted, self-controlled and autoregulated system.

The recording of peripheral neural signals is still challenging. Preclinical models have small nerve sizes and the connective tissue that surrounds the nerves (perineurium) attenuates the

weak electrical signals [9].

To overcome these limitations, we here adapted an existing intrafascicular electrode (Q-PINE) previously developed by our group [17] both to record and stimulate from the VN at the same time (VQ-PINE). Thanks to the adaptable structure of the Q-PINE, the design of the VQ-PINE was adapted to the histological analysis of porcine VN obtained.

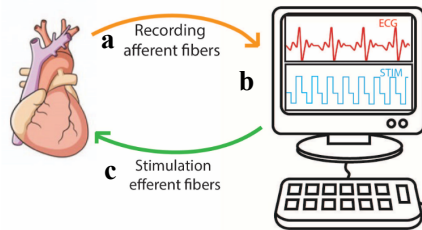This novel electrode should promote the development of a closed-loop system for clinical application.

Fig. 1: The heart rate is recorded from afferent fibers of VN which innervates the heart (a). The PC is analyzing in real-time the data acquired (b) and stimulates the efferent fibers of the same nerve accordingly to data recorded to maintain parameters in the physiological range (c).

II. MATERIALS AND METHODS

All experimental animal procedures were approved by the Italian Ministry of Health and were in accordance with the Italian law (D.lgs. 26/2014).

A. 3D model of the porcine vagus nerve

The histological evaluation of the left and right VN of the porcine model extracted at the cervical level was performed.

100 histological sections were used to calculate the medium diameter of the nerve.

A 3D model of the nerve was generated uploading the histological section in Solidworks (Dassault Systèmes, Fr).

B. Design of the multi-array intrafascicular electrode

The electrode 3D model here described has been developed from an existing intrafascicular electrode (Q-PINE) for porcine sciatic nerve previously developed by our group [16].

To adapt the Q-PINE to the VN a decrease in the overall size of the electrode was necessary. Porcine vagus nerves are smaller compared to the porcine sciatic nerve (roughly 2mm and 6mm diameter respectively).

The electrode (Fig. 2) is composed of a supporting platform and two silicon fixating portions that enclose the nerve. Four needles are perpendicularly inserted through the PCB and the supporting platform (Fig. 2B). Each one of them contains two 25μm thick Pt90/Ir10 microwires (Advent Research Materials, UK) coated with a PTFE layer of 5μm. The total outer diameter of the microwire is 35μm. Eight active sites (ASs) are available in the V-QPINE. The silicon portion docking system has been modified and the electrode dimensions have been reduced.

Using a laser cutter (VersaLaser, Polytech GmbH, GER) 150μm of the insulation layer are removed from the microwire to realize one AS. The AS can be seen in Fig.2C and 2D colored pink, yellow and green. The ASs colors in these two figures correspond to the correct needles in Fig. 2B.

The number and position of ASs were designed in order to achieve the maximum number of fascicles and increase electrode selectivity. The ASs were distributed over the whole cross-section of the nerve (Fig.2C). Along the longitudinal section, the ASs were placed at a different height (Fig.2D).

In order to increase the electrochemical performances of the ASs, the microwires are coated electrodepositing poly(3,4-ethylenedioxythiophene) (PEDOT).

Custom-made PCB (Cadline Srl, ITA) was developed and integrated into the supporting platform and connected to the microwires containing the ASs. A recorder or a stimulator can be attached to a cable connected to the PCB using a SAM8701-ND connector (Samtec Inc., USA).

Finally, to ensure the microwires stability after the implantation, the surgeon should apply a biocompatible glue (World Precision Instruments, LLC), on the bottom of the silicon portion. This will ensure mechanical stability.
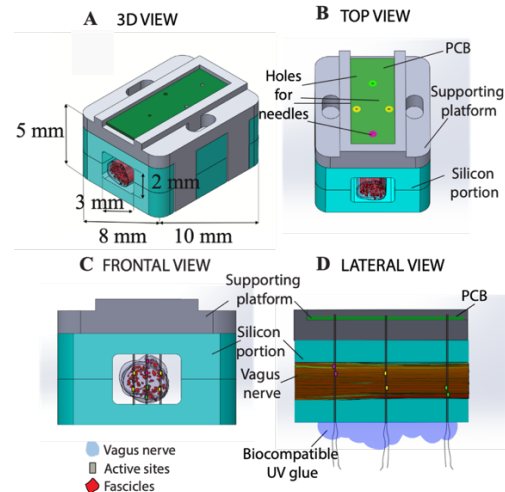

Fig. 2: A) 3D view of the electrode; B) top view of the electrode C) frontal view of the electrode; D) lateral view of the electrode

C. Electrochemical characterization

The ASs electrochemical characterization was performed in a custom-made faradaic cage before and after the PEDOT coating. The techniques used to characterize the electrochemical properties of the ASs were: electrochemical impedance spectroscopy (EIS), cyclic voltammetry (CV) and voltage transient measurements (VTm), as described by [17].

EIS, CV, and VTm were performed in a standard phosphate buffer solution (PBS), using a Gamry Reference 600 (Gamry Instruments, US) in a three-electrode configuration. The AS of the microwire was considered to be the working electrode. A large ($25x50mm^2$) Pt grid was used as a counter electrode and an Ag/AgCl electrode (Merck, USA) as a reference electrode.

A custom Matlab (Mathworks, USA) algorithm was developed to analyze data obtained from these measures. Values of impedance, cathodal charge storage capacity (CSCc) and maximum injectable charge (Qinj) were obtained with the algorithm.

III. RESULTS

The VN 3D model was developed based on the histology of a real nerve and it fits properly in the electrode (Fig 2).

The electrode dimensions are 8mm (width), 5mm (height) and 10mm (length) (Fig.2A). The hole between the silicon portions is 3mm large and 2mm long.

Data collected from the electrochemical measures are shown in Tab. 1. As expected, the PEDOT coating decreased the ASs impedance while increased the CSCc and Q-inj.

Parameter	No PEDOT coating	With PEDOT coating
Impedance (kΩ)	64.5 ± 16.24	1.70 ± 0.40
CSCc (mC/cm^2)	6.60 ± 1.45	28.0 ± 7.58
Q-inj (mC/cm^2)	0.14 ± 0.03	0.74 ± 0.30

Tab. 1: Statistical analysis of EIS, CV and VTm measurements before and after PEDOT coating.

IV. DISCUSSION

Here we described the design for the V-QPINE. The Q-PINE was successfully adapted for the implantation in the porcine VN. The estimated electrochemical parameters were similar to the Q-PINE suggesting the V-QPINE correct working.

The electrochemical parameters low standard deviation suggests high reliability of the coating procedure. EIS measurements suggest good recording properties since the PEDOT coated Pt/Ir wires showed a low impedance. Literature studies reported 5kΩ impedance for PEDOT coated electrodes [18], [19]. We obtained lower impedance values, reported as 1.7kΩ. CV and VTm measurements confirmed similar de-insulated properties of the Pt/Ir wires compared with the ones reported by Venkatraman [20]. The latter reported 8mC/cm^2 for CSCc and 0.13mC/cm^2 for Q-inj. Here we obtained a CSCc of 6.6mC/cm^2 and a Q-inj of 0.14mC/cm^2. This suggests a proper wire de-insulation. Castagnola et al. 2014 obtained a CSCc of 123 mC/cm^2 and a Q-inj of 2.92 mC/cm^2 for PEDOT coated Pt/Ir wires [19]. We obtained a lower increase of conduction properties with the PEDOT coating. The CSCc and Q-inj we reported were 28mC/cm^2 and 0.74mC/cm^2 respectively. This result in lower electrode stimulation capacity. An insufficient deposition charge or too short deposition time could be the reason. However, the electrochemical parameters are strictly dependent on the electrochemical setup, ASs shape and microwire material. The high variability in literature prevents proper comparisons.

The ASs were widely distributed throughout the nerve's sections. This should allow the recording of neural signals with a higher SNR and the selective stimulation of neural fibers. As for the Q-PINE, the silicone fixating portion will isolate the signal from surrounding noises, acting as an external shielding as suggested in Sadeghlo study [21].

The electrode is ready to be assembled and successively implanted. *In vivo* testing will be performed to demonstrate its neural selectivity and recording capacities. Physiological parameters will be monitored (e.g. heart rate) during the porcine VN recording and stimulation. The electrochemical characterization of post-surgery electrodes will show how stable the electrical coating is. If successful, the V-QPINE could close the feedback loop to control autonomic reflexes. An autoregulated system could allow patients suffering from chronic diseases to have a more regulated life.

ACKNOWLEDGMENT

REFERENCES

[1] Y. Kim and M. I. Romero-Ortega, "Material considerations for peripheral nerve interfacing," *MRS Bull.*, vol. 37, no. 6, pp. 573–580, Jun. 2012, doi: 10.1557/mrs.2012.99.
[2] "Heart Disease and Stroke Statistics—2019 Update: A Report From the American Heart Association," p. 473.
[3] "WHO | 2. Background," *WHO*. https://www.who.int/nutrition/topics/2_background/en/
[4] D. T. T. Plachta, N. Espinosa, M. Gierthmuehlen, O. Cota, T. C. Herrera, and T. Stieglitz, "Detection of baroreceptor activity in rat vagal nerve recording using a multi-channel cuff-electrode and real-time coherent averaging," in *2012 Annual International Conference of the IEEE Engineering in Medicine and Biology Society*, San Diego, CA, Aug. 2012, pp. 3416–3419, doi: 10.1109/EMBC.2012.6346699.
[5] "Adverse Effects of ²-Blocker Therapy for Patients With Heart Failure: A Quantitative Overview of Randomized Trials," *ARCH INTERN MED*, vol. 164, p. 6, 2004.
[6] R. Câmara and C. J. Griessenauer, "Chapter 27 - Anatomy of the Vagus Nerve," in *Nerves and Nerve Injuries*, R. S. Tubbs, E. Rizk, M. M. Shoja, M. Loukas, N. Barbaro, and R. J. Spinner, Eds. San Diego: Academic Press, 2015, pp. 385–397.
[7] L. K. McCorry, "Physiology of the Autonomic Nervous System," *Am. J. Pharm. Educ.*, p. 11.
[8] C. M. Noller, Y. A. Levine, T. M. Urakov, J. P. Aronson, and M. S. Nash, "Vagus Nerve Stimulation in Rodent Models: An Overview of Technical Considerations," *Front. Neurosci.*, vol. 13, p. 911, Sep. 2019, doi: 10.3389/fnins.2019.00911.
[9] S. Breit, A. Kupferberg, G. Rogler, and G. Hasler, "Vagus Nerve as Modulator of the Brain–Gut Axis in Psychiatric and Inflammatory Disorders," *Front. Psychiatry*, vol. 9, p. 44, Mar. 2018, doi: 10.3389/fpsyt.2018.00044.
[10] T. P. Zanos, "Recording and Decoding of Vagal Neural Signals Related to Changes in Physiological Parameters and Biomarkers of Disease," *Cold Spring Harb. Perspect. Med.*, p. a034157, Jan. 2019, doi: 10.1101/cshperspect.a034157.
[11] D. Guiraud *et al.*, "Vagus nerve stimulation: state of the art of stimulation and recording strategies to address autonomic function neuromodulation," *J. Neural Eng.*, vol. 13, no. 4, p. 041002, Aug. 2016, doi: 10.1088/1741-2560/13/4/041002.
[12] T. P. Zanos *et al.*, "Identification of cytokine-specific sensory neural signals by decoding murine vagus nerve activity," *Proc. Natl. Acad. Sci.*, vol. 115, no. 21, pp. E4843–E4852, May 2018, doi: 10.1073/pnas.1719083115.
[13] C. Sevcencu, T. N. Nielsen, B. Kjaergaard, and J. J. Struijk, "A Respiratory Marker Derived From Left Vagus Nerve Signals Recorded With Implantable Cuff Electrodes: A LEFT VAGUS NERVE RESPIRATORY MARKER," *Neuromodulation Technol. Neural Interface*, vol. 21, no. 3, pp. 269–275, Apr. 2018, doi: 10.1111/ner.12630.
[14] G. A. McCallum *et al.*, "Chronic interfacing with the autonomic nervous system using carbon nanotube (CNT) yarn electrodes," *Sci. Rep.*, vol. 7, no. 1, p. 11723, Dec. 2017, doi: 10.1038/s41598-017-10639-w.
[15] X. Navarro, T. B. Krueger, N. Lago, S. Micera, T. Stieglitz, and P. Dario, "A critical review of interfaces with the peripheral nervous system for the control of neuroprostheses and hybrid bionic systems," *J. Peripher. Nerv. Syst.*, vol. 10, no. 3, pp. 229–258, Sep. 2005, doi: 10.1111/j.1085-9489.2005.10303.x.
[16] I. Strauss *et al.*, "Floating array of intrafascicular soft electrodes to interface with the peripheral nerve," p. 3, 2018.
[17] S. Wilks, "Poly(3,4-ethylene dioxythiophene) (PEDOT) as a micro-neural interface material for electrostimulation," *Front. Neuroengineering*, vol. 2, 2009, doi: 10.3389/neuro.16.007.2009.
[18] S. Venkatraman *et al.*, "In vitro and in vivo evaluation of PEDOT microelectrodes for neural stimulation and recording," *IEEE Trans. Neural Syst. Rehabil. Eng. Publ. IEEE Eng. Med. Biol. Soc.*, vol. 19, no. 3, pp. 307–316, Jun. 2011, doi: 10.1109/TNSRE.2011.2109399.
[19] V. Castagnola, C. Bayon, E. Descamps, and C. Bergaud, "Morphology and conductivity of PEDOT layers produced by different electrochemical routes," *Synth. Met.*, vol. 189, pp. 7–16, Mar. 2014, doi: 10.1016/j.synthmet.2013.12.013.
[20] S. Venkatraman *et al.*, "In Vitro and In Vivo Evaluation of PEDOT Microelectrodes for Neural Stimulation and Recording," *IEEE Trans. Neural Syst. Rehabil. Eng.*, vol. 19, no. 3, pp. 307–316, Jun. 2011, doi: 10.1109/TNSRE.2011.2109399.
[21] B. Sadeghlo, "Design of a Peripheral Nerve Electrode for Improved Neural Recording of the Cervical Vagus Nerve," p. 60.

Detecting the neural processes of lie generation with low-cost EEG: a preliminary study

D. Garofalo[1], F.D. Nota[1], F. Zoleo[1], F. Bardozzo[1], M. Delli Priscoli[1], R. Tagliaferri[1], F. Esposito[1]

[1] *University of Salerno*

Abstract—Lying and being deceptive is a common and costly behaviour among human beings which has been studied from different perspectives and with a range of different protocols, with the aim of bringing to light the physiological mechanisms accompanying lie generation. The goal of this preliminary study was to investigate the feasibility of lie detection using a portable low cost device (Muse 2016, InteraXon Inc.) . EEG was recorded from 4 electrode sites (AF7, AF8, TP9, TP10) during a modified version of the Guilty Knowledge Test in 39 subjects. Joint time-frequency analysis revealed significant differences between deceptive and truthful responses. These differences were detected in three distinct time windows and covered the whole alpha band. The first time window well corresponds to the P300 component and highlights a neural desynchronization during the process of lie generation; the second window highlights an alpha synchronization; the third window highlights a neural synchronization covering also part of the low beta and high theta bands and reflects the variability in response times. These preliminary results indicate that the Muse device is potentially capable of detecting neural processes involved in human lie generation and could be possibly used for fast and low cost experimenting of lie detection systems outside laboratory environments. Moreover, the data coming from this exploratory analysis could be exploited in future studies by artificial intelligence techniques with the purpose of automatically detect guilty individuals.

Keywords—EEG, lie-detection, low-cost, GKT.

I. INTRODUCTION

Lie detection is a research area that, in the past few decades, has found many important applications in the legal, social and clinical fields [1]–[3]. The advantage of using EEG to measure the physiological responses associated with lie generation cognitive processes resides in the fact that it is way more difficult, sometimes impossible, to fake a cognitive process than a more peripheral physiological response. The most common protocol in lie detection is the Concealed Information Test (CIT) [4], usually referred to as the Guilty Knowledge Test (GKT) [5]–[7]. In the last decade this protocol has been used largely in Japan, while in other countries such as Lithuania, the possibility of adoption is under discussion; however, it is not considered legally valid in most countries. The GKT assumes that a guilty person possesses critical information known only to the people involved in the crime; this critical information is exploited in the method by presenting it to the subject as a series of rare stimuli (probes) embedded into a longer series of irrelevant stimuli. Among these, some specific stimuli (targets) are similar to the probes in that they elicit a unique response of the subjects, albeit these are only needed as an attention holder. This experimental design is a variant of the odd-ball paradigm which is commonly used in the EEG research. Particularly, it has been shown that a P300 event-related potential (ERP) response is elicited to infrequently presented probe or target stimuli embedded within frequently occurring task-irrelevant items [8], [9]. Until recently, these kinds of experiments have always been conducted in laboratory due to machinery not suited for outdoor experiments. Thanks to the development of dry electrodes [10], EEG technology has become portable and many new low-cost devices are being built every year and brought out of laboratory environment [11]–[13], with some of them showing good results in detecting P300 components [14]. The aim of this paper is to show how a modern portable low-cost EEG device could be used to measure some neural processes involved in human lie generation and therefore potentially suitable for a lie-detection system. ERP and event-related spectral perturbation (ERSP) analyses have been conducted to evaluate the statistical significance of the differences between responses measured in truth and lie trials. The proposed protocol for this investigation is the modified GKT, which is based on a card game similar to others adopted in literature [15]–[17]. The goal of the modified GKT is to minimize the emotional involvement of a subject [18]. In this work, experiments have been conducted in realistic environments to enable a fast and easy collection of EEG data. The low cost EEG device used is the Muse device that costs more than 100 times less than a medical device; one study compared it with an ActiChamp system and showed that Muse was sensible enough to conduct ERP analysis. [19].

II. MATERIALS AND METHODS

A. Participants and settings

The experiment involved 39 healthy subjects (7 females, 37 right-handed) with no history of mental disorder, with ages ranging from 17 to 62 and a mean age of 31.3 . Environment settings included parks, university classrooms and private houses. Before every experiment, sufficiently isolated places were identified to minimize distractions for the subjects.

B. Experimental protocol

Before the experiment, participants were instructed to lie during the card game in such a way that it would not have been possible to discover a secret card by simply analyzing the behavioral responses. The card game was implemented on an Android smartphone. A random card (probe) was initially shown to the subject who was asked to keep this card secret in memory. A series of 39 random cards appeared on the screen of a smartphone with an inter stimulus of 2 s; the subject

was instructed to answer "Yes" or "No" to the (implicit) question about the possible matching between the displayed card and the probe card by pressing the left or right button on a smartphone screen. As participants were asked to lie during the game, the suggested strategy was that they had to press "No" when the secret card occurred (probe trial) and "Yes" when a different card, freely chosen by them during the game, occurred (target trial). Otherwise, they had to press "No" to the occurrence of all other irrelevant cards (excluding the chosen target). As an additional attention control, at the end of each round, the probe, the target and one irrelevant card were shown to the participants who were asked to indicate the probe. Every subject did a first partial test without EEG recording, in order to understand the game mechanics. Probe and target cards randomly appeared more than once (min 1 max 4) during the experiment, with an average of 3.5 probes, 3.5 targets and 32 irrelevant stimuli. Participants did a minimum of 3 recorded experiment repetitions and a maximum of 5.

C. EEG Data Acquisition and pre-processing

The InteraXon's Muse 2016 headset system has a sampling rate of 256 Hz and five electrodes: three Ag electrodes are located analogous to Fpz, used as reference electrode, AF7 and AF8 and two additional electrodes made of conductive rubber, are located at TP9 and TP10. To stream the data from the headband, the Muse Direct application was running in background on an Android smartphone, while, on the same device, the card game application was executed in foreground. MATLAB's toolbox EEGLAB [20] has been used for the pre-processing and the statistical analysis of the EEG traces. Data were high pass filtered at 0.1 Hz and baseline corrected. Noise was removed at 50Hz with CleanLine, an EEGLAB plugin which adaptively estimates and removes sinusoidal artefacts. Excessively noisy trials were then removed by visual inspection. Lastly, 4 seconds epochs time locked to the stimulus presentation were extracted from single trials with 1 s of pre-stimulus baseline.

D. Exploratory analysis

The analysis has been made using EEGLAB and MATLAB. After the pre-processing steps, the trials have been divided into two categories: Truth and Lie. "Truth" groups all the irrelevant responses, while "Lie" groups probes and targets. The statistical analysis has been conducted using permutation statistics with 2000 permutations. All the trials in each of the two groups have been averaged and baseline corrected [-200 ms 0 ms] and then compared by using a paired t-test. To visually inspect the ERPs, ERP images were generated (Figure 2). ERP-image plots are 2-D transforms of epoched data expressed as 2-D images in which data epochs are first sorted along some relevant dimension (e.g. subject reaction time) and then smoothed (across adjacent trials and time points) and color-coded. The ERSP analysis has also been performed to analyse the EEG responses in the time-frequency domain (Figure 3). In EEGLAB, Morlet wavelets were used with the default parameters (3 cycles, 0.5). Namely, the
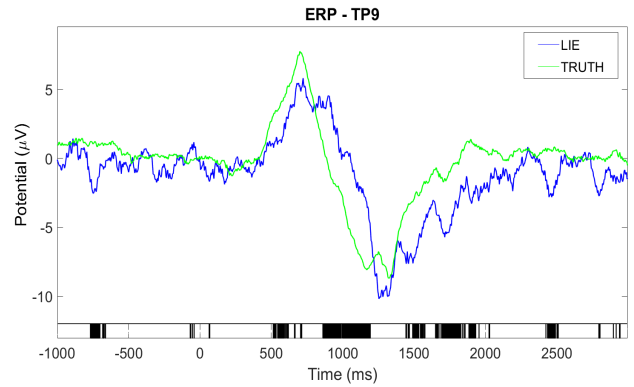

Fig. 1: Superimposed inter-subject grand average of lie (blue) and truth (green) trials. Black stripes indicate intervals of statistically significant (p<0.05) differences between the two conditions.
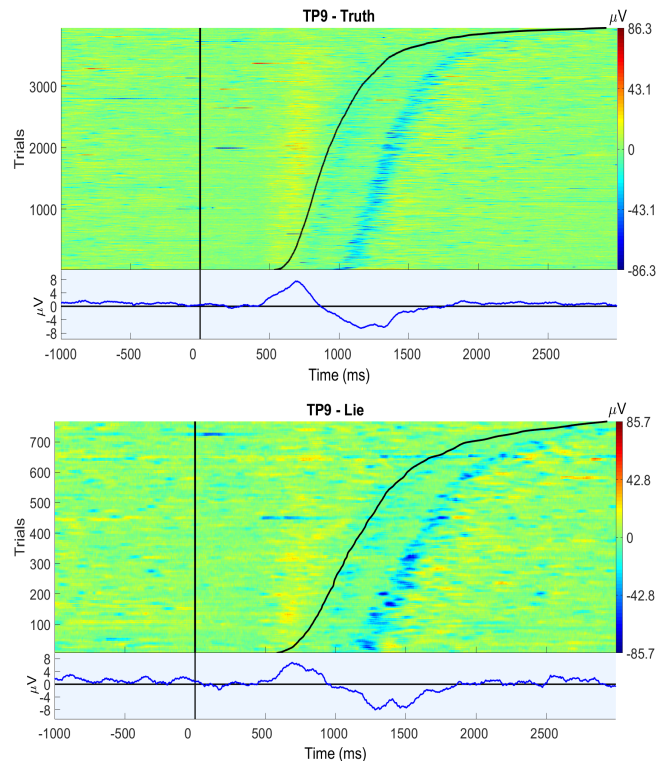

Fig. 2: ERP-image plots for Truth (upper) and Lie (bottom) trials. Trials are vertically stacked after being sorted by reaction times. The black curve denotes the moment in which subjects pressed the response button: this is visibly slower in Lie trials.

number of cycles in the wavelets was increased from lower to higher frequencies reaching half the number of cycles in the equivalent fast Fourier transform (FFT) window at its highest frequency.

III. RESULTS AND DISCUSSION

The most statistically significant results were obtained from the analysis of the electrode TP9. Although the electrode is on the left, which is close to the region controlling language, this might be also related to the fact that most subjects were
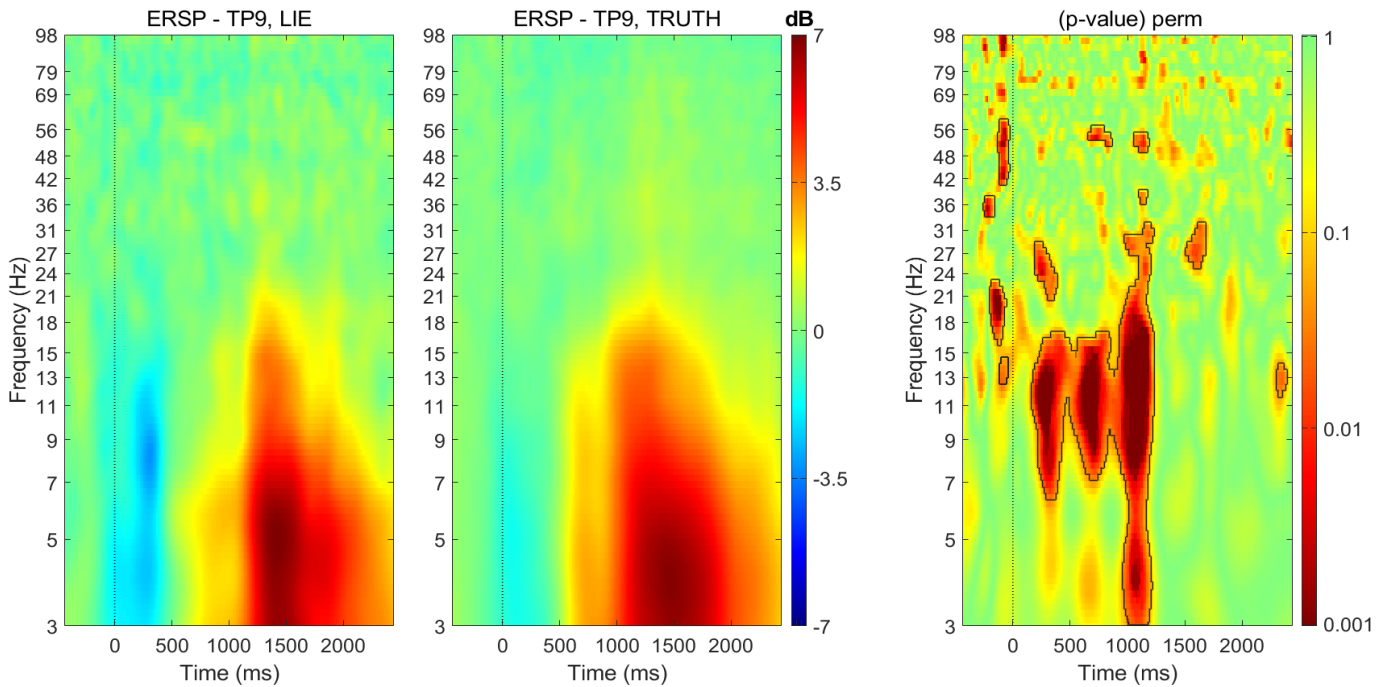
Fig. 3: ERSP analysis. Time-frequency plots of averaged ERSP responses from lie (left) and truth (center) trials. Time-frequency plot of the p-value for the differences between lie and truth trials (right) obtained with permutation testing. Statistically significant regions(p<0.05) are marked with a black line.

right-handed. In Figure 1, a positive peak is visible in the ERP response, starting at 500 ms and a subsequent negative peak at 1000 ms. The black bars under the time axis denote statistically significant differences, with a p-value less than 0.05, in the windows 500-600 ms and ~900-1200 ms. In Figure 2 the impact of the response times is even more evident. As shown in [21], [22], response times for telling a lie are slower. This clarifies the presence of the significant statistical difference seen before between 900-1200 ms as being the difference in response times.

The results of the ERSP analysis are shown in Figure 3. Three main time windows exhibited statistically significant differences between lie and truth responses (p<0.05); these differences are located respectively around 300 ms, 500 ms, 1000 ms and cover the whole alpha band (~7.5-15 Hz) and part of the low beta band. As lies almost certainly involve inhibitory neural processes, the observed changes in the alpha synchronization, especially in the two later time windows, could be related to the fact that alpha is often associated with inhibitory neural processes [23]. On the other hand, the earlier time window, around 300 ms, denotes a desynchronization response during the process of lying, thereby, given also a slight trend towards lower frequencies (theta rhythm), this is probably associated with the additional neural cost of telling a lie [24], [25]. This earlier response was not visible in the time domain. The second time-frequency window, around 500 ms, comes in conjunction with the positive peak in the time domain. As already observed by [17], the absence of a prominent P300 response could be due to the modified GKT protocol. This 500 ms peak is possibly a late positive

component associated with working memory and recognition of old/new stimuli [26]. The last time-frequency window, around 1000 ms, reflects the response times of the subjects and has a wider spectrum range respect to the first two. A preliminary attempt to distinguish between Lie and Truth classes with machine learning techniques has been performed using a Random Forest model. The input for training the model was the concatenation of the epoched time series (3 s epoch starting from stimulus onset) and their spectra (0-128 Hz) for each electrode. The best preliminary result obtained was a mean prediction accuracy of 66 percent on the test set. The mean accuracy has been obtained by applying k-fold cross validation (k=5).

IV. LIMITATIONS

Although this study is one of the few in Lie Detection that uses measurements within the wavelet domain, it does have some limitations. The first is the lack of midline electrodes, as it is well known that the P300 has a centro-parietal scalp distribution with its maximum over midline scalp sites [27]. The second important limitation is the intra and inter subject variability of the late positive response: all subjects showed this response but with slightly different latencies. This could probably be the reason why the first attempts with machine learning approaches on the dataset of this study did not bring good results, as also happened with the use of wavelet entropy [28]. The use of other wavelet features, such as wavelet entropy and coherence [28]–[30], has shown promising results in the detection of lies in recent years, therefore it could be further investigated as a support for the classification process.

V. CONCLUSION

The results of this study suggest that the Muse device could be sensitive to the effects of neural processes associated with lie generation in non standard laboratory conditions. This promotes the usage of the Muse device in portable (out of lab) applications where both ERP and ERSP measures represent an useful readout of complex cognitive processes such as lie generation. Future works could analyse the impact that different environment settings have on the experiment; moreover, a deeper systematic study should be conducted to understand the feasibility of an automatic lie detection process. With this aim artificial intelligence techniques, relying on the ERP/ERSP features illustrated in the present work, will be explored.

REFERENCES

[1] M. Gamer and S. Berti. Task relevance and recognition of concealed information have different influences on electrodermal activity and event-related brain potentials. *Psychophysiology*, 47(2):355–364, 2010.

[2] W. Ambach, S. Bursch, R. Stark, and D. Vaitl. A concealed information test with multimodal measurement. *International Journal of Psychophysiology*, 75(3):258–267, 2010.

[3] A. Ito, N. Abe, T. Fujii, A. Ueno, Y. Koseki, R. Hashimoto, S. Mugikura, S. Takahashi, and E. Mori. The role of the dorsolateral prefrontal cortex in deception when remembering neutral and emotional events. *Neuroscience research*, 69(2):121–128, 2011.

[4] D.T. Lykken. The GSR in the detection of guilt. *Journal of Applied Psychology*, 43(6):385, 1959.

[5] B. Verschuere, G. Ben-Shakhar, and E. Meijer. *Memory detection: Theory and application of the Concealed Information Test*. Cambridge University Press, 2011.

[6] E.H. Meijer, N.K. Selle, L. Elber, and G. Ben-Shakhar. Memory detection with the concealed information test: A meta analysis of skin conductance, respiration, heart rate, and p300 data. *Psychophysiology*, 51(9):879–904, 2014.

[7] J.P. Rosenfeld, G. Ben-Shakhar, and G. Ganis. Physiologically based methods of concealed memory detection. *Memory and law*, 2012.

[8] J.P. Rosenfeld. Event-related potentials in the detection of deception. handbook of polygraph testing, 2002.

[9] J.P. Rosenfeld. P300 in detecting concealed information. *Memory detection: Theory and application of the Concealed Information Test*, pages 63–89, 2011.

[10] L. Liao, C. Lin, K. McDowell, A.E. Wickenden, K. Gramann, T. Jung, L. Ko, and J. Chang. Biosensor technologies for augmented brain–computer interfaces in the next decades. *Proceedings of the IEEE*, 100(Special Centennial Issue):1553–1566, 2012.

[11] M.L. Pietto, M. Gatti, F. Raimondo, S.J. Lipina, and J.E. Kamienkowski. Electrophysiological approaches in the study of cognitive development outside the lab. *PloS one*, 13(11):e0206983, 2018.

[12] S. Debener, F. Minow, R. Emkes, K. Gandras, and M. De Vos. How about taking a low-cost, small, and wireless EEG for a walk? *Psychophysiology*, 49(11):1617–1621, 2012.

[13] J.WP Kuziek, A. Shienh, and K.E. Mathewson. Transitioning EEG experiments away from the laboratory using a raspberry pi 2. *Journal of neuroscience methods*, 277:75–82, 2017.

[14] A.F. Pérez-Vidal, C.D. Garcia-Beltran, A. Martínez-Sibaja, and R. Posada-Gómez. Use of the stockwell transform in the detection of p300 evoked potentials with low-cost brain sensors. *Sensors*, 18(5):1483, 2018.

[15] Y. Marchand, P.C. Inglis-Assaff, and C.D. Lefebvre. Impact of stimulus similarity between the probe and the irrelevant items during a card-playing deception detection task: The "irrelevants" are not irrelevant. *Journal of clinical and experimental neuropsychology*, 35(7):686–701, 2013.

[16] A.C. Merzagora, M. Izzetoglu, S. Bunce, and B. Onaral. Time-domain analysis of EEG during guilty knowledge test: Investigation of epoch extraction criteria. In *2007 29th Annual International Conference of the IEEE Engineering in Medicine and Biology Society*, pages 1302–1305. IEEE, 2007.

[17] A.C. Merzagora, S. Bunce, M. Izzetoglu, and B. Onaral. Wavelet analysis for EEG feature extraction in deception detection. In *2006 International Conference of the IEEE Engineering in Medicine and Biology Society*, pages 2434–2437. IEEE, 2006.

[18] D.T. Lykken. Why (some) americans believe in the lie detector while others believe in the guilty knowledge test. *Integrative Physiological and Behavioral Science*, 26(3):214–222, 1991.

[19] O.E. Krigolson, C. Williams, A. Norton, C.D. Hassall, and F.L. Colino. Choosing muse: Validation of a low-cost, portable EEG system for ERP research. *Frontiers in neuroscience*, 11:109, 2017.

[20] UC San Diego SSCN. Eeglab. https://sccn.ucsd.edu/eeglab/index.php. Accessed: 2020-01-17.

[21] H. Gibbons, R. Schnuerch, C. Wittinghofer, A. Armbrecht, and J. Stahl. Detection of deception: Event–related potential markers of attention and cognitive control during intentional false responses. *Psychophysiology*, 55(6):e13047, 2018.

[22] J. Olson, J.P. Rosenfeld, T. Kim, and E. Perrault. The effect of countermeasures against the reaction time based concealed information test on the p300 index of knowledge recognition: A combined rt and p300–based test. *International Journal of Psychophysiology*, 134:9–14, 2018.

[23] W. Klimesch, P. Sauseng, and S. Hanslmayr. EEG alpha oscillations: the inhibition–timing hypothesis. *Brain research reviews*, 53(1):63–88, 2007.

[24] K. Suchotzki, G. Crombez, F.TY Smulders, E. Meijer, and B. Verschuere. The cognitive mechanisms underlying deception: An event-related potential study. *International Journal of Psychophysiology*, 95(3):395–405, 2015.

[25] Y. Lo and P. Tseng. Electrophysiological markers of working memory usage as an index for truth-based lies. *Cognitive, Affective, & Behavioral Neuroscience*, 18(6):1089–1104, 2018.

[26] D. Friedman and R. Johnson Jr. Event-related potential (ERP) studies of memory encoding and retrieval: a selective review. *Microscopy research and technique*, 51(1):6–28, 2000.

[27] R. Johnson Jr. On the neural generators of the p300 component of the event–related potential. *Psychophysiology*, 30(1):90–97, 1993.

[28] J. Gao, J. Song, Y. Yang, S. Yao, J. Guan, H. Si, H. Zhou, S. Ge, and P. Lin. Deception decreases brain complexity. *IEEE journal of biomedical and health informatics*, 23(1):164–174, 2018.

[29] J. Gao, Y. Yang, W. Huang, P. Lin, S. Ge, H. Zheng, L. Gu, H. Zhou, C. Li, and N. Rao. Exploring time–and frequency–dependent functional connectivity and brain networks during deception with single–trial event–related potentials. *Scientific reports*, 6:37065, 2016.

[30] S. Dodia, D.R. Edla, A. Bablani, D. Ramesh, and V. Kuppili. An efficient EEG based deceit identification test using wavelet packet transform and linear discriminant analysis. *Journal of neuroscience methods*, 314:31–40, 2019.

Electrospun ultrathin scaffold for Bruch's membrane regeneration in retinal tissue engineering

B. Belgio[1], G. Dubini[1], F. Boschetti[1], and S. Mantero[1]

[1] *Department of Chemistry, Materials, and Chemical Engineering "Giulio Natta", Politecnico di Milano, Milano, Italy*

Abstract— **Currently there are no retinal tissue engineered grafts for clinical applications. Our project aims at designing a functional retinal tissue that could be implanted in patients suffering from age-related macular degeneration. To this end we will apply 3D electrospun ultrathin scaffolds and characterize their mechanical and biological properties using suitable cells.**

Keywords—**Retina, Tissue engineering, Electrospinning, Ophthalmology.**

I. INTRODUCTION

RETINA is a complex multi-layered tissue that absorbs, modulates, and transmits visual stimuli from the external world to the brain.

The outer retina is composed of retinal pigment epithelium (RPE). The RPE consists in a monolayer of polarized pigment cells which collaborate closely with the adjacent photoreceptors in maintaining visual function. RPE cells perform important roles including absorption of stray light, phagocytosis of outer segment of photoreceptors, maintenance of blood-retinal barrier, secretion of growth factors, and nourishment of the retinal visual cells [1]. The RPE lies on Bruch's membrane (BM) that is a thin (2-4 µm), acellular, extracellular matrix located between the retina and the choroid. Thanks to its permeable nature, the BM regulates the diffusion of biomolecules, nutrients, oxygen, fluids and metabolic waste between the outer retina and the choroidal blood supply [2]. As a vessel wall of the choroid, another crucial function of the BM is structural. Indeed, it serves as physical support for intact and functional RPE formation [2]. A healthy RPE together with a normal BM are essential for maintaining survival, integrity, homoeostasis, and function of the adjacent photoreceptors, and thus vision.

The dysfunction or degeneration of RPE cells results in different types of retinal diseases such as age-related macular degeneration (AMD). AMD is the principal cause of blindness in the elderly worldwide, affecting globally about 30-50 million individuals [3]. AMD consists in a progressive degeneration of the central retina due to age-related changes in BM and in the RPE. Aberrant neovascularization characterizes the wet form of AMD, which is responsible for 90% of AMD-associated severe visual impairment [4]. Currently, periodic intravitreal injections of anti-vascular endothelial growth factor (anti-VEGF) drugs are the gold standard therapy in the management of wet-AMD [5]. However, these treatment protocols are unable to restore tissue functionality, are expensive, and may lead to adverse effects, such as chorioretinal atrophy [5]. Hence, new strategies are needed to alleviate the progression of, or to recover the lost vision associated with this disease.

Subretinal surgery with resection of changes in the BM and subsequent RPE cell replacement therapy is one of the most promising approaches to restore retinal function. However, the subretinal injection of suspended RPE cells can lead to lack of structural organization into monolayer, significant cell death, and retinal fibrosis [6]. In addition, the RPE malfunction is not the only challenge for treatment, as the BM is also compromised in AMD. In fact, the BM should provide a proper microenvironment to support cell attachment and survival while maintaining cell functionality over time. For this reason, it has been proposed that RPE cells can be transplanted on a proper scaffold that acts as a BM substitute supporting mechanically and physically cell attachment, cell proliferation, and formation of a functional intact monolayer [6].

Many research efforts have focused on developing a biocompatible prosthetic BM to reconstruct retinal tissue *in vitro* [6]. In most studies, 2-D membranes with a closed dense structure have been utilized as scaffold for RPE monolayers [7]-[9]. Nevertheless, such a structure is in contrast to the open fibrillar structure of a native BM and can prevent nutrient diffusion. Furthermore, cells accomplish their function in a three-dimensional (3D) environment that resembles their natural habitat [10]. Therefore, the ideal BM-like scaffold probably needs to be designed as a 3D fibrillar mesh.

Recently electrospinning has been suggested as a promising technique to fabricate RPE scaffold as it permits generating 3D nanofibrous network topographies that are highly permeable for solutes thus facilitating cell adhesion and proliferation [11]. Polycaprolactone (PCL), a biodegradable aliphatic polyester with high tensile and elongation properties, has been widely used for tissue engineering applications as it was approved by U.S. Food and Drug Administration (FDA) [1]. Electrospun PCL nanofibers have been demonstrated to support the growth and proliferation of retinal cells [1], [12]. However, PCL hydrophobicity and hence the lack of recognition sites for cell adhesion limit its use as prosthetic BM material. Previous studies showed that the blending of silk fibroin (SF) with PCL and other synthetic polymers, significantly improved cell adhesion due to SF good biocompatibility [12]-[13]. Compared to synthetic materials, silk degradation products (peptides) do not considerably affect the pH or osmolarity at the implantation site.

Consequently, the aim of this study was to design and develop an ultrathin nanofibrous electrospun membrane composed of *Bombyx mori* silk fibroin (BMSF) blended with polycaprolactone (PCL) that would closely mimic the natural fibrous architecture of the human BM.

II. Materials And Methods

A. Electrospinning

The polymer solutions with a concentration of 15% (wt/v) were prepared by dissolving *Bombyx mori* silk fibroin (BMSF, Crea) and Polycaprolactone (PCL, Sigma) with a weight ratio of 5:95 (BMSF/PCL) in 98% formic acid (Sigma). EF300 electrospinning system (SKE Research Equipment, Leonardino s.r.l.) was used to fabricate the BMSF and PCL nanofibrous membranes. A voltage of +18 kV was applied to the needle 15 cm distant from the surface of the grounded collector. The polymer solution was delivered at a flow rate of 1.3 ml/h. Electrospinning was performed at a constant temperature (33.5 °C) and a relative humidity of 22%.

B. Characterization of electrospun membranes

Membranes were subjected to an examination of their physico-chemical and mechanical properties including physical morphology, stress-strain relation, elasticity, and permeability. To investigate the morphology, scaffolds were sputter coated with gold and observed with a scanning electron microscopy (SEM, Stereoscan 360, Cambridge Instruments) at 10 kV. ImageJ software (National Institute of Health, USA) was used to determine the membrane thickness, the fibre diameter, and packing density. 20 random fibres were measured to calculate the average fibre diameter. The packing density, presented as a percentage, was computed by counting the number of the fibres across each image, multiplying this by the average fibre diameter and then dividing by the width of the image.

For the mechanical measurements, scaffolds were cut into 5 x 32 mm samples. A material testing machine (Synergie 200, MTS Systems) equipped with a 100 N loading cell was used for the tensile test. Displacement was applied at 0.1 mm/s. Samples were first preconditioned four times and then pulled to failure. Measurements were repeated five times. The same protocol was applied to hydrated samples, i.e. samples submerged in saline solution for 1 hour. Young's modulus was calculated by measuring the slope of the initial linear region of the stress-strain curve.

To estimate permeability, a custom-made apparatus was employed containing two stainless-steel cylinders, a polyethylene filter, an O-Ring, and a capillary. Briefly, after inserting the sample properly between the two cylinders, we applied a constant hydrostatic pressure to the sample and measured the fluid volume through the sample over time. We then calculated permeability using Darcy's law, as in Eq. (1).

$$k = \frac{\Delta V * \mu * h}{\Delta t * A * \Delta P} \qquad (1)$$

Where k is the permeability, $\Delta V/\Delta t$ is the fluid volume over time, h is the sample thickness, A is the flow area, and ΔP is the applied hydrostatic pressure. Four different values of pressure were applied to each sample. The measurements were repeated three times.

C. The culture of ARPE-19 cells

ARPE-19 cells, a human retinal pigment epithelium (RPE) cell line obtained from American Type Culture Collection (ATCC), were cultured with DMEM/F12 (ATCC) supplemented with 10% fetal bovine serum (FBS, ATCC), 1% 100 U/ml penicillin (Gibco[TM]), and 100 µg/ml streptomycin (Gibco[TM]). Medium was changed regularly every 3 days until confluence. Cells were cultured at 37 °C and 5% CO_2.

D. Biocompatibility

To investigate the *in vitro* biocompatibility of the BMSF/PCL scaffolds, a direct contact cytotoxicity test was carried out. Scaffolds were soaked in 75% ethanol for 6 h followed by washing three times with sterilized phosphate saline buffer (PBS, Gibco[TM]). The ARPE-19 were seeded on 6-well plates at a density of 20000 cells/cm^2 and cultured in direct contact with the electrospun membranes for 3 days. Changes in cell morphology and cell viability were assessed using a fluorescent microscope (Olympus IX70). For cell viability, cells were stained with Live/Dead assay (Invitrogen[TM]).

E. Statistical analysis

Results are presented as mean ± standard deviation (SD). Statistical analyses were performed using Graphpad Prism Version 8 (Graphpad Software). Differences were considered statistically significant if the *p*-value was less than 0.05.

III. Results

A. Scaffold characterization

In this study, the BMSF/PCL membranes were successfully produced by electrospinning and appeared to be uniform as shown in Figure 1 (Fig. 1).
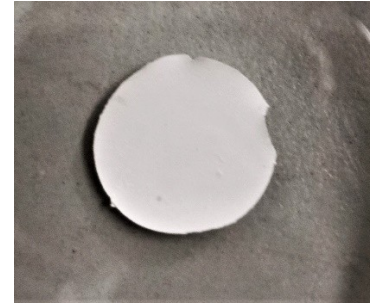

Fig. 1: Appearance of electrospun BMSF/PCL scaffolds.

The resulted scaffolds were constructed of randomly oriented fibres and thoroughly interconnected pore structures (Fig. 2). The electrospun membranes displayed a thickness of 44 µm, an average fibre diameter of 1217 ± 101 nm, and a fibre packing density of 63.76 ± 1.2%.
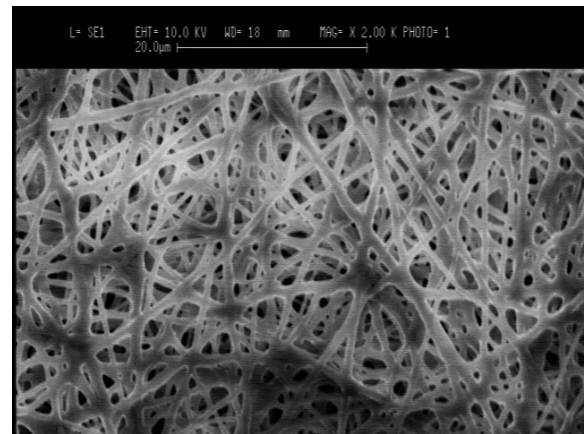

Fig. 2: Scanning electron microscopy images of electrospun BMSF/PCL scaffolds. Scale bar: 20 µm.

The mechanical properties of both hydrated and dry membranes were reflected by typical tensile stress-strain curves (Fig 3).
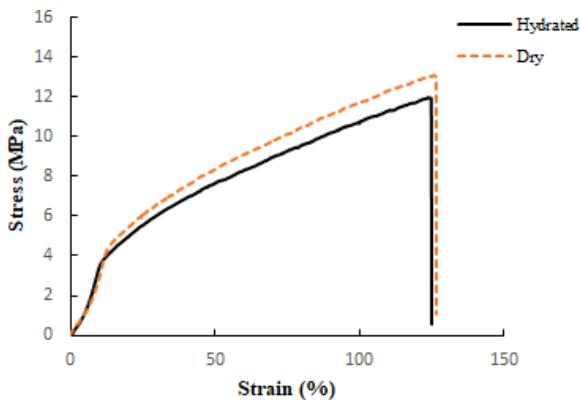

Fig. 3: Tensile stress versus strain curve of BMSF/PCL hydrated (black continuous line) and dry (dotted orange line) scaffolds.

The ultimate tensile strength of the dry membrane was 9.72 ± 2.47 MPa, with an ultimate strain of $100.4 \pm 31.6\%$ and a Young's modulus of 17.37 ± 1.99 MPa. The hydrated membrane had slightly higher values of ultimate tensile strength, ultimate strain and Young's modulus, of 10.234 ± 2.21 MPa, $118.6 \pm 25.9\%$ and 18.57 ± 4.47 MPa, respectively. No significant difference was found between mechanical properties of hydrated and dry scaffolds (Fig. 4).
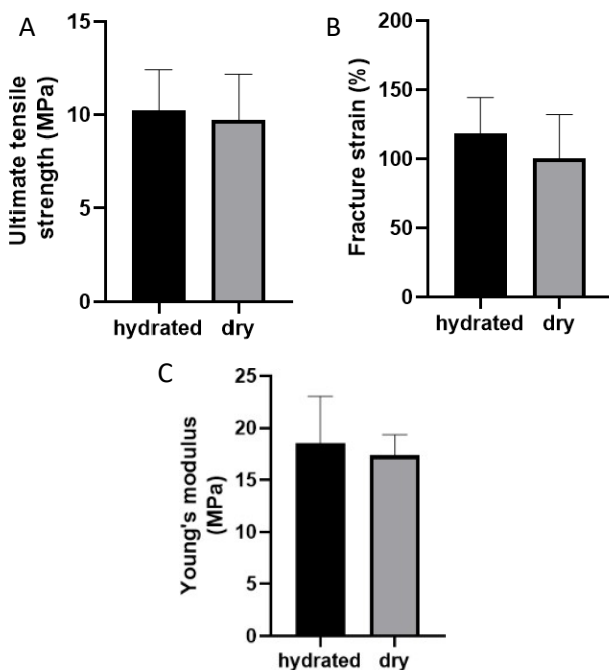
Fig. 4: **(A)** Ultimate tensile strength of hydrated (black column) and dry (grey column) scaffolds. **(B)** Fracture strain of hydrated (black column) and dry (grey column) scaffolds. **(C)** Young's modulus of hydrated (black column) and dry (grey column) scaffolds.

Membrane permeability was performed to assess how the fluid flows through the material. For instance, at a pressure of 3090 Pa the average permeability was $5.07 \times 10^{-18} \pm 1.99 \times 10^{-18}$ m^2.

Generally, the average permeability resulted to decrease with the increase of hydrostatic pressure ΔP (Fig. 5).
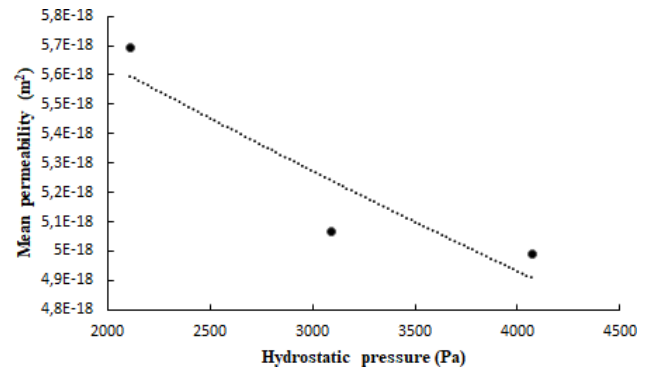
Fig. 5: Average permeability of BMSF/PCL scaffold versus hydrostatic pressure curve

B. Biocompatibility

We carried out preliminary tests to assess the scaffold biocompatibility *in vitro*. According to initial results (not shown) of these preliminary tests, ARPE-19 cells seemed to be viable after 3 days of direct contact with the retinal membranous scaffold. However, we will need to further investigate this hypothesis to confirm the scaffold suitability for retinal regeneration.

IV. DISCUSSION AND CONCLUSION

Impairment of the native RPE monolayer is a major pathologic feature of AMD. Transplantation of RPE with a carrier, instead of injections of cell suspension, seems to improve RPE survival, engraftment, and integration [13]. However, an ideal substrate for constructing a prosthetic BM with attached RPE cells has yet to be found. The perfect retinal scaffold should be thin enough to accommodate the subretinal space (5-90 µm), be permeable to allow biomolecules transfer, exhibit a non-linear stress/strain behavior with a Young's modulus of 6-14 MPa consistently with the native tissue, present an appropriate degradation time matched to synthesis of new extracellular matrix by cells, should favor cell adhesion, and maintain cell viability and normal function including the formation of a pigment epithelium [14].

In our study, the obtained scaffold showed structural and mechanical similarity to human BM, which has a random fibrillar network, a packing density of 48%, and a Young's modulus ranging from 6 to 14 MPa [11], [15]. In addition, we found out that scaffolds are suitable for cell culture and we are carrying out additional investigation with ARPE-19 cells in both static and dynamic conditions, as bioreactors support cell viability of 3D constructs by perfusion or diffusion system [16, 17]. However, to more closely imitate the BM, fibre diameters, membrane thickness, and the packing density need to be further reduced. The successful outcome of this study will inform the treatment of an optimal substrate as a basal support for RPE. Moreover, this work may lead to new studies where a second layer of photoreceptors can be bioprinted on the RPE.

V. ACKNOWLEDGMENT

REFERENCES

[1] P. Xiang, *et al*., "A novel Bruch's membrane-mimetic electrospun substrate scaffold for human retinal pigment epithelium cells," *Biomaterials*, vol. 35, pp. 9777-9788, September 2014.

[2] C. A. Curcio and M. Johnson, *Structure, function, and pathology of Bruch's membrane*, London: Elsevier, Inc., 2013, ch. 20.

[3] Colijn, Johanna M., *et al.*, "Prevalence of age-related macular degeneration in Europe," *Ophthalmology,* vol. 124, no. 12, 2017, pp. 1753–1763.

[4] N. C. Hunt, D. Hallam, V. Chichagova, D. H. Steel, and M. Lako, "The application of biomaterials to tissue engineering neural retina and retinal pigment epithelium," *Advanced Healthcare Materials*, vol. 7, 1800226, 2018.

[5] Fernández-Robredo, P., et al. "Current treatment limitations in age-related macular degeneration and future approaches based on cell therapy and tissue engineering." *Journal of Ophthalmology*, vol. 2014, pp. 1–13., January 2014.

[6] S. Royce Hynes and H. B. Lavik, "A tissue-engineered approach towards retinal repair: Scaffolds for cell transplantation to the subretinal space," Graefes Arch. Clin. Exp. Ophthalmol., vol. 248, pp. 763–778, February 2010.

[7] G. K. Srivastava, *et al.*, "Elastin-like recombinamers as substrates for retinal pigment epithelial cell growth," J Biomed Mater Res A, vol. 97, pp. 243–50, 2011.

[8] J. T. Lu, C. J. Lee, S. F. Bent, H. A. Fishman, and E. E. Sabelman, "Thin collagen film scaffolds for retinal epithelial cell culture," *Biomaterials*, vol. 28, pp.1486–94, 2007.

[9] E. Santos, R.M. Hernández, J. L. Pedraz, G. Orive, "Novel advances in the design of three-dimensional bio-scaffolds to control cell fate: translation from 2D to 3D," *Trends Biotechnol*, vol. 30, pp. 331–41, 2012.

[10] M. A. Asnaghi, *et al*., "Trends in biomedical engineering: focus on regenerative medicine," J Appl Biomater Biomech, vol. 9 no. 2, pp. 73-86, 2011.

[11] P. H. Warnke, *et al.* "Primordium of an artificial Bruch's membrane made of nanofibers for engineering of retinal pigment epithelium cell monolayers," *Acta Biomaterialia*, vol. 9, pp. 9414-9422, 2013.

[12] D. Zhang, et al., "Electrospun SF/PLCL nanofibrous membrane: a potential scaffold for retinal progenitor cell proliferation and differentiation", Scientific Reports, vol. 5, Article 14326, 2015.

[13] S. Popelka, *et al*. "A frame-supported ultrathin electrospun polymer membrane for transplantation of retinal pigment epithelial cells," *Biomedical Materials*, vol. 10, Article 045022, 2015.

[14] Y. S. E. Tan, P. J. Shi, C. Choo, A. Laude, and W. Y. Yeong, "Tissue engineering of retina and Bruch's membrane: a review of cells, materials, and processes," *Br J Ophthalmol*, vol. 102, pp. 1182–1187, 2018.

[15] W. H. Chan, *et al.* "Young's modulus of Bruch's membrane: Implications for AMD." *Investigative Ophthalmology & Visual Science*, Vol. 48, no. 13, pp. 2187, 2007.

[16] S. Mantero, N. Sadr, S. A. Riboldi, S. Lorenzoni, and F. M. Montevecchi, "A new electro-mechanical bioreactor for soft tissue engineering," *Journal of Applied Biomaterials & Biomechanics*, vol. 5 no. 2, pp. 107-116, 2007.

[17] L. Urbani, *et al.* "Multi-stage bioengineering of a layered oesophagus with in vitro expanded muscle and epithelial adult progenitors," *Nature Communications*, vol. 9, pp. 1-16, 2018.

Surface coated chitosan microbeads for the sustained release of drugs

P. Arnaldi[1], O. Monticelli[2], and L. Pastorino[1]

[1] *Department of Informatics, Bioengineering, Robotics and Systems Engineering, University of Genoa*
[2] *Department of Chemistry and Industrial Chemistry, University of Genoa*

Abstract - **The main objective of this work was to improve chitosan (CHI) microbeads drug release and degradation properties by the application of a poly-(styrene-co-maleic anhydride) (PSMA) surface coating. The effect of the coating on the surface properties of the CHI microbeads was characterized by means of FE-SEM analysis for the morphology and contact angle measurements for the wettability. Degradation tests in an enzymatic medium demonstrated the effectiveness of the treatment in terms of system protection. Cytotoxicity tests showed good cells compatibility, confirming the non-toxicity of the applied coating. Finally, drug release profiles in acidic conditions were analysed, demonstrating the potentiality of the PSMA/CHI system for sustained drug release applications.**

Keywords— **Chitosan, Poly-(styrene-co-maleic anhydride), Sustained Drug Release, Degradation.**

I. INTRODUCTION

Chitosan is undoubtly the most studied biopolymer of the 21st century cause of its unique features, including antimicrobial, non-toxicity and biocompatibility, which made it the perfect candidate for numerous bioapplications [1].

In particular, CHI resulted to have great potential as drug delivery carrier thanks to its mucoadhesiveness and a high charge density, improving the dissolution and the release of poorly soluble drugs [2]. The versatility of this polysaccharide has been exploited for several pharmaceutical applications, such as blood anticoagulants [3], ocular [4] and oral [5] drug delivery systems and wound healing [6]. Among all the drug delivery systems, nano and microparticles based ones gained great interest since they can be applied directly to the specific site, in various formulations [7]. For this reason, in this work we focused on the production and modification of chitosan microbeads as drugs carrier.

However, the use of chitosan is not without limitations and precautions due to its sensitivity to environmental conditions such as humidity, low pH media and the presence of enzymes capable to decompose its chains and speed up its degradation [8]. Another important limitation in the applicability of chitosan for pharmaceutical release is due to the "burst" release effect. In general, chemical crosslinking is applied in order to decrease the polymer degradation and tune the burst effect in drug release [9]. The benefits obtained from this type of treatment are often not enough to compensate the variation of the biological properties of the chitosan system brought by the crosslinker, which in some cases, like glutaraldehyde, could be cause of toxicity [10]. For this reason, the hypothesis on which we based our work was to realize chitosan particles by neutralization method using aerodynamically assisted jetting technique, i.e. avoiding the use of crosslinkers, and trying to confer the same properties as polymeric crosslinking, in terms of limiting the degradation of microbeads and the burst release of drugs, without changing the properties of the bulk polymer, through the application of a surface coating based on a biocompatible polymer. Moreover, another important effect of this approach is the possibility to vary the wettability of the polymer, characteristic that influence its response to bio-macromolecules.

Chitosan microbeads were surface covered with, poly-(styrene-co-maleic anhydride) (PSMA), a biocompatible polymer already used in numerous bioapplications [11],[12]. CHI microparticles were put in contact with a PSMA solution and the reaction between chitosan amino groups and maleic functionalities of PSMA was exploited to obtain an external coating. The characterization of the novel system was performed by FE-SEM and contact angle measurements, comparing all the results with the untreated samples. In order to evaluate the effect of the PSMA surface deposition on the biological properties of CHI, enzymatic degradation, cytotoxicity tests and the kinetic release of a model drug, were conducted.

II. MATERIALS AND METHODS

A. Materials

CHI medium molecular weight (75-85% deacetylated), acetic acid, ethanol, sodium hydroxide (NaOH), tetrahydrofuran (THF), citric acid, sodium phosphate dibasic and bovine serum albumin (BSA) were purchased from Sigma-Aldrich. PSMA (14% maleic content) was purchased from Nova Chemicals.

B. Production of Chitosan Microbeads

The preparation of Chitosan microbeads followed the procedure developed by Custódio et al. [13]. Briefly, a 1% w/v CHI solution was prepared by dissolving the polymer in a 0.1 M acetic acid aqueous solution. The obtained solution was extruded using a microencapsulation unit (Nisco Encapsulation Unit VAR J30) equipped with a conical nozzle (diameter of 0.25 mm). Gelation process was conducted collecting the generated microbeads into a neutralization solution (2% w/v NaOH dissolved in 60% v/v ethanol-distilled water solution) under continuous stirring for 45 min. Finally, CHI microbeads were centrifuged (1200 rpm for 5 min), neutralization solution was removed, and samples were washed, dispersed in distilled water and stored at 4 °C.

C. PSMA coating of CHI microbeads

CHI microbeads were dispersed in THF after water removal

and washed 3 times in the same solvent to assure no water content before being transferred in a three necked flask.

PSMA was dissolved in THF (0,5% w/v) and added dropwise to the flask. The reaction was conducted leaving the CHI microbeads in contact for 2 hours with the PSMA solution at 45 °C under continuous stirring. Afterwards, the suspension was centrifuged in order to remove the supernatant (1200 rpm for 5 minutes), and the obtained CHI/PSMA microbeads were subjected to 3 washing steps in distilled water.

D. Characaterization

FE-SEM micrographs (acquired by a Zeiss Supra 40 VP FE-SEM after sputter coating with carbon) were used to analyse the microbeads morphology. Contact angle tests (Basler as A780 contact angle analyser) were conducted on films to evaluate the effect of the PSMA surface coating on the wettability of CHI. Films were prepared by drop casting of a CHI solution (1% w/v). Afterwards, they were neutralized, washed with distilled water and left to dry overnight. PSMA-coated CHI films were obtained under the same conditions previously described for microbeads (paragraph C).

E. Enzymatic Degradation

Structure degradation of CHI and PSMA/CHI microbeads was tested by incubating for 21 days the samples in a PBS solution at physiological pH with a lysozyme concentration of 1.5 µg/ml. The degradation medium was refreshed every 4 days and optical contrast phase images were acquired by an inverted IX-51 Olympus microscope equipped with a DP70 digital camera (coupled with CPlan 10 N.A.) to analyze variations of the dimension and the shape of the samples.

F. Cytotoxicity Tests

Cell compatibility of microbeads was evaluated through an MTT based cell viability assay kit. Cells not exposed to samples were used as a blank control, while both CHI and PSMA/CHI microbeads were tested (experiments were carried out in triplicate).

MCF-7 cells (purchased from Interlab Cell Line Collection (ICLC) cell bank, San Martino Polyclinic Hospital Genova, Italy) were used in this study. Cells were cultured in Dulbecco's Modified Eagle's Medium (DMEM) supplemented with 10% v/v Fetal Bovine Serum (FBS) and 1% antibiotics, and incubated at 37 °C before being plated on a multi-well plate (2.5×10^5 cells/well) and exposed to the microbeads for 24 h (1.5×10^6 microbeads/well). MTT assay analysis was conducted with a UV/Vis Spectro-photometer (Agilent, Cary 60) at a wavelength of 565 nm.

G. Drug release in acidic medium

BSA protein was used as a model drug in order to evaluate the encapsulation efficiency of the microbeads and their release profiles. CHI microbeads were incubated in a BSA aqueous solution (0,5% w/v) at 37 °C overnight. Afterwards, CHI microbeads were centrifuged, the supernatant was collected, and the samples were rinsed with distilled water to remove the unloaded drugs. The protein content in the supernatant was evaluated by UV-vis spectroscopy referring to a previously established calibration curve of BSA dissolved in distilled water. All the measurements were conducted at 280 nm wavelength.

CHI microbeads Encapsulation Efficiency (EE) was obtained from Eq. (1).

$$EE(\%) = \frac{m_0 - m_s}{m_0} \cdot 100\% \qquad (1)$$

where m_0 is the BSA content in the loading solution and m_s is the amount of BSA in supernatant.

The BSA "post-loading" process was carried out on pure CHI microspheres. In order to evaluate the effect of the treatment on the release properties of the system, the protein-loaded microbeads were subjected to the same treatment as previously described (paragraph C). Citrate-Phosphate buffer solutions at pH=3 was prepared following the method developed by McIlvane [14] and used as release medium.

Release tests were performed at 37 °C by dispersing BSA-loaded CHI and PSMA/CHI microbeads in 12 ml of Citrate-Phosphate buffer solution. At fixed time steps (from 15 minutes to 300 minutes) 1 mL of release medium was withdrawn, to be spectrophotometrically analysed and replaced with the same volume of fresh buffer solution. Protein cumulative release (%) was obtained from the measurements of the absorbance of the withdrawn samples considering the dilution factor applied. The cumulative release tests were carried out in triplicate, reporting data as mean ± standard deviation (n = 3).

III. RESULTS

CHI microbeads surface morphology was analysed before and after the treatment with PSMA. FE-SEM micrographs showed clearly the deposition of the polymer on the surface of the beads through an external layer. The main observable effect of the treatment is the decrease of pores size (Fig. 1).
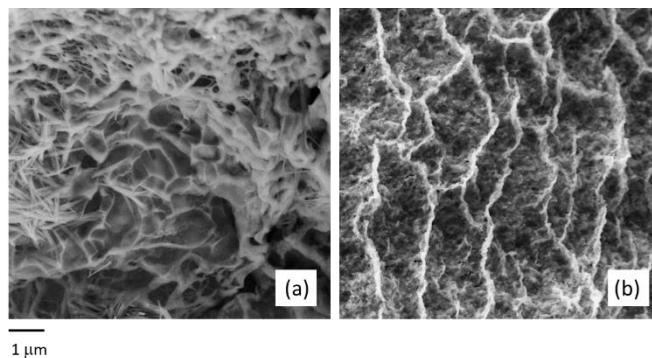

1 µm

Fig. 1: Surface SEM micrographs of CHI microbeads (a) and PSMA/CHI microbeads (b).

Contact angle measurements were conducted on both CHI and PSMA/CHI films.

TABLE I
CONTACT ANGLE MEASUREMENTS

Sample	Contact Angle [°]	Standard deviation
CHI	98,6	3,4
PSMA/CHI	88,7	3,1

The choice of using films instead of beads derived from the necessity to have an adequate system to analyse the solid-liquid interface angle after drop deposition. Measured data are reported in Table 1. The collected data showed that the surface bond with the PSMA led to an increase in the hydrophilicity of the chitosan-based system. This result is perfectly in line with the values reported in the literature for films based on pure PSMA [15], which has a contact angle of about 20° less than pure CHI ones [16].

To verify the degradation of the systems in physiological environment, CHI and PSMA/CHI microbeads were incubated for 21 days at 37 °C in a PBS lysozyme solution. Lysozyme was chosen because it is a common enzyme that can be found in the innate immune system [17] and is primarily responsible for in vivo degradation of CHI by the breakage of glycosidic bonds [18]. The effects of lysozyme on CHI and PSMA/CHI microbeads was analyzed by means of optical microscopy, comparing the morphology before and after the incubation in the degradation medium.
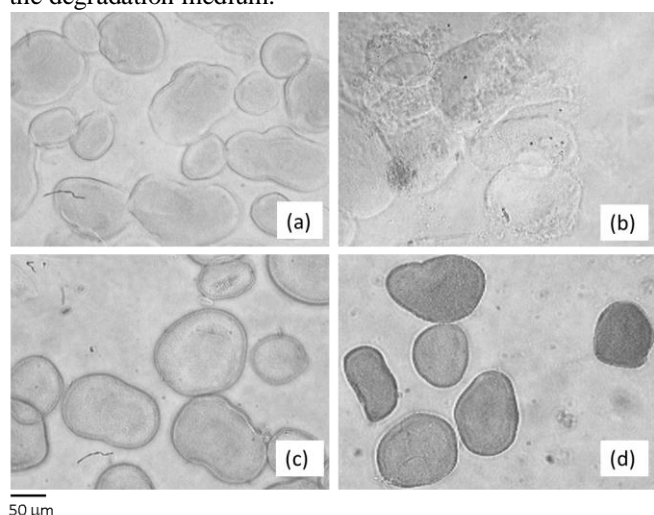
Fig. 2: Optical contrast phase micrographs of images of: (a) and (c) CHI and PSMA/CHI microbeads before incubation, (b) and (d) CHI and PSMA/CHI microbeads after 21 days in lysozyme solution.

As it can be observed in Fig. 2b, after 21 days in lysozyme solution, CHI microbeads lost their initial shape and gave rise to aggregates. Similar results have already been reported in previous studies [19].

The degradative effect of lysozyme is instead not observable regarding the samples coated with PSMA, as the beads have maintained their shape and structure for the whole time of the analysis conducted (Fig.2c-d). The use of PSMA as an external coating not only limits the diffusion of the lysozyme within the structure by reducing the porosity but in particular, since it is not subject to the degradation phenomenon of the lysozyme, it covers and minimizes the exposed surface of the matrix that the lysozyme can decompose.

Although biocompatibility properties of neat CHI and PSMA were already demonstrated [20],[21], cells viability tests were conducted in order to verify that the bond between the two polymers didn't lead to toxicity in the composite system. MCF-7 cells were subjected to exposure for 24 h to CHI and PSMA/CHI microbeads, to evaluate cytotoxicity by MTT assay. Cell viability values of 107±14% and 91±12% were obtained respectively for the CHI samples and the PSMA/CHI ones. The obtained values demonstrated that the coating procedure didn't affect cells viability, confirming the possibility of using the system developed for bioapplications.

Finally, to conclude the characterization of the composite microbeads, the drug loading and release properties were tested using BSA as model drug. Since a BSA "post-loading" process was used, the encapsulation efficiency was calculated on the pure CHI microbeads and was found to be 36,2±7,4%. The analysis of the beads release kinetics was carried out under acidic conditions. CHI microbeads showed a "burst" release mode in the first 15 minutes of incubation, releasing 68,6±3,2% of the encapsulated protein. "Burst" effect that was found to be significantly limited in PSMA/CHI microbeads, which released only 21,8±1,4% in the same time interval. This difference was maintained for the subsequent 5 hours in which cumulative release was tested. At the last time step the total amount of BSA released for the treated and untreated microbeads was 31,9±5,2% and 82,2±2,3% respectively. The data collected showed how the treatment can have a double action on the release properties of the system. The "burst" effect is probably reduced by the decrease in pore size, while an occurring interaction between PSMA and the protein may be responsible for the prolonged release effect.

IV. CONCLUSION

In this work, CHI microbeads were produced by neutralization-gelation method and subsequently coated by the application of a PSMA surface layer. The characterization results of the developed system, a marked resistance to the degrading action of enzymes and a release profile of a model drug in acidic medium considerably lower than the untreated system, suggested that this protective approach could be an effective method for fabricating chitosan-based drug carriers microbeads for oral sustained delivery applications.

REFERENCES

[1] D. Elieh-Ali-Komi & M. R. Hamblin. (2016). Chitin and chitosan: production and application of versatile biomedical nanomaterials. *International journal of advanced research*. 4.3, 411.

[2] N. Bhattarai, J. Gunn & M. Zhang. (2010). Chitosan-based hydrogels for controlled, localized drug delivery. *Advanced drug delivery reviews*. 62.1, 83-99.

[3] Y. Okamoto, R. Yano, K. Miyatake, I. Tomohiro, Y. Shigemasa & S. Minami. (2003). Effects of chitin and chitosan on blood coagulation. *Carbohydrate Polymers*. 53.3, 337-342.

[4] M. J. Alonso & A. Sánchez. (2003). The potential of chitosan in ocular drug delivery. *Journal of Pharmacy and Pharmacology*. 55.11, 1451-1463.

[5] K. Bowman & K. W. Leong. (2006). Chitosan nanoparticles for oral drug and gene delivery. *International journal of nanomedicine*. 1.2, 117.

[6] S. Ahmed & I. Saiqa. (2016). Chitosan based scaffolds and their applications in wound healing. *Achievements in the life sciences*. 10.1, 27-37.

[7] U. Garg, S. Chauhan, U. Nagaich, & N. Jain. (2019). Current advances in chitosan nanoparticles based drug delivery and targeting. *Advanced pharmaceutical bulletin*. 9.2, 195.

[8] E. Szymańska & K. Winnicka. (2015). Stability of chitosan - a challenge for pharmaceutical and biomedical applications. *Marine drugs*. 13.4, 1819-1846.

[9] A. Di Martino, P. Kucharczyk, Z. Capakova, P. Humpolicek & V. Sedlarik. (2017). Chitosan-based nanocomplexes for simultaneous loading, burst reduction and controlled release of doxorubicin and 5-fluorouracil, *Int. J. Biol. Macromol.* 102, 613–624.

[10] T. Banerjee, S. Mitra, A. Kumar Singh, R. Kumar Sharma & A. Maitra. (2002) Preparation, characterization and biodistribution of ultrafine chitosan nanoparticles. *Int. J. Pharm.*. 243, 93-105

[11] E. Dellacasa, M. Forouharshad, R. Rolandi, L. Pastorino & O. Monticelli. (2018). Poly (styrene-co-maleic anhydride) nanoparticles as protein carriers. *Materials Letters*. 220, 241-244.

[12] H. Singh, M.S. Jabbal, A. R. Ray & P. Vasudevan. (1984). Effect of anionic polymeric hydrogels on spermatozoa motility. *Biomaterials*. 5, 307-309.

[13] C. A. Custódio, V. E. Santo, M. B. Oliveira, M. E. Gomes, R. L. Reis & J. F. Mano. (2014). Functionalized microparticles producing scaffolds in combination with cells. *Advanced Functional Materials*. 24.10, 1391-1400.

[14] T. C. McIlvaine. (1921). A buffer solution for colorimetric comparison. *Journal of Biological Chemistry*. 49.1, 183-186.

[15] O. Monticelli, A. Fina, E. S. Cozza, M. Prato & V. Bruzzo. (2011). POSS vapor phase grafting: a novel method to modify polymer films. *J. Mater. Chem.*. 21, 18049–18054

[16] Y. Luo, X. Pan, Y. Ling, X. Wang & R. Su. (2014). Facile fabrication of chitosan active film with xylan via direct immersion. *Cellulose*. 21, 1873–1883.

[17] S. A. Ragland & K. C. Alison. (2017). From bacterial killing to immune modulation: recent insights into the functions of lysozyme. *PLoS pathogens*. 13.9.

[18] R. J. Nordtveit, K. M. Vårum, & O. Smidsrød. (1996). Degradation of partially N-acetylated chitosans with hen egg white and human lysozyme. *Carbohydrate polymers*. 29.2, 163-167.

[19] Z. Peng, Z. Li, F. Zhang, & X. Peng. (2014). In-Vitro Degradation and Cytotoxicity of Gelatin/Chitosan Microparticles for Drug Controlled Release. *Journal of Macromolecular Science, Part A*. 51.8, 646-652.

[20] P. J. VandeVord, H. W. Matthew, S. P. DeSilva, L. Mayton, B. Wu, & P. H. Wooley. (2002). Evaluation of the biocompatibility of a chitosan scaffold in mice. *Journal of Biomedical Materials Research*. 59.3, 585-590.

[21] M. J. Vicent & R. Duncan. (2006). Polymer conjugates: nanosized medicines for treating cancer. *Trends in biotechnology*. 24.1, 39-47.

Assessing Transfer Entropy as a functional connectivity measure via a Neural Mass Model

G. Ricci, E. Magosso, and M. Ursino

Department of Electric, Electronic and Information Engineering, University of Bologna, Campus of Cesena

Abstract— **The evaluation of brain connectivity plays a crucial role in the field of neuroscience. However, it is difficult to achieve a reliable estimation of connectivity from data, primarily due to the strong dependence of results on mathematical methods used for connectivity estimation. The aim of this work is to evaluate the reliability of the bivariate Transfer Entropy (TE) as a measure of functional connectivity. To this end, we used simulated data, generated using a neural mass model of two interconnected Regions of Interest (ROIs) with different connectivity strengths. TE estimates were evaluated against the model connectivity parameters, used as a "ground truth". Results suggest that TE can reliably estimate the strength of connectivity as long as neural populations work in their linear region. On the contrary, non-linear phenomena dramatically affect the measure.**

Keywords— **Bivariate Transfer Entropy, brain connectivity, synapses, non-linear neural phenomena.**

I. INTRODUCTION

PERPCEPTUAL, motor and cognitive processes depend on the coordinated interplay among specialized brain regions, connected via long-range synapses. Therefore, assessing the connectivity among brain regions is central to increase our knowledge on how brain functions are implemented in normal conditions and altered in pathological states. In the last decades, a large body of research has tackled the problem of inferring brain connectivity from both neuroimaging (fMRI) and neuroelectrical data (e.g. cortical activities reconstructed from EEG/MEG), providing different definitions of connectivity [1,2] and a large set of different measures [3-5].

Among the different definitions, *functional connectivity* is defined as the statistical dependence between two neural time series, usually measured via correlation or mutual information [5]. Other measures are based on the principle of Wiener-Granger influence [6]: a time series X has an influence on a time series Y (flow of information from X to Y) if the prediction on the future of Y from its own past is improved by incorporating the past of X. Some connectivity measures implementing this principle are based on linear multivariate autoregressive models [7-9], assuming linear interactions; however, this hypothesis is frequently invalid in case of neural processes where non-linear behaviours play a crucial role.

Transfer Entropy (TE) is an alternative measure of functional connectivity that reformulates the Granger's principle based on information theory quantities [10]: a signal X has an influence on a signal Y if the entropy on the present measurement of Y is reduced when the knowledge on the past of X is added to the past of Y. Compared to other methods, TE does not rely on any prior model of the interaction (i.e. it is model-free). For this reason, TE has experienced a rapid surge of interest in neuroscience to infer connectivity from neurophysiological data in absence of any a priori assumption [10,11]. However, a clear comprehension of virtues and pitfalls of TE as estimate of brain connectivity is still lacking.

A crucial aspect is that TE is not a direct measure of a coupling strength, and should be used with caution to measure a coupling parameter (such as the weight of synapses among two neural populations) and a causal-effect interaction. TE measures how much information is transferred from X to Y, a concept inherently different from causal coupling strength [11]. Indeed, while a high value of TE likely denotes the presence of a coupling strength (information cannot be transferred without coupling), a small value of TE might not necessarily indicate absence of a causal-effect interaction. For example, when one population enters into saturation (non-linear behavior) it transmits poor information to another population despite the existence of a strong coupling term.

In this study, we analyze the capacity of bivariate TE to infer the coupling strength between two interconnected Regions of Interest (ROIs). To this aim, we used simulated data to evaluate TE against a "ground truth". The simulated data were generated using a neural mass model (NMM) we implemented previously [12,13]. In the model, the neuroelectric activity in each ROI (representing a large cortical population) is described using a few state variables, and the two ROIs are connected via coupling terms mimicking long-range connections (excitatory or bi-synaptic inhibitory in type). Then, the values of TE were estimated from the simulated data, using the open-source Matlab toolbox TRENTOOL [14], and compared with the coupling terms assigned in the model. In particular, the following two main aims have been pursued: i) To analyze the relationship between the TE metrics and the strength of the model connectivity, both in case of excitatory and inhibitory connections. ii) To disclose how non-linearities can affect the TE-based inference of connectivity, showing that a change in a ROI working point may greatly modifies TE in face of the same assigned coupling strength.

II. METHODS

A. General theory of Transfer Entropy

In this section, the lower and upper case letters distinguish between scalar and vector variables; the bold and no-bold distinguish between random variables (either scalar or vector) and their realization.

Considering two time series generated by two stochastic processes, we can define, from each process, a time-dependent random state vector ($\boldsymbol{X}^m(t)$ and $\boldsymbol{Y}^n(t)$), whose particular observation can be written as follows:

$$X^m(t) = [x(t)\ x(t - \Delta t)\ \dots\ x(t - (m - 1) \cdot \Delta t)] \quad (1)$$
$$Y^n(t) = [y(t)\ y(t - \Delta t)\ \dots\ y(t - (n - 1) \cdot \Delta t)] \quad (2)$$

m and n are the embedding dimensions (i.e. how many past samples of the process are used); Δt is the embedding delay.

Let's now consider the random variable $\boldsymbol{y}(t + \Delta t)$ representing a future sample of the stochastic process. In case

of information flow from X to Y, the probability of $\boldsymbol{y}(t + \Delta t)$ conditioned by both $\boldsymbol{X}^m(t)$ and $\boldsymbol{Y}^n(t)$ should be different from the probability of $\boldsymbol{y}(t + \Delta t)$ conditioned by its past only. This effect can be quantified as a difference in Shannon entropy, i.e by evaluating the decrease in uncertainty that the past of X produces on the future of Y:

$$
\begin{aligned}
TE(X \to Y, l) = \; & S(\boldsymbol{y}(t + \Delta t)/\boldsymbol{Y}^n(t)) \\
& - S\big((\boldsymbol{y}(t + \Delta t)/\boldsymbol{X}^m(t - l \cdot \Delta t), \boldsymbol{Y}^n(t))\big) \quad (3)
\end{aligned}
$$

where $S(\cdot/\cdot)$ denotes the conditional Shannon Entropy. In Eq. (3) we used $\boldsymbol{X}^m(t - l \cdot \Delta t)$ instead of $\boldsymbol{X}^m(t)$, so to take into account that in neural systems, the influence of a signal on another is characterized by a pure delay (d), due to the travel time of action potentials along axons. Approximating the delay by l sampling periods ($d = l \cdot \Delta t$), the delayed signal $\boldsymbol{X}^m(t - d) = \boldsymbol{X}^m(t - l \cdot \Delta t)$ is used to define TE.

Based on Eq. (3), TE is asymmetric, hence it is a directional measure of information transfer; it catches both linear and non-linear relationships between time series, which is a fundamental aspect in neuroscience.
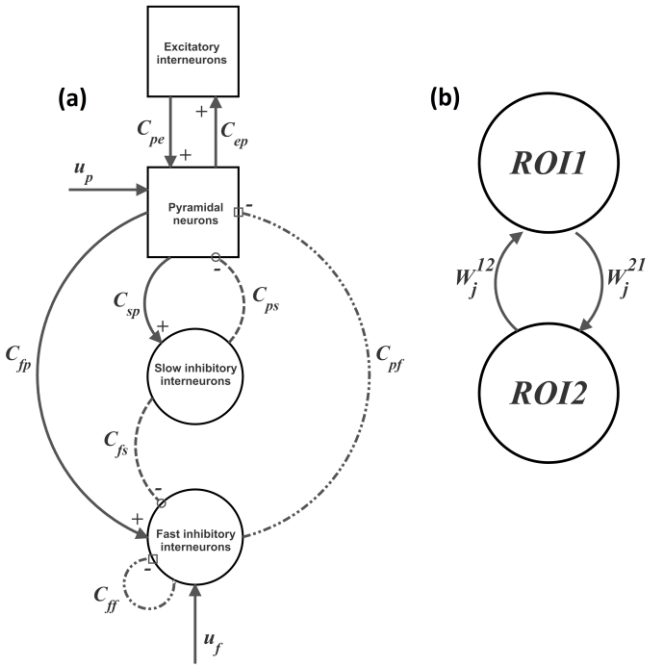
Fig. 1: a) Block diagram of the neural mass model used to simulate the dynamics in a single ROI. Continuous lines with arrows: glutamatergic excitatory synapses; dotted lines with open circles: GABAergic slower inhibitory synapses; dash-dotted lines with open squares: GABAergic faster inhibitory synapses. b) Schematic representation of a connection between two ROIs (ROI h and ROI k with $h = 1$ and $k = 2$; $j = p$ or f, see text).

B. Model of a single Region of Interest

A single ROI is modelled as the feedback arrangement among four neural populations: pyramidal neurons (p), excitatory interneurons (e), inhibitory interneurons with slow (s) and fast (f) synaptic kinetics (Fig. 1a). Each population receives an average postsynaptic membrane potential from other populations and converts it into an average density of spikes. This conversion is simulated through a static sigmoidal relationship, reproducing the non-linear neuronal behaviour.

To model the dynamics in a whole ROI, the four populations are connected via excitatory and inhibitory synapses (Fig. 1a), whose kinetics are described with a second order system. Three types of synapses have been considered: glutamatergic

excitatory synapses, for both pyramidal neurons and excitatory interneurons; GABAergic inhibitory synapses with slow dynamics; GABAergic inhibitory synapses with faster dynamics. The average number of synaptic contacts between couples of neural populations is represented by eight parameters C_{ij}, where the first subscript represents the post-synaptic population and the second refers to the pre-synaptic population. We assume that inputs to each ROI, representing all exogenous contributions from external sources, target only pyramidal ($u_p(t)$) and fast-inhibitory populations ($u_f(t)$) [12]. Since long-range connections in the brain are mediated only via excitatory glutamatergic synapses [15], inputs are filtered via the low-pass dynamics of the excitatory synapses.

C. Model of two interconnected ROIs

In order to study connectivity between regions, two ROIs (ROIh and ROIk) were interconnected through long-range excitatory connections (Fig. 1b). Here, the pre-synaptic and post-synaptic regions are denoted with the superscript k and h, respectively. To simulate connectivity, we assumed that the average spike density of pyramidal neurons of the pre-synaptic area (z_p^k) affects the target ROI via a weight factor, W_j^{hk} (where $j = p$ or f, depending on the synapse target) and a time delay, T. Since z represents a normalized dimensionless density of spikes, the parameters W, as well as the internal connections C in Fig. 1, have di dimension of mV. It is worth noting that the model makes use of two kind of long range connections between ROIs, both originating from pyramidal neurons: excitatory connections from pyramidal neurons in the source ROI to pyramidal neurons in the target ROI (W_p^{hk}), and bi-synaptic inhibitory connections (W_f^{hk}). The latter originate from pyramidal neurons in the source ROI and excite inhibitory interneurons in the target ROI; the latter, in turn inhibits the pyramidal neurons inside the target ROI.

Inputs u_p^h and/or u_f^h to the target ROI are defined as:

$$
u_j^h(t) = n_j^h(t) + W_j^{hk} z_p^k(t - T) \qquad j = p, f \qquad (4)
$$

where $n_j(t)$ is Gaussian white noise (mean value $m_j = 0$ if not specified differently, and variance $\sigma_j^2 = 9/dt$, where dt is the integration step) which accounts for all other external inputs. The variance $9/dt$ corresponds to a noise power density as high as 9. This value ensures that the two regions work mainly in the central linear region, with some moderate involvement of saturation non-linearity. The effect of higher noise, leading to higher non-linear effects, may be studied in a subsequent work. White noise was generated using the same seed for all different simulations; hence, TE differences among model configurations can be ascribed only to differences in synapses, not to individual random noise realizations.

In the following, TE^{hk} refers to the transfer entropy from ROIk to ROIh, that is $TE^{hk} = TE(ROIk \to ROIh)$.

D. Assignment of model parameters

A parameter configuration was given to each NMM to simulate a power spectral density with activity in the beta (about 20 Hz) and in the gamma range (above 30 Hz), typical brain rhythms in supplementary and pre-motor cortical areas [12]. Power spectral density was computed by applying the Welch method on the post-synaptic membrane potential of pyramidal neurons.

E. Model simulations and Transfer Entropy computation

Several NMM simulations were performed by using different coupling configurations between the two ROIs (i.e. modifying the parameters $W_j^{hk}, j = p, f$), and by modifying the mean value of the input noise to one region (to investigate non-linear effects). For each configuration, 10 trials of 60 seconds were generated using the NMM: each trial contained the time series of the pyramidal post-synaptic potentials of the two ROIs. The 10 trials were given as input to TRENTOOL [14] that computed the TE values of both the simulated data and surrogate data and provided a p value assessing whether the TE of the simulated data were significantly different from the surrogate data. The latter, computed internally by the software, do not incorporate information transfer but maintain the same statistical properties of the original data fed as input.

In section III, we refer to TE as the difference between simulated signals TE and surrogate data TE. Whenever no statistical significance (p>0.05) was achieved, the difference was set at zero. Changes in TE were compared with the corresponding changes in the true connection strengths assigned between the two ROIs. In particular, we looked for a linear relationship, assessing whether a progressive change in connectivity corresponds to a proportional change in TE.

III. RESULTS

A. Two interconnected ROIs

A set of simulations was performed using two ROIs (ROI1 and ROI2, i.e. $h = 1, k = 2$) linked by reciprocal excitatory and/or inhibitory connections. For each curve of Fig.2, the synapse W_j^{21} was set constant, while the synapse W_j^{12} was progressively increased $(j = p \text{ or } f)$. Hence, to better appreciate the linear relationship between TE and synaptic strength, only values of TE^{12} were reported vs the increasing synaptic strength (W_j^{12}). Even if not displayed, TE^{21} rose when the synapse W_j^{21} increased.

Fig. 2a depicts TE^{12} and TE^{21} estimated when the ROIs are linked via two *excitatory connections*. The synapse W_p^{12} was increased progressively from 0 to 80, at different values of W_p^{21}. We can note that: i) when the synapse is zero, synapse

W_p^{21} the relative TE is not significantly different from that of surrogate data and is negligible; ii) TE increases quite linearly with the strength of the synapse; iii) TE^{12} increases moderately when the reciprocal synapse increases.

Fig. 2b depicts the values of TE^{12} and TE^{21} estimated when the two ROIs are linked via reciprocal *inhibitory connections*. The synapse W_f^{12} was progressively increased from 0 to 40, at different values of the synapse W_f^{21}. As it is clear, TE increases with the value of the inhibitory synapse in the direction under study, but some differences are evident, compared with the excitatory case: i) the effects of inhibitory connections are about twofold more efficacious in information transmission compared with the excitatory ones; ii) the value of the inhibitory synapse in the other direction affects the estimation significantly. A large variability becomes especially evident when the first synapse (W_f^{12}) is higher than 20 and TE is computed at different values of W_f^{21}. Furthermore, when both inhibitory synapses (W_f^{21} and W_f^{12}) assume values $\geq$ 30, TRENTOOL failed to find the correct solution, providing an error. The problem is probably related with the reconstruction of states from scalar time series using time-delay embedding.

In Fig. 2c simulations were performed assuming two regions interconnected by an excitatory synapse W_p^{12}, which was progressively increased from 0 to 80, at different values of an inhibitory synapse W_f^{21}. These results are substantially similar to those in Fig.2a, indicating a linear and robust relationship between TE and the synapse strength. Indeed, TE increases linearly with the value of the excitatory synapse in the direction under study, and the value of the inhibitory synapse in the other direction has only a mild effect on the estimation.

B. Effect of the input mean value

The neural mass model used in this work is intrinsically non-linear. Due to non-linearity effects, information transfer may not reflect the true anatomical connectivity. Hence, it is of fundamental interest to assess how TE estimation may change when all synapses are fixed while the working point in neural populations is modified.

In order to test non-linear phenomena, we modified the mean value of the noise entering to pyramidal neurons in ROI1.
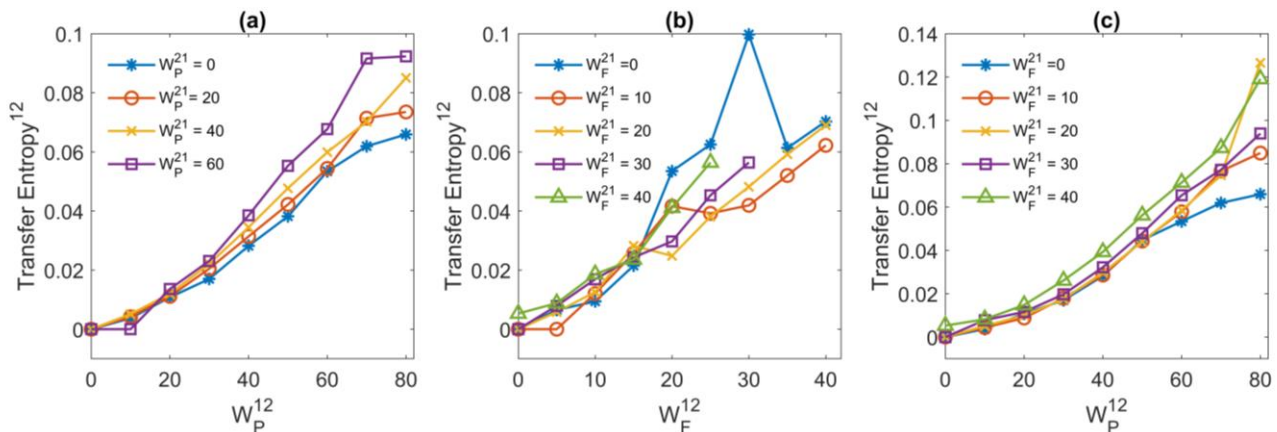

Fig.2: a) Dependence of TE on a feedback realized with two regions interconnected via reciprocal *excitatory* synapses. TE[12] increases quite linearly with the value of the excitatory synapse in the direction under study, and it is moderately affected by the value of the excitatory synapses in the other direction. b) Dependence of TE on a feedback realized with two regions interconnected via reciprocal *inhibitory* synapses. TE[12] increases with the value of the inhibitory synapse in the direction under study. Note that the effect of inhibitory synapses on TE is stronger than the effect of excitatory ones. c) Dependence of TE on a feedback including *both excitatory and inhibitory* synapses. TE[12] increases linearly with the value of the excitatory synapse in the direction under study; the value of the inhibitory synapse in the other direction has only a mild effect on the estimation. Here, the mean value of input noise was zero for both ROIs.
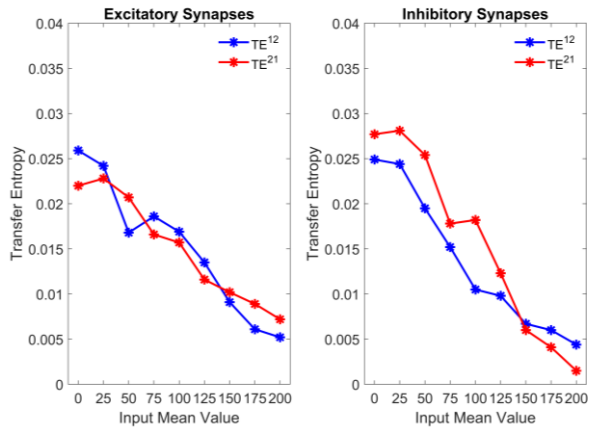
Fig. 3: Effect of the mean value of the input noise on the estimation of Transfer Entropy. The simulations have been performed using two interconnected regions, with excitatory synapses (left panel) and inhibitory synapses (right panel), and by varying the mean value of the noise entering to ROI 1. Transfer entropy decreases monotonically with the input mean value of noise.

Indeed, a change in the mean value shifts the working point along the sigmoidal relationship. Simulations (Fig 3) were performed using two interconnected regions, with the following reciprocal configuration of synapses: a) both excitatory $W_p^{12}=W_p^{21}=30$ (left panel) and b) both inhibitory $W_f^{12}=W_f^{21}=15$ (right panel). Results indicate that an increase in the mean value of the input to ROI1 causes a significant decline in the estimated value of TE^{21}. Indeed, the activity of pyramidal neurons in ROI1 approaches the upper saturation, and the temporal variance of this activity becomes less evident reducing the quantity of information transmitted from 1 to 2. TE^{12} decreases, too: indeed, also ROI2 exits from the central linear region, because of the strong excitation from ROI1.

We can conclude that, in the presence of a significant input excitation or inhibition to one ROI, TE starts to decrease since both regions can leave the linear working region, when information transmission is maximal, to enter a saturation zone. This is an example of how connectivity estimated by TE may be different from the anatomical connectivity, and extreme caution should be taken in interpreting TE values.

IV. DISCUSSION

In the last decade, the use of various methods to assess connectivity from neuroimaging and neuroelectrical data has received an enormous attention. However, much debate is still present on the reliability of these methods. In order to clarify this problem, we evaluated the significance of connectivity values derived from bivariate TE, using data generated through a NNM, with assigned connectivity parameters.

A first important result is that the TE algorithm can discriminate between the presence/absence of connectivity when two ROIs are interconnected. In all cases when model connectivity was set at zero or at an extremely low value ($W_p \leq 10$ or $W_f \leq 5$), the algorithm provided no significant difference between model signals and surrogate data (Fig. 2).

Another important result is that quite a linear relationship can be observed between the strength of the connection and the estimated value of TE, as long as the model is working in the linear region. The linear relationship is quite straightforward in case of excitatory synapses (Figs. 2a and 2c), and less precise in case of inhibitory synapses (Fig. 2b).

The main results of this study are the effects of non-linearities on TE estimation and how it strongly depends on the working point of populations. In particular, whenever a population of pyramidal neurons enters into a saturation region, its capacity to transmit information towards other ROIs drastically decreases(and hence TE, too), despite the presence of a strong synapse.

In conclusion, results suggest that bivariate TE can be a promising method to estimate the strength of connectivity if neural populations work in the linear region; on the contrary non-linear phenomena may play a critical role in the assessment of connectivity, since they significantly reduce the estimation of TE. We suggest that changes in connectivity, often reported in the literature, during different tasks or brain conditions, might not always reflect a true change in the connecting network, but rather a change in information transmission due to a different working point of the involved neural populations. Future works may include the analysis of the relationship between TE and connectivity in multivariate conditions (i.e., in case of more than two interconnected ROIs) and the effect of connectivity linking regions with different intrinsic rhythms (e.g. gamma vs. beta or beta vs. alpha).

REFERENCES

[1]   B. Horwitz, "The elusive concept of brain connectivity," *Neuroimage*, vol. 19(2 Pt 1), pp. 466-470, Jun, 2003.

[2]   K. J. Friston, "Functional and effective connectivity: a review,"*Brain Connect.*, vol. 1, pp. 13-36, 2011.

[3]   M. P. van den Heuvel and H. E. Hulshoff Pol, "Exploring the brain network: a review on resting-state fMRI functional connectivity," *Eur. Neuropsychopharmacol.*, vol. 20, pp. 519-534, Aug. 2010.

[4]   V. Sakkalis, "Review of advanced techniques for the estimation of brain connectivity measured with EEG/MEG," *Comput. Biol. Med.*, vol. 41, pp. 1110-1117, Dec. 2011.

[5]   H. E. Wang, C. G. Bénar, P. P.Quilichini, K. J. Friston, V. K. Jirsa, and C. Bernard, "A systematic framework for functional connectivity measures," *Front. Neurosci,*, vol 8. (article 405), pp. 1-22, Dec. 2014.

[6]   C. W. J. Granger, "Investigating Causal Relations by Econometric Models and Cross-spectral Methods," *Econometrica*, vol. 37, pp. 424-438, Aug. 1969.

[7]   K. Sameshima and L.A. Baccalá, "Using partial directed coherence to describe neuronal ensemble interactions,", *J. Neurosci. Methods.*, vol. 94, pp. 93-103, Dec. 1999

[8]   M. J. Kamiński and K. J. Blinowska, "A new method of the description of the information flow in the brain structures," *Biol. Cyber.*, vol. 65, pp. 203-2010M. Young, *The Techincal Writers Handbook.* Mill Valley, CA: University Science, 1989.

[9]   L. Astolfi et al., "Imaging functional brain connectivity patterns from high-resolution EEG and fMRI via graph theory," *Psychophysiology*, vol. 44, pp. 880-893, Nov. 2007.

[10] R. Vicente, M. Wibral, and M. Lindner, G. Pipa, "Transfer entropy—a model-free measure of effective connectivity for the neurosciences," *J. Comput. Neurosci.*, vol. 30, pp. 45-67, Feb. 2011.

[11] M. Wibral, R. Vicente, and M. Lindner, "Transfer entropy in neuroscience," in *Directed Information Measures in Neuroscience*, 1st ed., M. Wibral, R. Vicente, J. T. Lizier, Eds. Berlin: Springer, 2014, pp. 3-36.

[12] M. Ursino, F. Cona, M. Zavaglia, "The generation of rhythms within a cortical region: analysis of a neural mass model," *Neuroimage*, vol. 52, pp. 1080-1094, Sep. 2010.

[13] F. Cona, M. Zavaglia, M. Massimini, M. Rosanova and M. Ursino, "A neural mass model of interconnected regions simulates rhythm propagation observed via TMS-EEG," *Neuroimage*, vol. 57, pp. 1045-1058, Aug. 2011.

[14] M. Lindner, R. Vicente, V. Priesemann, and, M. Wibral, "TRENTOOL: A Matlab open source toolbox to analyse information flow in time series data with transfer entropy", *BMC Neurosci*, vol.12 (119), pp. 1-22, Nov. 2011.

[15] D. J. Felleman and D.C.Van Essen, "Distributed hierarchical processing in the primate cerebral cortex". *Cereb. Cortex* vol. 1, pp. 1–47, 1991.

Balance control after tripping: Margin of Stability and Limb Support Quotient

Alberto Finazzi[1], Adele Macrì Panarese[2,3], Paolo Gallina[1], Silvestro Micera[2,3,4], Vito Monaco[2,3,4,5]

[1]*Università degli Studi di Trieste*
[2]*The BioRoboticsInstitute, Scuola Superiore Sant'Anna, 56127 Pisa, Italy*
[3]*Department of Excellence in Robotics & AI, The BioRobotics Institute, ScuolaSuperioreSant'Anna, Pisa, Italy*
[4]*Bertarelli Foundation Chair in Translational Neuroengineering, Center for Neuroprosthetics and Institute of Bioengineering, School of Engineering, EcolePolytechniqueFederale de Lausanne*
[5]*IRCCS Fondazione Don Carlo Gnocchi, 20148 Milan, Italy*

Abstract—**The quantitative assessment of the biomechanical response represents a key issue to test the effectiveness of counteracting strategy against the fall risk. Accordingly, in this study we investigated the attitude of both the Margin of Stability in the sagittal plane (MoS$_{AP}$) and the Limb Support Quotient (LSQ) to reflect the lack of balance resulting after a tripping.**

Eight healthy young subjects were recruited for the experimental sessions and were asked to manage unexpected tripping-like perturbations while walking on a treadmill at normalized speed. Perturbations were delivered by a custom made mechatronic platform. The 3D whole body kinematics was collected during the experimental sessions. It was off-line used to compute MoS$_{AP}$ and LSQ during two consecutive right steps across the onset of the perturbation.

The data analysis revealed that both metrics pre and post perturbation were statistically different. In addition, the correlation between MoS$_{AP}$ and LSQ ranged between -0.45 and 0.31, and only after the perturbation onset the correlation coefficient was significant.

Results hence confirmed that the adopted experimental protocol can effectively alter the dynamics of healthy subjects, thus MoS$_{AP}$ and LSQ can likely document it. Results surprisingly revealed that values related to the adopted assessment tools were poorly correlated, despite both metrics are sensitive to the altered dynamics pre vs. post perturbation. Accordingly, we inferred that the balance control after a tripping might differently targets the stability along the two axes.

Keywords—**Tripping, Margin of Stability, Limb Support Quotient.**

I. INTRODUCTION

A large number of studies have highlighted that one over three adults +65 years old falls once a year, and the rate of falls further increases due to concomitant neuro-musculo-skeletal diseases (e.g., Parkinson's disease, lower limb amputation)[1]–[4]. Due to these critical events, fallers suffer fractures and other non-fatal injuries that worsen their quality of life [2], [5]. In addition, consequences of falls, in terms of cares and hospitalization, represent a significant burden for the society as a whole [2], [6]–[9]. Accordingly, the identification of effective strategies to counteract the fall risk is of primary importance to allow the fragile population to remain safe while maintaining autonomy during daily activities.

One of the key issues underlying the design of effective counteracting strategies against falling consists in accurately assessing the "stability" of a person in order to identify his/her related risk in a specific context. Noticeably, herein the term stability refers to the one's ability to recover his/her balance after an unexpected and acute perturbation likely occurring during daily activities (e.g., tripping, slipping).

Literature provides several assessment tools to investigate individuals' ability to counteract the lack of balance due to unexpected perturbations [10]. Among those, in this study we analysed the attitude of the Margin of Stability (MoS) and the Limb Support Quotient (LSQ) to reflect the lack of balance after a tripping.

The MoS represents the relative distance between the velocity-adjusted position of the centre of mass (usually called extrapolated centre of mass) and the base of support, and can be computed in both the frontal and in the sagittal plane [11] (see section II.C for further details). With respect tothe latter case, the MoS indicates how far the centre of mass will be projected behind (i.e., forward or backward) with respect the base of support, which in turn suggests how many steps are required to recover the stability [10]. Noticeably, from the theoretical viewpoint, the MoS should be computed by combining the whole body kinematics and the inertial properties of all body segments. Its accuracy is hence affected by several sources of errors (i.e., consistence of kinematic data, accuracy of the anthropometrical tables).

The LSQ was introduced by Yang and colleagues [12]and represents the ratio between the vertical velocity and the vertical position of the hip joints (see section II.C for further details). This assessment tool was shown to be sufficiently accurate to distinguish between fallers and non-fallers after a slippage, based on the evidence that fallers use to go lower at faster velocity than the counterpart. From the computational viewpoint, the LSQ can be assessed by using a simpler approach than the MoS, thus reducing the source of errors. Moreover, it is more prone to be used in experimental contexts involving devices that can potentially occlude markers (e.g., effectiveness of wearable robotics against the fall risk [13], [14]).

It is worth noting that, based on their definitions, these assessment tools refer to different biomechanical features of the reactive behaviour after a perturbation (i.e., vertical vs. antero-posterior axis respectively for the LSQ and the MoS). In spite of this, they are expected to be sensitive to the lack of

balance induced by an external perturbation.

Accordingly, in this study we investigated the relationship between LSQ and MoS. In particular, we tested a twofold hypothesis: 1. MoS and LSQ are sensitive to the altered dynamics induced by unexpected tripping like perturbations; 2. values of MoS and LSQ during the compensative stride are correlated. If these hypotheses were confirmed, we could infer that the lack of balance can be assessed by using two alternative tools suitable for different experimental contexts.

II. MATERIALS AND METHODS

A. Subjects and experimental protocol

A convenience sample of eight healthy young subjects were recruited for the experimental sessions. Age and anthropometrical features are reported in Table I. Participants were asked to manage unexpected tripping-like perturbations while walking on the treadmill.

More in details, before recording sessions were started, participants were asked to walk on a treadmill at normalized speed (Froude number = 0.15; see [15] for additional details) for about 3 min to accustom themselves. Then, they were exposed to an initial set of tripping-like perturbations to prevent the first perturbation-related bias [16], [17]. Overall, the acclimation period took about 10 min.

After that, participants underwent a set of 6 sequential trials where they were asked to manage unexpected tripping-like perturbations while listening music by earphones to prevent any adaptive behaviour elicited by auditory cues. The walking speed was kept at the same constant value during the whole session.

Background noise was kept under control and experimenters were not in the participants' visual field during the whole experimental session.

B. Experimental setup

To induce a trip during a walk on a treadmill, a portable mechatronic platform was designed to host and brake a nylon rope through a cam-based mechanism, as described in [18]. The nylon rope was connected, on one side, to the main frame of the mechatronic platform via a compliant spring, and, on the other side, to one of the participants' feet (Fig. 1).

During steady walking, the rope moved forward and backward, throughout a series of pulleys, according to the foot

TABLE I

	Mean ± Standard deviation
Age (years)	26.6±3.7
Weight (kg)	65.9±12.4
Height (m)	1.73± 0.07
Lower limb length[1] (m)	0.81±0.03
Walking speed(m/s)	1.09 ± 0.02

[1]*The lower limb leng this the distance between the external surface of*
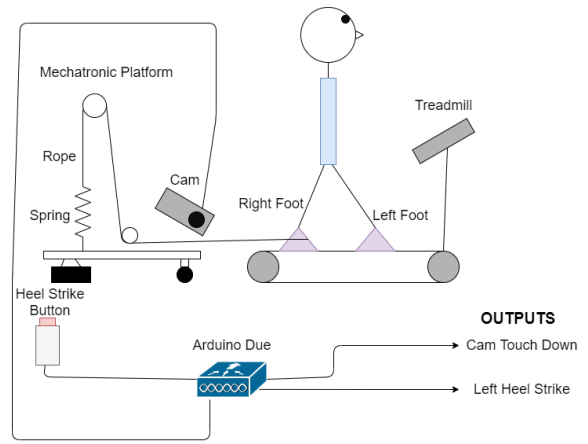
Figure 1 Schematic scheme of the experimental setup. The stiffness of the spring was 3 N/m while the rope could be likely considered inextensible.

motion. If timely enabled, the cam braked the rope and inhibited the forward movement of the foot toward the swing phase, thus emulating a trip. To prevent gait asymmetries the mechatronic platform was actually equipped with two rope-spring systems (the one, on the right limb, was provided with cam-braking mechanism, the other one was free; note: the second rope is not shown in Fig. 1 to make reading easier).

The control architecture was based on an Arduino Due microcontroller, and was designed to deliver a perturbation at the right toe off, thus the trip was always induced on the right limb. The onset of the perturbation (i.e., left heel strike) was triggered by an experienced experimenter, thus the rope was braked just after a forthcoming right toe-off. In addition, Arduino provided two more outputs for off-line data synchronization.

The experimental setup was also provided with a 8-camera stereophotogrammetric system (6 Vicon Bonita 10 and 2 Vicon Vero v2.2) to record the 3D whole body kinematics
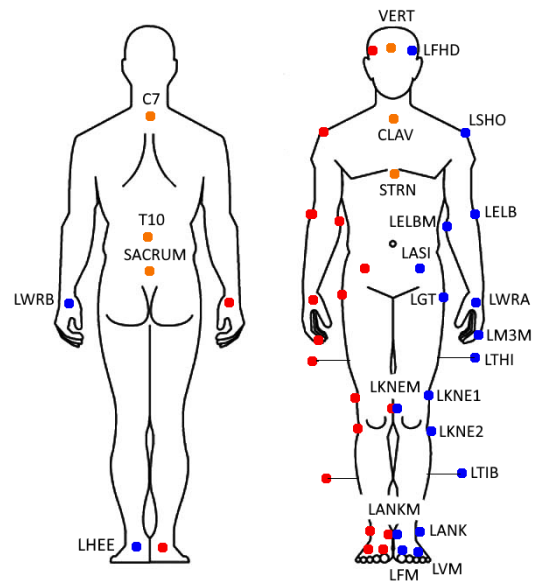
Figure 2 Representation of the 44 markers on anatomical landmarks. Labels are reported on the left side only to make reading easier.

(sample rate 100 Hz). Specifically, 44 markers were placed on anatomical landmarksas describe elsewhere [19] and reported in Fig. 2.

Kinematic data and onset of the perturbation were off-line synchronized by means of a logic pulse delivered by the microcontroller at the onset of the perturbation.

C. Data Analysis

The kinematic data were pre-processed in MATLAB environment (The MathWorks, Inc., Natick, MA, USA) to both fill gaps (spline interpolation) and remove high frequency artifacts (low pass zero-lag filtering, 3rd order Butterworth filter with cut off at 10 Hz). Then, the position of the whole body centre of mass (CoM) was computed as the weighed summation of the position of all body segment-related centre of mass. Inertial properties were estimated in accordance with the procedures described in [20] and modified by [21]. After that, we assessed both the Margin of Stability along the antero-position direction (MoS_{AP}) and the Limb Support Quotient (LSQ), as described below.

The MoS_{AP} is defined as the distance between the extrapolated CoM position and the boundaries of the base of support [11] and can be computed as follows:

$$MoS_{AP} = U_{MAX} - XCoM \qquad (1)$$

where U_{MAX} is the forward boundary of the base of support, i.e., first metatarsal head, and XCoM is the extrapolated CoM. The XCoM was calculated as:

$$XCoM = CoM_{AP} + \frac{C\dot{o}M_{AP}}{\sqrt{\frac{g}{h_{CoM}}}} \qquad (2)$$

where CoM_{AP} and $C\dot{o}M_{AP}$ respectively are the AP components of position and velocity of the CoM, h_{CoM} is the distance between CoM and floor while subjects were keeping the unperturbed upright stance, and g is the gravitationalacceleration (9.81 m/s^2).

The LSQ is usually computed as the ratio between normalized vertical velocity and normalized vertical position of the hip joint [12]. In this study it was instead computed as the ratio between normalized vertical velocity of the whole CoM and the normalized vertical position of the CoM, as follows:

$$LSQ = \frac{\widehat{C\dot{o}M_V}}{\widehat{CoM_V}} = \frac{C\dot{o}M_V / \sqrt{g \cdot h}}{CoM_V / h} \qquad (3)$$

where CoM_V and $C\dot{o}M_V$ respectively are vertical position and velocity of the CoM, g is the gravitational acceleration and h the subject's height.

After that, we assessed both the Margin of Stability along the antero-position posterior direction (MoS_{AP}) and the LSQ at three homologous time instants related to the right stance phase of the strides just before and just after the perturbation
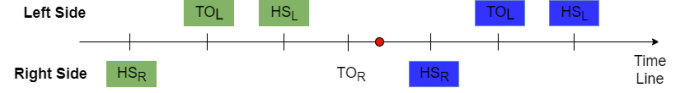
Figure 3 Order sequence of time instants across the onset of the perturbation. The red dot is the onset perturbation. The homologous time instants before and after the onset perturbation are highlighted by green and blue boxes respectively.

onset (Fig. 3): right heel strike (HS_R), left toe off (TO_L) and left heel strike (HS_L).

Finallyduration of the step and the double support phase before and after the onset of the perturbation were computed too.

D. Statistical Analysis

The hypothesis of normal distribution of all datasets and the homogeneity of variance of all homologous datasets were assessed by, respectively, the Kolmogorov-Smirnov normality test and the Levene's test. Since in many cases the related null hypotheses wererejected, we used nonparametric statistic tests. Specifically: the Mann-Whitney was used to test the equality of medians before vs. after the onset of the perturbation; the Spearman correlation coefficient was used to assess the strength of the relationship between the stability assessment tools (i.e., MoS_{AP} and LSQ).

Data processing and statistical analysis were carried out by using written MATLAB scripts. Significance was set at $\alpha < 0.05$.

III. RESULTS

Fig. 4 shows spatio-temporal parameters (i.e., step and double support duration) and stability parameters, before and after the onset of the perturbation (i.e., Walking vs. Tripping), for all time instants (i.e., HS_R, TO_L, and HS_L).The statistical analysis revealed that all metrics pre and post perturbation were statistically different, with the exception of LSQ at HS_R(p-value = 0.479).

The analysis of the correlation between MoS_{AP} and LSQ has shown that the Spearman correlation coefficient rangedbetween -0.45 and 0.31, and only after the onset of the perturbationit was significant.
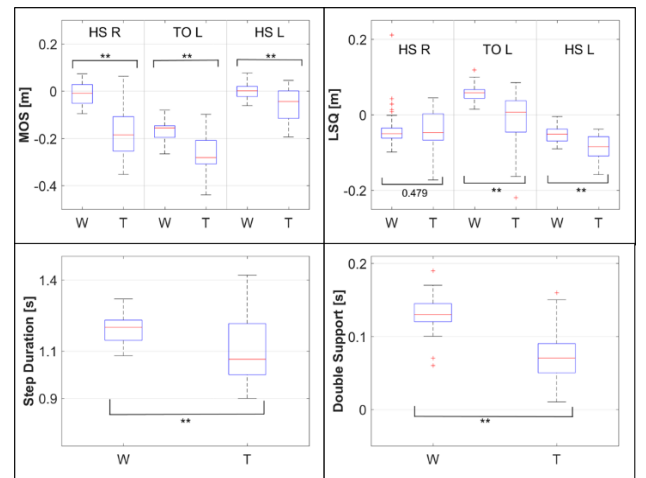

Figure 4 Boxplots of stability and temporal-spatial parameters with the relative p-values (** means p < 0.001). Labels W and T respectively refer to unperturbed walking and tripping

IV. DISCUSSION AND CONCLUSION

This study aimed at firstly testing the hypothesis that both the MoS$_{AP}$ and the LSQ can reliably recognize the altered dynamics resulting after an unexpected tripping induced while healthy subjects were steadily walking on a treadmill. In addition, we verified whether the two assessment tools (i.e., MoS$_{AP}$ and LSQ) are correlated, thus representing two alternative strategies to describe the state of a subject while reactively recovery the balance.

As expected, results confirmed that the adopted experimental protocol can effectively alter the dynamics of healthy subjects. In particular, after the perturbation:
- the duration of both spatio-temporal parameters decreased (Fig. 4) suggesting that participants needed faster consecutive steps to recovery their balance;
- the MoS$_{AP}$ became more negative, reflecting a forward shift of the extrapolated centre of mass involving a greater forward fall risk;
- the LSQ decreased, revealing a faster downward movement of the CoM in the step after the perturbation.

Surprisingly, results also revealed that values related to the adopted assessment toolswere low correlated. That is, despite MoS$_{AP}$ and LSQ appear sensitive to the lack of balance induced by an unexpected tripping-like perturbation, the reactive behaviour of the CoM along the fore-aft anterior-posterior axis is mostly unrelated to that along the vertical one.

We believe that this result is in part due to the anisotropy of the musculo-skeletal system (e.g., joints, stiffness, inertia) along the two axes. However, we cannot reject the hypothesis that the balance control after a tripping might differently targets the stability along the two axes. Specifically, the increased negative MoS$_{AP}$, in conjunction with a shorter step duration, after tripping, suggests that subjects rely on several compensatory steps in order to recovery the balance. However, with respect to the vertical axis, the smaller LSQ post perturbation might reflectthe need to control the whole body inertia by shifting downward the CoM in order to reduce the biomechanical demand underlying balance recovery. This hypothesis deserves further investigations.

REFERENCES

[1] M. Pijnappels, M. F. Bobbert, and J. H. Van Dieën, "Contribution of the support limb in control of angular momentum after tripping," *J. Biomech.*, vol. 37, no. 12, pp. 1811–1818, 2004.
[2] A. Danielsen, H. Olofsen, and B. A. Bremdal, "Increasing fall risk awareness using wearables: A fall risk awareness protocol," *J. Biomed. Inform.*, vol. 63, pp. 184–194, 2016.
[3] X. Hu and X. Qu, "Pre-impact fall detection," *Biomed. Eng. Online*, vol. 15, no. 1, pp. 1–16, 2016.
[4] H. Stolze, S. Klebe, C. Zechlin, C. Baecker, L. Friege, and G. Deuschl, "Falls in frequent neurological diseases: Prevalence, risk factors and aetiology," *J. Neurol.*, vol. 251, no. 1, pp. 79–84, 2004.
[5] C. Shirota, A. M. Simon, and T. A. Kuiken, "Trip recovery strategies following perturbations of variable duration," *J. Biomech.*, vol. 47, no. 11, pp. 2679–2684, 2014.
[6] M. N. Nyan, F. E. H. Tay, and E. Murugasu, "A wearable system for pre-impact fall detection," *J. Biomech.*, vol. 41, no. 16, pp. 3475–3481, 2008.
[7] D. Yoo, K. H. Seo, and B. C. Lee, "The effect of the most common gait perturbations on the compensatory limb's ankle, knee, and hip moments during the first stepping response," *Gait Posture*, vol. 71, no. November 2018, pp. 98–104, 2019.
[8] C. Smeesters, W. C. Hayes, and T. A. McMahon, "The threshold trip duration for which recovery is no longer possible is associated with strength and reaction time," *J. Biomech.*, vol. 34, no. 5, pp. 589–595, 2001.
[9] J. K. Lee, S. N. Robinovitch, and E. J. Park, "Inertial Sensing-Based Pre-Impact Detection of Falls Involving Near-Fall Scenarios," *IEEE Trans. Neural Syst. Rehabil. Eng.*, vol. 23, no. 2, pp. 258–266, 2015.
[10] S. M. Bruijn, O. G. Meijer, P. J. Beek, and J. H. Van Dieen, "Assessing the stability of human locomotion: A review of current measures," *J. R. Soc. Interface*, vol. 10, no. 83, 2013.
[11] M. Guaitolini, F. Aprigliano, A. Mannini, S. Micera, V. Monaco, and A. M. Sabatini, "Ambulatory assessment of the dynamic margin of stability using an inertial sensor network," *Sensors (Switzerland)*, vol. 19, no. 19, 2019.
[12] F. Yang, T. Bhatt, and Y. C. Pai, "Limits of recovery against slip-induced falls while walking," *J. Biomech.*, vol. 44, no. 15, pp. 2607–2613, 2011.
[13] V. Monaco et al., "An ecologically-controlled exoskeleton can improve balance recovery after slippage," *Sci. Rep.*, vol. 7, no. March, pp. 1–10, 2017.
[14] F. Aprigliano, V. Monaco, P. Tropea, D. Martelli, N. Vitiello, and S. Micera, "Effectiveness of a Robot-Mediated Strategy While Counteracting Multidirectional Slippages," *Robotica*, vol. 37, pp. 1–13, 2019.
[15] V. Monaco, L. A. Rinaldi, G. Macrì, and S. Micera, "During walking elders increase efforts at proximal joints and keep low kinetics at the ankle," *Clin. Biomech.*, vol. 24, no. 6, pp. 493–498, 2009.
[16] L. B. Oude Nijhuis, J. H. J. Allum, G. F. Borm, F. Honegger, S. Overeem, and B. R. Bloem, "Directional sensitivity of 'first trial' reactions in human balance control," *J. Neurophysiol.*, 2009.
[17] F. Aprigliano, D. Martelli, S. Micera, and V. Monaco, "Intersegmental coordination elicited by unexpected multidirectional slippinglike perturbations resembles that adopted during steady locomotion," *J. Neurophysiol.*, vol. 115, no. 2, pp. 728–740, 2016.
[18] F. Aprigliano, S. Micera, and V. Monaco, "Pre-Impact Detection Algorithm to Identify Tripping Events Using Wearable Sensors," *Sensors (Switzerland)*, 2019.
[19] D. Martelli, V. Monaco, L. Bassi Luciani, and S. Micera, "Angular momentum during unexpected multidirectional perturbations delivered while walking," *IEEE Trans. Biomed. Eng.*, vol. 60, no. 7, pp. 1785–1795, 2013.
[20] Zatsiorsky, V. M.,Seluyanov,V. N. & Chugunova, and L. G, "Methods of determining mass-inertial characteristics of human body segments." eds Chernyi, G. G. & Regirer, S. A., CRC Press, Massachusetts, USA, pp. 272–291, 1990.
[21] P. De Leva, "Adjustments to zatsiorsky-seluyanov's segment inertia parameters," *J. Biomech.*, 1996.

Impact of the shear stress on cultured human gut microbiota

F. Biagini[1], M. Calvigioni[2], E. Botte[1], A. Vecchione[2], F. Montemurro[1], C. De Maria[1], C. Magliaro[1], F. Celandroni[2], E. Ghelardi[2], and G. Vozzi[1]

[1] *Research Center "E. Piaggio" and Dipartimento di Ingegneria dell'Informazione, University of Pisa, Pisa, Italy;*
[2] *Department of Translational Research and New Technologies in Medicine and Surgery, University of Pisa, Pisa, Italy*

Abstract—In vitro **models of the human gut microbiota are widely used to study fermentation pattern of the microorganisms, their composition and the host-microbe interactions. Bioreactors and microfluidic devices are commonly designed to culture microorganisms from the human gut microbiota in a dynamic environment. Recent findings suggest that bacteria are influenced not only by the chemical environment, but also mechanical stimuli can affect their adhesion and proliferation. This work aims at evaluating the effects of the shear stress on the human gut microbiota. Specifically, we designed and fabricated a controlled shear stress chamber to evaluate the adhesion of the microorganisms under a constant fluid flow. Results show how, in a specific range, the shear stresses have a positive effect on biofilm formation for the *E. Coli* and the human gut microbiota.**

Keywords—**Gut microbiota, Shear stress, Dynamic culture, Bioreactor**

I. INTRODUCTION

THE human gut microbiota is considered as the last organ under research [1]. Several studies suggest that an altered microbiota composition can lead to the development of systemic diseases [2]–[5]. In this scenario, *in vitro* models of human gut microbiota are emerging as a powerful tool to understand the interactions between these microorganisms and other tissues of the human body [6].

Several dynamic *in vitro* models of the human gut microbiota have been developed in the last decades. Among them, the Simulator of the Human Intestinal Microbial Ecosystem (SHIME®) is composed by five reactors working in series for reproducing the environment (*e.g.,* pH, transit time) of the different tracts constituting the human gut [9]. Such a model and its updated version with the addition of the mucus [10] are considered the point of reference for studying the fermentation pattern of the microorganisms composing the human gut microbiota [11]. Other systems are purposely designed to reproduce the environment of a specific intestinal tract (e.g., the TIM-2 platform for mimicking the proximal colon environment [12]). To better understand the host-microbe interactions, co-culture of human intestinal cell lines and microorganisms from human gut microbiota were performed. In particular, Kim *et al.* [13] developed a gut-on-chip co-culturing CACO-2 cells and an intestinal microorganism (*Lactobacillus rhamnosus)* [13]. A recent work by Jalili-Firoozinezhad and coworkers [14] presents a novel anaerobic intestine-on-a-chip where human gut microbiota from infant faeces was co-cultured with CACO-2 epithelium.

However, all these dynamic models still lack on the systematic study of the effects of the mechanical stimuli on the cultured microorganisms due to the flow of culture medium. It is known the recirculation of medium boosts the proliferation of the bacteria, carrying anabolites and washing away the waste products [15]. However, the flow could also inhibit the proliferation of the bacteria, affecting the density of the biofilm and reducing its size. For example, Thomen *et al.* [16] studied the effect of the shear stress using *E.Coli* as the reference bacteria strain. In their work, they used bacteria directly immersed in the fluid and they found a value that inhibit the attachment of the planktonic bacteria and the resulting formation of the biofilm. Cremer *et al.* [17] suggest in their work that the physical forces due to a peristaltic mixing can affect the growth and the ecology of the microorganisms of the colon.

In this light, this work aims at understanding how the fluid flow in dynamic culture conditions affects the formation of the complex multi-species biofilm, such as that produced by the human gut microbiota. Specifically, we developed a controlled shear stress chamber where we firstly cultured two bacterial strains (*i.e.,* E. Coli and E. Faecalis) and then a complete human gut microbiota under different flow rates, evaluating the biofilm formation.

II. MATERIALS AND METHODS

A. Computation model of the controlled shear stress chamber

The culture chamber of the bioreactor was purposely designed to evaluate how the microorganisms react to the shear stress. Specifically, the chamber has a trunk of pyramid shape (Fig 1.a) to ensure an increase of the shear stress on its bottom wall from the inlet to the outlet. Finite element analysis (COMSOL Multiphysics) was performed in order to evaluate the fluid dynamics inside the chamber. Navier-stokes equations with laminar flow were solved inside the culture medium domain. A parametric model was applied to the problem to see how the shear stress curve change with different flow rates (Qin, ranging from 2.5 to 7.5 ml/min). Inlet and outlet of the model are shown in Fig 1.a. Domain and boundary condition are shown in Fig 1.b.

B. Fabrication of the controlled shear stress chamber

To fabricate the controlled shear stress chamber, different subtractive and additive techniques were used. The main body of the chamber was fabricated by milling (Roland SRM 20) a polyoxymethylene (POM) block; the screw-type connectors were made *ad hoc* by stereolithography (Form 2, Formlabs) using an epoxy resin (Formlabs); the polystyrene glass cap was cut using a laser cutter machine; the snap fit closure was made
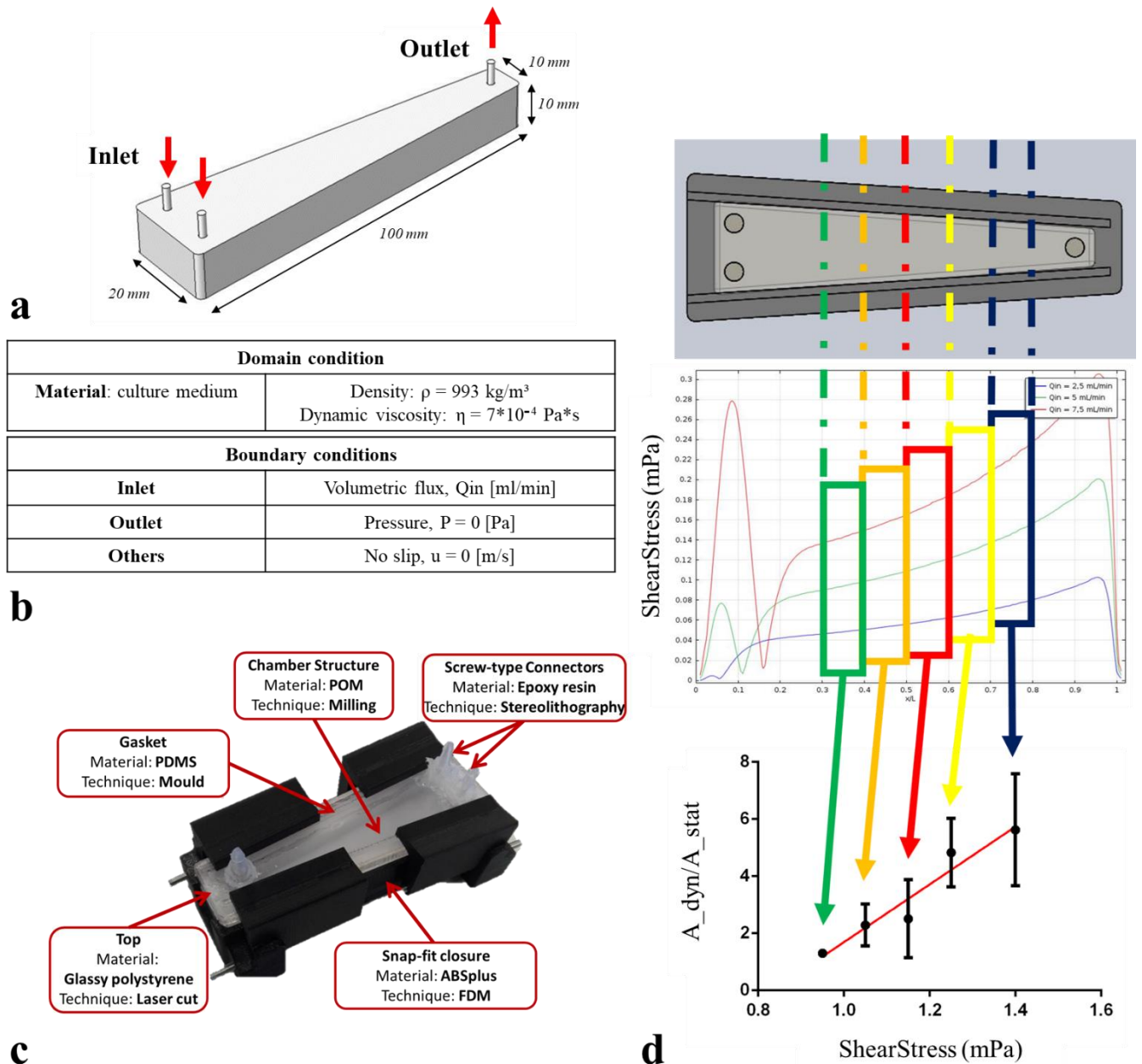
Figure 1: (a) CAD model of the controlled shear stress culture chamber;(b) parameters defined for the computational model. Data for culture medium have been taken from [19];(c) prototype of the controlled shear stress culture chamber;(d, from the top) top view of the culture chamber bottom wall; bottom wall shear stress (middle); (bottom) evaluation of the film formation, measured in the region where the shear stress presents a linear increase (A_dyn is the absorbance at 570 nm of the crystal violet essay in the dynamic tests, while A_stat is the same measurement under static conditions).

in ABS with a 3D FDM printer (Ultimaker Original) (Fig 1.b).A gasket was also fabricated to help the closure of the snap-fit system, pouring silicone (Sylgard 184, DowCorning) on a mold 3D printed by FDM.

C. Microorganisms preparation

Two reference microbial strains were selected: *Escherichia coli* ATCC 25922, *Enterococcus faecalis* ATCC 29212. These strains represent two common commensal of the human gut microbiota and are Gram-negative and Gram-positive, respectively.

Faecal samples collected from healthy donors were prepared following the European Guidelines for faecal microbiota transplantation [18]. Briefly, 30 g of fresh faeces

were dissolved in 150 ml of saline solution and filtered with Whatman membranes. Samples were stored at -80°C with 10% glycerol.

D. Dynamic tests and biofilm quantification

Bacteria were cultured on acetate strips (length 8 cm, width 1 cm, thickness 100-300 µm). Briefly, 600 µl of microbial suspension were seeded on the acetate strips and cultured for 24 hours using RPMI 1640 culture medium (Sigma-Aldrich). Human gut microbiota was cultured under anaerobic conditions.

Both dynamic and static tests, with the same amount of culture medium, were assessed. Static tests were used as positive control. Two dynamic tests were performed for 8 h each, under
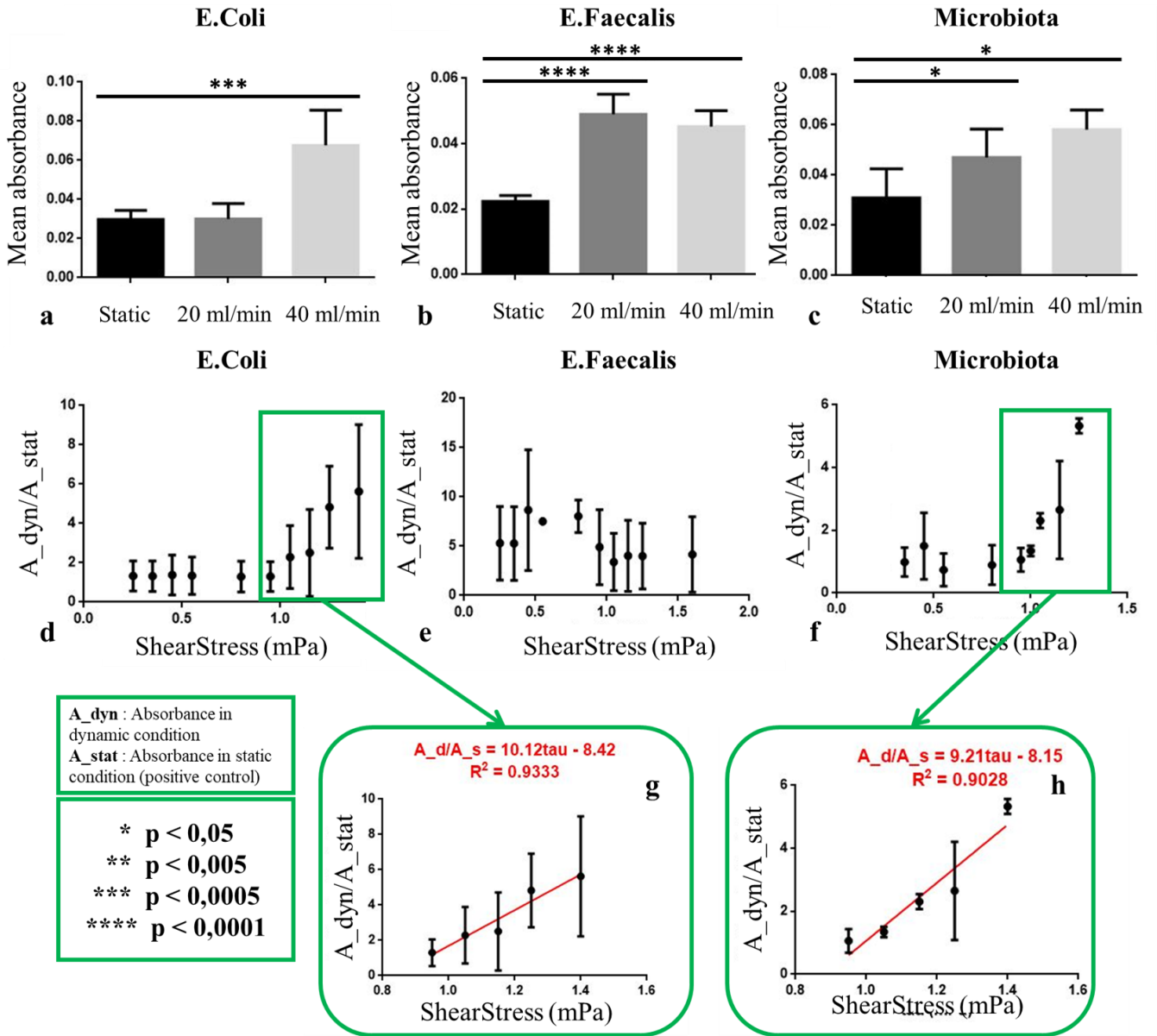
Figure 2: (a-c) Histograms of the mean absorbance, calculated over all the ROIs, for the two strains for the complete human gut microbiota; correlation between the ratio of absorbances (dynamic vs. static conditions) and the shear stress for the two strains (d, e) and for the complete human gut microbiota (f); (g-h). The statistically significant correlations in (g) and (h) correspond to 40 ml/m flux.

a flow of 20 ml/min and 40 ml/min, respectively. These flows were selected to understand if high fluxes could affect negatively (i.e. inhibition of the proliferation, detachment of the formed biofilm) the cultured bacteria. For the gut microbiota an anaerobic culture condition was used.

At the end of the test, the area of the strips where the wall shear stress presents a linear increase (Fig 1d) was divided into several region of interests (ROI), obtaining squares of 1 cm side. On each ROI, a crystal violet assay was performed in order to quantify the formation of a biofilm on the substrate. Briefly, samples were stained in a 24-well using 200 μl of 0.1% crystal violet for 30 min at RT [20]. After three washes with PBS 1X, samples were covered with 2 ml of ethanol (96% v/v) to solubilize the crystal violet. The crystal violet expelled from the microorganisms (correlated to the quantification of

bacteria biofilms) was evaluated in terms of Optical Density (OD) at 570 nm using a micro plate reader [21], [22].

E. Statistical analysis

Results are expressed as mean values ± standard deviations. All the statistical and correlation analyses were performed with the Prism 6 (GraphPad) software. Significance was set at a P value of $* < 0.05$, $** < 0.005$, $*** < 0.0005$, $**** < 0.0001$. For the correlation analysis a R > 0.90 was considered as statically significant.

III. RESULTS AND DISCUSSION

Fig 2.a-c show the mean value of the absorbance from ROIs subjected to increasing flow rates, for evaluating the effect of the flow on the whole substrate regardless of the shear stress

value. A t-test confirms a significant increase in bacterial biofilm production with respect to the static condition when a flow is applied, both for the individual bacterial strains (*E.Coli* and *E.Faecalis*) and the complete human gut microbiota. Only the *E.Coli* subjected to a flow of 20 ml/min does not respect this trend. The increase in biofilm production, evaluated as average on all the ROIs, can be related to an improved nutrient supply thanks to the dynamic culture conditions.

In order to evaluate the biofilm formation in the dynamic model with respect to the control as a function of the applied shear stress, the ratio between the absorbance of the ROIs obtained from the dynamic model and those of the static model was calculated. The values obtained for each ROI were plotted versus the average shear stress values obtained from the computational model in the different regions of the bioreactor (Fig 2.d-f, A_dyn referred to the dynamic tests, A_stat is referred to the static tests). Data show that the ratio between dynamic and static conditions is always greater than one, further suggesting the effects on microbiota well-being of the nutrient intake due to convective flux.

Finally, we assessed the effect of the shear stress on the formation of the biofilm performing correlation analysis on the data in Fig 2.d-f. The results showed a positive trend for *E.Coli* and the human gut microbiota subjected to a flow of 40 ml/min (shear stress ranges from 0.9 to 1.4 mPa) (Fig 2.g,h). Data suggest that mechanical stimuli due to the applied fluid flow increase the formation of a stable biofilm for both *E.Coli* and the human gut microbiota.

IV. CONCLUSION

In this work a controlled shear stress chamber was designed and manufactured to evaluate the effects of a flow induced shear stress on two microorganism strains and on the complete human gut microbiota. The results showed that the convective mass flux generated by the fluid flow improves the growth of bacteria with respect to the static control. In addition, a positive trend was observed at increasing shear rates for *E.Coli* and for the human gut microbiota, suggesting a relationship between the production of a stable biofilm and a mechanical stimulus. Future developments will focus on the investigation of bacteria behaviour under a wider range of shear stresses, in order to understand if there is a critical shear stress beyond which there is an inhibition of the bacteria proliferation and of the formation of a stable biofilm, thus guiding the design of a bioreactor specific for bacteria culturing.

REFERENCES

[1] F. Baquero and C. Nombela, "The microbiome as a human organ," Clinical Microbiology and Infection, vol. 18, no. SUPPL. 4. Blackwell Publishing Ltd, pp. 2–4, 2012.

[2] V. Braniste et al., "The gut microbiota influences blood-brain barrier permeability in mice," Sci. Transl. Med., vol. 6, no. 263, Nov. 2014.

[3] A. Abu-Shanab and E. M. M. Quigley, "The role of the gut microbiota in nonalcoholic fatty liver disease," Nat. Rev. Gastroenterol. Hepatol., vol. 7, no. 12, pp. 691–701, Dec. 2010.

[4] A. Keshavarzian et al., "Colonic bacterial composition in Parkinson's disease," Mov. Disord., vol. 30, no. 10, pp. 1351–1360, 2015.

[5] J. F. Cryan et al., "The microbiota-gut-brain axis," Physiol. Rev., vol. 99, no. 4, pp. 1877–2013, 2019.

[6] G. Trujillo-de Santiago, M. J. Lobo-Zegers, S. L. Montes-Fonseca, Y. S. Zhang, and M. M. Alvarez, "Gut-microbiota-on-a-chip: an enabling field for physiological research," Microphysiological Syst., vol. 1, pp. 1–1, 2018.

[7] T. L. Miller and M. J. Wolin, "Fermentation by the human large intestine microbial community in an in vitro semicontinuous culture system," Appl. Environ. Microbiol., vol. 42, no. 3, pp. 400–407, 1981.

[8] G. R. Gibson, J. H. Cummings, and G. T. Macfarlane, "Use of a three-stage continuous culture system to study the effect of mucin on dissimilatory sulfate reduction and methanogenesis by mixed populations of human gut bacteria.," Appl. Environ. Microbiol., vol. 54, no. 11, pp. 2750–2755, Nov. 1988.

[9] K. Molly, M. Vande Woestyne, and W. Verstraete, "Development of a 5-step multi-chamber reactor as a simulation of the human intestinal microbial ecosystem," Appl. Microbiol. Biotechnol., vol. 39, no. 2, pp. 254–258, May 1993.

[10] P. Van Den Abbeele et al., "Butyrate-producing Clostridium cluster XIVa species specifically colonize mucins in an in vitro gut model," ISME J., vol. 7, no. 5, pp. 949–961, May 2013.

[11] L. Liu et al., "Establishing a mucosal gut microbial community in vitro using an artificial simulator," PLoS One, vol. 13, no. 7, p. e0197692, Jul. 2018.

[12] M. Minekus et al., "A computer-controlled system to simulate conditions of the large intestine with peristaltic mixing, water absorption and absorption of fermentation products," Appl. Microbiol. Biotechnol., vol. 53, no. 1, pp. 108–114, Dec. 1999.

[13] H. J. Kim, D. Huh, G. Hamilton, and D. E. Ingber, "Human gut-on-a-chip inhabited by microbial flora that experiences intestinal peristalsis-like motions and flow," Lab Chip, vol. 12, no. 12, pp. 2165–2174, Jun. 2012.

[14] S. Jalili-Firoozinezhad et al., "A complex human gut microbiome cultured in an anaerobic intestine-on-a-chip," Nat. Biomed. Eng., vol. 3, no. 7, pp. 520–531, Jul. 2019.

[15] A. Persat et al., "The mechanical world of bacteria," Cell, vol. 161, no. 5. Cell Press, pp. 988–997, 30-May-2015.

[16] [16] P. Thomen, J. Robert, A. Monmeyran, A.-F. Bitbol, C. Douarche, and N. Henry, "Bacterial biofilm under flow: First a physical struggle to stay, then a matter of breathing," PLoS One, vol. 12, no. 4, p. e0175197, Apr. 2017.

[17] J. Cremer et al., "Effect of flow and peristaltic mixing on bacterial growth in a gut-like channel."

[18] G. Cammarota et al., "European consensus conference on faecal microbiota transplantation in clinical practice," Gut, vol. 66, no. 4, pp. 569–580, Apr. 2017.

[19] P. Buchwald, "A local glucose-and oxygen concentration-based insulin secretion model for pancreatic islets," Theor. Biol. Med. Model., vol. 8, no. 1, p. 20, Jun. 2011.

[20] G. D. Christensen et al., "Adherence of coagulase-negative staphylococci to plastic tissue culture plates: A quantitative model for the adherence of staphylococci to medical devices," J. Clin. Microbiol., vol. 22, no. 6, pp. 996–1006, 1985.

[21] J. G. E. Wijman, P. P. L. A. De Leeuw, R. Moezelaar, M. H. Zwietering, and T. Abee, "Air-liquid interface biofilms of Bacillus cereus: Formation, sporulation, and dispersion," Appl. Environ. Microbiol., vol. 73, no. 5, pp. 1481–1488, Mar. 2007.

[22] L. Crémet et al., "Comparison of three methods to study biofilm formation by clinical strains of Escherichia coli," Diagn. Microbiol. Infect. Dis., vol. 75, no. 3, pp. 252–255, Mar. 2013.H. Poor, *An Introduction to Signal Detection and Estimation*. New York: Springer-Verlag, 1985, ch. 4.

Pectin-based biomaterial ink for Green Tissue Engineering applications

A. Lapomarda[1,2], A. De Acutis[1,2], I. Chiesa[1,2,3], G. M. Fortunato[1,2], F. Montemurro[1], C. De Maria[1,2],
M. Mattioli Belmonte[4], R. Gottardi[3,5], G. Vozzi[1,2]

[1] *Research Center 'E. Piaggio', University of Pisa, Pisa, Italy*
[2] *Department of Ingegneria dell'Informazione, University of Pisa, Pisa, Italy*
[3] *Department of Pediatrics, Division of Pulmonary Medicine, The Children's Hospital of Philadelphia, Philadelphia, USA*
[4] *Department of Scienze Cliniche e Molecolari, Università Politecnica delle Marche, Ancona, Italy*
[5] *Fondazione Ri.MED, Palermo, Italy*

Abstract—**Green and non-toxic biomaterials obtained from renewable sources and processable through 3D bioprinting technologies are emerging as novel candidate materials to produce sustainable scaffolds for tissue engineering applications. Here, pectins from citrus peels were crosslinked for the first time with (3-Glycidyloxypropyl)trimethoxysilane (GPTMS) through a simple and one-pot procedure. GPTMS content affected the properties of freeze-dried pectin scaffolds in terms of porosity, water uptake and compressive modulus. Moreover, GPTMS improved pectins printability and did not negatively affect pectins cytocompatibility. Three-dimensional woodpile and complex anatomical shaped scaffolds with interconnected micro- and macropores were therefore bioprinted without the use of any additional support material. These results show the great potential of using pectin crosslinked with GPTMS as biomaterial ink to fabricate patient specific scaffolds, which could be used to promote tissue regeneration *in vivo*.**

Keywords— **tissue engineering, pectin, bioprinting, GPTMS**

I. Introduction

RESTORING the functions of native tissues is one of the main goals of tissue engineering (TE). This objective is achieved by using three-dimensional (3D) scaffolds able to mimic the biochemical signalling, topological (e.g., porosity) and mechanical properties (e.g., elastic modulus) of native tissues on micro- and macroscale [1]. The identification of the proper fabrication technology and biomaterials plays a fundamental role in producing functional scaffolds with a specific 3D architecture [2-3]. Recently, a great deal of attention has been attributed to the use of sustainable technologies and eco-friendly biomaterials derived from recycled sources (e.g. keratin extracted from chicken feathers [4], hydroxyapatite derived from egg shells [5], pectin derived from fruit pomace [6]) for the fabrication of TE scaffolds. Among these, pectins, polysaccharides constituting the cell walls of most of the plants [6], are finding different applications in the biomedical field (e.g. targeted drug delivery [7] and TE [8]) for their advantageous properties including biocompatibility, biodegradability and nontoxicity [9]. Moreover, pectins are soluble in green solvents (e.g., water) and form a gel when exposed to a certain amount of divalent cations (e.g., Ca^{2+}) [6]. Their poor rheological properties (viscosity and yield stress), however, limit their use through 3D bioprinting techniques. Only few examples of 3D bioprinted pectin-based scaffolds have been, in fact, reported in literature so far [10-11].

The crosslinking process based on the use of divalent cations is the most used approach to obtain water stable pectin scaffolds. This method is however generally characterized by a poor control over the complete and homogenous gelation throughout the scaffold and postprocessing treatments (especially in bioprinting) are often required [12]. Here, we address this challenge by using (3-glycidyloxypropyl)-trimethoxysilane (GPTMS) as pectin cross-linking agent for the first time. GPTMS is a cytocompatible crosslinker which allows to obtain materials with tunable physical properties (e.g., mechanical properties, water uptake, porosity [13]) in a simple and one-pot approach. Moreover, it has been shown that GPTMS contributes to improve the processability of natural [14] and synthetic [15] polymers.

In this work, we report on a new one-pot approach to prepare a pectin-GPTMS-based biomaterial ink. Particularly, we firstly investigated the effects of GPTMS content on the porosity, water uptake, mechanical properties, and cytocompatibility on microporous pectin-GPTMS sponges fabricated by freeze-drying. Then, we examined the processability of pectin-GPTMS-based biomaterial ink through 3D bioprinting. 3D mesoporous woodpile and complex anatomically shaped scaffolds were finally fabricated combining 3D bioprinting and freeze-drying techniques.

II. Materials And Methods

A. Preparation of Pectin-GPTMS Sponges

An aqueous solution of pectin (4% w/v) (Classic CU 701, degree of esterification 36%, Mw 100−400 kDa [16]) was prepared at 70 °C until pectin was completely dissolved. Thereafter, different amounts of GPTMS (Alfa Aesar) were added to obtain the mixtures presented in Table I, which were stirred at 70 °C for 40 min.

TABLE I
COMPOSITION OF PECTIN-GPTMS MIXTURES

Sample name	GPTMS (g/g pectin)
Pect	0
PectG1	0.107
PectG2	0.246
PectG3	0.492
PectG4	0.984

These mixtures were subsequently poured into custom-made cylindrical molds [17] (13 mm diameter × 10 mm height),

frozen overnight at −20 °C and then freeze-dried (BenchTop Pro-SP Scientific) at −60 °C for 24 h to obtain dry crosslinked pectin sponges. Finally, the resulting sponges were left on a heating plate at 37 °C for 4 days to further promote the completion of the cross-linking reaction between pectin and GPTMS. Non crosslinked pectin porous sponges (without GPTMS) were obtained with the same procedure.

B. Characterization of the Pectin-GPTMS Sponges.

Pore size and architecture in the dry pectin sponges (n = 3 per group) were analyzed on scanning electron microscopy (SEM, Philips XL 20 SEM) images through ImageJ software.

The porosity (P) of dry pectin sponges (n = 3 per group) was determined gravimetrically by applying eq. 1:

$$P\ (\%) = \left(1 - \frac{m_s}{\rho_m V_s}\right) \times 100 \tag{1}$$

where m_s and V_s are the measured weight and volume of the sponges, respectively. The theoretical density of the material (ρ_m) was determined measuring the mass and volume of squared samples (n = 10 per group) cored from nonporous solvent-casted films made of the Pectin-GPTMS mixtures (Table 1).

Water Uptake (WU) was obtained by soaking dry pectin sponges (n = 3 per group) in ultrapure water at 37 °C for 4 days. At predefined time points WU was calculated as described by Shirosaki et al. [13].

Compressive modulus of wet pectin sponges (n = 5 per group) was determined through uniaxial compressive test (Z005 series Zwick/Roell) using a 100 N loading cell, 0.01 s⁻¹ strain rate and a max compressive axial deformation of 30%.

C. Cell culture

Human mesenchymal stem cells (hMSCs, 5×10^4 cells/sponge) (RoosterBio) were seeded on the pectin-GPTMS sponges (n = 3 per group) previously sterilized and incubated overnight in growth medium (GM: Gibco FluoroBrite Dulbecco's Modified Eagle Medium, fetal bovine serum (10% v/v), penicillin/streptomycin/fungizone (2% v/v), sodium pyruvate (1% v/v), and glutaMAX (1% v/v)) at 37°C and 5% CO_2. Pure pectin sponges (Pect) were not analyzed due to their dissolution in the culture medium. Live and dead assay was carried out after 24 h, 72 h, 7 days, and 10 days of initial hMSCs seeding. Scaffolds were covered with calcein AM/ethidium homodimer solution (4 μM/ 8 μM) and incubated for 45 min in the dark. At each time point, maximum projection images were acquired with a fluorescence microscope (Keyence BSX710).

D. Printability investigation

PectG4 was selected to evaluate the effects of GPTMS on pectin printability. PectG4 mixture was further stirred for 4 h at 70 °C to induce an increment of viscosity, useful for the printing process [18]. The change of viscosity after 4h stirring and heating was confirmed by rheological experiments carried out on a HAAKE RheoStress 6000 (Thermo Scientific) with plate-cone (1° angle) measuring configuration. Measurements were performed at 20 °C (printing temperature) in the linear viscoelastic regime at the frequency range of $0.1 - 100$ s⁻¹. Additionally, the yield stress as function of shear rate ($0 - 100$ s⁻¹) was determined.

E. 3D bioprinting

A customized piston-driven extruder 3D bioprinter was used to bioprint 3D mesoporous scaffolds (previously designed and sliced on purpose by CAD and CAM software: Solidworks and Slic3r, respectively) with the viscous PectG4 biomaterial ink. A conical tapered plastic tip (22 G), a printing speed of 13 mm/s, and an extrusion rate of 18 ml/h were used, respectively. Woodpile structures (17 mm × 17 mm × 5.2 mm, with a total of 13 layers) were printed with a 1.8 mm spacing between adjacent strands. Once printed, the macroporous structures were frozen (−20 °C, overnight) and subsequently freeze-dried in order to promote the cross-linking process of GPTMS and introduce a microporosity into the macroporous structures. The fabrication process and the woodpile model of the printed scaffolds are shown in Fig. 1. Scaffold architecture and pore size were investigated through SEM, as previously described. A human nose and ear model were furthermore 3D printed to investigate the potentiality of this material to fabricate complex anatomically-shaped scaffolds.

III. RESULTS AND DISCUSSION

A. Characterization of the Pectin-GPTMS Sponges

Pectin sponges with an interconnected network of micropores were obtained by cross-linking the pectin with different amounts of GPTMS (Fig. 2). Preliminary attenuated total reflectance infrared spectroscopy (ATR-IR) show that during crosslinking process (pH = 2.7) the hydroxyl groups of GPTMS, deriving from the opening of the GPTMS oxirane ring, may react with the carbonyl groups of pectin. Moreover, we found evidence that in the meantime a siloxane network is formed. Pectin sponges showed suitable values of porosity for TE applications ($\geq 75\%$) (Table II) [20]. Particularly, the porosity of dry pectin sponges was found to decrease with increasing in GPTMS content (Pearson coefficient R = 0.98),
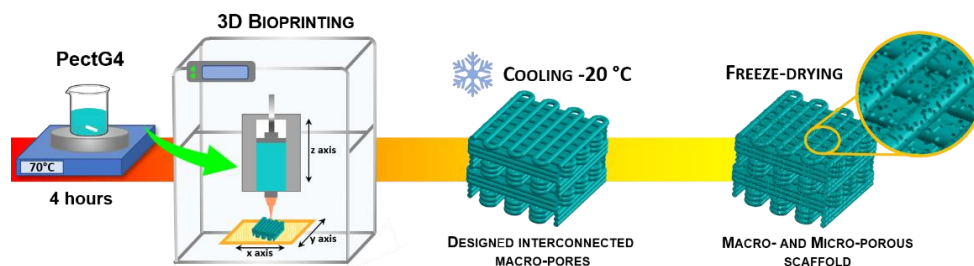

Fig. 1 Workflow of the fabrication of PectG4 woodpile scaffolds. After stirring for 4 h at 70 °C, PectG4 is loaded in the syringe of a custom-made piston-driven extruder 3D bioprinter, and a woodpile scaffold is 3D bioprinted. The scaffold is thereafter cooled at −20 °C and freeze-dried, and a mesoporous scaffold is finally obtained. Reprinted (adapted) with permission from [19]. Copyright (2020) American Chemical Society.
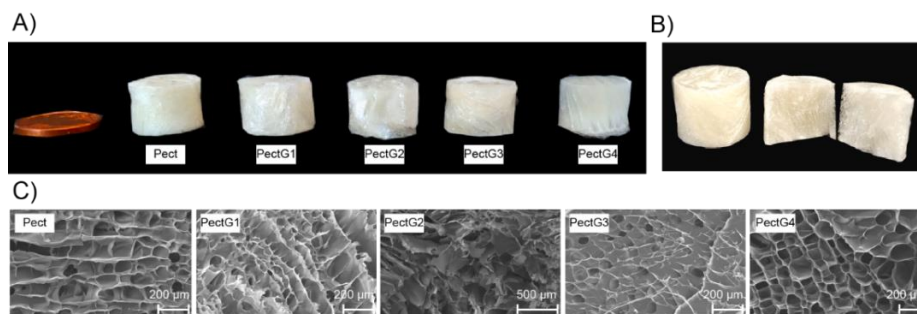
Fig. 2 (A-B) Representative images of Pect and PectG sponges after freeze-drying; (C) SEM images of the cross-section of Pect and PectG sponges (Pect, PectG1, PectG3, and PectG4, scale bar, 200 μm; PectG2, scale bar, 500 μm). Reprinted (adapted) with permission from [19]. Copyright (2020) American Chemical Society.

as also confirmed by Chao et al. in chitosan scaffold crosslinked with GPTMS [21]. However, GPTMS content did not affect the pore size in pectin sponges. An average pore size of 85 μm with a range of 50−140 and 20−200 μm were obtained for Pect and the PectG sponges, respectively. No statistical differences or correlations (R = 0.53) were observed among groups. This is in line with the results obtained by Shirosaki et al. [13].

Pectin sponges absorb water over time reaching a plateau value after 24

h at 37°C. GPTMS content strongly influences the WU of pectin-GPTMS sponges. WU decreased with increasing in GPTMS amount (R = − 0.98), as was also reported by Chao et al. for chitosan sponges [21]. The higher crosslinking density due to a higher amount of GPTMS explains this trend [22].

The compressive modulus of pectin-GPTMS sponges increased with increasing in GPTMS content (R = 0.99) as also shown by Shirosaki et al. in chitosan membranes [23]. Particularly, PectG4 sponges showed an almost 3-fold higher stiffness than PectG1 sponges. As previously described, this is due to an increase of crosslinking density in the pectin matrix.

TABLE II
PROPERTIES OF PECT-GPTMS SPONGES

Sample	Compressive Modulus (kPa)	Porosity (%)	Water Uptake (%)
Pect	-	86.9 ± 0.4	-
PectG1	67.4 ± 32.7	87.6 ± 1.2	1550 ± 24.3
PectG2	105.7 ± 17.4	85.4 ± 0.8	1309.7 ± 74.2
PectG3	180.7 ± 52.2	83.9 ± 0.4	1026.7 ± 47.2
PectG4	288 ± 78.1	77.5 ± 0.6	698.6 ± 49

B. Cell culture

Live and Dead assays on hMSCs seeded on the PectG sponges showed that, at all timepoints, cells were alive and homogeneously distributed and no dead cells could be observed (Fig. 3).
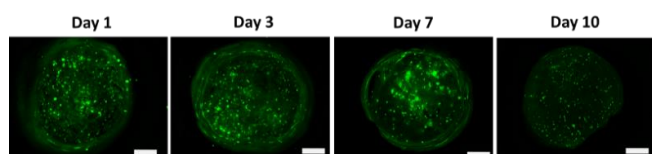
Fig. 3 Representative maximum projection images of a live assay at different time points on PectG4 sponges. (scale bar, 1 mm). Reprinted (adapted) with permission from [19]. Copyright (2020) American Chemical Society.

For brevity, only representative views at each timepoint are shown in Figure 3. Globally, the high viability of the hMSCs over time on PectG sponges proves that our newly developed GPTMS-based pectin cross-linking method does not negatively affect pectin cytocompatibility.

C. 3D Bioprinting of Micro- and Macroporous scaffolds.

The addition of GPTMS made the pectin suitable as ink for bioprinting due to the increase of viscosity and yield stress, as confirmed by rheological experiments (Fig. 4A). The introduction of GPTMS induced an increase of 40-folds of viscosity and the rise of the yield stress from 0.5 to 3 kPa. This increase was promoted by the GPTMS and pectin reaction at 70 °C for 4h. Globally, Pect and PectG4 both possessed a pseudoplastic flow behavior; the marked increase of the yield stress due to GPTMS contribution made PectG4 a Bingham pseudoplastic fluid. Thus, the rheological properties of PectG4 make it a promising ink for 3D bioprinting as the lower viscosity at higher shear rates allows for ready extrusion through the printer nozzle, and the higher yield stress in the absence of shear enables PectG4 to retain its shape without collapsing after extrusion.

D. 3D bioprinting

The combination of 3D bioprinting with freeze-drying allowed to fabricate mesoporous 3D woodpile structures (Fig. 4).
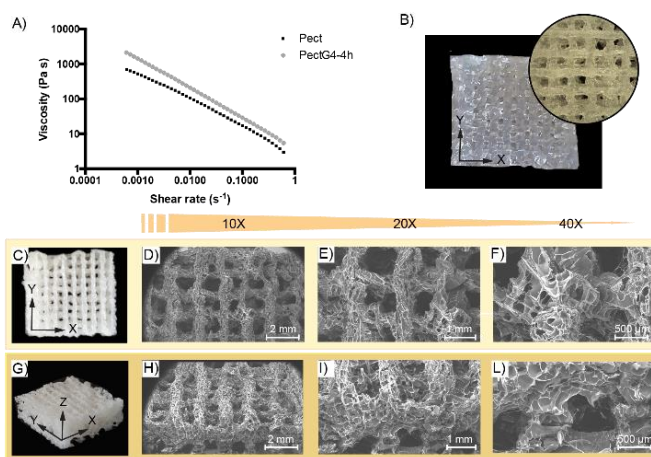

Fig- 4(A) Viscosity *vs* shear rate of Pect and PectG4; (B) PectG4 woodpile scaffold with a focus of the core part after bioprinting; (C, G) images of PectG4 woodpile scaffolds after freeze-drying; SEM images of woodpile scaffolds in (D−F) top and (H−L) lateral views (scale bars: D, H = 2 mm; E, I = 1 mm; F, L = 500 μm). Reprinted (adapted) with permission from [19]. Copyright (2020) American Chemical Society.

PectG4 woodpile structures possessed micropores of 130 ± 40 μm and 150 ± 70 μm on the xy and yz planes, respectively. As can be seen from the SEM images (Fig. 4 D-F, H-L), designed interconnected macropores of 1100 ± 200 and 1000 ± 200 μm were present in the xy and yz planes (refer to axes in Fig. 1). Moreover, no delamination between the different layers was observed, indicating that a chemical link between layers could be obtained. Fig. 5 shows pictures of 3D printed and freeze-dried models of human nose and ear. This confirms the high potential of PectG4 to be used as biomaterial ink for the production of complex shaped scaffolds, such as patient specific implants, which could be used to induce tissue regeneration *in vivo*.
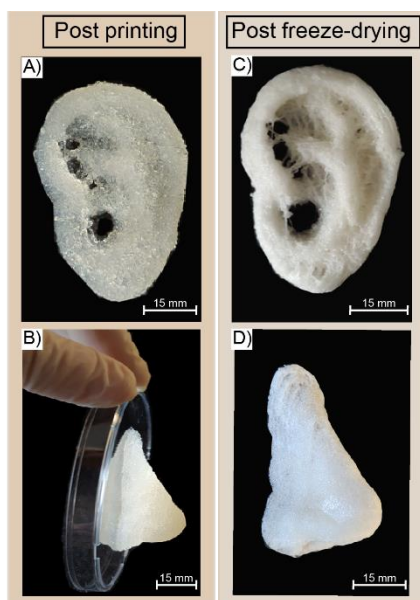
Fig. 5 3D printed structures of a ear and nose model immediately after bioprinting (A, B), and after freeze-drying (C, D). Reprinted (adapted) with permission from [19]. Copyright (2020) American Chemical Society.

E. Conclusions

Here, a one-pot preparation of a pectin-based biomaterial cross-linked with GPTMS was described for the first time. This material shows promising rheological properties to be used as biomaterial ink for the fabrication of complex 3D bioprinted anatomical shaped scaffold without the use of any support material. The GPTMS content directly affects porosity, compressive modulus and water uptake, while pore size and morphology are independent from this parameter. Notably, pectin-GPTMS sponges are cytocompatible: hMSCs remained alive up to the end of the experiments (10 days) and homogeneously colonized the scaffold. Globally, all these results showed the great potential of this newly developed biomaterial to be used as sustainable and versatile biomaterial ink for the biofabrication of cost-effective, sustainable, patient-specific scaffolds.

REFERENCES

[1] Ross, A. M.; Jiang, Z.; Bastmeyer, M.; Lahann, J. Physical aspects of cell culture substrates: Topography, roughness, and elasticity. Small 2012, 8, 336−355.

[2] O'Brien, F. J. Biomaterials and scaffolds for tissue engineering. Mater. Today 2011, 14, 88−95.

[3] Ma, P. X. Scaffolds for tissue fabrication. Mater. Today 2004, 7, 30−40.

[4] Yin, X. C.; Li, F. Y.; He, Y. F.; Wang, Y.; Wang, R. M. Study on effective extraction of chicken feather keratins and their films for controlling drug release. Biomater. Sci. 2013, 1, 528−536.

[5] Rivera, E. M.; Araiza, M.; Brostow, W.; Castano, V. M.; Dıaz-Estrada, et al. Synthesis of hydroxyapatite from eggshells. Mater. Lett. 1999, 41, 128−134.

[6] Sriamornsak, P. Chemistry of pectin and its pharmaceutical uses: A review. Silpakorn Univ. Sci. Technol. J. 2003, 3, 206−228

[7] Liu, L. S.; Fishman, M. L.; Kost, J.; Hicks, K. B. Pectin-based systems for colon-specific drug delivery via oral route. Biomaterials 2003, 24, 3333−3343.

[8] Neves, S. C.; Gomes, D. B.; Sousa, A.; Bidarra, S. J.; et al. Biofunctionalized pectin hydrogels as 3D cellular microenvironments. J. Mater. Chem. B 2015, 3, 2096−2108.

[9] Noreen, A.; Nazli, Z.-i-H.; Akram, J.; Rasul, I., et al. Pectins functionalized biomaterials; a new viable approach for biomedical applications: A review. Int. J. Biol. Macromol. 2017, 101, 254−272.

[10] Stealey, S.; Guo, X.; Ren, L.; Bryant, E., et al. Stability improvement and characterization of bioprinted pectin-based scaffold. J. Appl. Biomater. Funct. Mater. 2019, 17, 1−5.

[11] Banks, A.; Guo, X.; Chen, J.; Kumpaty, S.; Zhang, W. Novel bioprinting method using a pectin based bioink. Technol. Health Care 2017, 25, 651−655.

[12] Hajikhani, A.; Scocozza, F.; Conti, M.; Marino, M.; et al; Experimental characterization and computational modeling of hydrogel cross-linking for bioprinting applications. Int. J. Artif. Organs 2019, 42, 548−557.

[13] Shirosaki, Y.; Okayama, T.; Tsuru, K.; Hayakawa, S.; Osaka, A. Synthesis and cytocompatibility of porous chitosan-silicate hybrids for tissue engineering scaffold application. Chem. Eng. J. 2008, 137, 122−128.

[14] Gao, C.; Rahaman, M. N.; Gao, Q.; Teramoto, A.; Abe, K. Robotic deposition and in vitro characterization of 3D gelatin bioactive glass hybrid scaffolds for biomedical applications. J. Biomed. Mater. Res., Part A 2013, 101, 2027−2037.

[15] Tallia, F.; Russo, L.; Li, S.; Orrin, A. L. et al, Bouncing and 3D printable hybrids with self-healing properties. Mater. Horiz. 2018, 5, 849−860.

[16] Moreira, H. R.; Munarin, F.; Gentilini, R.; Visai, L.; et alInjectable pectin hydrogels produced by internal gelation: PH dependence of gelling and rheological properties. Carbohydr. Polym. 2014, 103, 339−347.

[17] Orsi, G., Fagnano, M., De Maria, C., Montemurro, F., & Vozzi, G. (2017). A new 3D concentration gradient maker and its application in building hydrogels with a 3D stiffness gradient. Journal of tissue engineering and regenerative medicine, 11(1), 256-264.

[18] Paxton, N., Smolan, W., Böck, T., Melchels, F., Groll, J., Jungst, T. (2017). Proposal to assess printability of bioinks for extrusion-based bioprinting and evaluation of rheological properties governing bioprintability. Biofabrication, 9(4), 044107.

[19] Lapomarda, A., De Acutis, A., Chiesa, I., Fortunato, G. M., Montemurro, F., et al. (2019). Pectin-GPTMS based biomaterial: toward a sustainable Bioprinting of 3D scaffolds for Tissue Engineering application. Biomacromolecules.

[20] Loh, Q. L.; Choong, C. Three-dimensional scaffolds for tissue engineering applications: Role of porosity and pore size. Tissue Eng., Part B 2013, 19, 485−502.

[21] Chao, A. C. Preparation of porous chitosan/GPTMS hybrid membrane and its application in affinity sorption for tyrosinase purification with Agaricus bisporus. J. Membr. Sci. 2008, 311, 306−318.

[22] Canal, T.; Peppas, N. A. Correlation between mesh size and equilibrium. J. Biomed. Mater. Res. 1989, 23, 1183−1193.

[23] Shirosaki, Y.; Tsuru, K.; Hayakawa, S.; Osaka, A., ;et al. Physical, chemical and in vitro biological profile of chitosan hybrid membrane as a function oforganosiloxane concentration. Acta Biomater. 2009, 5, 346−355.

Somatotopical feedback restoration in the lower limb through TENS: a feasibility study

A. Demofonti[1], A. Scarpelli[1], V. Iannelli[1], A.L. Ciancio[1], F. Cordella[1] and L. Zollo[1]

[1]Research Unit of Advanced Robotics and Human-centred Technologies, Campus Bio-Medico University of Rome, Italy

Abstract—Commercially available lower limb prostheses do not restore sensory feedback in amputees. Literature suggests that Transcutaneous Electrical Nerve Stimulation (TENS) can be a promising, non-invasive, somatotopic technique to elicit tactile sensation. This study aims at demonstrating the potentiality of TENS as a means for restoring somatotopic sensations in lower limb amputees. To this purpose an experimental protocol of charge and frequency modulation has been developed and applied to 15 healthy subjects. The referred sensations were characterized in terms of naturalness, depth, pain, intensity, quality and location. Results show that the delivered sensations were mostly described as an almost natural and superficial tingling during both phases. An increase of the quality (from no sensation to vibration) occurred when a higher quantity of charge is injected. A similar trend is reported also for the relationship between injected charge and referred sensation intensity which are mildly correlated (ρ=0.6431, Pearson coefficient). The extension of the elicited area proportionally increased with the stimulus intensity due to the increase of pulse width and pulse frequency in the charge and frequency modulation. The obtained results have made it possible to take a step forward for considering TENS as a valid somatotopic, non-invasive approach for restoring sensory feedback and hence, for testing the technique on trans-tibial amputees in order to integrate it in the future in a prosthetic system.

Keywords—Lower limb, sensory feedback restoration, tactile sensation, transcutaneous electrical nerve stimulation.

I. INTRODUCTION

Current lower limb prostheses support walking, bending the knee joint, absorbing and stabilizing stance during walking [1]. Relying on the tactile information from the stump-socket interface [2], people with lower limb amputation have to deal with risk of falls [3], reduced mobility [4] and increased cognitive burden [5]. Sensory feedback restoration could contribute to improve their quality of life and participation in activities of daily living [6]. Despite the high prevalence of lower limb loss [7], few studies have been conducted for the sensory feedback restoration in lower limb amputees.

Invasive techniques have obtained interesting results, such as the increasing of walking speed and the decreasing of mental and physical fatigue and metabolic cost, but they present disadvantages related to invasiveness, i.e. surgery, fibrotic reaction and weak long-term stability of the implant [8][9][10][11].

Different non-invasive methods have been tested. Despite the resulting benefit (improvement of gait symmetry and stability), most non-invasive systems are non-somatotopic since the elicited sensation is not felt in the missing leg using vibrotactile or electrotactile stimulation of the stump to convey touch events on the foot [1][12][13][14].

The ideal solution is to restore sensory information using a somatotopic approach because of the simplicity and intuitiveness, which allows for immediate and effortless integration of the feedback within the prostheses[15]. This is in contrast with non-somatotopic approaches, which necessarily introduce the need for training.

Transcutaneous Electrical Nerve Stimulation (TENS) uses superficial electrodes placed on the skin to electrically stimulate the underlying nerves and evoke referred tactile sensations. Evidence suggests that TENS can be a promising non-invasive, somatotopic sensory feedback approach for inducing referred sensations to the phantom foot of the amputees. In the literature, TENS has been used to allow the amputees to realize how the position of the center of pressure (CoP) changes during gait [16][17][18].

Moreover, the literature shows that TENS can reduce painful conditions, phantom pain and stump pain caused by amputation [19].

This study aims at demonstrating the potentiality of TENS as a means for restoring somatotopic sensations in lower limb amputees. A feasibility study has been performed on healthy subjects to fully characterize the evoked tactile sensation in the foot by transcutaneous electrical stimulation of the tibial nerve. Charge and frequency modulation have been used to evaluate different characteristics of the evoked sensations.

The paper is organized as follows. Section II describes the experimental setup and protocol. Section III reports and discusses results and Section IV is dedicated to the conclusion.

II. MATERIALS AND METHODS

A. Experimental setup

15 healthy subjects (5 males and 10 females) with a mean age of 24.5±1.7 years were recruited for the study. All subjects had no previous experiences with TENS and no neurological disorders. The study was authorized by the Ethic Committee of Campus Bio-Medico University of Rome in accordance with the Helsinki Declaration. The main aspects of the study were explained to the subjects and they signed an informed consent.

The used experimental setup is represented in Fig.1. It was composed of an electrical stimulator (A), a proprietary control software of the stimulator (B), two superficial electrodes (C) and a graphic user interface (D).
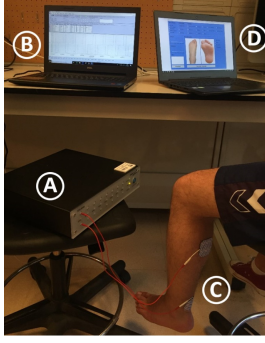
Fig. 1: Experimental setup. It was composed of an electrical stimulator (A), a proprietary control software of the stimulator (B), two superficial electrodes (C) and a graphic user interface (D).

The electrical stimuli were delivered by a fully programmable stimulator (STG4008, Multichannel System MCS GmbH, Reutlingen, Germany). The proprietary software (MC_Stimulus II) of the stimulator allows generating arbitrary waveforms.

Two square (50 mm side) commercial auto-adhesive and superficial electrodes (TensCare Ltd, Epsom, United Kingdom) were applied on the subject's left leg to stimulate the tibial nerve. The choice of stimulating the left leg rather than the right one has been arbitrary due to the symmetry of the human body with respect to the sagittal plane.

A custom-developed graphic user interface implemented in C# was used to record the main features of the elicited sensations. For each trial the subject was asked to indicate: the location, the naturalness, the depth, the quality, the intensity of the sensation and pain, if present. The naturalness was assessed using the following options: natural, almost natural, possibly natural, almost unnatural and unnatural. The depth was assessed choosing between superficial, deep and both. The quality was assessed using the following choices: touch/pression, vibration, tug, tingling, pinch, burning, cold, hot, ankle flexion, ankle extension, toes flexion, toes extension and nothing. The intensity and the pain of the sensation were reported in a scale from 0 to 10. In addition, the subject had to indicate on the GUI the location of the sensation using two pictures representing the foot instep and sole.

A symmetric biphasic square wave was used since it is the most used in the literature [10][11][16][17][18]. The stimulation parameters that have been varied are the Pulse Amplitude (PA), the Pulse Width (PW) and the Pulse Frequency (PF). No Interphase Delay (ID) has been used (see Fig.2).
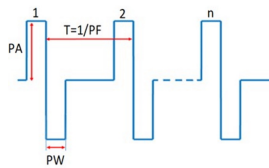
Fig. 2: Symmetric biphasic square wave used during the trials. The stimulation parameters are Pulse Amplitude (PA), Pulse Width (PW) and Pulse Frequency (PF).

B. Experimental Protocol

The experimental protocol was composed of three phases: electrodes positioning, charge modulation and frequency modulation. The first phase was aimed at identifying the optimal position of the electrodes. They have to be positioned upon the skin along the superficial path of the tibial nerve in order to stimulate it and elicit a sensation in the foot sole. The optimal positioning was identified by varying the location of the electrodes. In this phase the following parameters have been used: PW=500 μs, PF=500 Hz and the PA was incremented from 1 mA with a step of 0.1 mA until a value of PA at which the subject reported a well-defined and conformable sensation. This value of amplitude is above the sensation threshold, below the motor one and was kept constant during the whole experimental protocol.

In the second phase, a charge modulation was carried out. PF was fixed at 150 Hz and the PW was varied in the range 100÷500 μs with a step of 40 μs between a stimulus and the following one. At the end of the modulation, PW_m was selected. PW_m is a value of PW at which the reported sensation intensity was at least 3.

In the last phase, a frequency modulation was carried out. PW was settled to PW_m and the PF was varied in the range 50÷500 Hz with a step of 50 Hz from 50 to 200 Hz and a step of 100 Hz from 200 to 500 Hz between a stimulus and the following one.

The stimulation duration was settled to 1 s and kept constant during each of the three phases of the experimental protocol. The target ranges and the step increase of PA, PW and PF during electrodes positioning, charge modulation and frequency modulation, respectively, were used following preliminary tests and they were equal for each subject.

III. RESULTS

The maximum current amplitude delivered to the participants was specific for each subject; the mean value±SD (Standard Deviation) among the subjects was 8.4±0.9 mA. Table I shows the reported naturalness, depth, pain and quality of the sensation of each subject for each trial during both charge and frequency modulation.

During the charge modulation, sensations were generally described as natural, almost natural and possibly natural (respectively, in the 34%, 40% and 18% of the trials where the subjects reported a sensation). The number of trials where the subjects referred an almost unnatural and unnatural sensation is negligible: each of them is equal to 4%. The same trend was reported also for the frequency modulation, where a natural sensation was referred in 25% of the trials, almost natural in 26% and possibly natural in 38%. The stimulation evoked mostly superficial and painless sensations. During the charge modulation, 29% of the total number of trials did not elicit any sensation on the subjects. In the remaining trials the subjects reported a sensation of tingling, vibration and a mix of them. These three sensations were prevalent: their percentages are 27%, 4% and 22%, respectively. During frequency modulation,

TABLE I: CHARACTERISTICS OF THE ELICITED SENSATIONS FOR THE CHARGE AND FREQUENCY MODULATION

Charge Modulation							
Naturalness (117)		**Depth (117)**		**Pain (117)**		**Quality (165)**	
Natural	40	Superficial	82	0 (no pain)	110	Nothing	48
Almost natural	46	Deep	13	1,2,3	7	Tingling	44
Possibly natural	21	Both	22	4,5,6	0	Vibration	6
Almost unnatural	5			7,8,9	0	Tingling and Vibration	36
Unnatural	5			10 (most pain)	0	Others	31
Frequency Modulation							
Naturalness (105)		**Depth (105)**		**Pain (105)**		**Quality (105)**	
Natural	27	Superficial	72	0 (no pain)	101	Nothing	0
Almost natural	27	Deep	15	1,2,3	4	Tingling	26
Possibly natural	40	Both	18	4,5,6	0	Vibration	11
Almost unnatural	10			7,8,9	0	Tingling and Vibration	44
Unnatural	2			10 (most pain)	0	Others	23

The total number of trials for the charge modulation (117) and the frequency modulation (105) in naturalness, depth and pain differ from that of quality because the participant did not always feel a sensation in response to stimulus.

each stimulus elicited a sensation in the foot. As it can be seen in Table I, the number of times when the subjects did not report any sensation during the frequency modulation is zero. Since most of time the subjects reported "Nothing" as quality occurred at 100 μs, 140 μs and 180 μs, these first three values of PW should be too low to elicit a sensation according to our experimental set-up and protocol. In the remaining trials, the subjects reported sensations of tingling, vibration and a mix of them. These resulted the main qualities reported by the subjects with a percentage of 25%, 11% and 42%, respectively. The term "Others" in Table I indicates all the qualities and the combinations of them reported by the subjects in a negligible number of times (touch/pression, touch/pression and tingling, touch/pression and vibration and others).

The relationship between the injected charge and the perceived quality and between the injected charge and the referred sensation intensity were analysed (Fig.3 and Fig.4).

Fig. 4: Relationship between the injected charge and the referred sensation intensity during charge modulation.

Fig. 3: Relationship between the injected charge and the perceived quality. The + sign represents the outlier.

When a higher quantity of charge is injected, an increase of the perception (from nothing to vibration) occurred. The median charge values are 2.52 μC, 4.99 μC, 7.04 μC and 8.28 μC for nothing, tingling, tingling-vibration and vibration, respectively.
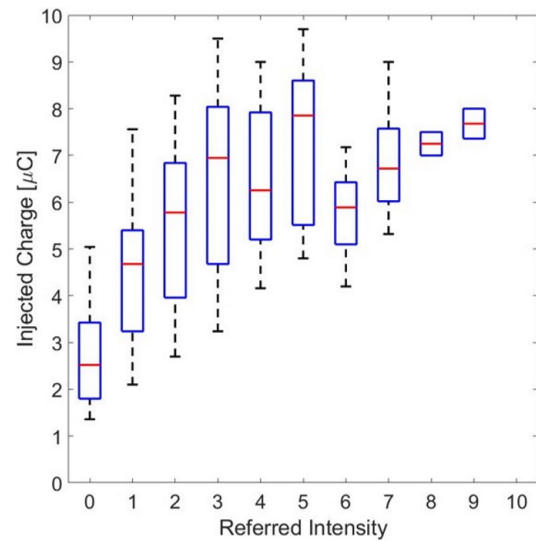
A similar trend is reported also for the relationship between injected charge and referred sensation intensity (ρ=0.6431, Pearson coefficient).

For each stimulus, each subject reported on a map the location of the referred sensations in the left foot's instep and sole. The elicited regions experienced during the charge and frequency modulation of the tibial nerve stimulation are represented in Fig.5. The regions referred by the subjects were overlapped in order to obtain a single picture indicating the mean region reported for three different levels of the stimulus intensity. As expected from the anatomy, the tibial nerve stimulation elicits the regions of the entire foot since under the laciniate ligament the nerve forks in two different branches (median and lateral plantar nerves) which innervate the foot sole. The extension of the elicited region proportionally increased with the stimulus intensity due to the increase of PW and PF in the charge and frequency modulation.
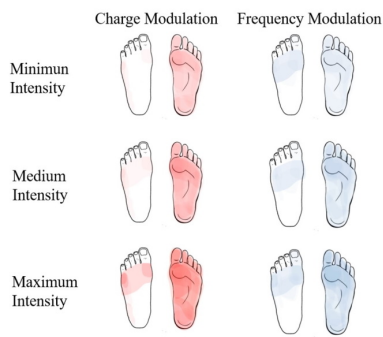
Fig. 5: Regions reported by the subjects after the charge (red) and frequency (blue) modulation. The regions indicated were overlapped in a left leg foot's instep and sole map. The areas depicted with a more vivid colour indicate the regions with a higher number of occurrences than others. Minimum intensity is PW=260 μs and PF=100 Hz; medium intensity is PW=380 μs and PF=300 Hz; maximum intensity is PW=500 μs and PF=500 Hz.

IV. CONCLUSION

This study aims to characterise the evoked tactile sensation in the foot induced by transcutaneous electrical nerve stimulation. An experimental protocol regarding the tibial nerve stimulation was defined and applied on 15 healthy subjects enrolled in the study. The protocol was composed of three phases: electrodes positioning, charge and frequency modulation. The main objective of the experiments was to characterise the type of referred sensation in term of naturalness, depth, pain, intensity, quality and location. During the charge modulation, the reported sensations were mostly described as almost natural and superficial tingling, whereas in the frequency modulation the sensation was mainly perceived as a possibly natural mix of tingling and vibration.

An increase of the quality (from nothing to vibration) occurred when a higher quantity of charge is injected. An analogue trend is reported also for the relationship between injected charge and referred sensation intensity (ρ=0.6431). The extension of the elicited region proportionally increased with the stimulus intensity due to the increase of PW and PF in the charge and frequency modulation. In conclusion, the obtained results are encouraging and they show the good potential of providing a tactile sensation on the foot by TENS.

Future work will be devoted to test the proposed system on lower limb amputees. In patients, a neural reorganization in the stump and movements in stump-socket interface could modify the tissue impedance: these two phenomena could negatively affect the elicitation of referred sensations and, in a general point of view, the overall system.

However, if TENS would be able to overcome this limits on patients and to confirm the already obtained results, it will represents a successfull somatotopical, non-invasive approach that could improve postural control in subjects with trans-tibial amputation.

ACKNOWLEDGEMENT

REFERENCES

[1] C. Dietrich, S. Nehrdich, S. Seifert, K.R. Blume, W.H. Miltner, G.O. Hofmann and T. Weiss, "Leg prosthesis with somatosensory feedback reduces phantom limb pain and increases functionality" *Frontiers in neurology*, 9, 270, 2018.

[2] A.F. Mak, M. Zhang and D.A. Boone, State-of-the-art research in lower-limb prosthetic biomechanics-socket interface: a review. *Journal of rehabilitation research and development*, 38(2), 161-174, 2001.

[3] W.C. Miller, M. Speechley and B. Deathe, "The prevalence and risk factors of falling and fear of falling among lower extremity amputees", *Archives of physical medicine and rehabilitation*, 82(8), 2001.

[4] L. Nolan, A. Wit, K. Dudziñski, A. Lees, M. Lake and M. Wychowañski, "Adjustments in gait symmetry with walking speed in trans-femoral and trans-tibial amputees", *Gait posture*, 17(2), 142-151, 2003.

[5] R.M. Williams, A.P. Turner, M. Orendurff, A.D. Segal, G.K. Klute, J. Pecoraro and J. Czerniecki, "Does having a computerized prosthetic knee influence cognitive performance during amputee walking?", *Archives of physical medicine and rehabilitation*, 87(7), 989-994, 2006.

[6] W.C. Miller, A.B. Deathe, M. Speechley and J. Koval, "The influence of falling, fear of falling, and balance confidence on prosthetic mobility and social activity among individuals with a lower extremity amputation", *Archives of physical medicine and rehabilitation*, 82(9), 2001.

[7] K. Ziegler-Graham, E.J. MacKenzie, P.L. Ephraim, T.G. Travison and R. Brookmeyer,"Estimating the prevalence of limb loss in the United States: 2005 to 2050",*Archives of physical medicine and rehabilitation*, 89(3), 422-429, 2008.

[8] T.R. Clites et al, "Proprioception from a neurally controlled lower-extremity prosthesis", *Science translational medicine*, 10(443), 2018.

[9] H. Charkhkar, C.E. Shell, P.D. Marasco, G.J. Pinault, D.J. Tyler and R.J. Triolo, "High-density peripheral nerve cuffs restore natural sensation to individuals with lower-limb amputations", *Journal of neural engineering*, 15(5), 2018.

[10] F.M. Petrini, G. Valle et al. "Enhancing functional abilities and cognitive integration of the lower limb prosthesis", *Science Translational Medicine*, 11(512), 2019.

[11] F.M. Petrini et al. "Sensory feedback restoration in leg amputees improves walking speed, metabolic cost and phantom pain", *Nature medicine*, 25(9), 2019.

[12] D. Rusaw, K. Hagberg, L. Nolan and N. Ramstrand, "Can vibratory feedback be used to improve postural stability in persons with transtibial limb loss?", *Journal of rehabilitation research and development*, 49(8), 1239-1254, 2012.

[13] S. Crea, B.B. Edin, K. Knaepen, R. Meeusen and N. Vitiello, "Time-discrete vibrotactile feedback contributes to improved gait symmetry in patients with lower limb amputations: case series", *Physical therapy*, 97(2), 198-207, 2017.

[14] J.A. Sabolich and G.M. Ortega, "Sense of feel for lower-limb amputees: a phase-one study", *JPO: Journal of Prosthetics and Orthotics*, 6(2), 36-41, 1994.

[15] F. Cordella, C. Gentile, L. Zollo, R. Barone, R. Sacchetti, A. Davalli, B. Siciliano and E. Guglielmelli, "A force-and-slippage control strategy for a poliarticulated prosthetic hand", IEEE International Conference on Robotics and Automation, 2016.

[16] S. Pfeifer, O. Caldiran, H. Vallery, R. Riener and A.H. Arieta, "Displaying centre of pressure location by electrotactile stimulation using phantom sensation", In Proceedings of the 2010 15th annual conference of the international functional electrical stimulation society, 2010.

[17] M. Seps, K. Dermitzakis and A.H. Arieta, "Study on lower back electrotactile stimulation characteristics for prosthetic sensory feedback", In 2011 IEEE/RSJ International Conference on Intelligent Robots and Systems (pp. 3454-3459).

[18] A. Pagel, A.H. Arieta, R. Riener and H. Vallery, "Effects of sensory augmentation on postural control and gait symmetry of transfemoral amputees: a case description", *Medical biological engineering computing*, 54(10), 1579-1589, 2016.

[19] M.I. Johnson, M.R. Mulvey and A.M. Bagnall, "Transcutaneous electrical nerve stimulation (TENS) for phantom pain and stump pain following amputation in adults", *Cochrane Database of Systematic Reviews*, (8), 2015.

A Dataset of DMPs for robot motion planning

C. Tamantini[1], C. Lauretti[1], F. Cordella[1] and L. Zollo[1]

[1] Research Unit of Advanced Robotics and Human-Centred Technologies,
Campus Bio-Medico University of Rome, Rome

Abstract—**Collaborative robots, working autonomously or in cooperation with humans, are used in industrial scenarios to help workers during the execution of repetitive and tiring activities that may lead to the onset of musculoskeletal disorders.**
This paper introduces a publicly available dataset of distinctive motion parameters (i.e. Dynamic Movement Primitives, DMPs) to be used for planning the motion of cooperative robots.
Learning by Demonstration methods were adopted to compute DMP parameters for common working activities, i.e. handling good, hammering and screwing, executed by human demonstrators. The computed DMP parameters were then stored inside the dataset. Once known the task to be performed and the target to be reached, the most appropriate set of DMP parameters is extracted from the dataset and the numerical integration of the DMP equation returns the robot desired Cartesian reference.
The dataset-based motion planner was tested in simulation: for each sub-task, several target points were used to plan trajectories. The obtained results, in terms of generalization capability of the motion planner, confirmed that the proposed approach is able to plan Cartesian trajectory for working activities with a mean Success Rate of 85% for the handling good, 67% for the hammering and 61% for the screwing tasks.

Keywords—**Dataset, Working Activities, Dynamical Movement Primitives, Human-robot interaction**

I. Introduction

The study of human motion can have important applications in several research areas, such as imitation learning, action recognition and motion generation for robotic platforms.

For these reasons, several motion capture datasets containing information about human movements have been built up and made available to the research community at the site https://francescacordella.com/ in the Dataset section. One of the largest motion capture dataset is the CMU Graphics Lab Motion Capture dataset [11]. It contains data about different kind of actions such as locomotion, sports and pantomime. The HDM05 dataset [16] includes 70 different motion classes. It was created for motion generation in computer animation. The Carnegie Mellon University built up two multimodal datasets [4] about food preparation while TUM Kitchen dataset [6] includes motion capture data of subjects setting the table. Another remarkable work is the KIT dataset [15] addressing the robot motion generation using imitation learning. From the literature analysis, two crucial aspects can be pointed out: datasets focusing on working activities are missing and all the available datasets need further elaboration in order to be used.

The advent of Industry 4.0 is strongly contributing to promote the use of collaborative robotics in industry to improve working conditions and reduce workload of industrial workers. A winning approach seems to be providing robotic systems with the capabilities of reproducing the human motion

behaviour [1]. This could increase the safety of interaction since the human user can somehow predict robot motion. Several solutions have been proposed in the literature to teach robots to move as humans. A valid approach has been found in motion planning based on dynamic motion primitives. As demonstrated in [2], the main advantages of these motion planning techniques are i) the generalization capabilities with respect to the environment variability, ii) the high level of anthropomorphism of the computed motion.

A dataset containing DMP parameters ready to be used for generating reference motion for robotic platforms in working environments can represent a contribution to the research community. Therefore, this paper proposes a dataset of working gestures created through a Learning by Demonstration approach, containing a set of distinctive motion parameters (i.e. Dynamic Movement Primitives parameters, DMPs), that can be used to plan the motion of robotic manipulators acting autonomously or in cooperation with humans. Such a trajectory planner is able to reproduce working actions through the modular composition of motor primitives.

II. Materials and Methods

Setup and Experimental Protocol

The adopted experimental setup is shown in Fig. 1. Motion capture data were collected by using the eigth cameras of the BTS Smart-DX optoelectronic system [10] with a frame rate of 60 Hz. The placement of retroreflective markers on anatomical landmarks followed the Rab protocol [5]. This way, it was possible to compute the trajectory of the wrist with respect to the shoulder frame.

Eight healthy subjects, 7 males and 1 female (mean age 27 ± 4), were asked to perform three common working activities, i.e. handling goods, hammering and screwing. The attention has been focused on these gestures since they represent the working tasks with the highest incidence of musculoskeletal disorders (MSDs) [14]. Worker safety may be improved with robotic assistance when these tasks have to be performed. A shelf unit, composed of three different levels, was positioned in front of the subject. The lower level was placed at the subject's shoulder height while the other shelves were placed at 0.19 m and 0.38 m above the first one. In order to investigate lateral load maneuvering, the shelf covered a circular sector of $\pi/3$ rad for 0.2 m of radius. The shelves were dimensioned following the directions of the International Organization of Standardizations ISO 11228-3 establishing ergonomic recommendations for repetitive working tasks involving the manual handling of low loads at high frequency.

Fig. 1: Experimental setup for the acquisition sessions.

Different conditions were assessed in this study: the target position (i.e. the load final position, the nail or the screw) was moved, from one recording to another, in 9 different points. In the first acquisition, the target was in front of the subject, 0.20 m distant. In the following recordings, it was moved at $\pi/6$ rad and $-\pi/6$ rad with respect to its initial position. This procedure was repeated at all the available heights. Two repetitions of each task and target position were collected.

Data Analysis

Tracked raw data were filtered with a 4th order low-pass Butterworth filter, with a cutoff frequency f_{cut} of 3 Hz. Such a value was chosen because noise and motion artifacts can be found at higher frequencies. It was confirmed by the results of a residual analysis performed on the collected data [18]. The f_{cut} of 3 Hz led to a residual RMS of $(5.9 \pm 1.6) \cdot 10^{-4}$ m for the hammering, i.e. the most impulsive task. Such a small residual confirmed that the chosen value of f_{cut} is suitable for the application.

All the working activities analyzed in this work were composed of different phases, each having its goal and motion features. In particular, the handling goods task is composed of three different sub-tasks: 1) to reach the load, 2) to "pick and place" the load at the proper position and 3) to return to the rest condition, also called homing. In the same way, the other two working gestures consist in: 1) reaching the working tool (i.e. the hammer or the screwdriver), 2) reaching the target, 3) performing the working activity, 4) releasing the working tool and 5) homing.

Dynamical Movement Primitives

The collected motion capture data was used to implement a trajectory planner for a robotic manipulator. A compact way to reproduce human complex motor behaviour consists in the non-linear dynamical system, called Dynamical Movement Primitives, proposed in [13, 3]. To be thorough, the fundamental equations of the DMP are reported in the following. A DMP is a non-linear second order system used to model motor behaviours, expressed as

$$\tau \ddot{y} = \alpha_z \left(\beta_z (g - y) - \dot{y} \right) + f \qquad (1)$$

where τ is a time constant, α_z and β_z are positive constants, g is the goal position and f is a forcing term that creates the landscape attractor of the system.

For discrete movements, the forcing term can be written as a weighed sum of a Gaussian Kernel basis functions Ψ, as follows

$$f(x) = \frac{\sum_{i=1}^{N} \Psi_i(x) \omega_i}{\sum_{i=1}^{N} \Psi_i(x)} x(g - y_0) \qquad (2)$$

The Gaussian functions Ψ_i are described as

$$\Psi_i(x) = \exp \left(\frac{1}{2\sigma_z^2} (c_i - x)^2 \right) \qquad (3)$$

where σ_z and c_i are the width and the centre of the Gaussian, respectively. The c_i centres are equally distributed over x. The state variable x is defined by $\tau \dot{x} = -\alpha_x x$, where α_x is a positive constant. By using a different formulation of the forcing term, it is possible to generate periodic pattern referred to as rhythmic DMPs

$$f(x) = \frac{\sum_{i=1}^{N} \Psi_i(x) \omega_i}{\sum_{i=1}^{N} \Psi_i(x)} r \qquad (4)$$

where the periodic function $\Psi_i(x)$ is given by

$$\Psi_i(x) = \exp \left(\frac{1}{2\sigma_z^2} (\cos(\phi - c_i) - 1) \right) \qquad (5)$$

where $\phi \in [0, 2\pi]$ is the phase angle of the oscillator in polar coordinates while r is the amplitude of the oscillation. A locally weighted regression (LWR) [8] can be exploited to identify the ω parameters from human demonstrations. The discrete formulation of the DMP were used for the reaching, moving and homing tasks. Conversely, rhythmic DMPs were conveniently adopted for the hammering and screwing tasks, since they can be seen as periodic movements.

Looking at the acquired kinematic data, it is important to outline that the wrist of the subjects does not rotate during the execution of the reaching, moving and homing tasks. Accordingly, DMP parameters that account for these tasks were referred only to the translations along the three axes. For the same reason, the parameters of the screwing sub-task are referred only to the rotations. The DMP parameters, in this case, were computed by using the Euler angle representation (i.e. Roll, Pitch and Yaw).

The DMP meta-parameters, i.e. α_z, β_z, α_x, σ_z and r, were experimentally retrieved and set as follows: $\alpha = 20$, $\beta_z = \alpha_z/4$, $\alpha_x = \alpha_z/3$, $\sigma_z = 0.0128$ and $r = 1$.

Motion Planner

The block scheme of the proposed DMP-based trajectory planner for a robot is shown in Fig. 2. Human motion trajectories are firstly recorded during the execution of the specific working activities. They are performed by healthy subjects and distinctive features (i.e. DMP parameters) are subsequently computed by using a LWR algorithm. Hence, a dataset of DMP parameters was built up (i.e. Off-line dataset building).

After the dataset is offline built, it can be used online: the user choose the working activity to perform with the robot assistance and the target position, then the most appropriate DMP parameters are extracted online from the dataset (DMP parameters selection). The nearest set of parameters used to compute the DMP equation and plan the motion for the desired task (DMP computation) is selected by means of a lookup table.

The dataset is made of M point clouds, where M represents the number of sub-tasks ($M = 13$), as evident from Table I.
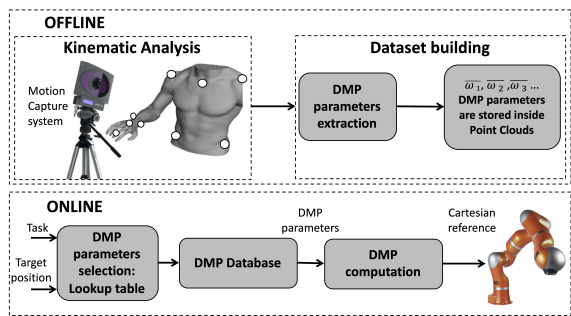
Fig. 2: Block scheme of the proposed motion planning system.
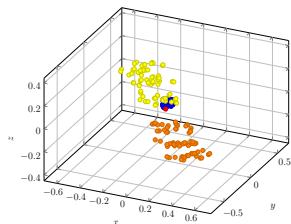

Fig. 3: Dataset of the handling good task. The red dot represents the initial position $\mathbf{p_0}$. The other points are those used to build up the DMP-dataset for an instance of *reaching*, *moving* or *homing*, respectively in blue, yellow and orange.

The points used to build up the dataset related to the handling goods task are reported in Fig. 3.

Evaluation Metrics

The proposed motion planner was validated in simulation. In particular, the simulated robot workspace was defined as follows: $x \in [-0.7, -0.45]$ m, $y \in [-0.35, 0.35]$ m and $z \in [0, 0.5]$ m. The targets used to test the planner for each sub-task have been placed in 990 different positions of the human-robot workspace. The initial position was $\mathbf{p_0} = [-0.5, 0.2, 0.15]^T$ m. These positions were obtained by dividing the entire workspace into cubic cells of 0.05 m side. The rhythmic DMPs of the hammering tasks were assessed by using each of the simulated point as initial and target position. The simulation workspace is reported in Fig. 4. For each simulated trajectory two conditions were checked:

1st Criterion: the trajectory is entirely contained within the workspace;

$$\mathbf{p}(t) \subset workspace \; \forall t \in [0, t_f]$$
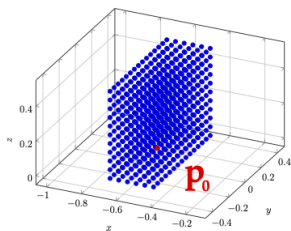
Fig. 4: Workspace used for the test in simulation. Blue points were used as a target positions while the red point represent the initial position $\mathbf{p_0}$

2nd Criterion: the target point $\mathbf{g}$ is reached with a small residual error;

$$\|\mathbf{p}(t_f) - \mathbf{g}\| < 0.015 \, m$$

The performance of the motion planner was evaluated at the end of the simulation by means of the success rate index

$$Success \, rate = (N_{succ}/N_{tot}) \cdot 100 \qquad (6)$$

where N_{succ} is the number of completed trajectories (i.e. the trajectories that satisfy both the previously listed criteria) and N_{tot} is the total number of simulated motions.

III. RESULTS

Fig. 5 shows a graphical representation of the trajectories that can be obtained by computing the DMP equations with the extracted parameters. In particular, Fig. 5A shows an example of a discrete DMP, computed for the reaching task. The Cartesian trajectories are very similar to the ones modeled by means of the Minimum Jerk theory [9]. 3D reaching tasks are naturally performed as quasi-monotonic trajectories with bell-shaped velocity profile [7]. Figure 5B reports the moving task. This differs from the previous one only for the z-axis (Fig. 1): which presents a sopra-elevation before reaching the goal. Additionally, in Fig. 5C-D both the Cartesian position and the Euler angles obtained by computing the DMP with the rhythmic formulation for the hammering task is shown. The Cartesian displacement highlights that the hammering task is condensed along the z-axis while some oscillations are visible in the other axes. At the same time, the prominent rotation during the hammering execution is around the y-axis. Finally, an example of rhythmic DMP computed for the screwing task is shown in Fig. 5E. It is worth observing that this task is performed as a pure rotation around the screwdriver axis, as observed during the acquisitions on human subjects.

The success rates obtained in simulation for each sub-tasks of the analyzed working gesture are reported in Table I. For the handling goods task, the trajectories that had a target point on the edge of the workspace did not meet the first criterion since they go out the workspace for a short period of time. Hammering task obtained the worst results. The hammering trajectory, reported in Fig. 5(a), is characterized by the peak along the z-axis. This motion features brings the trajectories out of the defined boundaries for some target points. This goes against the first criterion and leads to a success rate of 55.86% for the pure hammering gesture. The success rate of the screwing sub-task was not computed as this gesture was considered as a pure rotation around the screwdriver axis. The other sub-tasks of the screwing obtained low success rates. This could be related to the orientation of the tool to be reached. In fact, the reaching performances are impacted by the way the user approaches to the object before the grasping [12].

IV. CONCLUSION

This work presents a working gesture dataset, created through a Learning by demonstration approach, containing a set of distinctive motion parameters (i.e. Dynamic Movement Primitives, DMPs), that can be used to plan the motion of
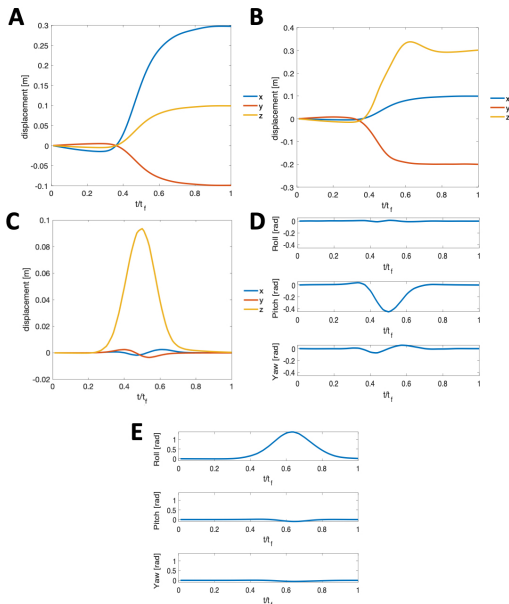
Fig. 5: Trajectories obtained by integrating the DMP parameters stored inside the proposed dataset. In A is reported a reaching, in B a pick and place, in C and D the Cartesian trajectory and the Euler angles for the hammering respectively while in E is shown the Euler angles for the screwing.

TABLE I: Success rates obtained in the simulation environment for the proposed motion planner.

Working gesture	sub-task	*Success rate*
Handling Goods	Reaching	81.81%
	Moving	82.42%
	Homing	90.90%
Hammering	Reaching of the hammer	78.79%
	Reaching of the nail	62.37%
	Hammering	55.86%
	Releasing of the hammer	75.75%
	Homing	62.22%
Screwing	Reaching of the screwdriver	56.24%
	Reaching of the screw	65.35%
	Screwing	—
	Releasing of the screwdriver	63.33%
	Homing	58.78%

robotic manipulators to perform such gestures, autonomously or in cooperation with a human. This learning method allows generalizing the trajectories with respect to target positions and robot kinematics and reproducing complex movements. Starting from the study of the kinematics of healthy subjects, the dataset was built up and used to generate Cartesian references for a manipulator. The DMP-based motion planner was validated in simulation. The generated trajectories have to meet specified criteria: i.e. the Cartesian reference contained within a predetermined workspace and a residual error less than 0.015 m. In particular, all the handling goods sub-tasks achieved success rates greater than 80%. The working sub-task that has achieved lower success rates in simulation is the hammering: the oscillation performed by the subject's wrist during the hammering does not satisfy the first criterion for some target positions.

Future work will be devoted to add information about the interaction forces [17] and to validate the proposed motion planner on a robotic platform in an experimental scenario of human-robot interaction during the execution of working activities.

REFERENCES
[1] C. Lauretti et al. "A Hybrid Joint/Cartesian DMP-Based Approach for Obstacle Avoidance of Anthropomorphic Assistive Robots". In: *International Journal of Social Robotics* 11.5 (2019).
[2] C. Lauretti et al. "Learning by demonstration for motion planning of upper-limb exoskeletons". In: *Frontiers in neurorobotics* 12 (2018).
[3] C. Lauretti et al. "Learning by demonstration for planning activities of daily living in rehabilitation and assistive robotics". In: *IEEE Robotics and Automation Letters* 2.3 (2017).
[4] F. Hodgins et al. "Guide to the carnegie mellon university multimodal activity (cmu-mmac) database". In: *CMU-RI-TR-08-22* (2009).
[5] G. Rab et al. "A method for determination of upper extremity kinematics". In: *Gait & posture* 15.2 (2002).
[6] M. Tenorth et al. "The TUM kitchen data set of everyday manipulation activities for motion tracking and action recognition". In: *2009 IEEE 12th International Conference on Computer Vision Workshops, ICCV Workshops*. IEEE. 2009.
[7] N. Fligge et al. "Minimum jerk for human catching movements in 3D". In: *2012 4th IEEE RAS & EMBS International Conference on Biomedical Robotics and Biomechatronics*. IEEE. 2012.
[8] S. Schaal et al. "Constructive incremental learning from only local information". In: *Neural computation* 10.8 (1998).
[9] T. Flash et al. "The coordination of arm movements: an experimentally confirmed mathematical model". In: *Journal of neuroscience* 5.7 (1985).
[10] *BTS Bioengineering*. URL: https://www.btsbioengineering.com/it/.
[11] *CMU Graphics Lab Motion Capture Database*. URL: http://mocap.cs.cmu.edu/.
[12] Patrizia Fattori et al. "Hand orientation during reach-to-grasp movements modulates neuronal activity in the medial posterior parietal area V6A". In: *Journal of Neuroscience* 29.6 (2009), pp. 1928–1936.
[13] A. J. Ijspeert et al. "Dynamical movement primitives: learning attractor models for motor behaviors". In: *Neural computation* 25.2 (2013).
[14] Dati Inail. *Andamento degli infortuni sul lavoro*. 2020.
[15] C. Mandery. "The KIT whole-body human motion database". In: 2015.
[16] M. Müller. "Documentation Mocap Database HDM05". In: (2007).
[17] Rocco Antonio Romeo et al. "Development and preliminary testing of an instrumented object for force analysis during grasping". In: *2015 37th Annual International Conference of the IEEE Engineering in Medicine and Biology Society (EMBC)*. IEEE. 2015, pp. 6720–6723.
[18] Ståle Andreas van Dorp Skogstad et al. "Filtering motion capture data for real-time applications". In: (2013).

An Innovative High-Fidelity Neonatal Pneumothorax Simulator

S. Maglio[1], S. Tognarelli[2], and A. Menciassi[2]

[1] University of Pisa, Pisa, Italy
[2] The BioRobotics Institute, Scuola Superiore Sant'Anna, Pisa

Abstract—**Pneumothorax represents a clinical emergency that needs to be solved within minutes and requires skilled clinicians. High-fidelity simulation allows for effective training involving the entire interventional technique, environment and gestures. However, available solutions lack of anatomical and physiological fidelity. With two airtight pressurized chambers and self-sealing needle insertion areas, the active simulator here presented overcomes the limitations of the existing solutions.**

Keywords—**Pneumothorax, high-fidelity, simulator, newborn.**

I. INTRODUCTION

PNEUMOTHORAX (PTX) is the presence of air in the pleural space, which causes a partial or complete collapse of the lung. Such collapse can lead to major clinical complications including death [1], [2]. PTX can occur spontaneously or following trauma or medical procedures. The incidence of PTX in the neonatal period is higher than in any other period of life and leads to death in 20% of cases [2]. Radiological survey showed an incidence of 1-2% of term neonates [1-2].

The PTX is an emergency condition and 1-2 minute delay in solving it can be fatal. Therefore, if a PTX is suspected, it is recommended to act immediately with the decompression procedure, even if it turns out that the suspect was wrong [3].

The first step of the decompression procedure consists of positioning the infant supine and inserting a Butterfly 25G needle at the mid-clavicular line (MCL) level in the 2nd or 3rd intercostal space (IS). The needle is inserted as close as possible to the lower rib to avoid any damage to the superior sensitive structures. The second step is the placement of a 14G Pleurocath needle for continuous air drainage in the 5th or 6th IS along the anterior-axillary line (AAL).

Simulation is currently a valid help for the neonatologists to improve interventional technique and comfort during the PTX decompression procedure. In addition, high-fidelity simulators offer the advantage of allowing to develop the required skills for successfully accomplish a PTX treatment by avoiding any risk and side effects for the patients [4].

A high-fidelity simulator is a device that reproduces as accurately as possible the environment in which the physicians work and the critical issues they are exposed to. In the case of neonatal PTX simulator, the following features are necessary:
- accurate simulation of the anatomical references both in terms of dimensions and mechanical properties;
- chest tension simulation, that is a symptom of tension PTX;
- reproduction of the return of syringe plunger when the PTX is solved: this feedback is fundamental because it indicates an empty pleural cavity;
- reproducing the tissue penetration feedback;
- allowing instrumentation access to the correct ISs.

Commercial solutions and research prototypes are currently available. Commercial simulators can be divided into specific PTX simulators only and neonatal simulators that include PTX features among the optional simulations. What is noticeable is that specific simulators are generally more accurate in reproduction structures that better simulate the pathology, but they always consist of adult manikins.

Neonatal simulators are generally more complete in terms of simulated emergencies, and PTX is only one of them. This leads to a poor simulation of the PTX anatomy and physiology, which is only reduced to an empty area beyond a dedicated access site (usually, a pad or a silicone cover). Moreover, generally in neonatal simulators there is only access along the AAL e and not along the MCL as required by the first step of the interventional medical procedure. To the best of the authors knowledge, the only PTX research prototypes reported in literature are [5], [6] together with four patents [7-10]. The two articles describe low-fidelity simulators, only one for newborn, and they present the same drawbacks of commercial simulators. The four patents describe technical solutions that allow simulating only specific components of the PTX. These solutions are intended for being integrated into existing manikins, resulting in low-fidelity devices.

In this framework, aim of this work, is the design, realization and preliminary assessment of a high-fidelity neonatal pneumothorax simulator that reproduces both the correct anatomy of the newborn' s chest and the PTX physiology. Chest tension is actively obtained through ad-hoc designed hardware and software components. The syringe plunger return feedback is reproduced by two pressurized airtight chambers. Finally, the simulator has two needle insertion areas in the third right and left ISs that provide the physiological tissue perforation feedback to the physician. Insertion areas were made with two self-sealing and replaceable pads for theoretically unlimited use of the device.

II. MATERIALS AND METHODS

A. Anatomy reproduction

In PTX simulation, reproducing the newborn anatomy means reproducing the physiological pleural space. The pleural space can be briefly described as an airtight chamber whose walls communicate with the lung, diaphragm, chest wall and mediastinum (figure 1A). Chest wall refers to all the components that constitute the external structure of the chest: rib cage, muscles, fat, and skin.

In the simulator, this airtight chamber was reproduced by reconstructing the mediastinum with the heart, the diaphragm, and the chest wall. These four structures were sealed together to form two isolated chambers containing the lungs. The

pleural membrane was simulated by a Kevlar sheet included in the replaceable pads (details reported below). A head and two arms were also added to the simulator torso to contribute to the high-fidelity visual experience (figure 1B).

Discussing with expert physicians, it was found that it is very important to recreate the entire working environment surrounding the user during the procedure to make the training as realistic and effective as possible.
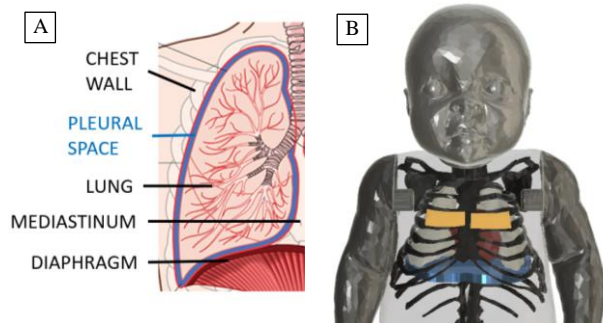

Fig. 1: A) Chest anatomy. B) Simulator conceptual design. Black: rib cage. White: lungs. Red: heart. Blue: diaphragm. Yellow: pads. Grey: arms and head. Transparent: skin.

Because of the complexity of the human anatomy and the need of a compliant material, Additive (AMT) and Formative (FMT) Manufacturing Technologies were identified as required manufacturing processes for realizing the simulator components.

The simulator skeleton was realized through Fused Deposition Modelling (FDM), an AMT technology. It was made in TPU 92A material with a Stratasys F370 3D printer (USA). The 3D model of the skeleton was obtained starting from an abdominal CT Scan of a 1-month neonate kindly provided by the neonatologists of the Neonatology unit of Azienda Ospedaliero Universitaria Pisana (AOUP). By the 3D Slicer 4.10.2 software [11], the primitive skeleton model was obtained. In MeshLab 2016.12 software (Italy), the model mesh was smoothed. Using Fusion 360 software (Autodesk, USA), the mesh was converted into a solid, trachea and bronchi were realized, and the different parts were joined together to obtain a single structure. The obtained model was printed at 110% of its regular dimension following the neonatologist advices.

The lungs, the heart, the diaphragm, the skeleton cover, the head, and the arms were made by casting technique. The casting is an FMT that consists of the injection of the liquid material, in this case the silicone, into a mould. The lungs, diaphragm and heart moulds were made in UV-curable resin by PolyJet printing (PJ) technique, which is an AMT technology available in the lab. The skeleton cover, head, and arms moulds were made in PA-12 material (USA) through the Multi Jet Fusion technique (MJF), an AMT technology provided by Zare S.r.l. company (Italy) (figure 2).

Fig. 2: Some moulds parts printed in PA-12 material.

All the moulds described below had reference structures that allowed the assembly of the components and holes for silicone injection and air outlet.

The lungs were made as two 2.3 mm thick shells reproducing the correct anatomical pulmonary shape to be inflated and thus simulate the breathing mechanism. They were realized by using Ecoflex 0030 silicone (Smooth-On, USA), as a compromise between softness and structural integrity of the structure. Lung moulds comprised the internal core and four external blocks that build up the mould body.

The heart was made as a full volume in Ecoflex 0030 silicone, respecting the pericardium anatomy but without functional properties. In fact, the effects of the PTX on the cardiovascular system were not addressed in this state of the project. The heart mould was created as two external blocks with a heart-shaped hollow. Both the lungs and heart moulds were realized starting from 3D models kindly provided by the Eindhoven University of Technology.

Chest wall was reproduced through the cover mould by creating a thickness of silicone that incorporates the skeleton. This thickness was designed by creating the mould core shaped like the inner surface of the rib cage and the mould body shaped like the desired simulator external surface.

The rib cage inner surface 3D model was obtained by coating the inside of the rib cage with cellophane and Soma Foama foam (Smooth-On) was poured into it. As the foam expanded, it took the interior shape of the rib cage and the desired surface was obtained. A 3D scanner (Go! SCAN 3D, Creaform, Canada) was used to generate the foam 3D model.

The cover mould core was designed to create the empty space for including the organs inside the simulator rib cage, the abdomen, and to realize the mediastinum, i.e. a 20mm thick silicone wall. It was split into five parts for an easy demoulding.

The simulator external surface was obtained starting from the CT scan and creating a volume that included all newborn's tissues. This model represented the newborn's chest with the arms. With the software mentioned above, the arms were removed, and two housings were created. The arms were separately realized and then reassembled.

The 3D model of the simulator external surface was used to design the cover mould body, which was split into five parts.

The cover mould provided also two housing windows for the pads. They were created using the pads 3D models described below. The models were split into two parts following the rib curvature: the external parts were joined to the cover mould body and the internal parts to the cover mould core.

The diaphragm was made from the cover mould core. It was shaped using the lungs bottom structure as reference and had a thickness of 7 mm to obtain acceptable structural integrity. Ecoflex 0030 was used for realizing the structure. The diaphragm mould was made by using a dedicated box split into two parts and with a diaphragm-shaped hollow inside.

The head and arms were realized with a rigid inner core, that was the mould core, subsequently incorporated in Ecoflex 0010 silicone. The moulds were realized with cores and bodies. The bodies were shaped reproducing the human arms and head structures. The arms 3D models were obtained from the newborn's CT scan as described above and the head 3D

model was obtained from the Thingiverse website, a website with free 3D models (www.thingiverse.com).

Considering that the pads were intended as two structures separated from the skeleton cover, there was the need for an additional cover that would make the surface of the simulator more homogeneous. This cover was called *skin*.

The skin was made as a thin layer of Ecoflex 0010 to be inserted over the skeleton cover as a kind of shirt that could be removed and replaced and that would allow the integration of arms and head with torso. Skin design required a dedicated mould equipped with a mould core shaped like the external surface of the skeleton cover and a mould body with an inner hollow shaped like the all tissues and organs model extracted from the newborn's CT scan. The skin mould body was split into three parts for easily demoulding.

B. Self-sealing and replaceable pads

The pads aim to replicate both the ability of human tissue to repair itself and the human tissue feedback during the needle insertion. We looked for a material that, once pierced with the needle, is able to close back the hole (i.e. the self-sealing ability). Two different materials were identified from the literature: Ecoflex Gel and Dragon Skin 10 mixed with Slacker (Smooth-On). These two materials are particularly sticky and have shown a good ability to close needle holes [8].

Since no references are available in literature to reproduce the human tissues feedback during the needle insertion, several samples were realized and tested with expert neonatologists asking them a feedback and making a comparison.

In pad design, under medical advice, the 3rd IS was chosen as the insertion area for the Butterfly 25G needle. The 14G Pleurocath needle insertion areas were not provided in the first version of the simulator here described because, with the available models, it was not possible to obtain proper tissues thicknesses comparable to the newborn anatomy.

Pads were realized in a layered structure following the physiological anatomy. From outside to inside, they replicate the skin, the fat tissue, the muscles, and the pleura.

In order to find the most appropriate materials that could simulate human tissues, the elastic modulus was analyzed. The silicones of the Ecoflex series were chosen. They have mechanical properties similar to those of human tissues and they were already used in literature to the same purposes [12].

The first test session was intended to test the correct layering of the pad. The pads were composed of three layers 5mm thick to a total thickness of 15mm, following literature [13]. In addition to silicone layers, Kevlar sheets were inserted, as it was necessary to add a structure that could provide a sensation like pleural perforation. In literature, pleura is described as a rigid tissue that once punctured provides a pop-like sensation. According to the physicians indications, two new pads were created. They had a thickness of 10 mm divided as follows: a 3 mm thick skin layer of Ecoflex 0010, a fat layer simulated with 6 mm thick Ecoflex Gel or 6 mm thick Dragon Skin 10 added with Slacker, and 1 mm thick Kevlar sheet fixed in the Ecoflex 0010 layer. In addition to the correct layering, we intended to test if during the needle insertion there were different feelings using one or the other of the two self-sealing materials. After this second test, the physicians reported a

correct layering and no differences between the two materials.

However, simulator skin was 2 mm thick, thus the final pads were realized as 1 mm thick inner layer (inn lyr) of Kevlar sheet fixed in Ecoflex 0010, 6 mm thick middle layer (mid lyr) of Ecoflex Gel and reducing the outer layer (out lyr) of Ecoflex 0010 to 1 mm of thickness (figure 3A). Finally, the pads have to be inserted into the simulator, thus they had to be shaped to fit the right IS. Pads 3D models, one for the right IS and one for the left IS, were created starting from the skeleton model. The pads moulds were obtained creating a box with a pad-shaped hollow and split into two parts (figure 3B).

During the needle insertion procedure, the user takes the lower rib as a reference and inserts the needle as close to the rib as possible. This procedure could most likely damage the simulator and cause it to lose its airtightness. Therefore, to overcome this problem, a 1mm thick structure, to be inserted into the pad, was created and shaped like the lower rib.

The pads moulds and the structures above the ribs were made in UV-curable resin by the PJ technique. To achieve even better adhesion to the structures above the ribs, they were coated with fabric.

Then, Ecoflex 0010 silicone was poured into the pad moulds, the structures above the ribs were placed inside and the excess of silicone was poured out. Once the silicone cured, the moulds were closed and Ecoflex Gel was injected with a syringe. After the cure time, the pads were demoulded and two sheets of Kevlar were shaped, incorporated in Ecoflex 0010 silicone and glued on the inner side of the pads.
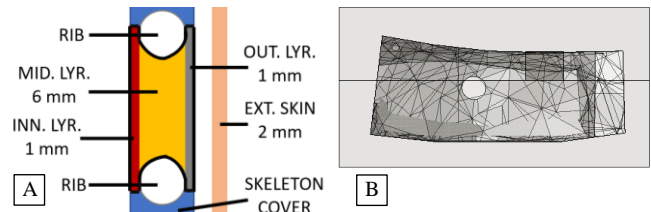

Fig. 3: (A) Sagittal section of the pad inserted in the simulator. (B) Pad mould.

C. Hardware

The simulator actively generates the tension inside the two airtight chambers through two air pumps (Makeblock, DC 12V/370-02PM) connected to two solenoid valves (Clippard, ST-3C-12-10-V), which allow or stop the airflow. The two airflows were then divided in two different ways, one directed inside the simulator, the other to a pressure sensor (NXP USA Inc., MPX5050DP). The pressure sensor was used to measure the pressure inside the airtight chamber and consequently to allow a parametric control of the system. The pumps and the solenoid valves were powered by 12V and 3A power supply (XP Power, VEL36US120-EU-JA) and controlled by the Arduino Uno microcontroller (Arduino AG, Italy) through four MOSFETs (Infineon Technologies, irfz44npbf-nd). The pressure sensors were powered and read by Arduino Uno.

D. Software

The simulator control and management software was implemented through LabView software (NI, USA). The software provides an interface for the physician to control: i) the reached pressures inside the simulator by using graphs and numerical outputs and ii) the two air pumps activation by two

switch buttons (figure 4). The interface is managed by LabView which communicates with the Arduino Uno board through the LINX software (Digilent, USA).
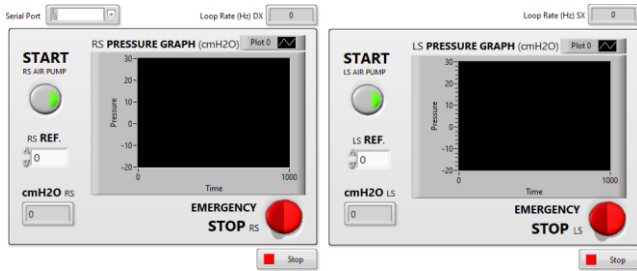

Fig. 4: Software interface.

Fig. 5: (A) Skeleton cover with pads. (B) Internal organs. (C) Simulator.

III. RESULTS

A. Pad self-sealing test

The self-sealing ability of the pad was investigated using a dedicated set-up. It was a cubic chamber where the pad was firmly glued instead of a face. The chamber was connected to the simulator hardware to create pressure inside and it was controlled by means of the simulator software. The inspected variables were pressure, number of holes and diameter of needles. Considering that a range from -5 cmH$_2$O to 25cmH$_2$O was associated with human tension in pneumothorax conditions [14], and assuming a safety factor of at least 4, a testing pressure value of 100 cmH$_2$O was set. The needles used were a Pleurocath 14G and a Butterfly 25G, as in clinical procedures. Pad failure was achieved after consequent 20 holes with Butterfly 25G needle and 15 holes with Pleurocath 14G needle. This guarantees to cover an entire simulator session test.

B. Assembly

The moulds were assembled and the silicone was poured into them. Once the silicone cured, the final simulator parts were demoulded and refined manually. The skeleton was incorporated into the silicone. The lungs and the heart were inserted into the skeleton cover and glued to the bronchi and mediastinum, respectively (figure 5B). The diaphragm was glued to the skeleton cover and to the heart in an anatomical position. Then the two pads were inserted into their housings and the Ecoflex 0010 silicone was poured to join the different parts and close holes (figure 5A). The two airtight chambers were made and connected to the simulator hardware through two tubes inserted and glued into the diaphragm. The skin was inserted over the skeleton cover, the arms were placed into their housings and glued to the skin and the head was stopped in the skeleton through a pin (figure 5C). Silicone glue was used, i.e. Sil-Poxy (Smooth-On).

The airtightness of the two chambers was verified by adding a fixed pressure of 50 cmH$_2$O and observing the pressure variations. Additionally, the continuity of the airways was assessed by ventilating the lungs with a neonatal ventilator.

Then the simulator was tested by the physicians asking them to simulate a PTX decompression procedure. The simulator answered very well to this first test, allowing to create the PTX and the physiological negative pressure of the pleural space. The physiological return of the syringe plunger was observed as in a real PTX decompression procedure.
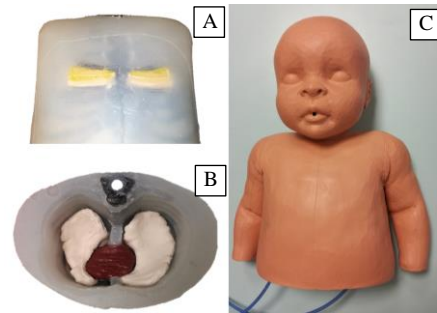
IV. CONCLUSION

Preliminary results confirmed the simulator as a valid technological solution for high-fidelity training course for neonatologists and paediatric residents. Future efforts will be dedicated to carry out specific experimental protocol for system validation involving both expert clinicians and residents. A deep comparison of the obtained results with that one reachable with other commercial PTX simulators could be also interesting for validating the proposed model.

ACKNOWLEDGEMENT

REFERENCES

[1] H. H. Duong et al., "Pneumothorax in neonates: trends, predictors and outcomes," *Journal of Neonatal-Perinatal Medicine*, vol. 7, pp. 29-30, 2014.

[2] H. Esme, Ö. Doğru, Ş. Eren, M. Korkmaz, and O. Solak, "The factors affecting persistent pneumothorax and mortality in neonatal PTX," *The Turkish Journal of Pediatrics*, vol. 50, pp. 242-246, May-June 2018.

[3] M. D. Cunningham, and T. L. Gomella, *Neonatology*, New York, PA: McGraw-Hill Medical, 2004.

[4] N. J. Maran, and R. J. Glavin, "Low- to high-fidelity simulation - a continuum of medical education?," *Medical Education*, vol. 37, pp. 22-28, 2003.

[5] V. Martinuzzi, E. C. Trabing, and D. E. Dow, "Pneumothorax training system," *in 2015 Proc. IME Cong. and Exp.*, pp. 1-6.

[6] A. O. Gupta, and J. Ramasethu, "An innovative nonanimal simulation trainer for chest tube insertion in neonates," *Pediatrics*, vol. 134, pp. 798-805, 2014.

[7] L. L. McCollum, "Pneumothorax diagnostic and treatment manikin," U.S. Patent 50 611 88A, Oct. 29, 1991.

[8] V. Duprez, O. H. Gomo, and E. Egelandsdal, "Simulator for medical training with detachable self-sealing hollow member," U.S. Patent 8100695B2, Jan. 24, 2012.

[9] R. F. Buckman, "System for simulating diagnostic features of tension pneumothorax and cardiac tamponade within a medical training manikin," European Patent 2787498A3, Nov. 26, 2014.

[10] Y. Fradette, Y. Cote, and C. Courtoy, "Removable tension-pneumothorax-simulator cartridge for use with a patient simulating mannequin," U.S. Patent 9953548B2, April 24, 2018.

[11] A. Fedorov et al., "3D Slicer as an image computing platform for the Quantitative Imaging Network," *Magnetic resonance imaging*, vol. 30, pp. 1323-41, 2012.

[12] J. L. Sparks, et al., "Use of silicone materials to simulate tissue biomechanics as related to deep tissue injury," *Advances in Skin and Wound Care*, vol. 28, pp. 59–68, 2015.

[13] G. Leonhard et al. (2019, Oct.) Determining optimal needle size for decompression of tension pneumothorax in children – a CT-based study. *Scandinavian Journal of Trauma, Resuscitation and Emergency Medicine*. [Online]. 27(1). Available: https://sjtrem.biomedcentral.com/track/pdf/10.1186/s13049-019-0671-x

[14] R. F. Johnston, J. H. Dovnarsky, "Pleural diseases," in: *Fishman's Pulmonary Diseases and Disorders*, AP ed. vol. 2. New York: MacGraw-Hill, 1980, pp. 1357–1375.

An innovative High-Fidelity simulator of cervical changes during labour

C. Luchini[1,2], S. Tognarelli[2], and A. Menciassi[2]

[1] *University of Pisa, Pisa, Italy*
[2] *The BioRobotics Institute, Scuola Superiore Sant'Anna, Pisa, Italy*

Abstract— **The assessment of cervical changes during labour is of paramount importance for a safe delivery. However, these measurements are manually carried out by gynaecologists, who provide subjective data strictly dependent on their experience and proprioceptive skills. For these reasons, simulation plays a central role in clinicians training processes. However, no simulators available on the market are able to actively and dynamically reproduce these changes. Aim of this work is to create, for the first time, a dynamic High-Fidelity simulator of cervical changes during labour, by using smart technologies such as granular jamming and Shape Memory Alloys materials.**

Keywords—**Cervical ripening, SMA, Granular jamming, High-Fidelity birth simulator.**

I. INTRODUCTION

THE human cervix during the pregnancy has a dual structural function: prior to term, it must work as a barrier both in terms of protection from external microorganisms and resisting the forces imposed by expanding uterus; and at term, the cervix must dilate under the influence of uterine contractions to allow the passage of the foetus. This dual functionality is obtained with a transformation called *cervical ripening*. It is a single continuous process that can be divided into four overlapping phases: softening, effacement, dilation and postpartum repair. *Softening* is carried out during the whole pregnancy, but it is accentuated during labour and it refers to softening of the cervical tissue; *effacement* (Fig. 1) refers to the gradual shortening and thinning of the cervix and it is usually evaluated in percentage from 0 (corresponding to 2 phalanges) to 100% (corresponding to less than 1 phalange); *dilation* refers to the gradual opening of the cervix to accommodate the passage of the foetus head into the vagina and it is measured in centimetres from 0 (totally closed) to 10 (totally open) cm; then the final phase of remodelling termed *postpartum repair*, ensuring recovery of tissue integrity and competency [1].

Fig. 1: Schematic representation of the effacement process of the cervix from 0% - on the left – to 100% - on the right.

The evaluation of the cervix status during labour, in particular of its length, dilation and softness is the only available intrapartum tool used by the medical doctors to manage delivery, and to make operative decisions, such as oxytocin use or caesarean delivery [2]. Currently, the cervical assessment is still performed in the same way of last centuries, namely with a manual vaginal exploration during which the consistency, effacement and dilation are assessed only through the use of two fingers (index and medium fingers). This evaluation is therefore strongly subjective and based on clinical experience of the medical doctor, thus reproducibility is very limited. Data reproducibility is the most important limit of the current evaluation of the delivery progress, because there is often more than one clinician taking part in the management of a single labour which usually entails several hours. Moreover, residents have to spend many hours in the delivery room for correctly learning how to make an accurate evaluation of the cervix, as there are no available alternatives in terms of training processes. In order to overcome this drawback, simulation is playing a fundamental role for residents learning and training.

"Simulator" is a general term referring to a physical object, device, situation or environment where a task or a series of tasks can be realistically and dynamically represented. Simulators in healthcare range from simple objects or training devices (i.e, low-fidelity simulators) to a technologically advanced mechanical or haptic systems representing a patient or a clinical environment (i.e, high-fidelity simulators) [3]. Specifically, currently available simulators of cervical changes during labour can be divided into two main categories: commercial simulators and simulator prototypes. The first one can be subdivided into two sub-categories: low-fidelity simulators [4-6], which include only simple cervix models reproducing different conditions of dilation and effacement that have to be manually interchanged during the labour phase simulation; high-fidelity simulators [7-9], which reproduce the physiological dimensions of the mother body. Also in this second case, the cervix is simulated with interchangeable passive elements. Regarding prototypes, there are several works using very simple technical solutions [10-12], but the most interesting one, in terms of used technical principle and obtained results, is the cervical simulator described in [13] and consisting of a toroid-shaped latex membrane filled with coffee powder. Effacement and dilation are simulated by exploiting the granular jamming principle by reaching the 35% of effacement and 1 cm of dilation, which are far less than a physiological 100% effacement and 10 cm dilation.

Based on the above premises, to the best of authors knowledge no High-Fidelity simulators that actively reproduce changes of the cervix during labour are available on the market or investigated by researchers. Aim of this paper is the design, developing and validation of a dynamic simulator capable of reproducing the physiological changes that occur in the cervix during labour, i.e. softening, effacement and dilation, that all together constitute the physiological phenomenon usually known as cervical ripening. By exploiting the support of expert gynaecologists of the University of Pisa and Azienda

Ospedaliero Universitaria Pisana (AOUP), different solutions such as 3D printing, granular jamming, shape memory alloy principle and rapid prototyping have been selected to be combined and to replicate the physiological behaviour of the cervix area.

II. MATERIALS AND METHODS

The whole structure of the proposed device (Fig. 2) can be divided into three main sub-systems assembled together in a dedicated support structure: each of the three sub-systems reproduces one of the main changes that occur in the cervix, i.e. softening, effacement and dilation. These phenomena do not occur simultaneously, but in a sequential way: first of all, cervix becomes soft, then the effacement occurs and, finally, dilation takes place. The same sequence of changes is accurately reproduced through two independent structures, one for softening – that is removable - and one for both effacement and dilation. Details are reported below.
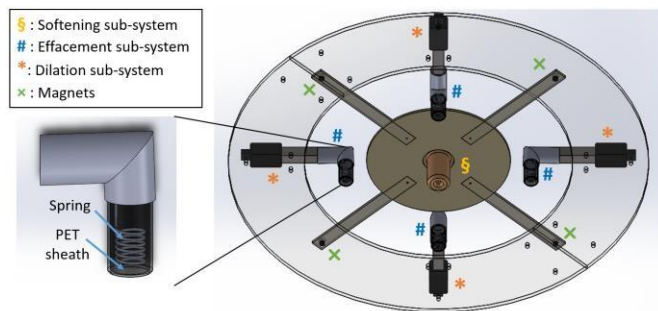
Fig. 2: CAD drawing of the whole structure and its sub-systems.

A. Softening sub-system

The softening process of the cervix is simulated by using granular jamming, a physical mechanism by which granular media can reversibly change between fluid- and solid-like states. When the granular material can flow freely, the object is soft and pliable. Tunable stiffness is achieved by applying and releasing vacuum on the structure enclosing the grains, forcing the grains to change state. Key elements of granular jamming are: the membrane, the internal particles and the vacuum system. In order to properly reproduce the cervical structure, a silicone membrane was realized through a molding manufacturing process. Clinicians were involved in several tests with different silicone, and Ecoflex 00-30 made by Smooth-On (Smooth-On Inc., USA) was recognised as the more similar to anatomical cervical tissues, both in terms of hardness and elasticity. A dedicated rapid prototyping mold, designed for replicating the anatomical structure of the human cervix, was realized with Project MJP 3600 MAX machine (3D Systems, USA). Then, the silicone membrane was filled with coffee powder, following the literature [14] evidence. A small flexible tube (2 mm in diameter) was integrated into the coffee powder inside the soft membrane for vacuum extraction and refilling; it is connected to an air pump motor (Makeblock Air Pump Motor, sku: 50000, DC 12.0 V/370-02PM) powered by a 12 V power supply. To control the cervical softening process, the air pump is connected (i.e., through a Mosfet transistor) with Arduino MEGA 2560 microcontroller (Arduino AG, Italy) used to activate or deactivate the air pump motor, thus to create vacuum or insert air inside the soft sub-structure and therefore simulate the cervix in its rigid or soft

state, respectively. The softening system prototype is shown in Fig. 3. Fig. 4 compare a human cervix and the prototype.
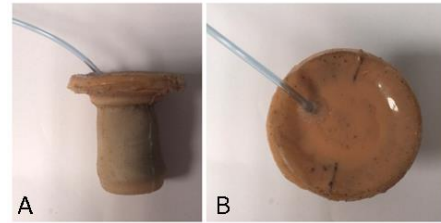

Fig. 3: Side (A) and top (B) view of the softening sub-system obtained by molding process. Silicone was colored by adding pink color to the Ecoflex 00-30 silicone (pink Silc Pig, Smooth-on, Inc., Texas, PA).
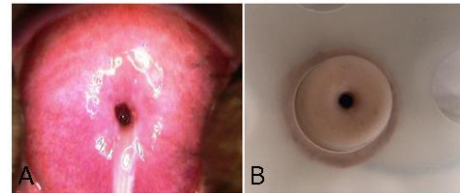

Fig. 4: Comparison between a real photo [15] of the human cervix (A) as observed by medical doctors during gynecological inspections and the bottom view of the softening system here realized.

In order to assemble the softening module with the rest of the simulator, a 3 mm thick circular crown was developed. It has a central hole for housing the body of the silicone structure (Fig. 2) and four bars equipped with four permanent magnets at one of their ends used for attaching and detaching the softening sub-structure from the whole cervix simulator (Fig. 8 as reference).

B. Effacement sub-system

Four similar yet independent structures were realized for simulating the cervix effacement process. Human cervix shows a circular shape, however, the four proposed structures allow to reduce the design complexity of the simulator while guaranteeing the ability to simulate both physiological and pathological shortening and thinning of cervix in preparation for childbirth. The fundamental element of each single structure is a Nitinol (NiTi) Shape Memory Alloy (SMA) spring as it represents the most suitable technology for the realization of a sub-system that change its length from 4 to 1 cm in a simple and quite fast way.

The SMA spring design phase is fundamental for guaranteeing the correct functioning of the entire sub-system. The best trade-off between anatomical behavior (during the active phase of the labour the human cervix reaches 1 cm length starting from 4 cm), actuator torque and activation current led to using 1 mm diameter NiTi wire for developing the thinning actuator; a torsion spring 8 mm in mean diameter and with 4 active spring turns was selected. During the fabrication procedure, the NiTi wire was tightly circled and constrained on a 8 mm diameter brass cylinder (Fig. 5A), and the whole system was placed in a pre-heated oven at 550°C. The heating treatment consists in keeping the wire inside the oven for 30 minutes, removing it and cooling rapidly by placing it in cold water. Due to the NiTi wire high stiffness, for each spring three consecutive thermal treatments were performed, so that the set shape correctly remains in memory in the wire. Finally, in order to select the most suitable electronic components of the sub-system, the voltage required for powering the thinning actuators was calculated. Spring resistance (R) was experimentally measured (R=0.3 Ω), and

considering the maximum current of 5 A as reported in literature [16], the maximum voltage value was calculated as 1.5 V.

Two commercial power supplies (RS components, Italy, product code: 739-7979) were included in the system, one of which drives two of the four SMA actuators, and experimental evidences confirmed that with a voltage of about 1.3 V and a current of about 3 A, the spring, once manually deformed reaching 4 cm, could smoothly return to its fabrication length. However, because SMA actuators were not able to maintain a regular shape if repeatedly solicited, NiTi spring was concentrically included into a Polyethylene (PET) 5 mm in diameter sheath (RS components, Milano, Italy, product code: 408-198). 10 mm diameter steel cylinder was used for assuring the required sheath internal diameter suitable to house the NiTi spring described above. PET sheath is then capable of stretch and shorten following the NiTi spring changes and it guarantees high system reliability. The sheath is then compacted as much as possible (starting length=1.5 cm) and its ends are locked on the rod; folding shape is then fixed by heating treatment (Fig. 5B).

In order to firmly join the NiTi spring and the sheath and then close the two ends of the structure, two rapid prototyped bases with an external diameter of 10 mm, a thickness of 0.8 mm and equipped with two miniaturized gold rings permanently fixed into two elliptical holes, were fabricated (Fig. 5C). After connecting the spring to the rings, the two bases were glued to the ends of the sheath. The entire structure was then covered with Ecoflex 00-10 silicone with the aim to guarantee the same feeling of physiological tissue (Fig. 5D).
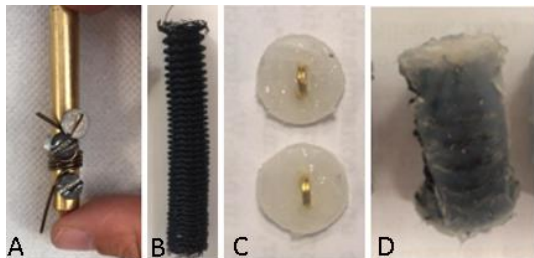
Fig. 5: NiTi spring firmly fixed to the 8 mm diameter brass cylinder (A); the final folding shape of the sheath after heat treatment (B); the two bases of the structure fabricated with 3D printer and equipped with gold rings firmly glued in the bases (C); the final complete structure (spring included in the sheath) covered with a layer of silicone (D).

The SMA actuators were controlled by an Arduino MEGA 2560 microcontroller together with an electronic circuit composed of a 4 channels DC 5V relay module (ELEGOO Inc., China). The power supplies cannot be directly connected to the Arduino as they generate too high current.

C. Dilation sub-system

Linear actuators are used to simulate the cervix dilation. Four L12-50-100-12-P Micro Linear Actuators made by Actuonix Motion Devices (Actuonix Motion Device Inc., Canada) were selected as the most suitable actuators, as they are small in size and show an intuitive control architecture. In addition, each motor has 5 cm of stroke, so by fixing them at 90° each other, the 10 cm cervix dilation required to accommodate the passage of baby head into the vagina, was reached.

Finally, for exploiting the Arduino MEGA 2560 microcontroller for the direct control of motor position too, a Linear Actuator Control Board (LAC) was used: it is a closed-loop control board specifically designed for Actuonix P-series micro actuators.

In order to join the dilation sub-system with the effacement one, a Silicone Smooth-On ECOFLEX 00-50 membrane of 2 mm thickness (Fig. 6A) was obtained with molding technique. The effacement sub-system described above was manually inserted into this membrane and fixed to the mobile end of the motor (Fig. 6B) exploiting a dedicated 3D printed mock-up already screwed to the motor (Fig. 6C). Lastly, considering the free space around the four sub-systems so realized, an artificial constraint was included (Fig. 6D) for limiting the length of the simulated cervix at 4 cm (when it is elongated), thus replicating anatomical features.
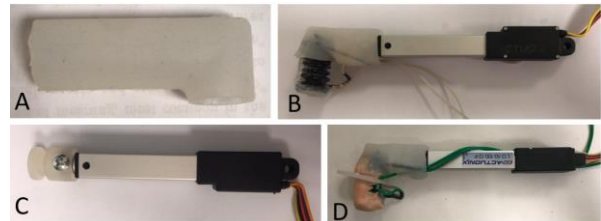

Fig. 6: Silicone membrane (A); inserting of the effacement sub-system into the silicone membrane (B); assembly of the connection element made by 3D printing with the linear actuator (C); complete assembly of dilation (*) and effacement (#) sub-systems (D).

D. Support Structure and Box for the electronic component

A dedicated support structure able to maintain the three sub-systems in the correct position and orientation, i.e. a circular crown of PMMA 3 mm thick, was designed in four single parts and fabricated by using Laser Cutter machine (Universal Laser Systems Inc., USA).

To reproduce the relative position between the mother and the gynaecologist during the pre-birth visits, the circular crown has to be maintained in a frontal position through two metal side bars fixed to a PMMA base, as shown in Fig. 7A.

Finally, in order to quickly and easily transport the simulator, thus to make easier the simulator application in multiple training centers, it was necessary to build a PMMA box containing all the electronic components (Fig. 7B).
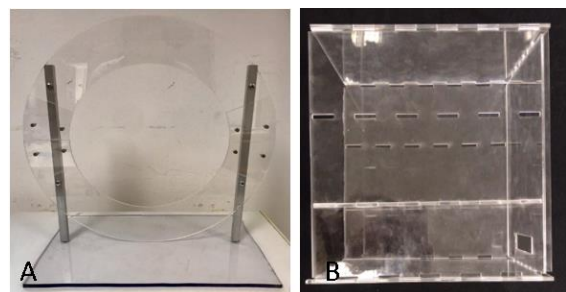

Fig. 7: Circular crown fixed (i.e., at 90°) to the PMMA base by two metal side bars and the PMMA base (A) and the box for electronic components (B).

III. RESULTS

The single components described in the previous paragraphs were assembled to reproduce the human cervix anatomy and physiology. In particular, linear actuators with the effacement sub-system were fixed with M4 screws to the circular crown, so that in the rest position (stroke of each motor equal to zero) the cervix dilation is 10 cm, and when the stroke of the motors is maximum (5 cm for each motor) a closed cervix is simulated. The softening sub-system was assembled with the rest of the structure thanks to four magnets included in both

sub-systems (i.e., PMMA circular crown and softening sub-system bars shown in Fig. 2). The overall assembly of the simulator is shown in Fig. 8.

The electronic components are positioned inside the Plexiglass box.
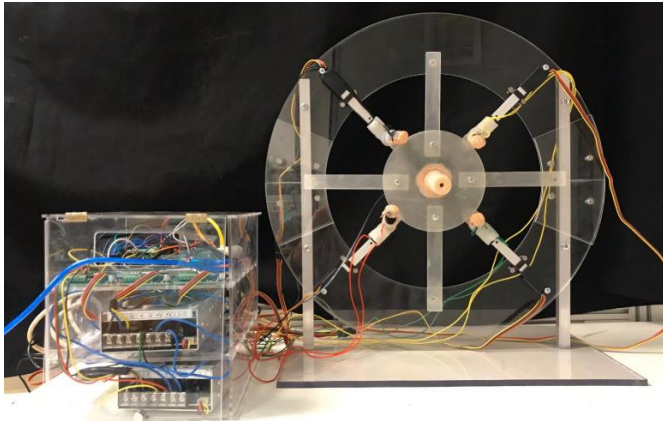

Fig. 8: Assembly of the simulator.

To control the entire simulator, an intuitive user interface (GUI) was created with LabVIEW 2019 (issued by National Instruments, USA). The GUI was made up of three distinct blocks for easily managing the three sub-systems (Fig. 9) guaranteeing the sequential behaviour of the human cervix changes: softening (Fig. 10A), then effacement and at the end dilation (Fig. 10B), exactly as it happens in nulliparous mother during labour. The gynaecologist is able to activate/deactivate each sub-system in a simple and intuitive way thanks to the presence of coloured buttons, switches and numbered slices.
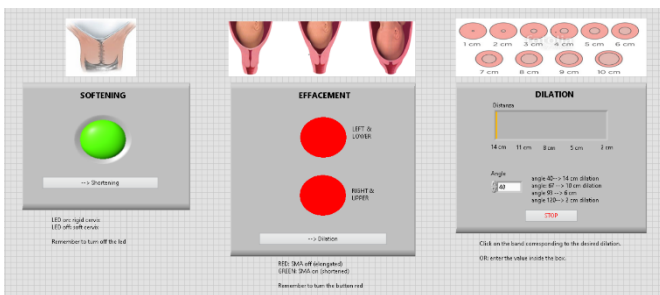
Fig. 9: The User Interface.
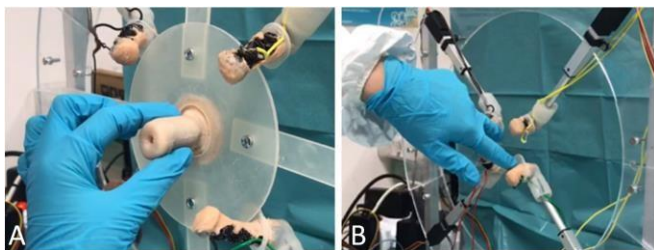
Fig. 10: Simulation of the softening (A) and effacement and dilation (B).

In order to validate the proposed system as a dynamic simulator for cervical changes during labour preliminary assessment phase was carried out involving four ten-year experience gynecologists Medical doctors confirmed the effectiveness of the proposed device in simulating the changes that occur in the cervix during labour, both in terms of used materials and technologies.

IV. CONCLUSION

Analysing the state of the art of both commercial gynaecological simulators and existing prototypes, it emerges that currently there are no systems that faithfully reproduce actively and dynamically the changes that occur in the human cervix during the labour. This work has the aim of creating a system capable of covering this gap, using different technologies and principles, such as granular jamming, SMA, 3D printing, laser cutting and linear actuation. The realized simulator paves the way for more innovative and technological training and teaching programs in gynaecology and obstetrics. Future efforts will be dedicated to validate the system by setting up a well-defined protocol; by including in the study residents in gynaecology and obstetrics (at least no. 50) of the faculty of Medicine of the University of Pisa we will obtain statistically valid data.

REFERENCES

[1] L. Peralta, G. Rus, N. Bochud, and F. S. Molina, "Mechanical assessment of cervical remodelling in pregnancy: Insight from a synthetic model," *Journal of Biomechanics*, vol. 48, no. 9, pp. 1557–1565, 2015.

[2] Woalder, "Cervical Evaluation: From Ancient Medicine to Precision Medicine," *Physiology & Behaviour*, vol. 176, no. 1, pp. 139–148, 2017.

[3] R. Gardner and D. B. Raemer, "Simulation in Obstetrics and Gynecology," vol. 35, pp. 97–127, 2008.

[4] "3B Scientific." [Online]. Available: https://www.3bscientific.it/3b-simulatore-di-stadi-del-parto-1020628-p94-3b-scientific,p_895_29087.html . [Accessed: 28-Aug-2019].

[5] "Birth International." [Online]. Available: https://birthinternational.com/product/individual-cervical-dilatation-models/ . [Accessed: 28-Aug-2019].

[6] "Childbirth graphics." [Online]. Available: https://www.childbirthgraphics.com/78916-Cloth-Cervix-Model-Set-5. [Accessed: 29-Aug-2019].

[7] "Limbs and Things." [Online]. Available: https://limbsandthings.com/us/products/80109/80109-prompt-flex-labor-progress-simulator/%7B%7Burl%7D%7D. [Accessed: 39-Aug-2019].

[8] "CAE." [Online]. Available: https://caehealthcare.com/patient-simulation/lucina/. [Accessed: 29-Aug-2019].

[9] "Alibaba.com." [Online]. Available: https://www.alibaba.com/product-detail/Dilated-and-Effaced-Demonstration-Cervix-Model_60667696727.html?spm=a2700.7724838.2017115.67.3ac12d3bvolUzH . [Accessed: 29-Aug-2019].

[10] S. L. York *et al.*, "Creation and Initial Assessment of a Second-Trimester Uterine Model," *Society for Simulation in Healthcare,* vol. 9, no. 3, pp. 199–202, 2014

[11] A. Pratinidhi and R. Patange, "Testing of simulation training device for assessment of cervical dilatation among nursing student of Karad, India," *Health Science Journal*, vol. 8, pp. 495–501, 2014.

[12] K. L. Shea and E. J. Rovera, "Vaginal Examination Simulation Using Citrus Fruit to Simulate Cervical Dilation and Effacement," *Cureus*, vol. 7, no. 9, pp. 1–8, 2015.

[13] M. J. Luk, D. Lobb, and J. A. Smith, "A Dynamic Compliance Cervix Phantom Robot for Latent Labor Simulation," *Soft Robotics*, vol. 5, no. 3, pp. 330–338, 2018.

[14] A. Cavallo, M. Brancadoro, S. Tognarelli, and A. Menciassi, "A Soft Retraction System for Surgery Based on Ferromagnetic Materials and Granular Jamming," *Soft Robotics*, vol 6, no. 2, pp. 161-173, 2019.

[15] "International Agency for Research on Cancer." [Online].Available: https://www.iarc.fr/. [Accessed: 28-Jan-2020]

[16] M. Salerno, S. Tognarelli, C. Quaglia, P. Dario, and A. Menciassi, "Anchoring frame for intra-abdominal surgery," *Int. J. Rob. Res.*, vol. 32, no. 3, pp. 360–370, 2013.

3D Printing open source non-critical spare parts of medical devices: the oxygen concentrator as a case study

L. Di Pietro[1], C. De Maria[1], G. Gallone[2] and A. Ahluwalia[1]

[1]Research Center "Enrico Piaggio" and Dept of Information Engineering, University of Pisa, Pisa, Italy
[2]Dept of Civil and Industrial Engineering, University of Pisa, Pisa, Italy

Abstract— **According to the World Health Organization the use of oxygen concentrators represents a suitable solution in contexts where oxygen supply is inappropriate or unavailable. However, the lack of spare parts, particularly its sieve beds, is one of the most important barriers for its sustainable use.**

3D printing technologies have been demonstrated to provide important advantages in the local production of devices. These appropriate technologies coupled with the open source design approach proposed by UBORA – a collaborative design e-platform - can solve the issues related to non-critical spare parts, without affecting the safety and certifiability of the device.

This paper presents a feasibility study to locally manufacture zeolite monoliths with interconnected channels as a substitute for zeolite pellets as sieve beds of the oxygen concentrator. Successful laboratory-scale 3D printing of monolith adsorbent, made of 13x zeolite powder and bentonite as a binder, is proposed. Compared to the commercial pellets, the monolith possesses higher macroporosity, a feature which is a benefit in the pressure swing adsorption air separation processes.

Keywords—**Medical device, Spare parts, Oxygen concentrator, Zeolite, 3D printing.**

I. INTRODUCTION

Health is a fundamental aspect of quality of life and it indirectly effects the capacity to produce and consume goods and services. Technology plays a fundamental role in improving the quality of health, being the fulcrum of an effective healthcare system. For these reasons, the 2030 Agenda for Sustainable Development Goals (SDGs), adopted by all United Nations Member States, clearly emphasizes the impact of the lack of appropriate medical devices (MDs) on health [1],[2].

In a worldwide market, assistance service and supply of consumables and spare parts profoundly affect the final costs of medical devices and technology, discouraging both manufactures, vendors and hospital managers from exploring the potential market. This is particularly true for developing countries where the lack of MD spare parts is one of the most important design barriers. [3].

Most medical equipment all over the world is manufactured in developed countries and it has been designed to operate in clean, sterile, climate-controlled environments, with reliable electricity. However, in low-resource settings (LRS), MDs are subjected to harsh environmental conditions including extreme climates, humidity, dust and power instability. These conditions cause more frequent failures and determine a higher request for spare parts, which are expensive and difficult to find. As a result, maintenance and repairing are as problematic as acquisition [3].

Indeed, devices designed for the developing world stop working as soon as the first replacement part is required. Recent studies conducted by Engineering World Health (EWH), revealed that a hospital in LRS finds it easier to request a new oxygen concentrator from their sponsors then to spend $5 to repair the concentrator already in possession [4].

II. 3D PRINTING IN THE MEDICAL FIELD

Additive Manufacturing processes, commonly known as 3D printing (3DP), are find their place in the biomedical field. mainly in the production of bespoke medical products and equipment, such as customized surgical tools, prostheses, and implants [5]-[8], anatomical models for surgical planning [9], and MDs. Apart from customization, benefits provided by the application of additive manufacturing in healthcare include an increased cost efficiency [10], enhanced productivity, democratization and collaboration [11],[12].

In a context where MD suppliers and manufacturers do not always have a satisfactory solution in many maintenance cases involving spare parts (e.g. no more after-sales service with still operating old MDs, sales of complete kits instead of single spare parts, overpricing of spare parts), and considering the constraints of maintenance workshops in hospitals (e.g. limited storage capacity and long delivery times), 3DP for MD spare parts can be a valuable solution for biomedical maintenance teams.

In this context, UBORA, the open Biomedical Engineering e-platform for collaborative deign, can be effectively used to develop safe and effective non-critical spare parts [13]. Through the UBORA e-platform, the biomedical engineering community can also share not only design and printing files of spare parts, but also the analysis of the technical needs, the risk management process, legal aspects, safety criteria and performance data, fundamental for maintaining the compliancy of the repaired devices with the medical device regulation [14].

III. OXYGEN CONCENTRATOR

Oxygen is one of the most basic medicines and despite the fact that it is included in the World Health Organization (WHO) list of essential medicines [15], oxygen supply is not widely available in developing countries [16]. In many acute illnesses, like hypoxemia (low level of oxygen in the blood),

treatment with oxygen is the fundamental part of the therapy. It is also essential for surgical care (e.g. in trauma and obstetrics) and anaesthesia. The reasons for the low availability of reliable oxygen supply are often associated with high cost and lack of infrastructure to install and maintain oxygen supply cylinders and piping [17]-[20].

Based on several studies conducted in different developing countries [21]-[23], the WHO recommends the use of oxygen concentrators, which are not only less expensive, but also more user friendly and reliable than a centralized oxygen supply.

The oxygen concentrator, according to EU Medical Device Regulation (MDR) 2017/745 is a Class IIA MD, and the relative Global Medical Device Nomenclature (GMDN) code is 12873. Its clinical purpose is to deliver low-flow, continuous, clean and concentrated oxygen from ambient air. According to ISO 80601-2-69 "*Medical electrical equipment - Part 2-69: Particular requirements for basic safety and essential performance of oxygen concentrator equipment*", the device must provide medical-grade oxygen (> 82 vol %) commonly between 5 and 10 L/min. Furthermore, a good-quality concentrator can provide a sustainable and reliable source of oxygen to several patients [24].

Currently, oxygen concentrators are based on an air separation process technique, Pressure Swing Adsorption (PSA), that produces oxygen enriched air. Atmospheric air is mainly composed of two gases, Nitrogen (N_2, 78%) and Oxygen (O_2, 21%). If N_2 is removed from air (e.g. absorbed onto a selective surface), the primary gas remaining will be O_2 with high purity.

The main components of the oxygen concentrator based on PSA are shown in Fig. *1*. Atmospheric air is drawn through a series of filters before moving through a compressor. The compressed air enters into the first sieve bed that contains zeolite, an adsorbent ceramic microporous material, able to adsorb N_2 at under high-pressure conditions (adsorption process). The selectivity for zeolite to adsorb N_2 compared to O2 is due to the interaction between electrostatic field of the cationic zeolite and the quadrupole moment of the N_2 which is three times higher than that of O_2 [25]. The most common zeolite for O_2 enrichment from air is 13X zeolite, usually in form of pellets or beads, to increase the surface area. The resulting O_2-enriched air is ready to be delivered to the patient using a nasal canula, oxygen mask or other accessories. In order to guarantee a continuous flow of O_2 to the patient, a two-sieve bed system, alternating adsorption and desorption, is used.

The flow rate must be adjustable by the users. The need of oxygen can change during therapy; in the case of premature newborns an excessive oxygen flow can cause harm. Using a stationary oxygen concentrator (AC-powered), with a continuous stream of oxygen at flow rate up to 10 L/min, equipped with multi-way flowmeter splitters, it is possible to split the oxygen flow and treat several patients (up to an entire paediatric ward) with different therapeutic needs at the same time [26],[27].
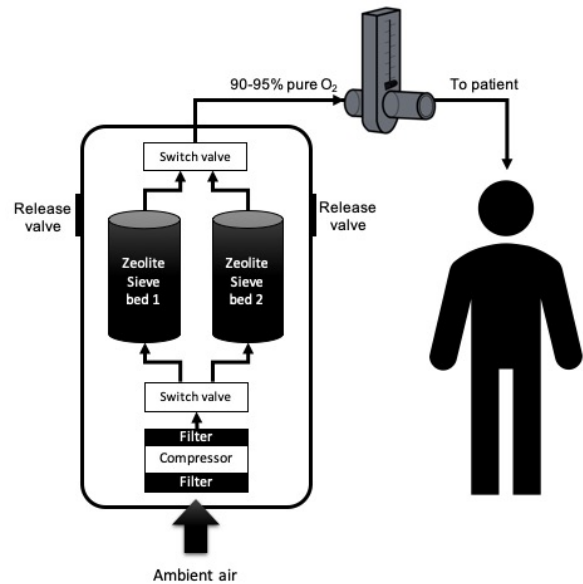

Fig. 1: Main components of the oxygen concentrator

According to Inogen®, one of the leading manufacturers of oxygen therapy solutions, the zeolite sieve beds have a variable duration depending on the quality of the air they draw in and on the volume of the daily use. Generally, a pair of sieve beds must be changed every 18-24 months, but in cases of intense use (12-18 hours per day) a replacement of the beds after 12-16 months is required. Hence, the replacement of the sieve beds for a stationary oxygen concentrator used in a LRS hospital, characterized by a dust environment, may be necessary more than one time per year.

A recent WHO publication [28] provides a detailed description of the requisite spare parts for the device in which the sieve beds are clearly crucial.

The objective of this work is to demonstrate the feasibility of fabricating reliable zeolite porous monoliths that can be used as sieve bed in order to increase the oxygen concentration. We have identified an extrusion-based 3D printing process as the enabling technology to produce zeolite monoliths as single solid structures featured with many interconnected macroporous channels. Compared to the pellet raw material, the 3D printed zeolite monoliths have the potential to be easily regenerated. Furthermore they present enhanced adsorption properties thanks to dynamics of air flow inside the purpose-designed channels, rendering them a suitable solution for the N_2 adsorption process in the oxygen concentrator [29].

The process for production monoliths from 13X zeolite powder is described in the following sections.

IV. FABRICATION OF 3D PRINTED ZEOLITE MONOLITHS

The steps for 3D printing a zeolite monolith are shown in Fig. *2*, and include paste preparation, forming, and finishing.
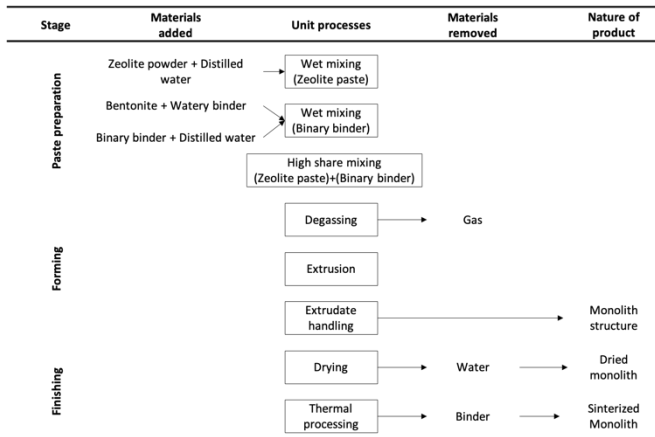
Fig. 2: Processing steps for manufacturing zeolite monolith

A. Paste preparation

Self-standing zeolite monolith was prepared from 13X zeolite powder (Molecular sieves, 13X, powder, Alfa Aesar®). The powder was mixed with a bentonite clay (Nanoclay Nanomer® PGV, Sigma-Aldrich), and a watery binder suspension containing colloidal silica (Ludox HS-40, Sigma Aldrich). In detail, a 50% w/w paste (zeolite paste) of 13X Zeolite in distilled water (milliQ) was obtained by 10 minutes sonication using a VC130 sonication probe (130, Sonics and Materials INC). The binary binder was obtained in two steps:

- *Step 1 – Paste A.* A 50% w/w paste of bentonite in watery binder was prepared by stirring for 10 minutes at room temperature.
- *Step 2 – binary binder.* A 50% w/w binary binder of Paste A in distilled water was prepared by stirring for 20 minutes at room temperature.

The binary binder system has been used to achieve a desired mechanical strength required to prevent cracking of channels or external perimeter of the structure. The final ink was obtained by mixing the zeolite paste with binary binder with a ratio of 1:1 and sonicating this mixture for 30 minutes.

B. Forming and Finishing

The monoliths were fabricated with a piston-driven extruder 3D printer, developed at the research center "Enrico Piaggio" (see

Fig. 3), using a 5 mL syringe with a conical nozzle (final diameter 0.7 mm).

A cylindrical monolith structure (20mm x 20mm x 15 mm) was designed in SolidWorks®, exported as a *.stl* file and sliced by Slic3r® that automatically generated the GCode for the 3D printer. The printing parameters, reported in Table 1, allow to fabricate a 0°-90° woodpile structure layer-by-layer, with a a pore diameter of 0.7mm. The structure was printed at 20°C and at 50% of relative humidity (RH).

When the printing process was completed, the monolith was dried at 20°C and RH 80% for 2 days. The drying step under controlled atmosphere was performed to prevent defects and cracks. Subsequently a calcination process (sintering) was applied at 700°C with a rate of 20°C/min in a temperature-controlled furnace for 4h.
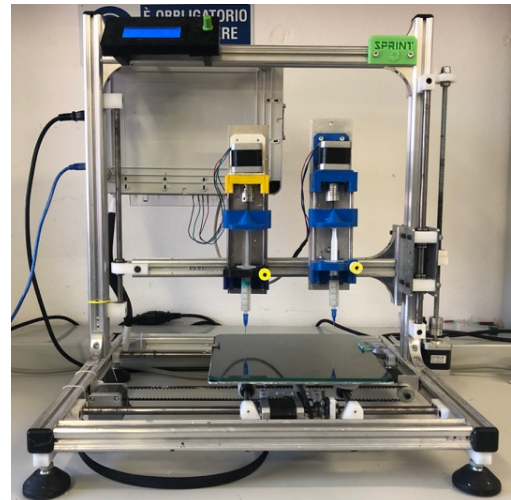

Fig. 3: Custom-made extrusion-based 3D printer

TABLE 1
Printing parameters set in Slicer to obtain the desired GCode

Layer height	0.7 mm
Fill density	50%
Fill pattern	Rectilinear
Fill angle	90°
Solid infill threshold area	70 mm^2
Print movement speed	8 mm/s
No-print movement speed	10 mm/s
Flow rate	160%
Nozzle diameter	0.8 mm
Perimeters	0
Solid layers	0

V. RESULTS AND DISCUSSIONS

This study describes the fabrication of 13X zeolite monoliths with interconnected channels (see

*Fig. 4*a, 3b) using the extrusion-based 3D printing technique. The post-processing after the printing (drying and sintering) did not result in relevant cracks on the structures (

*Fig. 4*c) demonstrating the reproducibility of the techniques employed to generate the structures.

Traditionally, zeolites extruded into monoliths are fabricated using the conventional extrusion processes [30]. In this study, we show that 3D Printing represents an enabling technology for fabricating complex geometries with desired configurations. Modifying printing parameters it should be possible to tune geometrical properties, such as cross section, channel size and wall thickness, which can be optimized to enhance the mechanical and adsorption properties.

VI. CONCLUSIONS

This work starts from the clinical need related to the lack of MD spare parts, which represents one of the most important barriers to access to quality health technologies in developing countries and is thus a prerequisite for global health equity.

We have explored the use of 3D printing as a reliable solution to locally produce sieve beds for an oxygen concentrator starting from row materials and proposing an easy-to-replicate production process (paste preparation, forming, and finishing).
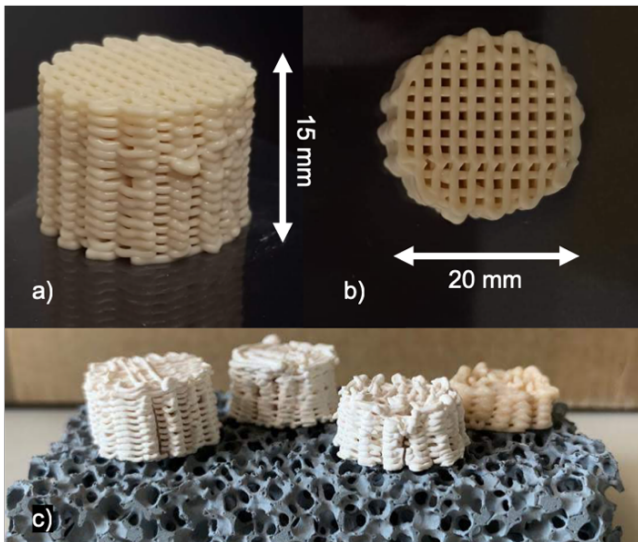
Fig. 4: Self-standing 13X zeolite: a) and b) monolith after printing; c) after the sintering process.

The use of this fabrication process enables the production of tailor-made design of structured adsorbents with the possibility of improving the oxygen purity at the output of the device. The results thus pave the way for further studies to characterise and optimise these monolith structures. Current efforts are focused on the structural analysis of the sieve beds, including dimensional tolerance analysis, air fluid-dynamic optimization, evaluation of absorption efficiency and assessment of regeneration potential.

REFERENCES

[1] Sustainable Development Goals. [Online]. Available: https://www.un.org/sustainabledevelopment/sustainable-development-goals/ [retrieved: January 2020]

[2] World Health Organization. *World health statistics 2016: monitoring health for the SDGs sustainable development goals*. World Health Organization, 2016.

[3] Malkin R. A. (2007). Barriers for medical devices for the developing world. *Expert review of medical devices*, 4(6), 759-763.

[4] Malkin, R. A. "Design of health care technologies for the developing world." *Annu. Rev. Biomed. Eng.* 9 (2007): 567-587.

[5] Banks, J. (2013). Adding value in additive manufacturing: researchers in the United Kingdom and Europe look to 3D printing for customization. *IEEE pulse*, 4(6), 22-26.

[6] Frame, M., & Huntley, J. S. (2012). Rapid prototyping in orthopaedic surgery: a user's guide. *The Scientific World Journal*, 2012.

[7] Mahaisavariya, B., Sitthiseripratip, K., Oris, P., & Tongdee, T. (2006). Rapid prototyping model for surgical planning of corrective osteotomy for cubitus varus: report of two cases. *Injury Extra*, 37(5), 176-180.

[8] Sheth, U., Theodoropoulos, J., & Abouali, J. (2015). Use of 3-dimensional printing for preoperative planning in the treatment of recurrent anterior shoulder instability. *Arthroscopy techniques*, 4(4), e311-e316

[9] Rengier, F., Mehndiratta, A., Von Tengg-Kobligk, H., Zechmann, C. M., Unterhinninghofen, R., Kauczor, H. U., & Giesel, F. L. (2010). 3D printing based on imaging data: review of medical applications. *International journal of computer assisted radiology and surgery*, 5(4), 335-341.

[10] Schubert, C., Van Langeveld, M. C., & Donoso, L. A. (2014). Innovations in 3D printing: a 3D overview from optics to organs. *British Journal of Ophthalmology*, 98(2), 159-161.

[11] Ahluwalia, A., De María, C., Díaz Lantada, A., Di Pietro, L., Ravizza, A., Mridha, M., ... & Leivobits, A. (2018). Towards Open Source Medical Devices. Current Situation, Inspiring Advances and Challenges.

[12] Ahluwalia, A., De Maria, C., & Díaz Lantada, A. (2018). The Kahawa Declaration: a manifesto for the democratization of medical technology. *Global Health Innovation*, 1(1), 1-4.

[13] Di Pietro, L., De Maria, C., Ravizza, A., & Ahluwalia, A. (2019, July). Co-design open-source medical devices: how to minimize the human error using UBORA e-infrastructure. In *2019 41st Annual International Conference of the IEEE Engineering in Medicine and Biology Society (EMBC)* (pp. 3730-3733). IEEE.

[14] UBORA: Euro-Africa Open Biomedical Engineering Innovation e-platform for Innovation through Education. [Online]. Available: https://platform.ubora-biomedical.org/ [retrieved: January 2020]

[15] World Health Organization Model List of Essential Medicines, 21st List, 2019. Geneva: World Health Organization; 2019. Licence: CC BY-NC-SA 3.0 IGO. [Online]. Available: https://apps.who.int/iris/bitstream/handle/10665/325771/WHO-MVP-EMP-IAU-2019.06-eng.pdf?ua=1 [retrieved: January 2020]

[16] Vo, D., Cherian, M. N., Bianchi, S., Noël, L., Lundeg, G., Taqdeer, A., ... & Ochroch, E. A. (2012). Anesthesia capacity in 22 low and middle income countries. *J Anesth Clin Res*, 3(4), 207.

[17] Duke T, Graham SM, Cherian MN, Ginsburg AS, English M, Howie S et al. Oxygen is an essential medicine: a call for international action. Int J Tuberc Lung Dis. 2010 November;14(11):1362–8.

[18] Howie SRC, Hill S, Ebonyi A, Krishnan G, Njie O, Sanneh M et al. Meeting oxygen needs in Africa: an options analysis from The Gambia. Bull World Health Organ. 2009 October 1;87(10):763–71.

[19] Duke T, Peel D, Graham S, Howie S, Enarson PM, Jacobson R. Oxygen concentrators: a practical guide for clinicians and technicians in developing countries. Ann Trop Paediatr. 2010 January;30(2):87–101.

[20] Mokuolu OA, Ajayi OA. Use of an oxygen concentrator in a Nigerian neonatal unit: economic implications and reliability. Ann Trop Paediatr. 2002 September 18;22(3):209–12.

[21] Dobson, M., Peel, D., & Khallaf, N. (1996). Field trial of oxygen concentrators in upper Egypt. *Lancet (London, England)*, 347(9015), 1597-1599.

[22] Litch, J. A., & Bishop, R. A. (2000). Oxygen concentrators for the delivery of supplemental oxygen in remote high-altitude areas. *Wilderness & environmental medicine*, 11(3), 189-191.

[23] Duke, T., Peel, D., Wandi, F., Subhi, R., Sa'avu, M., & Matai, S. (2010). Oxygen supplies for hospitals in Papua New Guinea: a comparison of the feasibility and cost-effectiveness of methods for different settings. *Papua New Guinea Medical Journal*, 53(3/4), 126

[24] World Health Organization. (2016). *Technical Specifications for Oxygen Concentrators: WHO Medical Device Technical Series*. World Health Organization.

[25] Hutson, N. D., Rege, S. U., & Yang, R. T. (1999). Mixed cation zeolites: LixAgy-X as a superior adsorbent for air separation. *AIChE journal*, 45(4), 724-734.

[26] Mokuolu, O. A., & Ajayi, O. A. (2002). Use of an oxygen concentrator in a Nigerian neonatal unit: economic implications and reliability. *Annals of tropical paediatrics*, 22(3), 209-212.

[27] Duke, T., Graham, S. M., Cherian, M. N., Ginsburg, A. S., English, M., Howie, S., ... & Union Oxygen Systems Working Group. (2010). Oxygen is an essential medicine: a call for international action [Unresolved issues]. *The International Journal of Tuberculosis and Lung Disease*, 14(11), 1362-1368.

[28] World Helath Organization. (2019). WHO-UNICEF technical specifications and guidance for oxygen therapy devices [Online]. Available: https://apps.who.int/iris/bitstream/handle/10665/329874/9789241516914-eng.pdf [retrieved: January 2020]

[29] Li, Y. Y., Perera, S. P., & Crittenden, B. D. (1998). Zeolite monoliths for air separation: part 1: manufacture and characterization. *Chemical Engineering Research and Design*, 76(8), 921-930.

[30] Govender, S., & Friedrich, H. B. (2017). Monoliths: a review of the basics, preparation methods and their relevance to oxidation. *Catalysts*, 7(2), 62.

MVAR estimation of source-level EEG connectivity in Parkinson's disease

E. Formaggio[1], M. Rubega[1], J. Rupil[2], S. Masiero[1,3], A. Del Felice[1,3], and G.M. Toffolo[2]

[1]*NEUROMOVE-Rehab, Department of Neuroscience, Section of Rehabilitation, University of Padova, Padova, Italy*
[2]*Department of Information Engineering, University of Padova, Padova, Italy*
[3]*Padova Neuroscience Center, University of Padova; Padova, Italy.*

Abstract— **Motor impairment and cognitive decline due to Parkinson's disease (PD) are mirrored by electroencephalography (EEG) changes detected in background activity and in functional connectivity at the cortico-subcortical and cortico-cortical levels. Investigating abnormalities of resting-state connectivity in PD may be relevant to our understanding of neurodegenerative disorders. In the present study, effective connectivity was investigated on source-level resting-state EEG signals in a group of 15 PD patients and in a group of 20 healthy control subjects. Causal connections were estimated using the well-accepted concept of Granger Causality, based on multivariate auto-regressive models, which provide information on both strength and directionality of the links. The resulting connection patterns were tested for significant differences between the two populations.**

The results revealed that effective connectivity is reduced in PD participants, with a depletion of links from frontal, parietal and occipital areas to the central areas. These cortices, which encompass motor cortices, appear thus functionally isolated in PD, stressing the neurophysiological basis at cortical level of PD.

Keywords— **EEG, Granger Causality, Parkinson's disease, multivariate autoregressive models.**

I. INTRODUCTION

EFFECTIVE connectivity concerns the influence that one neural system exerts over another (both directly or indirectly) and describes the direction of the functional interactions between brain regions. It can be measured by Multivariate Auto Regressive (MVAR) models and Granger Causality (GC) [1].

Among non-invasive functional brain imaging techniques, electroencephalography (EEG) is suitable for studying the temporal dynamics of functional cortical connectivity due to its high temporal resolution (millisecond time scale). EEG records neuronal oscillations, which are known to be altered (i.e. shifted towards faster frequencies over motor cortex) in Parkinson's disease (PD).

The main symptoms of this neurological syndrome arise as a consequence of denervation of the striatum, due to the loss of dopaminergic neurons in the substantia nigra [2]. This causes an imbalance in the modulatory activity of the neurotransmitter dopamine, that leads to excessive inhibition of basal ganglia output, for which the striatum represents the main input nucleus.

PD displays diverse neurophysiological signatures, which are linked to the disease pathophysiology [3]. A hallmark is the increase of beta power on the motor cortex, which reflects at scalp level the abnormal EEG rhythmic activity of basal ganglia. Pathological firing of the basal ganglia entrains oscillations within supplementary motor area, lateral premotor cortex, as well as frontal areas in various frequency. These abnormalities in oscillatory activity reflect alterations in connectivity in the cortico-striato-thalamo-cortical circuit [4], with impaired connectivity described also among cortical areas. Most of these data stem form magnetic resonance imaging (MRI) studies, using diverse functional or structural connectivity methods.

Our aim was to investigate causal connections based on EEG data, which are low-cost and easy to collect, to identify which cortical areas with altered function may impair other outputs. This would provide a neurotherapeutic target for future non-invasive stimulation techniques.

We estimated the Granger causality at the source level as a measure of effective connectivity and brain networks were extracted in order to compare PD with healthy subjects.

II. MATHERIALS AND METHODS

A. Participants

Fifteen people with PD (9 M; mean age 69 ± 6.3 years) were recruited from a Specialist Clinic [5]. Inclusion criteria were: diagnosis of idiopathic PD within the last 5 years; stable dose of antiparkinsonian therapy for at least 4 weeks; off-medication motor Hoen and Yahr 1–2. Exclusion criteria were: psychiatric disorder; benzodiazepine treatment, Mini Mental State Examination (MMSE) < 23. Control data from twenty healthy volunteers (9 M; mean age 45.75 ± 14.07 years) were obtained using the same EEG system.

B. EEG data acquisition

Ten minutes of eyes-open resting state EEG signal (32-channels system; BrainAmp 32MRplus, BrainProducts GmbH, Munich, Germany) were acquired using an analogic anti-aliasing band pass-filter at 0.1–1000 Hz and converted from analog to digital using a sampling rate of 5 KHz. The reference was between Fz/Cz and ground anterior to Fz.

C. EEG data analysis and source imaging

EEG data were band-pass filtered from 1 to 30 Hz and re-sampled using a sampling rate of 500 Hz. Artifacts (i.e., eye movements, cardiac activity, and scalp muscle contraction) were visually identified and removed using independent component analysis. The EEG data were processed using a common average reference and divided into epochs of 2 s.

Source-reconstructed time-series were obtained by using Brainstorm software [6]. First, a head model was created using a symmetric boundary element method based on the anatomy

derived from the ICBM152 brain [7]. Time-series of neuronal activity were reconstructed using minimum norm algorithm. Sources were constrained to the cortex and the reconstructed time-series were projected onto regions of interest (ROIs) as defined by the Brodmann atlas [8], where time-series for voxels within a ROI were averaged and used for connectivity analysis. ROIs were obtained merging Brodmann areas (BA) in frontal, central, parietal and occipital regions, grouped separately for left and right hemisphere, defined as follow: *central areas* - BA 1, 2, 3, 4, 6 (cL and cR); *frontal areas* - BA 8, 9, 10, 11, 44, 45, 46 (fL and fR); *parietal areas* - BA 5, 7, 30, 39, 40, 43 (pL and pR); *occipital areas* - BA 17, 18, 19 (oL and oR).

D. MVAR model and Granger Causality Index

Analysis was performed using the Multivariate Granger Causality Matlab® Toolbox (MVGC) [9]. MVAR models represent a parametric method for discrete-time signal description. Under the assumption of having m stochastic processes $y_i(n); i = 1..m$ they allow to take into account and reconstruct the evolution of each of them in terms of its past history, the past history of all the other signals and a contribution from white noise. This is expressed by the following equation:

$$\mathbf{y}(n) = \sum_{i=1}^{p} \mathbf{A}(i)\mathbf{y}(n-i) + \mathbf{u}(n) \qquad (1)$$

where $\mathbf{y}(n)$ is the vector of the n-th sample of the m processes, which has a deterministic component accompanied by the contribution of $\mathbf{u}(n)$ that represents the m-dimension vector of input white noise, with zero mean and diagonal covariance matrix $\mathbf{\Sigma_u}$. The term p and the $\mathbf{A}(i)$ matrices are respectively the model order and the model coefficient matrices. The model order defines the number of previous samples, from all the processes, that have to be considered in the expression of the current samples $\mathbf{y}(n)$; the weight of each of these samples is defined by the corresponding $\mathbf{A}(i)$ matrix. These matrices, together with $\mathbf{\Sigma_u}$, represent the model parameters that need to be identified in order to characterize the model itself.

According to Granger definition, a cause-effect relationship exists between two time series $y_i(n)$ and $y_j(n)$, with $i, j = 1 ....8$ and $i \neq j$, if the variance of the prediction error of $y_j(n)$, estimated with a MVAR model including all the m time series of $\mathbf{y}(n)$ (unrestricted model), is lower than the one resulting from a MVAR model from which $y_i(n)$ is excluded (restricted model). Hence, the Granger causality from $y_i(n)$ to $y_j(n)$ can be measured with Geweke's Granger Causality index, defined as:

$$GC_{y_i \to y_j|y} = \ln\frac{\tilde{\sigma}_j^2}{\sigma_j^2} \qquad (2)$$

where $\tilde{\sigma}_j^2$ and σ_j^2 are the variance of predicted error $u_j(n)$ for restricted and unrestricted model regression, respectively.

For each subject of each group the analysis was firstly carried out epoch-wise. At first, the order of MVAR model was selected: Akaike parsimony criterion (AIC) was used for this purpose [10]. AIC optimum order was evaluated for each epoch with an upper bound of $p = 20$: the order that was most frequently selected was then chosen as fixed for the subject ($p = 9$). Eq.1 was evaluated for all the possible pairs of ROIs

and the 8×8 matrix of GC indices represents causal strength among them, i.e. the (i, j) element of the GC matrix represents the strength of the influence that ROI j exerts on ROI i. F-test with Bonferroni correction was applied to check the statistical significance of each index ($p < 0.05$): if the null hypothesis, that error variances were not significantly different, was accepted, the value of the corresponding GC coefficient was forced to zero for the current epoch.

The overall estimate of Granger connection magnitudes at a single subject level was obtained by averaging the GC matrices across all epochs. The percentage of times epochs recognized as significant throughout the whole recording was also monitored for each subject.

Finally, for each group of subjects, the grand average GC matrix was evaluated and a graph of the connectivity network was depicted, evidencing the most relevant links, i.e. the ones recognized as significant in at least 75% of epochs. The 75% threshold was empirically chosen, since it allows a reasonable characterization of the networks using only those connections that are robust across epochs and subjects.

E. Statistical analysis

To obtain statistical inference regarding groups' differences in non-threshold connectivity matrices (GC values), a Mann-Whitney-Wilcoxon test ($p < 0.05$) was performed.

III. RESULTS

The average GC matrices for PD and control participants are shown in panels a and b of Fig. 1, the average percentage matrices in panels c and d, while in panels e and f the corresponding connectivity networks are depicted: the eight ROIs are the nodes, while the edges represent the most relevant connections among them. These graphs are i) directed since the asymmetry of the Granger matrix allows differentiating between in-going and out-going connections; ii) weighted since the strength of each edge is represented by the magnitude of the Granger coefficient, codified in Fig.1 by the colour of the arrows. Control group shows a higher number of connections compared to PD group and almost all of them are directed towards the central regions cR and cL (the motor cortex) (p<0.05). The patients' graph was overall poorer; only the connections form pL to cL and from oL to cL exceeded the threshold.

Comparison between the average GC matrices in the two groups (Fig.2) indicates a significantly stronger connections (p < 0.05) in controls vs. PD, from the occipital to the central areas, both in the right and left side, and from parietal to central area, only on the right side.

IV. CONCLUSION

A. Discussion

Our results provide evidence of connectivity abnormalities at cortical level in subjects with PD, with a functional alteration in the motor and visual systems, as shown in Fig. 2.
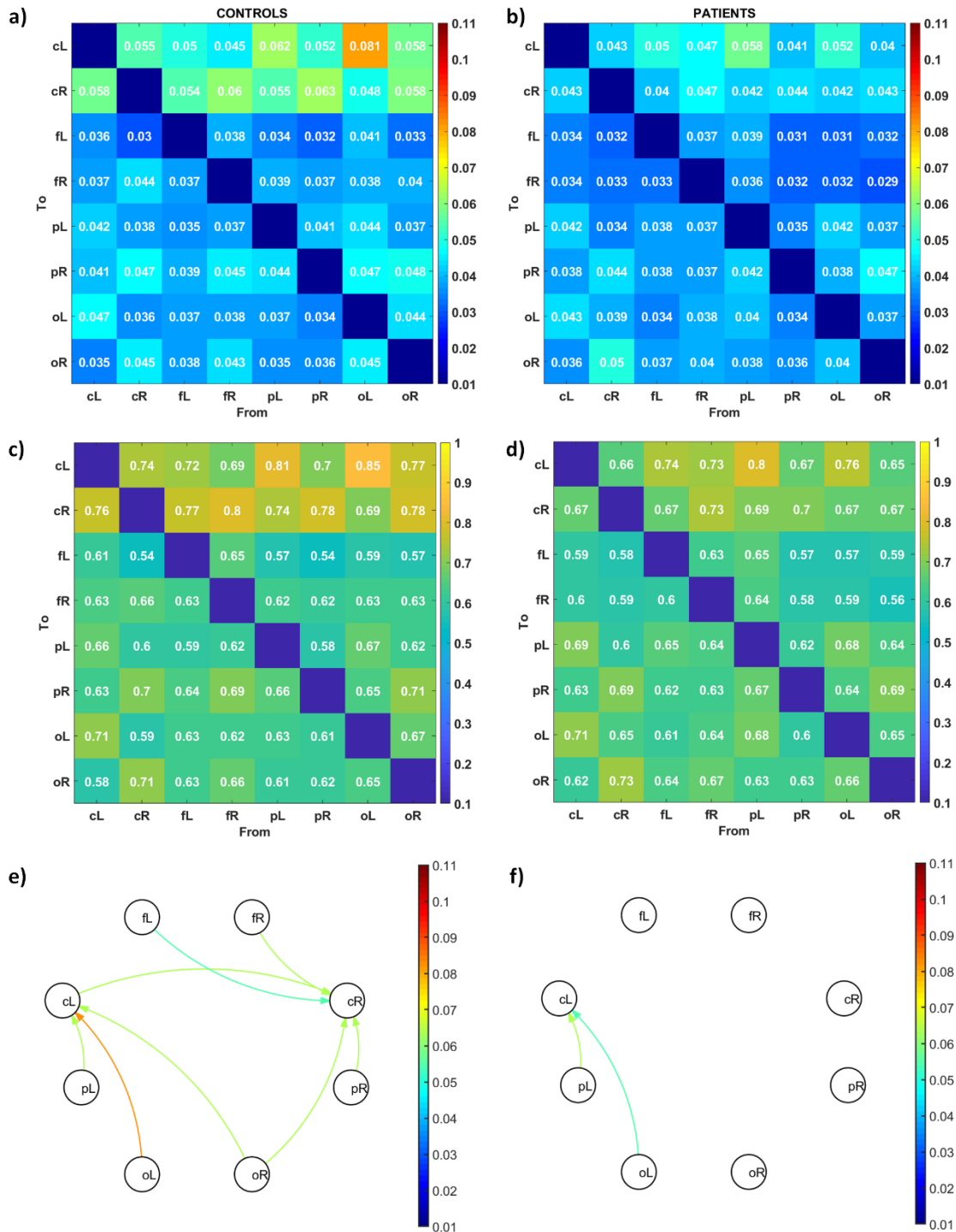
Fig. 1 UPPER PANELS. Grand-average GC matrices for Controls (a) and PD participants (b). Element (i,j) - where i indicates the row and j the column - represents the weight of the connection from ROI j to ROI i. The diagonal elements of the matrix are set to zero, since they represent connections from a ROI to itself (loops). MEDIUM PANELS. Grand-average percentage matrices for Controls (c) and PD participants (d). The percentage of times epochs recognized as significant throughout the whole recording. LOWER PANELS. Connectivity networks for Controls (e) and PD participants (f). Circles stands for the eight ROIs and arrows for directed connections. Colorbars represent the magnitude of the brain connections. Only the most relevant connections are shown, i.e. the ones recognized as significant in at least 75% of epochs.

These data offer a different perspective on the basal ganglia-thalamocortical loop, which is known to be dysfunctional in persons with PD [4]. In particular, cortico-motor areas resulted to be more isolated in PD.

Brain connectivity differences between healthy subjects and PD participants can be summarized into two main aspects: the depletion of connections towards the central areas, corresponding to the motor cortices, and the weakening of the links from the parietal and occipital ones towards motor regions. Overall, brain networks in PD resulted to be poorer than the healthy ones.

The isolation of motor areas may be coherent with the symptoms of the disease, which have a strong motor component (rigidity, bradykinesia, tremor, and postural instability). Data from functional MRI-based connectivity demonstrate diminished connections between basal ganglia

and motor cortices: we observe also a reduced interaction between these cortical areas, further supporting their pathophysiological role in PD.

Our results revealed that parietal and occipital connectivity changes play an important role in the characterization of PD participants' network. In fact, their causal influence on central areas was significantly reduced. Other imaging studies pointed out differences in the activation of these areas: Positron Emission Tomography (PET) investigation revealed that PD patients showed significantly lower relative cerebral blood flow in the bilateral occipital and posterior parietal cortex [11]. These results confirm the well-known neuropsychological trait of defective visuospatial integration, coupled with posterior areas (occipital, parietal and temporal) dysfunctions [12]-[13]. The reduced interaction of these posterior cortices with motor areas, shown by Granger causality, is further proof of the impact of this neuropsychological deficit on motor performance.
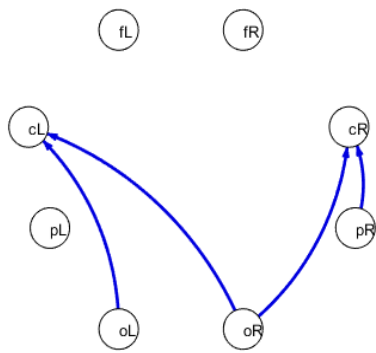
Fig. 2: Statistically significantly different edges (p < 0.05) in Controls vs PD as evaluated from the GC matrices. Circles stands for the eight ROIs and arrows for significant connections. Blue colour indicates controls > PD participants.

Impaired sensory-motor integration, reflected by the weakening of connections between parietal and central areas, is also confirmed by clinical signs: altered proprioception and sensation (i.e. the capability of recognizing body segment position in space) is considered the causal factor of some peculiar PD clinical pictures (i.e. Pisa syndrome) and becomes evident as isolated sign in the final stages of disease.

An unexpected finding was the predominance in controls of a right parieto-motor connection. An interesting hypothesis rests on the differential function of dominant and non-dominant limbs. In reaching movements, the non-dominant arm appears better adapted for achieving accurate final positions and the dominant one for specifying initial trajectory features, such as movement direction. According to this view, the right stronger information flow, even at rest, may signal the more detailed visuo-spatial control exerted on the left arm, which reaches targets with more accuracy.

B. Future development and limitations

Since recent works [14]-[15] provided direct evidence that scalp EEG can sense both cortical and subcortical signals, the promising results of this preliminary work in analysing the pathological topography of the brain network in PD may be supported by a high-density EEG study ($\geq$64 channels) exploiting an individual head model based on magnetic resonance imaging. Despite the exploited method for source reconstruction is computationally cheap and easy to implement, it relies on certain ad-hoc assumptions and constraints that can influence the accuracy of the results. Different assumptions embedded in the source localization method used to solve the inverse problem might lead to different results. Results might be also influenced by the choice of the brain parcellation and the method used to deal with the dipole orientation of all solution points in the same region of interest [16].

Moreover, control group should be age-matched. Aging processing may indeed slightly modulate brain connectivity producing differences among young, adult and elderly.

Connectivity analysis performed in frequency domain could improve the evaluation of pathological PD networks investigating also brain rhythms changes. A deviation from physiological frequency bands is indeed a hallmark of a wide group of pathologies as PD, namely oscillopathies.

Thresholding procedure could also be improve using an automatic method based for example on surrogate and uncorrelated data. Using a threshold of 50% all the connections appear in the graph, making difficult to grasp the differences between the two groups. The situation slightly improves with 60%, the 75% allows a reasonable characterization of the networks.

Brain connectivity changes related to pathophysiology may offer cues for the development of new therapeutic approaches. Effective connectivity analysis highlights differences in brain networks apparently related to PD symptoms. Treatments aimed at restoring physiological connectivity, in particular improving causal influence of parieto-occipital areas on the motor ones, might lead to a symptoms' improvement.

REFERENCES

[1] C. Granger, "Investigating causal relations by econometric models and cross Spectral methods," *Econometrica*, vol 37, pp. 424-438, 1969.

[2] M. Sharman, et al. "Parkinson's disease patients show reduced cortical-subcortical sensorimotor connectivity," *Movement Disorders*, vol. 28(4), pp. 447–454, 2013.

[3] A.K. Engel, P. Fries, "Beta-band oscillations-signalling the status quo?," *Curr. Opin. Neurobiol*, vol. 20(2), pp. 156–165, 2010.

[4] C. Hammond, H. Bergman, and P. Brown, "Pathological synchronization in parkinson's disease: networks, models and treatments," *Trends in neurosciences*, vol. 30(7), pp. 357–364, 2007.

[5] A. Del Felice, et al. "Personalized transcranial alternating current stimulation (tACS) and physical therapy to treat motor and cognitive symptoms in Parkinson's disease: A randomized cross-over trial," *Neuroimage Clin*, 22:101768, 2019.

[6] F. Tadel, S. Baillet, J. C. Mosher, D. Pantazis, and R. M. Leahy, "Brainstorm: a user-friendly application for meg/eeg analysis," *Computational intelligence and neuroscience*, vol. 2011, p. 13, 2011.

[7] J. Mazziotta, et al. "A four-dimensional probabilistic atlas of the human brain," *J. Am. Med. Inform. Assoc*, vol 8, pp, 401-430, 2001.

[8] K. Zilles and K. Amunts, "Centenary of brodmann's map—conception and fate," *Nature Reviews Neuroscience*, vol. 11(2), pp. 139-145, 2010.

[9] L. Barnett and A. K. Seth, "The mvgc multivariate granger causality toolbox: a new approach to granger-causal inference," *Journal of neuroscience methods*, vol. 223, pp. 50–68, 2014.

[10] H. Akaike, "A new look at the statistical model identification", *IEEE Trans. Autom. Control*, vol 19(6), pp. 716–723, 1974.

[11] Y. Abe, et al. "Occipital hypoperfusion in parkinson's disease without dementia: correlation to impaired cortical visual processing," *Journal of Neurology, Neurosurgery & Psychiatry*, vol. 74(4), pp. 419–422, 2003.

[12] G. Tropini, J. Chiang, Z.J. Wang, E. Ty, M.J. McKeown, "Altered directional connectivity in Parkinson's disease during performance of a visually guided task," *Neuroimage*, vol. 56(4), pp. 2144-2156, 2011.

[13] S. Kloeters, et al. "Impaired perception of human movements in Parkinson's disease," *Behav Brain Res*, vol. 317, pp. 88-94, 2017.

[14] F. Pizzo, et al. "Deep brain activities can be detected with magnetoencephalography," *Nat. Commun*, vol. 10(1), 971, 2019.

[15] M. Seeber, et al. "Subcortical electrophysiological activity is detectable with high-density EEG source imaging," *Nature communications* vol. 10(1):753, 2019.

[16] M. Rubega, et al. "Estimating EEG source dipole orientation based on singular-value decomposition for connectivity analysis," Brain topography vol. 32(4), pp. 704-719, 2019.

Polymeric microchambers arrays for cargo protection

S. Boi[1], V. Kudryavtseva[2,3], J. Zhang[2], A. Udalov[4], E. Shesterikov[4,5], S. Tverdokhlebov[3], L. Pastorino[1] and G. Sukhorukov[2]

[1] Department of Informatics, Bioengineering, Robotics and Systems Engineering, University of Genoa, Genoa, Italy
[2] School of Engineering and Materials Science, Queen Mary University of London, United Kingdom
[3] National Research Tomsk Polytechnic University, Russian Federation
[4] V.E. Zuev Institute of Atmospheric Optics, Russian Academy of Science, Siberian Branch, Russian Federation
[5] Tomsk State University of Control Systems and Radioelectronics, Russian Federation

Abstract— **Efficient depot systems for entrapment and long-term release of small water-soluble molecules are of pivotal importance for numerous applications. In this work, polylactic acid (PLA) was used to obtain arrays of micro-sized and tunable shaped microchambers containing various cargos and able to retain them up to several weeks, thus protecting them from dissolution and leakage.**

Keywords—**Microchambers, PLA, Drug delivery, Microprinting.**

I. INTRODUCTION

Encapsulation systems are urgently needed for the delivery of active molecules such as enzymes, cells, dyes or drugs for an extensive variety of advanced applications [1].
Particularly, micropacking is required for a wide range of applications, including drug delivery [2,3], diagnostics [4], tissue engineering [5], biosensors [7] membranes but also corrosion inhibition [6], templates for synthesis, optical systems [8] antifouling [9,10] self-healing materials [1] and coatings [6]. Small molecules (Mw < 1 kDa) encapsulation is still a request, due to the commonly employed encapsulation matrix like polyelectrolyte multilayers or liposomes being nanoporous. Fabrication of such polymeric composite systems is commonly achieved via layered nanodeposition approaches based on electrostatic-, hydrogen and van-der-Waals bonding. Nowadays, one of the most tunable and used layered deposition system consists in polyelectrolyte multilayers (PEM) based on layer-by-layer (LbL) self-assembly [9]. While storage of polymeric or chemically linked drugs within the bulk of PEM is possible, a site-specific release of precisely defined low quantities requires encapsulation within microchambers [12], because of capsule shell's high permeability.
Thus, the failure in encapsulating hydrophilic cargos with low molecular weights [7, 11] renders the entrapment of small molecules still a challenge.
Polylactic acid is an FDA approved biocompatible and biodegradable polymer and has already shown the ability to block the diffusion of small molecules from microchambers [12].

II. EXPERIMENTAL

A. Materials

Polylactic acid (PLA) (GoodFellow), poly(dimethylsiloxane) (PDMS) kit (Sylgard 184, Dow-Corning, Midland, MI), chloroform (VWR), carboxyfluorescein (CF, Sigma) were used as received without further purification.
Deionized (DI) water from a Milli-Q (Millipore, Darmstadt, Germany) water purification system was used to produce ultrapure water for the dipping and washing solutions.
The silicon masters used for PDMS-based pattern creation were produced by combination of photolithography and electroplating technique [13].

B. Fabrication of Patterned PDMS Stamp Based on Silicon Master

Patterned PDMS stamps with rectangular-shaped microwells were prepared by casting PDMS prepolymer and curing agent (10:1 ratio) onto silicon masters with micropillars. The PDMS was subsequently degassed for 30 min in vacuum and cured at 70 °C for 3 h. Then the PDMS was cut with a sharp surgery knife and lifted off the micropatterned master. PDMS stamp offering a negative replica of the master surface features were produced.

C. Fabrication of PLA microchambers

The utilized silicon master structures for microchamber production were rectangular structures with 13 μm lenght and 9 μm width positioned at 20 μm center-to-center distance. This chamber arrangement allowed for 250000 chambers to be placed on 1 cm^2.
PDMS stamps were dipped into 2% PLA solution for 2 s and then gently taken out and let dry in ambient conditions, allowing solvent evaporation.
Cargo loading was performed both by precipitation of a model drug solution and by dry powder spreading onto the stamp. For cargo loading by solution, PDMS stamps covered with a PLA layer were dipped into the cargo solution for 60 s. The sample was wiped with fuzz free cotton swabs to remove solution not filling the chambers and allowed to dry in air overnight at room temperature to evaporate solvent and facilitate cargo precipitation.
Microchambers sealing was obtained both by microcontact printing and by dip-coating. As regards sealing by dip-coating technique, PDMS stamp with loaded microchambers was dipped into 2% PLA solution for 2 s and gently removed and let dry at room temperature.
As regards sealing by microcontact printing, a flat PLA sheet without patterns was coated with PLA by dipping it for 2 s in 2% PLA solution and printing it under pressure for 30 s.

The sealed PLA microchamber arrays were then collected after lifting off the PDMS stamp.

D. Characterization.

Scanning electron microscopy (SEM) (FEI, Inspect-F) was used to assess PLA microchamber morphologies after 45s of gold sputter coating to ensure conductive samples. SEM observation was carried out using an accelerating voltage of 5 kV, a spot size of 3, and a working distance of approximately 10 mm. Confocal laser scanning microscopy (CLSM) images were obtained with a Leica TS confocal scanning system (Leica, Heidelberg, Germany) equipped with a 20× objective. The obtained microchamber arrays were washed three times in DI water and then kept into DI water or 0.01 M PBS for 8 weeks in order to assess CF protection ability of the developed drug delivery system. The fluorescence of the incubation media was measured by fluorescence spectroscopy (Perkin Elmer LS55), in order to evaluate potential CF dissolution and leakage from the carriers, up to 8 weeks.

III. RESULTS

PLA microchambers arrays were prepared from 2% PLA solution in chloroform. Figure 1 shows SEM micrographs of PDMS stamps dipped into PLA solution and dried (a), microwells loaded with model cargo carboxyfluorescein (b) and loaded microwells sealed by dip-coating (c) and microcontact printing (d). It can be noticed that the resulting films obtained by different sealing methods, appear very similar.
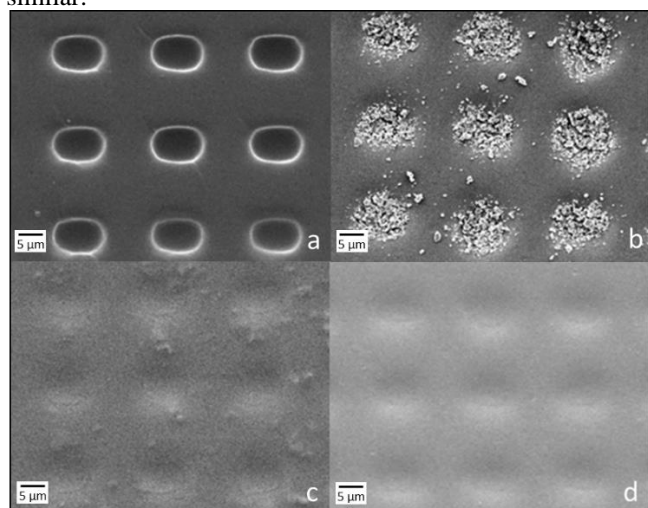
Fig. 1: SEM micrographs of the different steps of PLA microchambers production. PDMS stamps dipped into PLA solution and dried (a), microwells loaded with model cargo carboxyfluorescein (b), loaded microwells sealed by dip-coating (c) and by microcontact printing (d).

Figure 2 shows confocal laser scanning miroscopy images of PDMS stamps dipped into Nile red-marked PLA (red) and loaded with carboxyfluorescein (CF, green) (a) and microchambers sealed by microcontact printing with a sealing layer of red-marked PLA (b). It can be clearly seen that loaded CF can be found only into the microwells and little amount remains outside.
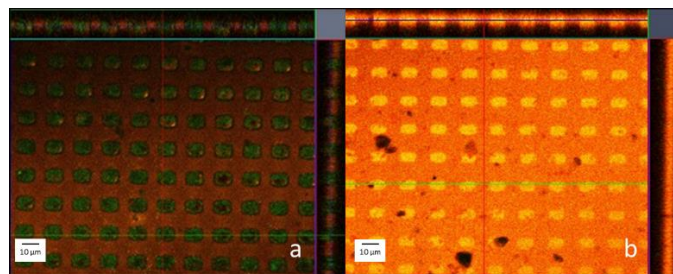

Fig. 2: Confocal laser scanning microscopy images of PDMS stamps dipped into PLA (red) and loaded with carboxyfluorescein (green) (a) and microchambers sealed by microcontact printing with a final layer of red-marked PLA (b).

After 8 weeks, no fluorescence was found in the incubation media, thus demonstrating that CF crystals were successfully retained into PLA microchamber arrays without cargo loss.

IV. CONCLUSIONS

PLA biocompatible and biodegradable microchambers were produced via a one-step dip-coating strategy. This procedure allows great tunability and versatility in the polymer choice and in the microchambers shape and size high controllability provided by the silicon master. Moreover, a wide range of possible cargo molecules (water-soluble, non-water soluble, low-molecular), as well as loading methods (in-situ crystallization of solutions, powder spreading in case of poorly water-soluble drugs), are allowed. Microchambers sealing can be performed by dip-coating or by microcontact printing. Hence, this variety of choices allows the selection of diverse release trigger stimuli, like laser-guided, high focused ultrasounds and magnetic fields.

Special emphasis is given to the fact that the encapsulated hydrophilic molecule is stably entrapped within submerged conditions up to 8 weeks, thus demonstrating microchambers ability to provide enough protection to small water-soluble molecules for a relatively long period of time without cargo dissolution and loss.

REFERENCES

[1] E. V. Skorb and H. Möhwald, Adv. Mater., 2013, 25, 5029–5043.
[2] Wu, Y. Wu, W. He, X. Lin, J. Sun and Q. He, Angew. Chem., Int. Ed., 2013, 125, 7138–7141.
[3] 3 Y. Wu, Z. Wu, X. Lin, Q. He and J. Li, ACS Nano, 2012, 6, 10910–10916.
[4] 4 K. A. Athanasiou, G. G. Niederauer and C. M. Agrawal, Biomaterials, 1996, 17, 93–102.
[5] 5 A. H. Faraji and P. Wipf, Bioorg. Med. Chem., 2009, 17, 2950–2962.
[6] D. Borisova, D. Akçakayıran, M. Schenderlein, H. Möhwald and D. G. Shchukin, Adv. Funct. Mater., 2013, 12, 3799–3812.
[7] Z. Siwy, L. Trofin, P. Kohli, L. a. Baker, C. Trautmann and C. R. Martin, J. Am. Chem. Soc., 2005, 127, 5000–5001.
[8] J. Shao, M. Xuan, L. Dai, T. Si, J. Li and Q. He, Angew. Chem., Int. Ed., 2015, 54, 12782–12787.
[9] J. Frueh, M. Gai, Z. Yang and Q. He, J. Nanosci. Nanotechnol., 2014, 14, 4341–4350.
[10] J. A. Callow and M. E. Callow, Nat. Commun., 2011, 2, 244.
[11] H. Gao, A. V. Sapelkin, M. M. Titirici and G. B. Sukhorukov, ACS Nano, 2016, 10, 9608–9615.
[12] M. Gai, J. Frueh, T. Tao, A. V. Petrov, V. V. Petrov, E. V. Shesterikov, S. I. Tverdokhlebov and G. B. Sukhorukov. Nanoscale,2017, 9, 7063-7070.
[13] I. A. Zykova, A. A. Udalov, V. L. Kudryavtseva, E. V. Shesterikov and S. I. Tverdokhlebov. IOP Conf Ser Mater Sci Eng, 2019, 511, 012037.

Model-based assessment of incretin effect from OGTT data in healthy subjects

M. Morettini[1], E. Creato[1], J. Di Monte[1], L. Ilari[1] and L. Burattini[1*]

[1] Department of Information Engineering, Università Politecnica delle Marche, Ancona (Italy)

*Corresponding author (l.burattini@univpm.it)

Abstract— **The incretin effect is a phenomenon in which insulin response to an Oral Glucose Tolerance Test (OGTT) is higher with respect to the insulin response to a matched isoglycaemic intravenous glucose infusion (I-IGI). The aim of this study was to simplify our previous model describing glucose-insulin regulatory system to allow assessment of the incretin effect in healthy subjects from OGTT glucose and insulin data, without using I-IGI data. The proposed model is characterized by four free parameters and was tested on mean data of two groups of healthy subjects. Free model parameters were estimated with a good precision (CV%<22) and provided values for the incretin effect very similar to the experimental ones (64.2 vs. 63 in the first group of subject and 77.7 vs. 78.1 in the second group). Thus, the proposed model seems to be promising, for the sake of a patient-oriented approach, to assess the incretin effect in healthy subjects only using OGTT glucose and insulin data.**

Keywords— **Glucose-dependent insulinotropic polypeptide, glucagon-like peptide-1, mathematical model, patient-oriented approach.**

I. Introduction

THE incretin effect represents a phenomenon in which oral glucose leads to a potentiated insulin response with respect to an intravenous glucose infusion even when the same plasma glucose concentration profiles ("isoglycaemia") are achieved. This is due to the fact that oral glucose, when absorbed in the gut, leads to the release of incretin hormones (glucose-dependent insulinotropic polypeptide, GIP, and glucagon-like peptide-1, GLP-1) from specialized cells in the gut, while intravenous glucose does not [1].

Incretin effect is usually quantified by comparing insulin response to two different tests: an Oral Glucose Tolerance Test (OGTT) and a matched Isoglycaemic Intravenous Glucose Infusion (I-IGI) in which isoglycaemia with the OGTT is imposed. Over the years, several mathematical models of the glucose-insulin regulatory system accounted for the incretin effect [2]-[10]. In some of these models [2], [6], [8]-[10], a simultaneous analysis of OGTT and I-IGI data is required; since two tests are needed in this case, assessment of incretin effect is demanding; moreover, differently from OGTT, I-IGI cannot be easily performed in clinical practice. Alternatively, mathematical description of incretin hormones dynamics have been introduced in other models and for parameter estimation, GIP and/or GLP-1 concentrations acquired during OGTT have been used in addition to glucose and insulin concentrations [3], [5], [6], [9], [10]. However, whilst a single test – the OGTT - is sometimes sufficient in some of these models, incretin hormones concentration is not usually measured during standard clinical practice, thus limiting applicability of such models.

Incretin-based therapies are currently used in the treatment of type 2 diabetes (T2D) [11] and the possibility to have a patient-oriented approach for the assessment of the incretin effect could provide an important tool to better understand the effect of such therapies and the pathophysiology of T2D. Thus, the aim of this study was to simplify our previous model [6] to allow assessment of the incretin effect in healthy subjects from OGTT glucose and insulin data, without using I-IGI data.

II. Materials and methods

A. Model formulation

The proposed model of the glucose-insulin regulatory system after glucose ingestion is shown in Figure 1. Assuming a glucose dose D (equal to 75 g, equivalent to 417 mmol), the rate of emptying of the oral glucose load into the gut $G_{empt}(t)$ (mmol·min^{-1}) is described as follows:

$$G_{empt}(t) = D \cdot \beta \cdot k_e^{\beta} \cdot t^{\beta-1} \cdot e^{[-(k_e \cdot t)^{\beta}]} \quad (1)$$

where k_e (min^{-1}) is a fractional transfer coefficient and β a dimensionless shape factor [6].

The gut is modelled as a single compartment and the rate of change of the amount of glucose into the gut $q_{gut}(t)$ (mmol) is described as follows:

$$\frac{dq_{gut}(t)}{dt} = -k_{abs} \cdot q_{gut}(t) + G_{empt}(t) \quad (2)$$

where k_{abs} (min^{-1}) is the rate constant of intestinal absorption [6]. Considering that only a fraction of the intestinal absorption (f) actually appears in plasma, the rate of appearance of ingested glucose into plasma $Ra_G(t)$ (mmol·min^{-1}) can be described as follows as previously done in [6]:

$$Ra_G(t) = f \cdot k_{abs} \cdot q_{gut}(t) \quad (3)$$

The rate of change in plasma glucose concentration $G(t)$ (mmol·l^{-1}) is described as previously done in [6] by the following differential equation:

$$\frac{dG(t)}{dt} = \frac{Ra_G(t)}{V} + \frac{HGB(t)}{V} - k_1 \cdot G(t) - k_2 \cdot I(t) + \gamma \cdot \frac{dI(t)}{dt} \quad (4)$$

where $HGB(t)$ (mmol·min^{-1}) represents the hepatic glucose balance and $I(t)$ (mU·l^{-1}) represents the plasma insulin concentration. Non-insulin-dependent and insulin-dependent glucose disappearance into tissues are regulated by the rate constants k_1 (min^{-1}) and k_2 (mmol·mU^{-1}·min^{-1}), respectively. The last term, regulated by the corrective factor γ (mmol·mU^{-1}), has the effect of sharpening the peak in the glucose curve. V (l) represents the distribution volume. $HGB(t)$ is controlled by both glucose and insulin according to

the following equation:

$$HGB(t) = HGB_b + M \cdot [G_b - G(t)] \cdot I(t) \quad (5)$$

where HGB_b is the basal hepatic glucose balance and was assumed equal to the value of 0.77 mmol·min^{-1} on the basis of previous considerations done in [6], G_b (mmol·l^{-1}) is the basal glucose concentration and M (L^2·mU^{-1}·min^{-1}) is a modulating factor. As previously done in [6], the ratio between non-insulin-dependent and insulin-dependent glucose disappearance into tissues (p) was assumed equal to 2 for basal conditions (with I_b representing basal insulin concentration in mU·l^{-1}), thus k_1 and k_2 in eq. (4) can be computed as follows:

$$k_1 = \frac{p}{p+1} \cdot \frac{HGB_b}{G_b \cdot V} \quad (6)$$

$$k_2 = \frac{1}{p+1} \cdot \frac{HGB_b}{I_b \cdot V} \quad (7)$$

The rate of change in plasma insulin concentration I(t) is described by the following differential equation:

$$\frac{dI(t)}{dt} = k_G \cdot G(t)^{1.3} + k_{INC} \cdot Ra_G(t) - k_9 \cdot I(t) + \lambda \quad (8)$$

where the first term accounts for post-hepatic insulin secretion due to glucose through the coefficient k_G (mU·min^{-1}· mmol$^{-1.3}$·L$^{-0.3}$). Differently from the original model [6], in the present model incretin hormones dynamics has not been directly described and the contribution of the incretin hormones to post-hepatic insulin secretion has been modelled with a control from the rate of appearance of ingested glucose into plasma through the coefficient k_{INC} (mU·mmol^{-1}·L^{-1}); the third term accounts for insulin clearance through the coefficient k_9 (min^{-1}) whereas λ (mU·L^{-1}·min^{-1}) is a constant term that can be derived by imposing the steady-state conditions:

$$\lambda = k_9 \cdot I_b - k_G \cdot G_b^{1.3} \quad (9)$$

Description, values and units for model variables and fixed model parameters are reported in Table I and II, respectively. The remaining independent parameters β, k_G, k_{INC}, and γ were automatically estimated from experimental data.

B. Reported experimental data

Data of plasma glucose and insulin concentration measured after an OGTT and a subsequent matched I-IGI, averaged over two groups of healthy subjects (HC1 [12] and HC2-group [13]) were considered. The OGTT protocol consists of a standard 75 g oral glucose administration (i.e. 1 g of glucose per kg body weight, BW, administered at time t = 0 min, and standardized to a 75 kg individual).

C. Parameter estimation

Parameter estimation has been performed in Matlab&Simulink® environment, through a weighted least squares (WLS) procedure. For each time point (t_i) of the OGTT protocol (being N the number of samples acquired during the OGTT), the model-predicted glucose $G_m(t_i)$ and insulin $I_m(t_i)$ have been simultaneously fitted to the glucose $G(t_i)$ and insulin $I(t_i)$ data from OGTT using the following sum of square error (SSE) expression:

$$SSE = \sum_{i=1}^{N} \left[\left(\frac{G_m(t_i) - G(t_i)}{\Gamma_{Gi}} \right)^2 + \left(\frac{I_m(t_i) - I(t_i)}{\Gamma_{Ii}} \right)^2 \right] \quad (10)$$

where the weights Γ_{Gi} and Γ_{Ii} were placed equal to 1.5% and 4% of $G(t_i)$ and $I(t_i)$, respectively, assuming normal distribution with zero mean for the measurement errors.

The quality of the fit was assessed by computing the root-mean-square error RMSE=√(SSE/2N), whereas the precision of all parameter estimates was expressed in terms of coefficient of variation CV(p_i)% = SDp_i /p_i · 100, being p_i and SDp_i the i-th component of the model parameters vector and the standard deviation of p_i, respectively. SDp_i was computed as the square root of the diagonal terms of the inverse of the Fisher information matrix.
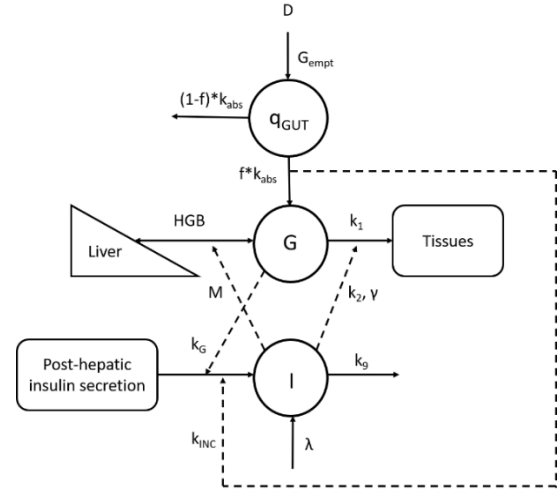

Fig. 1: Compartmental description of the proposed model.

D. Model validation and assessment of the incretin effect

After parameter estimation, model has been used to simulate insulin response to an I-IGI. To this purpose, Ra_G (t) was set to zero in eq. (8) and plasma glucose concentration during OGTT was used as input. Incretin effect has been assessed as the difference in integrated incremental insulin responses (over basal) between OGTT and matched I-IGI, expressed as percentage of the integrated incremental OGTT insulin response. Model validation has been performed by comparing the incretin effect obtained from the model to the one provided by the experimental data.

TABLE I
DESCRIPTION, BASAL VALUES AND UNITS FOR MODEL VARIABLES

Model variable	Description	Basal value	Units
$G_{empt}(t)$	Rate of emptying of glucose load into the gut	0	mmol·min^{-1}
$q_{GUT}(t)$	Amount of glucose in the gut	0	mmol
$Ra_G(t)$	Rate of appearance of ingested glucose into the plasma	0	mmol·min^{-1}
$HGB(t)$	Hepatic glucose balance	HGB_b=0.77	mmol·min^{-1}
$G(t)$	Plasma glucose concentration	G_b=fasting measurement	mmol·l^{-1}
$I(t)$	Plasma insulin concentration	I_b=fasting measurement	mU·l^{-1}

TABLE II
DESCRIPTION, VALUES AND UNITS FOR FIXED MODEL PARAMETERS

Parameter	Description	Value	Units
k_e	Fractional transfer coefficient for gastric emptying	0.011	min^{-1}
k_{abs}	Rate constant of intestinal absorption	0.22	min^{-1}
f	Fraction of the intestinal absorption appearing in plasma	0.90	-
p	Ratio between non-insulin-dependent and insulin dependent glucose disappearance	2	-
k_9	Rate constant for insulin clearance	0.1	min^{-1}
V	Distribution volume	15	l
M	Modulating factor for hepatic glucose balance	0.0029	$L^2 \cdot mU^{-1} \cdot min^{-1}$

Values for k_{abs}, f, p, k_9 and V were chosen on the basis of considerations reported in [6]; value for k_e was taken from [14]; value for M was chosen as the mean of values reported in [6].

III. RESULTS

Estimates for the four free model parameters are reported in Table III. Figure 2 shows the results of parameter estimation which was performed with RMSE values equal to 2.1 e 4.8 in the HC1 and HC2 group, respectively. Model validation results in terms of ability to fit I-IGI data are shown in Figure 2, whereas assessment of incretin effect is reported in Table IV.

TABLE III
ESTIMATES FOR FREE MODEL PARAMETERS

Parameter	Value		Units
	HC1	HC2	
β	1.08 (4%)	1.78 (1%)	-
k_G	0.78 (22%)	0.28 (2%)	$mU \cdot min^{-1} \cdot mmol^{-1.3} \cdot L^{-0.3}$
k_{INC}	1.67 (18%)	1.55 (1%)	$mU \cdot mmol^{-1} \cdot L^1$
γ	0 (-)	0.10 (1%)	$mmol \cdot mU^{-1}$

Estimates for free model parameters in the HC1 and HC2 groups; β (dimensionless shape factor for gastric emptying), k_G (coefficient for post-hepatic insulin response due to glucose), k_{INC} (coefficient for post-hepatic insulin response due to incretin) and γ (corrective factor for the glucose curve). Percent coefficient of variation (CV%) is reported in brackets.

TABLE IV
INCRETIN EFFECT

Group	Model	Experimental
HC1	64.2	63.0
HC2	77.7	78.1

IV. DISCUSSION

The model proposed in this study is a simplified version of the integrated model previously proposed by Burattini et al. [6]. The novel aspect of this model is in the definition of post-hepatic insulin response due to incretin effect, which is supposed to be directly regulated by the rate of glucose appearance into the plasma ($Ra_G(t)$), thus sparing the definition of incretin hormones dynamics and the need of measuring GIP and/or GLP-1 data from the OGTT. This assumption has been made on the basis of the experimental observation that the rate of intestinal glucose exposure is a major determinant of the secretion of GIP and GLP-1 and thus, of the incretin effect [14]. The simpler structure of this model with respect to the original one, reduced the number of parameters to be estimated (four instead of seven) and provided that free model parameters can be estimated only using data from OGTT, without performing a matched I-IGI.

All the model parameters were estimated with a good precision (CV%<22, see Table III). The parameters regulating post-hepatic insulin response due to glucose (k_G) and incretin (k_{INC}) and the corrective factor for the glucose curve (γ) have been considered as free parameters as done in [6]. Of note, the corrective factor γ may be necessary only to fit glucose curves with particular shape; in fact, in this study, γ was necessary to fit only HC2 but not HC1 data (in which $\gamma=0$, see Table III). With respect to the original model parameters, the modulating factor for hepatic glucose balance (M) and the fractional transfer coefficient for gastric emptying (k_e) were set to fixed values. However, this simplification did not affect capability of the model to assess incretin effect (see Table IV); further studies should assess the effect of this model assumption in providing reliable fluxes also in the gut and in the liver.

Model assumption on post-hepatic insulin response due to incretin effect, is similar to the one used in the model by Silber et al. [4], that introduced it as a linear function of the rate of glucose appearance into the plasma. However, in the model by Silber et al. [4] the rate of glucose appearance into the plasma was described by a piecewise linear model whereas, in this study, a system model for glucose absorption was considered [15]. Moreover, with respect to models with similar characteristics [7], the proposed model is characterized by a lower number of parameters.

The incretin effect is a complex phenomenon affecting glucose metabolism and also the metabolism of other nutrients [16]. Impairment of incretin effect have been shown in T2D and the mechanism seems to be related to an impaired beta-cell sensitivity to incretin hormones [17]. Being a key phenomenon in the pathophysiology of T2D, assessment of incretin effect is recommended to monitor subjects at increased T2D risk. Many efforts have been made to provide simple but reliable methodologies that can be useful to quantify processes (e.g. insulin sensitivity, glucose effectiveness, etc.) when a metabolic test is carried out [18]-[21]. The proposed model, after being validated in a wider population, may represent a step forward in the development of a patient-oriented approach to simply evaluate the incretin effect from OGTT glucose and insulin data.
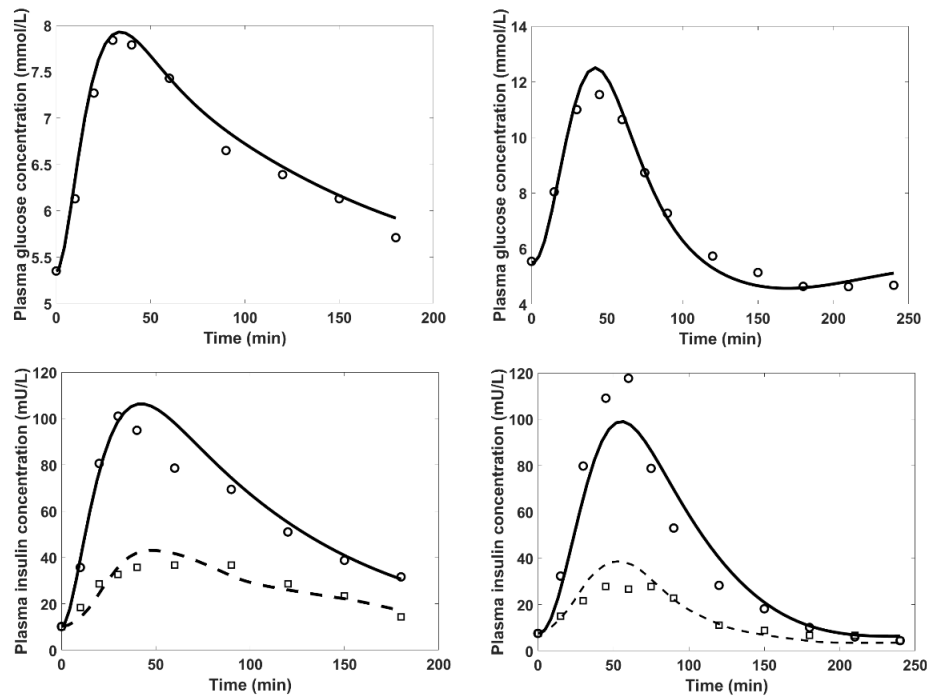
Fig. 2: Mean data of plasma glucose and insulin concentration during the OGTT (open circles) and the I-IGI (open squares) in the HC1 and HC2 group. Solid and dashed lines represent model prediction as result of the parameter estimation and model validation, respectively.

REFERENCES

[1]   M. A. Nauck, and J. J. Meier, "The incretin effect in healthy individuals and those with type 2 diabetes: physiology, pathophysiology, and response to therapeutic interventions," *Lancet Diabetes Endocrinol.,* vol. 4, pp. 525-536, Jun. 2016.

[2]   R. V. Overgaard, K. Jelic, M. Karlsson, J. E. Henriksen, and H. Madsen, "Mathematical beta cell model for insulin secretion following IVGTT and OGTT," *Ann. Biomed. Eng.,* vol. 34, pp. 1343-1354, Aug. 2006.

[3]   P. L. Brubaker, E. L. Ohayon, L. M. D'Alessandro, and K. H. Norwich, "A mathematical model of the oral glucose tolerance test illustrating the effects of the incretins," *Ann. Biomed. Eng.,* vol. 35, pp. 1286-1300, Jul. 2007.

[4]   H. E. Silber, N. Frey, and M. O. Karlsson, "An integrated glucose-insulin model to describe oral glucose tolerance test data in healthy volunteers," *J. Clin. Pharmacol.,* vol. 50, pp. 246–256, Mar. 2010.

[5]   S. Salinari, A. Bertuzzi, and G. Mingrone, "Intestinal transit of a glucose bolus and incretin kinetics: a mathematical model with application to the oral glucose tolerance test," *Am. J. Physiol. Endocrinol. Metab.,* vol. 300, pp. 955–965, Jun. 2011.

[6]   R. Burattini, and M. Morettini, "Identification of an integrated mathematical model of standard oral glucose tolerance test for characterization of insulin potentiation in health," *Comput. Methods Prog. Biomed.,* vol. 107, pp. 248–261, Aug. 2012.

[7]   A. De Gaetano, S. Panunzi S, A. Matone, A. Samson, J. Vrbikova, *et al.,* "Routine OGTT: a robust model including incretin effect for precise identification of insulin sensitivity and secretion in a single individual," *PLoS One,* vol. 8, pp. e70875, Aug. 2013.

[8]   A. Tura, E. Muscelli, A. Gastaldelli, E. Ferrannini, and A. Mari, "Altered pattern of the incretin effect as assessed by modelling in individuals with glucose tolerance ranging from normal to diabetic," *Diabetologia,* vol. 57, pp. 1199-1203, Jun. 2014.

[9]   O. Vahidi, K. E. Kwok, R. B. Gopaluni, and F. K. Knop, "A comprehensive compartmental model of blood glucose regulation for healthy and type 2 diabetic subjects," *Med. Biol. Eng. Comput.,* vol. 54, pp. 1383-1398, Sep. 2016.

[10] R. M. Røge, J. I. Bagger, O. Alskär, N. R. Kristensen, S. Klim, *et al.,* "Mathematical Modelling of Glucose-Dependent Insulinotropic Polypeptide and Glucagon-like Peptide-1 following Ingestion of Glucose," *Basic Clin. Pharmacol. Toxicol.,* vol. 121, pp. 290-297, Oct. 2017.

[11] J. J. Meier, and M. A. Nauck, "Incretin-based therapies: where will we be 50 years from now?," *Diabetologia,* vol. 58, pp. 1745-1750, Aug. 2015.

[12] E. Muscelli, A. Mari, A. Natali, B. D. Astiarraga, S. Camastra, *et al.,* "Impact of incretin hormones on β-cell function in subjects with normal or impaired glucose tolerance," *Am. J. Physiol. Endocrinol. Metab.,* vol. 291, pp. 1144–E1150, Dec. 2006.

[13] M. A. Nauck, A. El-Ouaghlidi, B. Gabrys, K. Hücking, J. J. Holst, *et al.,* "Secretion of incretin hormones (GIP and GLP-1) and incretin effect after oral glucose in first-degree relatives of patients with type 2 diabetes," *Regul. Pept.,* vol. 122, pp. 209–217, Nov. 2004.

[14] C. S. Marathe, C. K. Rayner, M. Bound, H. Checklin, S. Standfield, *et al.,* "Small intestinal glucose exposure determines the magnitude of the incretin effect in health and type 2 diabetes," *Diabetes,* vol. 63, pp. 2668-2675, Aug. 2014.

[15] C. Dalla Man, M. Camilleri, and C. Cobelli, "A system model of oral glucose absorption: validation on gold standard data," *IEEE Trans. Biomed. Eng.,* vol. 53, pp. 2472-2478, Dec. 2006.

[16] O. Lindgren, G. Pacini, A. Tura, J. J. Holst, C. F. Deacon, *et al.,* "Incretin effect after oral amino acid ingestion in humans," *J. Clin. Endocrinol. Metab.,* vol. 100, pp. 1172-1176, Mar. 2015.

[17] A. Tura A, J. I. Bagger, E. Ferrannini E, J. J. Holst, F. K. Knop, *et al.,* "Impaired beta cell sensitivity to incretins in type 2 diabetes is insufficiently compensated by higher incretin response," *Nutr. Metab. Cardiovasc. Dis.,* vol. 27, pp. 1123-1129, Dec. 2017.

[18] A. Tura, G. Chemello, J. Szendroedi, C. Göbl, K. Færch, *et al.,* "Prediction of clamp-derived insulin sensitivity from the oral glucose insulin sensitivity index," *Diabetologia,* vol. 61, pp. 1135-1141, May 2018.

[19] A. Tura, S. Sbrignadello, E. Succurro, L. Groop, G. Sesti, *et al.,* "An empirical index of insulin sensitivity from short IVGTT: validation against the minimal model and glucose clamp indices in patients with different clinical characteristics," *Diabetologia,* vol. 53, pp. 144-152, Jan. 2010.

[20] M. Morettini, F. Di Nardo, L. Burattini, S. Fioretti, C. Göbl, *et al.,* "Assessment of glucose effectiveness from short IVGTT in individuals with different degrees of glucose tolerance," *Acta Diabetol.,* vol. 55, pp. 1011-1018, Oct. 2018.

[21] M. Morettini, C. Castriota, C. Göbl, A. Kautzky-Willer, G. Pacini, *et al.,* "Glucose effectiveness from short insulin-modified IVGTT and its application to the study of women with previous gestational diabetes mellitus," *Diabetes Metab. J.,* vol. 44, pp. 286-294, Apr. 2020.

Electrocardiographic Alternans in Hemodialysis: A Case Report

I. Marcantoni[1], J. Di Monte[1], C. Leoni[1], Z. Mansour[1], A. Sbrollini[1], M. Morettini[1] and L. Burattini[1]*

[1] *Department of Information Engineering, Università Politecnica delle Marche, Ancona, Italy*

* Corresponding author: l.burattini@univpm.it

Abstract— **Hemodialysis (HD) is a clinical procedure used to treat patients suffering of chronic kidney failure. Unfortunately, HD patients are at a high risk of sudden cardiac death (SCD). To evaluate SCD risk, it is useful to analyze the electrocardiographic signal (ECG). One of the most popular indexes to investigate SCD is T-wave alternans (TWA), related to the ventricular repolarization segment of the ECG. Electrocardiographic alternans (ECGA), i.e. the prevalent nature of electrical alternans, though, represents a more complete analysis of the cardiac electrical activity, including also the possible presence of alternans on P wave (PWA) and QRS (QRSA), related to atrial depolarization and repolarization phases, respectively. Aim of this study was to obtain a complete evaluation of ECGA on a HD patient during a HD day, by means of the Heart-Rate Adaptive Match filter (HRAMF) method. HRAMF was applied for ECGA analysis on a continuous Holter ECG recording. Considering four macro-time periods PRE-HD, IN-HD, POST-HD and NT-HD (before, during, after HD and during the night, respectively), ECGA was identified as TWA and presented high values ($>15\mu V$) in PRE-HD (51 µV) and IN-HD (53 µV), highlighting how these periods are characterized by a higher SCD risk. Two hours after the end of HD, ECGA decreased due to the treatment, able to rebalance electrolytes concentrations. Statistical differences were found between PRE-HD and POST-HD, and PRE-HD and NT-HD ($p<10^{-3}$). The study suggested a higher cardiac risk (mostly affecting ventricular repolarization) in HD patients; this risk is lower after the end of HD session.**

Keywords—**Hemodialysis, Sudden cardiac death, Electrocardiographic alternans, Heart-rate adaptive match filter.**

I. INTRODUCTION

HEMODIALYSIS (HD) is a clinical procedure mainly used to treat patients suffering of chronic kidney failure: it replaces the kidneys' function, filtering the blood from toxic substances by means of an external machine. It has been observed that, in HD patients, the risk of sudden cardiac death (SCD) increases due to the higher incidence of arrhythmias and heart failure [1], [2]. Investigation of SCD risk is possible through surface electrocardiography. Electrocardiogram (ECG) is the recording of the electrical heart activity and depending on the location of electrodes, it is possible to observe the cardiac activity from different standpoints, i.e. the 12-standard leads: I, II, III (Fundamental); V1, V2, V3, V4, V5, V6 (Precordial); aVR, aVl, aVF (Unipolar).

Each cardiac beat in the ECG is characterized by three main waves: P wave, QRS complex and T wave, that represent, respectively, the atrial depolarization, the ventricular depolarization (as well as the atrial repolarization) and the ventricular repolarization. One of the most popular risk ECG indexes of SCD is T-wave alternans (TWA). TWA is an electrophysiological phenomenon occurring at stable heart rate (HR), characterized by beat-to-beat variations (ABAB pattern) in the morphology, amplitude, duration and possibly polarity of T wave. TWA was studied to evaluate cardiac risk in several pathological states, e.g. epilepsy, acute myocardial infarction and implanted cardiac defibrillator [3]–[5].

TWA was first studied on HD in 2007, in a small population: among these patients, 7 out of 9 showed TWA [6]. The following study, in 2009, reported that physical exercise failed to reduce TWA [7]. Another study showed that end stage renal disease patients present more abnormal TWA values than left ventricle hypertrophy ones (57.7% vs 26.7%) [8]. The fact that these studies neglected intra-HD session periods inspired other researchers to include them in their analyses. Indeed, in 2011, a study on continuous 72-hours ECG recordings considered three 24-hours periods for risk stratification (with the second day containing HD). Results showed increased TWA values in 27 out of 28 patients in at least one of the three experimental intervals [9]. Other findings were observed in a study over a 48-hours period, where the distribution of TWA peaks remained constant, while mean TWA increased during HD and returned to baseline two hours after HD [10]. In 2019, a case report endorsed results by [10], though detected TWA amplitude was higher [11].

Alternans of other ECG waves, such as P-wave alternans (PWA) and QRS alternans (QRSA), were less emphasized in clinical research than TWA. Actually, TWA reflects the electrical activity of ventricular heart cells. Since action potential acts on all cardiac sites, it seems appropriate to consider the possible alternans of all the ECG waves in order to detect ECG alternans (ECGA). ECGA is the prevalent nature of electrical alternans that may affect the ECG, i.e. PWA, QRSA or TWA [12]. Considering that each ECG wave represents a different electrical phase in the cardiac function, PWA and QRSA may act as indices to detect atrial fibrillation [13], supraventricular and ventricular tachycardia [14]. The few studies that concentrated on the consequences of HD on the cardiac electrical cycle did not consider PWA or QRSA but focused only on amplitude and especially duration of P wave and QRS, evaluating them with manual methods, e.g. magnifying glass and calipers, before and after HD [15], [16]. A complete overview of ECGA was not fully covered until now and only first steps in this direction were made considering simulated data [12].

Aim of this case report was to detect ECGA by means of the Heart-Rate Adaptive Match filter (HRAMF) method [17] (according to its adaptation as described in [12]) on real data acquired on a HD patient, also evaluating ECGA trend before, during and after HD in order to investigate the effect of HD on the ECGA amplitude.

II. Materials and Methods

A. Case description

A male patient (82 years old), who was diagnosed with chronic kidney failure and therefore was treated with HD procedures, was the subject of a 12-standard lead (I, II, III, V1, V2, V3, V4, V5, V6, aVR, aVL, aVF) ECG recording, continuously acquired for 24 hours in a HD day. Continuous ECG recording was obtained by means of a wearable 12-lead M12 Global Instrumentation® digital Holter ECG recorder (Manlius, NY, sampling rate: 1000 Hz). Acquisition began at 11:00 am (hour zero) of a HD treatment day and ended at 11:00 am of the next day, with HD starting at 4:00 pm and lasting 4 hours. Normal daily activities (walking, eating and sleeping) were performed during the recording by the subject, who rested lying on his back in the course of HD [11].

The study was conducted in compliance with the ethical principles of the Helsinki Declaration and approved by the institutional expert committee; the patient gave his informed consent prior to testing.

B. Heart-rate adaptive match filter to evaluate electrocardiographic alternans

All ECG acquisition leads were analyzed through the heart-rate adaptive match filter (HRAMF) method. Analysis was performed by Matlab2018b. Each ECG lead was pre-processed before being tested for ECGA identification through HRAMF method [17]. ECG leads were divided into recursively (every 1 s) extracted windows, each with a duration of 150 s so as to contain at least 128 beats. All windows were down sampled from 1000 Hz to 200 Hz. Pan-Tompkins algorithm was applied to locate R-peak positions, which were then used to identify ECG waves fiducial points (i.e. the onset, offset and maximum points of the P, QRS and T waves). A band-pass filter (0.3-35 Hz) was used to remove low and high frequency components and baseline. Ectopic or noisy beats were replaced with the median of all the beats in the window. Windows in which the number of replaced beats was not higher than 10 and the HR standard deviation was at most 10% mean HR were considered suitable for ECGA analysis [17], while ECGA detection was not performed in the windows that did not match such conditions. ECGA analysis was finally performed by the HRAMF on suitable windows. HRAMF method was introduced about 10 years ago for TWA identification. For this study, the adapted version of HRAMF to identify PWA, QRSA and TWA was used [12]. This adapted version keeps the theoretical approach of the original one. It consists in a HR adaptive narrow-band passing filter centered around a frequency value (fECGA) equal to half mean HR, i.e. the characteristic frequency of ECGA. In particular, this 6th-order bidirectional Butterworth band-pass filter, with passing band of 0.12 Hz centered in fECGA, is constructed with, first, a low-pass filter (cut-off frequency fECGA+dfECGA, dfECGA=0.06 Hz) and then a high-pass filter (cut-off frequency fECGA−dfECGA), applied in cascade [17]. One of the outputs of HRAMF is a pseudo-sinusoidal signal with maxima and minima over the alternans center of mass, when it is present (or a zero-constant signal, when it is not present) [12]. Indeed, the identification of the prevalent alternans defining ECGA depends on the location of alternans center of mass in each ECG beat. The occurrence rate (%) of ECGA center of mass on P (PWA), QRS (QRSA), and T (TWA) waves is computed for each suitable window and the most occurring kind of alternans is estimated. The most frequent kind of alternans is the ECGA for the considered window. Thus, the amplitude quantification of the defined ECGA for each beat follows. Indeed, the other output of HRAMF is a vector containing the ECGA amplitude for all the beats of the window. Then, median values for ECGA amplitudes are computed, to properly evaluate possible non-normal distributions in some analyzed windows.

C. Statistical analysis

In order to highlight the prevalent nature of ECGA, mean percentages of occurrence rate of PWA, QRSA and TWA were computed for all the time periods and all the leads. According to the percentages obtained, only the amplitude values of the prevalent alternans, i.e. ECGA, were reported.

ECGA amplitude values were computed at different time intervals during the day, thus the recording was divided into four macro-time periods: PRE-HD, from 11:00 am to 4:00 pm, preceding HD; IN-HD, from 4:00 pm to 8:00 pm, corresponding to the whole HD session; POST-HD, from 8:00 pm to 1:00 am, representing the period immediately after HD; NT-HD, from 1:00 am to 6:00 am, corresponding to the night period following HD. Based on the Kolmogorov-Smirnov test and being commonly used in statistical analysis, Lilliefors test was applied to evaluate the normality of distributions for HR and ECGA values, for each time period and each lead. Thus, 50th [25th;75th] percentiles, were chosen to represent non-normal distributions. Moreover, the percentage of number of windows accepted for ECGA analysis (NW%) was computed for all the time periods and for all leads. Additional analysis was carried out by computing median ECGA values over all leads. Wilcoxon rank-sum test was applied for statistical comparisons among ECGA distributions in the four macro-time periods. Statistical significance p was set to 0.05 in all cases. Normal reference ECGA values relied on previous studies performed on normal male subjects using the same method, even if referring only to TWA [18], [19] and ECGA values were considered high if overcoming 15 µV.

III. Results

The frequency of PWA, QRSA and TWA, in terms of percentages, can be found in Table I. For all time periods and among all leads, TWA was the prevalent alternans since it presented the highest occurrence rate (81% across all leads and macro periods) with respect to PWA (11%) and QRSA (8%).

In Table II, distributions for ECGA can be found, represented by means of median values since all distributions were not normal. All values but one, in correspondence of lead I in NT-HD, overcame 15 µV, considered as physiological threshold. ECGA presented high values in PRE-HD (62 µV, lead V5), and even more during IN-HD (66 µV, V6), and started to decrease in the subsequent time periods, POST-HD (43 µV, III) and NT-HD (38 µV, II and III). Interquartile difference showed the same decreasing behavior from PRE-HD to NT-HD.

TABLE I
ALTERNANS OCCURRENCE RATE (%)

	PRE-HD			IN-HD			POST-HD			NT-HD			Tot PERIODS		
	PWA	QRSA	TWA	PWA	QRSA	TWA	PWA	QRSA	TWA	PWA	QRSA	TWA	PWA	QRSA	TWA
I	10	7	83	19	9	72	11	8	81	11	9	80	13	8	79
II	10	7	83	13	8	79	10	6	84	8	5	87	10	7	83
III	11	6	83	12	7	81	9	5	86	7	5	88	10	6	84
V1	10	7	83	11	7	82	9	6	85	9	6	85	10	7	83
V2	11	7	82	12	10	78	10	6	84	8	6	86	10	7	83
V3	10	7	83	12	7	81	9	6	85	8	5	87	10	6	84
V4	10	7	83	12	10	78	10	8	82	11	7	82	11	8	81
V5	12	8	80	17	10	73	11	8	81	12	8	80	13	9	78
V6	11	8	81	10	8	82	20	16	64	12	9	79	13	10	77
aVR	11	7	82	13	8	79	12	8	80	10	6	84	12	7	81
aVL	10	7	83	11	8	81	11	6	83	9	6	85	10	7	83
aVF	10	6	84	9	6	85	12	7	81	9	7	84	10	7	83
Tot	10	7	83	13	8	79	11	8	81	10	7	83	11	8	81

Percentages of occurrence rate of PWA, QRSA and TWA, computed in each time period and lead.

NW% was lower or equal to 70% among all leads, with windows being rejected especially during PRE-HD and IN-HD periods. The patient's HR presented median values ranging from 59 bpm in PRE-HD and NT-HD to 66 bpm in POST-HD, as shown in Table II. Peak HR values were around 80 bpm for all time periods. Statistical differences between PRE-HD and POST-HD ($p=8.04 \cdot 10^{-4}$), and between PRE-HD and NT-HD ($p=1.93 \cdot 10^{-4}$), were present. Also, IN-HD and POST-HD ($p=3.36 \cdot 10^{-4}$), and NT-HD ($p=1.37 \cdot 10^{-4}$) showed statistical differences. There was no statistical difference instead between PRE-HD and IN-HD ($p=0.60$) and between POST-HD and NT-HD ($p=0.12$).

These results are ensured by the ECGA trends represented in Fig. 1, where rejected windows, identified by a default value equal to -1, were not plotted, but time-occurrence information were kept. A median peak was obtained during HD, while values decreased two hours after the end of HD, below 50 µV.

IV. DISCUSSION

This case report constitutes the first time that real ECGA was studied in a HD patient by means of HRAMF method, as ECGA may represent a complete view of the cardiac activity from an electrical standpoint. In fact, as previously described, ECGA is defined as the prevalent nature of alternans in the ECG, that can reveal itself as PWA, QRSA or TWA.

TABLE II
ECGA AMPLITUDE (µV)

	ECGA				NW%
	PRE-HD	IN-HD	POST-HD	NT-HD	
I	33 [27;41]	31 [27;46]	19 [15;29]	13 [10;17]	31
II	54 [35;75]	57 [46;76]	34 [25;47]	38 [27;57]	61
III	51 [32;84]	54 [41;80]	43 [29;76]	38 [28;56]	47
V1	32 [24;45]	37 [32;41]	24 [17;34]	24 [17;37]	44
V2	43 [30;57]	40 [35;44]	28 [18;45]	22 [17;31]	30
V3	57 [36;82]	52 [42;72]	40 [27;59]	37 [27;52]	59
V4	55 [31;74]	55 [41;73]	21 [16;37]	17 [13;25]	66
V5	62 [38;92]	59 [42;77]	28 [19;42]	18 [14;23]	70
V6	42 [30;63]	66 [47;112]	37 [32;47]	24 [14;40]	29
aVR	58 [40;82]	52 [33;79]	37 [28;53]	21 [15;33]	62
aVL	50 [35;66]	46 [34;70]	25 [17;35]	19 [14;28]	59
aVF	38 [29;53]	56 [45;68]	19 [14;29]	20 [14;31]	47
Tot	51 [32;70]	53 [41;73]	28 [19;44]*	22 [15;32]*	53
HR	59 [57;62]	62 [61;65]	66 [65;68]	59 [58;63]	100

HR (bpm) and ECGA distributions expressed as $50^{th}[25^{th};75^{th}]$ percentile. NW is reported in percentage. * PRE-HD vs POST-HD and NT-HD; IN-HD vs POST-HD and NT-HD: $P<10^{-3}$.

Alternans occurrence rate (Table I) for all time periods and all leads, showed that ECGA center of mass especially fell within the temporal ranges defined by onset and offset positions of the T wave. According to these results, TWA was the prevalent alternans, so ECGA was identified as TWA and ECGA amplitude distributions correspond to TWA amplitude ones (Table II and Fig. 1). Here ECGA showed increased values and variability (assessable as interquartile range) before and during HD, as well as a peak between the first and second hour of IN-HD. A double consideration can be drawn: ECGA amplitude highlighted these periods may be characterized by a higher SCD risk, ECGA expression as TWA highlighted the risk is especially linked to electrical anomalies of ventricular repolarization. ECGA decreased two hours after the end of the treatment (with variability also decreasing in POST-HD and NT-HD), stabilizing around values lower than 50 µV possibly due to the rebalancing of ionic concentrations in the blood, following HD treatment. The presence of a ECGA peak in IN-HD (Fig. 1) can find a possible explanation in the fact that, before and during HD treatment, electrolytes concentrations shifts and cardiac distress [9], [10] can lead to a high number of ectopic beats (as confirmed by the high rate of rejected windows in PRE-HD and IN-HD, Table II).

The trend here described endorsed results presented in [10], even if used identification methods are different. Compared with the results of [11], obtained from the same data,
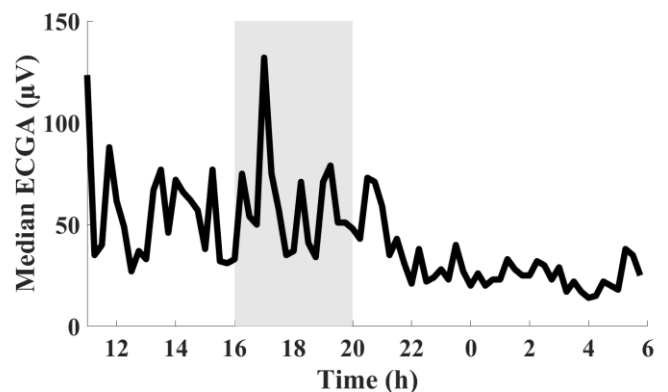

Fig. 1: ECGA trend, described through median values computed in intervals of 15 min over the whole ECG recording and all leads. Grey area corresponds to IN-HD period.

amplitude values reported in Table II were slightly lower, likely due to the computation of median values in each window instead of mean values, considered preferable and more reliable especially in case of non-normal distributions. Despite the similarities, [11] did not take into account the possibility of having PWA and QRSA as well. In fact, as showed by Table I, all four macro-time periods presented PWA and QRSA, even though in small percentages. Analogous behavior is also visible among the leads (Table I), even if lead V6 in POST-HD was characterized by a higher frequency of occurrence for PWA (20%) and QRSA (16%), while TWA reached its lowest percentage value (64%) compared with all other leads and time periods. A possible explanation for such variations in percentages could be the lead dependency of TWA [20], concept that could be extended also to PWA and QRSA. Moreover, lead dependency influences TWA amplitude [20], as shown in Table II, where each lead presented different median values compared to the others, independently of the time periods considered.

In addition, TWA amplitude computed in this study could be overestimated, since in [12] it has been noted that ECGA amplitude is always overvalued in case of multiple-wave alternans. The fluctuation of the wave considered as prevalent is inevitably affected by the fluctuation of the other waves [12]: indeed, fluid rebalancing in HD leads to changes in the QRS amplitude, and in turn brings changes in the P wave [15] and perhaps also in the T wave segment and vice versa (as mentioned before, in this case report TWA was always the prevalent alternans and therefore represented ECGA). In the future, new researches regarding ECGA may focus on the goodness of ECGA amplitude estimation occurring in situations of multiple-wave alternans.

Despite this being a study focused on a single patient (and with a single ECGA identification method), ECGA proved to be a useful index to evaluate SCD risk during HD; in fact, ECGA evaluation allows a more specific evaluation of cardiac risk, possible only after a wider observation of all the phases of the electrical heart cycle. This wider perspective has to be preferred since alternans detection of P wave and QRS complex may help in the identification of pathologies related to the atrial chambers, not included in only TWA-investigation approach. Deeper analysis about ECGA on a wider HD population and with different ECGA identification methods will be needed in the future.

V. CONCLUSION

This case report evaluated ECGA on a HD patient by means of HRAMF, revealing an identification of ECGA with TWA. Preliminary but promising results suggested a higher cardiac risk (mostly affecting ventricular repolarization) in HD patients with respect to healthy subjects; this risk becomes lower after the end of HD.

REFERENCES

[1] A. Rich, "Morbidity and mortality," *USRDS 2008 Annual Data Report*. National Institutes of Health, National Institute of Diabetes and Digestive and Renal Diseases, pp. 129–146, 2008.

[2] M. Cozzolino, M. Mangano, A. Stucchi, P. Ciceri, F. Conte, *et al.*, "Cardiovascular disease in dialysis patients," *Nephrol. Dial. Transplant.*, vol. 33, pp. iii28–iii34, Oct. 2018.

[3] I. Marcantoni, V. Cerquetti, V. Cotechini, M. Lattanzi, A. Sbrollini, *et al.*, "T-wave alternans in partial epileptic patients," in *2018 Proc. 45th Computing in Cardiology (CinC) Conf.*, pp. 1-4.

[4] L. Burattini, S. Bini, and R. Burattini, "Repolarization alternans heterogeneity in healthy subjects and acute myocardial infarction patients," *Med. Eng. Phys.*, vol. 34, pp. 305-312, Apr. 2012.

[5] L. Burattini, S. Man, and C. A. Swenne, "The power of exercise-induced T-wave alternans to predict ventricular arrhythmias in patients with implanted cardiac defibrillator," *J. Healthc. Eng.*, vol. 4, pp. 167-184, June 2013.

[6] A. N. Friedman, W. J. Groh, and M. Das, "A pilot study in hemodialysis of an electrophysiological tool to measure sudden cardiac death risk," *Clin. Nephrol.*, vol. 68, pp. 159-164, Sept. 2007.

[7] E. J. Kouidi, D. M. Grekas, and A. P. Deligiannis, "Effects of exercise training on noninvasive cardiac measures in patients undergoing longterm hemodialysis: a randomized controlled trial," *Am. J. Kidney Dis.*, vol. 54, pp. 511-521, Sept. 2009.

[8] R. K. Patel, P. B. Mark, C. Halliday, T. Steedman, H. J. Dargie, *et al.*, "Microvolt T-wave alternans in end-stage renal disease patients—associations with uremic cardiomyopathy," *Clin. J. Am. Soc. Nephrol.*, vol. 6, pp. 519-527, Mar. 2011.

[9] E. A. Secemsky, R. L. Verrier, G. Cooke, C. Ghossein, H. Subacius, *et al.*, "High prevalence of cardiac autonomic dysfunction and T-wave alternans in dialysis patients," *Heart Rhythm*, vol. 8, pp. 592-598, Apr. 2011.

[10] D. Green, V. Batchvarov, C. Wijesekara, P. A. Kalra, and A. J. Camm, "Dialysis-dependent changes in ventricular repolarization," *Pacing Clin. Electrophysiol.*, vol. 35, pp. 703-710, June 2012.

[11] C. Leoni, I. Marcantoni, A. Sbrollini, M. Morettini and L. Burattini, "TWA Identifier for cardiac risk self-monitoring during hemodialysis: a case report," in *2019 Proc. IEEE 23rd International Symposium on Consumer Technologies (ISCT) Conf.*, pp. 143-146.

[12] I. Marcantoni, D. Calabrese, G. Chiriatti, R. Melchionda, B. Pambianco, *et al.*, "Electrocardiographic alternans: a new approach, " in *2019 Proc. 15th Mediterranean Conference on Medical and Biological Engineering and Computing (MEDICON) Conf.*, pp. 159-166.

[13] E. Siniorakis, S. Arvanitakis, P. Tzevelekos, N. Giannakopoulos, and S. Limberi, "P-wave alternans predicting imminent atrial flutter," *Cardiol. J.*, vol. 24, pp. 706–707, Sept. 2017.

[14] P. Maury, and J. Metzger, "Alternans in QRS amplitude during ventricular tachycardia," *Pacing Clin. Electrophysiol.*, vol. 25, pp. 142–150, Feb. 2002.

[15] J. E. Madias, "Increases in P-wave duration and dispersion after hemodialysis are totally (or partially) due to the procedure-induced alleviation of the body fluid overload: a hypothesis with strong experimental support," *Ann. Noninvasive Electrocardiol.*, vol. 10, pp.129–133, Apr. 2005.

[16] A. Drighil, J. E. Madias, M. Yazidi, M. Bennani, A. Bennis, *et al.*, "P-wave and QRS complex measurements in patients undergoing hemodialysis," *J. Electrocardiol.*, vol. 41, pp. 60.e1-60.e7, Jan.-Feb. 2008.

[17] L. Burattini, W. Zareba, and R. Burattini, "Adaptive match filter based method for time vs. amplitude characterization of microvolt ECG T-wave alternans," *Ann. Biomed. Eng.*, vol. 36, pp. 1558-1564, Sept. 2008.

[18] L. Burattini, W. Zareba, and R. Burattini, "Assessment of physiological amplitude, duration, and magnitude of ECG T-wave alternans," *Ann. Noninvasive Electrocardiol.*, vol. 14, pp. 366-374, Oct. 2009.

[19] L. Burattini, W. Zareba, and R. Burattini, "Identification of gender-related normality regions for T-wave alternans," *Ann. Noninvasive Electrocardiol.*, vol. 15, pp.328-336, Oct. 2010.

[20] L. Burattini, S. Man, R. Burattini, and C. A. Swenne, "Comparison of standard versus orthogonal ECG leads for T-wave alternans identification," *Ann. Noninvasive Electrocardiol.*, vol. 17, pp. 130-140, Apr. 2012.

Novel recurrence features for prefall and fall detection in backward and forward fall types

A. Nasim[1], D.C. Nchekwube[1], E. Khorasani[1], N.E. Van der Maaden[1,2], M. Morettini[1] and L. Burattini[1]

[1] *Universita' Politecnica delle Marche, Ancona, Italy*
[2] *Eindhoven University of Technology, Eindhoven, Netherlands*

Abstract—**Injuries caused by different types of falls are one of the vital health threats to the elder community living independent or otherwise. Characterization and detection of a fall event can trigger an alert and minimize the damage. This work presents recurrence quantification parameters as novel features for characterization of a fall event in case of backward and forward types of falls using data acquired through wearable sensors. Computing cross recurrence plots and recurrence parameters; recurrence rate (RR), determinism (DET) and line entropy (ENT) for pre-fall, fall and post-fall phases, the level of signal stability and non-stability is quantified. The recurrence parameters show a stable behaviour in case of pre-fall (RR=0.74, DET=0.85, ENT=4.36) and chaotic behaviour in case of fall (RR=0.39 DET=0.80, ENT=3.13). To assess the discriminating capability of novel recurrence features, a support vector machine (SVM) is used to perform binary classification for prefall and fall classes. The SVM results in overall accuracy of 76% with a positive prediction of 82% for fall and 70% for pre-fall events. The results indicate that recurrence metrics are successfully able to characterize a sudden fall event and could be used in designing fall detection algorithms using wearable sensors.**

Keywords—**recurrence quantification analysis, fall detection, wearable sensor, support vector machine.**

I. INTRODUCTION

With the increase in human lifetime years over the last decades, the percentage of elderly people in the world keeps growing. The desire to stay at home and live independently can result in dangerous situations including undetected and harmful falls [1]. Falls in older adults often occur during walking and trunk position. Therefore, analysis of trunk movements during gait could present a viable approach to the development of such methods [4]. There are different ways to detect falls such as through vision or a wearable sensor [5]. Detection of fall is important and nowadays various practical solutions are presented for assisting the elderly against falls via detecting falls and triggering notification alarms calling for help as soon as falls occur in order to diminish fall consequences [2]. Novel algorithms and sensing devices can provide solutions to detect falls and generate alerts for first aid and rescue. The biggest challenge in the development of these algorithms and sensors is the flexibility to distinguish multiple kinds of falls during daily life scenarios. The common daily life activities include standing, walking on levelled ground, upstairs or downstairs, sitting down or getting up from a chair, running, jumping, lying down or getting up from the bed, and picking up object from floor, carrying load etc. [6] which could possibly lead to a fall event.

Recurrence is a fundamental property of dynamical systems, which can be exploited to characterize the system's behaviour in time-varying states. Recurrence analysis has been used successfully as a tool for describing complex dynamic systems that are inadequately characterized by standard methods for time-series data analysis [9], [8]. Cross recurrence plots (CRPs) produce readily interpretable visualizations of two input signals that provide insight into the characteristics of changing system states and also provide tools to assess repeated patterns, sequences, and regime shifts both quantitatively and qualitatively [10]. Recurrence quantification analysis (RQA) [11] has recently gained importance regarding constantly changing complex signals for the identification, quantification and assessment of synchronization patterns. This method can be used to represent signals into time-changing regular and irregular system states. Recurrence plots have been shown to be a valuable data visualization tool for the analysis of dynamic systems in a variety of scientific application areas for e.g. neuroscience [9], engineering [12], biology [13], geosciences [15], behavioural sciences [14] specifically gait analysis [3] and other research disciplines.

The currently selected database [16], [7] offers a collection of different types of falls performed by human subjects using a MARG sensor positioned at the subject's waist, placement usually considered to measure human kinematics when inertial sensors are adopted [17]. This work uses the 3-D movement signals recorded from accelerometer and gyroscope embedded in the sensing device for the analysis of fall detection. RQA was performed and CRPs are plotted using both the squared vector magnitude for acceleration calculated using x, y and z-axis data and the orientation pitch angle around the y-axis. Each time-series recorded was thresholded according to the value of 'g'to identify and analyse the pre-fall, fall and post-fall states separately. CRPs and quantification metrics; recurrence rate, determinism and entropy were computed for two simulated falls: forward and backward. The distinguishing capabilities of the calculated novel RQA metrics are then tested using a basic support vctor machine (SVM) for the binary classification of pre-fall and fall states.

The paper is organized as follows: Section-I introduces fall detection algorithms in wearable sensing and RQA. In section-II the methodology, RQA feature extraction and classification metrics are presented. In section-III the results are reported while in section-IV, a discussion on the achieved goals is presented. Section V concludes the paper.

II. MATERIALS AND METHODS

A. Data

The data [16] were collected from an experiment performed by 8 healthy participants (6 males and 2 females) with an average age 25.37 ± 2.56 years and weight 76.62 ± 10.59 Kgs. The data consist of 8 types of self-initiated falls of which 4 directed forward (falling on knees ending up lying, ending in lateral position, ending up lying, ending up lying with recovery) and 4 directed backward (falling sitting ending up lying, ending in lateral position, ending up lying, ending up lying with recovery). Every type of fall was performed 3 times by each participant while wearing a MARG (Magnetic Angular Rate and Gravity) multi-sensory device, tied to the waist. The duration of the trials was different for each fall, participant and trial. The required data consist of 14 parameters of which 5 were used in the analysis: time in 's' acceleration along the x, y and z-axis and squared vector magnitude measured in terms of gravitational acceleration in m/s^2.
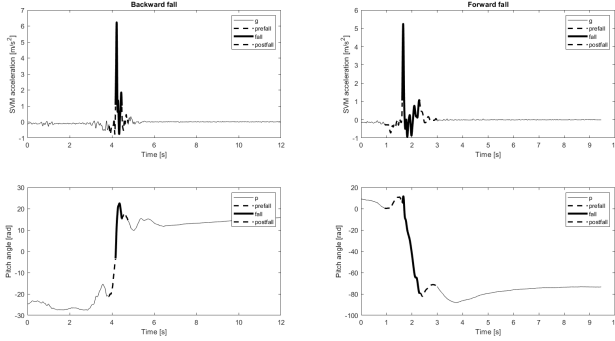
Fig. 1: Input signals, (a) squared vector magnitude of 'g' and (b) pitch angle 'p', both thresholded on $g \leq 9.8 m/s^2$ to represent pre-fall and post-fall phases and $g > 9.8 m/s^2$ to define fall phase

B. Mathematical Formulation

Squared vector magnitude of gravitational acceleration denoted by ga and the orientation pitch angle around the y-axis denoted by p are used as input signals for the computation of cross recurrence plots. For both signals the recording in number of samples is written as $ga_i(n)$ and $p_i(n)$ with $0 \leq n \leq N$ and $1 \leq i \leq 3$ where N is the total number of samples in each signal and i represents the number of equal-lengthed sections i.e. prefall, fall and postfall with respect to threshold on $ga \geq 1g$ for fall and $ga \leq 1g$ for pre-fall and post-fall (where g = 9.8 m/s^2).

Fig. 1 shows the 2 signals used as input for 8 different subcategories of backward and forward falls plotted against time. The 3 sections in which the signals are divided into are displayed: the solid line represents fall and the dotted line before and after it represent pre-fall and post-fall respectively. CRPs are then calculated for all three sections separately, so pre-fall, fall and post-fall, resulting into 3 cross recurrence matrices $r_i(n)$ using eq. 1:

$$r_i = \begin{cases} 1 & d(ga_i, p_i) \leq \rho \\ 0 & else \end{cases} \quad (1)$$

where 'd' is the distance metric, in the current case euclidean distance $d(ga_i, p_i) = euclidean(ga_i, p_i)$ and 'ρ' is the threshold used as a measure of closeness of points in the CRP and the recurrence metrics are calculated on the thresholded CRPs. In the last step of methodology, a simple SVM classifier is implemented to assess the detection accuracy for pre-fall and fall events using recurrence parameters as novel features. The test-train data split applied here is 50-50. The data was labeled with a 0 for pre-fall and a 1 for fall. After shuffling the data the classification was performed on the test data and the results are represented in terms of accuracy and positive detection rate.

C. RQA feature extraction

Recurrence features for pre-fall, fall and post-fall phases are calculated as mentioned below:

1) Recurrence Rate (RR): The recurrence rate is calculated as in eq. 2. and corresponds with the probability that a specific state will recur. High recurrence rates show a more periodic and less chaotic signal.

$$RR = \frac{1}{M} \sum_{i=1}^{M} r_i(\rho) \quad (2)$$

2) Determinism (DET): Determinism calculated as in eq. 3 and is defined as the ratio of recurrence points that form diagonal structures (of at least length l_{min}) to all recurrence points.

$$DET = \frac{\sum_{l=l_{min}}^{M} lP(l)}{\sum_{l=1}^{M} lP(l)} \quad (3)$$

3) Entropy (ENT): The entropy of the distribution of the diagonal lines lengths $p(l)$ of $r_i(\rho)$ and measured by eq. 4:

$$ENT = - \sum_{l=l_{min}}^{M} Mp(l) l_n(p(l)) \quad (4)$$

where, 'M' is the length of a single phase in the 3-phase division of $ga_i(n)$, 'i' being 1, 2 or 3.

D. Classification metrics

SVM binary classification results are reported in terms of accuracy (Acc) and positive predictivity (+P) as given in eq. 5 and 6 respectively:

$$Acc = \frac{TP + TN}{TP + TN + FP + FN} \quad (5)$$

$$+P = \frac{TP}{TP + FP} \quad (6)$$

where, TP = truely identified positives (pre-fall instances), TN = truely identified negatives (fall instances), FP = falsely identified positives and FN = falsely identified negatives.

TABLE I: RECURRENCE METRICS FOR FALL SIMULATIONS AND THRESHOLDED SECTIONS

Falltype	Recurrence Rate (RR)			Determinism (DET)			Entropy (ENT)		
	Pre-fall	Fall	Post-Fall	Pre-fall	Fall	Post-Fall	Pre-fall	Fall	Post-Fall
Forward									
Kneelying	0.937	0.335	0.071	1.000	1.000	0.166	6.056	3.920	0.561
LateralPosition	0.965	0.716	0.571	1.000	1.000	0.788	5.262	4.462	3.604
Lying	0.403	0.105	0.005	0.542	0.375	0.042	2.785	1.446	0.079
LyingRecovery	0.417	0.070	0.090	0.500	0.250	0.125	2.846	0.973	0.711
Backward									
LateralPosition	0.774	0.623	0.504	0.872	0.958	0.657	4.152	3.995	2.977
Lying	0.798	0.287	0.111	0.958	0.957	0.166	4.518	3.024	0.717
LyingRecovery	0.835	0.246	0.098	0.986	0.914	0.207	4.932	3.208	0.901
Sitting	0.818	0.725	0.542	0.958	0.958	0.625	4.301	4.018	2.750

Threshold ρ for eq. 2, 3 and 4 is set at 25.2, selected after hit and trial to maximize the detection accuracy in eq. 5 of SVM classification algorithm in the second step of methodology. Results are presented for 8 fall subcategories and 3 phases as mean over 24 records (8 subjects and 3 simulation runs). The significance of the results is tested using Lilliefor's test setting $p < 0.05$. Total records processed are 192 (8 subcategories of falls, 24 records each).

III. RESULTS

From the CRPs for pre-fall, fall and post-fall computed using 'ga' and 'p' the values of RR, DET and ENT are reported in Table I. RR for pre-fall section has an average of 0.937, 0.965, 0.403 and 0.417 respectively for fall phases of knee lying, lateral position, lying, lying recovery. This is for the case of forward fall. Likewise, for backward fall, average values are respectively 0.774, 0.798, 0.835 and 0.818. For the fall section of the signal, average values are 0.335, 0.716, 0.105 and 0.070 and 0.623, 0.287, 0.246 and 0.725 for forward and backward fall respectively. For the Post-fall section the average values are 0.071, 0.571, 0.005, 0.090 and 0.504, 0.111, 0.098, 0.542 for forward and backward fall respectively. DET rate average values for pre-fall section of forward fall activity are 0.999, 0.999, 0.542 and 0.500. For backward fall, 0.872, 0.958, 0.986 and 0.958. Average values for the fall section of forward fall activity are 0.999, 0.999, 0.375 and 0.250. While for backward fall, 0.958, 0.957, 0.914 and 0.958. For the Post-fall section the average values are 0.166, 0.788, 0.042, 0.125 and 0.657, 0.166, 0.207, 0.625 for forward and backward fall respectively. Average ENT values for the pre-fall section of forward fall activity are respectively 6.056, 5.262, 2.785 and 2.846. For backward fall, 4.152, 4.518, 4.932 and 4.301. For the fall section of forward fall activity, average values are 3.920, 4.462, 1.446 and 0.973. While for backward fall, average values are 3.995, 3.024, 3.208 and 4.018. For the Post-fall section the average values are 0.561, 3.604, 0.079, 0.711 and 2.977, 0.717, 0.901, 2.750 for forward and backward fall respectively.

Comparing 'ga' and 'p' signals in Fig. 1, the time section of activity with respect to the occurring fall action overlap. The confusion matrix of the result of the support vector machine is shown in Table II. A detection rate of 70% and 82% was achieved for pre-fall and fall respectively with overall classification accuracy of 76%.

IV. DISCUSSION

In addition to the squared vector magnitude 'ga' and 'p', other signals e.g. roll and yaw are available in the dataset. Different signal pairs were tried but 'ga' and 'p' gave the best result in case of the backward and forward fall types studied. Out of three angles available, 'p' was observed to have more dynamics for both backward and forward fall cases. Mean values of recurrence rate for the fall activities are higher for the pre-fall section than the fall section.

Table. I shows the mean values of the recurrence metrics for each fall case calculated for 24 tests - 8 subjects and 3 trials each. In our analysis and discussion we only compare the sections pre-fall and fall since the aim of the study is to detect prefall and fall. The highest recurrence is seen for the pre-fall phase and least for the fall phase showing that the signal is least disrupted while pre-fall and highly disrupted for the fall event. High probability value for determinism depicts a less chaotic subject movement and low probability value represents a more chaotic subject movement, hence representing a fall. High values of determinism are observed during the pre-fall states and low vales are reported during the fall states. High value of line entropy is reported in the case of pre-fall and low value in case of fall phase showing less signal disruption contained in the non-fall state and signal disruption during the fall state.

TABLE II: CONFUSION MATRIX FOR PRE-FALL AND FALL USING SVM

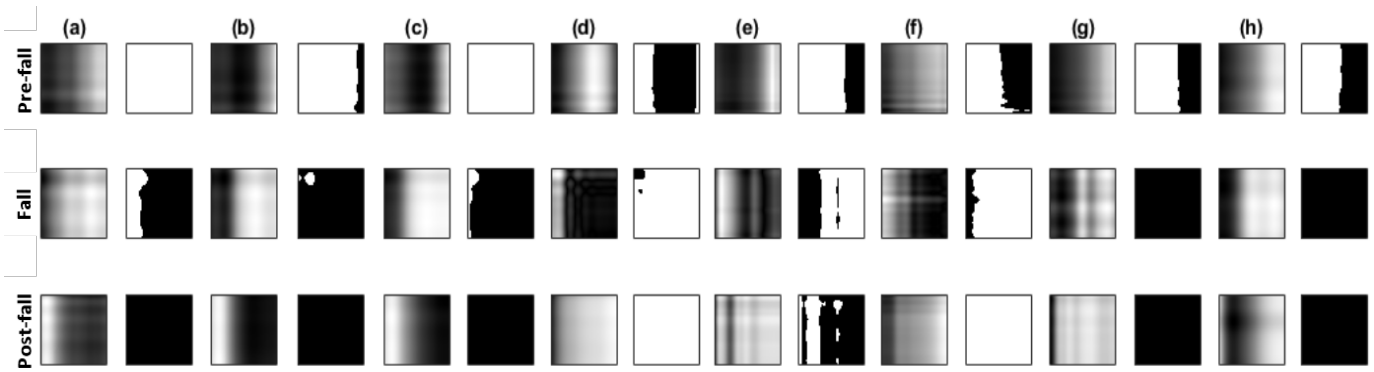| True/Predicted	Pre-fall	Fall
Pre-fall	67	29
Fall	17	79

Fig. 2: Cross recurrence plots for backward fall: (a) lateral, (b) lying, (c) lying recovery, (d) sitting, and for forward fall (e) knee lying, (f) lateral position, (g) lying, (h) lying recovery (left side: without threshold; right side: with threshold)

Fig. 2 shows CRPs for all eight kinds of falls i.e. backward fall: (a) lateral, (b) lying, (c) lying recovery, (d) sitting, and for forward fall (e) knee lying, (f) lateral position, (g) lying, (h) lying recovery for all three phases of fall. These output CRPs correspond to the inputs shown in Fig. 1. Using the reason that detecting a pre-fall and fall event is more important leading to appropriate prevention measures, the SVM is set to classify only pre-fall and fall event. In the selection of the threshold, the tested values were in the range: 0.1 to 60 and selected the optimum that produced maximum overall accuracy at SVM output. Fig. 2 also shows some similarity between different falls but it is seen distinctions are better made with the recurrence metrics as shown comparing for instance Fig. 2 (g) and Fig. 2 (h). Table. II shows confusion matrix for pre-fall and fall detection. Further studies on a larger population could improve the detection rate achieved through SVM using parameter optimization procedures. Application of more complex deep learning algorithms could improve the detection accuracy. Also since falls entail more profound changes in pitch recordings compared to roll and yaw, quantification analysis on pitch angle data alone can be studied and compared to the detection produced using CRPs of 'ga' and 'p' .

V. CONCLUSION

In this study, RQA was performed to detect falls using data acquired through wearable sensors. The results show that using novel RQA features produces good fall detection rate of 70% and 82% for pre-fall and fall respectively which results in an overall detection rate of 76%. Hence, RQA features are able to well-characterize the dynamics of a fall.

ACKNOWLEDGEMENT

REFERENCES

[1] T. Luxton, and J. Riglin, "Preventing falls in older people: a multi-agency approach," Nurs. Older. People., vol. 15, no. 2, pp. 18–21, 2003.

[2] N. El-Bendary, Q. Tan, F.C. Pivot and A, Lam, "Fall detection and prevention for the elderly: A review of trends and challenges," International Journal on Smart Sensing & Intelligent Systems, vol. 6, no. 3, pp. 842–856, 2013.

[3] F. S. Labini, A. Meli, Y. P. Ivanenko and D. Tufarelli, "Recurrence quantification analysis of gait in normal and hypovestibular subjects," Gait Posture, vol. 6, no. 3, pp. 842–856, 2013.

[4] F. Riva, M. J. P.Toebes, M. A. G. M. Pijnappels, R .Stagni and J. H. Van Dieen, "Estimating fall risk with inertial sensors using gait stability measures that do not require step detection," Gait Posture, vol. 38, no. 2, pp. 170–1741, June 2013.

[5] M. Mubashir, L. Shao, and L. Seed, "A survey on fall detection: Principles and approaches," Neurocomputing, vol. 100, pp. 144–152, Jan. 2013.

[6] P. Natthapon, S. Thiemjarus, and E. Nantajeewarawat, "Automatic fall monitoring: A review.," Sensors, vol. 14, no. 7, pp. 12900–12936, July 2014.

[7] A. Nasim, M. Morettini, I. Marcantoni, A. Sbrollini, L. Burattini, "Recurrence Analysis of Human Body Movements during Activities of Daily Living," IEEE 23rd International Symposium on Consumer Technologies (ISCT), pp. 157–160, June 2019.

[8] A. Nasim, I. Marcantoni, A. Sbrollini, M. Morettini, L. Burattini, "Recurrence Quantification Analysis for Motion Artifacts in Wearable ECG Sensors," IEEE 23rd International Symposium on Consumer Technologies (ISCT), pp. 206–209, June 2019.

[9] N. C. Anderson, W. F. Bischof, K. E Laidlaw, E. F.Risko and A. Kingstone, "Recurrence quantification analysis of eye movements," Behav. Res. Methods., vol. 45, no. 3, pp. 842–856, Sep. 2013.

[10] T. R. Brick, A. L. Gray, and A. D Staples, "Recurrence quantification for the analysis of coupled processes in aging," J. Gerontol. B. Psychol. Sci. Soc. Sci., vol. 73, no. 1, pp. 134–147, Sep. 2017.

[11] N. Marwan, M. C. Romano, M. Thiel, and J. Kurths, "Recurrence plots for the analysis of complex systems," Phys. Rep., vol. 438, no. 5-6, pp. 237–329, Jan. 2007.

[12] C. O. Ilie, O. Alexa, I. Lespezeanu, M. Marinescu, and D. Grosu, "Recurrence plot analysis to study parameters of a gasoline engine," Applied Mechanics and Materials, vol. 823, pp. 323–328, Jan. 2016.

[13] P. Melillo, R. Izzo, A. Orrico, P. Scala, M. Attanasio, M. Mirra, N. De Luca, and L. Pecchia, "Automatic prediction of cardiovascular and cerebrovascular events using heart rate variability analysis," PLoS One., vol. 10, no. 3, p. e0118504, Mar. 2015.

[14] J. Morton, T. A. Wheeler, and M. J. Kochenderfer, "Analysis of recurrent neural networks for probabilistic modeling of driver behavior," IEEE Trans. Intell. Transp. Syst., vol. 18, no. 5, pp. 1289–1298, Sep. 2016.

[15] R.V. Donner and S.M Barbosa, "Nonlinear Time Series Analysis in the Geosciences-Applications in Climatology," Geodynamics and Solar-Terrestrial Physics, vol. 112, 2008.

[16] V. Cotechini, A. Belli, L. Palma, M. Morettini, L. Burattini, and P. Pierleoni, "A dataset for the development and optimization of fall detection algorithms based on wearable sensors," Data in Brief, vol. 23, p. 103839, Apr. 2019.

[17] S. Cardarelli, A. Mengarelli, A. Tigrini, A. Strazza, F. Di Nardo, S. Fioretti and F. Verdini, "Single IMU displacement and orientation estimation of human center of mass: A magnetometer-free approach," IEEE Trans. Instrum. Meas., Dec. 2019.

Preliminary Design and Validation of an Implantable Artificial Bladder

S. Pane, V. Iacovacci, T. Mazzocchi, L. Ricotti, and A. Menciassi

The BioRobotics Institute, Scuola Superiore Sant'Anna, Pisa, Italy
Department of Excellence in Robotics & AI, Scuola Superiore Sant'Anna, Pisa, Italy

Abstract— **Substituting the functionalities of natural organs with artificial devices is an ambitious bioengineering challenge. This study proposes an artificial solution for the restoration of natural bladder functionalities (e.g. upon natural bladder removal for cancer treatment). The design of the artificial bladder system (ABS) is tailored around clinical needs. On one hand, a smart structural design enables to functionalize the internal walls with proper materials and to prevent reflux with custom unidirectional valves. On the other hand, a novel magnetic sensing strategy, combined with embedded electronics for efficient powering and wireless data transfer, allows to potentially restore bladder filling sensitivity. The performances of the system were validated preliminarily on the bench, achieving relative error in volume estimation below 12%. Finally, cadaver experiments allowed to demonstrate the implantability and the overall feasibility of the proposed solution, confirming the stability of wireless connection within a 100 cm distance from the implant.**

Keywords— **Artificial bladder, sensorized artificial organs, implantable medical devices, magnetic sensing.**

I. INTRODUCTION

Restoring lost organ functions is a great challenge in the field of medical devices and artificial organs. Replacing natural bladder functions and anatomy upon radical cystectomy or neurological disorders represents a particularly interesting case study [1]. Most of the works available in the state of the art concern the treatment of neurological disorders such as overactive bladder through sacral neurostimulator or artificial detrusor systems [2], [3]. However, this does not apply when, upon muscle invasive bladder cancer, radical cystectomy is performed and the natural anatomy has to be replaced.

Upon bladder resection, the anatomy and the ability to collect urinary fluids are restored, at present, through orthotopic bladders, i.e. through the reconstruction of the bladder sack using autologous tissues from the patient intestine [4]. Although effective, this intervention carries severe complications, including non-physiological electrolyte exchanges, reduced patient's quality of life and high rates of re-operation [5].

On the other hand, the development of artificial and bioartificial bladder counterparts would overcome such limitations. The design of the first artificial bladder system (ABS) dates back to the '60s. However, the outcomes of research efforts in this field are rather poor today, especially in terms of medium and long-term stability, due to the lack of a structure guaranteeing at the same time optimal sealing, resistance to urinary encrustations and ability to restore lost bladder functions (in terms of fluid collections and filling state sensitivity).

To overcome such barriers and to develop a novel effective fully implantable ABS, a smart design should be combined with proper materials, thus guaranteeing at the same time safe interaction with the surrounding tissues and resistance to urinary encrustations. From a functional viewpoint, if the ABS can rely on passive voiding, e.g. through an abdominal torsion to produce pressure in the bladder (i.e. the Valsalva maneuver [6]), it should integrate an active sensing apparatus to enable filling state monitoring. In this sense, a proper volume sensing strategy and a bi-directional communication protocol between the human and the implant are key factors.

In this framework, this paper aims to propose an integrated ABS design tailored around clinical needs. The ABS can change its internal volume to guarantee urine collection without producing any stretch in its internal walls.

To provide the patient with information on the implant filling status in real-time, the device includes an on-board volume monitoring system. The integration of functional components (e.g. anti-reflux check-valves and tools for surgical anchorage and connection with the natural portions of the urinary system) guarantees the implantability of the ABS.

II. SYSTEM OVERVIEW

A. Device Architecture

The proposed ABS is devised as a fully implantable system with geometry and dimensions enabling its implant in the pelvic cavity (Fig. 1a), in place of the natural bladder. The ABS holds a volume of 260 mL in the full configuration, thus guaranteeing a capacity comparable to the natural organ in adults [7].

Based on a novel design patented by the authors [8], the proposed ABS can undergo volumetric changes and collect urine without any stretching of the constitutive walls. The non-stretchability of the walls allows a functionalization with proper coatings intended to provide resistance to urinary encrustations [9]. Possible stretching of the functional coating, typically obtained by metallic materials, could induce the formation of cracks acting as the starting points for urine crystallization.

The ABS structure consists of four flexible non-stretchable walls obtained from multilayered sheets of polypropylene (PP) and acetate. PP was selected for its biocompatibility and thermoplastic properties which allow a simple fabrication, whereas acetate was interposed between PP sheets to
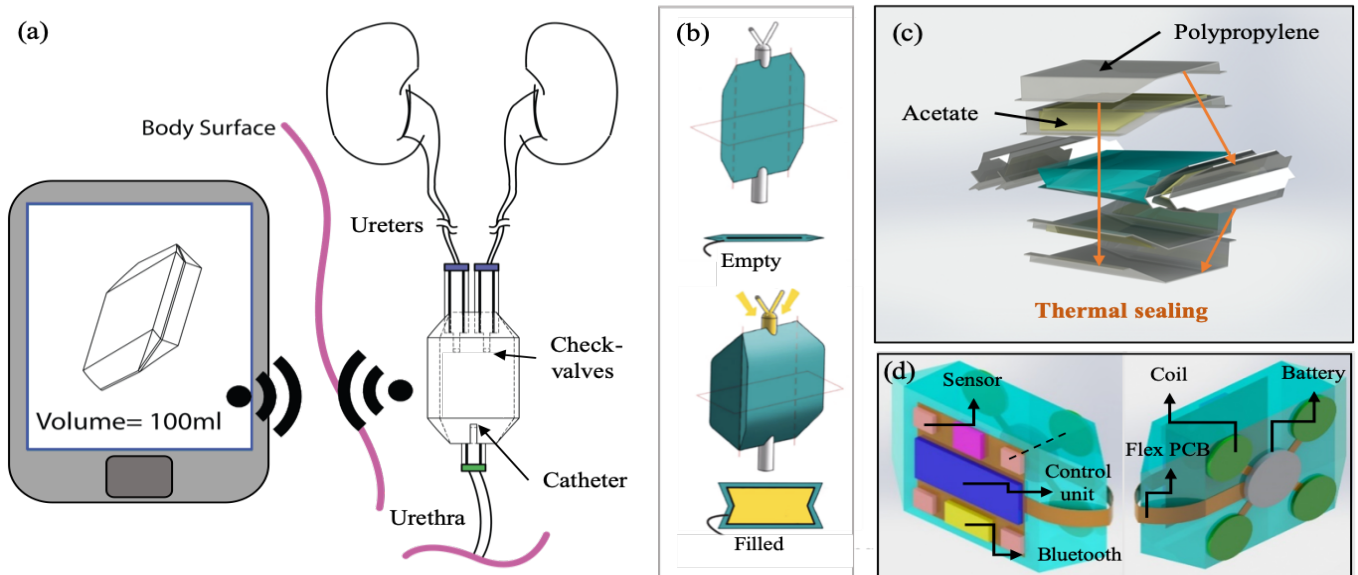
Figure 1. System Overview. (a) Schematization of the implant site and interface of the device with the user. (b) Device shape transitions due to urinary fluid collection. (c) Exploded view of the materials and fabrication steps employed to obtain the proposed ABS. (d) Representation of on-board embedded electronics

selectively add rigidity to the structure. During fabrication, the bag is pre-shaped by thermal sealing so as to obtain hinges on the lateral walls. Such components enable the structure to self-fold upon decrease in internal volume (walls approaching each other) and expand upon increase (walls moving away from each other). This behavior favors shape transitions due to urinary fluid collection (Fig. 1b-c).

The proposed ABS is equipped with internal volume estimation and data transmission electronics to counterbalance the lack of natural proprioception. In particular, real-time volume estimation is enabled by magnetic field-based distance measurements and by a dedicated volume reconstruction algorithm robust to possible ABS structural deformations.

The on-board electronics, encapsulated within the ABS walls (Fig. 1d), is powered by an implantable Lithium-Ion battery and enabled volume monitoring and data transfer (*via* Bluetooth) to the patient through an external user interface (e.g. a tablet).

The ABS includes three fluidic ports and fixing hinges to enable connection with ureters/urethra and anchoring to the pubic bone, respectively. The upper fluidic ports consist of custom unidirectional fluidic valves, with the role of inhibiting reflux from the ABS to the kidneys. Such valves consist of two soft membranes prolonged from the channels port inside the ABS internal volume. When the internal pressure arises (e.g. due to abdominal torsion through the Valsalva maneuver) the membranes approach each other thus causing valve closure.

On the other hand, the fixing hinges enable anchoring to the pubic bone by guaranteeing at the same time no free movement of the ABS within the pelvic cavity and easier performance of the Valsalva maneuver.

B. Volume Sensing System

The implemented volume sensing strategy relies on the combination of high-sensitivity digital tri-axial magneto-resistive sensors (MRS) and planar electromagnetic coils (EMC) controlled by the on-board electronics. Coils were preferred over permanent magnets for their uniform magnetic field distribution and for enabling differential field readings (field "ON" and field "OFF").

For the sake of simplicity the geometry of the proposed ABS can be approximated to a trapezoid prism, so that the volume can be reconstructed from the evaluation of the four corner edges. To this aim, four EMC and four MRS were distributed on opposite ABS walls while keeping the co-axiality between coil and sensor in each couple (Fig. 1d). An on-board microcontroller unit enables to activate each sensor-coil couple sequentially. In this way, the relative distance can be reconstructed without any interference produced by adjacent non-coaxial coils.

The relative distance between the coil and the sensor is retrieved by comparing the sensor readings with a lookup table, correlating a magnetic field value with the distance between field source (coil) and sensor. Such a table was obtained by solving a Biot-Savart model of the EMC, validated by comparison with field measurements. The distance estimation routine is executed for each coil-sensor pair sequentially, to avoid cross-talk field interferences, and finally, a volume estimation is provided. A Bluetooth Low Energy (BLE) communication protocol provides computed volume data to an external device. As a result of code profiling, we identified an average execution time of 100 ms, necessary to wake up the system (generally in power-down mode) from a remote user interface and obtain a volume estimation.

Low-power characteristics of the selected electronic components, coupled with the power down management libraries available in the Arduino programming environment, guarantee extended lifetime for the device. Power analysis revealed that the ABS has an average battery consumption of 500 mAh per year if considering 4-5 volume readings per day. This implies that a duration of 10 years can be achieved by integrating commercial batteries with 5000 mAh capacity, which dimensions are still suitable for a chronically implanted device.
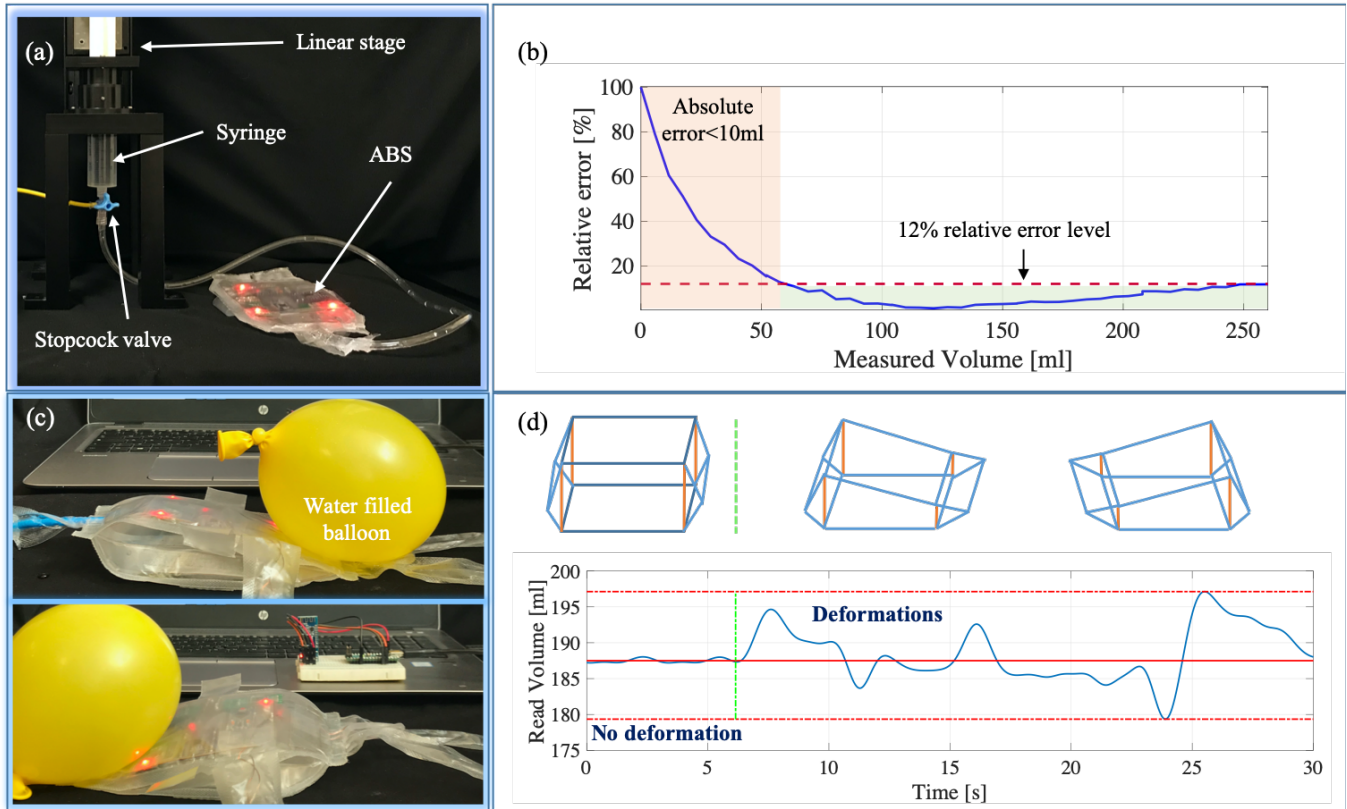
Figure 2. Bench tests. (a) Experimental setup for estimating volume measurement performances. (b) Trend of the relative error function in the measuring range (blue), 12% level threshold (red). (c) Water filled balloon used to produce deformations of the structure mimicking adjacent organs pressures. (d) Tracking of the variation in the measurements due to deformations of the structure.

III. SYSTEM VALIDATION

A. Bench tests

The ABS was tested on the bench to validate the volume monitoring system. In this regard, we assessed the trend of the relative error function over the whole measuring range (0 – 260 mL). 260 mL of water were injected by 26 successive steps of 10 mL through a syringe actuated by a linear stage, (Fig. 2a). After each injection, the estimated volume was compared with the real one to obtain the error function (Fig. 2b). Results show that for relatively low internal volumes (below 50 mL), the sensing system presents high percentages of relative error. This is an intrinsic consequence of the fabrication workflow: due to geometrical imperfections, the walls are not completely flat and the structure is never fully collapsed in the empty configuration. Nevertheless, the corresponding absolute errors in this range are tolerable (below 10 mL). For higher amounts of collected liquid (above 50 mL) the relative error function lays below a 12% threshold. The presented results are obtained as the average of 6 repeated experiments, to assess possible variability and to verify the stability of the measurements.

To demonstrate the robustness of the proposed sensing strategy to mechanical deformations of the structure, we monitored the data when applying random pressure configurations onto the ABS walls. The pressure was exerted through the weight of a water filled balloon, intended to simulate surrounding organs/tissues behavior (Fig. 2c). During deformations, the internal volume was kept constant (around 200 mL). By this test, we were able to verify that deformations of the ABS produce a variation in the volume reading that is between ±5% of the real value (Fig. 2d).

B. Cadaver test

As a further step forward in the ABS assessment, we validated the implantability and the correct operation of the sensing and communication modules *ex-vivo* on human anatomy. In particular, the surgical implant procedure and connection with residual urinary system segments (ureters and urethra) were performed on a male cadaver (78 years old, 188 cm eight, 70 kg weight - Fig. 3a). This *ex-vivo* test allowed to verify that the dimensions of the device matched the implant site (Fig. 3b) and that the surgical implant procedure was actually feasible. The surgeons (transplantation specialists) proceeded with the anchorage to the pubic bone and ultimately with the connection of ABS channels to biological channels (ureters) through urethral anastomosis (Fig. 3c). In order to enable also functional tests to be performed, a urethral catheter was placed to allow controlled filling and voiding of the ABS.

Last, we assessed the BLE communication reliability by verifying the absence of latencies or data losses in the transmitted signal. To this extent, the abdomen was surgically closed to recreate normal implant conditions. Data were collected while positioning the external interface at various distances from the implanted device. Tests verified that neither data losses nor latencies happened within a range of around 100 *cm* (Fig. 3d), thus enabling the integration of wearable or pocket-held user interfaces.
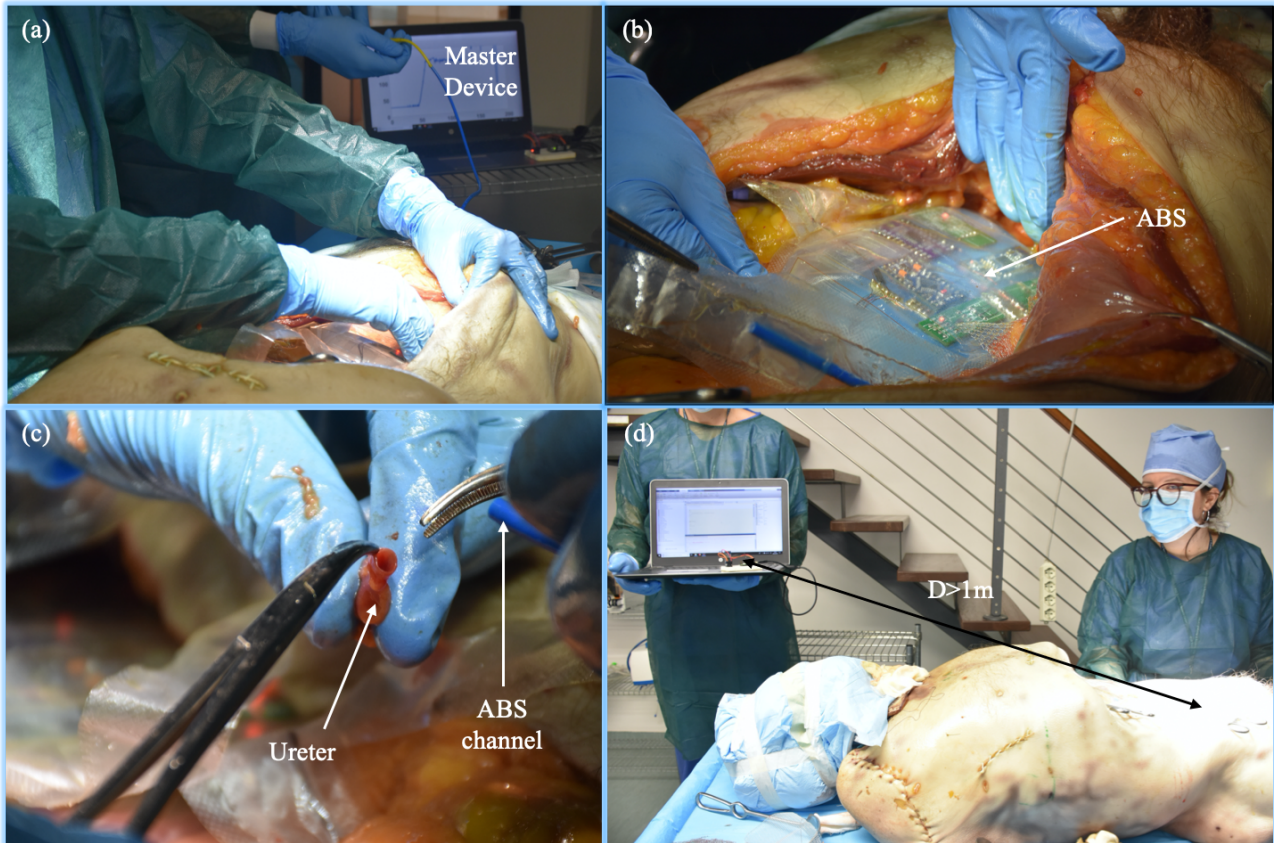
Figure 3. Cadaver test. (a) Procedure of implantation performed by transplantation surgeons. (b) Verification that ABS geometry and size fit the pelvic cavity. (c) Procedure of connection with ureters by urethral anastomosis. (d) Assessment of reliability of communication protocol within a 100cm range.

IV. CONCLUSIONS AND FUTURE PERSPECTIVES

This study proposes an artificial solution for the restoration of natural bladder functionalities (e.g. upon removal due to cancer treatment).

The proposed integrated system features an efficient structural design for enabling smart coating functionalization and reflux prevention with custom unidirectional valves. A novel magnetic sensing solution, combined with embedded electronics for efficient powering and wireless data transfer, allows to potentially restore micturition sensitivity.

Preliminary bench tests validated the performances of the device and cadaver experiments demonstrated the overall feasibility of the proposed solution.

Future research shall direct on ensuring device bio- and immune-compatibility by integrating proper biomaterials. Eventually, an artificial actuation strategy could substitute manually performed voiding actions.

REFERENCES

[1] O. El-Taji, A. Q. Khattak, and S. A. Hussain, "Bladder reconstruction: the past, present and future," *Oncol. Lett.*, vol. 10, no. 1, pp. 3–10, 2015.

[2] A. D. Mickle *et al.*, "A wireless closed-loop system for optogenetic peripheral neuromodulation," *Nature*, vol. 565, no. 7739, p. 361, 2019.

[3] X. Yang *et al.*, "Soft Artificial Bladder Detrusor," *Adv. Healthc. Mater.*, vol. 7, no. 6, p. 1701014, 2018.

[4] J. K. Nam, T. N. Kim, S. W. Park, S. D. Lee, and M. K. Chung, "The Studer orthotopic neobladder: long-term (more than 10 years) functional outcomes, urodynamic features, and complications," *Yonsei Med. J.*, vol. 54, no. 3, pp. 690–695, 2013.

[5] C. Wiesner *et al.*, "Continent cutaneous urinary diversion: long-term follow-up of more than 800 patients with ileocecal reservoirs," *World J. Urol.*, vol. 24, no. 3, pp. 315–318, 2006.

[6] M. Lavdaniti and S. Zyga, "Quality of Life in Elderly Bladder Cancer Patients Following a Cystectomy," in *GeNeDis 2016*, Springer, 2017, pp. 297–300.

[7] E. S. Lukacz *et al.*, "A healthy bladder: a consensus statement," *Int. J. Clin. Pract.*, vol. 65, no. 10, pp. 1026–1036, 2011.

[8] L. Fontana, R., Iacovacci, V., Mazzocchi, T., Menciassi, A., Pinzi, N., Ricotti, "Artificial Bladder." p. WO2017145128A1, 2017.

[9] A. Cardona, V. Iacovacci, T. Mazzocchi, A. Menciassi, and L. Ricotti, "Novel Nanostructured Coating on PDMS Substrates Featuring High Resistance to Urine," *ACS Appl. Bio Mater.*, vol. 2, no. 1, pp. 255–265, 2018.

Advanced Firmware and Hardware for Multiscale and Multimaterial Bioprinting

A. F. Bonatti[1], G. M. Fortunato[1], A. Lapomarda[1], A. De Acutis[1], C. De Maria[1], C. Vitale Brovarone[2], G. Vozzi[1]

[1]*Research Center E. Piaggio and Dpt. of Information Engineering, University of Pisa, Pisa, Italy*
[2]*Department of Applied Science and Technology, Politecnico di Torino, Turin, Italy*

Abstract—**Bioprinting allows precise deposition of multiple materials at different scale lengths, to fabricate complex scaffolds which mimic the natural tissue cues. A novel trend in the design of 3D Bioprinters is the integration of multiple fabrication techniques into the same machine, to speed-up the scaffold fabrication process and increase the scaffold functionalities. Even if multi-technique bioprinters have reached the market, their implementation is far from being optimized. In this work we present a novel printing platform with high accuracy that implements two of the most commonly used Bioprinting strategies, namely piston-actuated extrusion and thermal drop-on-demand inkjet. Here we firstly present a method to find the optimal printing parameters, and then proof-of-concept printed shapes to validate the developed platform.**

Keywords—**3D Bioprinting, Multimaterial, Multiscale.**

I. INTRODUCTION

The term Bioprinting refers to 'the use of computer-aided transfer processes for patterning and assembly of living and non-living materials with a prescribed 2D or 3D organization to produce bio-engineered structures serving in regenerative medicine, pharmacokinetics, and basic cell biology studies' [1], [2].

Compared to conventional scaffold fabrication technologies (e.g. particulate leaching, freeze-drying), Bioprinting offers several advantages, including the ability to create highly complex porous scaffolds and anatomically correct patient-tailored shapes. Moreover, Bioprinting technologies allow printing multiple biomaterials, cells and biomolecules together in precise spatial locations with high resolution, accuracy and repeatability. These properties can be exploited to fabricate complex 3D constructs containing gradients of biomaterials, cells and biomolecules [3]–[5].

The combination of multiple techniques, materials and cell types is a novel trend in Bioprinting, and promises to fabricate constructs which can mimic the geometry, complexity and functions of human tissues [6].

Currently, this research field is experiencing a rapid transformation from basic research to emerging industry [7]. The market growth is expected to be driven by new printing technologies, as well as the expansion of new applications beyond the medical field [8]. However, although the technology has reached commercialization, the integration of multiple printing techniques is far from being reliable, as highlighted by several researches on multimaterial scaffolds which employ consecutive use of different bioprinters with different technologies [1].

In this context, we present a newly designed bioprinting platform, which integrates thermal drop-on-demand inkjet and extrusion techniques in the same machine. We have introduced, for the first time, LinuxCNC, an open-source software system for numerical control of machines such as lathes, cutters, etc, at the core of a Bioprinter. This work will show the potential of this innovative printing platform by firstly defining the optimal printing parameters for the two technologies, and then printing a series of illustrative shapes, creating ink-based three-dimensional objects into a polymeric gel support.

II. MATERIALS AND METHODS

A. Hardware design

The printing module is attached to the z-stage of a cartesian three axis micro-positioner. The axes are controlled by linear stepper actuators that regulate positioning of the end-effector up to 10 µm accuracy. For each axis, magnetic encoders are used to implement a closed-loop position control, ensuring a final accuracy below 5 microns.
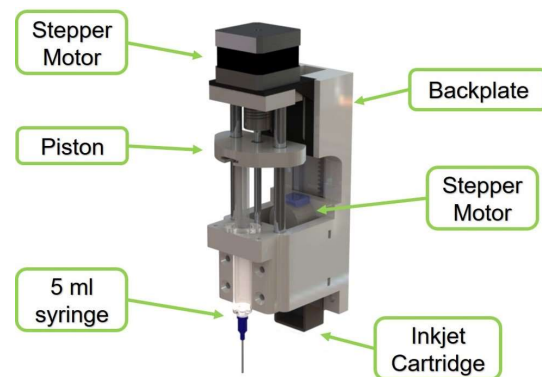

Fig. 1: Rendering of the final printing module, with the different components highlighted.

The printing module includes: a syringe for gel extrusion, and a cartridge for inkjet printing (Fig. 1). The former consists of a 5ml syringe pump, in which the rotation of the driving motor shaft is converted to linear movement of the stage through a lead-screw mechanism. The inkjet part consists of a cartridge support for the HP C6602 thermal cartridge. This specific cartridge has 12 nozzles with a diameter of 80 µm. The nozzles are aligned and spaced of 260 µm, effectively turning the system into a native 96 DPI ink printer. However, the printer resolution can be further increased thanks to high position accuracy of the micro-positioner (below the nozzle spacing).

The cartridge can be moved in the printing position thanks to a stepper motor to eliminate alignment problems with the extrusion module, and to reduce the bulk volume of the printing tool, for easily printing in multiwell plates or petri dishes.

Specifically, when the inkjet printing module is activated, the cartridge is moved above the target surface, while the syringe extruder is in a safe upper position. On the opposite, when the extrusion module is active, the tip of the nozzle is positioned at a distance specified by the layer height (a parameter which indicates the thickness of the layers being printed), while the cartridge is moved upwards.

B. Software and Firmware

The real-time control and the interpolation of axes movements with the printing tools are achieved thanks to the real-time operating system LinuxCNC, interfaced with MESA breakout boards to motor drivers. LinuxCNC is based upon a Hardware Abstraction Layer (HAL), which masks what is behind the machine hardware from the software point of view. Each hardware component is described as a black-box element; as a result, the program does not care about how it works *internally*, but consider only its inputs and outputs [9]. In this work, the modularity of HAL and LinuxCNC was exploited by adding "black boxes" of the above described printing modules to the ones of the motorized axis, and by synchronizing their movement within the printing task, through a proper definition of the g-code.

The g-code generation process is performed through a custom Graphical User Interface (GUI) programmed in Python. The GUI purpose is to guide the user in creating the g-code for printing complex three-dimensional ink structures inside extruded support ones.

Briefly, the user needs to first define a .stl file for the 3D ink shape and one for the gel support. Inside the GUI, the slicing program Slic3r can be directly called to obtain the final extrusion g-code with user specified printing parameters.
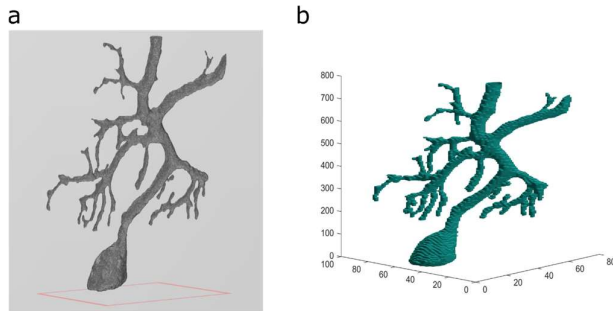
Fig. 2: Mesh slicing example, (a) the mesh for a neuron structure, and (b) the final result visualized as a stack of binary images.

Regarding the ink shape, a custom slicing program 'cuts' the ink .stl at given heights, outputting binary images corresponding to the contours of the sliced mesh (Fig. 2). The images are then converted to g-code through a custom defined program, and the corresponding files are merged with the g-code for the extruded support based on user inputs.

Optimization of the printing parameters for both the extrusion and inkjet technologies are reported in the Printing Experiments section.

C. Materials Formulation

Two different concentration of Pluronic F127 (Sigma-Aldrich, Italy) were prepared, namely 20% wt and 38% wt. The protocol for the material preparation is reported in [10]. Briefly, after heating ultrapure water at 90°C on a magnetic stirrer, the Pluronic F127 powder was added while mixing the solution at low speed. The solution was then manually stirred with a spatula until uniform dissolution of the Pluronic powder. Finally, the solution was left to rest overnight at 4°C and stirred again before printing.

For the inkjet printing, a commercial aqueous solution black ink from HP was used as purchased, without any modifications. All the printing experiments were conducted at room temperature and on microscope glass slides.

III. PRINTING EXPERIMENTS

A. Extrusion optimal parameters

During all extrusion printing tests a conical needle with an internal final diameter equal to $D = 0.41 \, mm$ was used. Preliminary tests with Pluronic hydrogels were conducted to evaluate the correct extrusion parameters.

The effect on the printed line diameter of the following four main variables was evaluated: the speed of the tool-head v, the extrusion multiplier EM, the ratio between the layer height and diameter of the syringe needle LH/D, and the Pluronic concentration C. The EM parameter is a slicing parameters which allows to finely control the flow rate of material during printing, for reducing the effect of die-swell immediately after the extrusion that depends on the viscoelastic behavior of each specific material: $EM > 1$ means that more material will be extruded than the standard setting, while $EM < 1$ represents the opposite case.

The tested values for the four parameters are reported in Table I.

TABLE I
MAIN PARAMETER FOR EXTRUSION PRINTING

Parameter Name	Values
v	1 mm/s; 1.7 mm/s; 2.4 mm/s; 3 mm/s
EM	1; 1.3; 1.5
LH/D	60%; 70%; 80%
C	20%; 38%

Simple lines were printed on a microscope glass slide, each representing a different combination of the parameters in Table I. For each combination five lines were printed (for a total of 360 lines), to extract statistical information during the analysis phase.

A photograph was taken for each printed line using an optical microscope, and the line diameter was computed by using a semi-automatic segmentation procedure in Matlab. Briefly, the images were binarized through the Otsu thresholding method by using an automatic global threshold. The binarized images were then manually cropped in order to select a Region Of Interest (ROI), and the cropped ROI were analyzed by computing its Bounding Box (Fig. 3). The width of the BB was then converted to millimeters by multiplying it with the px/mm ratio for the given set-up.
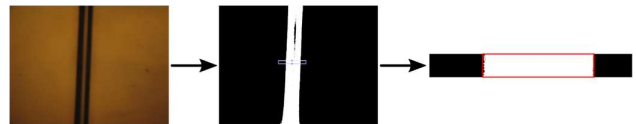

Fig. 3: Steps to the segmentation process: loading the image and binarization, manually choosing a ROI, and computing the strand diameter from the Bounding Box width.
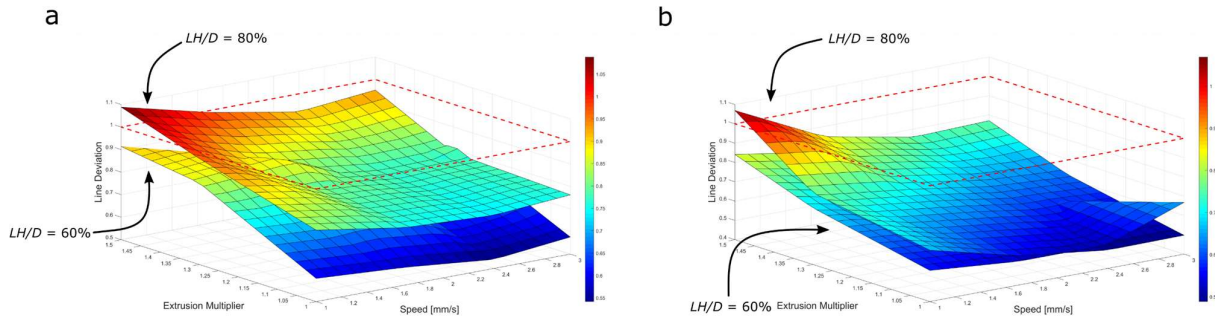
Fig. 4: 3D plot distribution of the Line Deviation parameter by varying the four parameters in Table I. The dashed red line indicates the plane for LD = 1, which is considered as the 'ideal' value for optimal line fidelity. In (a) the plot for 20% wt Pluronic concentration; and in (b) the one for 38% wt.

To evaluate line fidelity (i.e. how much the printed line deviates from its theorical diameter), the Line Deviation (LD) parameter was computed through Eq. (1):

$$LD = \frac{D_p}{D_t} \qquad (1)$$

where D_p is the printed line diameter found through image segmentation, and D_t is the theorical diameter computed by the slicing program during the g-code generation process. Ideally, the best combination of parameters should yield lines with a fidelity as close to unity as possible. The case of $LD > 1$ highlights thicker lines, while $LD < 1$ thinner ones.

B. Inkjet optimal height

A series of inkjet printing tests were conducted to evaluate the influence of the cartridge distance (indicated as "height") respect to the printing surface on the final droplet shape. A simple pattern of a square of 12x12 single ink dots was printed by using different heights: starting from 2 mm over the surface and increasing up to 6 mm with steps of 1 mm each (for a total of 5 tested heights). The printing speed was kept constant at 3 mm/s during these experiments.

Photos of the printed pattern were taken using an optical microscope and quantitatively analyzed in terms of their roundness to determine the optimal printing height.

Briefly, the images were segmented in Matlab by firstly using morphological operations on the grayscale data (i.e. opening-by-reconstruction and closing-by-reconstruction). These preliminary operations were important to better separate the foreground (the printed droplets) from the background. Then, the images were binarized using a global Otsu threshold, the droplets at the image edges were deleted, and morphological erosion was performed to better separate the connected components. Finally, small droplets were deleted by area filtering, to ensure that the analysis regarded only the main droplets and not the smaller satellite ones.

IV. RESULTS

A. Evaluation of the optimal extrusion parameters

The line deviation parameter distribution was plotted in a 3D graph for better result visualization of the results and can be seen in Fig. 4. The plots highlight that a combination of higher LH/D ratios and EM at lower speeds yields the better line fidelity (i.e. $LD \approx 1$).

Data also indicate that at higher Pluronic concentration, the same speeds and LH/D ratios require a higher EM value (i.e. more material outflow) to reach optimal line fidelity.

B. Evaluation of the optimal inkjet height

Using the previously described segmentation process, for each segmented droplet the circularity was evaluated as:

$$C = \frac{4\pi A}{P} \qquad (2)$$

where A is the area of the droplet (i.e. total number of white pixels) and P its perimeter (i.e. number of contour pixels). In general, $C \leq 1$, where $C = 1$ means a perfectly circular droplet. Circularity data were acquired for each printing height and can be seen in Fig. 5, alongside the results of the segmentation.
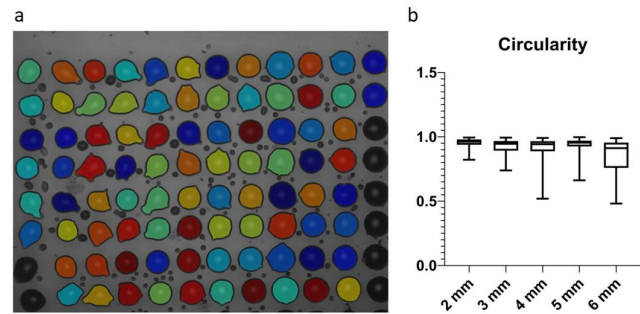
Fig. 5: (a) results from the droplet segmentation for a height of 2 mm, visualized as a coloured layer over the grayscale of the original image. (b) Box-and-whiskers plot of the droplets printed at different heights.

A non-parametric Kruskal-Wallis statistic test was performed to infer if there was any statistically significant difference between the median of the 5 groups. The null hypothesis (i.e. the medians of the groups are all the same) was rejected with a $\alpha = 0.05$, and multiple comparison tests confirmed that lower heights give better circularity and better deposition.

C. Example shapes printing

Starting from the results of the previous section, a series of test shapes were printed to explore the potentialities of the bioprinter in creating complex 3D patterns of low-viscous ink, including extreme overhangs and non-continuous shapes.

The support gel shape was obtained by defining the CAD model for a parallelepiped in Solidworks® and then slicing it to obtain the final g-code. In a similar manner, the ink 3D shape was generated by slicing a .stl file, as previously described in the Software and Firmware section.

The printing strategy consisted in extruding a support layer and, immediately after, inkjet printing a specific pattern. The

process was then repeated for all layers of the support structure.

TABLE II
PRINTING PARAMETERS FOR THE PROOF-OF-CONCEPT SHAPES

Parameter Name	Value
LH/D	70%
EM	1.3
v	3 mm/s
Infill Pattern	Rectilinear
Infill Density	90%
Infill Angle	90°

Pluronic at 38% wt was used as support gel, while water-based ink with black colour was used for patterning. Table II highlights the main extrusion parameters used during the proof-of-concept prints. Regarding the inkjet cartridge height, an intermediate value of 4 mm was chosen to avoid any collisions with the printed structure during the process. Fig. 6 and Fig. 7 show the results for an inclined plane and 'dog' bone shape.
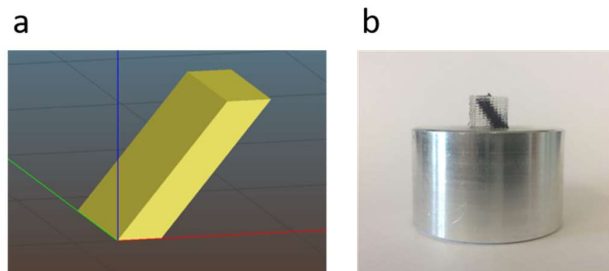
Fig. 6: Example of the inclined plan model: (a) visualization of the mesh file (as seen in the Slic3r preview), and (b) the printed structure.
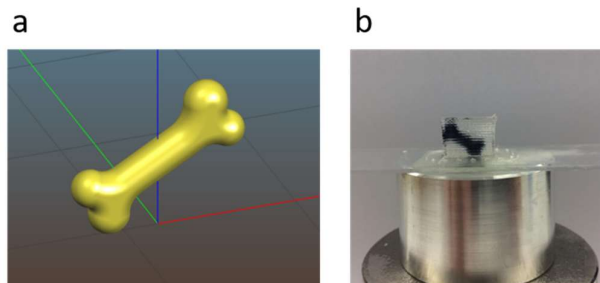
Fig. 7: Example of the dog bone model: (a) the mesh file (as seen in the Slic3r preview), and (b) the printed structure.

V. CONCLUSION

We presented the innovative hardware-software bioprinting platform based on open source tools, that grants micrometric accuracy and integrates two of the main technologies currently available. The simultaneous use of multiple technique on the same 3D bioprinter can improve the scaffolds properties (e.g. local functionalization with inkjet-printed growth factors), and will allow the fabrication of complex multimaterial and multiscale structures, e.g. by jetting a gelling agent (e.g. $CaCl_2$) or directly living cells.

REFERENCES

[1] L. Moroni, T. Boland, J. A. Burdick, C. De Maria, B. Derby, G. Forgacs, *et al.*, "Biofabrication: A Guide to Technology and Terminology," *Trends Biotechnol.*, vol. 36, no. 4, pp. 384–402, 2018.

[2] J. Groll, T. Boland, T. Blunk, J. A. Burdick, D.-W. Cho, P. D. Dalton, *et al.*, "Biofabrication: reappraising the definition of an evolving field.," *Biofabrication*, vol. 8, no. 1, p. 013001, 2016.

[3] R. Pantani and L. S. Turng, "Manufacturing of advanced biodegradable polymeric components," *J. Appl. Polym. Sci.*, vol. 132, no. 48, 2015.

[4] Y. J. Seol, H. W. Kang, S. J. Lee, A. Atala, and J. J. Yoo, "Bioprinting technology and its applications," *Eur. J. Cardio-thoracic Surg.*, vol. 46, no. 3, pp. 342–348, 2014.

[5] X. Zhang and Y. Zhang, "Tissue Engineering Applications of Three-Dimensional Bioprinting," *Cell Biochem. Biophys.*, vol. 72, no. 3, pp. 777–782, 2015.

[6] C. De Maria, G. Vozzi, and L. Moroni, "Multimaterial, heterogeneous, and multicellular three-dimensional bioprinting," *MRS Bull.*, pp. 578–584, 2017.

[7] A. Arslan-Yildiz, R. El Assal, P. Chen, S. Guven, F. Inci, and U. Demirci, "Towards artificial tissue models: Past, present, and future of 3D bioprinting," *Biofabrication*, vol. 8, no. 1, p. 0, 2016.

[8] D. Choudhury, S. Anand, and M. W. Naing, "The Arrival of Commercial Bioprinters - Towards 3D Bioprinting Revolution!," *Int. J. Bioprinting*, vol. 4, no. 2, pp. 1–20, 2018.

[9] T. Staroveški, T. Udiljak, and D. Brezak, "LinuxCNC - The enhanced machine controller: Application and an overview," *Teh. Vjesn.*, vol. 20, no. 6, pp. 1103–1110, 2013.

[10] I. R. Schmolka, "Artificial skin I. Preparation and properties of pluronic F127 gels for treatment of burns," *J. Biomed. Mater. Res.*, vol. 6, no. 6, pp. 571–582, 1972.

Boosting automated palynology via microfluidics and machine learning

M. D'Orazio[1,#], R. Reale[2,#], A. De Ninno[2,3], M. A. Brighetti[4], A. Mencattini[1], L. Businaro[3],
E. Martinelli[1], P. Bisegna[2], A. Travaglini[4] and F. Caselli[2,*]

[1] *Department of Electronic Engineering, University of Rome Tor Vergata*
[2] *Department of Civil Engineering and Computer Science, University of Rome Tor Vergata*
[3] *Institute for Photonics and Nanotechnology, Italian National Research Council*
[4] *Department of Biology, University of Rome Tor Vergata*
[#] *Equal contribution;* [*] *E-mail: caselli@ing.uniroma2.it*

Abstract—In allergology and environmental monitoring, there is a pressing need for fast and simple approaches for the analysis of pollen grains. In this work, we propose the use of microfluidic impedance cytometry, a label-free electrical characterization technique, in combination with machine learning-based image processing. Preliminary results show that this *electro-optical cytometry* provides high-content information useful for characterization of grain conditions and taxa classification.

Keywords—Microfluidic impedance cytometry, Machine learning, Automated palynology, Allergy studies.

I. INTRODUCTION

Palynology is an interdisciplinary science at the intersection of geology and biology. In particular, the analysis of pollen grains has a number of notable applications such as allergy studies, environmental monitoring and maximization of breeding efficiency. The recent WHO meeting indicated aerobiological monitoring as an important tool to improve the quality of life in an urban environment, a goal defined among the urgency measures described in the Legislative Decree n. 111 of 14 October 2019. Whereas traditional techniques for pollen analysis are laborious and time consuming, automated systems have the potential to improve the speed, quality and size of pollen studies with reduced costs [1]. In the last two decades, several optical approaches for the automatic analysis of pollen grains have been proposed [2], [3], [4], [5]. Moreover, the use of microfluidic impedance spectroscopy has recently been pioneered by Di Berardino et al. [6]. Notwithstanding the recent progress in automated palynology, the ideal system providing simplicity, portability as well as accuracy and consistency has yet to be developed [1].

Here we propose a microfluidic approach for single-particle, high-throughput analysis of pollen grains based on electrical characterization and simultaneous optical imaging inside a microfluidic impedance cytometer (Figure 1). The electrical characterization exploits a peculiar measurement setup and a multi-frequency approach that enable an accurate estimation of particle size and dielectric properties [7], [8] (cf. Section II-B). The electrical traces are also exploited to identify the image frames that contain a pollen grain, thus greatly reducing the burden of image processing. Image analysis of pollen grains

is based on a deep convolutional neural network followed by a support vector machine classifier (cf. Section II-C). Preliminary results reported in Section III show that, due to the richness of obtained information, this multimodal approach is uniquely posed for pollen analysis.

II. METHODS

A. Sample collection and preparation

Dry pollen grains of seven different taxa (Cupressus, Fagus, Fraxinus, Juglans, Ligustrum, Ostrya, Platanus) were collected by the Aerobiological Monitoring Center of the University of Rome Tor Vergata. Pollen grains were suspended in a saline buffer augmented with 150 mg/ml sucrose, to reduce grain sedimentation, and spiked with 10 μm diameter polystyrene beads (Sigma-Aldrich), as internal reference for the impedance measurements. Final sample concentrations were approximately 10^5 grains/ml for each taxon, and 10^4 grains/ml for the beads. Before the experiments, samples were filtered with 50 μm filters (Cell Tricks) to prevent the risk of channel clogging. Samples were injected into the microfluidic chip by a syringe pump (Harvard Apparatus) at a rate of 90 μl/min.

B. Microfluidic impedance cytometry

The microfluidic impedance chip was fabricated with standard microfabrication techniques, as reported previously [7], [9]. Briefly, the chip consists of a glass microscope slide with integrated gold microelectrodes, bonded to a PDMS-embedded microchannel. As shown in Figure 1, the sensing region comprises two pairs of coplanar electrodes housed in lateral channels. The main channel is 120 μm wide and 60 μm high. Lateral channels are 90 μm wide with a 90 μm spacing. An original wiring scheme with stimulation on diagonally opposite electrodes is used (cf. caption of Figure 1). Stimulations frequencies are 0.5 MHz and 10 MHz. Event detection in the impedance data stream is performed with the algorithm described in Ref. [10], whereas for feature extraction the template fitting strategy introduced in [11] is used, providing electric diameters D and phases Φ at each frequency.
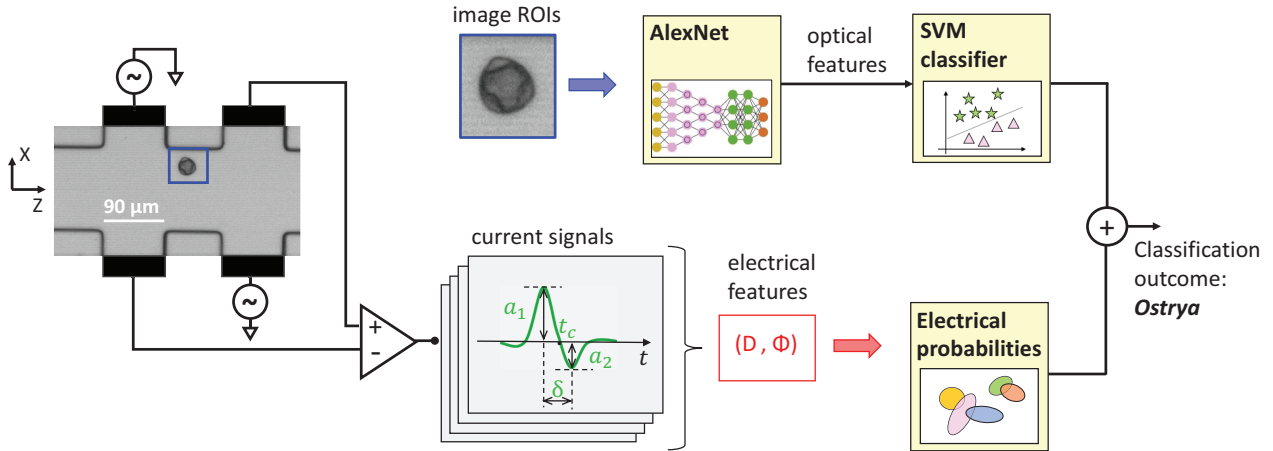
Fig. 1: Principle of multimodal analysis of pollen grains. A simple microfluidic impedance chip with four coplanar electrodes is used. Multifrequency AC voltage is applied to diagonally opposite electrodes and the differential current flowing through the other electrodes is collected. Upon the passage of a pollen grain, after demodulation, each frequency channel yields two asymmetric bipolar Gaussian impedance traces (in-phase and out-of-phase components). The features of the latter traces are used to obtain electrical parameters (i.e., electric diameter D at 0.5 MHz and electric phase Φ at 10 MHz) useful for taxa discrimination. The impedance traces are synchronized with the optical image acquisition and therefore allow to identify the image frames containing the pollen grain. By means of automatic image segmentation, a region of interest (ROI) containing the pollen grain is extracted and fed to a deep convolutional neural network (AlexNET) providing a large number of optical features. The latter are fed to a support vector machine classifier (SVM).

C. Image acquisition and processing

The sample flow through the detection area is acquired using a high-speed camera (Photron Mini UX100, frame rate 4000 fps, shutter time 3.9 μs) connected to an inverted microscope (Zeiss Axio Observer, 10x objective). Events detected in the impedance data stream are matched to their optical frames with a custom Matlab script.

Image processing is performed as follows. First, a background subtraction is applied in order to eliminate all the confounding structures of the microfluidic device that may alter the pollen analysis. Then, frames containing at least a pollen grain are analyzed by an object identification algorithm based on the Circular Hough Transform (CHT) [12], a method specifically developed to automatically detect circular object in a grayscale image. In this way, the approach allows retrieving more than one pollen grain in the same environment (as in case of coincidences). After the detection, a Region Of Interest (ROI) is automatically extracted around each grain for a further local processing. The ROIs collected are used as input to a pretrained Deep Learning CNN network, Alexnet [13], with the aim to implement transfer learning. More in details, each ROI is coded by the network into a set of numerical descriptors that the network considered relevant for its representation according to its elsewhere performed learning procedure. The descriptors are fed into a multiclass Support Vector Machine classifier [14] with linear kernel with the aim to recognize the taxonomy group of each pollen grain. To obtain a unique response for the same sequence of frames the final classes assigned by the SVM model are then combined using different logics of consensus, i.e., the maximum score class, the most voted class.

III. RESULTS

A. Electrical characterization of hydration status

As shown in Figure 2, electrical characterization alone is suited for hydration/viability studies. In particular, three different sub-populations of Cupressus sempervirens L. are clearly distinguished in the density plot of the electric diameter D at 0.5 MHz against the phase Φ at 10 MHz. As confirmed by visual inspection of corresponding optical images, those sub-populations respectively correspond to hydrated pollen grains, grains with ruptured exine, and split-off exine shells (panel (a)). We monitored the relative amount of each sub-population during a timeframe of 24 hours. As expected, during the time course of pollen hydration, the number of intact grains is progressively reduced, in favour of an increased number of ruptured grains and exine shells (Fig. 2(b)).

B. Image-based taxa classification

As a preliminary investigation, the image-based classifier was tested on a mixture of seven taxa (Cupressus, Fagus, Fraxinus, Juglans, Ligustrum, Ostrya, Platanus). A unique label was assigned to the different sub-populations of Cupressus. We used a cross-validation strategy by repeated subsampling the 80% of the features extracted on the labelled dataset for training and the 20% for testing. The procedure has been repeated for 1000 times. Classification results have been evaluated by the accuracy of classification for each taxonomy group. The resulting confusion matrix is shown in Figure 3. The average accuracy obtained is 87%. In some cases, misclassification could be attributed to coincidences, i.e., two grains passing simultaneously in the sensing zone. As shown recently by our
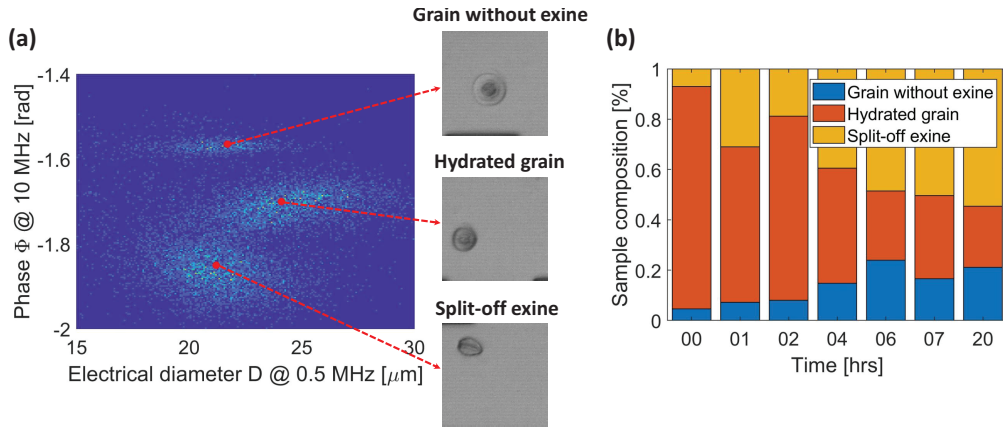
Fig. 2: Impedance spectroscopy of Cupressus sempervirens L. (a) Density plot of the electric diameter D at 0.5 MHz against the phase Φ at 10 MHz. Three clusters are identified, corresponding to hydrated grains, grains without exine (having dilated intine), and exine shells. (b) Time course of sample composition. It is evident the the number of intact grains decreses with time, in favour of an increased number of grains without exine and exine shells.
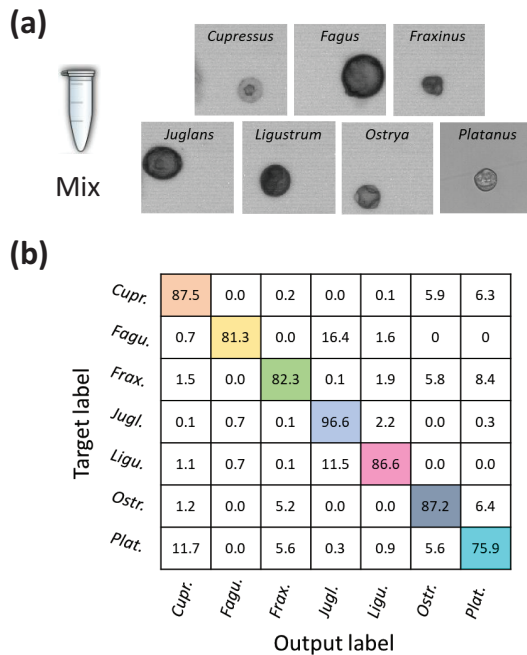

Fig. 3: (a) Representative microscopy images of pollen grains from the seven different taxa. (b) Confusion matrix of taxa classification.

group, coincidences can be identified and resolved by suited processing of the electrical data streams [15].

IV. CONCLUSIONS

We have proposed a multimodal approach for high-throughput automated palynology based on microfluidic impedance cytometry and simultaneous optical imaging. Impedance traces and optical images both provide high-content information useful for pollen characterization and taxa classification. Future work will deal with the development of a classifier that exploits both electrical and optical features at the same time. In particular, several approaches will be compared, such as [16]: product rule, sum rule, max rule, min rule, median rule and majority vote rule. The optimal combination strategy will be identified. Moreover, real-time processing will be pursued, exploiting a neural network approach for the analysis of the impedance traces [17].

REFERENCES

[1] K. A. Holt and K. D. Bennett, "Principles and methods for automated palynology," New Phytologist, vol. 203(3), pp. 735-742, 2014.

[2] R. Blank and P. Papireddy Vinayaka and M. W. Tahir and J. Yong and M. J. Vellekoop and W. Lang, "Comparison of Several Optical Methods for an Automated Fungal Spore Sensor System Concept," IEEE Sensors Journal, vol. 16, pp. 5596–5602, 2016.

[3] J. Oteros, G. Pusch, I. Weichenmeier, et al. "Automatic and Online Pollen Monitoring," Int. Arch. Allergy Immunol. 2015;167(3):158-166.

[4] J. Schiele, A. Damialis, F. Rabe et al. "Automated Classification of Airborne Pollen using Neural Networks," Conf. Proc. IEEE Eng. Med. Biol. Soc. 2019;2019:4474-4478.

[5] I. Šaulien, L. Šukien, G. Valiuliset al. "Automatic pollen recognition with the Rapid-E particle counter: the first-level procedure, experience and next steps," Atmospheric Measurement Techniques, vol. 12, pp. 3435–3452.

[6] I. Heidmann, G. Schade-Kampmann, J. Lambalk, M. Ottiger and M. Di Berardino, "Impedance Flow Cytometry: A Novel Technique in Pollen Analysis," PLoS ONE, vol. 11, e0165531, 2016.

[7] F. Caselli, A. De Ninno, R. Reale, L. Businaro and P. Bisegna, "A novel wiring scheme for standard chips enabling high-accuracy impedance cytometry," Sensors and Actuators B: Chemical, vol. 256, pp. 580-589, 2018.

[8] R. Reale, A. De Ninno, L. Businaro, P. Bisegna and F. Caselli, "High-throughput electrical position detection of single flowing particles/cells with non-spherical shape," Lab Chip, vol. 19, pp. 1818-1827, 2019.

[9] R. Reale, A. De Ninno, L. Businaro, P. Bisegna and F. Caselli, "Electrical measurement of cross-sectional position of particles flowing through a microchannel," Microfluidics and Nanofluidics, vol. 22, pp. 41, 2018.

[10] F. Caselli and P. Bisegna, "A simple and robust event-detection algorithm for single-cell impedance cytometry," IEEE Transactions on Biomedical Engineering, vol. 63, pp. 415-422, 2016.

[11] A. De Ninno, R. Reale, A. Giovinazzo, F. R. Bertani, L. Businaro and P. Bisegna, C. Matteucci and F. Caselli, "High-throughput label-free characterization of viable, necrotic and apoptotic human lymphoma cells in a coplanar-electrode microfluidic impedance chip," Biosensors and Bioelectronics, vol. 150, n. 111887, 2020

[12] H. K Yuen, J. Princen, J. Illingworth, and J. Kittler, "Comparative study of Hough transform methods for circle finding," Image and Vision Computing, vol. 8, pp. 7177, 1990.

[13] O. Russakovsky, J. Deng, H. Su et al., "ImageNet Large Scale Visual Recognition Challenge," International Journal of Computer Vision (IJCV), vol. 115, pp. 211252, 2015.

[14] C. Cortes and V. Vapnik, "Support-Vector Networks," Machine Learning, vol. 20, pp. 273-297, 1995.

[15] F. Caselli, A. De Ninno, R. Reale, L. Businaro and P. Bisegna, "A Bayesian approach for coincidence resolution in microfluidic impedance cytometry," IEEE Transactions on Biomedical Engineering, doi: 10.1109/TBME.2020.2995364.

[16] J. Kittler, M. Hatef, R. P. W. Duin and J. Matas, "On combining classifiers," in IEEE Transactions on Pattern Analysis and Machine Intelligence, vol. 20, no. 3, pp. 226-239.

[17] C. Honrado, J. S. McGrath, R. Reale, P. Bisegna, N. S. Swami and F. Caselli, "A neural network approach for real-time particle/cell characterization in microfluidic impedance cytometry," in Analytical and Bioanalytical Chemistry, vol. 412, pp. 3835–3845.

A hydrogel channel-based system to model the blood flow dynamic stimuli

C. Vitale[1*], A. Fedi[1,2*], G. Varani[1], A. Marrella[1], M. Fato[2], and S. Scaglione[1]

1 National Research Council of Italy, IEIIT Institute
2 University of Genoa

*These authors equally contributed

Abstract—**Metastasis is a dynamic process involving the dissemination of circulating tumour cells (CTCs) through the bloodstream to distant tissues within the body. An improved understanding of the fluid flow induced mechanical forces experienced by CTCs in the blood flow is crucial for fully explicating the metastatic steps and defining vulnerable CTC conditions for therapeutic intervention. Nevertheless, the development of an *in vitro* platform mimicking able to mimic the dynamic stimuli occurring during metastasis still remains a challenge. We here developed a 3D hydrogel-based tissue model provided with an inner channel resembling the vascularization of the metastatic tumor tissue. The mechanical properties of two different hydrogels (i.e. fibrin and alginate) were measured; glucose mass transport resembling the blood flow through the hydrogels was analyzed by performing a computational fluid-dynamic (CFD) analysis. Moreover, this system has been used to evaluate the shear forces inducing fluid flow effects on high metastatic breast cancer cells (MDA-MB-231) circulating within the hydrogel-based channel.**

Keywords—**CTCs, CFD, hydrogel, shear stress.**

I. Introduction

CTCs are viable cells which circulate in blood after detaching from a primary tumour [1]. Over the past decade, different studies showed that these cells cover a key role in tumour progression [2]. An improved understanding of the mechanical forces encountered by CTCs in fluids is crucial for fully elucidating the metastatic cascade and delineating vulnerable CTCs states for therapeutic intervention [3]. In fact, CTCs must be able to withstand different fluid-dynamical stress when they circulate, in order to survive and to adhere to the endothelial wall, to finally extravasate to origin a secondary tumour [4].

Moreover, the migration of CTCs require their interaction with the surrounding extracellular matrix (ECM) [5]. With the development of tissue engineering, hydrogels have been widely used as three-dimensional (3D) scaffolds because of their advantageous properties similar to those of the native ECM [6]-[7]. In fact, tissue mechanical properties, mass transport and, the high degree of diffusivity of growth factors, oxygen, and nutrients also condition cellular behaviour [8]. In particular, glucose is fundamental for tumour growth, as cancer cells use a higher quantity of this nutrient than healthy cells. This increased glycolysis provides tumoral cells different advantages, including the ability to survive even in the absence of oxygen, to produce essential elements (lactate) for the growth of the tumour mass and the establishment of an extremely favourable surrounding environment [9]. Currently, there is the need to develop *in vitro* models taking into account these aspects and where to study the impact of fluid forces on CTCs. In this context, an *in silico* analysis can be extremely useful both to simulate the nutrients diffusion kinetic in advanced *in vitro* models, with the ultimate goal to design a reliable model of metastasis, and both to systematically predict the cell response to various biomechanical forces [10].

We designed a fluidic system, where CTCs can experience blood flow physiological forces, within an "ECM-like" system. In particular, we realized a hydrogel matrix provided with a linear channel, which can be directly connected with an external fluidic system. Two kinds of hydrogels have been used and compared: alginate and fibrin. Alginate was chosen because it is bio-inert, easy-to-use, cheap [11], while fibrin was selected for its higher biocompatibility and bioactivity [12]. Mechanical characterization of the gels and nutrients diffusion studies within the hydrogel have been carried out. Subsequently, the platform has been used for the circulation of high metastatic breast cancer cells (MDA-MB-231) under physiological fluid shear stress (FSS) conditions, in order to evaluate shear stress effects con CTCs.

II. Materials and Methods

A. Hydrogel realization and characterization

A mold was realized through 3D printing technology (Form 2, Formlabs) with the aim to fabricate a hydrogel, composed by a sphere (diameter = 1 cm), to mimic the metastatic tumour mass [13], and a channel, where CTCs could migrate. We tested two different materials to realize the hydrogel: alginate and fibrin. Briefly, alginate powder (Manugel GMB, FMC Biopolymer) was dissolved in physiologic solution at the concentration of 1% w/v, subsequently the cross-linking was obtained into the mold by adding a 0.5 M calcium chloride solution ($CaCl_2$) [14], whereas fibrin hydrogel was formed by casting fibrinogen (20 mg/ml) from human plasma (F3879 Sigma) and thrombin (10 U/ml) in $CaCl_2$ 5 mM solution of thrombin from human plasma (T6884 Sigma). The channel was created though the insertion of a 21G-needle within the mold, before the addition of the polymers. After the cross-linking, the needle was gently removed leaving a cavity inside the gel. Both hydrogels were mechanically characterized at a frequency through a dynamic mechanical analysis (DMA). Finally, perfusion tests have been carried out to verify the fluidic continuity between the channel and an external fluidic circuit connected to a peristaltic pump. The flow rate was set to obtain a capillary velocity (1 cm/s) within the channel.
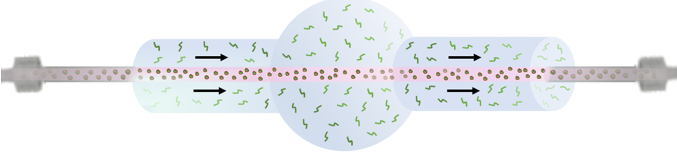
Fig. 1: Schematic representation of the hydrogel matrix resembling the metastatic tumour tissue with the vascular linear channel where growth factors and CTC flow.

B. Glucose absorption study

A release study of glucose was carried out to calculate the experimental diffusion coefficient of glucose within the two hydrogels. Alginate was poured in the cross-linker $CaCl_2$ bath whereas fibrinogen was poured in a thrombin one. Then, hydrogel beads were soaked in 4 ml of deionized water containing glucose at the initial concentration of 200 mg/ml. 1ml of solution was sampled every hour for 8 hours and the glucose absorbance read at 193 nm by using a spectrophotometer. A calibration curve was used to quantify the amount of glucose absorbed by hydrogels.

C. Computational fluid-dynamics (CFD) analysis

A theoretical model, based on the Continuity law and energy balance, was developed to analyse the fluid-structure interaction and the transport of diluted nutrients through the hydrogel. This model was implemented by using the Laminar Fluid Flow model of Comsol Multiphysics 5.3a assuming i) a laminar flow, ii) an incompressible Newtonian fluid. The solving equations are the Navier-Stokes ones:

$$\begin{cases} \rho\left[\frac{\partial u_f}{\partial t} + u_f \cdot (\nabla u_f)\right] = -\nabla p + \mu(\nabla^2 u_f) \\ (\nabla \cdot u_f) = 0 \end{cases} \quad (1)$$

where u_f is the fluid velocity and p the pressure across the circuit. The values of density ρ (1000 kg/m^3) and viscosity μ (1.05·10^{-3} Pa·s) of water at room temperature (25 °C) were used. A no-slip boundary condition was fixed, instead, as initial condition, velocity and pressure were set to zero. To create a pressure gradient within the channel, in order to generate the fluid motion, as input a flow rate was set, while as output a pressure equal to zero has been set, avoiding a return flow.

The interaction between a fluid and a solid structure, including both fluid pressure and viscous forces, has been studied by using the Fluid-Structure Interaction (FSI) module of Comsol Multiphysics 5.3a. In particular, we analyzed the fluid-dynamic load on the structure, i.e. the hydrogel matrix, especially in terms of channel deformation. The equations to be solved were chosen by the software according to the kind of material defined, which, in our case, has been approximated to isotropic linear elastic, given the results obtained from the dynamic mechanical tests on alginate and fibrin. Therefore, the structural model equations are:

- Equation of motion, an expression of Newton's second law:

$$\nabla \cdot \sigma_s + F_v = \rho_h \frac{\partial u_2}{\partial t^2} \quad (2)$$

where σ_s is the Cauchy stress tensor, F_v the body force

per unit volume, ρ_h is the hydrogel density and u_2 the displacement vector;

- Strain-displacement equation:

$$\varepsilon = \frac{1}{2}\left[\nabla u_2 + (\nabla u_2)^T\right] \quad (3)$$

Where ε is the strain tensor;

- Constitutive law for the structural material:

$$\sigma_s = \left[\frac{E\upsilon}{(1+\upsilon)(1-2\upsilon)}\nabla\cdot u_2\right]I + \left[\frac{E}{1+\upsilon}\right]\varepsilon \quad (4)$$

where E is the Young Modulus and υ the Poisson coefficient;

- Equation of normal components, which allows to couple the fluid dynamics with the solids mechanics:

$$\sigma_s \cdot n = \sigma_f \cdot n \quad (5)$$

where n is the normal vector on the channel walls and σ_f the fluid stress tensor;

- Constitutive law for a Newtonian fluid:

$$\sigma_f = -p_f I + \mu\left[\nabla u_f + \left(\nabla u_f\right)^T\right] - \frac{2}{3}\mu\left(\nabla\cdot u_f\right)I \quad (6)$$

The initial displacement was assumed void.

Cells need to exchange nutrients and gases with the surrounding environment to survive once the colonization and the metastatic process has occurred. Thus, it is important to predict and evaluate their distribution inside the hydrogel. In particular, we focused on the glucose transport as the main component of the cellular metabolism. Therefore, we performed a mass transport analysis also considering other two contributions including a convection term, due to the presence of a velocity field (u_f) and a reaction term (R). This parameter defines the component consumption or production because of cells metabolism and can be described by the Michaelis-Menten reaction. Thus, the general form to describe the mass transport can be written as:

$$\nabla\cdot(-D\nabla c) + u_f\cdot\nabla c = R \quad (7)$$

where D is the diffusion coefficient of the component at 37 °C, obtained through experimental glucose release studies for both alginate and fibrin, and c the concentration of the component. Moreover, two borderline cases were considered for our analysis: i) a continuous refill of the culture medium into the bioreactor and ii) no culture medium refill.

D. Shear stress effects on circulating breast cancer cells

We used metastatic breast cancer cells (MDA-MB-231) as CTCs. They circulated within the whole fluidic system under physiological shear stress conditions (5 Dyne/cm^2) [15]-[16]. In order to obtain this value, the flow rate was calculated by the inverse formula of Poiseuille's law for a cylindric tube as:

$$Q = \frac{\pi r^3 \tau}{4\mu} \quad (8)$$

Moreover, given the results of preliminary perfusion tests, only fibrin was used as hydrogel material. The cell line was expanded in Dulbecco's Modified Eagle's Medium (DMEM) enriched with 10% Fetal Bovine Serum (FBS), 1% L-glutamine and 1% penicillin/streptomycin (all from Sigma Aldrich). Cells were enzymatically detached with 0.05% trypsin, counted and injected within the circuit with a density of 1·10^5 cells/ml, while the fibrin gel was prepared using the

protocol described above. Since we have focused on the circulation of the cells through the fluidic channel and the shear forces effects on them, after 24 hours the viability was evaluated through a live/dead assay (Sigma Aldrich).

III. RESULTS

A. CFD simulations and perfusion tests

Computational simulations allowed us to obtain velocity profile and shear stress distribution within the hydrogel channel. Moreover, starting from this, we analyzed the fluid-dynamic load transmitted to the hydrogel through the FDI. The maximum shear stress value is 0.5 Pa, namely 5 Dyne/cm^2, according to the Eq. 8. The fluid-dynamic load transmitted to the hydrogel is represented in figure 2 (A), which turned out to be higher at the gel-tips interface: it means that this point is crucial for the fluidic continuity between the hydrogel channel and the external system, rather than the entire channel itself. Therefore, this interface is a critical point for the hydraulic seal of the whole fluidic system.
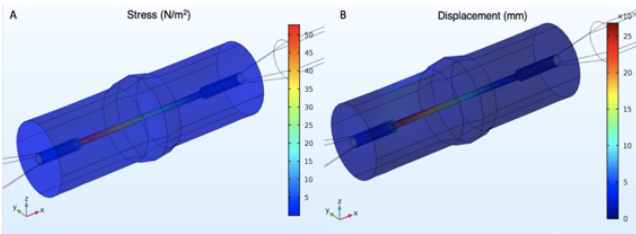
Fig. 2: Stress (A) and displacement of the channel (B).

Moreover, only a perfect cross-linking and channel formation can ensure no liquid leakage. As it is shown in figure 2 (B), the strain caused by the fluid load on the hydrogel, compared to the diameter of the channel, is only 0.3% for the flow rate imposed on the peristaltic pump in order to obtain a FSS of 5 Dyne/cm^2.

Perfusion tests were performed to experimentally compare the resistance to the fluid passage in alginate and fibrin hydrogels. These tests confirm the CFD simulations, showing the ability of the hydrogels to withstand the fluidical forces.

In particular, as it is shown in figure 3, the fibrin gel resulted better than alginate one, showing a lower dispersion of liquid within the polymeric matrix of the hydrogel. Moreover, the fibrin hydrogel allowed to obtain an excellent fluidic continuity between the inner channel and the external fluidic circuit for longer times (data not shown). This can be due to the well-known adhesive properties of the fibrin [17], that in this case well adhered over the plastic tubes.
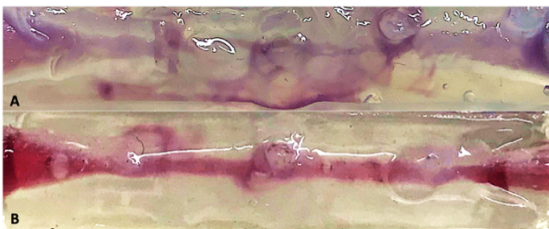
Fig. 3: Perfusion test on alginate (A) and fibrin (B).

For what concerns the mechanical characterization, the elastic and viscous modulus values are reported in figure 4. For both materials, the elastic component was found to be higher than the viscous one. Tests have been performed at a frequency of 1 Hz. It is interesting to note that even if the best material in terms of resistance to fluidic stimuli was fibrin, the Young Modulus is significantly higher for alginate hydrogel.
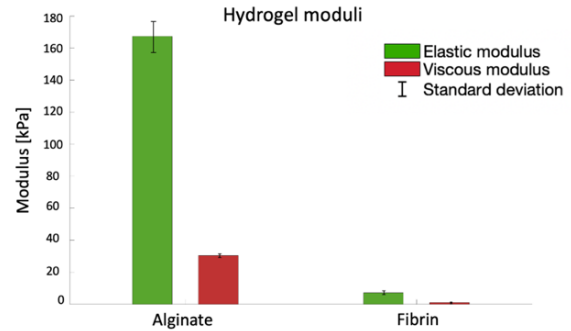

Fig. 4: Storage and loss moduli of alginate and fibrin hydrogels.

Given these results, in the following computational simulations, both the hydrogels have been modelled as a simple linear elastic material and the values obtained by DMA were used as input parameters for the simulations.

B. Glucose transport studies

Experimental data obtained from glucose release studies over time on alginate and fibrin hydrogel samples, are reported in figure 5.
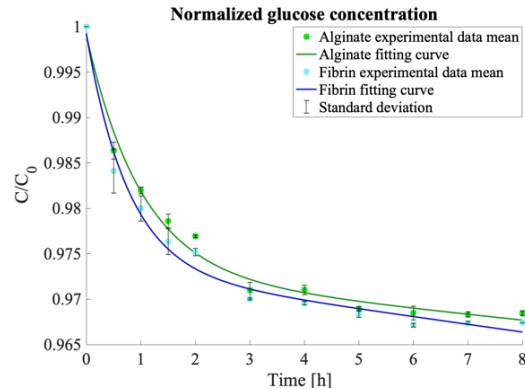

Fig. 5: Medium glucose concentration (C) normalized with respect to the initial medium glucose concentration (C$_0$ = 200 mg/ml) at different time points.

The glucose diffusivity within the two hydrogels was calculated by the best fitting of the data obtained from the experimental release studies. Then, such parameter was used as input value for the mass transport simulations to model the diffusion process through the hydrogels.

Since the diffusion coefficients were found to be similar for the two materials (5·10^{-10} m^2/s for alginate; 4.38·10^{-10} m^2/s for fibrin), glucose transport analysis was performed considering only fibrin hydrogel.

Different time points were examined. Since in the experimental studies the hydrogels were saturated with glucose after 8 hours, the simulation was carried out up to 8 hours. Glucose distribution within the hydrogel in the case of continuous culture medium refilling in the environment

simulating the culture chamber is shown in figure 6, while the one without refill is shown in figure 7. The refill mode has a clear effect on the glucose concentration profiles within the hydrogel, ensuring a homogeneous distribution of the metabolite within the material. Therefore, the condition of continuous refill of the medium is necessary since it provides a uniform glucose supply for the CTCs migrated in the gel.
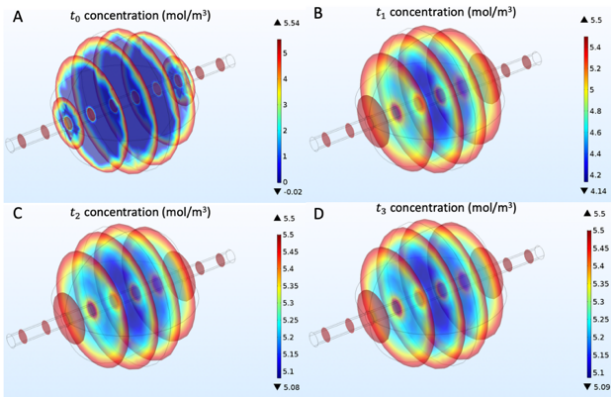

Fig. 6: Glucose concentration with medium refill at different time point: t_0 = 0h (A), t_1 = 1h (B), t_2 = 4h (C), t_3 = 8h (D).
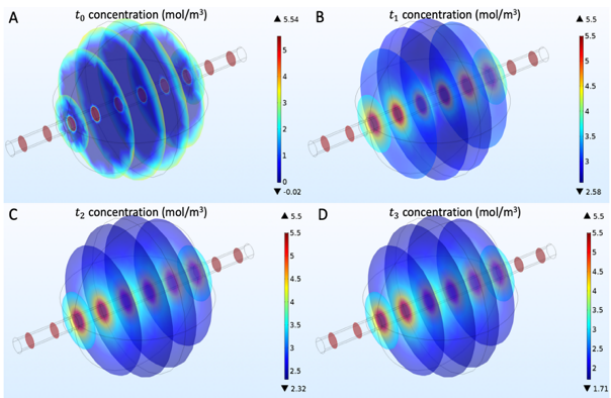
Fig. 7: Glucose concentration without medium refill at different time point: t_0 = 0h (A), t_1 = 1h (B), t_2 = 4h (C), t_3 = 8h (D).

C. Shear stress effects on circulating breast cancer cells

High metastatic breast adenocarcinoma cells (MDA-MB-231) circulated within the whole fluidic system under 5 Dyne/cm^2 of shear stress conditions for 24 hours. At the end of the experiment, the cell suspension was recovered from the circuit and cell viability was assessed through the dead/alive assay. The cell viability after circulation was about 80% in line with the literature data [16].

IV. CONCLUSION

In this work, a hydrogel channel-based system has been realized to reproduce the blood flow-associated forces experienced by CTCs and the first steps of the metastatic cascade. The system is composed by a 3D hydrogel modelling the metastatic mass provided with an inner linear channel resembling the tumor vascularization, where cells and nutrients can flow with physiological fluid flow parameters. As first analysis, the mechanical stability and glucose diffusion of two polymeric-based hydrogels, alginate and fibrin, have been tested, revealing that this last is more resistant to the fluid flow. Mechanical analysis of the hydrogels showed that both the hydrogels can be modelled as elastic materials and that the elastic modulus of alginate is significantly higher than fibrin, even if the fibrin channel was more suitable to withstand the fluid flow. These data, together with the hydrogel diffusivity, have been used as input of CFD simulations to predict glucose transport kinetic within the hydrogels. In particular, glucose transport simulations showed that it is necessary to recirculate the culture medium within the system to ensure a homogeneous distribution of glucose. Moreover, MDA-MB-231 injected within the system showed a cell viability about 80% after 24 hours of circulation, accordingly with the literature. Therefore, this hydrogel-based system has been fluidically validated and fibrin hydrogel has been selected for further tests. Moreover, the platform's versatility enables to set different shear stress conditions study the effects of different fluid-dynamical stimuli on CTCs circulation, by changing the vessel diameter or by setting different flow rate.

REFERENCES

[1] Song, Ping, et al. "DNA hydrogel with aptamer-toehold-based recognition, cloaking, and decloaking of circulating tumor cells for live cell analysis." Nano letters 17.9 (2017): 5193-5198.

[2] Pantel, Klaus, and Catherine Alix-Panabieres. *"Functional studies on viable circulating tumor cells."* Clinical chemistry 62.2 (2016): 328-334.

[3] Follain, Gautier, et al. *"Fluids and their mechanics in tumour transit: shaping metastasis."* Nature Reviews Cancer (2019): 1-18.

[4] Mitchell, Michael J., and Michael R. King. *"Computational and experimental models of cancer cell response to fluid shear stress."* Frontiers in oncology 3 (2013): 44.

[5] Pathak, Amit, and Sanjay Kumar. *"Independent regulation of tumor cell migration by matrix stiffness and confinement."* Proceedings of the National Academy of Sciences 109.26 (2012): 10334-10339.

[6] Marrella, Alessandra, et al. *"Enhanced mechanical performances and bioactivity of cell laden-graphene oxide/alginate hydrogels open new scenario for articular tissue engineering applications."* Carbon 115 (2017): 608-616.

[7] Marrella, Alessandra, et al. *"3D porous gelatin/PVA hydrogel as meniscus substitute using alginate micro-particles as porogens."* Polymers 10.4 (2018): 380.

[8] Marrella, Alessandra, et al. *"Topographical features of graphene-oxide-functionalized substrates modulate cancer and healthy cell adhesion based on the cell tissue of origin."* ACS applied materials & interfaces 10.49 (2018): 41978-41985.

[9] Annibaldi, Alessandro, and Christian Widmann. *"Glucose metabolism in cancer cells."* Current Opinion in Clinical Nutrition & Metabolic Care 13.4 (2010): 466-470.

[10] Mitchell, Michael J., and Michael R. King. *"Computational and experimental models of cancer cell response to fluid shear stress."* Frontiers in oncology 3 (2013): 44.

[11] Kaklamani, Georgia, et al. *"Mechanical properties of alginate hydrogels manufactured using external gelation."* Journal of the mechanical behavior of biomedical materials 36 (2014): 135-142.

[12] Haugh, Matthew G., et al. *"The application of plastic compression to modulate fibrin hydrogel mechanical properties."* Journal of the mechanical behavior of biomedical materials 16 (2012): 66-72.

[13] Sefidgar, Mostafa, et al. *"Effect of tumor shape, size, and tissue transport properties on drug delivery to solid tumors."* Journal of biological engineering 8.1 (2014): 12.

[14] Marrella, Alessandra, et al. *"Cell-laden hydrogel as a clinical-relevant 3D model for analyzing neuroblastoma growth, immunophenotype and susceptibility to therapies."* Frontiers in immunology 10 (2019): 1876.

[15] Regmi, Sagar, Afu Fu, and Kathy Qian Luo. *"High shear stresses under exercise condition destroy circulating tumor cells in a microfluidic system."* Scientific reports 7.1 (2017): 1-12.

[16] Fu, Afu, et al. *"High expression of MnSOD promotes survival of circulating breast cancer cells and increases their resistance to doxorubicin."* Oncotarget 7.31 (2016): 50239.

[17] Spicer, Patrick P., and Antonios G. Mikos. *"Fibrin glue as a drug delivery system."* Journal of controlled release 148.1 (2010): 49-55.

Are your cells alive?

A. De Ninno[1,2], R. Reale[1], A. Giovinazzo[3], F. R. Bertani[2], L. Businaro[2], P. Bisegna[1], C. Matteucci[3], and F. Caselli[1,*]

[1] *Department of Civil Engineering and Computer Science, University of Rome Tor Vergata*
[2] *Institute for Photonics and Nanotechnologies, Italian National Research Council*
[3] *Department of Experimental Medicine, University of Rome Tor Vergata*
* *E-mail: caselli@ing.uniroma2.it*

Abstract—The study and the characterization of cell death mechanisms are fundamental to unravel cell behavior in normal and harsh conditions, with important implication to understand disease pathogenesis and treatment. In this work, we use electrical impedance spectroscopy as a label-free methodology to characterize viable, necrotic and apoptotic human lymphoma U937 cells. The results suggest that, at low frequency (0.5 MHz), signal magnitude enables the discrimination between viable/necrotic cells and cell fragments, whereas phase information allows discriminating between viable cells and necrotic cells. At higher frequency (10 MHz) two subpopulations of cell fragments are distinguished. This work substantiates the prominent role of electrical impedance spectroscopy for the development of next-generation cell viability assays.

Keywords—Cell viability, Impedance cytometry, Microfluidics, Single-cell analysis.

I. INTRODUCTION

Cell death characterization is essential in cell biology research, and specific recommendations have been drawn up for the classification of the different types and modality of cell death discovered so far [1]. Apoptosis is a physiological form of programmed cell death whereby a cell provokes its own demise in response to a stimulus, whereas necrosis occurs when cells are irreversibly damaged by an external trauma. A critical issue in chemotherapy drugs development is the type of resulting cell death, both for the containment of inflammatory or immunosuppressive response, and to avoid the mechanism of resistance to the therapy [2].

Traditional death/viability assays involve laborious sample preparation and expensive equipment or reagents [3]. In particular, flow cytometry [4] predominantly relies on fluorescent labeling, which may be time-consuming and alter natural biological functions [5]. Microfluidic lab-on-a-chip solutions promise simpler procedures and greatly reduced costs [6], [7], [8], [9], with tremendous benefit for pharmaceutical and life-science research. In particular, label-free approaches are especially attractive, because they preserve cell native behaviour and therapeutic potential [10], [11].

Since changes in cell physiology are known to result in changes in dielectric properties of the cell [12], lab-on-a-chip devices for cell electrical phenotyping have the potential for label-free death/viability assays. In particular, microfluidic impedance spectroscopy [13], [14], potentially enabling high-throughput multiparametric analysis, is particularly attractive to perform viability assays. In a typical impedance chip, suspended particles flow through a microchannel and two electrode pairs are used to measure the variation in channel impedance induced by the passage of a particle. The impedance variation is exploited to characterize particle properties. Recently, the possibility to analyze the impedance trace in real-time using neural networks has been reported [15]. However, resolution and accuracy of microfluidic impedance spectroscopy is challenged by the positional dependence of the measured signals, i.e. identical particles flowing along different trajectories in the microchannel provide different signals [13], [16], [17], [18].

In this work, we address the label-free discrimination of viable, necrotic and apoptotic human lymphoma U937 cells in a microfluidic impedance cytometer. The U937 cell line [19] is widely used in cell biology research, however its electrical phenotyping has received limited attention. In order to keep the system as simple as possible, thus maximizing its potential for low-cost and portable implementation, a chip layout with three coplanar electrodes is used and no focusing mechanisms are implemented. Due to the presence of both intact cells and apoptotic bodies, size-heterogeneous samples are expected. Accordingly, position blurring cannot be easily eliminated by optimization of channel dimensions. In order to mitigate the positional dependence of the measured signals, an enhanced version of the compensation strategy previously introduced by Errico et al. [20] is used. Experimental campaigns involving control samples and samples treated with heat-shock (to induce necrosis) or etoposide (to induce apoptosis) are performed. Thousands of cells are measured at high-throughput ($\approx$200 cell/s) and flow cytometry analysis is used for validation. The results of the present work (Section III) show that the recorded electrical fingerprints provide high-content information useful for cell discrimination, and bring microfluidic impedance spectroscopy in a prominent position for next-generation cell viability assays.

II. MATERIALS AND METHODS

A. Microfluidic impedance cytometer

A schematic representation of the microfluidic impedance chip is shown in Figure 1(a). The microchannel is filled with a conductive fluid and a multifrequency AC voltage signal (0.5 and 10 MHz, 2.5 V each) is applied to the central electrode by an impedance spectroscope. The difference in current collected from the lateral electrodes is measured with a transimpedance
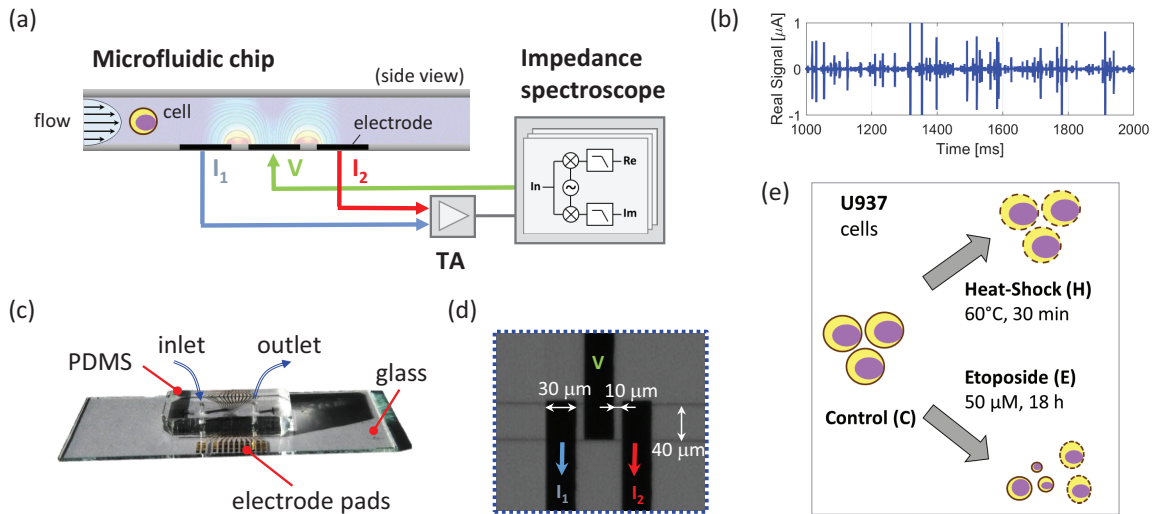
Fig. 1: (a) Operation mode of the microfluidic impedance cytometer: an impedance spectroscope provides a multifrequency AC voltage signal (V) to the central electrode of the microfluidic chip, and receives as differential input the current signals I_1 and I_2 collected from the lateral electrodes and conditioned by a transimpedance amplifier (TA). (b) Real part of the differential current demodulated at 0.5 MHz (exemplary data stream shown). (c) Microfluidic impedance chip. (d) Bright-field image of the sensing region (top view, channel height is 21 μm). (e) Experimental protocol. Human lymphoma U937 cells are treated with heath-shock (H) or etoposide (E) to induce necrosis or apoptosis, respectively. Untreated cells (C) are used as control.

amplifier and demodulated by the spectroscope, providing the in-phase (real) and out-of-phase (imaginary) components of each frequency channel. A portion of a typical datastream (real part, relevant to one frequency channel) is reported in Figure 1(b). The passage of a flowing particle is recorded as a pair of opposite peaks [21].

The microfluidic impedance chip consists of a microchannel with coplanar microelectrodes integrated at the bottom of a microscope glass slide (Figure 1(c,d)), and was fabricated as previously described [22]. In the sensing region the channel cross-sectional area is 40 μm wide and 21 μm high; electrodes are 30 μm wide with a 10 μm spacing.

B. Sample preparation

Human histiocytic lymphoma U937 cells, originally obtained from Zooprofilactic Institute (Brescia, Italy), were grown in suspension culture at a density of 4×10^5 cells/ml in RPMI 1640 supplemented with 10% fetal bovine serum (FBS), 2 mM glutamine, 50 U/ml penicillin and 50 U/ml streptomycin at 37°C in a 5% CO_2-humified atmosphere for 18 h. To induce necrosis, after 15 h of culture cells were exposed to a heat shock by incubation for 30 min at 60 °C in a water bath, then washed in phosphate-buffered saline (PBS; Sigma-Aldrich) for 5 min at 1000 g, and incubated in culture medium for other 3 h at 37 °C in a 5% CO_2-humified atmosphere. Apoptosis was induced with etoposide (Sigma-Aldrich) treatment at the concentration of 50 μM for 18 h. Dimethyl sulfoxide (DMSO; Sigma-Aldrich) was used as diluent for etoposide and was referred as vehicle in control condition. The experimental protocol is pictured in Figure 1(e). A mixed sample, containing cells from the control, heat-shock and etoposide samples, was also prepared. Samples were spiked with polystyrene beads

(6 μm diameter, PolySciences) for internal reference. Samples were injected into the microfluidic chip by a syringe pump (Harvard Apparatus) at a rate of 10 μl/min.

C. Impedance data processing

Event detection in the data stream was performed with the algorithm described in Ref. [23]. For feature extraction, a novel template fitting strategy was implemented, taking into account all the complex frequency channels at the same time. To this aim, a suited bipolar Gaussian template was considered, characterized by the following features: a frequency-dependent complex amplitude a, a frequency-independent real peak-width control σ, and a frequency-independent real peak-to-peak time δ. A least-square approach was used to fit the template to each detected event.

The following features were considered for discrimination:

- electrical diameter $D = G\,|a_{0.5}|^{1/3}$, where $a_{0.5}$ denotes complex amplitude at 0.5 MHz, $|\cdot|$ denotes absolute value, and G is a gain factor accounting for the electronic circuitry;
- phase of a at 0.5 MHz, denoted by $\Phi_{0.5}$;
- phase of a at 10 MHz, denoted by Φ_{10}.

The shape parameter σ/δ of the signal pulse, correlating with the particle trajectory height, was also computed. Moreover, since the signal phase depends on a number of factors related to the physical properties of the complete system [24], [10], the phase features $\Phi_{0.5}$ and Φ_{10} were normalized by subtracting their average value computed for the bead population, so they have the meaning of phase shift with respect to beads.
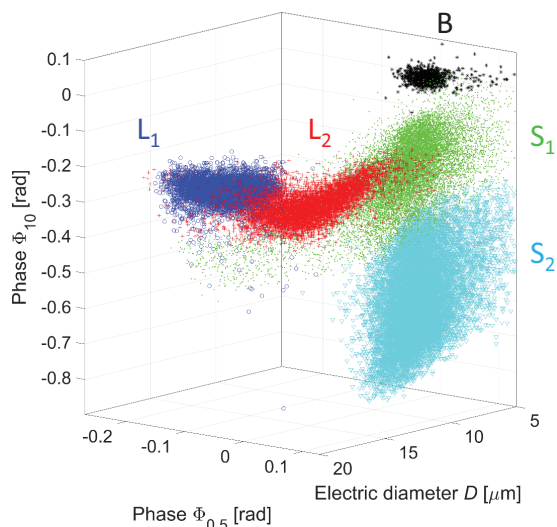
Fig. 2: 3D scatter plot of electrical diameter, phase at 0.5 MHz and phase at 10 MHz, relevant to the mixed sample. Data points are labeled according to the population they belong to.

III. RESULTS

Canonical hallmarks of apoptotic cell death include cell shrinkage, maintenance of plasma membrane integrity, nuclear fragmentation and formation of apoptotic bodies. In contrast, necrosis is characterized, among other features, by an early swelling and increased permeability with break-down of the plasma membrane integrity. Accordingly, different size and dielectric properties are expected for apoptotic, necrotic and viable cells, and this should reflect in different impedance signatures. In fact, the electrical diameter D is a metric of cell size [25], [20], whereas the electric phase depends on cell membrane properties [26].

The 3D scatter plot of the electrical features D, $\Phi_{0.5}$ and Φ_{10} relevant to the mixed sample is shown in Figure 2. These results overlap the results obtained by the single sample analysis (data not shown). Five clusters can be identified. Particularly, besides the beads (B), two clusters with small electric diameters (S_1 and S_2) and two clusters with large electric diameter (L_1 and L_2) are found. All clusters exhibit a negative high-frequency phase shift with respect to the beads. Clusters S_1 and S_2 exhibit different values of high-frequency phase Φ_{10}, whereas clusters L_1 and L_2 exhibit different values of low-frequency phase $\Phi_{0.5}$. As thoroughly discussed in Ref. [22], clusters L_1 and L_2 reasonably correspond to viable and necrotic cells, respectively, while clusters S_1 and S_2 represent two subpopulations of apoptotic bodies/cell debris, characterized by permeable or intact membrane, respectively.

Figure 3 shows a representative snapshot of a cell from cluster L_1 flowing through the sensing zone of the cytometer. The impedance signals generated by the flowing cell are also visualized, and the corresponding values of the electric phases $\Phi_{0.5}$ and Φ_{10} are marked in the relevant density plot.

IV. CONCLUSIONS

An impedance-based label-free analysis of viable, necrotic and apoptotic human lymphoma cells was reported. Necrosis was induced with heat-shock, whereas apoptosis was induced with etoposide. Electrical fingerprints from thousands of cells were measured and significant differences were found among untreated cells, cells treated with heat-shock, and cells treated with etoposide. Overall, the results of the impedance-based analysis suggest that the electrical diameter at low frequency is effective for size-based discrimination between viable/necrotic cells and apoptotic bodies, whereas the electrical phase at low frequency is effective to discriminate between viable and necrotic cells based on intact or damaged plasma membrane.

REFERENCES

[1] L. Galluzzi and et al., "Molecular mechanisms of cell death: recommendations of the nomenclature committee on cell death 2018," *Cell Death and Differentiation*, vol. 25, no. 3, pp. 486–541, 2018.

[2] J. Zhang, X. Lou, L. Jin, R. Zhou, S. Liu, N. Xu, and D. J. Liao, "Necrosis, and then stress induced necrosis-like cell death, but not apoptosis, should be the preferred cell death mode for chemotherapy: clearance of a few misconceptions," *Oncoscience*, vol. 1, no. 6, pp. 407–422, 2014.

[3] B. S. Cummings, L. P. Wills, and R. G. Schnellmann, "Measurement of cell death in mammalian cells," *Current Protocols in Pharmacology*, vol. 56, no. 1, pp. 12.8.1–12.8.24, 2012.

[4] H. Shapiro, *Practical Flow Cytometry, 4th Edition*. Wiley, 2003.

[5] K. Hiramatsu, T. Ideguchi, Y. Yonamine, S. Lee, Y. Luo, K. Hashimoto, T. Ito, M. Hase, J. Park, Y. Kasai, S. Sakuma, T. Hayakawa, F. Arai, Y. Hoshino, and K. Goda, "High-throughput label-free molecular fingerprinting flow cytometry," *Sci Adv.*, vol. 5, no. 1, p. eaau0241, 2019.

[6] A. Valero, F. Merino, F. Wolbers, R. Luttge, I. Vermes, H. Andersson, and A. van den Berg, "Apoptotic cell death dynamics of HL60 cells studied using a microfluidic cell trap device," *Lab Chip*, vol. 5, pp. 49–55, 2005.

[7] W. Donald, S. Joanna, and D. Zbigniew, "Cytometry in cell necrobiology revisited. Recent advances and new vistas," *Cytometry Part A*, vol. 77, no. 7, pp. 591–606, 2010.

[8] C. Petchakup, K. H. H. Li, and H. W. Hou, "Advances in single cell impedance cytometry for biomedical applications," *Micromachines*, vol. 8, no. 3, 2017.

[9] R. Reale, A. De Ninno, L. Businaro, P. Bisegna, and F. Caselli, "High-throughput electrical position detection of single flowing particles/cells with non-spherical shape," *Lab Chip*, vol. 19, pp. 1818–1827, 2019.

[10] E. Rollo, E. Tenaglia, R. Genolet, E. Bianchi, A. Harari, G. Coukos, and C. Guiducci, "Label-free identification of activated T lymphocytes through tridimensional microsensors on chip," *Biosensors and Bioelectronics*, vol. 94, pp. 193–199, 2017.

[11] P. Bagnaninchi and N. Drummond, "Real-time label-free monitoring of adipose-derived stem cell differentiation with electric cell-substrate impedance sensing," *Proceedings of the National Academy of Sciences of the United States of America*, vol. 108, no. 16, pp. 6462–6467, 2011.

[12] M. Nikolic-Jaric, T. Cabel, E. Salimi, A. Bhide, K. Braasch, M. Butler, G. Bridges, and D. Thomson, "Differential electronic detector to monitor apoptosis using dielectrophoresis-induced translation of flowing cells (dielectrophoresis cytometry)," *Biomicrofluidics.*, vol. 7, no. 2, 2013.

[13] K. C. Cheung, M. Di Berardino, G. Schade-Kampmann, M. Hebeisen, A. Pierzchalski, J. Bocsi, A. Mittag, and A. Tárnok, "Microfluidic impedance-based flow cytometry," *Cytometry Part A*, vol. 77, no. 7, pp. 648–666, 2010.
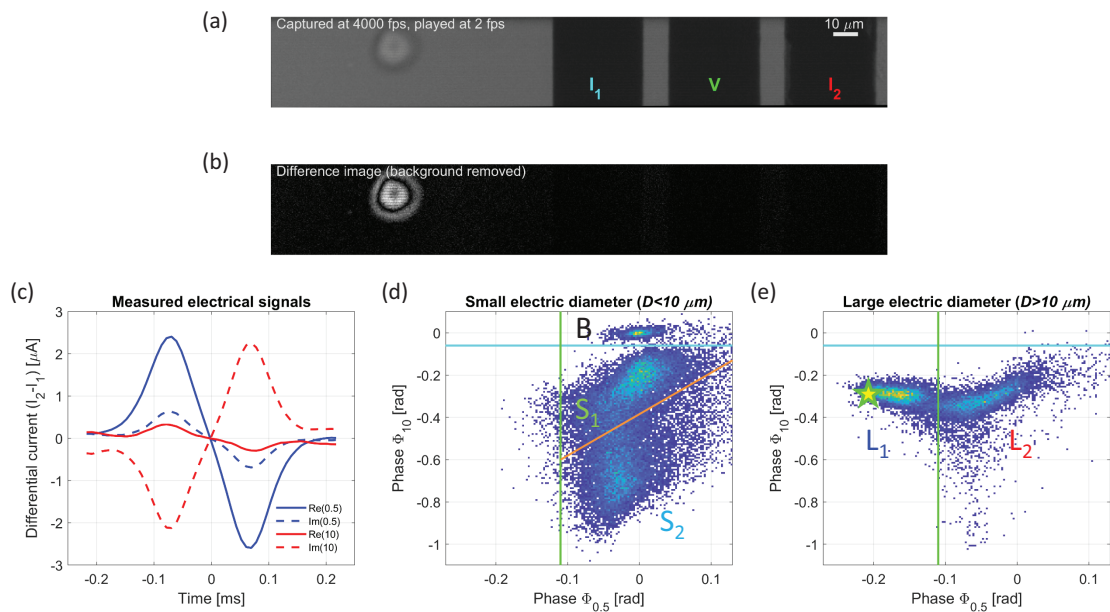
Fig. 3: (a) Optical image of a cell flowing through the microfluidic chip, and (b) difference between the image and the background (i.e., image of the empty channel). (c) Impedance signals generated by the flowing cell (real and imaginary parts for both 0.5 MHz and 10 MHz frequency channels). (d,e) Density plots of electric phases $\Phi_{0.5}$ and Φ_{10}, with a gating on (d) small cells or (e) large cells. The features of the cell shown in panel (a) are marked with a yellow star.

[14] T. Sun and H. Morgan, "Single-cell microfluidic impedance cytometry: a review," *Microfluid. Nanofluid.*, vol. 8, no. 4, pp. 423–443, 2010.

[15] C. Honrado, J. S. McGrath, R. Reale, P. Bisegna, N. S. Swami, and F. Caselli, "A neural network approach for real-time particle/cell characterization in microfluidic impedance cytometry," *Analytical and Bioanalytical Chemistry*, vol. 412, pp. 3835–3845, 2020.

[16] D. Spencer and H. Morgan, "Positional dependence of particles in microfludic impedance cytometry," *Lab Chip*, vol. 11, no. 7, pp. 1234–1239, 2011.

[17] F. Caselli, A. De Ninno, R. Reale, L. Businaro, and P. Bisegna, "A novel wiring scheme for standard chips enabling high-accuracy impedance cytometry," *Sensors and Actuators B: Chemical*, vol. 256, pp. 580–589, 2018.

[18] R. Reale, A. De Ninno, L. Businaro, P. Bisegna, and F. Caselli, "Electrical measurement of cross-sectional position of particles flowing through a microchannel," *Microfluidics and Nanofluidics*, vol. 22, no. 4, p. 41, 2018.

[19] C. Sundström and K. Nilsson, "Establishment and characterization of a human histiocytic lymphoma cell line (u937)," *International Journal of Cancer*, vol. 17, no. 5, pp. 565–577, 1976.

[20] V. Errico, A. De Ninno, F. R. Bertani, L. Businaro, P. Bisegna, and F. Caselli, "Mitigating positional dependence in coplanar electrode Coulter-type microfluidic devices," *Sensors and Actuators B: Chemical*, vol. 247, pp. 580–586, 2017.

[21] T. Sun, C. van Berkel, N. G. Green, and H. Morgan, "Digital signal processing methods for impedance microfluidic cytometry," *Microfluid. Nanofluid.*, vol. 6, no. 2, pp. 179–187, 2009.

[22] A. D. Ninno, R. Reale, A. Giovinazzo, F. R. Bertani, L. Businaro, P. Bisegna, C. Matteucci, and F. Caselli, "High-throughput label-free characterization of viable, necrotic and apoptotic human lymphoma cells in a coplanar-electrode microfluidic impedance chip," *Biosensors and Bioelectronics*, vol. 150, p. 111887, 2020.

[23] F. Caselli and P. Bisegna, "A simple and robust event-detection algorithm for single-cell impedance cytometry," *IEEE Trans Biomed Eng*, vol. 63, no. 2, pp. 415–422, 2016.

[24] N. Haandbæk, S. C. Bürgel, F. Rudolf, F. Heer, and A. Hierlemann, "Characterization of single yeast cell phenotypes using microfluidic impedance cytometry and optical imaging," *ACS Sens*, vol. 1, no. 8, pp. 1020–1027, 2016.

[25] S. Gawad, K. Cheung, U. Seger, A. Bertsch, and P. Renaud, "Dielectric spectroscopy in a micromachined flow cytometer: theoretical and practical considerations," *Lab Chip*, vol. 4, no. 3, pp. 241–251, 2004.

[26] A. Pierzchalski, M. Hebeisen, A. Mittag, M. D. Berardino, and A. Tarnok, "Label-free single cell analysis with a chip-based impedance flow cytometer," in *Imaging, Manipulation, and Analysis of Biomolecules, Cells, and Tissues VIII*, D. L. Farkas, D. V. Nicolau, and R. C. Leif, Eds., vol. 7568, International Society for Optics and Photonics. SPIE, 2010, pp. 256–266.

Towards classification of ovarian cancer via micro-arrays data analysis

Diego Liberati

CNR-IEIIT@DEIB-POLIMI Italy diego.liberati@polimi.it

Abstract— **The classification of micro-arrays data relative to ovarian cancer is approached without using any a priori information via a specially designed technique, consisting of cascading two clustering algorithms, namely PDDP, recalled, and well known K-means. Then validation is made by investigating correlations between the obtained clustering and the a priori clinical classification, possibly suggesting new and useful information on the investigated disease**

Keywords— **Data analysis for biomedical diagnosis, Ovarian Cancer DNA micro-arrays, Data-mining, Clustering.**
.

I. INTRODUCTION

In the last years DNA-micro-arrays have revealed themselves one of the most effective technologies to study the gene profile of a subject and in particular to examine the values of genes expression in patients affected by cancer disease [1]. In this study an unsupervised clustering has been performed, with the following aims [2][3]:

- to select the most significant gene information and reduce the problem's dimensionality;
- to create a classification of patients affected by cancer;
- to extract the genes most likely featuring the obtained clustering

The data analysis procedure we propose consists of 4 steps. The first two are devoted to preliminary data processing, while the third is devoted to data clustering. Finally, we proceed to the selection of the most relevant genes for pathology classification. More in detail, the four steps can be outlined as follows:

1. A drastic reduction in the number of genes dealt with is obtained thanks to a pruning based on the analysis of inter-subject variance. This will enable passing from the original 8665 genes to 227 only.
2. To define a hierarchy in the remaining set of genes, we resort to a principal component analysis; in this way it is possible to point out the most significant variables for clustering.
3. The adopted clustering procedure follows the unsupervised point of view, namely the classification is achieved without using a priori information on the patient's pathology so as to automatically highlight the (possibly unknown) patient casuistry. The clustering algorithm is a combination of the classical *k-means* technique [4][5] with the most recently developed PDDP algorithm proposed in [6]. According to the analysis provided in [7], cascading these two algorithms results in a significant improvement of performances.

4. By analyzing the obtained results, the number of genes for the detection of the various pathologies is further reduced (*gene shrinking*). In this way the classification is eventually based on a minimum number of genes.

II. METHODS AND MATERIALS

A. Data set

The data-base is constituted by 8665 gene expression data over 48 subjects suffering from Ovarian Cancer, at National Institute against Cancer, Milano. Each patient is thus determined by an 8665-dimensional vector of real numbers each measuring the expression of the corresponding gene in a Euclidean space. A simple measure of the genomic difference between two patients can be obtained by resorting to the distance among the corresponding two vectors. In order to ease algebraic manipulations of data, the data-set can be also represented by means of a real matrix S^0 of dimension 48x8665, the entry s_{ij}^0 of which measures the *expression* of the jth gene for the ith patient. Each subject is a priori clinically classified by means of the following variables (types):

- ➢ Histology, namely the kind of ovarian cancer;
- ➢ Response to treatment: that is the reduction of mass's cancer after surgical operation and chemotherapy;
- ➢ Response to treatment with platinum and taxolo, as above (where platinum and taxolo are two of the most used substances in chemotherapy);
- ➢ Disease free survival, that means the relapse of disease;
- ➢ Overall survival, that means the time of survival after surgery;
- ➢ p53 status, where p53 is a gene often not activated in cancer disease;
- ➢ Age at onset, showing the age of the patient.

each potentially assuming a defined set of few values (terms) here not fully reported for the sake of space: unfortunately for some type of classification, terms of classification are not always available, mainly because it is not always possible to define a classification for samples of genes grown and analysed in vitro.

B. Data pre-processing

A typical bottleneck in DNA micro-arrays experiments, making the classification problem even harder, is the difficulty to collect a high number of homogeneous subjects: not only a big matrix is involved, but such matrix has a huge number of variables (8665 genes) with a very small number of samples (48 subjects). Needless to say, finding the most significant

coordinates among these 8665 variables is of paramount importance to model the data distribution and, consequently, to perform clustering (following Section C). In this work, the search of the most significant coordinates is performed in two steps:

- A preliminary gene pruning is first performed in order to eliminate those variables which are per-se of little significance.
- The most significant gene combinations are determined by resorting to the known Principal Component Analysis (PCA).

B.1 Preliminary pruning

The first reduction of the problem dimensionality is obtained through a simple univariate analysis. Precisely, the variance of the expression values is computed for each gene across the patients, in order to have a first indicator of the relative inter-subject expression variability, done by the

formula $\frac{1}{N}\sum_{1}^{N} {}_{j}\big[s_{ij} - w_i\big]^2$ for the ith patient, where w_i is the mean of the considered values. Then, the genes whose variability is below a defined threshold are rejected leading to a first pruning. The simple idea behind such a procedure is that if the variability of a gene expression over the subjects is small, then that gene is similarly expressed for each patient and hence is not useful for classification purposes. The variance is relatively small for thousands of genes. Having selected a suitable threshold equal to 0,2, 8438 genes were pruned. So, attention has been focused on 227 genes only. In the sequel the remaining 48x227 data matrix will be denoted by S.

Here the critical issue was of course the choice of the cut-off level, which is in fact a tuning parameter of the method. To this end, note that the adopted level may be possibly decided on the basis of biological considerations (e.g. it is known that the natural variability of gene expressions between homogenous subjects is no greater than a certain level), technological knowledge (taking into account DNA micro-arrays measurement confidence) or simply following empirical considerations (e.g. imposing either a maximum of residual variables or a maximum fraction of variance to be discarded). Refining may be then made, like in the present results, iterating all the following procedure for a few reasonable values of the threshold around the value initially selected, and then ex-post decide what is the most effective value in order to comply with the tradeoff not to discard useful information nor to keep noise.

B.2. Principal component analysis

Principal Component Analysis [5] [8] is a known multivariate analysis by means of which it is possible to bring into evidence the linear combinations of variables with higher inter-subject variance, namely those combinations which are most useful for classification. More precisely, PCA returns a new set of orthogonal coordinates for the 227-dimensional data space resulting from the previous gene-pruning step. The new coordinates are ordered in such a way that the first one, the so called first principal component, denotes the direction with the greatest inter-subject variance, the second one (the second principal component) has the greatest inter-subject variance among all the directions orthogonal to the first component, and

so on. The computation of the principal components of S is made easy by the fact that, if the columns of S have zero mean, the first principal component is the eigenvector associated with the largest eigenvalue of the covariance matrix $S^T S$. Analogously, the second principal component is the eigenvector corresponding to the second largest eigenvalue of $S^T S$, and so on [5].

Remark 1: *The requirement that the columns of S have zero mean can be fulfilled considering in place of S the unbiased matrix $S - e \cdot w$, where $e = [1,1,...,1]^T$ and w, the so called centroid of S, is a vector $[w_1, w_2, ..., w_p]$ with*

$$w_k = \frac{1}{N}\sum_{i=1}^{N} s_{ik}, \quad k = 1,2,...,p$$

($[s_{i1}, s_{i2}, ..., s_{ip}]$ is ith row of S, $i = 1,2,...,N$).

Since the eigenvalues of $S^T S$ are the (square of the) singular values of S, PCA can be performed through the singular value decomposition (SVD) of S. In this regard, we recall that any real valued matrix S (square or rectangular) can be decomposed as $S = U\Sigma V$, where Σ is a diagonal matrix with the same dimension of S whose non null elements are the singular values of S, and U and V are orthonormal unitary square matrices, namely the inverse of U coincides with its transpose ($U^{-1} = U^T$) and analogously for V. Interestingly enough, the columns of V are the eigenvectors of $S^T S$, namely the principal components. As it is well known, there are many efficient algorithms for computing the SVD [9] available in existing software tools. Thanks to the PCA analysis the dimensionality of the problem has been reduced from 227 to 10. The final dimension of 10 refers to the number of linear combinations of genes considered as the most significant ones from the PCA analysis, still accounting for the large majority of the initial covariance.

C. Clustering

The clustering of the data obtained at the end of the preliminary data processing described above is performed according to following basic rationale: maximize the intra-similarity within each cluster and minimize the inter-similarity of two different clusters. In practice we pursue this objective as follows:

a) the set of data is portioned in two subsets (bisecting procedure) by initially applying an algorithm called PDDP [6] and then the known *k-means* [4] procedure.
b) when advisable one or both clusters obtained as output of step a) are again sub-partitioned in two clusters re-applying PDDP followed by *k-means*.

Obviously, the procedure can be iterated until a suitable number of clusters is obtained.

D. Gene Shrinking

Going through PDDP and K-means, it can be seen that the final data bisection is performed according to the following (linear) classification rule (c_L and c_R are the final centroids returned by the K-means algorithm):

$$\begin{cases} x_i \in X_L & \text{if } \ x_i \cdot u \leq K \\ x_i \in X_R & \text{if } \ x_i \cdot u > K \end{cases} \qquad (1)$$

where $u = (c_R - c_L)/\|c_R - c_L\|$ and $K = 0,5 \cdot (c_R + c_L) \cdot u$.

The problem within this expression is that if the linear inequalities above are referred to the original coordinates (i.e. the genes), we obtain a classifier depending on all the 227 relevant genes, characterizing each patient. This in turn imply that the expression above is of minor interest from a biological perspective as it involves too many genes. For this reason, the classification procedure outlined in Section 4 has been complemented with a "gene shrinking" technique in order to detect which are the (hopefully few) genes actually relevant for the classification.

The approach we propose is the following one. Suppose that vector u above is written as $[u_1, u_2, \ldots, u_{???}]$ where, without any loss of generality, these components are sorted by decreasing values of $|u_i|$. In a sense, $|u_i|$ measures the importance of the ith variable for the classification. Then, we consider $u' = [u_1, \ldots, u_{???-1}, 0]$ in place of u in (1) and search for a partitioning threshold K' ($K' \neq K$ in general) such that the original data partition is preserved. If such K' exist, a new classifier based on (227-1) genes only is obtained. This procedure can be iterated, eliminating one by one all the less relevant component of u. The stopping rule is determined by a certain $u' = [u_1, \ldots, u_{l-1}, 0, \ldots, 0]$ for which no K' preserves the original data partition. This returns $u_1, \ldots, u_l$ as the genes actually relevant for the patient classification.
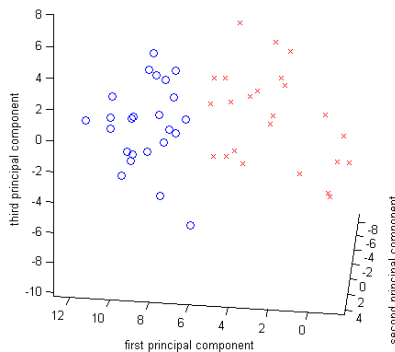
Fig. 1: **PDDP+K-means data partition ("x"=cluster R, "o"=cluster**

III. RESULTS AND DISCUSSION

A. Main splitting

The set of 48 subjects has been first subdivided into two clusters named L and R (each happening to be of the same cardinality of 24 subjects). Such bisection is basically performed orthogonally to the first principal component (Fig. 1), thus simplifying the following "gene shrinking". Interestingly enough, similarities arise between our unsupervised classification form data and a priori clinical classification, the terms of classification showing large difference between cluster L and R, over a large percentage of subjects, being the more interesting ones. Concerning **histology**, we notice that terms 1, 3, and 5 (together including about one third of subjects), mainly belong to cluster L, while

term 2 (even if it would have notable weight) does not provide (like term 4) useful information , because of the almost equal distribution of subjects in both clusters L and R. Finally, it has to be mentioned that subjects classified according to terms 6, 7, 8 and 9 fully belong to cluster R: all these terms are linked to tumour cells grown in vitro, thus it could be argued that cluster R performs a quite effective characterization of in vitro (as opposite of in vivo) assays. This fact could imply that, through the different expression of some genes, it would become possible to verify how the in vitro growth involves different biological gene expression, and a changes the complex partially unknown gene coregulations/pathways, with respect to what happens in vivo;

concerning **response to treatment (without or with platinum and taxolo** the results are comparable, as clinically expected) and there's a significant predominance of cluster L mainly tending to include subjects sensible to treatment, while many "NA" mainly fall in cluster R.

concerning **disease free survival, overall survival, p53 status** and **age at onset** we notice that L mainly clusters both opposite terms, while R is again mainly representative of "NA".

The substantive presence of the "NA" in cluster R is congruent to the fact that such NA labelling for classification types other than histology is quite common for in vitro cells. The final gene-shrinking step leads to a very small number of significant genes needed for such classification, namely 31 genes. The corresponding K' introduced at the end of section II.D after equation 1, through which the classification is made is equal to 2,98. The existence of a complex bio-molecular network of gene co-regulation and of pathways of gene control may explain the need of just a few core genes to identify the edge of classification, being the further information provided by the other genes not any more needed.

B. Second iteration: further splitting

After the first bisection, the PDDP+k-means algorithm has been re-applied once more to both the obtained clusters order to *yield* the sub-clusters named LL ed LR (each with 12 subjects), for the cluster L (as shown in Table 2), and RL (with 11 subjects) and RR (with 13 subjects), for the cluster R. Results in Table 2 suggest the following interpretation:

concerning **histology**, terms 1 and 3, being together more than half of the considered population, account for almost all the subjects clustered in LL, while term 2, accounting for almost all the residual subjects, well belongs to cluster LR, thus appearing to mainly identify type 2, namely *ovarian serous carcinoma*, the most frequent malignant form.in the analyzed context . Incidentally, no subjects belong to types 6, 7, 8, 9, since they have already been all classified in cluster R in the previous step;

concerning **response to treatment (without or with platinum and/or taxol),** and **disease free survival** the results are quite interesting from a prognostic point of view; in fact term A mainly clusters in LR while term B mainly clusters in LL, helping to blindly forecast prognosis;

overall survival, **p53 status** and **age at onset** do not exhibit interesting correlation with clustering instead.

Gene shrinking extracted a number of 98 genes, needed for the sub-clustering of L in LL and LR, then much bigger than the only 31 genes needed at previous step classifying in L and R, probably because a larger quantity of information is required to refine classification.

The sub-clustering of R in RL and RR shows that:

concerning histology, terms 1 and 9 clusters in RL, together with most of the subjects belonging to term 2. Types 4 to 8 belong to cluster RR (types 6 to 8 feature in vitro cells);

concerning response to treatment (without or with platinum and taxolo), disease free survival, overall survival (even if an important presence of terms "NA" has to be taken into account) and p53 status the quite sharp opposition between the high percentage of subjects in cluster RL with response A, as opposite to the high percentage in cluster RR of subjects with response B, is useful in prognosis , while age at onset, whose results are not so well defined, is not.

Gene shrinking reduces to 45 genes the minimal need for clustering R in RL and RR.

A possible further partition of (some of the) four described clusters, that would be of help if more than one type would be almost fully clustered together in only one partition, would not help in the present case, being the data already mostly sparse across clusters.

IV. CONCLUSION

A technique of unsupervised learning has been proposed in order to mine ovarian cancer micro-arrays data with the aim to help to develop a tool able to learn only form gene expression data how to classify the observed variability in ovarian cancer. Such technique basically consists in re- arranging the data in such a way to more easily subsequently prune the redundant information, before clustering and finally coming back to the original frame. Such approach has already proved successful [2] in a simpler problem in this very context, namely classifying leukemia [1]. In that case, better classification with a need of fewer genes was obtained with respect to the original work of Golub and co-workers. The results in the present paper are not equally sharp, probably due to the higher complexity of the problem, together with the present availability of only a few homogeneous samples for each histological type. Nevertheless, the proposed approach was able to suggest some partitioning of interest. In fact, taking into account the two subsequent partition steps described in the previous result section, one can notice that in vitro tumors cluster together in RR, where on the other side a fraction of clear cells and secondary form different tumor also falls, while all borderline alone do constitute cluster RL. For the other types of histology, unfortunately, such a sharp partitioning is not yet available (only a tendency to LL for both not differentiated and endometrial is apparent), nor the minimal set of genes needed for the partitioning seems to be small enough yet to allow direct biological experimentation. Also for prognostic classification, LR is preferred, but not really sensitive nor specific as one would like, when treatment is useful, and survival is improved both on quality and quantity. p53 is slightly more activate in LR. Age at the onset does not really appear to matter.

Further investigation with a more extensive data base is thus needed to assess if the proposed approach, already successful in other problems in some way quite similar to the one under analysis, like also a recent confirmation of a hypothesized pathway in leukemia differential diagnosis [3] could really be of help, maybe together with other methods, in discriminating ovarian cancer histology with a lower need of biological analysis, and/or in suggesting prognosis, and/or in extracting a real core of a few genes whose systems biology could assist in explaining key issues in cancer

REFERENCES

[1] Golub, T.R., D.K. Slonim, P. Tamayo, C. Huard, M. Gaasenbeek, J.P. Mesirov, H. Coller, M. Loh, J.R. Downing, M.A. Caligiuri, C.D. Bloomfield, and E.S. Lander (1999): 'Molecular Classification of Cancer: Class Discovery and Class Prediction by Gene Expression', Science 286:531-537
[2] Garatti S., Bittanti S Liberati D. Maffezzoli A (2007); An unsupervised clustering approach for leukaemia classification based on DNA micro-arrays data, Intelligent Data Analysis 11 (2), 175-188
[3] Grassi S., Palumbo S, Mariotti V, Liberati D et al (2019): The Wnt Pathway is Relevant for the BCR-ABL-1 Independent Resistance in Chronic Myeloid Leukemia, Frontiers in oncology 9, 532
[4] MacQueen, J. (1967): "Some methods for classification and analysis of multivariate observations". In Proceeedings of the Fifth Berkeley Symposium on Mathematical Statistics and Probability, LM LE Cam & J Neyman (eds.), Univeristy of California Press, Berkeley, pp. 291-297.
[5] Hand, D., H. Mannila, P. Smyth (2001). "Principles of Data-Mining". The MIT press, Cambridge, Massachusetts, USA
[6] Boley, D.L (1998). "Principal Direction Divisive Partitioning". Data Mining and Knowledge Discovery, 2(4):325-344.
[7] Savaresi, S.M., D.L. Boley (2001). "On the performance of bisecting K-means and PDDP". 1st SIAM Conference on Data Mining, Chicago, IL, USA, paper n.5, pp.1-14
[8] O'Connel, M.J. (1974), Search Program for Significant Variables, Comp. Phys. Comm. 8, 49.
[9] Golub, G.H., C.F. van Loan (1996). Matrix Computations (3rd edition). The Johns Hopkins University Press

A new motor-driven smart prosthetic socket

L. Paternò[1], C. Quaglia[1], M. Ibrahimi[1], E. Gruppioni[2], L. Ricotti[1] and A. Menciassi[1]

[1]*The BioRobotics Institute, Department of Excellence in Robotics and AI, Scuola Superiore Sant'Anna, Pisa (PI), Italy*
[2]*INAIL Centro Protesi, Budrio (BO), Italy*

Abstract—**Lower residual limbs gradually change in volume overtime, thus affecting the fitting of prosthetic sockets. This is one of the most commonly reported complains from prosthetic users. This work aims at proposing the design and development of a new motor-driven adjustable socket for transfemoral amputees to compensate for limb volume fluctuations. The smart socket includes an inner flexible socket and an outer rigid socket made of four symmetric struts, which are kept together by a tensioning system at the proximal region. Each strut is fixed to an *ad hoc* movable attachment mechanism including a traditional female prosthetic pyramidal adapter to be mounted on different commercial prosthetic knees. The actuation system consists of an electric motor and a reduction gear mechanism, connected to the tensioning system. The actuation is contained in a wearable housing to be carried on the low back of the patient by a belt.**

To test the new socket functionality, a transfemoral residual limb mock-up has been manufactured. The volume of the mock-up can be increased up to +33% of the initial volume thanks to an internal hydraulic chamber. The new socket can compensate for volume fluctuations up to +21.4%.

Keywords— **motor-driven socket, smart prosthetic socket, transfemoral residual limb, volume compensation.**

I. INTRODUCTION

Lower limb amputations affect the quality of life of a significant number of people all over the world. From 2001 to 2010 an average of 11639 people underwent a lower limb amputation each year, only in Italy [1]. Among them, 58.6% were affected by diabetes. The most recent data of the Italian Ministry of Health report that the number of lower-limb amputations was equal to 12115 in the year 2018, with an average age of approximately 80 years [2]. The total number of lower limb amputations is expected to further increase, due to the higher life expectancy and the growing incidence of diabetes and peripheral vascular disease (PVD) [3].

Concerning lower limb prostheses, crucial aspect for patient comfort is the human-machine interface, *i.e.* the prosthetic socket [3]. Several factors influence such an interface: pressures and shear stresses applied on the tissues might lead to dermatological problems; temperature increments due to the artificial socket barrier can compromise the limb thermoregulatory system; volume and shape changes of the residual limb can dramatically affect the fit and the comfort of the prosthesis, both in the short and in the long term.

The socket creates a mechanical coupling between the residual limb and the prosthesis. To do that properly it has to replicate the residual limb shape perfectly and to compensate its volume fluctuations over time [3].

Short term volume fluctuations of transtibial residual limbs have been evaluated by Zachariah *et al.* [4]. A median volume increment of 6.0% ± 3.6% (range: 2.4% ÷10.9%) has been reported, with no consistent differences between proximal and distal areas. Sanders *et al.* [5] measured tissue extracellular fluid volume variations of four transtibial amputees during 5-minutes walking. Test results show a volume change with an absolute median value of 0.5%. Concerning transfemoral residual limbs, the short term volume fluctuations due to physical activity were found in the range from −1.25% to +3.09%, after prosthesis doffing [6]. Over a 6-hours period, they ranged from 0.5% to 7.5% [7]. Long term volume changes can vary from –2.0% to +12.6% (absolute median: 2.1%) over two weeks in transtibial amputees [4], while a case study of a transfemoral amputee wearing a Northwestern University Flexible Sub-ischial Vacuum (NU-FlexSIV) socket over a decade reported a volume change of 31.3% [8].

Based on these values, the need of a prosthetic socket able to adapt to the residual limb volume and to guarantee proper fitting and comfort over time, clearly emerges. The efficacy of a manually adjustable prosthetic socket has already been demonstrated [9]. Anyhow, the main issue of prosthetic users is to identify the correct socket fitting to be applied. An excessive tightening can cause blood occlusions, dermatological problems and volume reductions; while insufficient tightening increases the fall risk and the pistoning effect. Nevertheless, only a few studies have been dedicated to the design of an automatic adjustable prosthetic socket system [3]. Automatic sockets that adjust liquid within bladders, pads or other inserts have been proposed, but they cannot allow uniform deformations, uniform stress distributions, and adequate stability. For this reason, the most promising automatic adjustable socket solutions in the state-of-the-art are the ones based on motor-driven adjustable mechanisms; they are composed of one or more moving panels in the socket structure controlled by a motor actuation system linked to a tensioning mechanism [10]. However, only solutions for transtibial amputees have been investigated and no studies have been found in the state-of-the-art about motor-driven adjustable sockets for transfemoral patients, who undergo significant volume fluctuations as well. Also, these transtibial solutions are based on cabled-panel adjustable designs, which allow for the compensation of limb volume fluctuations only in the specific residual limb areas covered by the panels. This can lead to non-uniform stress distributions on tissues.

This paper presents a new motor-driven adjustable socket for transfemoral amputees, based on four rigid struts that can adapt to the residual limb volume changes over time.

II. MATERIALS AND METHODS

A. Smart prosthetic socket

A new smart prosthetic socket for transfemoral amputees has

been designed to provide compensation to residual limb volume fluctuations. The proposed socket can be divided into three main components (Fig. 1): the socket, the movable attachment mechanism to be mounted on the prosthetic knee and the actuation system.
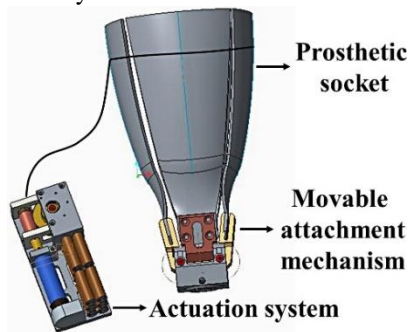

Fig. 1. Design of the new smart prosthetic socket proposed in this paper.

1) Socket

Differently from previous works, grounded on traditional manual cabled-panel adjustable socket, in this work a different structure is proposed to allow for the volume compensation of the overall residual limb. The proposed new socket is characterized by a sub-ischial design which has been obtained following the rules described in [11] to fabricate the new NU-FlexSIV Socket. The sub-ischial design is characterized by lower proximal trim lines that do not intimately interact with the pelvis. However, based on patient's requirements, also more traditional designs (*e.g.* Quadrilateral or Ischial Containment Sockets) can be used.

The socket includes a flexible inner socket and a rigid outer socket as shown in Fig. 2. The inner socket (white socket in Fig. 2) is made of Flex Ethyl Vinyl Acetate (EVA-Flex, Össur Europe BV, Italy). It was manufactured by thermoforming technique on the positive cast of a transfemoral residual limb, provided by a prosthetic center. Subsequently, the structure was cut in a symmetrical 'flower' shape with gradually flattened edges to avoid high pressures due to the uneven internal surface. The outer socket is a carbon-fiber-laminated socket (black socket in Fig. 2), made of four symmetrical struts, to be fixed at their distal end into specific enclosures of the movable attachment.
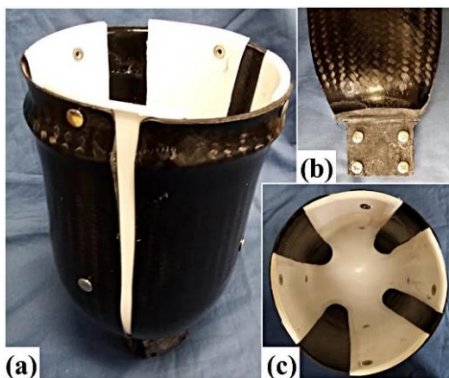
Fig. 2. (a) The new socket composed by an inner flexible socket (white) and an outer carbon-fiber-laminated rigid socket (black). (b) Distal end of one outer rigid strut which has to be fixed in the specific enclosure of the movable attachment mechanism. (c) Internal surface of the new socket.

The rigid socket was manufactured by a traditional

lamination process, which also guarantees a more lightweight solution. In order to optimally fit the struts at their distal ends in the attachment enclosures, an *ad hoc* template was designed to be positioned at the apex of the residual limb positive cast (Fig. 3a). The scan of the positive cast with the flexible socket was acquired by a 3D optical scanner (GO!SCAN50, Creaform, Inc., Lévis, CA). Then, a boolean subtraction between the template CAD and the scan was done in Netfabb as in Fig. 3b. This allows accurate positioning of the template on the cast apex and, subsequently, an accurate coupling of the socket to the movable attachment. However, for very long residual limbs, it could be insufficient and other designs have to be used.

The final template was fabricated by ProJet 3600 HD Max (3D Systems, USA) 3D printer, lubricated by a PTFE (Teflon) spray (VMDITALIA, Italy) and placed at the apex of the positive cast (Fig. 3c). In addition, before starting the lamination, a plastic tube was positioned at the proximal region of the positive cast between the carbon laminates. This allowed for creating an empty space for the next integration of the Bowden cable of the tensioning system.

Once manufactured, the socket was cut into four symmetric struts to allow relative movements and to guarantee the traditional medio-lateral and antero-posterior grips of the socket design (Fig. 2). A Bowden cable was finally mounted.
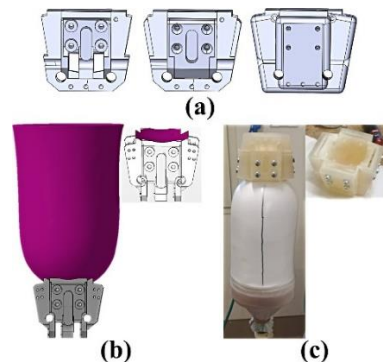

Fig. 3. (a) CAD of the template for the lamination process, designed to obtain the rigid distal ends of the outer socket struts. (b) Boolean subtraction between the scan of the residual limb positive cast and the template; c) 3D printed template positioned on the distal apex of the positive cast with the inner flexible socket.

2) Movable attachment mechanism

The movable attachment mechanism is composed of four parts able to rotate thanks to rotary joints linked to a fixed base (Fig. 4).
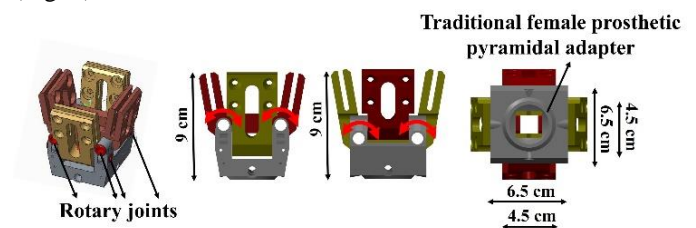

Fig. 4. CAD of the movable attachment mechanism.

Each movable part is fixed with four M5 screws to the struts of the outer rigid socket (Fig. 5a), thus allowing the regulation of their positioning when the length of the Bowden cable is changed.
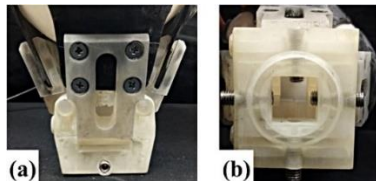
Fig. 5. (a) Preliminary prototype of the movable attachment mechanism, manufactured by 3D printing. (b) The new attachment replicates in the bottom part a traditional female prosthetic pyramidal adapter.

The bottom part base of the attachment replicates a traditional female prosthetic pyramidal adapter to facilitate the integration of the new smart socket with different prosthetic knees (Fig. 5b). In order to preliminary test the system, a prototype of the movable attachment mechanism was 3D printed; the final movable attachment will be made of titanium alloy, to optimize weight and strength.

3) Actuation system

The actuation system is used to change the Bowden cable length/ tension and, consequently, to adjust the socket size thanks to the rotary joints of the new attachment. It consists of an electric 23 mm diameter Faulhaber motor with a maximum torque of 0.02 Nm and a reduction gear system that can pull/ push the Bowden cable positioned all around the proximal rigid socket struts (Fig. 6).
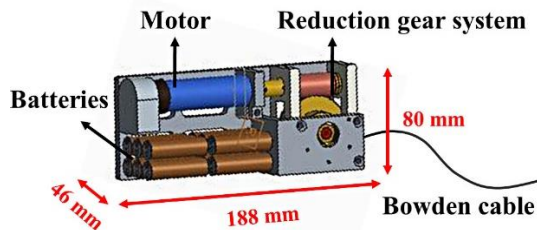
Fig. 6. CAD of the actuation system of the smart socket.

The actuation system is contained in a specific housing that the patient can wear around the low back thanks to a belt. The housing was 3D printed and the actuation system was assembled inside it (Fig. 7).

The final smart prosthetic socket system is shown in Fig. 7. The weight of the socket and movable attachment mechanism was 1.9 kg (Table I), which is acceptable for clinical use. Indeed, it was evaluated that an increment of up to 2.5 kg did not significantly affect the walking parameters [12]. The socket could change the length of the Bowden cable and, then, the socket diameter, of around 10 cm, modulating its volume in the range from 2.8 dm^3 to 3.4 dm^3, also thanks to the movable attachment at the distal base, which can rotate of an angle of 30 degrees.
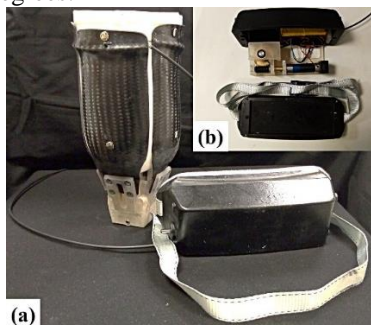

Fig. 7. (a) The final prototype of the new smart prosthetic socket and (b) the actuation system.

TABLE I
WEIGHT OF THE SMART SOCKET COMPONENTS

Components	Weight (g)
Socket	770
Movable attachment mechanism	1130
Actuation system (electric motor)	700 (195)
Total system	2600

B. Transfemoral mock up to mimic residual limb volume fluctuations

To test the performances of the smart prosthetic socket, an *ad hoc* transfemoral residual limb mock-up capable of changing its volume was developed. It allowed to effectively simulate volume fluctuations affecting transfemoral residual limbs and to assess the new socket compensation capabilities.

An anatomical functional model of the hip joint was used to reproduce the skeletal structure (NS 51, SOMSO-PLAST®, Sonneberg, Germany) (Fig. 8a). This functional model can perform the ante-version, retro-version, abduction, inner and outer rotation of the thigh. The muscles, fat, and skin were made of silicone materials, which highly mimic the mechanical properties of lower residual limb tissues [13]. To reproduce muscles, specific molds were fabricated by wrapping plaster bandages around the muscle replica of an anatomical leg model. Once the plaster dried, the muscles replica were removed obtaining the final molds for the silicone curing (Fig. 8b). Then, the silicone Dragon Skin 20 colored with pink Silc Pig (Smooth-on Inc., Macungie, PA) was poured into the molds (Fig. 8b).

Fig. 8. (a) Anatomical functional model of the hip joint. (b) Example of a plaster mold. (c) Manufactured silicone muscle.

The muscles were fixed in position on the hip model and put within the negative cast of the patient's residual limb. The internal surface of the negative cast was covered with a 5 mm-thick plastic layer and, then, filled with silicone Ecoflex 0010 (Smooth-on Inc., Macungie, PA) to simulate the fat tissue. Then, such a plastic layer was removed and the external surface of the fat was covered with a 1 mm-thick plastic layer. The space was filled with Dragon Skin 10 to simulate the skin. When it was poured, the 1 mm-thick plastic layer was removed thus obtaining an empty chamber for the fluidic actuation. The chamber was sealed by using the silicone glue Sil-Poxy (Smooth-on Inc., Macungie, PA) and two 5 mm tubes were connected to the chamber. A prosthetic Silcare Breathe Liner (Endolite, Blatchford Products Ltd, United Kingdom) was rolled on the final limb mock-up (Fig. 9).
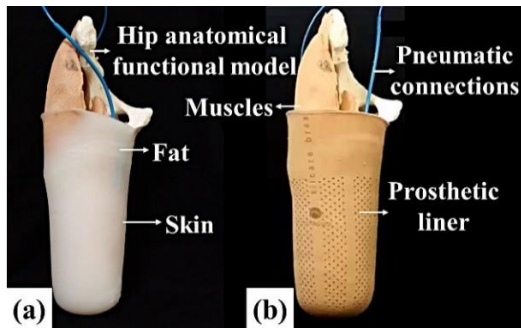
Fig. 9. Transfemoral residual limb mock up without (a) and with (a) the prosthetic Silcare Breathe Liner.

To test the volume change capability of the limb mock-up, the pneumatic tubes were connected to an air compressor (JUNIOR 30; ABAC) and the imposed inlet pressure was read through a digital pressure sensor (Series SWCN; Camozzi spa).

III. RESULTS

The transfemoral residual limb mock-up was able to change its volume in the range:

$V_0 = 5.1$ dm^3 at P = 0 bar;

$V_{max} = 6.8$ dm^3 at P = 1.5 bar;

allowing for a volume fluctuation up to +33%. The final bench test system including the new smart socket and the transfemoral residual limb mock-up is shown in Fig. 10.

By using a piezoresistive pressure sensor (Tekscan, model 5101) at the mock-up/ socket interface it was possible to verify that the new smart socket could follow the volume changes of the residual limb mock-up, adjusting the length of the Bowden cable by manually activating/ deactivating the actuation system (Fig. 10). This may enable, in the future, an optimal control of the stresses applied to the tissues in order to avoid dermatological problems.
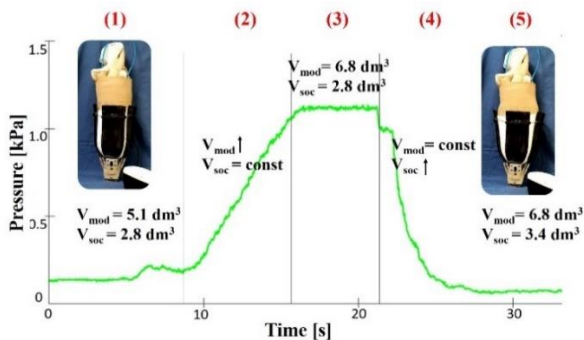
Fig. 10. Pressure curve measured at the residual limb model/ socket interface: (1) At the beginning, the residual limb model volume (Vmod) and the socket volume (Vsoc) were constant at their initial value. (2) Then, the model was inflated reaching its maximum volume and causing a pressure increment followed by (3) a constant trend. (4) The Bowden cable length of the smart socket was regulated for the volume adaptation of the socket to the limb, reducing the interfacial pressure and (5) reaching again the initial pressure value.

IV. CONCLUSION

The design and development of a smart motor-driven prosthetic socket for transfemoral amputees has been presented compensating the volume fluctuations of a residual limb mock-up overtime. The socket volume could be regulated between 2.8 dm^3 and 3.4 dm^3 thanks to a movable attachment that can rotate of 30 degrees and a tensioning mechanism, whose length is tuned by the actuation system contained in a wearable housing. The length of the Bowden cable could be varied by 10 cm, thus regulating the socket struts position thanks to the movable attachment at the distal base. This allowed the compensation of a maximum volume fluctuations equal to +21.4%.

Future efforts will be focused on the integration of a sensorized liner able to measure pressures applied on tissues. By implementing an automatic volume control based on a specific pressure threshold, it will be possible to obtain a self-adaptation of the socket to interfacial pressures, thus compensating the volume changes in real-time and in closed-loop.

REFERENCES

[1] F. L. Lombardo, *et al.*, "Lower Extremity Amputations in Persons with and without Diabetes in Italy: 2001–2010," *PLoS One*, vol. 9, no. 1, p. e86405, Jan. 2014.

[2] "Statistiche sull'incidenza delle amputazioni in Italia: analisi dati SDO del Ministero della Salute anni 2010-2018." INAIL, Direzione centrale assistenza protesica e riabilitazione, 2019.

[3] L. Paterno,*et al.*, "Sockets for Limb Prostheses: A Review of Existing Technologies and Open Challenges," *IEEE Trans. Biomed. Eng.*, vol. 65, no. 9, pp. 1996–2010, Sep. 2018.

[4] S. G. Zachariah, R. Saxena, J. R. Fergason, and J. E. Sanders, "Shape and volume change in the transtibial residuum over the short term: Preliminary investigation of six subjects," vol. 41, no. 5, pp. 683–694.

[5] J. E. Sanders, D. S. Harrison, K. J. Allyn, and T. R. Myers, "Clinical Utility of In-Socket Residual Limb Volume Change Measurement: Case Study Results," *Prosthet. Orthot. Int.*, vol. 33, no. 4, pp. 378–390, Dec. 2009.

[6] L. Paternò, M. Ibrahimi, E. Rosini, A. Menciassi, and L. Ricotti, "Transfemoral residual limb volume change due to physical activity," in *Biosystems and Biorobotics*, vol. 21, Springer International Publishing, 2019, pp. 146–150.

[7] M. Staker, K. Ryan, and K. LaBat, "Medicine and Design Investigate Residual Limb Volume Fluctuations: Three Case Studies," *Australas. Med. J.*, pp. 156–161, Nov. 2008.

[8] S. Fatone, J. Yohay, and R. Caldwell, "Change in residual limb size over time in the NU-FlexSIV socket: A case study.," *Prosthet. Orthot. Int.*, vol. 42, no. 6, pp. 620–625, Dec. 2018.

[9] J. T. Kahle, T. D. Klenow, and M. J. Highsmith, " Comparative Effectiveness of an Adjustable Transfemoral Prosthetic Interface Accommodating Volume Fluctuation: Case Study ," *Technol. Innov.*, vol. 18, no. 2, pp. 175–183, Sep. 2016.

[10] J. E. Sanders *et al.*, "A motor-driven adjustable prosthetic socket operated using a mobile phone app: A technical note," *Med. Eng. Phys.*, vol. 68, pp. 94–100, Jun. 2019.

[11] S. Fatone and R. Caldwell, "Northwestern University Flexible Subischial Vacuum Socket for persons with transfemoral amputation-Part 1: Description of technique.," *Prosthet. Orthot. Int.*, vol. 41, no. 3, pp. 237–245, Jun. 2017.

[12] R. W. Selles, *Weighing weight : effect of below-knee prosthetic inertial properties on gait*. 2002.

[13] J. L. Sparks *et al.*, "Use of Silicone Materials to Simulate Tissue Biomechanics as Related to Deep Tissue Injury," *Adv. Skin Wound Care*, vol. 28, no. 2, pp. 59–68, Feb. 2015.

Design of novel ventricular chambers: comparison of three different models

V. Candela[1], M. Todesco[1], G. Meneghetti[1], A. Fabozzo[2], G. Gerosa[2], A. Bagno[1]

[1] *Department of Industrial Engineering, University of Padua, via Marzolo 9, 35131, Padova, Italy*
[2] *Department of Cardiac, Thoracic and Vascular Sciences, University of Padova, via Giustiniani 2, 35127, Padova, Italy*

Abstract — **Mechanical circulatory supports have to be carefully designed with the aim of increasing hemocompatibility and avoiding blood stagnation to prevent thromboembolic events. Explicit FEM analysis of three different designs was preliminary performed by means of LS-DYNA to assess pros and cons of each model. A hemocompatible polycarbonate urethane was chosen to simulate material's mechanical characteristics.**

Keywords— **ventricular chamber, FEM analysis, design, LS-DYNA.**

I. INTRODUCTION

TOTAL ARTIFICIAL HEARTS, also known as TAHs, are mechanical circulatory supports that replace biological hearts in case of refractory end-stage heart failure [1]. TAHs are mostly applied as bridge-to-transplantation devices, but they are currently receiving a growing interest as destination-therapy solutions; indeed, many drawbacks are still limiting their exploitation (i.e. dimensions, power supply, cardiac output, …).

Nowadays, CardioWest TAH represents the only device that already received the FDA approval and CE mark: up to date, it has been implanted in more than 1300 patients [1]. Another promising device is the Carmat TAH, which is equipped with highly sophisticated electronics [2]. These two TAHs share the same working principle: their ventricular chambers are made of a rigid dome and a flexible membrane; the back and forth motion of the membrane produces systolic and diastolic effects, making the blood flow possible. This design assures the pulsatile flow, but many researchers are currently evaluating the possibility to use non-pulsatile pumps, i.e. rotary ones. These latter come from the success of rotary Left Ventricular Assist Devices (LVADs). The possibility to sustain life without a physiologic blood flow was confirmed by Golding et al. in 1980 [3], but the long-term usage of a continuous flow pump can lead to many collateral risks, such as microvascular dysfunction and haemorrhages [4].

Through a preliminary FEM analysis, the present work investigates three different ventricular chamber's geometries as possible innovative solutions for a novel pulsatile device. The simulated material is a polycarbonate urethane (PCU), well known for its bio- and hemocompatibility.

The computational analysis aimed at examining the tensile state of stresses and deformations generated in the material during one systolic and diastolic cycle: too high stresses or strains can result in the early failure of the device.

The simulations showed how to improve the design of the pulsatile chamber.

II. MATERIALS AND METHODS

A. 3D models

Three different linear geometries were developed starting from an initial concept of a bellow-like pump [5]. The original sketch shows an ellipsoidal flexible chamber provided with two one-way heart valves. Compression and expansion of the chamber (thanks to an electromagnetic actuator) operates the motion of the chamber; valves assure the correct blood flow. 3D real-scale models were created using AutoDesk Fusion 360.

The first model has a three-sphere-shaped geometry (Figure 1): two one-way heart valves (21 mm) are located inside the necks between the central chamber and the lateral ones. The second model (Figure 2) was designed to avoid excessive radial expansion when the central chamber reaches maximum axial compression. In this case, valves (31 mm) are placed at the level of the two rigid plates. The third model (Figure 3) is aimed at eliminating the rigid plates: this is possible thanks to a pair of specifically–designed valves (50 mm). In this configuration, valves are able to compress the rib in the middle, working as the plates work in the previous models. Thus, this geometry does not produce excessive radial expansion.

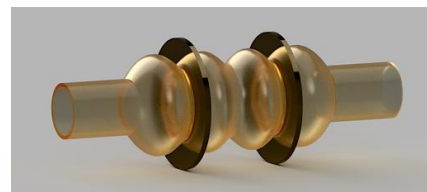Fig.1: First model: two rigid plates compress the central compartment

Fig. 2: Second model: it avoids excessive radial expansion

Fig. 3: Third model: the use of rigid plates is not necessary

B. Element formulation

The geometry of each chamber was imported in LS-DYNA Pre-Post. Each chamber was approximated as a thin-wall object and shell elements (2 mm thick) were used. The plates were idealized as rigid bodies: a solid elements mesh was used for these components.

The prototype's material was described trough *MAT_MOONEY-RIVLIN_RUBBER model (Material Type 27) to simulate the rubber-like behaviour of the PCU. The rigid plates were described with *MAT_RIGID (Material Type 20), inputting the properties of Aluminium (i.e. Young's Modulus, Poisson's ratio and density). Viscoelastic effects are considered.

C. PCU mechanical properties

The mechanical characterization of PCU (ChronoFlex AR-LT, AdvanSource Biomaterials, Wilmington, MA, US) was fundamental to get the data that were used in the material's cards (data not shown). Uniaxial tensile test was performed (with an elongation rate of 1 mm/s) using dog bone shaped sample. The acquired stress-strain engineering curve was uploaded in LS-DYNA. The Poisson's ratio was also measured: during the tensile test thickness, width and gage length were taken at different elongations using a digital caliber. The average value of the Poisson's ratio was used in the material's card in LS-DYNA. A density of 1200 kg/m^3 was considered.

D. Contacts and constrains

Contacts are necessary to avoid elements penetration: to this purpose AUTOMATIC_SINGLE_SURFACE and AUTOMATIC_SURFACE_TO_SURFACE were defined for preventing penetration between shell elements, and shell and solid elements, respectively.

In the models provided with the rigid plates, another contact was defined: TIED_NODES_TO_ SURFACE. It allowed to stick the prototype's nodes set (corresponding to the valve's region, this set is the slave part) to one of the two plates (master part); this contact was useful for avoiding any kind of sliding between the ventricular chamber and the plates.

Translation and rotation of the nodes/elements of the cylindrical regions were constrained in all directions: in fact, these parts will be fixed to the chassis of the device. Moreover, the rigid plates/valve locations are free to move back and forth only following the pump axial direction. Constrains are represented in Figure 4.
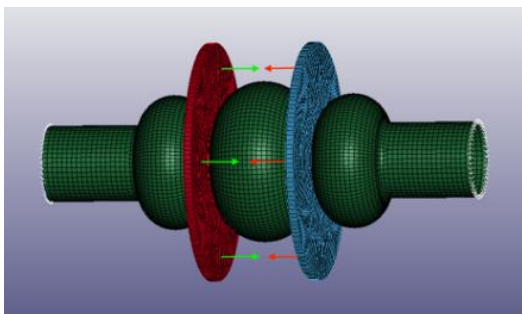

Fig. 4: Constrains are applied to the first model: to the cylindrical extremities (white rings) and to the moving plates (green and red arrows). Plates can get back to the original position)

E. Actuation

In order to mimic the actuation of each prototype, the symmetric motion of the rigid plates (or of the valves) was defined: a displacement vs. time curve was associated to the moving components using BOUNDARY_PRESCRIBED_ MOTION. A preliminary assessment was aimed at estimating the capacity of the prototypes to withstand the imposed displacement of the valves/rigid plates after one cycle. The critical state of stress and highest strains were identified to check if they are low enough for a possible fatigue analysis. The study was carried out without considering fluid dynamics.

The movement of the plates/valves is very fast: they need to go forth and back at least 2 times per second to achieve a minimum flowrate of 5 L/min. The prototypes have an internal capacity from 60 mL to 70 mL and the internal fluid is supposed to be not completely ejected.

III. RESULTS

A. Stresses and strains

The three-sphere-shaped prototype (Figure 5) reached less than 1 MPa stress (von Mises stresses are illustrated in the legends of Figures 5, 6 and 7) when the central chamber is completely flattened, with a maximum engineering strain of 18.3%. These values are low, but the diameter of the central compartment largely increased during compression: from 66 to nearly 80 mm. For this reason, this model was discarded.

The second prototype (Figure 6) developed 0.9 MPa and a strain of 19.5% in the necking region between the two rigid plates. This model negligibly increased its maximum diameter (from 55 to 57 mm) and it will be considered for further investigations.

The last model (Figure 7) did not appreciably change its diameter (from 60 to 65 mm), but it showed much higher stresses and strains with respect to the first two prototypes: 3.5 MPa with an engineering strain of 60%. These values were reached because of the design of the lateral compartments: the motion of the two valves caused an intensive stretch in these regions during the chamber's compression. However, stresses and strain can be reduced by modifying the geometry of these regions.

IV. CONCLUSION

This preliminary computational analysis of three different ventricular chambers allowed identifying the most suitable geometries. In particular, the second model assures a negligible increase of diameter and low stresses; the third model has to be re-designed to reduce stresses and deformation.

Further analyses are needed, in particular fatigue tests and fluid dynamics simulations, before moving to the production of a real prototype for the functional trials. These latter will validate the numerical models and will be performed by means of a mock circulatory loop reproducing several hemodynamic conditions.

Current investigations are aimed at identifying the best geometry for the development of an innovative TAH: its major novelty will be due to the composition of the inner chamber coating. The chamber will be fabricated by coupling a

polymeric material (polycarbonate urethane), which is responsible for the mechanical resistance, with a biological decellularized tissue (animal pericardium), which is in direct contact with blood. The biological layer will assure high hemocompatibility, also being prone to endothelialization by circulating cells.
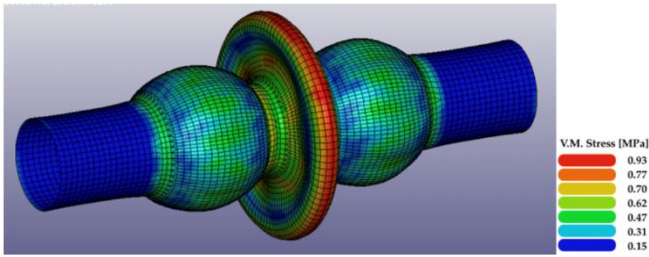

Fig. 5: First model: effective stresses when the ventricular chamber is flattened (the rigid plates are not shown): maximum values are in red
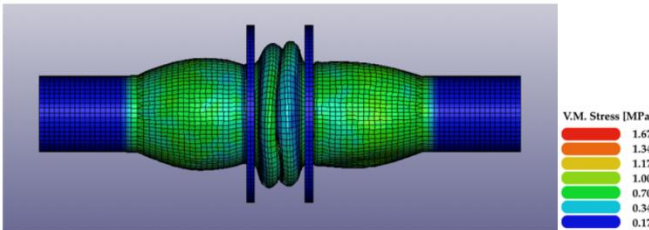

Fig. 6: Second model at the maximum compression: stresses are shown. The highest values are in the middle of the two ribs
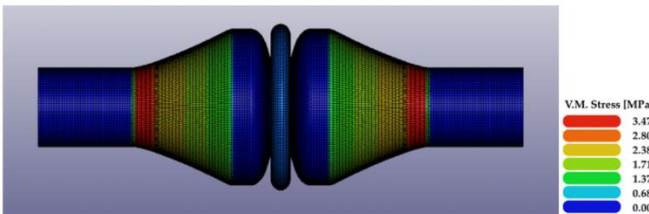

Fig. 7: Third model at the maximal compression: stresses of 3.5 MPa are in red

V. CONCLUSION

This preliminary computational analysis of three different ventricular chambers allowed identifying the most suitable geometries. In particular, the second model assures a negligible increase of diameter and low stresses; the third model has to be re-designed to reduce stresses and deformation.

Further analyses are needed, in particular fatigue tests and fluid dynamics simulations, before moving to the production of a real prototype for the functional trials. These latter will validate the numerical models and will be performed by means of a mock circulatory loop reproducing several hemodynamic conditions.

Current investigations are aimed at identifying the best geometry for the development of an innovative TAH: its major novelty will be due to the composition of the inner chamber coating. The chamber will be fabricated by coupling a polymeric material (polycarbonate urethane), which is responsible for the mechanical resistance, with a biological decellularized tissue (animal pericardium), which is in direct contact with blood. The biological layer will assure high hemocompatibility, also being prone to endothelialization by circulating cells.

REFERENCES

[1] T. Lee, G. Torregrossa (2018), Total Artificial Heart – Encyclopedia of Cardiovascular Research and Medicine, *Elsevier Inc*, pp. 545-557.
[2] A. Carpentier, C. Latrémouille, B. Cholley, D.M. Smadja, J.C. Roussel, E. Boissier, J.N. Trochu, J.P. Gueffet, M. Treillot, P. Bizouarn, D. Méléard, M.F. Boughenou, O. Ponzio, M. Grimmé, A. Capel, P. Jansen, A. Hagège, M. Desnos, J.N. Fabiani, D. Duveau (2015), First clinical use of a bioprosthetic total artificial heart: report of two cases, *Lancet*, vol. 386, pp. 1556-1563.
[3] P.A. Smith, W.E. Cohn, O.H. Frazier (2018), Total Artificial Heart, Mechanical Circulatory and Respiratory Support, *Academic Press*, pp. 221-244.
[4] J. Vašku, J. Wotke, P. Dobšák, A. Baba, A. Rejthar, Š. Kutchtíčková, K. Imachi, Y. Abe, I. Saito, T. Isoyama, S. Nitta, T. Yambe (2007), Acute and chronic consequences of non-pulsatile blood flow pattern in long-term total artificial heart experiment, *Pathophysiology*, vol. 14, Issue 2, pp. 87-95.
[5] S.T.G. Scuri, F. Mantovani, T. Perlato, G. Gerosa, F.M. Susin, inventors, E. Tomasi, S.T.G. Scuri, F. Mantovani, T. Perlato, G. Gerosa, Iguzzini Illuminazione S.P.A., applicants, Artificial Heart. United States patent US 2016/0310651A1. 2016 October 27.

A Dual-Branched Convolutional Neural Network for P300 detection and feature interpretation

D. Borra[1], S. Fantozzi[1], and E. Magosso[1]

[1] *Department of Electrical, Electronic and Information Engineering "Guglielmo Marconi" (DEI), University of Bologna*

Abstract— **Brain-Computer Interfaces rely on machine learning algorithms to decode electroencephalographic (EEG) signals. Advances in machine learning – as represented by Convolutional Neural Networks (CNNs) – were recently applied to EEG signals to decode the P300 evoked response with outstanding results. In this study, a novel multi-scale CNN was proposed and compared with several CNNs designed for P300 detection. These algorithms were applied to a large cross-session P300 dataset. The proposed CNN provided higher accuracy, on average 95.3% across subjects. Furthermore, the interpretation of the learned features was provided via saliency maps.**

Keywords—**Convolutional neural networks, electro-encephalogram, P300, saliency maps.**

I. INTRODUCTION

THE P300 evoked response is an attention-dependent event-related potential (ERP) first reported in the electroencephalographic (EEG) signals by Sutton et al. [1]. This ERP component is characterized by a positive deflection peaking between 300 and 450 ms after the stimulus onset and can be evoked in an oddball paradigm, where an infrequent stimulus (target) is presented to the user immersed in a sequence of frequent stimuli (background). Topographically, the P300 is most pronounced around the midline EEG electrodes, with maximum amplitudes in the parietal region [2]. This response can be used as neural signal in Brain-Computer Interfaces (BCIs) [3]. For example, in recent years, P300-based BCIs have been proposed to provide an alternative way of communication for patients with an impaired muscular control [4], and to improve social attention skills in Autism Spectrum Disorder (ASD) [5]. Traditional BCI paradigms for P300 detection include feature extraction and selection stages, manually designed according to experience, and traditional machine learning algorithms (e.g. support vector machines and linear discriminant analysis). However, feature extraction is hypothesis-driven and a strong a priori knowledge about the EEG signals is exploited to design the features. Furthermore, the feature extraction and classification steps are performed separately, thus the extracted features may not be optimal for classification. Recently, Convolutional Neural Networks (CNNs) have achieved outstanding results in computer vision applications, especially with images and time series [6]. CNNs automatically extract features from the data maximizing the between-class discriminability and finalize the classification task in an end-to-end fashion from raw/light pre-processed inputs. Despite these advantages, CNNs include some drawbacks such as the lack of direct interpretability of the extracted features and the introduction of a large number of trainable parameters. In order to interpret CNN features, several post-hoc interpretation techniques (i.e. methods to be applied after the network parameter optimization) were proposed for computer vision to explain the relevant features that drive the CNN decision [7]. The gradient of the CNN output with respect to its input example, named saliency map, is a straightforward representation of the relevant features that drive the CNN decision.

Cecotti et al. [8] first developed a 5-layer CNN for P300 detection. This architecture was the first of a series of models in which the convolution along the spatial dimension is performed at first and then along the temporal dimension. Recent advances in these models include the use of parallel temporal convolutions in order to extract multi-resolution temporal patterns (see BranchedNet [9]) in the deeper layers. Alternative solutions were then proposed, moving the temporal convolution to the shallower layers as a mixed spatio-temporal convolution (see OCNN [10]) or as the first layer before the spatial filtering (see EEGNet [11]). In addition, EEGNet introduced non-standard convolutional layers such as depthwise and separable convolutions, that reduce the number of trainable parameters. Recently, we proposed a CNN based on EEGNet for the P300 detection challenge promoted by the International Federation of Medical and Biological Engineering (IFMBE https://www.medicon2019.org/scientific-challenge/). The proposed solution [12] ranked 1st, its accuracy beating by >8% other algorithms, including deeper CNNs [13] with more trainable parameters, and traditional machine learning pipelines.

Exploring novel CNN architectures is of relevance not only as to the methodological aspects (to improve the theoretical insights into design principles of CNN for EEG decoding) but also as to basic knowledge (to increase our comprehension of the neural correlates underlying the decoded classes, via interpretation of extracted features), as well as for its practical impacts on BCI-based cognitive and motor rehabilitation.

In this study, we present a novel CNN architecture based on the main recent advances for P300 detection. This architecture modifies EEGNet by including - downstream the shallow temporal and spatial convolution layers - two separated branches (similarly as in BranchedNet [9]) extracting temporal patterns at two different resolutions and using this multi-resolution information for classification. The performance of this architecture has been compared to other state-of-the-art CNNs on a large P300 dataset. Moreover, saliency maps are used to explain the most relevant temporal and spatial features that drive the discrimination between the P300 and non-P300

response in the proposed CNN.

II. METHODS

A. Dataset

The dataset was made available by IFMBE for the 2019 Scientific Challenge Competition (https://www.medicon2019.org/scientific-challenge/). It was obtained in a feasibility clinical trial in which a P300-based BCI was tested on 15 youngsters with ASD to follow social cues [5] provided to the user in a virtual environment with 8 flashing objects. Each participant's dataset was acquired during 7 recording sessions; each session contained calibration data (20 blocks of recordings) and online data (50 blocks). Each block contains a repetition of N runs (N=10 for the calibration data and N varies across sessions for the online data). In each run, 8 trials were acquired; in each trial one of the 8 objects flashed in the virtual environment. Only one of these trials contained the P300 response and was related to the target object the user was looking at. All runs within the same block were associated to the same target object to decode. The overall session data contains an important class unbalancing (7:1 for the non-P300 and P300 classes). Signals were recorded at 250 Hz from 8 electrodes (C3, Cz, C4, CPz, P3, Pz, P4, POz) and the reference was placed at the right ear and the ground electrode at AFz. These signals were notch filtered at 50 Hz and filtered between 2 and 30 Hz.

B. Pre-processing

Epochs were defined from -100 to 1000 ms relative to the event stimulus. Furthermore, to reduce the computational cost, signals were downsampled at 128 Hz. Thus, the resulting single trial had shape of (1,8,140), representing the CNN input. We adopted a cross-session training strategy to augment the dataset, i.e. the trials of a specific subject were merged together across sessions (31066±2218trials, mean±std. dev. across participants).

C. Branched-EEGNet

Inspired by recent innovations in terms of multi-scale temporal pattern extraction (BranchedNet [9]) and architecture compactness (EEGNet [12]), a dual-branched EEGNet (named Branched-EEGNet) was designed to decode the P300 evoked response at the single trial level. The proposed network is composed by 4 main blocks (named "branches") as represented in Fig. 1. A *common branch* learned 8 frequency filters with shape (1,65) in the temporal convolutional layer ("Conv2D" in Fig. 1), and then the spatial depthwise convolutional layer ("DepthConv2D" in Fig. 1) learned 2 frequency-specific spatial filters with shape (8,1) for each temporal filter (i.e. a total number of 16 filters). These first two layers provided a straightforward way to learn frequency-specific spatial filters. Lastly, the neurons of the spatial filtering layer were activated with an Exponential Linear Unit (ELU) function $(f(x) = x, x > 0$ and $f(x) = \exp(x) - 1, x \leq 0)$, average pooled ("AvgPool2D" in Fig. 1) with a pool size of (1,4) and a dropout layer was included to increase the generalization capability. The output of this branch had shape (16,1,35). Subsequently, temporal patterns at two different scales were learned via separable convolutions ("SepConv2D" in Fig. 1) from the frequency-specific spatial activations. The

high-resolution branch learned temporal patterns on roughly 150 ms of the common branch output, while the *low-resolution branch* on roughly 500 ms (this was the temporal kernel size in the original EEGNet [11]). The small and large kernels should be able to learn high and low frequency patterns from the input, respectively [9]. Furthermore, the ratio between the small and large kernel sizes used here was approx. the same as in BranchedNet [9] (i.e. 1/4, keeping odd kernel sizes). Then, the neurons of these layers were activated via an ELU function, average pooled with a pool size of (1,8) and a dropout layer was also included. At the end of these parallel temporal convolutions, the *classification branch* finalizes the decoding task by concatenating the features at different scales (i.e. multi-scale features with shape (32,1,4)), unrolling the values along one single dimension and using a single fully-connected layer containing 2 neurons, one for each class (P300 and non-P300 classes). To output conditional probabilities $P(y = 0|\mathbf{X})$ and $P(y = 1|\mathbf{X})$, where y is the output category ("0" non-P300, "1" P300) and $\mathbf{X}$ the input trial, the neurons of this densely connected layer were activated with a softmax activation function.
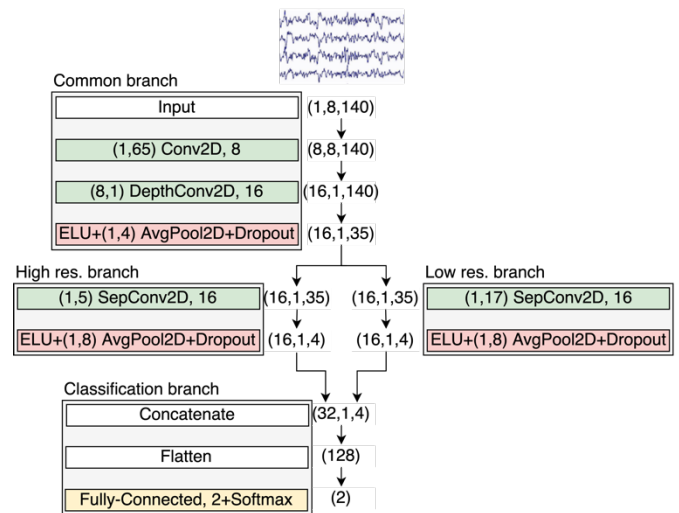

Fig. 1: Branched-EEGNet. The main layers are represented in boxes and the corresponding output sizes are displayed in brackets. Each convolutional layer (green boxes) is followed by a batch normalization layer.

All convolutions were performed with a zero-padding such that the output dimension matches with the input dimension. After each convolutional layer, a batch normalization layer was added to improve the generalization. The dropout rate was set to 0.25 as in [12] for cross-session trainings. The weights and biases were randomly initialized with a Xavier uniform initialization scheme and to zero, respectively. The cross-entropy between the empirical probability distribution defined by the training labels and the probability distribution defined by the model was minimized via Adam with a learning rate of 1e-3, a mini-batch size of 64 and a maximum number of epochs of 500. To address the class unbalance, a single mini-batch of data was composed by a proportion of 50–50% of the two classes randomly selecting the trials within the dataset. To increase the generalization capability and reduce the computational time, early stopping was performed, by interrupting the optimization when the validation loss did not decrease for 50 consecutive epochs.

D. Performance evaluation

In addition to Branched-EEGNet, other CNNs were re-implemented and compared to the proposed architecture. These included OCNN [10], BranchedNet [9] and EEGNet [12] with the hyper-parameters set as in the original papers. The total number of trainable parameters was 1650, 5418, 1386, 1882, respectively for OCNN, BranchedNet, EEGNet, Branched-EEGNet. The networks were compared using a Wilcoxon signed-ranked test and the Bonferroni correction was used to correct for multiple tests. The target object (or target block) decoding accuracy, defined as the ratio between the number of corrected predicted blocks and the total number of blocks, was used as performance metric as it was the one adopted for the challenge. To do so, the single-trial P300 probabilities corresponding to each flashed object in the scene were averaged together across runs belonging to a specific block and the target object of a specific block was decoded as the one with maximum average probability. The performance of the networks was evaluated in within-subject trainings: each network was trained using the participant's trials recorded across multiple sessions, leading to subject-specific CNNs. Four-fold cross-validation was used on the total subject's dataset (containing both calibration and online data). To perform early stopping in the P300 detection, a validation set containing 20% of the trials was selected from the training set maintaining the class proportion.

E. Post-hoc interpretation: saliency maps

To interpret the features driving Branched-EEGNet decision, saliency maps were computed once the within-subject trainings ended, by backpropagating the gradient of the P300 class output with respect to the layer's input back to a target layer. This interpretation technique represents the relevant features of the target layer that drive the network's decision. In this study, the target layer was the input layer and thus, the features of interest were the EEG electrode locations and time samples. For each participant, the saliency maps were computed for each test trial belonging to the P300 class, averaged across trials and normalized between [-1, 1]. Then, these within-subject maps were averaged across subjects, obtaining the *average saliency map*, represented as a 2D heat-map along the channel and time dimensions. Furthermore, for each participant the absolute value of the saliency maps was computed, averaged across the trials, and then averaged across all EEG channels (most discriminative time samples) and across all the time samples (most discriminative electrodes). The resulting maps were normalized between [0, 1] for each participant and finally averaged across participants (*average most discriminative time samples* and *average most discriminative electrodes*).

III. RESULTS

A. Performance metric

Fig. 2 displays the results obtained with the re-implemented CNNs and the proposed Branched-EEGNet. Branched-EEGNet scored an average target object accuracy of 95.3±0.6% (mean±std. error of the mean) statistically outperforming OCNN and BranchedNet (with P-values of

5.96e-11 and 6.17e-06, respectively), while did not outperformed significantly EEGNet (P-value of 0.20) that scored an average accuracy of 94.8±0.7%. Notably, Branched-EEGNet was computationally more lightweight than BranchedNet (approx. 0.35 times) and lightly heavier than the compared single-branched designs (approx. 1.14 and 1.36 times compared to OCNN and EEGNet, respectively).
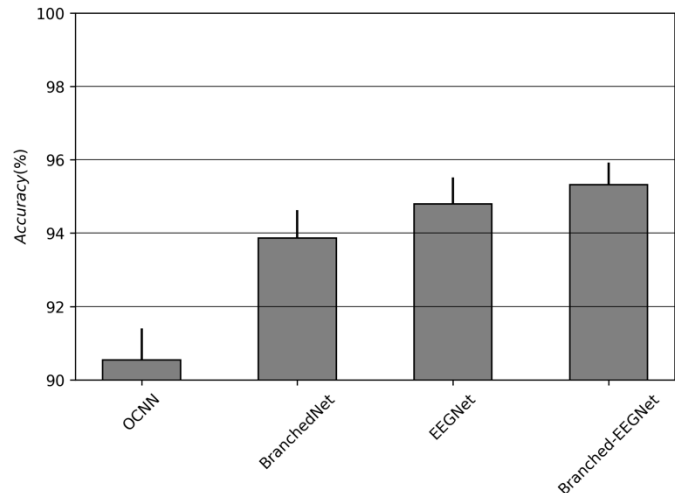

Fig. 2: Performance comparison between the tested CNNs. Mean values across folds and subjects are displayed as grey bars, while the error bars represent the standard error of the mean.

B. Post-hoc interpretation: saliency maps

In Fig. 3 the average saliency map is reported alongside with the average most discriminative electrodes and time samples. The electrodes P3, Pz, P4, POz show larger gradients (both positive and negative) from 300 to 600 ms post stimulus (Fig. 3a). Positive and negative gradients correspond respectively to positive and negative EEG signal deflections that positively contribute to the P300 decoding decision. Accordingly, the most discriminative electrodes across the whole epoch resulted P3, Pz, P4 and POz (Fig. 3b). The temporal distribution of the gradient peaks approx. between 400-500 ms post stimulus (Fig. 3c); however, other peaks appear also in other intervals (e.g. less prominent peaks between 500-600 ms and 150-250 ms). Each peak of this distribution could reflect a specific neural process modulated by the user attention to the target object. These spatial and temporal visualizations match the well-known P300 component spatio-temporal distribution [2].

IV. DISCUSSION

In this study, four CNNs were compared for P300 decoding task. All the CNNs performed well above the chance level (12.5%). Furthermore, in this study, we demonstrated that – when applied to P300 decoding task – a dual-branched CNN based on an architecture where the temporal convolution is performed before the spatial filtering outperformed significantly OCNN and BranchedNet, a similar architecture in which the order of these convolutions is reversed. Branched-EEGNet scored the highest average performance metric across subjects, but without statistical significance when compared with EEGNet. The used CNNs worked directly with raw/lightly pre-processed data with high-dimensionality and extracted automatically the relevant features to better discriminate between the conditions. This is particularly

relevant as this framework can be used to discover information about the target cognitive task by adopting an appropriate post-hoc interpretation technique.
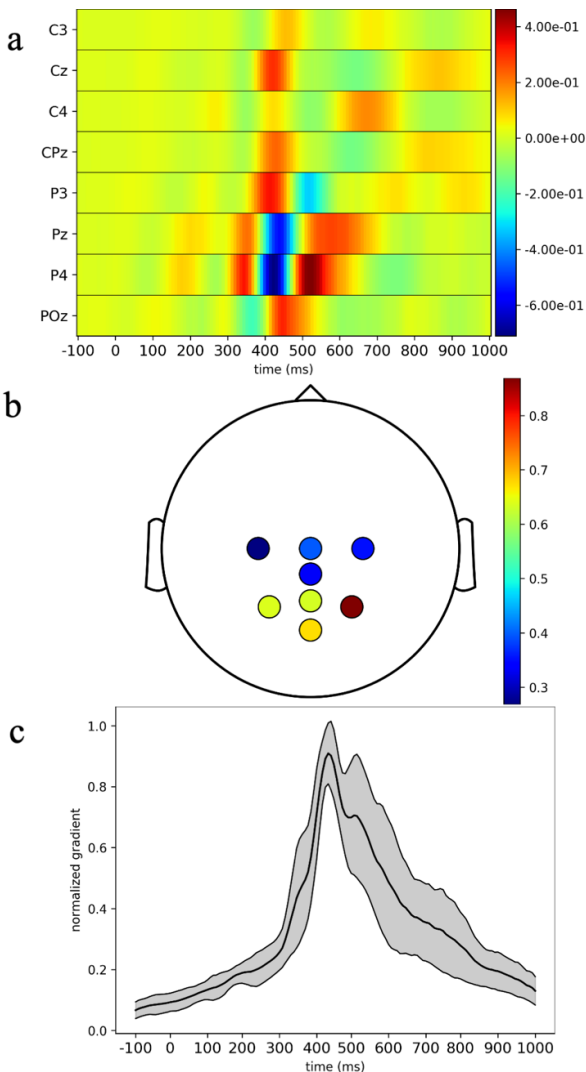

Fig. 3: Saliency maps. (a) Average maps obtained across the test trials of the subjects. The absolute value of the maps was averaged across the test trials of the subjects and across the temporal – (b) most discriminative electrodes – and spatial dimensions – (c) most discriminative time samples (the mean value is displayed with a bold line, while the grey-shaded area represent the mean value ±std. dev.).

Among the available electrodes, P3, Pz, P4 and POz were the most discriminative ones; this is in line with previous studies in which the montage was optimized comprising 5-8 electrodes [14] [15], including P3, Pz and P4. The most discriminative time period is approx. around 300-500 ms as Amaral et al. [5] found in the same dataset. The multi-scale feature extraction realized via the double branch did not significantly outperform EEGNet (including a single branch) in this specific classification task. However, the potential advantage of this design solution could emerge in other conditions such as applying this network to other classification tasks, or in transfer-leaning, i.e. when transferring the knowledge of pre-trained CNNs to a new user to potentially reduce the amount of training data. Furthermore, a deep analysis on the effect of hyper-parameters of the dual-branch and of different pre-processing procedures could be performed in future studies to better investigate this solution. Lastly, in

agreement with [9], the saliency maps not only allow visualization of CNN learned features but may represent a tool for further ERP investigation. Indeed, training a CNN to discriminate between the different investigated conditions, and visualizing the corresponding saliency maps could provide insights about the spatio-temporal distribution of the different neural correlates. In perspective, the comparison between saliency maps related to early and late trials/recording sessions in neurological patients, could be used to design biomarkers useful to monitor the course of neurological disorders and assess the effect of the rehabilitation training.

REFERENCES

[1] S. Sutton, P. Tueting, J. Zubin, E.R. John, "Information delivery and the sensory evoked potential", *Science*, vol. 155, pp. 1436–1439, March 1967

[2] J. Polich, "Updating P300: an integrative theory of P3a and P3b", *Clinical Neurophysiology*, vol. 118, pp. 2128–2148, June 2007

[3] R. A. Ramadan, A. V. Vasilakos, "Brain computer interface: control signals review", *Neurocomputing*, vol. 223, pp. 26-44, February 2017

[4] E. W. Sellers, E. Donchin "A P300-based brain–computer interface: Initial tests by ALS patients", *Clinical Neurophysiology*, vol. 117, pp. 538-548, March 2006

[5] C. Amaral et al., "A Feasibility Clinical Trial to Improve Social Attention in Autistic Spectrum Disorder (ASD) Using a Brain Computer Interface", *Frontiers in Neuroscience*, vol. 12:477, July 2018

[6] Y. LeCun, Y. Bengio, G. Hinton, "Deep learning", *Nature*, vol. 521, pp. 436-444, May 2015

[7] G. Montavon, W. Samek, K.-R. Müller, "Methods for interpreting and understanding deep neural networks", *Digital Signal Processing*, vol. 73, pp. 1-15, February 2018

[8] H. Cecotti, A. Graser, "Convolutional neural networks for P300 detection with application to brain-computer interfaces", *IEEE Transactions on Pattern Analysis and Machine Intelligence*, vol. 33, pp. 433-445, March 2011

[9] A. Farahat, C. Reichert, C. M. Sweeney-Reed, H. Hinrichs, "Convolutional neural networks for decoding of covert attention focus and saliency maps for EEG feature visualization", *Journal of Neural Engineering*, vol. 16, October 2019

[10] H. Shan, Y. Liu, T. Stefanov, "A simple convolutional neural network for accurate P300 detection and character spelling in brain computer interface" *Proceedings of the 27th International Joint Conference on Artificial Intelligence*, pp. 1604–1610, July 2018

[11] V. J. Lawhern et al., "EEGNet: a compact convolutional neural network for EEG-based brain–computer interfaces", *Journal of Neural Engineering*, vol. 15, July 2018

[12] D. Borra, S. Fantozzi, E. Magosso, "Convolutional Neural Network for a P300 Brain-Computer Interface to Improve Social Attention in Autistic Spectrum Disorder" *IFMBE Proceedings of XV Mediterranean Conference on Medical and Biological Engineering and Computing*, pp. 1837-1843, September 2019

[13] E. Santamaría-Vázquez, V. Martínez-Cagigal, J. Gomez-Pilar, R. Hornero, "Deep Learning Architecture Based on the Combination of Convolutional and Recurrent Layers for ERP-Based Brain-Computer Interfaces", *IFMBE Proceedings of XV Mediterranean Conference on Medical and Biological Engineering and Computing*, pp. 1844-1852, September 2019

[14] D. J. Krusienski et al., "A comparison of classification techniques for the P300 Speller", *Journal of Neural Engineering*, vol. 3, October 2006

[15] D. J. Krusienski et al., "Toward enhanced P300 speller performance", *Journal of Neuroscience Methods*, vol. 167, pp. 15-21, January 2008

Rapid and affordable prototyping of bioinspired microfluidic networks for Tissue Engineering

G. Pacetta[1], A. De Acutis[1,2], F. Montemurro[1], C. De Maria[1,2] and G. Vozzi[1,2]

[1] Research Center "E. Piaggio", University of Pisa, Pisa, Italy
[2] Department of Ingegneria dell'Informazione, University of Pisa, Pisa, Italy

Abstract—**Traditional approaches for the fabrication of microfluidic technologies for Tissue Engineering (TE) usually rely on expensive facilities and long-manufacturing time. Here, we gave an overview of a novel procedure to rapidly prototype bioinspired polydimethylsiloxane (PDMS)-based microfluidic networks for many TE application with an affordable equipment. The proposed approach is based on the combination of a laser engraving process with consecutive PDMS double casting procedures to fabricate a microfluidic network mimicking the retinal vasculature in only 2 hours. To prove the compatibility of the produced microfluidic structure to create microfluidic prototypes, it was sealed to a glass substrate to form a closed microchannels system for preliminary fluid flow tests.**

Keywords—**Microfluidic device, vascular microfluidic network, tissue engineering, PDMS, laser cutting, PDMS double casting.**

I. INTRODUCTION

THE human vasculature network, allowing blood to flow throughout tissues for delivering of nutrients and oxygen, removing metabolic waste and regulating pH and temperature, plays a pivotal role in maintaining cells homeostasis and is closely related to several diseases [1].

Accordingly, huge efforts have been made in the field of Tissue Engineering (TE) to fabricate three-dimensional (3D) in vitro models endowed of a perfusable microvascular network to better mimic the in vivo environment of native tissue to be used in applications involving diseases modelling and drug screening [2]. Thus, advances in the development of new microfluidic technologies for engineering vascular networks has provided powerful microfluidics devices for enabling reliable 3D in vitro models and engineered tissues in lab-on-a-chips [3].

Soft lithography (SL) is one of the most common fabrication techniques to engineer vascular networks for TE microfluidics (SL). This technique is based on printing and replica molding using mechanically soft and biocompatible elastomeric materials (i.e. Polydimethylsiloxane, PDMS) stamps or moulds with the patterns of interest [4]. SL allows to fabricate channels for microfluidics with a high accuracy, resolution (down to 1 µm) and complexity [5], [6]. In opposition, microfluidics fabrication using SL still relies on quite costly, time consuming and human labor-intensive photolithographic processes for developing cleanroom-manufactured SU-8 masters [7], which are limited in high-resource settings.

In order to go beyond all these limitations rapid fabrication techniques based on common or easily affordable laboratory equipment have been proposed as alternative the traditional methods to develop cost-effective and more customizable networks for TE microfluidic devices. These techniques include 3D printing, molding, laser ablation and micromilling approach [8], [9].

In this context we present the workflow of a novel fabrication methods to prototype high quality PDMS-based bioinspired microfluidic networks in a time and cost-saving manner. The presented fabrication method, based on a combination of a laser engraving process with consecutive PDMS double casting procedures (i.e. moulding PDMS in a PDMS master), allowed the fabrication of a PDMS microfluidic network mimicking the human retinal vasculature. The quality of the fabricated microfluidic network was assessed by an optical analysis. Lastly, as a demonstration of the microfluidic network functionality, it was integrated in a microfluidic system to perform fluid flow tests.

II. MATERIALS AND METHODS

A. Fabrication of a bioinspired microfluid network

The proposed fabrication method can be described as 4-step process. The first is the fabrication of a PDMS female mold (FM) by laser engraving a pattern mimicking the human retinal vascular network (RVN) on a thin PDSM spin-coated layer. The second step involves the fabrication of a reusable male mold (MM) by double PDMS casting in the FM. In the third step the desired RVN is obtained by PDMS double casting in the MM. As last, RVN channels are properly functionalized to serve as cell cultivation substrates for TE applications. An easily affordable Sylgard 184® (Dow-Corning) mixed in a 10 (base) : 1 (curing agent) ratio by weight, once debubbled, was the material used in all steps to produce PDMS part. The entire fabrication process is summarized in Fig. 1, while each step is described below.

(i) Fabrication of the FM: firstly, 3 ml of PDMS were spin-coated on a glass slide (25 mm x 35 mm) for 60 s at 270 rpm to form a homogeneous layer height of 300 µm which in turn determines the desired channel depth (Fig. 1(a)). Then the PDMS was cured in oven for 20 min at 100°C (Fig. 1 (b)). After curing, a 60 W CO_2 laser cutter (Speedy 100, Trotec) was used to engrave the PDMS layer to create the pattern of the desired bioinspired microfluidic network (Fig. 1(c)). Particularly, a 2D vector illustration of a human RVN (Fig. 2(b)) was generated from Indocyanine Green Angiography (ICGA) images (Fig. 2(a)) and processed using image processing and vector-based drawing software (Adobe Photoshop and Adobe Illustrator) (Fig. 2(b)) and subsequently imported on the JobControl® laser software. The RVN microfluidic pattern was composed of microchannels with a width between 75 and 480 µm. To transfer the RVN pattern on the PDMS layer, the laser power, spot size, ablation resolution

and ablation velocity were set as 1.2 W, 70 μm, 1000 dpi and 0.9 cm/s to obtain the highest engraving quality in term of debris formation, and precision of channels profile. The RVN pattern was transferred using a line-by-line raster engraving process to not limit the channel width to the spot laser dimension. The engraving process was repeated two times with same setting to achieve more defined channels. After the engraving procedure, the engraved PDMS film was sonicated in an ethanol-water solution (70% v/v) (Sigma Aldrich) at power of 4 W for removing debris produced by the laser (Fig. 1(d))). Then, the engraved PDMS film was placed on a hot plate at 40°C to enhance the evaporation of the ethanol-water solution (Sigma Aldrich) thus getting the desired PDMS FM.

(ii) Fabrication of the MM: a two-step FM surface treatment was required to ensure an excellent demoulding procedure for the fabrication of reusable MM via PDMS double casting. Firstly, a small amount of surfactant solution (i.e. 10% w/w soft-soap in 70% v/v ethanol-water) was applied into a single point of the network (Fig. 1(e))). From this point the surfactant solution spreads in all the microfluidic network under the action of capillary forces. Subsequently, the FM was placed on a hot plate at 40°C to enhance the solvent evaporation and thus the surfactant deposition. Then a commercial mould release agent (Mann Ease Release™ 200, Smooth-On) was sprayed on the PDMS in accordance with the manufacturer's instructions Fig. 1(f). Following the surface treatment, the FM (with the engraved pattern upwards) was then placed in a custom-made aluminum holder and 3 ml of uncured PDMS were poured over the engraved PDMS using a plastic syringe until covering the whole FM surface. The holder was then placed into a vacuum chamber for 3 min in order to enhance the penetration of the casted PDMS inside the engraved channels. Next, the holder was placed in oven to cure the PDMS for 10 min at 150°C (Fig. 1(g)). Finally, the MM was obtained by gently peeling off the cured PDMS from the FM (Fig. 1(h)).

(iii) Fabrication of the microfluidic RVN: firstly, the commercial mould release agent was sprayed all over the MM as the only surface treatment to ensure an excellent double casting procedure (Fig. 1(i)). Subsequently, the MM was placed in a custom-made aluminum holder (with the embossed pattern upwards) and 3 ml of PDMS were poured over the surface until a homogeneous layer was obtained. The holder was then placed in a vacuum chamber for 3 min to facilitate PDMS penetration among the spaces of the network in relief. Thereafter, the holder was put in oven for 10 min at 150°C to cure the PDMS (Fig. 1(j)). Hence, the microfluidic RVN was obtained by gently peeling off the cured PDMS from the MM (Fig. 1(k)).

(iv) Microfluidic RVN chemical surface modification: since PDMS is very hydrophobic when cured, the surface of the microfluidic RVN was functionalized with a coating of gelatin (Type A, Sigma Aldrich) crosslinked with 3-glycidoxypropyltrimethoxysilane (GPTMS) (Sigma Aldrich) to support cell adhesion. Prior to coating, a salinization of microfluidic RVN surface was performed to encourage a stable and long-term attachment of the gelatin coating to the RVN surface. Particularly, the surface functionalization was performed by dipping the microfluidic RVN in a 3-aminopropyltriethoxysilane (APTES)-ethanol solution (50% v/v) (Sigma Aldrich) for 5 min (Fig. 1(l)). Then the drained microfluidic RVN was washed in acid acetic-water solution (33% v/v) (Sigma Aldrich) and then dried in a vacuum chamber for 1 min (Fig. 1(m)). After functionalization, 150 μL of gelatin solution (10% w/v in 90% acid acetic-water) crosslinked with GPTMS (3.68% v/v) was poured on the microfluidic RVN surface and subsequently put in a vacuum chamber for 1 min to facilitate the penetration of the solution into the channels. Finally, the gelatin solution was uniformly distributed over the microfluidic RVN by spin-coating for 120 sec at 2000 rpm (Fig. 1(n, o)).
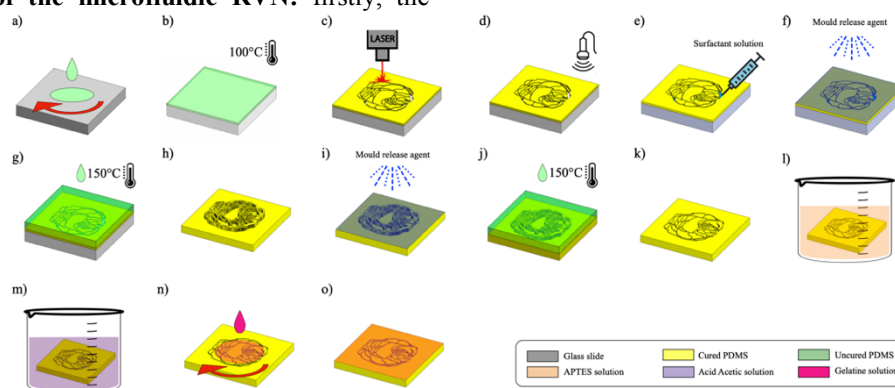

Fig. 1: Schematic illustration of the microfluidic RVN fabrication process. a) spin-coating of PDMS on a glass slide. b) curing of PDMS for 20 min at 100°C. c) FM fabrication by PDMS laser engraving. d) FM cleaning by sonication. e) application of the surfactant solution inside the FM channels. f) spraying of the mould release agent on the FM surface. g) PDMS deposition over the FM and PDMS curing for 10 min at 150°C. h) MM fabrication by peeling of the cured PDMS from the FM. i) spraying of the mould release agent on the MM surface. J) PDMS deposition over the FM and PDMS curing for 10 min at 150°C. k) microfluidic RVN fabrication by peeling of the cured PDMS from the MM. l), m) RVN surface chemical modification. n), o) RVN surface functionalization whit a gelatine spin-coated layer.

B. Optical analysis of the microfluidic RVN

The quality of the fabricated part was optically analysed in term of replication fidelity of features using a Leica DM6M. Particularly, the images acquired were processed with the Leica Map DCM 3D software to measure how the final

dimension (i.e. channels depth and width) replicated the original design.

C. Microfluidic RVN system fabrication

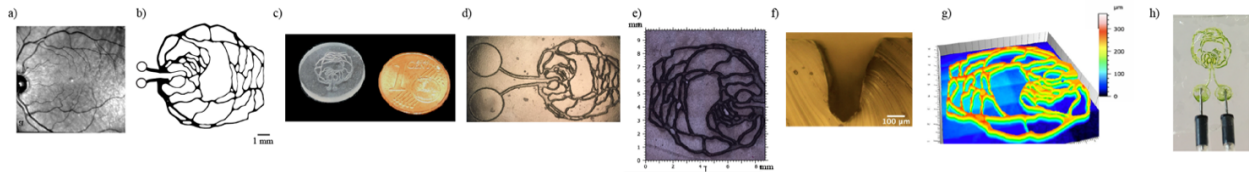Immediately after the chemical surface modification the microfluidic RVN was bonded to a glass slide previously silanized to enable the immobilization of gelatin. Once the gelatin crosslinked, a closed channel system was achieved. Finally, a fluid (i.e. food dye in DI water) was inject in the inlet hole manually by to assess the functionality of the system.

Fig. 2: a) Indocyanine green angiography image of a retinal vasculature. b) RVN designed pattern. c) picture of the fabricated microfluidic RVN. d) picture of the fabricated MM. e) microscope image of the microfluidic RVN. f) side view of a RVN microfluidic channel. g) channels depth map of the microfluidic RVN. h) picture of the microfluidic system after the perfusion test.

III. Results and discussion

Figure 2 (c) shows the final fabricated microfluidic RVN. The microscope image of the microfluidic RVN demonstrated the high quality of the proposed method in term of 2D designed pattern geometry replication fidelity starting from the FM and the MM (Fig. 2(d, e)). Through a comparison of microscope image of the microfluidic RVN (Fig. 2(e)) with the designed 2D pattern it was found that the average error in term of channel width was about 50.93 ± 12.32 μm. More specifically, the minimum and the maximum widths were 27% and 5% larger than the designed dimension, respectively. This mismatch, especially in channels with a smaller width, mainly depends on the laser spot size and could be reduced by equipping the laser cutter machine with an additional optical component. It was also found that average channel depth (Fig. 2(f)) was 298.4 ± 16.3 μm. Although this value was very close to the designed one, it was not uniform over the channels width. A more uniform depth distribution could be achieved by finding the right trade-off between laser power and resolution. From the analysis of the microscope image it was possible to achieve a map of the depth's distribution of all the RVN channels (Fig. 2 (g)). Finally, the absence of leaks or blockages during the fluid flow test demonstrated the functionality of the fabricated microfluidic structure (Fig. 2(h)).

IV. Conclusion

In this study a rapid fabrication process to fabricate bioinspired microvasculature networks in low-resource settings for TE application was presented. Importantly, this study demonstrated that a good quality bioinspired microfluidic network could be readily achieved without expensive cleanroom equipment and lithography process (more than 30k € for cleanroom facilities) thus reducing the overall fabrication set up to a spin-coater (~ 6k €), oven (~ 2k €) and laser cutter (~ 12k €), PDMS (~ 180 €/kg) and other common chemical consumables (~ 1.5k €). As evidence, a functional PDMS microfluidic RVN system with reasonable resolution was fabricated from a MM achieved a PDMS double casting process started on a thin laser engraved PDMS layer. The overall fabrication process was completed in about 2 h. Since the MM could be used several times if not damaged, the total fabrication time could even be halved. Based on the presented result, the proposed fabrication approach has the potential to significantly facilitate the fabrication of TE microfluidic technology for biomimetic 3D in vitro models. However, further studies will be carried out to optimize the entire fabrication procedure in term of quality of the fabricated microfluidic channels (e.g. surface roughness, channel depth and width), in term of accuracy and repeatability, and to evaluate their biological importance in an in vitro model of the human eye.

References

[1] X. Wang, Q. Sun and J. Pei, "Microfluidic-based 3D engineered microvascular networks and their applications in vascularized microtumor models," *Micromachines*, vol. 9, no. 10, pp. 1–26, 2018.

[2] B. Zhang, A. Korolj, B. F. L. Lai and M. Radisic, "Advances in organ-on-a-chip engineering," *Nature Reviews Materials*, vol. 3, no. 8, pp. 257–278, 2018.

[3] N. K. Inamdar and J. T. Borenstein, "Microfluidic cell culture models for tissue engineering," *Current Opinion Biotechnology.*, vol. 22, no. 5, pp. 681–689, 2011.

[4] G. M. Whitesides, E. Ostuni, S. Takayama, X. Jiang, and D. E. Ingber, "Soft Lithography in Biology and Biochemistry," *Annual Review of Biomedical Engineering*, Vol 3, no.1, pp. 335-373, 2001.

[5] L. M. Bellan, H. Chamberlain, D. Wu and R. Langer, "Microfluidic Vascular Networks for Engineered Tissues," *Microfluidic Cell Culture System*, pp. 223-245, 2013.

[6] J. H. Huang, A. Jayaraman, and V. M. Ugaz, "Microvascular Networks for Tissue Engineering," *Microfluidic Cell Culture System*, pp-27-52, 2013.

[7] S. P. Desai, D. M. Freeman, and J. Voldman, "Plastic masters - Rigid templates for soft lithography," *Lab Chip*, vol. 9, no. 11, pp. 1631–1637, 2009.

[8] H.-B. Liu, and H. Q. Gong, "Templateless prototyping of polydimethylsiloxane microfluidic structures using a pulsed CO 2 laser," *J. Micromechanics Microengineering*, vol. 19, no. 3, 2009.

[9] Z. Isiksacan, M. T. Guler, B. Aydogdu, I. Bilican, and C. Elbuken, "Rapid fabrication of microfluidic PDMS devices from reusable PDMS molds using laser ablation," *J. Micromechanics Microengineering*, vol. 26, no. 3, 2016.

Radiomics-based prediction of head and neck cancer recurrence: a multi-centric MRI study

M. Bologna[1], V. D. A Corino[1], G. Calareso[2], S. Alfieri[2], R. Romanò[2], L. Locati[2], L. Licitra[2] and L. T. Mainardi[1]

[1] Department of Electronics, Information and Bioengineering (DEIB), Politecnico di Milano, Milan, Italy
[2] Fondazione IRCCS Istituto Nazionale dei Tumori, Milan, Italy

Abstract—In this study, a classifier for head and neck cancer (HNC) recurrence was developed using MRI radiomics. In total, 51 patients (10 recurrences) from 8 different hospitals were included in this study. For each patient the following MRI-sequences were available: T1-weighted; T1-weighted with fat suppression and contrast enhancement; T2-weighted. A total of 2553 radiomic features were extracted from the images. In order to reduce the dimensionality, features selection based on features, stability and correlation was performed. Synthetic minority oversampling technique (SMOTE) was used to balance the classes. Least absolute shrinkage and selection operator (LASSO) logistic regression was used to perform the classification. A 10-fold cross-validation was performed and an unbiased estimate of the classifier sensitivity, specificity and area under the curve (AUC) were computed. Model sensitivity and specificity were 90% and 68% respectively and the AUC was 0.80. The radiomic classifier could be useful to perform a preliminary stratification, allowing to optimize the follow-up strategy for high risk patients in a more efficient and cost-effective way.

Keywords—Radiomics, head and neck cancer, magnetic resonance imaging.

I. INTRODUCTION

ONE of the main issues related to head and neck cancer (HNC) treatment is tumor recurrence, i.e. the return of the tumor, years after the end of the treatment. In order to promptly detect the presence of a recurrence, multiple control examinations are required, which increases the cost for the national health systems of the different nations. A stratification performed before treatment could be useful to guide the follow-up management in order to make it more efficient (e.g. by reducing the number of examinations in the low risk group) thus reducing the cost for the national health system and increasing the quality of life of the patient.

Medical imaging could potentially be a non-invasive and low-cost tool to perform such baseline stratification. In particular, a radiomic approach, consisting in the extraction and mining of hundreds or thousands of quantitative features from medical imaging [1], may be useful for the purpose. As a matter of fact, radiomics has been successfully used in the past for tumor prognosis, classification and prediction of response to treatment [2]–[4]. While classification models for HNC were developed for computed tomography (CT), studies based on magnetic resonance imaging (MRI) focused only on nasopharyngeal carcinoma (NPC), and not on other subsites. Since MRI provides better contrast and more versatility than other imaging techniques, it could potentially provide more information compared to CT. However, since MRI signal is not standardized and may depend on a multitude of different image acquisition parameters, it may be difficult to compare images coming from different hospitals or acquired with different protocols [1]. To the knowledge of the authors, no MRI-radiomic signature based on multi-centric study was developed for the classification of recurrence risk in HNC.

In this study, MRI images from a multi-centric cohort of HNC patients will be used to develop and validate a classifier for cancer recurrence (high and low risk), to provide an efficient and objective way to stratify patients before treatment, thus allowing to optimize their follow-up strategy.

II. MATERIALS AND METHODS

A. Clinical dataset

The dataset used for this study consisted is a subset of 51 patients with HNC that were acquired from 8 different Italian hospitals. The ethical committee of each center approved the study and all patients gave their written informed consent. All patients' data were anonymized prior to the analysis. The main clinical data of the patients are reported in Table I. All the patients undergo the optimal treatment based on prognostic factors such as Stage TNM, HPV status and tumor subsite, which were uniformly distributed across centers.

TABLE I
CLINICAL AND FOLLOW-UP DATA OF THE ANALYZED DATASET

Characteristic	Value
Number of patients	51
Age at diagnosis	64 [55-69]
Sex	42 males; 9 females
Number of recurrences	10

Quantitative parameters are reported as median and inter-quartile range

B. MRI images acquisition

MRI data were acquired for each of the patient and the following MRI sequences were available: pre-contrast T1-weighted images (T1w), post-contrast fat-saturated T1-weighted images (T1wCont); T2-weighted (T2w) MRI, without contrast. The protocol and the scanner used for MRI acquisition were not standardized among the clinical center. An example of the three sequences acquired for the study is displayed in Figure 1.

C. Image segmentation and preprocessing

An expert radiologist (G.C.) performed manual segmentation of the region of interest (ROI), which in this study was the main tumor (Fig. 1). The segmentation was performed on the T2w image and the same segmentation was used for the T1w images as well. No registration among the

image types was performed since misalignment due to movement was negligible (Figure 1).

Preprocessing of the MRI images included image denoise with a gaussian filter and a bias field correction using the N4ITK [5] to correct for potential effects due to inhomogeneity of the magnetic field. Z-score standardization was performed to ensure the range of intensity in the MRI images was the same. Last, the images were resampled to a common isotropic resolution of 2 mm (as in [3]) using B-spline interpolation. Intensity values of the MRI were discretized using 32-bins histogram discretization. The preprocessing was performed in MATLAB 2018a (the Mathworks, Natick, MA, USA), using wrappers for other software like 3D Slicer or Pyradiomics. MATLAB was also used for all the following analysis performed on the MRI images and radiomic features.
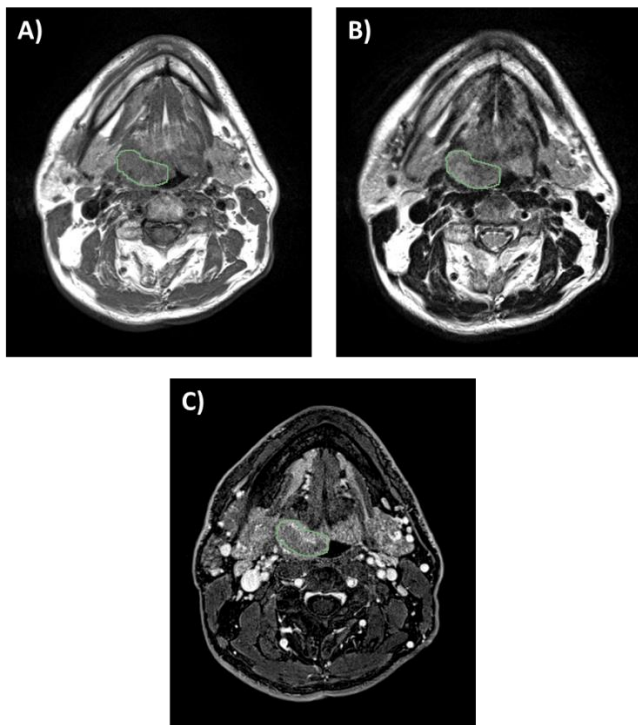

Fig. 1: Example of images used for the study: T1-weighted image (A); T2-weighted image (B); T1-weighted fat sat image (C).

D. Radiomic features extraction

Radiomic features were extracted using open source software Pyradiomics [6]. Features of different categories were considered [7]: 14 shape and size (SS) features; 18 first order statistics (FOS) features; 75 textural features, of which 24 computed on grey level co-occurrence matrix (GLCM), 16 computed on grey level run-length matrix (GLRLM), 16 computed on grey level size zone matrix (GLSZM), 5 computed on from neighborhood grey tone different matrix (NGTDM), 14 from grey level dependence matrix (GLDM). FOS and textural features were also computed on 8 different wavelet transforms [2]. From each MRI sequence 851 features were extracted for a total of 2553 features per patient.

E. Training of the radiomic classifier

The pipeline used for the training of a radiomic signature comprised different steps.

The first step of the pipeline was features normalization. The

different radiomic features were defined in different ranges, spanning several orders of magnitudes. This may be an issue for the following analyses. Z-score normalization was used to standardize the range of the features, normalizing the mean value to 0 and the standard deviation was 1.

The second step was the a-priori removal of features that were known to be unstable to sources of variability such as variations in the image acquisition parameters, or geometrical transformations of the ROI. To identify such groups of unstable features, procedure described in previous studies [8], [9] were extended to the entire features set (2553 features). The intra-class correlation coefficient [10] was used as a metric of stability. Only the features with ICC>0.75 (as defined by [11]) for both tests (ROI manipulation and random variation of image acquisition parameters) were selected.

The third step consisted of a correlation-based features selection, performed to ensure a set of features with low internal redundancy. Spearman correlation coefficient ρ was computed for each pair of features and in case a pair had $|\rho| > 0.85$, only the features with the lower mean Spearman coefficient with all the others was selected.

The fourth step of signature training consisted in the fitting of a least absolute shrinkage and selection operator (LASSO) with a logistic regression model [12] for the classification of recurrence risk (high or low risk). The optimal value of λ (the hyperparameter that controls the number of features used in the logistic regression model), was optimized through internal 10-fold cross-validation. To overcome the issue of the imbalance of the classes, synthetic minority oversampling technique (SMOTE) [13] was used on the training set in each iteration of the internal cross-validation. The radiomic score was given by the linear combination of the radiomic features selected by the LASSO and their corresponding regression coefficients.

F. Evaluation of signature performance

Stratified 10-fold cross-validation was used to obtain an unbiased prediction of the risk class for each patient, as well as an unbiased estimation of the radiomic score. Sensitivity and specificity of the classifier were computed, as well as the area under the receiver operating characteristic curve (AUC) for the radiomic score.

III. RESULTS AND DISCUSSION

A. Radiomic classifier training

In total, 678 features were considered stable. Of these, 64 were non-redundant. Two features (*T1wCont_waveletLLL_ngtdm_Complexity* and *T2w_waveletLLH_firstorder_Mean*) were selected for the classifier. The optimal value of λ for the LASSO was 0.08. The coefficients of the selected features, together with their mean and standard deviations are reported in Table II.

TABLE II
DETAILS OF THE FEATURES USED IN THE RADIOMIC CLASSIFIER

Feature name	Regression coefficient	Mean ± SD
T1wCont_WaveletLLL_ Complexity	-0.62	740.79 ± 232.50
T2w_WaveletLLH_ Mean	0.02	-0.02 ± 0.03

B. Evaluation of model performance

The AUC of the cross-validated radiomic score was 0.80 (see Fig.2). In cross-validation, the sensitivity and specificity of the classification were 90% and 68% respectively. The mean sensitivity to both classes was 79%. Table III shows more detail on the classification of the patients. By looking at Fig.2 it can be seen that the default threshold, i.e. a value of 0 for the score of LASSO logistic regression (corresponding to a probability of recurrence of 0.5), is not equal to the optimal point of the classification. If the optimal point threshold (corresponding to a probability of 0.55) was used, the sensitivity would stay the same, but the specificity would increase up to 76%. This situation corresponds to the point of the ROC curve that is closer to the top-left corner of the graph (marked by a green circle in Fig.2). The models used in 10-fold cross validation were of course different from the one reported in subsection IIIA but they still provide an estimate of the predictive performance of the radiomic signature and risk on unseen data.
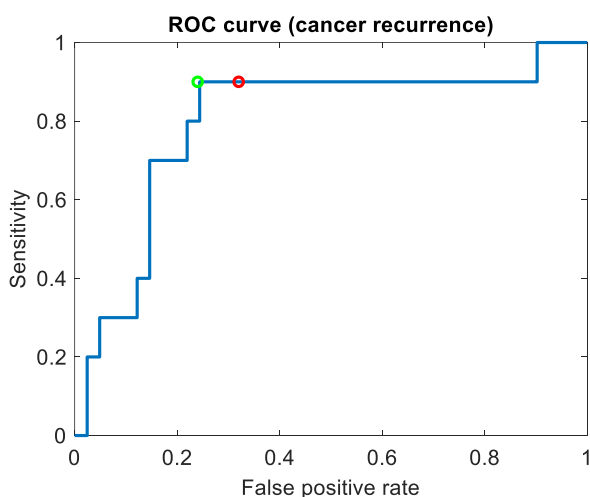

Fig. 2: Receiver operating characteristic (ROC) curve for the radiomic score. The position on the curve given by the default cut-off value is marked with the red circle, while the position of the optimal cut-off is marked with the green circle.

TABLE III
PERFORMANCE OF THE RADIOMICS–BASED CLASSIFICATION

Metric	RADIOMIC MODEL
True positives	9
True negatives	28
False positives	13
False negatives	1
Sensitivity	90 %
Specificity	68 %
AUC	0.80

C. Discussion of the results

The results obtained during the cross-validation show how radiomics can be used to improve the clinical practice. Instead of performing a more intensive monitoring on all the patients,

which guarantees 100% sensitivity and 0% specificity, the radiomic classifier splits the patients in high and low risk group, increasing the specificity to 68% with only a small reduction in the sensitivity, which decreases to 90%. Also, as can be seen in Fig.2, the default cut-off for the radiomic score (assigning positive value to high risk class and vice-versa) is not the optimal point of the ROC curve. If the optimal cut-off was chosen, the specificity would increase up to 76%, while the sensitivity would stay the same (green dot in Fig.2). This would mean reduced number of patients in the high-risk group, leading to a reduced number of unnecessary examinations. Also, the high AUC of the radiomic score may suggest that it can be used as a new feature inside a multiparametric model including clinical variables, allowing to further improve the stratification of the patients.

It is also important to note that the results achieved were good even if the analyzed cohort was multi-centric, suggesting that with the right pre-processing of the images and the features radiomics could still be applicable in multi-centric studies.

In the study, 10-fold cross validation was used to estimate the performance of a radiomic based classifier trained with the workflow described in section IIE, and once cross-validation was performed the final model (presented in subsection IIIA) was trained on the entire dataset to be used for future applications. However, an external validation set is lacking. The next future development of the study is to perform such external validation to assess the robustness of the methodology.

Another possible future development could be to perform multivariate prognostic analysis

IV. CONCLUSION

A radiomics-based classifier for cancer recurrence was developed, and the potential advantages of using radiomics signature in the clinical practice was highlighted. A radiomics-based classifier may be a useful tool to be used in the future for patients' stratification.

REFERENCES

[1] V. Kumar *et al.*, "Radiomics: The process and the challenges," *Magn. Reson. Imaging*, vol. 30, no. 9, pp. 1234–1248, 2012.

[2] H. J. W. L. Aerts *et al.*, "Decoding tumour phenotype by noninvasive imaging using a quantitative radiomics approach," *Nat. Commun.*, vol. 5, p. 4006, 2014.

[3] R. T. Leijenaar *et al.*, "Development and validation of a radiomic signature to predict HPV (p16) status from standard CT imaging: a multicenter study," *Br. J. Radiol.*, vol. 91, no. 1086, p. 20170498, 2018.

[4] G. Wang, L. He, C. Yuan, Y. Huang, Z. Liu, and C. Liang, "Pretreatment MR imaging radiomics signatures for response prediction to induction chemotherapy in patients with nasopharyngeal carcinoma," *Eur. J. Radiol.*, vol. 98, pp. 100–106, 2018.

[5] N. J. Tustison, P. A. Cook, and J. C. Gee, "N4ITK: improved N3 bias correction," *IEEE Trans. Med. Imaging*, vol. 29, no. 6, pp. 1310–1320, 2010.

[6] J. J. M. van Griethuysen *et al.*, "Computational Radiomics System to Decode the Radiographic Phenotype," *Cancer Res.*, vol. 77, no. 21, pp. e104–e107, 2017.

[7] "Pyradiomics features description," *https://pyradiomics.readthedocs.io/en/2.1.0/features.html*, 2018. .

[8] M. Bologna *et al.*, "Assessment of Stability and Discrimination Capacity of Radiomic Features on Apparent Diffusion Coefficient Images," *J. Digit. Imaging*, vol. 31, no. 6, pp. 879–894, May 2018.

[9]   M. Bologna, V. Corino, and L. Mainardi, "Technical Note : Virtual phantom analyses for preprocessing evaluation and detection of a robust feature set for MRI-radiomics of the brain," *Med. Phys.*, 2019.

[10]   K. O. Mcgraw, "Forming Inferences About Some Intraclass Correlation Coefficients," *Psychol. Methods*, vol. 1, no. 1, pp. 30–46, 1996.

[11]   T. K. Koo and M. Y. Li, "A Guideline of Selecting and Reporting Intraclass Correlation Coefficients for Reliability Research," *J. Chiropr. Med.*, vol. 15, no. 2, pp. 155–163, 2016.

[12]   R. Tibshirani, "Regression Shrinkage and Selection via the Lasso.," *J. R. Stat. Soc.*, vol. 58, no. 1, pp. 267–288, 2016.

[13]   N. V. Chawla, K. W. Bowyer, L. O. Hall, and W. P. Kegelmeyer, "SMOTE: Synthetic Minority Over-sampling Technique," *J. Artif. Intell. Res.*, vol. 16, pp. 321–357, 2002.

Neural response to acoustic stimulation mediated by piezoelectric nanoparticles

M. Pisano[1], M.Tedesco[2], M. Brofiga[1], P. Massobrio[1], A. Marino[3], G. Ciofani[3] and R.Raiteri[1,4]

[1] *Department of Informatics, Bioengineering, Robotics, and System Engineering, University of Genova, Italy*
[2] *3Brain AG, Switzerland*
[3] *Istituto Italiano di Tecnologia, Smart Bio-Interfaces, Pontedera (Pisa), Italy*
[4] *CNR-Institute of Biophysics, Via De Marini, 6, 16149, Genova, Italy*

Abstract— **Nowadays, the most commonly employed neuromodulation approaches either require invasive procedures (such as surgical implantation of electrodes or photon-emitting devices), or lack sensitivity and selectivity being based on electromagnetic fields. One of the challenges in the field of neuroengineering is to identify new stimulation strategies, which balance efficacy with invasiveness. A promising family of non-invasive neuromodulation approaches exploits ultrasound (US), which can be focused to reach deep brain regions through the skull. In this work, we investigate the *in vitro* electrophysiological response of cortical networks, treated with piezoelectric barium titanate nanoparticles (BTNPs), to US pulses. We observed that US causes a reproducible and reversible increase of the network activity. Without BTNPs or with non-piezoelectric BTNPs, the US stimulus does not affect the spontaneous electrical activity of the network.**

Keywords—**Ultrasound neuromodulation, piezoelectric nanoparticles, Micro-Electrode-Arrays.**

I. INTRODUCTION

NEURAL stimulation is an essential technique to restore lost neural functions and correct disordered neural circuits in some neurological diseases. Some of the most commonly employed neuromodulation approaches require invasive procedures, e.g. electrical neural stimulation [1]. This type of stimulation has the capability to recover different symptoms in several diseases (e.g. depression, Alzheimer's disease, and schizophrenia) but problems occur in terms of biocompatibility [2] and surgery [3]. Multiple alternative and less invasive neuromodulation techniques, based on electromagnetic fields, have been released over the past decades (e.g. transcranial magnetic stimulation, transcranial direct current stimulation); however, the intrinsic limit of such methods is the poor spatial resolution (in the order of centimeters) [4] [5].

For this reason, wireless and non-invasive stimulation of the central nervous system is considered a critical issue, not only for the treatment of a variety of pathological conditions, such as, epilepsy, chronic pain, and obsessive-compulsive disorders, but also for reducing the debilitating motor symptoms of movement disorders such as Parkinson's disease, dystonia, and essential tremor.

Ultrasound (US) offers the attractive combination of non-invasiveness (it can be exploited for trans-cranial stimulation without the requirement of surgical processes), and relatively high spatial resolution (it can be focused virtually anywhere within the brain with a spatial resolution of few mm) [6]. For these reasons, US represents an ideal and safe source of mechanical energy that can be efficiently transduced into biologically relevant electrical cues. Effects of US propagation on biological tissues are at the basis of US medical diagnostic imaging; effects of US pressure waves on biological tissues have been studied for safety (US dosimetry [7]), therapeutic (tissue ablation [8]), local drug delivery [9], thrombolysis [10], as well as imaging purposes (e.g., US localization microscopy).

For neuromodulation, short pulses at low amplitudes are used to minimize thermal effects (i.e. heating) [11] and provide mechanical actuation through radiation force avoiding cavitation. Several *in vivo* and *in vitro* studies showed either excitatory or inhibitory neuronal responses to directly applied US [12], [13].

Coupling nanomaterials to transduce the US primary stimulus has the potential advantage of a better-defined and controlled stimulation mechanism, which renders the stimulation more selective. We recently showed that piezoelectric BTNPs, in response to US, induce Ca^{2+} influx on SH-SY5Y-derived neurons [6] and modulate the electrophysiological activity of primary neuronal cultures from rat embryos [14][15]. In this work, we investigate the US stimulation coupled with BTNPs on *in vitro* primary cultures of cortical neurons to induce neuronal activation.

II. MATERIALS AND METHODS

A. Cell culture

The experimental protocol for the cell culture was approved by the European Animal Care Legislation (2010/63/EU), by the Italian Ministry of Health in accordance with the D.L. 116/1992, and by the guidelines of the University of Genova.

All neurons were cultured onto commercial 60 Micro-Electrode Array (MEA) devices (Multi Channel Systems MCS GmbH, Germany). The day before the neuronal culture preparation, MEAs were sterilized in the oven at 120°C and pre-treated with the adhesion factor poly-L-Ornithine at 50 µg/ml concentration. Cortex was extracted and dissociated from E18 embryos old. The tissue was enzymatically dissociated with 0.125% of Trypsin/Hank's solution containing 0.05% DNAse (all Sigma Aldrich). Then, the proteolytic digestion was stopped with a solution of Neurobasal medium supplemented with 10% fetal bovine serum (FBS, Sigma Aldrich). The medium was removed and replaced with a new medium supplemented with 1% Glutamax, 2% B-27, 1% penicillin–streptomycin (all from Invitrogen Life Technologies) and without FBS. After a mechanical dissociation mediated by a fire-polished Pasteur pipette, cells were counted using Trypan Blue and plated on the MEA chips. A cell density of about 1500 cell/mm^2 was

chosen. MEAs were then recovered inside an incubator at 5% CO_2 and 37 °C. After Day 1 neuronal processes should begin to be visible. Neurons were fed every seven days by replacing half of the total culture medium with fresh one.

B. BTNPs

We used piezoelectric non-centrosymmetric BTNPs, characterized by a tetragonal crystal phase (1144DY, from Nanostructured & Amorphous Materials, Inc. Houston, TX). The supplier provided nanomaterial composition and its level of purity: BaO/ TiO2 0.999-1.001; APS 300nm; SSA 3.5-3.7m2 /g; purity 99.9%.

The BTNPs were dispersed in Neurobasal medium at 1mg/ml concentration. The day before the experiment the nanoparticles solution was sonicated for a few hours to obtain a homogeneous suspension and subsequently diluted in cell culture medium to reach the final concentration of 50 μg/ml; BTNPs unspecifically bind the plasma membrane as observed by confocal microscopy. In control experiments, primary cultures on MEA were incubated with analogue BTNPs characterized by a centrosymmetric cubic crystal structure (1143DY, from Nanostructured & Amorphous Materials), thus not showing piezoelectric behavior. The last control cultures consisted in neurons without nanoparticles.

C. Technical equipment

US at 1 MHz frequency and relatively low intensity (~1 W/cm^2) was generated using commercial source driven by a high voltage pulse generator (Sonidel, model SonoPore KTAC-4000) equipped with a disc piezoelectric transducer. US reached the MEA chamber through a thin thermoplastic film coated with a layer of acoustic gel. The pressure field generated by the piezoelectric transducer was experimentally characterized using a dummy MEA equipped with a miniaturize hydrophone (Teledyne RESON, model TC4038). US stimulation was applied as a train of pulses, whose main parameters are: total duration of the pulse train, pulse periodicity, duty cycle, and US wave amplitude and frequency.

Electrophysiological activity of neuronal networks was recorded by the commercial system MEA2100 (MCS). Raw data from each of the 60 electrodes of the array were acquired with the system software (MC Rack), at the sampling frequency of 10 kHz. We also recorded a trigger signal for the US source to reconstruct the exact timing of the generated US pulses.

D. US stimulation protocol

After 20 days in vitro (DIV), we recorded spontaneous neuronal activity in absence of nanoparticles, to control the cells vitality. Then, we added the BTNPs as mentioned above and we delivered the stimulation protocol. Right before and after the stimulation we recorded five minutes of spontaneous activity (i.e. pre-stimulation and post-stimulation stages). The stimulation stage consisted of a train of US pulses generated with 2 s periodicity for a total duration of 180 seconds, (i.e. 90 periods) as shown in Figure 1. We tested different duty cycles in the range from 25% to 75%.

In order to verify the effects of US exposure on the network activity, we performed an electrical test-stimulus before and after each experiment.
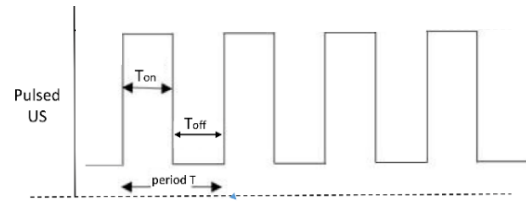

Figure 1: Example of US pulses train with a DC = 50% used for stimulation.

E. Data analysis

Data analysis was partly performed using SpyCode software [16], and partly using custom scripts developed in MatLab (The Mathwork, Natik, US). Raw data were pre-processed by using the spike detection algorithm described in [17] to extract the neuronal firing activity. All parameters were averaged over the whole array of active electrodes. To evaluate the spiking analysis we calculated two parameters: i) instantaneous firing rate, defined as the number spikes in a small window Δt of each single channel and then averaging among the active electrodes of the MEA, ii) mean firing rate (MFR), defined as the number of spikes in a certain time interval divided by the duration of the interval. To calculate the MFR values, we considered 90 s before and after the stimulation ("pre" and "post" intervals) and over 90 consecutive periods during which the US was switched on ("US_{on}" intervals) or off ("US_{off}" intervals). Moreover, we evaluated the MFR_{ratio}, defined as:

$$MFR_{ratio} = \frac{MFR_{on} - MFR_{off}}{MFR_{on} + MFR_{off}}$$

MFR_{ratio} can spans between -1 and 1: the first case would means that all spiking activity was during the "US_{off}" intervals, while the second one would means that spiking activity was only during the "US_{on}" intervals. In addition, bursting activity, detected by the string method [18], was characterized by the three following parameters, such as the bursting rate (BR), the burst duration (BD), and the number of spikes in each burst (SpkxBurst). The mean values of these parameters were calculated before, during, and after US stimulation.

III. RESULTS

In this section, we report results coming from the recordings of cortical cultures after 21 days in vitro (DIV). This allows a network development to a mature stage, when the electrophysiological activity is stable. In order to assess the changes in the activity of the cultures in the presence of US stimulation we calculated, for each experiments, a raster-plot that shows the spikes, represented with points, as a function of the recording electrode and time. Figure 2 reports 10 seconds of one representative raster plot, during the stimulation stage.
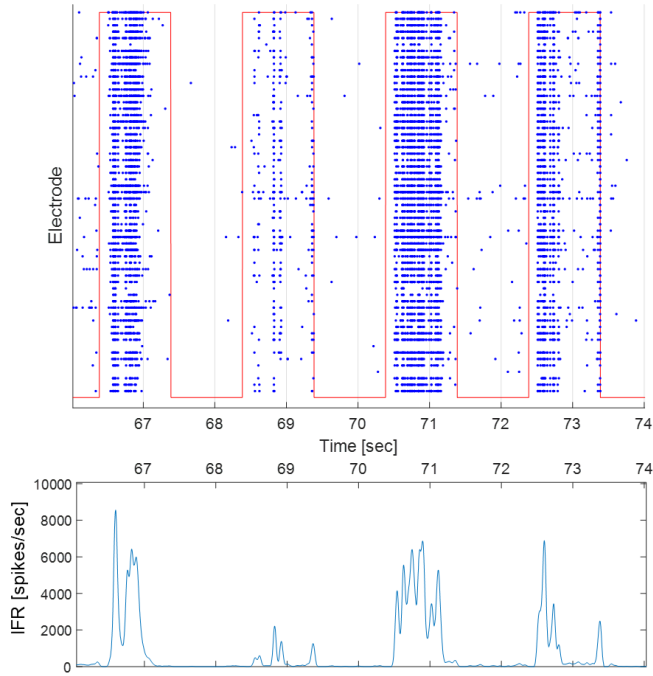
Figure 2: MEA recording of the electrical activity in primary neurons during BTNP-assisted and US-driven piezoelectric stimulation. (Top) Raster plot recorded from 60 microelectrodes during the train of US stimulations (single pulse duration = 1 s, pulse frequency = 0.5 Hz); (Bottom) Trend over time of the instantaneous firing rate.

The red line superimposed over the raster plot indicates the switching on and off of the US wave. It is evident that the entire neuronal network increases its activity when the US is switched on. The instantaneous firing rate depicted in the lower graph of Figure 2 shows a peak of about 8000 spikes/s during the USon intervals.

MFR was also calculated in order to quantify the increase in electrical activity. Table 1 shows the remarkable increases of the MFR parameter averaged over the 90 US pulses of two consecutive stimulation stages of a representative experiment, with the corresponding standard deviations (std); such increase is both repeatable and reversible.

TABLE 1
MFR [spike/sec]

Time Point	MFR value	std
Pre	1.568	0.2
US_on	8.6429	0.4
US_off	1.6406	0.2
Post	0.8167	0.14
US_on	18.0965	0.4
US_off	0.2865	0.06
Post	0.4898	0.08

Figure 3 shows a graphical representation of the change in the firing activity of a neuronal network pre-incubated with piezoelectric BTNPs during the stimulation stage of a representative experiment. MFR_{ratio} parameter is plotted as a function of the US pulse number in the pulse train; it can be observed that the MFR_{ratio} value spans preferably from +0.6 to +1 which means an increase of the spiking activity in US_{on} interval with respect to US_{off} intervals (See Methods-Data Analysis).

Also, we performed a MFR_{ratio} comparison of three different experimental configurations: i) cultures incubated with piezoelectric BTNPs, ii) cultures incubated with non-piezoelectric BTNPs, iii) cultures without nanoparticles, respectively. The last two configurations show MRF_{ratio} values close to zero and this means that, in absence of piezoelectric nanomaterials, the US stimulation was unable to induce relevant response in the neuronal network.
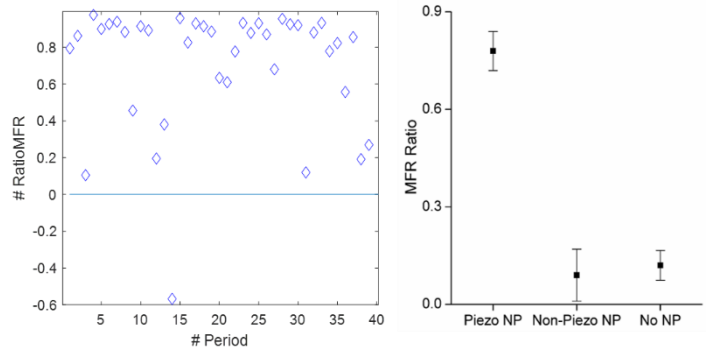

Figure 3: Analysis of the MFR ratio in response to piezoelectric stimulation. Left: MFR ratio measured for each T period in an interconnected neuronal network pre-incubated with piezoelectric BTNPs. Right: MFR ratio averaged with standard deviation over the whole electrode array. Values obtained with Piezoelectric BTNPs (Piezo NP) are compared with control experiments: neuronal networks pre-incubated with non-piezoelectric BTNPs, or incubated without NPs.

Figure 4 shows results of the bursting activity. As well as for the spiking activity, the US stimulation induce an increase of about 80% in the bursting rate activity (MBR). It is worth to notice that the electrophysiological activity of the cortical cultures returns to normal MBR value (*i.e,* MBR_{pre} and MBR_{post}) when the US is switching off. Moreover, during the stimulation, the bursts are longer and with a higher number of spikes than the ones of the other intervals, as the BD and SpkXBursts values show. These activity changes may be interpreted such as an increase of information transmission into the network induced by the US stimulation. Assessing the all obtained results, we speculate that the effects of our US stimulation protocol do not evoke any plastic change at the network level because they are limited to the USon intervals only.
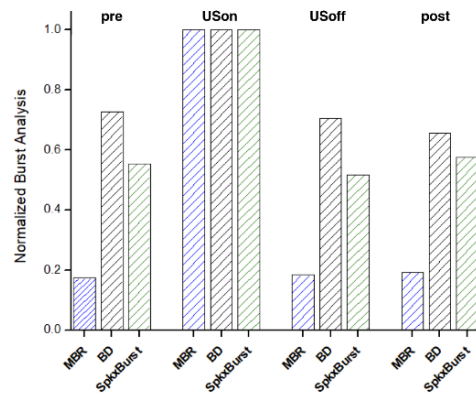

Figure 4: Network burst activity before, during, and after US stimulation for a representative experiment with piezoelectric NPs. Different parameters are plotted for each interval: mean burst rate (MBR), burst duration (BD), inter burst interval (IBI), and number of spikes per burst (SpkxBurst). Mean values are normalized with respect to the maximum during the experiment. Reproduced from [15] with permission

Although preliminary, such results suggest and offer an interesting opportunity to exploit US as a remote stimulation signal for a highly selective neuromodulation strategy based on nanoparticles. This methods cannot be defined as entirely non-invasive for the presence of the nanoparticles, however, the absence of genetic intervention, proposed in several other US based studies [19], presents some advantages. Moreover, the nanoparticles could be decorated with antibodies to address specific sub-populations of neurons in the central nervous system, with virtually single cell resolution.

REFERENCES

[1]   C. Hassler, T. Boretius, and T. Stieglitz, "Polymers for neural implants," *J. Polym. Sci. Part B Polym. Phys.*, vol. 49, no. 1, pp. 18–33, Jan. 2011, doi: 10.1002/polb.22169.

[2]   C. Marin and E. Fernández, "Biocompatibility of intracortical microelectrodes: Current status and future prospects," *Front. Neuroeng.*, vol. 3, no. MAY, May 2010, doi: 10.3389/fneng.2010.00008.

[3]   J. M. Bronstein *et al.*, "Deep brain stimulation for Parkinson disease an expert consensus and review of key issues," *Archives of Neurology*, vol. 68, no. 2. pp. 165–171, Feb. 2011, doi: 10.1001/archneurol.2010.260.

[4]   A. Thielscher, A. Opitz, and M. Windhoff, "Impact of the gyral geometry on the electric field induced by transcranial magnetic stimulation," *Neuroimage*, vol. 54, no. 1, pp. 234–243, Jan. 2011, doi: 10.1016/j.neuroimage.2010.07.061.

[5]   A. Thielscher and T. Kammer, "Electric field properties of two commercial figure-8 coils in TMS: Calculation of focality and efficiency," *Clin. Neurophysiol.*, vol. 115, no. 7, pp. 1697–1708, Jul. 2004, doi: 10.1016/j.clinph.2004.02.019.

[6]   A. Marino *et al.*, "Piezoelectric Nanoparticle-Assisted Wireless Neuronal Stimulation," *ACS Nano*, vol. 9, no. 7, pp. 7678–7689, Jul. 2015, doi: 10.1021/acsnano.5b03162.

[7]   W. D. O'Brien, "Ultrasound-biophysics mechanisms," *Progress in Biophysics and Molecular Biology*, vol. 93, no. 1–3. NIH Public Access, pp. 212–255, Jan. 2007, doi: 10.1016/j.pbiomolbio.2006.07.010.

[8]   G. K. Hesley, K. R. Gorny, and D. A. Woodrum, "MR-guided focused ultrasound for the treatment of uterine fibroids," *CardioVascular and Interventional Radiology*, vol. 36, no. 1. Springer, pp. 5–13, Feb. 28, 2013, doi: 10.1007/s00270-012-0367-3.

[9]   A. Carpentier *et al.*, "Clinical trial of blood-brain barrier disruption by pulsed ultrasound," *Sci. Transl. Med.*, vol. 8, no. 343, pp. 343re2-343re2, Jun. 2016, doi: 10.1126/scitranslmed.aaf6086.

[10]   K. B. Bader, G. Bouchoux, and C. K. Holland, "Sonothrombolysis," *Advances in Experimental Medicine and Biology*, vol. 880. Springer New York LLC, pp. 339–362, Jan. 01, 2016, doi: 10.1007/978-3-319-22536-4_19.

[11]   G. Ciofani *et al.*, "Enhancement of neurite outgrowth in neuronal-like cells following boron nitride nanotube-mediated stimulation," *ACS Nano*, vol. 4, no. 10, pp. 6267–6277, Oct. 2010, doi: 10.1021/nn101985a.

[12]   O. Naor, S. Krupa, and S. Shoham, "Ultrasonic neuromodulation," *J. Neural Eng.*, vol. 13, no. 3, p. 031003, May 2016, doi: 10.1088/1741-2560/13/3/031003.

[13]   J. Blackmore, S. Shrivastava, J. Sallet, C. R. Butler, and R. O. Cleveland, "Ultrasound Neuromodulation: A Review of Results, Mechanisms and Safety," *Ultrasound in Medicine and Biology*, vol. 45, no. 7. Elsevier USA, pp. 1509–1536, Jul. 01, 2019, doi: 10.1016/j.ultrasmedbio.2018.12.015.

[14]   C. Rojas *et al.*, "Acoustic stimulation can induce a selective neural network response mediated by piezoelectric nanoparticles.," *J. Neural Eng.*, vol. 15, no. 3, p. 036016, 2018, doi: 10.1088/1741-2552/aaa140.

[15]   A. Marino *et al.*, "Nanomaterial-Assisted Acoustic Neural Stimulation," in *Neural Interface Engineering*, Cham: Springer International Publishing, 2020, pp. 347–363.

[16]   L. L. Bologna *et al.*, "Investigating neuronal activity by SPYCODE multi-channel data analyzer," *Neural Networks*, vol. 23, no. 6, pp. 685–697, Aug. 2010, doi: 10.1016/j.neunet.2010.05.002.

[17]   A. Maccione, M. Gandolfo, P. Massobrio, A. Novellino, S. Martinoia, and M. Chiappalone, "A novel algorithm for precise identification of spikes in extracellularly recorded neuronal signals," *J. Neurosci. Methods*, vol. 177, no. 1, pp. 241–249, 2009, doi: 10.1016/j.jneumeth.2008.09.026.

[18]   M. Chiappalone, A. Novellino, I. Vajda, A. Vato, S. Martinoia, and J. van Pelt, "Burst detection algorithms for the analysis of spatio-temporal patterns in cortical networks of neurons," *Neurocomputing*, vol. 65–66, no. SPEC. ISS., pp. 653–662, 2005, doi: 10.1016/j.neucom.2004.10.094.

[19]   S. Ibsen, A. Tong, C. Schutt, S. Esener, and S. H. Chalasani, "Sonogenetics is a non-invasive approach to activating neurons in Caenorhabditis elegans," *Nat. Commun.*, vol. 6, no. 1, pp. 1–12, Sep. 2015, doi: 10.1038/ncomms9264.

Tensile properties of porcine retina

B. Belgio[1], S. Ragazzini[1], P. Arpa[2], V. De Molfetta[2], S. Mantero[1], and F. Boschetti[1]

[1] *Department of Chemistry, Materials and Chemical Engineering, "Giulio Natta", Politecnico di Milano, 20133 Milan, Italy*

[2] *S. Gerardo Hospital, Monza Brianza, Italy*

Abstract—**The mechanical properties of the retina has not received much attention, probably due to the fact that retina is very fragile and that its main function is not related to mechanical support. In this study, we provide a protocol to isolate the retina and perform tensile testing on porcine retinal tissues. Moreover, we present our preliminary results. These show a short linear region followed by a relatively wide non-linear region characterized by peaks. Additional tests will be carried out to confirm these preliminary findings.**

Keywords—**Retina, tensile test, mechanical parameters, ophthalmology.**

I. Introduction

THE retina, lining the posterior wall of the eye, is a thin neurosensory membrane responsible for absorption of the light and transmission of this signal to the brain through the optic nerve. It is composed of multiple layers of different cells including retinal epithelial cells (RPE), photoreceptors, glial cells and neurons (Fig.1). These cells are supplied either by the central retinal artery and its branches which perfuse the anterior retina or by the choroid that provides nutrients and oxygen to the outer retina through Bruch's membrane (BM).
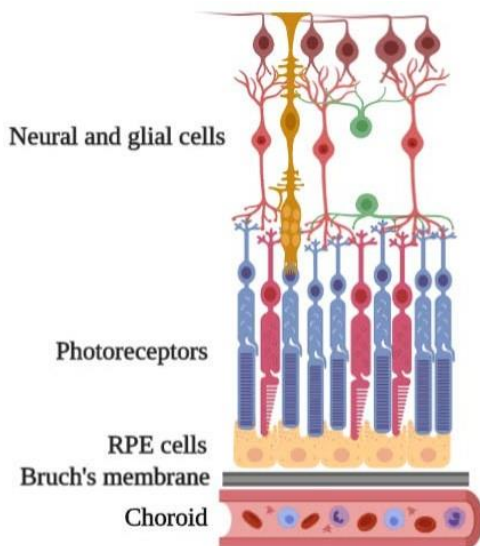

Fig. 1: Schematic illustrating the cellular composition of the retina

The mechanical properties of the retinal tissue are scarcely investigated probably because of its extreme structural fragility [1], [2], [3]. Hence, retina results to be difficult to be isolated and manipulated.

Although the retina does not play a key role in mechanical support, the knowledge of its mechanical response is important for a variety of reasons. For instance, it helps completely understand the retinal physiology. In addition, it allows to build both *in silico* and *in vitro* models used for investigating retinal physiology and pathologies such as age-related macular degeneration (AMD), glaucoma, retinitis pigmentosa, diabetic retinopathy [4], [5]. In high-income countries, these diseases account for a large proportion of blind or visually impaired people [6]. Moreover, they are difficult to treat, mostly because topical administration presents limited access to the retina and systemic administration requires high doses with consequent undesired effects. Intravitreal injections represent an alternative but they are invasive, expensive, and unable to restore tissue functionality [6]. Knowing retinal biomechanical properties is also fundamental to develop retinal functional tissue engineered prostheses that can be implanted in patients suffering from one of the diseases previously mentioned. Another reason to examine mechanical properties of retinal tissue is to understand and to prevent the risks of detachment during surgical procedures (i.e. vitrectomy). Indeed, during vitrectomy, which consists in removal and consequent replacement of the vitreous, retinal tear can be caused with subsequent cell loss resulting in retinal detachment [1].

Here, we present the preliminary results of tensile tests performed on pig retinal tissues.

II. Materials and Methods

A. Sample collection

Pig eyes were collected from a local abattoir (Fumagalli Industria Alimentare, Tavernerio (CO), Italy), within 1 hour post mortem. Pigs were nine months old.

B. Sample preparation

The eyeballs were cleaned from adipose tissue and conjunctiva (Fig. 2A). Using a scalpel to make a circular cut on the sclera at the cornea level, we carefully removed, in sequence, cornea, iris, crystalline lens, and vitreous (Fig. 2 B). Then the retina was cautiously detached from the back wall of the posterior chamber (Fig. 2C), and preserved in PBS solution (P4417, SIGMA) at 4 °C until testing. Before testing, 11x5 mm retinal samples were obtained.
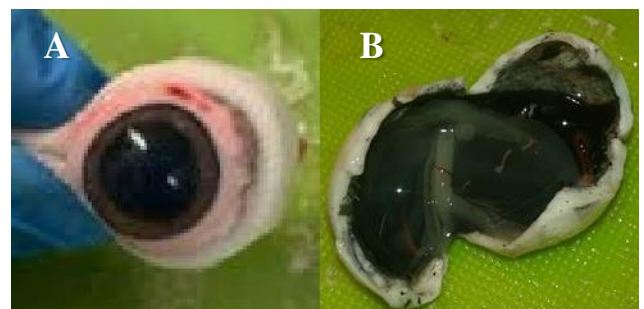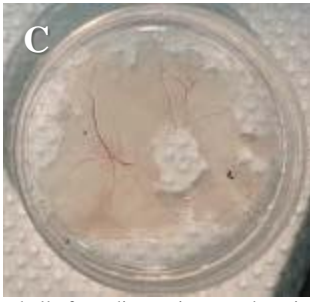
Fig. 2: **(A)** Clean eyeball after adipose tissue and conjunctiva removal. **(B)** Isolation and detachment of retina from the back of the eye. **(C)** Detached retina preserved in PBS.

C. Experimental apparatus and protocol

For the mechanical measurements, retinal samples were clamped between the grips of an electromechanical testing machine (TC3F, EBERS), equipped with a 1 lb load cell (Fig. 3). Grips were made of knurled stainless steel and clamping was obtained manually by screws. Silicone sheets were interposed between clamps and retina to preserve the sample integrity. After five preconditioning cycles, consisting in stretching the samples up to 1 mm and back to zero at a strain rate of 0.88 %/s, samples were pulled until failure at a velocity of 0.88 %/s at room temperature.
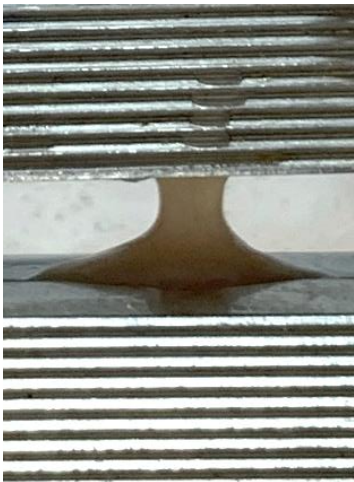

Fig. 3: Porcine retina clamped between the grips of the tensile testing machine

D. Definition of Biomechanical Terms

From the force (N) – elongation (mm) data, we calculated the stress (MPa) as the ratio of the applied force to the original cross section area (mm^2), and the strain as the change of length divided by the original length. The original cross section area was calculated as the multiplication of the initial thickness by the initial width, both evaluated through the ImageJ software (National Institutes of Health, USA). The gap between the clamps was considered as the original length. The elastic modulus (E) was extracted from the stress-strain plots as the linear portion of the curve before the change of the slope. The yield stress (Y) was defined as the point of change of slope in the first linear elastic region of the stress-strain curve. The failure stress was set to the maximum stress value.

E. Statistical analysis

Results of E, Y and failure stress are presented as average ± standard deviation (SD).

III. RESULTS

A. Stress-Strain Measurements

A typical stress-strain curve of retinal samples under tensile tests is shown in Fig. 4. The curve exhibited a narrow initial linear region followed by a wide region of plastic behavior presenting several peaks probably due to micro-ruptures in the tissue.
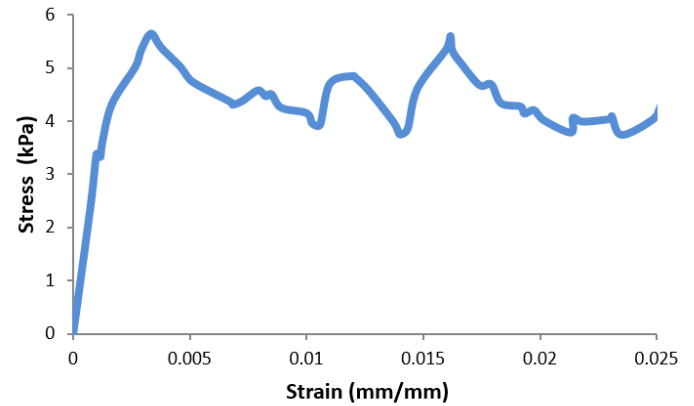

Fig. 4: Tensile stress versus strain curve of retinal specimens at room temperature

A close-up view of the first portion of the curve displays an initial elastic region followed by yielding before rupture.
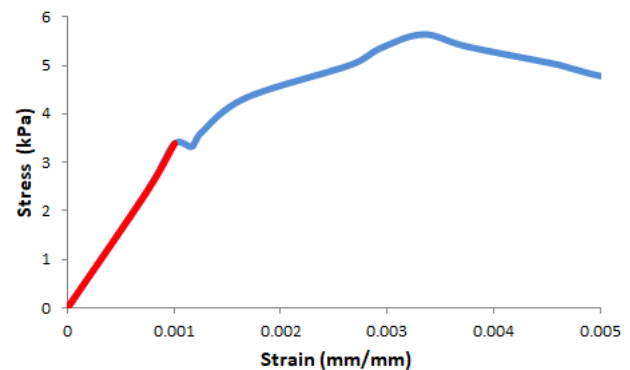

Fig. 5: Zoom in of the stress-strain relationship shown in Fig. 4. The red line represents the initial elastic region before plastic deformation.

For the stress-strain measurements of retinal tissue, five samples (n=5) were tested and their resulting curves were analyzed. The elastic modulus E at room temperature was on average 2.87 ± 1.29 MPa with values ranging from 1,65 MPa to 5 MPa. The Y and the failure stress resulted to be 3.67 ± 2 kPa and 7.428 ± 3.62 kPa respectively. Table I outlines the average values and the SDs of the biomechanical parameters taken into account, namely E, Y, and failure stress.

TABLE I
BIOMECHANICAL PARAMETERS

Parameter	Average value	Standard deviation (SD)
Elastic modulus (E) (MPa)	2.87	1.29
Yield stress (Y) (kPa)	3.67	2
Failure stress (kPa)	7.428	3.62

Table I shows the average values and the SDs of the biomechanical parameters analysed in this study

IV. DISCUSSION AND CONCLUSION

Considering the initial tests (n=5) that we performed, we can hypothesize that the biomechanical behaviour of the retina is characterized by a short linear region of elastic deformation and a relatively wide non-linear region of plastic deformation. Nevertheless, these results are still preliminary. Hence, currently we are carrying out additional tests that are necessary to obtain more significant data and to compare our findings with those of the previous studies [1], [3].

REFERENCES

[1] G. Wollensak, and E. Spoerl, "Biomechanical characteristics of retina," *Retina, the Journal of Retinal and Vitreous Diseases*, vol. 24, no. 6, pp. 967-970, 2004.

[2] W. Wu, W. H. Peters, M. E. Hammer, "Basic mechanical properties of retina in simple elongation," *Journal of Biomechanical Engineering*, vol. 109, pp. 65-67, February 1987.

[3] K. Chen, and J. D. Weiland, "Anisotropic and inhomogeneous mechanical characteristics of the retina," *Journal of Biomechanics*, vol. 43, pp. 1417-1421, 2010.

[4] M. Ferroni, M. G. Cereda, and F. Boschetti, "A Combined Approach for the Analysis of Ocular Fluid Dynamics in the Presence of Saccadic Movements," *Ann Biomed Eng.*, vol. 46, pp. 2091-2101, August 2018.

[5] M. Ferroni, M. G. Cereda, and F. Boschetti, "Saccadic movement effects on intraocular drug delivery for a wet-AMD clinical case," *Journal for Modelling in Ophthalmology*, vol. 2, pp. 86-91, 2018.

[6] N. C. Hunt, D. Hallam, V. Chichagova, D. H. Steel, and M. Lako, "The application of biomaterials to tissue engineering neural retina and retinal pigment epithelium," *Advanced Healthcare Materials*, vol. 7, 1800226, 2018.

SensRing, a wearable ring-shaped device for measuring kinematics in reach-to-grasp tasks

G. Galperti[1], E. Rovini[1,2], L. Fiorini[1,2], G. Mancioppi[1,2], R. Zeghari[3], A. Gros[3], V. Manera[3] and F. Cavallo[1,2,4]

[1] The BioRobotics Institute, Scuola Superiore Sant'Anna, Pisa, Italy
[2] Department of Excellence in Robotics and AI, Scuola Superiore Sant'Anna, Pisa, Italy
[3] CoBTeK lab of the Université Cote d'Azur, Nice, France
[4] Department of Industrial Engineering, University of Florence, Florence, Italy

Abstract—**Reach-to-grasp (RG) actions have been recently studied to evaluate action planning and how intentions in performing a movement modify its kinematics. Studying the kinematics of these action sequences can point out important information on motor planning and control in several pathologies, including neurodegenerative diseases. Currently, RG analysis is mainly based on optoelectronic systems, which provide accurate movement tracking but are time-consuming, expensive and limited to some constrained research spaces. In this study, SensRing, a ring-shaped wearable system has been proposed to record inertial data in an easy and non-invasive way. A reach-to-grasp protocol was applied in a population of 20 healthy young controls (HYC) and 19 healthy older controls (HOC) where subjects were instructed to reach towards and grasp a can to drink (DRINK), to place it on a cup (IND) or to pass it to another partner (SOC). Results indicate that motor patterns are sensitive to experimental conditions. Precisely, SensRing can differentiate similar actions that differ for end-goals (DRINK vs IND/SOC) or for social intentions (IND vs SOC). Moreover, HOC kinematic patterns significantly differ from HYC; this shows the potentiality of SensRing to explore age-related changes in kinematics of RG actions and it provides the ability to extend these studies on patients with neurodegenerative pathologies that can have impairments in motor planning or social interaction.**

Keywords—**reach-to-grasp, ring-shaped sensor, action planning, social intention.**

I. INTRODUCTION

P rior social purposes can shape the way we perform actions. For instance, someone could grasp an object with the intent of touch it, use it, lift it, move it, or pass it. Experimental studies based on reach-to-grasp protocols showed that intentions influence action planning so that differences in kinematic features are evident according to the goal to be achieved, although the to-be-grasped object remains the same [1]. This can be attested by asking subjects to reach and grasp an object, and then to perform subsequent actions with different aims (e.g. lift it, place it in a container, pour its content, pass it to a partner, pass it to a partner while communicating with him). These paradigms spotted the role of end-goals and social intentions in motor planning. Therefore, such paradigm is becoming crucial to show how action kinematics is sensitive to the final goal and how the social context is characterized by the interaction with a partner [2].

The kinematic analysis of these action sequences, decomposing them in reach-to-grasp (RG) and move (M) tasks, can provide relevant information about changes in motor performance during aging, as well as about deficits in action planning and control in several clinical populations, including

people with Parkinson's disease [3], stroke [4], and autism spectrum disorder [5]. Previous studies on RG protocols showed how older people perform simple reach and grasp actions in a different way compared to young subjects [6], [7]. Kinematic modifications could be either the result of physical decline due to age, leading to abnormalities in motor patterns, or the result of compensation strategies due to the deterioration of other systems [8]. Monitoring such changes in simple daily actions during aging can be remarkably informative in clinical practice, especially in the context of neurodegenerative diseases, such as Alzheimer's Disease. However, up to now, most studies have been performed in research settings because current technology, based on 3D optoelectronic motion capture systems, is time-consuming, invasive, and limited to dedicated space.

Recently, we developed an innovative ring-shaped wearable system, named SensRing, that can record kinematic data from the hand. We selected a reach-to-grasp protocol consisting of three tasks with different end-goals (i.e. drinking, placing, passing), all involving the grasping of an object, and tested it in a population of 39 subjects (20 younger healthy subjects, and 19 older healthy adults). In this context, we aim at i) verifying the effectiveness and usability of SensRing, assessing motor performances through an RG protocol. Our goal is to investigate whether the system could differentiate reaching actions that differ in terms of end-goal, or social intentions; then, we aim at ii) studying whether SensRing could identify distinct motor patterns, related to subjects' ages.

II. MATERIAL AND METHODS

A. Instrumentation

SensRing is a ring-shaped wearable sensor, worn on the proximal phalanx of the index finger, able to full track the orientation and movement of the finger (Fig. 1). It is characterized by a 9-axes inertial measurement unit (IMU) LSM9DS1 (STMicroelectronics, Italy), which includes 3D,

Fig. 1: Left: SensRing device. Right: Setup for reach-to-grasp protocol.

TABLE I.
KINEMATIC PARAMETERS EXTRACTED FROM SENSRING.

Variable	Parameter	Definition
IAV	Integral of the magnitude of the acceleration vector	It represents a value correlated to the energy expenditure [m/s].
SMV	Signal Magnitude Vector	It indicates the degree of movement intensity.
SMA	Signal Magnitude Area	It indicates the fluctuation degree of the acceleration signal.
rmseJ	Root mean square of the Jerk	It represents the smoothness of the movement [m/s^3].
SKEW	Skewness	It is a measure of the asymmetry of the distribution.
KURT	Kurtosis	It is a measure of the shape of the tail of the distribution.
T	Execution Time	It represents the time spent to make the movement [s].
Vpeak	Amplitude of peak velocity	It is the amplitude of the peak velocity during the movement [m/s].
Tvpeak	Time of peak velocity	It is the time instant corresponding to the peak velocity [s].
Treact	Reaction time	It indicates the time elapsed from the beep to start the movement [s].
EXC	Amplitude of maximum hand excursion	It indicates the angular excursion of the hand during the grasping of the object [deg].
Texc	Time of maximum excursion	It is the time instant corresponding to the maximum aperture of the hand [s].

digital linear acceleration sensor (full scale: ±2/±4/±8/±16 g), 3D digital angular rate sensor (full scale: ±245/±500/±2000 dps) and 3D digital magnetic sensor (full scale: ±4/±8/±12/±16 gauss). It is based on an ARM®Cortex™-M3 32-bit STM32-F103 microcontroller (STMicroelectronics, Italy) which acquires, filters and stores data at a frequency of 50 Hz. These data are then transmitted towards a generic control station through a wireless communication based on the Rigado BMD-350 Bluetooth serial device, using a dongle. In this study, the device was powered by a small, rechargeable, and light polymer lithium battery, externally fixed to the wrist with an elastic band. A dedicated interface, based on C# language, has been developed in Microsoft Visual Studio 2019 to manage the connection and the transmission of sensors data from SensRing. Acquired data are then saved in specific directories as text files.

B. Participants

Twenty healthy young controls (HYC) (11 females, 9 males, mean age ± standard deviation (SD) 33.15±10.15 years old) and nineteen healthy older controls (HOC) (14 females, 5 males, mean age ± SD 63.42±9.93 years old) voluntarily took part in the study, carried out at the Nice Research Memory Center (CMRR) & Cognition Behaviour Technology laboratory (CoBTeK). All participants were right-handed. All the subjects signed a written informed consent and the study procedure was performed in accordance with the Declaration of Helsinki and approved by the ethical committee CPP Ile de France (N° IDRCB: 2019-A00342-55).

C. The Reach-to-grasp Protocol

The subjects were asked to wear SensRing on the proximal phalanx of the index finger of the dominant hand. During this study, also the SensHand wearable inertial system was used for acquiring data (Fig. 1), but its analysis is out of the scope of this paper. As described in [2], participants were sitting in front of a table with the hand in the starting position, 3 cm away from the edge of the table in a midsagittal position, 15 cm away from the midsection. Three exercises, adapted from other experimental studies that investigated reach-to-grasp sequences [1], [2] were chosen to evaluate the performance of the subjects. After 5 seconds of acquiring the initial static position, a tone indicated to the subject of starting the task. For these exercises, a can was positioned on a table in front of the

participant at 21 cm from the hand starting position along the midsagittal plane (Fig. 1). For each of the three exercises randomly selected, 10 repetitions were done: i) Drink (DRINK): the subject had to reach the can, grasp it and lift it up to drink; ii) Individual (IND): the subject had to reach the bottle, grasp it and put inside a cup, placed on the table and located 28 cm at the right side with respect to the initial position of the bottle. After each repetition, the can was repositioned on its initial position; iii) Social (SOC): the subject had to reach the can, grasp it, and pass it to a partner. The partner seated to the right side of the table with the hand resting on the target position ready to take the can. After each repetition, the partner repositioned the can on its initial position.

D. Data Analysis

Inertial data acquired with SensRing were stored and offline processed by using MATLAB R2018a (The MathWorks, Inc., Natick, MA, USA). Triaxial accelerations and triaxial angular velocities, provided by the accelerometer and gyroscope, were pre-processed with a fourth-order low-pass digital Butterworth filter using a 5 Hz cut-off frequency to erase high-frequency noise. Custom made algorithms were implemented for signal segmentation to identify the characteristic times of each exercise.

Each gesture was decomposed in the *reach-to-grasp* (RG) and the *move* (M) phases. For each exercise, a set of kinematic parameters was obtained from acceleration and angular velocities of the SensRing (Table I). All the parameters were calculated both in the RG and the M phase, except for the reaction time, the amplitude and time of maximum hand excursion that were measured during RG phase only. Totally, 21 parameters composed the dataset of each exercise, including 12 features for the RG and 9 for the M phase. Some biomechanical parameters are taken from [9], [10], where more information about the computation of these parameters are detailed. Other parameters have been chosen because, as previously demonstrated by [2], they are sensitive to variations in social context, such as: the amplitude of peak velocity during both the RG and the M phases with the corresponding time instant and the amplitude of maximum aperture of the hand during the reaching phase with its associated time instant. Data were expressed as mean ± SD for all the conditions, both for the HYC and the HOC groups. Preliminary analysis was conducted on data to check for normality by using the Kolmogorov-Smirnov test. According to the results of the test,
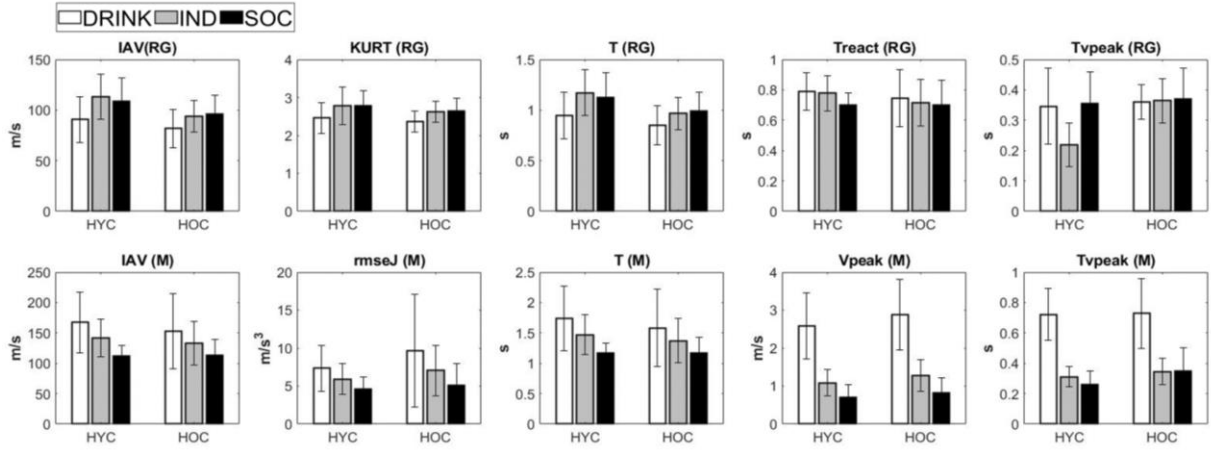
Fig. 2: Graphical representation for significant parameters within conditions (DRINK, IND, SOC) for HYC and HOC groups.

data were not normally distributed, so non-parametric statistical tests were used.

Specifically, two analyses were proceeded on data:

- *Intra-group analysis*, both for HYC and HOC, to investigate significant differences (p<0.05) among the movements over the three experimental conditions (DRINK, IND, SOC). Here, for each dependent variable, the means of each participant was entered in the Wilcoxon test.
- *Inter-group analysis* to study the influence of age in performing simple RG sequences. The non-parametric Mann-Whitney U-Test was applied to investigate significant differences (p<0.05) in motor parameters between the two groups.

III. RESULTS

The aim of this paper was to study the use of SensRing wearable device to have quantitative analysis on sequences of reach-to-grasp and move actions, in order to investigate how motor goals affect the way people move and plan the actions. First, the intra-group analysis aims at calculating the performance of the subjects by investigating differences in motor patterns due to differences among the three experimental conditions. Second, the inter-group study points out differences in movement executions related to age in those two groups.

Intra-group HYC analysis: for the RG phase, the experimental condition DRINK was significantly different (p<0.05) for IAV, SMV, SMA, KURT, T both from SOC and IND. Moreover, DRINK differ only from SOC concerning Reaction time, whereas Vpeak, Tvpeak and Texc are statistically different when comparing DRINK with IND. Furthermore, significant differences were obtained for the Tvpeak and Treact when comparing IND vs. SOC condition. Concerning the M phase, the IAV, rmseJ, SKEW, KURT, T, Vpeak, Tvpeak are statistically different between IND and SOC condition. A graphical representation of the main significant parameters is shown in Fig. 2.

Intra-group HOC analysis: for the RG phase, the IAV, SMV, SMA, KURT, T can differentiate the DRINK both from the IND and SOC conditions. Moreover, the rmseJ was found significantly different when comparing the IND from the SOC experimental task. Regarding the M phase, significant differences were found comparing the IND and SOC condition in the IAV, rmseJ, KURT, T, Vpeak.

Inter-group analysis: all the significant features able to distinguish between HOC and HYC are reported in Table II.

TABLE II.
SIGNIFICANT KINEMATIC PARAMETERS FOR INTER-GROUP ANALYSIS.

Task	Features	HYC Mean±SD	HOC Mean±SD	p-value
DRINK	SMV (M)	96.07±0.81	96.63±1.01	0.0445
	KURT (M)	2.77±0.67	2.42±0.65	0.0444
	Vpeak (RG)	0.73±0.52	1.08±0.49	0.0436
IND	IAV (RG)	113.24±22.01	94.03±15.80	0.0052
	SMV (RG)	96.57±0.74	97.28±1.16	0.0416
	SMV (M)	96.24±0.54	96.94±0.86	0.0086
	SMA (M)	2.77±0.12	2.88±0.13	0.0294
	T (RG)	1.17±0.23	0.97±0.16	0.0036
	Vpeak (RG)	0.85±0.54	1.29±0.41	0.0255
	Tvpeak (RG)	0.31±0.07	0.35±0.09	<0.0001
SOC	SMV (M)	96.30±0.97	97.11±1.09	0.0220
	T (RG)	1.12±0.24	0.99±1.09	0.0363
	Vpeak (RG)	0.84±0.46	1.15±0.33	0.0255
	Tvpeak (RG)	0.26±0.09	0.35±0.15	0.0444

IV. DISCUSSION AND CONCLUSION

Nowadays, the optic systems, relying on infrared cameras, represent the gold standard for fine motor assessment. Those systems generate reliable movement data but, conversely, require space and a sizable amount of time to setup. Therefore, we presented SensRing, an innovative wearable ring-shaped device that aims at facilitating such analysis, providing accurate measurements. Achieved results from accuracy evaluation tests [11], even if obtained from a small dataset, are very promising in terms of reliability of the measures from the SensRing and make the device suitable to support clinicians in daily practice to objectify motor evaluations. In this study, SensRing was used to collect movement information during an RG protocol. According to the literature, human hand movements, for instance, reach and grasp an object, are characterized by the use of specific motor patterns associated with the action end-goal [1], [2]. These authors showed that the intention to perform a movement could shape its kinematics, regardless of physical constraints (the object to be grasped or the movement to reach the object). The kinematics revealed different motor patterns according to the action that followed the grasping. In our work, we aim at investigating motor planning and the role of intentions by asking participants to perform three tasks using the same object: i)

grasp a filled can and lift it up to drink (DRINK condition), ii) grasp and place it on a target position represented by a cup with matching size as the object (IND/placing condition), iii) grasp and pass it to a partner (SOC/passing condition). The rationale behind these tasks was that: the drinking action is a low-accuracy task that served for performing a different action in terms of end-goal and final position; the placing (high-accuracy) and passing tasks are two similar actions in terms of movement, but different for the goal and the context (individual or social conditions). The hypothesis are i) to find in these groups of neurologically healthy controls, differences in motor patterns able to differentiate the first phase of the movement (i.e. reaching and grasping the object) which is the same for the three tasks, according to the type of end-goal and to investigate whether different aims and intentions shapes the second phase of the movement (i.e. placing or passing the object). Then, ii) to find age-related changes of motor patterns by comparing the young and older groups. For this purpose, we partitioned each task into two successive phases, the reach-to-grasp part that was the same for the three exercises and the move part that should change in terms of motor planning (DRINK vs IND,SOC) or in terms of social intentions (IND vs SOC). Consistently with our first hypothesis, the execution of motor actions (reaching and grasping an object) is not only determined by the physical properties of the object (shape or size), but also by subject's intentions. Among the significant parameters for the two groups, the estimated energy expenditure (IAV), the kurtosis (KURT) and the execution time (T) during the RG phase are lower for the drinking condition, which can be considered a low-accuracy task performed individually. These parameters appear higher for the other two tasks, which require more precise and careful motor planning. Indeed, subjects had to precisely place the object into a container (with a matching size) or to carefully pass the object to the partner. Moreover, HYC exhibited an anticipated peak velocity (Tvpeak) and took longer (Treact) to initiate the placing action compared to the passing one. This aspect might reflect that the motor planning of an object insertion into the container requires a higher degree of cognitive resources if compared to passing an object to a partner. Concerning the moving phase, as expected, SensRing has been able to differentiate the DRINK motor sequences from IND and SOC conditions. Indeed, they are actions with completely different goals and final movement positions. Interestingly, significant differences have been found during the IND and SOC moving phases, which consist of the same movement but different goal (placing vs passing) and context (individual vs social). Some parameters, such as the estimated energy expenditure, the smoothness of the movement (rmseJ) and the execution time are higher for the placing condition, suggesting higher efforts for the high-accuracy task. Moreover, a lower and anticipated peak velocity for the social conditions suggested a more careful approach when the subject had to interact with another partner. Then, we compared the motor performances of young and old controls to verify if SensRing could identify differences in motor patterns related to the age. Previous studies have already demonstrated that along with aging can occur changes in movement executions, which might reflect a compensation strategy due to decline in cognitive and/or physical control systems [6]. Older subjects tend to perform longer movements and adopted different grasping strategies [8], showing a lower accuracy in

performing those actions [7]. Tracking age-related changes in the kinematics of grasping actions can be very important for the clinical practice, especially for neurodegenerative diseases. In the present study, we managed to find significant differences in motor patterns between the two groups by using a non-invasive and easy to use device. Our work enriches the present literature, presenting a breakthrough technology that did not rely on optoelectronic motion capture systems, which due to their drawbacks in terms of time and space, hamper the potentiality of such protocols in clinical settings. However, this work presents some limitations related to the reduced number of involved subjects and the recruitment of only right-handed persons. Nevertheless, the obtained results are promising, and the experimental protocol can be easily replicated in further studies to enlarge the dataset.

In conclusion, SensRing could be a proper alternative to optoelectronic systems in evaluating motor performances during reach-to-grasp protocols. It is easy-to-use, not time-consuming and it does not require ample spaces. Indeed, it can be adopted in hospital settings but also at home. Future works involve the application of this protocol in patients with neurodegenerative diseases (e.g., PD, stroke, autism spectrum disorder), to investigate whether SensRing could be applied in medical practice to support clinicians in motor evaluation.

REFERENCES

[1] C. Ansuini, L. Giosa, L. Turella, G. Altoè, and U. Castiello, "An object for an action, the same object for other actions: Effects on hand shaping," Exp. Brain Res., vol. 185, no. 1, pp. 111–119, 2008.

[2] C. Becchio, L. Sartori, M. Bulgheroni, and U. Castiello, "The case of Dr . Jekyll and Mr . Hyde : A kinematic study on social intention," vol. 17, pp. 557–564, 2008.

[3] E. Straulino, T. Scaravilli, and U. Castiello, "ScienceDirect Social intentions in Parkinson ' s disease patients : A kinematic study," CORTEX, vol. 70, pp. 179–188, 2015.

[4] A. Viau, A. G. Feldman, B. J. McFadyen, and M. F. Levin, "Reaching in reality and virtual reality: A comparison of movement kinematics in healthy subjects and in adults with hemiparesis," J. Neuroeng. Rehabil., vol. 1, pp. 1–7, 2004.

[5] L. A. R. Sacrey, T. Germani, S. E. Bryson, and L. Zwaigenbaum, "Reaching and grasping in autism spectrum disorder: A review of recent literature," Front. Neurol., vol. 5 JAN, no. January, 2014.

[6] K. M. B. Bennett and U. Castiello, "Reach to grasp: Changes with age," Journals Gerontol., vol. 49, no. 1, pp. 1–7, 1994.

[7] Y. Tamaru, Y. Naito, and T. Nishikawa, "Earlier and greater hand pre-shaping in the elderly: a study based on kinematic analysis of reaching movements to grasp objects," Psychogeriatrics, vol. 17, no. 6, pp. 382–388, 2017.

[8] A. Cicerale, E. Ambron, A. Lingnau, and R. I. Rumiati, "A kinematic analysis of age-related changes in grasping to use and grasping to move common objects," Acta Psychol. (Amst.)., vol. 151, pp. 134–142, 2014.

[9] F. Cavallo, G. Megali, S. Sinigaglia, O. Tonet, and P. Dario, "A biomechanical analysis of surgeon ' s gesture in a laparoscopic virtual scenario ."

[10] D. Figo, P. C. Diniz, D. R. Ferreira, and J. M. P. Cardoso, "Preprocessing techniques for context recognition from accelerometer data," Pers. Ubiquitous Comput., vol. 14, no. 7, pp. 645–662, 2010.

[11] E. Rovini, G. Galperti, L. Fiorini, G. Mancioppi, V. Manera, & F. Cavallo, (2020), "SensRing, a novel wearable ring-shaped device for objective analysis of reach-to-grasp movements", Accepted in IEEE Eng Med Biol Soc. (EMBC) 2020, July 20-24, 2020, Montreal, Canada.

Driving neuronal network connectivity with a modular alginate mask

M. Brofiga[1]*, E. Dellacasa[1]*, E. Vitali[1], D. Di Lisa[1], P. Massobrio [1] and L. Pastorino[1]

[1] *Department of Informatics, Bioengineering, Robotics, System Engineering (DIBRIS),*
University of Genova, Genova, Italy
martina.brofiga@dibris.unige.it, elena.dellacasa@edu.unige.it
* These authors contributed equally to this work

Abstract—The engineering and modelling of neuronal networks are aimed at understanding the complex mechanisms of communication and the development of the central nervous system. Conventional modelling methods deal with the building of networks with a pre-programmed and unalterable structure and, though they offer good reproducibility, they have limitations to mimic dynamical changes we observe *in vivo*. This work aims at engineering a neuronal network following a topology through the design and development of a biopolymeric mask with controlled and modular geometry.

Keywords—Micro-Electrode Arrays, removable alginate mask, engineered neuronal network.

I. INTRODUCTION

The interplay between the morphological and functional features of neuronal circuits is one of the current significant challenges in the field of neuroengineering and computational neuroscience. If it is reasonable to assume that network connectivity acts on the expressed electrophysiological activity, it is also evident that the same activity modulates the morphological structure of the network: a fundamental physiological phenomenon like synaptic plasticity implies a remodeling of the neural circuits depending on activity. Repetitive activation patterns can reinforce particular synaptic pathways and depress others [1]. These evidences imply that connectivity and dynamics are highly interdependent and interact in a bidirectional way. The main problem concerning the study of the relationship between structure and function is related to the modular and hierarchical organization of the brain [2], [3]. The high *in vivo* brain complexity, due to the numerous connections among the different brain regions, the high number of input that each region receives, and the intricate connectivity inside each assembly do not allow to easily understand the role of each neuronal population. Nonetheless, despite the significant progress in electrophysiology and imaging that has allowed access to complex *in vivo* circuits, the neuronal motifs recordings are still minimal. As a result of these limitations, alternative methods have been developed over the years that allow the study of the structure-function relationship. Primary dissociated neuronal cultures are an elegant powerful experimental tool to investigate and describe both electrophysiological and morphological properties of neuronal networks which guarantee a trade-off between controllability/observability and similarity to the *in vivo* nervous system. The electrophysiological activity of such neuronal assemblies can be extracellularly recorded by means of Micro-Electrode Arrays (MEAs). Up to now, most of the works make use of uniform networks [4], [5], [6], [7], [8], [9], which do not fully mimic the complex organization as well as the functional complexity of the human brain *in vivo* [10], [11], [12]. Indeed, neuronal networks of the brain have small-world properties with scattered connectivity, locally clustered, and with some long-range connections that mediate short path lengths between any pair of regions [13]. Controlling the topological features of neuronal networks on MEAs and predetermining their connectivity has been the topic of extensive studies in the past decade. Techniques including micro-contact printing [14], [15], UV irradiation [16], and photolithography [17] have allowed to design networks with different topological architectures. However, these methods define networks with a preprogrammed and unalterable structure, showing limitations in the reproduction of structural changes in a controlled manner. This study aims to design the topology of a neuronal network and to trigger and drive the connections among different neuronal sub-populations at different time points. To this purpose, a patterned surface with selected bio-adhesive areas for neurons deposition and growth has been developed. In particular, poly-L-lysine and chitosan were chosen as adhesion factors and let to adsorb as uniform thin films onto planar supports. A micrometric alginate-based mask, with specific microwell was placed onto the bio-adhesive films to confine the position of the cellular cell bodies in predetermined area. Chitosan was chosen as an alternative substrate to the classic Poly-L-lysine because of its previously demonstrated properties of neuron attachment and growth enhancement [18]. Alginate was chosen, in its hydrogel form, because of its known cell-repellent properties [19] that ensure neurons to be confined within the microwells. In addition, the alginate hydrogel can be removed with weak chemical treatments, avoiding the neural culture to be damaged during the mask removal and then resulting in unaltered growth of neuritic processes and communication between different sub-populations.

II. MATERIALS AND METHODS

A. Alginate mask

The MIMIC (micromolding in capillaries) technique was used to create the alginate mask. To this end, a silicon master with 120 microwells was designed and developed (Scriba Nanotechnologie S.r.l) in a layout that reflects the configuration of a MEA with 120 recording sites. This device was chosen since a more significant number of electrodes will allow signal propagation in the neural network to be evaluated. The microwells are 10 μm in height, 100 μm in diameter and have a center-center distance of 200 μm (reflecting MEA features) (Fig.1).
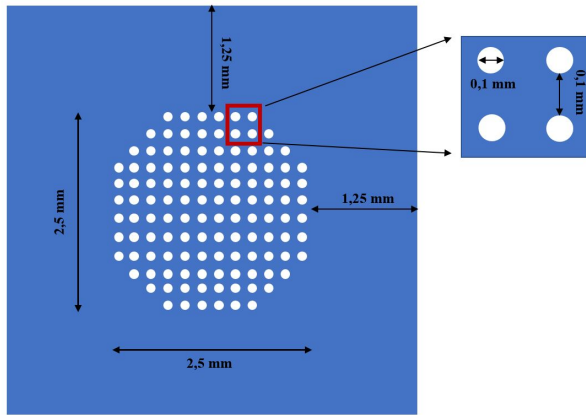

Fig. 1: Sketch of the developed device with a zoom on the holes area.

A mixture of poly-dimethyl-siloxane prepolymer (PDMS) and curing agent (10:1 w/w) was poured onto the mold and left for 20 minutes at 80 °C for the creation of the polymeric mask with the pillars. The final polymeric device was used as mold for the alginate MIMIC. To selectively hydrophilize the surface as support for the mask fabrication, and allow the alginate to flow through the pillars, the polymeric mold was placed onto cover-slips with the pillar facing downwards, for oxygen plasma treatment (120 sec at 30 W). The mold was then placed on glass slides previously sterilized in the oven at 120 °C for 3 hours and precoated overnight with the adhesion factors. Two different adhesion factors were tested: poly-L-lysine 0.1 mg/ml and chitosan 1% in acetic acid 0.1 M. 5μl of alginate aqueous solution 0.1% (w/v) was deposited near one side of the polymeric mold and it filled the channels formed between the polymeric device and the slide by capillarity. Then 40 μl of alginate crosslinking solution, 1% (w/v) calcium chloride ($CaCl_2$), was poured and the system was left to crosslink overnight. The day after, the PDMS mold was removed and the surface was washed with Milli-Q water three times, removing exceeding residues of alginate hydrogel not adhering onto the bio-adhesive area. Before proceeding with the neuronal cell plating, everything was sterilized using 70% (v/v) ethanol for 30 minutes.

B. Cell culture

All the procedures executed for the preparation of cell cultures for experimental purposes were carried out in compliance with the legislative decree of the Ministry of Health (DL 116/1992) and the guidelines of the University of Genova, to reduce the number of animals needed for testing and their suffering. In this project, we used cultures of dissociated neurons from cortex of embryonic rats, at gestational day 18. Briefly, the cerebral cortices were dissected out from the brain and dissociated first by enzymatic digestion in Trypsin 0.125% and DNAse solution for 20 min at 37 °C. Once the necessary time has elapsed, the action of the trypsin enzyme is blocked by washing in soil containing fetal bovine serum (FBS). Due to the use of the fine-tipped Pasteur pipette, the enzymatic dissociation was accompanied by the mechanical one. The resulting single cells were suspended in Neurobasal medium supplemented with 2% B$-$27, 1% Glutamax$-$I and 1% Pen-Strep solution. Dissociated neurons were afterwards plated onto the glass slides in a 30 μl drop covering the electrode region; the final density obtained was about 10'000 cell/mm^2. The devices were stored in the incubator at constant temperature (37 °C), humidity (95%) and 5% CO_2. 50% of the medium was changed approximately weekly, but the frequency with which medium is changed is related to the proper development of the culture itself. Glia proliferation was not prevented by adding anti-mitotic drugs, because it had an essential role in the nervous system; thus, the culture contained all the types of cells present at the time of extraction.

C. Removal of the alginate mask

After three days *in vitro*, the alginate mask removal protocol was tested. The hydrogel was dissolved by exposing it to a 10 mM sodium carbonate solution (Na_2CO_3) for 5 minutes in incubator. Then, samples were washed: a first washing in DPBS (Dulbecco's phosphate-buffered solution) was followed by two washes with the culture medium, in order to remove any calcium crystal eventually formed due to the alginate hydrogel dissolution.

D. Morphological characterization

The cultures were fixed at room temperature for 20 minutes in 4% paraformaldehyde (PFA) in phosphate buffer solution (PBS). Permeabilization was obtained with PBS containing 0.05% Triton-X100 for 5 minutes at room temperature and the non-specific binding of antibodies was blocked with an incubation of 35 minutes in a blocking buffer solution consisting of PBS, 0.3% BSA (bovine serum albumin) and 0.5% FBS (fetal bovine serum). Cultures have been incubated with primary antibody diluted in a PBS Blocking buffer for 90 minutes at room temperature. Then, cultures have been washed three times with PBS and finally exposed to secondary antibodies for 30 minutes. As primary antibodies

were used MAP2 1:500 and DAPI 1:1000.

III. RESULTS

The samples were fixed at 3 days *in vitro* (DIV), before the removal of the alginate mask, and at 18 DIV to observe the morphological properties of the neuronal network after the mask removal. Figure 2 shows some significant results at 3 DIV: in the case of the use of poly-L-lysine as adhesion factor (Fig. 2A), strong containment of the cellular somata was obtained, while the use of chitosan did not guarantee cell isolation (Fig.2B).
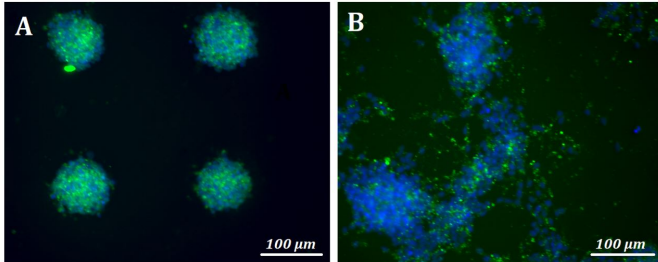

Fig. 2: Morphological image of the 3 DIV neuronal network: the nuclei (DAPI) are highlighted in blue while the neurites (MAP2) are in green. A) Poly-L-lysine B) Chitosan.

The lack of cellular confinement using chitosan as adhesion factor was due to the lower electrostatic force between alginate and chitosan compared to that observed between alginate and poly-L-lysine. Indeed, poly-L-lysine has an isoelectric point (pI) that spans from 9 to 11 [20], whereas chitosan has a acidic dissociation constant (pKa) of 6.8 [21], behaving as strong and weak polycation respectively, considering the physiological conditions under which we operate (pH = 7.4). This leads to a stronger interaction between poly-L-lysine and alginate, so that the hydrogel mask doesn't break during the PDMS mold detach. The difference in the use of chitosan or poly-L-lysine as bio-adhesive films was demonstrated by dispersing 4% (v/v) carboxylated microspheres (FluoSpheres Carboxylate-Modified Microspheres, 0.2 m, red fluorescent (580/605), 2% solids, Thermo Fisher Scientific) in the alginate solution. Figure 3 compares how inhomogeneous and poorly defined the alginate mask appears using chitosan (right) or poly-L-lysine (left) as substrate.
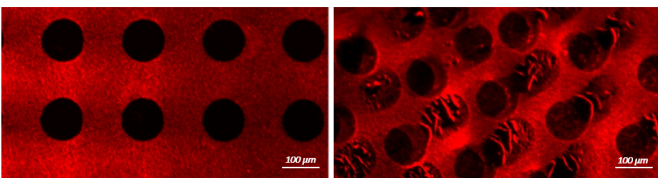

Fig. 3: Fluorescence image of the hydrogel using a chitosan-coated (left) poly-L-lysine-coated (right) substrate.

It was possible to check at 18 DIV (15 days since the removal of the alginate mask) how the removal protocol worked and how the neuronal development has not been affected. Figure
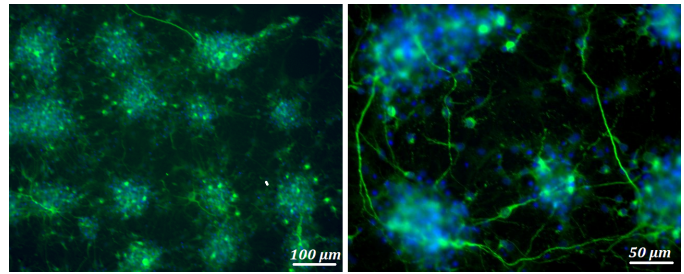

Fig. 4: Fluorescence image of the network interconnected at 18 DIV with two different zooms: left 10X and right 20X.

4 shows how neuritic processes among the various clusters have developed to establish structural relations between the clusters and thus to define a linked network.

IV. CONCLUSION AND PERSPECTIVE

In this study, an experimental approach was proposed to define an engineered network that allows for its topology modulation through dynamic control of the adhesion surface. For this purpose, a bioinert and biocompatible hydrogel with predefined geometry, and which can be removed under conditions compatible with neuronal viability, was used. Such characteristics allowed cell deposition and neuritis growth to be isolated in specific regions. The hydrogel mask removal at a predetermined time-point (3 DIV) made the substrate to switch from the repellent to adhesive for neuronal cells, triggering spontaneous growth of the connections between the different clusters.

The final goal of this research will be to characterize the interplay between structure and function of the neuronal network, evaluated by means of the electrophysiological activity recorded by Micro-Electrode Arrays (MEAs). The aforementioned protocol should be adapted to the MEA surface. The process of removing the alginate mask should be postponed to at least 12 DIV, when the maturation of the sub-populations is such as to allow the activity recordings. This will make it possible, taking into account the maturation of the network, to evaluate the changes made to its structure: from the clustered to the connected network.

V. ACKNOWLEDGMENTS

REFERENCES

[1] G. Q. Bi and M. M. Poo, "Synaptic modifications in cultured hippocampal neurons: Dependence on spike timing, synaptic strength, and postsynaptic cell type," *Journal of Neuroscience*, vol. 18, pp. 10464–10472, dec 1998.

[2] V. Mountcastle, "The columnar organization of the neocortex," *Brain*, vol. 120, pp. 701–722, apr 1997.

[3] E. Bullmore and O. Sporns, "Complex brain networks: Graph theoretical analysis of structural and functional systems," mar 2009.

[4] D. Wagenaar, J. Pine, and S. Potter, "An extremely rich repertoire of bursting patterns during the development of cortical cultures," *BMC Neuroscience*, vol. 7, p. 11, feb 2006.

[5] M. Chiappalone, P. Massobrio, and S. Martinoia, "Network plasticity in cortical assemblies," *European Journal of Neuroscience*, vol. 28, pp. 221–237, jul 2008.

[6] V. Pasquale, P. Massobrio, L. Bologna, M. Chiappalone, and S. Martinoia, "Self-organization and neuronal avalanches in networks of dissociated cortical neurons," *Neuroscience*, vol. 153, pp. 1354–1369, jun 2008.

[7] D. A. Wagenaar, J. Pine, and S. M. Potter, "Effective parameters for stimulation of dissociated cultures using multi-electrode arrays," *Journal of Neuroscience Methods*, vol. 138, pp. 27–37, sep 2004.

[8] E. Defranchi, A. Novellino, M. Whelan, S. Vogel, T. Ramirez, B. van Ravenzwaay, and R. Landsiedel, "Feasibility Assessment of Micro-Electrode Chip Assay as a Method of Detecting Neurotoxicity in vitro," *Frontiers in Neuroengineering*, vol. 4, 2011.

[9] J. D. Rolston, D. A. Wagenaar, and S. M. Potter, "Precisely timed spatiotemporal patterns of neural activity in dissociated cortical cultures," *Neuroscience*, vol. 148, pp. 294–303, aug 2007.

[10] E. Macis, M. Tedesco, P. Massobrio, R. Raiteri, and S. Martinoia, "An automated microdrop delivery system for neuronal network patterning on microelectrode arrays," *Journal of Neuroscience Methods*, vol. 161, pp. 88–95, mar 2007.

[11] M. Shein Idelson, E. Ben-Jacob, and Y. Hanein, "Innate Synchronous Oscillations in Freely-Organized Small Neuronal Circuits," *PLoS ONE*, vol. 5, no. 12, 2010.

[12] J. Erickson, A. Tooker, Y. C. Tai, and J. Pine, "Caged neuron MEA: A system for long-term investigation of cultured neural network connectivity," *Journal of Neuroscience Methods*, vol. 175, pp. 1–16, oct 2008.

[13] D. S. Bassett and E. Bullmore, "Small-World Brain Networks," *The Neuroscientist*, vol. 12, pp. 512–523, dec 2006.

[14] J. C. Chang, G. J. Brewer, and B. C. Wheeler, "A modified microstamping technique enhances polylysine transfer and neuronal cell patterning," *Biomaterials*, vol. 24, no. 17, pp. 2863–2870, 2003.

[15] E. Marconi, T. Nieus, A. Maccione, P. Valente, A. Simi, M. Messa, S. Dante, P. Baldelli, L. Berdondini, and F. Benfenati, "Emergent Functional Properties of Neuronal Networks with Controlled Topology," *PLoS ONE*, vol. 7, p. e34648, apr 2012.

[16] M. Suzuki, K. Ikeda, M. Yamaguchi, S. N. Kudoh, K. Yokoyama, R. Satoh, D. Ito, M. Nagayama, T. Uchida, and K. Gohara, "Neuronal cell patterning on a multi-electrode array for a network analysis platform," *Biomaterials*, vol. 34, pp. 5210–5217, jul 2013.

[17] T. Zhou, S. F. Perry, Y. Berdichevsky, S. Petryna, V. Fluck, and S. Tatic-Lucic, "Multi-electrode array capable of supporting precisely patterned hippocampal neuronal networks," *Biomedical Microdevices*, vol. 17, no. 1, 2015.

[18] M. T. Tedesco, D. Di Lisa, P. Massobrio, N. Colistra, M. Pesce, T. Catelani, E. Dellacasa, R. Raiteri, S. Martinoia, and L. Pastorino, "Soft chitosan microbeads scaffold for 3D functional neuronal networks," *Biomaterials*, vol. 156, pp. 159–171, feb 2018.

[19] M. Morra and C. Cassinelli, "Force measurements on cell repellant and cell adhesive alginic acid coated surfaces," *Colloids and Surfaces B: Biointerfaces*, vol. 18, pp. 249–259, oct 2000.

[20] J.-H. Choi, S.-O. Kim, E. Linardy, E. C. Dreaden, V. P. Zhdanov, P. T. Hammond, and N.-J. Cho, "Influence of pH and Surface Chemistry on Poly-L-lysine Adsorption onto Solid Supports Investigated by Quartz Crystal Microbalance with Dissipation Monitoring," *The Journal of Physical Chemistry B*, vol. 119, pp. 10554–10565, aug 2015.

Ultrasound-triggered permeabilization of polyelectrolyte microcapsules

M. Pisano[1], M. Clerici[1], D. Di Lisa[1], R. Raiteri[1,2] and L. Pastorino[1]

[1] *Department of Informatics, Bioengineering, Robotics and System Engineering (DIBRIS), University of Genova, Genova, Italy.*
[2] *CNR-Institute of Biophysics, Genova, Italy*

Abstract— **Despite the extensive research effort, the development of advanced drug delivery systems with controlled release properties and successful pharmacological activity continues to be a major challenge. This study aims to establish an experimental protocol to release a model drug, doxorubicin, stored in polyelectrolyte microcapsules, fabricated with the layer-by-layer technique, using an ultrasound (US) treatment applied with a commercial biomedical device. The US based delivery system was first characterized in terms of microcapsule rupture and model drug release and then tested *in vitro* using breast cancer cells. Overall, the obtained results demonstrate that by using a suitable US source, without damaging human tissues and respecting biocompatible mechanical index values, it is possible to trigger the drug release from polyelectrolyte microcapsules in a controlled fashion.**

Keywords—**drug delivery, ultrasound, microcapsules.**

I. INTRODUCTION

A mong actively growing fields of studies, the development of drug targeted delivery systems with controlled release is an actual subject of great interest in the biomaterials research area, which combines chemistry, materials science and modern medicine [1].

This research area is especially important in curing dangerous diseases, such as cancer. Malignant tumours, together with heart diseases, are the major cause of death in the developed world [2]. In this case, highly effective but toxic drugs are usually employed, such as the chemotherapeutic agent doxorubicin (DOX), which is one of the most commonly used drugs in cancer treatment and that is based on the concept of suppressing tumour growth. It is an anthracycline antibiotic, which has high anti-tumour activity against many types of cancer, particularly breast and ovarian cancers. However, it has high cardiotoxicity, causing myocardial damage. To minimize chemotherapeutic agents toxicity and reduce unwanted side effects that affect both diseased and healthy tissues, it is advisable that only the damaged part of the organism be treated [3], hence the increasing need for efficient and controllable drug delivery systems [4].

The most promising approach to solve this problem is to entrap toxic drugs in the inner volume of microcontainers [5] (e.g. liposomes, microspheres and polymeric microcapsules), with diameters from 1 to 100 μm. Different microcontainers have different stimuli-responsive behaviours. Encapsulation of anti-tumour drugs in liposomes and micelles (especially polymeric micelles) alters the pharmacokinetics and distribution of these agents and reduces their cytotoxicity [4]. One of the simplest but most successful approaches to synthesize microcapsules is the layer-by-layer (LbL) assembly technique, which consists of assembling a multilayer thin film on a solid charged support by the spontaneous sequential adsorption of oppositely charged species from aqueous solutions [6]. The main advantages of microcapsules fabricated by the LbL technique are their loading capacity and the possibility to precisely tailor their properties by choosing the capsule components [7]. In fact, they are sensitive to different chemical parameters in the surrounding environment, i.e. temperature, pH, sugar concentration, etc. In response to external physical stimuli such as a magnetic field, light or ultrasound, they can also hold or release encapsulated materials [1].

US technology is generally regarded as safe and cost-effective, and it is becoming widely applied in the biomedical area due to its non-invasive nature [4]. Moreover, US represents an effective method for achieving spatiotemporal regulation of drug release at the desired site, preventing harmful side effects to healthy tissues. Indeed, ultrasonic waves can be tuned in terms of frequency and amplitude to penetrate deep inside the body and damage the microcontainer shell to release the encapsulated drug without damaging the surrounding tissues [5].

As relates to the application of US to polyelectrolyte microcapsules, it is worth to note that in the literature US are applied using ultrasonic baths or ultrasonic cell disruptors and homogenizers [8]. In this study, we developed a protocol for the US-triggered permeabilization of polyelectrolyte microcapsules by using a biomedical US source working under conditions compatible with cells and tissues. The model drug, doxorubicin hydrochloride, was loaded into the microcapsule volume and its release under US stimulation was characterized.

We have qualitatively tested the efficacy of this system using fluorescence and confocal microscopy, and quantitatively checked the release of DOX using Uv-vis spectroscopy. Finally, we carried out *in vitro* experiments to evaluate the cytotoxicity of the developed protocol, testing the effect of US on empty and filled microcapsules placed in contact with tumour cell, i.e. MCF-7 breast cancer cell line.

II. MATERIALS AND METHODS

A. *Polyelectrolyte microcapsules*

The microstructured polyelectrolytes capsules (NPCs) were fabricated by the layer-by-layer deposition of a polyelectrolyte multilayer onto the surface of sacrificial calcium carbonate microparticles. Namely, calcium carbonate ($CaCO_3$) microparticles were synthesized by co-precipitation of equal volumes of calcium chloride ($CaCl_2$ 0,33M) and sodium
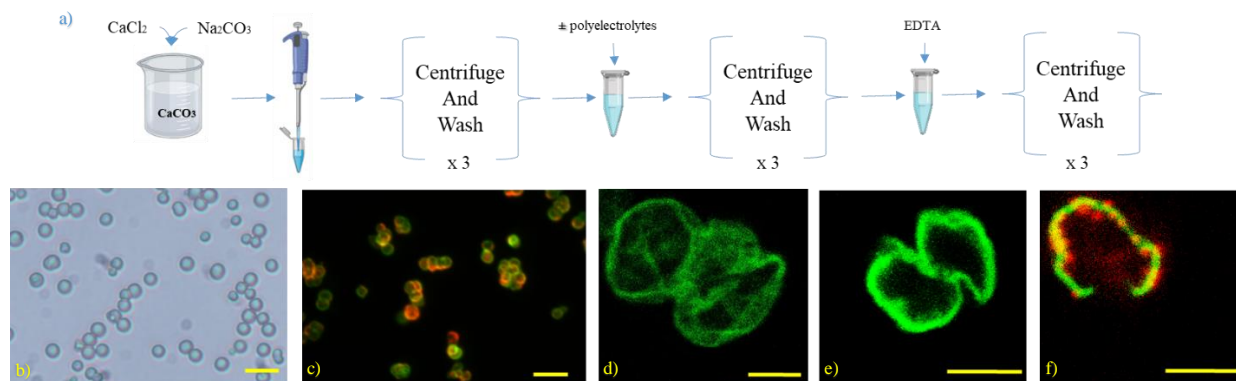
Figure 1: a) Schematic of polyelectrolyte capsule fabrication by layer-by-layer (LbL) assembly. b) Optical image: polyelectrolyte microcapsules before the EDTA treatment, scale bar:10μm. c) Fluorescence microscope: polyelectrolyte microcapsules filled with Fluo-Spheres^{TM} (red) and with FITC-dextran layer (green). Scale bar: 10 μm. d-f) Confocal image: respectively non sonicated, empty sonicated and filled sonicated microcapsules.

carbonate (Na_2CO_3 0,33M). The so-obtained microparticles were exposed alternatively to solutions of the positive or negative polyelectrolytes for their deposition. The first one was anionic polystyrene sulfonate (PSS 1mg/m) followed by cationic poly-allamine hydrochloride (PAH 1mg/m). The procedure was repeated, alternating PSS and PAH solutions, to four bilayers. At the end, the covered $CaCO_3$ microparticles were exposed to an ethylenediaminetetraacetic acid solution (EDTA 0.2M) to decomposes the internal core, used as templates, and to obtain the final microcapsules. Figure 1a) shows the process, while 1b) shows the final result.

We made another trial with synthetic polyelectrolytes, using fluorescent materials. We filled the NPCs with fluorescent nanoparticles, Fluo-Spheres™ carboxylate-modified microspheres. These were co-precipitated with $CaCl_2$ 0.33 M solution. Then Na_2CO_3 0.33 M solution was added. Therefore, we got the $CaCO_3$ core visible in red fluorescence. With the same process described above, we then made two bilayers (PSS / PAH) and two bilayers (FITC-dex / PAH) and added the last layer of PSS. In this case, the concentration of PSS and PAH was 2 mg/ml. In this way, microcapsules were visible in both red and green fluorescence, as shown in Figure 1c).

In the end, to evaluate the effect of the proposed drug delivery system directly on an immortalized cell line, synthetic polyelectrolyte microcapsules, filled with DOX, were used. DOX was added to Na_2CO_3 to reach the final concentration of 0,25 mg/ml. The obtained solution was rapidly coprecipatated with $CaCl_2$ and the L-b-L process, as above, was repeated. In the reported experiments, microcapsules containing about 25 μg of DOX were added to the culture medium and incubated.

B. Cell culture

The human breast adenocarcinoma MCF-7 cells were purchased from the Interlab Cell Line Collection (ICLC) cell bank (San Martino Polyclinic Hospital Genova, Italy). MCF-7 cells were cultured in a fully humidified atmosphere in the presence of 5% (v/v) CO_2 at 37 °C in Dulbecco's Modified Eagle's Medium (DMEM) supplemented with 10% (v/v) fetal bovine serum (FBS), 1% antibiotics (diluted from a stock solution containing 5000 U/ml Penicillin, 5000 mg/ml Streptomycin) and 2 mM glutamine. When reaching more than 80% confluence, the cells were detached by using 0.25% Trypsin, plated onto petri dishes (Ø 35 mm) with a cell density

of 1.6×10^6 cells/petri and incubated for 24h. After 24h, cells were exposed at different conditions: DOX-loaded microcapsules with and without US stimulation as well as empty microcapsules with and without US stimulation. In particular, 100 μl of unloaded and loaded microcapsules were diluted directly in the culture medium. Moreover, cells directly treated and no treated with US stimulation were cultured as a control in order to evaluate the cell response to US. The US stimulation was applied immediately after the addition of the microcapsules onto cells.

C. Ultrasound stimulation

A US source consisting of a driving unit and a piezoelectric transducer operating at 1 MHz (model SP100 sonoporator, Sonidel Limited, Ireland), was used to perform the ultrasonic stimulation. Trains of US pulses with different intensities, periods, and duty cycles were applied to NPCs. The advantage of a pulsed stimulation is that thermal effects are reduced. In this way, a higher intensity could be set than with a continuous wave.

For the characterization of US effects on NPCs, 0.5 ml solution containing microcapsules was poured into a 10 x 40 mm Petri dish and 2 ml of Mill-Q water was added. The piezoelectric transducer was then positioned over the Petri dish, partly immersed in the solution. The US stimulation pattern consisted of 5 and 10 minutes of US pulses with a period of 10 ms, 20% duty cycle, and intensities in the 1,5 - 2 W/cm^2 range.

D. Imaging

Optical (bright field) and fluorescence microscopy images were taken before and after US treatment, to qualitatively observe changes in NPCs shape and fluorescence intensity when filled with fluorescent nanoparticles.

An Olympus IX51/TH4-200 microscope and a Leica DMIRE2 confocal microscope were used. ImageJ software was used for the image analysis.

E. Spectrophotometry

The amount of DOX encapsulated inside the microcapsules was assessed, using a UV-Vis spectrophotometer (Cary 60 model, Agilent Technologies). All solutions were analyzed at

the wavelength of 481 nm with a calibration curve in Milli-Q water. The DOX calibration curve was:

$$Abs = 23,44279\,x + 0,01093 \qquad (1)$$

which was calculated with different solutions at different doxorubicin concentrations, setting absorbance as y-coordinate and concentration as x-coordinate. To detect the unknown concentration of the test sample it was sufficient to prepare a dilution in Milli-Q solvent, determine the absorbance value, and derive the relevant concentration value using the calibration curve. Also, the encapsulation efficiency (EE%) was calculated in the following way:

$$EE\% = \frac{DOX_{total} - DOX_{free}}{DOX_{tot}} * 100 \qquad (2)$$

where DOX_{tot} is the amount of initial doxorubicin and DOX_{free} is the released doxorubicin by the NPCs. The quantity of released DOX (RD%) was evaluated in 1 ml of not sonicated microcapsules, as a control sample, and in 1 ml of microcapsules sonicated at different intensities and times and it was calculated with following equation:

$$RD\% = \frac{DOX_{realesed}}{DOX_{encapsulated}} * 100 \qquad (3)$$

F. In vitro cytotoxicity assay

Cell viability was assessed after 24 hours using the cell viability assay kit MTT. Each experiment was carried out in triplicate. The MTT assay is used to estimate the effect and potential cytotoxicity of the system *in vitro* and it is based on the capability of mitochondrial dehydrogenases of viable cells to cleave 3-(4,5-dimethylthiazol-2-yl)-2,5-diphenyltetrazolium bromide (MTT) yielding insoluble formazan crystals, which are solubilized in isopropyl-alcohol. The formazan product, which is a consequence of MTT reduction, was analysed spectrophotometrically (565 nm) after dissolution in isopropyl-alcohol. Cell viability (CV%) was calculated as follow:

$$CV\% = \frac{abs_{samples}}{abs_{control}} * 100 \qquad (4)$$

G. Chemicals and Technical equipment

The sources of the chemicals used to create synthetic microcapsules are as follows: poly-allylamine hydrochloride (PAH, Mw = 70 kDa), sodium polystyrene sulfonate (PSS, Mw = 70 kDa,), calcium chloride dehydrate (CaCl2), sodium carbonate (Na2CO3), ethylenediaminetetraacetic acid (EDTA) and fluorescein isothiocyanate-dextran (FITC-dextran) were purchased from Sigma-Aldrich. For release tests we used doxorubicin hydrochloride, phosphate-buffered saline (PBS), isopropyl-alcohol and methylthiazolyldiphenyl-tetrazolium bromide (MTT) from Sigma-Aldrich. Fluo-Spheres™ carboxylate-modified microspheres were purchased from Thermo Fisher Scientific. All reagents for cell culture were purchased from Invitrogen. The technical equipment used consists of Eppendorf Centrifuge 5804 R, FALC-F70 magnetic stirrer, Scientific Industries Vortex-Genie 2, Techno Kartell TK3S stirrer, Sartorius TE124S Talent Analytical Balance, FALC HK2200 ultrasonic bath.

III. RESULTS

We first characterized empty and FluoSpheres™ filled microcapsules, with fluorescence and confocal microscope in order to check for breakage, and we observe two completely different behaviours. In Figure 1 (d-e) it is possible to observe that empty microcapsules, when sonicated with our protocol, do not break but shrink themselves, decreasing their areas in a significant way. Values in Table 1 highlight this result.

TABLE I
AREA OF NPCS (μm^2)

Not sonicated	Sonicated
56,04	32,60
51,81	31,45
76,07	45,68
71,59	43,77
67,41	46,14
63,86	34,17

On the contrary, filled microcapsules tend to break when sonicated, letting the internal substances get out. This behavioural difference is probably due to the presence of the support given by the nanoparticles inside the microcapsules or to its absence.

Once the experimental protocol to break microcapsules with US was established, the quantity of released DOX after US stimulation was measured using UV-vis spectrophotometry. Microcapsules filled with DOX with the efficiency of encapsulation (EE%) of about 50% were used. More precisely, we employed microcapsules with 0.085 mg/ml of doxorubicin encapsulated. Table II shows the increase of DOX concentration into the solution with sonicated microcapsules compared to solution with non-sonicated ones.

TABLE II
DOX RELEASE [μg/ml]

Time Point	Control	Sonicated
10 min	0.046	0.259
1 hour	0.131	0.558

The achieved results show that even if US treatment has an immediate effect, the release continues also in the subsequent time.

Finally, the system was tested directly on MCF7-cells, and the MTT assay was carried out to characterize the *in vitro* cytotoxicity of the system. Cell viability (CV%) was estimated 24h after the stimulation. Results are shown in Table III.

TABLE III
CELL VIABILITY (CV%)

Sample	CV%
Control	100%
Empty Microcapsules (EM)	95,6%
EM with US	98,1%
Microcapsules with DOX (DM)	114,6%
DM with US	63,3%

For empty synthetic microcapsules, with and without US stimulation, CV% remained very high when compared with the control sample. This result means that our system is biocompatible and does not cause damages to cells. Regarding cells exposed to DOX-loaded microcapsules, there is a difference between them and the control sample for two different reasons. On the one hand, there has been an increased cells proliferation in microcapsules with DOX but without US, and this has probably been due to the minimal release of the drug from microcapsules, which, as confirmed in the published literature [9], could cause this effect in low concentration dosage. This means that this system, if not stimulated, is able to limit the release due to the porosity of the capsules. On the other hand, microcapsules filled with DOX and stimulated at 1.5 W/cm^2 for 10 minutes show a significant (p < 0,05, compared to control using Kruskal-Wallis test) decrease in CV%, which means that DOX is released slowly, allowing cells to absorb it, thus causing cell degradation. This percentage value could rise by increasing the administration of the capsules number and therefore the concentration of DOX that would be released, while the power of ultrasound should not increase to avoid thermal effects. Therefore, the obtained results overall confirm that US treatment, in conditions that respect biocompatible mechanical index values, has an effect on the microcapsules system and triggers the DOX release by breakage in a controlled fashion.

REFERENCES

[1] A. M. Pavlov, V. Saez, A. Cobley, J. Graves, G. B. Sukhorukov, and T. J. Mason, "Controlled protein release from microcapsules with composite shells using high frequency ultrasound—potential for in vivo medical use," Soft Matter, vol. 7, no. 9, pp. 4341–4347, 2011.
[2] E. W. Neuse, "Synthetic polymers as drug-delivery vehicles in medicine," Metal-based drugs, vol. 2008, 2008.
[3] C. F. Thorn, C. Oshiro, S. Marsh, T. Hernandez-Boussard, H. McLeod, T. E. Klein, and R. B. Altman, "DOXorubicin pathways: pharmacodynamics and adverse effects," Pharmacogenetics and genomics, vol. 21, no. 7, p. 440, 2011.
[4] S. E. Ahmed, A. M. Martins, and G. A. Husseini, "The use of ultrasound to release chemotherapeutic drugs from micelles and liposomes," Journal of drug targeting, vol. 23, no. 1, pp. 16–42, 2015.
[5] D. G. Shchukin, D. A. Gorin, and H. M¨ohwald, "Ultrasonically induced opening of polyelectrolyte microcontainers," Langmuir, vol. 22, no. 17, pp. 7400–7404, 2006.
[6] H. Gao, D. Wen, and G. B. Sukhorukov, "Composite silica nanoparticle/polyelectrolyte microcapsules with reduced permeability and enhanced ultrasound sensitivity," Journal of materials chemistry b, vol. 3, no. 9, pp. 1888–1897, 2015.
[7] B. G. De Geest, A. G. Skirtach, A. A. Mamedov, A. A. Antipov, N. A. Kotov, S. C. De Smedt, and G. B. Sukhorukov, "Ultrasound-triggered release from multilayered capsules," small, vol. 3, no. 5, pp. 804–808, 2007.
[8] De Geest, B. G., Skirtach, A. G., Mamedov, A. A., Antipov, A. A., Kotov, N. A., De Smedt, S. C., & Sukhorukov, G. B. "Ultrasound-triggered release from multilayered capsules." small, 3(5), 804-808, 2007

[9] P. Vichi and T. R. Tritton, "Stimulation of growth in human and murine cells by adriamycin," Cancer research, vol. 49, no. 10, pp. 2679–2682, 1989.

The suitability of Gait Variable Scores for Myotonic Dystrophy types classification

M. Lofrumento, E. Judica, B. Fossati, M. Corbo and P. Tropea

MOTION Lab, Department of Neurorehabilitation Sciences, Casa Cura Policlinico, Milan, Italy

Abstract—**Myotonic Dystrophy is a rare neuromuscular disorder caused by a genetic anomaly. Currently, two major types of DM are recognized: type 1 (DM1) and type 2 (DM2). In both, gait and balance can be severely impaired. Focusing on locomotion, weakness affects mostly the distal muscles (lower legs) in subjects with DM1 and the proximal muscles (pelvis and hips) in subjects with DM2. To date, locomotive functional deficits are investigated through clinical assessment.**

The quantification of the functional limitations related to DM type using Gait Profile Score (GPS) and/or Gait Variable Scores (GVSs) is the aim of this study.

Six patients with DM1 and DM2 underwent gait analysis. Differences induced by the DM typology concerning spatiotemporal parameters and kinematics scores, calculated as GVSs and GPS, were assessed. Spatiotemporal parameters and GPS, although altered in comparison with normative data, did not reveal any significant effect of the pathology, while specific GVSs (distal for DM1, proximal for DM2) were strictly related to DM type.

Therefore, Gait Profile Score can differentiate Myotonic Dystrophy from unaffected people. However, only a deeper investigation by means of Gait Variable Scores can discriminate and quantify DM types, identifying also the joints more affected by the disease. This could be beneficial in order to track the evolution of the muscular involvement and to guide specific rehabilitation program.

Keywords—**Myotonic Dystrophy, gait analysis, gait profile score, rehabilitation.**

I. INTRODUCTION

MYOTONIC Dystrophy (DM) is a rare and progressive neuromuscular disorder with genetic transmission. It is one of the most complex pathologies ever known and it is the most common adult muscular dystrophy, characterized by progressive muscle wasting and weakness [1]. It is a multi-systemic progressive disorder affecting the muscular, respiratory, cardiac, nervous and endocrine systems.

Currently, two major types of DM are recognized: type 1 (DM1 or Steinert's disease) and type 2 (DM2 or PROMM) [2].

Individuals with DM1 can present symptoms at different ages and are predisposed to the phenomenon of "anticipation", that is the occurrence of increasing disease severity at an earlier age with each generation [3]. Instead, congenital phenotypes have not been ascribed to DM2 yet and most patients are adult. Weakness and wasting (atrophy) are prominent features in DM1 while muscle pain and myotonia interest DM2. Moreover, individuals with DM1 manifest facial and distal limb weakness whereas individuals with DM2 are affected by proximal weakness [1].

In both DM1 and DM2, gait and balance can be severely impaired, and patients have a significantly increased risk for falls when compared to normal population [4]. Also because of multi-organ involvement, their quality of life tend to progressively worsen. Even though motor impairment, such as limited walking perimeter and gait speed, is frequently reported in clinical settings, it has not been thoroughly addressed in the scientific scenario, and the therapeutic approach remains poorly defined.

As for locomotion, weakness and atrophy affect mostly the distal muscles (lower leg) in subjects with DM1 and the proximal muscles (pelvis and hips) in subjects with DM2 [1].

Gait analysis has increasingly become a routinely clinical tool to investigate and better understand the pathomechanics of gait abnormalities [5]. Anyway, the DM gait environment with a clear distinction between its two types has not been deeply explored yet. Some evidences are reported for DM1, probably due to the late discovery of DM2. As for kinematic patterns of DM1 subjects, the distal muscle weakness resulted in a steppage gait [6] and abnormalities at the knee and ankle joints [7], while the risk of fall was studied in relation to lower limb muscle strength and spatiotemporal parameters [4].

Concerning comparison of DM1 and DM2, during dual-task walking, both patients differed in their temporal and stride characteristics compared to healthy subjects [8].

The quantification of the functional limitations related to DM could be beneficial in order to guide a rehabilitation program. Due to the systemic nature of this pathology, which involves also cognitive disorders, there is no indication of a standard specific physical therapy program. Improvements in balance were registered in DM1 patients after a rehabilitation program focused on strength, endurance and static and dynamic balance [9], but, except for gait speed, there was no reference to changes in kinematic patterns.

At this regard, it is worth highlighting that the interpretation of the huge amount of three-dimensional data generated by gait analysis is not so straightforward. Therefore, recently, synthetic indexes have been made. Particularly, the Gait Profile Score (GPS) provides a global measure of quality of an individual's walking by calculating the deviations from normative dataset of gait kinematic patterns.

The strength of GPS consists in evaluating the separate contributions of nine kinematic variables (i.e., pelvic tilt, obliquity, and rotation, hip flexion, abduction and rotation, knee flexion, ankle dorsiflexion and foot progression, for both sides of the body) by first calculating the Gait Variable Score (GVS).

GPS and GVSs have been already validated in a wide range of diseases [10]–[13]. However, to our knowledge, no studies have previously employed the GPS to characterize DMs' gait.

Based on these considerations, we aimed to evaluate the applicability of GPS and GVS in individuals with different types of DM. In our hypothesis, GPS and GVS will be considered a clinically relevant tool if they result able to detect the differences between DM1 and DM2 kinematics and

provide a quantitative measure to a possible rehabilitation scenario. In this perspective, we expect that GPS, as global measure, will not detect the alterations between the two DM types. Conversely, GVSs will highlight which joint kinematics differs between DM1 and DM2, providing also some hints for customizing rehabilitation treatments.

II. METHODS

A. Participants and evaluation procedure

Six individuals affected by Myotonic Dystrophy (three DM1 and three DM2) were enrolled at Casa Cura Policlinico (CCP), a neurologic rehabilitation hospital in Milan.

The inclusion criteria were as follows: i) age > 18 years; ii) diagnosis of Myotonic Dystrophy.

Exclusion criteria were: i) insufficient cognitive and language abilities to understand and follow instructions (Mini Mental State Examination (MMSE) <24/30); ii) inability to independently walk on level ground (Functional Ambulation Categories (FAC) ≤3); iii) deficit in visual acuity; iv) refusal to sign consent form.

The diagnosis of Myotonic Dystrophy was previously established by genetic analysis, through biomolecular analysis for DM1 and Fluorescence in situ Hybridization (FISH) for DM2. Patients signed a written informed consent prior to participation. The study was approved by the Local Ethics Committee (Comitato Etico Milano Area 2, resolution 723_2019bis, ID:1109) and was in accordance with the Declaration of Helsinki.

The evaluation was carried out at the Motion Lab of CCP using a 6-cameras optoelectronic system (VICON, Oxford, UK) with a sampling rate of 100 Hz. Sixteen spherical retro-reflective passive markers (14 mm diameter) were placed on the patients' pelvis and lower limbs according to Plug-In-Gait model (VICON, Oxford, UK). Particularly, for both left and right side, markers were attached on: anterior and posterior superior iliac spines for the pelvis; lateral epicondyle of the femurs and over the lateral surface of the thighs, lateral malleolus and over the lateral surface of the shanks, calcaneus and second metatarsal head.

After familiarization with the environment, the subjects were asked to walk barefoot at their own natural pace along a 10-m walkway. At least six trials were collected for each subject to guarantee the consistency of the data.

Normative reference data (means and standard deviations), employed in the routine use for clinical gait analysis services (MOTION Lab, Casa di Cura del Policlinico (CCP), Milan, Italy), was used as reference population.

B. Data processing and GPS calculation

Raw data were pre-processed and processed using the Nexus software (VICON, Oxford, UK) to calculate the spatiotemporal and kinematic parameters for each trial performed by the patients. For each subject, four gait cycles for each side were considered for the analysis. Time-series curves were normalized over 51 points.

The following spatiotemporal parameters were obtained: cadence (step/min), walking speed (m/s), stride and step lengths (m), stride and step time (s), and duration of single and double supports and of foot-off, opposite foot-off and opposite foot-contact (expressed as percentage of gait cycle, %GC).

The following kinematic outputs were obtained: pelvic tilt, rotation and obliquity, hip flexion-extension, adduction-abduction and rotation, knee flexion-extension, ankle dorsiflexion and foot progression.

The nine kinematic outputs were used to calculate the Gait Variable Scores (GVSs) (one for each kinematic time-series) and the Gait Profile Score (GPS), in a customized script in MATLAB (MathWorks Inc., Natick, MA, US). Previous work has provided a detailed description for the GPS and GVSs analysis [10]. Briefly, after the normalization of the kinematic time-series over the gait cycle, the GVS (expressed in degrees) was estimated as the Root Mean Square (RMS) difference between a patient's data and the mean value obtained from tests performed on the unaffected population (Eq. (1)).

$$GVS_i = \sqrt{\frac{1}{T}\sum_{t=1}^{T}\left(x_{i,t} - \overline{x_{ref}}_{i,t}\right)^2} \qquad (1)$$

where: i is the number of kinematic variable used; t is the specific time point in the gait cycle; x is the value of the ith gait variable; x_{ref} is the mean of that variable at the same time instant for the reference population; T is equal to 51 (i.e., time series curves length).

Then, the GPS was computed as the RMS average of all the GVS values [10], as showed in Eq. (2):

$$GPS = \sqrt{\frac{1}{N}\sum_{i=1}^{N} GVS_i^2} \qquad (2)$$

where N represents the number of GVS (in our case, N=9 for each side).

Higher GVSs and GPS values, larger the deviations from a physiological gait pattern.

C. Statistical analysis

The mean value between left and right side was used in order to consider people to be the unit of analysis rather than limbs [14].

The Wilcoxon test was used to verify whether the patient's spatiotemporal gait parameters were significantly affected by the pathological group. To investigate possible differences between the two groups (DM1 and DM2 subjects) in regards to their GVS/GPS kinematics characteristics, a t-test for independent samples was used.

Data were processed by using custom routines developed under Matlab environment (Mathworks Inc., Natick, MA, USA). For all statistical tests, the significance was set at α = 0.05.

III. RESULTS

Three DM1 patients (1 Female, 46.7 ± 6.5 years) and three DM2 patients (3 Female, 66.3 ± 11.7 years) were enrolled.

Table I shows the results for the spatiotemporal gait parameters, while Table II shows the GPS and GVS values calculated for the two groups.

In relation to the spatiotemporal parameters, statistical analysis did not show significant differences between subjects' groups (p-values>0.05 for each parameters). The differences between groups are negligible and without any specific trend.

Concerning the kinematic parameters evaluated using the synthetic index Gait Profile Score, results showed a smaller, but negligible, deviation from a physiological gait pattern for DM1 group, without statistical significance between groups (p-values=0.245).

TABLE I
COMPARISON BETWEEN SPATIOTEMPORAL PARAMETERS OF GAIT IN INDIVIDUALS WITH DM1 AND DM2

Parameter	DM1	DM2	p-value
Cadence [steps/min]	92.85 (15.53)	95.78 (9.89)	0.588
Walking speed [m/s]	0.73 (0.33)	0.67 (0.24)	0.855
Single support [%GC]	35.70 (3.02)	35.75 (4.75)	0.699
Double support [%GC]	28.50 (5.97)	29.08 (9.51)	0.370
Foot-off [%GC]	64.20 (3.09)	64.85 (5.32)	0.731
Opposite Foot Contact [%GC]	50.02 (1.17)	50.32 (2.12)	0.900
Opposite Foot Off [%GC]	14.33 (2.46)	14.57 (4.62)	0.484
Stance phase [%GC]	0.66 (0.11)	0.63 (0.06)	0.619
Swing phase [%GC]	0.45 (0.13)	0.41 (0.11)	0.816
Step width [m]	0.18 (0.02)	0.15 (0.04)	0.415
Stride length [m]	0.90 (0.25)	0.83 (0.21)	0.785
Stride Time [s]	1.32 (0.21)	1.27 (0.12)	0.697

Values are expressed as mean (SD) across trials and subjects, for the specific group (DM1 and DM2).In the last column, the Wilcoxon test's p-values for differences between the two groups are reported.

TABLE II
COMPARISON BETWEEN GPS AND GVS VALUES IN INDIVIDUALS WITH DM1 AND DM2

	Parameter	DM1	DM2	p-value
	GPS [°]	12.75 (3.06)	13.88 (3.56)	0.245
	Pelvic Tilt	**14.69 (4.77)**	**19.17 (8.42)**	**0.028**
	Pelvic Rotation	3.57 (1.11)	3.71 (1.33)	0.698
	Pelvic Obliquity	4.64 (2.15)	5.42 (1.17)	0.127
G	**Hip Flex–Extension**	**16.74 (5.67)**	**25.24 (8.63)**	**<0.0001**
V S	Hip Abd–Adduction	3.98 (2.19)	3.11 (1.24)	0.098
[°]	Hip Rotation	19.64 (8.75)	17.26 (7.64)	0.322
	Knee Flex–Extension	13.35 (5.02)	14.60 (1.93)	0.264
	Ankle Dorsiflexion	**12.59 (4.83)**	**6.75 (1.24)**	**<0.0001**
	Foot Progression	**8.98 (3.45)**	**4.60 (1.57)**	**<0.0001**

Values are expressed as mean (SD) across trials and subjects, for the specific group (DM1 and DM2).In the last column, the t-test's p-values for differences between the two groups are reported. p < 0.05 are in bold.

As for the specific kinematic parameters concerning the Gait Variable Scores analysis, two variables were significantly higher (large distance from physiological gait pattern) for DM1 group and two variables were significantly higher for DM2 subjects. Specifically, DM1 subjects showed a better performance regarding the pelvic tilt and the hip flex–extension (p-values = 0.028 and p-values < 0.0001, respectively), while subjects with DM2 presented a better performance for ankle dorsiflexion and foot progression (p<0.0001, for both variables).

IV. DISCUSSION

DM is a complex, rare neuromuscular disease characterized by progressive muscle wasting and weakness, and its clinical course is progressive. Measuring changes over short periods and differences in DM types is therefore crucial for the suitability of rehabilitation treatments. Current clinical scales are focused on the disease progression and not on the patients' functional abilities; consequently, they are scarcely suitable for rehabilitation trials.

In order to avoid the complexity of the interpretation of the spatial data generated by optoelectronic gait analysis, in the present study a synthetic index to differentiate walking impairment in patients with DM1 and DM2 was tested.

Overall, spatiotemporal gait parameters showed a slower walking speed than a healthy behaviour, probably related to a combination of short stride length and slow cadence resulting in an impaired gait performance (normative data: walking speed = 1.3 m/s; stride length = 1.32 m, cadence = 118 steps/min) (Table I). This behaviour could be a strategy aimed to enhance stability and reducing the fall risk.

Interestingly, the gait spatiotemporal parameters did not show any significant differences between the two groups (Table I, forth column), suggesting that a "macroscopic" view of walking does not allow the arising of different muscular anomalies.

Regarding kinematics, for the GPS, that takes into account all the kinematic patterns along the gait cycle, all DM subjects (both DM1 and DM2) showed a value greater than 10° (Table II, second row), denoting a general picture of impaired gait [10]. Nevertheless, this index seems not appropriate to highlight a distinction between DM1 and DM2. This result was expected, since its global nature, even if finer than spatiotemporal parameters.

Although spatiotemporal parameters and GPS are able to discriminate between DM subjects and healthy subjects, these measures are not a valid tool to differentiate the whole ambulation and the impairment of the singular joint movement across DM type.

Instead, it is noteworthy that GVS, referred to variables confined to the plane of progression of the pelvis, hip, ankle and the foot progression, significantly differ between the DM1 and DM2 group.

In particular, as reported in Table II (bold lines), a better performance resulted in DM1 subjects related to the proximal joints (DM1<DM2 for pelvic tilt and hip flexion/extension (respectively, p < 0.0001 and p = 0.028)) while DM2 subjects showed a better performance mainly in distal segments (DM1>DM2 for ankle dorsiflexion and foot progression (both p < 0.0001)).

These results seem to accurately reflect the clinical finding about a major involvement of distal muscles in DM1, and the major involvement of proximal muscles in DM2.

Regarding the knee joint, no statistical difference (p = 0.264) was found between DM1 and DM2 subjects for knee flexion/extension. It might depend on the "neutral" location of the knee with respect to the distal and proximal limb extremities. Both DM1 and DM2 subjects showed GVS values greater than 10° (Table II) that, as mentioned before [10], indicates an impaired knee flexion/extension movement. While for DM1 subjects an anomalous behaviour for the knee (knee hyperextension) is actually documented in a previous study [5], the kinematic patterns of DM2 subjects have not

been examined yet. From our results it could be inferred that knee impairments interest also DM2 individuals. Additionally, it would be interesting to verify if, with the evolution of the disease, GVS is able to reflect potential differences in knee flexion/extension between DM1 and DM2.

On the whole, these all outcomes offer a quantitative measure of impairment regarding the two types of DM, resulting in a useful tool for supporting clinical diagnosis and therapy.

The use of GVS in the neurological practice has a great potential, as these preliminary data can impact the clinical approach to the DM patient for two main reasons. First, it can help to track the evolution of the muscular involvement, intra-individual and inter-individual, as in the same family, and monitor the answer to different treatments. Especially for DM1, which is a slowly progressive disease, GVS can notify the gradual substitution of less effected muscles to perform movement and, therefore, monitor the progression of the disease. Second, as often patients with DM show signs of cognitive impairment and poor insight of the disease [14], refined indexes of gait analysis can be important objective signs of muscular impairment that may suggest new therapeutic and rehabilitation approach.

In addition, in the rehabilitation field, GVS can quantify the deviation from healthy behaviour in order to guide and monitor the effect of training. In literature, very few studies investigated the effect of a rehabilitation training on DM patients and none reported a possible association between objective parameters of impairment and function in static and dynamic settings. In this perspective, the GVS can, to some extent, measure periodically the effectiveness of a training program, notifying the distance from the desired gait pattern. Intended with this meaning of measure of discrepancy from the healthy, this index can be adopted also to monitor and evaluate other conditions and exercises, like climbing the stairs to test balance.

Although part of the results (i.e., the affected gait of DM patients compared with normative data) are in line with other similar studies [8] , the major limitation of this paper is the very small number of patients included. As further implementation, we intend to enrol a major number of patients in order to reinforce the consistency of our results. In addition, a clinical characterization, in term of functional scales for the evaluation of specific lower limbs joints, could be helpful to correlate the instrumental findings with the clinical ones.

V. Conclusion

The present study aimed to characterize the locomotion of individuals affected by Myotonic Dystrophy using GPS and GVSs as synthetic indexes of gait. The objective was to obtain a distinction between DM1 and DM2, based on their different functional deficits in walking activity. Since locomotion impairments are common and highly invalidating in these, often young, patients, gait analysis is a compelling candidate tool to measure ambulatory injury.

Although spatiotemporal parameters and the Gait Profile Score did not show difference between the two types of DM, these two metrics are a global measure of the gait anomaly.

Most importantly, our finding is that the Gait Variable Score resulted suitable to point out the different kinematic features peculiar to the two groups. Therefore, GVS represents a powerful index not only to characterize but also quantify the disabilities of DM1 and DM2 patients.

References

[1] G. Meola and R. Cardani, "Myotonic Dystrophy Type 2: An Update on Clinical Aspects, Genetic and Pathomolecular Mechanism," *J. Neuromuscul. Dis.*, vol. 2, pp. S59–S71, 2015, doi: 10.3233/JND-150088.

[2] C. Turner and D. Hilton-Jones, "The myotonic dystrophies: Diagnosis and management," *Journal of Neurology, Neurosurgery and Psychiatry*, vol. 81, no. 4. BMJ Publishing Group, pp. 358–367, 2010, doi: 10.1136/jnnp.2008.158261.

[3] T. D. Bird, *Myotonic Dystrophy Type 1*. 1993.

[4] C. M. Wiles, M. E. Busse, C. M. Sampson, M. T. Rogers, J. Fenton-May, and R. Van Deursen, "Falls and stumbles in myotonic dystrophy," *J. Neurol. Neurosurg. Psychiatry*, vol. 77, no. 3, pp. 393–396, Mar. 2006, doi: 10.1136/jnnp.2005.066258.

[5] M. Galli *et al.*, "Gait pattern in myotonic dystrophy (Steinert disease): A kinematic, kinetic and EMG evaluation using 3D gait analysis," *J. Neurol. Sci.*, vol. 314, no. 1–2, pp. 83–87, Mar. 2012, doi: 10.1016/j.jns.2011.10.026.

[6] R. B. Wright, D. M. Yoder, J. L. Costa, and T. P. Andriacchi, "Characterization of gait parameters in adult-onset myotonic dystrophy: abnormal hip motion.," *Arch. Phys. Med. Rehabil.*, vol. 76, no. 1, pp. 33–8, Jan. 1995, doi: 10.1016/s0003-9993(95)80039-5.

[7] F. Moreno Izco, M. Mendioroz Iriarte, J. J. Poza Aldea, J. F. Martí Massó, and A. López de Munain, "[Analysis of gait and movement of upper limbs in muscular dystrophies].," *Neurologia*, vol. 20, no. 7, pp. 341–8, Sep. 2005.

[8] S. Radovanović *et al.*, "Comparison of temporal and stride characteristics in myotonic dystrophies type 1 and 2 during dual-task walking," *Gait Posture*, vol. 44, pp. 194–199, Feb. 2016, doi: 10.1016/j.gaitpost.2015.12.020.

[9] B. Missaoui *et al.*, "Capacités posturolocomotrices et maladie de Steinert. Évaluation à court terme d'un programme de rééducation," *Ann. Phys. Rehabil. Med.*, vol. 53, no. 6–7, pp. 387–398, Aug. 2010, doi: 10.1016/j.rehab.2010.06.004.

[10] R. Baker *et al.*, "The Gait Profile Score and Movement Analysis Profile," *Gait Posture*, vol. 30, no. 3, pp. 265–269, Oct. 2009, doi: 10.1016/j.gaitpost.2009.05.020.

[11] G. Coghe *et al.*, "Quantifying gait impairment in individuals affected by Charcot-Marie-Tooth disease: the usefulness of gait profile score and gait variable score," *Disability and Rehabilitation*, Taylor and Francis Ltd, 2018.

[12] M. A. de Souza *et al.*, "The use of the gait profile score and gait variable score in individuals with Duchenne Muscular Dystrophy," *J. Biomech.*, Jan. 2019, doi: 10.1016/j.jbiomech.2019.109485.

[13] D. S. Speciali, E. M. Oliveira, J. R. Cardoso, J. C. F. Correa, R. Baker, and P. R. G. Lucareli, "Gait profile score and movement analysis profile in patients with Parkinson's disease during concurrent cognitive load," *Brazilian J. Phys. Ther.*, vol. 18, no. 4, pp. 315–322, 2014, doi: 10.1590/bjpt-rbf.2014.0049.

[14] J. S. Kalkman *et al.*, "Experienced fatigue in facioscapulohumeral dystrophy, myotonic dystrophy, and HMSN-I," *J. Neurol. Neurosurg. Psychiatry*, vol. 76, no. 10, pp. 1406–1409, Oct. 2005, doi: 10.1136/jnnp.2004.050005.

Personalized Linear Data-Driven Algorithms for Real-Time Glucose Forecasting in Type 1 Diabetes

F. Prendin[1], S. Del Favero[1], G. Sparacino[1], and A. Facchinetti[1]

[1] *Department of Information Engineering, University of Padova, Italy*

Abstract—**Minimally-invasive subcutaneous Continuous Glucose Monitoring (CGM) sensors have become an important tool in the daily management of Type 1 Diabetes (T1D). In particular, CGM sensors enable the real-time prediction of future glucose levels, which can be proactively used to prevent, or mitigate, upcoming critical events such as hypoglycemic episodes. Several prediction methods, both linear and nonlinear, have been proposed in literature for such a scope. The aim of this work is to perform a head-to-head comparison of personalized linear data-driven algorithms based on CGM data only, in terms both of accuracy of the prediction of future glucose levels and of correct forecasting of hypoglycemic episodes. Autoregressive (AR), Autoregressive Moving Average (ARMA) and Autoregressive Integrated Moving Average (ARIMA) are considered as candidate model class, Prediction Error Method (PEM) and Bayesian Information Criterion (BIC) for identification. Using a prediction horizon (PH) of 30 minutes, a total of 11 algorithms are evaluated on a dataset composed by 124 CGM traces monitored for 10 days by the Dexcom G6 CGM sensor, a product that has been launched in the market in 2018.**

Results show that ARIMA model outperforms all the other methodologies in terms of glucose level prediction and hypoglycaemia forecasting.

Keywords—**Continuous Glucose Monitoring, Black-Box model, Hypoglycemia, Model personalization.**

I. INTRODUCTION

TYPE 1 diabetes (T1D) is an autoimmune metabolic disease characterized by a deficient insulin secretion due to the destruction of the pancreatic beta cells, which compromises the complex physiological feedback systems regulating blood glucose (BG) levels in the body. To keep BG within a normal range ([70-180] mg/dL), common T1D therapy includes diet and physical exercise, as well as, insulin administrations, tuned according to self-monitoring of blood glucose 3-4 times a day.

The management of T1D has been recently revolutionized by the introduction of Continuous Glucose Monitoring (CGM) devices, subcutaneous non-invasive sensors providing real-time glycemic measures every 5 minutes for up to 10 days. CGM sensors currently available in the market are embedded with visual/acoustic real-time alarms to warn the user when the measured glucose concentration exceeds the thresholds of hypoglycemia (e.g. 70 mg/dL) and hyperglycemia (e.g. 180 mg/dL). The combined availability of real-time information on glucose dynamics and alerts has proved to be key in improving glucose control [1]. However, the large amount of data coming from CGM sensors can also be used to predict, rather than simply detect [2], such critical episodes, e.g. by appropriately modelling the CGM time series and using such a model to perform a real-time ahead-of-time prediction of the future glucose concentration. The real-time forecasting of the future glucose concentration, coupled with suitable preventive alert strategies, will enable to suggest important preventive actions, e.g. the suggestion of assuming suitable snacks to reduce the frequency and impact of hypoglycemia.

In the recent years, several algorithms for the prediction of future glucose levels have been developed, exploiting both CGM data only [3] and CGM data plus other information such as injected insulin, the amount of carbohydrates (CHO) assumed during a meal and physical activity, [4], [5], [6]. As shown in [7], the use of exogenous data allows enhancing prediction performance if compared to algorithms based on CGM data only. However, recording information about physical activity, or even CHO and injected insulin, requires the use of additional devices such as insulin pumps, mobile applications or wearable tracker devices. All of these devices must be able to communicate and elaborate information each other.

To the best of our knowledge, such systems are not already available to the majority of diabetic individuals, suggesting that the investigation of algorithms based on CGM data only is still of large interest.

Despite in literature a great number of algorithms have been developed, both linear and nonlinear, a performance comparison of predictive algorithms on the same dataset, collected with one of the newest sensors, is still missing. Therefore, in this paper we provide a head-to-head comparison of real-time personalized linear algorithms for glucose prediction fed by CGM data only, by assessing both the accuracy of the predicted profiles and the capability of forecasting upcoming hypoglycemic events.

II. DATASET

Data consist of 124 CGM traces (provided by Dexcom, Inc. San Diego, CA) collected in T1D people during a pivotal study (2016) on the G6 CGM sensor for 10 days. The sampling time is 5 minutes. The absence of daily calibrations and the accuracy of the CGM readings, are two features that have increased the use of such device between T1D subjects [2].

For each subject, CGM data are suitably divided in training and test set. We found, in a preliminary analysis, that a training set of 400 CGM samples (about 33 hours) is sufficient to identify a personalized model.

Then, predictive algorithms are evaluated on the test set, approximately 9 days.

III. METHODS

In this work, two main configurations of increasing complexity have been implemented to develop linear predictive algorithms.

A first option is to derive a subject-specific algorithm, in such a way that the large inter-individual variability, which characterizes T1D individuals, could be learnt from CGM data.

Another option is the identification of multiple predictors for each individual, in particular one for the day and one for the night period. This approach is more sophisticated, but it results also to be much more computationally demanding.

A. Linear Data-Driven Models under evaluation

We consider three linear model classes: autoregressive (AR), autoregressive moving-average (ARMA) and autoregressive integrated moving-average (ARIMA) models [8].

The ARIMA models, which are a generalization of AR and ARMA models, can be described by the following equation:

$$A(q)y(t) = \frac{C(q)}{(1-q^{-1})^d} e(t) \qquad (1)$$

where $A(q) = [1 + a_1 q^{-1} + \ldots + a_p q^{-p}]$, $C(q) = [1 + c_1 q^{-1} + \ldots + c_m q^{-m}]$, q^{-1} is the backward shift operator, $e(t)$ is the noise term assumed to be identically, independent distributed (i.i.d.), $y(t)$ are the CGM readings. We refer to ARIMA as ARIMA(p, m, d) by indicating the order of the AR, MA and I part respectively. In this work we consider only $d = 1$, in order to correct handle CGM bias and time drifts.

As for as the choice of model complexity is concerned, common strategies used for defining the number of parameters to be estimated are: Akaike Information Criterion (AIC), Bayesian Information Criterion (BIC) and Cross Validation (CV) [8]. A preliminary analysis showed that not significant differences in predictive performance can be seen among these methods, therefore we choose BIC to select the best model orders.

As for as parameter estimation is concerned, the state-of-art approach is the Prediction Error Method (PEM), based on the minimization of the one-step prediction error. The term step stands for sampling time, i.e. 5 minutes in this work. An alternative we investigated, is the minimization of the 30-minute ahead prediction error. Intra-patient variability could be described efficiency by involving models with fixed structure and time variant parameters, therefore we apply recursive least squares (RLS) parameters estimation to AR(1), as described in [9]. A last option considered is the regularized PEM approach [10], which adds to standard PEM cost function a regularization term (a prior on the unknown coefficients) to prevent overfitting.

Finally, once the model has been identified, the k-step ahead predictor is derived by applying the linear Kalman filter theory [8]. In this work we will always use a k=6-step ahead prediction, corresponding to a prediction horizon of PH=30 min.

B. Assessment of the algorithms

Combining all the models presented with several configurations, we derive 11 algorithms. Such algorithms were compared considering both glucose values prediction and hypoglycaemia event detection.

1) Glucose value prediction metrics

The accuracy of the predicted profiles is evaluated using three metrics.

Root Mean Square Error (RMSE):

$$RMSE(PH) = \sqrt{\frac{1}{N} \sum_{t=1}^{N} (y(t) - \hat{y}(t|t - PH))^2} \qquad (2)$$

where PH is the prediction horizon, N is the length of the CGM data of the test set, y(t) is the current CGM value, ŷ(t|t-PH) is its PH steps ahead prediction.

Coefficient of Determination (COD):

$$COD(PH) = 100 * \left(1 - \frac{\|y(t) - \hat{y}(t|t - PH)\|_2^2}{\|y(t) - \bar{y}(t)\|_2^2} \right) \qquad (3)$$

where ȳ is the mean of CGM data, y(t) and ŷ(t|t-PH) are described as previously.

COD counts for the variance explained by the predictive model with respect to the total variance of the signal. Its maximum value is 100%.

The delay existing between the target signal and the predicted one can be computed as the temporal shift that minimizes the square of the mean quadratic error between these two signals:

$$de =$$

$$arg \min_{j \in [0, PH]} \left[\frac{1}{N} \sum_{t=1}^{N-PH} \left(\hat{y}\big((t|t - PH) + j\big) - y(t) \right)^2 \right] \qquad (4)$$

then, the time gain granted by the prediction:

$$TG = PH - de \qquad (5)$$

2) Hypoglycemic prediction metrics

In the following, we will assume that n hypoglycemia occurs when a measured CGM value falls below 70 mg/dL (hypoglycemic threshold) with the previous 6 readings above this threshold. Hypoglycemic alarms are generated using the same definition, but on the predicted signal.

Considering a Detection Window (DW) of 45 minutes, we assign:

- True Positive (TP): if an alarm is raised at least 5 minutes before the hypoglycemic event and at most DW minutes before that episode;
- False Positive (FP): if an alarm is raised but no event occurred in the following DW minutes;
- False Negative (FN): if no alarm is raised at least 5 minutes before the event.

It is useful noting that defining True Negative (TN) would be of a limited interest here since the dataset is strongly unbalanced [11].

Finally, for any of the 124 CGM traces the following metrics can be computed:

$$Precision = \frac{TP}{TP + FP} \tag{6}$$

$$Recall = \frac{TP}{TP + FN} \tag{7}$$

$$F1 - score = 2 * \frac{Precision * Recall}{Precision + Recall} \tag{8}$$

Precision is the ratio of correct alarms over the total alarms generated. Recall is the ratio of correctly detected hypoglycemic events over the total and F1-score is the harmonic mean of the two metrics. We also compute the FP-per-day index, since the dataset is strongly unbalanced.

IV. RESULTS

Results about glucose prediction and hypoglycemic event detection are reported in Table I. For sake of conciseness, we report only 6 out of the 11 models investigated.

Individualized AR models provide the lowest RMSE: 22.6 mg/dL, but the detection of hypoglycemic event is not satisfactory: Recall and Precision are around 33% and 47%, respectively.

Personalized ARIMA allows mitigating the impact of slow changes in glucose mean concentration and the predicted profiles are more adherent to the CGM signal, as in Fig. 1.
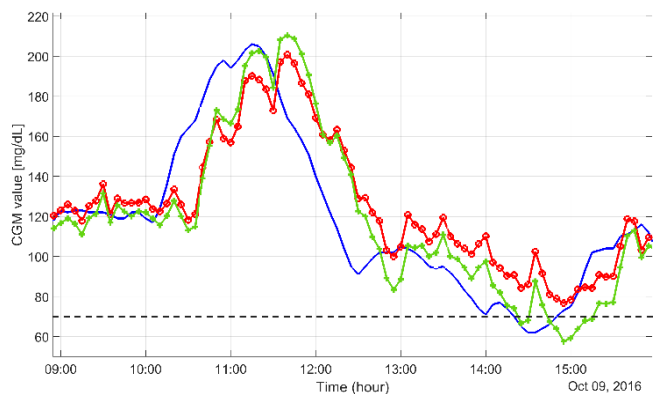
Fig. 1: CGM data (blue line), 30-minute ahead prediction (red line) personalized AR(10) and (green line) personalized ARIMA(2,0,1). Hypoglycemic threshold (black dashed line).

Individualized ARIMA model provides accurate prediction also when CGM data fall below the hypoglycemic threshold (as visible in Fig. 1 after 14:00); in such a way an alert could warn the subject of an upcoming hypoglycemia, while the AR model is not able to predict that specific future event. Despite the RMSE is about 22.7 mg/dL (slightly higher than AR), ARIMA models allow obtaining very satisfactory Recall and Precision scores (83% and 64%, respectively), with a median time gain of 10 minutes.

Models derived by the minimization of the 30-minute prediction error achieve similar performance to those identified using the standard PEM approach. For instance, for AR models identified in such a way we obtained: RMSE: 22.93%, COD: 84.73%, Recall: 21.8%, Precision: 44.03%.

The day and night specific algorithms provide a higher RMSE (25.2 mg/dL) than previous models, while the ability to predict hypoglycemic events is comparable to the other algorithms, suggesting that this additional complexity in the model structure does not improve the performance.

Regularized AR models, which require a more complicate identification procedure, achieve RMSE of 23.3 mg/dL, and Recall and Precision of 37% and 49.5% respectively, and thus not providing any visible improvement with respect to other models.

Finally, AR-RLS(1) shows the highest RMSE (28.5 mg/dL), since it is very sensitive to noisy CGM values. However, Recall and Precision are particularly high: 82% and 60%. The median TG is 15 minutes.

TABLE I
PERSONALIZED LINEAR ALGORITHMS RESULTS, PH = 30 MIN

Algorithm	Glucose Prediction Metrics	Hypoglycemic Event Detection Metrics
Individual AR	RMSE: 22.64 mg/dL COD: 85.64%	F1-score: 39.31% Recall: 33.45% Precision: 47.65% FP/day: 0.51 TG: 10 min
Individual ARIMA	RMSE: 22.69 mg/dL COD: 85.65%	F1-score: 71.84% Recall: 82.69% Precision: 63.50% FP/day: 0.65 TG: 10 min
Individual AR 30-minute prediction error	RMSE: 22.93 mg/dL COD: 84.73%	F1-score: 29.14% Recall: 21.77% Precision: 44.03% FP/day: 0.38 TG: 10 min
Individual day and night ARIMA	RMSE: 25.18 mg/dL COD: 83.53%	F1-score: 65.35% Recall: 78.37% Precision: 56.04% FP/day: 0. 84 TG: 15 min
Individual AR regularized	RMSE: 23.27 mg/dL COD: 83.59%	F1-score: 42.32% Recall: 36.96% Precision: 49.49% FP/day: 0. 51 TG: 10 min
Individual RLS AR (1)	RMSE: 28.44 mg/dL COD: 79.56%	F1-score: 69.17% Recall: 82.14% Precision: 59.74% FP/day: 0. 86 TG: 15 min

Median values of the metrics for 6 out of the 11 models presented in this study.

V. CONCLUSIONS

The effective prediction of blood glucose levels or forecasting of hypoglycemic episodes is a crucial task since that it can play an important role in improving the effectiveness of T1D therapy.

In this work we have implemented and compared 11 glucose prediction algorithms fed by CGM data only and based on linear models. The goodness of such algorithms has been evaluated on 124 CGM traces monitored with the Dexcom G6 sensor for 10 days, in terms of accuracy of glucose levels prediction and capability of forecasting hypoglycemic events.

The best performing algorithm is individual ARIMA, which

outperforms all other methodologies in terms of hypoglycaemia event detection.

Finally, the RMSE results presented in this work (around 22 mg/dL) are in line with literature works based on CGM data only [3], [6], [9], [12] which ranges from 18.9 mg/dL up to 27 mg/dL. Moreover, the algorithms proposed in this work have a practically relevant advantage: they require 33 hours of CGM data for training, while the great part of the algorithms based on deep learning models needed a large amount of data and they are more computation demanding.

In another contribution by our group [13], we address the issue of predicting future BG using CGM data, insulin and CHO signals as exogenous inputs, based on linear black-box models. The methods presented in [13] achieved a RMSE = ~12 mg/dL at PH = 30 minutes. It should be noticed that, although exogenous inputs are expected to improve the prediction accuracy, a direct comparison could be misleading since the dataset used in this work is more challenging (10-day CGM data recorded in free living conditions).

We refer the interested reader to [6] for a systematic review of the main works related to glucose prediction techniques since this goes beyond the scope of this paper.

Further developments of this work will be the implementation of personalized machine learning algorithms which, thanks to the possibility of learning complex subject-specific patterns from CGM data, might improve glucose prediction performance.

REFERENCES

[1] N. Camerlingo, M. Vettoretti, S. Del Favero, et al., "A Real-Time Continuous Glucose Monitoring-Based Algorithm to Trigger Hypotraments to Prevent/Mitigate Hypoglycemic Events," *Diabetes Technol Ther.* Vol. 21, pp. 644-655, 2019.

[2] M. Vettoretti, G. Cappon, G. Acciaroli, et al., "Continuous Glucose Monitoring: Current Use in Diabetes Management and Possible Future Applications," J. Diabetes Sci Technol. Vol 5, pp. 1064-1071, 2018.

[3] J. Yang, L. Li, Y. Shi., et al., "An ARIMA Model With Adaptative Orders for Predicting Blood Glucose Concentrations and Hypoglycemia," *IEEE J. Biomed Health Inform*, vol. 23, pp. 1251–1260, 2018.

[4] K. Li, J. Daniels, C. Liu, et al., "Convolutional Reccurrent Neural Networks for Glucose Prediction," *IEEE J. Biomed Health Inform*, 2019.

[5] C. Zecchin, A. Facchinetti, G. Sparacino, et al., "Jump Neural Network for Online Short-Term Prediction of Blood Glucose from Continuous Glucose Monitoring Sensor and Meal Information," *Comput. Methods Programs Biomed.*, vol. 113, pp. 144-152, 2014.

[6] S. Oviedo, J. Vehì, R. Calm, et al., "A Review of Personalized Blood Glucose Prediction Strategies for T1DM patients," *Int J. Numer Methos Biomed Eng.*, vol. 33, pp. e2833, 2017.

[7] C. Zecchin, A. Facchinetti, G. Sparacino, et al., "How Much is short-Term Glucose Prediction in Type 1 Diabetes Improved by Adding Insulin Delivery and Meal Content Information to CGM Data? A Proof-of-Concept Study," *J. Diabetes Sci Technol.*, vol. 10, pp. 1149-1160, 2016.

[8] L. Ljung, *System Identification-Theory for the User*, 2nd ed. Upper Saddle River, NJ: Prentice-Hall, 1999.

[9] G. Sparacino, F. Zanderigo, S. Corazza, et al., "Glucose Concentration can be Predicted Ahead in Time from Continuous Glucose Monitoring Sensor Time-Series," *IEEE Trans. Biomed Eng.*, vol. 54, pp. 931–937, 2007.

[10] G. Pillonetto, F. Dinuzzo, T. Chen, et al., "Kernel Methods in System Identification, Machine Learning and Function Estimation: a Survey," *Automatica*, vol. 50, pp. 657–682, 2014.

[11] T. Saito, M. Rehmsmeier, "The Precision-Recall Plot is More Informative than the ROC Plot When Evaluating Binary Classifiers on Imbalanced Datasets," *PloS one*, vol. 50, 2015.

[12] D. A. Finan, F. J. Doyle III, C. C. Palerm, et al., "Experimental Evaluation of a Recursive Model Identification Technique for Type 1 Diabetes," *J. Diabetes Sci Technol.*, vol. 3, pp. 1192-1202, 2009

[13] S. Faccioli, A. Facchinetti, G. Sparacino, and S. Del Favero, "Comparison of Parametric Linear Techniques for Glucose Prediction in Type-1 Diabetes," in Proc. of the Italian National Bioengineering Group (GNB 2020+1), 2020.

Sensitivity to carb-counting error in the T1D management

C. Roversi[1], M. Vettoretti[1], S. Del Favero[1], A. Facchinetti[1] and G. Sparacino[1],
on behalf of Hypo-RESOLVE Consortium
[1] Department of Information Engineering, University of Padova, Padova, Italy

Abstract— In type 1 diabetes (T1D) therapy, patients need to take an exogenous insulin dose at mealtime in order to compensate the rise in glycaemia caused by carbohydrates (CHO) intake. To properly tune the meal insulin dose, the patient needs to estimate the amount of CHO. Errors in CHO estimation are, however, common and can have a negative impact on the quality of glycaemic control. The aim of this work is to quantify how much different levels of carb-counting error affect the overall glycaemic control. This sensitivity study is performed in silico using the popular T1D patient decision simulator. In 100 virtual subjects simulated for 7 days, different levels of carb-counting error are generated with Gaussian distributions varying the error mean from -10% to +10% and standard deviation ranging from 0% to 50%. The effect of the error is evaluated by computing time inside (TIR), above (TAR) and below (TBR) the target glycaemic range using the absence of error as reference case. We found that random errors globally deteriorate the glycaemic control; systematic underestimation lead to, on average, up to 5.2% more of TAR than the reference case, while systematic overestimation results in up to 0.8% more of TBR. Such results could be useful to assist diabetologists in patients' therapy adjustments or training.

Keywords—type 1 diabetes, carb-counting error, glycaemic control, simulation.

I. INTRODUCTION

TYPE I diabetes (T1D) is a chronic disease that causes instability in blood glucose concentration (BG) due to the lack of insulin production by pancreatic beta-cells. Consequently, BG concentration can exceed the safe range. While prolonged hyperglycaemia (i.e. BG>180 mg/dl) can lead to long-term complications such as retinopathy, nephropathy and neuropathy, hypoglycaemia (i.e. BG<70 mg/dl) can be extremely dangerous in the short-term since it might lead to coma and even death [1]. To maintain BG concentration within the safe range, T1D patients must properly tune exogenous insulin doses [2], a task facilitated by frequent monitoring of BG concentration by continuous glucose monitoring (CGM) sensors [3],[4]. In particular, at mealtime T1D subjects need to estimate the meal carbohydrates (CHO) amount, an action called carb-counting, and then compute the size of the insulin bolus by using a mathematical formula [5]. Accurate carb-counting requires a specific training and knowledge about the CHO content of different foods and meals. Therefore, carb-counting is a difficult task for T1D subjects, who frequently commit errors which can influence the postprandial BG excursion.

While, according to an in-vivo clinical trial performed by Smart et al [6], an error of ±10 g per meal or snack on a meal size of 60 g would not significantly deteriorate the postprandial control, some literature works have underlined that subjects made much larger errors [7]-[9]. Moreover, a regression model of the carb-counting error was developed by involving, as predictors, meal, subject and therapy characteristic, showing that the error strongly depends on meal CHO amount and type [10].

The quantitative impact of carb-counting error on glycaemic control in T1D patients has been investigated only partly. In particular, CHO underestimation can cause post-prandial hyperglycaemia, while CHO overestimation can lead to hypoglycaemic episodes [9],[11],[12]. A possible limit of the quantification in a real life setting of the impact of the carb-counting errors is that, since many conditions may affect the daily glycaemic profile of T1D subjects (e.g. insulin sensitivity variability, different amount and time of the meals consumed, error in meal amount estimation, physical activity and others), it is difficult to isolate the contribution of only a single factor. These limitations can be overcome by in silico experiments, in which the impact of each factor can be isolated by performing multiple simulations in which a single factor is changed and all the other factors are fixed.

The aim of this work is to perform a sensitivity analysis of the impact of carb-counting error on glucose control by using the popular T1D patient decision simulator [13].

II. METHODS

A. Simulation scenario

The T1D patient decision simulator [13], based on the well-known FDA-approved UVA/Padova T1D physiological model [14], is a simulation tool that allows performing in silico trials in T1D and was shown to reproduce realistic treatment scenarios [13]. The simulator, in particular, permits to test the impact of deviations from the ideal situation, either due to error of technologies or patient mistakes, without any risk for real patients.

In particular, the T1D patient decision simulator [13], schematically represented in Fig. 1, is constructed by connecting the UVA/Padova T1D model [15] (block A), that describes the physiology of T1D, with mathematical descriptions of glucose monitor devices [16],[17] (block B), insulin pump [18] (block D) and patient's behaviour in making the treatment decisions (block C). In particular, Block C also models the possible mistakes made by patients in tuning CHO intakes and insulin doses according to glucose measurements, such as carb-counting errors. In this work, we used the simulator to perform a 7-day simulation in 100 virtual subjects with 3 meals per day (i.e. breakfast, lunch and dinner) and therapy based on non-adjunctive CGM use.

Meal amounts are randomly generated from Gaussian distributions fitted on the real data extracted from Brazeau et al [8]. The entire simulation is repeated for different values of the mean and the standard deviation of carb-counting error as described in Section II.B.
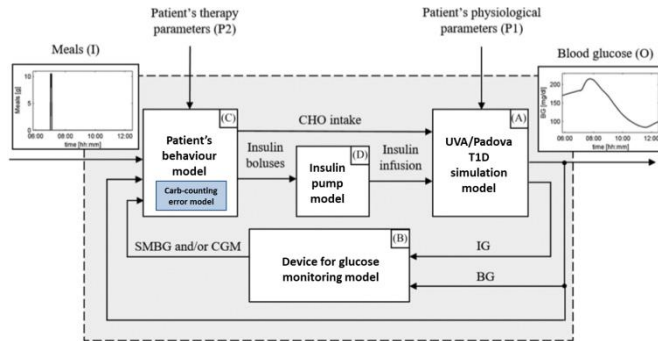

Fig. 1: Schematic block representation of the T1D patient decision simulator. Arrows entering each block are inputs, while arrows exiting are outputs. The input of the simulator is the sequence of meals (I), while the output is the BG concentration profile (O). The simulator includes parameters describing the patient physiology (P1) and therapy (P2).

B. Carb-counting error generation

We simulate the percentage CHO estimation error e by using a Gaussian distribution, with mean M and standard deviation SD:

$$e \sim N(M, SD) \qquad (1)$$

The analysis performed in [10] on real data shows an approximatively symmetric distribution of the carb-counting errors, justifying the use of the Gaussian distribution to simulate the error. Moreover, a Gaussian distribution easily permits to match the parameters of the distribution with the behavior of patients in real life: the mean M accounts for the systematic error, while the standard deviation SD for the random error.

Different sign and magnitude of the error are tested by using different mean and standard deviation values. In particular, we tested mean values of -10%, -5%, 0%, +5% and +10%. For each of the mean value, we tested different values of standard deviation, which are 0%, 10%, 20%, 30%, 40% and 50%. A mean value of 0% means that no systematic error is present, while a standard deviation value of 0% accounts for the absence of random error. Such values of carb-counting error parameters have been chosen after the analysis of the real data published by Brazeau et al [8].

Each of the Gaussian distribution is then truncated at -100%, which means a CHO estimate of 0 g, and +100%, which means a CHO estimate of twice the real meal amount, in order to avoid unrealistic CHO counting error realizations.

The reference case for the problem under study is the scenario in which carb-counting error is absent, that is

$$e \sim N(M = 0, SD = 0) \qquad (2)$$

C. Evaluation of the effect of carb-counting error

The impact of different carb-counting error values on the subjects' glycaemic control is evaluated by computing from the 100 subjects' glycaemic profile the following metrics:
- Time In target Range (TIR), i.e. percentage of BG values between 70 and 180 mg/dl;
- Time Above Range (TAR), i.e. percentage of BG values greater than 180 mg/dl;
- Time Below Range (TBR), i.e. percentage of BG values less than 70 mg/dl.

In addition, for each of the 100 virtual subjects and in each of the simulation performed, we compute also the difference time metrics compared to the reference case. For example, for the time spent in the target range, the difference time is computed as the difference between the time spent in the target range when a certain carb-counting error is made and the one obtained when no carb-counting error is made:

$$\Delta TIR = TIR(M = m, SD = sd) - TIR(M = 0, SD = 0)$$
$$(3)$$

Results are analysed via boxplot representation, bidimensional maps and plot of the time metrics' curves.

III. RESULTS

Fig. 2 reports via boxplot representation the time metrics difference distributions (ΔTIR, ΔTBR and ΔTAR), when the carb-counting error is generated using Gaussian distribution with a standard deviation equal to 0 and different values of the error mean, i.e. -10%, -5%, +5%, +10%, respectively. From a clinical perspective, Fig. 2 shows the impact of the systematic error in carb-counting on the glycaemic control, in absence of random error. We can see that systematic underestimations of the meal CHO content (i.e. error mean equal to -5% and -10%) lead to more TAR and less time in TIR than the reference case for the majority of subjects. Instead, systematic overestimations (i.e. error mean equal to +5% and +10%) lead to more TIR at the expense of an increase of TBR for the majority of subjects, which can lead to severe short-term complications.
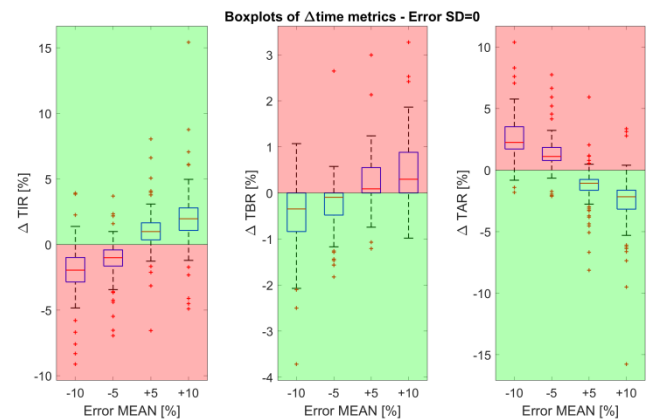

Fig. 2: Boxplot representation of the distribution of ΔTIR (on the left), ΔTBR (in the middle) and ΔTAR (on the right), obtained by varying carb-counting error mean and setting error SD equal to 0. A zero value for the y-axis corresponds to the reference case. In red zones, the glycaemic control is worse than the reference case, while in the green ones it is better. Red horizontal lines represent median, boxes mark interquartile ranges, dashed lines the whiskers, while red crosses are the outliers.

Fig. 3 reports via boxplot representation the time metrics

differences distribution (ΔTIR, ΔTBR and ΔTAR), when the Gaussian distributions of carb-counting error have mean equal to 0 and different values of standard deviation, which vary from 10% to 50%. Therefore, Fig. 3 shows the impact of the random error on the glycaemic control metrics, in absence of systematic error. The increase of random error apparently results in a deterioration of glycaemic control, i.e. lower TIR and higher TAR and TBR.
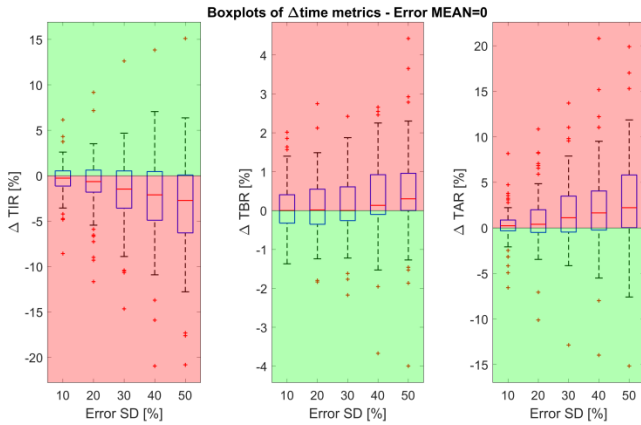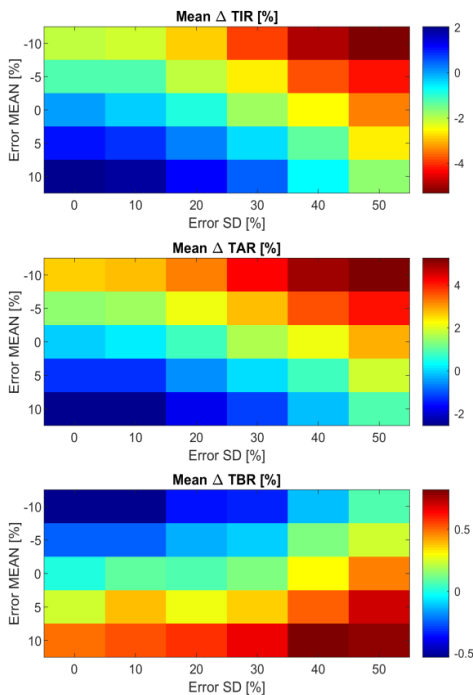

Fig. 3: Boxplot representation of the distribution of ΔTIR (on the left), ΔTBR (in the middle) and ΔTAR (on the right), obtained by varying carb-counting error SD and setting error mean equal to 0. A zero value for the y-axis corresponds to the reference case. In red zones, the glycaemic control is worse than the reference case, while in the green ones it is better. Red horizontal lines represent median, boxes mark interquantile ranges, dashed lines the whiskers, while red crosses are the outliers.

Fig. 4: Bidimensional maps of the mean among the 100 virtual subjects of ΔTIR (on top), ΔTAR (in the middle) and ΔTBR (below), for all combinations of carb-counting error mean and SD tested. In each map, the x-axis represents error SD, while the y-axis the error mean. Each color represents a different quantitative value of the metric, reported by the legends on the right of each map.

Fig. 4 reports the bidimensional maps of the mean among the 100 subjects of the difference time metrics for each simulation. Systematic underestimation with high random error lead to up to 5.2% more of mean TAR and 5.3% less of mean TIR compared to the reference. Note that, according to the International Consensus on time in ranges [19], a difference of 5% in TIR is clinically significant for T1D individuals. Regarding the cases with systematic overestimation, the presence of large random error results in up to a 0.8% increase of TBR over the reference. The virtual subjects intake of hypotreatment, i.e. small amount of CHO consumed by T1D subjects to compensate an excessive drop in BG concentration caused, for example, by a too high insulin dose, probably mitigate the variation in TBR due to carb-counting error.

The mean among the 100 virtual subjects of the time metrics is plotted in Fig. 5 and Fig. 6 for different values of carb-counting error mean and standard deviation, respectively. While the starting point of each curves is different, depending on either the error mean (in Fig. 5) or the standard deviation (in Fig. 6), the plots present a similar trend, approximatively linear, with a different rate of change for the different time metrics.
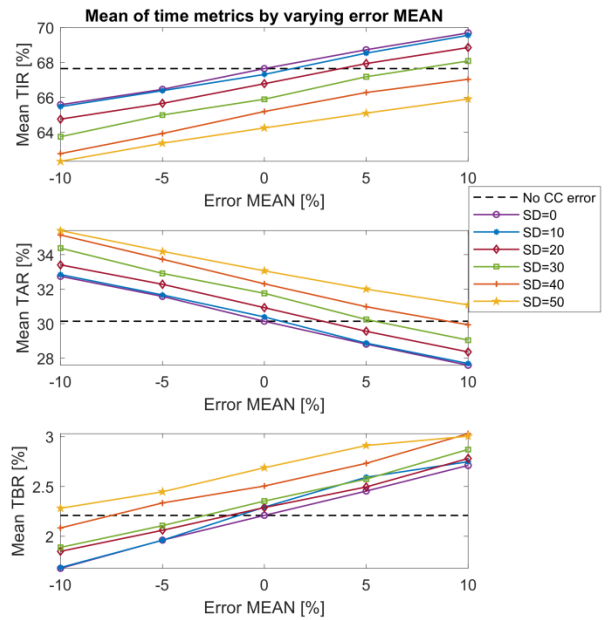

Fig. 5: Plot of the mean among the 100 virtual subjects of TIR (on top), TAR (in the middle) and TBR (below), by varying carb-counting error mean. The curves have different colors based on the error SD value. Dashed lines represent the values of the time metrics in the reference case.

IV. CONCLUSION

Carb-counting error is one of the most common mistake committed by T1D subjects in the insulin therapy. In the present study, we perform a sensitivity analysis aimed at quantifying the impact of the error in meal CHO amount estimation on the subjects glycaemic control.

Results highlight that carb-counting errors deteriorate the overall glycaemic control of T1D patients by increasing the
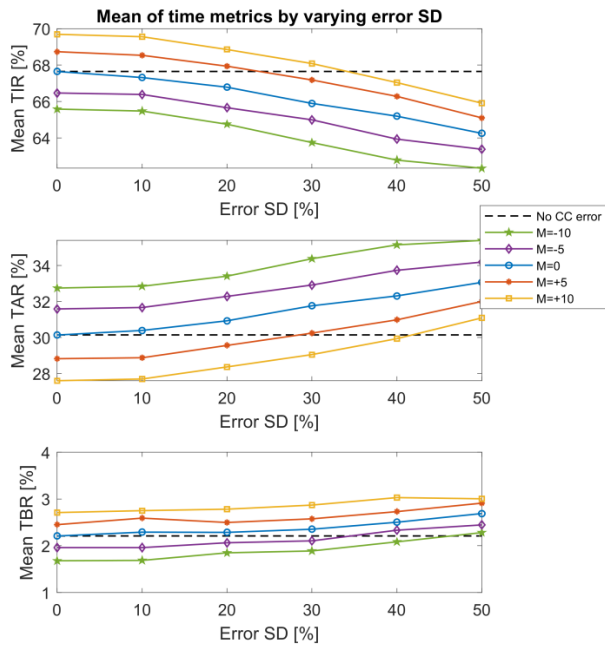
Fig. 6: Plot of the mean among the 100 virtual subjects of TIR (on top), TAR (in the middle) and TBR (below), by varying carb-counting error SD. The curves have different colors based on the error mean value. Dashed lines represent the values of the time metrics in the reference case.

time spent outside the safe range, motivating a deeper analysis on this topic. This evidence may be useful to clinicians to refine educational session for T1D subjects about meal CHO estimation and to identify an acceptable range of the error, i.e. error which do not significantly deteriorate the glycaemic control.

The trend obtained for the time metrics by varying the two parameters of the error, i.e. error mean (Fig. 5) and standard deviation (Fig. 6), suggests that the relationship between variations of carb-counting error mean/standard deviation and the change of glycaemic metrics can be modelled. For example, a mathematical formula could be developed that summarizes what variation on time metrics is expected from a variation of the carb-counting error mean or standard deviation. Such a formula could be useful to define actionable rules, i.e. acceptable range of the carb-counting errors, which would assist diabetologists in patients' therapy adjustments or training. Moreover, the awareness of the potential risk in misestimating meal CHO amount (e.g. the increasing in TIR) would motivate patients to better perform this critical task.

Finally, the current work is a first part of a wider study aiming at analysing the relative impact of some of the main behavioural factors, including e.g. carb-counting error, responsiveness to CGM alerts, early or delayed boluses, which can potentially influence the glycaemic control, with a particular attention to hypoglycaemia.

REFERENCES

[1]   D. Daneman, "Type 1 diabetes", Lancet, vol. 367, pp. 847-858, 2006.
[2]   D. E. De Witt, and I. B. Hirsch, "Outpatient insulin therapy in type 1 and type 2 diabetes mellitus," JAMA, vol. 289, pp. 2254-2264, 2003.
[3]   G. Cappon, G. Acciaroli, M. Vettoretti, A. Facchinetti, and G. Sparacino, "Wearable continuous glucose monitoring sensors: a revolution in diabetes management," Electronics, vol. 6, pp. 65-81, 2017.
[4]   Vettoretti, G. Cappon, G. Acciaroli, A. Facchinetti, and G. Sparacino, "Continuous glucose monitoring: current use in diabetes management and possible future applications," J Diabetes Sci Technol, vol. 12, pp. 1064-1071, 2018.
[5]   S. Schmidt, and K. Norgaard, "Bolus calculator," J Diabetes Sci Technol, vol. 8, pp. 1035-1041, 2014.
[6]   C. E. Smart, K. Boss, J. A. Edge, C. E. Collins, K. Colyvas§, et al, "Children and adolescents on intensive insulin therapy maintain postprandial glycaemic control without precise carbohydrate counting," Diabetic Medicine, vol. 26, pp. 279-285, 2009.
[7]   L. T. Meade, and W.E. Rushton, "Accuracy of carbohydrate counting in adults," Clin Diabetes Journal, vol. 34, pp. 142-147, 2016.
[8]   A. S. Brazeau, H. Mircescu, K. Desjardins, C. Leroux, I. Strychar, et al, "Carbohydrate Counting Accuracy and Blood Glucose Variability in Adults With Type 1 Diabetes," Diabetes Res. Clin. Pract., vol. 99, pp. 19-23, 2013.
[9]   F. Reiterer, G. Freckmann, and L. Del Re, "Impact of carbohydrate counting errors on glycemic control in type 1 diabetes," Science Direct, vol. 51, pp. 186-191, 2018.
[10] C. Roversi, M. Vettoretti, S. Del Favero, A. Facchinetti, and G. Sparacino, on behalf of the Hypo-RESOLVE Consortium, "Modeling carbohydrate counting error in type 1 diabetes management", Diabetes Technology and Therapeutics, vol. 22, 2020.
[11] C. E. Smart, B. R. King, P. McElduff , and C. E. Collins, "In children using intensive insulin therapy, a 20-g variation in carbohydrate amount significantly impacts on postprandial glycaemia," Diabetic Medicine, vol. 29, pp. e21-24, 2012.
[12] A. Deeb, A. Al Hajeri, I. Alhmoundi, and N. Nagelkerke, "Accurate carbohydrate counting is an important determinant of postprandial glycemia in children and adolescents with type I diabetes on insulin pump therapy," J Diabetes Sci Technol, vol. 11, pp. 753-758, 2017.
[13] M. Vettoretti, A. Facchinetti, G. Sparacino, and C. Cobelli, "Type 1 diabetes patient decision simulator for in silico testing safety and effectiveness of insulin treatments," IEEE Trans Biomed Eng, vol.65, pp.1281-1290, 2018.
[14] R. Visentin, E. Campos-Nanez, M. Schiavon, D. Lv, M. Vettoretti, M. Breton, et al, "The UVA/Padova type 1 diabetes simulator goes from single meal to single day," J Diabetes Sci Technol, vol. 12, pp. 273-281, 2018.
[15] C. Dalla Man, F. Micheletto, D. Lv, M. Breton, B. Kovatchev, et al, "The UVA/PADOVA type 1 diabetes simulator: new features," J Diabetes Sci Technol, vol. 8, pp. 26-34, 2014.
[16] M. Vettoretti, A. Facchinetti, G. Sparacino, and C. Cobelli, "A model of self-monitoring blood glucose measurement error," J Diabetes Sci Technol, vol. 11, pp. 724-735, 2017.
[17] M. Vettoretti, C. Battocchio, G. Sparacino, and A. Facchinetti, "Development of an error model for factory-calibrated countinuous glucose monitoring sensor with 10-day lifetime," Sensors, vol.19, 2019.
[18] M. Vettoretti, and A. Facchinetti, "Combining continuous glucose monitoring and insulin pumps to automatically tune the basal insulin infusion in diabetes therapy: a review," Biomed Eng Online, vol.18, 2019.
[19] T. Battelino, T. Danne, R. M. Bergenstal, S. A. Amiel, R. Beck, et al, "Clinical targets for continuous glucose monitoring data interpretation: recommendations from the international consensus on time in range," Diabetes Care, vol. 42, pp. 1593-1603, 2019.

Bioactive silica-based glass nanoparticles containing boron and copper

E. Piatti[1], M. Miola[1], and E. Vernè[1]

[1] Department of Applied Science and Technology, Politecnico di Torino, Turin, Italy

Abstract—**Because of their ability to bond with living tissues and release ions, stimulating new tissue growth, bioactive glasses are good candidates for tissue-engineering applications. Innovative bioactive glass compositions containing boron and copper have been prepared via sol-gel and characterized using SEM, EDS, FTIR, XRD, BET and bioactivity analysis.**

Keywords—**Bioactive glass, sol-gel, Copper, Boron**

I. Introduction

Bioactive glasses (BGs) are amorphous materials that are able to bond with living tissues and stimulate new tissue growth, without formation of an undesirable fibrous encapsulation [1]–[3]. The bonding with the hard tissues, such as bone and teeth, through a hydroxyapatite (HA) layer formation, has been widely documented [4]–[6]. Moreover, during their dissolution process, BGs can release ions with therapeutic effect. According to the released ions, for example, BGs can promote osteogenesis [7] and angiogenesis [8], [9], stimulate hard and soft tissue growth [10], [11] and have antibacterial properties [12]–[14].

The first bioactive biomaterial was a silicate glass containing sodium, calcium and phosphorus ions, known as Bioglass®, that was developed by Hench et al. in 1969 [15]. Nowadays many BGs with different chemical compositions are available.

Among others, BGs containing copper [16], [17] or boron [5], [10], [18] are largely investigated, especially because of the antibacterial [8], [9], [19] and angiogenic [9], [20]–[22] properties of these elements.

Very few studies have been carried out on glasses incorporating both ions. Recently, borosilicate glasses have been doped with copper by different researcher groups [23]–[26]. In 2015 Shailajha et al. [27] have successfully doped some sodium phosphoborate glasses with CuO. The synthesis of Cu-doped borate glasses have been also reported [26], [28], [29]. In all mentioned experimental studies, glass powders were produced through the melting-quenching technique. Only few of the above cited studies have potential biomedical application [23], [24], [26].

In this study, we report the sol-gel synthesis of a bioactive glass doped with boron and copper. On the basis of authors knowledge, there are not any other works based on sol-gel bioactive glasses containing both B and Cu ions for therapeutic applications, in details they could be potentially used as bioactive fillers in a polymeric matrix for soft tissue engineering applications.

II. Materials and methods

A. Materials

For the synthesis of the bioactive glasses, tetraethyl orthosilicate (TEOS) $C_8H_{20}O_4Si$ at 99% (Sigma Aldrich), triethyl phosphate (TEP) $C_6H_{15}O_4P$ at 99% (Alfa Aesar), calcium nitrate tetrahydrate $Ca(NO_3)_2 \cdot 4H_2O$, copper nitrate trihydrate $Cu(NO_3)_2 \cdot 3H_2O$ (Fluka) and boric acid H_3BO_3 at 99% (Sigma Aldrich) were used as precursors for SiO_2, P_2O_5, CaO, CuO and B_2O_3, respectively. Distilled water and ethanol (EtOH, Sigma Aldrich) were used as solvents. To achieve an acid-base co-catalysed synthesis, nitric acid (HNO_3) at 70% (Sigma Aldrich) and ammonia solution NH_4OH at 28-30% (Emsure) were used as hydrolysis catalyst and gelling catalyst, respectively.

B. Glass synthesis

Three different glass compositions, shown in Table I, were synthesized. To compare different synthesis strategies, two synthesis methods were carried out simultaneously. In both cases, the glasses were synthesized through a modified Stöber method, hydrolysing TEOS in an acidic media (using nitric acid) and adding a certain amount of ammonia solution (NH_4OH 2M).

TABLE I
GLASS COMPOSITION

Glass	SiO_2	P_2O_5	CaO	B_2O_3	CuO
S	77	9	14	---	---
SB	62	9	14	15	---
SBCu	62	9	9	15	5

Synthesis 1: The first step of the synthesis was the acid hydrolysis of TEOS: a solution of EtOH, H_2O, HNO_3 2M and TEOS, with molar ratio (H_2O+HNO_3):TEOS equal to 8, was left under gentle and constant magnetic stirring for 1 h. At this point, NH_4OH 2M was dropped during vigorous magnetic stirring, monitoring the pH increase. The addition of NH_4OH was stopped when a final pH between 8.3 – 9 was reached. Therefore, the other glass precursors were added to the silica gel in a basic condition, at time interval of 30 min under gently magnetic stirring, according to a fixed order (TEP, $Ca(NO_3)_2 \cdot 4H_2O$, $Cu(NO_3)_2 \cdot 3H_2O$, and boric acid H_3BO_3). At this point the steps of drying at 60 °C in a heater for 48 h and later at 700 °C in muffle furnace (Manfredi OVMAT2009) for 2 h were carried out. Glasses prepared through this synthesis process were called S1, SB1 and SBCu1.

Synthesis 2: after the acid hydrolysis of TEOS took place, all other precursors were added to the acid solution. 30 min after the addition of the last precursor, NH_4OH 2M was added dropwise until the solution became a gel characterized by a pH of 8.3 – 9. As in synthesis 1, the obtained gels were dried at 60 °C in a heater for 48 h and then calcinated at 700 °C in furnace for 2 h. Glasses prepared through this synthesis process were called S2, SB2 and SBCu2.

III. CHARACTERIZATION

A. Morphological and compositional characterization

The morphological and compositional analysis was carried out by means of Field Emission Scanning Electron Microscopy (FE-SEM - Gemini SUPRATM 40 Zeiss, Germany) equipped with Energy Dispersive Spectroscopy (EDS). The samples were prepared attaching the glass powders on an aluminium stub using a double-side carbon tape and sputtering them with chromium.

B. X-ray diffraction characterization

To assess the samples structure, an X-ray diffraction (XRD) analysis was performed by means of a X'Pert diffractometer, using the Bragg Brentano camera geometry and the Cu-Ka incident radiation, setting the source voltage at 40 kV, the current at 30 mA, the incident wavelength λ at 1.5405 Å, the step size Δ(2θ) at 0.02°, the counting time at 1 s per step and varying the analysis degree 2θ between 10° to 70°. The obtained spectra were analysed by X'Pert HighScore program equipped with PCPDFWIN database.

C. FTIR analysis

The structure analysis of glasses was performed with Fourier Transform Infrared Spectroscopy, using the KBr pellet method. The Thermo Scientific Nicolet iS50 FT-IR Spectrometer, equipped with OMNIC software, was used in transmission with a selected number of spectral scans of 32, a resolution of 4 cm^{-1} and a wavenumber range between 4000 and 525 cm^{-1}.

D. BET measurements

The N_2 adsorption and desorption measurements were performed using the analyzer ASAP 2020 Plus (Micrometrics, United States) and the particle surface area was calculated according to the Brunauer, Emmett, Teller method (BET method).

E. In vitro acellular bioactivity test

To evaluate *in vitro* the samples bioactivity, the synthesized glasses were soaked in a simulated body fluid (SBF) solution. The SBF solution is an acellular aqueous solution, buffered at physiological pH and having an ionic composition and concentration similar to those of the inorganic part of human plasma, in order to mimic the human plasma itself. The SBF solution was prepared according to Kokubo protocol [30]. The ratio between glass powders and SBF solution for samples soaking was 1:1 [31]. The samples were kept at 37 °C in an orbital shaker at 100 rpm, without renewing the SBF solution. Four time points were taken into consideration: 1, 3, 7 and 14 days. During immersion time, the pH of the SBF solution was investigated after 1, 3, 5, 7, 10, 12 and 14 days. At each time point, samples were removed from SBF, rinsed with deionized water, centrifugated at 5000 rpm for 10 minutes and dried in an incubator at 37 °C. Finally, the samples were analysed using SEM-EDS and XRD.

IV. RESULTS

A. Morphological and compositional characterization

Nanosized round-shaped particles, with a certain degree of aggregation, were obtained for all syntheses and compositions, without significant change in morphology, size and aggregation; SBCu1 is shown as example in Fig. 1. The mean particle size of all glasses is smaller than 100 nm, with a predominant diameter of about 50 nm.

The EDS patterns confirm the composition of the glasses, with the exception of boron that was not possible to quantify because of its small amount and an underestimated amount of phosphorus compared to the theoretical composition.
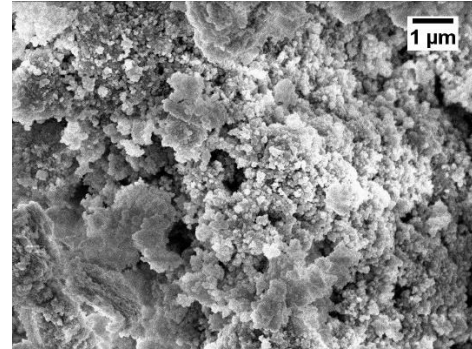

Fig. 1: SEM micrograph of SBCu1 (30.00 KX of magnification)

B. FTIR analysis

As seen in the FTIR spectra (reported in Fig. 2), in case of B-doped glasses, the presence of new peaks were observed: a large peak between 1200 cm^{-1} and 1600 cm^{-1} and two smaller peaks at 942 cm^{-1} and at 650 cm^{-1}, that can be attributed to B–O bond stretching vibrations of triangular [BO_3] elementary units [32], [33], B–O bond stretching vibrations of tetrahedral [BO_4] units [34] and borosiloxane bonds [35], respectively.

Thus, FTIR analysis confirmed the presence of boron ions in the glass matrix.
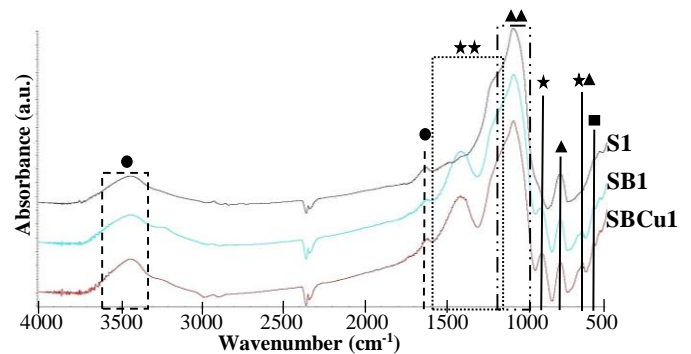
▲▲ Si-O-Si asymmetric stretching   ★▲ Borosiloxane bond vibration
▲ Si-O-Si symmetric stretching   ● Silanol group vibration
★★ B-O stretching of [BO_3]   ■ O-P-O bending vibration
★ B-O stretching of [BO_4]

Fig. 2: FTIR spectra of S1, SB1 and SBCu1 glasses

The typical peaks of the silicate network were clearly seen, in particular the shoulder between 1000 and 1200 cm^{-1} and the peak at 800 cm^{-1}, that are characteristic of Si-O-Si asymmetric [36], [37] and symmetric stretching vibration [36], [38], respectively.

The peak around 600 cm^{-1} is related to harmonics of P-O-P bending vibrations [18], [39].

It was not possible to distinguish vibrations that can be assigned to Cu–O bond, because they are revealed at wavenumbers lower than 400 cm^{-1} [40].

The broad band between 3600 and 3375 cm^{-1} and the peak at 1653 cm^{-1} are referred to the SiO-H stretching of surface silanols hydrogen-bonded to molecular water (SiO-H$\cdots$H$_2$O) and show the hygroscopic nature of these glasses [41]–[44].

C. X-ray diffraction characterization

The XRD patterns (Fig. 3) show the typical amorphous broad halo between 15° and 35°, one sharp peak around 32° and two smaller peaks at 26° and 40°, that can be attributed to a calcium silicate Ca$_2$SiO$_4$ (code 00-033-0303).
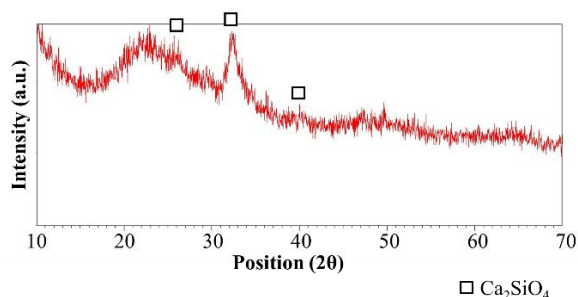

Fig. 3: XRD spectrum of SBCu2 glass

D. BET measurements

As reported in Table II, the surface area of the glasses prepared by synthesis 1 is bigger and the area values decreased with the addition of the doping elements. The B and Cu co-doped glass (SBCu1 and SBCu2) nanoparticles have the smallest areas, compared to the other glass compositions.

TABLE II
BET SURFACE AREA MEASURED

Surface area (m²/g)		
Glass	Synthesis 1	Synthesis 2
S	244	193
SB	132	69
SBCu	67	55

E. In vitro acellular bioactivity test

The bioactivity of the synthesized glasses is confirmed by XRD analysis: after immersion in SBF, XRD patterns show new peaks, that can be ascribed to HA (00-001-1008), as shown in Fig. 4 (SBCu2 glass as example).
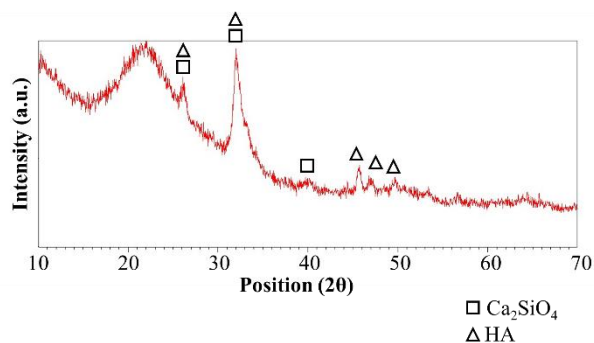

Fig. 4: XRD spectrum of SBCu2 after 14 days of immersion in SBF

Plotting the EDS results in terms of variations in P and Ca concentration versus immersion time, it is possible to observe that the amount of phosphorous and calcium on the surface of the synthesized glasses increased during soaking time and the Ca/P atomic ratios were similar to the ratio value for stoichiometric HA (1.67), in particular in case of the glass compositions containing both boron and copper. Remarkable pH variations versus soaking time and between the different synthesized glasses were not observed and the pH remained in the range 7.34–7.56, showing a slight increase in its value by increasing soaking, in agreement with literature results [45], [46].

V. CONCLUSION

Sol-gel bioactive glasses doped with copper and boron have been successfully synthesized by modifying the Stöber method.

The chemical and physical characterization showed that the synthesized glass nanoparticles are almost spherical and bioactive, and they present a certain degree of aggregation. Any significant difference was observed between the two different used syntheses and among the different investigated compositions in terms of bioactivity. In order to avoid particle aggregation, the optimisation of synthesis processes is in progress.

REFERENCES

[1] K. Zheng and A. R. Boccaccini, "Sol-gel processing of bioactive glass nanoparticles: A review," *Adv. Colloid Interface Sci.*, vol. 249, pp. 363–373, 2017.

[2] M. Mačković *et al.*, "Bioactive glass (type 45S5) nanoparticles: in vitro reactivity on nanoscale and biocompatibility," *J. Nanoparticle Res.*, vol. 14, pp. 1-22, 2012.

[3] A. M. Deliormanlı and M. Yıldırım, "Sol-gel synthesis of 13-93 bioactive glass powders containing therapeutic agents," *J. Aust. Ceram. Soc.*, vol. 52, pp. 9–19, 2016.

[4] V. Miguez-Pacheco, D. De Ligny, J. Schmidt, R. Detsch, and A. R. Boccaccini, "Development and characterization of niobium-releasing silicate bioactive glasses for tissue engineering applications," *J. Eur. Ceram. Soc.*, vol. 38, pp. 871–876, 2018.

[5] R. L. Ciceo, D. Trandafir, T. Radu, O. Ponta, and V. Simon, "Synthesis, characterisation and in vitro evaluation of sol–gel derived SiO2–P2O5–CaO–B2O3 bioactive system," *Ceram. Int.*, vol. 40, pp. 9517–9524, 2014.

[6] S. Romeis *et al.*, "Top-down processing of submicron 45S5 Bioglass ® for enhanced in vitro bioactivity and biocompatibility," *Procedia Eng.*, vol. 102, pp. 534–541, 2015.

[7] A. López-Noriega *et al.*, "Ordered Mesoporous Bioactive Glasses for Bone Tissue Regeneration," *Chem. Mater.*, vol. 18, pp. 3137–3144, 2006.

[8] X. Wang *et al.*, "Biocomposites of copper-containing mesoporous bioactive glass and nanofibrillated cellulose: Biocompatibility and angiogenic promotion in chronic wound healing application," *Acta Biomater.*, vol. 46, pp. 286–298, 2016.

[9] C. Wu *et al.*, "Copper-containing mesoporous bioactive glass scaffolds with multifunctional properties of angiogenesis capacity, osteostimulation and antibacterial activity," *Biomaterials*, vol. 34, pp. 422–433, 2013.

[10] P. Balasubramanian, T. Büttner, V. M. Pacheco, and A. R. Boccaccini, "Boron-containing bioactive glasses in bone and soft tissue engineering," *J. Eur. Ceram. Soc.*, vol. 38, pp. 855–869, 2018.

[11] F. Lv *et al.*, "A conducive bioceramic / polymer composite biomaterial for diabetic wound healing," *Acta Biomater.*, vol. 60, pp. 128–143, 2017.

[12] J. S. Fernandes, P. Gentile, R. A. Pires, R. L. Reis, and P. V Hatton, "Multifunctional bioactive glass and glass-ceramic biomaterials with antibacterial properties for repair and regeneration of bone tissue," *Acta Biomater.*, vol. 59, pp. 2–11, 2017.

[13] S. Kaya, M. Cresswell, and A. R. Boccaccini, "Mesoporous silica-based bioactive glasses for antibiotic-free antibacterial applications," *Mater.*

Sci. Eng. C, vol. 83, pp. 99–107, 2018.

[14] Y. Goh *et al.*, "In-vitro characterization of antibacterial bioactive glass containing ceria," *Ceram. Int.*, vol. 40, pp. 729–737, 2014.

[15] C. Wanpeng and L. L. Hench, "Bioactive Materials," *Ceram. Int.*, vol. 22, pp. 493–507, 1996.

[16] J. Bejarano, P. Caviedes, and H. Palza, "Sol–gel synthesis and in vitro bioactivity of copper and zinc-doped silicate bioactive glasses and glass-ceramics," *Biomed. Mater.*, vol. 10, pp. 1–13, 2015.

[17] A. Bari *et al.*, "Copper-containing mesoporous bioactive glass nanoparticles as multifunctional agent for bone regeneration," *Acta Biomater.*, vol. 55, pp. 493–504, 2017.

[18] H. Yin *et al.*, "Fabrication and characterization of strontium-doped borate-based bioactive glass scaffolds for bone tissue engineering," *J. Alloys Compd.*, vol. 743, pp. 564–569, 2018.

[19] J. Li *et al.*, "Preparation of copper-containing bioactive glass/eggshell membrane nanocomposites for improving angiogenesis, antibacterial activity and wound healing," *Acta Biomater.*, vol. 36, pp. 254–266, 2016.

[20] Y. Lin, W. Xiao, B. Sonny Bal, and M. N. Rahaman, "Effect of copper-doped silicate 13–93 bioactive glass scaffolds on the response of MC3T3-E1 cells in vitro and on bone regeneration and angiogenesis in rat calvarial defects in vivo," *Mater. Sci. Eng. C*, vol. 67, pp. 440–452, 2016.

[21] S. Zhao *et al.*, "Wound dressings composed of copper-doped borate bioactive glass micro fibers stimulate angiogenesis and heal full-thickness skin defects in a rodent model," *Biomaterials*, vol. 53, pp. 379-391, 2015.

[22] C. Gérard, L. Bordeleau, J. Barralet, and C. J. Doillon, "The stimulation of angiogenesis and collagen deposition by copper," *Biomaterials*, vol. 31, pp. 824–831, 2010.

[23] E. Kulczycki *et al.*, "Stimulation of Methanotroph Activity by Cu-Substituted Borosilicate Glass Stimulation of Methanotroph Activity by Cu-Substituted," *Geomicrobiol. J.*, vol. 28, pp. 1–10, 2011.

[24] H. Wang *et al.*, "Influence of Cu doping in borosilicate bioactive glass and the properties of its derived scaffolds," *Mater. Sci. Eng. C*, vol. 58, pp. 194–203, 2016.

[25] E. Meechoowas, M. Müller, C. Rüssel, "Redox relaxation in a sodium borosilicate glass doped with copper and arsenic, antimony, or tin," *J. Non. Cryst. Solids*, vol. 356, pp. 2528–2533, 2010.

[26] K. Schuhladen, X. Wang, L. Hupa, and A. R. Boccaccini, "Dissolution of borate and borosilicate bioactive glasses and the influence of ion (Zn, Cu) doping in different solutions," *J. Non. Cryst. Solids*, vol. 502, pp. 22–34, 2018.

[27] S. Shailajha, K. Geetha, P. Vasantharani, and S. P. S. Abdul, "Effects of copper on the preparation and characterization of Na–Ca–P borate glasses," *Spectrochim. Acta Part A Mol. Biomol. Spectrosc.*, vol. 138, pp. 846–856, 2015.

[28] K. H. Obayes, H. Wagiran, R. Hussin, and M. A. Saeed, "A new strontium/copper co-doped lithium borate glass composition with improved dosimetric features," *J. Lumin.*, vol. 176, pp. 202–211, 2016.

[29] Z. Y. Yao *et al.*, "Structure and mechanical properties of copper–lead and copper–zinc borate glasses," *J. Non. Cryst. Solids*, vol. 435, pp. 55–68, 2016.

[30] T. Kokubo and H. Takadama, "How useful is SBF in predicting in vivo bone bioactivity?," *Biomaterials*, vol. 27, pp. 2907–2915, 2006.

[31] M. Magallanes-Perdomo, S. Meille, J. Chenal, E. Pacard, and J. Chevalier, "Bioactivity modulation of Bioglass ® powder by thermal treatment," *J. Eur. Ceram. Soc.*, vol. 32, pp. 2765–2775, 2012.

[32] I. Kashif and A. Ratep, "Role of copper metal or oxide on physical properties of lithium borate glass," *J. Mol. Struct.*, vol. 1102, pp. 1–5, 2015.

[33] H. Doweidar, G. El-Damrawi, and M. Al-Zaibani, "Distribution of species in Na2O–CaO–B2O3 glasses as probed by FTIR," *Vib. Spectrosc.*, vol. 68, pp. 91–95, 2013.

[34] E. E. Horopanitis *et al.*, "Identification of the presence of crystalline phase in lithiated boron oxide ionic glass conductors," *Mater. Sci. Eng. B*, vol. 165, pp. 156–159, 2009.

[35] S. Grandi *et al.*, "SiO2-B2O3 xerogels: The problem of boron leaching," *J. Non. Cryst. Solids*, vol. 358, pp. 1631–1637, 2012.

[36] A. A. El-Rashidy *et al.*, "Preparation and in vitro characterization of silver-doped bioactive glass nanoparticles fabricated using a sol-gel process and modified Stöber method," *J. Non. Cryst. Solids*, vol. 483, pp. 26–36, 2018.

[37] A. M. El-Kady, A. F. Ali, R. A. Rizk, and M. M. Ahmed, "Synthesis, characterization and microbiological response of silver doped bioactive glass nanoparticles," *Ceram. Int.*, vol. 38, pp. 177–188, 2012.

[38] S. Zhao, Y. Li, and D. Li, "Synthesis and in vitro bioactivity of CaO–SiO2–P2O5 mesoporous microspheres," *Microporous Mesoporous Mater.*, vol. 135, pp. 67–73, 2010.

[39] Y. Goh, A. Z. Alshemary, M. Akram, M. R. A. Kadir, and R. Hussain, "In vitro study of nano-sized zinc doped bioactive glass," *Mater. Chem. Phys.*, vol. 137, pp. 1031–1038, 2013.

[40] V. Giannoulatou *et al.*, "Magnesium calcium silicate bioactive glass doped with copper ions," *J. Non. Cryst. Solids*, vol. 500, pp. 98–109, 2018.

[41] H. E. Çamurlu, E. Akarsu, O. Arslan, and S. Mathur, "Nanocomposite glass coatings containing hexagonal boron nitride nanoparticles," *Ceram. Int.*, vol. 42, pp. 8856–8862, 2016.

[42] T. S. Perova, M. Nolan-Jonas, J. McGilp, H. S. Gamble, "Borosilicate glass nanolayer as a spin-on dopant source: FTIR and spectroscopic ellipsometry investigations," *J. Mater. Sci. Mater. Electron.*, vol. 27, pp. 6292–6304, 2016.

[43] R. G. Furlan *et al.*, "Preparation and characterization of boron-based bioglass by sol−gel process," *J. Sol-Gel Sci. Technol.*, pp. 181–191, 2018.

[44] R. Koohkan, T. Hooshmand, M. Tahriri, and D. Mohebbi-Kalhori, "Synthesis, characterization and in vitro bioactivity of mesoporous copper silicate bioactive glasses," *Ceram. Int.*, vol. 44, pp. 2390–2399, 2018.

[45] M. Mozafari, F. Moztarzadeh, and M. Tahriri, "Investigation of the physico-chemical reactivity of a mesoporous bioactive SiO2–CaO–P2O5 glass in simulated body fluid," *J. Non. Cryst. Solids*, vol. 356, pp. 1470–1478, 2010.

[46] S. M. Ahmadi, A. Behnamghader, and A. Asefnejaad, "Sol-gel synthesis, characterization and in vitro evaluation of SiO2−CaO−P2O5 Bioactive glass nanoparticles with various CaO/P2O5 ratios," *Dig. J. Nanomater. Biostructures*, vol. 12, pp. 847–860, 2017.

Neuroimaging biomarkers toward an optimized and personalized AOT

M. Ottaviani[1], P. Romano[1], S. Pournajaf[1], M. Goffredo[1], F. Marinozzi[2], F. Bini[2], M. Franceschini[1,3], and F. Infarinato[1]

[1]*IRCCS San Raffaele Pisana, Rome (Italy)*
[2]*Department of Mechanical and Aerospace Engineering, "Sapienza" University of Rome, Rome (Italy)*
[3] *San Raffaele University, Rome (Italy)*

Abstract— **Stroke is the second leading cause of death in industrialized countries. In recent years, some scientific studies have focused on the search for new non-invasive strategies which contribute to the functional recovery of stroke patients. Action Observation Therapy (AOT) is one of them. This rehabilitative approach is aimed at facilitating neural plasticity toward the reconstruction of impaired motor functions through the stimulation of motor cortex via visual stimuli containing actions. This study was carried out fitting into this research context, proposing an analysis of the electroencephalographic signals acquired during an action observation protocol. The aim of the work is to identify, through the study of the desynchronization and synchronization index (ERD/ERS), the categories of gestures that cause greater cortical activation to optimize intervention based on AOT protocol. The results showed that the behavior of motor cortex during the visualization of motor gestures is statistically different respect to control videos (not human actions) with a p-value < 0.03 for mu band (8-13 Hz) and p-value < 0.0001 for beta band (15-20 Hz). Another key result based on time course of signals power showed that the control stimuli cause less desynchronization in the motor area compared to visual motor stimuli.**

Keywords—**AOT, EEG, Rehabilitation, Stroke**

I. INTRODUCTION

Stroke is a major cause of death and a major cause of long-term disability that interferes with the good quality of life in western countries [1]. From the point of view of functional improvement, rehabilitation interventions are the main component of the patient's care pathway [2], [3], [4].

In recent years, in order to improve the recovery of Activity of Daily Living (ADL), new non-invasive strategies for rehabilitation treatment have been proposed as an alternative to traditional physical and occupational therapies [5], [6].

Interest in the use of Action Observation Therapy (AOT) is increased as a new method of rehabilitation of patients affected by stroke [7]. This approach is based on the functions of the Mirror Neuron System (MNS; [8], [9]). Extensive research over the past 20 years on human MNS (hMNS) has shown its importance not only in recognizing action but also in motor intentions and other social cognitive functions [10], [11]. Finally, since mirror neurons are also recruited in case of brain damage, MNS can provide satisfactory rehabilitation results [12], [13].

AOT takes advantage of the mirror system properties to restore brain function despite patient impairment [14] and appears to be a good example of translational medicine, from basic neuroscience to rehabilitation.

Both active movement and the observation of an action performed by another individual cause the desynchronization of mu (8-13 Hz) and beta (15-20 Hz) rhythms in electroencephalographic signals (EEG) localized in the sensorimotor areas [15], [16]. However, to date, specific guidelines on rehabilitation protocols based on AOT are limited; recently, Zhu et al. [17] highlighted the greater activation in the primary motor cortex induced by observing action movements and execution in the meantime with a MEG study and concluded underlying necessity to find the most appropriate strategies and approaches to enhance the stroke patients' performance. It is important to define a correct stimulation protocol with suitable visual stimuli in terms of kind of actions. Activity variations in the primary motor cortex are analyzed in this paper to define effects and changes on EEG oscillatory activity in healthy subjects determined by different motor actions on video. This work aims to build solid basis for future AOT guidelines that will lead to provide optimized protocols addressed to hemi paretic post-stroke patients rehabilitation.

II. METHODS

A. Subjects

Eleven subjects (7 male and 4 female, average age 61.64±3.68) with no neurological disorder were enrolled for a single-day EEG recording protocol. Subjects were asked to carefully observe the actions acted out by people in video clips.

B. Stimulation protocol

The stimulation protocol was carried out ensuring the synchronization between the two devices, one for the signals acquisition and one for videos administration, administration protocol was realized using a Psychopy 2.0 code (Open Science Tools Ltd). Protocol was divided into two steps: 6 minutes resting state EEG recording with open (3 minutes) and closed eyes (3 minutes) and 15 min AOT simulation that includes 40 videos (eight videos for each categories) repeated three times randomly, for a total of 120 stimuli.

Visual stimuli were recorded considering a neutral background, uniform ambient light and keeping the actors of the videos in focus. The proposed videos could belong to one of the following five categories:

1) No Human Control Actions (NHCA), control videos not containing humans but only natural landscapes in movement.
2) Human Control Actions (HCA), control videos containing gestures not finalized to a specific action (i.e. arm slow movements with fixed direction and without an interaction with objects).
3) Self Care Actions (SCA), a video of body care-oriented gestures.

4) External Actions (EA), video of gestures oriented to the use of everyday objects.

5) Feeding Actions (FA), gestures aimed at the action of eating.

The stimulation protocol included a first part (evt1) to allow synchronization of the motor and premotor areas. The temporal length of the stimulus depends on a variable called jitter randomly extracted from a uniform distribution of values between 3 and 4 s. The second phase (evt2) of 500 ms containing a fixation cross to increase the attention to the center of the screen. Finally, the video stimulus (evt3) of about 4 s was shown (Fig.1).

In random moments, an attention game (evt4) was proposed to increase attention and avoid the phenomena of habituation. The random stimulus temporal length relied on the response time of patient.

Finally, each Human Action (HA, i.e. categories 3, 4, 5) contained two subparts called respectively Reaching (time interval during which the actor reaches the object) and Grasping (time interval during which the actor finalizes utilization of kept in hand object). The duration of them depended on videos and different trigger events were chosen to set the phases. Generally, Reaching and Grasping segments lasted about 500 ms after video starting and about 2.5 s after video starting respectively.

Fig.1 Trials configuration: Intertrial (black screen, evt1, about 3-4 s according to jitter variable), white cross (evt2, 500 ms), video (stimulus, evt3, 4 s)

C. EEG recording and pre-processing

EEG registration was performed using a 128-channel Geodesic EGI system. The recorded signals were subsequently imported into MATLAB environment (Mathworks, Natick, MA, USA; v. 2019a) and underwent a pre-processing protocol through the EEGLAB tools composed of:
- Band-pass filtering (0.5 - 45 Hz) with a FIR filter based on Hamming window
- Removal of bad channels (with critically compromised by artifacts signals or distorted signals because of bad contact with the scalp)
- Independent Component Analysis (ICA)
- Average Re-reference.

After this step, an in-house tool developed in MATLAB (i) filtered them with respect of 2 bands of interest (mu and beta), (ii) segmented signals according to events trigger obtained with the use of Psychopy code and (iii) averaged them spatially by parameterizing the left and right motor areas.

Finally, the event-related desynchronization and synchronization of EEG rhythms for each category was calculated. The ERD/ERS computing procedure followed two approaches: Calculation of temporal power and Calculation of energy spectral density.

In the first case the classical theory was applied [18], with the calculation of the averaged temporal power waveform between all trials in each category compared to pre-event reference, normalized on the power of the reference, as evinced by the following formula:

$$P_{ref} = \frac{1}{|T_{ref}|} \sum_{t \in T_{Ref}} |P|$$

$$ERD[t] := \frac{E[P_t] - E[P_{ref}]}{E[P_{ref}]}, t \in T$$

P is the instantaneous power, P_{ref} is the signal power of evt1 in the selected time window T_{ref}, P_t represents the power of entire phase evt3 and E[.] refers to expected value. Its expected value expresses an average of the signal power map at a time lag and the two frequency bands of interest (mu and beta). The choice of the best pre-event reference was made with a floating window of 1.5 seconds length. The window, initially placed at the beginning of the segment preceding the stimulus, moves along the phase evt1 and identifies the temporal region with the least variation (evaluated by derivate calculation) in signal power.

The other case is aimed at considering the normalized ratio between areas under the Power Spectral Density (PSD) of the stimulus and pre-stimulus segments. In this case videos belonging to categories 3, 4, 5 have been further subdivided into the two before said segments of Grasping and Reaching actions.

D. Statistical Analysis

After checking the normality of data with Kolmogorov-Smirnov (alpha equal to 0.05), 1-way ANOVA test (alpha equal to 0.05) was performed. This test was used to evaluate the statistically significant differences of normalized power spectral density areas of EEG signals segmented in trials depending on NHCA, HCA and HA categories, the latter one divided in Reaching and Grasping. The evaluation occurred for both mu and beta bands in the primary motor cortex. Subsequently, post-hoc analysis was performed using Bonferroni test (alpha equal to 0.05) to realize paired data comparisons in order to identify statistic differences between categories and which one causes the major neuronal enrollment.

III. RESULTS

The ERD/ERS analysis provided two kinds of results, one for the signal power time-series, as shown in Fig.2, and one for the power spectral density area, as shown in Fig.3, both scaled for intertrial behavior. In the first case the average across subjects with shaded standard deviation ERD/ERS time waveform are shown separately in left and right motor cortex areas: the graphic illustrates the pattern of ERD/ERS along evt3 in both mu and beta bands for each category during NHCA, HCA and HA videos.

In the second case EEG signals recorded by channels above left (C3 and neighbors) and right (C4 and neighbors) motor cortex areas were averaged to obtain a single area, since no evident differences between the two hemispheric sides were highlighted.
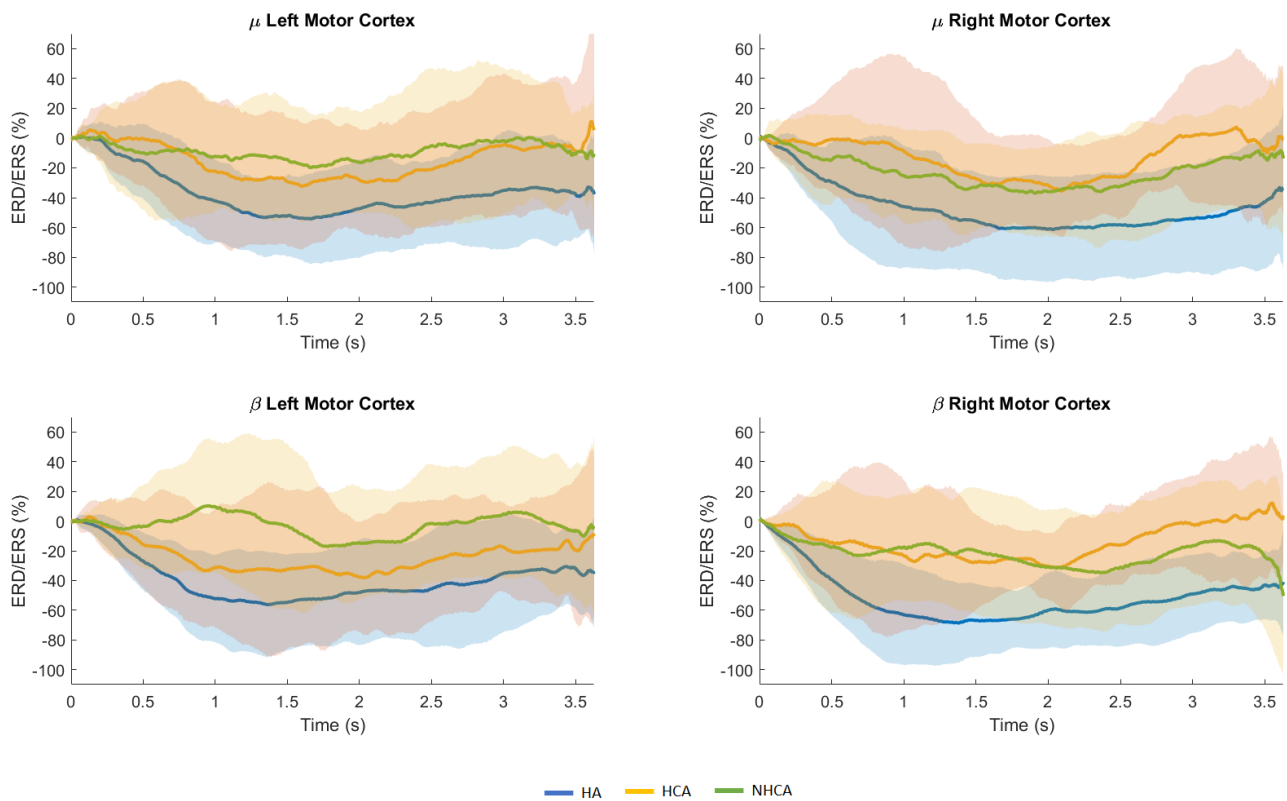
Fig.2 Average and standard deviation across subjects of ERD/ERS time waveform during NHCA (green line) , HCA (orange line) and HA (blue line) videos visualization. Waveforms start from 300 ms after the onset stimulus and finish at the end of video (evt3). ERD/ERS equal to zero represents the reference with respect to which the curves are scaled.

The statistical tests were performed for the power spectral density area values in mu and beta bands, to detect a comparison between biomarkers obtained from averaged trials collected into categories. As shown in Fig.3, ANOVA test returned a p-value < 0.0004 for mu band and a p-value < 0.000001 for beta band. The multiple comparison showed statistically significant differences between the ERD/ERS of the three macro categories. Particularly, there were clear differences between HCA, HA (both Reaching and Grasping) and NHCA. Bonferroni post-hoc test confirmed these differences in mu band (p < 0.03) and in beta band (p < 0.0001).

IV. DISCUSSION

AOT is a new neuro-rehabilitation approach capable of evoking a brain response by observing videos of daily life gestures performed by a human actor. This technique aims to promote the motor cortex through the mirror neuron system activation like previously discussed.
The main goal of the work concerned the validation and discrimination of visual stimuli able to elicit the greater neuronal recruitment of the mirror system and the identification of indexes to be used to predict rehabilitation outcomes. For this purpose, EEG recordings on healthy subjects were performed during the observation of short videos randomly administered. Videos were recorded excluding environmental noises and disturbances, and subdivided in groups (NHCA, HCA and HA) depending on the type of actions and the presence/absence of human subjects and

objects. Specific biomarkers associated to event-related synchronization or desynchronization (ERD/ERS) patterns of EEG rhythms were calculated to validate video categories who are suitable to AOT and select which type of visual stimuli will be most effective in inducing motor excitability.
This analysis requested the implementation of an in-house algorithm for the classification of cortical responses, from 128-channel EEG recordings. The EEG signals were filtered, artifact-removed, segmented into categories.
Mu and beta rhythms suppression on the motor cortex are considered as neuro-markers of MNS activation [19], [20]: event-related modulation of signals temporal power and power spectral density compared to pre-event window was evaluated in the two mu and beta bands of interest for each videos category.
The averaged temporal power waveforms (ERD/ERS trend along video observation) make it possible to notice how different stimuli administered imply different neuronal patterns and behavior of primary motor cortex. In particular, both mu and beta oscillatory rhythms reflect a greater suppression during arm moving observation in respect with not finalized actions or environment in movement; these results were found both in the right and in the left hemispheres. We can notice that there aren't substantial and remarkable elements to distinguish the attitude of neuronal activity between NHCA and HCA categories, whereas the patterns of waveform inherent HA is reproducible for all cases: they show the stronger suppression around 1.5 s after the beginning of graphs and then a rising versus a slight re-
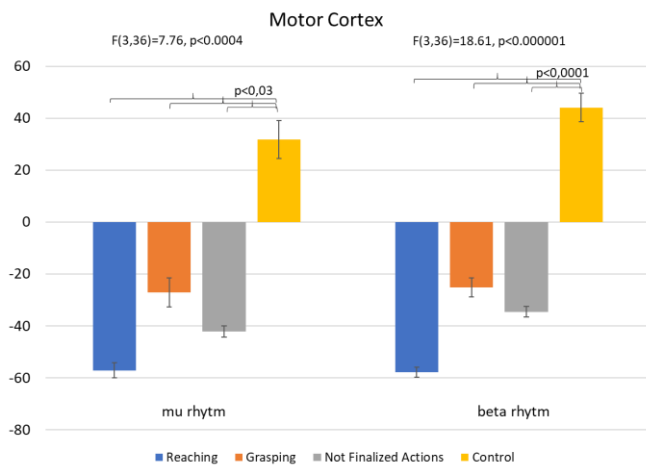
Fig.3 Multiple comparison between normalized power spectral density areas of EEG signals segmented in trials depending on visual stimuli.

synchronization. This examination of different suppression characteristics for not action visual stimuli denotes the specific involvement of the mirror system activity in our analysis.

Subsequently HA were further subdivided into two segments, namely Reaching and Grasping, referring to the phase of the action shown in the visual stimuli and ERD/ERS in the frequency domain was evaluated for four categories, referring to previous black screen intertrial. The obtained figure 3 could suggest that it is possible to discriminate the landscape images from a human gesture, and to recognize the phases that compose the movement using EEG markers. In particular, the finalized and not finalized gestures enroll a neuronal rhythms desynchronization that is not found during not human control videos observation. These results confirmed that the NHCA provide the largest synchronization in both mu and beta rhythms and this reflects in absence of activation of motor cortex circuit by MNS. This situation respects precedent findings: NHCA don't require the execution of movements by an individual and therefore arouse less motor interest from the observer. Furthermore, although data doesn't return a statistically significant difference between Reaching, Grasping and HCA, the histogram reveals that Reaching actions category enhances the neuronal response of the primary motor cortex.

The results showed that AOT administered with these recorded videos is an effective method to easily enroll the mirror neuron system and suggest the possibility of applying this protocol to post-stroke patients, generating an effect on the clinical management of rehabilitation therapies. These findings will lead to the selection of an optimal AOT exercise protocol.

Further studies will be executed to make a certain assessment of the progress of desynchronization during observation of different type of gestures, with the aim to define a more efficient therapeutic protocol for the upper limb rehabilitation.

REFERENCES

[1] Gosman-Hedström,G.,Claesson, L.,Blomstrand, C.,"Consequences of severity at stroke onset for health-related quality of life (HRQL) and informal care: a 1-year follow-up in elderly stroke survivors.",*Archives of gerontology and geriatrics*, 2008, 47.1: 79-91.

[2] Pollock, A., Baer, G., Campbell, P., Choo, P. L., Forster, A., Morris, J., ... & Langhorne, P. "Physical rehabilitation approaches for the recovery of function and mobility following stroke.", *Cochrane Database of Systematic Reviews*, 2014, 4.

[3] Iosa, M., Bini, F., Marinozzi, F., Fusco, A., Morone, G., Koch, G., Cinnera, A. M., Bonnì, S., Paolucci, S. "Stability and Harmony of Gait in Patients with Subacute Stroke", *J. Med. Biol. Eng.*, 2016, vol. 36, pp. 635-643.

[4] Iosa, M., Morone, G., Bini, F., Fusco, A., Paolucci, S., Marinozzi, F. "The connection between anthropometry and gait harmony unveiled through the lens of the golden ratio", *Neuroscience Letters*, 2016, vol. 612, pp. 138-144.

[5] Zeng, W., Guo, Y., Wu, G., Liu, X., & Fang, Q., "Mirror therapy for motor function of the upper extremity in patients with stroke: a meta-analysis.", *Journal of rehabilitation medicine*, 2018, 50.1: 8-15.

[6] Laver, K. E., Lange, B., George, S., Deutsch, J. E., Saposnik, G., & Crotty, M., "Virtual reality for stroke rehabilitation.", *Cochrane database of systematic reviews*, 2017, 11.

[7] Peng, T. H., Zhu, J. D., Chen, C. C., Tai, R. Y., Lee, C. Y., & Hsieh, Y. W., "Action observation therapy for improving arm function, walking ability, and daily activity performance after stroke: a systematic review and meta-analysis.", *Clinical rehabilitation*, 2019, Vol. 33(8) pp. 1277–1285.

[8] Bonini, L., & Ferrari, P. F., "Evolution of mirror systems: a simple mechanism for complex cognitive functions.", *Annals of the New York Academy of Sciences*, 2011, 1225.1: 166.

[9] Fogassi, L., Ferrari, P. F., Gesierich, B., Rozzi, S., Chersi, F., &Rizzolatti, G., "Parietal lobe: from action organization to intention understanding." *Science*, 2005, 308.5722: 662-667.

[10] Rizzolatti, G., Cattaneo, L., Fabbri-Destro, M., &Rozzi, S., "Cortical mechanisms underlying the organization of goal-directed actions and mirror neuron-based action understanding."*Physiological reviews*, 2014, 94.2: 655-706.

[11] Bonini, L., Ferrari, P. F., &Fogassi, L. "Neurophysiological bases underlying the organization of intentional actions and the understanding of others' intention." *Consciousness and cognition*, 2013, 22.3: 1095-1104.

[12] Franceschini, M., Agosti, M., Cantagallo, A., Sale, P., Mancuso, M., & Buccino, G., "Mirror neurons: action observation treatment as a tool in stroke rehabilitation.", *Eur J Phys Rehabil Med*, 2010, 46.4: 517-523.

[13] Buccino, G., "Action observation treatment: a novel tool in neurorehabilitation.", *Philosophical Transactions of the Royal Society B: Biological Sciences*, 2014, 369.1644: 20130185.

[14] Tani, M., Ono, Y., Matsubara, M., Ohmatsu, S., Yukawa, Y., Kohno, M., & Tominaga, T., "Action observation facilitates motor cortical activity in patients with stroke and hemiplegia.", *Neuroscience research*, 2018, 133: 7-14.

[15] Cochin, S., Barthelemy, C., Roux, S., & Martineau, J., "Observation and execution of movement: similarities demonstrated by quantified electroencephalography.", *European Journal of Neuroscience*, 1999, 11.5: 1839-1842.

[16] Lopez, S., Bini, F., Del Percio, C., Marinozzi, F., Celletti, C., Suppa, A., Staltari, E., Camerota, F., Babiloni, C. "Electroencephalographic Sensorimotor Rhythms are modulated in the Acute Phase Following Focal Vibration in Healthy Subjects", *Neuroscience*, 2017, vol. 352, pp. 236-248.

[17] Zhu, J. D., Cheng, C. H., Tseng, Y. J., Chou, C. C., Chen, C. C., Hsieh, Y. W., & Liao, Y. H., "Modulation of Motor Cortical Activities by Action Observation and Execution in Patients with Stroke: An MEG Study.", *Neural plasticity*, 2019, 2019.

[18] Pfurtscheller, G., & Da Silva, F. L.,"Event-related EEG/MEG synchronization and desynchronization: basic principles.",*Clinical neurophysiology*, 1999, 110.11: 1842-1857.

[19] Gros, I. T., Panasiti, M. S., & Chakrabarti, B.. The plasticity of the mirror system: How reward learning modulates cortical motor simulation of others. Neuropsychologia, 2015, 70, 255-262.

[20] Simon, S., & Mukamel, R.. Power modulation of electroencephalogram mu and beta frequency depends on perceived level of observed actions. Brain and behavior, 2016, 6(8), e00494.

Strategies to speed up the standardized bone plates mechanical testing for regulatory purposes

M. Terzini[1], G. Serino[1], A.T. Lugas[1], G. Dichio[1], P. Costa[2] and A.L. Audenino[1]

[1] Polito^{BIO}Med Lab, Department of Mechanical and Aerospace Engineering, Politecnico di Torino, Turin, Italy

[2] Intrauma S.p.A., Rivoli, Italy

Abstract— Bone plates for osteosynthesis are biomechanically and mechanically tested for safety and regulatory purposes. The test campaigns recommended by the standards have very high associated costs, as well as unreasonable times from the market point of view. In this work, a strategy is proposed to reduce the number of tests needed to identify the fatigue strength of osteosynthesis plates and to establish an application-specific performance level.

Keywords—Bone plate, Mechanical testing, ASTM F382, Finite Element Analysis

I. INTRODUCTION

IN silico testing of osteosynthesis medical devices, such as bone plates, is generally addressed by two main approaches: (1) the biomechanical testing, aimed at the device evaluation under physiological loading condition and described in several scientific articles, and (2) the mechanical testing, mainly conducted for regulatory purposes. Indeed, bone plates, as well as all medical devices, need to be mechanically evaluated prior to marketing and, with this aim, manufacturers apply test methods published as ASTM standards. In particular, ASTM F382 is the most recent and most used testing standard applicable for metallic bone plates [1]. This specification establishes consistent methods to define the geometric and performance characteristics of bone plates, but it does not claim to simulate physiological biomechanics for a specific anatomical region. As a matter of fact, ASTM standards do not define acceptable levels of performance as insufficient knowledge is, to date, available to predict the consequences of the osteosynthesis device use in individual patients for specific daily activities (Scope 1.2 in [1]). ASTM standards main goal in therefore to establish a reference test method which can be executed in each accredited laboratory, thus delivering objective results for direct predicate comparison. However, the complexity of clinical and biomechanical scenarios caused a huge variety of bone plates concepts to emerge (e.g. locking compression plates, dynamic compression plates, variable angle-locking compression plates) intended for different types of bones and also for specific bones in different anatomical regions. This broad framework doubtless complicates the definition of a "harmonized testing approach" [2]. In fact, the standard states that in cases when the structurally critical region of the bone plate lies in a non-uniform region, it may be impossible to fit this non-uniform region in the recommended test configuration and it may be therefore necessary to evaluate the plate bending properties using a different test method. Yet, no additional indications are given regarding what the "different test method" should be.

From a practical point of view, ASTM F382 suggests quasi-static and dynamic 4-Point-Bending tests to evaluate the bending stiffness, the bending structural stiffness, the bending strength and the cyclic bending fatigue performance of the bone plate. Carrying out a test campaign of this magnitude requires a huge financial outlay by the manufacturers, as well as a considerable use of time and equipment. From our experience we have estimated an overall test time by type of plate equal, at best, to about 180 hours without interruption. Most of this time is necessary for dynamic tests, for which the standard suggests a load frequency of 5 Hz and a number of cycles for "runout" of 1000000. The loading range to sweep is determined during quasi-static testing, and a logarithmic graph of the applied bending moment versus number of cycles to failure should be created (M-N diagram). To provide a complete picture of the regulatory process, it is finally useful to mention that: any deviation from the standard must be duly justified, which forces manufacturers to stick to the standard faithfully; each new osteosynthesis device testing result should be compared to an already marketed predicate device, suggesting that better performance would be summed up in "greater mechanical strength" instead of greater similarity to the physiological behaviour of the bone district to be repaired.

In this study a contoured distal femur plate was mechanically tested according to ASTM F382 and exploiting the testing strategy proposed in section A1.6.2.1, which states that bone plates that do not directly fit into the test setup can be attached to rigid extension segments. A complete static and dynamic test campaign was carried out to measure the static and the fatigue bending properties of the bone plate. Thanks to the Finite Element Analysis, well-established technique for the analysis of mechanical and biomechanical constructs [3]–[5], *in silico* models were implemented to (1) replicate the *in vitro* test in order to guide the choice of the load range in which to search for the "runout" load, (2) investigate the bone-plate construct in order to build up a rationale able to compare experimental results with plausible physiological loading conditions.

II. MATERIALS AND METHODS

A. Standardized mechanical testing of the bone plates

Quasi-static tests were performed in order to measure the bending stiffness and the bending strength of a Ti6Al4V distal femur plate using a 4-Point Bending test according to ASTM F382-17 Annex A1. The bone plate material tensile properties are $E = 120\ GPa$, $\sigma_y = 941.9\ MPa$ and $\sigma_{UTS} = 991.8\ MPa$. As previously stated, the tested bone plate does not have a sufficiently long section of symmetry, therefore, according to A1.6.2.1, rigid extension segments (material AISI 630,

W1.4542 – Heat Treatment H900) were used to effectively lengthen the bone plate so that the bone plate can be tested with the 4-Point Bending test method (Fig. 1). The testing set-up, schematized in Fig. 1, is mainly composed of:

- two loading rollers of equal diameter (10 mm) positioned so that at least two screw holes are located between them. Their distance, namely the centre span distance, is marked by the letter a, and it is equal to 83 mm.
- Four support rollers, located at equal distance away from the adjacent loading roller, namely, the loading span $h = 64.5 \; mm$.
- A bone plate rigidly fixed to two extensions through 9 screws.

The support rollers are positioned on holders designed to be constrained on the testing machine base (Instron E3000), while the loading rollers are rigidly connected to a spherical joint, able to equally distribute the applied load to the plate.
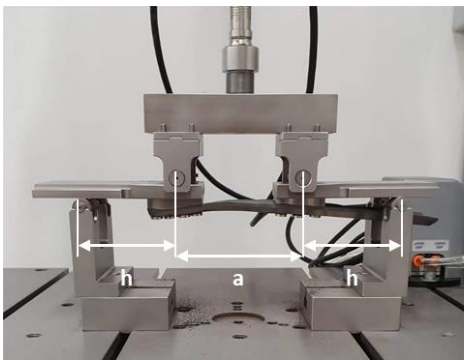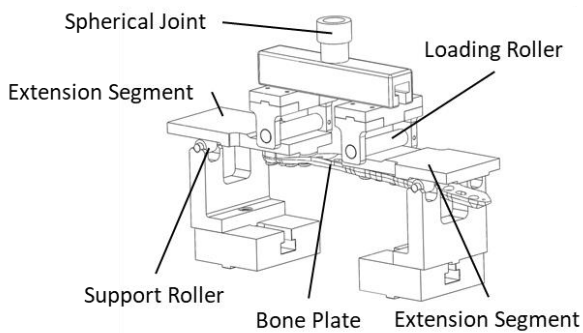
Fig. 1: (Top) 4-Point-Bending testing set-up and (Bottom) characterizing distances a (center span) and h (loading span)

Four plates were tested till failure at 5 mm/min, and from resulting load-displacement data the bending stiffness k and the bending strength were extracted. This latter was computed at the proof load, namely at the intersection point between the load-displacement curve and the 2% offset displacement line (Fig. 2), as in Eq. (1).

$$bending\ strength = \frac{Ph}{2} \qquad (1)$$

where P is the proof load and h is the loading span distance.

A 2% offset was used in place of the recommended 0.2% offset to determine the proof load because a 0.2% offset would not allow for enough displacement to identify a yield load.

Exploiting the same set-up, five more plates were tested dynamically to determine the plate fatigue life over a range of

maximum bending moment levels according to ASTM F382-17 Annex A2. Tests were performed in load control, and maximum load magnitudes were determine starting from the 75% of the bending strength and gradually reducing the load until identifying the load that led to the "runout". For each maximum load, the minimum of the sinusoidal waveform was computed as the 10% of the maximum load (i.e. adopting an R-ratio of 0.1 as recommended by the standard).
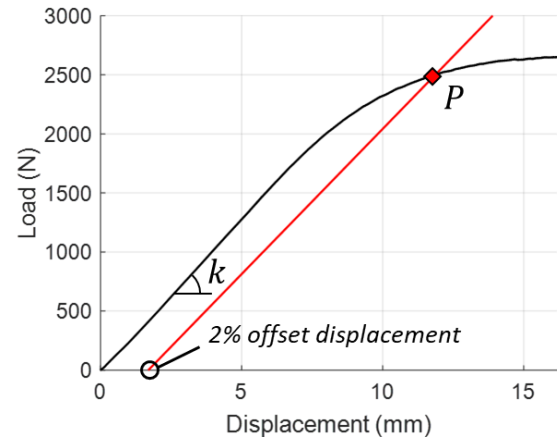

Fig. 2: Typical load-displacement curve with indication of the proof load P, the bending stiffness k and the 2% offset displacement computed ad $0.02 * a$.

Tests were performed at 5 Hz. Each test was ended when either a functional failure was attained, or the test reached 1000000 cycles. The "runout" situation was repeated on three different samples.

B. Finite Element Model of the mechanical testing

A Finite Element Model (FEM) of the bone plate has been implemented starting from the plate meshing (706476 Tet elements). The plate material was considered as ideal elastic-plastic. To simplify the FEM model the testing set-up described in the previous section has been replaced by adequate boundary conditions suitable for applying the desired moment to the plate. Indeed, two multi point constraints were generated on two node sets, selected in correspondence with the holes occupied by the first head screw (Fig. 3 (A)) and the first tail screw (Fig. 3 (B)).
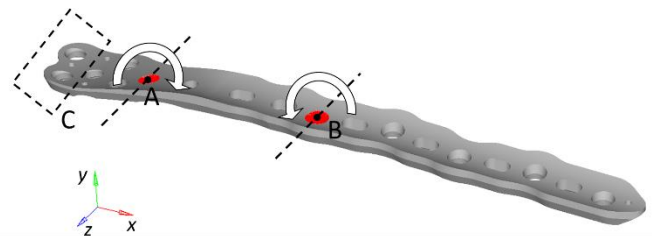

Fig. 3: Boundary conditions of the FE model.

The plate head extremity (Fig. 3 (C)) was fully fixed, and two bending moments of opposite direction were applied to nodes A and B. The bending moments M were computed from the experimental load L following Eq. (2).

$$M = \frac{Lh}{2} \qquad (2)$$

The maximum Von Mises stress (σ_{max}) was finally positioned on a constant-life fatigue diagram in order to predict the plate "runout" or rupture. In detail, assuming an R-ratio of

0.1 as recommended by the standard, the mean stress (σ_m) and the stress amplitude (σ_a) were computed from σ_{max} according to Eq. (3) and Eq. (4) respectively.

$$\sigma_m = \frac{\sigma_{max} + 0.1\,\sigma_{max}}{2} \qquad (3)$$

$$\sigma_a = \frac{\sigma_{max} - 0.1\,\sigma_{max}}{2} \qquad (4)$$

C. Finite Element Model of the biomechanical testing

Being not straightforward the comparison between the bending strength of the bone plate, resulting from the experimental 4-Point-Bending tests, and the level of performance needed for the specific biomechanical application, a FEM model of a bone-plate construct was implemented. Based on the work of Gervais et al [6], a standard Sawbones femur, distally fractured, was assembled with the bone plate and solicited with patient specific loads (Fig. 4). Bone plate was constrained to the bone through rigid links at the screw holes. It must be underlined that this choice represents a strong simplification, as it does not consider the preloading of the screws nor their structural contribution. However, this condition was considered the most critical for the bone plate, as it presupposes a direct load transfer through the bone plate. The plate material was considered as ideal elastic-plastic, while the bone was considered as linear elastic with $E = 20\ GPa$ for the healthy bone and $E = 1\ GPa$ for the fracture gap. The bone-plate construct was meshed with 936322 Tet elements, and the screws was modelled as rigids.
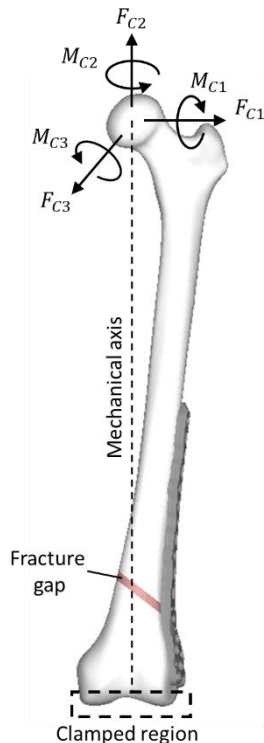

Fig. 4: Boundary conditions applied to the bone-plate FE model [6].

TABLE I
LOADS APPLIED TO THE BONE-PLATE CONSTRUCT [6]

F_{C1}	F_{C2}	F_{C3}	M_{C1}	M_{C2}	M_{C3}
7 N	-738 N	156 N	-85 Nm	8 Nm	45 Nm

Table I lists the loads applied in order to deduce the maximum Von Mises stress of the plate in physiological loading conditions.

III. RESULTS

A. Standardized mechanical testing of the bone plates

The four bone plates tested under quasi-static conditions exhibited plastic deformation, and there were no fractures during the tests. The obtained mean bending strength is equal to 78617.62 ± 3464.14 Nmm, while the mean proof load is equal to 2437.76 ± 107.42 N. Fig. 5 shows the M-N diagram extracted from the fatigue tests. Two out of three plates exhibited fracture initiating from one of the screw holes, while the others reached the "runout" with an applied bending moment equal to 29025 Nmm.
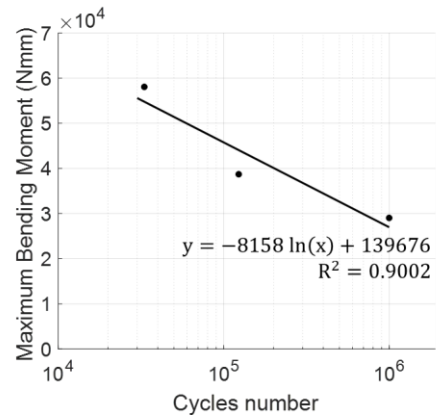

Fig. 5: M-N Diagram

B. Finite Element Model of the mechanical testing

Fig. 6 shows the Von Mises stress state of the plate resultant from a 29025 Nmm bending moment.
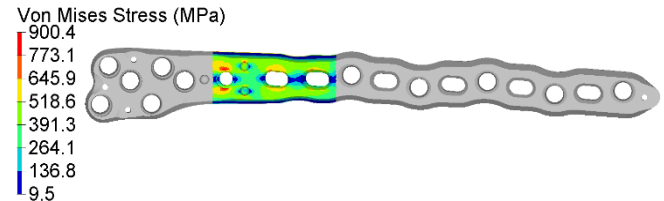

Fig. 6: Von Mises Stress distribution in the tested area resulting from a 29025 Nmm bending moment. The maximum value, equal to 900.4 MPa, is located on the experimentally fractured hole.

The maximum stress was located on a constant-life fatigue diagram (red dot in Fig. 7) where the horizontal axis represents the static loading while the vertical axis represents the alternate loading. The blue line delimits an area where no yielding is permitted and a life of at least 1000000 cycles is required. However, is it possible to work in the area delimited by the blue line and the dotted line, especially in cases where the local yielding is sufficiently minute and, therefore, the material may strain-strengthen causing the yielding to cease [7].

The constant-life fatigue diagram is based on an extremely conservative method [7]. Indeed, with respect to our experimental evidence (red dot – Fig. 7), the black dot in Fig. 7 locates the predicted "runout" at 25800 Nmm of maximum bending, thus determining a Factor of Safety (FoS) of 1.12.
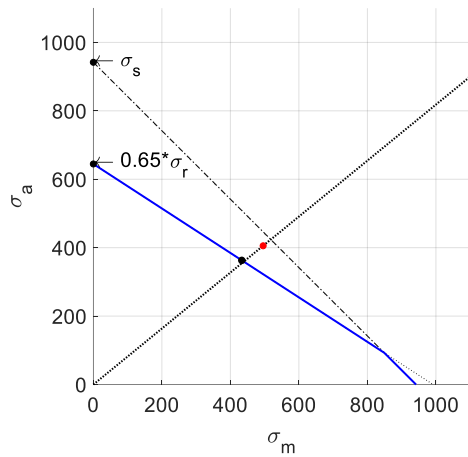
Fig. 7: Constant-life fatigue diagram for Ti6Al4V. The red dot represents the maximum Von Mises stress obtained at a 29025 Nmm bending moment. The black dot refers to the predicted 1000000 cycles fatigue limit. The $0.65\sigma_r$ point was defined from [7].

C. Finite Element Model of the biomechanical testing

The comparison between mechanical testing and biomechanical testing, experimentally arduous, it is allowed *in silico* by the analysis of the stress state in the two load conditions.
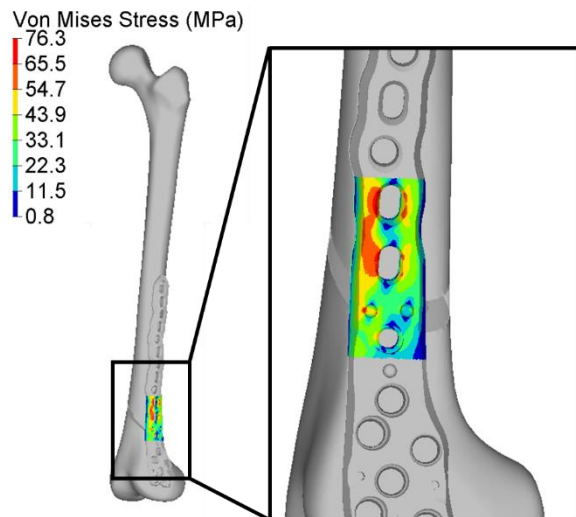

Fig. 8: Von Mises Stress distribution in the area of interest of the bone plate, under physiological load conditions.

A maximum value of 76.3 MPa is reached in the plate under physiological load conditions, suggesting that the plate being analyzed is sufficiently performing for the clinical application. Indeed, the "runout" bending moment caused a maximum Von Mises stress an order of magnitude higher than that experienced in the biomechanical configuration. However, it should be stress that the simulated loadings concern the condition of a patient in the healing phase who is already allowed to apply the entire load during the walk. Realistically, in a post-operative phase in which the bone callous is not yet in formation, the load allowed will be considerably less.

IV. CONCLUSION

In this work *in vitro* and *in silico* tests were performed on a bone plate pending certification. Although the standard

mentions the possible use of numerical models only to identify the most critical area to be tested, numerical models can be useful not only to select the loads around which to look for the "runout", but also to establish a level of performance needed for the specific biomechanical application. The critical issues related to the uncontrollable variables that the device will encounter in clinical use complicate the evaluation of what may happen *in vivo*. Nevertheless, one cannot ignore the knowledge of structural mechanics that can guide not only the design of the devices, but also their mechanical evaluation. Through FE models, the stress state of the metallic plate can be estimated under prescribed loading conditions (as an example, here we predicted the 1000000 cycles life of the distal femur plate with a FoS of 1.12), thus restricting the range of loads to be investigated by standardized mechanical testing. The consequent reduction of the times involved in the experimental tests, in any case essential, would have a substantial impact on the costs for the manufacturer. Moreover, an *in silico* replica of the bone-plate construct can identify a minimum level of performance, necessary for the mechanical success of the implant, thus releasing the manufacturer from the comparison with a predicate device.

REFERENCES

[1]   "ASTM F382-17, Standard Specification and Test Method for Metallic Bone Plates,." ASTM International, 100 Barr Harbor Drive, PO Box C700, West Conshohocken, PA 19428-2959, United States, pp. 1–12, 2017.

[2]   H. Schorler, F. Capanni, M. Gaashan, R. Wendlandt, and C. Jürgens, "Bone plates for osteosynthesis – a systematic review of test methods and parameters for biomechanical testing," pp. 1–9, 2016.

[3]   M. Terzini, A. Aldieri, L. Rinaudo, G. Osella, A. L. Audenino, *et al.*, "DXA-derived Finite Element models to enhance the hip fracture risk prediction," no. October, pp. 1–2, 2019.

[4]   A. Aldieri, M. Terzini, G. Osella, A. M. Priola, A. Angeli, *et al.*, "Osteoporotic Hip Fracture Prediction: Is T-Score-Based Criterion Enough? A Hip Structural Analysis-Based Model," *J. Biomech. Eng.*, vol. 140, no. 11, 2018.

[5]   D. Putzer, M. Nogler, M. Terzini, R. Mannara, and C. Bignardi, "A finite element analysis for a new short stem concept design with spherical bone interface for hip resurfacing," *Int. J. Mech. Eng. Technol.*, vol. 9, no. 3, 2018.

[6]   B. Gervais, A. Vadean, M. Brochu, and M. Raison, "Influence of the load modelling during gait on the stress distribution in a femoral implant," *Multibody Syst Dyn*, pp. 93–105, 2018.

[7]   K. M. M. Robert C. Juvinall, *Fundamentals of Machine Component Design*, Fifth Edit. 2012

Filtering techniques for whole body vibration artefact removal from low-SNR sEMG signals

S. Ranaldi[1], C. D'Anna[1], F. Botta[1], A. Scorza[1], A, Rossi[1], C. Foti[2], S. Faraci[2], S.A. Sciuto[1], M. Schmid[1] and S. Conforto[1]

[1] *Department of Engineering, University Roma Tre*
[2] *Physical and Rehabilitation Medicine, Clinical Sciences and Translational Medicine DPT, Tor Vergata University, Rome*

Abstract—**Whole body vibration exercise is hypothesized to result in an increase of the neural drive to muscle; however, the sEMG signal recorded during vibration exercise is corrupted by a high-power harmonic noise. In this work, several different Fourier-domain techniques (spectral interpolation, Hampel filtering) for vibration artefact removal are compared on simulated signals. Although spectral interpolation can yield some slightly better performances with respect to other methods, its behaviour is strongly dependent on the processing choices, while Hampel filtering maintains acceptable performance regardless of changes in its parameters.**

Keywords—**sEMG, signal processing, whole body vibration.**

I. INTRODUCTION

WHOLE body vibration (WBV) has been hypothesized to affect positively the EMG activity during a variety of different contractions [1]-[8]. However, surface EMG recordings during WBV are affected by a non-negligible high-frequency movement artefact coming from the vibration of the probes. Since different research groups have adopted different processing schemes for denoising these signals [9], it is still not completely clear whether WBV actually increases the sEMG activity.

In the literature [10], it has been shown how the presence of this artefact increases the RMS amplitude of the sEMG signal, thus generating a potential misleading effect on the interpretation of the results. Conversely, it has been hypothesized that the sEMG response to vibration exercise is composed of a non-negligible stretch reflex activity at the stimulation frequency, thus raising the point that a complete removal of the activity in those frequency ranges can remove some of the physiologically meaningful information [11].

WBV typically works at frequencies ranging from 10 to 50 Hz [12][13]: these values imply that vibration noise cannot be treated with the standard processing methods used for the removal of movement artefacts. Moreover, in addition to the fundamental frequencies, the resulting noise is characterized by several higher order harmonic components that fall within the central part of the sEMG power spectra. In order to manage these features of vibration artefact, different procedures have been proposed in the literature, starting from multiple notch filters centered at the fundamental frequency and its harmonics to spectrum interpolation methods [9]. Other strategies require additional signals to be recorded, such as acceleration from a point that is close to the sEMG probe [14]. While all these methods have been found to yield valid results, they all depend on the *a priori* knowledge of the fundamental frequency.

A possible automatic solution to the problem of identify and remove vibration artefact is given by the frequency-domain Hampel filter [15]. This filter has been used in the framework of harmonic noise in different physiological signals [16] and it

has then been characterized in the general case of removing periodical interference from the sEMG signal [17]. However, the performance of this filter in very low Signal to Noise Ratio (SNR) scenarios such as the ones recorded during WBV exercises is still missing from the literature.

In this work, different vibration artefact removal techniques will be tested on a dataset of simulated sEMG data at very low SNR. Results will be compared in terms of typical amplitude and frequency parameters, as well as in terms of the accuracy in separating the artefact from the sEMG signal.

II. METHODS

A. Filtering procedures

In order to check the influence of the filtering procedure on the analysis of WBV signals, different filtering algorithms have been implemented:

- Multiple notch filtering (**N**): after the identification of the fundamental frequency and its harmonics, a single notch filter with a 2 Hz bandwidth has been applied on the signal;
- Spectral interpolation (**I**): the spectrum in the frequency band, centered in each interference frequency of width W, has been substituted with its cubic spline interpolation [18];
- Hampel filtering (**H**): a sliding window of length W is applied on the power spectrum, with a 1-sample shift interval. If the central point of the window is a statistical outlier, that point is substituted with the median value of all the samples in the window. A different version of this method has also been applied on both real and imaginary part of the Fourier transform as in [17] (**HF**).

For both **H** and **HF** W has been chosen to be 10 Hz (narrow) or 16 Hz (wide), while for **I** the same values were set to 2 Hz (narrow) or 4 Hz (wide). Harmonic detection has been carried out, for **N** and **I**, by selecting the location of the maximum of the power spectrum as the fundamental frequency and searching for its harmonics accordingly.

For **I** and **H**, after the modification of the power spectrum, the inverse Fourier transform has been applied using the original phase information in order to be able to evaluate parameters in the time-domain.

B. Simulated data

Synthetic sEMG data were generated using the Stulen-De Luca filter [19], imposing 50 Hz and 150 Hz as low and high cut-off frequencies and a sampling frequency of 1 kHz. Data were simulated with different lengths (1, 3 and 5 seconds). The vibration artefact has been simulated at 30 and 50 Hz; in

addition to the fundamental frequency, the first 8 harmonics were included, with decreasing power, according to the following:

$$s(t) = \sum_{n=1}^{9} \frac{1}{2^n} \sin(2\pi n f t)$$

The interference signal was modulated with a Hamming window of the same length of the signal, scaled and shifted in amplitude so to have values ranging from 0.8 to 1. The amplitude of the interference signal was scaled in order to obtain a signal-to-noise ratio in the range of approximately -10 dB and -3 dB.

For each combination of the parameters above, 50 different realizations were generated. An example of the spectrum of a simulated signal is given in Fig. 1.
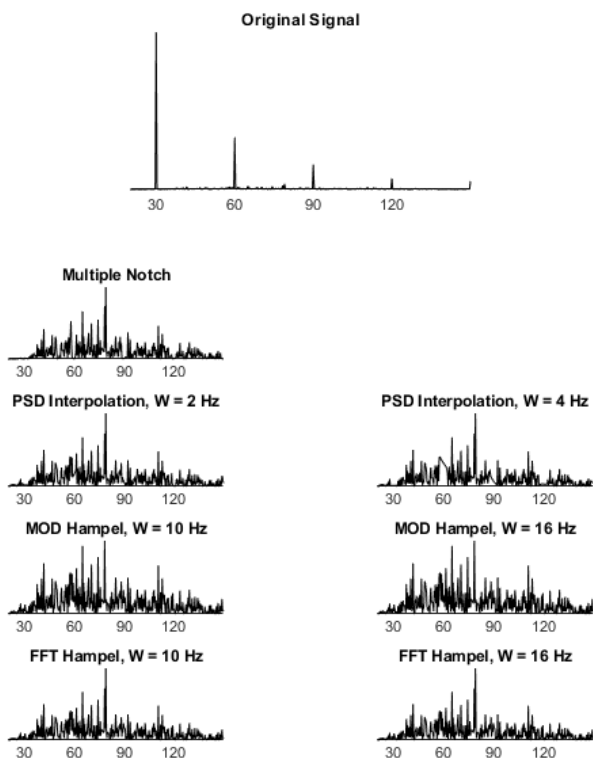
Fig. 1: Spectra of the original corrupted signal (i.e. simulated signal sEMG after the inclusion of the synthetic interference) and of the filter outputs in the range 20-150 Hz.

C. Quality parameters

The performance of the different filters has been evaluated in terms of:

- Absolute error in the identification of the mean (**eMean**) and median (**eMed**) frequencies
- Absolute error in the RMS value of the signal (**eRMS**)
- Cosine similarity between the original interference and the difference between noisy and filtered signals (**cInt**) as a measure of the ability of the filter to remove and isolate the interference
- Cosine similarity between the amplitude envelope of the interference and of the filtered signal

(**cMod**), as a measure of the ability of the filter to eliminate any modulation in the interference from the sEMG signal

All errors were evaluated with respect to the signal before the inclusion of the synthetic interference.

The comparison between methods has been carried out regardless of the simulation parameters (SNR, interference frequency and signal length); this has been done in order to identify general trends on an extremely heterogeneous sample. As a drawback, this implicit variability results in the fact that no inferential statistics has been carried out on the results.

D. Example of experimental data

A signal recorded during a vibration perturbation has been used as a qualitative benchmark to show the outcomes of the different filters in terms of power spectral density. For this purpose, a subject was asked to maintain a half squat position for 45 seconds when on a vibration platform (Nemes Bosco LX-B Health, Mikkeli, Finland); the platform was turned on at a nominal frequency of 30 Hz from second 15 to 30. This experimental procedure has been chosen since such a posture has been recurrently adopted in WBV interventions [20]-[22]. Signals from bilateral *vastus lateralis*, *vastus medialis* and *semitendinosus* muscles were recorded during the whole trial using wireless lightweight sEMG probes (BTS FREEEMG). For this analysis, only the central 3 seconds of the portion of the signal corresponding to the vibration were analysed using the aforementioned filters.

For this analysis only one experimental signal has been used for testing, and no quantitative parameters have been calculated.

III. RESULTS

An example of the outcomes in terms of power spectral density of the different filters is given in Fig. 1 for a portion of the sEMG frequency band. While the Hampel procedures seem not to distort the shape of the spectra, **N** and **I** behaviour results in macroscopic alterations in the PSD; in particular, **I** introduces significant distortions when the window length is larger.

Results presented in Fig. 2 show a quite high variability in terms of median absolute deviation, even if some trends can be identified. In general, regardless of the distortion introduced in the power spectral density, the interpolation filter shows the lowest **eRMS**, with values of **eMean** and **eMed** comparable with the Hampel filter applied on the modulus of the FFT. Results in terms of **cInt** and **cMod** do not show significant differences for all the tested filters. Lower values of **eRMS**, **eMean**, **eMed** and **cMod** reflect better performance of the filters in preserving the original signal features, while higher values of **cInt** indicate a better identification of the vibration artefact.

Each bar refers to data from the complete dataset (50 realizations, 3 window lengths, 2 vibration frequencies and 2 SNR values. 600 values in total).
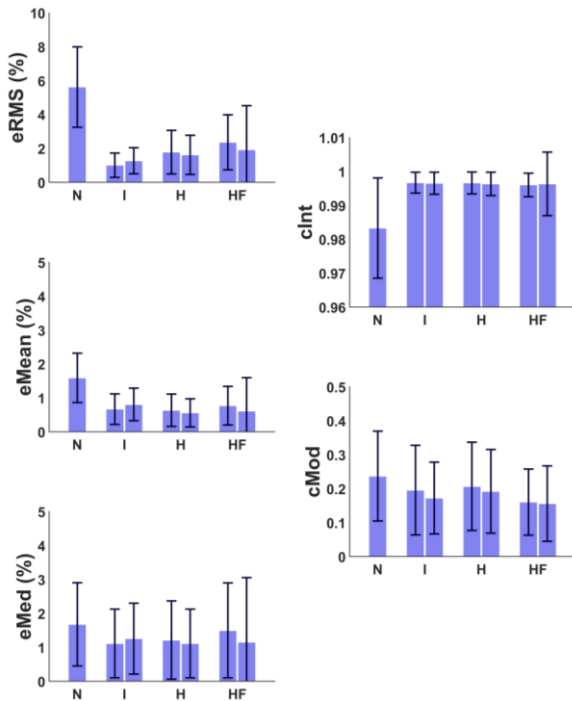
Fig. 2: Performance of the different filters on average across all conditions (median ± median absolute deviation). The bars for I, H and HF refer to the different window lengths (left: narrow; right: wide). The different ranges on the y axis are arranged according to the meaning of the parameters.

Results from the test on experimental signals are shown in Fig. 3 for the *vastus medialis* muscle, in the range 20-150 Hz. The results are coherent with what has been found on simulated data; the shape of the typical sEMG spectrum is recovered after each one of the tested filters. The only significant distortions are found, in accordance with the simulated data, when **I** is applied with a large window.
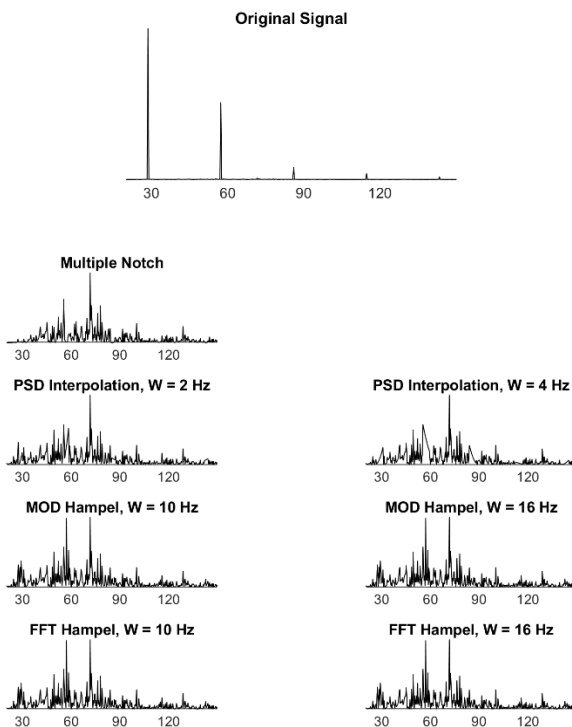

Fig. 3: Example of the spectra of the original measured signal and of the filter outputs in the range 20-150 Hz.

IV. DISCUSSION AND CONCLUSION

In this work, a qualitative assessment of the performance of different filters for the removal of WBV artefact from the sEMG signal has been presented; the simulations have been carried out on a dataset characterized by a high degree of intrinsic variability. The nature of the tested signals has been chosen in order to identify general trends, and all the results will be discussed without a statistical support.

The presented results show how, even when the signal to noise ratio is extremely low, it is possible to filter the vibration artefact from the sEMG signal without losing meaningful information. The significant variability of the results of the simulations is due to the different tested scenarios in terms of length of the signal and frequency and SNR of the interference. Despite this limitation, it is possible to draw some general conclusions: the parameter on which the processing method seems to have the maximum effect is the RMS value, while for the mean and median frequencies all the tested methods reach an accuracy of about 2%. These results are mostly coherent with what has been presented before in literature [9][17] and all the differences with those previous studies can be reasonably ascribed to the wide differences in terms of simulated SNR.

Based on the apparent trends that are visible in the results of this simulation, it could be concluded that both the interpolation and the Hampel filter are the most appropriate choices when analysing vibration exercise EMG data. It should be noted, however, that the simulated signals were characterized by very sharp interference pulses that are detectable with small windows; in real experiments, different external factors can increase the effect in amplitude modulation of the interference, thus enlarging the bandwidth of the frequency spikes. In these scenarios, using an interpolation window greater than 2 Hz can significantly distort the power spectrum, detrimentally affecting the performance of the interpolation filter. Moreover, the Hampel filter behaviour depends on several different parameters, among which the outlier detection method, that can be finely tuned in order to reduce the invasiveness of the filter in all the frequency ranges in which the interference is not present.

The analysis on **cInt** and **cMod** showed that, although all the filters reasonably eliminate any modulation effect of the interference from the sEMG signal, both the interpolation filter and the module-based Hampel seem to have a slightly better performance in the isolation of the noise signal. This implies that, with respect to the other tested procedures, these two strategies are more conservative and selective in the reduction of the noise, with a lower impact on the sEMG frequency content.

Any potential difference in the performance of the FFT-based Hampel filtering, with respect to the modulus-based, are probably to be ascribed to the nature of the filter itself. Being the real and imaginary part of the FFT a zero-mean signal, it is highly likely that when the outlier is detected, that point is substituted with a value close to zero, implementing what is essentially a very narrow-band notch filter. Applying the Hampel filter on a positive-definite signal such as the modulus of the FFT decreases the probability of the filtered value to be

close to zero, thus creating a behaviour that is closer to the one of a fine-tuned interpolation filter.

In conclusion, it has to be remarked that both notch filter and interpolation methods require either an *a priori* knowledge of the frequency characteristics of the interference or a detection step. While it is easy to implement several methods for the detection of the steep peaks in correspondence of the fundamental and harmonic frequencies of the noise, it can be difficult to define the width of the spectral peaks and consequently set the optimal window length. Hampel filtering, in contrast, does not require the identification of the peak locations and it is supposed to be less affected by the window length, maintaining the error at values lower than 5% in the identification of all the parameters; as a consequence, it is reasonable to adopt a well-tuned Hampel filtering to denoise vibration exercise sEMG signals when the knowledge on the nature and features of the artefact are not known accurately.

REFERENCES

[1] A. Fratini, A. La Gatta, P. Bifulco, M. Romano, and M. Cesarelli, 'Muscle motion and EMG activity in vibration treatment', Medical Engineering & Physics, vol. 31, no. 9, pp. 1166–1172, Nov. 2009, doi: 10.1016/j.medengphy.2009.07.014.

[2] Morel, Danielle & Marín, Pedro & Moreira-Marconi, Eloá & Dionello, Carla & Bernardo-Filho, Mario. (2018). Can Whole-Body Vibration Exercises in Different Positions Change Muscular Activity of Upper Limbs? A Randomized Trial. Dose-Response. 16. 155932581880436. 10.1177/1559325818804361.

[3] Kaçoğlu, Celil & Gurol, Baris. (2016). Effect of body position during whole body vibration on acute jumping performance. Baltic Journal of Sport and Health Sciences. 3. 8-12. 10.33607/bjshs.v3i102.59.

[4] Ji, Q., He, H., Zhang, C., Lu, C., Zheng, Y., Luo, X., He, C., 'Effects of whole-body vibration on neuromuscular performance in individuals with spinal cord injury: A systematic review', Clin Rehabil., 2017 Oct; 31(10), 1279-1291.

[5] D. Simsek, 'Different fatigue-resistant leg muscles and EMG response during whole-body vibration', Journal of Electromyography and Kinesiology, Volume 37, December 2017, Pages 147-154.

[6] Sousa-Gonçalves, C.R.; Paineiras-Domingos, L.L.; Teixeira-Silva, Y.; Amadeu, T.; Lírio, A.P.S.; Francisca-Santos, A.; De Souza, L.F.F.; Pereira, M.J.S.; Melo-Oliveira, M.E.S.; Meirelles, A.G.; Guimarães-Lourenço, G.M.; Reis-Silva, A.; Moreira-Marconi, E.; Moura-Fernandes, M.C.; Xavier, V.L.; Mulder, A.R.P.; Lacerda, A.C.R.; Mendonça, V.A.; Bachur, J.A.; Taiar, R.; Sartorio, A.; Sá-Caputo, D.C.; Bernardo-Filho, M. Evaluation of Whole-Body Vibration Exercise on Neuromuscular Activation Through Electromyographic Pattern of Vastus Lateralis Muscle and on Range of Motion of Knees in Metabolic Syndrome: A Quasi-Randomized Cross-Over Controlled Trial. Appl. Sci. 2019, 9, 4997.

[7] D. Simsek, 'Different fatigue-resistant leg muscles and EMG response during whole-body vibration', Journal of Electromyography and Kinesiology, Volume 37, December 2017, Pages 147-154.

[8] Bosco, Carmelo, Marco Cardinale, and Olga Tsarpela. "Influence of vibration on mechanical power and electromyogram activity in human arm flexor muscles." European journal of applied physiology and occupational physiology 79.4 (1999): 306-311.

[9] K. Lienhard, A. Cabasson, O. Meste, and S. S. Colson, 'Comparison of sEMG processing methods during whole-body vibration exercise', Journal of Electromyography and Kinesiology, vol. 25, no. 6, pp. 833–840, Dec. 2015, doi: 10.1016/j.jelekin.2015.10.005.

[10] A. Fratini, M. Cesarelli, P. Bifulco, and M. Romano, 'Relevance of motion artifact in electromyography recordings during vibration treatment', Journal of Electromyography and Kinesiology, vol. 19, no. 4, pp. 710–718, Aug. 2009, doi: 10.1016/j.jelekin.2008.04.005.

[11] R. Ritzmann, A. Kramer, M. Gruber, A. Gollhofer, and W. Taube, 'EMG activity during whole body vibration: motion artifacts or stretch reflexes?', Eur J Appl Physiol, vol. 110, no. 1, pp. 143–151, Sep. 2010, doi: 10.1007/s00421-010-1483-x.

[12] Rossi, A., Orsini, F., Botta, F., Scorza, A., Schinaia, L., Bibbo, D., Sciuto, S.A. A novel method for whole body vibration platform characterization for clinical applications (2017) 22nd IMEKO TC4

International Symposium and 20th International Workshop on ADC Modelling and Testing 2017: Supporting World Development Through Electrical and Electronic Measurements, 2017-September, pp. 159-163.

[13] Orsini, F., Rossi, A., Scorza, A., Botta, F., Sciuto, S.A. A comparison between a commercial WBV platform and an experimental prototype (2017) 22nd IMEKO TC4 International Symposium and 20th International Workshop on ADC Modelling and Testing 2017: Supporting World Development Through Electrical and Electronic Measurements, 2017-September, pp. 154-158.

[14] A. Fratini, M. Cesarelli, P. Bifulco, A. La Gatta, M. Romano, and G. Pasquariello, 'Acceleration driven adaptive filter to remove motion artifact from EMG recordings in Whole Body Vibration', in 11th Mediterranean Conference on Medical and Biomedical Engineering and Computing 2007, Berlin, Heidelberg, 2007, pp. 990–993, doi: 10.1007/978-3-540-73044-6_256.

[15] R. K. Pearson, Y. Neuvo, J. Astola, and M. Gabbouj, 'Generalized Hampel Filters', EURASIP J. Adv. Signal Process., vol. 2016, no. 1, p. 87, Aug. 2016, doi: 10.1186/s13634-016-0383-6.

[16] D. P. Allen, E. L. Stegemöller, C. Zadikoff, J. M. Rosenow, and C. D. MacKinnon, 'Suppression of deep brain stimulation artifacts from the electroencephalogram by frequency-domain Hampel filtering', Clinical Neurophysiology, vol. 121, no. 8, pp. 1227–1232, Aug. 2010, doi: 10.1016/j.clinph.2010.02.156.

[17] D. P. Allen, 'A frequency domain Hampel filter for blind rejection of sinusoidal interference from electromyograms', Journal of Neuroscience Methods, vol. 177, no. 2, pp. 303–310, Mar. 2009, doi: 10.1016/j.jneumeth.2008.10.019.

[18] S. Leske and S. S. Dalal, 'Reducing power line noise in EEG and MEG data via spectrum interpolation', NeuroImage, vol. 189, pp. 763–776, Apr. 2019, doi: 10.1016/j.neuroimage.2019.01.026.

[19] F. B. Stulen and C. J. De Luca, 'Frequency Parameters of the Myoelectric Signal as a Measure of Muscle Conduction Velocity', IEEE Transactions on Biomedical Engineering, vol. BME-28, no. 7, pp. 515–523, Jul. 1981, doi: 10.1109/TBME.1981.324738.

[20] A. Krause, K. Lee, K. Freyler, T. Bührer, A. Gollhofer, R. Ritzmann, 'Whole-body vibration impedes the deterioration of postural control in patients with multiple sclerosis', Multiple Sclerosis and Related Disorders, Volume 31, June 2019, Pages 134-140.

[21] Huang M, Tang CY, Pang MYC. Use of whole body vibration in individuals with chronic stroke: Transmissibility and signal purity. J Biomech., 2018 May, 73, Pages 80-91.

[22] D. J. Cochrane, S. R. Stannard, 'Acute whole body vibration training increases vertical jump and flexibility performance in elite female field hockey players', Br J Sports Med, 2005, 39, Pages 860–865.

DXA-based Finite Element models to improve hip fracture risk prediction: a comparison with CT-based models

A. Aldieri[1], M. Terzini[1], C. Bignardi[1] and A. L. Audenino[1]

[1] PolitoBIOMed Lab, Department of Mechanical and Aerospace Engineering, Politecnico di Torino, Turin, Italy

Abstract—In light of the urgent need to enhance the current osteoporotic hip fracture risk assessment, CT- and DXA-based Finite Element simulations reproducing a sideways fall have been performed and their outcomes compared for a cohort of 28 patients. In spite of their projective nature, DXA-based models would be indeed already clinically attainable. The 2D and 3D outcomes were only moderately correlated, suggesting CT- and DXA-based models do not appear equivalent. In this light, DXA, which produces a 2D projective image, suffers from the positioning error, so that DXA images might show a proximal femur shape altered compared to the real 3D one. Interestingly however, the same patients were highlighted as at higher risk by the 2D and 3D predictors.

Keywords—Osteoporosis, Hip Fracture, Fracture Risk Prediction, Finite Element Models.

I. INTRODUCTION

OSTEOPOROSIS is a metabolic disorder which mainly affects post-menopausal women and which induces progressive loss and deterioration of the bone tissue silently, until a fracture occurs. 200 million people are currently affected by this disorder globally [1], and its incidence is expected to grow dramatically over the next years [2]. Among osteoporotic fractures, hip fractures are considered to be particularly devastating because of the severe aftermaths they entail as well as the related costs [2].

At present, the presence of osteoporosis is assessed based on the Bone Mineral Density (BMD) measurement using 2D Dual X-rays Absorptiometry (DXA) images. Comparing the patient-specific BMD value with that related to a standard young population, T-score, the gold-standard for patients classification, is computed. However, T-score predictive weaknesses have increasingly been highlighted in literature [2]. In light of this, aiming to enhance the current gold-standard predictive performances, and given that geometry represents an important determinant of bone strength, proximal femur geometrical descriptors achievable directly from DXA images, namely the Hip Structural Analysis (HSA) variables [3], have been considered, although with disparate results in assessing the most relevant to the fracture risk. Besides, Finite Element (FE) models have been investigated, able to integrate patient-specific geometry, a variety of loading conditions and patient-specific heterogeneous material properties. (Quantitative) Computed Tomography (CT)-based 3D FE models would be extremely accurate, but CT does not represent the first-choice exam in this context. Hence, to meet the clinical reality, 2D DXA-based FE models have also been developed to investigate their potentialities as supportive risk predictors [5], [6]. In this study we exploited the simultaneous availability of proximal femur CT and DXA images for a cohort of 28 post-menopausal women with a double aim: 1)

the assessment of the HSA variables most relevant to the fracture risk estimated from CT-based FE analyses; 2) the comparison between CT- and DXA-based FE analyses outcomes.

II. MATERIALS & METHODS

Twenty-eight post-menopausal female subjects, aged from 55 to 81 years (treated in San Luigi Gonzaga Hospital in Orbassano, Italy), were involved in the present study after having signed an informed consent. Patients with available clinical data, DXA derived information and CT scans acquired in the same year were selected. Only the proximal portion of the femur was considered.

A. CT-based FE construction

Three-dimensional subject-specific geometric models of the proximal femur were built through a semi-automatic segmentation procedure on the CT images. Following the meshing procedure (1.2 mm size ten-nodes tetrahedral elements, found consistent with [12]), based on a sensitivity analysis on principal strains, heterogeneous material properties were mapped onto the FE models. A linear elastic model was adopted, and Young's modulus determined based on the following density-elasticity relationship [7]:

$$E = 15.010 \, \rho_{app}^{2.18}, \quad if \; \rho_{app} \leq 0.28 \; g/cm^3 \qquad (1)$$

$$E = 6.850 \, \rho_{app}^{1.49}, \quad if \; \rho_{app} > 0.28 \frac{g}{cm^3}, \qquad (2)$$

where E is the Young's modulus, expressed in GPa, and ρ_{app} is the apparent density, computed from CT-derived Hounsfield Unit (HU) values, in g/cm^3. The relation between HU and ρ_{app}, was assessed through a pseudo-calibration procedure [8].

Static FE simulations were performed reproducing a sideways fall condition. Two different spatial configurations of the proximal femurs were investigated: 1) a neutral one, where femurs were aligned with respect to neck and shaft axes, 2) a tilted configuration, obtained including a 30° internal and 15° medial rotations with respect to the neck and shaft axes. The two different configurations were studied applying the same boundary conditions, shown in [9]. Briefly, the impact load was applied on the trochanter, head nodes were bound to the ground by means of spring elements with a 10000 N/mm stiffness, the distal nodes of the proximal femur models were connected through link elements to a reference node positioned 0.1 m distally, acting as a pivotal hinge.

B. DXA-based FE construction

The 2D geometric models were extracted from DXA scans.

According to a widely adopted approach in the field [5], [6], [10] the femur was modelled as a plate with thickness determined based on the HSA femoral neck width W. Specifically, the subject-specific element thickness t was calculated such that the area and area moment of inertia of a rectangular cross-section with thickness t matched those of a circular cross-section with diameter W: $t = \frac{3.5\,\pi\,W}{16}$ [5], assuming the real cross-section at the neck to be circular. Plane-stress triangular elements (0.5 mm sized 6 nodes elements) were used. Local BMD values were assigned thanks to the pixel-by-pixel BMD maps availability. In particular, ρ_{app} values were derived from DXA BMD according to [5]:

$$\rho_v = \frac{BMD}{t}\frac{1.89}{1.05}, \quad (3)$$

$$\rho_{app} = \frac{\rho_v}{1.14\cdot 0.598}. \quad (4)$$

Young's modulus values were computed using the same empirical relationships [7] used in the three-dimensional case (Equations (1), (2)).

Boundary conditions were applied coherently with those presented in the previous section and in [11]. Again, two different configurations were explored: 1) the neutral one, where 2D models were aligned to the shaft axis and the impact load applied perpendicularly to it; 2) the tilted one, where proximal femurs were medially rotated by 15° in the frontal plane. Due to the two-dimensionality of the problem the internal rotation could not be included.

C. Post-processing

The post-processing phase was based on principal strains extraction in both the 3D [12], [14] and 2D [10] analyses: minimum (ε_1) and maximum (ε_3) principal strains were extracted at each element centroid; for each mesh element, a compressive or tensile predominance was assessed and a Risk Factor (RF) could be calculated [12] as:

$$RF = \frac{\varepsilon_{max}}{\varepsilon_{lim}}, \quad (5)$$

where ε_{max} refers to the prevailing tensile or compressive principal strain ($\varepsilon_{max} = \max(|\varepsilon_1|, \varepsilon_3)$), and ε_{lim} represents the tensile or compressive threshold (0.0074 in tension, 0.0104 in compression) [13].

Two fracture risk predictors, the Femoral Strength (FS) and Risk Fracture Index (RFI) were estimated both in the 2D and 3D cases. The FS, i.e. the impact load causing the onset of a fracture, was estimated linearly increasing the impact load up to the onset of the fracture predicted at the failure of a number of contiguous elements (3D case: number of superficial contiguous elements exceeding 0.3% [14]; 2D case: number of contiguous elements exceeding 0.15% [5], [10]). The RFI was defined as the highest RF value identified (3D case: among the superficial elements; 2D case: over the whole model) at a patient-specific impact load assessed using a 1 Degree of Freedom mass-spring damper system [9]. Comparing the FS and RFI between the neutral and inclined configurations (RFI_N, RFI_I and FS_N, FS_I), the most critical values were identified:

$$FS = \min(FS_N, FS_I) \quad (6)$$

$$RFI = \max(RFI_N, RFI_I). \quad (7)$$

With regard to the 2D and 3D case, they will be addressed as FS_{2D}, FS_{3D} and RFI_{2D}, RFI_{3D} respectively.

Aiming to assess the HSA parameters most meaningful with respect to the afore-mentioned risk predictors, multilinear regression analyses were carried out after performing a collinearity diagnosis on the variables based on the Variance Inflation Factor (VIF) calculation [15]. The relative importance of the regression models and of the selected HSA variables was eventually assessed using the Akaike Information Criterion (AIC) [16].

III. RESULTS

The inclined configuration resulted the most critical one, showing, both in the 3D and 2D case, lower FS and highest RFI values.

If the FS_{2D}, FS_{3D} and RFI_{2D}, RFI_{3D} are compared (Fig. 1), the correlation between the CT- and DXA-based outcomes turns out to be significant, but modest: regressing the 3D predictors on the 2D ones, the RFI_{2D} could explain only a small portion of the RFI_{3D} variance, R^2 being 0.26 ($p < 0.0057$). As for the FS_{2D}, it managed to explain nearly half of the variance of the corresponding FS_{3D} ($R^2 = 0.46$, $p < 0.0001$). Hence, the CT- and DXA-based predictors would not be judged equivalent, given that most of the three-dimensional predictors cannot be accounted for by the two-dimensional ones.
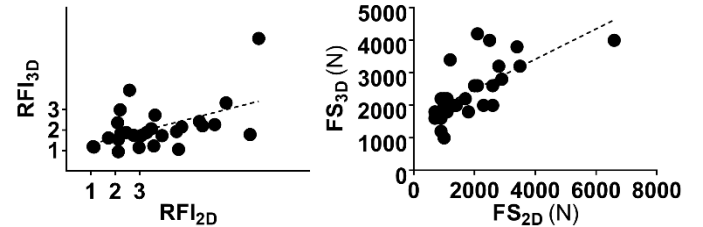

Figure 1: Comparison between the two- and three-dimensional RFI (left) and FS (right).

From this perspective, Fig. 2 displays the comparison between the 3D and 2D RF distribution for the 28 patients at the estimated patient-specific impact load in the tilted configuration. For visualization purposes, only RF values above the 90th percentile are shown. As visible, a consistent co-localization of the regions interested by the highest RF values cannot be found between the three- and two-dimensional models. However, it is interesting to notice that the patients highlighted by large areas of RF above the 90th percentile threshold or exhibiting extremely high RF values ($RF > 2$) are often the same.

Fig. 3 and Fig. 4 display, respectively, the comparison between the 2D and 3D fracture risk indices and T-score classification. The two patients displayed using empty circles are two additional patients who had fractured in the year following the DXA image, but for whom CT images were not available, preventing the 3D models construction.

Fig. 3 shows the values as extracted from the FE analyses for the whole dataset, while Fig. 4 shows the values as computed from the FE outcomes for the 28 patients, but as predicted by
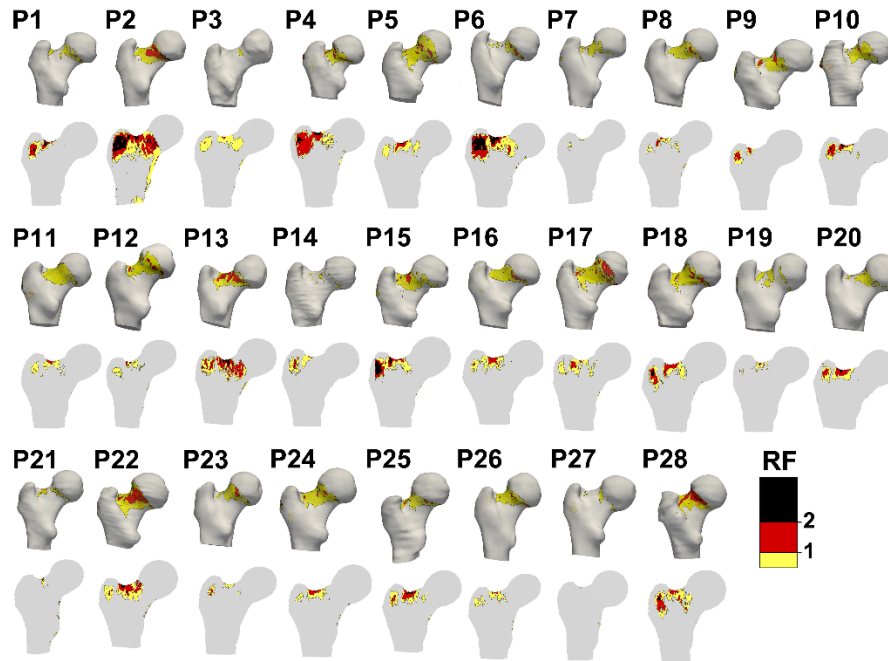
Figure 2: RF distribution in the CT- and DXA-based models related to the inclined configuration at the patient-specific impact-load. Only *RF* values above the 90th percentile are shown (0.51 for the 3D models, 0.6 for the 2D models.

the optimal regression model (Table I) for the afore-mentioned fractured patients. In spite of the discrepancies pointed out previously, the predictors manage to better stratify patients belonging to the same T-score range, with particular attention to the osteopenic ones: some appear indeed as at higher risk, and have been highlighted depicting them with empty diamonds.
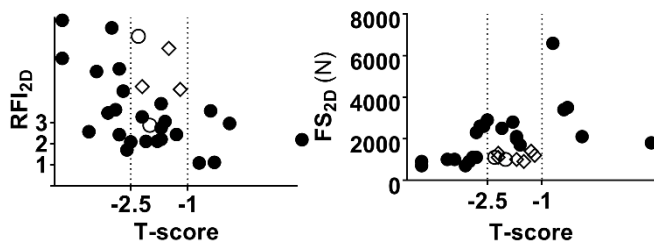
Figure 3: RFI_{2D} and FS_{2D} compared with the T-score. The three standard ranges of the T-score are highlighted: no osteoporosis/osteopenia: T-score > -1; osteopenia: -2:5 < T-score > -1; osteoporosis: T-score < -2:5. Empty circles refer to the two fractured patients predicted values, empty diamond to the non-osteoporotic patients looking at higher risk. Significant correlations were found (RFI_{2D}: R = 0.48; p < 0.007, FS_{2D}: R = 0:.54; p < 0.002).

In particular, the same patients are located in the higher risk region by both the FS_{2D} and FS_{3D}, and analogously by both the RFI_{2D} and RFI_{3D}. Only one patient, highlighted as at higher risk by both the 2D indices, is not highlighted as so by the 3D ones. The two fractured patients are correctly placed in the low FS_{2D} and FS_{3D} region, but only one manages to outdistance the other osteopenic patients if the RFI is considered. That is probably due to the BMI-dependent definition of the impact load on which the RFI definition was based on: characterized by an extremely low BMI, a modest impact load was employed within the FE analyses, which resulted in moderate strain levels.

Eventually, Table I presents the HSA variables included in the best three regression models according to AIC for each fracture risk predictors, while Table II presents the first four most relevant variables with respect to the 2D and 3D fracture risk predictors, as ranked by the Akaike cumulative weights. Interestingly, the Buckling Ratio (BR) and the Cross-Sectional Moment of Inertia (CSMI) are consistently contemplated by all the predictors. This might point out the fundamental role played by the bone resistance to bending, which is dominant during sideways falls, but is also consistent with the idea that osteoporosis degrades strength by reducing cortical stability.
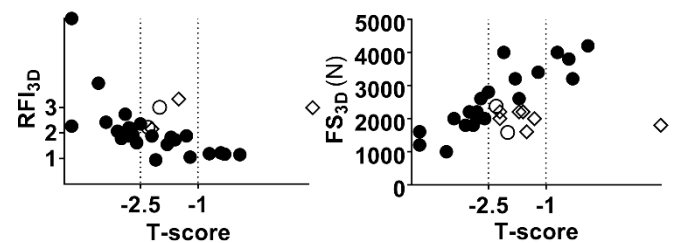

Figure 4: RFI3D and FS_{3D} compared with the T-score. RFI_{3D}: R = 0:42; p < 0:02, FS_{3D}: R = 0:52; p < 0:003).

However, the BR and CSMI are intrinsically associated to the BMD itself, being determined based on the image pixels intensity. Therefore, it is not straightforward to assess if the geometrical features they gather are predominant with respect to the BMD-related ones. As for the Hip Axis Length (HAL) and Neck Shaft Angle (NSA), which are independent of the image pixels intensity, they did not turn out to be equally highlighted by all the fracture risk predictors. Nevertheless, in spite of the differences, and with particular regard to the HAL, they emerged as meaningful on the whole. In this background, the limited consistency found with regard to the NSA and HAL might be partially explained considering Fig. 5. It highlights how, for some patients, noticeable differences in geometry exist if the CT- and DXA-based models are compared. Considering the NSA indeed, opposite conclusions would be

drawn looking at the CT- or DXA-based geometries. Related to the DXA projective nature, this could have presumably affected the AIC-based regression analysis outcomes.

TABLE I
BEST REGRESSION MODELS

	Variables	R_{adj}^2	w
RFI₃D	{NSA, BR_{nn}}	0.457	0.091
	{NSA, CSMI_{nn}, BR_{nn}}	0.483	0.071
	{HAL, NSA, BR_{nn}, BR_{fs}}	0.513	0.059
RFI₂D	{CSMI_{it}, BR_{nn}}	0.289	0.064
	{HAL, BR_{nn}}	0.284	0.058
	{HAL, BR_{nn}, BR_{fs}}	0.319	0.052
FS₃D	{CSMI_{nn}, BR_{nn}, BR_{fs}}	0.566	0.065
	{CSMI_{nn}, BR_{nn}}	0.531	0.054
	{HAL, CSMI_{nn}, BR_{nn}, BR_{fs}}	0.589	0.049
FS₂D	{NSA, CSMI_{nn}, BR_{nn}, BR_{fs}}	0.619	0.119
	{NSA, CSMI_{nn}, BR_{fs}}	0.577	0.068
	{NSA, CSMI_{nn}, CSMI_{it}, W_{it}, BR_{fs}}	0.631	0.064

The best three regression models according to AIC are presented together with the corresponding adjusted R² and Akaike weight *w*.

TABLE II
RANKED HSA VARIABLES

HSA var.	w_+	HSA var.	w_+	HSA var.	w_+	HSA var.	w_+
RFI₃D		**RFI₂D**		**FS₃D**		**FS₂D**	
BR*	0.93	BR*	0.88	CSMI	0.87	CSMI	0.96
NSA	0.82	HAL	0.50	BR+	0.62	NSA	0.93
BR+	0.46	BR+	0.44	BR*	0.62	BR+	0.76
HAL	0.32	CSMI	0.37	HAL	0.41	BR*	0.45

The first four HSA variables as ranked according to the cumulative Akaike weights w_+, which establish the relative importance of each predictor variable. *variable computed at the narrow neck; +variable computed at the femoral shaft. The CSMI is always referred to the narrow neck.
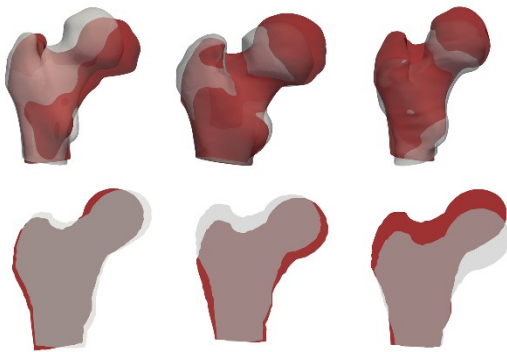

Figure 5: Comparison between DXA- and CT-based geometries for 3 patients (in columns). In red the patient with highest (DXA-derived) NSA is depicted.

Of course, the limited number of patients considered does represent a limitation which is worth mentioning. In addition, the lack of follow-up information for this cohort did not allow to draw solid and absolute conclusions about the actual classification performances of the extracted risk predictors. Rather, a relative comparison was carried out, and larger cohorts with known fracture status will help in getting further insights.

IV. CONCLUSION

CT- and DXA- derived FE models for 28 patients were compared. Although not appearing to be equivalent, they managed to highlight the same patients as at higher risk. The relevant HSA variables pointed out the predominant role of the resistance to the bending stress occurring sideways falls in both cases. Attention should be paid when dealing with DXA-derived shapes which, affected by its projective nature, might alter the 3D real features of the patient-specific geometry.

REFERENCES

[1] J. T. Lin, and J. M. Lane, "Osteoporosis: a review" in *Clinical Orthopaedics and Related Research*, vol. 425, pp. 216–134, 2004.
[2] O. Strom, F. Borgstrom, J. A. Kanis, J. Compston, C. Cooper, E. V. McCloskey, B. Jonsson, "Osteoporosis: burden, health care provision and opportunities in the EU" in *Archives of osteoporosis*, vol. 6(1-2), pp. 59–155, 2011.
[3] T. Beck, "Measuring the structural strength of bones with dual-energy X-ray absorptiometry: principles, technical limitations, and future possibilities" in *Osteoporosis International*, vol. 14(5), pp. 81–88, 2003.
[4] J. S. Gregory, R. M. Aspden, "Femoral geometry as a risk factor for osteoporotic hip fracture in men and women" in *Clinical Orthopaedics and Related Research*, vol. 30(10), pp. 1275–1286, 2008.
[5] K. E. Naylor, E. V. McCloskey, R. Eastell, L. Yang, "Use of DXA-based finite element analysis of the proximal femur in a longitudinal study of hip fracture" in *Journal of Bone and Mineral Research*, vol. 28(5), pp. 1014–1021, 2013.
[6] L. Yang, L. Palermo, D. M. Black, R. Eastell, Richard, "Prediction of incident hip fracture with the estimated femoral strength by finite element analysis of DXA scans in the study of osteoporotic fractures" in *Journal of Bone and Mineral Research*, vol. 29(12), pp. 2594–2600, 2014.
[7] E. F. Morgan, H. H. Bayraktar, T. M. Keaveny, "Trabecular bone modulus–density relationships depend on anatomic site" in *Journal of biomechanics*, vol. 36(7), pp. 897–904, 2003.
[8] C. M. Ford, T. M. Keaveny, W. C. Hayes, "The effect of impact direction on the structural capacity of the proximal femur during falls" in *Journal of Bone and Mineral Research*, vol. 11(3), pp. 377–383, 1996.
[9] A. Aldieri, M. Terzini, G. Osella, A. M. Priola, A. Angeli, A. Veltri, A. L. Audenino, C. Bignardi, "Osteoporotic hip fracture prediction: I T-score-based criterion enough? A hip structural analysis-based model" in *Journal of biomechanical engineering*, vol. 140(11), pp. 111004, 2018.
[10] E. Dall'Ara, R. Eastell, M. Viceconti, D. Pahr, L. Yang, L "Experimental validation of DXA-based finite element models for prediction of femoral strength" in *Journal of the mechanical behavior of biomedical materials*, vol. 63, pp. 17–25, 2016.
[11] M. Terzini, A. Aldieri, L. Rinaudo, G. Osella, A. L. Audenino, C. Bignardi, C., Improving the hip fracture risk prediction through 2D finite element models from DXA images: validation against 3D models, in *Frontiers in bioengineering and biotechnology*, vol. 7, pp. 220, 2019.
[12] E. Schileo, F. Taddei, L. Cristofolini, M. Viceconti, "Subject-specific finite element models implementing a maximum principal strain criterion are able to estimate failure risk and fracture location on huma femurs tested in vitro" in *Journal of biomechanics*, vol. 41(2), pp. 35 367, 2008.
[13] H. H. Bayraktar, E. F. Morgan, G. L. Niebur, G. E. Morris, E. K. Wong, ET. M. Keaveny, "Comparison of the elastic and yield properties of human femoral trabecular and cortical bone tissue" in *Journal of biomechanics*, vol. 37(1), pp. 27–35, 2004.
[14] E. Schileo, L. Balistreri, L. Grassi, L. Cristofolini, F. Taddei, "To what extent can linear finite element models of human femora predict failure under stance and fall loading configurations?" in *Journal of biomechanics*, vol. 47(14), pp. 3531–3538, 2014.
[15] E. Walker, "Detection of collinearity-influential observations" in Communications in Statistics-Theory and Methods, vol. 18(5), pp. 1675–1690, 1989.
[16] H. Akaike, "A new look at the statistical model identification" in IEEE Transaction on automatic control, vol. 19(6), pp. 716–723, 1974.

Design and development of an origami-based pump for soft robotics wearable applications

G. Bondì[1,2], D. Zrinscak[1,2], and M. Cianchetti[1,2]

[1] *The BioRobotics Insitute, Scuola Superiore Sant'Anna, Pisa*
[2] *Department of Excellence in Robotics & AI, Scuola Superiore Sant'Anna, Pisa*

Abstract—Wearable assistive devices have recently exploited soft robotics principles in order to expand the possibilities for a safe interaction and cooperation while assisting the patient. One of the most common actuation solutions are soft fluidic actuators, given their ability to expand, contract or bend. While they show major advantages such as high specific power and a wide range of available motions, their major drawback lies in the need of a bulky fluidic power source. In the state-of-the-art, several different means of providing pressure for an untethered operation have been used. However, they all present limitations as insufficient flow rate and pressure, limited volume capacity or complex modelling and control. This paper focuses on the design and development of a proof-of-concept lightweight pump for soft robotics applications, that exploits Shape Memory Alloys and an origami mechanical structure to produce a volumetric difference and the displacement of a stored fluid. Two existing volumetric origami models – the origami waterbomb and the Kresling cylinder – were selected and their kinematic studied analytically. FEM simulations were performed to confirm the analytical modelling and get insights into folding behaviour. Prototypes were fabricated and actuated with SMA spring actuators. They were then tested, showing that the proposed origami pump is capable of delivering an output specific pressure in line with the values presented in the state-of-the-art.

Keywords—Soft robotics, wearable, origami, soft pump.

I. INTRODUCTION

One of the most significant and recent challenges of robotics has been the use of soft materials and compliant mechanisms, aiming to obtain a gentle and safe interaction with the environment and with humans. Indeed, the use of soft matter has paved the way for several biomedical applications in which a soft interaction with a patient should be preferred [1], as in the case of rehabilitation or assistive wearable devices.

Flexible fluidic actuators (FFAs) have become prominent, between several actuation solutions in the development of novel soft robots, given their ability to expand, contract or bend. While soft fluidic actuators have major advantages, such as high specific power and a wide range of available motions, their major drawback lies in the need of a fluidic power source and a complex electromechanical system, which may result bulky [2]. Although tethered designs may work well in a stationary configuration, mobile or wearable soft robots, instead, would significantly benefit from sustained untethered operation.

Having in mind small-scale wearable applications, the system should be as compact and lightweight as possible, while supplying enough pressure and energy for long-term operation.

The gauge pressure required for powering small pneumatic actuators usually ranges from 50 to 500 kPa [3], [4].

In the state-of-the-art, several means of providing pressure for untethered operation have been used, such as mechanical compression [5], storage of previously compressed gas [6], phase change and many different chemical reactions [7]. However, all these methods present limitations: on-board micro-compressors generally provide insufficient flow rate and pressure, while often being heavy; weight is a problem for pressurized gas tanks, too, which also suffer from a limited volume capacity; chemical reactions are usually difficult to model and control.

To build an independently operating soft robot, one of the key challenges would be the design and implementation of a soft and lightweight pneumatic pressure source to actuate the pneumatic network. This challenge is particularly true in the case of rehabilitation and wearable robots. The soft nature of these devices provides several advantages especially in at-home assistance: they have a broader range of motion which increases user mobility, they can ensure a safer human-robot interaction thanks to soft and compliant materials that, generally, also lower fabrication cost and, finally, they are lightweight and portable [8], [9].

These advantages could be considered as well for the proposed soft pump, whose control will be greatly simplified by employing an origami structure with an on-off activation mechanism actuated by Shape Memory Alloys, that are the optimal actuation solution for this design owing to their high work density, their low weight, silence and cleanliness.

II. CONCEPT DESIGN

This paper focuses on the design, fabrication and characterization of a proof-of-concept soft lightweight pump inspired by volumetric origami. This subclass of origami is known for the ability to host a certain volume, and the theoretic complete compression, when folded. The novelty lies in the idea of exploiting the origami structure as a active reservoir, able to produce a specific pressure difference upon contraction, and thus, displace the stored fluid. Origami, indeed, has recently proved to be a valuable tool to develop various engineering applications and has also inspired the manufacturing and design of robots [10].

This component may be employed in a variety of applications – e.g. a pneumatic source for FFAs – and it can be embedded in a distributed soft pumping network. By
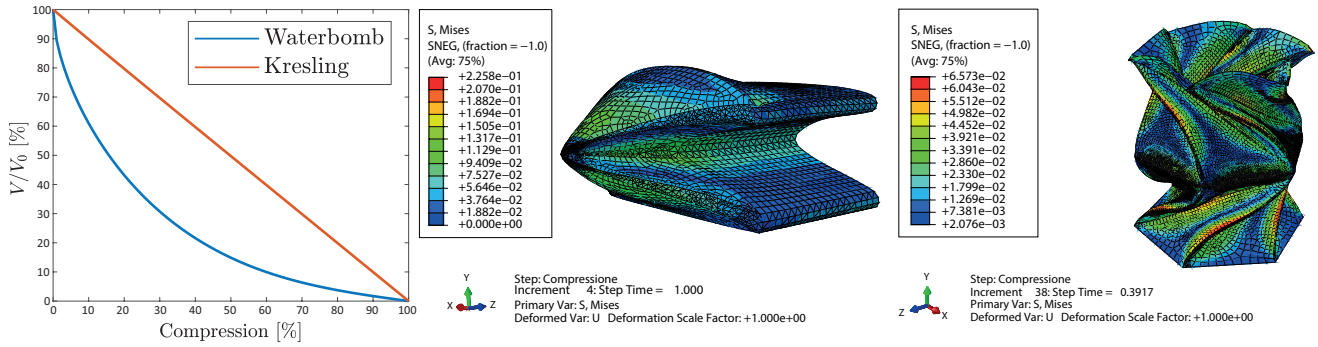
Fig. 1: Analytical and FEM models results. *Left*: comparison between the volume evolution of an origami waterbomb and an origami cylinder with Kresling pattern; *Center*: maximum Equivalent Von Mises stresses for a origami waterbomb; *Right*: maximum Equivalent Von Mises stresses for a two-layers Kresling cylinder.

coupling the single pumps in series or parallel to achieve a particular desired final pressure, and it can be a feasible solution for wearable applications, freeing the user from a bulky compressor by distributing the pumping system on the user himself.

The soft robotics glove developed by Polygerinos and colleagues [8], in which soft actuators that induce specific trajectories support the range of motion of individual fingers, is a suitable example of an application which can define some general requirements for the design of the device:

- Lightweight: to be wearable and portable, the proposed pump should weight in the order of 10^1 g;
- Low profile: to be wearable and distributed, the pump should have a limited thickness and shouldn't protrude more than $3 - 4$ cm;
- High specific pressures: around 1 bar/kg;
- Medium/high flow rates: around 10 ml/(min kg);
- Scalable system: if the final performance indexes are not sufficient to the final application, it should be possible to connect several unit pumps into series or parallel configuration for a correct management of output pressures and flow rates.
- Frequency requirements, considering a rehabilitation application, are not of primary concern.

SMAs are metal alloys capable of undergoing a certain strain, and subsequently recover their original shape when heated: owing to their high work density, their low weight, silence, and cleanliness, they have been used extensively in soft robotics in several applications [11] and, although they show a major drawback in being slow, they are also the optimal actuation solution for the proposed origami pump, while a major drawback is their slowness

III. MATERIALS AND METHODS

As there is no standard model for robogami, the general methodology followed to develop the proposed origami pump was proposed in [12]: it requires the design and development to be carried on simultaneously.

A. Volumetric origami assessment

At the beginning, an evaluation of existing volumetric origami structures was carried out, considering that model should have minimum movements at the base, to keep a stable interface between the pump and the underlying layer; have a fixed area at the base; be as lightweight as possible; maximize volume displacement.

The *origami waterbomb* and *Kresling cylinder* were chosen as the ones that adhered most to the application requirements. Then, kinematic models of the two origami were developed to obtain an analytical formulation of their volume depending on their compression, to choose the most suitable design for the application. While an analytical formulation of the origami waterbomb volume was already present in the literature [13], as well as numerous works focusing on the Kresling cylinder kinematics and bistability properties [14], [15] a formulation of the internal volume of this latter model was still missing in the state-of-the-art. Thus, during the design phase, to have a comparison with the origami waterbomb volume, an analytical formulation of the volume for a generic origami-based cylinder with Kresling pattern was derived while considering its folding kinematics.

Calling $V(h)$ the volume of the origami when at height h and considering an origami compressing from a certain h_0 to 0, it is possible to define volume variation as $\frac{V(h)}{V(h_0)} \times 100\%$ and structure compression as $\frac{h - h_0}{h_0} \times 100\%$. Their relationship for the two origami structures is displayed in Figure 1: from this comparison is possible to observe a major difference in compression efficiency between the two structures, given that with the same compression the origami waterbomb has a greater volume variation.

B. Simulations

In the following step, FEM simulations were performed, aiming to verify the kinematic models and gain insights into folding behaviour and stresses developed at vertices and hinges. Simulations were performed using Abaqus/CAE 6.14-1 (Dassault Systemes Simulia Corp., Providence, RI, USA). Simulations pointed out, as presented in Figure 1, that, as desired, the waterbomb compresses until its geometric limit

due to faces thickness, and cap vertices, being characterized by low stresses, could easily host air outlet ports. Instead, a two-layers Kresling cylinder could not compress completely: for this reason, as well as for the aforementioned volume variation, the Kresling cylinder design was discarded, and its investigation was not carried further.

C. Fabrication

Origami fabrication is performed in a layer-by-layer 2D manner, with each layer 0.5 mm thick, as displayed in Figure 2. A flexible matrix of DragonSkin^{TM} 30 (Smooth-On, Macungie, Pennsylvania) is reinforced in the rigid faces of the origami waterbomb with FR-4 tiles (McMaster-Carr, Douglasville, Georgia). In this way it is possible to have a sealed structure, with thin walls and enhanced flexibility at the hinges. The device is then assembled in 3D and TPU outlet tubes and SMA spring actuators are attached on it using SmoothOn Sil-Poxy silicone rubber adhesive. A total of three origami waterbombs were fabricated.
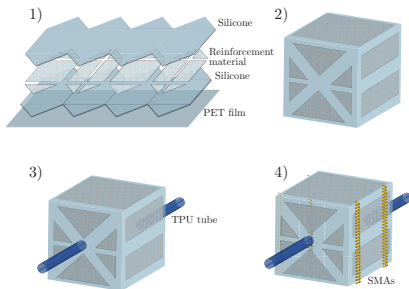

Fig. 2: Summary of the four main steps to fabricate the waterbomb origami pump.

Regarding the actuation, to compress the origami simmetrically and to avoid mechanical singularities (given by an outward buckling of the side faces), the number of SMA spring actuators considered was equal to four, one per each vertical edge of the waterbomb. These were modelled and fabricated according to the method proposed in [16], using a value of force obtained by the test described in Section III.D. The chosen shape memory wire was the G/w/0.300/c040 (Saes Getters, Lainate, Italy). The number of coils was chosen to have the maximum expanded length of the actuators equal to the waterbomb side length (3 cm).

SMA wires were then connected to electrical wires using amp connectors; their extremities are attached together so that the four SMA spring actuators are electrically and mechanically in parallel.

D. Prototype characterization

Three tests were performed to characterize the three final prototypes, of which one is shown in Figure 3. First, a measure of the required compression force, used to dimension SMA spring actuators, was performed with a mechanical testing machine, (Instron, Norwood, Massachusetts, US), lowering its load cell at speed of 10 mm/min from a pre-compressed configuration of the origami, and keeping the outlet ports open.
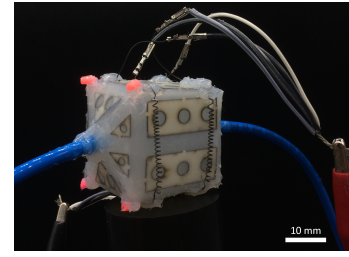

Fig. 3: Final origami waterbomb soft pump prototype. The device is approximable to a cube with side length of 3 cm that weighs 18 g, in line with the first two design requirements.

The measure was repeated ten times per sample. The reference value employed for SMA dimensioning was over-estimated as 2 N.

Then, still considering open outlets and actuating the device with SMA, a measure of the origami contraction rate was performed employed colored optical markers and video recordings of the contraction analyzed with Tracker. Finally, using the setup of Figure 4, the output pressure obtained from the prototype using SMA spring actuators was measured after having connected the two outlets to a SWCN-V01-P3-2 digital manometer (Camozzi, Brescia, Italy). These last two tests were performed three times per sample.
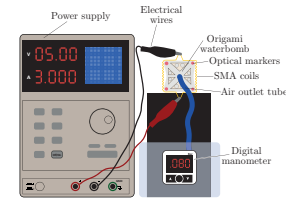

Fig. 4: Schematic of experimental setup.

IV. RESULTS AND DISCUSSION

Results from the aforementioned tests are shown, for just one representative sample, in Figure 5. Regarding the compression test, it is possible to see that, after a peak in the compression force, it starts decreasing: this happens once the sides begin to fold inside the origami. The maximum force was over-dimensioned considering 2 N as a reference value to select the shape memory wires between the available ones.

Concerning the contraction rate, it was possible to observe that the two sides of each sample had different actuation timings, likely due to fabrication differences in the silicone, SMA spring actuators and in their coupling technique with silicone glue, which can have uninvestigated thermal effects. However, it was possible to identify a heating phase, an activation phase, and a stabilization phase and, by considering an estimate of the origami waterbomb volume obtained applying its analytical volume formulation, to find out the compression rate, fitting the activation phase with a line.

Considering only one side it was found, as expected, that actuation timing only depends on the driving current value: the higher the current, the higher the power dissipated by
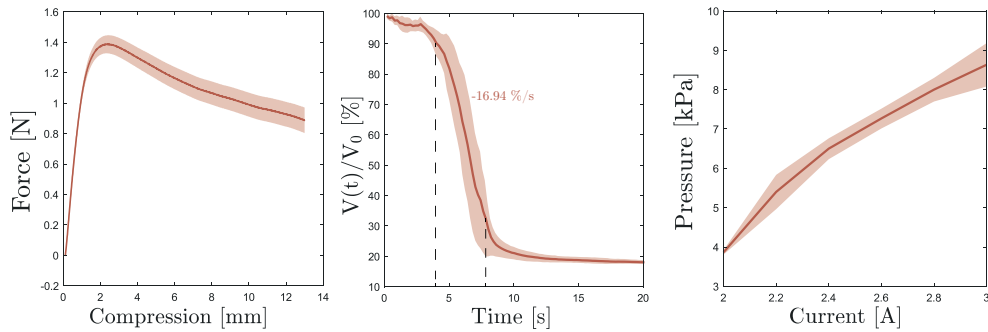
Fig. 5: Results obtained for the origami waterbomb sample 1. *Left*: mean force required for compression; *Center*: mean volume variation over time; *Right*: mean maximum output pressure produced in function of the total driving current.

Joule effect while the actuator is heating faster. When the activation temperature is reached, the change of shape occurs immediately. The high values of driving current are a major drawback to the system: for this reason a further design optimization step, in terms of total number of SMA and their electrical connection, is fundamental.

In the same activation time interval, higher values of output pressure are obtained for higher driving current values, as shown in Figure 5 (right), until a maximum value of approximately 9 kPa. Further optimization of the SMA design could decrease the driving currents, while other parameters to take into consideration are pressure losses along tubings.

Although a fully characterized prototype would need a design optimization and an improved control of SMA and flow rate measures, as a first step towards a scalable system, we have achieved a lightweight and low profile device (side length: 3 cm; weight: 18 g) capable, as shown by Figure 6, of delivering an output specific pressure in line with the values presented in the state of the art.

V. CONCLUSION

While serving as an additional validation of the robogami design methodology of [12], and contributing in laying down the foundations of a formalization of the origami robotics field, this work proposed a proof-of-concept lightweight pumping device, stemming from the need of portable fluidic sources in soft robotics wearable application.
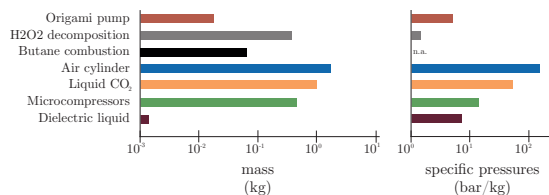

Fig. 6: Comparison, in terms of mass and specific pressures of the proposed origami pump with other existing solutions for on-board pressure generation. Data adapted from [3].

Indeed, for the first time soft robotics principles have been combined with origami solutions to lay the foundations for a novel pressure source device, employable in wearable robotics,

opening up new possibilities and applications of origami in the bioengineering field.

REFERENCES

[1] M. Cianchetti, C. Laschi, A. Menciassi, and Paolo Dario, "Biomedical applications of soft robotics," Nature Reviews Materials, vol. 3, pp. 143–153, Jun. 2018.

[2] F. Schmitt, O. Piccin, L. Barbe, and B. Bayle, "Soft Robots Manufacturing: A Review," Frontiers in Robotics and AI, vol. 5, no. 84, Jul. 2018.

[3] M. Wehner et al., "Pneumatic Energy Sources for Autonomous and Wearable Soft Robotics," Soft Robotics, vol. 1, no. 4, pp. 263–274, Oct. 2014.

[4] M. Adami and A. Seibel, "On-Board Pneumatic Pressure Generation Methods for Soft Robotics Applications," Actuators, vol. 8, no. 1, Dec. 2018.

[5] M. T. Tolley et al., "A Resilient, Untethered Soft Robot," Soft Robotics, vol. 1, no. 3, pp. 213–223, Aug. 2014

[6] A. D. Marchese, C. D. Onal, and D. Rus, "Autonomous Soft Robotic Fish Capable of Escape Maneuvers Using Fluidic Elastomer Actuators," Soft Robotics, vol. 1, no. 1, pp. 75–87, Feb. 2014

[7] R. F. Shepherd, et al., "Using Explosions to Power a Soft Robot," Angewandte Chemie International Edition, vol. 52, no. 10, pp. 2892–2896, Mar. 2013.

[8] P. Polygerinos, Z. Wang, K. C. Galloway, R. J. Wood, and C. J. Walsh, "Soft robotic glove for combined assistance and at-home rehabilitation," Robotics and Autonomous Systems, no. 73, pp. 135–143, 2015.

[9] M. Wehner, Y. L. Park, R. J. Wood, and T. Moore, "Experimental Characterization of Components for Active Soft Orthotics," presented at The Fourth IEEE RAS/EMBS International Conference on Biomedical Robotics and Biomechatronics, Roma, Italy, Jun. 24–27, 2012.

[10] D. Rus and M. T. Tolley, "Design, fabrication and control of origami robots," Nature Reviews Materials, vol. 3, no. 6, pp. 101–112, May 2018.

[11] M. Cianchetti, "Fundamentals on the Use of Shape Memory Alloys in Soft Robotics," in Interdisciplinary Mechatronics, M.K. Habib and J.P. Davim, Ed. Hoboken NJ: John Wiley & Sons, Inc., 2013.

[12] Z. Zhakypov and J. Paik, "Design Methodology for Constructing Multimaterial Origami Robots and Machines," IEEE Trans. Robotics, vol. 34, no. 1, pp. 151–165, Feb. 2018.

[13] F. Schmitt, O. Piccin, L. Barbe, and B. Bayle. "An Origami-Inspired Flexible Pneumatic Actuator," presented at the IEEE/RSJ International Conference on Intelligent Robots and Systems (IROS), Madrid, Spain, Oct. 1–5, 2018.

[14] C. Jianguo, D. Xiaowei, Z. Ya, F. Jian, and T. Yongming, "Bistable Behavior of the Cylindrical Origami Structure With Kresling Pattern," Journal of Mechanical Design, vol. 137, pp. 1–8, Jun. 2015.

[15] C. Jianguo, L. Yangqing, M. Ruijun, F. Jian, and Z. Ya, "Nonrigidly Foldability Analysis of Kresling Cylindrical Origami," Journal of Mechanisms and Robotics, vol. 9, no. 4, Jun. 2017.

[16] M. Follador, M. Cianchetti, A. Arienti, and C. Laschi, "A general method for the design and fabrication of shape memory alloy active spring actuators," Smart Materials and Structures, vol. 21, pp. 115029–115039, Aug. 2012.

A Multibody Model for Ligament Balancing Assessment in Total Knee Arthroplasty

G. Putame[1], M. Terzini[1], S. Borrelli[1], C. Bignardi[1] and A.L. Audenino[1]

[1] PolitoBIOMed Lab, Department of Mechanical and Aerospace Engineering, Politecnico di Torino, Turin, Italy

Abstract— **Total knee arthroplasty (TKA) is the most common surgical procedure for the treatment of chronic degenerative pathologies of the knee. A correct implant positioning together with an optimal ligament balancing are mandatory to achieve the best surgical outcomes. The aim of this study was the development of a prothesized knee multibody model able to provide valuable information for the collateral ligaments balancing. The developed model has proven to be able to predict quantitative information in agreement with experimental studies. Results from implant variations highlight the predominant role of the insert thickness in increasing the forces involved in the knee balance.**

Keywords—**Multibody model, Total Knee Arthroplasty, Collateral Ligaments Balancing, Surgical Preplanning**

I. INTRODUCTION

CHRONIC degenerative pathologies of the knee, such as osteoarthritis, arthrosis and osteoporosis are among the main causes for disability and pain in the modern society [1]. When the non-surgical treatments fail, the implant of joint prothesis after bone resection is usually suggested. Total Knee Arthroplasty (TKA) is the most common surgical procedure for the treatment of these pathologies, and it implies the replacement of the damaged articular surfaces of the knee with metal and plastic components. In general, total knee implants consist of three parts: a femur component, a tibial tray, and an insert. In case of need, also a patellar component can be added. The main goals of the TKA are pain alleviation and recovery of the functional stability of the knee joint. To date, although the surgical procedure is well-established, there is still a revision risk equal to 5% at 10 years [2]. A successful surgical outcome depends on various technical factors including proper bone resection, correct alignment of the implant components, and, above all, an adequate soft tissues balancing. In particular, ligament balancing is a dominant factor in postoperative patient satisfaction and implant longevity [3]. Indeed, excessively tight ligaments can lead to articular pain, stiffness, and reduction of the range of motion. In contrast, overly loose ligaments can generate complications associated with joint instability. In addition, misalignment and imbalance may produce a concentration of the tibiofemoral loads which could trigger wear phenomena at the contact interfaces, thus shortening the implant lifetime. Traditionally, to achieve an appropriate balance, surgeons can adjust implant alignment or perform soft-tissue releases. However, these methods typically rely on the surgeon's experience and his subjective evaluations.

Motivated by the need to minimize the complications caused by the subjectivity of ligament balancing, in the last decades several devices able to provide quantitative intraoperative measurements of the ligament balancing have been developed (e.g. eLIBRA, Zimmer Inc., Warsaw, USA and Verasense, OrthoSensor Inc., Dania Beach, FL). On the other hand, computer-assisted orthopaedic surgery (CAOS) approaches are helping in improving the accuracy of implant three-dimensional alignment [4]. Although these tools provide a more quantitative evaluation of contact forces and alignments, the intraoperative measurement of the ligament forces throughout the flexion motion is still an open challenge being still qualitatively assessed through manual trial movements. In order to address this lack of information, the integration of biomechanical simulations into the surgical procedure appears promising. Recently, some attempts have been made to include biomechanical simulation into the surgical decision-making process for orthopaedic interventions. For instance, a biomechanical guidance system was proposed by Armand and co-workers [5] to intraoperatively simulate different tasks scenarios (e.g. walking, sitting), thus predicting the contact pressure distribution in the hip joint and optimizing the joint alignment in a periacetabular osteotomy. It should be stressed that the implementation of patient-specific models is arduous since they require detailed anatomical information as well as the mechanical properties of the involved biological tissues. However, the development of a properly simplified model, such as multibody models [6]–[9], coupled with the aforementioned sensing devices and CAOS systems, could lead to a better understanding of the joint biomechanics as well as provide more effective information to support surgeons during the surgical preplanning and the intraoperative phases.

In this context, the present study aimed at the implementation of a multibody model of a prothesized knee able to predict the traction forces exerted by the collateral ligaments throughout a passive knee flexion and in the presence of different implant configurations. In order to test the feasibility of integrating the simulation into a clinical pathway, a custom-made software interface was also implemented able to interactively modify the insert thickness and the tibial tray slopes on both the coronal and sagittal planes, thereby, investigating how such variations impact on the ligaments forces.

II. MATERIALS AND METHODS

A. Multibody model

The multibody model of a prothesized left knee (Fig. 1) was created in ADAMS (MSC Software Corporation, Santa Ana, CA) by assembling the geometries of the femur and tibia bones (Sawbones® Europe AB, Malmoe, Sweden) together with a total knee prosthesis (Gruppo BioImpianti s.r.l., Milan, IT). The prosthesis insert consists of polyethylene (UHMWPE) and presents a posterior stabilized design characterized by a

symmetrical mediolateral shape. In order to distinguish between medial and lateral tibiofemoral contact force, the insert geometry was split along its sagittal plane obtaining two symmetrical rigid bodies. Average densities were assigned to the femur (1000 kg/m^3), the tibia (2740 kg/m^3), the implant metal components (4850 kg/m^3) and the polyethylene insert (960 kg/m^3).
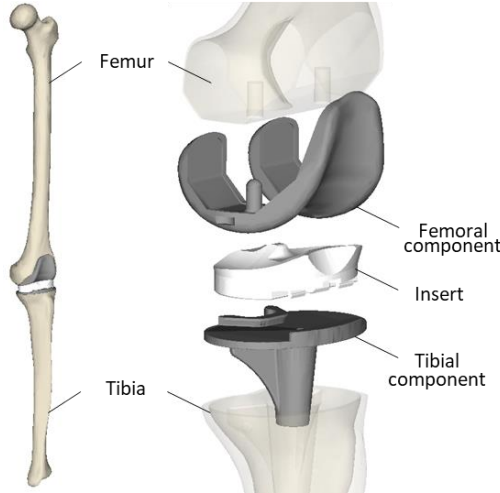

Fig. 1: Prothesized knee model geometry (left) and exploded view showing the TKA implant components (right).

Deformable contacts were defined by means of an Hertz's law-based formulation between the femoral component and each of the two insert parts, also considering a friction force between the articular surfaces [10]. Table I lists the contacts parameters.

TABLE I
CONTACT PARAMETERS

Parameter	Value
Stiffness (K)	72800 N/mm$^{2.5}$
Max damping (Cmax)	966 Ns/mm
Max penetration (δmax)	0.01 mm
Power exponent (e)	2.5
Static friction coefficient	0.03
Dynamic friction coefficient	0.01

The medial (MCL) and lateral (LCL) collateral ligaments were included in the model. Each ligament was split into three bundles, resulting in six bundles in total: MCL anterior (aMCL), intermediate (iMCL) and posterior (pMCL) bundle; LCL anterior (aLCL), superior (sLCL) and posterior (pLCL) bundle. This split allows considering the ligament structure in bundles with their different constraining contribution. Figure 2 shows the positions of the origin and insertion points and the bundles orientations of each ligament.

Ligaments bundles were modelled as nonlinear springs [7], [9], [11] whose force-strain relationship is described by the following nonlinear piecewise function:

$$f = \begin{cases} -k(\varepsilon - \varepsilon_L), & \varepsilon > 2\varepsilon_L \\ -0.25\, k \frac{\varepsilon^2}{\varepsilon_L}, & 0 \le \varepsilon \le 2\varepsilon_L \\ 0, & \varepsilon < 0 \end{cases} \quad (1)$$

where ε is the ligament strain, ε_L is a reference value of strain equal to 0.03 and k is the stiffness parameter, expressed as

force per unit strain, of each different ligament bundle.
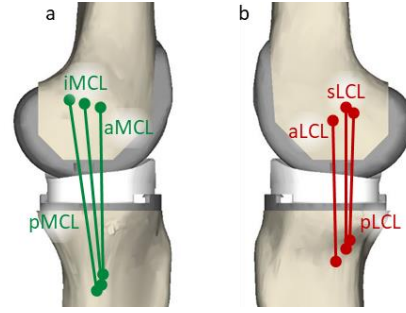

Fig. 2: (a) Medial view of the knee model in extension showing the medial collateral ligament bundles; (b) Lateral view of the knee model showing the lateral collateral ligament bundles.

The adopted stiffness parameters k for each ligament bundle are shown in Table II.

TABLE II
LIGAMENTS STIFFNESS PARAMETERS [12]

Ligament bundle	k (N)
aMCL	2750
iMCL	2750
pMCL	2750
aLCL	2000
sLCL	2000
pLCL	2000

The zero-load length of each ligament bundle was tuned by iteratively performing the simulation of a passive knee flexion and simultaneously adjusting the ligament zero-load lengths following the strategy propose by Guess and co-workers [13] based on two hypotheses: during the passive movement of the knee throughout its range of motion (1) every ligament bundle is stretched, and (2) the force exerted by each bundle should be below 50 N. In particular, in this work, the zero-load lengths were iteratively corrected by steps of 1% with respect to the initial zero-load lengths until the two assumptions were satisfied. Furthermore, the bundles attachment points were adjusted to agree with the bundles recruitment patterns reported in literature [11].

B. Passive flexion simulation

In order to assess the model behaviour, a passive flexion simulation was performed. While the femur was fixed in space, the tibial segment kinematic was restrained proximally by only the contacts and ligaments forces. A bushing element was used to prescribe to the tibia a passive knee flexion ranging from 5° extension up to 110° flexion. This bushing element is defined between a reference part, fixed to the distal tibial segment, and a dummy part connected to the model ground through a revolute joint located between the femoral condyles. In complete extension, the reference and the dummy part are overlapped. When an angular motion is prescribed at the revolute joint, the dummy part rotation causes the activation of the bushing element, which generates a force proportional to the distance d$_x$ between the reference and the dummy part (Fig. 3). Due to this force, the tibial segment is dragged along the flexion until the target flexion angle of 110° is reached. This method (1) allows the imposition of the desired motion regardless of the force required to impose the motion itself,

and (2) minimizes undesired constraints that could affect the measured tibiofemoral contact force.
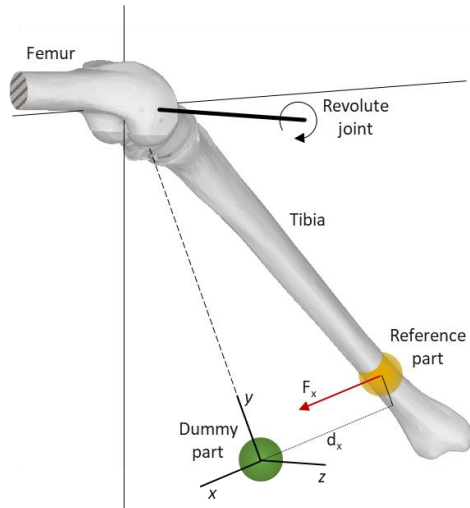

Fig. 3: Schematic diagram of the passive flexion motion imposition. The force (F_x), generated by the bushing, is applied to the tibia along the x axis of the dummy part (green) local reference system. The force magnitude is proportional to the distance (d_x) between the reference part (orange) and the dummy part, measured along the x axis. For sake of clarity, the distance d_x is here oversized.

C. Implant variation

Once the zero-load ligament lengths were optimized, the resulting model was taken as balanced reference configuration to investigate the impact of the insert thickness and tibial tray slope variation on the ligament forces.
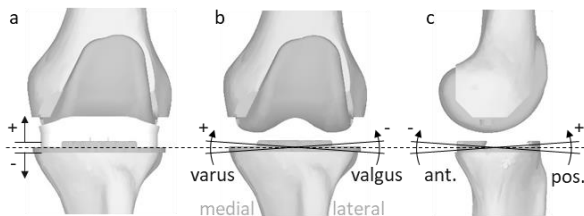

Fig. 4: Insert thickness variation (a), tibial component slope variation on the coronal plane (b) and on the sagittal plane (c).

The insert thickness was therefore varied between ±2 mm by steps of 1 mm, whereas the varus/valgus and posterior/anterior slopes of the tibial component were modified between ±4° by steps of 2°. In the model, the insert distance from the upper surface of the tibial tray was increased and decreased to mimic a higher and lower insert thickness, respectively. Similarly, the tibial component was tilted with respect to a point centred on the tibial tray (Fig. 4).
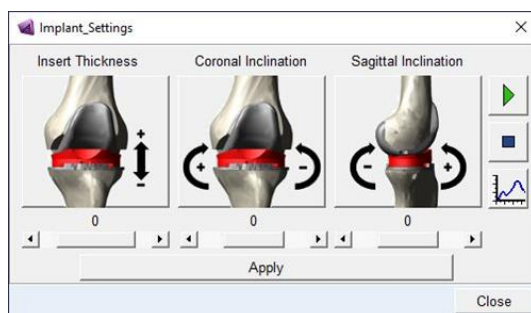

Fig. 5: Custom-made software interactive interface.

A custom-made software interface was implemented (Fig. 5) to interactively modify the implant parameters of the model. In addition, the interactive interface allows for: a quick setting of the model view on the coronal or sagittal plane; the starting and stopping of the simulation; the visualization of the simulation results.

III. RESULTS AND DISCUSSION

A. Balanced condition

The initial ligament refinement allowed obtaining the balanced knee model which was considered as baseline to assess the impact of the different implant variations in terms of generated ligaments forces and tibiofemoral contact forces.
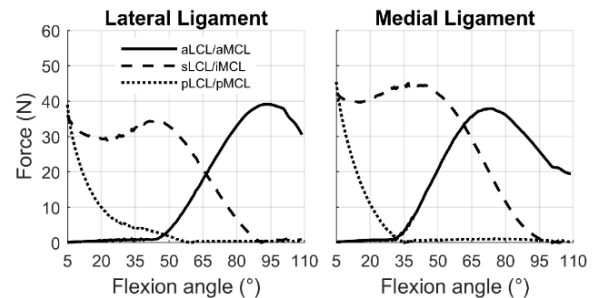

Fig. 6: Ligament traction forces resulting from the balanced condition.

As regards the ligament optimization process, all the obtained bundles traction forces resulted below the threshold of 50 N suggested by Guess [13]. Moreover, the bundles recruitment patterns were found to be consistent with what reported by [11] (Fig. 6). What stands out is the trend similarity in lateral and medial matching bundles. For example, as the lateral posterior bundle force decreases during the passive flexion from 5° to 55°, also the medial posterior bundle force decreases from 5° to 35°.

B. Implant variation

Regarding the implant positioning, Fig. 7 shows that valgus and varus slope changes mainly generate an increase in the lateral and in the medial ligament forces, respectively.
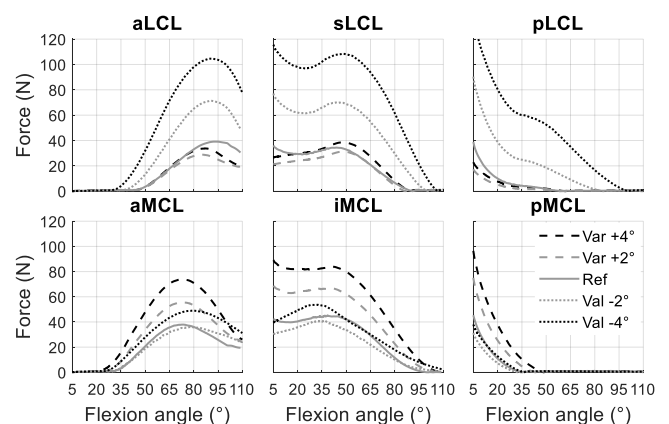

Fig. 7: Impact of the varus/valgus tilt on the ligament forces.

Higher valgus slopes mostly affect the lateral ligament, which results clearly tougher than the medial one. On the other side, varus slopes produce the medial ligament tautening and, secondarily, a partial lateral loosening.

Conversely, changes in the slope of the tibial component on the sagittal plane produces ligaments forces trends not

dissimilar from the reference condition (Fig. 8). Indeed, it is visible in the sLCL graph that the highest force difference corresponds to barely 1.5 times the related reference value. However, higher anterior slopes lead, in accordance with the literature [14], [15], to higher joint forces and vice versa.
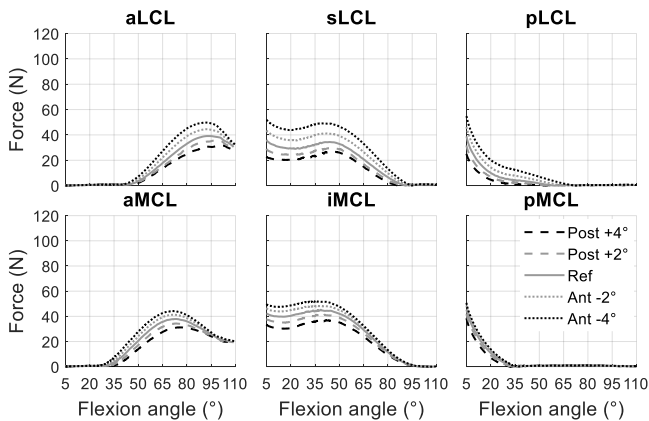

Fig. 8: Impact of the anterior/posterior tilt on the ligament forces.

As far as the insert thickness is concerned, both medial and lateral ligaments are equally affected by an increase/decrease in the bundle force due to the insert thickening/thinning (Fig. 9). What is striking is the significant forces changes caused by the insert thickening with respect to the insert thinning. This is evident in the case of the +2 mm insert for the pLCL, where a 3.3 fold increase with respect to the reference trend is visible at 5° of flexion.
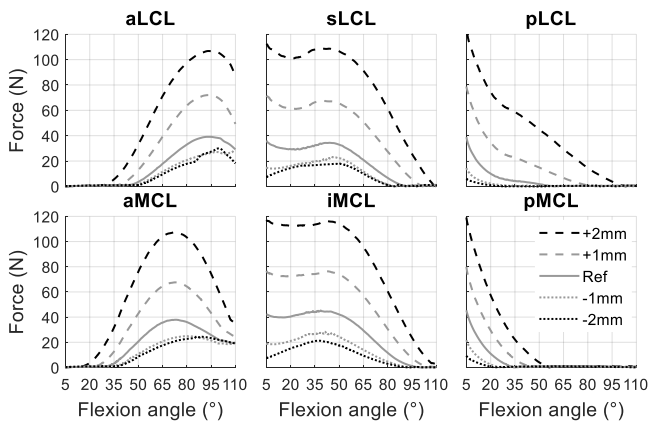

Fig. 9: Impact of the insert thickness on the ligament forces.

Although presenting some limitations, such as the simplification of the soft tissue structures surrounding the knee joint, the only investigation of the passive flexion motion, and the absence of the extensor mechanism of the knee, the model developed in this study has proven to be able to rapidly predict significant quantitative information in agreement with experimental studies. Moreover, the used ligament tuning method, showed its suitability in generating the ligament balancing needed as reference condition. In addition, the performed analysis highlights the high sensitivity of the ligament balancing to variations within 2 mm of insert thickness and 4° of tibial tray slope.

IV. CONCLUSION

Thanks to its computational efficiency (i.e. short simulation time), the here presented model in combination with a

furtherly improved software interface and the already available sensing devices, might be the first step toward the implementation of a valuable tool aimed to assisting the surgeon in both preoperative or intraoperative evaluations of the ligaments balancing during TKA.

REFERENCES

[1]   G. Zheng and L. P. Nolte, "Computer-Assisted Orthopedic Surgery: Current State and Future Perspective," *Front. Surg.*, vol. 2, no. December, Dec. 2015.

[2]   R. Popescu, E. G. Haritinian, and S. Cristea, "Relevance of Finite Element in Total Knee Arthroplasty - Literature Review," *Chirurgia (Bucur).*, vol. 114, no. 4, p. 437, 2019.

[3]   C. R. Smith, M. F. Vignos, R. L. Lenhart, J. Kaiser, and D. G. Thelen, "The Influence of Component Alignment and Ligament Properties on Tibiofemoral Contact Forces in Total Knee Replacement," *J. Biomech. Eng.*, vol. 138, no. 2, Feb. 2016.

[4]   N. Sugano, "Computer-assisted orthopedic surgery," *J. Orthop. Sci.*, vol. 8, no. 3, pp. 442–448, May 2003.

[5]   M. Armand, R. Grupp, R. Murphy, R. Hegman, R. Armiger, *et al.*, "Biomechanical guidance system for periacetabular osteotomy," in *Advances in Experimental Medicine and Biology*, vol. 1093, G. Zheng, W. Tian, and X. Zhuang, Eds. Singapore: Springer Singapore, 2018, pp. 169–179.

[6]   E. Zanetti, M. Terzini, L. Mossa, C. Bignardi, P. Costa, *et al.*, "A structural numerical model for the optimization of double pelvic osteotomy in the early treatment of canine hip dysplasia," *Vet. Comp. Orthop. Traumatol.*, vol. 30, no. 04, pp. 256–264, 2017.

[7]   M. Terzini, E. M. Zanetti, A. L. Audenino, G. Putame, L. Gastaldi, *et al.*, "Multibody modelling of ligamentous and bony stabilizers in the human elbow," *Muscle Ligaments Tendons J.*, vol. 07, no. 04, p. 493, 2019.

[8]   G. Pascoletti, F. Cianetti, G. Putame, M. Terzini, and E. M. Zanetti, "Numerical simulation of an intramedullary Elastic Nail: Expansion phase and load-bearing behavior," *Front. Bioeng. Biotechnol.*, vol. 6, 2018.

[9]   G. Putame, M. Terzini, C. Bignardi, B. Beale, D. Hulse, *et al.*, "Surgical Treatments for Canine Anterior Cruciate Ligament Rupture: Assessing Functional Recovery Through Multibody Comparative Analysis," *Front. Bioeng. Biotechnol.*, vol. 7, no. AUG, pp. 1–11, Aug. 2019.

[10]   A. P. Stylianou, T. M. Guess, and M. Kia, "Multibody Muscle Driven Model of an Instrumented Prosthetic Knee During Squat and Toe Rise Motions," *J. Biomech. Eng.*, vol. 135, no. 4, p. 041008, 2013.

[11]   L. Blankevoort, R. Huiskes, and A. de Lange, "Recruitment of Knee Joint Ligaments," *J. Biomech. Eng.*, vol. 113, no. 1, p. 94, 1991.

[12]   M. A. Marra, V. Vanheule, R. Fluit, B. H. F. J. M. Koopman, J. Rasmussen, *et al.*, "A Subject-Specific Musculoskeletal Modeling Framework to Predict In Vivo Mechanics of Total Knee Arthroplasty," *J. Biomech. Eng.*, vol. 137, no. 2, p. 020904, Feb. 2015.

[13]   T. M. Guess and S. Razu, "Loading of the medial meniscus in the ACL deficient knee: A multibody computational study," *Med. Eng. Phys.*, vol. 41, no. 3, pp. 26–34, Mar. 2017.

[14]   M. Kebbach, R. Grawe, A. Geier, E. Winter, P. Bergschmidt, *et al.*, "Effect of surgical parameters on the biomechanical behaviour of bicondylar total knee endoprostheses – A robot-assisted test method based on a musculoskeletal model," *Sci. Rep.*, vol. 9, no. 1, p. 14504, Dec. 2019.

[15]   Z. Chen, L. Wang, Y. Liu, J. He, Q. Lian, *et al.*, "Effect of component mal-rotation on knee loading in total knee arthroplasty using multi-body dynamics modeling under a simulated walking gait," *J. Orthop. Res.*, vol. 33, no. 9, pp. 1287–1296, Sep. 2015.

Mapping the sEMG distribution over the forearm for grip myotonia characterization: methodological aspects

E. Tricomi[1,2], A. Botter[2,3], P. Tropea[1], G.L. Cerone[2], E. Judica[1], B. Fossati[1],
M. Corbo[1] and M. Gazzoni[2,3]

[1] Department of Neurorehabilitation Sciences, Casa Cura Policlinico, Milan, Italy;
[2] Laboratory for Engineering of the Neuromuscular System (LISiN), DET, Politecnico di Torino, Turin, Italy
[3] PolitoBIOMed Lab, Politecnico di Torino, Turin, Italy

Abstract—**Grip myotonia is one of the main symptoms of Myotonic Dystrophy, a rare neuromuscular disorder caused by a genetic anomaly. To date, myotonic discharges (i.e., delayed relaxation of a muscle after voluntary contraction) are mainly investigated through needle EMG. Surface EMG detected with multiple, closely-spaced electrodes (High Density sEMG - HDsEMG) over a group of muscles allows to identify and study the contribution of individual muscles to a contraction. This feature is potentially relevant in the characterization of myotonia.**

The present study is aimed to investigate the use of HDsEMG to characterize EMG activity distribution of the extrinsic wrist and finger flexors during tasks that usually elicit myotonia. Six healthy subjects underwent experimental examination. According to sEMG amplitude distributions, a grid of 96 electrodes organized in 12 rows and 8 columns is required to identify all the surface muscles contributing to myotonic discharges. As a proof of concept, this finding was tested on a Myotonic Dystrophy patient. The presence of spatially localized regions of muscle activity over the electrode grid was observed.

Keywords—**HDsEMG, Upper limb, Myotonia, Myotonic Dystrophy**

I. INTRODUCTION

MYOTONIC Dystrophy (DM) is one of the most complex pathologies ever known. It is a rare and slowly progressive genetic disorder that affects the neuromuscular system. It is inherited in a dominant pattern and with the worsening of symptoms over time [1]. Up to the present, two forms of DM have been identified: Myotonic Dystrophy Type 1 (DM1 or Steinert's disease) and Myotonic Dystrophy Type 2 (DM2 or PROMM).

Myotonic dystrophy is mainly characterized, among a wide number of symptoms, by the presence of myotonia [1], [2]. Myotonia can be defined as excessive and prolonged muscle excitability and muscle contraction at rest, right after percussion or at the end of the excitatory stimulus [3]. This symptom brings to the visible clinical effect of a delayed relaxation of skeletal muscles resulting in muscle stiffness and pain [4]. Myotonia may affect different muscles, such as facial, tongue, or bulbar muscles, even though one of the main feature of the pathology relies on handgrip myotonia [5].

Needle electromyography is still the gold standard to confirm the presence of myotonic discharges [6]. Nevertheless, due to its invasiveness and limited detection volume, needle EMG presents a number of drawbacks [7], [8]. With the development of High-Density surface Electromyography (HDsEMG), a technique that uses multiple closely-spaced electrodes overlying a muscle or a group of

muscles [9], [10], it became possible to sample the muscular electrical activity over a large surface area and to extract information about the peripheral and central properties of the neuromuscular system in a non-invasive manner [11]. With respect to needle EMG, with surface electrodes the distance and the tissue interposed between the skin and muscle fibres act as a filter decreasing the high frequency components of the EMG signal and, as a consequence, the amplitude. This inherent problem has limited sEMG diagnostic applicability. Nevertheless, the development of analysis of spatio-temporal information provided by grids of electrodes has increased the applicability of the surface EMG method [6].

Focusing on grip myotonia, the muscles of interest are those of the ventral compartment of the forearm, which perform wrist and fingers flexion and wrist pronation. Being small the region of interest and the flexor muscles intertwined, a detection system covering the most of the active area over the flexors should be used to sample the most of the muscle activity. In this context, the optimal detection system should be that allowing to identify different spatial patterns of sEMG activity associated with different hand and fingers movements. This requires an appropriate sampling of sEMG spatial distribution over the muscles of interest.

The aim of the present study was to investigate sEMG distribution over wrist and finger extrinsic flexor muscles to identify the features of the detection system, in terms of dimensions and positioning over the forearm, able to provide a representative information about the activation of these muscles. This is a methodological step for the identification of muscles contributing to grip myotonia in patients with Myotonic Dystrophy.

This preliminary study was performed on healthy volunteers and the results were tested on a patient as proof of concept.

II. MATERIALS AND METHODS

A. Participants

Six healthy subjects were enrolled for the experimental procedure (three females, age: 25±2 years, weight: 61±12 kg, height: 170±10 cm). All subjects reported no upper limb pathologies. Before the beginning of the experiments all subjects signed an informed consent. All research procedures were in accordance with the Declaration of Helsinki and were approved by the Local Ethics Committee (Comitato Etico Milano Area 2, resolution 718_2019bis, ID:1112).

B. Experimental setup

The subjects' right forearm was used for testing. Muscle activity was recorded by a detection system consisting of three bi-dimensional electrode grids, each one composed of 32 Ag surface electrodes equally spaced by 10 mm in rows and columns. The three grids were organized to form a unique electrode grid of 96 electrodes in 12 rows and 8 columns. This detection system covered most of the skin area over the flexor muscles in the ventral portion of the forearm.

Before placing the electrode grid, the skin was accurately scrubbed and a line was drawn between the point of insertion of the distal biceps tendon and the radial styloid process. The length and proximal circumference of the forearm were measured. The length of the forearm was measured as the distance between the point of insertion of the distal biceps tendon and the radial styloid process; the circumference of the forearm was measured at 1/3 of the forearm length starting from the proximal reference point. The grid was then placed aligning the first column with the drawn line, and the first row at 3 cm from the point on the distal biceps tendon insertion.

C. Protocol

Participants seated in a chair with the forearm in horizontal position and mid-pronation at about 120° flexion. Being grip myotonia elicited by tasks involving wrist and fingers flexors, the subjects were asked to perform and maintain for 5 seconds the following isometric contractions: i) wrist flexion with the wrist kept in neutral position; ii) pressing little, ring, middle, and index fingers against the thumb one by one with the other fingers relaxed and the wrist in neutral position; iii) grasping a rigid cylindric object at medium force level; iv) grasping a soft cylindric object at medium force level.

D. Data acquisition

sEMG signals were collected through miniaturized wireless and modular acquisition systems for HD-sEMG (LISiN, Politecnico di Torino and OTBioelettronica) performing the conditioning, sampling, and wireless transmission of monopolar sEMG signals, sampled at 2048 samples/s with 16-bit resolution [12]. Each electrode grid was connected to a module of the acquisition system, and the three modules were connected to a single reference electrode placed over the elbow. Figure 1 shows the detection system with the relative positioning and the modules of the acquisition system.

E. Data processing

The investigation was carried out following the methodology described in [13]. For each subject and each task, the signals collected from the electrode grid were passband filtered between 20 Hz and 400 Hz with a fourth-order Butterworth filter. Signal quality was assessed through visual analysis in the time domain, and bad channels (i.e., sporadic channels showing instable baseline or high power line interference) were replaced using a linear interpolation of the neighbours.

To localize the barycentre of muscle activation over the electrode grid during the performed tasks, the monopolar amplitude distribution of sEMG was obtained computing the root mean square (RMS) of each channel of the grid during a 1-second signal epoch in the middle of the contraction (seconds: 2-3). For the barycentre computation, the channels
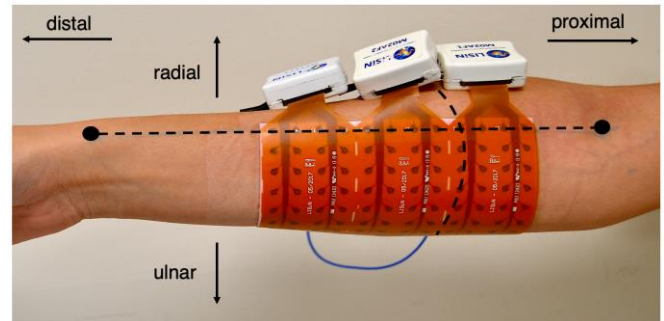

Fig. 1 Position of the detection system over the ventral portion of the forearm and the three modular acquisition systems for HDsEMG. The detection system was placed aligning the first column with the line linking the point on the distal biceps tendon and the one over the radial styloid process, and the first row was placed at 3 cm from the point on the distal biceps tendon.

with an RMS value higher than 70% of the maximum RMS value were identified and considered as the cluster of activation [12]. The barycentre was then computed weighting the RMS values of the identified channels with the respective coordinates over the grid. When more than one cluster of activation was identified in a specific task, a barycentre for each of the identified active areas was computed. Indeed, different clusters could represent different muscles. The position of the barycentre was then normalized with respect to the anatomical measures of the subjects (proximal circumference and length of the forearm, for X and Y coordinates, respectively) and used to compare the location of the active areas among subjects. For the Y coordinate, it was considered that the grid was placed at 3 cm from the insertion point of the distal tendon of the biceps muscle.

In the end, the distribution of the mean number of active channels across the six subjects for each electrode grid was assessed. The last analysis was performed in order to understand if the punctual information of the barycentre could be considered as representative of the whole active area for the requested tasks.

III. RESULTS

The average forearm length was 24.0 ± 1.3 cm (mean ± standard deviation), whereas the proximal forearm circumference was 21.1 ± 7.5 cm.

Examples of colour maps and barycentre identification for each task from a representative subject are shown in Figure 2. For the different tasks a different monopolar sEMG amplitude distribution was obtained. In relation with the defined threshold, almost every task showed only one cluster of activation. Only the task "Wrist Flexion" showed two clusters in every subject, therefore one barycentre for each cluster was identified. The positions of the mean barycentre of the clusters of activation across the six subjects are represented in Figure 3, subdivided by task. The distribution of the barycentres averaged across the six subjects for the tested tasks ranged from 27% to 55% of the forearm length and from 17% to 27% of the forearm circumference.

The bar plots in Figure 4 provide the mean number of the active channels across the six subjects for each matrix with one side standard error. According to the results shown in the bar plots, each grid presents at least the 20% of the total number of channels (32 for each grid) belonging to the cluster of active channels in every task.
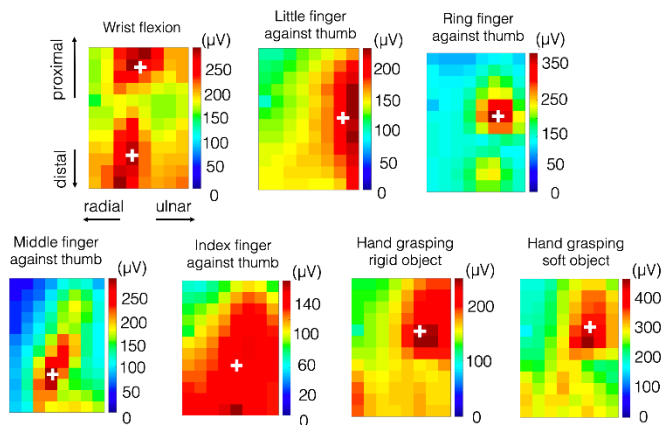
Fig. 2 sEMG amplitude distributions (RMS) over the forearm during the seven tasks of a representative subject (S1). The colour bar ranges from zero (blue) to the peak of amplitude (in µV) of the map (red). The white cross represents the barycentre of the channels that overcome the threshold of the 70% of the maximum RMS value.
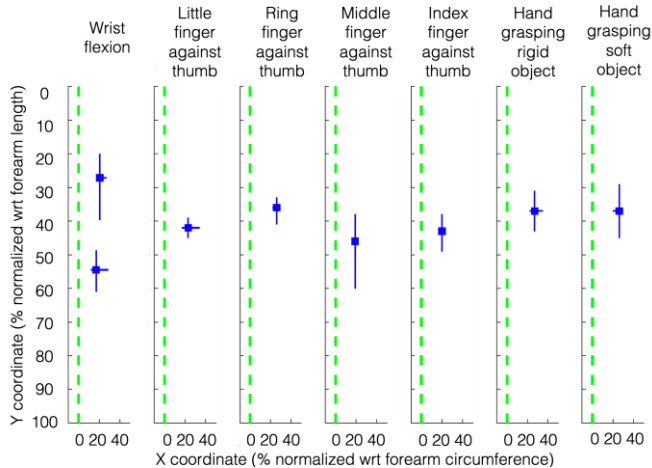

Fig. 3 Barycentre averaged across all subjects shown for each task. The y-axis represents the normalized length of the forearm (0% point of insertion of tendon and 100% the radius styloid process). The x-axis represents the normalized circumference of the forearm. The green, dashed line represents the line linking the point on the distal biceps tendon and the one over the radius styloid process.
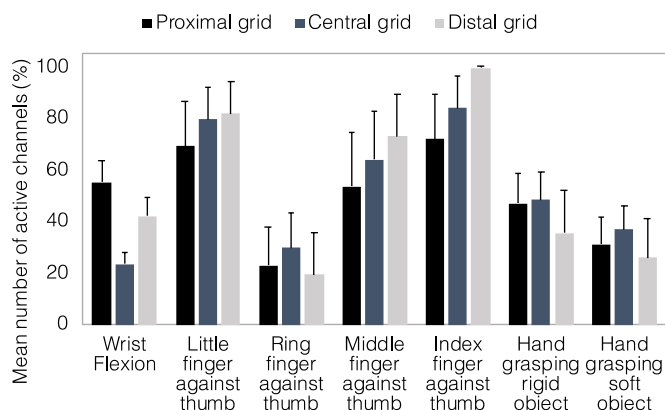

Fig. 4 Number of channels (% of total number of electrodes of each grid) belonging to the activation cluster for each electrode grid and for each task averaged (and standard error) across the six subjects.

IV. DISCUSSION

The purpose of the current study was to investigate the distribution of sEMG activity over the wrist and finger extrinsic flexor muscles to identify the HDsEMG detection system dimension and positioning able to provide a representative information of muscle activation. The long-term goal is to use such a system to non-invasively investigate the activity of individual muscles contributing to myotonia in DM. Indeed, a detection system able to adequately sample muscle activity is necessary when analysing phenomena that may involve the abnormal activation and deactivation of different muscles, such as myotonia.

According to the distributions of the mean barycentre among the subjects, we considered the possibility to reduce the electrode grids from three to two grids (i.e., from 96 to 64 electrodes) to be placed over the 27% and 55% of the forearm length. Indeed, the length of two grids (i.e., 8 cm) could cover this range (i.e., 28% of the forearm length ~ 7 cm).

Nevertheless, considering that the barycentre is a piece of punctual information, the mean barycentre could not always be considered as representative of the active areas for each subject for the tested tasks. Indeed, placing the threshold to identify the most active region at the 70% of the maximum RMS value, in some tasks, a larger cluster of activation was identified. The analysis of the number of active channels in each grid confirmed that in some of the tested contractions (e.g., the tasks Little finger, Middle finger, and Index finger against the thumb) more than the 50% of the total number of channels of each grid belongs to the activation cluster, making the narrow zone identified by the barycentre not so representative of the active region. Since subjects had different dimensions of the forearm and, as a consequence, a different correspondence between the electrodes and the underlying muscles, data about the extension of the clusters of activation showed a high intra-subject variability. On average each electrode grid presented at least the 20% of the 32 channels being part of the cluster of activation. Therefore, relying only upon the mean barycentre and the range and reducing the detection system to two grids, active muscles and portions of the forearm would be excluded. On the above lines, a conservative approach was preferred to avoid the loss of important information regarding the sEMG amplitude distributions over forearm muscles during hand and wrist motor control.

In the present study, we identified the "optimal" configuration in terms of extension of the covered forearm area and positioning of the electrode grids. Thus, the 96-electrodes grid configuration was considered as the detection system able to adequately sample the activity of flexor muscles in the forearm region during fingers and wrist movements.

As limitation of this study, it is important to note that the density of the spatial sampling was not taken into consideration. However, the results shown in Figure 4 seem to suggest that a reduction of the spatial sampling, by increasing the inter-electrode distance (thus reducing the number of electrodes), may allow to maintain the same sampled area. Further study should investigate this issue.

V. PROOF OF CONCEPT

The identified configuration was tested in one DM subject (male; 30 years) recruited through Casa di Cura del Policlinico (CCP), a neurologic rehabilitation hospital in Milan. The subject, with a diagnosis of DM confirmed through DNA analysis, presented clinically evocable myotonia in the upper

limb without upper limb orthopaedic impairment or presence of other severe clinical problems. The enrolled subject was informed about the purpose of the study and signed informed consent forms. The experimentation was approved by the Local Ethics Committee and was in accordance with the Declaration of Helsinki.

The patient was asked to grasp the handle of a handgrip dynamometer for 3 seconds and to release the grip as fast as he could after the 3-seconds contraction. During the relaxation phase, the subject was asked not to stretch the fingers for 10 seconds to avoid the recording of the contribution of finger extensors. This task was repeated for six trials. The presence of myotonia during the relaxation was confirmed by the subject and documented by a neurologist.

The recorded sEMG signals were processed offline. They were bandpass filtered with a fourth-order Butterworth filter with cut frequencies of 20 and 400 Hz and visualized in bipolar configuration. The muscle relaxation phase was analysed to investigate the potentialities of the proposed detection system.

Figure 5 provides a 0.5 seconds epoch of the signals collected from the patient during the relaxation phase following the 3-seconds isometric muscle contraction of the first trial. From a preliminary visual inspection of the collected signals during the manifestation of clinical myotonia, the presence of spatially localized regions of muscle activity over the electrode grid was noticed.
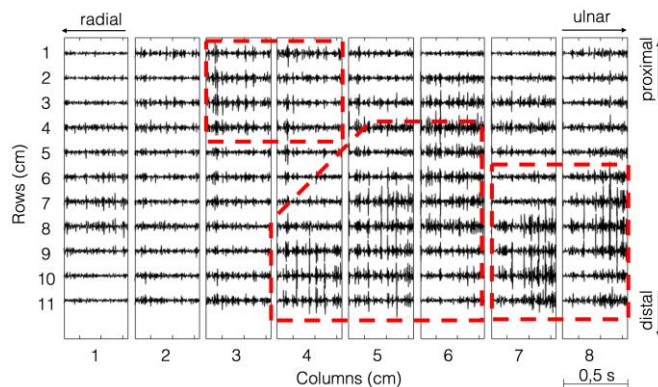

Fig. 5 Half second-epoch of single differential signals collected from a DM patient during grip release after 3 seconds of isometric muscle contraction. The red dashed lines highlight the presence of a sustained localized muscle activity during muscle relaxation phase.

The application of the identified detection system to a real case of documented myotonia and the preliminary analysis of the collected signals (visual inspection) resulted in localized regions of muscle activity. This result may suggest the possibility to discriminate between normal and abnormal muscle activity and, eventually, to spatially identify the muscles or muscle portions involved in the clinically evident poor relaxation by means of the proposed detection system. Even so, this proof of concept brings to the necessity to expand the evaluations to a larger sample of subjects in order to verify the potentialities of the proposed detection system for the investigation of myotonia.

Regarding the technical limitations of the proposed methods, it is important to note the possibility to study the contribution of a limited number of muscles (the superficial ones), crosstalk related problems, and the time required for data analysis and proper quantification [9], [13]. These limitations will be investigated in future studies.

To our knowledge, the applicability of HDsEMG technique for the investigation of myotonia was not documented to date. Since HDsEMG allows the investigation of global muscle activity information as well as single motor units properties and recruitment, it may represent a valid technique to analyse the phenomenon of myotonia. In this scenario, the possibility to identify muscles involved in the abnormal muscle activity may be helpful for different clinical purposes, such as a targeted upper limb rehabilitation or a modulation of the pharmacological treatment.

VI. CONCLUSION

In order to offer a representative information of muscle activation of flexor muscles in the forearm to investigate their individual contribution during myotonia in DM, a 96-electrodes grid configuration was considered an appropriate detection system.

The proof of concept on a Myotonic Dystrophy patient suggested that the outlined detection system may be able to identify the different regions of the ventral portion of the forearm involved in a persisted muscle activity. Hence, the preliminary results bring to hypothesize the applicability of the identified detection system for the study of myotonia in DM and other related neuromuscular diseases.

REFERENCES

[1] A. Aldehag, H. Jonsson, J. Lindblad, A. Kottorp, T. Ansved, and M. Kierkegaard, "Effects of hand-training in persons with myotonic dystrophy type 1-a randomised controlled cross-over pilot study," *Disabil. Rehabil.*, vol. 35, no. 21, pp. 1798–1807, 2013.

[2] L. Machuca-Tzili, D. Brook, and D. Hilton-Jones, "Clinical and molecular aspects of the myotonic dystrophies: A review," *Muscle and Nerve*, vol. 35, no. 21, pp. 1798–1807, 2005.

[3] T. Kurihara, "New classification and treatment for myotonic disorders," *Internal Medicine*, vol. 44, no. 10. pp. 1027–1032, 18-Nov-2005.

[4] M. K. Hehir and E. L. Logigian, "Electrodiagnosis of Myotonic Disorders," *Phys. Med. Rehabil. Clin. N. Am.*, vol. 24, no. 1, pp. 209–220, 2013.

[5] G. Meola, "Clinical aspects, molecular pathomechanisms and management of myotonic dystrophies," *Acta Myol.*, vol. 32, no. 3, pp. 154–165, 2013.

[6] A. Fuglsang-Frederiksen, "The role of different EMG methods in evaluating myopathy," *Clin. Neurophysiol.*, vol. 117, pp. 1173–1189, 2006.

[7] A. Holobar, D. Farina, M. Gazzoni, R. Merletti, and D. Zazula, "Estimating motor unit discharge patterns from high-density surface electromyogram," *Clin. Neurophysiol.*, vol. 120, pp. 551–562, 2009.

[8] M. J. Zwarts and D. F. Stegeman, "Multichannel surface EMG: Basic aspects and clinical utility," *Muscle and Nerve*, vol. 28, no. 1. pp. 1–17, 01-Jul-2003.

[9] G. Drost, *High-density surface EMG: pathophysiological insights and clinical applications*. 2007.

[10] G. Drost, D. F. Stegeman, B. G. M. van Engelen, and M. J. Zwarts, "Clinical applications of high-density surface EMG: A systematic review," *J. Electromyogr. Kinesiol.*, vol. 16, pp. 586–602, 2006.

[11] R. Merletti, A. Holobar, and D. Farina, "Analysis of motor units with high-density surface electromyography," *J. Electromyogr. Kinesiol.*, vol. 18, no. 6, pp. 879–890, 2008.

[12] G. L. Cerone, A. Botter, and M. Gazzoni, "A modular, smart, and wearable system for high density sEMG detection," *IEEE Trans. Biomed. Eng.* **66**, 3371–3380 (2019)

[13] A. Gallina and A. Botter, "Spatial localization of electromyographic amplitude distributions associated to the activation of dorsal forearm muscles," Front Physiol. 2013 Dec 13;4:367.

Poincaré Image-Based Atrial Fibrillation Detection for Photoplethysmography Signals

G. García-Isla[1], V.D.A. Corino[1], and L.T. Mainardi[1]

[1] *Dipartimento di Elettronica, Informatica e Bioingegneria (DEIB), Politecnico di Milano*

Abstract—Early atrial fibrillation (AF) detection is of major importance to prevent thromboembolic events and myocardial tissue deterioration among others. Given the asymptomatic nature of many AF episodes, its detection can be challenging. Photoplethysmography (PPG) monitoring technology is accessible to the general public and could be used for mass screening of AF. In this paper a Poincaré Image and Altas-based methodology is applied to PP intervals in order to evaluate its capacity to detect AF.

Simulated PPG signals with a 30 dB signal to noise ratio (SNR) were used. One hundred signals were simulated for AF and one hundred for normal sinus rhythm (NSR). Poincaré plots were built using a time window of 60, 30 and 20 s. Poincaré Images were then computed using the Poincaré Plots with a bin size of 20 ms and a X and Y limit of (-800,800) ms. 80% of the Poincaré Images of each rhythm were used to create the Poincaré Atlases by averaging the Images. The remaining 20% were classified using normalized mutual information (MI) metric. The process was iterated in a ten fold cross-validation.

AF classification attained an accuracy of 93.89%±2.16, 93.10%±1.47 and 89.47%±3.10 for the time windows of 60, 30 and 20 s, respectively. Results demonstrate the capability of the method used to detect AF episodes and to classify both RR intervals extracted from ECG signals and PPG PPi. A wider PPG dataset with more cardiac rhythms could be used to evaluate the performance in classifying other rhythms.

Keywords—Inter-systolic series (PPi), arrhythmia, cardiac monitoring, mutual information (MI).

I. INTRODUCTION

Atrial fibrillation (AF) is the most prevalent cardiac arrhythmia, affecting 1-2% of global population. It is characterized by a pathological atrial depolarization pattern and an irregularly irregular ventricular activation. In spite of not representing a direct life-threatening condition, AF increases the risk of thromboembolic events and is linked to a deterioration of myocardial tissue and high morbidity and mortality levels. The early detection and monitoring of its development is of major importance in order to apply the correct treatment and prevent these late events. Nevertheless, many paroxysmal AF (PAF) episodes remain asymptomatic, which makes their detection challenging [1].

AF mass screening could help diagnose patients on time. The initiation of an appropriate treatment could prevent myocardial tissue deterioration, an unexpected thromboembolic event or even cardiac failure. Cardiac monitoring has been typically performed through electrocardiogram (ECG) recordings using different devices, from a 12 lead ECG to implanted loop recorders (ILR) to hand-held recorders. Currently ILR are the only long-term monitoring alternative that provide a constant registering for a prolonged period of time. However, they cannot be used to screen global population due to the high costs implied and the need of a invasive procedure for implantation of the device. ILR are only implanted on patients under AF risk or that had already suffered from AF at some point. Likewise, event recorders are typically based just on short 30 s registration, which makes the detection of asymptomatic paroxysmal AF episodes rather difficult. Other ambulatory ECG devices as 24 or 48 hours Holter monitoring are only used when a risk is suspected or after an anomalous event, as they require of manual data revision by a cardiologist. Furthermore, they also do not guarantee that a paroxysmal event can be captured during the 24 or 48 hours recording [2]. The emerging noninvasive photoplethysmography (PPG) technology, integrated in smartphones, wristbands and smartwatches could help in the detection of PAF episodes accessible to the general public. PPG is a technique that allows to monitor the haemodynamical changes of the vascular system. It is based on an optical technology by which the tissue is illuminated by an emitting source with light of a certain wavelength and its reflection or diffusion is captured by a receptor [3]. After identification of systolic peaks position, the inter-systolic series (PPi) can be derived and analyzed similarly to the RR interval series [4].

In this paper we explore the possibility of using a methodology previously described in [5] and applied on ECG signals, to classify PPi intervals obtained from simulated PPG signals in AF and normal sinus rhythm (NSR). This methodology relies on the computation of Poincaré Images and Poincaré Atlases that capture the mean behaviour of ventricular activation during different cardiac rhythms. Other studies relying only on RRi were based on the description of certain parameters and thresholds describing ventricular patterns [6]–[9]. Differently, the applied methodology uses ventricular activation represented on the Poincaré Plot as a whole, rather than as a combination of parameters that may offer an incomplete description of RRi behaviour.

II. MATERIALS AND METHODS

A. PPG data

PPG signals included in the study were simulated according to [4]. The model uses RR interval series, obtained from annotated ECG recordings, as input for generating a PPG signal. The model accounts for the presence of premature beats by introducing amplitude and time scale factors which modify pulse width and amplitude, thus making it possible to simulate

ectopic beats and certain rhythms such as bigeminy known to cause false alarms in RR interval-based AF detection. Two-hundreds PPG signals (100 in AF and 100 in NSR) corresponding to 300 RR intervals were generated. Systolic and diastolic peak positions were identified as in [10]. The inter-systolic series was computed (PPi) and further analyzed.

B. Image generation

In ECG signals, the Poincaré plot is the graphical representation of one RR interval, RR_i, versus the previous one, RR_{i-1}. A different version of the Poincaré plot that follows the same criteria, uses the δRR instead, defined as Eq. 1

$$\delta RR_i = RR_{i-1} - RR_i \tag{1}$$

Even though Poincaré Plots are typically used for RR data, the same concept can be applied to the PP intervals found in PPG signals. For each PPG signal a sliding window of 20, 30 and 60 s without overlap was used to generate the δRR Poincaré plots from the previously computed PPi. Poincaré Images were computed from the Poincaré plots as previously described in [5]. Each Poincaré plot was discretized into its pixelated version as a 2D histogram. The bin size used to generate the pixels was 20 ms. The counting of the number of $(\delta PPi_n, \delta PPi_{n-1})$ points of the Poincaré plot present inside the limits of a determined bin, accounted for the resultant value of each bin. A common range of (-800, 800) ms was established for all Poincaré plots prior to conversion to Poincaré Images. The dimensions of all the resultant Images were [80x80] pixels. Values in individual Images were then converted into probability maps and transformed into the uint16 scale in order to be discretized.

C. Poincaré Atlases

Poincaré Atlases attempt to capture and represent the typical pattern represented by a certain cardiac rhythm as registered by PPG. Atlases were created using the 80% of the Poincaré Images generated for each of the rhythms; NSR and AF. They were computed by averaging the probability maps of the Poincaré Images as in Eq.2

$$A_r = \frac{1}{M_r} \sum_{m=1}^{M_r} \frac{P_m^{(r)}}{N_m^{(r)}} \tag{2}$$

where $P_m^{(r)}$ is the Poincaré Image of the mth epoch of rhythm r in the dataset, $N_m^{(r)}$ the total number of PP points in the Poincaré Image and and M_r is the total number of Images of rhythm r. Values were posteriorly transformed into uint16 scale.

D. Normalized mutual information

Mutual Information (MI) measures the dependency between two random variables and how one contributes to the degree of uncertainty about the other. It is a metric commonly used in medical image registration for both 2D and 3D images [11], [12]. It captures the statistical relationship between two images by computing two image's joint entropy. MI can be
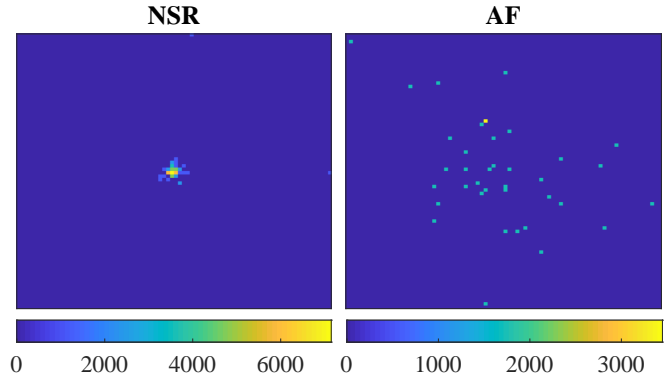

Fig. 1: Example of one of one NSR and AF Poincaré Image for a time window of 60 s and a bin size of 20ms.

described using different mathematical expressions as joint entropy, Kullball–Leibler distance or Shannon Entropy as in Eq.3.

$$I(A, B) = H(B) - H(B/A) \tag{3}$$

where A and B are the two images for which MI is being computed, $H(B)$ is the Shannon Entropy of B and $H(B/A)$ is the conditional entropy of the images' pixels conditional probabilities $p(b/a)$ [13].

MI was computed between each of the remaining 20% of the Images of NSR and AF not used for the computation of the atlas and the two Poincaré Atlases. Individual images were classified as one determined rhythm according to the maximum MI value obtained with the available Atlases i.e. an image was classified as AF only if the value if

$$MI(P_m^{(r)}, A_{AF}) > MI(P_m^{(r)}, A_{NSR}) \tag{4}$$

Where A_{AF} and A_{NSR} are the AF and the NSR Atlases, respectively. The process was iterated in a ten fold cross-validation for more consistent results.

III. RESULTS

A. Poincaré Images

Table I gathers the number of images generated for each of the rhythms of study using the three time windows as well as the number of signals used to compute them. An example of one NSR and AF Poincaré Images computed for a time window of 60 s and a bin size of 20 ms is displayed in Figure 1.

TABLE I: IMAGES GENERATED FOR AF AND NSR FOR EACH OF THE TIME WINDOWS.

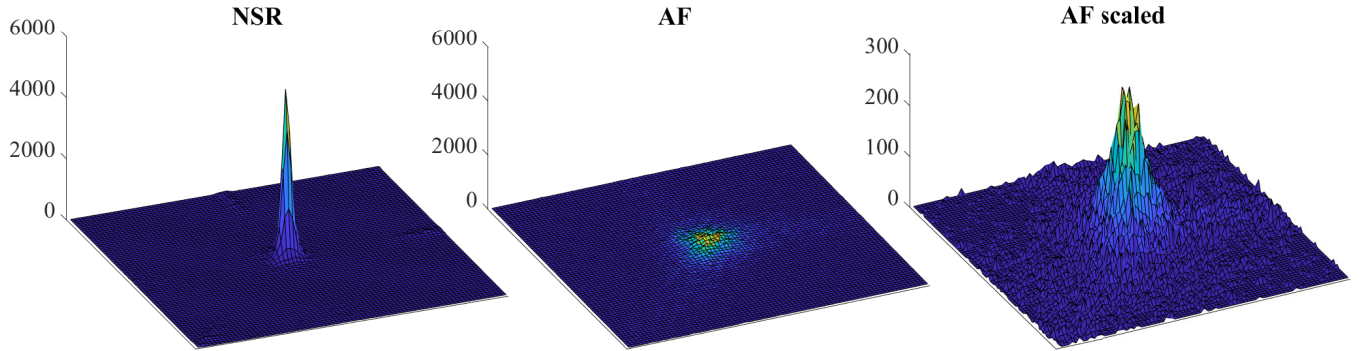| Time Window	NSR	AF	Signals
20 s	1137	1032	100
30 s	738	669	100
60 s	347	311	100

Fig. 2: Example of one of the ten pairs of Poincaré Atlases generated for NSR and AF displayed in 3D dimensions. Values are probability maps values transformed into Uint16 scale. The scale of the AF Poincaré Atlas has been scaled for proper visualization
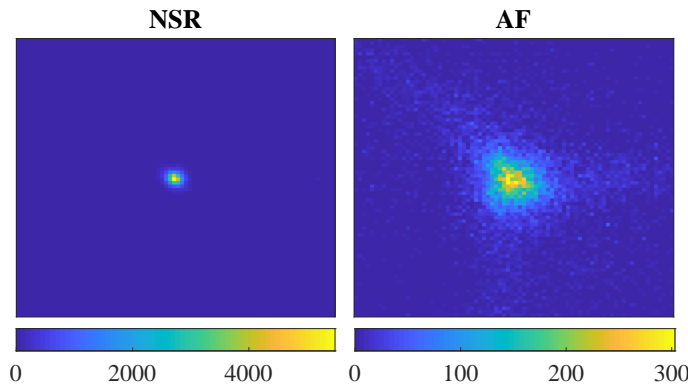

Fig. 3: Example of one of the ten pairs of Poincaré Atlases generated visualized as a Poincaré Image for NSR and AF. Values are probability maps values transformed into Uint16 scale.

Figure 3 represent one of the ten sets of Poincaré Atlases for NSR and AF generated after the ten fold cross-validation for a time window of 60 s and a bin size of 20 ms. Instead, in Figure 2 a 3D version of the Poincaré Atlases can be appreciated.

B. Classification results

Accuracy, sensitivity and specificity values and standard deviations after the ten fold cross-validation are shown in Table II. The values presented correspond to the classification of the 20% of AF Poincaré Images of each time window. As the time window was lengthened the classification performance increased, yielding a 93.89% of accuracy for 60 s. Specificity values was always higher than sensitivity ones.

TABLE II: CLASSIFICATION RESULTS FOR THE DIFFERENT AF TIME WINDOWS AND BIN SIZE 20ms

Time Window	Acc. (%)	Se. (%)	Sp. (%)
20 s	89.47±3.10	93.57±1.07	85.62±6.24
30 s	93.10±1.47	97.70±0.96	88.92±3.11
60 s	93.89±2.16	100±0.00	88.41±4.01

Acc., se. and sp. account for accuracy, sensitivity and specificity, respectively.

IV. DISCUSSION

The main finding of this work is the capability of detecting AF segments on PPG signals using δPPi Poincaré Images. The usage of Poincaré Atlases applied directly on PPG Poincaré Images managed to translate the same methodology applied previously in [5] to pulsatile signals. Guidelines define 30 s as the minimum duration of a relevant PAF episode to be considered AF [14]. However, the best classification results in terms of accuracy, sensitivity and specificity were obtained for a time window of 60 s. Performance worsened as the time window was reduced. Nevertheless, high results over 93% accuracy were yet obtained for a time window of 30 s. This paper represents one of the few that has attempted to apply the same methodology used for AF detection using RRI to detect AF with PPi. Even thought RRi and PPi share many characteristics, they also entail relevant differences both in the intervals themselves and in the amount of noise present in signals of origin.

Given that the memory and power requirements for the algorithm to be implemented are very low, the presented methodology could be suitable for its implementation on a PPG device for a constant patient monitoring. In addition, the high sensitivity achieved could help detect asymptomatic AF as well as more regular episodes. A lower sensitivity could lead to the underestimation of the AF burden suffered by the patient. The proposed classification methodology directly integrates noise into the definition of a rhythm's Poincaré Image pattern by its inclusion in the Poincaré Atlas, relative to each rhythm. By tunning the parameters used to build the Poincaré Images the compromise between sensitivity and specificity could be altered to prevent the hindering effect of noise. Furthermore, arrhythmia detection by Poincaré Image and Atlas analysis could enable its generalization into more rhythms apart from AF and NSR as it was shown on [5]. A wider annotated dataset with other rhythms would be necessary in order to prove this on PPG signals. Being able to capture different rhythms using these signals could provide a cheap and accessible way of cardiac constant monitoring on a broad population and consequently, the premature detection

of possible electrophysiological disorders.

Nevertheless, the vulnerability to noise and artifacts of pulsatile morphology compared to electrocardiographic lead to bad–quality signals, which trigger many false positives [2]. Many algorithms obtaining high performance on AF detection were evaluated on controlled datasets with a rather low amount of noise, not applicable to the real-life ambulatory signals [10], [15]. It is thus, important to be able to quantify and control the amount of noise contained in the signals used for the development and testing of the classification algorithm in order to make it as reliable as possible.

ACKNOWLEDGEMENT

REFERENCES

[1] C. T. January, L. S. Wann, J. S. Alpert, H. Calkins, J. E. Cigarroa, J. C. Cleveland, J. B. Conti, P. T. Ellinor, M. D. Ezekowitz, M. E. Field, K. T. Murray, R. L. Sacco, W. G. Stevenson, P. J. Tchou, C. M. Tracy, and C. W. Yancy, "2014 AHA/ACC/HRS guideline for the management of patients with atrial fibrillation: A report of the American college of Cardiology/American heart association task force on practice guidelines and the heart rhythm society," *Journal of the American College of Cardiology*, vol. 64, no. 21, pp. e1–e76, 2014.

[2] L. Sörnmo, A. Petr, V. Marozas, and P. E. C. G. Databases, "Atrial Fibrillation from an Engineering Perspective," pp. 49–71, 2018. [Online]. Available: http://link.springer.com/10.1007/978-3-319-68515-1

[3] K. H. Shelley, "Photoplethysmography: Beyond the calculation of arterial oxygen saturation and heart rate," *Anesthesia and Analgesia*, vol. 105, no. SUPPL. 6, pp. 31–36, 2007.

[4] A. Sološenko, A. Petrėnas, V. Marozas, and L. Sörnmo, "Modeling of the photoplethysmogram during atrial fibrillation," *Computers in Biology and Medicine*, vol. 81, no. October 2016, pp. 130–138, 2017.

[5] G. García-Isla, V. D. Corino, and L. T. Mainardi, "Cardiac Tachyarrhythmia Detection by Poincaré Plot-Based Image Analysis," in *Computing in Cardiology*, Singapore, 2019.

[6] J. Park, S. Lee, and M. Jeon, "Atrial fibrillation detection by heart rate variability in Poincare plot," *BioMedical Engineering Online*, vol. 8, pp. 1–12, 2009.

[7] S. Sarkar, D. Ritscher, and R. Mehra, "Communications A Detector for a Chronic Implantable Atrial," *IEEE Transactions on Biomedical Engineering*, vol. 55, no. 3, pp. 1219–1224, 2008.

[8] J. Lian, L. Wang, and D. Muessig, "A simple method to detect atrial fibrillation using RR intervals," *American Journal of Cardiology*, vol. 107, no. 10, pp. 1494–1497, 2011.

[9] K. Monahan, Y. Song, K. Loparo, R. Mehra, F. E. Harrell, and S. Redline, "Automated detection of atrial fibrillation from the electrocardiogram channel of polysomnograms," *Sleep and Breathing*, vol. 20, no. 2, pp. 515–522, 2016.

[10] V. D. Corino, R. Laureanti, L. Ferranti, G. Scarpini, F. Lombardi, and L. T. Mainardi, "Detection of atrial fibrillation episodes using a wristband device," *Physiological Measurement*, vol. 38, no. 5, pp. 787–799, 2017.

[11] P. Viola and W. I. William M., "Alignment by Maximization of Mutual Information," *International Journal of Computer Vision*, vol. 24, no. 2, pp. 137–154, 1997.

[12] F. Maes, A. Collignon, D. Vandermeulen, G. Marchal, and P. Suetens, "Multi-modality image registration by maximization of mutual information," *Proceedings of the Workship on Mathematical Methods in Biomedical Image Analysis*, vol. 16, no. 2, pp. 14–22, 1996.

[13] J. Pluim, "Mutual information based registration of medical images," *Ponsen & Looijen*, vol. XX, pp. 1–21, 2000.

[14] A. J. Camm, P. Kirchhof, G. Y. H. Lip, U. Schotten, I. Savelieva, and E. Al., "Guidelines for the management of atrial fibrillation: The Task Force for the Management of Atrial Fibrillation of the European Society of Cardiology (ESC)," *Europace*, vol. 12, no. 10, pp. 1360–1420, 2010. [Online]. Available: https://academic.oup.com/europace/article-lookup/doi/10.1093/europace/euq350

[15] P. H. Chan, C. K. Wong, Y. C. Poh, L. Pun, W. W. C. Leung, Y. F. Wong, M. M. Y. Wong, M. Z. Poh, D. W. S. Chu, and C. W. Siu, "Diagnostic Performance of a Smartphone-Based Photoplethysmographic Application for Atrial Fibrillation Screening in a Primary Care Setting," *Journal of the American Heart Association*, vol. 5, no. 7, pp. 1–7, 2016.

Smoking effect on the circadian rhythm of blood pressure in hypertensive subjects

G. Silveri[1], L. Pascazio[2], A. Miladinović[1], M. Ajčević[1] and A. Accardo[1]

[1] Department of Engineering and Architecture, University of Trieste, Trieste 34127, Italy
[2] Department of Medical, Surgical and Health Care, CS of Geriatrics, University of Trieste, Trieste 34127, Italy

Abstract—The use of office measurement of Blood Pressure (BP) as well as of the mean on day-time, on night-time or on 24h does not accurately describe the changes of the BP circadian rhythm. Moreover, several risk factors affect this rhythm but until now possible alterations, due to the presence of such risk factors considered separately, were not been yet studied. Cigarette smoking is one of the most relevant risk factors increasing cardiovascular morbidity and mortality. The aim of this study is to evaluate quantitatively and with a suitable temporal detail how the smoking influences the BP circadian rhythm in normotensive and hypertensive subjects excluding those who presented other risk factors like obesity, dyslipidemia and diabetes mellitus. Holter BP monitoring coming from 618 subjects was used and the behaviour on 24h was examined separately in normotensive and hypertensive subjects either smokers or non-smokers. Four intervals with alternate different characteristics were found in the BP rhythm and regression lines approximated them in order to evaluate the changing rate of BP in each period. Results showed higher values from 10:00 to 02:00 in hypertensive smokers than non-smokers and significant differences between normotensive smokers and non-smokers between 10:00 and 19:00. The changing rate between 10:00 and 14:30 was higher in non-smokers than in smokers for both normotensive and hypertensive subjects while the opposite was found in the other three periods. The different velocity rates of BP changes during 24h, could be associated with different risk levels of cardiovascular disease.

Keywords—Smoking, Hypertension, Circadian Rhythm, Blood Pressure.

I. INTRODUCTION

BLOOD pressure (BP) is a biological signal that has a circadian rhythm related to the cardiovascular system. The development of cardiovascular disease is mainly associated with the increase of some risk factors like high-density lipoprotein-cholesterol ratio, excess weight, elevated blood sugar level and hypertension. The latter is frequently associated with the incidence of stroke, myocardial infarction, heart failure and death. In hypertensive population, smoking increases the development of cardiovascular events [1]-[2] due to endothelial dysfunction, producing organ damages [3]-[4]. Moreover, it is known that to smoke a cigarette produces, because of vasoconstriction, an acute increase in blood pressure in normotensive subjects for at least 15 minutes, with a peak elevation ranging from 3 to 12 mmHg of systolic blood pressure (SBP) and from 5 to 10 mmHg of diastolic one (DBP) [5]. Moreover, in an epidemiological study, Al-Safi found that normotensive smokers had significant higher office blood pressure compared with non-smokers [6]. However, in order to better evaluate the subjects' physiological condition and to correctly diagnose and manage hypertension, the 24h Ambulatory BP Monitoring (ABPM) has proven to be more appropriate than the conventional office BP measure [7]. Thus,

other studies related to 24h BP monitoring found that, even though office BP levels were comparable between normotensive smokers and non-smokers, ABPM in smokers maintained a higher day-time systolic value than in non-smokers [8]-[9]. This is in contrast with the results of Mikkelsen et al. [10], in which they highlighted in a cohort of normotensive adults from 20 to 79 years old, that smokers exhibited slightly lower BP ambulatory blood pressure compared with non-smokers during day and night.

Furthermore, also in hypertensive subjects smoking has been shown to induce an acute rise in blood pressure in office condition [11]. Comparing hypertensive smokers and non-smokers, Bang et al. found that there was no difference between smokers and non-smokers in office conditions. On the contrary, by using ABPM, they underlined that smokers had a significant higher systolic and diastolic blood pressure in the period between 06:00 and 22:00 (day-time). In addition, they highlighted that the difference between office and day-time ABPM was significant and lower only for diastolic BP in the hypertensive smokers compared to non-smokers [12]. Some studies [9], [13] confirmed a higher day-time BP level in hypertensive smokers compared to hypertensive non-smokers; other authors [14] highlighted that also the mean on 24h was significantly higher in hypertensive smokers while the difference between smokers and non-smokers in the night-time (22:00 to 06:00) was not significant.

However, the use of a single value (office as well as mean on day-time, on night-time or on 24h) only approximatively describes the changes due to the circadian rhythm of BP occurring during 24h. A better temporal definition of the changes occurring in BP during 24h can also be useful to identify with greater accuracy not only possible pressure peaks but also how quickly changes occur in BP.

Therefore, in this study, we examine with a fine temporal resolution how the BP changes along 24h in normotensive and hypertensive smokers compared to non-smokers, in intervals of 15 or 30 minutes. Moreover, to reduce the effects of other cardiovascular risk factors such as obesity, dyslipidemia and diabetic mellitus, which generally are positively associated with BP, increasing its value [15]-[16], we studied hypertensive and normotensive subjects did not present these risk factors.

II. MATERIALS AND METHODS

The study population consisted of 618 subjects afferent to the Geriatric Department of the Trieste, from June 2016 to September 2016. This retrospective study was carried out on subjects who met these inclusion criteria: no clinical or laboratory evidence of secondary arterial hypertension, absence of clinical evidence of hypertension-related

complications and no cardiac disease. According to current guidelines, subjects were classified based on office BP readings, as hypertensive (SBP≥140 mmHg and/or DBP≥90 mmHg) or normotensive (SBP<140 mmHg and DBP<90 mmHg) [17]. The smoking, obesity, diabetes mellitus and dyslipidemia risk factors were collected on physical examination at the time of visit, in accordance with international guidelines [18]. We excluded subjects that presented at least one of these risk factors; the remaining subjects (Table I) were divided into 32 hypertensive smokers (HS) and 113 non-smokers (HNS), 20 normotensive smokers (NHS) and 83 non-smokers (NHNS) presenting comparable age. Non-smokers were defined as those who had not smoked for at least a year. The measurement procedures were in accordance with the institutional guidelines and the principles of Helsinki Declaration. All the subjects gave their informed consent.

TABLE I
SUBJECT GROUPS

| Groups | Age | Gender | |
		Male	Female
NHNS	59±16	46	37
NHS	54±15	13	7
HNS	56±13	58	55
HS	52±14	18	14

The BP was measured in office condition around at 9:00, as the average of two consecutive readings and then in ambulatory way, along the 24h, by using a Holter Blood Pressure Monitor (Mobil-O-Graph® NG, IEM gmbh Stolberg, Germany) [17]. The portable monitor was programmed to obtain ambulatory blood pressure each 15-min interval throughout the day-time (6:00 to 22:00) and each 30-min interval throughout the night-time (22:00 to 6:00). No patient received additional medication that might affect the circadian blood pressure. Written instruction was given on how to use the Holter Blood Pressure Monitor was given to participants individually.

The circadian trend of the mean values of SBP and DBP was separately examined for H, HS, NHS and NHNS subject groups. Since the BP profiles during 24h showed to be bimodal with two maxima and two minima, we subdivided the 24h into four intervals. In each period the quite linear trend was fitted by a regression line. Slopes, intercepts, R^2 and p-value parameters were calculated for each line. Finally, we compared the trends between normotensive smokers and non-smokers and between hypertensive smokers and non-smokers for each interval, by using the Wilcoxon rank sum test (p<0.05).

III. RESULTS

The median values (±1SD) of BP in the four subject groups for each period as well as during day- and night-time are reported in Table II. The differences between circadian SBP and DBP values in hypertensive smokers compared with non-smokers were significant in the three periods between 10:00 and 02:00 (p<0.05) and also considering the day-time from 06:00 to 22:00 (p<0.0001). Moreover, in normotensive

subjects, the difference between smokers and non-smokers was significant only for SBP values between 10:00 and 19:00 (p<0.04), as well as in day-time and night-time (p<0.003).

Figure 1 shows the circadian rhythms of SBP and DBP among the subjects in the four groups and the linear approximations in the four periods in which we separated each rhythm. All the trends decrease between 10:00 and 14:30 and between 19:15 and 02:00, while the increase from 14:45 to 19:00 and from 2:30 to 09:45 and their behavior was approximated, both for SBP and DBP, by linear regressions (Fig.1) presenting slopes that differ among groups and intervals (Tab III).

TABLE II
25TH AND 75TH PERCENTILES OF BP PRESSURES (IN MMHG) IN THE FOUR SUBJECT GROUPS FOR EACH PERIOD AND DURING DAY- AND NIGHT-TIMES. DIFFERENCES BETWEEN SMOKERS AND NON-SMOKERS: #P<0.04, * P<0.05, §P<0.003, $P<0.0001

Systolic BP	NHNS	NHS	HNS	HS
10:00-14:30	124-128#	121-126#	137-143*	142-146*
14:45-19:00	124-126#	121-125#	134-137*	136-144*
19:15-02:00	116-127	112-125	121-138*	126-144*
02:30-09:45	113-122	109-122	120-139	120-134
Day-time	122-127§	120-125§	134-140$	136-145$
Night-time	113-116§	107-113§	118-121	118-125
Dyastolic BP				
10:00-14:30	77-81	77-81	88-90*	88-93*
14:45-19:00	76-78	77-81	83-86*	85-91*
19:15-02:00	68-79	71-79	72-85*	75-91*
02:30-09:45	66-75	68-79	73-86	72-84
Day-time	75-80	77-81	83-88$	85-92$
Night-time	66-68	67-71	69-74	70-77

In particular, the slopes were generally greater for SBP in smokers than in non-smokers (in both hypertensive and normotensive subjects) in the three periods after 14.45 while an opposite trend was present between 10.00 and 14.30 with slope values greater in non-smokers. For DBP the slopes were quite similar among the subject groups, excluded HS, in the three periods after 14.45 while from 14.45 to 02.00 in the HS group, the slopes were much higher. As for SBP, also for DBP, in the first period, between 10.00 and 14.45, the slopes were greater in non-smokers than in smokers.

TABLE III
SLOPES (m IN MMHG/HOUR) AND INTERCEPTS (q IN MMHG) OF THE REGRESSION LINES BETWEEN HOURS OF THE DAY AND BP, IN THE FOUR GROUPS FOR EACH PERIOD. *NO SIGNIFICANTLY DIFFERENT FROM ZERO.

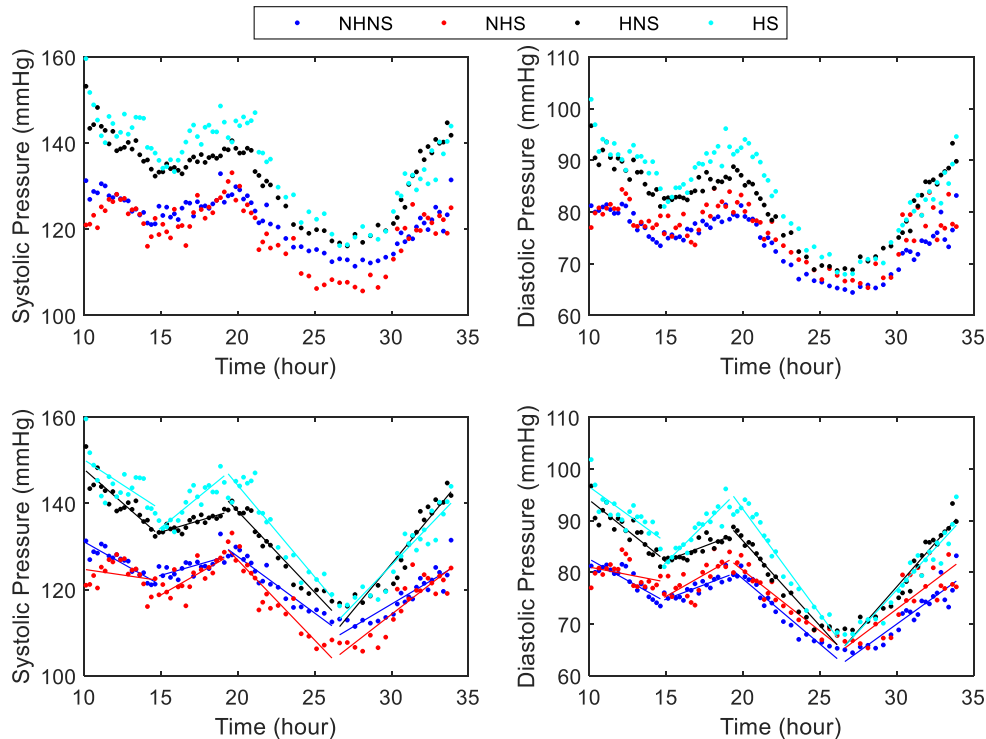| | NHNS | | NHS | | HNS | | HS | |
Systolic BP	m	q	m	q	m	q	m	q
10:00-14:30	-2.01	151	-0.52*	130	-3.13	179	-2.32	173
14:45-19:00	1.03	108	2.04	88	1.06	117	2.92	90
19:15-02:00	-2.62	180	-3.71	201	-3.77	213	-4.25	229
02:30-09:45	2.12	53	2.77	31	4.32	-4	3.71	14
Dyastolic BP	m	q	m	q	m	q	m	q
10:00-14:30	-1.67	99	-0.58*	86	-2.37	118	-2.15	118
14:45-19:00	1.13	59	1.69	50	1.13	65	2.95	38
19:15-02:00	-2.52	129	-2.34	127	-3.28	152	-4.04	173
02:30-09:45	2.15	6	2.24	6	3.39	-24	3.22	-20

Fig. 1:Circadian Systolic and Diastolic BP rhythms in Hypertensive Smokers (HS), Hypertensive Non-Smokers (HNS), Normotensive Smokers (NHS) and Normotensive Non-Smokers (NHNS) together with the linear approximations in the four separate periods.

R-squared determination coefficient presented values between 0.40 and 0.95 for both SBP and DBP, confirming a good linear approximation. The only interval in which the BP presented a quite constant behaviour was between 10:00 and 14:30 in normotensive smokers. In all the other cases the slopes were significantly ($p<0.01$) different from zero.

IV. DISCUSSION

In this study, we considered subjects eventually affected by one cardiovascular risk factor (smoking) not taking into account other risk factors that could modify the circadian BP rhythms. Although the effects of smoking on BP are complex with evidence that it increases the risk of renovascular, malignant and masked hypertension [19], to our knowledge no other authors have studied the influence of smoking on the circadian rhythm separating the effects of other risk factors. Thus, our study is the first that evaluate the effect of smoking on the circadian BP rhythm. To assess BP values, we used the ABPM that is more predictive than office BP in estimating cardiovascular risks because of a more through information.

The study pointed out four well definite periods during 24h in hypertensive as well as in normotensive smokers and non-smokers. One of the main findings was that the normotensive subjects presented higher mean values of SBP in non-smokers than in smokers confirming the result of Mikkelsen [10] although opposite to those of [8]-[9], during day-time. The lower BP values in normotensive smokers presenting between 10:00 to 19:00 cannot be justified by the known pharmacological effect of nicotine that increases the BP [20]. One possible explanation for the lower BP in normotensive smokers could be the tolerance developed of the nicotine effects [18]. On the other hand, hypertensive smokers presented significant higher values than non-smokers along the periods between 10:00 and 02:00 while during the

awaking, the behaviour was opposite. These results confirm the findings of numerous authors [9], [12]-[14] on day-time, enlarging the time interval in which this occurs. The direct pharmacological effects of nicotine in different daily activities reduced during the night-time could explain this fact.

Furthermore, by linearly approximating the behaviour of the circadian rhythm in each of the four characteristic periods, it was possible to analyze as quickly the BP changed along 24h. In particular, in the first period the slopes were different among the four subject groups, showing different velocity changes of BP (both SBP and DBP) with higher values in both hypertensive and normotensive non-smokers than in smokers. On the contrary, in the successive three periods, the smokers had slopes generally greater than non-smokers in both hypertensive and normotensive subjects. The values were similar between smokers and non-smokers only during the third period for DBP in normotensive subjects and the fourth period, the awaking, for SBP in hypertensive subjects. A possible explanation of the latter behavior could be that during awakening, BP variations are mostly regulated by the autonomic nervous system that minimizes the effect of smoking.

The slopes could be used to quantify the morning blood pressure surge as well as the night blood pressure fall, associated with acute cardiovascular effects [21]. Hence, we can conclude that the different linear velocity rates of BP changes during 24h may be associated with different risk levels of cardiovascular disease. However, more clinical data are necessary to confirm this hypothesis.

V. CONCLUSION

Our study allowed describing with an appropriate time resolution the circadian BP rhythm in smokers and non-smokers hypertensive and normotensive subjects. We

highlighted significant differences between smokers and non-smokers in both hypertensive and normotensive subjects, especially during day-time. More interesting, the rates of change of both SBP and DBP in the four intervals were different in the four groups of subjects, higher in non-smokers between 9:00 and 14:30 and in smokers in the other three periods.

REFERENCES

[1] K.S. Lee, C.Y. Park, K.H. Meng, et al., "The association of cigarette smoking and alcohol consumption with other cardiovascular risk factors in men from Seoul, Korea," *Ann Epidemiol*,vol.8, pp.31-8,1998.

[2] A. Menotti, A. Keys, H. Blackburn, et al., " Comparison of multivariate predictive power of major risk factors for coronary artery disease in different countries: results from eight nations of the seven countries study, 25 year follow up," *J. Cardiovasc. Risk*.,vol.3, pp.69– 75,1996.

[3] J.S. Jensen, P. Clausen, K. Borch-Johnsen, et al., "Detecting microalbuminuria by urinary albumin/creatinine concentration ration," *Nephrol. Dial. Transplant.,* vol.12, pp. 6-9, 1997.

[4] R. Pedrinelli, G. Dell'Omo, V. Di Bello, et al., "Microalbuminuria, an integrated marker of cardiovascular risk in essential hypertension," *J. Human. Hypertens.*, vol.16, pp.79-89, 2002.

[5] P.E. Cryer, M.W. Haymond, J.V. Santiago, S.D. Shah, "Norepinephrine and epinephrine release and adrenergic mediation of smoking-associated hemodynamic and metabolic events," *N. Engl. J. Med.*, vol. 295, pp. 573–577, 1976.

[6] S. A. Al-Safi, "Does smoking affect blood pressure and heart rate?," *Eur. J. Cardiovasc. Nurs.*, vol.4, pp.286-289, 2005.

[7] P. Palatini, M. Penzo, A. Racioppa, et al., "Clinical relevance of nighttime blood pressure and of daytime blood pressure variability," *Arch. Intern. Med.*, vol. 152, pp.1855–1860, 1992.

[8] M.S. Green, E. Jucha,Y. Luz, "Blood pressure in smokers and nonsmokers: epidemiological findings," *Am. Heart J.*, vol.5, pp. 932-940, 1986.

[9] S.J. Mann, G.D. James, R.S. Wang, et al., "Elevation of ambulatory systolic blood pressure in hypertensive smokers," *J.A.M.A.*, vol.265, pp. 2226-2228, 1991.

[10] K.L. Mikkelsen, N. Wiinberg, A. Hoegholm, et al., "Smoking related to 24-h ambulatory blood pressure and heart rate: a study in 352 normotensive Danish subjects," *Am. J. Hypertens.*, vol.10, pp. 483-491, 1997.

[11] P.Omvik, "How smoking effects blood pressure," *Blood Press.*, vol.5, pp. 71-77, 1996.

[12] L.E. Bang, L. Buttenschon, K.S. Kristensen, T.L. Svendsen "Do we undertreat hypertensive smokers? A comparison between smoking and non-smoking hypertensive," *Blood Press. Monit.*, vol.5, pp. 271-274, 2000.

[13] K. Soresan, K. Kristensen, L. Bang, T. Svendsen, N. Wiinberg, L. Buttenschon, U. Talleruphuus, "Increased systolic ambulatory blood pressure and microalbuminuria in treated and non-treated hypertensive smokers," *Blood Press.,* vol. 13, pp. 362-368, 2004.

[14] P. Verdecchia, G. Schillaci, C. Borgioni, A. Ciucci, I. Zampi, M. Battistelli, "Cigarette smoking, ambulatory blood pressure and cardiac hypertrophy in essential hypertension," *J. Hypertension*, vol.13, pp. 1209–1215, 1995.

[15] G. Mancia, R. Facchetti, M. Bombelli, et al., "Relationship of office, home, and ambulatory blood pressure to blood glucose and lipid variables in the PAMELA population," *Hypertension*, vol. 45, pp.1072–1077, 2005.

[16] D. Ettehad, CA Emdin, A Kiran, et al., "Blood pressure lowering for prevention of cardiovascular disease and death: a systematic review and meta-analysis," *Lancet*, vol. 387, pp.957–967, 2016.

[17] G. Mancia, R. Fagard, K. Narkiewicz, et al. "2013 ESH/ESC guide-lines for the management of arterial hypertension: the Task Force for the Management of Arterial Hypertension of the European Society of Hypertension (ESH) and of the European Society of Cardiology (ESC)," *Eur. Heart J.*, vol. 34, pp. 2159–2219, 2013.

[18] M.G. Myers, N.L. Benowitz, J.D. Dubbin, et al., "Cardiovascular effects of smoking in patients with ischemic heart disease," *Chest*, vol. 93, pp.14-19, 1988.

[19] A. Virdis, C. Giannarelli, M. Fritsch Neves, S. Taddei, L. Ghiadoni, "Cigarette smoking and hypertension," *Curr. Pharm. Des.*, vol. 16, pp. 2518-2525, 2010.

[20] D. Robertson, C.J. Tseng, M. Appalsamy, "Smoking and mechanisms of cardiovascular control," *Am. Heart J.*, vol. 115, pp. 258-263, 1988.

[21] L. Chen, G. Yang, "Recent advances in circadian rhythms in cardiovascular system," *Front. Pharmacol.*, vol. 6, pp. 71, 2015.

Influence of cartilage thickness on Human Femur Neck: a 3D Stress-Strain Analysis

Andrada Pica[1], Fabiano Bini[1], Andrea Marinozzi[2], and Franco Marinozzi[1]

[1]*Department of Mechanical and Aerospace Engineering, "Sapienza" University of Rome, Rome (Italy)*
[2]*Orthopedy and Traumatology Area, "Campus Bio-Medico" University, Rome (Italy)*

Abstract—**Articular cartilage is a fundamental part of the hip joint. Finite element (FE) analysis is performed on a 3D model of the proximal part of the human femur with the aim to assess the influence of the cartilage thickness on the stress and strain patterns within the bone structure. We considered decreasing values of cartilage thickness in order to mimic structural changes due to aging. A loading condition simulating the stance phase of gait in a healthy subject is applied to the FE model. For different values of the cartilage thickness of the FE model, principal stresses and strains are calculated within a section sited in proximity of the femur neck. The results suggest that cartilage morphology is a parameter that might be studied as one of the factors contributing risk of fracture.**

Keywords — **3D FEM, Human Femur Neck, Articular Cartilage.**

I. INTRODUCTION

THE increase of elderly population is expected to contribute to a rise in the number of femoral neck fractures over the coming decades. Since these fractures account for 50 percent of the proximal femoral fractures and lead to considerable socioeconomic implications [1], there is long standing interest in accurate identification of subjects at risk [2], [3]. Extensive research has been performed to determine the relationships between the structural stability and the geometrical and material factors of bone tissue, namely size, distribution and content of mineral. Computational and numerical modelling have been proposed as powerful non-invasive methods to investigate bone structure and processes [4] – [7]. Generally, finite element (FE) models are used to predict the mechanical response of the femur under different loading scenarios, in healthy and pathological conditions [8] - [14], and to complement experimental studies [15] - [18].

In the hip joint, the articular cartilage, the cortical and trabecular bone form a functional unit that is adapted to transfer the load to the lower joints. The articular cartilage is a soft connective tissue that covers the bone extremities in the synovial joints. It provides a low friction surface that facilitate the motion between the components of the joint [19]. Previous studies have referred that cartilage thickness is a key factor in the appropriate functioning of the joint [19]-[20]. Several works have examined the morphology of the cartilage in the human hip joint and reported the cartilage thickness to be in the range from 0.25 to 3 mm [21]. Investigations have shown that cartilage geometric size varies among individuals and it is influenced by the aging process [20]. A decrease of the cartilage thickness is observed with advancing age, but in absence of pathologies as osteoarthritis, cartilage integrity is preserved [20]. Previous FE studies that incorporated the articular cartilage in the hip joint model have focused their analysis on the mechanical response of the cartilage [22] or in

the stress pattern within the acetabulum region [8]. Thus, the influence of the cartilage geometry on the stress and strain pattern within the femur is not well established. In the present study, we developed a FE model of the proximal part of the human femur and analysed the mechanical behaviour for decreasing values of cartilage thickness. A hip joint loading condition simulating the stance phase of gait is implemented. In this manner, we aim to assess the variations in the stress and strain response in a healthy femur during the aging process.

The results are consistent with the hypothesis that a thicker cartilage minimizes the stress as it provides a distribution of the loads over a larger contact area [19] - [20].

II. METHODS

The 3D geometric model of the proximal half of the human femur is based on Computer Tomography (CT) images provided by the National Library of Medicine in Maryland (USA). The coordinate system follows the ISB recommendations [23] (Fig.1). The 3D geometric model includes an inner trabecular region, an external cortical zone and a cartilage shell that covers the femur head. We investigate the role of the cartilage thickness on the stress and strain distribution by sequentially decreasing the thickness of the cartilage from 3 mm to 0.25 mm with a step size of 0.25 mm [21]. We also considered the condition of femur head without cartilage, indicated successively as 0 mm cartilage thickness case.

A non-uniform FE tetrahedral mesh was generated. A refinement in the regions of femur head and neck (Fig.1a) is developed with mesh elements characterized by edge lengths varying between $0.02t_i$ and $0.1t_i$, where t_i is the thickness of the cartilage, cortical and trabecular region respectively. The minimum size element is 5 μm. In Table 1 we indicate the number of mesh elements and the number of degrees of freedom achieved for the FE model.

We modelled the femur structure assuming linear, elastic, homogeneous and isotropic material behaviour. We assigned the apparent elastic moduli of the cortical and trabecular tissue following the relations [24]:

$$E_{cortical} = 2065 \cdot \rho_{app}^{3.09} \qquad (1)$$
$$E_{trabecular} = 1904 \cdot \rho_{app}^{1.64} \qquad (2)$$

where $E_{cortical}$ and $E_{trabecular}$ are the Young's moduli, expressed in MPa, of the cortical and trabecular regions, respectively. The apparent density ρ_{app} is assumed to be 2 g/cm³ for the cortical bone [24] and 0.7 g/cm³ for the trabecular tissue [24].

The achieved values of the elastic modulus are also in agreement with experimental data [15], [17]-[18]. According to [24], we assume average values for the Poisson's ratio, namely a value of 0.12 for the cancellous bone and 0.3 for the cortical shell. The cartilage layer is characterized by a Young's modulus of 15 MPa and a Poisson's ratio of 0.4 [25].
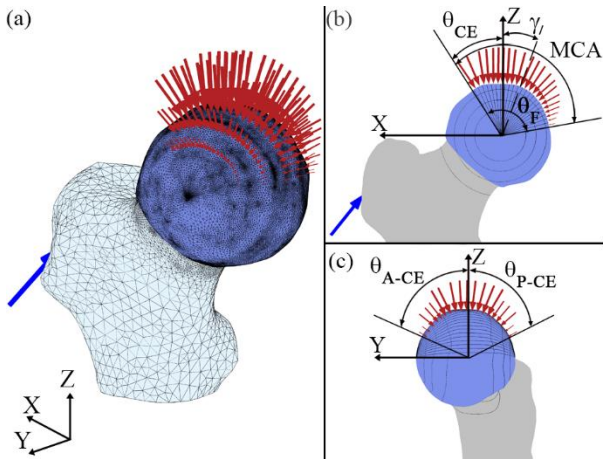
Fig.1: 3D meshed model of the femur. The blue shell represents the femoral cartilage. The red arrows illustrate the load distribution that acts over the femoral head while the blue arrow indicates the concentrated muscular force. In (b) and (c) we showed the load distribution in the coronal plane, i.e. XZ plane, and in the sagittal plane, i.e. YZ plane, respectively, that acts over the most solicited sections.

Appropriate boundary conditions are set to better mimic the load transfer between the acetabulum and the femur head. The size of the main contact area (MCA) is assessed by considering radiographic parameters, i.e. the centre-edge angles of Wiberg (θ_{CE}), that estimate the acetabular coverage of the femur head. According to [12], in the XZ plane, θ_{CE} correlates with the extension of the MCA, characterized by the angle θ_F. For a normal hip, a θ_{CE} value of 30° and a θ_F value of 110° are assumed [12]. In the YZ plane, the estimation of the acetabular contact surface with the femoral head is described by the anterior ($\theta_{A\text{-}CE}$) and posterior ($\theta_{P\text{-}CE}$) angles of Wiberg. According to [26], we set both $\theta_{A\text{-}CE}$ and $\theta_{P\text{-}CE}$ to 60°.

We assumed that the force that acts over the MCA is directed normally to the surface. We supposed friction-free boundary conditions since, in the healthy condition, the articular surfaces are well lubricated and subject to low coefficient of friction [7]. According to experimental data [16] and mathematical models [7], the magnitude of the force distributed over the MCA during the stance phase of gait reaches 244 percent of the body mass. For a typical subject of an estimated mass of 70 kg, the hip joint force corresponds to 1673 N.

We applied a load configuration [7], [12] that simulate the stance phase of gait in a healthy subject. In the XZ plane, i.e. coronal plane, the load distribution is characterized by a cosine function of the angle γ (Fig. 1b), which is defined as the angle between the Z- axis and the generic point on the MCA [7].

TABLE I
Statistics of the FE model

Cartilage thickness (mm)	Number of mesh elements	Degrees of freedom
0	4 815 811	19 490 283
0.25	6 956 326	29 484 189
0.50	7 372 307	30 673 071
0.75	6 935 226	28 751 847
1.00	7 130 359	29 526 891
1.25	7 130 079	29 495 970
1.50	7 464 714	30 765 504
1.75	7 139 926	29 479 209
2.00	6 799 045	27 998 646
2.25	7 131 812	29 427 708
2.50	7 465 010	30 691 488
2.75	7 215 290	29 727 885
3.00	6 767 905	27 918 963

In the YZ plane, i.e. sagittal plane, we adopt a symmetric parabolic distribution of the load on the femur head [12]. The maximum value is achieved in the centre of the contact surface, which is assumed to be in correspondence of the Z-axis (Fig. 1c). A detailed description of the load distribution applied on the MCA is reported in [11].

Apart from the hip joint force, the contribution of the major muscles, that act on the proximal femur during the stance phase of gait is incorporated in the model. As a simplification, the muscle forces were assumed to be applied at the same point, which is scaled [27] to the current geometric model from [28]. The muscle force magnitude and orientation are taken from [28] and indicated in Table II.

The nodes at the distal end of the femur are fully constrained in order to prevent any movement in the plane [9]-[10].

To optimize the computational cost, the stationary FE problem is solved by means of the smoothed algebraic multigrid (SAMG) iterative solver.

III. RESULTS AND DISCUSSIONS

In physiological conditions, articular cartilage has the function to ensure that the joint load is spread over a sufficiently large portion of the articular surface within the femur head [29]. The aging process leads to a progressive thinning of the cartilage, which is simulated in the FE approach by spanning over 13 values of cartilage thickness, namely from 3 mm to 0 mm. We evaluated the principal stress and strain distributions in the most solicited section, in proximity of the femoral neck (Fig. 2). This section is distant from joint surface according to [29].

In Fig. 2 we illustrate the distributions of the principal stress (2a) and strain (2c) predicted in the neck section of the FE model characterized by the thickest cartilage shell, i.e. 3 mm. In Fig. 2b and Fig. 2d we represent the colour map of the incremental values of stress and strain, respectively, that allow to obtain the corresponding distributions in the femur neck in the critical condition without cartilage.

The peak values of the maximum and minimum principal stresses achieved from the femur neck section of the FE model characterized by different values of cartilage thickness are illustrated in Fig. 3. The maximum principal stress represents the first principal stress (σ_1), while the minimum principal stress corresponds to the third principal stress (σ_3). Also in Fig. 4 we depicted the peak values of the maximum and minimum principal strains spanning the values of cartilage thickness considered for the FE model. The maximum and minimum principal strains correspond to the first (ε_1) and third (ε_3) principal strains, respectively.

Mainly, it can be noticed that the progressive decrease of the cartilage thickness leads to an increment of the magnitude of the maximum and minimum principal stresses and strains. We observed an increase of roughly 18 percent of the absolute value of σ_1 and of approximately 13 percent of σ_3 between

TABLE II
Muscular forces

Muscle name	Force magnitude (percent of BW)		
	X	Y	Z
Gluteal muscles	-58	-4.3	86.5
Tensor fascia latae proximal part	-7.2	-11.6	13.2
Tensor fascia latae distal part	0.5	0.7	-19

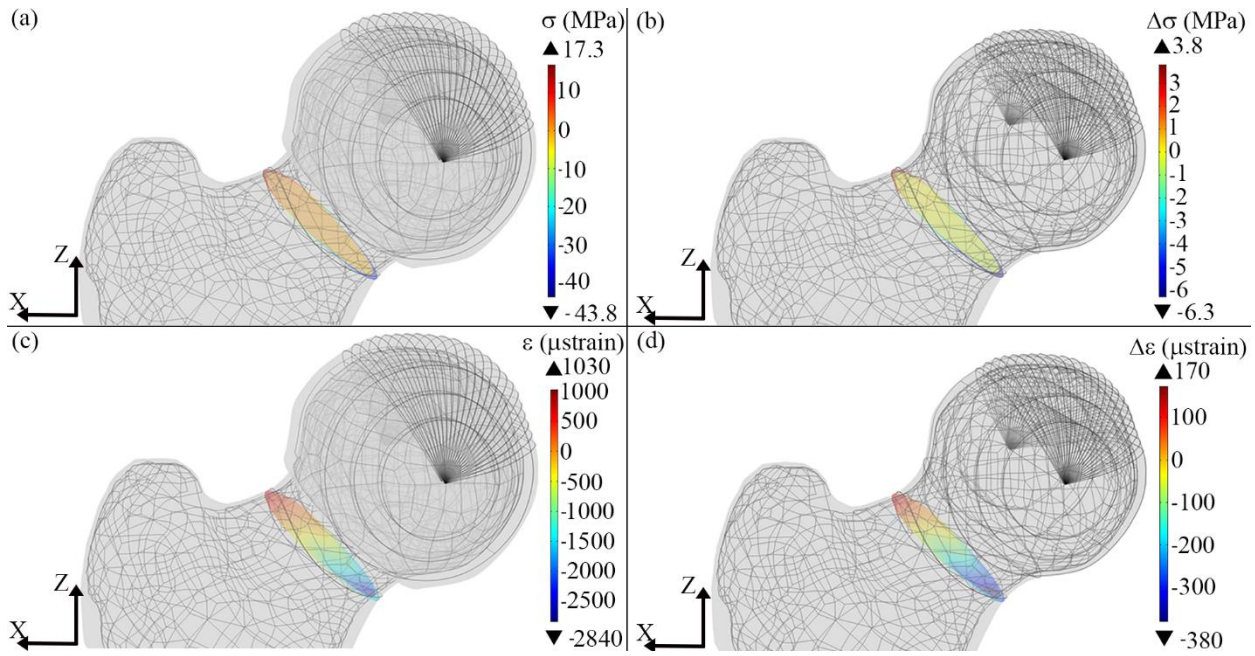The muscular forces (in percentage of bodyweight BW) are expressed in the coordinate system of the femur

Fig. 2: Stress (a) and strain (c) pattern in correspondence of the most solicited slice of the femoral neck for the FE model characterized by 3 mm cartilage shell and incremental values of stress (b) and strain (d) that allow to obtain the stress and strain distribution predicted by the FE model at 0 mm cartilage.

the condition with the thickest cartilage shell, i.e. 3 mm and the case without cartilage, i.e. 0 mm. The peak magnitude of the maximum and minimum principal strains, respectively, follow the same monotonous increasing trend described for the principal stresses. An increment of nearly 14 percent for ε_1 and of 12 percent for ε_3, is assessed between the condition with the cartilage thickness of 3 mm and the theoretical condition of absence of cartilage. Therefore, the diminution of the cartilage thickness enhances the likelihood of structural failure of the femur neck.

The maximum and minimum principal stress and strain achieved in the present study are in the same range with the outcomes of previous FE models that analyse healthy

conditions of the hip joint [30], [31]. The predicted distributions of stress and strain are also consistent with results obtained from experimental measurements [15], [32].

It is worth mentioning that our study has certain limitations. We assumed as structural change due to aging only the variation of the cartilage thickness. Other age-related modifications concerning the subject body mass or bone tissue elastic properties were not considered since the main scope of this study was to assess the impact of the cartilage thickness in the stress and strain patterns. Future investigations should analyse how the variation of multiple parameters affect the structural response of the tissue. Moreover, we adopted the hypothesis of linear, elastic, homogeneous and isotropic
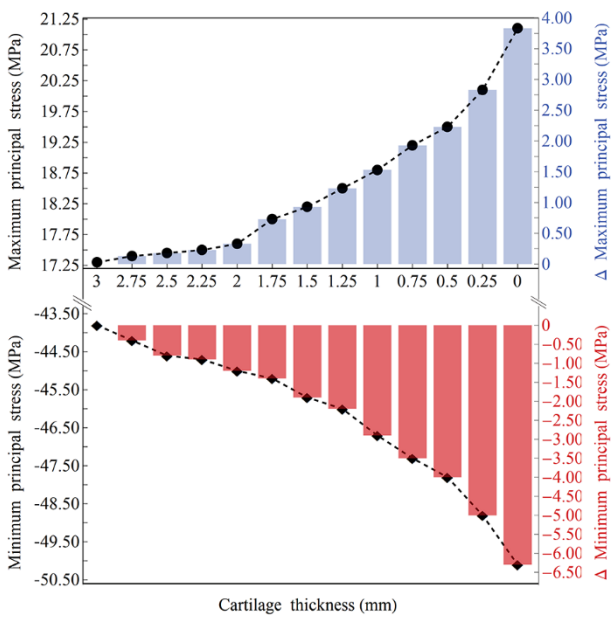

Fig. 3: Peak values of the maximum (dots) and minimum (diamonds) principal stress in correspondence of the most solicited slice of the femoral neck for FE model with cartilage shell spanning from 3 mm to 0 mm. Bar charts represent the increment of stress with cartilage thinning.
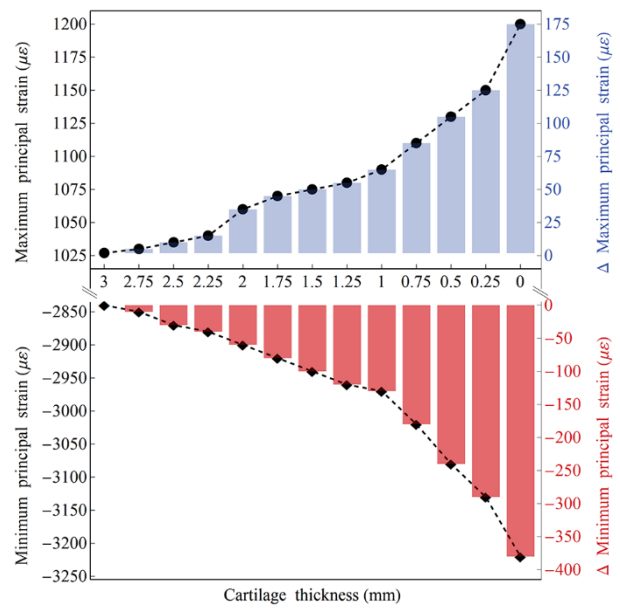

Fig. 4: Peak values of the maximum (dots) and minimum (diamonds) principal strain in correspondence of the most solicited slice of the femoral neck for FE model with cartilage shell spanning from 3 mm to 0 mm. Bar charts represent the increment of strain with cartilage thinning.

material for the femur head. Although this approach is not physiologic, it is frequently used in biomechanical FE models [10], [12], [31] as a first attempt in investigating complex mechanically induced processes in bone.

FE analysis is not introduced in the clinical workflow of the assessment of femoral fracture risk since CT scan does not represent the first-choice exam to investigate it. Emerging techniques [33] allow to develop FE models from X-ray and dual X-Ray absorptiometry scans. In this manner, also the described FE method can be integrated in the clinical protocol.

IV. CONCLUSION

We assessed that the changes in cartilage thickness may meaningfully affect the biomechanics of the femur head. The current outcomes could allow further investigations of the joint behaviour in presence of loading conditions that simulate healthy and pathological gait [34]-[38]. FE approach provides support for predictive studies of risk fracture assessment [2], [3], [13], [14], of properties of bone or bone biosensors [39].

Age associated variations in the articular cartilage provide a basis upon which osteoarthritis can be initiated. The current model could be adapted to investigate the importance of cartilage in the functionality of the hip joint also in age related pathological conditions.

REFERENCES

[1] G. Holt et al., "Changes in population demographics and the future incidence of hip fracture", *Injury, Int. J Care Injured* 40: 722-726, 2009.

[2] M. Terzini et al., "Improving the hip fracture risk prediction through 2D finite element models from DXA images: validation against 3D models", *Front. Bioeng. Biotechnol.*, 7:220, 2019.

[3] Aldieri et al., "Osteoporotic hip fracture prediction: is T-score-based criterion enough? A hip structural analysis-based model", *J Biomech Eng.*, 140(11): 111004, 2018.

[4] F. Bini, A. Pica, A. Marinozzi, F. Marinozzi, "A 3D Model of the Effect of Tortuosity and Constrictivity on the Diffusion in Mineralized Collagen Fibril" *Scientific Reports* vol. 9: 1, Article number 2658,2019

[5] F. Bini, A. Pica, A. Marinozzi, F. Marinozzi, "3D diffusion model within the collagen apatite porosity: an insight to the nanostructure of human trabecular bone" *PLoS ONE* 12(12), e0189041, 2017.

[6] F. Bini, A. Pica, S. Novelli, A. Marinozzi, F. Marinozzi, "3D-FEM Modeling of iso-concentration maps in single trabecula from human femur head", *VipIMAGE 2019 – Proceedings of the VII ECCOMAS Thematic conference on computational vision and medical image processing. J.M. Tavares and R.M.N. Jorge (Editors)*, 2019.

[7] M. Ipavec et al., "Mathematical modelling of stress in the hip during gait", *J Biomech* 32: 1229-1235, 1999.

[8] Ghosh R., Pal B., Ghosh D., Gupta S., "Finite element analysis of a hemi-pelvis: the effect of inclusion of cartilage layer on acetabular stresses and strain", *Comput. Methods Biomech. Biomed. Eng.*, 18:7, 697-710, 2015.

[9] F. Marinozzi, F. Bini, A. De Paolis, R. De Luca, A. Marinozzi, "Effects of hip osteoarthritis on mechanical stimulation of trabecular bone: A finite element study", *J. Med. Biol. Eng.*, 35(4), 535–544, 2015.

[10] F. Marinozzi et al., "A finite element analysis of altered load distribution within femoral head in osteoarthritis", *Comput. Methods Biomech. Biomed. Eng. Imaging Vis.*, 3(2), 84–90, 2015.

[11] F Bini, A. Pica, A. Marinozzi, F. Marinozzi, "Prediction of Stress and Strain Patterns from Load Rearrangement in Human Osteoarthritic Femur Head: Finite Element Study with the Integration of Muscular Forces and Friction Contact", *In Tavares J., Fernandes P. (eds) New developments on computational methods and imaging in biomechanics and biomedical engineering. Lecture notes in computational vision and biomechanics, vol. 33 Springer, Cham*, 2019.

[12] A. Iglic, V. Kralj- Iglic, M. Daniel, A. Macek-Lebar, "Computer determination of contact stress distribution and size of weight bearing area in the human hip joint", *Comput. Methods Biomech. Biomed. Eng.*, Vol. 5 (2), pp. 185–192, 2002.

[13] Z. Altai, M. Qasim, X. Li, M. Viceconti, "The effect of boundary and loading conditions on patient classification using finite element

[14] M. Qasim et al., "Patient-specific finite element estimated femur strength as a predictor of the risk of hip fracture: the effect of methodological determinants", *Osteoporos Int*, 27: 2815-2822, 2016.

[15] F. Marinozzi, F. Bini, A. Marinozzi, "Evidence of entropic elasticity of human bone trabeculae at low strains", *J. Biomech.* 44:5, 988-991, 2011.

[16] G. Bergmann, A. Bender, J. Dymke, G. Duda, P. Damm, "Standardized loads acting in hip implants", *PLoS ONE* 11(5): e0155612, 2016.

[17] F. Bini, A. Marinozzi, F. Marinozzi, F. Patanè, "Microtensile measurements of single trabeculae stiffness in human femur", *J. Biomech.*, 35(11), 1515–1519, 2002.

[18] F. Marinozzi et al., "Technique for bone volume measurement from human femur head samples by classification of micro-CT image histograms", *Ann. I. Super. Sanità*. 49(3): 300-305, 2013.

[19] V. C. Mow, G. A. Ateshian, R. L. Spilker, "Biomechanics of diarthrodial joints: a review of twenty years of progress", *J Biomech Eng.*, 115(4B): 460-467, 1993.

[20] M. Lotz, R.F. Loeser, "Effects of aging on articular cartilage homeostasis", *Bone* 51:241-248, 2012.

[21] H. J. Kurrat, W Oberlander, "The thickness of the cartilage in the hip joint", *J.Anat*. 126: 145-155, 1978.

[22] J. Li, T. D. Stewart, Z. Jin, R. K. Wilcox, J. Fisher, "The influence of size, clearance, cartilage properties, thickness and hemiarthroplasty on the contact mechanics of the hip joint with biphasic layer", *J. Biomech* 46: 1641-1647, 2013.

[23] Wu et al., "ISB recommendation on definitions of joint coordinate system of various joints for the reporting of human joint motion—part I: ankle, hip, and spine", *J Biomech* 35: 543-548, 2002.

[24] D. C. Wirtz et al., "Critical evaluation of known bone material properties to realize anisotropic FE simulation of the proximal femur", *J Biomech* 33: 1325-1330, 2000.

[25] G. E. Kempson, "The mechanical properties of articular cartilage", In *Sokoloff L (Ed.) The joint and synovial fluids*, pp 177-238, 1970.

[26] D. Miyasaka et al., "Three-dimensional assessment of femoral head coverage in normal and dysplastic hips: a novel method". *Acta Med. Okayama*, 68(5): 277-284, 2014.

[27] M. Viceconti, M. Ansaloni, M. Baleani, A. Toni, "The muscle standardized femur: a step forward in the replication of numerical studies in biomechanics", *Proc. IMechE, Part H: Journal of Engineering in Medicine*, 217(2), 105–110, 2003.

[28] M. O. Heller et al., "Determination of muscle loading at the hip joint for use in pre-clinical testing". *J. Biomech.*, 38(5), 1155–1163, 2005.

[29] M. Viceconti, "Multiscale modelling of the skeletal system", Cambridge, Cambridge University Press, pp 89-90, 2011.

[30] J.H. Marangalou, K. Ito, B. van Rietbergen, "A new approach to determine the accuracy of morphology–elasticity relationships in continuum FE analyses of human proximal femur", *J. Biomech* 45: 2884-2892, 2012.

[31] B. Van Rietbergen, R. Huiskes, F. Eckstein, P. Ruegsegger." Trabecular Bone Tissue Strains in the Healthy and Osteoporotic Human Femur." *J Bone Min. Res*, 18, 1781–1788, 2003.

[32] M. M. Juszczyk, L. Cristofolini, M. Viceconti, "The human proximal femur behaves linearly elastic up to failure under physiological loading conditions", *J Biomech*, 44: 2259-2266, 2011.

[33] L. Grassi, S.P. Väänänen, M. Ristinmaa, J.S. Jurvelin, H. Isaksson., "Prediction of femoral strength using 3D finite element models reconstructed from DXA images: validation against experiments", *Biomech Model Mechanobiol*, 16: 989-1000, 2017

[34] M. Iosa et al., "The connection between anthropometry and gait harmony unveiled through the lens of the golden ratio", *Neuroscience Letters*, Volume 612, Pages 138-144, 2016.

[35] M. Serrao et al., "Harmony as a convergence attractor that minimizes the energy expenditure and variability in physiological gait and the loss of harmony in cerebellar ataxia" *Clinical Biomechanics*. 48:15-23, 2017.

[36] M. Serrao et al. "Progression of Gait Ataxia in Patients with Degenerative Cerebellar Disorders: a 4-Year Follow-Up Study", *The Cerebellum*, 16:3; 629-637, 2017.

[37] M. Serrao et al. "Identification of specific gait patterns in patients with Cerebellar Ataxia, Spastic Paraplegia and Parkinson's Disease: a non-hierarchical cluster analysis", *Hum. Movement Sci.*, 57: 267-279, 2018.

[38] M. Rinaldi et al., "Increased lower limb muscle coactivation reduces gait performance and increases metabolic cost in patients with hereditary spastic paraparesis", *Clinical Biomechanics*, vol. 48, pp.63-72, 2017.

[39] R. Araneo et al., "Thermal-electric model for piezoelectric ZnO nanowires", *Nanotechnology*, vol. 26, pp. 265402, 2015.

[*] predicted risk of fracture", *Clin. Biomech. (Bristol, Avon)*, 68: 137-143, 2019.

Modelling the Meal Variability of Individuals with Type 1 Diabetes under Free-Living Conditions

N. Camerlingo[1], M. Vettoretti[1], S. Del Favero[1], A. Facchinetti[1], G. M. Di Nunzio[1], and G. Sparacino[1],
on behalf of the Hypo-RESOLVE Consortium

[1] *Department of Information Engineering, University of Padova*

Abstract—In-silico clinical trials (ISCTs) have been widely used in the last years to accelerate research in Type 1 diabetes (T1D) management. Numerous simulation tools have been proposed in the literature to model the physiological response of T1D patients to meal and insulin inputs, but most of them fail in realistically describing the behavioural and lifestyle factors affecting glucose control. This calls for new investigations, like those carried out in this paper where we develop and validate new models describing the meal variability of T1D patients in terms of carbohydrates amount and timing of the three main meals (breakfast, lunch, dinner) and the snacks. For this purpose, we use a dataset collected in 32 patients with T1D, monitored for up to 6 months under free-living conditions. The developed models will be incorporated in a popular T1D simulator to allow more realistic ISCTs.

Keywords—Type 1 diabetes, behavioural factors, support vector machine, simulation models.

I. INTRODUCTION

TYPE 1 diabetes (T1D) is a chronic metabolic disease characterized by the pancreas inability to produce sufficient amounts of insulin, a hormone responsible for blood glucose (BG) counter regulation. T1D standard therapy consists in diet, physical exercise, and exogenous insulin infusions, which are fundamental to keep BG concentration within the safety range (70 – 180 mg/dL) [1]. The recent advent of continuous glucose monitoring (CGM) sensors, which can monitor glucose concentration almost continuously [2], allows the development of new treatments that can improve T1D therapy [3 – 4]. Before being tested in trials on humans, such innovative treatments can be tested in in-silico clinical trials (ISCTs). ISCTs are widely used in T1D research since they allow carrying out a vast number of experiments that can be repeated under controlled conditions, providing evidence to support and better design trials on humans, with great economical and human cost savings [5]. ISCTs require mathematical models mimicking physiological response and lifestyle of T1D patients. Several simulation tools were proposed in the literature that accurately describe the T1D patient physiology [6 – 8]. However, these simulators do not describe with precision some of the behavioural aspects of patients' lifestyle, which can remarkably affect glucose control. A first attempt to take these aspects into account and enable more realistic ISCTs was made in Vettoretti et al. [9], where a model of the patient's behaviour in making the treatment decisions was proposed to complement the so-called UVA/Padova T1D simulator. However, the proposed model of meal variability was still suboptimal because it considered meal times uncorrelated among each other and did not include a model of the snacks.

In this work, we aim to overcome these limitations by developing models describing the T1D patients' variability in

tuning breakfast, lunch, dinner and snack, under free-living conditions. Specifically, we will derive models describing the carbohydrate (CHO) amount of each meal intake, and the time between two consecutive meals. Then, we will also determine a group of variables that influence the likelihood of consuming a snack during the day.

II. DATASET

In this paper, the models are developed on data collected under free-living conditions by a crossover study made for the AP@home EU project [10]. This study involved 32 patients with T1D aged 18-69 years from three different European medical centres. Subjects were randomly assigned to 2 months of artificial pancreas (AP) from dinner to waking up plus sensor augmented pump (SAP) therapy during the day, versus 2 months of SAP use only. A subgroup of 20 subjects was monitored in a further 1-month trial under AP therapy for all the day [11]. Then, 18 out of the previous 20 subjects underwent the last 1-month follow up with a personalized AP for all the day [12].

The CHO amount and the time of all the meals and insulin injections were reported on a diary during the SAP therapy, and on a smartphone platform [13] during the AP therapy.

III. MODEL DEVELOPMENT

A. Meals labelling

All the meal intakes were labelled as either main meals (i.e., breakfast, lunch and dinner) or snacks in order to model them separately. Firstly, all the "fragmented" meals were detected and assembled. A meal is defined "fragmented" if it is reported by patients as several temporally close sub-meals (e.g., during a lunch, the main course can be reported apart from the dessert, even if they belong to the same meal). Specifically, two meals in the same 25-min window were incorporated in a single meal, whose CHO amount was set equal to the sum of the two sub-meals' CHO amount, consumed at the same time of the earliest sub-meal.

Then, the main meals were identified as those with the bigger CHO amount amongst all the meals registered in specific time windows: 4:00 am – 11:30 am for breakfast, 11:35 am – 4:30 pm for lunch, 4:35 pm – 3:55 am for dinner. The other meal intakes could be either snacks or hypotreatments (i.e., fast acting CHO ingested when low glucose values are detected). Since in the AP scenario the hypotreatments are already labelled, after the main meals identification, all the other CHO consumptions were supposed to be snacks. In the SAP scenario, once the main meals have been identified, the other CHO intakes (i.e., snacks andhypotreatments) were not labelled and, thus, were not

assigned to a specific CHO intake category.

The labelling step provided 11,460 main meals (3,643 breakfasts, 3,837 lunches, 3,980 dinners) and 1,218 snacks.

B. Meal time and amount modelling

To represent the meal habits of the T1D patient, we modelled the following seven quantities: breakfast, lunch, dinner and snack CHO amounts, time between consecutive main meals (i.e., breakfast-lunch and lunch-dinner) and time between snacks and previous main meals. For each quantity of interest, we randomly split the available data into training set (cardinality: 70%) and test set (cardinality: 30%). Training set data were used to fit a set of candidate probability density function (PDF) models. In particular, 10 PDF models were considered: Gaussian, lognormal, loglogistic, gamma, generalized-extreme-value (gev), t-Student, exponential, inverse Gaussian, logistic and uniform. The parameters of these PDFs were estimated by Maximum Likelihood (ML). Each model was then validated on the test set data, by applying the one-sample Kolmogorov-Smirnov (KS) goodness of fit test (significance level α = 0.05), a nonparametric test of the null hypothesis that the population cumulative distribution function (CDF) of the test set data is equal to the hypothesized CDF (fitted on the training set).

Since multiple comparisons between the 10 tested distributions were performed simultaneously, α was lowered by a factor of 45, according to the Bonferroni correction. The procedure was re-iterated for 100 different training-test set splits and the percentage of simulated samples for which the KS test rejected H0 over the 100 iterations was calculated for each model, that is expected to be small if the identified model performs well. Finally, for each quantity, the PDF model providing the lowest rate of rejection is selected as final model and identified on the entire dataset.

C. Determination of predictors for snack time

Unlike the main meals, which are consumed three times per day for almost all the trial, snack consumption is much more irregular: according to the dataset under analysis, the probability of consuming at least one snack per day is 37.14%, with the number of snacks per day ranging between 0 and 6. To model the snack habits of the T1D patient, we looked for possible variables influencing the snack consumption time. Specifically, we derived a classifier able to predict if a snack is present or not in a future time window.

A dataset to derive the model was built as follows. We splitted each subject's trial into 3-hour contiguous windows, and labelled them with "1", if at least one snack was consumed inside the window, or "0" otherwise. Then, the following 15 variables were extracted as possible predictors of the labels: subject's age and body weight (BW), CHO amount of a meal consumed in the previous 1-hour, 4-hour and 6-hour windows and the related time from that meal (if no meal was detected, CHO amount was set to 0 and the time was set to the previous window duration), CHO amount of the last meal intake and time from the last meal intake, mean CGM in the previous 1-hour and 4-hour windows, first CGM value of the current 3-hour window, CGM rate-of-change in the previous 1-h window, time of the current 3-hour window (categorical variable equal to 1, 2, 3, 4 if the first sample of the window is
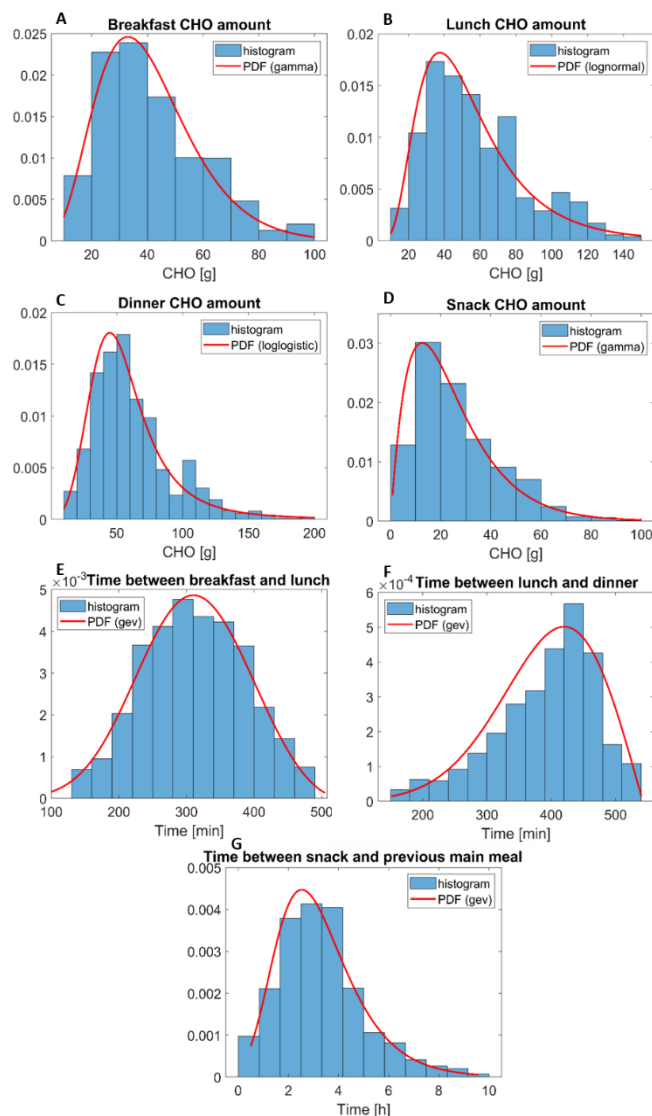

Figure 1. Histograms (blue) and estimated PDF models (red) of the following data: breakfast CHO amount (panel A), lunch CHO amount (panel B), dinner CHO amount (panel C), snack CHO amount (panel D), time between breakfast and lunch (E), time between lunch and dinner (F), time between main meal and following snack (G).

in the interval 5:00 am – 10:55 am, 11:00 am – 4:55 pm, 5:00 pm – 10:55 pm, 11:00 pm – 4:55 am, respectively).

In this way, we obtained a dataset with 8405 observations and 15 features, 1028 observations with label "0", 7377 observations with label "1". The dataset was divided into a training set (80%) and a test set (20%). The features were normalized through the z-score standardization using the mean and the standard deviation of the features in the training set.

The training set underwent a 20-fold CV, resulting in a ranked feature list and an average classification performance measure. As classifier, we implemented a nonlinear Support Vector Machine, which mapped the inputs into a high-dimensional feature space through the Gaussian kernel. At each CV iteration, a recursive feature elimination (RFE) was performed, obtaining a ranking of the features according to their contribution to the area under the Receiver Operating Characteristic curve (AUC-ROC). In particular, at each step of the RFE, the less important feature (i.e., the one that once removed provides the smallest deterioration of AUC-ROC)

was removed. The 20 ranked features lists obtained from the 20 CV iteration were then aggregated into a single ranked list, using the Borda method [14]. The optimal feature number n_{opt} was chosen as the number of feature maximizing the average AUC-ROC value in CV. Finally, the model containing the top n_{opt} variables of the aggregated ranked list was trained on the whole training set and validated on the test set. Since, the score value provided as output by the SVM model is a measure of distance, in order to obtain a probability value, the final model output is given as input to a sigmoid function:

$$S(x) = \frac{1}{1 + e^{-\alpha x + \beta}} \tag{1}$$

which transforms the SVM score into the posterior probability of having a snack. The parameters α and β were fixed by minimization of the classification error in a 10-fold CV over the training set.

IV. RESULTS

Histograms and estimated PDFs of breakfast, lunch, dinner and snack CHO amount, time between breakfast-lunch and lunch-dinner, time between snack and previous main meals, are reported in Fig. 1. Among all the considered PDF models , the ones allowing the lowest rate of rejection of the one-sample KS test were selected. As a result, breakfast and snack CHO amount are modelled by gamma distributions, lunch and dinner CHO amount are modelled by a lognormal and a loglogistic distribution, respectively. Time between breakfast-lunch and lunch-dinner and time between snack and previous main meal are all modelled by gev distributions. Tab. 1 reports the estimated parameters of all the distributions and the rejection rate of the KS test.

The feature selection step provided the average classification performance curve, depicted in Fig. 2, and the aggregated ranked feature list, shown in Tab. 2. Specifically,
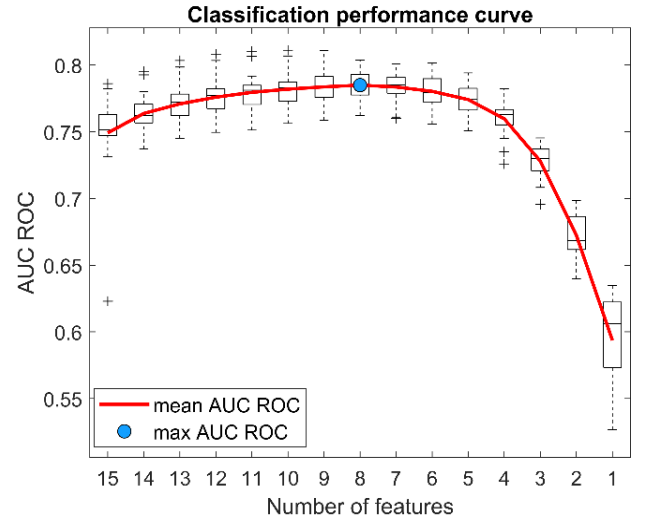

Figure 2. Boxplot of the AUC-ROC for a decreasing number of features, over the 20 iterations of CV. Average curve (red) and maximum AUC-ROC value (blue circle).

Fig. 2 shows the boxplots of the AUC-ROC over the 20 iterations of CV, for a decreasing number of predictors. The red curve represents the mean AUC, whose maximum (blue dot) is obtained with 8 features. Then, the selected features are the 8 features with the highest Borda score in Tab. 2 (reported in brackets): time of the current 3-hour window (272), time from the last meal intake (240), patient's BW (232), patient's age (221), mean CGM of the previous 1-hour window (151), time from the meal consumed in the previous 4-hour window (139), CHO amount of the meal consumed in the previous 4-hour window (130), CHO amount of the meal consumed in the previous 6-hour window (128).

The ROC curve obtained when applying the final SVM model to the test set is reported in Fig. 3. The resulting AU-ROC is equal to 0.756. As further performance metrics, we

TABLE I
MEAL HABITS MODELS

Variable	PDF model	Estimated parameters	KS test rejection rate [%]
Breakfast CHO amount	$F(x; \alpha, \lambda) = \dfrac{\lambda^{\alpha} x^{\alpha-1} e^{-\lambda x}}{\Gamma(\alpha)}$	$\alpha = 5.290$ $\lambda = 7.696$	41
Lunch CHO amount	$F(x; \mu, \sigma) = \dfrac{\exp\left(-\dfrac{(\ln x - \mu)^2}{2\sigma^2}\right)}{x\sqrt{2\pi}\sigma}$	$\mu = 3.884$ $\sigma = 0.518$	30
Dinner CHO amount	$F(x; \alpha, \beta) = \dfrac{\left(\dfrac{\beta}{\alpha}\right)\left(\dfrac{x}{\alpha}\right)^{\beta-1}}{\left(1 + \left(\dfrac{x}{\alpha}\right)^{\beta}\right)^2}$	$\alpha = 0.284$ $\beta = 3.977$	32
Snack CHO amount	$F(x; \alpha, \lambda) = \dfrac{\lambda^{\alpha} x^{\alpha-1} e^{-\lambda x}}{\Gamma(\alpha)}$	$\alpha = 2.060$ $\lambda = 11.88$	2
Time between Breakfast-Lunch	$F(x; \mu, \sigma, \xi) = \exp\left\{-\left[1 + \xi\left(\dfrac{x-\mu}{\sigma}\right)\right]^{-\frac{1}{\xi}}\right\}^2$	$\mu = 282.9$ $\sigma = 79.98$ $\xi = -0.320$	22
Time between Lunch-Dinner	$F(x; \mu, \sigma, \xi) = \exp\left\{-\left[1 + \xi\left(\dfrac{x-\mu}{\sigma}\right)\right]^{-\frac{1}{\xi}}\right\}^2$	$\mu = 374.9$ $\sigma = 84.86$ $\xi = -0.472$	9
Time between Main meal-Snack	$F(x; \mu, \sigma, \xi) = \exp\left\{-\left[1 + \xi\left(\dfrac{x-\mu}{\sigma}\right)\right]^{-\frac{1}{\xi}}\right\}^2$	$\mu = 147.4$ $\sigma = 81.97$ $\xi = -0.016$	6

TABLE II
RANKING OF THE VARIABLES FOR FEATURE SELECTION STEP

Variable	Borda score
Time of the current 3-h window	272
Time from the last meal intake	240
Patient's BW	232
Patient's age	221
Mean CGM of the previous 1-h window	151
Time from the previous 4-h window meal	139
CHO amount of the previous 4-h window meal	130
CHO amount of the previous 6-h window meal	128
CHO amount of the last meal intake	127
Time from the previous 6-h window meal	113
Mean CGM of the previous 4-h window	79
Current CGM	76
CGM rate-of-change in the previous 1-h window	66
CHO amount of the previous 1-h window meal	64
Time from the previous 1-h window meal	62
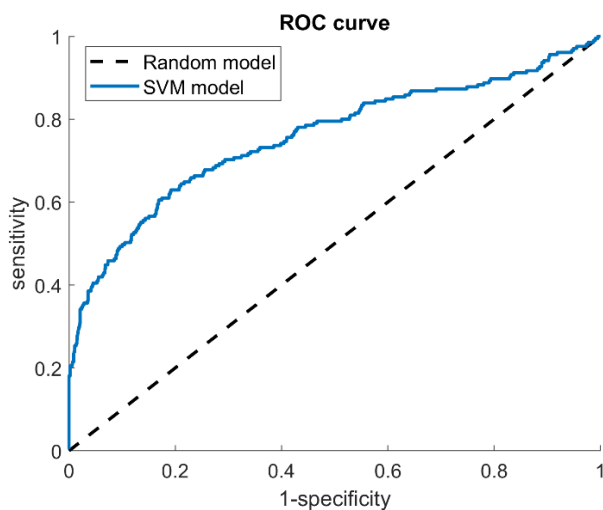
Figure 3. ROC curve: comparison between the random model (dashed black line) and the SVM model (blue curve) performance.

computed accuracy, sensitivity and specificity [15]. To obtain a good trade-off between sensitivity and specificity, we selected the threshold on the posterior probability equal to 0.071. With this threshold accuracy was 0.737, sensitivity was 0.699, and specificity was 0.742.

V. CONCLUSION

While the potential of existing T1D simulators in accelerating research in diabetes technology is well-established, the simulators currently available in the diabetes technology research community still lack a realistic description of some behavioural aspects of T1D patients that can greatly impact glucose control. In this work, we proposed new models describing CHO amount and timing of breakfast, lunch, dinner and snack of European subjects with T1D, under free-living conditions. The developed models can be incorporated in T1D simulators, to allow a more realistic description of patients' behaviour and, thus, more reliable ISCTs.

As a future development, the availability of a larger dataset could help refining the models, for example by linking the meal habits to the living country. Future work will also concern the development of models describing different behavioural characteristics of the T1D patient, such as the responsiveness to CGM sensor alarms and alerts and the insulin dosing behaviour under several insulin regimens.

REFERENCES

[1] American Diabetes Association, "Standards of Medical Care in Diabetes - 2019", in *Diabetes Care*, vol. 42(1), 2019.
[2] G. Cappon, M. Vettoretti, G. Sparacino et al., "Continuous glucose monitoring sensors for diabetes management: A review of technologies and applications", in *Diabetes Metab. J,* vol.43(4), pp. 383-397, 2019.
[3] M. Vettoretti, G. Cappon, G. Acciaroli, et al., "Continuous Glucose Monitoring: Current Use in Diabetes Management and Possible Future Applications", in *J. Diabetes Sci. Technol.,* vol. 12(5), pp. 1064-1071, 2018.
[4] N. Camerlingo, M. Vettoretti, S. Del Favero, et al., "A Real-Time Continuous Glucose Monitoring-Based Algorithm to Trigger Hypotreatments to Prevent/Mitigate Hypoglycemic Events", in *Diabetes Technol. Ther.,* vol. 21(11), pp. 644-655, 2019.
[5] M. Viceconti, A. Henney and E. Morley-Fletcher, "In silico clinical trials: how computer simulation will transform the biomedical industry", in *Int. J. Clin. Trials,* vol. 3(2), pp. 37-46, 2016.
[6] R. Visentin, E. Campos-Nanez, M. Schiavon, et al., "The UVA/Padova Type 1 Diabetes Simulator Goes From Single Meal to Single Day", in *J. Diabetes Sci. Technol.,* vol. 12(2), pp. 273-281, 2018.
[7] R. Hovorka, F. Shojaee-Moradie, P. Carroll, et al., "Partitioning glucose distribution/transport, disposal, and endogenous production during IVGTT", in *Am. J. Physiol. Endocrinol. Metab,* vol. 282(5), pp. E992-E1007, 2002.
[8] M. Rashid, S. Samadi, M. Sevil, et al., "Simulation software for assessment of nonlinear and adaptive multivariable control algorithms: Glucose-insulin dynamics in Type 1 diabetes", in *Comput. Chem. Eng.,* vol. 130(2), pp. 106565-106582, 2019.
[9] M. Vettoretti, A. Facchinetti, G. Sparacino et al., "Type-1 diabetes patient decision simulator for in silico testing safety and effectiveness of insulin treatments", in *IEEE Trans. Biomed. Eng.,* vol. 65(6), pp. 1281-1290, 2018.
[10] J. Kropff, S. Del Favero, J. Place et al., "2 month evening and night closed-loop glucose control in patients with type 1 diabetes under free-living conditions: a randomised crossover trial", in *Lancet Diabetes Endo.,* vol. 3(12), pp. 939-947, 2015.
[11] E. Renard, A. Farret, J. Kropff, et al., "Day-and-Night Closed-Loop Glucose Control in Patients With Type 1 Diabetes Under Free-Living Conditions: Results of a Single-Arm 1-Month Experience Compared With a Previously Reported Feasibility Study of Evening and Night at Home", in *Diabetes Care,* vol. 39, pp. 1151-1160, 2016.
[12] M. Messori, J. Kropff, S. Del Favero, et al., "Individually Adaptive Artificial Pancreas in Subjects with Type 1 Diabetes: A One-Month Proof-of-Concept Trial in Free-Living Conditions", in *Diabetes Technol. Ther.,* vol. 19(10), pp. 560-571, 2017.
[13] P. Keith-Hynes, P. Guerlain, S. Mize, et al., "DiAs user interface: a patient-centric interface for mobile artificial pancreas systems", in *J. Diabetes Sci. Technol.,* vol. 7(6), pp. 1416-1426, 2013.
[14] G. Jurman, S. Merler, A. Barla, et al. "Algebraic stability indicators for ranked lists in molecular profiling", in *Bioinformatics*, vol. 24(2), pp. 258-264, 2008.
[15] P. Baldi, S. Brunak, Y. Chauvin, et al., "Assessing the accuracy of prediction algorithms for classification: an overview", in *Bioinformatics,* vol. 16(5), pp. 412-424, 2000.

Stereo-PIV study of the flow across an axial pump for circulatory support

G. D'Avenio[1], U. Morbiducci[2], C. Del Gaudio[3], and M. Grigioni[1]

[1] *National Center for Innovative Technologies in Public Health, Istituto Superiore di Sanità, Rome, Italy*
[2] *PolitoBioMEDLab, Department of Mechanical and Aerospace Engineering, Politecnico di Torino, Turin, Italy*
[3] *Edoardo Amaldi Foundation, Rome, Italy*

Abstract—**Mechanical support to the circulation is an increasingly successful therapeutic option. Use of such support is still not free from complications, though, especially thromboembolism. In this study, a Stereo-PIV investigation of the flow field associated to an axial pump physically modelled in vitro, similar to a commercial device, is presented. The measurement of the full Reynolds stress tensor enabled to reveal fine details of the turbulence associated to the device, thanks to the capability of stereo PIV to investigate flow in very small channels.**

Keywords—**Fluid dynamics, Circulatory support devices, turbulence, blood trauma.**

I. INTRODUCTION

BLOOD pumps have become a widespread tool in the clinical praxis. They support the natural circulation whenever at least one ventricle fails to exert sufficient mechanical power, due to reversible or irreversible diseases. In the former case, typical of infections undermining the cardiac biomechanics, the pump must support the patient during the treatment, until physiological conditions are restored [1]. For patients with irreversible pathologies, mechanical support is also advantageous, since it can be thought of as bridge to transplantation [2] (allowing the patient to remain in the waiting list until organ availability), or ar least as a bridge to destination, when treatments – strictly defined – are not available (transplantation included), given the conditions of the patient [3-4].

Even though much experience has been gained with regard to blood pump, especially ventricular assist devices (VADs), these devices are still not free from significant complications, such as hemolysis and thromboembolism. Elevated flow stresses generated by non physiologic flow, especially owing to the rotating parts of the assist device, may trigger platelet activation and, ultimately, cause thromboembolism. The solution of this problem is evidently a critical factor for the long-term success of VADs and similar devices.

In this study, we addressed experimentally in vitro the analysis of the flow generated by a VAD prototype, modelled after a VAD already present in the European market.

The pump was studied to understand the dynamical effects on the flow field (stress on blood) due to the particular design adopted, using different stages (rotor, stator and transition between the two), considering above all the small space available for the fluid flow, constrained between the pump inner structure and housing.

A prototype of the impeller was designed to study the blood motion characteristics within the pump model, on the basis of images of seeded flow, by means of the Stereo-PIV (Particle Image Velocimetry) technique. Unlike traditional 2D PIV, Stereo PIV allows to measure all 3 velocity components, thus yielding the full Reynolds stress tensor in the measurement domain. Final results of the experimental campaign carried out at ISS facilities showed relevant parameters for blood damage.

II. MATERIALS AND METHODS

A. Pump model

The 3D investigation of the axial pump was planned in order to highlight the peculiar feature of the flow field generated by such a device.

The in vitro model was designed as a scaled-up (3:1) version of an impeller similar to that of a commercial device, built with transparent PMMA resin to achieve optical access for Stereo-PIV investigation.

It must be underlined that the pump is not cylindrically symmetrical; in the rotor part, moreover, the screw thread has a variable pitch (Fig. 1), contributing to a more complex flow, with even less homogeneously distributed turbulence. Also the phase relative to the instant when the rotor crosses the stator must be considered important.

B. Stereo-PIV setup

The Stereo-PIV assessment of a complex implantable device is useful to highlight the possible limitations of a two-dimensional velocimetric study. In the latter case, the most evident limitation would be clearly the impossibility of obtaining the full Reynolds stress tensor.

The main characteristics of the ISS Stereo PIV System used to obtain the full three-dimensional characterisation of fluid within the axial pump model are the following:

- Two cameras, capable of recording 1280x1024 pixel images in frame-straddling mode. The cameras are arranged in the Scheimpflug configuration by means of rotatable lens and camera body seats.
- A pulsed double-head Nd-YAG laser (Brilliant Twins, Quantel, France) was used to generate a light sheet, via a light arm arrangement.
- Dual-plane targets for calibrating the Stereo-PIV set-up without the need for translating the target itself. Both commercial (TSI Inc., USA) and original targets (designed at the ISS) have been employed during the project. For this application, also an optically generated target (i.e., a lattice of light intensity maxima) has been evaluated.
- Translation stage with stepper motor and autocalibration

at start-up.
- Commercial software for Stereo-PIV analysis (Insight, TSI Inc., USA).
- Original software, written in order to:
  - enable PIV analysis in batch mode;
  - perform the preprocessing (background subtraction) of the particle images pertaining to a given experimental phase;
  - check the quality of the calibration (dewarping of particle images, calculation of disparity maps [5]).

The axial pump was operated at 260 rps, by selecting the proper speed with the control knob of the control unit. Rhodamine-coated particles of 10 μm diameter were used to seed the flow. Low-pass filters were mounted on the cameras' objectives in order to record only the fluorescence emitted from the particles. The use of fluorescent particles allowed us to avoid an excess of reflections, which would have made impossibile to obtain reliable measurements. Moreover, the use of fluorescent particles allowed to avoid the preprocessing stage of removing the background illumination.
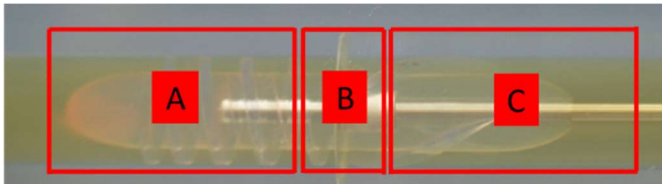

Fig. 1 – Detailed view of the pump model: the rotor (stator) is at the left (right) part of the image. A, B and C denote the interrogation windows considered in the Stereo-PIV study; A and C, in turn, were subdivided in three experimental windows to cover the entire flow field, since the length of the pump is much larger than its width. Zone A was decomposed in three views (A1, A2, A3, from the leftmost position). A similar decomposition was adopted for zone C.

C. Optical setup

A series of 7 images was needed to record the entire structure of the axial pump, from the beginning of the rotor to the end of the stator (proceeding in the flow direction), for appropriate spatial resolution, considering the aspect ratio of the pump model (Fig. 1). This was suggested also by the optical setup, which allowed to have an uniformly focused flow field across the model width: the adopted optics were 105-mm focal length objectives with the use of focal length duplicators.

One z-plane was considered for the measurements. Taking into account the residual refractive index mismatch between fluid and PMMA (1.472 (at 23°C) vs. 1.487 - 1.490, respectively), the plane z=0 was chosen for the measurements, thereby excluding off-axis positions of the measurement plane, in order to avoid any inclination of the laser sheet with respect to the vertical, caused by the difference in the refractive index. This effect would have been greater with increasing distance from z=0. Hence, the plane containing the pump axis was chosen for the measurements.

The angle between cameras (symmetrically disposed about the normal to the pump axis) was set at 60 degrees, in view of the goal of obtaining a reliable measurement of the cross-plane velocity W. Owing to this rather large inclination of the cameras with respect to the pump model, some details could

not be viewed as with a 2D analysis. In particular, the thin region between rotor and stator could not be imaged simultaneously by the two cameras, so that no 3D measurements could be obtained in that region.

Moreover, the above-mentioned choice of z=0 rendered very thin the measurable flow region, which was additionally decreased by the imaging at different angles of the helicoidal thread on the rotor.

The entire extension of the pump was covered by shifting the Stereo cameras and recording a portion of the flow field. 3 views were chosen to characterize the region A. The views have been numbered as A1, A2, A3, starting from the initial part of the rotor. Similarly, after the series of images at the interface region B, the regions C1, C2 and C3 were considered for the flow around the stator.

Preliminary investigations have highlighted a negligible phase dependency of the flow field in the region upstream of the rotor-stator transition, as well as downstream of the latter. Then we measured the flow field in these regions at 0° phase.

In zone B, instead, the phase scan was carried out for the following phase positions:
-160,-120,-100,-80,-60,-40,-20,-10,-5-,0, 5, 10, 20, 40, 60, 80, 100, 120,160 degrees.

D. Stereo–PIV calibration

Three-dimensional PIV is based on the same fundamental principle as human eyesight, or Stereoscopic vision: slightly different images are captured by the eyes and, from the comparison of these two images, the brain derives a three-dimensional interpretation. Stereo PIV, with each one of the two cameras playing the role of "eyes", measures displacements rather than actual velocities (as two-dimensional PIV does). The accuracy in the determination of the out-of-plane displacement (i.e. velocity) is related to the angle between the two cameras: the larger this angle, the more accurate is the determination of the out-of-plane displacement (with a restricted optical access, a smaller angle must be used, and a cost of accuracy in determining the third velocity component must be paid).

The actual Stereo measurements begin with conventional two-dimensional PIV processing of simultaneous recordings from the two cameras. This produces two two-dimensional vector maps showing the instantaneous flow field as seen from each of the cameras. Then, using a calibration procedure, the points in the chosen interrogation grid are mapped from the light sheet plane onto the left and right image planes (CCD-chip). With a two-dimensional displacement seen from both left and right camera, estimated at the same point in physical space, the true three-dimensional particle displacement can be calculated by solving the equations obtained in the calibration phase. Owing to this somewhat lengthy procedure, it must be remarked that the correct Stereo PIV calibration is an essential prerequisite for the accurate measurement of the three components of the velocity vector field in the investigated flow domain.

It is common to adopt a completely empirical approach for Stereo PIV calibration by placing a planar target, consisting of a grid of regularly spaced marks at the position of the light

sheet and moving the target by a specified amount in the out-of-plane direction to two or more z-positions [6]. At each z-position a calibration function with sufficient degrees of freedom is used to map the world xy-plane to each camera plane, while the difference between z-planes provides the z-derivatives of the mapping function necessary for reconstructing the three velocity components. This empirical approach has the advantage that all image distortions arising from imperfect lenses or light path irregularities e.g. from air/glass/water interfaces are compensated automatically in one step.

The calibration of the 3D PIV system was carried out using the PIV software (INSIGHT 5.0), together with PIVCalib, a software supplied with INSIGHT.

The calibration or mapping process uses a calibration target, which is a rectangular grid of marker points with known (x, y, z) locations. The target is mounted on a traverse (moving stage) and imaged at different z positions or, alternatively, a target with two planes is used without traversing, and positioned in the fluid. The latter option was chosen for the measurements at ISS premises, due to the difficulty in traversing a target in the small and not easily accessible space available to the flow.

The distance between the two planes of the target was $\Delta z=0.5$ mm. Each dot of a 7x7 rectangular grid (spacing: 5 mm) was relative to one of the two planes, in an alternate fashion (along each diagonal, the z coordinate was the same). The light sheet was aligned midway between the two target planes.

The initial step of the procedure consisted of recording the calibration images, that is, capturing and saving a set of images of the calibration target that can be analyzed and used as data points for the calibration file. For 3D operation, pairs of left and right images are captured as CalxxL.tif and CalxxR.tif and stored in the experiment's Calibration folder. With the two-plane target only one set of calibration images is used. In order to have satisfying results, the cameras were focused on the light sheet plane, then the target was positioned in the field of view of t

he cameras, using a large f-number to have a sufficient depth of field for having the two planes in focus.

The PIVCalib software makes use of a fiducial point (a crosshair), to determine univocally the center of the target. Thus, the entire target needs not be imaged, to derive the mapping function between world coordinates and camera coordinates.

After the selection of a suitable threshold for the light intensity and the definition of the proper grid parameters, the software is capable of analyzing the calibration images; before this step, the user can visually ascertain that the markers on the target are interpreted correctly, as for both position and priority, by the software.

By means of the "Create Calibration File" option, a *.cal file is generated, which is used to generate the 3D flow fields on the basis of the measurements relative to the left and right camera images.

More specifically, once the calibration images over the range of the lightsheet thickness are acquired, a set of calibration points filling the entire measurement volume is collected to build up the mapping functions. For each camera, six polynomial equations can be found by a least squares method, i. e., three fluid to image mapping functions:

$$X = f(x, y, z) \qquad (1)$$
$$Y = g(x, y, z) \qquad (2)$$
$$Z = h(x, y, z) \qquad (3)$$

and three image to fluid mapping functions:

$$x = f_2(X,Y) \qquad (4)$$
$$y = g_2(X,Y) \qquad (5)$$
$$z = h_2(X,Y) \qquad (6)$$

Being the image a two-dimensional object, it follows that in Eq. (3) all the polynomial coefficients are zero (since $Z = 0$); moreover, the image to fluid mapping is done with z set to zero. Equations from (4) to (6) can be used to show image locations mapped into the $z = 0$ fluid plane.

E. Reynolds shear stresses

Stereo PIV enables to measure the complete Reynolds stress tensor, whence the maximum turbulence shear stress (TSS_{max}) can be calculated rigorously. This quantity represents the maximum value of the Reynolds shear stress on a generic surface passing through a given point, and has been often used to quantify to maximum load on blood constituents [9].

Being the Reynolds stress tensor a real-valued symmetrical tensor, it is well known that a suitable coordinate system exists such as the Reynolds tensor can be expressed in the form

$$T = \rho \overline{u_i u_k} = \begin{bmatrix} \sigma_1 & 0 & 0 \\ 0 & \sigma_2 & 0 \\ 0 & 0 & \sigma_3 \end{bmatrix} \qquad ()$$

with σ_1, σ_2 and σ_3 representing the principal normal stresses [10], ordered usually as follows: $\sigma_1 \geq \sigma_2 \geq \sigma_3$. This coordinate system is composed of the Reynolds tensor's eigenvectors directions, and is termed principal coordinate system. It can be demonstrated [10] that the maximum Reynolds shear stress acting on a surface element can be expressed simply as $TSS_{max} = \dfrac{\sigma_1 - \sigma_3}{2}$.

III. RESULTS

In the zone of the rotor, hereby covered in the regions A1, A2, A3, the flow field is, as predictable, affected by the presence of the helicoidal thread on the rotor itself. In Fig. 2, relative to the region A3, the W velocity field (bottom panel) depicts the cross-plane velocity, which was found to have higher values with respect to the in-plane velocity components (U, V). The peaks in W correspond to the space between the helicoidal thread's projection on the laser sheet plane. The flow transported by threads is thus visualized.

The values in the colorbars are expressed in m/s. In the abscissae, the distance (mm) from the stator is reported.

As for the turbulence shear stress, in the region A the highest values on a global standpoint were found immediately upstream of the interaction zone (x=0) thanks to the threads' action. In Fig. 3 the shear stresses are reported for the phase 120°. The maximum value of TSS_{max} (412.2 Pa) was found, in this angular position of the rotor, at x=-4.86 mm, y=-3.7 mm.

In this same location, $\text{TSS}_{\max,2D}$ calculated with the in-plane velocity components (U and V), as in a 2D PIV investigation, was only 8.58 Pa, due to the disposition of the Principal Normal Stresses with respect to the coordinate system used in the analysis. This confirms the need of 3D analysis with such complex flows.

The result about the maximum value of $\text{TSS}_{\max}$ is reassuring with respect to blood damage created by the pump: in a previous investigation [8], a value of 400 Pa was proposed for the inception of hemolysis due to turbulence shear stresses. Actually, as demonstrated in [9] by means of Principal Stress Analysis, such a threshold value should be recalculated to at least 600 Pa, so that a safe margin for hemolysis was found in our study.

A potential limitation of the study is given by the fact that a scaled-up model of the pump has been chosen, in order to have a more detailed view of the space between the rotor and the housing. Nevertheless, besides the geometric similarity between model and pump, it must be underlined that the Reynolds number relative to the model was similar to that of the original pump operating in the assisted circulation, although a perfect match could not be attained, owing to the fact that, in order to match the refractive index of the casing, a fluid with a rather high kinematic viscosity (kerosene) had to be selected.
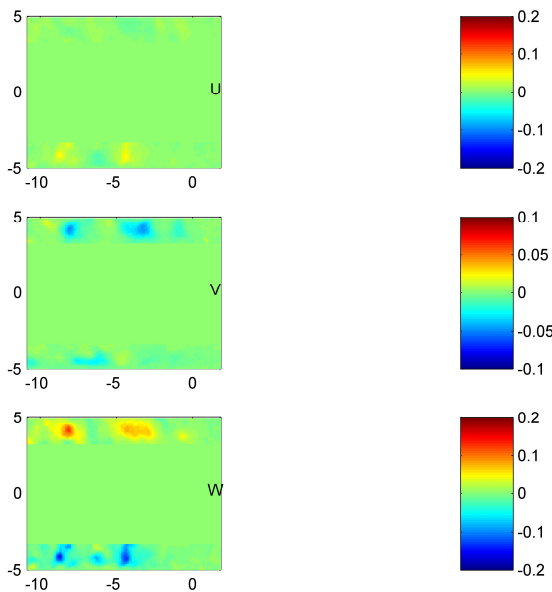
in a scaled-up version, did not lend itself easily to an experimental assessment, given the small space left between stator/rotor and housing of the pump. Hence, it was necessary to use fluorescent particles, otherwise the light scattered by the solid boundaries to the flow would have rendered it impossible to have a sufficient signal-to-noise ratio.

The results show clearly that a 3D study is necessary for this type of device: the comparison between the Reynolds stresses obtained with the full Reynolds tensor and with a 2D subset of the latter yielded completely different values, due to the particular local rotation of the eigenvectors of the Reynolds tensor, which could not be taken into account by selecting a couple of velocity components in the laboratory frame and performing a Principal Stress Analysis on such velocity components.

Even though stereo PIV does not attain the spatial resolution made possible by Computational Fluid Dynamics (CFD) studies, it has the capability of measuring directly the instantaneous flow field in the device, without resorting to the approximations required to calculate velocities and pressures in turbulent regimes (e.g., [11]). In this view, the experimental characterization of axial pumps and other implantable devices gives critical information about the turbulence associated to the device, thereby contributing to assess its propensity for blood trauma (hemolysis and/or thrombogenesis) already at the bench, prior to any in vivo investigation.

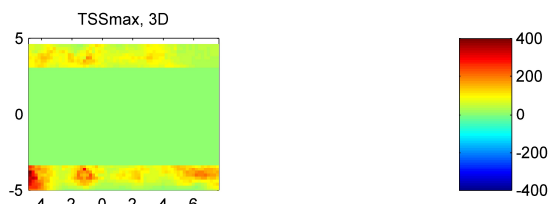Fig. 2 – Velocity components (m/s), zone A3

Fig. 3 – TSS$_{\max}$ (Pa), zone B

IV. CONCLUSION

An experimental investigation of the flow field associated to an axial pump model was presented. The device, even though

REFERENCES

[1] M. Ibrahim, M.H. Yacoub, "Bridge to Recovery and Weaning Protocols", *Heart Failure Clin* 10 (2014) S47–S55, http://dx.doi.org/10.1016/j.hfc.2013.08.004
[2] L. W. Miller, F. D. Pagani, S. D. Russell, R. John, A. J. Boyle, K. D. Aaronson, J. V. Conte, Y. Naka, D. Mancini, R. M. Delgado, T. E. MacGillivray, D. J. Farrar, O. H. Frazier, "Use of a continuous-flow device in patients awaiting heart transplantation", New England Journal of Medicine, 357(9):885-896, DOI: 10.1056/NEJMoa067758
[3] M. S. Slaughter, J. G. Rogers, C. A. Milano, S. D. Russell, J. V. Conte, D. Feldman, B. Sun, A. J. Tatooles, R. M. Delgado, J. W. Long, T. C. Wozniak, W. Ghumman, D. J. Farrar, and O. H. Frazier, "Advanced Heart Failure Treated with Continuous-Flow Left Ventricular Assist Device"
[4] K. Lietz, J. W. Long, A. G. Kfoury, M. S. Slaughter, M. A. Silver, C. A. Milano, J. G. Rogers, Y. Naka, D. Mancini, L. W. Miller, "Outcomes of left ventricular assist device implantation as destination therapy in the post-REMATCH era - Implications for patient selection", CIRCULATION, 116(5): 497-505
[5] B. Wieneke, "Stereo-PIV using self-calibration on particle images", Experiments in Fluids, 2005, 39(2): 267-280, DOI: 10.1007/s00348-005-0962-z
[6] Soloff SM, Adrian EJ and Liu ZC, "Distortion compensation for generalized stereoscopic particle image velocimetry", *Meas. Sci. Technol.* 8 (12):1441-1454, 1997
[7] Fontaine, A.A., Ellis, J.T., Healy, T.M., Hopmeyer, J., Yoganathan,A.P., "Identification of peak stresses in cardiac prostheses.A comparison of two-dimensional versus three-dimensional principal stress analyses", *ASAIO Journal*, 42:154-163, 1996
[8] Sallam A.M., Hwang N.H.C., "Human red blood cell hemolysis in a turbulent shear flow: contribution of Reynolds shear stresses", *Biorheology* 21:783-797, 1984
[9] Grigioni M., Daniele C., D'Avenio G., Barbaro V., "A discussion on the threshold limit for hemolysis related to Reynolds shear stress", *J Biomech*. 32(10):1107-12, 1999
[10] Malvern LE, Introduction to the mechanics of a continuous medium. Prentice Hall Inc., Englewood Cliffs, New Jersey, 1977
[11] Yakhot et al., "Development of turbulence models for shear flows by a double expansion technique", Physics of Fluids A 1992, 4(7):1510-1520

Image processing for rheological characterization of blood under flow

G. D'Avenio[1], P. Caprari[2], C. Daniele[1], and M Grigioni[1]

[1] *National Center for Innovative Technologies in Public Health, Istituto Superiore di Sanità, Rome, Italy*
[2] *National Center for the Control and Evaluation of Medicines, Istituto Superiore di Sanità, Rome, Italy*

Abstract— **Red blood cells (RBCs) have a critical role in the behaviour of blood under flow. Normally the RBCs have the capacity to aggregate in the presence of plasma proteins but the aggregates are dispersed by the shear stress generated by the blood flow; propensity to aggregation is critical in determining blood rheology. This study presents a software tool capable to determine, by means of analysis of erythrocytes images under flow, the aggregation - disaggregation patterns of RBCs, either obtained from controls or pathological patients. The results of the analysis of actual images of physiological RBC under different shear rates confirm the effectiveness of the proposed method.**

Keywords—**Blood flow, aggregation, image processing, blood rheology.**

I. INTRODUCTION

RED blood cells (RBCs) have a critical role in the behaviour of blood under flow: blood rheology is determined by several RBC properties, such as cell deformability and aggregation propensity. Haematological diseases characterized by morphological and structural alterations in RBCs may be associated with hemorheological abnormalities. Image processing tools, analysing RBC images under different flow conditions, can be very useful to evaluate quantitatively how RBCs reacts to mechanical loading induced by increasing shear rates. Such tools could also determine, in principle, the pathological profile of the patient.

Normally the RBCs have the capacity to aggregate in the presence of plasma proteins. Such aggregates are nevertheless easily dispersed by the shear stress generated by the blood flow [1]. Structural alterations in RBCs might induce the formation of larger and stronger aggregates that are resistant to dispersion by fluid shear stress; alternatively, smaller and weaker aggregates can be formed that are easily disaggregated.

This study presents a software tool capable to determine the aggregation - disaggregation patterns of RBCs, either obtained from controls or pathological patients.

II. MATERIALS AND METHODS

A custom software was written in the Matlab environment to analyze video sequences of RBCs under flow. The software calculates, for each frame, the number and size of the clusters of RBCs, by non-linear filtering of the images. Thus, the time course of the mean cluster area could be identified, for the operating conditions of the recording (i.e., shear rate).

Each video frame is partitioned in smaller domains, and the histogram of intensity values in each subsection of the image is calculated. Thus, the average intensities associated to the peak values of the background's and of the erythrocytes' distributions (see example in Fig. 1) are combined together, in order to form a local optimum intensity threshold (equal to the

semisum of the two previously mentioned average values). This local thresholding allows the software to tackle also non-uniform illumination of the image, such as in Fig. 2.

After binarizing each subimage with the relative threshold, the binarized version of the original frame is obtained. Then, spurious groups of pixels are removed with morphological opening ([2]), using structuring elements of lower size than that of a single RBC.
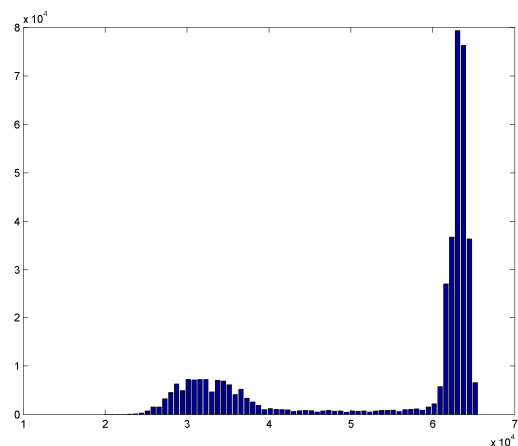

Fig. 1 - Histogram of the intensities in a typical RBC image. A roughly Gaussian bimodal distribution can be noticed, given by the erythrocytes (left) and background (right) contribution

Erythrocytes' images under microscope have a much brighter center than their border, due to their biconcave shape. Thus, upon binarization the image can present ring-like structures, instead of a connected domain of points (Fig. 3). This effect is dealt with by removing from the image all connected components (objects) that have fewer than N pixels, where N is a suitable fraction of the RBC size. This is done by morphologically opening the image, with a structuring element of suitable size (Fig. 4).

Finally, all remaining connected components in the image (i.e., single or aggregated erythrocytes) are labeled, making it possible to measure the centroid and area of each labeled cluster. The total area of aggregates, as well as the average area of the aggregates and the number of clusters in each image are then computed.

The result of the procedure is shown in Fig. 5, referring to the examples in Fig. 2: notwithstanding the not ideal illumination conditions, the difference in the number of pixels identified as belonging to the same clusters of RBCs between the two images is very small (0.6%).

Of course, the examples shown in Fig. 2 are representative

of the series of recordings obtained with different experimental conditions and different patient samples. They have been selected only for the sake of clarity, since they provide both isolated RBCs and cell fragments, which can be difficult to deal with, in an automatic approach to erythrocyte segmentation.

The experimental part of this study has been carried out using the Rheo-Microscope (Anton Paar), constituted by a glass parallel-plate rheometer, and an optical microscope. Whole blood was subjected at 37 °C to increasing shear rates (between 1 and 250 s^{-1}) and simultaneously imaged with a CCD camera. Video sequences of the flowing RBCs were subsequently analyzed. The Rheo-Microscope's imaged view of blood flow is optimized for homogeneity of characteristics of the sample, after positioning the latter on the glass plate. After extraction of each video frame, the entire image was used for segmentation, at each shear rate.
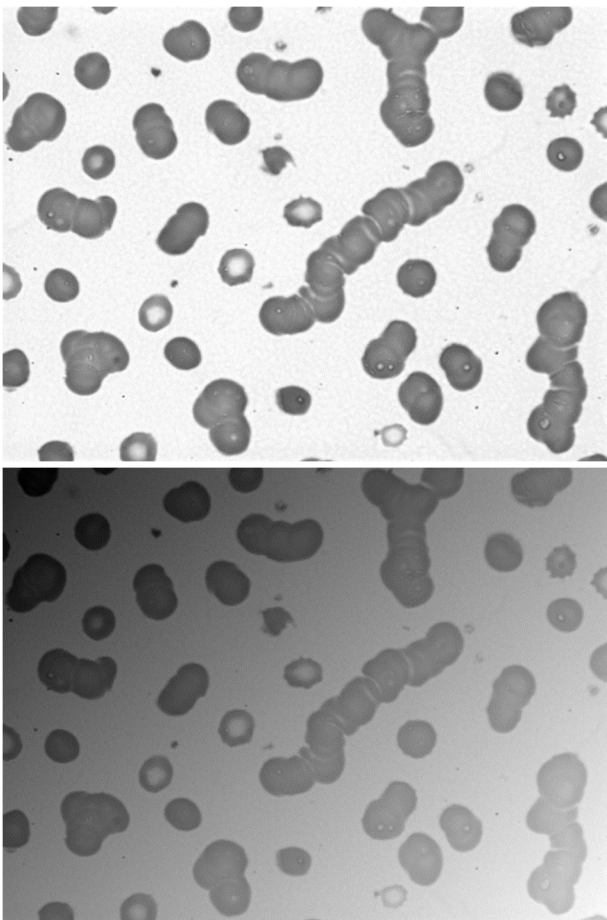

Fig. 2. -Typical images of aggregating erythrocytes, in ideal illumination conditions (top) and with illumination gradients (bottom)

III. RESULTS

A preliminary evaluation of the algorithm was carried out by means of synthetic images of aggregating RBCs, randomly disposed in the image. N=1000 synthetic images were generated, and added with gaussian white noise of increasingly higher level, in order so simulate varying degrees of signal-to-noise ratio. The image SNR is defined as follows:

$$SNR = 10\log_{10}\frac{\sigma_s}{\sigma_n} \qquad (1)$$

σ_s^2 and σ_n^2 being the variance of the original and the noise image, respectively. The algorithm was found to be relatively insensitive to additive white noise, at least up to SNR=10 dB (Fig. 6).
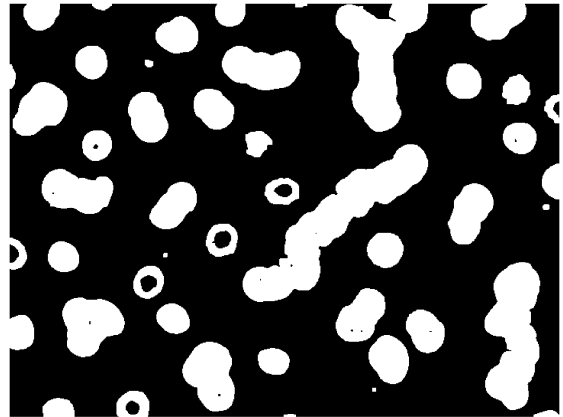

Fig. 3 - Image of aggregating erythrocytes, after local thresholding: there are a number of segmented RBCs with only their periphery marked as belonging to a cellular structure. The ring-like structures correspond to the biconcave shape of the RBC, whose central region if thinner than its edge.
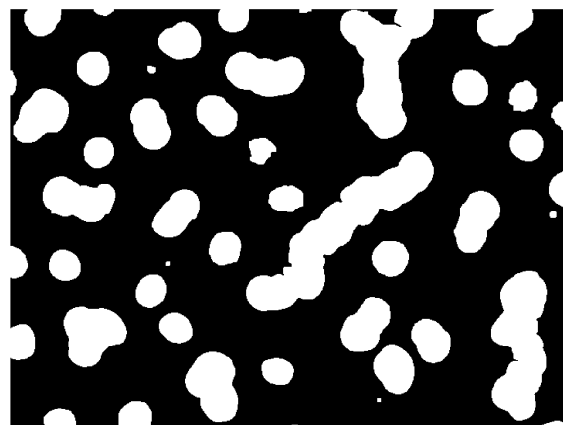

Fig. 4 - Result of the operation of morphological opening on the image in Fig. 2. The ring-like structures are replaced by correct shapes

The software was then tested with RBC video sequences from the Rheo-Microscope. As shown in Fig. 7, the number of clusters was found to be steadily increasing, after the start of the rheometer's plate movement (vertical line). The rate of increase of clusters (1/s) is calculated by least–square-fitting the data comprised between two limit points (red circles).

The results of the analysis are reported in table I. At lower shear rate, 50 s^{-1}, the mechanical load caused the aggregates to break down (table I and Fig. 8). This applied for 50 as well as for 100 s^{-1} SR values, the latter causing a rate of increase of cluster number which was almost double of that associated to the former.

Finally, at 200 s^{-1}, the applied shear was high enough to cause immediate fragmentation, and a low, negative value of the rate of increase of cluster number was found (table I and Fig. 9).
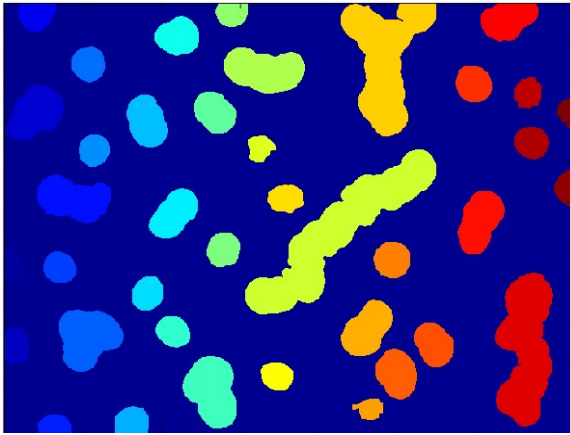
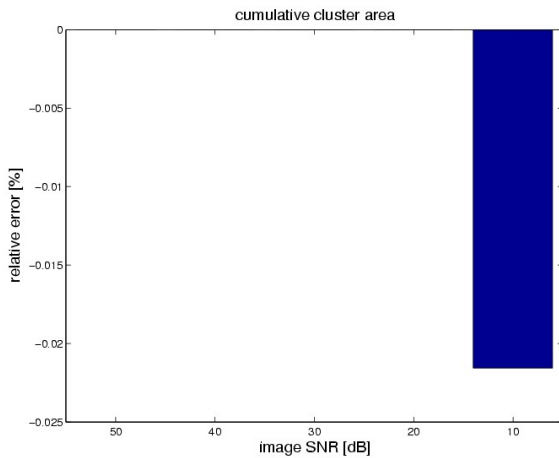Fig. 5 -Result of the segmentation of the image in Fig. 2. Each labeled cluster is shown with a different colour.

Fig. 6 - Relative error (%) for the cumulative cluster area, as a function of the image SNR
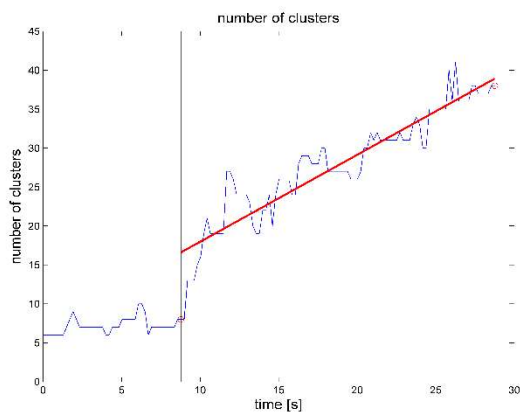
Table I. Rate of increase of cluster number (RI), after analysis of a sample of physiological blood under Rheo-microscope.

SR [s^{-1}]	50	100	200
RI [s^{-1}]	0.66	1.18	-0.20

IV. DISCUSSION

Other studies about automatic processing of hematological images have been proposed in the past. For instance, Gering et al [3] report a method for counting nucleated erythrocytes from digital micrographs of thin blood smears, which enables to estimate intensity of hematozoan infections in non-mammalian vertebrate hosts. This method, which subjects blood images to automatic thresholding and particle analysis, uses ImageJ, a Java-based open source software tool, developed at the U.S. National Institutes of Health (http://rsb.info.nih.gov/ ij/index.html).

The main image enhancements operations provided by ImageJ are: smoothing, sharpening, edge detection, median filtering and thresholding on both grayscale and RGB color images, brightness and contrast interactive adjustment.

The method by Gering et al [3] is aimed at segmentation of single RBCs, so it does not lend itself to cluster analysis, as opposed to our method. Moreover, the hereby presented software supports local automatic thresholding, which is not usually supported by general-purpose image processing software; the local determination of the optimal threshold for binarization is required to avoid unrealistic segmentation results, due to uneven illuination.

Our method uses morphological operators to post-process blood images after thresholding, whereas this procedure is not provided as a standard feature, in other image processing softwares. For instance, in [3] an ad-hoc range of pixel count was selected, in order to individuate erythrocyte nuclei. The range may not be always appropriate, depending on the experimental conditions and the blood sample characteristics.
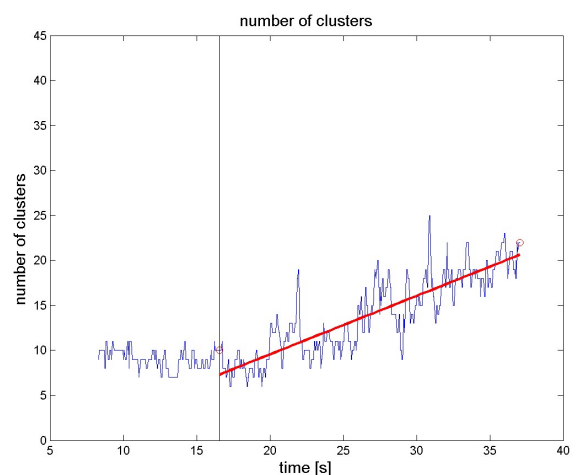

Fig. 7 - Analysis of the video recording of flowing erythrocytes, at shear rate=100 s^{-1}. The number of clusters is shown against time. The number of clusters is steadily increasing, after the start of the rheometer (vertical line).

Fig. 8 - Analysis of the video recording of flowing erythrocytes, at shear rate=50 s^{-1}. The number of clusters is shown against time. The number of clusters is steadily increasing, after the start of the rheometer (vertical line).
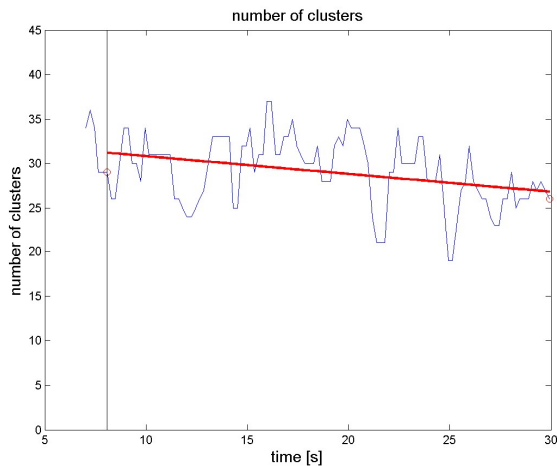
Fig. 9 - Analysis of the video recording of flowing erythrocytes, at shear rate=200 s^{-1}. The number of clusters is shown against time. At this high shear rate, the behaviour of the RBC aggregates is completely different from that reported in Fig. 7.

It must be underlined that the blood smears considered by Gering et al [3] had been previously subjected to staining, in order to enhance the contrast between nuclei and RBC cytoplasm, whereas our study addresses the analysis of unstained blood images, thus rendering the experimental effort much more simple.

Several other literature studies (e.g., [4]) have considered blood smears slides as the data for evaluating the analysis method. In this work, instead, we considered video frames from the rheometer's standard camera, thus with lower resoluton and image quality than what can be obtained with digitized microscopic slides.

The problem of uneven illumination can hinder automatic processing of microscopic images [5], since it is something that is not always recognized by the operator, who generally automatically compensates inhomogeneities of this sort, while perceiving the image. The software hereby proposed can deal with such a problem (Fig. 2), allowing for local thresholding of images.

Previous works in related areas have also used morphological operators: In [6], grey-scale granulometry based on opening with disk-shaped elements (flat and hemispherical) was applied. These structuring element were used to enhance the roundness and the compactness of the red cells, in conjunction with the classical watershed algorithm, while a disk-shaped flat structuring element was used to separate overlapping cells. These methods make use of previous knowledge of the red blood cell structure, as opposed to traditional watershed-based algorithms.

In our study, morphological operators were not used to alter the morphological features (e.g., roundness/compactness) of RBCs (this would have not been useful, since the RBCs were generally found in aggregates), but to perform filtering of cell shapes after thresholding (i.e., pruning of stray pixels related to image noise, and correction of ring-like structures due to the biconcavity of RBCs).

An often-cited method for monitoring RBC aggregability

under shear was proposed in [7]. In this work, image processing was applied to differentiate aggregates by segmentation of the background. Such operation was not clearly described, though, hence it is not possible to rigorously compare the approach with that hereby presented. In particular, it is not possible to assess if an uneven illumination can impact on the accuracy of the analysis. Anyhow, all of the parameters yielded by the method presented in [7], i.e., projected aggregate area, number of cells per aggregate, aggregate distribution, etc., are also provided by our method. Moreover, the center of mass of single aggregates is also computed, so that the relative trajectory as a function of time can be calculated.

The study was intended principally to provide a tool for the characterization of blood rheological properties: the propensity of erythrocytes aggregates to fragment under shear can be quantified as the rate of increase (RI) of cluster number. Actually, enhanced RBC aggregation has been observed and implicated in the pathophysiology of many pathological states (cardiovascular diseases, sickle cell disease, thalassemia) [8]. Hence, the determination of the aggregation - disaggregation patterns of RBCs, by means of the proposed method, might be useful to highlight the presence of rheological alterations affecting the microcirculation, thus constituting a quantitative diagnostic tool.

V. CONCLUSION

Image analysis was found to be capable to yield useful information on the erythrocyte aggregation. The correlation of the hemorheological profile of healthy and pathological subjects with RBCs flow behaviour is an interesting possibility, that needs to be further investigated .

REFERENCES

[1] Neu, B. Red blood cell aggregation. O.K. Baskurt et al. (Eds) 2007. Handbook of Hemorheology and Hemodynamics. Amsterdam. IOS press pp. 114-136.
[2] Dougherty ER 1992. An Introduction to Morphological Image Processing. ISBN 0-8194-0845-X
[3] Gering E and Atkinson CT. 2004. A Rapid Method for Counting Nucleated Erythrocytes on Stained Blood Smears by Digital Image Analysis. Journal of Parasitology, 90 (4): 879-881.
[4] Govind D, Lutnick B, Tomaszewski JE, Sarder P 2018. Automated erythrocyte detectionand classification from whole slide images. "J. Med. Imag.5(2), 027501,
[5] Leong FJWM, Brady M, McGee J. 2003. Correction of uneven illumination (vignetting) in digital microscopy images. J Clin Pathol, 56:619-621.
[6] Di Ruberto C, Dempster A, Khan S, Jarra B. 2002. Analysis of infected blood cell images using morphological operators. Image and Vision Computing 20:133–146
[7] Chen S, Barshtein G, Gavish B, Mahler Y, Yedgar S. 1994. Monitoring of red blood cell aggregability in a flow-chamber by computerized image analysis. Clinical Hemorheology, 14, 497–508.
[8] Baskurt OK. Mechanisms of blood rheology alterations. O.K. Baskurt et al. (Eds) 2007. Handbook of Hemorheology and Hemodynamics. Amsterdam. IOS press pp.170-190.

Performance of Dual-Augmented Lagrangian Method and Common Spatial Patterns applied in classification of Motor-Imagery BCI

A. Miladinović[1], M. Ajčević[1], G. Silveri[1], A. Accardo[1]

[1] *Department of Engineering and Architecture, University of Trieste, Italy*

Abstract—**Motor-imagery based brain-computer interfaces (MI-BCI) have the potential to become ground-breaking technologies for neurorehabilitation, the reestablishment of non-muscular communication and commands for patients suffering from neuronal disorders and disabilities, but also outside of clinical practice, for video game control and other entertainment purposes. However, due to the noisy nature of the used EEG signal, reliable BCI systems require specialized procedures for features optimization and extraction. This paper compares the two approaches, the Common Spatial Patterns with Linear Discriminant Analysis classifier (CSP-LDA), widely used in BCI for extracting features in Motor Imagery (MI) tasks, and the Dual-Augmented Lagrangian (DAL) framework with three different regularization methods: group sparsity with row groups (DAL-GLR), dual-spectrum (DAL-DS) and l1-norm regularization (DAL-L1). The test has been performed on 7 healthy subjects performing 5 BCI-MI sessions each. The preliminary results show that DAL-GLR method outperforms standard CSP-LDA, presenting 6.9% lower misclassification error (p-value = 0.008) and demonstrate the advantage of DAL framework for MI-BCI.**

Keywords—**brain-computer interface (BCI), electroencephalography (EEG), motor-imagery (MI).**

I. INTRODUCTION

THE purpose of BCI research is to establish communication between computers and the brain bypassing peripheral nerves. The approach can be used to regain communication capabilities in the cases of certain types of neurological conditions [1], control of a prosthetic arm or wheelchair [2], and furthermore, by combining different strategies [3] as neurorehabilitation tools for patients suffering from Parkinson's disease [4], post-Stroke [5], Attention-Deficit Hyperactivity Disorders [6], Autism Spectrum Disorder [7] and other neurological conditions.

The most commonly used BCI technique is based on electroencephalography since it provides a non-invasive, easily applicable, and relatively affordable measurement of the electrical activity generated on the scalp as a consequence of the brain activity. However, despite its advantages, the acquired signal quality may vary due to the low signal-to-noise ratio caused by external factors such as powerline of 50Hz and man-made noise, but also internal non-task related brain and muscular activity. Nonetheless, the signal has high time-resolution; it suffers from low spatial resolution caused by tissue volume conduction and non-stationarity caused by changes in the subject's overall brain state during the experiment (e.g., a prominent increase of alpha burst caused

by drowsiness). Therefore, the application of conventional statistical analysis leads to poor performance and, in many cases, fail to produce a reliable real-time prediction of the user's brain state. Therefore, one of the biggest challenges in BCI is how to extract a small number of robust and informative features from the EEG data by applying various data-driven approaches. One of the most commonly used techniques for the transformation of sensor space (raw EEG data) into a new lower rank space is Common Spatial Patterns (CSP) [8]. Various studies [8]–[10] demonstrated that the pre-processing steps mostly influence the performance of the BCI system, and in that regard, it is demonstrated in [11] that relatively simple classifiers, such as Linear Discriminant Analysis (LDA) [8], can provide optimal results and outperform more complex classification techniques. Still, most data-driven approaches, including CSP, as reported in [12] tries to solve non-convex optimisation problems, and subdivided independent steps of feature extraction, and classification increases the chances of suboptimal BCI models leading to general poorer performances and lower resilience to the noises [13].

In that regard, in this paper we explored the performance of an alternative framework, the Dual-Augmented Lagrangian (DAL) [14], [15], that tries to eliminate problems of multiple local minima by merging the process of feature extraction, dimensionality reduction, and classification into one process [14]. The further aim is to provide a comparison of the performance of CSP and DAL for motor-imagery based brain-computer interface in a real-life scenario applied to a group of healthy subjects.

II. MATERIALS AND METHODS

A. Study population

The experiment was conducted on 7 healthy (3 males and 4 females) with a mean age of 21 years (standard deviation= 1.6) right-handed (Edinburgh Handedness Inventory) participants.

All subjects were right-handed, with no history of neurological disorders and BCI naïve.

This study has been approved by the local ethics committee and has been performed in accordance with the ethical standards laid down in the 1964 Declaration of Helsinki and its later amendments. All participants released their informed consent.

B. BCI protocol

Each subject underwent 5 sessions of right-hand Motor-Imagery controlled BCI feedback administered in two weeks.

Each session consisted of initial calibration phase in which subjects had a task to perform a repetitive MI right-hand task when the command in the form of the arrow appeared on the screen in the duration (see Fig.1), and, conversely, stay in rest when the image disappears (two-class classification problem). The number of repetitions was set to 30 for each class, leading to a total of 60 acquired trials for each session. The acquired data is then used for the subsequent online phase where the cursor was controlled by the subject's volitional EEG processed with the produced BCI model.
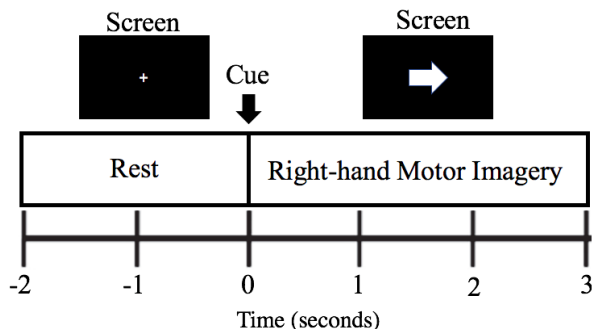

Fig. 1: Depiction of the presented stimulus on the screen for a single run during initial calibration phase

C. EEG acquisition

The acquisition of 11 channel EEG was performed using OpenBCI (OpenBCI, New York, NY, USA) and Ag/AgCl electrodes (SpesMedica, Genova, Italy) placed at standard 10-20 locations covering the motor areas (F3, Fz, F4, T3, C3, Cz, C4, T4, P3, Pz, P4) as reported in Fig.2. The signals were recorded with 250 Hz sample frequency and subsequently downsampled to 128Hz and pre-processed with the 6-32 Hz 2nd order Butterworth digital bandpass filter. During the experiment, the electrode impedances were kept below 5 kΩ. The BCILAB [16] and MATLAB® (The MathWorks Inc., Natick, MA) were used for real-time processing, as well as for later offline analysis.
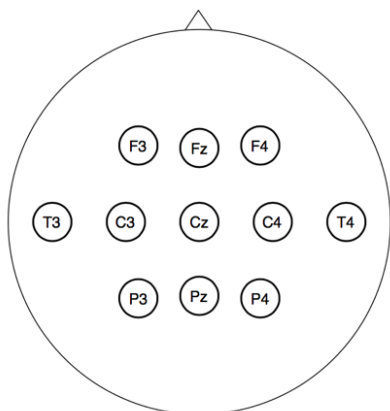
.

Fig. 2: Schematic of electrode placement for MI-BCI

The performance of DAL has been explored with tree type of regularisation strategies proposed in [14] applicable to the augmented weight matrix: (1) group sparsity with row groups (DAL-GLR), suggested in the cases where the emphasis is on channel selection, and there are a low number of temporally distributed activity patterns, (2) dual-spectral optimal where there are few informative constellations over time combining both power and time-domain segments (DAL-DS), and finally, (3) standard Euclidean l1-norm regularization that focuses on the temporal aspect.

At the same time, the CSP-LDA algorithm has been used as described in previous work [9], maximizing signal variance (power) for 3 patterns for each class. After the application of the spatial filter, the data are fed in the LDA classifier with automatic shrinkage regularization parameters [8].

The optimization of regularization parameters in all cases was performed using 5-fold blockwise cross-validation with 5 trials, whereas the final misclassification error of the model was estimated using 10-fold blockwise cross-validation with the same margin of 5 trials.

D. Statistical analysis

Differences in misclassification errors were tested by repeated-measure analysis of variance (ANOVA). Bonferroni corrections were used for post-hoc multiple comparisons.

III. RESULTS

The session mean misclassification error obtained by models produced by CSP-LDA, DAL-GLR, DAL-DS, and DAL-L1 approaches is reported in Table 1 for each of the 7 subjects. The misclassification error of the DAL-GLR ($30.7\% \pm 6.3$) was significantly lower compared to CSP (37.6 ± 8.7) (p-value = 0.008). No significant difference in total error was found between CSP-LDA and DAL-DS (p-value = 0.060), and DAL-L1 (p-value = 0.095), although, on average, both cases presented a slightly lower error. No significant differences were observed among DAL-based methods

IV. DISCUSSION

Motor-Imagery BCI has the potential to be used as a neurorehabilitation tool that can improve motor and cognitive abilities in patients and subjects affected by various disorders [4]–[7].

TABLE I
MISCLASSIFICATION ERROR (%) AND STANDARD DEVIATION OBTAINED BY THE CSP-LDA, DAL-GLR, DAL-DS, AND DAL-L1 METHODS, RESPECTIVELY, FOR 7 HEALTHY SUBJECTS OVER 5 BCI SESSIONS PERFORMED FOR EACH SUBJECT. FOR EACH PATIENT, THE LOWEST ERROR IS MARKED IN BOLDFACE.

Subjects	CSP-LDA	DAL-GLR	DAL-DS	DAL-L1
1	40.1±4.9	25.2±0.3	**24.9**±0.3	25.3±0.7
2	47.6±3.5	25.7±1.0	**24.9**±0.4	25.4±1.3
3	37.9±5.1	**32.5**±5.7	35.8±6.4	33.4±5.5
4	37.0±9.5	**33.9**±11.4	34.3±8.2	34.4±12.0
5	**25.1**±4.9	30.8±3.9	30.8±7.0	33.6±8.2
6	**31.5**±4.8	31.5±5.5	33.7±7.8	31.9±4.5
7	44.3±4.0	**35.2**±4.9	38.4±6.2	38.0±5.7
Average	37.6±8.7	**30.7**±6.3	31.8±7.4	31.7±7.4

To improve the reliability of BCI systems, a proper model that personalizes the model for each subject, and each session has to produce. The violation of the Machine Learning premises, such as unpredicted non-stationarity of the features [13], imposes a challenge to produce a reliable BCI model using a standard optimization technique. Therefore, the developed frameworks have to be also properly tested and evaluated on subjects producing real-life application scenarios.

This study compared the performance of two approaches for two-class MI-based BCI, the traditional CSP algorithm, and the DAL method with three different regularisation strategies. The study was performed on 7 healthy subjects. The approach DAL with the group sparsity regularization DAL-GLR outperforms standard CSP-LDA algorithm when the task elicits changes in power band ratios at the particular scalp locations, such as mu/alpha power decrease and beta increase (beta rebound) in the case of Motor-Imagery [2]. The execution of Motor Imagery activates Sensory-motor areas that are located contralaterally of the imagined hand [10], and in our case, the highest activation produces by right-hand is expected on the C3 electrode. The precise topographical location of expected cortex activation explains why DAL-GLR, optimized for channel selection, produces the lowest misclassification error on average.

The better accuracy DAL in respect to the CSP of 6.9% (p-value = 0.008) demonstrate the superiority of the framework that blurs the boundary between subsequent machine-learning steps because it provides an immediate loop for optimization of regularization parameters, which is not the case in CSP where the feature extraction and reduction are separated from the classification process.

Nonetheless, due to a small test, it is difficult to draw any firm conclusions for the other two regularization approaches DAL-DS and DAL-L1, despite statistically nonsignificant differences also present lower error in comparison to CSP. Evidence from [14] shows DAL-DS outperforms the DAL-GLR when applied to slow cortical potentials. However, in the case of our experiment, the findings demonstrate activation of the precise brain location and on higher frequencies (alpha/beta), which is not demonstrated in the case of the study in [14]. Despite not optimal in all cases, we can observe that the DAL-DS presented the lowest classification error in two of seven subjects, which can lead to a debate that the differences among DAL approaches should be further investigated in a larger dataset.

V. CONCLUSION

In conclusion, this preliminary study showed that among selected approaches, DAL-GLR provides the best classification performance among the tested approach. It also demonstrates the supremacy of DAL methods over the standardized CSP-LDA machine learning framework. However, the results obtained should be confirmed in a study with a larger number of participants

ACKNOWLEDGEMENT

A. Miladinović is supported by the European Social Fund (ESF) - FVG.

REFERENCES

[1]   J. R. Wolpaw, N. Birbaumer, D. J. McFarland, G. Pfurtscheller, and T. M. Vaughan, "Brain–computer interfaces for communication and control," Clin. Neurophysiol., vol. 113, no. 6, pp. 767–791, Jun. 2002, doi: 10.1016/S1388-2457(02)00057-3.

[2]   M. A. L. Nicolelis, "Brain–machine interfaces to restore motor function and probe neural circuits," Nat. Rev. Neurosci., vol. 4, no. 5, pp. 417–422, May 2003, doi: 10.1038/nrn1105.

[3]   A. Miladinović et al., "Combined and Singular Effects of Action Observation and Motor Imagery Paradigms on Resting-State Sensorimotor Rhythms," in XV Mediterranean Conference on Medical and Biological Engineering and Computing – MEDICON 2019, vol. 76, J. Henriques, N. Neves, and P. de Carvalho, Eds. Cham: Springer International Publishing, 2020, pp. 1129–1137.

[4]   L. Subramanian et al., "Real-Time Functional Magnetic Resonance Imaging Neurofeedback for Treatment of Parkinson's Disease," J. Neurosci., vol. 31, no. 45, pp. 16309–16317, Nov. 2011, doi: 10.1523/JNEUROSCI.3498-11.2011.

[5]   K. K. Ang et al., "A clinical evaluation of non-invasive motor imagery-based brain-computer interface in stroke," in 2008 30th Annual International Conference of the IEEE Engineering in Medicine and Biology Society, Vancouver, BC, 2008, pp. 4178–4181, doi: 10.1109/IEMBS.2008.4650130.

[6]   C. G. Lim et al., "A Brain-Computer Interface Based Attention Training Program for Treating Attention Deficit Hyperactivity Disorder," PLoS ONE, vol. 7, no. 10, p. e46692, Oct. 2012, doi: 10.1371/journal.pone.0046692.

[7]   A. Miladinović et al., "Slow Cortical Potential BCI Classification Using Sparse Variational Bayesian Logistic Regression with Automatic Relevance Determination," in XV Mediterranean Conference on Medical and Biological Engineering and Computing – MEDICON 2019, vol. 76, J. Henriques, N. Neves, and P. de Carvalho, Eds. Cham: Springer International Publishing, 2020, pp. 1853–1860.

[8]   C. Vidaurre, M. Kawanabe, P. von Bünau, B. Blankertz, and K. R. Müller, "Toward Unsupervised Adaptation of LDA for Brain–Computer Interfaces," IEEE Trans. Biomed. Eng., vol. 58, no. 3, pp. 587–597, Mar. 2011, doi: 10.1109/TBME.2010.2093133.

[9]   F. Lotte and Cuntai Guan, "Regularizing Common Spatial Patterns to Improve BCI Designs: Unified Theory and New Algorithms," IEEE Trans. Biomed. Eng., vol. 58, no. 2, pp. 355–362, Feb. 2011, doi: 10.1109/TBME.2010.2082539.

[10]   H. Ramoser, J. Muller-Gerking, and G. Pfurtscheller, "Optimal spatial filtering of single trial EEG during imagined hand movement," IEEE Trans. Rehabil. Eng., vol. 8, no. 4, pp. 441–446, Dec. 2000, doi: 10.1109/86.895946.

[11]   V. P. Oikonomou, K. Georgiadis, G. Liaros, S. Nikolopoulos, and I. Kompatsiaris, "A Comparison Study on EEG Signal Processing Techniques Using Motor Imagery EEG Data," in 2017 IEEE 30th International Symposium on Computer-Based Medical Systems (CBMS), 2017, pp. 781–786, doi: 10.1109/CBMS.2017.113.

[12]   M. Dyrholm, C. Christoforou, and L. C. Parra, "Bilinear discriminant component analysis," J. Mach. Learn. Res., vol. 8, pp. 1097–1111, 2007.

[13]   R. Tomioka, K. Aihara, and K.-R. Müller, "Logistic regression for single trial EEG classification," presented at the Advances in Neural Information Processing Systems, 2007, pp. 1377–1384.

[14]   R. Tomioka and K.-R. Müller, "A regularized discriminative framework for EEG analysis with application to brain–computer interface," NeuroImage, vol. 49, no. 1, pp. 415–432, Jan. 2010, doi: 10.1016/j.neuroimage.2009.07.045.

[15]   R. Tomioka and M. Sugiyama, "Dual-Augmented Lagrangian Method for Efficient Sparse Reconstruction," IEEE Signal Process. Lett., vol. 16, pp. 1067–1070, 2009, doi: 10.1109/LSP.2009.2030111.

[16]   C. A. Kothe and S. Makeig, "BCILAB: a platform for brain–computer interface development," J. Neural Eng., vol. 10, no. 5, p. 056014, Oct. 2013, doi: 10.1088/1741-2560/10/5/056014.

Human Activity Recognition through Wearable Sensors: a Deep Learning Approach

D. Fortunato[1,2], M. Ghislieri[1,2], S. Rosati[1,2], G. Balestra[1,2], M. Knaflitz[1,2], and V. Agostini[1,2]

[1] *Department of Electronics and Telecommunications of Politecnico di Torino, 10129, Torino, Italy.*
[2] *PoliTo[BIO]MedLab of Politecnico di Torino, 10129, Torino, Italy.*

Abstract—**Human Activity Recognition (HAR) can be performed through an actigraph that: 1) records 3D accelerometric and gyroscopic signals, 2) classifies different activities of daily living, such as walking (ground level, uphill, downhill), ascending or descending stairs, upright quiet standing, and sitting. The aim of this work is to introduce a deep learning classification approach, based on Long Short-Term Memory (LSTM) neural networks, that can be easily implemented on a HAR actigraph. Among 360 different models, the best LSTM was chosen and its properties described. The classifier accuracy ranges from 92% (for uphill walking) to 100% (for sitting). Differently from previously described HAR classifiers, the proposed classifier requires neither signal pre-processing, nor feature extraction and selection.**

Keywords—**LSTM, MIMU, HAR, Actigraph.**

I. INTRODUCTION

IN the last years, Human Activity Recognition (HAR) has become a research field of great interest for medical applications. In particular, HAR was successfully applied for monitoring of the elderly [1], remote detection of falls [2], medical diagnosis [3], and rehabilitation [4]. A HAR system is usually composed of two components: (1) a wearable device equipped with magneto-inertial sensors called MIMU (i.e., accelerometer, gyroscope, and magnetometer sensors) used to acquire human movements during different tasks, and (2) a processing tool used to process the acquired data and to recognize the activity performed at a given instant by the subject.

Most of the commercially available HAR systems rely on a) miniaturized MIMU sensors that perform the sensing and digitalizing of the inertial signals, b) a microcontroller for data storage and/or transmission to an external system, and c) the processing application that is installed on the external system, that generally consists of a PC, a tablet, or a smartphone. However, a stand-alone device, able both to acquire inertial signals for long periods of time and to recognize human activities, would be essential for all those applications that require real-time feedback.

In this context, our research group designed and realized a MIMU-based micro-processed device for real-time HAR [5] – [7]. This small and lightweight device is equipped with a microcontroller with enough internal memory to store the inertial signals and to support the implementation of a classifier for activity recognition. In a previous work [5], five different classifiers based on machine learning were built up to recognize seven daily-life activities: level walking, uphill and downhill walking, ascending or descending stairs, standing, and sitting. Among all classifiers that were tested, the Decision Tree was selected to be implemented into the microcontroller. This classifier requires a reduced number of input features and has a lower computational cost with respect to other classifiers. To properly recognize human activities, all the approaches previously studied require a feature extraction and selection step. However, the identification of the correct set of input features for the classifier is a challenging and still open issue when dealing with HAR [7], [8]. Alternative methods, such as Deep Learning approaches, are being explored to overcome the limitations of the previous HAR classifiers. Among the Deep Learning approaches, Long Short-Term Memory (LSTM) neural networks have been chosen for our purpose. This choice is justified by the fact that LSTM neural networks are a widely used type of Recurrent Neural Network (RNN), specifically designed to recognize patterns in sequential data [9], such as accelerometer and gyroscope signals. In the last years, several approaches for HAR based on LSTM neural networks were proposed in literature. The authors in [10] built a two-layers LSTM model that allows the automatic extraction and selection of the optimal set of input features to detect human activities in different application domains. In [11] the role of feature extractor was assigned to a Convolutional Neural Network (CNN) that provides higher-level abstract representations of low-level raw time-series signals to an LSTM model. Ref. [12] analyzed appropriate training procedures for several deep learning approaches to HAR including deep LSTM networks. Instead of using single LSTM models the work [13] built various LSTM networks and fused them in score-level to improve HAR performance.

The aim of this contribution is to assess if this approach (based on LSTM classification) can be used as an alternative to the previous classifier (based on Decision Tree classification) implemented on the MIMU-based micro-processed device.

II. MATERIALS AND METHODS

A. Sample Population and Experimental Setup

A sample population consisting of 61 healthy subjects (age: 22 years ± 2 years, gender: 33 females and 28 males, height: 169.9 cm ± 8.3 cm, weight: 64.3 kg ± 11.0 kg), with no history of physical disabilities or recent injuries, was retrospectively analyzed using inertial sensor data in our database [7]. During the test previously performed, subjects were asked to perform seven different activities: level
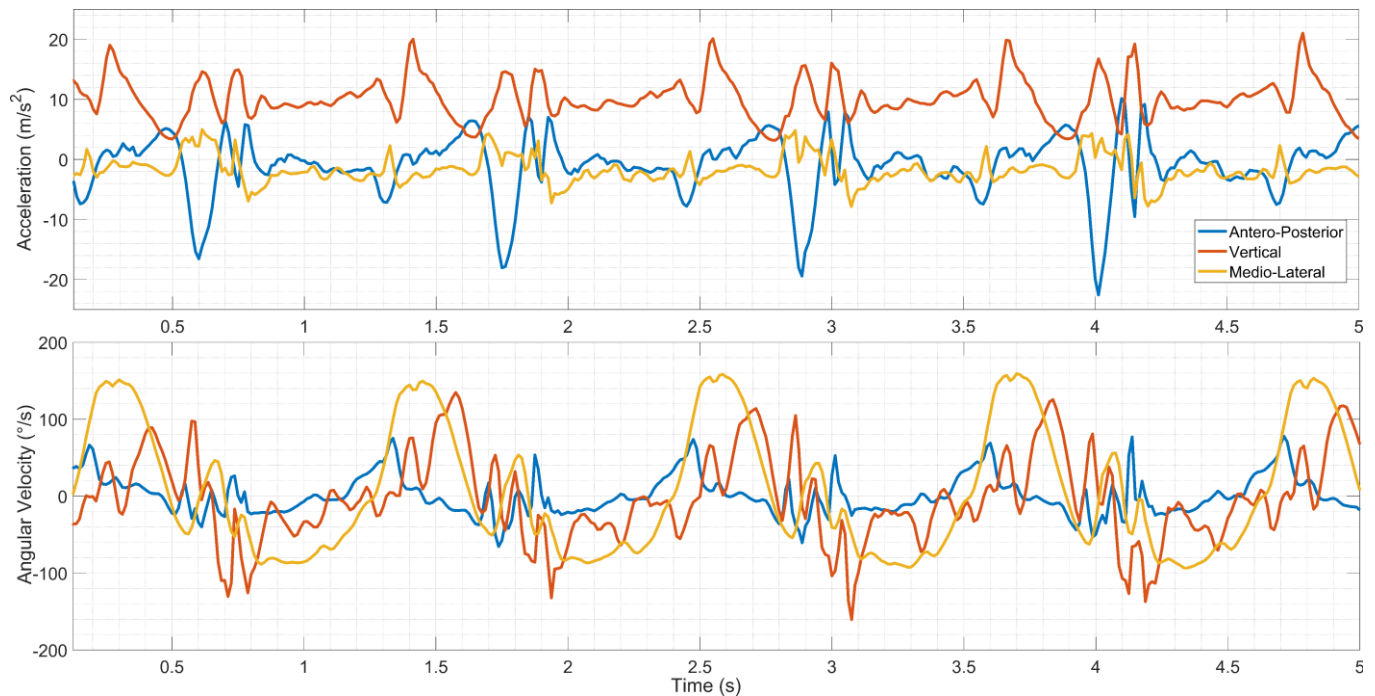
Figure 1. Example of inertial signals acquired by accelerometer (top) and gyroscope (bottom) during 5 seconds of level walking of a healthy subject.

walking, uphill and downhill walking, stairs ascending and descending, upright standing, and sitting. Each activity, performed in indoor and outdoor areas, lasted approximately 50 s and was repeated five times by each subject.

Each subject signed an informed consent form. The experimental protocol conformed to the Helsinki declaration on medical research involving human volunteers.

B. Data Acquisition

A MIMU-based micro-processed device designed and developed at our lab, and now produced and distributed by Medical Technology (Italy), was used to acquire the signals [5], [7], [14]. This device is based on a tri-axial accelerometer, a tri-axial gyroscope, and a tri-axial magnetometer. The measurement range is ± 4 g for the accelerometer, ± 2000 °/s for the gyroscope, and ± 4 G for the magnetometer. The sampling frequency for all the acquired signals is equal to 80 Hz.

In this study, only the inertial signals (i.e., accelerometer and gyroscope signals) acquired from each axis were considered for activity recognition, hence six different signals were used as input features of the LSTM neural network.

Figure 1 represents an example of the signals acquired by the accelerometer and gyroscope sensors fixed on the right thigh of a healthy subject during level walking.

The wearable device was fixed on the lateral side of the right thigh by means of an elastic belt. The y-axis was oriented in the down-top vertical direction, the x-axis was aligned to the antero-posterior direction, and the z-axis was aligned to the medio-lateral direction. Figure 2 shows the MIMU-based wearable device fixed on a volunteer during upright standing.

C. Long Short-Term Memory Neural Network (LSTM)

Long Short-Term Memory (LSTM) neural networks are a widely used type of artificial neural network specifically designed to recognize patterns in sequential data, such as numerical time series, texts, and audio tracks [9]. These networks were introduced by Hochreiter and Schmidhuber in 1997 [15] and represent an extension of the Recurrent Neural Networks, allowing for a better assessment of the time-dependencies in sequential data. Actually, the LSTM neural network represents the state of the art in natural language
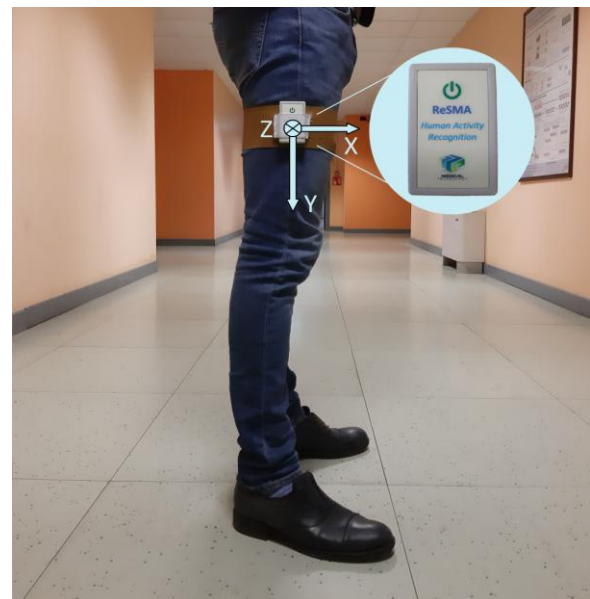

Figure 2. Experimental setup of a subject wearing the MIMU-based micro-processed device (actigraph) by means of an elastic belt on the lateral side of the right thigh. The y-axis is oriented in the down-top vertical direction, the x-axis is aligned to the antero-posterior direction, and the z-axis is aligned to the medio-lateral direction.

processing and speech recognition problems [16].

In this study, we implemented a simple LSTM model to classify seven different activities starting from sequential data acquired from the accelerometric and gyroscopic sensors. The model presents the following structure:

i. *Input sequence layer*
ii. *LSTM layer* used to learn the time-dependence from the accelerometer and gyroscope signals
iii. *Fully connected layer* used to convert the output size of the previous layers into the number of activities to be recognized
iv. *Softmax layer* used to compute the belonging probability for every possible class
v. *Classification output layer* used to compute the cost function

To define the best LSTM model for human activity recognition, the entire dataset was divided into three different sets called training set, validation set (or developing set), and test set, respectively. The training set (70%) was used to train the LSTM, while the validation set (15%) was used to evaluate the accuracy of the network and to avoid the overfitting of the training data. Finally, the overall classification accuracy of the LSTM model was evaluated by considering the test set (15%) only.

The algorithm for the definition of the best LSTM model was developed in MATLAB® release R2019b (The MathWorks Inc., Natick, MA, USA). The processing was performed on a workstation with a 3.20 GHz i7-8700 CPU, 32 Gb of RAM memory and 64-bit version of Windows 10.

III. RESULTS

The dataset that was retrospectively analyzed in this contribution consists of 427 different 50-s epochs of accelerometer and gyroscope signals. Each of the 427 epochs of the dataset was a $n \times m$ matrix, where n was equal to 6 (i.e. 3 accelerometer and 3 gyroscope signals) and m was equal to the number of samples collected within a 50-s epoch. During the training step, the training set was further split into smaller subsets, called mini-batches, to speed up the optimization algorithm. A mini-batch size of 64 epochs was used for each of the tested LSTM models.

TABLE I
DETAILS OF THE BEST LSTM MODEL

LSTM Layers	Properties
Sequence input layer	6 input features
LSTM layer	225 hidden units, sequence-to-sequence architecture
Fully connected layer	7 units
Softmax layer	Softmax activation function (threshold = 0.5)
Classification output layer	7 classes

A. LSTM Model

To define the best LSTM model for the detection of the proposed activities we used a brute-force approach. Specifically, 360 different models were tested using the neural network toolbox of MATLAB®. All the tested models had a sequence input layer consisting of 6 units (3 accelerometer and 3 gyroscope signals) and a fully connected output layer consisting of 7 units (number of activities to be recognized). The tested models differ in terms of number of LSTM layers, number of hidden units for each LSTM layer, learning rate (α), and drop period (δ). Two different values of number of hidden LSTM layers ($n = 1, 2$), nine different numbers of hidden units in each LSTM layer ($n_{units} = 100, 125, 150, 175, 200, 225, 250, 275,$ and 300), five different values of learning rate ($\alpha = 0.01, 0.015, 0.02, 0.025, 0.03$), and eight different drop rate values ($\delta = 10, 15, 20, 25, 30, 35, 40, 45$) were tested. The performance of the LSTM classifiers was assessed by computing the overall classification accuracy, defined as the number of correctly classified epochs normalized by the total number of epochs in the test set.

The best LSTM model was selected among all the tested networks as the one with the highest overall classification accuracy, discarding those networks with a difference between the training and validation accuracy higher than 4%. Moreover, accuracy and loss curves of the remaining models were carefully assessed to avoid overfitting or underfitting of the training data.

Figure 3 shows the distribution of the classification accuracies for each of the 7 activities among all the 360 tested LSTM neural networks. Results revealed a different

TABLE II
CLASSIFICATION ACCURACY OF THE BEST LSTM MODEL

|		Predicted						
		Ascending Stairs	Descending Stairs	Downhill Walking	Level Walking	Sitting	Upright Stance	Uphill Walking
True	Ascending Stairs	**98.7**	0.6	0.4	0.5	0.0	0.0	1.1
	Descending Stairs	0.1	**97.2**	0.5	0.2	0.0	0.1	1.6
	Downhill Walking	0.2	1.1	**92.7**	2.9	0.0	0.0	0.8
	Level Walking	0.2	0.2	5.4	**93.4**	0.0	0.0	3.2
	Sitting	0.0	0.1	0.1	0.1	**100.0**	0.0	0.5
	Upright Stance	0.1	0.4	0.4	1.3	0.0	**99.9**	0.9
	Uphill Walking	0.8	0.5	0.5	1.5	0.0	0.0	**92.0**
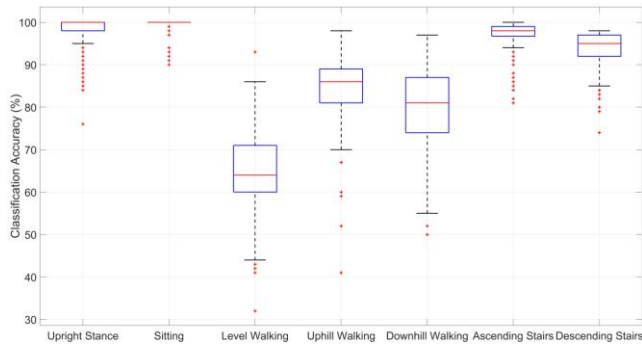
Figure 3. Boxplot of the classification accuracies for each of the 7 activities among all the 360 tested LSTM neural networks. The performances achieved in the classification of the upright stance, sitting, ascending and descending stairs activities are consistent across the different LSTM architectures. Instead, the classification accuracies achieved in the classification of the level, uphill and downhill walking activities are strongly affected by the selection of the architecture

accuracy of the LSTM classifiers for different activities and architectures of the neural networks. The accuracy achieved in the classification of the upright stance, sitting, ascending and descending stairs are consistent across the different architectures of the LSTM classifier, while those in the classification of level, uphill and downhill walking are strongly dependent on the selection of the architecture parameters.

Table I shows the properties of the LSTM architecture that achieved the highest test classification accuracy, while the relative confusion matrix is represented in Table II.

IV. DISCUSSION AND CONCLUSIONS

Among the deep learning approaches, the LSTM was initially selected as a promising classifier to perform human activity recognition of different activities of daily living (level walking, uphill and downhill walking, stairs ascending and descending, upright stance, and sitting), from accelerometric and gyroscopic signals. Different models of LSTM artificial neural networks were evaluated and the most performant architecture was chosen among 360 that were tested. This architecture allows for achieving classification accuracies ranging from 92% (for uphill walking) up to 100% (for sitting).

The results revealed that the smaller accuracy is achieved in the classification of uphill walking (92.0%), downhill walking (92.7%), and level walking (93.4%). The slightly higher percentage of misclassifications for these activities is not surprising. In fact, the inertial signals share very similar patterns among level walking and uphill/downhill walking on slopes of approximately ±5% of incline.

The proposed LSTM classifier can be easily implemented and has the following advantages: 1) it provides a very high classification accuracy, 2) it does not require any pre-processing step on the MIMU signals, 3) it does not require any feature extraction and selection procedure.

In future works, a cascade LSTM neural network will be considered to overcome the limitations of the proposed

LSTM architecture in the classification of level, uphill and downhill walking activities.

REFERENCES

[1] Y. Wang, S. Cang, and H. Yu, "A Data Fusion-Based Hybrid Sensory System for Older People's Daily Activity and Daily Routine Recognition," *IEEE Sens. J.*, vol. 18, no. 16, pp. 6874–6888, 2018.

[2] P. Tsinganos and A. Skodras, "On the comparison of wearable sensor data fusion to a single sensor machine learning technique in fall detection," *Sensors (Switzerland)*, vol. 18, no. 2, 2018.

[3] S. González, J. Sedano, J. R. Villar, E. Corchado, Á. Herrero, and B. Baruque, "Features and models for human activity recognition," *Neurocomputing*, vol. 167, pp. 52–60, 2015.

[4] S. H. Roy *et al.*, "A Combined sEMG and Accelerometer System for Monitoring Functional Activity in Stroke," *IEEE Trans. Neural Syst. Rehabil. Eng.*, vol. 17, no. 6, pp. 585–594, 2009.

[5] G. De Leonardis *et al.*, "Human Activity Recognition by Wearable Sensors," in *2018 IEEE International Symposium on Medical Measurements and Applications (MeMeA) Proceedings*, 2018.

[6] G. De Leonardis *et al.*, "Human Activity Recognition by Wearable Sensors : Comparison of different classifiers for real-time applications," *MeMeA 2018 - 2018 IEEE Int. Symp. Med. Meas. Appl. Proc.*, pp. 1–6, 2018.

[7] S. Rosati, G. Balestra, and M. Knaflitz, "Comparison of different sets of features for human activity recognition by wearable sensors," *Sensors (Switzerland)*, vol. 18, no. 12, 2018.

[8] S. J. Preece, J. Y. Goulermas, L. P. J. Kenney, D. Howard, K. Meijer, and R. Crompton, "Activity identification using body-mounted sensors—a review of classification techniques," *Physiol. Meas.*, vol. 30, no. 4, pp. R1–R33, 2009.

[9] A. Graves, "Generating Sequences With Recurrent Neural Networks," pp. 1–43, 2013.

[10] Y. Chen, K. Zhong, J. Zhang, Q. Sun, and X. Zhao, "LSTM Networks for Mobile Human Activity Recognition," 2016.

[11] F. J. Ordóñez and D. Roggen, "Deep convolutional and LSTM recurrent neural networks for multimodal wearable activity recognition," *Sensors (Switzerland)*, 2016.

[12] N. Y. Hammerla, S. Halloran, and T. Plötz, "Deep, convolutional, and recurrent models for human activity recognition using wearables," in *IJCAI International Joint Conference on Artificial Intelligence*, 2016.

[13] Y. Guan and T. Plötz, "Ensembles of Deep LSTM Learners for Activity Recognition using Wearables," *Proc. ACM Interactive, Mobile, Wearable Ubiquitous Technol.*, 2017.

[14] G. De Leonardis, D. Fortunato, C. M. Gianfreda, S. Rosati, G. Balestra, and M. Knaflitz, "An innovative microprocessor-based system for Human Activity Recognition: A fast and reliable classification algorithm," *Gait Posture*, vol. 66, pp. S14–S15, 2018.

[15] S. Hochreiter and J. Schmidhuber, "Long Short-Term Memory," *Neural Comput.*, vol. 9, no. 8, pp. 1735–1780, Nov. 1997.

[16] Y. Goldberg, "Neural Network Methods for Natural Language Processing," *Synth. Lect. Hum. Lang. Technol.*, vol. 10, no. 1, pp. 1–309, Apr. 2017.

An Augmented-Reality App to communicate through the eye-gaze

M. Rossi[1,2], G. D'Avenio[2], F. Cincotti[1,3], and M. Grigioni[2]

[1] Department of Computer, Control and Management Engineering, Sapienza University of Rome
[2] National Center for Technological Innovation in Public Health, Istituto Superiore di Sanità, Rome
[3] Neuroelectric Imaging and BCI Lab, Santa Lucia Foundation, IRCCS, Rome

Abstract— **Language disorders are considered a main cause for worsening the people quality of life. Especially in children, these disorders may involve future emotional and intellectual issues. Technological solutions for augmented and alternative communication aim to simplify and increase communication properties of individuals who have difficulties using the most common communicational channels. For people who suffer from language disorders and motor problems, a device capable of convert the gaze into a cursor control on a display could be the only solution. We developed an augmented reality App for a commercial smart glasses, able to track user's gaze and equipped with a "text-to speech" technology, designed for children as a communication device, that allows users to have face-to-face conversations, improve social relations and express their personal potential only by choosing specific pictograms using eye-gaze only.**

Keywords— smart glasses, augmented communication, gaze tracking.

I. INTRODUCTION

Developmental language disorder is considered a cause of public health concern. In children, it implicates an increased risk of school failure and can be a cause of social, emotional, and behavioral issues. In general, statistics (Fig. 1) estimates that about 7.5% of children (age 3-17), have a clinically significant language disorder that is considered to be a direct cause that impedes learning. On the other hand, 2.3% of children with language impairment presents an associated medical diagnoses and/or intellectual disorder [1].
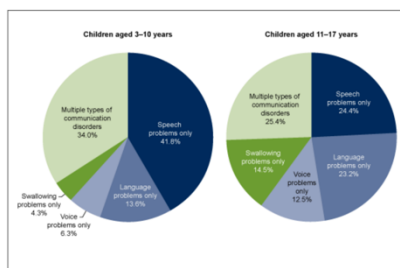

Fig. 1. Percentage distribution of types of communication disorders among children aged 3–17 years with a communication disorder during the year 2012 (Data are based on household interviews with parents or adult caregivers of children in a sample of the civilian noninstitutionalized U.S. population. SOURCE: CDC/NCHS, National Health Interview Survey, 2012).

Specific language impairment (SLI), one of common developmental disorders (7-8% incidence in kindergarten) is a communication disorder characterized by issues in acquiring and usage of the most common communication channel, in particular written and oral language. Even though this disorder's causes are unknown, studies suggest that it has genetic routes. In fact, approximately 50-70% of SLI patients have at least one relative with language disorder [2]. In addition to the above-mentioned factor, language impairment is caused by other diseases such as, neurodevelopmental disorders (autism spectrum disorders, down syndrome, cerebral palsy, etc.) or degenerative neurological conditions (e.g., primary progressive aphasia) [3]. Individuals presenting such disabilities must necessarily lay on others to satisfy their essential needs [4]. The communication difficulties occur during the interaction with parents, but it is especially accentuated while interfacing with strangers [5].

Functional impairments limit children to fully live their childhood. By participating in meaningful activities, children could develop certain skills, learn to self-express and are better engaged in social activities [6].

II. AUGMENTATIVE AND ALTERNATIVE COMMUNICATION

The possibility to inform other individuals regarding their needs and preferences is fundamental for establishing solid social relations [4]. In order to maintain an acceptable social life, have decision-making abilities and the capability to indicate needs and willingness, an effective communication method is necessary.

Augmented and Alternative Communication (AAC) has become an essential part of intervention programs for those persons who have difficulties utilizing common communication channels [7]. Some children are using low-tech devices such as tables or books containing images and, by indicating with fingers or pointing with eyes, it is possible to interpret their intention. However, if children involved are presenting motor impairments as well, it gets more complicated. A possibility is to understand where the child is looking, but more frequently parents are interacting with simple ''yes or no questions'', on which children are able to respond, for example, by showing different facial expressions or by orientating their gaze up and down [5]. Hence, it is necessary the employment of devices able of detect these features automatically.

A. Assistive Technologies

International Organization for Standardization defines Assistive Technology (AT) as "any product (including devices, equipment, instruments and software), especially produced or generally available, used by or for persons with disability, for participation, to protect, support, train, measure or substitute for body functions/structures and activities, or to prevent impairments, activity limitations or participation restrictions" [8]. Even though, AT technologies may offer a treatment for the patient or at least reduce its disability, it may act as an equalizer, by being a factor that offers to a disabled child the opportunity to be dedicated to activities while having the success as peers children without disorders [6]. With support of computers, children develop a new awareness toward the importance of using a communication code [9]. In literature, various studies reported that technology have the potential to

"free" children from their disability and to enable them to show their real potential [10]. Computer ATs could in fact support clinicians, educationalists and parents to improve children's participation into diverse childhood occupations and to develop their own occupational role [6].

Advances in mobile technologies have provided new tools for the communication [3]. For example, tablet utility has been already proved in this field which resulted as favorable compared to traditional techniques that utilize *picture cards* [7]. Recently, interest in the use of portable media player and smartphones as speech-generating devices has increased. In general, these new technologies are smaller and more financially affordable in comparison with traditional AAC devices [3].

Children who have language impairment as well as motor disabilities are unable to interact with traditional input devices (mouse, keyboard, joystick, touchscreen, etc.) in an appropriate way [11]. To match users with particular needs, alternative Human Computer Interfaces have been adopted. Several studies used *gesture recognition* techniques, capable of recognize automatically some specific hand gestures and translate it into vocal outputs [12]. However, this technology has some limitations: technological (use of a camera or a glove), statistical (based on an error prone statistical model) and physical (requires accurate hands and fingers movements) [13]. Other studies used as an input a bio-signal registration. For example, muscle electrical activity signals (EMG) (e.g. [14]), especially from facial muscles; or brain-computer interface (BCI), most of which are based on electroencephalogram signal (e.g., [15]). In relation to EMG-based systems, BCI doesn't require any motor input. However, BCI requires a long preparation time [16].

B. Gaze-based AT

Already in the last decade of the past century, many researchers started to assess the possibility to support individuals affected by both language and motor impairments with employments of gaze-based AT [11], [17], [18], [19]. Eye-gaze technology could provide a mean to access AAC electronic systems in a fast, reliable and more independent way [20]. So, this technology can improve children's quality of life and provide a hope for a child's future inclusion in society.

Several ways could be used to interface eye-gaze systems with computers or an AAC technology, some are surface electrodes around eyes (electrooculogram), video imaging, gaze-tracking or eye-tracking to measure the line of gaze view [22]. A device that integrates gaze-tracking, a screen showing a keyboard or an image and a text-to-speech (TTS) technology allows to communicate by dwelling the gaze on the element for a time at least equal than a prefixed time period or by blinking or winking [23]. Previous researches have reported positive results regarding the usage of gaze-based AT by people with serious motor impairment to carry out activities of daily living (e.g., [24]).

We have developed a communication, augmented-reality based system for children, affected by language and motor disabilities, to be implemented for a head-mounted display (HMD). Throughout the HMD, users can select the icons shown on the display, by pointing his/her gaze for more than a programmable period, so that it activates the related function.

III. APP IMPLEMENTATION AND DESIGN

The set-up used in the present study is a commercial HMD (Fig. 2), able to detect the direction of user's gaze and it is equipped with TTS technology. The App was implemented with "Unity 3D", a cross-platform game engine, and a plugin provided by the HMD's manufacturer.

Fig. 2.   The commercial HMD used in this study.

Fig. 3 shows the interface menu that appears when the App is executed. While the user is exploring the surrounding environment, the cursor (the "white dot", showed at the center of Fig.3) indicates where he/she is looking.
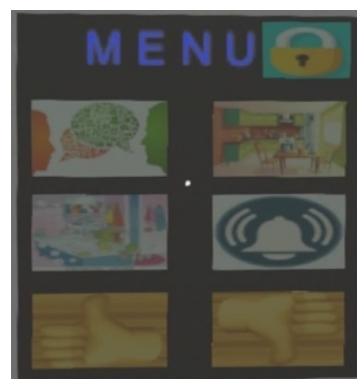

Fig. 3.   The figure shows the layout display showed on the HMD when executed. On the top right an icon (lock) is displayed that blocks the App. The four central icons allows to open the related sub-menus. The bottom two icon (Yes or No) give the specific vocal answer.

At each icon of the menu is associated a programmed function:

- The icon representing the lock allows the user to block the selection when the user doesn't need it, to avoid false selection;

- In the bottom section of the menu, icons related to specific answer, positive (on the right) and negative (on the left) are displayed. When one of these options is selected the HMD reads out the answer.

- At each one of the four central icons, a sub-menu is associated. When the cursor is overlapping with an icon, the word associated with it is displayed.

The selection of an element passes through 3 steps, to avoid, or at least limit, false selections [23], [25]: when the cursor is overlapping with an icon, the word related to it is displayed (left panel of Fig. 4); if the gaze dwells for longer than 1 second, the color of the displayed word changes (right panel of Fig. 4); if the cursor stays for 1 more second, the element is considered selected.

Fig. 4. The figure shows a comparison between the icons previous the selection. On the left, white word, is displayed on the icon for cursor pointing for less than 1 second; on the right, green word, for cursor pointing between 1 and 2 seconds from the instant which the cursor and the icon are overlapped.

IV. DISCUSSION

The eye-gaze interfaces can be an efficient input mean because eye-gaze is natural, fast and involved muscles are subjected to little efforts [22]. A previous study engaging amyotrophic lateral sclerosis patients have demonstrated that subjects who used eye-gaze devices were less depressed and showed an improved quality of life in comparison to whom were using a phonetic board [26]. The introduction of eye-gaze controlled computers at home and school could enhance children's communication skills, allowing them to express their desires and to carry out recreative activities [27], as well as improving their social activities (for example, choosing their game mate [28] or which song to be listen at school [20]). Employing augmented-reality communicators, as illustrated in this paper, allows to have a face-to-face conversation, without losing the non-verbal conversational component. This type of system requires only a brief learning period [16] and a low workload [29].

The choice in this study to use sentences rather than showing a keyboard was made with the purpose to reduce the downtime during the conversation [23]; moreover, the employment of pictogram was originated by the fact that disabled people, children in particular, prefer symbolic images instead of words [13]. Regarding fixation time to the eye-gaze selections of an element, previous researchers (e.g., [25], [30]) stated that few hundred of milliseconds are considered to be a good tradeoff between false selections and speed of communication. Due to the fact that our system is developed for disabled individuals, we set a threshold for the selections that equals to 2 seconds.

On the other hand, technological limits are related to gaze-based AT. In general, accuracy could be not considered as good as a traditional mouse, for both technological and eye-features properties. In fact, eye-movement are subconscious, while a total and constant eyes' control is required. Furthermore, in particular people with disabilities may find difficult to search and select simultaneously [22].

Concerning literature results, only few studies have applied the standard ISO 9421-9 for the evaluation of performance, comfort and effort requested by devices. Mass adoption of those criteria would improve the results strength and simplify the comparison [31].

V. CONCLUSION

Although gaze-based AT are available, nowadays only a small group of children can access it, in part due to the high cost [11] and because parents have doubts that children with both serious physical and cognitive impairments are able to control a device with their eyes [32]. At the date, children use the device only for a short time period, and mostly on request rather than on their own initiative [6], but parents are convinced that there is a gap between what the child can do today and what would be able to do in the future thanks to AT gaze-based and, in addition, they are convinced that it is correct to continue investing in this technology [5]. Another aspect that should not be underestimated is that classmates would be curious and interested about the technology and this can lead to a greater inclusion of the disabled person with his peers [28].

We have performed a pilot study to get feedback from healthy subjects about the implementation of the App and we are making changes based on the reports. Therefore, we are planning an experimental study to evaluate the usability of the proposed system, initially starting from a group of children who do not have disabilities.

REFERENCES

[1] C. F. Norbury, D. Gooch, C. Wray, G. Baird, T. Charman, E. Simonoff, G. Vamvakas, and A. Pickles, "The impact of nonverbal ability on prevalence and clinical presentation of language disorder: evidence from a population study," Journal of Child Psychology and Psychiatry, 57, 1247 – 257, May 2016.

[2] https://www.nidcd.nih.gov/health/specific-language-impairment

[3] D. McNaughton and J. Light, "The iPad and mobile technology revolution: Benefits and challenges for individuals who require augmentative and alternative communication," Augmentative and Alternative Communication, 29, 107–116, 2003.

[4] C. V. Fleming, G. M. Wheeler, H. I. Cannella-Malone, A. R. Basbagill, Y. C. Chung, and K.G. Day, "An evaluation of the use of eye gaze to measure preference of individuals with severe physical and developmental disabilities," Developmental Neurorehabilitation, 13, 266–275, Aug. 2010.

[5] M. Borgestig, P. Rytterström, and H. Hemmingsson, "Gazed-based assistive technology used in daily life by children with severe physical impairments - Parents' experiences," Developmental Neurorehabilitation, 20:5, 301–308, Aug. 2016.

[6] J. Chantry J and C. Dunford, "How do computer assistive technologies enhance participation in childhood occupations for children with multiple and complex disabilities? A review of the current literature," British Journal of Occupal Therapy, 73(8): 351–365., June 2010.

[7] M. Flores, K. Musgrove, S. Renner, V. Hinton, S. Strozier, S.Franklin, and D. Hil, "A comparison of communication using the Apple iPad and a picture-based communication system", Augmentative and Alternative Communication, 28, pp. 74-84, Jan. 2012.

[8] https://www.iso.org/obp/ui/#iso:std:iso:9999:ed-6:v1:en

[9] S. Besio and A. L. Salminen, "Children and youngsters and technology," Technology and Disability, 16 (3), 115–117, 2004

[10] T. Hasselbring and C. Williams Glaser, "Use of computer technolgy to help students with special needs: the future of children," Children and Computer Technology, 10(2), 102-22, 2000.

[11] C. L. Chen, C. Y. Wu, H. C. Chen, W. H. Hong, W. Y. Liu, A. Wong, C. Y. Chung, and H. C. Hsu, "Application of a novel integrated pointing device apparatus for children with cerebral palsy," Chang Gung Med J, 29: 380– 7, July 2006.

[12] P. Matetelki, M. Pataki, S. Turbucz, and L. Kovacs, "An assistive interpreter tool using glove-based hand gesture recognition," IEEE Canada International Humanitarian Technology Conference, pp. 1-5, June 2014.

[13] K. Wolk, A. Wolk, and W. Glinkowski, "A cross-lingual mobile medical communication system prototype for foreigners and subjects with speech hearing and mental disabilities based on pictograms," Computational and Mathematical Methods in Medicine, vol. 2017, pp. 1-9, 2017.

[14] C.A. Chin CA, A. Barreto, and M. Adjouadi, "Enhanced real-time cursor control algorithm, based on the spectral analysis of electromyograms," Biomedical Science and Instrumentation 42: 249–54, Feb. 2006.

[15] F. Cincotti, D. Mattia, F. Aloise, S. Bufalari, G. Schalk, G. Oriolo, A. Cherubini, M. G. Marciani, and F. Babiloni, "Non-invasive brain-computer interface system: Towards its application as assistive technology," Brain Res. Bull., vol. 75, no. 6, pp. 796-803, Apr. 2008.

[16] E. Pasqualotto, T. Matuz T, S. Federici, C. A. Ruf, M. Bartl, M. O. Belardinelli, N. Birbaumer, and S. Halder, "Usability and Workload of Access Technology for People With Severe Motor Impairment, A Comparison of Brain-Computer Interfacing and Eye Tracking," Neurorehabil Neural Repair, 29: 950–7, Mar. 2015.

[17] J. ANGELO, C. DETERDING, AND J. WEISMAN, "COMPARING THREE HEAD-POINTING SYSTEM USING A SINGLE-SUBJECT DESIGN," ASSISITIVE TECHNOLOGY 3(2): 43–49, JAN. 1991.

[18] D. G. Evans, R. Drew, and P. Blenkhorn, "Controlling mouse pointer position using an infrared head-operated joystick," IEEE Trans. Rehab. Eng., vol. 8, no. 1, pp. 107-117, Mar. 2000.

[19] G.E. Lancioni, N. N. Singh, M. F. O'Reilly, J. Sigafoos, C. Chiapparino, F. Stasolla, and D. Oliva, " Using an optical sensor and a scanning keyboard emulator to facilitate writing by persons with pervasive motor disabilities", J Dev Phys Disabil, 19:593–603, May 2007.

[20] K. van Niekerk and K. Tönsing, "Eye gaze technology: A South African perspective," Disability and Rehabilitation: Assistive Technology, 10(4), 340–6, Oct. 2014.

[21] P. Rytterström, M. Borgestig, and H. Hemmingsson, "Hope and technology: Other-oriented hope related to eye gaze technology for children with severe disabilities," Int. J. Environ. Res. Public Health, 16, 1667, May 2019.

[22] L. J. Ball, A. S. Nordness, S. K. Fager, K. Kersch, B. Mohr, G. L. Pattee, and D. R. Beukelman, "Eye-gaze access to AAC technology for people with amyotrophic lateral sclerosis," Journal of Medical Speech-Language Pathology, 18:11–23, Sep. 2010.

[23] P. Majaranta and K. J. Rih, "Twenty Years of Eye Typing: Systems and Design Issues," Proc. Symp. Eye Tracking Research and Applications, pp. 15-22, Jan. 2002.

[24] A. Calvo, A. Chiò, E. Castellina, F. Corno, L. Farinetti, P. Ghiglione, V. Pasian, and A. Vignola, "Eye Tracking Impact on Quality-of-Life of ALS Patients," 11th International Conference on Computers Helping People with Special Needs, Linz (AT), p. 70–77, 2008.

[25] P. Majaranta, S. MacKenzie, A. Aula A, and K. J. Räihä, "Effects of feedback and dwell time on eye typing speed and accuracy". Universal Access in the Information Society, 5 (2): 199-208, Aug. 2006.

[26] C.S. Hwang, H. H. Weng, L. F. Wang, C. H. Tsai, and H. T. Chang, "An Eye-Tracking Assistive Device Improves the Quality of Life for ALS Patients and Reduces the Caregivers' Burden", J Mot Behav, 46(4):233–8, 2014.

[27] A.J. Hornof and A. Cavender, "EyeDraw: enabling children with severe motor impairments to draw with their eyes," Proceedings of ACM CHI 2005: Conference on Human Factors in Computing Systems, pp. 161-170, 2005.

[28] P. Rytterström, M. Borgestig, and H. Hemmingsson, "Teachers' experiences of using eye gaze-controlled computers for pupils with severe motor impairments and without speech,". Eur. J. Spec. Needs Educ, 31, 506–519, June 2016.

[29] I. Käthner, A. Kübler, and S. Halder, "Comparison of eye tracking electrooculography and an auditory brain-computer interface for binary communication: a case study with a participant in the locked-in state," Journal of neuroengineering and rehabilitation, vol. 12, no. 1, pp. 76, 2015.

[30] D. M. Stampe and E. M. Reingold, "Selection by looking: A novel computer interface and its application to psychological research" in J. M. Findlay, R. Walker, and R. W. Kentridge (eds.), Eye movement research: Mechanisms, processes and applications, Elsevier, Amsterdam, 467-478, 1995.

[31] T. C. Davies, S. Mudge, S. Ameratunga and N. S. Stott, "Enabling self-directed computer use for individuals with cerebral palsy: a systematic review of assistive devices and technologies," Dev Med Child Neurol, 52:510– 6, Jan. 2010.

[32] M. Borgestig, J. Sandqvist, R. Parsons, T. Falkmer, and H. Hemmingsson, "Eye gaze performance for children with severe physical impairments using gaze-based assistive technology – a longitudinal study," Assistive Technology, 28:2, 93–102, May 2016.

An application of DMAIC methodology for reducing voluntary departures from an Emergency Department

G. Improta[1], M. Romano[2], C. Ricciardi[3], C. Cosentino[2], and F. Amato[4]

[1] Department of Public Health, School of Medicine and Surgery, University of Naples "Federico II"
[2] Department of Experimental and Clinical Medicine (DMSC), University "Magna Graecia" of Catanzaro
[3] Department of Advanced Medical Sciences, University of Naples "Federico II"
[4] Department of Electrical Engineering and Information Technology (DIETI), University of Naples "Federico II"

Abstract— The Emergency Department (ED) is a zone of a hospital where usually the healthcare staff has to face sudden and serious heathy problems. On the other side, patients find themselves in a situation of great emotion, discomfort and anxiety, aggravated by the expectation that, in cases of lesser severity, it can be long and badly tolerated. Furthermore, during access, patients and caregivers must undertake visits, assessments, consultations and bureaucratic procedures that can be long and complicated, due to inadequate or inaccurate information. In these conditions, waiting times can often be very long and / or patients can decide to abandon the ED. In this work, a combination of important managerial methodologies, Lean Six Sigma and DMAIC cycle (Define, Measure, Analyse, Improve, Control) are employed at an important hospital of South Italy in order to improve the emergency care process as well as the patient experience. It is a retrospective study, for which the historical times of access to the ED were analysed for the years 2015 and 2016. During this period, to improve the reception of patients and to reduce voluntary departures, two digital monitors were being designed and installed in the waiting room of the ED, which allow the visualization of the overall situation at the ED itself. The visualization is of course totally dynamic, i.e. the layout varies according to the data taken into consideration. In conclusion, the adopted approach impacts on the entrance and waiting times of patients in the ED and improves the general patient experience.

Keywords—DMAIC, Emergency department, health management, LSS.

I. INTRODUCTION

IT is known that the emergency is the department of a hospital responsible for the provision of medical and surgical care to patients arriving in need of immediate care. Of course, Emergency Department (ED) personnel may also respond to sudden situations happening within the hospital, such as cardiac arrests. In order to face every kind of pathology, it uses the cooperation of all the clinical specialities of the hospital. Hence, it can represent the heart of the hospital, meaning that it covers a strategic role and has to be properly managed both from an organizational perspective and a human one.

The mission of the ED is to guarantee prompt intervention, and adequate and optimal responses for each kind of person for urgent and emergency reasons. Therefore, the need to improve the cost of care, the speed of service, the patient safety and satisfaction, and to reduce crowding are now goals widely accepted [1].

In this context, another very important goal among hospital directors is to reduce the number of people which voluntary leave the ED without finishing the assistance path and even at

its beginning.

In order to understand in depth this phenomenon, during the last years, it has been studied from different points of view, organizational, managerial and it has been also studied the psychology of people in a queue. In [2] were analysed patients in an ED; they found that the abandonment is influenced mainly by the queue's length and flow. Other authors investigated, in a more quantitative way, which factors affect patients' decision during their waiting in an ED, they are waiting time, queue length, and service rate [3]. All these factors influence patient's propensity of leaving the waiting area without being seen by a physician.

Moreover, patients with more severe conditions abandon the ED before the ones with less severe conditions, that leads to the serious problem of risking adverse health consequences due to the absence or delay of a treatment.

Nowadays, it is known that managerial approaches together with statistical tools and simulation models [4], [5] can be adopted to improve healthcare processes and help in the decision-making as well as machine learning techniques [6], [7] and other data processing algorithms [8], [9]. Analogously, some specific tools can be also employed to reduce inefficiencies and limit the voluntary departures by an ED.

Before continuing, it is necessary to explain that the Italian Health System provides a colour code to divide patients into groups according to their severity (triage method).

The triage method is used primarily upon the arrival of patients in the ED, where access to treatment does not take place on the basis of the order of arrival but on the priority of their conditions. Practically, each patient which arrives at an ED is evaluated by nurses who as quickly as possible evaluate the patient's clinical condition and his/her evolutionary risk and assigns an urgency colour code: white for the non-urgent patients (they will also pay a ticket), green for the non-urgent patients that need a specialist treatment, yellow for a partial urgency, red for urgencies [10].

This paper aims to analyse the issue of number of voluntary departures (meaning by this the situations in which the patient leaves the department before any action) or abandonment (meaning by this the situations in which the patient leaves the department during the care path) and length of stay (LOS) in an ED.

To this aim, a Lean Six Sigma (LSS) approach with the problem-solving strategy of DMAIC cycle (Define, Measure, Analyse, Improve and Control) was employed to find the best solution and analyse the results, the "as-is" and the "to be" processes are then compared.

These methodologies were chosen since have potentialities

that are strengthened when the two approaches are "integrated" [11]. Moreover, their application in healthcare [12] has introduced novelties (such as integrated care pathways or fast track surgery) which have already demonstrated to give robust opportunities to lead to a general improvement, also in ED [1], [13], [14], [15].

II. METHODS

A. Hints of LSS

LSS is a managerial methodology employed firstly in industrial processes and then in healthcare organizations [16], [17] to tackle quality issues by improving quality, speed, customer satisfaction and costs; for processing biomedical data [18], [19]; analyse clinical pathways [20], [21]; and others [22]. It was born 20 years ago from the combination of two previous methodologies Lean Thinking and Six Sigma, already well-known in Japan and USA in Eighties, and has been applied by industries in a first period and in healthcare afterwards. While Lean Thinking [1] deals with speed and efficiency of the process' flow, Six Sigma regards precision and accuracy, in order to reduce variability and make more "stable" the process over the time [23], [24].

The former guarantees that the resources are working on the correct activities, while the latter guarantees that all the things are completed right the first time [12].

B. Hints of DMAIC

Let us remember that DMAIC [23] is a problem-solving strategy that is often adopted together with LSS. It consists in 5 cyclical phases driven by data for the continuous improvement of a process [25]:

• Define phase: makes clear and precise the problem that will be faced and consequently the objective to be reached.

• Measure phase: shows the as-is process (quantitatively, defining also the critical to quality (CTQ), i.e. the parameter to be improved), and involves the data collection in order to understand what type of errors were occurring.

• Analyse phase: the team analysis the as-is process to comprehend why errors are generated by detecting the key variables that most likely create process variations.

• Improve phase: mainly through brainstorming, the team identifies potential solutions for selecting, among the potential corrective actions, the best ones that can be useful for the identified problems during the analysis phase.

• Control phase: looks at the "to-be" process to guarantee a long-run result. The major aim of control phase is to sustain the improvements. Tools are put in place to ensure that under the corrected process the key variables remain within the maximum acceptable ranges over time.

C. Methods

As required by LSS improvement process [16], the DMAIC roadmap was adopted as tool to perform the study. Data for all the patients involved in the present study, personal, anamnestic and clinical variables, was collected from printed medical records and digital information system database of an important public hospital[1]. Data was collected from January

---

[1] The hospital is here not cited for privacy reasons

2015 to December 2016. Data gathered during the first year (90.312) represents the control group, and data about patients involved in 2016 (87662) represents the study group. The total sample of patients was 177974.

Let us show in more detail the application of the DMAIC phases in this study.

• *Define phase*: the problem to be solved was to reduce the LOS of patients and the number of patients leaving the ED before being visited. These parameters represent hence the CTQ.

• *Measure phase*: for each patient, the following information were stored: gender, age, date of Triage, admission, hospitalization.

About the LOS CTQ, it was measured in minutes elapsed staying in the ED.

About the CTQ consisting in the number of patients leaving the ED, two parameters were defined: the number of "Leave Without Being Seen" (LWBS) and number of "Leave Before Medical Record" (LBMR).

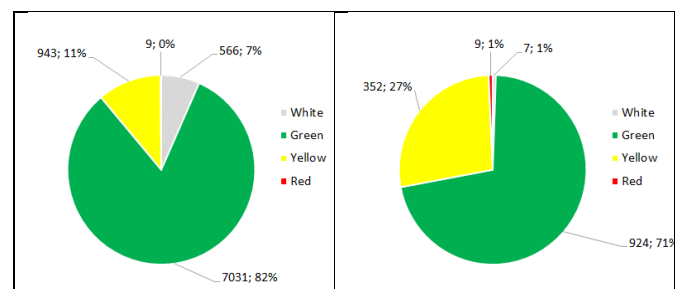In the following figures 1 and 2, the analysis carried out to measure the CTQs of the "as-is" process are shown.

Figure 1. On the left, number of LWBS patients for each assigned triage code; on the left; number of LBMR patients on the right.
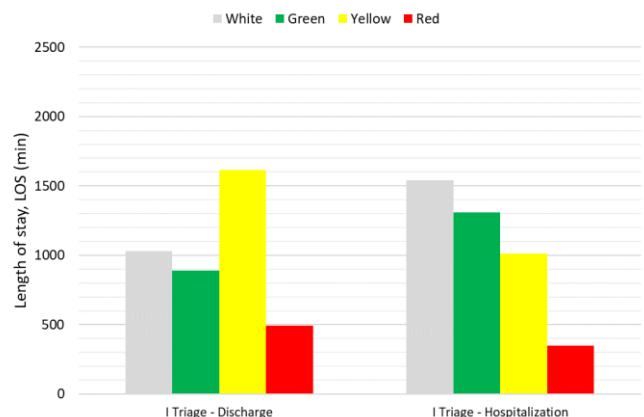

Figure 2. Los at different steps of the first aid process measured before improvement.

• *Analyse phase*: the team, composed both from engineers and clinicians, who shared the tasks of statistical analyses, process analysis and meetings for updating the project status, isolated the main activities recognised in the previous phases and identified sources of wastes, delays and inefficiencies.

At the end of the analysis phase, an Ishikawa diagram was drawn (Fig. 3).
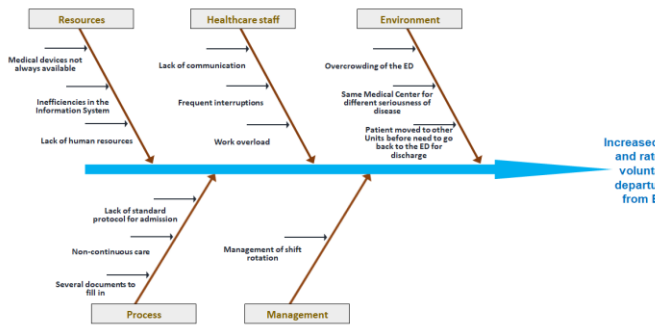
Figure 3. Ishikawa Diagram.

Among the different causes leading to the increase of LOS and voluntary departures from ED, the research team identified as more important:
- − the overcrowding of the ED
- − the patients' movement around the ED and other Units, very often useless
- − the lack of communication and information between patients and medical staff.

• *Improve phase*: In this phase, in order to solve the above emerged problems, as corrective action, the implementation of digital monitors for patients' acceptance was decided (Fig. 4).

Figure 4. Digital monitors for patients' acceptance.

The digital monitor on the left of Fig. 4 shows the overview of the crowding situation, in particular the status of three boxes: medical, orthopaedic and gynaecological; i.e. how many people are visiting, how many are waiting for the report, how many are under observation and how many are waiting for the hospitalisation. Obviously, for each category, the colour code is also reported.

The digital monitor on the right depicts the status of singular patients, i.e. their actual position in the care path.

• *Control phase*: as expected at this stage, the team looked at the "to-be" process, by monitoring over time, the process parameters chosen in the measure phase. After collecting the new data, in order to establish if the corrective action yielded to an effective improvement of the CTQ parameters' performances, a statistical analysis was carried out. In particular, a *t*-test (95% confidence interval) was performed to compare the average LOS between the groups before and after the implementation of the digital monitors, while a Chi-square test was used to compare the voluntary departure rates from the ED (LWBS and LBMR parameters). All statistical tests were carried out using SPSS software (IBM, version 20).

III. RESULTS

In this section, the results obtained in the control phase are reported, i.e. after the installation of the digital monitors, of course with reference to the performances' parameters defined in the measure phase.

A. *Performances of the to-be process*

Parameters here shown are: LWBS, LBMR and LOS.

In order to make simpler and faster the comparison with the situation of the as-is process, the same kind of representation has been chosen.
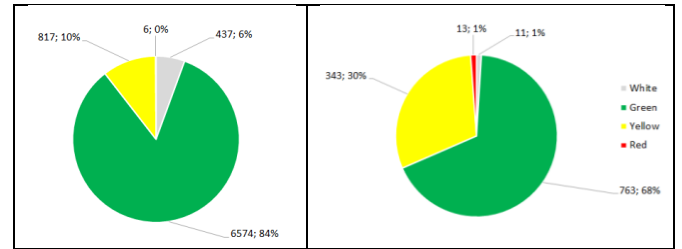

Figure 5. On the left, number of LWBS patients for each assigned triage code; on the left; number of LBMR patients on the right.
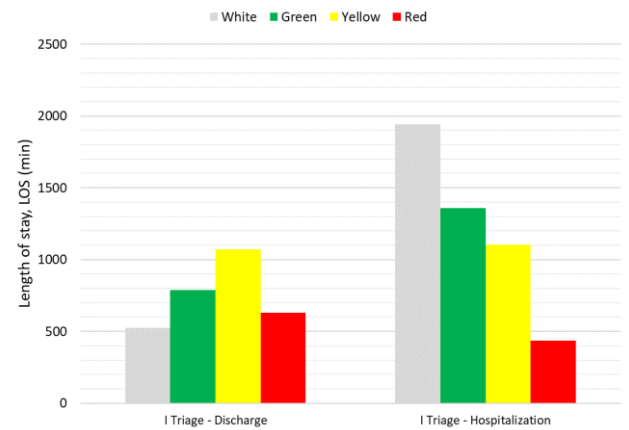

Figure 6. LOS at different steps of the first aid process measured after improvement.

B. *Statistical analysis*

In Table I the results of the statistical analysis are reported.

TABLE I
COMPARISON BETWEEN BOTH VOLUNTARY DEPARTURES AND LOS BEFORE AND AFTER THE CORRECTIVE ACTION

	Before improvement	After improvement	p value
LWBS [%]	9.46	8.94	0.0001
LBMR [%]	1.43	1.29	0.01
LOS (Triage – Discharge) [min]	1119.99	879.50	0.0001
LOS (Triage – Hospitalization) [min]	1068.16	1135.99	0.0003

All colour codes are here considered.

Finally, in order to ensure the sustainability of the results in the long run, the team planned the following actions:
• periodical review meetings to evaluate the status of the process implementation;
• internal auditing to verify the implemented solutions;
• periodical updates of the measurements.

IV. CONCLUSION

The adoption in healthcare of methodologies born and developed in industrial contexts has become a widespread practice and a useful strategic operation in order to achieve the excellence both as business and quality of processes. The LSS DMAIC methodology proved to be a helpful tool to identify wastes also in the ED care process, to find possible solutions, to measure and control the improvements through data gathering and statistical analysis.

The case here faced, the implementation of digital monitors, for patients' acceptance, demonstrated to be an effective way to reduce the overall ED care process and to enhance the general satisfaction of the staff (topic not explicitly treated for necessity of brevity). However, as shown in Figs. 5 and 6 and in Table I, not all the parameters showed an improvement. In particular, as far as the LOS, the comparison between Figg 2 and 6 shows a decrease in the triage-discharge LOS but an increase in the triage-hospitalization LOS. This can be explained by the fact that in 2016 there are fewer dropouts from the ED, i.e. reduced LWBS and LBMR (see Figg. 1 and 5), which lengthen hospitalization time because of the increased number of patients waiting for medical visits. Conversely, patients who do not need hospitalization are quickly discharged from the ED thanks to the leaner patients flow granted by the ED monitors.

These results suggest that the implemented process must be perfected, likely in all phases of the DMAIC cycle (of course except of the Define phase, because the problem to be solved does not change). For example, in the Measure phase, satisfaction of patients and staff should be added as CTQ parameters. As consequence, in the Improvement phase, questionnaires to submit to patients (or their companions) and ED personnel should to be planned. Furthermore, all personnel have to be identified by identification plates with name and role. Arrows on the floors could be traced to better identify the paths that patients must follow. That could have also an indirect positive effect: a decrease in overcrowding in some areas of ED, where patients who do not know where to go tend to stop. Indeed, another important topic that heavily affects ED functioning is precisely its overcrowding. In the control phase, patients should be divided in subsets according to the colour-code of the triage, in order to identify whose patients' category shows the most critical issues.

In conclusion, it is still possible to say that the adoption of the DMAIC cycle in the ED of a national hospital had a positive impact on the care process and on the department management.

REFERENCES

[1] R. J. Holden, "Lean Thinking in Emergency Departments: A Critical Review". *Annals of Emergency Medicine*, Vol. 57, No. 3, March 2011.

[2] R. Batt, C. Terwiesch, "Waiting patiently: An empirical study of queue abandonment in an emergency department". *Management Science*, 61(1), 39–59, 2015.

[3] E. Bolandifar, N. DeHoratius, T. Olsen, J. Wiler, "An empirical study of the behavior of patients who leave the emergency department without being seen". *Journal of Operations Management*, 65(5), 430-446, 2019.

[4] G. Improta, M. Romano, M. V. Di Cicco, A. Ferraro, A. Borrelli, C. Verdoliva, M. triassi, M. Cesarelli, "Lean thinking to improve emergency department throughput at AORN Cardarelli hospital". *BMC health services research*, 18.1: 914, 2018.

[5] G. Improta, G. Balato, M. Romano, A. M. Ponsiglione, E. Raiola, M. A. Russo, P. Cuccaro, L. C. Santillo, M. Cesarelli, "Improving performances of the knee replacement surgery process by applying DMAIC principles". Journal of evaluation in clinical practice, 23(6), 1401-1407, 2017

[6] C. Ricciardi, V. Cantoni, G. Improta, L. Iuppariello, I. Latessa, et al., "Application of data mining in a cohort of Italian subjects undergoing myocardial perfusion imaging at an academic medical center. *Computer Methods and Programs in Biomedicine*, 105343, 2020.

[7] V. Romeo, R. Cuocolo, C. Ricciardi, L. Ugga, S. Cocoza, et al., "Prediction of Tumor Grade and Nodal Status in Oropharyngeal and Oral Cavity Squamous-cell Carcinoma Using a Radiomic Approach. *Anticancer Research*, 40(1), 271-280, 2020.

[8] M. Romano, G. D'Addio, F. Clemente, A.M. Ponsiglione, G. Improtaand M. Cesarelli, "Symbolic dynamic and frequency analysis in foetal monitoring," *In 2014 IEEE International Symposium on Medical Measurements and Applications (MeMeA)* (pp. 1-5). IEEE, 2014.

[9] M. Romano, P. Bifulco, A.M. Ponsiglione, G. D. Gargiulo, F. Amato, and M. Cesarelli, "Evaluation of floatingline and foetal heart rate variability. *Biomedical Signal Processing and Control*, 39, 185-196, 2018.

[10] Ministero della Salute. "Linee di indirizzo nazionali sul triage intraospedaliero", 2012.

[11] J. Antony, P. Palsuk, S. Gupta, D. Mishra, P. Barach, "Six Sigma in healthcare: a systematic review of the literature". *International Journal of Quality & Reliability Management*, 35.5: 1075-1092, 2018.

[12] A. Laureani, A., J. Antony, "Leadership and Lean Six Sigma: a systematic literature review". *Total Quality Management & Business Excellence*, 30(1-2), 53-81, 2019.

[13] A. H. Tettey, S. E. Gholston, P. Welch, S. Dyas, S, "Application of Lean Six Sigma to Improve Inventory Management in an Emergency Department". *Journal of Management & Engineering Integration*, 9(1), 126-132, 2016.

[14] N. Mandahawi, M. Shurrab, S. Al-Shihabi, A. A. Abdallah, Y. M. Alfarah, "Utilizing Six Sigma to improve the processing time: a simulation study at an emergency department". *Journal of Industrial and Production Engineering*, 34(7), 495-503, 2016.

[15] S. L. Furterer, "Applying Lean Six Sigma methods to reduce length of stay in a hospital's emergency department". *Quality Engineering*, 30(3), 389-404, 2016.

[16] S. A. Albliwi, J. Antony, S. A. H. Lim, "A systematic review of Lean Six Sigma for the manufacturing industry". *Business Process Management Journal*, 21(3), 665–691, 2015.

[17] D. B. Henrique, D. B., M. Godinho Filho, "A systematic literature review of empirical research in Lean and Six Sigma in healthcare", *Total Quality Management & Business Excellence*, 1-21, 2018.

[18] C. Ricciardi, A. Fiorillo, A. Valente, A. Borrelli, C. Verdoliva, M. Triassi and G. Improta, "Lean Six Sigma approach to reduce LOS through a diagnostic-therapeutic-assistance path at A.O.R.N. A. Cardarelli", *The TQM Journal*, Vol. 31 No. 5, pp. 657-672, 2019.

[19] G. Improta, C. Ricciardi, A. Borrelli, A. D'alessandro, C. Verdoliva, and M. Cesarelli, "The application of six sigma to reduce the pre-operative length of hospital stay at the hospital Antonio Cardarelli", *International Journal of Lean Six Sigma*, 2019.

[20] G. Improta, G. Balato, C. Ricciardi, M.A. Russo, I. Santalucia, M. Triassi and M. Cesarelli, "Lean Six Sigma in healthcare", *The TQM Journal*, 2019.

[21] C. Ricciardi, G. Balato, M. Romano, I. Santalucia, M. Cesarelli, and G. Improta, "Fast track surgery for knee replacement surgery: a lean six sigma approach", *The TQM Journal*, 2020.

[22] G. Improta, G. Guizzi, C. Ricciardi, V. Giordano, A.M. Ponsiglione, G. Converso and M. Triassi, "Agile Six Sigma in Healthcare: Case Study at Santobono Pediatric Hospital", *International Journal of Environmental Research and Public Health*, 17(3), 1052, 2020.

[23] G. Ankitha, M. J. Aida, K. Sreenath, k. Vishnu Vettekkaram, M. Kaliyan, D. Britto, S. H. Sherief, S. Thangavel, "Application of Six Sigma DMAIC Methodology to Reduce Medication Errors in a Major Trauma Care Centre in India", *Indian Journal of Pharmacy Practice*, Vol 11, Issue 4, Oct-Dec, 2018.

[24] J. van den Heuvel, R. J.M.M. Does, J. P.S. Verver, "Six Sigma in healthcare: lessons learned from a hospital", *Int. J. Six Sigma and Competitive Advantage*, Vol. 1, No. 4, 2005.

[25] M. Sokovic, D. Pavletic, K. K. Pipan, "Quality improvement methodologies–PDCA cycle, RADAR matrix, DMAIC and DFSS", *Journal of achievements in materials and manufacturing engineering*, 43.1: 476-483, 2010.

Unobtrusive monitoring of stress indicators: a preliminary evaluation at rest

V.C. Zuccalà[1,2], R. Favilla[1], and G. Coppini[1]

[1] *Institute of Clinical Physiology of the National Research Council*
[2] *Department of Electrical, Electronic, and Information Engineering "Guglielmo Marconi" of the University of Bologna*

Abstract—**Monitoring individual well-being is central in developing novel disease prevention strategies. In this work we describe a simple setup to monitor a set of stress indicators including heart rate and heart rate variability, respiratory rate, and galvanic skin response using unobtrusive devices. Data obtained from the observation of twelve volunteers observed in resting state are summarized. The volunteers were divided into two groups based on age (25-35 years for group I and 55-65 years for group II).**

Keywords—**Well-being, stress, heart rate, respiratory rate, galvanic skin response.**

I. INTRODUCTION

INDIVIDUAL lifestyle is universally recognised as a key factor in disease prevention [1]. It is well known that lifestyle interventions are effective tools for reducing the risk and incidence of major illnesses including, but not limited to, cardiovascular and metabolic diseases. On the other hand, lifestyle habits are tightly linked to personal well-being. The latter indicates the state or condition of being in good physical and mental health and it is not surprising that monitoring individual well-being is central in developing novel prevention strategies. As a matter of fact, there is a growing general awareness of lifestyle relevance and a generalised trend to become an active part in monitoring, preserving, and improving personal wellness. In this respect, self-monitoring technology has gained a central role, resulting in the diffusions of dedicated devices, apps and services to assess our wellness and advising us on how to improve it [2].

Stress is a common state of emotional strain that plays a crucial role in everyday quality of life and is one of the main factors impacting on personal risk [3]. Stress is usually a state of tension produced when person responds to demands and pressures arising from external sources (e.g. work, family, and social environment) as well as those internally generated (e.g. self-imposed demands and obligations, self-criticism). This state consists of several complementary and interacting components (i.e. cognitive, affective, and psycho-physiological) [4]. Furthermore, chronic stress carries a wide range of health-related diseases, including cardiovascular diseases, cerebrovascular diseases, diabetes, and immune deficiencies. Due to the adverse effects of stress in our daily life, stress management has been receiving an increasing attention in health-care and well-being research [5][6][7]. In this respect, stress related factors, together with the development of personalised coping strategies, are of paramount importance.

As described in [8], autonomic nervous systems (ANS) controls the response of organs in our body such as the heart, stomach, and intestines. The parasympathetic ANS branch is responsible for nourishing, calming the nerves to return to the regular function, healing, and regeneration. On the contrary, the sympathetic branch is accountable for activating the glands and organs for defending the body from the threat. The ANS activation may be accompanied by many bodily reactions, such as increased heart rate (HR), and respiratory rate (RR), rapid blood flow to the muscle, activation of sweat glands which is linked to changes in skin conductance. Therefore, analysing these phenomena by monitoring related physiological parameters may allow to detect stress conditions.

This work is part of a research project aiming at building a model able to quantify the individual wellness status based on unobtrusive measurements and self-reported data. In particular, we focused on the assessment of resting status as a preliminary step to analyse the individual response to stress stimuli. Evaluating the status in the absence of external stimuli is crucial to assess and understand individual stimuli responses.

To this end we designed an experimental setup based on the integration of simple unobtrusive devices monitoring skin blood volume pulses (BVPs), respiratory rate, and galvanic skin response (GSR). The effectiveness of this setup was evaluated on a small sample of volunteers. Data were recorded in resting conditions and analysed as described in the following sections.

II. METHODS

A. Study's participants

Twelve healthy volunteers were enrolled. The sample was split into two groups: group I was composed by six voluntaries (4 females and 2 males) with age between 25 and 35 (mean 29, min. 25, max. 35); group II was composed by six voluntaries (4 females and 2 males) with age between 55 and 65 (mean 60.16, min. 53, max. 63). The experimental protocol received the Ethical Clearance certification (0050349/2019, July 09th, 2019) by the Council National Research Committee for Research Ethics and Bioethics. Written informed consent was obtained from all volunteers included in this study. In order to explain the experiment, an information sheet was distributed to the volunteers. No user pre-training was performed.

B. Experimental setup

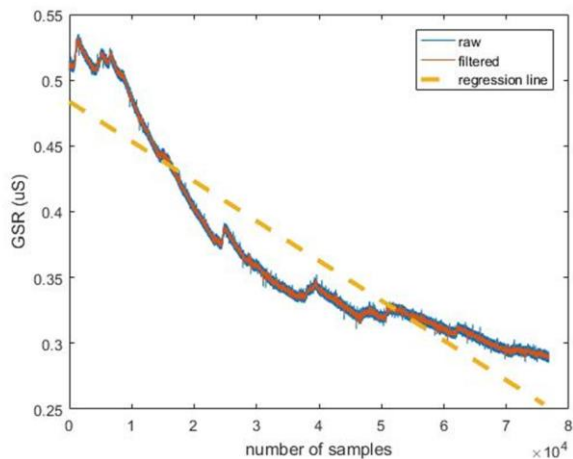The following set of the non-medical commercial devices were used:

Figure 1 A typical GSR record. The raw and the filtered signals of the skin conductivity of a subject during the resting state are shown. The regression line (obtained by the linear regression) is the average slope of the signal.

- Gigabit Ethernet camera with a CMOS monochrome sensor (UI-55240SE-NIR-GL, IDS GmbH, De). The camera was operated at 133 fps with an image matrix of 352 x 224 pixel, 8 bits/pixel. The video images were saved in real time in raw format by a Mac minicomputer (Intel Core i7 dual-core processor with 3 GHz, 16 GB RAM, and 500 GB SSD). In order to enhance the plethysmographic signal, the camera mounted an optical band-pass filter centred at 560 nm with a bandwidth of 40 nm [9].
- Bioaharness 3 Zephyr chest belt for the respiratory rate measure.
- Shimmer3 GSR for the galvanic skin response signal acquisition.

The subjects were sitting still in front of a computer. The chair had a headrest to contain head motion and making the recording comfortable for the volunteer. The subjects were illuminated by a white LED light source. At first the volunteer was invited to provide some base data: age, sex, weight, height, current perceived stress level through the perceived stress scale, and physical activity through the rapid assessment of physical activity questionnaire. The camera was positioned on a tripod at a distance of about one meter from the subject. The Bioharness 3 Zephyr chest belt was positioned around the chest with the centre line of the device directly under the armpit. The two electrodes of the Shimmer3 GSR were positioned on the palmar surface of the proximal phalanx of the index and of the middle finger, respectively.

After the sensors calibration was asked to the subject to close his/her eyes and to relax. The subject's signals were recorded for five minutes in resting state.

C. Video signal analysis

The video signal was analysed as described in [10]. According to [10], to extract the heart rate and the heart rate variability (HRV) parameters, image grey levels were averaged in the three automatically selected regions of interest (ROIs), which provided three time signals $x_1(t)$, $x_2(t)$, and $x_3(t)$. They were detrended by subtracting a 2 s time

TABLE I
RESULTS SUMMARY

Parameter	Group I	Group II
NN (ms)	823.24 (171.19)	849.98 (50.87)
SDNN (ms)	86.98 (52.02)	90.01 (48.32)
LF (%)	56.54 (47.44)	54.06 (9.92)
HF (%)	43.46 (44.44)	45.94 (9.92)
LF/HF	1.32 (1.73)	1.18 (0.52)
RR (bpm)	14.92 (3.86)	13.29 (0.66)
GSR (slope)	-4.15×10^{-4} (1.16×10^{-3})	-1.62×10^{-3} (3.08×10^{-3})

For each group, the median and the interquartile range, in brackets, of HR and HRV parameters (NN, SDNN, LF, HF, LF/HF), respiratory rate (RR), and the slope of the skin conductivity trend (GSR$_{slope}$) are reported.

average and were jointly processed through independent component analysis (ICA) as implemented in FastICA algorithm [11]; three new sequences $y_1(t)$, $y_2(t)$, and $y_3(t)$ were so obtained, each representing a different signal contribution. The spectra of $y_1(t)$, $y_2(t)$, and $y_3(t)$ were analysed. The component $y_s(t)$ having the highest peak in the range from 0.75 Hz to 2.0 Hz was selected as blood volume pulse (BVP) component. The $y_s(t)$ was then filtered using a FIR band-pass filter implemented via Hamming window, with lower cut-off at 0.75 Hz (45 bpm) and upper cut-off at 2 Hz (120 bpm). After filtering, BVP peaks were detected. Finally, the tachogram for each BVP peak sequence was computed. The NN and SDNN values were extracted from the tachogram. Analysis of HRV was performed by power density spectrum (PSD) estimation using the Lomb-Scargle periodogram. The values of low frequency (LF) and high frequency (HF) contribute to PSD, along with the ratio LF/HF values were calculated.

D. Respiratory rate signal analysis

Respiratory rate was measured through Bioaharness 3 Zephyr. The device provides respiratory rate at 1 Hz sampling frequency. The values of the median and the interquartile range were calculated.

E. Galvanic skin response signal analysis

Galvanic skin response was measured through Shimmer3 GSR. The skin conductivity was sampled at 256 Hz. The interfering main frequency (50 Hz) was removed from the signal by a notch filter. The average slope of the descending

portion of the signal was estimated by linear regression (see Figure 1).

III. RESULTS

Collected data were analysed for the two groups separately. In table I, the median and the interquartile range of all the data are reported.

The median (interquartile range) NN as calculated from the video signal is 823.24 ms (171.19 ms) and 849.98 ms (50.87 ms) for group I and group II respectively. This parameter is smaller in group I than in group II. The median (interquartile range) RR as measured through Bioaharness 3 Zephyr is 14.92 bpm (3.86 bpm) and 13.29 bpm (0.66 bpm) for group I and group II respectively. This parameter is smaller in group II than in group I. The variability of NN and RR in group II is lower than in group I. As shown in Figure 1, the skin conductivity decreases when the subject relaxes. The median (interquartile range) of the slope of the skin conductivity trend is -4.15×10^{-4} (1.16×10^{-3}) and -1.62×10^{-3} (3.08×10^{-3}) for group I and group II respectively. This suggests that skin conductivity of group II decreases faster than that one of group I.

IV. CONCLUSION

This study defined an experimental setup based on simple unobtrusive devices monitoring skin blood volume pulses, respiratory rate, and galvanic skin response. Imaging plethysmography was used to monitor the blood volume pulses using a video camera. The respiratory rate was monitored trough the Bioaharness 3 Zephyr chest belt and the galvanic skin response was monitored though the Shimmer3 GSR. Data from two groups of volunteers with different age ranges were recorded in resting state.

The results indicate that the variability of NN and RR is smaller in group II than in group I. The skin conductance decreases when the subject relaxes and decreases faster in group II than in group I.

The experimental setup turned out robust and reliable for unobtrusively monitoring the physiological signals taken into account, permitting us to extract relevant parameters from two groups of volunteers. Especially, the camera returns information of the heart rate in a contactless way. The camera together with the Bioaharness 3 Zephyr chest belt and the Shimmer3 GSR could allow to measure vital signs in environments of daily life and during others activities as driving, playing a video game, brushing teeth.

In order to deepen our investigation also appraising the statistical significance of the observed differences in collected data, we have planned to extend the sample size. Twenty subjects per group are currently under evaluation. In this population, the described setup will be used to monitor the volunteers' response to stressing stimuli implemented by simple computer games. This is expected to provide a quantitative description of a relevant stress-related component of the individual well-being.

REFERENCES

[1] F. Sassi and J. Hurst, "The prevention of lifestyle related chronic disease: an economic framework", *OECD Health Working Papers*, 2008.

[2] Kevin Anderson, Oksana Burford, and Lynne Emmerton, "Mobile health apps to facilitate self-care: a qualitative study of user experiences", *Plos one*, vol. 11, n. 5, 2016.

[3] T. B. VanItallie, "Stress: A risk factor for serious illness", *Metabolism*, vol. 51, n. 6, pp. 40–45, 2002.

[4] N. Schneiderman, G. Ironson, and S. D. Siegel, "Stress and health: psychological, behavioural, and biological determinants", *Annu. Rev. Clin. Psychol.*, vol. 1, pp. 607-628, 2005.

[5] Y. Ayzenberg, J. H. Rivera, and R. Picard, "Feel: frequent EDA and event logging – a mobile social interaction stress monitoring system", *CHI'12 Extended Abstracts on Human Factors in Computing System,* ACM, pp. 2357-2362, 2012.

[6] J. Bakker, L. Holenderski, R. Kocielnik, M. Pechenizkiy, and N. Sidorova, "Stress@work: from measuring stress to its understanding, precidtion and handling with personalized coaching", *Proceedings of 2nd ACM SIGHIT International Health Informatics Symposium*, ACM, pp. 673-678, 2012.

[7] Y. Deng, D. Hsu, Z. Wu, and C. H. Chu, "Feature selection and combination for stress identification using correlation and diversity", *2012 12th International Symposium on Pervasive Systems, Algorithms and Networks*, IEEE, pp. 37-43, 2012.

[8] H. Kurniawan, A. V. Maslov, and M. Pechenizkiy, "Stress detection from speech and galvanic skin response signals", *Proceedings of the 26th IEEE International Symposium on Computer-Based Medical Systems*, IEEE, pp. 209-214, 2013.

[9] W. Verkruysse, L. O. Svaasand, and J. S. Nelson, "Remote plethysmographic imaging using ambient light", *Opt. Express*, vol. 16, n. 26, pp. 21434-21445, 2008.

[10] R. Favilla, V. C. Zuccalà, and G. Coppini, "Heart Rate and Heart Rate Variability from Single-Channel Video and ICA Integration of Multiple Signals", *IEEE journal of biomedical and health informatics*, 2018.

[11] A Hyvärinen, "Fast and robust fixed-point algorithms for independent component analysis", *IEEE Transaction Neural Network*, n. 3, pp. 626-634, May 1999.

No-reference evaluation of the reconstructed images in single-shot K-Edge Subtraction X-ray Computed Tomography

G. Saccomano[1], V. Di Trapani[2], P. Delogu[2] and F. Brun[1]

[1] *Dipartimento di Ingegneria e Architettura, Università degli Studi di Trieste, Trieste, Italy*

[2] *Dipartimento Scienze fisiche, della Terra e dell'ambiente, Università degli Studi di Siena, Siena, Italy*

Abstract—**Single-shot K-Edge Subtraction X-ray Computed Tomography (CT) with a multi-threshold photon-counting detector is an interesting approach to favour low-dose analyses of a known contrast agent with promising applications *in vivo*. To assess the minimum detectable concentration of the contrast agent and to favour possible radiation dose reduction and/or faster acquisition time, a significant role is played by the tomographic reconstruction algorithm. By considering experimental images, this work evaluates three CT reconstruction methods and different acquisition statistics via a no-reference assessment of contrast-to-noise ratio and spatial resolution. The results support that, although computationally expensive, a SART-TV reconstruction approach yields adequate results even when a limited number of projections is available.**

Keywords—**spectral imaging, photon counting detector, computed tomography, iterative reconstruction.**

I. INTRODUCTION

Within the field of X-ray spectral imaging [1], K-Edge Subtraction (KES) considers the sharp rise of the absorption coefficient at the K-edge of a specific element such as e.g. an injected contrast agent. This imaging technique requires the acquisition of two digital images at different energies at either side of the K-edge of the element to be detected and it can be applied to Computed Tomography (CT). The logarithmic subtraction of these "low" and "high" energy images enhances the presence of the element whereas the other structures have negligible (or negative) contrast, thus favoring further image segmentation and analysis.

KES imaging with conventional polychromatic sources is of great interest and it would be desirable to obtain the energy images in a *single shot* by separating the spectrum in (at least) two parts, i.e. below and above the K-edge of an element. An X-ray Photon Counting Detector (XPCD) is the most promising tool for single-shot KES imaging [2], since it is equipped with a real time multi-threshold discrimination system and it is therefore capable to acquire perfectly co-registered data over multiple energy bins in a single scan.

This work considers different reconstruction methods for X-ray KES CT images of Ba solutions. Experimental images acquired with the Pixie-III detector [3]–[6] are analyzed. This work aims at evaluating different KES CT reconstruction algorithms by proposing a simple no-reference quality evaluation method based on an assessment of contrast-to-noise

ratio and spatial resolution directly from the reconstructed images. The ultimate goals of this work are: i) to investigate if refined iterative reconstruction algorithms for KES-CT allow to detect subtle concentrations of a contrast agent thanks to a better noise compensation and ii) to speculate about the reconstruction algorithm that, among the considered ones, better tolerates a projection decimation since this generally favors a radiation dose reduction and/or faster acquisition times.

II. MATERIALS AND METHODS

A. Sample preparation

A test object composed of polypropylene 350 µl small tubes filled with different dilutions of $BaCl_2$ (Carlo Erba Reagents — 122 mg/ml) and de-ionized water was prepared. Fig. 1 depicts a sketch of this test object together with its setup with respect to the beam and the detector.
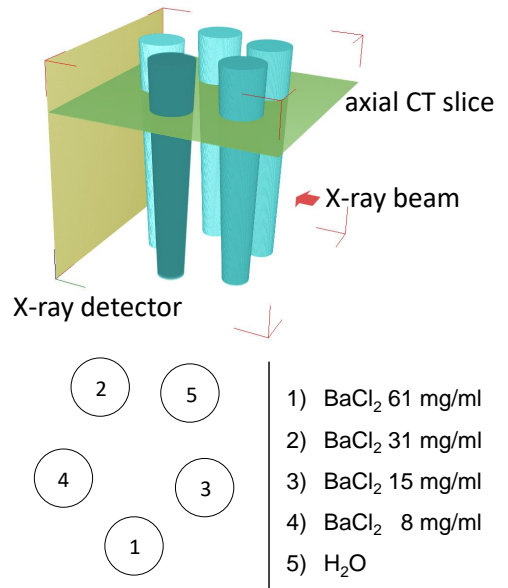

Fig. 1: Sketch of KES CT imaging setup (top panel) and the considered test object composed of different pipettes filled with a Ba solution with the order and composition as it results from an axial CT slice (bottom panel).
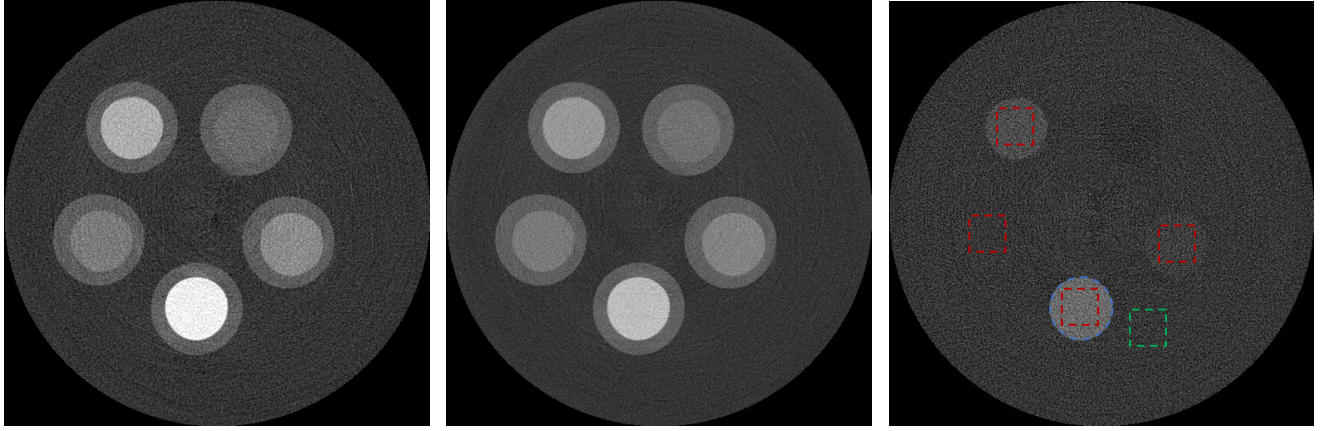
Fig. 2: CT axial slice (512×512 pixels) reconstructed with FDK of the considered test object: a) low-energy image; (b) high-energy image; c) resulting KES image where only the Ba content within the small tubes results highlighted. Resulting isotropic voxel size is $50\times50\times50$ µm^3. The same window/level gray-value settings are used for the three images. The highlighted ROIs are used for quantitative analysis. [Scale bar = 5 mm]

B. CT acquisition

A micro-focus Hamamatsu X-ray source (tube voltage: 20 to 90 kV, tube current: 0 to 200 µA, maximum output: 8 W, focal spot size: 5 µm) and a CdTe Pixirad-1/Pixie-III detector (sensitive area: 31.7×25.0 mm^2 organized as a 512×402 pixels on a square matrix at 62 µm pitch) were used. The detector was configured in Neighbor Pixel Inhibit - Pixel Summing Mode (NPISUM) [5]. This mode is specifically designed to favor energy resolution [6].

Thanks to its two programmable energy thresholds E_{low} and E_{high}, the detector outputs in a single exposure two images, hereafter referred as to "low" (in the energy range $[E_{low},E_{high}]$) and "high" (in the range $[E_{high},+\infty]$). Fig. 2 reports a sample slice of these "low", "high" and KES datasets.

For this work the following acquisition settings were used: X-ray tube voltage = 50 kV, current = 160 µA, 1mm Al filter, exposure time = 1 s, detector energy thresholds E_{low} = 28.0 keV, E_{high} = 38.0 keV. These settings result from the optimization reported in [7]. The cone-beam CT geometry setttings are: distance source-to-object D_{SO} = 200 mm, distance source-to-detector D_{SD} = 250 mm, 720 projections over 360 degrees in "step and go" mode. Projection averaging over 10 images was applied. The nominal voxel size of the reconstructed 512×512 axial slices is $50\times50\times50$ µm^3.

C. Image pre-processing

In addition to conventional flat-fielding, a custom automatic detection and removal non-linear filter was used to compensate for a few observed defective pixels. This filter considers a 5×5 neighborhood and its median gray value m. If the absolute difference between the gray-level of the central pixel and m is above a user-specified fixed threshold δ, the value of the central pixel is then replaced. The replaced value is not m but it is the median of the set composed by the pixels that satisfy the previous condition, i.e. having the absolute difference between their gray level and m below the threshold.

D. Reconstruction algorithms

In this work the following reconstruction algorithms were considered: FDK, OS-SART, and SART-TV. The implementation available in the open-source software TIGRE was used [8]. Default parameters were considered for each algorithm except for the filtering of the FDK where "shepp-logan" was applied and for the λ parameter of SART-TV (λ = 500 was set). For the SART-based algorithms 200 iterations were applied. To simulate different acquisition statistics, projections were decimated in order to have three input datasets composed of 720, 360, and 180 projections, respectively. For each considered algorithm, a post-reconstruction ring-removal filter was applied directly to the reconstructed slices [9].

E. Quantitative analysis

The reconstructed images were quantitatively compared in terms of spatial resolution Δx and contrast-to-noise ratio CNR by considering the central slice of the reconstructed volume. The circular edge method with a logistic curve-fitting technique [10] was used to asses the spatial resolution as Full Width Half Maximum (FWHM) of the first derivative of the edge spread function. The circular edge reported in blue in Fig, 2 was considered. The Regions-of-Interests (ROIs) reported in red as well as reference ROI$_0$ highlighted in green in Fig, 2 were used to compute the mean μ and standard deviation σ of the gray levels. Then CNR for each ROI i-th was determined as:

$$CNR_i = \frac{|\mu_i - \mu_0|}{\sqrt{(\sigma_i^2 + \sigma_0^2)/2}}. \tag{1}$$

A simple quality characteristic Q defined as:

$$Q = \frac{CNR_1}{\Delta x} \tag{2}$$

is here proposed to combine CNR and spatial resolution information in a single metric.

TABLE I: Results of the quantitative analysis of CNR

Algorithm	CNR_1	CNR_2	CNR_3	CNR_4
FDK ∣ 720	2.48	1.14	0.43	0.06
FDK ∣ 360	1.66	0.76	0.29	0.03
FDK ∣ 180	1.15	0.51	0.19	0.02
OS-SART ∣ 720	1.19	0.54	0.24	0.05
OS-SART ∣ 360	1.27	0.55	0.22	0.02
OS-SART ∣ 180	1.59	0.71	0.26	0.01
SART-TV ∣ 720	5.81	2.64	1.01	0.11
SART-TV ∣ 360	6.18	3.04	1.10	0.12
SART-TV ∣ 180	6.78	3.06	1.14	0.16

TABLE II: Results of the quantitative analysis of Δx and Q

Algorithm	Δx [mm]	Q [mm^{-1}]
FDK ∣ 720	0.091	27.1
FDK ∣ 360	0.089	18.7
FDK ∣ 180	0.096	12.1
OS-SART ∣ 720	0.077	15.4
OS-SART ∣ 360	0.075	16.9
OS-SART ∣ 180	0.134	11.9
SART-TV ∣ 720	0.106	54.8
SART-TV ∣ 360	0.126	49.0
SART-TV ∣ 180	0.169	39.9

III. RESULTS AND DISCUSSION

Table I reports the quantitative results of the assessment of CNR for each considered Ba dilutions. It can be noticed that although the pipette filled with the minimum concentration of Ba results hard to detect for all the considered algorithms, an interesting difference is observed for the pipette filled with 15 mg/ml of BaCl$_2$. The images reconstructed with SART-TV present a value for CNR_3 above 1 for each considered projection decimation. It is worthy to note also that CNR values for the FDK images decrease when reducing the number of available projections. This is not true for the SART-based algorithms where a better noise handling with a consequently smoothing effect results in increasing CNR values for ROI$_1$ and ROI$_2$. These results support that SART-TV allow to detect a subtle concentrations of the contrast agent thanks to its better noise compensation even when a limited number of projections is available.

Because higher values for CNR might be related to a worsening of the spatial resolution, the previous observation needs to take into account the quantitative results for Δx and Q reported in Table II. It can be observed that for FDK the value of Q increases coherently when more projections are available. This observation does not hold for OS-SART. Interestingly, the highest value of Q for OS-SART is recorded for the case considering 360 projections, thus suggesting that 720 projections are not necessary for the reconstruction of a 512×512 image with this algorithm. While the assessed spatial resolution for FDK is superior to the one for the SART-TV case, the assessed Δx values for SART-TV might be acceptable for an experimental voxel size of $50 \times 50 \times 50$ µm^3.

The computed quality measurements still support the use of FDK when a high number of projections are collected, especially for applications in which spatial resolution has to be privileged. However, the loss in Δx for SART-TV might be tolerated for practical applications where the detectability of subtle concentrations has to be favored. Moreover, although a more refined and detailed investigation is required, the λ parameter of SART-TV seems to act as a trade-off between these two aspects, thus allowing an application-dependent fine tuning of the final quality of the reconstructed images. This option is not available for the FDK algorithm.

Computational requirements are of course different for the three considered algorithms, being FDK the fastest reconstruction approach and SART-TV the most computationally intense. Refined investigations are required to optimize the number of iterations required by the SART-based techniques. It is reasonable to assume that 200 iterations as considered in this work are more than abundant for the vast majority of the applications. A convergence analysis is required to optimize the computational aspects of a SART-based reconstruction workflow.

REFERENCES

[1] E. Fredenberg, "Spectral and dual-energy X-ray imaging for medical applications," *Nuclear Instruments and Methods in Physics Research, Section A: Accelerators, Spectrometers, Detectors and Associated Equipment*, vol. 878, pp. 74–87, 2018.

[2] J. Schlomka, E. Roessl, R. Dorscheid, S. Dill, G. Martens, T. Istel, and et al., "Experimental feasibility of multi-energy photon-counting k-edge imaging in pre-clinical computed tomography," *Physics in Medicine and Biology*, vol. 53, no. 15, pp. 4031–4047, 2008.

[3] F. Brun, V. Di Trapani, D. Dreossi, R. Longo, P. Delogu, and L. Rigon, "K-edge spectral computed tomography with a photon counting detector and discrete reconstruction," *Annual International Conference of the IEEE Engineering in Medicine and Biology Society*, vol. 2018, pp. 5245–5248, 2018.

[4] F. Brun, V. Di Trapani, D. Dreossi, L. Rigon, R. Longo, and P. Delogu, "Towards in vivo K-edge X-ray micro-CT with the Pixirad-I/Pixie-III detector," *IFMBE Proceedings*, vol. 68, no. 1, pp. 123–126, 2019.

[5] V. Di Trapani, A. Bravin, F. Brun, D. Dreossi, R. Longo, A. Mittone, and et al., "Characterization of noise and efficiency of the pixirad-1/pixie-III CdTe x-ray imaging detector," *Journal of Instrumentation*, vol. 13, pp. C12008–C12008, dec 2018.

[6] V. Di Trapani, A. Bravin, F. Brun, D. Dreossi, R. Longo, A. Mittone, and et al., "Characterization of the acquisition modes implemented in Pixirad-1/Pixie-III X-ray Detector: Effects of charge sharing correction on spectral resolution and image quality," *Nuclear Instruments and Methods in Physics Research, Section A: Accelerators, Spectrometers, Detectors and Associated Equipment*, vol. 955, p. 163220, 2020.

[7] F. Brun, V. D. Trapani, J. Albers, P. Sacco, D. Dreossi, L. Brombal, and et al., "Single-shot K-Edge subtraction X-ray discrete computed tomography with a polychromatic source and the Pixie-III detector," *Physics in Medicine Biology*, 2020, published on-line DOI:10.1088/1361-6560/ab7105.

[8] A. Biguri, M. Dosanjh, S. Hancock, and M. Soleimani, "TIGRE: A MATLAB-GPU toolbox for CBCT image reconstruction," *Biomedical Physics and Engineering Express*, vol. 2, no. 5, 2016.

[9] F. Brun, A. Accardo, G. Kourousias, D. Dreossi, and R. Pugliese, "Effective implementation of ring artifacts removal filters for synchrotron radiation microtomographic images," *International Symposium on Image and Signal Processing and Analysis, ISPA*, pp. 672–676, 2013.

[10] T. Takenaga, S. Katsuragawa, M. Goto, M. Hatemura, Y. Uchiyama, and J. Shiraishi, "Modulation transfer function measurement of ct images by use of a circular edge method with a logistic curve-fitting technique," *Radiological Physics and Technology*, vol. 8, pp. 53–59, Jan 2015.
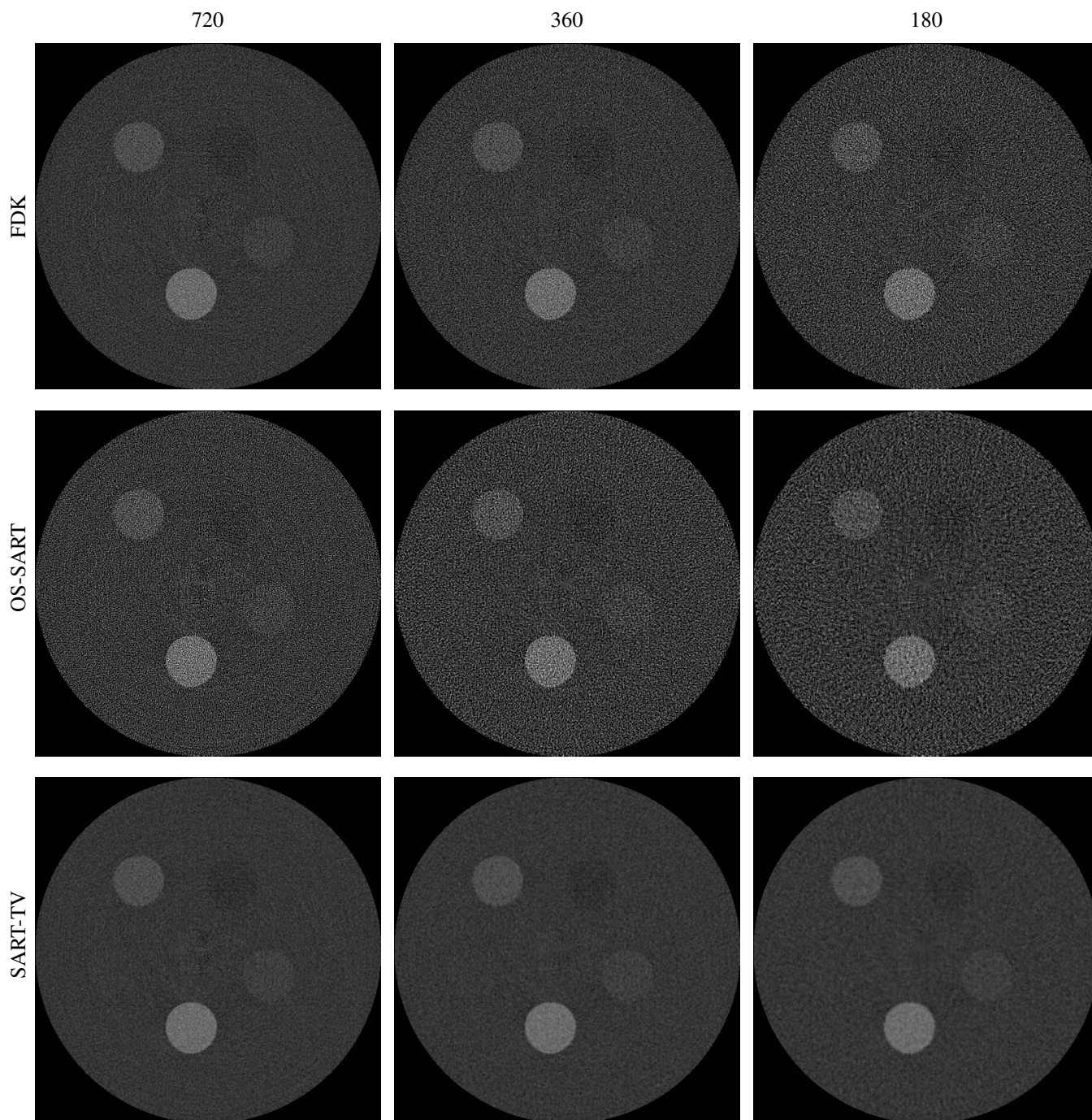
Fig. 3: A representative axial slice for each of the considered reconstruction algorithm and for the three different angular sampling (i.e. number of projections). From top to bottom: FDK, OS-SART, and SART-TV. From left to right: 720, 360, and 180 projections.

Fontan Computational Hemodynamics: Impact of Inlet Velocity Profile Features with Implications on Clinically Relevant Parameters

M. Lodi Rizzini[1], P. Tasso[1], D. Gallo[1], G. D'Avenio[2], A Secinaro[3],
A. Amodeo[3], U. Morbiducci[1] and M. Grigioni[2]

[1] *PolitoBio^MEDLab, Department of Mechanical and Aerospace Engineering, Politecnico di Torino, Turin, Italy*
[2] *Istituto Superiore di Sanità, Department of Technology and Health, Rome, Italy*
[3] *Ospedale Pediatrico Bambino Gesù, Department of Pediatric Cardiology and Cardiac Surgery, Rome, Italy*

Abstract — **Total cavopulmonary connection (TCPC) is a surgical technique adopted for univentricular heart disease treatment affected by complications related to thrombus formation and energy dissipation. Computational fluid dynamics (CFD) has been largely adopted to assess Fontan hemodynamics, both in relation to surgical planning/ optimization, and to long-term complications risk. However, CFD models necessarily imply the use of assumptions/idealizations contributing to the budget of uncertainty affecting the results and potentially limiting their translational application. In this perspective, in this study we explore the impact of the shape of inflow velocity profiles, used as boundary conditions and not easily quantifiable in vivo in a clinical framework, on the local hemodynamics in CFD models of TCPC. To do that, using generalized analytical formulations we generated 3D velocity profiles and used them in CFD simulations as inflow venous boundary conditions. The findings of the study suggest that considering a fully 3D velocity profile with in-plane components, instead of the most common through-plane only velocity profile, promotes helical flow in the connection, thus increasing also the average WSS in the graft (reducing the risk of thrombus formation), and reduces the hydraulic energy losses.**

Keywords—**Fontan, Thrombus risk, Viscous Dissipation Rate**

I. INTRODUCTION

UNIVENTRICULAR heart is a congenital disease with an incidence of about 2% in pediatric patients with heart diseases [1]. This pathological condition consists in the presence of a single ventricle chamber, with the ultimate consequence of oxygenated and deoxygenated blood mixing [1]. The main complications for this pathology are low blood saturation, chronic cyanosis, and heart failure as a result of volumetric overload. If untreated, this pathological state leads to patients death before 16 years old in the 70% of cases [1]. The most common surgical technique adopted to treat these patients is the Fontan procedure [2]. This surgical techniques consists of three consecutive steps to gradually separate systemic and pulmonary circulations through a connection between the two venae cava and pulmonary arteries [2]. The Fontan procedure is palliative and present complication risks, the most relevant being systemic and pulmonary thrombus formation [3] and an inadequate connection efficiency [4]. These risks are clearly related to the complex venous hemodynamics [3], which could lead to connection failure [5].

In recent years, the coupling of medical imaging and computational fluid dynamics (CFD) has been extensively developed and applied to study cardiovascular flows, taking advantage of the possibility to obtain highly resolved hemodynamics in anatomically realistic arterial models. In this sense, CFD has been a powerful instrument to assess Fontan hemodynamics, both in relation to surgical planning and/or optimization and to long-term complications [6]. In the context of a subject-specific oriented approach, 4D flow MRI has emerged as able to provide the anatomical and hemodynamic inputs to even more realistic, fully personalized Fontan flow simulations. The importance of adopting realistic inflow BCs was recently highlighted in cardiovascular flows [7], and very recently investigated also in TCPC models [8].

Motivated from these evidences, the aim of this work was to explore the hemodynamics in a patient-specific 3D model of TCPC with CFD simulations, focusing on the impact of inflow velocity profile features on TCPC hemodynamics, with a tightly controlled approach. To do that, different velocity profiles were analytically generated and prescribed at the inlets (i.e., the superior and inferior cava veins). The impact of the inflow velocity profiles features was evaluated in terms of: (1) thrombus formation risk, considering low wall shear stress as an indicator of low/recirculating flow (which is a hallmark of thrombogenicity), (2) intravascular flow features, assessing helical and vortical flow features, and (3) connection efficiency in terms of hydraulic power losses and viscous dissipation rate.

II. MATERIALS AND METHODS

A. Fluid Dynamics Simulation and Boundary Conditions

In a patient-specific 3D model of TCPC, the governing equations of fluid motion were solved in their discretized form under unsteady-state conditions, adopting the finite element-based open-source code SimVascular (http://simvascular.github.io/). To ensure a grid-independent solution of the flow field, an average element size of $0.675 \cdot 10^{-3}$ m with a near-wall refinement consisting of 3 tetrahedral boundary layers with a decreasing ratio of 0.6 was adopted after a sensitivity analysis. The resulting mesh cardinality was of 3.5 million elements. Blood rheology was assumed to be Newtonian (density $\rho = 1060$ kg/m^3; dynamic viscosity $\mu = 0.004$ Pa·s) [9]. Vessels wall was assumed to be rigid, no-slip conditions were prescribed at wall boundaries. Concerning the outflow sections, hydraulic resistance values based on data proposed in the literature [10] were imposed at the left pulmonary artery

(LPA) and at the two right pulmonary arteries (RPA1 and RPA2, respectively), as depicted in Fig. 1. In detail, the value of $2.76 \cdot 10^7$ kg/m^{4}s was imposed as hydraulic resistance at LPA outflow section (R_{LPA}) and as total resistance at the two RPA outflow sections. The hydraulic resistance values at the two RPA were set according to the Murray's law [11], obtaining values equal to $5.70 \cdot 10^7$ kg/m^{4}s and $5.35 \cdot 10^7$ kg/m^{4}s, respectively. At the inflow sections at the superior and inferior vena cava (SVC and IVC, respectively), Dirichlet boundary conditions were imposed in terms of 3D velocity profiles, as detailed in the following section.

B. Inflow Velocity Profiles

The 3D velocity profiles at the SVC and IVC inflow sections were built up as given by the combination of two components: a through-plane (TP) component, in the direction of the axis of the vessel and thus orthogonal to the inflow section, and an in-plane (IP) component, orthogonal to the direction of axis of the vessel and this lying on inflow section plane. Due to the lack of patient-specific hemodynamic data, here we used the venous flow rate waveforms of another patient, rescaled to the inlet SVC and IVC areas. Using inflow rate waveforms, the Womersley theory [12] was applied to obtain the instantaneous local TP velocity components at SVC and IVC inlet sections. The presence of the IP component as part of the inflow velocity profile was modelled accounting for two possible configurations as representative of secondary flow in the caval veins. More in detail, we considered the presence of (1) one single vortex structure, and (2) Dean-like two-vortices. To generate the secondary flow structures, here two analytical formulations were used, generalized to fit realistic non-circular cross-sections of blood vessels. In detail, starting from the polar coordinate system (r, ϑ) defined on the inlet surface, we defined a new generalized polar coordinate system (r', ϑ'):

$$\begin{cases} r' = \frac{r}{R(\vartheta)} \\ \vartheta' = \vartheta \end{cases} \tag{1}$$

where $R(\vartheta)$ is the variable radius of inlet surface. This allows to have values of r' ranging from 0 to 1 (0 at the surface geometric centre and 1 at each point of surface boundary).
The first formulation, describing one vortex secondary flow configuration (Fig. 1), was obtained generalizing the equation proposed elsewhere [13], as follows:

$$\begin{cases} \boldsymbol{v}_{\vartheta\prime}(r', \vartheta') = k_{\vartheta\prime}[1 - r'^2]r'\boldsymbol{u}_{\vartheta\prime} \\ \boldsymbol{v}_{r\prime}(r', \vartheta') = k_{r\prime}[1 - r'^2]r'\boldsymbol{u}_{r\prime} \end{cases} \tag{2}$$

where $\boldsymbol{u}_{r\prime}$ and $\boldsymbol{u}_{\vartheta}$ are unit vectors along the radial and angular direction respectively, and $k_{\vartheta\prime}$ and $k_{r\prime}$ are constant parameters regulating the angular and radial component of IP velocity, respectively. In this study the values $k_{\vartheta\prime}=5$ and $k_{r\prime}=1$ were considered to obtain the single-vortex secondary flow configuration. The second formulation describes a double-vortex secondary flow configuration, obtained generalizing to non-circular cross-sections the Dean formulation for secondary flows in curved pipes [14]:

$$\begin{cases} \boldsymbol{v}_{\vartheta\prime}(r', \vartheta) = (1 - r'^2)(4 - 23r'^2 + 7r'^4)\cos(\vartheta')\boldsymbol{u}_{\vartheta\prime} \\ \boldsymbol{v}_{r\prime}(r', \vartheta) = (1 - r'^2)^2(4 - r'^2)\sin(\vartheta')\boldsymbol{u}_{r\prime} \end{cases} \tag{3}$$

On both the SVC and IVC inlet sections, the local value of the IP component of the inflow velocity was then scaled to the instantaneous inflow rate waveform according to:

$$\boldsymbol{v}_{ip}(r', \vartheta', t) = C\frac{Q(t)}{S}\frac{\boldsymbol{v}_{\vartheta\prime}(r\prime,\vartheta\prime)+\boldsymbol{v}_{r\prime}(r\prime,\vartheta\prime)}{|\boldsymbol{v}_{\vartheta\prime}(r\prime,\vartheta\prime)+\boldsymbol{v}_{r\prime}(r\prime,\vartheta)|_{mean}} \tag{4}$$

where $Q(t)$ is time-dependent inlet flow rate, S is the inlet surface area and C is a scaling factor representing the TP/IP components ratio. Here the values set for the scaling factor are C=0.33 and C=0.66, corresponding to a magnitude ratio of the local IP and TP velocity components equal to 33% and 66%, respectively. Summarizing, five unsteady-state simulations were performed on the same TCPC model with different velocity profiles as inflow boundary condition (TABLE I): the one-dimensional, TP-only Womersley velocity profile was used as reference case, and four three-dimensional profiles made by the composition of Womersley profile as TP component and different IP components.

TABLE I

Profile Name	TP velocity	IP velocity	IP/TP
Reference	Womersley	No IP velocity	0.00
Double Vortex IP33	Womersley	Double Vortex	0.33
Double Vortex IP66	Womersley	Double Vortex	0.66
Single Vortex IP33	Womersley	Single Vortex	0.33
Single Vortex IP66	Womersley	Single Vortex	0.66

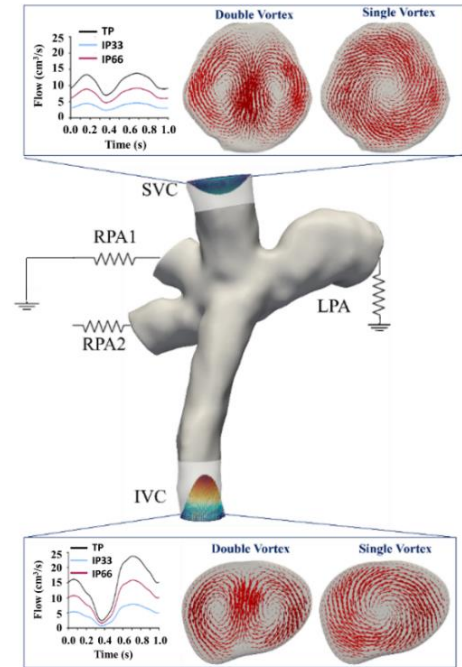Schematic table of the different velocity profiles adopted in the study

Fig. 1: Schematic of BCs applied at inflow and outflow sections of the TCPC model. Upper and lower panels: details about inflow BCs, at SVC and IVC respectively, showing the time dependant flowrate of TP and scaled amount of IP. IP velocity scaled vectors for double and single vortex configurations respectively are also shown in the panels.

C. Hemodynamic Descriptors

The near-wall hemodynamics was characterized in terms of time-averaged wall shear stress (TAWSS), as indicator of low velocity/ stagnation regions, computed as:

$$\text{TAWSS}(s) = \frac{1}{T}\int_0^T |\boldsymbol{\tau}_w(\boldsymbol{s}, t)|dt \tag{5}$$

where T is the time duration of the cardiac cycle, $\boldsymbol{\tau}_w$ the wall shear stress vector, and $\boldsymbol{s}$ the position at the wall. Moreover, the intravascular flow features were analysed in terms of helical flow and vorticity. In particular, to visualize helical flow patterns, the local normalized helicity (LNH) was computed as follows [15]:

$$LNH = \frac{\boldsymbol{v}(s,t)\cdot\boldsymbol{\omega}(s,t)}{|\boldsymbol{v}(s,t)\cdot\boldsymbol{\omega}(s,t)|} = \cos\varphi \qquad (6)$$

where φ is the angle between the velocity ($\boldsymbol{v}$) and vorticity ($\boldsymbol{\omega}$) vector. The analysis was completed evaluating the efficiency of the TCPC in terms of hydraulic power and energy dissipation. In detail, the instantaneous hydraulic power losses ($\dot{E}$) [16] was evaluated as follows:

$$\dot{E}(t) = -\int_{IN} p(\boldsymbol{s},t)\boldsymbol{v}(\boldsymbol{s},t)\cdot\boldsymbol{u}_n(\boldsymbol{s})dS - \int_{IN}\frac{1}{2}\rho|\boldsymbol{v}(\boldsymbol{s},t)|^2\boldsymbol{v}(\boldsymbol{s},t)\cdot\boldsymbol{u}_n(\boldsymbol{s})dS -$$
$$\int_{OUT} p(\boldsymbol{s},t)\boldsymbol{v}(\boldsymbol{s},t)\cdot\boldsymbol{u}_n(\boldsymbol{s})dS - \int_{OUT}\frac{1}{2}\rho|\boldsymbol{v}(\boldsymbol{s},t)|^2\boldsymbol{v}(\boldsymbol{s},t)\cdot\boldsymbol{u}_n(\boldsymbol{s})dS \quad (7)$$

where p is the pressure and $\boldsymbol{u}_n$ the outward unit vector normal to inlet/outlet sections.

The local viscous dissipation rate (VDR) [8] in the TCPC fluid domain was evaluated as:

$$VDR(\boldsymbol{s},t) = \mu\left[2\left(\frac{\partial v_x}{\partial x}\right)^2 + 2\left(\frac{\partial v_y}{\partial y}\right)^2 + 2\left(\frac{\partial v_z}{\partial z}\right)^2 + \left(\frac{\partial v_x}{\partial y} + \frac{\partial v_y}{\partial x}\right)^2 + \left(\frac{\partial v_x}{\partial z} + \frac{\partial v_z}{\partial x}\right)^2 + \left(\frac{\partial v_y}{\partial z} + \frac{\partial v_z}{\partial y}\right)^2\right] \qquad (8)$$

where v_x, v_y and v_z are the three velocity components in the cartesian coordinate system. The TCPC was characterized in terms volumetric VDR as follows:

$$VDR_{tot}(t) = \int_V VDR(\boldsymbol{s},t)dV \qquad (9)$$

where V is the whole TCPC fluid volume.

III. RESULTS

The surface areas at the luminal surface subjected to TAWSS values lower than 0.4 Pa are presented in Fig. 2. From a qualitative point of view, it can be noticed that, especially in the graft area, TAWSS values are higher if an IP velocity component is prescribed at the inflow sections. The quantitative evaluation of the surface exposed to low WSS (Fig. 2) confirms the previous observation, corroborating that the imposition of purely TP velocity profiles at the inflow sections leads to a larger exposure to low TAWSS. Helical flow patterns are shown in Fig. 3 in terms of isosurfaces of cycle average LNH. By visual inspection, it emerges that the cases with 3D velocity profiles as inflow BC present a larger counter-rotating helical patterns, differently from the reference TP-only inflow BC velocity profiles. Finally, differences in viscous dissipation rate within the TCPC for the different inflow BC velocity profiles can be observed in Fig. 4 in terms of streamlines of the cycle-average flow field (colour-coded with VDR values). It can be noticed that the TP-only inflow BC case presents high VDR values, particularly in the anastomosis region. These qualitative observations are confirmed by the quantitative analysis in Fig. 5. All 3D inflow velocity profile BCs cases are characterized by cycle-average power loss values and VDR_{tot} lower that than the TP-only case, except for the power loss of case double vortex IP66.

We can conclude that TCPC power losses are sensitive to the shape of the inflow velocity profiles with maximum

percentage difference of 12% between reference velocity profile and single vortex IP66.
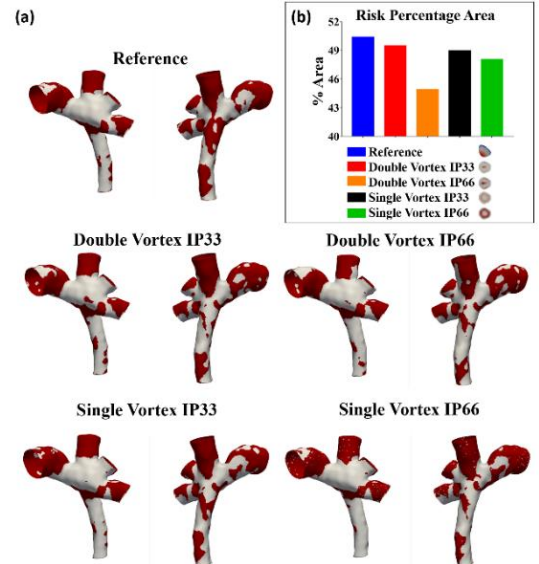

Fig. 2: (a) 3D model surfaces areas subjected to TAWSS < 0.4 Pa and (b) percentage histogram of surface subjected to low WSS.
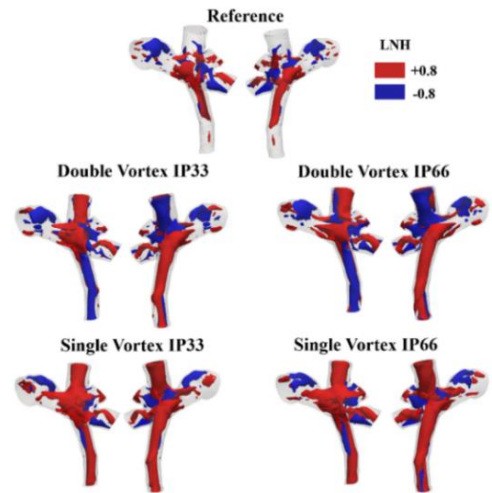

Fig. 3: LNH iso-surfaces for the five velocity profiles imposed, thresholds was set at ±0.8 for visualization purposes. righthanded and lefthanded structures are coloured in red and blue respectively.
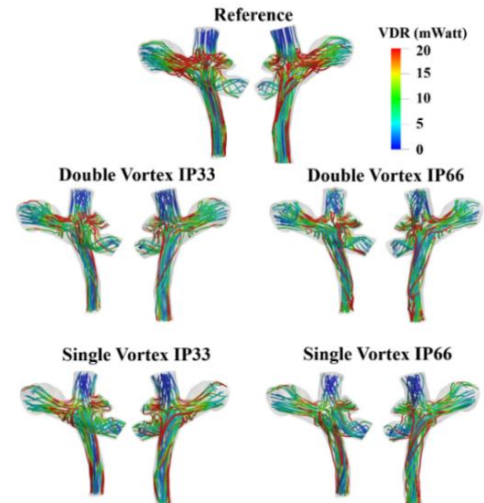

Fig. 4: Colormaps of streamlines according to VDR for the five velocity profiles imposed.

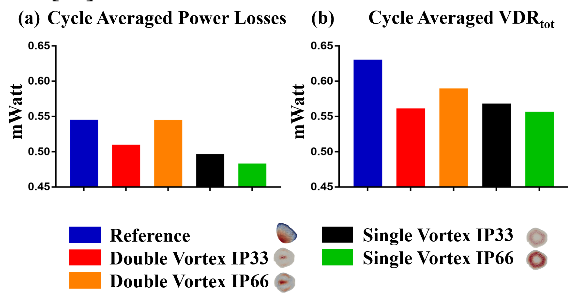The obtained results are comparable with values reported in literature [17].

(a) Cycle Averaged Power Losses   **(b) Cycle Averaged VDR$_{tot}$**

Fig. 5: Histograms of cycle average values of (a) power losses and (b) viscous dissipation rate for the five different velocity profiles imposed.

IV. DISCUSSIONS AND CONCLUSION

It is well established that the TCPC local hemodynamics play a key role in the long-term outcome [4], [8]. In this context, CFD is a powerful tool to investigate the patient specific TCPC hemodynamics. The importance of realistic inflow BCs in cardiovascular flow simulations was recently established [7] and very recently studied also in TCPC models [8]. Due to the impact of assumptions/idealizations in personalized in silico hemodynamics, here we investigated whether the shape of the venous velocity profiles applied as BC at SVC and IVC inlet sections of TCPC computational hemodynamics models impacts the hemodynamics of the anastomosis region. To this aim, analytical, generalized velocity profiles were assembled, based on fluid mechanics theory and CFD simulations were carried out on a TCPC model. The findings of this study suggest that the presence of an IP component in the velocity profile prescribed as venous inflow BC, compared to a purely TP profile, increases local TAWSS values, especially in the IVC graft region. This result also suggests a beneficial role for IP velocity in reducing the hemodynamic risk of thrombus formation. From the analysis of intravascular flow features, it emerged that the presence of IP components in the inflow velocity profile imparts a higher level of organization in the blood flowing through the TCPC, not only in the IVC and SVC regions but also in the anastomosis region, ultimately contributing to lower the hydraulic power losses and viscous dissipation rate. This suggests that the establishment of large scale, distinguishable helical flow patterns inside the TCPC could contribute to improve the energetic efficiency of the connection [18]. These considerations also open the way to rethink how to design the graft and shape the connection, to target a proper shaping of helical flow patterns in the TCPC. There are some limitations that could weaken the findings of this study. Firstly, we used the TP-only Womersley profile as reference instead of an *in-vivo* measured velocity profile. This choice was based on recent evidences reporting that the use of Womersley profile in TCPC CFD models does not show statistically significant differences in hemodynamics descriptors with respect to the patient-specific 3D velocity profile [8]. Secondly, our findings are based on the analysis of one model only. Finally, here we assumed rigid walls, an assumption extensively adopted in computational studies of TCPC hemodynamics [9-10, 16], because it was reported that it has moderate influence power

losses computation . To conclude, one strong point of the here presented analysis on TCPC is that it can be easily extended to all those computational hemodynamic studies where fully 3D conditions at boundaries are not available or difficult to measure.

REFERENCES

[1] P. Khairy, N. Poirier, L.-A. e. Mercier, *"Univentricular Heart"*, Circulation, *115*, 800-812, 2007.

[2] F. Fontan, E. Baudet, *"Surgical reapair of tricuspid atresia"*, Thorax *26*, 8, 1971.

[3] P. D. Coon, J. Rychik, R. T. Novello, P. S. Ro, J. W. Gaynor, T. L. Spray, *"Thrombus formation after the Fontan operation"*, The Annals of Thoracic Surgery, *71*, 5, 2001.

[4] M. Grigioni, C. Daniele, C. Del Gaudio, U. Morbiducci, A. Balducci, G. D'Avenio, A. Amodeo, V. Barbaro, R. Di Donato, *"Numerical simulation of a realistic total cavo-pulmonary connection: Effect of unbalanced pulmonary resistences on hydrodynamic performance"*, The International Journal of Artificial Organs, *26*, 10, 2003.

[5] L. P. Dasi, K. Pekkan, H. Katajima, A. P. Yoganathan, *"Functional Analysis of Fontan Energy Dissipation"*, Journal of Biomechanics, *41*, 13, 2008.

[6] C. M. Haggerty, M. Restrepo, E. Tang, D. A. de Zélicourt, K. S. Sundareswaran, L. Mirabella, J. Bethel, K. K. Whitehead, M. A. Fogel, A. P. Yoganathan, *"Fontan hemodynamics from 100 patient-specific cardiac magnetic resonance studies: A computational fluid dynamics analysis"*, The Journal of Thoracic and Cardiovascular Surgery, *148*, 1481-1489, 2014.

[7] U. Morbiducci, R. Ponzini, D. Gallo, C. Bignardi, G. Rizzo, *"Inflow boundary conditions for image-based computational hemodynamics: Impact of idealized versus measured velocity profiles in the human aorta"*, Journal of Biomechanics, *46*, 102-109, 2013.

[8] Z. A. Wei, C. Huddleston, P. M. Trusty, S. Singh-Gryzbon, M. A. Fogel, A. Veneziani, A. P. Yoganathan, *"Analysis of Inlet Velocity Profiles in Numerical Assessment of Fontan Hemodynamics"*, Annals of Biomedical Engineering, *47*, 2258-2270, 2019.

[9] K. K. Whitehead, K. Pekkan, H. D. Kitajima, S. M. Paridon, A. P. Yoganathan, M. A. Fogel, *"Nonlinear Power Loss During Exercise in Single-Ventricle Patients After the Fontan: Insights From Computational Fluid Dynamics"*, Circulation, *116*, I-165-I-171, 2007.

[10] F. Migliavacca, G. Dubini, E. L. Bove, M. R. de Leval, *"Computational Fluid Dynamics Simulations in Realistic 3-D Geometries of the Total Cavopulmonary Anastomosis: The Influence of the Inferior Caval Anastomosis"*, Journal of Biomechanical Engineering, *125*, 805-813, 2003.

[11] T. F. Sherman, *"On Connecting Large Vessel to Small"*, Journal of General Physiology, *78*, 23, 1981.

[12] J. R. Womersley, *"Method for the Calculation of Velocity, Rate of Flow and Viscous Drag in Arteries When the Pressure Gradient Is Known"*, Journal of Physiology, *127*, 11, 1955.

[13] L. Zovatto, G. Pedrizzetti, *"Optimal helical entry flow in a helical vessel"*, Fluid Dynamics Research, *50*, 065503, 2018.

[14] W. R. Dean, *"Note on the motion of fluid in a curved pipe"*, The London, Edinburgh, and Dublin Philosophical Magazine and Journal of Science, *4*, 16, 1927.

[15] D. Gallo, D. A. Steinman, P. B. Bijari, U. Morbiducci, *"Helical flow in carotid bifurcation as surrogate marker of exposure to disturbed shear"*, Journal of Biomechanics, *45*, 2398-2404, 2012.

[16] M. Grigioni, G. D'Avenio, A. Amodeo, R. M. Di Donato, *"Power dissipation associated with surgical operations' hemodynamics: Critical issues and application to the total cavopulmonary connection"*, Journal of Biomechanics, *39*, 1583-1594, 2006.

[17] Z. A. Wei, M. Tree, P. M. Trusty, W. Wu, S. Singh-Gryzbon, A. Yoganathan, *"The Advantages of Viscous Dissipation Rate over Simplified Power Loss as a Fontan Hemodynamic Metric"*, Annals of Biomedical Engineering, *46*, 404-416, 2017.

[18] A. Amodeo, M. Grigioni, G. Oppido, C. Daniele, G. D'Avenio, G. Pedrizzetti, S. Giannico, S. Filippelli, R. M. Di Donato, *"The beneficial vortex and best spatial arrangement in total extracardiac cavopulmonary connection"*, The Journal of Thoracic and Cardiovascular Surgery, *124*, 471-478, 2002.

A neuromorphic haptic feedback for lower limb sensory substitution

J. D'Abbraccio[1], S. Prasanna[1], I. Cesini[1], F. Dell'Agnello[1], S. Crea[1,2], N. Vitiello[1,2], A. Mazzoni[1] and C.M. Oddo[1]

[1] *Scuola Superiore Sant'Anna, The BioRobotics Institute and Department of Excellence in Robotics and AI, Pisa, Italy*
[2] *Fondazione Don Carlo Gnocchi, Milan, Italy*

Abstract—**Individuals suffering from the amputation of a lower limb experience a worsening of life quality and participation to daily activities. Even with efficient lower limb prostheses enabling the patient to walk again, the loss of functionality and sensory information from the foot receptors results in abnormal gait and balance. In this work, we present a non-invasive vibrotactile feedback based on neuromorphic encoding of sensory stimuli from an integrated insole and the related wearable haptic system for sensory remapping. The effectiveness of the overall system in non-invasively enabling the perception of both limb placement and terrain features has been preliminarily tested with a healthy volunteer. By considering both the softness and evenness of a smooth floor, artificial grass and a rocky terrain, the subject correctly recognized the three textures with an overall accuracy of 58.3%. The accuracy reached 87.6% in the discrimination between the rocky terrain and the even ones (smooth floor and artificial grass). The promising psychophysical results achieved pave the way for the assessment of the neuromorphic strategy with larger cohorts of subjects, before going through the target population.**

Keywords—**Lower limb amputees, neuromorphic haptic feedback, vibrotactile stimulation, sensory substitution**

I. INTRODUCTION

PERSONS experiencing the amputation of a lower limb suffer from a significant impairment of the sensorimotor system, since the amputation results in a severe limitation of effectiveness of muscle and tendon proprioceptors and loss of the information encoded by the mechanoreceptors of the foot while walking. Besides gait abnormalities and deficient balance [1]–[5], the lack of sensory feedback also entails an increase of the cognitive effort [6], physical fatigue [7] and fear of falling [3] when using a lower limb prosthesis, as well as a worsening of life quality and participation to daily activities of amputees [8]. The addition of an artificial sensory feedback matching and enriching information from the unimpaired sensory modalities may allow for the integration of the artificial limb within the impaired sensorimotor system and lead to a mitigation of the side effects following the amputation.

A wide range of systems conveying sensory information about the foot-ground interaction and other kinematic parameters by means of visual [9], acoustic [4] [9], electro-tactile [10] and haptic feedback [2] [8], [11]–[13] have been proposed to recover a more physiological gait pattern. Nevertheless, a large part of these solutions does not consider the possibility to provide information also about the terrain conditions, even if this might be critical for the patient, for instance to determine walking speed.

The present work reports about a preliminary assessment with a single healthy subject of the performance of a wearable haptic device providing a vibrotactile feedback grounded on a neuromorphic approach [14] in allowing the user to perceive both the position of the prosthetic foot in the space and floor texture features while walking.

II. MATERIALS & METHODS

A. The wearable haptic system and the feedback strategy

The wearable haptic system is a stand-alone device conceived for sensory remapping and substitution in people suffering from lower limb impairments compromising the natural sensorimotor functions and, specifically, for those who experienced an amputation of the limb. The prototype consists of two main submodules, with the addition of a haptic control unit allowing for the wireless data collection and streaming, as well as for encoding gait information into vibrotactile stimulation. The sensing module (Fig. 1.B) of the system is made of a pressure-sensitive shoe and its electronics, estimating the foot-ground interaction thanks to an optoelectronic sensor array in the form of an insole [15]. The haptic module (Fig. 1.A) is a textile belt adjustable in size equipped with a 3D-printed box enclosing the control unit and three coin-shaped cylindrical eccentric motors (Pico Vibe 304-116, Precision Microdrives) for the real-time provision of a unilateral vibrotactile stimulation at the waist level. These actuators are small (5 mm in diameter), lightweight (1.2 g) and they can be actuated in 15 ms. The vibrotactile units (VTs) are embedded in a polymeric matrix (PolyDiMethylSiloxane (PDMS), Sylgard® 184 Silicone Elsatomer, Dow Corning) to enhance the comfort of the contact with the skin and increase the contact area, without hindering the vibrations transmission. With respect to the wearer's waist circumference and to the side of the lower limb impairment, the three VTs are located at a distance of 9 cm from each other along the surface of the belt in contact with the body skin [16]. Depending on the objective of the specific application, the VTs can be actuated according to multiple feedback strategies by simply tuning frequency, amplitude and pattern of activation [1], [17], [18]. To provide information about both discrete gait events and floor texture features (i.e. evenness and softness), an innovative strategy relying on a neuromorphic spike-based approach was implemented. In particular, the readings of the integrated shoe are mapped onto three VT units, in accordance with stance phases (heel-strike, flat-foot and toe-off). Each stance phase, in turn, is then used for commanding the activation of the VTs by means of a neuronal model. Such a
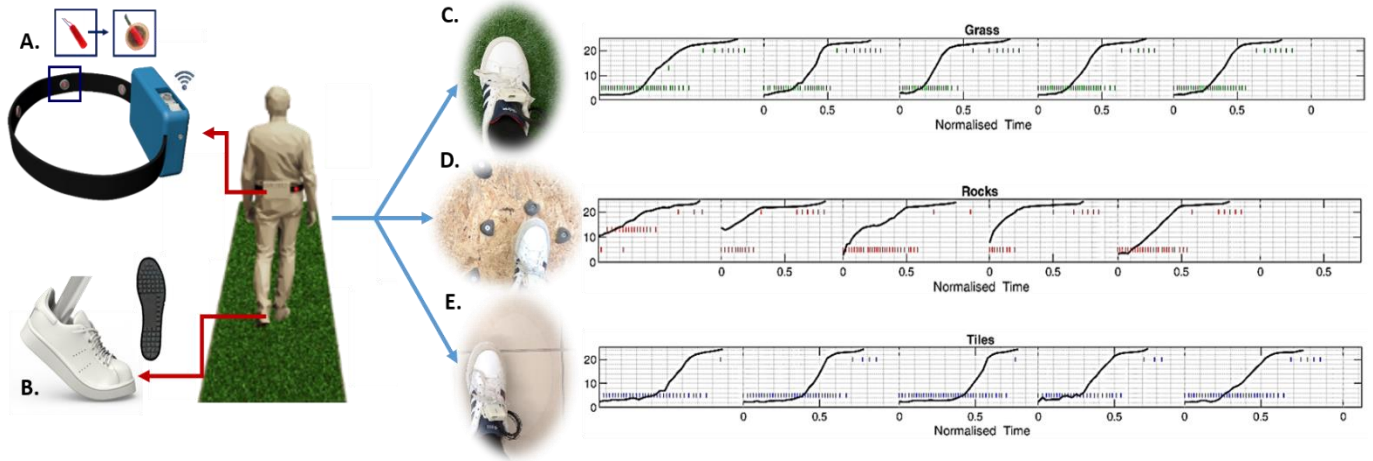
Fig. 1: The haptic feedback system. Overview of the device consisting of a haptic interface equipped with 3 vibrotactile units and the control unit (A) and a pressure-sensitive shoe (B). C-D-E show the floor textures and the corresponding activation patterns of the VT units along with the progression of the center of pressure (CoP) under the foot sole.

model includes three Izhikevich artificial neurons (associated to VT1 near to the spine, VT2 on the side and VT3 near to the navel, respectively, and hence sensitive to heel-strike, flat-foot and toe-off) with a Regular Spiking neuron dynamics at 16 kHz [14], [19]. The neuronal model relies on the following two-dimensional system of differential equations:

$$\begin{cases} \dfrac{dv}{dt} = \dfrac{0.04}{sV}v^2 + \dfrac{5}{s}v + 140\dfrac{V}{s} - u + I & (1) \\ \qquad\quad \dfrac{du}{dt} = a(bv - u) & (2) \end{cases}$$

in which v and u are variables representing the membrane potential and the membrane recovery of a neuron, respectively. The parameters a and b are set according to [14], [20] to obtain a regular spiking dynamics for the artificial neurons ($A = 0.02$; $B = \frac{0.2}{s}$). When the injected current I excites the neuron, a spike is fired until it exceeds the after-spike reset threshold of 30 mV, which leads to the reset of v and u variables.

The I input current to each ith neuron is given by Eq. (3):

$$I_{VTi}^n = g_{VTi}max(w_{VTi}^T x^n, 0) \qquad (3)$$

where x^n are the raw sensor array readings, g_{VTi} are the gains and w_{VTi}^T are the afferent receptive field weights determining the identification of the stance phase and, thus, the enabling of the corresponding VT for 15 ms. In the experimental activities, the gain values, g_{VTi} = [72.17, 32.08, 38.42], were set for the neurons depicting the heel-strike (VTi = VT1), the flat-foot (VTi = VT2) and the toe-off (VTi = VT3) events, respectively, while the afferent receptive field weights were defined as $w^T{}_{VT1}$ = [-0.17, -0.24, 1.00], $w^T{}_{VT2}$ = [-0.00, 0.98, 0.00] and $w^T{}_{VT3}$ = [0.32, -0.08, -0.00]. In line with this activation mechanism, the neuromorphic strategy conveys both the spatial mapping of the foot-ground contact and the contact pressure through the modulation of the vibration intensity given by changes in the firing rate (Fig. 1.C-E).

B. Experimental setup

　To artificially reproduce the features of terrains with

different softness and evenness, three floor textures have been fabricated. Specifically, three 7.5 m straight paths replicating the softness of grass (Fig. 1.C), the unevenness of a rocky trail (Fig. 1.D) and the smoothness of a floor (Fig. 1.E), were reproduced in order to assess whether the presented vibrotactile stimulation allowed for the recognition of the terrain.

C. Experimental protocol

　A healthy male volunteer joined the experiment consisting of two consecutive sessions, namely familiarization and playback phase. During the familiarization, it was asked to the subject to wear the haptic system and to accomplish a locomotor task of over-ground walking along each reproduced terrain. In particular, the participant was asked to walk at his natural speed along each floor texture in order to get used to the vibrotactile stimulation and recognize, if any, its features in terms of activation patterns of VTs, intensity and duration of the provided stimuli. Towards the comparison of all the terrain-based stimulations, the subject performed 4 consecutive walks on the same floor texture before going through the others, for a total of 16 trials along each surface. The vibrotactile feedback provided in the familiarization stage was recorded at 1 kHz and shuffled in order to have a set of 48 randomized stimulations for the playback session. In particular, in this phase, the participant was asked to discriminate the terrains, being instructed to identify each perceived stimulation as originated by only one among the tested terrains.

D. Data analysis

　A psychophysical evaluation of the subject performance collected in the playback session was computed through a Matlab routine to carry out the confusion matrix for a 3 classes-based classification. Since both the grass and the floor terrains exhibited the same evenness, subject's performance in a 2 classes-based classification were also evaluated.

III. Results

The confusion matrices about the performance of the subject in texture discrimination through vibrotactile feedback are reported in Fig. 2. According to the results of the 3 classes classification (Fig. 2.A), the subject was able to correctly recognize the three terrain types with an overall accuracy of 58.4%. By solely relying on the provided neuromorphic-based stimulation, the subject was able to discriminate the rocky terrain from both the artificial grass and the smooth floor with an accuracy of 81.3%. On the other hand, the participant mostly misclassified the smooth floor with artificial grass (50.0%) and vice versa (43.8%). With reference to a 2 terrains classification (Fig. 2.B) based on the recognition of an even (smooth floor and grass) from an uneven terrain (rocky terrain), the overall accuracy of the subject raised up to 87.6%.
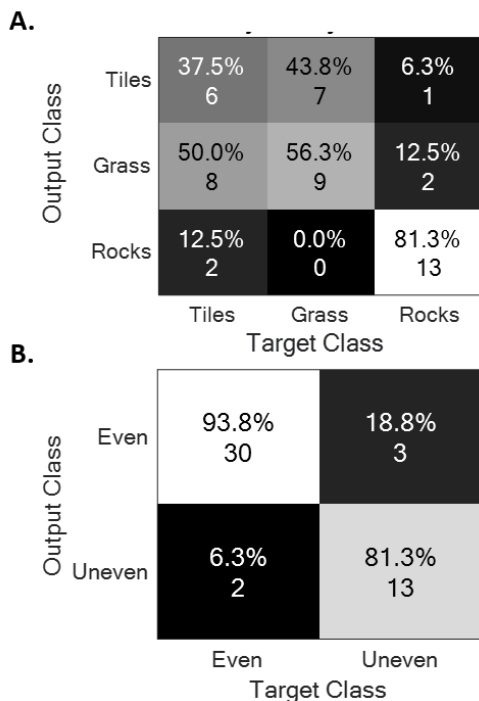
Fig. 2: Confusion matrices reporting the subject's performance in the recognition of three floor textures (A) and even from uneven terrains (B).

IV. Conclusion

A wearable haptic system and novel neuromorphic feedback strategy providing information about pressure distribution under the foot sole were presented. The effectiveness of the corresponding vibrotactile stimulation in allowing for the perception of both limb placement and characteristics of the contact surface was preliminarily tested with a single volunteer healthy subject. When tested with the more challenging task of recognizing a smooth surface from artificial grass, the accuracy was suboptimal. On the other hand, psychophysical results showed the neuromorphic stimulations enabled the recognition of uneven terrains, which is of clinical relevance.

These promising results will fuel the validation of the spike-based strategy with a larger sample of healthy subjects before going through lower limb amputees.

References

[1] S. Crea, C. Cipriani, M. Donati, M. C. Carrozza, and N. Vitiello, "Providing Time-Discrete Gait Information by Wearable Feedback Apparatus for Lower-Limb Amputees: Usability and Functional Validation," *IEEE Trans. Neural Syst. Rehabil. Eng.*, vol. 23, no. 2, pp. 250–257, 2015, doi: 10.1109/TNSRE.2014.2365548.

[2] A. Plauche, D. Villarreal, and R. D. Gregg, "A Haptic Feedback System for Phase-Based Sensory Restoration in Above-Knee Prosthetic Leg Users," *IEEE Trans. Haptics*, vol. 9, no. 3, pp. 421–426, 2016, doi: 10.1109/TOH.2016.2580507.

[3] W. C. Miller *et al.*, "The Influence of Falling , Fear of Falling , and Balance Confidence on Prosthetic Mobility and Social Activity Among Individuals With a Lower Extremity Amputation," vol. 82, no. September, pp. 1238–1244, 2001, doi: 10.1053/apmr.2001.25079.

[4] L. Yang, P. S. Dyer, R. J. Carson, J. B. Webster, K. Bo Foreman, and S. J. M. Bamberg, "Utilization of a lower extremity ambulatory feedback system to reduce gait asymmetry in transtibial amputation gait," *Gait Posture*, vol. 36, no. 3, pp. 631–634, 2012, doi: 10.1016/j.gaitpost.2012.04.004.

[5] P. B. Shull and D. D. Damian, "Haptic wearables as sensory replacement, sensory augmentation and trainer - A review," *J. Neuroeng. Rehabil.*, vol. 12, no. 1, pp. 1–13, 2015, doi: 10.1186/s12984-015-0055-z.

[6] B. W. Heller, D. Datta, and J. Howitt, "Clinical Rehabilitation," 2000, doi: 10.1191/0269215500cr345oa.

[7] L. Nolan, "Adjustments in gait symmetry with walking speed in trans-femoraland trans-tibial amputees," *Gait Posture*, vol. 17, pp. 142–151, 2003, doi: 10.1016/S0966-6362(02)00066-8.

[8] C. Lauretti *et al.*, "A vibrotactile stimulation system for improving postural control and knee joint proprioception in lower-limb amputees," *2017 26th IEEE Int. Symp. Robot Hum. Interact. Commun.*, pp. 88–93, 2017, doi: 10.1109/ROMAN.2017.8172285.

[9] et al Zambarbieri D., "Sensory feedback for lower limb prostheses," *Intell. Syst. Technol. Rehabil. Eng.*, 2001.

[10] A. Pagel, A. H. Arieta, R. Riener, and H. Vallery, "Effects of sensory augmentation on postural control

and gait symmetry of transfemoral amputees: a case description," *Med. Biol. Eng. Comput.*, vol. 54, no. 10, pp. 1579–1589, 2016, doi: 10.1007/s11517-015-1432-2.

[11]   A. Sie, D. Boe, and E. Rombokas, "Design and Evaluation of a Wearable Haptic Feedback System for Lower Limb Prostheses during Stair Descent," *Proc. IEEE RAS EMBS Int. Conf. Biomed. Robot. Biomechatronics*, vol. 2018-Augus, pp. 219–224, 2018, doi: 10.1109/BIOROB.2018.8487652.

[12]   S. Crea, B. B. Edin, K. Knaepen, R. Meeusen, and N. Vitiello, "Time-Discrete Vibrotactile Feedback Contributes to Improved Gait Symmetry in Patients With Lower Limb Amputations: Case Series," vol. 97, no. 2, 2017.

[13]   R. E. Fan *et al.*, "A prototype haptic feedback system for lower-limb prostheses and sensory neuropathy," *Stud. Health Technol. Inform.*, vol. 132, no. 3, pp. 270–277, 2008, doi: 10.1590/0103-8478cr20161016.

[14]   E. M. Izhikevich, "Simple model of spiking neurons," *IEEE Trans. Neural Networks*, vol. 14, no. 6, pp. 1569–1572, 2003, doi: 10.1109/TNN.2003.820440.

[15]   E. Martini *et al.*, "Pressure-Sensitive Insoles for Real-Time Gait-Related Applications," *Sensors* , vol. 20, no. 5. 2020, doi: 10.3390/s20051448.

[16]   I. Cesini *et al.*, "Perception of time-discrete haptic feedback on the waist is invariant with gait events," *IEEE Trans. Neural Syst. Rehabil. Eng.*, 2020, doi: 10.1109/tnsre.2020.2984913.

[17]   I. Cesini *et al.*, "A wearable haptic feedback system for assisting lower-limb amputees in multiple locomotion tasks," in *International Symposium on Wearable Robotics*, 2018, pp. 115–119.

[18]   M. Filosa *et al.*, "A new sensory feedback system for lower-limb amputees: Assessment of discrete vibrotactile stimuli perception during walking," in *International Symposium on Wearable Robotics*, 2018, pp. 105–109.

[19]   S. Prasanna *et al.*, "Neuromorphic tactile sensor array based on fiber Bragg gratings to encode object qualities," in *Optics and Photonics for Information Processing XIII*, 2019, vol. 11136, p. 1113608.

[20]   C. M. Oddo *et al.*, "Intraneural stimulation elicits discrimination of textural features by artificial fingertip in intact and amputee humans," *Elife*, vol. 5, p. e09148, 2016, doi: 10.7554/eLife.09148.

Detecting low-to-moderate isometric muscle activity through a generalized CWT-based technique

T. Varrecchia*, C. D'Anna*, D. Bibbo, M. Schmid, S. Conforto

Department of Engineering, Roma Tre University, Via Vito Volterra 62, Rome, Italy
These two authors contributed equally to the study

Abstract— **A recently introduced generalization of a Continuous Wavelet Transform-based (gCWT) algorithm for the detection of muscular activation from EMG recordings, previously tested in silico on synthetic and semi-synthetic data, is here applied for the detection of experimental data. Healthy young adults were requested to isometrically contract the upper trapezius while seated, and a visual bio-feedback was implemented to maintain the level of the upper trapezius activity between 5% and the 10% of the maximum voluntary contraction. Difference of duration between the estimated muscular activity and the force exertion captured by a pressure switch was calculated for both the gCWT technique and an amplitude-based technique, using the Teager-Kaiser Energy Operator (TKE). Difference of duration resulted in line with uncertainties associated with the variations in electromechanical delay (EMD) and relaxation-EMD reported in the literature, and they were found lower than those obtained with TKE.**

Keywords—**Muscle Activity Detection, Continuous wavelet transform (CWT), Upper Trapezius.**

I. INTRODUCTION

DETECTING muscular activity through surface EMG is a challenging task in those conditions where exerted muscle force is low, or when the activity comes from muscles that are far from the pickup site [1]. The combination of these two elements leads to reduced SNR, and the EMG signals that are characterized by these components have been recently denoted as "weak and noisy": they display low amplitudes, they may be generated by a reduced number of motor units, and may be associated with a low firing rate [2]. These conditions are, however, very frequent in a variety of application fields: they are common when prosthetic control is performed through the detection of the residual muscular activation in amputee subjects [3]; they are present in ergonomics, when tonic muscular activity is sustained for long periods with low-level contractions (e.g. shoulder/neck muscles activity during computer work or upright stance) [4]; they often appear in association with pathologies that lead to muscular weakness [5].

In all the cited conditions, the estimation of muscular activity onset through the traditional amplitude-based techniques (see e.g. [6]) or visual inspection of surface electromyograms [7] may display suboptimal performance. These classical techniques are in fact able to accurately detect muscular activations when the difference between the EMG activity at rest and that displayed during contraction is high, the level of background noise is relatively small, and the

muscle activation is characterized by an abrupt change of the signal power.

When dealing with weak and noisy EMG signals, methods have been developed to detach from amplitude-based approaches [8]: Lee and colleagues [9] used a Kalman smoother, while Zhang and Zhou [10] and Chen et al. [11] introduced two different approaches based on sample and fuzzy entropy; Staude [12] proposed a method based on the generalized likelihood ratio; the maximum likelihood method proposed by Xu and colleagues [13] improved the generalized likelihood ratio test with an adaptive threshold technique based on the SNR estimation; D'Anna et al. [14] proposed a clustering-based method that receives as inputs specific frequency characteristics of the EMG signal.

A Continuous Wavelet transform-based method introduced by Merlo and colleagues [15] was subsequently generalized by Varrecchia and colleagues, who tested its performance on synthetic and semi-synthetic data [16]. Generalization was achieved by including the possibility to iteratively determine and update the threshold for detection based on the estimation of the SNR, thus allowing to widen the applicability of the method to a class of signals where the hypotheses required by the traditional method could not be met. This approach was proven effective *in silico* for SNR values down to -2 dB.

Following along with the results obtained in silico on the generalized CWT approach, the objective of the present work is to apply the same technique for the detection of muscular activations from data taken on experimental conditions characterized by low-to-moderate muscular activations.

II. MATERIALS AND METHODS

In this section, we will describe the experimental set-up and the procedure for data recording first, and then we will focus on the processing steps included in the generalized CWT approach (gCWT), together with the description of the metrics used to evaluate the detection accuracy.

A. Participants and experimental set-up

A convenience sample of 3 healthy young individuals participated to the study. After informed consent being taken, a surface EMG probe (StepPC, DEMItalia, Italy) integrating Ag/AgCl surface electrodes (Kendall ARBO, inter-electrode distance 2 cm) was placed over the right side of the upper trapezius (UT) muscle belly in the direction of the muscle fibres, according to the European Recommendations for Surface Electromyography [17]. The reference electrode was placed on the acromial end of the collarbone. The adopted probe includes a first stage differential amplifier followed by

a second stage band-pass active filter [20-400 Hz], with an overall common mode rejection ratio around 100dB. The probe is powered with a stabilized dual voltage supply (±5 V) and its output is cable connected to the A/D converter.
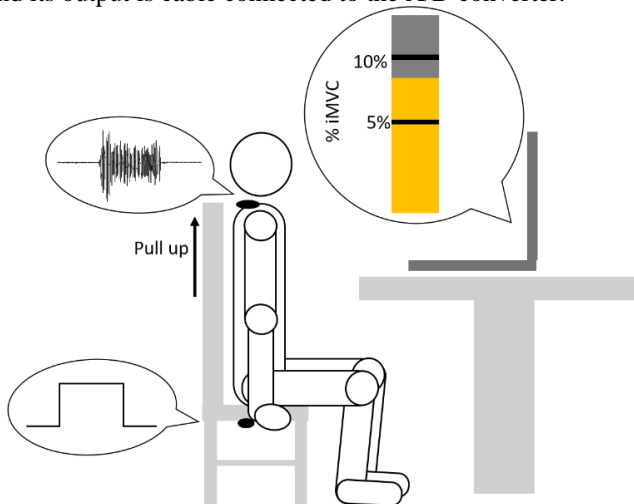

Fig. 1 Experimental procedure with visual feedback.

Individuals were requested to perform an isometric maximum voluntary contraction (iMVC) first, and then maintain, for a specified duration, a value of muscular contraction between 5% and 10% of the iMVC.

In order to inform the individuals on the amount of muscular contraction being exerted, a custom visual biofeedback (VBF) was implemented in LabVIEW code (National Instruments Corporation), which showed the instantaneous value of muscular contraction (taken by considering the root mean square value on a window 500 ms long, relative to the same value obtained during the iMVC), together with the bar limits corresponding to 5% and 10%. The task that the individuals were requested to perform to activate the UT was the same defined to calculate the iMVC [17]. Each participant repeated the task four times, with a rest period of 60 s between consecutive repetitions, thus summing up to a total of 12 trials. A simplified representation of the experimental set-up is showed in Figure 1.
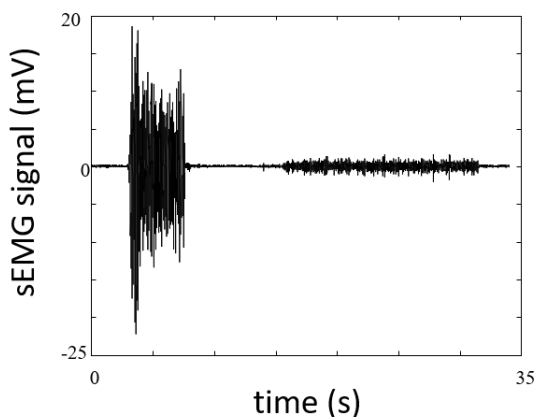
Fig. 2 An example of acquired isometric maximum voluntary contractions (iMVC) signal followed by the acquired signal in the range 5-10% of iMVC.

In order to provide a timing reference for the muscular activation in this isometric task, arms were lying along the trunk with hands gripping the bottom side of the seat, which was equipped with a pressure switch. With this configuration, the muscular contraction of the upper trapezius determines a corresponding pressure which was sensed by the sensor. The pressure switch was powered with a stabilized dual voltage supply (±5 V), and it was connected to the same ADC structure, to guarantee synchronization. In this way, it was possible to know the reference duration of the task within the 5-10% of iMVC. Before the experimental task and after iMVC recording, individuals were allowed a period of training to familiarize with the VBF, and to maintain a stable muscular activity in the 5-10% range.

B. Data processing and gCWT-based detection technique

Surface EMG data were digitally filtered (bandwidth 10-400 Hz), then the detection technique was applied, as in the following.

The first step for the estimation is the calculation of the continuous wavelet transform. In this case, we chose the Mexican Hat as prototype function, as it has been proven to be an effective mother wavelet for the analysis of EMG data [16]. CWT can be calculated for a variety of decomposition levels a, whose maximum number dictates the computational burden of the algorithm. The detection algorithm is constituted of the following three steps:

1) Definition of the minimum level of decomposition value a_{min}: CWT is calculated from a = 1 to a = a_{min}. In particular, the procedure to identify a_{min} is the following: the power of the CWT coefficients is estimated on windows lasting 200 ms and the coefficient of variation (CV) is evaluated. The level of decomposition a_{min} is then determined as the first level presenting a coefficient of variation lower than a given threshold set at 0.1.

2) Detection cycle:

   i. For each iteration i, starting from the value a_{min} determined in the previous initialization step, an objective function $\eta(t)_i$ is calculated according to the following:

   $$\eta(t)_i = max\{CWT(a,t)\}_{a=a_{min}}^{i} \quad (2)$$

   ii. $\eta(t)_i$ is processed to extract power values calculated on windows lasting 200 ms [16]. The series of the power values allowed a first classification of the signal into two different contributions. The lowest value of the series is attributed to *noise* (P_n) so considering the relative window as the part of the signal characterized by noise only. The remaining signal is considered as containing a superposition of noise and signal and is used to calculate the *signal+noise* power (P_{s+n}). With these values the SNR for the first iteration of the algorithm is calculated.

   iii. An inner cycle is then initialized, where a first-guess threshold (th_1) is estimated on the $\eta(t)_i$ function. This step is iteratively calculated as in the following:

   $$th_h = \gamma * max_\eta, h = 1 \quad (3)$$

where h is the current iteration of the algorithm, max_η is the maximum value contained in the window of $\eta(t)_i$ used to estimate P_n, and γ is calculated as follows:

$$\gamma = \sqrt{\frac{P_s}{P_n}} = \sqrt{\frac{P_{s+n} - P_n}{P_n}} \qquad (4)$$

iv. Each time sample of the vector t is classified as either a burst or inter-burst based on the chosen threshold th_h.

v. After the detection process, the SNR estimation is updated by considering the burst-interburst classification obtained at the previous step, as in [18].

vi. The relative difference between two consecutive SNR estimations is evaluated, and the iteration stops if this difference is lower than 1E-3, otherwise the threshold is updated, and steps iv. and v. are repeated.

vii. Then the detection is refined by a post-processing manipulation to reject or merge spurious transitions and to merge events that can be considered as belonging to the same contraction [15].

3) The maximum level of decomposition is chosen based on the estimation of the muscular activity for two successive values: if it is lower than 1%, the maximum level of decomposition (a_{max}) is determined.

C. Evaluation of results

Results for real signals were evaluated in terms of difference of duration (DoD) for the EMG activity: it is calculated as the temporal difference between the duration of the nominal muscular activity (Reference Activity Duration, *RAD*) estimated using the pressure switch data, and the Estimated Burst Duration (EBD), taken by running the proposed technique on the EMG data. We opted to consider the duration, since there will be a difference coming from the electromechanical delay [19], which would affect both onset timings and offset timings.

$$DoD = RAD - EBD \qquad (5)$$

For the sake of comparison, DoD was also calculated by using the Teager-Kaiser Estimation (TKE) technique introduced in [6]. In the case of gCWT, we also calculated the average number of decomposition levels n_{lev}, to provide an indication of the computational burden associated with the estimation. The corresponding estimated SNR was also calculated for each trial.

III. RESULTS

Figure 3 shows an example of acquired signal (in black) and the estimation of the muscular activity (in red). Table 1 reports the group mean values of DoD for both the gCWT and TKE, the number of decomposition levels for gCWT, and the corresponding estimated SNR for all real sEMG signals (3 subjects x 4 repetitions).

Difference of duration was on average lower than that obtained from TKE, and in general it did not exceed 100 ms. It was, for the vast majority of the cases, positive, and this

meant that overall duration of the EMG burst, as estimated from both techniques, was on average shorter than the duration of the exerted force.

TABLE I
PARAMETERS OF DETECTION ACCURACY

	gCWT	TKE
DoD [ms]	65.90 ± 49.43	80.90 ± 53.44
n_{lev}	4.10 ± 1.19	n.a.
$SNR_{estimated}$ [dB]	16.15 ± 3.14	16.15 ± 3.14

Values of Difference of Duration (*DoD*), number of decomposition levels n_{lev}, and estimated SNR (SNR$_{estimated}$) for the tested techniques. Group mean values ± standard deviation.

It may be speculated that this difference is associated with a different electromechanical delay between the onset phase and the offset phase (the so-called relaxation-EMD, [20]). We could not exclude that, given the low amount of activity chosen in the experiments, there may be uncertainties in the transition phases of muscular contraction. The number of levels varied between 4 and 5, and the estimated SNR resulted in the range 12-19 dB.
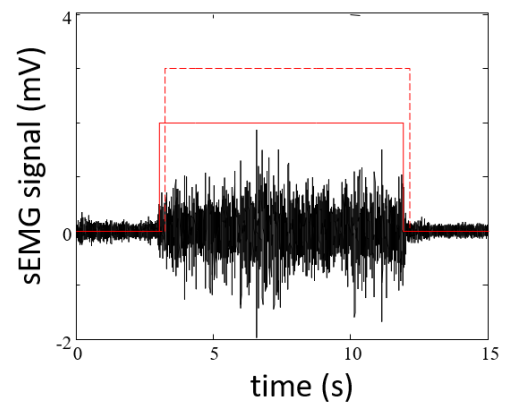

Fig. 3. An example of acquired signal (in black), the gCWT muscular estimation (red line), the pressure switch signal (dotted red line)

IV. CONCLUSIONS

When muscular activity falls below 10% of maximal voluntary contraction, the activation of muscles may be often characterized by the presence of a reduced number of recruited motor units, and a low firing rate [21]. The combination of these two elements makes the process of accurately detecting muscular activity nontrivial, and amplitude-based algorithms for EMG detection may not be the optimal solution. In this contribution, we applied a generalized CWT-based algorithm to estimate the duration of EMG activity in isometric muscular contractions performed at low-to-moderate values, and the obtained values on the limited dataset analyzed in this contribution, despite being higher than those obtained in silico, are in line with the limits of accuracy associated with the electromechanical delay variations taken from pressure switches.

Future studies will be needed, to statistically substantiate the results obtained in this work, and to optimize the parameters for the detection algorithm, with special reference to the choice

of the prototype function to be used, and the numerical choices for the stopping criteria in the iterative part of the algorithm.

REFERENCES

[1] G. Staude et al., "Onset detection in surface electromyographic signals: A systematic comparison of methods," *EURASIP J Appl. Signal Process*, no. 2, pp. 67–81, Dec. 2001

[2] D. Yang et al., "Accurate EMG onset detection in pathological, weak and noisy myoelectric signals", *Biomed Signal Process Control*, vol. 33, pp. 306–315, 2017.

[3] S. Micera, J. Carpaneto, S. Raspopovic. "Control of hand prostheses using peripheral information", *IEEE Rev. Biomed Eng*, vol. 3, pp. 48–68, 2010.

[4] E.S. Chumanov et al., "Changes in muscle activation patterns when running step rate is increased", *Gait Posture*, vol. 36, no. 2, pp. 231-235, 2012.

[5] C. De Marchis et al., "An optimized method for tremor detection and temporal tracking through repeated second order moment calculations on the surface EMG signal", *Med Eng Phys*, vol. 34, no. 9, pp. 1268-1277, 2012.

[6] X. Li et al., "Teager–Kaiser energy operation of surface EMG improves muscle activity onset detection", *Ann Biomed. Eng* Vol. 35, no. 9 1532–1538, 2007.

[7] A.S. Ferreira, F.S. Guimaraes, R.C.S. Silva, M.A.R. Magalhaes "Effects of supervised practice on the accuracy of observers for manual segmentation of simulated electromyograms", *Kinesiology*, vol. 46, no. 2, 2014.

[8] G. Vannozzi et al., "Automatic detection of surface EMG activation timing using a wavelet transform based method", *J. Electromyogr Kinesiol*, vol. 20, no. 4, pp. 767-772, 2010.

[9] J. Lee et al., "Detection of onset and offset time of muscle activity in surface EMGs using the Kalman smoother", *World Congress on Medical Physics and Biomedical Engineering 2006 IFMBE Proceedings*, pp. 1103–1106, 2007.

[10] X. Zhang, P. Zhou, "Sample entropy analysis of surface EMG for improved muscle activity onset detection against spurious background spikes", *J. Electromyogr Kinesiol*, vol. 22, pp. 901–907, 2012.

[11] W. Chen et al., "Characterization of surface EMG signal based on fuzzy entropy", *IEEE Trans Neural Syst Rehabil Eng*, vol. 1, no. 2, pp. 266-272, 2007.

[12] G.H. Staude, "Precise onset detection of human motor responses using a whitening filter and the log-likelihood-ratio test", *IEEE Trans. Biomed Eng*, vol. 48, pp. 1292–1305, 2001.

[13] Q. Xu et al., "An adaptive algorithm for the determination of the onset and offset of muscle contraction by EMG signal processing", *IEEE Trans. Neural Syst Rehabil Eng*, vol. 21, pp. 65–73, 2013.

[14] C. D'Anna et al., "Using the frequency signature to detect muscular activity in weak and noisy myoelectric signals", *Biomed Signal Process Control*, vol. 52, pp. 69-76, 2019.

[15] A. Merlo et al., "A fast and reliable technique for muscle activity detection from surface EMG signals", *IEEE Trans. Biomed Eng*, vol. 50, no. 3, pp. 316-23, March 2003.

[16] T. Varrecchia et al, "Generalization of a wavelet-based algorithm to adaptively detect activation intervals in weak and noisy myoelectric signals", *Biomed Signal Process Control*, 58, 101838.

[17] H.J. Hermens, B. Freriks, C. Disselhorst-Klug, G. Rau, "Development of recommendations for SEMG sensors and sensor placement procedures". J. Electromyogr. Kinesiol. 10 (5), 361–374, 2000.

[18] G. Severini et al., "Novel formulation of a double threshold algorithm for the estimation of muscle activation intervals designed for variable SNR environments", *J. Electromyogr. Kinesiol*, vol. 22 (6), pp. 878-885, 2012.

[19] S. Conforto et al. "How much can we trust the electromechanical delay estimated by using electromyography?", In 2006 International Conference of the IEEE Engineering in Medicine and Biology Society, pp. 1256-1259. IEEE, 2006.

[20] T. J. Roberts, A.M. Gabaldón, A.M., "Interpreting muscle function from EMG: lessons learned from direct measurements of muscle force", Integrative and comparative biology, 48(2), pp.312-320, 2008.

[21] R.A. Conwit et al, "Firing rate analysis using decomposition-enhanced spike triggered averaging in the quadriceps femoris", *Muscle Nerve*, 21(10), pp.1338-1340, 1998.

Clinical and technology-based assessment of an innovative integrated rehabilitation programme for persons affected by Parkinson's disease

G.P. Salvi[1], A. Quarenghi[1], E. Sigismondi[1], E. Mion[2], M. Simonini[1], and S. Mazzoleni[3,4]

[1] *U.O. Riabilitazione Neuromotoria – Istituto Clinico Quarenghi, San Pellegrino Terme, Italy*
[2] *Scuola di Specializzazione in Medicina fisica e riabilitativa, Università di Pavia, Italy*
[3] *The BioRobotics Institute, Scuola Superiore Sant'Anna, Pisa, Italy*
[4] *Department of Excellence in Robotics and AI, Scuola Superiore Sant'Anna, Pisa, Italy*

Abstract—The aim of this study is to evaluate the effects of an integrated rehabilitation treatment of persons affected by Parkinson's disease based on neuromotor exercises, unstable platform and treadmill walk. Seventy-nine patients (42 men, 37 women; mean age 68,2±9 years) affected by Parkinson's disease diagnosed more than 12 months prior to the study were recruited. Each patient underwent a 4-week rehabilitation programme composed by 20 sessions (5 sessions/week), including 30 minutes of neuromotor exercises aimed at improving the swing phase, facilitation and modulation of dynamic load, step training with obstacles overcoming and stairs execution. In addition, during each rehabilitation session each patient has carried out 15 minutes of proprioceptive exercise on an unstable platform and 15 minutes of treadmill gait. The Unified Parkinson's Disease Rating Scale (UPDRS) and the Functional Independence Measure (FIM) were used as clinical outcome measures. A stability index and an oscillation index were computed.

The results showed significant improvement of clinical outcome measures and stability and oscillation index at the end of the integrated rehabilitation programme.

Keywords—Parkinson, gait, posture, assessment.

I. INTRODUCTION

Parkinson's disease is a progressive neurodegenerative caused by basal ganglia dysfunction and mainly characterised, even if not exclusively, by a triad of motor signs composed by rest tremor, bradykinesia and rigidity.

The motor framework of the pathology, therefore, is characterised by alteration of the timing of muscle activation with a hindrance of fine motor skills, slowness in the execution of voluntary movements, reduction of postural reflexes with difficulty in walking and propension to falls. The rehabilitation protocols currently offered to persons with Parkinson's disease include treatments aimed at reducing hypertonicity, straightening posture, improving balance and walking pattern [1]-[3].

The use of different technologies in the rehabilitation domain is essential to stimulate neuroplasticity that is the ability of brain cells to change in response to intrinsic and extrinsic factors. It is a continuous process able to promote short-, medium- and long-term remodeling of neurosynaptic organisation, with the aim of optimizing the functioning of neural networks following brain injury.

Neuroplasticity is enhanced by repetitive tasks. Different robotic devices were used in this study in order to improve both neuroplasticity and patients' compliance: changing tasks and devices make training sessions more attractive.

Evidence-based approaches to rehabilitation are known to improve physical functioning, strength, balance, gait and health-related quality of life among persons with Parkinson's disease [4]: the rehabilitation programme proposed in this study aims to improve independence of these persons in activities of daily living (ADLs) after discharge.

The aim of this study is to evaluate the effects of an integrated rehabilitation treatment of persons affected by Parkinson's disease based on neuromotor exercises, unstable platform and treadmill walk.

II. METHODS

At the Neuromotor Rehabilitation Dept. of Istituto Clinico "Quarenghi" in San Pellegrino Terme (Bergamo), Italy, n=79 patients (42 men, 37 women; mean age 68,2±9 years) affected by Parkinson's disease were recruited. Inclusion criteria: disease diagnosed more than 12 months prior to the study, Skin integrity (i.e., no bedsores). Exclusion criteria: cognitive impairment (Mini Mental State Exam score < 24/30), cardiovascular clinical instability (i.e. severe heart failure), osteoarticular limitations (i.e., arthrodesis).

Neuromotor exercises with respect to traditional exercises aim to improve global coordination, trunk control and trunk extension and balance and core stability. Each patient underwent a 4-week rehabilitation programme composed by 20 sessions (5 sessions/week), including 30 minutes of neuromotor exercises aimed at improving the swing phase, facilitation and modulation of dynamic load, step training with obstacles overcoming and stairs execution. The physical therapist supervised each patient during the rehabilitation programme. In addition, during each rehabilitation session each patient has carried out 15 minutes of proprioceptive exercise on an unstable platform (Biodex Balance System SD®) and 15 minutes of treadmill gait (Biodex Gait Trainer®). The unstable platform offers 12 different levels of instability from the lowest (lack of instability) to the highest (high instability). In order to assess each patient's balance control, the highest level of instability was used. A "reaching target time" was used as reference task: the patient had to move his/her centre of gravity on the platform and he/she was requested to hit an object shown on the screen in front of him/her by means of a virtual arrow. The speed during the treadmill walking was set to fit each patient skill: the average skill speed was 2 km/h. At the end of rehabilitation programme

the physical therapist provided each patient with a list of exercises to be performed at home. The physical therapist assessed and supervised the exercises by means of a videocall.

The analysis of stability and oscillation in orthostatic condition can be carried out by using the unstable platform based on the computation of a) the Stability Index (SI), defined as the angular excursion of the patient's center of gravity, and b) the Oscillation Index (OI), defined as the SI standard deviation. Both indices are evaluated under two modalities: a) open eyes and b) closed eyes open on a rigid and soft surface. The use of the treadmill, at the running speed feasible to the patient, the evaluation of the step length, gait speed and load distribution while walking can be carried out during the treadmill gait training. The Unified Parkinson's Disease Rating Scale (UPDRS) was administered for assessing the disability deriving from the pathology, and the Functional Independence Measure (FIM), for assessing the autonomy during execution of ADLs.
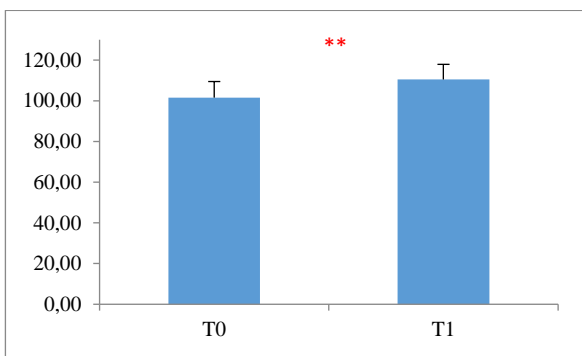
Fig. 1: Functional Independence Measure (FIM) score at admission (T0) and discharge (T1) expressed as mean and standard deviation. Legend: **, $p < 0,001$.

III. RESULTS

A statistically significant improvement of the FIM (Figure 1) and UPDRS (Figure 2) was observed. In addition, the step length (Figure 3) and the walking speed (Figure 4) also showed a significant improvement.

A statistically significant improvement of SI on a stable surface, both with open eyes (Figure 5) and closed eyes (Figure 6) was observed. Finally, significant improvements of the OI on a stable surface with open eyes (Figure 7) and the OI on a soft surface with closed eyes (Figure 8) were found.
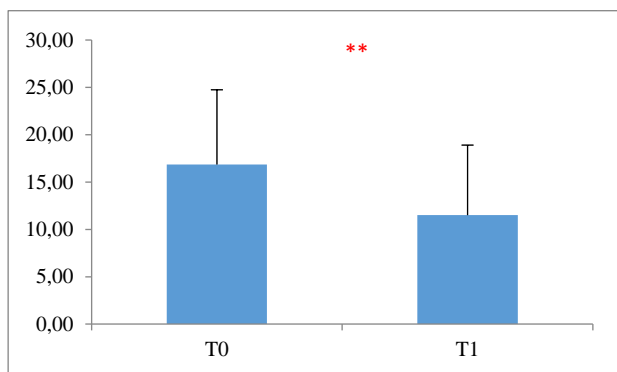

Fig. 2: Unified Parkinson's Disease Rating Scale score at admission (T0) and discharge (T1) expressed as mean and standard deviation. Legend: **, $p < 0,001$.
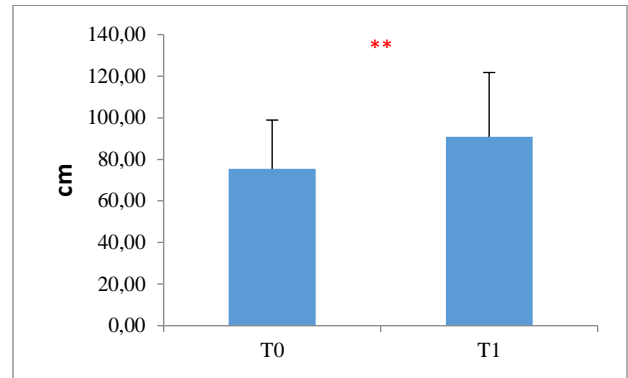

Fig. 3: Step length at admission (T0) and discharge (T1) expressed as mean and standard deviation. Legend: **, $p < 0,001$.
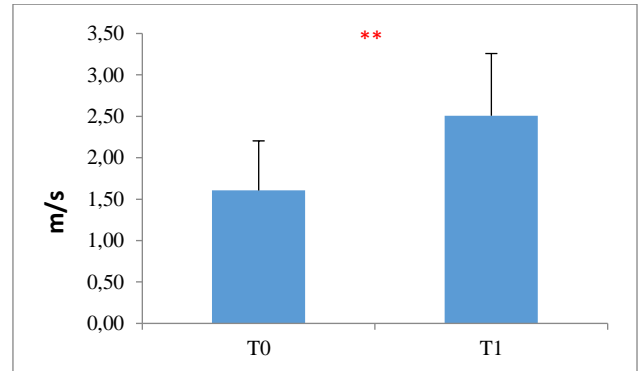

Fig. 4: Walking speed at admission (T0) and discharge (T1) expressed as mean and standard deviation. Legend: **, $p < 0,001$.

IV. CONCLUSION

The preliminary results of the study show that the proposed integrated rehabilitation treatment for persons affected by the Parkinson's disease indicate a potential improvement in terms of balance, gait parameters, disability linked to the pathology and independence in ADLs.

The proposed rehabilitation treatment also proved to be useful to counteract parkinsonian symptoms.

It is therefore desirable that the training based on unstable platform and treadmill may be included into the rehabilitation programmes of persons affected by the Parkinson's disease in conjunction with traditional neuromotor exercises.
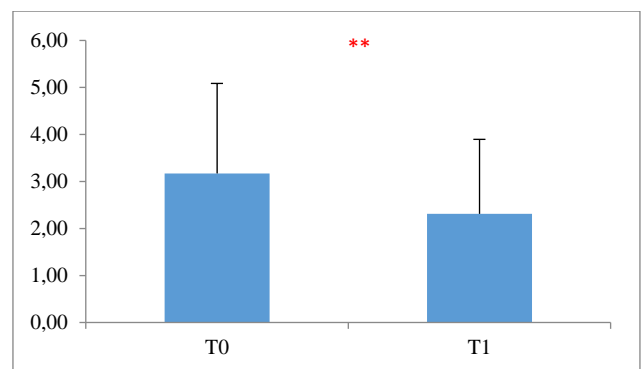

Fig. 5: Stability index with open eyes on stable surface at admission (T0) and discharge (T1) expressed as mean and standard deviation. Legend: **, $p < 0,001$.
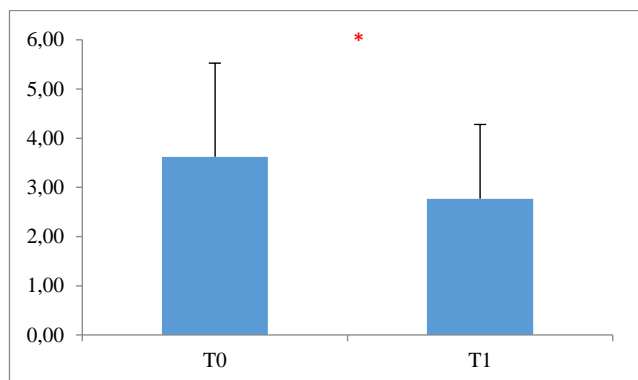
Fig. 6: Stability index with open eyes on stable surface at admission (T0) and discharge (T1) expressed as mean and standard deviation. Legend: *, p < 0,05.

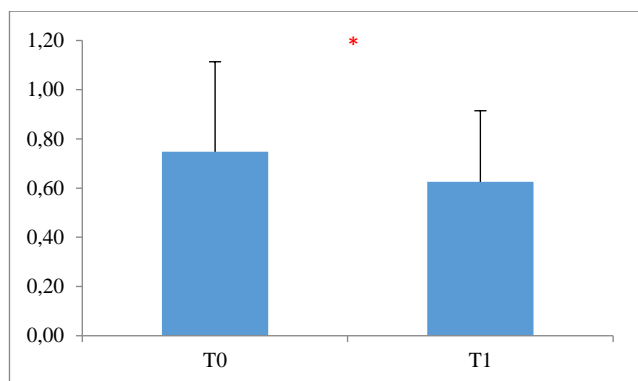

Fig. 7: Oscillation index with open eyes on stable surface at admission (T0) and discharge (T1) expressed as mean and standard deviation. Legend: *, p < 0,05.
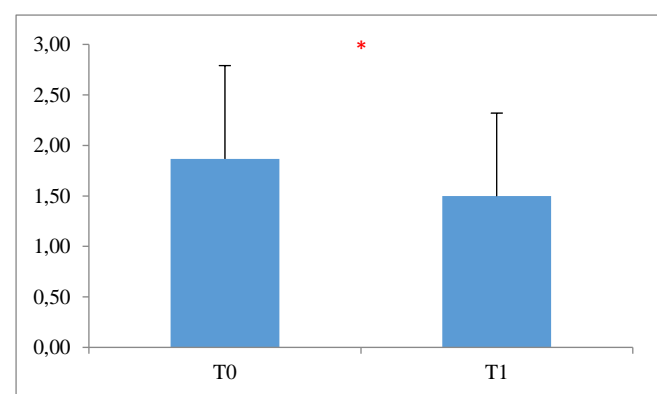

Fig. 8: Oscillation index with closed eyes on soft surface at admission (T0) and discharge (T1) expressed as mean and standard deviation. Legend: *, p < 0,05.

REFERENCES

[1] C. Schlenstedt, S. Paschen, A. Kruse, J. Raethjen, B. Weisser, and G. Deuschl, "Resistance versus balance training to improve postural control in Parkinson's disease: A randomized rater blinded controlled study," *PLoS One* 2015;10:e0140584.

[2] B.E. Fisher, A.D. Wu, G.J. Salem, J. Song, C.H. Lin, J. Yip, S. Cen, J. Gordon, M. Jakowec, and G. Petzinger, "The effect of exercise training in improving motor performance and corticomotor excitability in people with early Parkinson's disease," *Arch Phys Med Rehab* 2008; 89:1221-1229.

[3] C. Silva-Batista, D.M. Corcos, and H. Roschel, "Resistance training with instability for patients with Parkinson's disease," *Med Sci Sports Exerc* 2016; 48:1678–87.

[4] M.J. Falvo, B.K. Schilling, and G.M. Earhart, "Parkinson's disease and resistive exercise: rationale, review, and recommendations." *Mov Disord.* 2008; 23(1):1-11.

Preventive Healthcare through Air Pollution Exposure Modeling: the example of PULSE in Pavia

D. Pala[1], L. Zurlo[1], M. Franzini[2], V. Casella[2], R. Bellazzi[1], D. Vito[1] and C. Larizza[1]

[1] *Department of Electrical, Computer and Biomedical Engineering, University of Pavia, Pavia, Italy*
[2] *Department of Civil Engineering and Architecture, University of Pavia, Pavia, Italy*

Abstract—**Since the beginning of the last century, most of the world's population has been concentrating in the urban areas, and this trend is expected to continue in the next decades. With the increasing urbanization, health hazards such as air pollution are rising, increasing the necessity of interventions by the health policy makers. Due to its high industrialization level and its peculiar geographical position, the plain region known as Pianura Padana, in northern Italy, is frequently affected by extremely high pollution levels during the winter months, leading to an increased risk of respiratory diseases and premature mortality in the population. Several solutions that aim at limiting the pollution sources and rise awareness in the population are being developed. In this paper, a pollution monitoring system developed by the University of Pavia is presented. This system consists of a dense network of low-cost sensors paired with a smartphone App that helps the population to know the exact pollution level in every spot of the city of Pavia and organize outdoor activities accordingly. The system has been developed as part of the European union's PULSE project, briefly described at the beginning of this paper.**

Keywords—**Public Health, Air Pollution, Sensors, Exposure.**

I. INTRODUCTION

THE percentage of the world's population living in the urban areas is projected to increase in the next decades [1]. Rising industrialization, urbanization and heterogeneity are leading to new challenges for public health and quality of life in the population. The prevalence of conditions such as asthma and cardiovascular diseases is increasing due to a change in lifestyle and air quality [2] [3]. This enlightens the necessity of targeted interventions to increase citizens' quality of life and decrease their health risks.

To this end, the European Commission project named PULSE (Participatory Urban Living for Sustainable Environments) unifies several institutions around the world and works with the municipalities of 7 cities – Barcelona, Birmingham, Paris, Pavia, New York, Singapore and Keelung – to develop a multi-technological system to assist the population in the prevention and treatment of asthma, type 2 diabetes and cardiovascular diseases. The system created in PULSE features several parts, such as a personal App for the citizens, a set of air quality sensors, a WebGIS and dashboards for the public health operators. Citizens are directly involved in an exchange paradigm as they send their own data and receive feedbacks and suggestions about their health in return.

The University of Pavia, Italy, contributes to the technical implementation of the project and works together with the local municipality and health agency to involve the population in the project, transforming the city of Pavia in a PULSE test site.

This paper describes the implementation developed in Pavia, where a dense network of 40 air quality sensors has been deployed and paired with a smartphone app that makes air quality monitoring easy and accessible to the whole population, giving them feedbacks, increasing awareness and helping them organize outdoor activities in a way that minimizes health risk.

II. AIR POLLUTION: THE CASE OF PAVIA

Extensive research has proved the link between air pollution and the increased risk of respiratory and cardiovascular diseases [4]. Some studies even showed how high levels of some pollutants (e.g. PM2.5) can be associated to a higher risk of developing diabetes [5].

Even if its dimensions are limited (population around 71,000 inhabitants) and there aren't any extremely industrialized sites in the vicinity, the city of Pavia is often affected by high pollution levels, especially in the winter months. Pavia is located in the *Pianura Padana*, a large plain region located in the north of Italy that represents the most populated and industrialized area of Italy and one of the most industrialized in Europe. Being closed on 3 sides by the mountains, during the winter months, especially in a high atmospheric pressure situation where cold and heavy air is compressed to the ground, the air tends to stagnate in this area for long periods, generating a dramatic increase in the pollution levels that is easily notable even far from the major cities [6]. This phenomenon is worsened by the almost total absence of wind and the frequent presence of fog, that carries the pollutants in its small drops increasing their toxicity [7]. So far, local initiatives such as traffic or house heating limitations have been taken in order to limit the risks associated to high pollution, but the problem remains.

III. THE PURPLEAIR SENSOR NETWORK

One of the innovative aspects of PULSE is the participative paradigm that allows the citizens to be directly involved in the system, allowing them to be followed almost individually, thanks to a personalized risk calculator and a feedback system. The University of Pavia applies the same concept to fight the pollution problem, with a system that allows the citizens to be constantly informed about the situation in the city and its implications. This system features a unified infrastructure for the acquisition, visualization, management and sharing of the data made of several parts:

- A dense sensor network (40 sensors as to January 2020);
- ThingSpeak cloud service, for data storage;
- UNIPV server, connected with the main PULSE server, storing raw sensors data;
- A dedicated App, named PULSE@PV.

The sensor network is mainly composed of PurpleAir sensors, these are little, light and non-invasive devices that can be drilled over every kind of wall and require just an electrical outlet and Wi-Fi connection. These sensors have been installed on several public and private buildings throughout the city, thanks to the cooperation of the municipality and some volunteers. PurpleAir sensors measure PM2.5 and PM10 together with some meteorological conditions such as temperature and humidity every 2 minutes. Each sensor measures these quantities using two different channels (A and B), then the average of the two measurements is used. The detailed specifications of these sensors are available on the website https://www2.purpleair.com/products/purpleair-pa-ii#MainContent. More air quality data are available from the official monitoring station deployed by the local environmental protection agency (ARPA), that owns two high precision stations that measure PM2.5, PM10, NO_2 and CO. The ARPA portal allows to download historical air quality data for free.

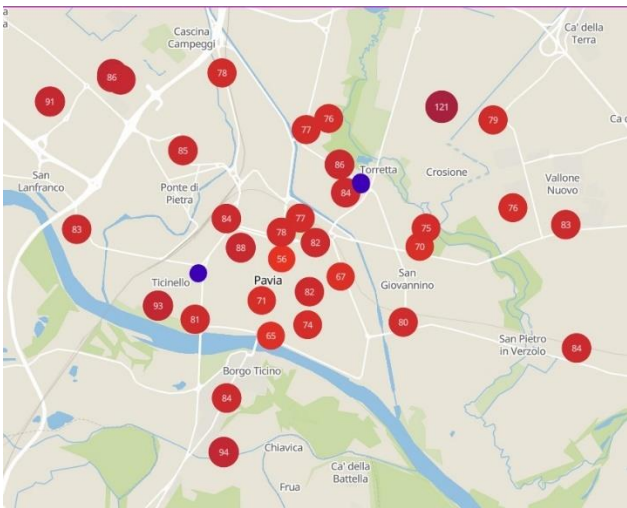Figure 1 shows a map of the sensors currently functioning.

Fig. 1: map of the air quality sensors currently functioning in Pavia. The PurpleAir sensors are colored in red and show their PM2.5 real time measurement, whereas the ARPA monitoring stations are highlighted in blue.

All the data coming from the sensors are stored in a dedicate database in the UNIPV server and can be accessed through basic SQL queries and Java methods. The latest measurements can be visualized also on the PurpleAir website, after authentication, using a detailed portal. The user can choose to either visualize the data of a specific sensor (figure 2) or those of several sensors together (figure 3).
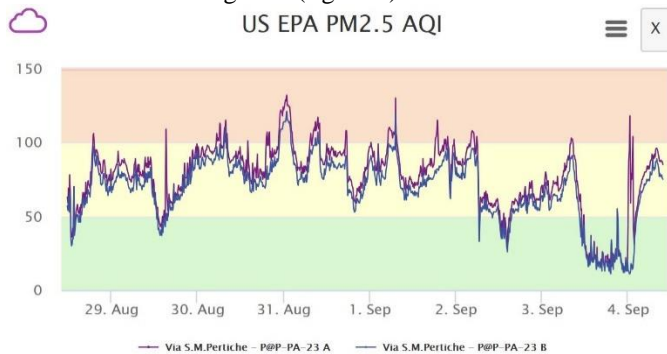

Fig. 2: Summary data of one week of channel A and B US EPA PM2.5 measurements of a selected sensor.
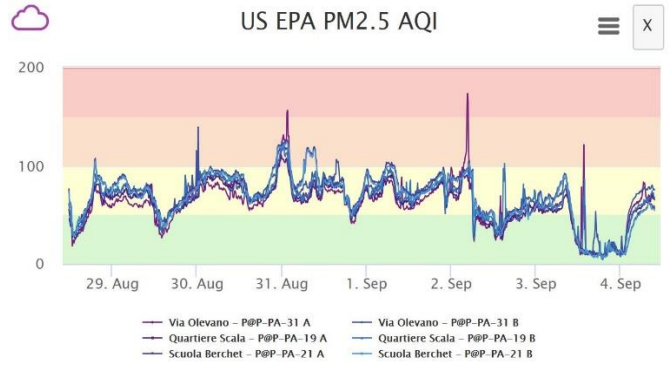

Fig. 3: Summary data of one week of measurements of 3 different sensors selected together.

To test the reliability of the PurpleAir sensors, some devices have been placed close to an official ARPA monitoring station in order to compute the correlation between the devices' measurements. ARPA sensors are official high quality devices, very precise and expensive, whereas PurpleAir sensors are low-cost domestic devices (the cost of each sensor is $200-250), so it is logical to assume that the accuracy of their measurements will be lower compared to the official stations' ones. In spite of this, the possibility to purchase a relatively high number of sensors at a moderate price allows to create a dense network that makes it easier to estimate the real values of pollution in all the points of the city [8], integrating the low-cost sensors' measurements with the official ones and performing a proper calibration. In our case, in all the comparisons we obtained high correlation scores (>0.8), and we observed that there was a small offset (<10 µg/m^3) in the PM2.5 and PM10 measurements between our sensors and the ARPA's ones. Figure 4 reports an example of a specific sensor located 120m from one of the official ones, concerning PM2.5.
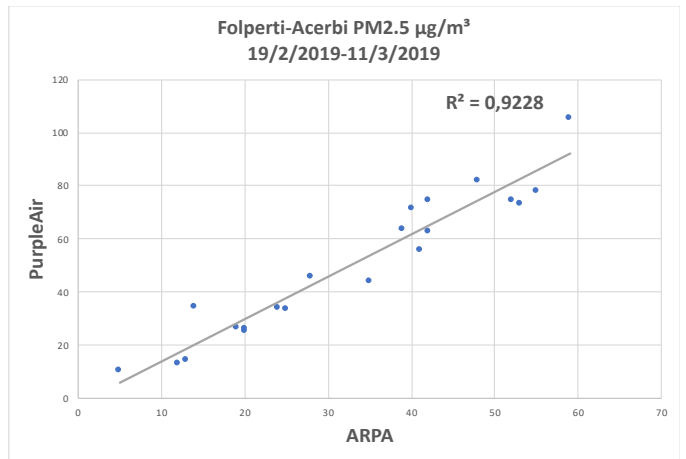

Fig. 4: Comparison of the daily averages measured by one PurpleAir sensor and the closest ARPA sensor. Correcting for a small offset, the correlation score was very high (0.9228).

The sensor network is used mainly in 3 different ways:

- Establishment of a link between the sensors's data and the PULSE@PV App that keeps the user informed about air quality and the current situation in his/her vicinity.
- Correlation studies on the link between pollution and health outcomes, integrating the data with health data

about hospitalizations, mortality and ER visits, available thanks to the cooperation with the local health agency and the hospitals. Both AQ and health data are integrated also with socioeconomic and demographic factors, that play an important role in the development and progression of a disease, as demonstrated in other studies performed within PULSE [9] [10];

- Interpolation of the data coming from the sensors in order to create a homogeneous pollution map usable for the computation of air pollution in every spot of the city and for the estimation of personal exposure of the users, thanks to the GPS tracking functionality of their mobile devices.

IV. THE PULSE@PV APP

The data coming from the sensors are constantly extracted by the ThingSpeak cloud service and stored in a proper database. The PULSE@PV App accesses these data for elaboration and visualization. This App features a simple layout and allows the citizens to be constantly informed about the city's air quality, through the following main functions:

- Visualization of the PM10 value measured in real-time by the nearest sensor. This value can be visualized directly in the home page of the app.
- Visualization of a list of all the sensors that were active in the last 30 minutes, with a feedback icon associated to each one of them, indicating whether the measured value represents a safe air quality status or a potentially dangerous situation for health. The sensors are ordered by distance.
- Visualization of the latest measurements of PM2.5, PM10, temperature and humidity of each sensor.
- Visualization of a map of all the sensors deployed and functioning in the city, color-coded according to the health hazard deriving from their measurements.

Besides color-coding (the US EPA colour cording for each pollutant is used), short sentences are paired to the sensors' measurements visualized on the app, providing a brief explanation of the danger involved in being exposed to the specific amount of pollution. Finally, the users can access an informative page that explains what the app and the project are about and how the data will be used. Figure 5 provides an illustration of the main functionalities of the app.

PULSE@PV can be used together with the official PULSE app, named *Pulsair*, that provides detailed feedback on the health risk of every single user through the use of risk models based on personal data, that allows to compute a personalized risk of developing or worsening asthma, type 2 diabetes or cardiovascular diseases.

At this time (updated on January 2020), PULSE@PV has been downloaded by almost 200 users counting both Android and IOS users.
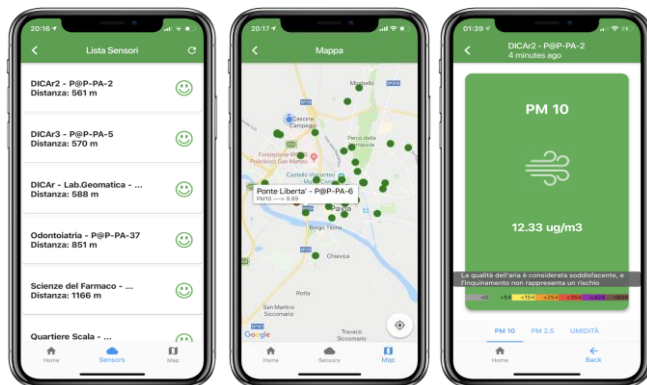

Fig. 5: Screenshot of the PULSE@PV App. From the left: the list of sensors ordered by distance with a feedback icon, a map of the sensors, the most recent measurement of the nearest sensor with an accompanying sentence that provides the danger level associated to the pollution status.

V. PERSONAL EXPOSURE CALCULATOR

Thanks to the great number of sensors deployed in Pavia, another system that aims at reducing the effect of pollution on the population by following each person individually is currently under development: a personal pollution exposure calculator. This system exploits two main parts of the technology developed in PULSE:

- The data coming from the dense sensor network deployed in Pavia, interpolated in space;
- The GPS tracking functionality of PULSE's app, that uses the geolocation feature of the users' phones.

At the present time, this system is under refinement in the city of Pavia, but future plans are to extend it to the other cities participating in PULSE and integrate it in the PULSE dashboards, i.e. a visualization tool which policy makers will be provided with to be constantly informed about several health and social indicators in their city, which can be used to take informed decisions and targeted interventions.

In the personal exposure calculator, each user, after reading and agreeing to a detailed consent form, is followed all day long with the GPS tracking. Meanwhile data coming from the sensors are continuously stored and interpolated in a homogeneous map. A trajectory is then drawn considering the user's movement and finally an estimation of the cumulative intake of pollutants that were breathed is calculated. This operation is performed through an estimation of the number of breaths that were taken by the user in each minute of the day and the correspondent air volume intake, considering three different levels of physical activity: standing still, walking, running. These quantities where estimated after an accurate research in literature [11] and are reported in Table I.

TABLE I
AIR INTAKE ESTIMATION BASED ON PHYSICAL ACTIVITY

Speed (Km/h)	Number of breaths per minute	Air volume per breath (liters)
0 - 2	15	0.6
2 - 6	28	1.8
>6	40	2.5

Figure 6 shows an example of the interpolated pollution measurement, obtained applying the Inverse Distance Weighting algorithm to the PurpleAir sensors, whereas figure 7 shows a simulated trajectory of a user that moves in the city through the day. These data are used to compute the cumulative personal exposure that influences the user's personal risk of respiratory diseases.
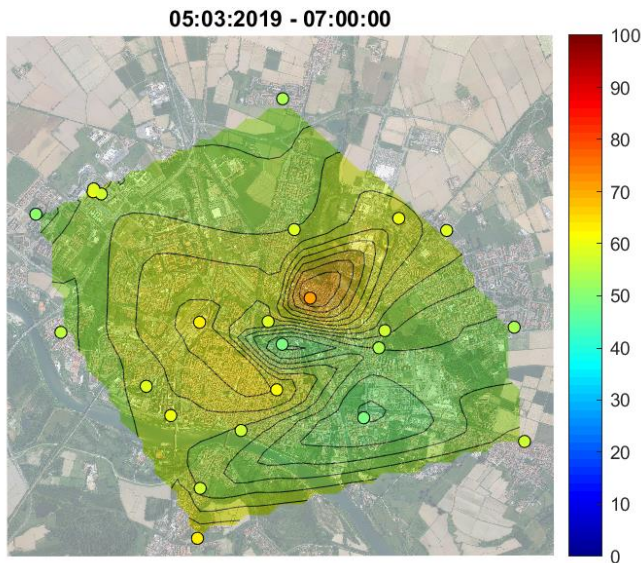

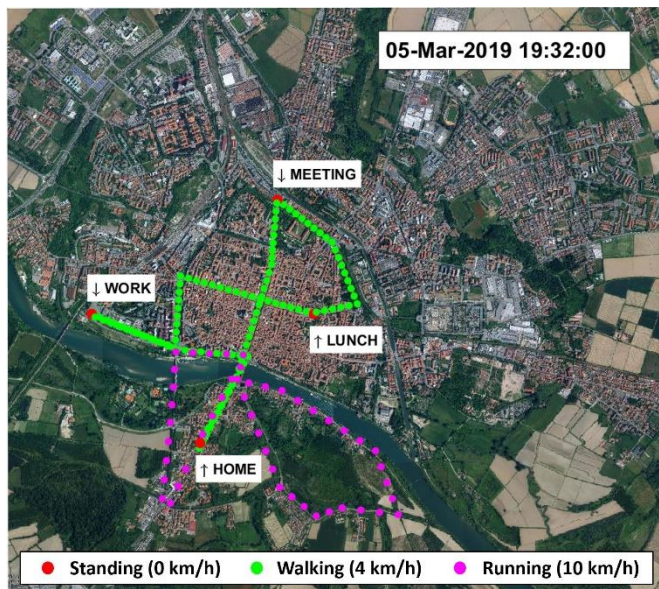Fig. 6: Interpolated map of the PM10 levels in a specific time frame.

Fig. 7: Simulated trajectory of a user in a specific day.

VI. CONCLUSIONS

This paper briefly describes a new integrated system that has been developed by the University of Pavia in the context of the European project PULSE. It has been demonstrated how air pollution can affect human health increasing the probability to contract several diseases and reducing quality of life. Being this a known problem, several interventions are taken every year by the municipalities of all the world to reduce emissions and increase awareness over the population. Nevertheless, cardiovascular and respiratory diseases are becoming more diffuse every year. The aim of PULSE and other similar projects is to use the new technology advancements in the

fields of mobile devices, GPS tracking and Big Data analytics to create a dynamic environment in which citizens can be constantly assisted and feel safe thanks to a personalized risk assessment, and policy makers can improve citizens' lives with an eased intervention process. This paper shows an example of how this can be achieved thanks to affordable sensor technology and advanced app development. Future developments will be the improvement of the personal exposure calculator using more precise physical activity data and the integration of all these systems in the PULSE dashboards.

REFERENCES

[1] World Health Organization and UN-Habitat, *Global report on urban health: equitable healthier cities for sustainable development*. World Health Organization, 2016.

[2] C. Anandan, U. Nurmatov, O. C. P. van Schayck, and A. Sheikh, "Is the prevalence of asthma declining? Systematic review of epidemiological studies," *Allergy*, vol. 65, no. 2, pp. 152–167, Feb. 2010, doi: 10.1111/j.1398-9995.2009.02244.x.

[3] M. Guarnieri and J. R. Balmes, "Outdoor air pollution and asthma," *Lancet Lond. Engl.*, vol. 383, no. 9928, pp. 1581–1592, May 2014, doi: 10.1016/S0140-6736(14)60617-6.

[4] B.-J. Lee, B. Kim, and K. Lee, "Air pollution exposure and cardiovascular disease," *Toxicol. Res.*, vol. 30, no. 2, pp. 71–75, Jun. 2014, doi: 10.5487/TR.2014.30.2.071.

[5] S. Feng, D. Gao, F. Liao, F. Zhou, and X. Wang, "The health effects of ambient PM2.5 and potential mechanisms," *Ecotoxicol. Environ. Saf.*, vol. 128, pp. 67–74, Jun. 2016, doi: 10.1016/j.ecoenv.2016.01.030.

[6] "'We breathe in poison': Why the Po Valley is one of the most polluted places in Italy," 28-Feb-2019. [Online]. Available: https://www.thelocal.it/20190228/po-valley-air-pollution-italy. [Accessed: 14-Jan-2020].

[7] S. Decesari *et al.*, "Enhanced toxicity of aerosol in fog conditions in the Po Valley, Italy," *Atmospheric Chem. Phys.*, vol. 17, no. 12, pp. 7721–7731, Jun. 2017, doi: https://doi.org/10.5194/acp-17-7721-2017.

[8] P. Kumar *et al.*, "The rise of low-cost sensing for managing air pollution in cities," *Environ. Int.*, vol. 75, pp. 199–205, Feb. 2015, doi: 10.1016/j.envint.2014.11.019.

[9] Pala D, Pagán J, Parimbelli E, Rocca MT, Bellazzi R and Casella V, "Spatial enablement to support environmental, demographic, socioeconomics, and health data integration and analysis for big cities: a case study with asthma hospitalizations in New York City." *Front. Med.* 6:84. 2019. doi: 10.3389/fmed.2019.00084

[10] R. Bellazzi *et al.*, "Transfer Learning for urban landscape clustering and correlation with health indexes," in *How AI Impacts Urban Living and Public Health*, Cham, 2019, pp. 143–153, doi: 10.1007/978-3-030-32785-9_13.

[11] "Your lungs and exercise," *Breathe*, vol. 12, no. 1, pp. 97–100, Mar. 2016, doi: 10.1183/20734735.ELF121.

Harmonisation of medical devices classification systems: development of a generalised approach starting from hip prostheses.
A first example of an international and standardised nomenclature to be integrated within the European Medical Device Nomenclature

M. Franzò[1,2], E. Carrani[1], M. Asaro[3], E. Caton[4], K. Tucker[5], R. Armstrong[4], E. Young[6], L. Sampaolo[7]
F. Bini[2], F. Marinozzi[2] and M. Torre[1]

[1] Scientific Secretariat of the Presidency, Italian National Institute of Health, Rome (Italy)
[2] Department of Mechanical and Aerospace Engineering, "Sapienza" University of Rome, Rome (Italy)
[3] European Medical Device Nomenclature implementation working Group, Trieste (Italy)
[4] Northgate Public Services, London (United Kingdom)
[5] ODEP, Beyond Compliance, London (United Kingdom)
[6] National Joint Registry for England, Wales, Northern Ireland and the Isle of Man, London (United Kingdom)
[7] National Centre for Disease Prevention and Health Promotion, Italian National Institute of Health, Rome (Italy)

Abstract— **Medical device (MD) nomenclatures are essential for market surveillance and vigilance activities. Currently, more than 25 arthroplasty Registries are established in Europe, each of them based on a different MD nomenclature. A common and shared nomenclature of orthopaedic implants is important to analyse implant performance across different national databases referring to a unique definition of its characteristics. Aim of this study is to describe an approach to compare and harmonise two different nomenclatures: a first step towards the organization of an international nomenclature of medical devices**.

Keywords— **medical devices, nomenclature, EMDN, CND**

I. INTRODUCTION

MEDICAL device (MD) nomenclatures are essential for market surveillance and vigilance activities. They allow to organize medical devices in homogeneous categories of products intended to perform a similar diagnostic or therapeutic intervention [1]. Currently, more than 25 arthroplasty Registries are established in Europe [2], each of them based on a different MD nomenclature.

The National Joint Registry for England, Wales, Northern Ireland and the Isle of Man (NJR) [3] introduced a new component nomenclature for hip and knee in 2018/19 [4]. Recently, NJR has upgraded its component database and classification, in cooperation with the EndoProthesen Register Deutschland (EPRD). This classification (NJR-EPRD nomenclature) is currently used in both countries. The Italian Arthroplasty Registry (RIAP) [5] uses the National Classification of Medical Devices (CND) established in 2007 by the Italian Ministry of Health (MoH) [6]. On 4th March 2019, the EU Commission adopted the CND nomenclature as a base to support the activity of the future European database of medical devices Eudamed [7]. As for joint prostheses, RIAP is supporting the project to extend CND to the EU level and develop the EU nomenclature EMDN (European Medical Device Nomenclature). The adoption of an internationally recognised medical devices nomenclature available free of charge to facilitate the functioning of Eudamed was recommended by the EU Regulation 2017/745 [8].

Moreover, a common and shared nomenclature is needed to support patient safety, define and name innovative technologies, classify the devices for regulatory approval [9].

The aim of this study is to describe the results of the comparison and harmonisation of two different MD nomenclatures for hip prostheses: a first example of a standardised and international nomenclature to be proposed as integration within the EMDN. Moreover, starting from this result, a generalised approach is proposed.

This work was performed within the framework of the cooperation recently set up between RIAP and NJR, in order to organise a single international database of the orthopaedic prostheses implanted in both countries. Thanks to this cooperation, the NJR-EPRD nomenclature was available for this study.

II. MATERIAL AND METHOD

A. Tools and sources of data

The following tools and databases were used:
1. CND
2. NJR-EPRD nomenclature
3. RIAP MD Dictionary
4. RIAP Database
5. MD National Database of the Italian MoH

1. CND
CND is structured as a hierarchical classification. It is organized in 22 anatomical/functional categories, each one identified by a letter and organised in groups and sub-groups structured in several levels (up to 7). Implantable prosthetic devices are described in Category P and subdivided in groups and sub-groups according to specific technical characteristics (anatomic component, type, fixation method, material) [10].

2. NJR-EPRD nomenclature
NJR-EPRD nomenclature has a flat/non-hierarchical structure. It provides each component of the joint with groups of specific technical characteristics (type, material, fixation method, design, size), each one including several attributes. Therefore, a device can be described by a set of attributes taken from different groups. This architecture is dynamic, comprehensive and flexible. It supports validation through incorporation of business rules, easy upload of data by manufacturers and, finally, ease and speed of computational analysis of the underlying database.

3. RIAP MD Dictionary
The RIAP MD Dictionary is a database of the implanted MD built by RIAP in close cooperation with manufacturers. Currently, it includes more than 66.000 implants (hip, knee and shoulder) described by catalogue code (Ref. code), manufacturer, MD description, CND code [11].

4. RIAP Database
The RIAP Database includes about 430.000 surgical procedures recorded since 2006 for hip, knee and shoulder. The collected data describe procedure and implanted devices, including joint, type of procedure, diagnosis for primary intervention and revision, fixation method, manufacturer and catalogue code. About 1.67 million of implanted devices are recorded [11].

5. MD National Database of the Italian MoH
The MD National Database of the Italian MoH is a database of all the devices marketed in Italy. It is available on an online platform. MD information on manufacturer, CND code and device description is public available, while devices' technical datasheets can be consulted only through private access [12].

B. Method
Comparison between CND and NJR-EPRD nomenclatures was performed considering NJR-EPRD nomenclature as the "reference nomenclature" and CND as the "compared nomenclature", with the aim of updating CND and, consequently, EMDN. The comparison was made for hip prostheses.

Given the differences between CND and NJR classification systems, the translation of the English terminology was made before comparing them. Cultural adaptation of the devices' features was accomplished by studying the devices' descriptions available in the RIAP Dictionary, the technical datasheets available in the MD National Database and, finally, the commercial catalogues and scientific publications.

Each final level of CND was compared with all the attributes considered by the NJR-EPRD nomenclature, looking for a possible correspondence of each CND final level with one or more attributes of the NJR-EPRD nomenclature with the aim to build an association table.

Since the NJR-EPRD nomenclature considers more attributes than the CND final levels, in some cases a unique association of the two nomenclatures could not be established. In these cases, the following further analyses were performed for each "non-associated" attribute:

a. for each type of device, the "non-associated" attribute was searched in the MD description field of the RIAP MD Dictionary and a list of devices of interest was built (including their Ref. code and CND code);

b. using the Ref. code, frequency of implantation of the listed devices was measured in the RIAP Database;

c. the most frequently implanted devices having "non-associated" attributes were more deeply investigated both for the design and characteristics, by studying the technical datasheets available from the MD National Database of the Italian MoH and the commercial catalogues available online, and for their performance, by analysing scientific publications and Registries reports.

New sub-groups relevant to "non-associated" attributes were included in CND and EMDN nomenclatures for devices having: high frequency of implantation; high recurrence in the RIAP MD Dictionary; innovative design; technical characteristics potentially influencing their performance.

One or more "non-associated" attributes were considered to define each new sub-group according to the essential principles of the CND and EMDN classification system. When needed, additional levels were considered.

Finally, a generalised approach was developed from the steps followed to define the hip prostheses sub-groups integrated in EMDN.

III. RESULTS

A. New sub-groups included in EMDN
Table I reports the new sub-groups selected for inclusion in EMDN with the corresponding combination of attributes identified in the NJR-EPRD nomenclature. They consider the following devices: polyethylene acetabular inserts, fixed-neck femoral stems for primary surgery, modular neck femoral stems for primary surgery, femoral stems for revision surgery, biarticular cups.

For polyethylene acetabular inserts, standard, eccentric, lipped and constrained attributes were selected because they were highly recurrent in the description of the devices collected in the RIAP Dictionary.

For the femoral stems, the cultural adaptation resulted in the change of the terms "non-modular" and "modular", previously used by CND, in "fixed-neck" and "modular neck".

For the "straight" "modular neck femoral stems – primary surgery", the attributes i) one-piece, ii) proximal component (two-pieces) and iii) distal component (two-pieces) were selected, due to both their high recurrence in the RIAP MD Dictionary and their potential influence on device performance.

For the biarticular cups, the "preassembled" and "modular" attributes were selected to find the association between CND and NJR-EPRD nomenclature s.

TABLE I
HIP PROSTHESIS: NEW SUB-GROUPS INTRODUCED IN EMDN

EMDN sub-group			NJR-EPRD
level$_i$	level$_{i+1}$	level$_{i+2}$	COMPONENT: attributes
polyethylene acetabular inserts	standard		ACETABULAR INSERT: standard, polyethylene
	eccentric		ACETABULAR INSERT: Angulated, polyethylene
	lipped		ACETABULAR INSERT: lipped, polyethylene
	constrained		ACETABULAR INSERT: constrained, polyethylene
fixed-neck femoral stems - primary surgery	straight		FEMORAL COMPONENT: modular head stem, straight
	anatomical		FEMORAL COMPONENT: modular head stem, anatomical
	conservative		FEMORAL COMPONENT: metaphyseal prosthesis
modular neck femoral stems -primary surgery	straight	one-piece	FEMORAL COMPONENT: femoral stem with modular neck, straight
		two-pieces proximal	FEMORAL COMPONENT: femoral stem proximal section, straight
		two-pieces distal	FEMORAL ACCESSORY: stem central section, straight
	anatomical		FEMORAL COMPONENT: femoral stem with modular neck, anatomical
	conservative		FEMORAL COMPONENT: metaphyseal prosthesis with modular neck
femoral stems - revision surgery	fixed-neck		FEMORAL COMPONENT: modular head stem, revision specific
	modular		FEMORAL COMPONENT: femoral stem with modular neck and femoral stem proximal section, revision specific
biarticular cups	preassembled		MODULAR HEAD: bipolar monobloc
	modular		MODULAR HEAD: bipolar modular head and bipolar modular insert

B. The generalised approach

Aim of the generalised approach is to compare two different nomenclatures of medical devices and update or check the "compared nomenclature", using the other one as "reference nomenclature". It is structured in 3 steps (Table II).

The first step consists in the analysis of both nomenclatures and in the study of their classifications systems to highlight their differences.

If the two nomenclatures are written in different languages, the translation and cultural adaptation of the terms (steps 2 and 2a) are needed. To do this, implant information could be essential.

The step 3 consists in the comparison of each class of the two nomenclatures. Aim of this step is to find for every class of the reference nomenclature a correspondent class of the compared nomenclature. Studies of both devices' biomechanical features and material properties could provide useful information to find a correct association.

If the comparison of the two nomenclatures results in a unique association between classes, the process ends with step 3, being both nomenclatures harmonised.

If a unique association between the classes cannot be established, the introduction of new classes or new classification branches is made following step 3a and 3b.

In step 3a, the core set of features characterising the new classes or the new classification branches is defined. This selection mainly analyses features of devices having high frequency of implantation, innovative design, and technical characteristics potentially influencing the performance. This information can be collected by consulting Registries databases, MD datasheets, scientific publications and Registries reports.

In the last step (step 3b), the classes and sub-classes defined in the previous step are included in the comparative nomenclature according to the structure of its classification system.

TABLE II
GENERALISED APPROACH

step	description
1	Collection of nomenclatures and analysis of their classification systems
2	Translation of terms (if needed, go to step 2a, otherwise skip to step 3)
2a	Cultural adaptation of devices' features
3	Comparison between each class of the reference nomenclature (1) and each class of the compared nomenclature (2) and association of the classes. If the comparison does not result in a unique association, go to step 3a.
3a	Selection of a core set of features relevant to the non-associated classes to define new classes and sub-classes
3b	Inclusion of the new classes and sub-classes in the nomenclature (2) to ensure consistency between the two nomenclatures

IV. DISCUSSION

The comparison of CND and NJR-EPRD nomenclature s showed that they are harmonised in the individuation of the technical characteristics of the hip joint prostheses [13]. Every CND sub-group finds its equivalent class in NJR-EPRD nomenclature when type, fixation methods and material are considered. Since the NJR-EPRD nomenclature considers more attributes than the CND final levels, a unique association between all the elements of the two nomenclatures cannot be established.

Information collected by consulting MD Databases, RIAP Database and scientific literature was essential both to compare the CND final level with the NJR-EPRD nomenclature attributes and to define the evidence of the need to classify devices having some particular attributes otherwise included in a more general class. To integrate the new proposed sub-groups it was essential to include additional levels in CND and EMDN. This integration was made respecting the basic principle of CND and EMDN i.e. to consider in the nomenclature only final levels that are described by an essential core set of features.

Exchange of information about MD among different registries and databases is a recognised need [9], [14]. Therefore, several studies compared the structure of the classification systems or the characteristics of different MD nomenclatures adopted either in Europe or in the rest of the world [15]-[18].

This study implemented a comparison of two nomenclatures with the aim of defining a harmonised nomenclature. For hip prostheses, this process allowed to include in the EMDN some new sub-groups that allow a more detailed description of devices otherwise misclassified or assigned to a more general group. It has to be highlighted that the criteria defined for the selection of the subgroups were based on the results provided by the MD registries (for example frequency of use and outcomes of specific devices). Moreover, starting from the specific case of hip prostheses, a generalised approach was presented. This approach can be applied to two different nomenclatures in order to develop a unified harmonised one.

The limit of this study is that the generalised approach was developed by extrapolating only the results obtained for hip prostheses and by comparing only two nomenclatures.

V. CONCLUSION

Data from Registries are essential for patient safety and for health systems management. More profound analysis is possible when data from different Registries are combined.

A Medical Devices Nomenclature is a pillar of a Registry. Therefore, harmonising different MD nomenclatures is a first step towards a common language for recording and reporting comparable medical devices outcomes from Registries of different countries.

The proposed approach allowed to compare two different nomenclatures and to harmonise them as far as possible.

Given that the results of the comparison performed in this study turned out as a first propose of updating the EMDN, it may be possible to obtain a unique and harmonized nomenclature in Europe, by applying this approach to other nomenclatures. To reach this goal, further studies need to be performed to validate the approach against other devices, other nomenclatures and other classification systems.

REFERENCES

[1] E. Stella "The Italian system of medical devices and the database of the ministry of health (BD/RDM)" International Strategic Workshop "Tools to identify and characterize implantable devices: the perspective of the RIAP-NJR collaboration". Rome, 1/3/2018 (www.riap.iss.it)

[2] NORE Network of Orthopaedic Registries of Europe (https://www.efort.org/about-us/nore/)

[3] http://www.njrcentre.org.uk/njrcentre/default.aspx

[4] https://reports.njrcentre.org.uk/Tracking-implant-performance

[5] www.iss.it/riap

[6] Italy. Decreto del Ministero della salute 20 febbraio 2007. Approvazione della Classificazione Nazionale dei Dispositivi Medici (CND). Gazzetta Ufficiale – Serie Generale N. 63, 16 marzo 2007.

[7] EU Commission official press release. Medical Devices Nomenclature. Available:https://ec.europa.eu/docsroom/documents/34264/attachments /1/translations/en/renditions/native

[8] Regulation (EU) 2017/745 of the European Parliament and of the Council of 5 April 2017 on medical devices, amending Directive 2001/83/EC, Regulation (EC) No 178/2002 and Regulation (EC) No 1223/2009 and repealing Council Directives 90/385/EEC and 93/42/EEC (Text with EEA relevance) Available: https://eur-lex.europa.eu/legal-content/EN/TXT/PDF/?uri=CELEX:32017R0745

[9] World Health Organization. Standardization of medical devices nomenclature: International classification, coding and nomenclature of medical devices. Executive board 145th session 30April 2019 Available: https://apps.who.int/gb/ebwha/pdf_files/EB145/B145_3-en.pdf

[10] Italian Classification of Medical Devices Available: http://www.salute.gov.it/imgs/C_17_pagineAree_328_listaFile_itemName_15_file.pdf

[11] M. Torre, I. Luzi, E. Carrani, L. Leone, E. Romanini, G. Zanoli (Eds). Italian Arthroplasty Registry Project. Concept, development, start-up. First Report. Rome, Il Pensiero Scientifico Editore, 2014. Available: http://riap.iss.it/riap/en/activities/reports/2014/11/17/firts-report-2014-executive-summary/

[12] Ministry of Health. Medical Devices Data Bank, User Manual Medical Device Manufacturer profile. Available: http://www.salute.gov.it/imgs/C_17_pagineAree_395_listaFile_itemName_7_file.pdf

[13] M. Torre, M. Franzò, E. Carrani, L. Sampaolo, F. Marinozzi et al. "A new collaboration on the horizon: the National Joint Registry (NJR) and the Italian Arthroplasty Registry (RIAP) towards an agreement upon a common component database and device classification systems harmonization" 8th International Congress of Arthroplasty Registries Leiden, The Netherlands, June 1-3, 2019

[14] G. A. W. Denissen, L. N. van Steenbergen, W. T. Lollinga, N. J. J. Verdonschot, B. W. Schreurs, R. G. H. H. Nelissen "Generic implant classification enables comparison across implant designs: the Dutch Arthroplasty Register implant library" EFORT Open Rev, Vol. 4, pp 345-350, 2019

[15] C. Niederländer, P. Wahlster, C. Kriza, P. Kolominsky-Rabas "Registries of implantable medical devices in Europe", Elsevier Journals Health Policy, 2013

[16] T. G. Maak, J. D. Wylie "Medical Device Regulation: A Comparison of the United States and the European Union (Review Article)" The Journal of the American Academy of Orthopaedic Surgeons, vol. 24, No. 8,2016

[17] C. Henschke, D. Panteli, M. Perleth, R. Busse, "Taxonomy of medical devices in the logic of health technology assessment", International Journal of Technology Assessment in Health Care, vol. 31, Issue 5, pp. 324-330, 2015

[18] C. S. Niederländer, C. Kriza, P. Kolominsky-Rabas, "Quality criteria for medical device registries: best practice approaches for improving patient safety – a systematic review of international experiences, Expert Review of Medical Devices", vol. 14, pp. 49-64, 2017

Deep learning for improving in room imaging in radiotherapy: CBCT to synthetic CT conversion

P. Zaffino[1,*], R. Raso[2], M.C. Angiocchi[2], M. Merola[1], S. Canino[2], M. Nonnis[2], A. Bavasso[3], C. Mezzotero[3], R.A. Anoja[2], E. Mazzei[3], and M.F. Spadea[1]

[1] *Magna Graecia University, Department of Experimental and Clinical Medicine, Catanzaro, Italy.*
[2] *Azienda Ospedaliera Pugliese-Ciaccio, SOC Fisica Sanitaria, Catanzaro, Italy.*
[3] *Azienda Ospedaliera Pugliese-Ciaccio, UOC Radioterapia Oncologica e Radiobiologia, Catanzaro, Italy.*
* *Corresponding author, p.zaffino@unicz.it*

Abstract—The aim of this work was to test a deep learning based approach to convert Cone Beam Computed Tomography (CBCT) into Computed Tomography (CT) images for adaptive radiotherapy purposes. The algorithm was tested and validated on a cohort of 40 prostate cancer patients. A 2D U-net style network made of 5 levels was trained to remap CBCT intensities. Going deeper into the encoding part, feature image size was reduced and the number of filters was increased. The opposite happened for the decoding path. For each level, direct connections between encoding and decoding sides were present. The network was trained 3 times on 2D image pairs (CBCT as input and CT as ground truth) sliced in the axial, sagittal and coronal plane respectively. The final CT value for each voxel was obtained by running an intensity voting procedure on three candidate outputs. Conversion accuracy was quantified in terms of Mean Absolute Error (MAE) and Mean Error (ME) between sCT and CT. An average value of 31.3 ± 1.6 and -1.9 ± 4.0 Hounsfield units was obtained respectively for MAE and ME. sCT generation took 3.5 minutes on average. Future effort will be to assess accuracy from a dosimetric and tissue segmentation point of view.

Keywords—Synthetic CT, Adaptive radiotherapy, Image guided radiotherapy, CBCT.

I. INTRODUCTION

Radiotherapy is a widespread strategy for treating cancer. Accurate tumor targeting and organs at risk sparing play a key role for the success of the therapy. High precision treatments are guided by imaging, not only in the planning stage, but also during dose delivery. The standard workflow for Image Guided RadioTherapy (IGRT) requires: 1) the acquisition of a planning Computed Tomography (pCT) scan, for tumor and Organs At Risk (OARs) segmentation, beam geometry design and dose computation; in this regard, several automatic solutions have been proposed for automatic segmentation of tumors and OARs [1], [2], [3], [4], [5], [6], [7], [8], [9], [10], [11], [12] and image quality improvement [13], [14]; 2) the acquisition of planar or volumetric images at the time of treatment (*in room* imaging). The latter modality poses a question about balancing high image quality in 3D (for tissue identification and dose calculation) and fast acquisition and reconstruction (for compatibility with clinical procedures)[15], [16]. Several options have been proposed and adopted in IGRT [17], [18], [19]. Among these, Cone Beam CT (CBCT) is an increasing used modality, especially in the pelvic district [20],

[21], since it offers 3D reconstructions of the organs, and, in principle, it can be used for dose computation and plan adaptation in real time. However, due to the low signal to noise ratio and low contrast, CBCT is not actually used for calculating the dose at the time of therapy. So, in case of large anatomical discrepancy, the patient has to be scanned with a new CT. This event entails additional ionizing dose to the patient and delays the clinical workflow. In order to overcome this issue, a possible solution is to convert the CBCT into a synthetic CT (sCT). The generation of sCT from other images modality is currently a hot topic in radiotherapy, since it can offer several advantages. In the planning stage, sCT can be obtained from Magnetic Resonance Imaging (MRI) acquisition [22], [23], [24], [25], [26], [27], [28], [29], where MRI offer better soft tissue contrast for tumor and OARs segmentation. However, CBCT is much more spread over the clinic and the possibility to convert CBCT to sCT has a higher impact at the moment. Many approaches proposed in literature are based on bulk assignment [30], [31], and deformable registration [32], [33], [34]. Unfortunately the first strategy provides limited conversion accuracy, the latter is time consuming and prone to registration errors. In this work, we investigated the feasibility of a Deep Learning (DL) algorithm for converting CBCT into sCT. The procedure was tested in the framework of prostate radiotherapy, where CBCT represents the current state of the art in IGRT.

II. MATERIALS AND METHODS

A. Dataset

A cohort of 40 patients diagnosed with prostate cancer and eligible for radiotherapy were enrolled in this retrospective study. For each patient, the pCT and the first CBCT of the treatment were used. All the patients were scanned and treated at "Azienda Ospedaliera Pugliese-Ciaccio", Catanzaro, Italy. pCT volume consisted of a stack of 166 slices on average (min-max 127-223), with a thickness of 3 mm in the superior-inferior direction; each slice had an acquisition matrix of $512 * 512$ pixels and the 3D spatial resolution was 1.1*1.1*3 mm . CBCT had size of 410*410 pixels in the cross-sectional image and a number of slices equal to 88, for a final voxel dimension of $1.0 * 1.0 * 3.0$ mm.
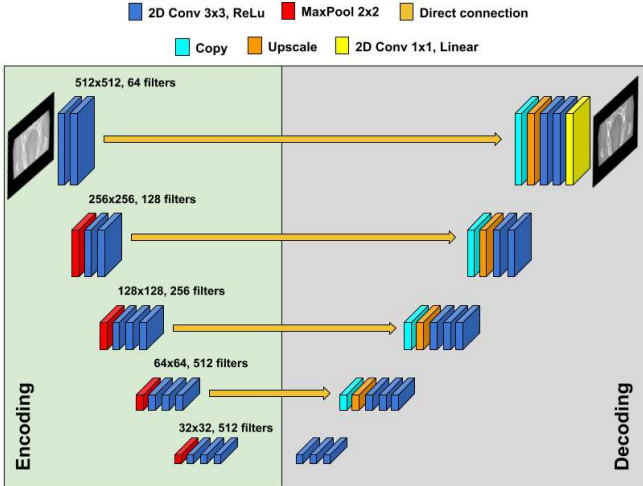
Fig. 1: Architecture of the 2D network used for CBCT to sCT conversion.

B. Preprocessing

Before feeding the data into the network, some preprocessing steps were required. First of all, each volume was masked to remove the couch. Then, all pCTs, usually with a larger field of view than CBCT in the superior inferior direction, were cropped, thus removing the part of the patient that was not acquired in room. Due to the large difference in patient positioning and internal organ filling (in particular bladder, rectum, and intestine), each CBCT was registered on its matching pCT. Accurate anatomical matching between pair of images is fundamental to let the network learn the exact intensity remapping. The registration workflow consisted of a rigid alignment executed by Elastix [35], followed by 2 B-spline deformable registration stages ran by Plastimatch [36]. Mutual information was used as registration metric and regularization term was introduced to discard solutions that did not preserve anatomy.

C. Deep learning netowrk and training

The DL algorithm used in this work was the same proposed by our group [24] for MRI to sCT conversion. An encoder-decoder 2D network was used to convert CBCT slice to sCT slice. Network architecture is depicted in Fig. 1. pCT was used as ground truth for training and Mean Absolute Error (MAE, Eq. 1) was chosen as loss function.

The dataset was randomly split in 50% for testing (20 cases), 42% for training (17 cases) and 8% for validation (3 cases). Data augmentation (translations and mirroring) was used to maximize the amount of training examples. Three networks were trained, providing in input 2D slices extracted in axial, sagittal and coronal view respectively. In this way, a set of optimal weights was identified for each possible view.

D. Testing

For each testing patient, the CBCT was fed into the network in axial, sagittal and coronal view. This led to generate three candidate for sCT, on basis of the different view used to stack the converted 2D slices. According to [24], the final sCT was obtained by running intensity voting across the three volumes. In particular, voxel-wise median value was used. Conversion accuracy was quantified in terms of MAE and Mean Error (ME, Eq. 2).

$$MAE = \frac{\sum_{n}^{1} |pCT - sCT|}{n} \quad (1)$$

$$ME = \frac{\sum_{n}^{1} pCT - sCT}{n} \quad (2)$$

Training and conversion time were also recorded in order to asses the usability of the proposed algorithm in a real clinical workflow.

III. Results

As a result of the testing, a median $\pm$ interquartiles MAE equal to 31.3 ± 1.6 HU (Hounsfield Units) was obtained. The best converted image volume had MAE of 25.2 HU; the worst 38.5 HU. Median $\pm$ interquartiles ME was -1.9 ± 4.0 HU (max-min range $-13.3/4.7$ HU). Fig. 2 shows an exemplary average case, including spatial distribution of conversion error. Higher conversion error was found where anatomic matching between CBCT and pCT was not correctly recovered by image registration. This mainly involved the intestine. Training time was equal to 4 days, converting a single testing case took 3.5 minutes.

IV. Discussions

Daily patient anatomy assessment is an essential step to guarantee the optimal radiotherapy treatment. In this context, CBCT are widely used to check patient positioning and internal organ filling. However, in case patient's replan is required, dose computation and tissue contouring can not be reliable executed on this image modality. In this work, we investigated the possibility to convert CBCT in sCT by using an existing algorithm developed by our group for MRI to sCT conversion. When this algorithm was first introduced, its validation was executed on brain MRI, that was not affected by important anatomical changes over time. In that case, the algorithm proved to be able to generate accurate sCT. The same framework already proved to be able to accurately convert CBCT in head and neck district [37]. The anatomical district chosen for this study, instead, is the pelvic region, where significant anatomical changes happen from day-to-day. All patients enrolled in this study underwent prostate radiotherapy treatment. Due to the high difference in patient positioning and bladder/rectum and intestine filling, rigid and deformable registrations were required. Training time was about 4 days, that is an offline process that does not affect the clinical workflow. Real sCT generation, actually made of three different conversions, was compatible with the normal routine timing (3.5 mins). Conversion accuracy was satisfying, with a minimum/maximum MAE equal to 25.2/38.5 HU (ME $-13.3/4.7$ HU). If we analyze spatial error distribution, higher
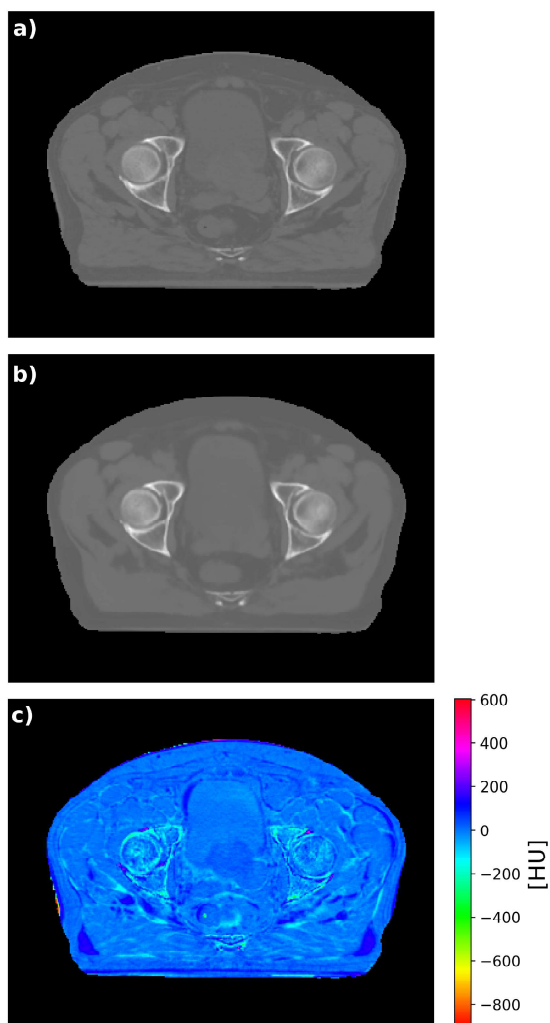
Fig. 2: Exemplary case of CBCT to sCT conversion. In panel a and in panel b the pCT and the sCT are depicted respectively. Panel c shows the error distribution map between pCT and sCT.

error was found where tissues were not perfectly aligned by image registration. This was because the deformable registration was deliberately not pushed, in order to guarantee the anatomical consistency of spatial transformation obtained. In fact, when there are significant anatomical differences to be recovered, the registration process can converge to a numerically valid solution, but without any anatomical meaning. In order to avoid this, penalties for irregular vector field and a limited number optimization steps can help to discard unreasonable geometrical transformations. Since anatomical mismatch affected also the training step, conversion accuracy was highly dependent on the anatomical correspondence of the paired images provided as input. In the light of this, and considering the large anatomical differences from day to day affecting the pelvic district, the obtained results are remarkable. In a real scenario, once the network has been trained on paired and matching images to remap intensities, the daily CBCT will be converted without performing any image registration. As a result, on the contrary of the current clinical strategy that generates a sCT by registering the pCT on the CBCT, our strategy does not introduce any uncertainties due to image registration and does not require the usage of additional images. Dosimetric analysis and tissue contouring executed directly on sCT, will be the next steps to be investigated, in order to further quantify the effectiveness of the proposed methodology. Finally, we want to underline that the main advantage of using CBCT is its widely availability in every clinical radiotherapy facility. In this way, all the sites having a CBCT installed, can take advantage of such algorithm, enabling a more accurate plan adaption.

V. CONCLUSION

In this preliminary work, we investigated the possibility to convert CBCT into sCT for a better radiotherapy plan adaptation. An already developed algorithm for MRI to sCT conversion was used. Even if the anatomical district (pelivs) was challenging due to not negligible organ filling difference, the algorithm proved to achieve satisfying conversion accuracy. Future efforts will be to execute dose computation and tissue contouring on the generated images.

REFERENCES

[1] G. A. Whitfield, P. Price, G. J. Price, and C. J. Moore, "Automated delineation of radiotherapy volumes: are we going in the right direction?," *The British journal of radiology*, vol. 86, no. 1021, pp. 20110718–20110718, 2013.

[2] P. Zaffino, G. Pernelle, A. Mastmeyer, A. Mehrtash, H. Zhang, R. Kikinis, T. Kapur, and M. F. Spadea, "Fully automatic catheter segmentation in mri with 3d convolutional neural networks: application to mri-guided gynecologic brachytherapy," *Physics in Medicine & Biology*, vol. 64, no. 16, p. 165008, 2019.

[3] P. Zaffino, D. Ciardo, P. Raudaschl, K. Fritscher, R. Ricotti, D. Alterio, G. Marvaso, C. Fodor, G. Baroni, F. Amato, *et al.*, "Multi atlas based segmentation: should we prefer the best atlas group over the group of best atlases?," *Physics in Medicine & Biology*, vol. 63, no. 12, p. 12NT01, 2018.

[4] K. Fritscher, P. Raudaschl, P. Zaffino, M. F. Spadea, G. C. Sharp, and R. Schubert, "Deep neural networks for fast segmentation of 3d medical images," in *International Conference on Medical Image Computing and Computer-Assisted Intervention*, pp. 158–165, Springer, 2016.

[5] P. Zaffino, D. Ciardo, G. Piperno, L. Travaini, S. Comi, A. Ferrari, D. Alterio, B. Jereczek-Fossa, R. Orecchia, G. Baroni, *et al.*, "Radiotherapy of hodgkin and non-hodgkin lymphoma: A nonrigid image-based registration method for automatic localization of prechemotherapy gross tumor volume," *Technology in cancer research & treatment*, vol. 15, no. 2, pp. 355–364, 2016.

[6] E. Tappeiner, S. Pröll, M. Hönig, P. F. Raudaschl, P. Zaffino, M. F. Spadea, G. C. Sharp, R. Schubert, and K. Fritscher, "Multi-organ segmentation of the head and neck area: an efficient hierarchical neural networks approach," *International journal of computer assisted radiology and surgery*, vol. 14, no. 5, pp. 745–754, 2019.

[7] D. Ciardo, M. A. Gerardi, S. Vigorito, A. Morra, V. Dell'Acqua, F. J. Diaz, F. Cattani, P. Zaffino, R. Ricotti, M. F. Spadea, *et al.*, "Atlas-based segmentation in breast cancer radiotherapy: Evaluation of specific and generic-purpose atlases," *The Breast*, vol. 32, pp. 44–52, 2017.

[8] G. Sharp, K. D. Fritscher, V. Pekar, M. Peroni, N. Shusharina, H. Veeraraghavan, and J. Yang, "Vision 20/20: perspectives on automated image segmentation for radiotherapy," *Medical physics*, vol. 41, no. 5, 2014.

[9] P. F. Raudaschl, P. Zaffino, G. C. Sharp, M. F. Spadea, A. Chen, B. M. Dawant, T. Albrecht, T. Gass, C. Langguth, M. Lüthi, *et al.*, "Evaluation of segmentation methods on head and neck ct: auto-segmentation challenge 2015," *Medical physics*, vol. 44, no. 5, pp. 2020–2036, 2017.

[10] K. D. Fritscher, M. Peroni, P. Zaffino, M. F. Spadea, R. Schubert, and G. Sharp, "Automatic segmentation of head and neck ct images for radiotherapy treatment planning using multiple atlases, statistical appearance models, and geodesic active contours," *Medical physics*, vol. 41, no. 5, p. 051910, 2014.

[11] P. Aljabar, R. A. Heckemann, A. Hammers, J. V. Hajnal, and D. Rueckert, "Multi-atlas based segmentation of brain images: atlas selection and its effect on accuracy," *Neuroimage*, vol. 46, no. 3, pp. 726–738, 2009.

[12] F. Milletari, N. Navab, and S.-A. Ahmadi, "V-net: Fully convolutional neural networks for volumetric medical image segmentation," in *2016 Fourth International Conference on 3D Vision (3DV)*, pp. 565–571, IEEE, 2016.

[13] M. F. Spadea, J. Verburg, G. Baroni, and J. Seco, "Dosimetric assessment of a novel metal artifact reduction method in ct images," *Journal of applied clinical medical physics*, vol. 14, no. 1, pp. 299–304, 2013.

[14] E. Meyer, R. Raupach, M. Lell, B. Schmidt, and M. Kachelrieß, "Normalized metal artifact reduction (nmar) in computed tomography," *Medical physics*, vol. 37, no. 10, pp. 5482–5493, 2010.

[15] M. F. Spadea, A. Fassi, P. Zaffino, M. Riboldi, G. Baroni, N. Depauw, and J. Seco, "Contrast-enhanced proton radiography for patient set-up by using x-ray ct prior knowledge," *International Journal of Radiation Oncology* Biology* Physics*, vol. 90, no. 3, pp. 628–636, 2014.

[16] J. Seco, M. Oumano, N. Depauw, M. F. Dias, R. P. Teixeira, and M. F. Spadea, "Characterizing the modulation transfer function (mtf) of proton/carbon radiography using monte carlo simulations," *Medical physics*, vol. 40, no. 9, p. 091717, 2013.

[17] D. Verellen, M. De Ridder, N. Linthout, K. Tournel, G. Soete, and G. Storme, "Innovations in image-guided radiotherapy," *Nature Reviews Cancer*, vol. 7, no. 12, pp. 949–960, 2007.

[18] L. A. Dawson and M. B. Sharpe, "Image-guided radiotherapy: rationale, benefits, and limitations," *The lancet oncology*, vol. 7, no. 10, pp. 848–858, 2006.

[19] A. Choudhury, G. Budgell, R. MacKay, S. Falk, C. Faivre-Finn, M. Dubec, M. van Herk, and A. McWilliam, "The future of image-guided radiotherapy," *Clinical Oncology*, vol. 29, no. 10, pp. 662–666, 2017.

[20] H. Guan and H. Dong, "Dose calculation accuracy using cone-beam ct (cbct) for pelvic adaptive radiotherapy," *Physics in Medicine & Biology*, vol. 54, no. 20, p. 6239, 2009.

[21] O. Morin, A. Gillis, J. Chen, M. Aubin, M. K. Bucci, M. Roach III, and J. Pouliot, "Megavoltage cone-beam ct: system description and clinical applications," *Medical Dosimetry*, vol. 31, no. 1, pp. 51–61, 2006.

[22] D. Winkel, G. H. Bol, P. S. Kroon, B. van Asselen, S. S. Hackett, A. M. Werensteijn-Honingh, M. P. Intven, W. S. Eppinga, R. H. Tijssen, L. G. Kerkmeijer, *et al.*, "Adaptive radiotherapy: the elekta unity mr-linac concept," *Clinical and translational radiation oncology*, vol. 18, pp. 54–59, 2019.

[23] G. Pileggi, C. Speier, G. C. Sharp, D. Izquierdo Garcia, C. Catana, J. Pursley, F. Amato, J. Seco, and M. F. Spadea, "Proton range shift analysis on brain pseudo-ct generated from t1 and t2 mr," *Acta Oncologica*, vol. 57, no. 11, pp. 1521–1531, 2018.

[24] M. F. Spadea, G. Pileggi, P. Zaffino, P. Salome, C. Catana, D. Izquierdo-Garcia, F. Amato, and J. Seco, "Deep convolution neural network (dcnn) multiplane approach to synthetic ct generation from mr images—application in brain proton therapy," *International Journal of Radiation Oncology* Biology* Physics*, vol. 105, no. 3, pp. 495–503, 2019.

[25] X. Han, "Mr-based synthetic ct generation using a deep convolutional neural network method," *Medical physics*, vol. 44, no. 4, pp. 1408–1419, 2017.

[26] M. Maspero, M. H. Savenije, A. M. Dinkla, P. R. Seevinck, M. P. Intven, I. M. Jurgenliemk-Schulz, L. G. Kerkmeijer, and C. A. van den Berg, "Dose evaluation of fast synthetic-ct generation using a generative adversarial network for general pelvis mr-only radiotherapy," *Physics in Medicine & Biology*, vol. 63, no. 18, p. 185001, 2018.

[27] E. Johnstone, J. J. Wyatt, A. M. Henry, S. C. Short, D. Sebag-Montefiore, L. Murray, C. G. Kelly, H. M. McCallum, and R. Speight, "Systematic review of synthetic computed tomography generation methodologies for use in magnetic resonance imaging–only radiation therapy," *International Journal of Radiation Oncology* Biology* Physics*, vol. 100, no. 1, pp. 199–217, 2018.

[28] X. Liang, L. Chen, D. Nguyen, Z. Zhou, X. Gu, M. Yang, J. Wang, and S. Jiang, "Generating synthesized computed tomography (ct) from cone-beam computed tomography (cbct) using cyclegan for adaptive radiation

therapy," *Physics in Medicine & Biology*, vol. 64, no. 12, p. 125002, 2019.

[29] Y. Li, J. Zhu, Z. Liu, J. Teng, Q. Xie, L. Zhang, X. Liu, J. Shi, and L. Chen, "A preliminary study of using a deep convolution neural network to generate synthesized ct images based on cbct for adaptive radiotherapy of nasopharyngeal carcinoma," *Physics in Medicine & Biology*, vol. 64, no. 14, p. 145010, 2019.

[30] B. Whelan, S. Kumar, J. Dowling, J. Begg, J. Lambert, K. Lim, S. K. Vinod, P. B. Greer, and L. Holloway, "Utilising pseudo-ct data for dose calculation and plan optimization in adaptive radiotherapy," *Australasian physical & engineering sciences in medicine*, vol. 38, no. 4, pp. 561–568, 2015.

[31] N. Tyagi, S. Fontenla, J. Zhang, M. Cloutier, M. Kadbi, J. Mechalakos, M. Zelefsky, J. Deasy, and M. Hunt, "Dosimetric and workflow evaluation of first commercial synthetic ct software for clinical use in pelvis," *Physics in Medicine & Biology*, vol. 62, no. 8, p. 2961, 2017.

[32] D. Paquin, D. Levy, and L. Xing, "Multiscale registration of planning ct and daily cone beam ct images for adaptive radiation therapy," *Medical physics*, vol. 36, no. 1, pp. 4–11, 2009.

[33] Y. Lou, T. Niu, X. Jia, P. A. Vela, L. Zhu, and A. R. Tannenbaum, "Joint ct/cbct deformable registration and cbct enhancement for cancer radiotherapy," *Medical image analysis*, vol. 17, no. 3, pp. 387–400, 2013.

[34] M. Peroni, D. Ciardo, M. F. Spadea, M. Riboldi, S. Comi, D. Alterio, G. Baroni, and R. Orecchia, "Automatic segmentation and online virtualct in head-and-neck adaptive radiation therapy," *International Journal of Radiation Oncology* Biology* Physics*, vol. 84, no. 3, pp. e427–e433, 2012.

[35] S. Klein, M. Staring, K. Murphy, M. A. Viergever, and J. P. Pluim, "Elastix: a toolbox for intensity-based medical image registration," *IEEE transactions on medical imaging*, vol. 29, no. 1, pp. 196–205, 2009.

[36] P. Zaffino, P. Raudaschl, K. Fritscher, G. C. Sharp, and M. F. Spadea, "Plastimatch mabs, an open source tool for automatic image segmentation," *Medical physics*, vol. 43, no. 9, pp. 5155–5160, 2016.

[37] A. Thummerer, P. Zaffino, A. Meijers, G. G. Marmitt, J. Seco, R. J. Steenbakkers, J. A. Langendijk, S. Both, M. F. Spadea, and A.-C. Knopf, "Comparison of cbct based synthetic ct methods suitable for proton dose calculations in adaptive proton therapy," *Physics in Medicine & Biology*, 2020.

Five years of Lean Six Sigma in the healthcare: an overview of main tools and results

G. Improta[1], A.M. Ponsiglione[2], A. Scala[1], D. Di Laura[3], L.S. D'Angiolella[3] and G. Cesarelli[4,5]

[1] Department of Public Health, School of Medicine and Surgery, University of Naples "Federico II"
[2] Department of Electrical Engineering and Information Technology (DIETI), University of Naples "Federico II"
[3] Research Centre on Public Health (CESP), University of Milano "Bicocca"
[4] Department of Chemical, Materials and Production Engineering (DiCMaPI), University of Naples "Federico II"
[5] Istituto Italiano di Tecnologia - Center for Advanced Biomaterials for Healthcare (CABHC), Naples, italy

Abstract— **Lean thinking in healthcare focuses on simplifying processes by acknowledging value-added activities from the patient's perspective and applying it to services that can reduce waste. The concept of Six Sigma theory offers an approach to problem solving and involves a strong organizational framework consisting of a redesigning a product, which then results in the elimination of defects. Over the last decade, a strong synergy between Lean and Six Sigma has developed, creating Lean Six Sigma. Several researchers investigated best practices to implement Lean Six Sigma in healthcare. The following presents summaries of the literature. Nineteen studies published in the last five years have been included.**

Keywords—**Lean Six Sigma, DMAIC, Healthcare.**

I. INTRODUCTION

SINCE the 1970s, also in the healthcare, the competition has increased on factors such as zero defects, process time reduction, price and relevant customisation. This scenario is the opposite of the so-called "Mass production", in which there is a huge demand for services and products and services are provided with low-cost resources and with poor personalisation and quality [1], [2]. Nowadays, this is true especially in the healthcare sector, where waste of resources and bad management of patients are the main causes of inefficiency. In order to optimize the health expenditure wastes and improve care processes, Lean and Six Sigma methodologies have been recently applied to public and private hospitals. On one hand, Lean thinking is focused on the extreme simplification of the patient mainstream with the intention of avoiding any kind of waste (it aims at "*doing things quickly*"), while on the other hand the Six Sigma uses powerful tools to understand and reduce process variation (it aims at "*doing things right*", i.e. defect free) [3]. Despite the literature about Lean and Six Sigma in the healthcare is relatively recent, studies show that significant accomplishments can be achieved using the tools offered by either Lean or Six Sigma or even the combination of the two, i.e. Lean Six Sigma (LSS) [3], [4], [5]. The latter, has been proved to be an effective approach in the healthcare

II. METHODOLOGY

Successful LSS applications in the healthcare published in the last five years have been collected using both PubMed database and Semantic Scholar database for searching. Results were filtered by publication year "from 01/01/2015 to 31/12/2019", publication type "journal article" and word included in the title "Lean Six Sigma". In the following, we report about main tools and results of three representative studies per year from 2015 to 2017 and five representative studies per year from 2018 to 2019.

III. RESULTS

A. Literature overview

Damato et al. [6] assessed the effectiveness of using LSS to improve blood collection processes at an Emergency Care Center (ECC). Through observations and interviews, they identified the non-value-added activities and selected the seven factors affecting negatively the examined process. LSS helped to pinpoint hemolysis as a key inefficiency in blood collection process. Improvement actions chosen after the process analysis and the interviews lead to a decrease in the hemolysis by 91%.

In their work, Improta et al. [7] used the "*Define, Measure, Analyze, Improve, and Control*" (DMAIC) cycle, at the Complex Operative Unit (UOC) of Orthopedics and Traumatology of the University Hospital 'Federico II', to reduce the inappropriate prolongation of the length of stay (LOS) for patients undergoing hip replacement surgery. The average LOS was reduced from 18.9 to 10.6 days (−44%). The same experience was subsequently repeated and adapted to the knee replacement surgery [8]. In this second case the LOS was reduced from 14.2 to 8.3 days (−42%).

Sanders et al. [9] applied Lean and Six Sigma tools in the reduction of turnaround time (TAT) for Emergency Departments (ED). The project results included: a 50 percent decrease in vials used for testing, a 50% decrease in unused or extra specimens, a 90% decrease in ED specimens without orders, a 30% decrease in complete blood count analysis (CBCA) Median TAT, a 50% decrease in CBCA TAT Variation, a 10% decrease in Troponin TAT Variation, an 18.2% decrease in URPN TAT Variation, and a 2-5 min decrease in ED registered nurses' rainbow draw time. This case study demonstrated how the quantitative power of Six Sigma and the speed of Lean worked in harmony to improve the blood draw process for a 1,000 bed tertiary care hospital.

Basta et al. [10] applied LSS to dispatch 90% of medical reports on the day of the patient's visit by improving the logistic process. This study was conducted at Gastro Intestinal Oncology Center Amsterdam (GIOCA), following the DMAIC. Data on 195 medical reports were collected and evaluated between December 2012 and February 2013. The quality and frequency of communication between hospital and

primary care can influence health care quality. Therefore, the study aimed to investigate whether the proportion of reports dispatched from GIOCA within 1 day could be increased to 90%, using the LSS. However, a regular evaluation of the process needs to be performed in order to maintain the goal of >90% of the reports dispatched on the same day as the patient's visit.

Agarwal et al. [11] adopted LSS to improve the operational efficiency of elective and urgent cardiac catheterization procedures. The study included diagnostic coronary angiography, percutaneous coronary interventions, structural interventions and peripheral interventions performed between June 2009 and December 2012. A considerable improvement was observed in the turn-time (from 43.6% to 56.6%, p<0.001) and in the percentage of manual sheath-pulls performed in the catheterization laboratory (from 60.7% to 22.7%, p <0.001).

Bhat et al. [12] applied LSS to reduce the Turn-Around-Time (TAT) of medical records preparation process and thus to improve the productivity and performance of the department. The root causes for the problem were identified and validated through data-based analysis from LSS tool box, at different stages in the project. As a result of this project, the TAT was reduced from average 19 minutes to 8 minutes and the standard deviation was reduced by one-tenth, which was a remarkable achievement for department under study. This was resulted in the reduction in the work-in-process inventory of medical records from 40 units to 0 at the end of the day. The cost benefit analysis by the finance department revealed that the hospital was able to save US $20,000 annually in terms of human resources and related overhead costs.

Montella et al. [13] applied LSS to reduce the number of patients affected by sentinel bacterial infections who are at risk of healthcare–associated infections (HAI). The LSS methodology was applied in the general surgery department by using a multidisciplinary team of both physicians and academics. The methodology allowed the identification of variables that influenced the risk of HAIs and the implementation of corrective actions to improve the care process, thereby reducing the percentage of infected patients. The application of the corrective actions led to a reduction of the percentage of colonized patients from 0.37% to 0.21%.

Tagge et al. [14] applied LSS to improve efficiency of an academic children's hospital using the DMAIC. Six hundred twelve cases were included in the seven Children's Hospital operating rooms (OR) over a 6-month period. Turnover Time (interval between patient OR departure and arrival of the subsequent patient) decreased from a median of 41 min in the baseline period to 32 min in the intervention period. Turnaround Time (interval between surgical dressing application and subsequent surgical incision) decreased from a median 81.5 min in the baseline period to 71 min in the intervention period.

Inal et al. [15] used LSS to simplify the laboratory work process and decrease the turnaround time by eliminating non-value- adding steps. Delay times in the reception area were measured on different days of the week and the average delay time was calculated. The pre-analytical process in the reception area was improved by eliminating 3 h and 22.5 min of non-value- adding work. Turnaround time also improved for stat samples from 68 to 59 min after applying Lean. Steps prone to medical errors and posing potential biological hazards to receptionists were reduced from 30% to 3%. This Lean analysis also improved TATs for urgent samples, which were subject to the same problems described above. By the end of the study, the average TAT had improved by 9 min (99% CI: 8-11 min), and this achievement was maintained in the following months.

Mancosu et al. [16] considered, in their study, the 2D-2D whole-breast radiotherapy repositioning process. The aim was to apply LSS methodologies to redesign the process in order to avoid errors in the set-up procedure. The team applied the DMAIC and the process was retrospectively measured over 30 months (July 2014-December 2016). Poka-yoke and visual management were considered for advancing the process. The new procedure was checked over 6 months (January-June 2017). Results gained were: AZS (almost zero shift) reduction, an improvement in distribution and outlier reduction verified by Kurtosis diminution. Lastly, using LSS in a radiotherapy department made possible the redesign of the breast repositioning matching procedure.

Steere et al. [17] used LSS methodology to improve occlusion management at Hartford Hospital. Among most frequent complications related to central venous access devices (CVADs) is catheter occlusion. Infusion treatment with catheters in facility represents more than 90% of acute care hospital patients and CVADs are in use in approximately 50% of intensive care patients. For this reason, CVADs occlusion evaluation in terms of catheter function, flushing and reflux was very useful. Application of Six Sigma DMAIC and 5ps principles led to a significant and durable improvement for Hertford Hospital. Staff communication, goal setting established a staff culture that is continually striving for better outcomes. DMAIC stages allowed identification of areas of deficiency for CVAD occlusion management, flushing and supply use. Among interventions there are the replacement of negative displacement needleless connectors with antireflux needleless connectors and speciality team assessment before tissue plasminogen activator use. In a 26 months study, the hospital recorded an overall reduction of 69% in tissue plasminogen activator use. Furthermore, it was achieved a considerable cost-cutting, reduction of treatment delays and of medical complications and elimination of unnecessary medications and procedures.

Schmidt et al. [18] demonstrated how LSS methodology, usually not applied in research administration, can be used to evaluate process in translational science in academic health center. Using DMAIC, pilot project program review process was completely remodelled leading to a two months' reduction of the final assignment decision to project financing. This achievement led to an increasing satisfaction of applicants thanks to quality and utility of reviewers' actions. These results also highlighted the importance of improving the experience of both applicants and reviewers. For this reason, there will always be a second round of surveys in order to achieve continuous improvements of the aforesaid process.

Improta et al. [19] applied LSS to reduce the risk of healthcare-associated infections (HAI) in areas of clinical medicine at the Federico II University Hospital in Naples.

DMAIC was utilised to identify root causes of risks in order to eliminate them and then to improve the whole process. Data were collected for 28,000 patients hospitalized between January 2011 and December 2016. Data from hospital database included: days of hospitalization, infections and number of diagnostic and therapeutic procedures. Among infected patients, the most prevalent sentinel bacteria were determined. The pre-intervention (January 2011 to December 2014) and post-intervention (January 2015 to December 2016) phases were compared to analyse effects of the project. To find out any causes, staff was asked to fill in a questionnaire in order to investigate protocols, procedures and precautionary actions adopted by the healthcare staff to limit the risk of HAIs. The questionnaire highlighted the lack of both standardised procedures to prevent infections and information of HAIs; it helped finding out corrective actions to improve the whole process as, for example, the introduction of best practices for hand hygiene and staff development making healthcare professionals and patients aware of HAIs risks and consequences. Results of implemented actions made it possible to reduce percentage of colonized patients from 0,36% to 0,19% confirming effectiveness of LSS.

Study of Birmingham et al. [20] aimed to ensure a routine repeat head tomography (RRHCT) to all trauma center geriatric patients who suffered a fall and are taking preinjury anticoagulant or antiplatelet (ACAP) medications. One of the risks of a fall is the delayed intracranial hemorrhage (DICH). Collected data were used to understand if RRHCT was performed or not. Further interesting variables were collected: age, injury severity score (ISS), Glasgow coma score, do not resuscitate order status and ACAP use. DMAIC methodology was used as a guideline to improve the process. Frequencies and percentages were analyzed to evaluate RRHCT practices. Simple logistic regression was used to examine conjunctions between patient characteristics and RRHCT performance. Pearson χ^2 test was used to determine the difference in the distribution of missed RRHCT changed after the operation. Main achievement is that missed RRHCT rate has dropped from 15% to 0%. In particular, it was implemented in medical records an automated warning poke yoke within the process where the user cannot advance to complete the medical record without first addressing the clinical implications of the RRHCT.

LSS based on DMAIC was used at A.O.R.N. A. Cardarelli (Naples) to reduce LOS through a diagnostic-therapeutic-assistance path (DTAP). Ricciardi et al. [21] studied two groups of patients who were operated due to a femur fracture during the 14 months before and after the introduction of the DTAP. The variables used for the study were: age, gender, cardiovascular disease, diabetes, American Society of Anaesthesiologists (ASA) score and allergies. In this study, many tools of LSS were exploited, like value stream map, Ishikawa diagram and statistical tests, but also analysis of the processes identifying value adding and non-value-adding activities and elimination of wastes, according to Lean Thinking. The reduction of LOS was statistically significant in all the subset of patients, so the implementation of DTAP brought advantages for both hospital and patients. Hospital will benefit from less costs (a consequence of the reduction of

LOS) and more available free beds and patients will benefit from a shorter hospital stay and a faster recovery.

Al-Zain et al. [22] used LSS to reduce patient waiting time in a Kuwaiti private hospital obstetrics and gynaecology clinic. Thanks to DMAIC, root causes and improvement actions were identified. Three most significant issues were a lack of scheduling, over-processing and delays caused by doctors. Solutions to these issues were suggested and simulated using Arena simulation software. The results were very significant: waiting time for appointments patients on Saturdays had 67% reduction whilst weekdays got 46%.

The research of Antony et al. [23] had the aim to reduce medication errors in the Norwegian Public Healthcare context. The findings of the study revealed that the most of medications errors in Norwegian hospitals occur in the administration phase, and thus this phase should be targeted for improvement. The study found that Lean and Six Sigma has not been widely applied as complete methodologies to reduce medication errors in the Norwegian healthcare context though PDCA (Plan, Do, Check, Act), which is repetitive 4-stages model used to achieve continuous improvement while DMAIC is a data-driven 5-stages improvement cycle used for enhancing and stabilizing processes, was identified as a popular improvement methodology. A mixed method approach was used to gather data from participants working in the four regions served by the Norway Health Authorities. Due to the large geographical area, it was difficult to reach participants from all health regions in Norway. However, the study managed to assess the current status of LSS implementation through the participants' perspectives.

Studies by Davies et al. [24] had the aim to improve efficiency in hospital day care unit through an environmental redesign. Aforesaid studies lasted 10 months, from October 2016 to July 2017. Pre-intervention data collection lasted three months, from November to January 2017. Intervention phase lasted three months as well, from February to April 2017. Lastly, post-intervention evaluation lasted from May to July 2017. The use of DMAIC helped the team achieving the following results: an average reduction of patient turnaround times (PTT) by 15 minutes per patient, an increasing in nursing time and an improvement in nurse-patient ratio. Using LSS methodology along with improvements focused on the environmental redesign of an hospital day care unit can ease the releasing time of nursing staff to concentrate on direct patient care. This study highlighted how teamwork can be useful in creating positive work organization attitude in order to reach improvements and beneficial change.

Hynes et al. [25] considered using LSS methodology to improve the turnaround time (TAT) for inpatient peripherally inserted central catheter (PICC) placement. The study included hospitalized patients for PICC placement in an interventional radiology department based in an academic teaching hospital with a national referral base. TAT for PICC line placement were registered for 6 months before final implementation and, subsequently, at the 6-month and 2-year follow-up points. Applying DMAIC methodology a significant mean TAT reduction was achieved, despite a 13,8% increase in overall interventional radiological activity. The study demonstrated that applying LSS to the entire PICC placement process it was

possible to identify areas of improvement and introduce simple and effective solutions, leading to a significant TAT reduction.

B. Summary table

Table 1 summarizes main LSS tools adopted in the literature.

TABLE I.
SUMMARY OF THE LITERATURE REVIEW

First Author (Year)	Lean and Six Sigma tools	Location
Damato et al. (2015)	Observations, interviews	USA
Sanders et al. (2015)	DMAIC	USA
Improta et al. (2015)	DMAIC	Italy
Basta et al. (2016)	DMAIC	Netherlands
Agarwal et al. (2016)	VSM, Kaizen	USA
Bhat et al. (2016)	DMAIC	India
Montella et al. (2017)	DMAIC	Italy
Inal et al. (2017)	DMAIC	Turkey
Tagge et al. (2017)	DMAIC	USA
Mancosu et al. (2018)	DMAIC, poka-yoke, visual management	Italy
Steere et al. (2018)	DMAIC	USA
Schmidt et al. (2018)	DMAIC	USA
Improta et al. (2018)	DMAIC	Italy
Birmingham et al. (2018)	DMAIC, logistic regression, χ^2 test	USA
Ricciardi et al. (2019)	DMAIC, t-test, χ^2 test	Italy
Al-Zain et al. (2019)	DMAIC	Kuwait
Antony et al. (2019)	PDCA, surveys, interviews	Norway
Davies et al. (2019)	DMAIC	Ireland
Hynes et al. (2019)	DMAIC	Ireland

DMAIC: Define, Measure, Analyze, Improve, Control; DES: Discrete Event Simulation; VSM: Value Stream Map

IV. CONCLUSION

Lean and Six Sigma principles have been successfully adapted to the healthcare environment enabling hospitals and clinics to streamline their operations and to focus on value as perceived by their patients. Many healthcare organizations have sought the support of lean manufacturing to improve their efficiency. Most recent contributions on applications of the DMAIC demonstrate its ability to increase the performances of healthcare processes, reducing wastes and saving the public health expenses. Promising outcomes of such studies encourage interest from the healthcare sector.

REFERENCES

[1] M. L. George, "Lean six sigma for service–Conquer complexity and achieve major cost reductions in less than a year," *New York*, 2003.

[2] A. Chiarini, "Lean thinking implementation in the public healthcare: results from Italy," In *17th Toulon-Verona Conference Excellence in Services*, 2014.

[3] H. Bevan, "Lean Six Sigma: some basic concepts," *NHS Institute for Innovation and Improvement*, 2006.

[4] G. Improta, M. Romano, M.V. Di Cicco, A. Ferraro, A. Borrelli, et al., "Lean thinking to improve emergency department throughput at AORN Cardarelli hospital," *BMC health services research*, 18(1), 914, 2018.

[5] G. Improta, G. Guizzi, C. Ricciardi, V. Giordano, A.M. Ponsiglione, et al., "Agile Six Sigma in Healthcare: Case Study at Santobono Pediatric Hospital," *International Journal of Environmental Research and Public Health*, 17(3), 1052, 2020.

[6] C. Damato and D. Rickard, "Using Lean-Six Sigma to reduce hemolysis in the emergency care center in a collaborative quality improvement project with the hospital laboratory," *The Joint Commission Journal on Quality and Patient Safety*, 41(3), 99-AP1, 2015.

[7] G. Improta, G. Balato, M. Romano, F. Carpentieri, P. Bifulco, et al., "Lean Six Sigma: a new approach to the management of patients undergoing prosthetic hip replacement surgery," *Journal of evaluation in clinical practice*, 21(4), 662-672, 2015.

[8] G. Improta, G. Balato, M. Romano, A. M. Ponsiglione, E. Raiola, et al., "Improving performances of the knee replacement surgery process by applying DMAIC principles," *Journal of evaluation in clinical practice*, 23(6), 1401-1407, 2017.

[9] J. H. Sanders and T. Karr, "Improving ED specimen TAT using lean Six Sigma," *International journal of health care quality assurance*, 2015.

[10] Y. L. Basta, I. M. Zwetsloot, J. H. Klinkenbijl, T. Rohof, M.M. Monster, et al., "Decreasing the dispatch time of medical reports sent from hospital to primary care with Lean Six Sigma," *Journal of evaluation in clinical practice*, 22(5), 690-698, 2016.

[11] S. Agarwal, J. J. Gallo, A. Parashar, K. K. Agarwal, S. G. Ellis, et al., "Impact of lean six sigma process improvement methodology on cardiac catheterization laboratory efficiency," *Cardiovascular Revascularization Medicine*, 17(2), 95-101, 2016.

[12] S. Bhat, E. V. Gijo and N. A. Jnanesh, "Productivity and performance improvement in the medical records department of a hospital," *International Journal of Productivity and Performance Management*, 2016

[13] E. Montella, M.V. Di Cicco, A. Ferraro, P. Centobelli, E. Raiola, et al., "The application of Lean Six Sigma methodology to reduce the risk of healthcare–associated infections in surgery departments," *Journal of evaluation in clinical practice*, 23(3), 530-539, 2017.

[14] E. P. Tagge, A. S. Thirumoorthi, J. Lenart, C. Garberoglio and K. W. Mitchell, "Improving operating room efficiency in academic children's hospital using Lean Six Sigma methodology," *Journal of pediatric surgery*, 52(6), 1040-1044, 2017.

[15] T. C. Inal, O. Goruroglu Ozturk, F. Kibar, S. Cetiner, S. Matyar, et al., "Lean six sigma methodologies improve clinical laboratory efficiency and reduce turnaround times," *Journal of clinical laboratory analysis*, 32(1), e22180, 2018.

[16] P. Mancosu, G. Nicolini, G. Goretti, F. De Rose, D. Franceschini, et al., "Applying Lean-Six-Sigma Methodology in radiotherapy: Lessons learned by the breast daily repositioning case," *Radiotherapy and Oncology*, 127(2), 326-331, 2018.

[17] L. Steere, M. Rousseau and L. Durland, "Lean Six Sigma for intravenous therapy optimization: a hospital use of Lean thinking to improve occlusion management," *Journal of the Association for Vascular Access*, 23(1), 42-50, 2018.

[18] S. Schmidt, L. A. Shay, C. Saygin, K. Schulz, R. A. Clark and P. K. Shireman, "Improving pilot project application and review processes: A novel application of lean six sigma in translational science," *Journal of clinical and translational science*, 2(3), 135-138, 2018.

[19] G. Improta, M. Cesarelli, P. Montuori, L. C. Santillo and M. Triassi, "Reducing the risk of healthcare-associated infections through Lean Six Sigma: The case of the medicine areas at the Federico II University Hospital in Naples (Italy) ," *Journal of evaluation in clinical practice*, 24(2), 338-346, 2018.

[20] L. E. Birmingham, A. Sedorovich, N. Mann and R. I. George, "Using Lean Six Sigma to Improve Delayed Intracranial Hemorrhage Screening in a Geriatric Trauma Population," *Quality Management in Healthcare*, 27(4), 199-203, 2018.

[21] C. Ricciardi, A. Fiorillo, A. S. Valente, A. Borrelli, C. Verdoliva, et al., "Lean Six Sigma approach to reduce LOS through a diagnostic-therapeutic-assistance path at A.O.R.N. A Cardarelli," *The TQM Journal*, 2019.

[22] Y. Al-Zain, L. Al-Fandi, M. Arafeh, S. Salim, S. Al-Quraini, et al., "Implementing Lean Six Sigma in a Kuwaiti private hospital," *International journal of health care quality assurance*, 2019.

[23] J. Antony, S. C. Forthun, Y. Trakulsunti, T. Farrington, J. McFarlane, et al., "An exploratory study into the use of lean six sigma to reduce medication errors in the Norwegian public healthcare context," *Leadership in Health Services*, 2019.

[24] C. Davies, C. Lyons and R. Whyte, "Optimizing nursing time in a day care unit: Quality improvement using Lean Six Sigma methodology," *International Journal for Quality in Health Care*, 31(Supp 1), 22-28, 2019.

[25] J. P. Hynes, A. S. Murray, O. M. Murray, S. K. Eustace, S. Gilchrist, et al., "Use of Lean Six Sigma methodology shows reduction of inpatient waiting time for peripherally inserted central catheter placement," *Clinical radiology*, 74(9), 733-e5, 2019.

From Mocap data to inertial data through a biomechanical model to classify countermeasure exercises performed on ISS

M. Ravizza[1], A. Pedrocchi[1], J. DeWitt[2] and G. Ferrigno[1]
[1]*Department of Electronics, Information and Bioengineering (DEIB), Politecnico di Milano, Italy;*
[2]*KBR NASA Johnson Space Center (JSC), Houston, USA.*

Abstract— **On board the International Space Station (ISS) resistive training is essential to reduce the effects of musculoskeletal system deconditioning due to weightlessness. However, it could be equally dangerous or not useful if performed with inappropriate techniques. Thus, a system based on inertial sensors able to monitor astronauts has been thought. In this work, an OpenSim biomechanical model was used to reproduce motion of countermeasure target exercises and to simulate inertial sensors put on the model. This was done starting from kinematic data collected with motion capture system (mocap), because no inertial data were available. Then, it was explored a possible approach to build the classifier able to automatically recognize 'correct' and 'wrong' techniques of execution. Two machine learning algorithms were compared and results in terms of accuracy were encouraging.**

Keywords— **Microgravity, biomechanics, inertial sensors, machine learning**

I. INTRODUCTION

DURING space missions astronauts are inserted in an environment that significantly differs from that on Earth. Weightlessness induces a series of human body changes and adaptations involving different systems: cardiovascular, respiratory, visual and, especially, musculoskeletal. The unloading of bones and muscles in microgravity produces rapid and severe mineral loss and reduction of muscle mass and muscle strength [1]. In current flights, recovery time is not critical, but space agencies are planning long-duration missions (LDMs) to Moon and Mars [2], so these physiological effects must be considered. To prevent deconditioning, crewmembers perform resistive exercises on board the International Space Station (ISS) thanks to the Advance Resistive Exercise Device (ARED). It simulates the use of weights in microgravity generating a constant load that can be changed from 0 to 272 kg [3]. Currently, ground teams communicate with crew by using a real-time audio/video system to ensure correct lifting technique. However, the more the distance from the Earth, the longer the communication delay. Therefore, feedback during LDMs to Moon and Mars will become more difficult to receive. Wrong techniques of execution, especially by using high loads, could decrease efficacy of training and may involve risk of injuries, as well documented in literature [4]-[6]. This study is inserted in a project that aims to design a biofeedback system based on a small set of wearable inertial sensors, suitable in microgravity,

and machine learning algorithms to supervise crew members during their daily training. Currently, no inertial sensor data of exercises performed with ARED are available, but only kinematic and dynamic experimental data collected by using a motion capture system and force plates at NASA Johnson Space Center (JSC) in Houston, where the on-ground ARED model is installed. For this reason, it is needed to use a personalized biomechanical model in order to extract acceleration signals in different virtual body points, where real inertial sensors would be put. The model is inserted in a virtual environment where target exercises, proposed on ISS, are simulated in microgravity or weightlessness conditions. Executions in different configurations, both correct and wrong ones, are required and a set of biomechanical variables associated with a musculoskeletal risk level should be extracted. Thus, corrective information must be provided with different types of biofeedback easy to interpret.

This work was focused on: (a) the extraction of acceleration signals by using a biomechanical model in OpenSim virtual environment. This was done starting from data collected with motion capture system related to correct and wrong exercise techniques. This point is necessary because, currently, no real data acquired with inertial sensors are available; (b) the development of a classifier able to automatically classify a technique between correct and wrong. This was done starting from simulated inertial data. At the moment, these analyses were completed with data collected at Luigi Divieti laboratory at Politecnico di Milano of two subjects performing target exercises, in correct and wrong forms, with barbell and weights. Currently, the study is going on by elaborating kinematic data collected at NASA JSC of six subjects performing target exercises in correct form. Exercises under analysis are normal stance squat (NS), wide stance squat (WS) and normal deadlift (ND). Currently, on board the ISS it is installed the motion capture system ELITE S2 [7] that is going to be substituted because it is now obsolete. As soon as a new system will be available, in-flight data collection will be planned in order to enlarge our dataset and to improve the classifier.

II. MATERIALS AND METHODS

A. Participants

Two voluntary athletes (one man, 170 cm, 65 kg, 30 year; one woman, 164 cm, 54 kg, 25 year) participated to the data collection at Politecnico di Milano. Six non-astronaut subjects (three women, 161.8±7.2cm, 60.0±7.8kg, 31.3±6.8year; three

men, 174±8.5cm, 70.8±13.2kg, 31.8±4.8years) were recruited at NASA JSC. All subjects were healthy and had experiences with the proposed resistance exercises.

B. Experimental protocol

Motion data at Politecnico di Milano were collected using motion capture system SMART DX 400 (BTS Bioengineering S.p.A, Milan, Italy), composed by 8 TV cameras with 100 Hz sampling frequency; Ground Reaction Forces (GRFs) were measured by 2 force plates (AMTI, USA). The marker-set was chosen according to the one previously used for data collected at NASA JSC. A total of 43 retro - reflective markers were placed on body excluding upper limbs (fig. 1) and 2 on the extremities of the bar. Placement were as follow, considering both sides: dorsal margin of first and fifth metatarsal heads, lateral midfoot, most posterior aspect of calcaneus, most lateral and medial point of malleolus, bank of 3 markers on lateral thigh, lateral knee, bank of 3 markers on lateral shank, prominence of greater trochanter, most anterior and most posterior superior iliac spine (ASIS, PSIS), xiphoid process, supraclavicular notch, 10th thoracic vertebrae, vertebra prominens, 3 markers on head.
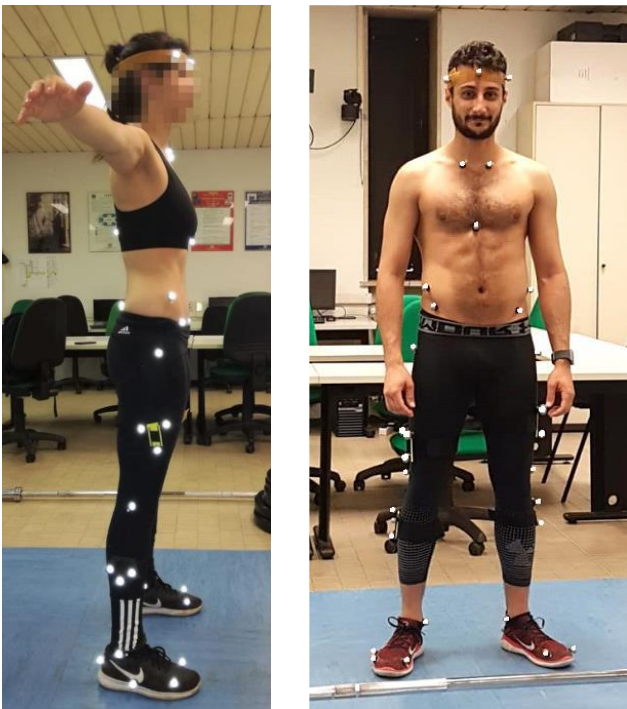
Fig. 1: marker placement for data collection at Politecnico di Milano

Each subject performed one set of 4 repetitions of normal squat, wide stance squat and normal deadlift with correct execution, similarly to that collected at NASA JSC. Additionally, they performed one set of each kind of wrong technique with a number of repetitions varying from 2 to 4 basing on the individual sensations, to avoid injuries. External loads were in the range of 75-80% of maximal isometric strength (ISO-MAX).

The experimental data prior collected at NASA JSC with ARED were acquired at 250 Hz by 11 cameras SMART-D (BTS Bioengineering S.p.A., Milan, Italy) and GRFs were collected at 1000 Hz by 2 force plates incorporated in the ARED foot platform (Model 9261, Kistler). All subjects involved in the experiment performed one set of four repetitions of the target exercises in correct configuration, with an external load of 75% ISO-MAX.

The protocol adopted, the correct and wrong techniques, were reviewed and approved by NASA Astronaut Strength, Conditioning and Rehabilitation (ASCR) specialists.

C. Correct and wrong techniques

The good form of normal squat requires to start from a standing position and to maintain the trunk straight. Moving down, knees are flexed to reach an angle equal or greater than 90° and then extended to return to the starting position. Wide squat differs from normal squat in placement of feet that show a separation 1.5-2 times larger. To minimize risk of trauma and ensure maximal lower limb muscles activation, optimal squat technique requires: upright trunk to maintain spine in a neutral position, with a slightly lordotic lumbar spine; knees tracking over toes, so without bring them closer and avoiding to overcome the toes; heels in contact with the floor, to prevent forward lean of the trunk; tibiae parallel to the upright torso; gaze forwards or upwards [5],[8],[9]. The deviations from the correct techniques were: rounded back (RB), valgus knees (KV), knees overcoming toes (KOT), raised heels (RH) and shallow squat (SQ).

As concern normal deadlift, the optimal technique requires to start in partial squatting, with natural width of feet and with arms coming down outside the legs to reach the bar. Then, hip and shoulders have to be lifted at the same time maintaining a natural position of the spine. It is necessary to respect some features to avoid inefficacy of training and/or injuries: hip joints have to be maintained higher than knees, to prevent forward lean of the trunk; upright trunk to maintain spine in a neutral position; shoulder blades adduced, slightly in front of bar; gaze forwards [4], [10]. Wrong executions were: rounded back (RB), bar over shoulders (BOS) and hyperextension of the back at the end of lifting (HB).

D. Data analysis and biomechanical simulation

OpenSim [11] is an open-source software used to build individual biomechanical models and to compute joint angles and moments. The model used for the analysis was the published skeletal model with 12 segments and 23 degrees of freedom (dof). Hip joint was modelled as a ball-and-socket joint with 3 dof, while knee and ankle as single dof hinge joints. The same model was utilized by DeWitt et al. [12] and Mummidivarapu et al. [13] to identify the optimal body weight replacement in weightlessness during squat. Fregly et. Al [14] combine the published extension of the same model, which includes also all upper-body joints [15], with three-dimensional computer-aided design (CAD) geometry of ARED to simulate squat exercise in microgravity. Custom script using Matlab R2019a were used to pre-process data, to create files in compatible format with OpenSim and to elaborate its output. Raw data were interpolated with a cubic spline function to fill gaps and filtered with a 6th order Butterworth low pass filter with a cut-off frequency of 5 Hz. External loads were added by considering a constant vertical force applied on the shoulders of the model, on the mid-point of the barbell (fig. 2).
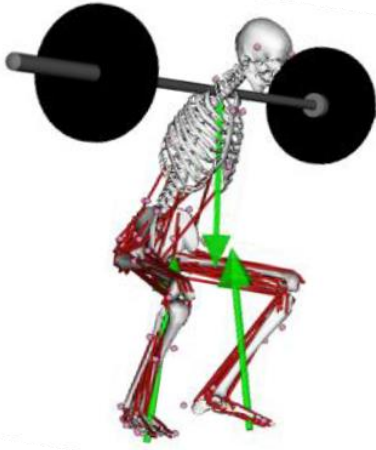
Fig. 2: screenshot of the model during simulation of correct squat. GRFs and external force due to the barbell are shown in green.

Output coming from OpenSim were elaborated in order to compare results between correct and wrong techniques with non-parametric Wilcoxon-Mann-Whitney test. For each exercise and each subject, joint angle and joint moment average and standard deviation of all repetitions were computed. For squat and wide squat, one cycle begins (0%) with hip and knee joints extended, it continues with their flexion and terminates (100%) returning to the initial position. For deadlift is the opposite: the cycle starts with knee and hip joints flexed, it proceeds with their extension and ends returning to the initial position.

E. Inertial sensors simulation and classifier development

The Analyses Tool of OpenSim was used to simulate inertial sensors, so to extract acceleration data in different body points related to each kind of training exercise and execution. This tool allows to compute trajectory, velocity and acceleration of body points properly specified by user. To do this, it is needed to specify the coordinates of the points involved, the name of the segment in which they are located and the reference system in which they are expressed. The chosen points were sternum, sacrum, mid-thigh and mid-shank. Despite the few simulated acceleration data available, it was explored a method to build a classifier based on machine learning algorithms. The classification was limited to a binary one in order to distinguish performance between correct and wrong, without differentiating the various mistakes. Two supervised learning methods were compared: Artificial Neural Network (ANN) and Support Vector Machine (SVM). Four sensors were simulated, each one gave three acceleration signals, one per axis. Accelerations related to each repetition were extracted, filtered with a 2nd order Butterworth low-pass filter with cut-off frequency of 2 Hz and normalised in time. Basing on works in literature [16], [17], features both in time domain (e.g. mean, max, min, variance, standard deviation, etc.) and frequency domain (e.g. energy, mean, max, min, band power, etc.) were extracted. Principal component analysis (PCA) [18] is one of the most used techniques for dimensionality reduction. It was chosen in this work to reduce the feature set and, thus, to facilitate the subsequent learning and generalization steps of machine learning algorithms. Workflow can be seen in the scheme below (figure 3).

III. RESULTS

A. Comparison between correct and wrong techniques

The hypothesis of not equality of joint angles and joint moments in the sagittal plane between correct and wrong techniques was statistically demonstrated with Wilcoxon-Mann-Whitney test ($p < 0.05$).

B. Comparison between ARED and barbell kinematics

Both correlation and the hypothesis of equality of joint
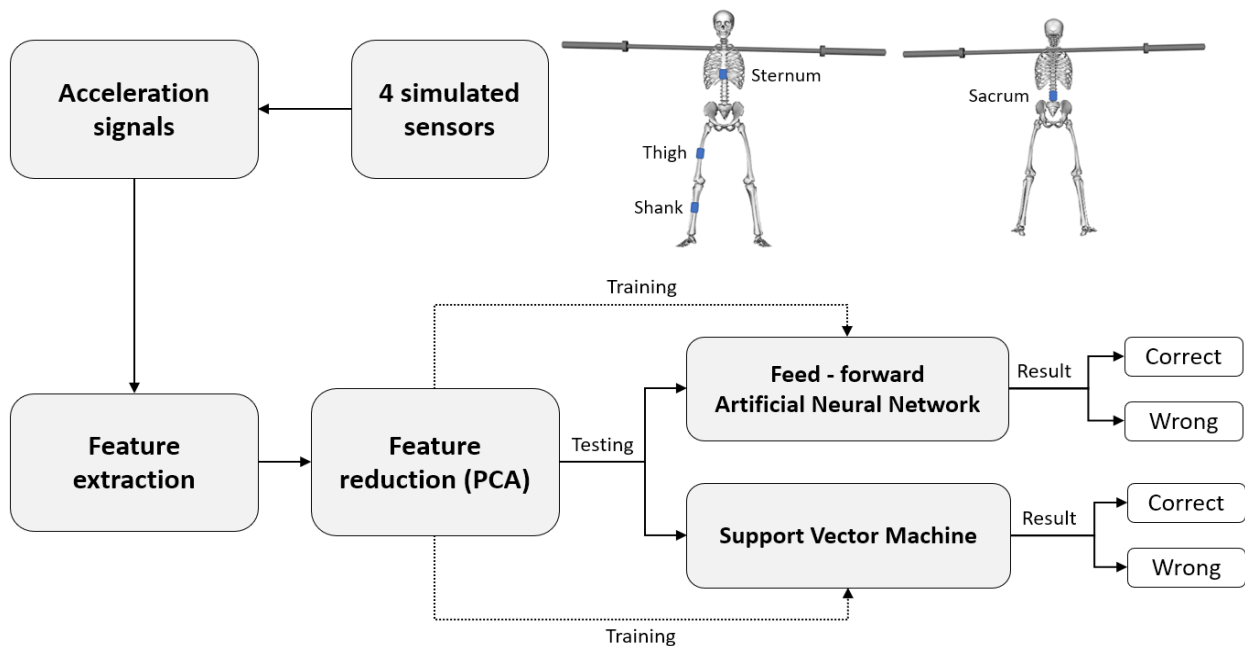

Fig. 3: workflow from sensor simulation to binary classification.

angles in the sagittal plane between ARED kinematics and barbell kinematics were statistically demonstrated with Wilcoxon-Mann-Whitney test (p < 0.05). Thus, no statistical differences were observed between kinematics of exercises performed with ARED and barbell.

C. Performance of the classifier

From each simulated acceleration signal, a total of 304 features per single repetition were extracted. For example, considering normal squat, dataset was composed by 40 rows, given that two subjects performed 4 repetitions of correct and each type of wrong technique, and 304 columns. PCA reduced the original datasets, composed by 304 features, to 12 for normal squat, 9 for wide squat and 10 for normal deadlift. Then, rows were labelled as 1 for correct execution and 0 for wrong. Datasets were divided to create subsets needed to train, validate and test the machine learning algorithms, considering a percentage of 80%, 5% and 15% of observations respectively. ANN and SVM performance were compared computing accuracy according to the formula Eq. (1) (TP = true positive, TN = true negative, FP = false positive, FN = false negative).

$$Accuracy = \frac{TP+TN}{TP+TN+FP+FN} \quad (1)$$

As shown in table I, for squat and deadlift SVM was more accurate, instead ANN showed better results for wide squat.

TABLE I
ACCURACY OF MACHINE LEARNING ALGORITHMS

	SQUAT	WIDESQUAT	DEADLIFT
ANN	83.3%	75%	60%
SVM	88%	71.4%	85.7%

IV. CONCLUSIONS

The procedure adopted in this work to simulate inertial sensors, given that no acceleration data related to exercise preformed with ARED were available, was effective despite the small amount of available data. Further investigations are needed to enlarge datasets and to improve the performance of the classifier, but these preliminary results could be seen as encouraging to consider this approach as working solution. Currently, the study is going on by analyzing data collected at NASA JSC and it will be supported by in-flight data, once available.

REFERENCES

[1] G. C. Demontis, M. M. Germani, E. G. Caiani, I. Barravecchia, C. Passino, D. Angeloni, "Human pathophysiological adaptations to the space environment," *Frontiers in physiology*, vol. 8, 547, August 2017.
[2] B. Dickey (2008, June 19), "Outposts on the Moon, Footprints on Mars: NASA's future exploration plan," NASA 50th magazine-50 Years Exploration and Discovery, https://www.nasa.gov/50th/50th_magazine/futureExploration.html.
[3] N. Petersen, P. Jaekel, A. Rosenberg, T. Weber, J. Scott, et al. "Exercise in space: the European Space Agency approach to in-flight exercise countermeasures for long-duration missions on ISS," *Extreme Physiology & Medicine,* vol. 5 9, August 02, 2016.
[4] V. Bengtsson, L. Berglund, U. Aasa, "Narrative review of injuries in powerlifting with special reference to their association to the squat, bench press and deadlift," *BMJ Open Sport & Exercise Medicine,* vol. 4 issue 1, July 14, 2018.
[5] G. D. Myer, A. M. Kushner, J. L. Brent, B. J. Schoenfeld, J. Hugentobler, et al. "The back squat: a proposed assessment of functional deficits and technical factors that limit performance," *Strength and conditioning journal*, vol. 36, pp. 4-27, December 01, 2015.
[6] K. Spencer, M. Croiss, "The effect of increasing loading on powerlifting movement from during the squat and deadlift," *Journal of Human Sport and Exercise,* vol.10, num. 3, pp. 764-774, 2015.
[7] G. Neri, G. Ferrigno, A. Pedrocchi, G. Baroni, V. Zolesi, et al. "Elite S2 – A new instrument for multifactorial movement analysis on the International Space Station," *54th International Astronautical Congress of the International Astronautical Federation, the International Academy of Astronauts and the International Institute of Space Law*, 29 September – 3 October, 2003.
[8] S. Lorenzetti, M. Ostermann, F. Zeidler, P. Zimmer, L. Jentsch, et al. "How to squat? Effects of various stance widths, foot placement angles and level of experience on knee, hip and trunk motion and loading," *BMC Sport Science, Medicine and Rehabilitation,* vol. 10, issue 14, July 17, 2018.
[9] P. Comfort, J. J. McMahon, T. J. Suchomel, "Optimizing squat technique - Revisited," *Strength and Conditioning Journal,* vol. 40, issue 6, pp. 68-74, December 2018.
[10] M. Hales, "Improving the deadlift: understanding biomechanical constraints and physiological adaptations to resistance exercise," *Strength and Conditioning Journal,* vol. 32, issue 4, pp. 44-51, August 2010.
[11] S. L. Delp, F. C. Anderson, A. S. Arnold, P. Loan, A. Habib, et al., "OpenSim: open-source software to create and analyze dynamic simulations of movement," *IEEE Transactions Biomedical Engineering,* vol. 52, issue 11, pp. 1940-1950, November 2007.
[12] J. J. DeWitt, R. S. Fincke, R. L. Logan, M. E. Gullliams, L. L. Ploutz-Snyder, "Load variation influences on joint work during squat exercise in reduced gravity," *35th Annual meeting of the American Society of Biomechanics,* 10-13 August, 2011.
[13] S. S. Mummidivarapu, G. Scaffner, "A method for determining body weight replacement load during squat exercise in weightlessness," *47th International Conference on Environmental Systems,* 16-20 July, 2017.
[14] B. J. Fregly, C. D. Fregly, B. T. Kim, "Computational prediction of muscle moments during ARED squat exercise on the International Space Station," *Journal of Biomechanical Engineering,* vol. 137, issue 12, December 2015.
[15] S. R. Hamner, A. Seth, S. L. Delp, "Muscle contributions to propulsion and support during running," *Journal of Biomechanics,* vol. 43, issue 14, pp. 2790-2716, 2010, 19 October, 2010.
[16] I. Farkas, E. Doran, "Activity recognition from acceleration data collected with a tri-axial accelerometer," *Acta Technica Napocensis,* vol. 52, number 2, 2011.
[17] C.B. Erdas, I. Atasoy, A. Koray, H. Ogul, "Integrating gestures for accelerometer-based activity recognition," *Procedia Computer Science*, vol. 98, pp. 522–527, 2016.
[18] I. T. Joliffe, *Principal Component Analysis,* Springer – Berlag, New York, 1986.

Play-Draw-Write: usability and acceptance of a tablet app for the early screening of handwriting difficulties in kindergartners

L.G. Dui[1], F. Lunardini[1], C. Termine[2], M. Matteucci[1] and S. Ferrante[1]

[1] *Politecnico di Milano, Department of Electronics, Information and Bioengineering*
[2] *Università dell'Insubria di Varese, Department of Medicine and Surgery*

Abstract—**Dysgraphia is a Learning Disability that prevents from mastering handwriting. It is belatedly diagnosed, with negative consequences on children's life. To anticipate Dysgraphia screening to a pre-literacy age, we present *Play-Draw-Write*, a tablet-based application designed to assess handwriting-related features, starting from drawing. It focuses on different aspects of graphical gesture production, such as rhythmicity and speed-accuracy tradeoff, but also to the possible alteration which might occur in gesture production itself, in free drawing. Preliminary inspection of quantitative parameters extracted from the app games suggests their potential in detecting children considered at risk of developing delays in graphical abilities, according to their teachers' judgement. In this work, we focus on children's opinion in terms of system acceptance and usability, to enable a longitudinal monitoring through our app and a better evaluation of the direction of possible corrections. Results from usability and acceptance questionnaires on 177 children revealed that they liked playing with the app, and wish to use it again, even when encountering some difficulties. These results are a first step toward an early, easy, and broad screening of Dysgraphia, before handwriting is learnt.**

Keywords—**Dysgraphia, screening, pre-literacy, usability.**

I. INTRODUCTION

HANDWRITING is a complex activity mastered during the first three years of primary school [1]. 5 to 27% of children [2], [3] experience difficulties in this learning process, with negative consequences on their behaviour, school performance, and whole life [4]. Dysgraphia is recognised as a Learning Disability [5] which requires specific intervention. Its diagnosis requires to evaluate handwriting itself [6]. In the meantime, it can be confused with transient difficulties, or not recognised at all, with the risk of exacerbating the related problems. To improve the pre-diagnostic process, some schools are implementing specific observational programs with trained teachers, starting from the last year of kindergarten, reporting abnormalities in grasping position, posture, coordination, dexterity, and other abilities related to future handwriting production.[4] However, observation only cannot disclose some subtle yet relevant characteristics of the writing gesture, which might hide the real causes of the observed weakness, nor quantitatively evaluate small improvements, which can help distinguishing between a transient delay and the Learning Disability itself.

Therefore, innovative solutions must be adopted, to help achieving an early screening of Dysgraphia. Such tools must meet specific requirements: first, they must provide objective parameters to characterize gesture production that are likely altered in dysgraphic handwriting; second, they must be sensitive to children's development, to allow the discrimination of longitudinal improvements; third, they must be designed to anticipate the screening to a pre-literacy age; fourth, they must be easily usable, in order to broaden the screening even to non-trained personnel; fifth, they must engage children, to facilitate repetitive test administration.

To meet the first need, we considered two main features usually altered in dysgraphic children. First, they are reported to experience problems in following rhythms [7], with difficulties in reproducing tapping sequences. Such rhythmical impairment, in handwriting, can be referred as the isochrony and homothety principles. Together, they predict speed modulation to keep absolute and relative writing time approximately constant across changes in size [8]. Both these aspects are proven to be altered in Dyslexia and Dysgraphia [9]. Second, we considered alteration in the speed-accuracy tradeoff (SAT), as dysgraphic handwriting is characterized by poor quality and fast executions, with several pauses between strokes [10], [11]. Importantly, handwriting SAT was proven to be sensitive to age-related changes [12], thus being suitable for a longitudinal monitoring. In addition, several parameters, such as pressure, frequency content, pen tilt, or smoothness, are proven to be effective in discriminating between normal and dysgraphic handwring [13], [14]. To anticipate the screening to a pre-literacy age, the same alterations reported in handwriting must be investigated in symbols drawing, both with imposed constraints to study rhythm and SAT, and in a freer execution. To allow a broader evaluation, we propose the use of commercial tablets, which additionally allow for gamification resulting in increased children involvement. Moreover, the use of commercial styli paired with tablets permit to collect different parameters, for a compete gesture characterization.

This study has 2 goals: (i) to present a novel solution which enables a complete characterization of children in terms of handwriting abilities, through the analysis of drawings in a pre-literacy stage; (ii) to test usability and acceptance of the new tool.

II. METHODS

A. Material

We developed *Play-Draw-Write*, an application in Unity 2018.3.2f1, for an iPad 6, with Apple Pencil 1. Stylus position, pressure, altitude, and azimuth angles are sampled at 240 Hz.

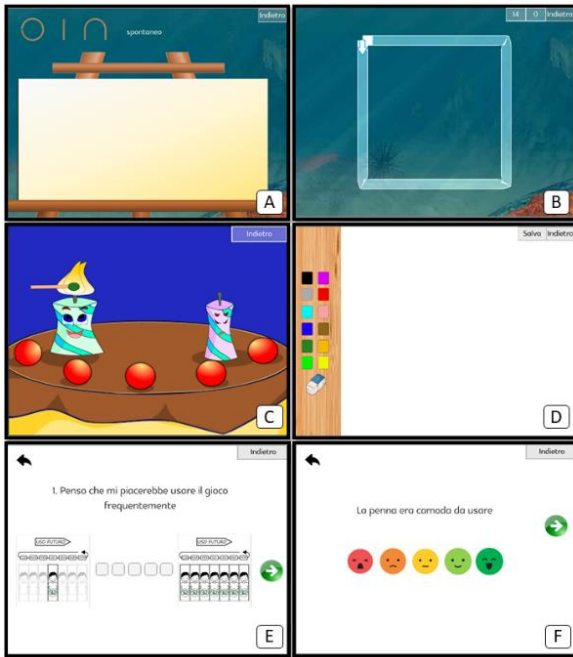The app presents four games and two questionnaires.

Figure 1: Application interfaces. Panel A: Copy Game. Panel B: Tunnel Game. Panel C: Song Game. Panel D: Drawing Game. Panel E: usability questionnaire (P-SUS). Panel F: acceptance questionnaire.

The Copy Game (Fig. 1A) presents an empty canvas and an example of a symbol (a square) or a sequence of symbols (a circle, a line, and a reversed U) to copy. In addition, the system suggests a modality for copying: spontaneous, big, or small. This game is designed to study isochrony in symbols, as speed modulation is expected when asked to draw bigger or smaller. Thus, we calculated the instantaneous speed as the derivative between successive points, and we averaged it to obtain a single mean value, to be compared between modalities. In addition, the sequence allows homothety evaluation, as the fraction of time dedicated to each symbol with respect to the total sequence can be studied between modalities.

The Tunnel Game (Fig. 1B) is designed to study SAT both in symbols (a square) and in a portion of word ("ele"). The game presents 14 tunnels of varying amplitude and width, to create five different indexes of difficulty (ID) [12], as per the steering law [15]. For each execution, we computed the total movement time (MT), and the linear regression between ID and MT, in order to evaluate its significance.

The Song Game (Fig. 1C) reproduces the "Happy birthday" song, as in [16]. The canvas presents two candles and users are asked to use the stylus to continuously draw back and forth between the two candles to light them on. To guide in the rhythm, candles increase their size and show a happy face when they are supposed to be lit, according to the rhythm. The increase in size is progressively reduced throughout the game, to check if children can keep up with the task, also with a reduced visual guidance. Furthermore, during the second stanza, volume is progressively lowered, to check if children can keep up with the rhythm without the acoustic hint. Thus we evaluated the horizontal movements of the stylus in the different phases of the song, in respect to the rhythm of the song.

The Drawing Game (Fig. 1D) presents an empty canvas, a color palette, and a rubber. The requirement is to draw a child.

This game is intended to investigate if even free drawing can be informative in predicting future handwriting abilities.

The usability questionnaire (Fig. 1E) is the System Usability Scale (SUS) [17] paired with pictures inspired by the Pictorial SUS (P-SUS) [18], to help children in the comprehension.

The acceptance questionnaire (Fig. 1F) presents 5-point likert scale questions, whose answers are visually guided by emoticons, from really sad (totally disagree) to really happy (completely agree):

1. Was the pen comfortable to use?
2. Was the pen light?
3. Do you prefer this pen rather than those you always use?
4. Did you enjoy the game and do you wish to continue using it at home?
5. Are you satisfied with the experience?

To test for users' reaction to the new tool, we performed frequency analysis of each item of both the P-SUS and the acceptance questionnaire. For the P-SUS, we additionally computed the total score [17].

B. Participants and Protocol

Children from the last year of kindergarten without known pathologies were enrolled in the study. Teachers' judgement about their graphical skills development were collected, to stratify participants between Typically Developing (TD) and at Risk of a graphical-related delay (R).

The experimental sessions were carried out under the supervision of a trained researcher who was providing oral explanation. Subjects were seated at a table, with the tablet in front of them. The complete protocol lasted about 20 minutes and was structured as follow:

Copy Game:
1. Copy a square in 3 ways: spontaneous, big, and small;
2. Copy a sequence in 3 ways: spontaneous, big, and small;
Tunnel Game:
3. View a tutorial of steering into a square-shaped tunnel, as fast as possible without crossing the borders;
4. Make a trial of steering in the square-shaped tunnel;
5. Steer 14 square-shaped tunnels, with random ID order;
6. Repeat steps 3-5 for the word-shaped tunnel ("ele")
Song Game:
7. View a tutorial;
8. Make a trial;
9. Play the game;
Drawing Game:
10. Draw a child;
Usability and acceptance:
11. Answer the 10 P-SUS questions;
12. Answer the 5 acceptance questions;

Written informed consent was signed by participants' parents, and the procedure was approved by the Politecnico di Milano Ethical Committee n. 24/2019.

III. RESULTS

177 children participated in the study, 26.5% of them were assigned to the R group, according to teachers' judgement. They were 94 males and 83 females, aged 5 years and 6 months old ± 3 months. 22 were left-handed, 9 showed ambidextrous attitude. 55 of them never used a tablet before and only 15 have previously used a stylus.

Fig. 2 reports frequency analysis for each question of the usability and acceptance questionnaires. The P-SUS score resulted in a mean value of 78.4 ± 15.0.
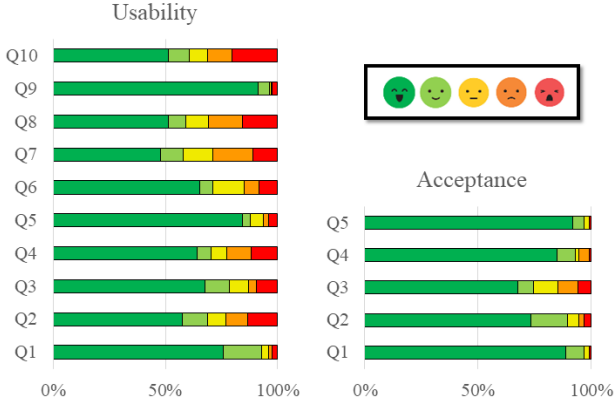

Figure 2: Questionnaire results. Each line reports the answers to a specific question, labelled as Q and its progressive number. Dark green: most positive, red: most negative answers (SUS even answers are mirrored for consistency).

We now report an exploratory analysis of the main features that can be extracted from the execution of each game. Exemplifying subjects, from R and TD groups, are chosen.

Fig. 3 shows an example from the Copy Game execution of two R children and a TD child, in the spontaneous modality. R children show that drawing difficulties can have different causes: in (A) we have a quivering execution, visible from both the drawing outcome and the speed fluctuation; in (B), even if the drawing outcome seems normal, there are several starts and stops (visible from the Speed panel), which suggest an effort in producing the final drawing. Regarding the Speed VS modality panel, isochrony alterations can be disclosed in R children: in both cases, the small modality is executed faster than the spontaneous one, and in (B) there is also evidence of an insufficient increase in speed for the big modality. No alterations are visible for the TD children (C). As for the Tunnel Game, Fig. 4 reports an example of a R child and a TD child. It can be noticed that the linear relationship between the ID and the MT predicted by the steering law is not respected by the R child. As for the Song Game, Fig. 5 shows the execution of one R and one TD child. The y axis represents the horizontal projection of the pen position, moved to alternatively reach the candles. The R child clearly shows a difficulty in perceiving the correct rhythm and to keep it constant when visual and auditory aids are inhibited. As for the Drawing Game, the examples reported in Fig. 6 show a different level of details and complexity of the representation and a different space awareness (R child draws on the Save and Back buttons).

IV. DISCUSSION

In this work, we present *Play-Draw-Write*, a tablet-based application designed to anticipate the screening for handwriting problems to an age in which handwriting is not learned yet. Dysgraphic handwriting presents problems in several aspects, which we believe can be abstracted from handwriting itself and can thus be shared with other activities, such as drawing. In this way, the first step in the screening for Dysgraphia should be anticipated to pre-literacy age, so that specific interventions can be planned.
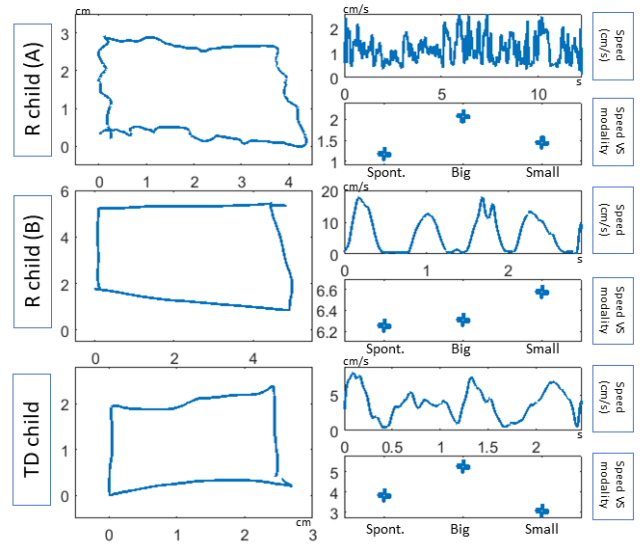

Figure 3. Example of the execution of square in the spontaneous modality for two R children (A and B) and one TD child. For each child, drawing outcome (in cm), speed (in cm/s) and comparison between speed and modality are reported.
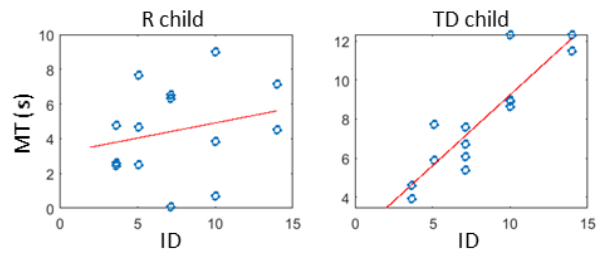

Figure 4. Example of Tunnel Game execution for one R and one TD child. Blue dots are the 14 repetitions of the game, the red line is the linear regression between index of difficulty (ID) and movement time (MT).
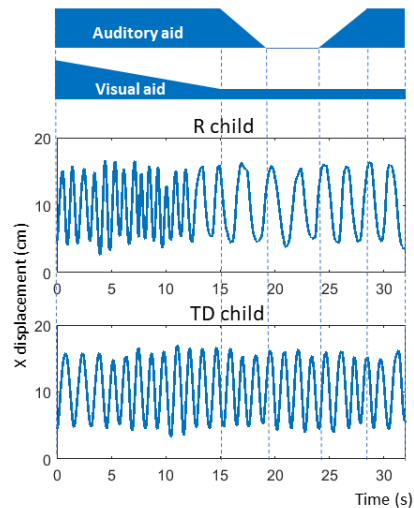

Figure 5. Song Game executed by one R and one TD child. X axis: time in seconds. Y axis: horizontal projection of pen position in centimeters. On top of the graphs, the blue bars indicate the intensity of auditory and visual aids.

Figure 6. Examples of the Drawing Game execution for a R and a TD child.

Examples of alterations in Dysgraphia are related to rhythm, both intended as the ability to follow an external imposed tempo [7], and the capacity to adapt the execution speed to keep constancy in writing words [9]. To this extent, our app presented both a pure rhythmical game and a game aimed at testing homothety and isochrony [8]. A preliminary inspection of the execution of these games show their potential in detecting children at risk of developing graphical problems, according to their teacher's judgement.

Our app allows also the study of another characteristic proper of gesture execution, that is the speed-accuracy tradeoff (SAT). Preliminary tests with the dedicated game show that it is suitable to study SAT in drawing, as well as in writing [12]. Finally, our app provides a free drawing canvas, to study, in a more natural task for children, possible alterations of other parameters of gesture production, such as smoothness, pressure, stylus inclination, but also drawing strategy and the drawing outcome. Specific indications about the aspects and skills more demanding for each child – potentially extracted from the execution of the app games – can help teachers and trainers adapt and improve potential empowerment programs of weak abilities.

We tested the app on 177 kindergartners to evaluate usability and acceptance. The app was rated as Good to Excellent [19]. A deeper inspection of single items suggests that the most positive feedback regarded the sense of comfort during system usage (Q9: 96.5% of positive answers), the will of frequently reuse the system (Q1: 93.1%), and the functions integration (Q5: 87.9%). Some children found the system difficult and wish to be helped in its usage (Q2: 23.0% of negative answers; Q3:12.7%; Q4: 22.5%). The items with a higher incidence of negative feedback are related to the estimated time to learn the game for their peers (Q7: 29.0% of negative answers), the cumbersomeness (Q8: 30.6%) and the need of learning several things before being able to use the system (Q10: 31.2%). Again, it might be that difficulty in interpreting the requests affected children's answers.

Concerning acceptance, the enthusiastic response to almost all the questions confirmed that tablet and stylus can be leveraged for this kind of evaluation. Children who reported to be satisfied by the experience were more than 97%. Therefore, the app can be easily leveraged for a repetitive evaluation, in a longitudinal monitoring perspective.

As a future work, we will leverage the acquired data to build machine learning models, with the aim of discriminating the risk of developing a delay in graphical abilities. Moreover, we plan to continue monitoring children to understand their evolution, in response to the games, and to leverage the acquired data to predict long-term risk of developing Dysgraphia.

To conclude, we developed an application designed to study parameters related to Dysgraphia in pre-literacy drawings.

Engaging features make it suitable for longitudinal monitoring. Indeed, our app enables to detect potential weaknesses at an early stage, to monitor their evolution, and to predict the risk of developing Dysgraphia.

REFERENCES

[1] A. Overvelde and W. Hulstijn, "Handwriting development in grade 2 and grade 3 primary school children with normal, at risk, or dysgraphic characteristics," *Res. Dev. Disabil.*, vol. 32, no. 2, pp. 540–548, 2011.

[2] M. Al-Yagon *et al.*, " The Proposed Changes for DSM-5 for SLD and ADHD ," *J. Learn. Disabil.*, vol. 46, no. 1, pp. 58–72, 2012.

[3] R. Karlsdottir and T. Stefansson, "Problems in Developing Functional Handwriting," *Percept. Mot. Skills*, vol. 94, no. 2, pp. 623–662, 2002.

[4] K. P. Feder and A. Majnemer, "Handwriting development, competency, and intervention," *Developmental Medicine and Child Neurology*, vol. 49, no. 4. pp. 312–317, 2007.

[5] American Psychiatric Association, *Diagnostic and Statistical Manual of Mental Disorders 1. American Psychiatric Association.* 2013.

[6] L. Hamstra-Bletz and A. W. Blöte, "A longitudinal study on dysgraphic handwriting in primary school.," *J. Learn. Disabil.*, vol. 26, no. 10, pp. 689–699, 1993.

[7] H. Ben-Pazi, S. Kukke, and T. D. Sanger, "Poor penmanship in children correlates with abnormal rhythmic tapping: A broad functional temporal impairment," *J. Child Neurol.*, vol. 22, no. 5, pp. 543–549, 2007.

[8] P. Viviani and C. Terzuolo, "Trajectory determines movement dynamics," *Neuroscience*, vol. 7, no. 2, pp. 431–437, 1982.

[9] E. Pagliarini *et al.*, "Dyslexic children fail to comply with the rhythmic constraints of handwriting," *Hum. Mov. Sci.*, vol. 42, pp. 161–182, 2015.

[10] M. M. Prunty, A. L. Barnett, K. Wilmut, and M. S. Plumb, "Handwriting speed in children with Developmental Coordination Disorder: Are they really slower?," *Res. Dev. Disabil.*, vol. 34, no. 9, pp. 2927–2936, 2013.

[11] V. Paz-Villagrán, J. Danna, and J. L. Velay, "Lifts and stops in proficient and dysgraphic handwriting," *Hum. Mov. Sci.*, vol. 33, no. 1, pp. 381–394, 2014.

[12] L. G. Dui, F. Lunardini, and S. Ferrante, "A tablet-based application to study the Speed- Accuracy tradeoff in handwriting throughout lifespan," in *E-Health and Bioengineering (EHB 2019)*, 2019, no. In press.

[13] T. Asselborn *et al.*, "Automated human-level diagnosis of dysgraphia using a consumer tablet," *npj Digit. Med.*, vol. 1, no. 1, 2018.

[14] J. Mekyska, M. Faundez-Zanuy, Z. Mzourek, Z. Galaz, Z. Smekal, and S. Rosenblum, "Identification and Rating of Developmental Dysgraphia by Handwriting Analysis," *IEEE Trans. Human-Machine Syst.*, vol. 47, no. 2, pp. 235–248, 2017.

[15] J. Accot and S. Zhai, "Beyond Fitts' law: models for trajectory-based HCI tasks," *Proc. ACM SIGCHI Conf. ...*, pp. 295–301, 1997.

[16] K. Overy, R. I. Nicolson, A. J. Fawcett, and E. F. Clarke, "Dyslexia and music: Measuring musical timing skills," *Dyslexia*, 2003.

[17] J. Brooke, "SUS-A quick and dirty usability scale," *Usability Eval. Ind.*, 1996.

[18] J. Baumgartner, N. Frei, M. Kleinke, J. Sauer, and A. Sonderegger, "Pictorial System Usability Scale (P-SUS): Developing an instrument for measuring perceived usability," in *Conference on Human Factors in Computing Systems - Proceedings*, 2019.

[19] "Determining what individual SUS scores mean: adding an adjective rating scale," *Determ. what Individ. SUS scores mean adding an adjective Rat. scale*, 2009.

Geometric alterations of capillary network in hypertension: preliminary results

V. Altamore[1], F. Giardini[2], C. Olianti[2], I. Costantini[1], L.Sacconi[2,3], L. Bocchi[1,2]

[1] *University of Florence, Florence, 50100, Italy*
[2] *European Laboratory for Non-Linear Spectroscopy, Florence, 50019, Italy*
[3] *National Institute of Optics, National Research Council, 50125, Florence, Italy*

Abstract—**Hypertension plays an important role in the development of heart damage. In this paper we analyze the topological properties of the capillary network in control and Spontaneously Hypertensive Rat (SHR) heart tissue. Sectional images were segmented, using the Otsu method, and the Hausdorff dimension of the capillary network is evaluated using the box-counting algorithm. Preliminary results indicate SHR images present a slightly worse correspondence with the fractal model, a higher variability between different depths, and a lower fractal dimension.**

Keywords—**Capillary network, fractal model, hypertension**

I. INTRODUCTION

Arterial hypertension is a key condition in the study of several kidney, brain and cardiac pathologies. The important role of arterial bed vasomotion in the blood pressure and flow automatic regulation [1], [2] is clear , as well as peripheral vessel network morphology and pathological remodeling[3], [4].

The Spontaneously Hypertensive Rat (SHR) appeared to be one of the more useful animal model in the study of arterial hypertension and vascular remodeling. In this context, the alterations on capillary network are not yet completely examined. Previous investigation were based on bi-dimensional analyses of the capillary architecture, due to technical limitations that precluded the three-dimensional investigation of the network. These studies were based on histo-morphometrical analyses performed with standard eosin-hematoxyline staining. For example, this method provides both quantitative and qualitative analyses of capillary architecture, but it is restricted to two dimensions[5], [6].

Other studies took advantages from the Vascular Corrosion Casting (VCC), based on TEM microscopy, allowing 3D visualization of the microvasculature and high-resolution[7]. This technique is, however, limited to the reconstruction of very small volumes. A different group of methods employs the optical fluorescence microscopy for investigating morphological features[8], [9]. Optical imaging offers great advantages, but light scattering limits its application range, as it prevents deep penetration of the light into the tissue[10].

The utilization of the optical clearing procedure CLARITY[11] in combination with refractive index matching agents, in particular of 2-2 Thiodiethanol (TDE)[12], allows a strong reduction of light scattering yielding a great efficacy in clarifying murine cardiac tissues[13], [14]. Recently, reconstruction of the whole mouse brain vasculature has been obtained by combining the staining protocol based on vascular perfusion with the BSA-FITC gel[15], with CLARITY/TDE clearing. This method generates a large signal-to-noise ratio coupled with Two-Photon Fluorescent Microscopy (TPFM) detection, and provides a high- quality imaging of the specimen. This method, optimized for heart tissue, will allow a 3D high resolution reconstruction of the capillary network in large specimen. It leads to the generation of a huge amount of data, requiring the optimization of proper automatic analyses of the vascular network.

In this context, we want evaluate the differences in vascular network topology between normal and SHR animals. To this aim, we explore the fractal analysis of the vascular tree to estimate the complexity of the network, using the classical box counting method. Fractal geometry, indeed, proved very effective in capturing alteration of complex network architectures, and in particular in the analysis of microcirculatory patterns[16]. The present work, in particular, analyzes the fractal dimension of single 2D frames of different depths in the tissue, as a preliminary method before the 3D analysis. Indeed, given the acquisition geometry, spatial resolution is intrinsically lower in the z axis, making necessary to introduce an interpolation step to equalize resolutions. Thus, a comparison between 2D and 3D analysis can help in assessing the effect of the interpolation step on the results. In this work, we performed a preliminary test, where we analyzed the feasibility of the proposed algorithm for assessing its capability of discriminating differences between controls and SHR.

II. MATERIALS AND METHODS

The procedure is based on the analysis of the coronary network in large volumes of rats heart tissue. Vascular reconstruction is obtained by tissue clarification and 3D casting of the vessels with a fluorescent gel. Two-photon non-linear optical microscopy is used to acquire the signals. Image segmentation is applied to allow a 2D investigation of the fractal dimensionality of the capillary network. Pathological (SHR) and control rats (Wistar-Kyoto Rats, WKY) are used.

A. Data set

Samples of the coronary vascular network of cardiac tissue of some rats were examined. Each sample is about ($450 \times 450 \times 300$)μm, represented as a series of 2D frames. The data

set is composed of 151 frames from SHR animals, and 189 frames from control subjects.

B. Preprocessing

The 3D acquisition method produces a large number of images, arranged in stacks. This data structure reflects the different spatial resolution of the acquisition process in the different directions. In particular, the resolution along the depth of the tissue (z axis, pixel size $2\,\mu m$) is lower with respect to the resolution in each tissue layer (x and y axes, pixel size $0.439\,\mu m$). This difference prevents a direct application of any fractal measurement. A 3D analysis would needs a re-sampled step, interpolating neighboring frames using a re-sample factor of 4.55 to obtain an isotropic 3D image. However, in this work we focused on the feasibility of the fractal analysis approach evaluating fractal properties on each 2D frame before interpolation.

Images are acquired in the RGB scale, but no significant information about the topology is embedded in the chrominance and saturation channels. Thus, the images are converted in gray scale, before a segmentation step aimed at identification of the capillary network.

Given the high quality of the image, as shown in fig. 1a, segmentation has been carried out by using a global threshold, estimated separately on each frame. A simple Otsu segmentation proved effective, being able to produce a good segmentation also of smaller vessels, as shown in fig. 1b.

C. Fractal model

The estimation of fractal dimension is possible both on gray-scale images and on binary images. In case of a gray-scale image, most methods introduce a 3-D representations, where an image is transformed into a surface composed of points in the 3-D space. This surface is generated by associating each pixel in the image with a height in the 3-D space, corresponding to its gray level. Thus, a given pixel at coordinates (x, y), having gray level $I(x, y)$ corresponds to the point with coordinates $(x, y, I(x, y))$ in 3D space. Therefore, the fractal dimension estimates the increased complexity of a 2D set embedded in the 3D space.

In case of binary images, the image is considered as a sparse set of points embedded in the 2D space; in our case, we consider the sparse set of white (i.e. vessels) points. Thus, we estimate the dimension of a set of 0D elements embedded in the 2D space.

Independently of these differences, several measures of fractal dimension have been proposed. In particular, we focused on the Haussdorf dimension, which is is the measure most frequently used in image analysis, because of the ease of implementation and the good experimental results. The Haussdorf dimension is estimated using the box-counting method[17], which is based on the estimation of the number N_ϵ of boxes of size ϵ required to cover the set representing the image.

For each value of ϵ, the image is subdivided in squares of size ϵ, and for each square s the number of boxes $N(s)$
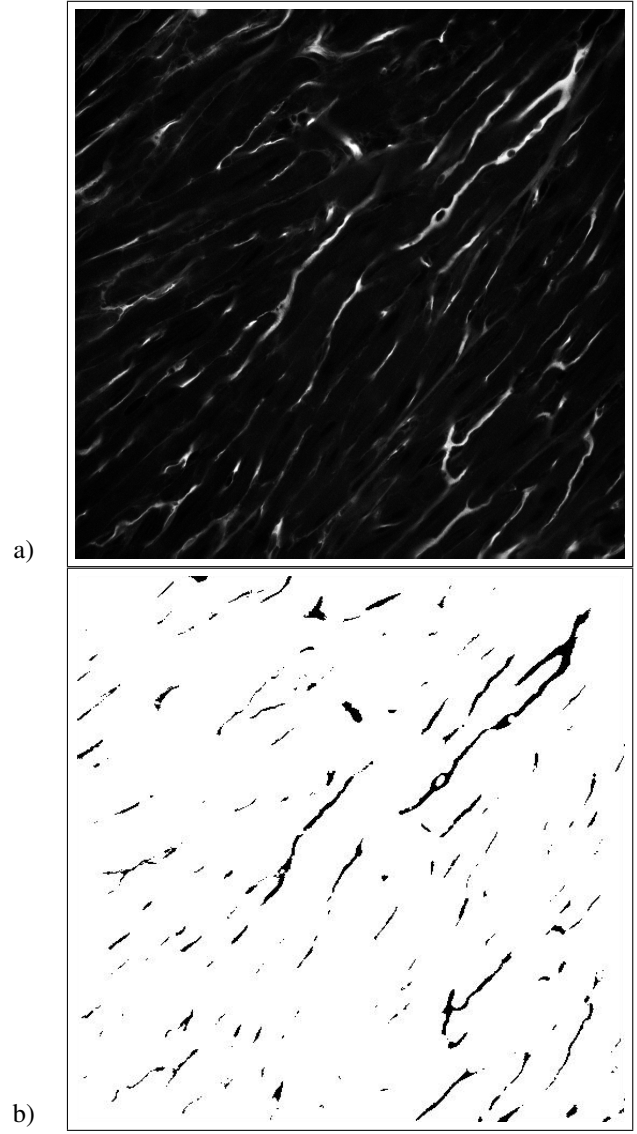
a)

b)

Fig. 1. a) A representative frame of a murine heart sample tissue is shown, where capillary network is obtained with fluorescent gel casting and two-photon microscopy; b) Otsu segmentation; in the segmented image, signal is inverted for better visualization.

required for covering the corresponding portion of the data set is evaluated. In the 3D case (gray scale images), the number of boxes is estimated as:

$$N_s^g = \text{ceiling}\left(\frac{max_s(\delta t_{(x,y)}) - min_s(\delta t_{(x,y)})}{\epsilon}\right) \quad (1)$$

while in case of binary images, the number of boxes is estimated as:

$$N_s^b = \begin{cases} 0 & \text{if no points belong to s} \\ 1 & \text{otherwise} \end{cases} \quad (2)$$

The fractal dimension H is then estimated as the slope of the regression line between $N_\epsilon = \sum_s(N_s)$ vs. $\log \epsilon$, over a suitable range of values of ϵ. This range can be estimated by visual inspection of the curve N_ϵ vs. $\log \epsilon$; the curve is approximately linear over the range of values of ϵ where the
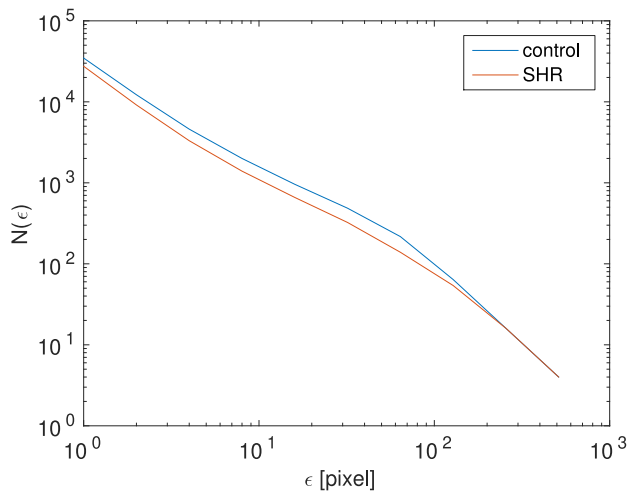
Fig. 2. Sample plot indicating the linear relationship between ϵ and $N(\epsilon)$ for a sample SHR and control case.

Fig. 3. Box plot of the fractal dimension for control and SHR images, respectively.

image has fractal properties, deviating from linearity both for larger and smaller values of ϵ. The estimation of the value of H is performed with classical Least Squares algorithm.

III. RESULTS

The first step of elaborations aimed to assess whether gray-scale or binary images were more suitable for estimating the vessel morphology. From a theoretical viewpoint, the study of the morphology closely relates to a vessel presence/absence criterion that to a "vessel intensity" evaluation, although the latter may provide information about the partial volume effect. However, the high spatial resolution of the data set reduces the effect of partial volume.

Accordingly with this assumption, also supported by some preliminary tests carried out on gray scale images, we opted for the analysis of binary images. The range of variability for the box dimension can be estimated by plotting (in logarithmic scale) the curve N_ϵ vs. $\log \epsilon$. As shown in fig. 2, the relation is almost linear over a large range of scales, thus confirming the suitability of a fractal model to describe the morphology of the vessel network. Visual analysis of the plot indicates that the whole range of scales is suitable for estimating the Haussdorf dimension, thus we selected values of ϵ ranging from 1 to 512 pixel.

The fractal dimension was estimated for all available frames; the correlation r between $\log(N_\epsilon)$ vs. $\log \epsilon$ indicates a strong agreement with a linear relationship, with correlation (expressed as mean $\pm$ standard deviation) $r = 0.9947 \pm 0.0033$ (normal cases $r = 0.9943 \pm 0.0025$, SHR $r = 0.9951 \pm 0.0040$), thus confirming once more the suitability of the fractal model.

The distribution of the fractal dimension D for all frames is shown in fig. 3, while numerical value for mean and standard deviation of estimated values are reported in table I.
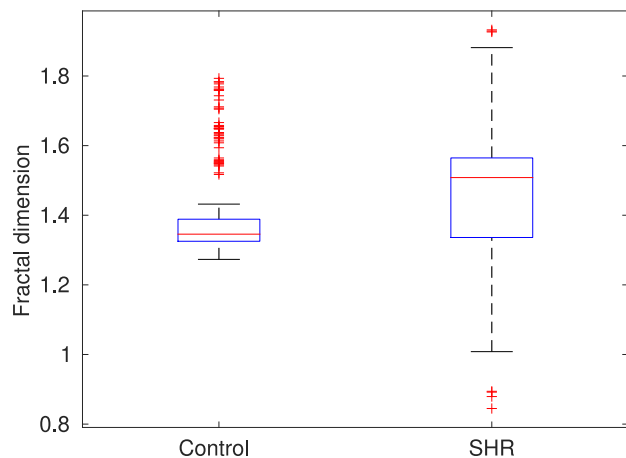
TABLE I
AVERAGE AND STANDARD DEVIATION OF CORRELATION AND FRACTAL DIMENSION. $p < 0.05$ VALUES INDICATE STATISTICALLY SIGNIFICANT DIFFERENCE BETWEEN CONTROLS AND SHR

	Whole dataset	Control	SHR	p
Average correlation	0.9947	0.9943	0.9951	0.044
Standard deviation	0.0033	0.0025	0.0040	
Average H	1.4347	1.4061	1.4706	0.002
Standard deviation	0.1840	0.1366	0.2254	

IV. CONCLUSIONS AND DISCUSSION

Given the small size of the data set, this work focuses on the assessment of the method and the variability of the fractal dimension in different frames and in the different groups. Results indicate that control frames have a small variability, while SHR frames present a much larger variability, suggesting the capillary network is much more irregular. However, the control frames presents several outliers. A closer inspection indicates that outliers corresponds only to frames in the external layers of the tissue, where part of the frames contains larger vessels and some regions having visible structural differences.

In all images, the values of the correlation measured between box size and number of boxes indicates the fractal model is very well suited to describe the structure of the network. A deeper analysis could even improve the estimation procedure, as the plot in fig. 2 suggests there is an inflection point in the curve, that may reflect a change of fractal properties between larger and smaller vessels. Again, the correlation in SHR frames is significantly lower than in control images, although it is still very high. In SHR subjects, indeed, the inflection point appear more visible, suggesting a larger change.

These results show that this approach will be suitable for an accurate 3D multi-scale estimation of the vessel morphology. Also, it is necessary to acquire a much larger data set in order to fully assess the differences between the two group and the physiological variability inside each group. Moreover, it would be interesting to evaluate changes of the parameter with age.

The algorithm needs to be enhanced and validated according to two aspects: first, a deeper analysis of the impact of the binarization algorithm on the estimated values should be performed; preliminary results indicate that a different threshold mostly affects the box counts at smaller sizes, with modest impact on larger scales. Therefore, we expect a variation in the threshold will not dramatically affect the average slope of the curve. Also, the automatic threshold selection performed by the Otsu method does not introduce subjectivity in the procedure. Second, we are working to extend the method to exploit the full 3D structure of the capillary tree, that is available in our dataset. Assuming the topology of the capillary network is isotropic, we expect no significant differences should be present in the 3D analysis; however, the 3D approach would be beneficial both because of the larger number of boxes, thus increasing robustness of the estimate, and fir its ability to detect the presence of anisotropies or spatial irregularities in the fractal distribution, as suggested by the 2D estimates. Unfortunately, the non-integer re-sampling required to obtains isotropic 3D data would introduce significant approximation and interpolation artifacts. We envisage two possible solution for overcoming this issue, in order not to jeopardize the estimation procedure: either a specialized interpolation method needs to be developed, or a custom box counting algorithm, keeping account the different spatial resolution will be deigned.

REFERENCES

[1] P. Bagher and S. S. Segal, "Regulation of blood flow in the microcirculation: role of conducted vasodilation," *Acta Physiol (Oxf)*, vol. 202(3), p. 271-284, 07 2011.

[2] L. Bocchi, A. Evangelisti, M. Barrella, L. Scatizzi, and M. Bevilacqua, "Recovery of 0.1hz microvascular skin blood flow in dysautonomic diabetic (type 2) neuropathy by using frequency rhythmic electrical modulation system (frems)," *Medical Engineering and Physics*, vol. 32, no. 4, pp. 407–413, 2010.

[3] C. Aalkjær, D. Boedtkjer, and V. Matchkov, "Vasomotion – what is currently thought?" *Acta Physiol (Oxf)*, vol. 202(3), p. 253-269, 04 2011.

[4] B. Schwartzkopff, W. Motz, H. Frenzel, M. Vogt, S. Knauer, and B. E. Strauer, "Structural and functional alterations of the intramyocardial coronary arterioles in patients with arterial hypertension." *Circulation*, vol. 88, no. 3, pp. 993–1003, 1993. [Online]. Available: https://www.ahajournals.org/doi/abs/10.1161/01.CIR.88.3.993

[5] K. Imamura, "Ultrastructural aspect of left ventricular hypertrophy in spontaneously hypertensive rats: A qualitative and quantitative study," *Japanese Circulation Journal*, vol. 42, no. 8, pp. 979–1002, 1978.

[6] J.-W. Gu, L. Fortepiani, J. Reckelhoff, T. Adair, J. Wang, and J. Hall, "Increased expression of vascular endothelial growth factor and capillary density in hearts of spontaneously hypertensive rats," *Microcirculation*, vol. 11, no. 8, pp. 689–697, 2004.

[7] I. Giuvărășteanu, "Scanning electron microscopy of vascular corrosion casts - standard method for studying microvessels," *Romanian journal of morphology and embryology = Revue roumaine de morphologie et embryologie*, vol. 48, pp. 257–61, 02 2007.

[8] M. Campisi, Y. Shin, T. Osaki, C. Hajal, V. Chiono, and R. Kamm, "3d self-organized microvascular model of the human blood-brain barrier with endothelial cells, pericytes and astrocytes," *Biomaterials*, vol. 180, pp. 117–129, 2018.

[9] M. Righi, M. Belleri, M. Presta, and A. Giacomini, "Quantification of 3d brain microangioarchitectures in an animal model of krabbe disease," *International journal of molecular sciences*, vol. 20, no. 10, 2019.

[10] I. Costantini, G. Mazzamuto, A. Laurino, E. Lazzeri, L. Sacconi, M. Neri, A. Simonetto, M. Roffilli, L. Silvestri, and F. Pavone, "Three-dimensional analysis of human brain cytoarchitectonics by means of a switch/tde-combined clearing method," in *Progress in Biomedical Optics and Imaging - Proceedings of SPIE*, vol. 11076, 2019.

[11] K. Chung, J. Wallace, S.-Y. Kim, S. Kalyanasundaram, A. Andalman, T. Davidson, J. Mirzabekov, K. Zalocusky, J. Mattis, A. Denisin, S. Pak, H. Bernstein, C. Ramakrishnan, L. Grosenick, V. Gradinaru, and K. Deisseroth, "Structural and molecular interrogation of intact biological systems," *Nature*, vol. 497, 04 2013.

[12] I. Costantini, J.-P. Ghobril, A. P. Di Giovanna, A. L. Allegra Mascaro, L. Silvestri, M. C. Müllenbroich, L. Onofri, V. Conti, F. Vanzi, L. Sacconi, R. Guerrini, H. Markram, G. Iannello, and F. Pavone, "A versatile clearing agent for multi-modal brain imaging," *Scientific reports*, vol. 5, 04 2015.

[13] A. Di Bona, V. Vita, I. Costantini, and T. Zaglia, "Towards a clearer view of sympathetic innervation of cardiac and skeletal muscles," *Progress in Biophysics and Molecular Biology*, 2019.

[14] N. Pianca, A. Di Bona, E. Lazzeri, I. Costantini, M. Franzoso, V. Prando, A. Armani, S. Rizzo, M. Fedrigo, A. Angelini, C. Basso, F. Pavone, M. Rubart, L. Sacconi, T. Zaglia, and M. Mongillo, "Cardiac sympathetic innervation network shapes the myocardium by locally controlling cardiomyocyte size through the cellular proteolytic machinery," *Journal of Physiology*, vol. 597, no. 14, pp. 3639–3656, 2019.

[15] P. Tsai, J. Kaufhold, P. Blinder, B. Friedman, P. Drew, H. Karten, P. Lyden, and D. Kleinfeld, "Correlations of neuronal and microvascular densities in murine cortex revealed by direct counting and colocalization of nuclei and vessels," *The Journal of neuroscience : the official journal of the Society for Neuroscience*, vol. 29, pp. 14553–70, 11 2009.

[16] L. Frassineti, F. Giardini, A. Perrella, M. Sorelli, L. Sacconi, and L. Bocchi, "Evaluation of spatial distribution of skin blood flow using optical imaging," in *IFMBE Proceedings*, vol. 62, 2017, pp. 74–80.

[17] N. Sarkar and B. B. Chaudhuri, "An efficient differential box-counting approach to compute fractal dimension of image," *IEEE Transactions on Systems, Man, and Cybernetics*, vol. 24, no. 1, pp. 115–120, Jan 1994.

Development of a capnometer for extracorporeal life support devices: compensation of the temperature effect on the mid-IR LED

M. Bellancini[1], L. Cercenelli[2], S. Severi[1] and E. Marcelli[2]

[1] DEI-Electric,Electronic and Information Dept., University of Bologna, Bologna, Italy
[2] DIMES-Experimental Diagnostic and Specialty Medicine Dept., University of Bologna, Bologna, Italy

Abstract—Measurement of carbon dioxide (CO_2) in medical application is a well established clinical procedure to evaluate patient's respiratory functionality. Even though measurement of CO_2 is associated with the respiratory monitoring filed, its application has been proven useful also in extracorporeal life support application (ECLS) . In order to measure the CO_2 concentration removed through the extracorporeal circulation procedure, a capnometer (CO_2 sensor) is applied at the exhaust port of the membrane oxygenator. In ECLS procedures, water vapor condensation at the oxygenator exhaust port often prevents the CO_2 concentration measure. To avoid the water vapor condensation adverse effect, a heating system can be implemented in the CO_2 sensor. This work focuses in the analysis of the temperature effect introduced by the heating system on a prototype of CO_2 sensor specifically designed for ECLS application, and proposes a method to compensate the temperature effect on the sensor optical signal. The proposed method consists in a real-time algorithm for temperature compensation that exploits a compensation coefficient experimentally determined, that allows to reduce signal variation due to thermal oscillations of the heating system.

Keywords—Capnometry, mid-IR, temperature compensation, extracorporeal life support devices.

I. INTRODUCTION

Capnometry is the measurement of carbon dioxide (CO_2) concentration in respiratory gases [1]. Even if the traditional use of capnometry is related to respiratory monitoring field, the use of this measurement in extracorporeal life support application, such as cardiopulmonary bypass (CPB) and extracorporeal membrane oxygenation (ECMO) has been proved [2], [3]. In particular, a capnometer (CO_2 sensor) can be placed at the exhaust port of an extracorporeal oxygenator ("oxygenator exhaust capnometry") in order to monitor the CO_2 removed from the patient. Oxygenator exhaust capnometry could represent a useful tool for ExtraCorporeal Life Support (ECLS) devices and procedures like ECCO2R (Extracorporeal Carbon Dioxide Removal) and ECMO (Extracorporeal Membrane Oxygenation), providing data relevant to CO_2 removal rate and allowing the operator to set the optimal treatment parameters (e.g blood flow and sweep gas flow), as well as to monitor the progress of the therapy. The working principle of capnometry is well known, and it is based on mid-infrared spectroscopy: CO_2 molecules have the ability to absorb infrared energy in the wavelength region between 4200-4300 nm; as the infrared light is passed through a sample of gas, the amount of infrared light absorbed is proportional to the concentration of CO_2 in the sample, as described by the Bourger-Lambert-Beer's Law [4]. Emission and detection of the wavelengths of interest for CO_2 spectroscopy can be obtained using LED and a Photodiode (PD) that work in the mid-IR region. Despite its relative easiness, the oxygenator exhaust capnometry is not routinely applied, since some practical issues remain to be solved to provide a reliable measurement of CO_2 removal from the patient. One of the main obstacles to CO_2 measurement at the exhaust port of a membrane oxygenator is the condensation of the water vapor contained in the gas exhaust on the optical elements of the CO_2 sensor. The water vapor condensation causes degradation of the signal acquired by the sensor and therefore an incorrect estimation of CO_2 concentration. A method that can be used to avoid water vapour condensation on the sensor consists in the implementation of a heating system that increases the temperature of the sensor. However, temperature variations on the optical elements introduced by the heating system affect the measured signal and consequently the CO_2 estimation. This work addresses the issue relevant to temperature effect on the performances of the emitter mid-IR LED of a CO_2 sensor designed for ECLS application and describes a compensation method proposed to solve this issue.

II. MATERIAL AND METHODS

The sensor used for this study is a prototype of a capnometer specifically designed for extracorporeal applications. The sensor can be directly attached to the exhaust port of a membrane oxygenator allowing the gas to flow inside a measuring chamber crossed by the infrared beam. The developed CO_2 sensor is made up by three subsections:

1) emission stage for the generation of the mid-IR beam;
2) receiver stage for the detection, conditioning and amplification of the optical signal after CO_2 absorption;
3) CPU for signal acquisition, processing and communication with a host device.

For both emission and detection of the mid-IR beam, optical elements of InAsSb/InAs (LED Microsensor NT, Saint-Petersburg, Russia) are used. The gas flows inside a plastic cuvette (**Fig. 1-b**), mid-IR beam generated by the emitter LED (**Fig. 1-a 4**) crosses the gas contained in the plastic cuvette, and
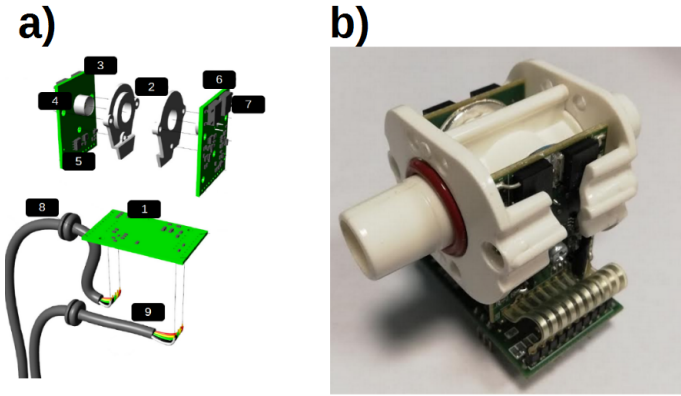
Fig. 1: a) Exploded drawing of the CO_2 sensor: 1) CPU board; 2) aluminum rings; 3) emitter board; 4) InAsSb/InAs element; 5) digital temperature sensor; 6) receiver board; 7) heating resistances; 8) Flow sensor communication cable; 9) power supply/RS-485 cable. b) Assembly of the developed CO_2 and plastic cuvette.

Fig. 2: Simulated emitted optical power

Fig. 3: (a) Output of the numerical simulation for the emitted optical power using the acquired temperature data, (b) Acquired signal from the capnomter, (c) Acquired temperature data.

is detected by the receiver element (**Fig. 1-a 6**). The optical signal is then amplified, conditioned and acquired by the CPU board(**Fig. 1-a 1**). Observing the variation of the acquired signal the concentration of CO_2 is determined. The implemented heating system is composed by: resistances mounted on rear of the electronics boards that generates heat(**Fig. 1-a 7**); an aluminum ring that surrounds the optical elements (**Fig. 1-a 2**) and conduces the generated heat along the measuring chamber; digital temperature sensor for the temperature monitoring(**Fig. 1-a 5**). CPU controls the temperature of the emitter and the receiver stages by switching ON and OFF the current circulating in the resistances. In order to prevent water vapor condensation, the system temperature is set at 42 °C, since the oxygenator exhaust gas temperature during ECLS procedure is around 38 °C. Data relevant to optical signal and temperature at the emitter and receiver stages are transmitted on RS-485 communication line, and acquired through a PC software.

III. THEORETICAL ANALYSIS

A. Mathematical description of temperature effect on the mid-IR LED

From literature it is known that emission power for InAsSb/InAs LEDs can be mathematically described by a Lorentzian function [5]:

$$P_{LED}(\lambda, T) = \frac{P0}{\pi} \cdot \frac{\Delta\lambda(T)}{\Delta\lambda(T)^2 + (\lambda - \lambda max(T))^2} \quad (1)$$

where P0 is the total output power [μW], λ is the wavelength [nm], $\Delta\lambda$ and λmax are the FWHM and peak wavelength of the emission spectra, respectively. Within the temperature range 0-50°C the following relationships are valid: $\Delta\lambda(T) \sim$ 0.1 $\lambda max(T)$ and dλmax/dT=4.5 nm/ °C. Solving equation (1) it is possible to describe the LED emission spectra at different temperatures, as well as the dependence between the temperature of the optical element and the emission power of the optical element, as reported in **Fig. 2**. A negative
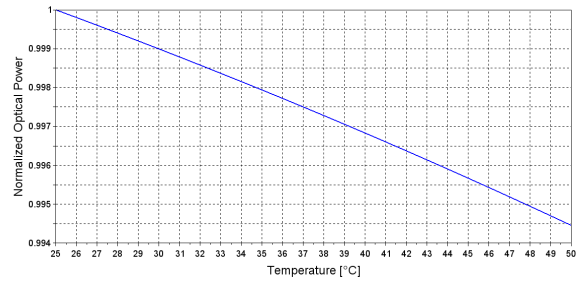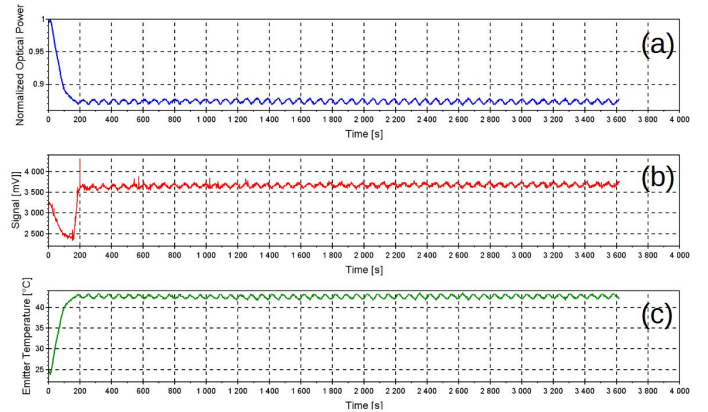
correlation between temperature and emitted power can be observed.

B. Numerical Simulation of Capnometer Signal

Numerical simulation, performed using Matlab, allows description of the signal decrease due to the initial temperature increase, related to the activation of the heating system, as well as description of the signal oscillations due to temperature variations related to the hysteretic behaviour of the heating system controller. This behaviour, described by numerical simulation (**Fig. 3-a**), is also verified by the acquired data (**Fig. 3-b**), confirming the correctness of the theoretical analysis. In **Fig. 3-b**, the signal increase in the initial portion of the figure is due to an higher current provided to the emitter LED by the system, necessary to allow the sensor to work properly. As shown in **Fig. 3-c** , the implemented heating system introduces oscillation in the optical element temperature, and therefore in the optical signal. In order to improve sensor accuracy a method to stabilize the optical signal is therefore needed.

IV. DEVELOPMENT OF THE COMPENSATION ALGORITHM

Linear correlation between the optical power and the temperature, as highlighted by the theoretical analysis, has been checked for the real system, by analysing the correlation between the acquired signal and the temperature of the emitter stage. Since the temperature sensor is not placed next to
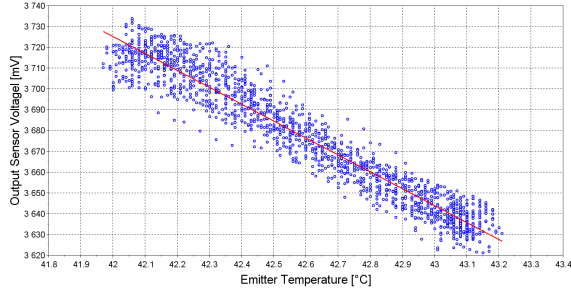
Fig. 4: Experimental evaluation of correlation between emitted output power and emitter stage temperature. Blue dots represent the sampled value of the output sensor voltage at several temperatures of the emitter stage. Red line represents the linear regression of the data.

Fig. 5: Comparison between the output of the compensation algorithm (blue) and the output of the filter currently implemented in the prototype (dashed red). In yellow, the originally acquired capnometer signal.

the optical element but is in contact with the aluminium ring of the heating system, temperature dynamics recorded by the temperature sensor does not represent the temperature dynamics of the optical elements. The reason is the thermal inertia introduced by the aluminium element, that introduces a delay in heat diffusion. Therefore, in order to correct the error in the acquisition of temperature data due to the position of the temperature sensor, digital filtering has been implemented on optical and temperature signal. In particular, two moving average filters with different windows width have been used to filter the acquired signal and the temperature. Using of the above mentioned filters allows to compensate the delay of the heat diffusion, and obtain temperature data that better describe the optical element temperature changes. Further, in order to study the effect of the temperature on the emitter stage, the heating system of the receiver stage has been disabled. In this way the signal data acquired are not affected by the temperature effect on the receiver stage. **Fig. 4** shows the distribution of the acquired signal values over optical element temperature and the relevant regression line, defined by a coefficient R^2=0.932. The experimental results confirm the negative correlation between emitted optical power and optical element temperature. Based on the obtained linear regression, a compensation algorithm has been developed, as expressed in Equation (2):

$$Signal_{adjusted} = Signal_{filtered} + (T_{ref} - T_{filtered}) \cdot r \quad (2)$$

where $Signal_{adjusted}$ is the signal compensated for the temperature effect, $Signal_{filtered}$ is the output of the moving average filter applied to the acquired signal, T_{ref} is a reference temperature (mean value of the emitter stage temperature at steady state), $T_{filtered}$ is the output of the moving average filter applied to the temperature data. Output of the compensation algorithm has been further filtered through a moving average filter to improve signal stability. The proposed compensation algorithm allows the real-time correction of the signal acquired by sensor. In order to check efficiency of the proposed solution, compensation algorithm output has been compared to the optical signal filtered with a moving average filter, with filtering width of 90
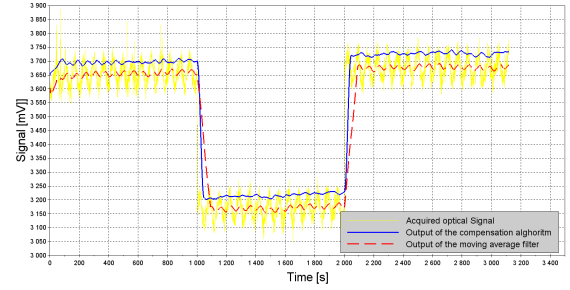
samples (to compensate the temperature variation period of the sensor). The new solution based on the proposed compensation algorithm gives a result similar to the one obtained with the moving average in terms of signal stability (SD= + 6.29 mV vs SD= + 7.38 mV) . However, the compensation algorithm allows a shorter response time, as reported in **Fig. 5**. in which a signal variation has been introduced applying a gas flow with CO_2 concentration of 2,5%. The increment of CO_2 causes the signal to decrease from approx. 3650 mV (signal value with environmental CO_2 concentration) to approx. 3200 mV. Further, as shown by **Fig. 5**, without any compensation, due to thermal effect the optical signal is characterized by high instability that reduce the accuracy of the sensor. Without any compensation, when a gas with CO_2 concentration of 2,5 % is applied at the sensor inlet, the concentration measured by the sensor is 2,5 % $\pm$ 1 %. With the proposed compensation method when a gas with CO_2 concentration of 2,5 % is applied at the sensor inlet, the concentration measured by the sensor is 2,5 % $\pm$ 0,1 %.

V. CONCLUSION

Temperature variation of the emitter optical element of the developed CO_2 affects optical signal stability, therefore in order to improve sensor accuracy a method to compensate this adverse effect needs to be implemented. Sensor signal variation, caused by the heating system implemented to avoid water vapour condensation, has been described through numerical simulation based on mathematical formulation found in the literature. A negative linear correlation between the capnometer signal and the emitter optical element temperature was found and was confirmed by experimental data acquired through the sensor prototype. Based on this analysis a compensation algorithm was implemented. The new solution based on the compensation algorithm allows to obtain a stable signal, improving the response time of the sensor, and higher accuracy . Future improvements will involve the analysis of the temperature effect on the receiver (PD) stage, and eventually the update of the compensation algorithm in order to take also this effect into account.

REFERENCES

[1] Daniel P. Davis. "Quantitative capnometry as a critical resuscitation tool". In Journal of Trauma Nursing 12.2 (2005), p. 40.

[2] Baraka et al. "Oxygenator exhaust capnography for prediction of arterial carbon dioxide tension during hypothermic cardiopulmonary bypass". In The journal of extra-corporeal technology 37.2 (2005), p. 192.

[3] Montalti et al. "Continuous monitoring of membrane lung carbon dioxide removal during ECMO: experimental testing of a new volumetric capnometer". In Perfusion (2019), pp. 538–543.

[4] T.-V. Dinh, I.-Y. Choi, Y.-S. Son and J.-C. Kim, "A review on non-dispersive infrared gas sensors: Improvement of sensor detection limit and interference correction". In Sensors and Actuators B: Chemical (2016), pp. 529–538.

[5] Aleksandrov et al. "Simulation of characteristics of optical gas sensors based on diode optopairs operating in the mid-IR spectral range". In Technical Physics 54.6 (2009), pp. 874–881.

Unassisted in-vitro simulation of superior cavo pulmonary shunt for evaluation of pathophysiological issue

F. De Gaetano[1], M. Griselli[2] and M.L Costantino[1]

[1] *LaBS, Dept. of Chemistry, Materials and Chemical Engineering "Giulio Natta", Politecnico di Milano, Milan, ITALY*
[2] *Division of Pediatric Cardiac Surgery, Dept. of Surgery, University of Minnesota Masonic Children's Hospital, MN, USA*

Abstract— In this study, a new in-vitro test bench of the bidirectional superior cavo-pulmonary connection (BCPC), which can mimic realistic conditions, was developed to provide the physician with a platform onto which to test surgical procedures outcomes by acquiring local measurements of the relevant hemodynamic quantities. Using values of resistances and compliance from literature data, a simplified lumped parameters model was designed to fit patients from 2 to 5 years. The mock loop circulation developed in this work was validated by using the in-vivo catheterization data from 20 patients.

All the parameters were first set to obtain physiological condition. Then four different dysfunctions were mimicked: diastolic dysfunction, systolic dysfunction, cavo-pulmonary intrinsic failure and a complex mix of these failures.

The measured pressure and flow rate showed an excellent correlation with the clinical catheterization data acquired in BCPC. This new in-vitro test bench can be a handy tool capable of providing better insight on how to treat these patients and which devices to employ in different clinical scenarios.

*Keywords—*Bidirectional superior cavo pulmonary connection, in-vitro test bench, paediatric circulation, TCPC.

I. INTRODUCTION

Mechanical circulatory support (MCS) for failing single ventricle physiology is a complex and challenging problem, which has not yet been satisfactorily addressed.

Today, the total cavo-pulmonary connection (TCPC) is performed as the final stage to achieve the so-called "Fontan Circulation", and this is obtained through two- or three-stage strategy for children suffering from a wide range congenital cardiac defects not suitable for two-ventricle repair. The bidirectional superior cavopulmonary connection (BCPC), historically and still inappropriately called "Glenn procedure", remains a fundamental intermediate step for these kinds of patients towards the "Fontan circulation".

Many centres advocate the intermediate palliation with a BCPC to improve the long-term outcome of the Fontan circulation [1], [2]. The advantages of BCPC as primary or second-stage palliative procedure include the relief of the volume load on the single ventricle, improvement in atrioventricular valve regurgitation, avoidance of pulmonary artery distortion after pulmonary artery banding or systemic-to-pulmonary artery shunts and prevention of the possible pulmonary vascular obstructive disease that can be developed with prolonged systemic-to-pulmonary shunting [3].

Clinical data show that the BCPC provides excellent early and midterm palliation, with a low incidence of reoperation [4]–[6].

Nowadays, the perioperative mortality rate has declined to 2%, due to improved patient selection, better adjustment of pulmonary blood flow, and to the refinement of the BCPC [7]. Perfect univentricular physiology is, however, an elusive goal. The TCPC represents the best haemodynamic compromise, but it could result in a cluster of multi-organ complications. Recently, an increasing number of single ventricle patients surviving the various stages of palliation showed a severe deterioration of the haemodynamic state requiring mechanical assist support. In-vitro simulation of the clinical situation, which can mimic realistic conditions [8], would provide the physician with a platform onto which to test surgical procedures outcomes by acquiring local measurements of the relevant hemodynamic quantities. Several models of the single-ventricle Fontan and failing Fontan circulation were developed [9]–[11] but, despite the importance, there is a lack of in-vitro model mimicking the BCPC [12]. Development of an in-vitro test bench reproducing the BCPC may provide more targeted treatment options to solve the underlying causes of failure. The optimal management of patients with single ventricular physiology complicated by pulmonary hypertension and elevated pulmonary vascular resistance (PVR) remains undefined [13]. The test bench developed in this work can be an optimal tool to investigate the best way to manage patients with failing cavo-pulmonary circulation. This in-vitro system is aimed at reproducing the proper haemodynamic conditions.

II. MATERIALS AND METHODS

In the MCS here described, the BCPC was schematized by using a single ventricle connected both to the lower body (LB) and to the upper body (UB) circulation. The superior vena cava (SVC) connects the UB to the pulmonary circulation, while the inferior vena cava (IVC) connects the LB to the common atrium. The loop is closed by connecting the pulmonary circulation to the common atrium (Fig.1). UB, LB and pulmonary circulation were each one described by a variable linear resistance, compliance, and imposed inertance elements.

These elements allow the replication of the haemodynamics both in physiological and in pathological BCPC patients. The single ventricle was reproduced by using a 15 cc pulsatile VAD (Excor®, Berlin Heart, Germany). The Ikus Driving Unit (Berlin Heart, Germany) was set to give to the VAD the right supply pressure to control the stroke volume, the heart rate and the systolic ratio.
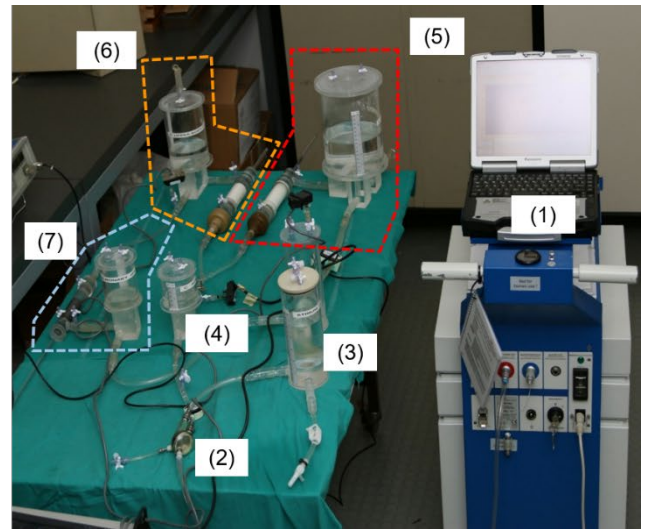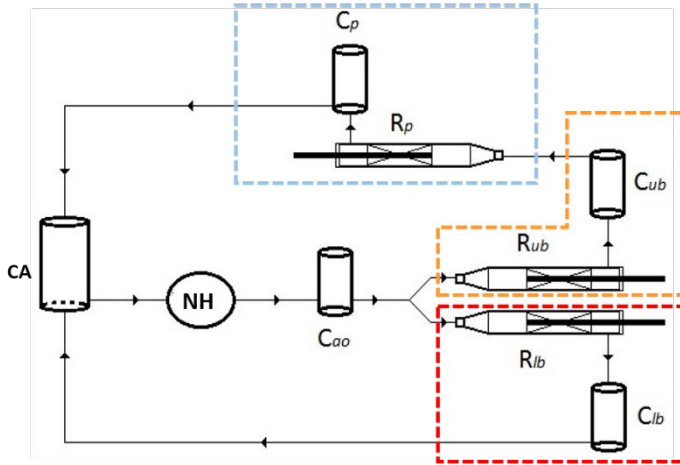
Fig. 1 Sketch (left) and picture (right) of the in-vitro test bench. The test bench is made by the Ikus unit (1), the native heart (NH) obtained using a 15 cc Excor® VAD (2), the common atrium (CA, 3), the aortic compliance (C_{ao}, 4) and the lower body (5), upper body (6) and pulmonary (7) blocks.

With references to the value of resistances and compliance from literature data [14], a simplified lumped parameters model was designed to fit patients from 2 years (BSA = 0.55 m²) to 5 years (BSA = 0.74 m²). To verify the reliability of the lumped parameter model in both physiological and pathological conditions, an electrical equivalent of the test bench was implemented in Simulink (Matlab®, Mathworks, MA, USA). It is important to remark that this mathematical model was created only to aid in the construction of the in-vitro test bench and not to support the clinical decision. All the value of the parameters used to mimic the BCPC physiological conditions in 4 years old patients are summarized in Table I. After the validation comparing the mathematical model with in-vivo catheterization performed on 20 patients, the elements of the MCS were built up.

In general, the solution chosen to make up hydraulic resistances consisted in preparing arrays of tubes of small diameter [15] [16]. If a rigid tube was used to build the resistance, the Poiseuille's law would be used to calculate the value of the resistance. It would thus be possible to obtain the desired value of the hydraulic resistance by adding an appropriate number of identical tube elements connected in parallel. With this solution, it is possible to get different values of resistances, but their setting could result quite difficult in replicating both pathological and physiological values with a single component. If a range of different values would need to be simulated, other resistors should be developed, and their dimensions could result quite large.

To overcome this issue, we developed the resistance elements taking into account Darcy's law that describes the fluid flow through a porous medium. Different cylinders with different porosity were 3D printed (3D Printer M2, Makergear, Ohio, USA) using a layer resolution of 50 μm, a nozzle size of 0.35 mm and a brass plate heated at 110°C. The 3D printed cylinders were tested to evaluate permeability. After setting the cross-section area (A) of the resistive element, and knowing the permeability (k), the length (L) was set to obtain the maximum resistance. A, k and L are set and selected to reproduce the values of resistances from literature data using water as working fluid in the test-bench. A sliding stick

inserted into the porous cylinder allows setting different values of the resistance. Moving the bar all along the length, the wet area can be increased or decreased reducing or increasing the hydraulic resistance, respectively (Fig. 2).
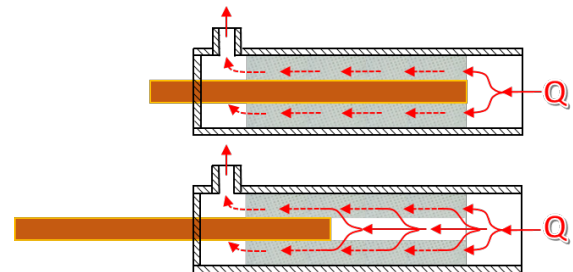

Fig. 2 Sketch of the resistor made by a porous cylinder (in grey) with a sliding stick inside used to modify the value of the resistance. Q is the flowrate that comes from right to left.

The physical solutions to obtain compliances are based on the use of the elastic properties of air. The hydro-pneumatic compliance consists of a tank partially filled with liquid with a volume of air above it. The inertial effects are present in all the types of lumped parameter hydraulic components and cannot be eliminated but rather minimized. Connection tubes are always present in hydraulic circulatory models and are, in general, the most crucial source of inertial effects. The proper choice of the connection tubes dimensions can help in controlling the role of inertial components in the circuit. The MCS was equipped with ¼"- to ½" internal diameter Tygon tubing with negligible compliance.

Instantaneous flow rates were measured by using a transit-time ultrasound flowmeter (HT110 series, Transonic System, Ithaca, NY, USA).

Pressures were measured by pressure transducers (140 PC pressure sensor, Honeywell, NY, USA). Flow and pressure were sampled at 200Hz using a proper acquisition system DAQPad-6020E (National Instruments, Inc., Austin, TX, USA). Water at 22°C (density of ρ = 1000 kg/m³ and viscosity of μ = 0.001 Pa·s) was used in these experiments. All the tests were performed setting the Ikus Driving Unit at a heart rate of 130 bpm and systolic time of 35%.

TABLE I

Par.	Value	Par.	Value
R_{AO}	$4.00 \left[\frac{mmHg \cdot min}{l}\right]$	L_{AO}	$3.0 \cdot 10^{-3} \left[\frac{mmHg \cdot s^2}{l}\right]$
R_{UB}	$0.65 \left[\frac{mmHg \cdot min}{l}\right]$	C_{AO}	$3.0 \cdot 10^{-4} \left[\frac{l}{mmHg}\right]$
R_{LB}	$0.82 \left[\frac{mmHg \cdot min}{l}\right]$	L_{UB}	$6.0 \cdot 10^{-4} \left[\frac{mmHg \cdot s^2}{l}\right]$
R_P	$5.00 \left[\frac{mmHg \cdot min}{l}\right]$	C_{UB}	$1.6 \cdot 10^{-3} \left[\frac{l}{mmHg}\right]$
R_{IVC}	$0.50 \left[\frac{mmHg \cdot min}{l}\right]$	L_{LB}	$1.8 \cdot 10^{-3} \left[\frac{mmHg \cdot s^2}{l}\right]$
R_{SVC}	$0.10 \left[\frac{mmHg \cdot min}{l}\right]$	C_{LB}	$4.3 \cdot 10^{-3} \left[\frac{l}{mmHg}\right]$
L_P	$1.9 \cdot 10^{-3} \left[\frac{mmHg \cdot s^2}{l}\right]$	C_P	$5.3 \cdot 10^{-3} \left[\frac{l}{mmHg}\right]$

Parameters used in the electrical model of the BCPC physiological conditions, then replicated in the in-vitro test bench.

Physiological conditions were replicated and compared with catheterization data obtained from 20 children with Glenn circulation. BCPC circulation can fail for many reasons. Systolic dysfunction, diastolic dysfunction, elevated PVR, and a combination these "failing" Glenn physiology [17], were simulated.

III. RESULTS

Measured pressure and flow values are compared directly to the catheterizations obtained from 20 patients (Table 2) aged 4 years old on average (BSA = 0.68 m^2). Signals were averaged on 30 seconds of contiguous cycles. Systolic and diastolic pressures were set in the physiological condition at 115 mmHg and -17.5 mmHg, respectively, to achieve an ejection fraction of 66%.

Setting the Glenn resistance, the resistance of the shunt, to "physiological" value of 1 wood unit (1 WU = 1 mmHg · min · l^{-1}) it was possible to achieve a mean flow rate equal to 1.32 ± 0.07 l/min, a mean aortic pressure (MAP) of 87 mmHg a pulmonary arterial pressure (PAP) of 10 mmHg and an atrial pressure (AP) of 4 mmHg.

The trans-gradient pressure (TGP) the difference between PAP and AP is 4 mmHg. All these values are very close to the in-vivo catheterizations, only the PAP (and consequently the TGP) in the in-vitro test was 1 mmHg higher than the pressure in the in-vivo conditions. Four different dysfunctions were replicated. To mimic the diastolic dysfunction, the diastolic pressure was increased from -17.5 mmHg to -12.5 mmHg, the systolic pressure was kept constant at 115 mmHg, and the aortic resistance was adjusted (decreased) to obtain the same flow rate of the physiological condition (1.32 l/min). In these conditions, the PAP remains constant while the MAP decreases to 75 mmHg. As expected with the diastolic dysfunction, the AP raise from 6 to 8.2 mmHg. Starting from the physiological condition, to take off the systolic dysfunction, only the diastolic pressure was increased from -17.5 mmHg to -10 mmHg. As expected, the flow rate and consequently, the MAP decrease to 0.95 l/min and 58 mmHg, respectively. Even in this case, the AP increase a lot from 6 to 9.8 mmHg while the PAP raises from 11 to 12 mmHg. To mimic the elevate PVR dysfunction, characterized by a very high cavo-pulmonary resistance that can lead to increased pulmonary artery pressures, the Glenn resistance was set to the pathological value of 4 WU. As anticipated, the cardiac output and the MAP does not chance from the physiological condition, while the PAP and the AP step up to 16 mmHg and 8.8 mmHg, respectively. In addition, the TGP increase from 6 mmHg to 8.8 mmHg. In the end, a complex mix of the previous failures was mimicked. Starting from physiological conditions, diastolic pressure and Glenn resistance were increased to 100 mmHg and 4 WU, respectively while the systolic pressure was reduced to 100 mmHg. Despite the decreasing of the cardiac output from 1.32 l/min to 1.1 l/min, the PAP increased from 10 mmHg to 16 mmHg, and the AP moved from 6 mmHg to 10 mmHg, the highest value ever achieved during these experiments.

TABLE II

Param.	Units	In-Vivo	In-Vitro				
		Physiological	Physiological	Diastolic dysfunction	Systolic dysfunction	Elevate PVR	Mixed type
Systolic Pressure	$[mmHg]$	[-]	115	115	115	115	100
Diastolic Pressure	$[mmHg]$	[-]	-17.5	-12.5	-10.0	-17.5	-10.0
Glenn Resistance	$\left[\frac{mmHg \cdot min}{l}\right]$	[-]	1	1	1	4	4
Flow rate	$[l/min]$	1.30	1.32	1.32	0.95	1.30	1.10
PAP	$[mmHg]$	11.3	10.0	11.0	12.0	16.0	16.2
AP	$[mmHg]$	6.2	7.0	8.2	9.8	8.8	10.0
TGP	$[mmHg]$	5.1	4.0	3.0	2.0	7.0	6.0
MAP	$[mmHg]$	70-90	87	75	58	86	70

Data obtained from catheterization and in-vitro tests. The catheterization data came from 20 children that were in stable Glenn circulatory conditions at the Newcastle Childhood Hospital (UK). Systolic and diastolic pressure were set by the Ikus while Glenn resistance was set in the test bench. Physiological condition, systolic dysfunction, diastolic dysfunction, elevated pulmonary vascular resistance (PVR), and a combination these "failing" Glenn physiology (Mixed type) were reproduced.

As expected, due to the decreasing of the cardiac output and having kept the aortic resistant constant, the MAP decreased from 87 mmHg to 70 mmHg. Table 2 resumes the variations of flow rate, PAP, AP, TGP and MAP both in in-vivo (physiological) and in-vitro (physiological or failure) conditions.

IV. Discussion

We believe we have developed a very detailed in-vitro model of the bidirectional cavo-pulmonary circulation amenable of adjustments due to changing pathophysiological conditions. The measured pressure and flow rate showed an excellent correlation with the catheterization data from 20 patients in a BCPC pre-TCPC. Four pathological BCPC circulations were well reproduced by changing one parameter at a time or all at once. Observation of the response of the "patient" by changing one parameter at a time or all at once is possible with this model, allowing us to understand how to establish the most suitable MCS. In all the pathological conditions mimicked, the AP increased. It is well known [17] that it is necessary to employ a MCS not only to restore the correct cardiac output but also to offload the atrium and reduce the AP, the PAP and consequently the TGP. The selection strategy for patients who benefit the most from the device continues to evolve. It remains controversial which type of MCS we should use, either VA-ECMO or VADs (with continuous or pulsatile flow, axial or centrifugal) and in which positions (atrial-arterial or ventricular-arterial cannulation). It has been proposed that the optimal mechanism for supporting univentricular patients depends on the aetiology of failure [17], for this reason, a tool capable of reproducing different mechanism of failures could be very useful to understand better how to treat these patients. In several clinical scenarios it remains controversial which type of MCS surgeons should use; using this new in-vitro test bench, it is possible to set patient-specific parameters to understand better how to treat this patient and which device is more appropriate for that pathology. In the experiments reported in this work, we have used the Berlin Heart Excor pulsatile pump as baseline native heart and ventricular assist device. The reason for this choice was mainly related to the size of patients whose cardiac catheterisation data were used as a reference. These children with single ventricle failure nowadays are only supported with Berlin Heart Excor being it the only available device for small size patients. However, the mock circulatory system can be easily connected to other ventricular assist devices like non-pulsatile pumps, either axial or centrifugal, leaving the Berlin Heart Excor as native heart as it allows easy adjustments to mimic the different types of failure and can allow reproducing the effects of the neurohormonal response (i.e. vasoconstriction due to low cardiac output etc.), by adjusting upper and lower body resistance. The proposed mock circulatory system can also be easily turned into a TCPC model by connecting the inferior vena cava draining the LB to the pulmonary artery system instead of the left atrium, or into the already mentioned and reproduced clinical scenarios or be connected to other different assist devices.

References

[1] Freedom RM, Nykanen D, Benson LN. The physiology of the bidirectional cavopulmonary connection. Ann Thorac Surg. 1998;66(2):664-667. doi:10.1016/S0003-4975(98)00618-3.

[2] Kopf GS, Laks H, Stansel HC, Hellenbrand WE, Kleinman CS, Talner NS. Thirty-year follow-up of superior vena cava-pulmonary artery (Glenn) shunts. J Thorac Cardiovasc Surg. 1990;100(5):661-662.

[3] Reddy VM, McElhinney DB, Moore P, Haas GS, Hanley FL. Outcomes after bidirectional cavopulmonary shunt in infants less than 6 months old. J Am Coll Cardiol. 1997;29(6):1365-1370. doi:10.1016/S0735-1097(97)00068-5.

[4] Lamberti JJ, Spicer RL, Waldman JD, et al. The bidirectional cavopulmonary shunt. J Thorac Cardiovasc Surg. 1990;100(1):22-30.

[5] Hopkins RA, Armstrong BE, Serwer GA, Peterson RJ, Oldham HN. Physiological rationale for a bidirectional cavopulmonary shunt. A versatile complement to the Fontan principle. J Thorac Cardiovasc Surg. 1985;90(3):391-398.

[6] Bridges ND, Jonas R a, Mayer JE, Flanagan MF, Keane JF, Castaneda a R. Bidirectional cavopulmonary anastomosis as interim palliation for high-risk Fontan candidates. Early results. Circulation. 1990;82(5 Suppl):IV170-6.

[7] Mondésert B, Marcotte F, Mongeon FP, et al. Fontan circulation: Success or failure? Can J Cardiol. 2013;29(7):811-820. doi:10.1016/j.cjca.2012.12.009.

[8] Bagai A, O'Brien S, Al Lawati H, et al. Mentored simulation training improves procedural skills in cardiac catheterization: A randomized, controlled pilot study. Circ Cardiovasc Interv. 2012;5(5):672-679. doi:10.1161/CIRCINTERVENTIONS.112.970772.

[9] Dur O, Lara M, Arnold D, et al. Pulsatile in vitro simulation of the pediatric univentricular circulation for evaluation of cardiopulmonary assist scenarios. Artif Organs. 2009;33(11):967-976. doi:10.1111/j.1525-1594.2009.00951.x.

[10] Di Molfetta A, Amodeo A, Fresiello L, et al. Simulation of Ventricular, Cavo-Pulmonary, and Biventricular Ventricular Assist Devices in Failing Fontan. Artif Organs. 2015;39(7):550-558. doi:10.1111/aor.12434.

[11] Pantalos GM, Ionan C, Koenig SC, et al. Expanded pediatric cardiovascular simulator for research and training. ASAIO J. 2010;56(1):67-72. doi:10.1097/MAT.0b013e3181c838ae.

[12] Zhou J, Esmaily-Moghadam M, Conover TA, Hsia TY, Marsden AL, Figliola RS. In Vitro Assessment of the Assisted Bidirectional Glenn Procedure for Stage One Single Ventricle Repair. Cardiovasc Eng Technol. 2015;6(3):256-267. doi:10.1007/s13239-015-0232-z.

[13] Hussain A, Arfi AM, Hussamuddin M, et al. Comparative Outcome of Bidirectional Glenn Shunt in Patients With Pulmonary Vascular Resistance ≥ 3.5 Woods Units Versus < 3.5 Woods Units. Am J Cardiol. 2008;102(7):907-912. doi:10.1016/j.amjcard.2008.04.063.

[14] Baretta A, Corsini C, Yang W, et al. Virtual Surgeries in Patients with Congenital Heart Disease: A Multi-scale Modelling Test Case. Philos Trans A Math Phys Eng Sci. 2011;369(1954):4316-4330. doi:10.1098/rsta.2011.0130.

[15] Vukicevic M, Chiulli JA, Conover T, et al. Mock circulatory system of the Fontan circulation to study respiration effects on venous flow behavior. ASAIO J. 2013;100(2):253-260. doi:10.1016/j.pestbp.2011.02.012.Investigations.

[16] Kung EO, Taylor CA. Development of a Physical Windkessel Module to Re-Create In Vivo Vascular Flow Impedance for In Vitro Experiments. Cardiovasc Eng Technol. 2011;2(1):2-14. doi:10.1007/s13239-010-0030-6.

[17] Horne D, Conway J, Rebeyka IM, Buchholz H. Mechanical Circulatory Support in Univentricular Hearts: Current Management. Semin Thorac Cardiovasc Surg Pediatr Card Surg Annu. 2015;18(1):17-24. doi:10.1053/j.pcsu.2015.02.002.

Thermosensitive hydrogels for the encapsulation of primary and human derived neuronal cells

Donatella Di Lisa[1], Elena Dellacasa [1], Lorenzo Muzzi [1], Alberto Lagazzo [2], Monica Frega[3], Sergio Martinoia[1] and Laura Pastorino[1]

[1]*University of Genova, Dept. of Informatics, Bioengineering, Robotics and System Engineering, Via Opera Pia 13, 16145 Genova, Italy*
[2]*University of Genova, Dept. of Civil, Chemical and Environmental, Via Opera Pia 15, 16145 Genova, Italy*
[3]*University of Twente, Dept. of Clinical neurophysiology, University of Twente, Drienerlolaan 5, 7522 NB Enschede, Netherlands*

Abstract- **Thermosensitive chitosan-based hydrogel was developed to encapsulate neuronal cells and to support neuronal network development. In particular, the goal of this study was to demonstrate the versatility of this hydrogel to be used as an artificial matrix for 3D neuronal networks in vitro studies and as an injectable-hydrogel for the in-vivo applications or innovative ink for 3D bioprinter. To this aim, chitosan thermogels were fabricated and characterized by different techniques. The scaffold was used to encapsulate primary rat neurons and human-induced neurons cultures to carry out morphological characterization by immunofluorescence techniques.**

Keywords— Chitosan, thermogel, injectability, h-iPSCs, 3D neuronal networks.

I. INTRODUCTION

Over the past decade, hydrogels, in particular biopolymeric ones, have gained great attention due to their potentialities in the field of tissue engineering and regenerative medicine [1]-[3]. Hydrogels are generally biocompatible, biodegradable and most importantly mimic the extracellular matrix (ECM) architecture, representing thus ideal biomaterials for 3D scaffolds fabrication, specifically for soft tissue [4], [5]. Moreover, engineered natural biomaterials, able to perform the sol-gel transition in the presence of cells under specific external stimuli, have been proposed [6]. Such kind of biomaterials are either based on components of the ECM such as collagen and hyaluronic acid [7]- [9], or complex ECM derivatives, such as Matrigel [10], and present the great advantage of allowing cell encapsulation in the hydrogel network. The great interest in these stimuli responsive hydrogels relays in the possibility to encapsulate cells, in their application as inks in 3D bioprinting and in their *in vivo* injectability [11].

Despite great advancements in this field, the applications of stimuli responsive hydrogels for the encapsulation of neurons, for the development of 3D neuronal networks, are still limited. This is mainly due to the necessity of developing a soft yet stable and bioactive hydrogel able to sustain neurons in long-term cultures [12]. The main hydrogels used for this specific application are Matrigel and GelMa [13]. However, Matrigel presents several limitations, mainly related to high batch to batch variability and low stability over time, whereas the photo-crosslinking process of GelMA raises concerns related to the possible impact on cells of such treatment [14,15].

Recently, we have demonstrated that the cationic polysaccharide chitosan (CHI) by itself is able to sustain neuronal adhesion and growth and we have proposed the use of this biopolymer for the development of 3D scaffold for neuronal networks development [16].

CHI is derived from the deacetylation of chitin, the main structural component of crustacean exoskeletons. CHI exhibits antibacterial and antioxidant activity, wound-healing properties, and low immunogenicity [17]- [18]. CHI is soluble in dilute acidic solutions below its pKa (6-6.8) and can be physically of chemically cross-linked to produce matrixes for drug delivery of cell seeding [19].

Most interesting, CHI in combination with basic compounds, such as β-glycerol phosphate (βGP), becomes thermosensitive in diluted acids and can undergo gelation around body temperature [20]. Different thermosensitive CHI formulations have been developed and used for in-situ bone and cartilage regeneration [21].

In the search of an alternative material for the encapsulation of neurons, in the present work we have explored the possibility of developing a chitosan based formulation which is liquid at room temperature and has a pH compatible with cells and becomes a gel as at body temperature, without imparting neuronal functions.

CHI based thermosensitive formulations were developed and characterized by scanning electron microscopy, mechanical and injectability testing. The optimized formulation was used for the encapsulation of primary cortical neurons and of neurons differentiated from human derived induced pluripotent stem cells. We demonstrated that the thermosensitive CHI formulation is able to sustained the viability and the growth of the two different cell populations in vitro. Furthermore, thanks to its injectability, the formulation is an excellent candidate for minimally invasive therapeutic cell delivery and an alternative ink for 3D bioprinting.

II. MATERIALS AND METHODS

A. Materials

CHI was purified following the method described by Qian and Glanville [22]. CHI solutions of 3% and 2.5% (w/v) were prepared by dissolving purified CHI powder in 0.1 M acetic acid. The stirring was kept at room temperature overnight, and then the solutions were sterilized by autoclave at 120°C for 20 min and stored at 4°C.

βGP was used as gelling agent at two different concentrations obtained dissolving βGP at 7% and 18% in water. Their temperature-dependent gelation mechanism was found to involve the heat-induced transfer of protons from CHI to

glycerol phosphate, which reduces the repulsive forces among positively charged ammonium groups and allows interaction of CHI chains. Gelling agent solutions were sterilized by filtration through 0.2μm syringe filters and stored at 4°C.

All reagents were from Sigma-Aldrich.

B. Cell cultures

Primary neurons and cortical astrocytes were obtained from embryonic Sprague-Dawley rats at gestational day 18 under sterile conditions. The experimental protocol was approved by the European Animal Care Legislation (2010/63/EU), by the Italian Ministry of Health in accordance with the D.L. 116/1992 and by the guidelines of the University of Genova. All efforts were made to reduce the number of animals used for the project and to minimize their suffering.

The rtTA/Ngn2 positive h-iPSCs line, generated from fibroblast withdrawn from a healthy donor, was kindly provided by Frega et al [23]. Briefly, for the generation of this line, hiPSCs were transduced with rtTA/Ngn2 lentiviruses and were selected by g418/puromycin, as described in [24]. Induced excitatory cortical neurons (iNeurons) were generated by overexpressing the neuronal determinant Neurogenin 2 (NgN2) upon doxycycline treatment.
Cultures were maintained in incubator at 37°C in a 5% CO2, 95% humidity atmosphere for 3/4 weeks by replacing half of the medium once a week.

C. Preparation of CHI/ βGP thermogels for Cell Encapsulation

CHI/ βGP thermogels were prepared at room temperature by mixing sterilized CHI solutions with sterilized βGP gelling agent solutions added drop by drop. All the hydrogels had a final concentration of 2% (w/v) chitosan.

3D neuronal cultures were obtained by growing dissociated primary neurons (E18) and iNeurons mixed with cortical astrocytes (ratio 1:1). Hydrogels were prepared in two consecutive steps: CHI was first mixed with βGP to create a solution with physiological pH at 4° C. The cell suspension (in culture media) was added to CHI/βGP solution and mixed with a pipette and the 50 μl of neuron-CHI/ βGP solution was poured in a PDMS (poly-dimethyl siloxane) mold and incubated a 37°C, (Fig.1).
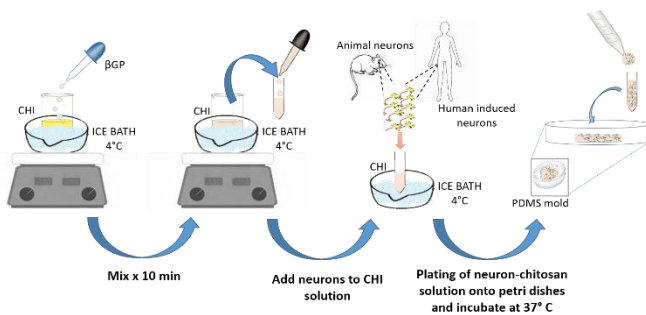

Fig 1: Preparation steps of 3D networks encapsulated inside CHI/βGP thermogel.

D. Mechanical characterization

The dynamic mechanical compressive analysis (DMA) were performed with home-made apparatus with frequency range between 1-100 Hz with prestrain of 10 % at room temperature. The tests were carried out on samples with cells.
Injectability tests was performed by using load cell of 500 N and speed 200 mm/min in a physiological solution at 37° C. 1 ml syringe with a needle (Ø 1mm) was loaded with gel prewarmed at 37°C for 5 min.

E. SEM characterization

The hydrogels were then kept (in liquid nitrogen) at −196° C overnight and freeze-dried under vacuum for 24 h. Each sample were coated with gold layer before analysis. The analysis was performed with SEM Hitachi S-2005 in SE.

F. 3D neuronal networks characterization

The immunocytochemistry characterization was carried out to assess the expression of specific neuronal markers, MAP-2 for neuronal cells and DAPI for nucleus. An Olympus BX-51 upright microscope was used for immunofluorescence evaluation of the biological samples.

III. RESULTS

A. Gelling dynamics characterization

Both 2.5% and 3% CHI solutions were mixed with the proper amount of βGP, and the gelation time at 37°C were monitored (Fig 2).
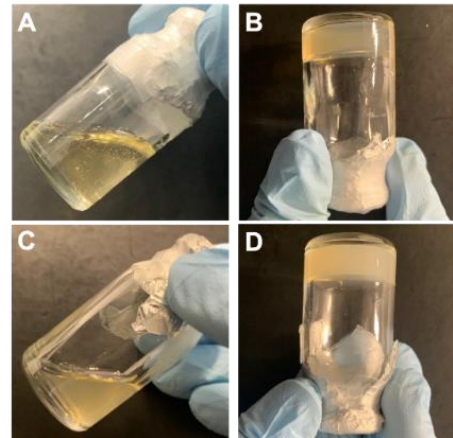

Fig.2: CHI (2.5%)- βGP (18% w/v) solution before gelation (A) and after gelation (B). CHI (3%)- βGP (7% w/v) solution before gelation (C) and after gelation (D).

2.5% CHI thermogel reached the complete gelation after 13 minutes of incubation, while 3% CHI thermogel reached the complete gelation after 7 minutes.

B. Mechanical characterization

Both 3% and 2.5% CHI thermogelling solution were then mixed with the cell suspension and let to gel in round PDMS molds with 5 mm of diameter and 1 mm of height (Fig 3).

The Elastic Modulus measured by DMA were found to be 13.9 kPa for 2.5% CHI thermogel and 19.6 kPa for 3% CHI thermogel, which are comparable with the elastic modulus values of brain tissue [25,26].

Fig 3: Injectability of CHI/ βGP thermogel immersed in saline at 37 °C Aspect of extruded thermogel (yellow arrow).

The injectability evaluation was perfomed for both 2.5% and 3% CHI/ βGP thermogels. The experimental results demonstrated that only the 3% CHI/ βGP formulation was suitable for a correct extrusion (Fig 3), while the 2.5% CHI/ βGP formulation showed non-continuous flow and didn't gel during the extrusion process.

C. SEM characterization

Before cell encapsulation, both 2.5% and 3% CHI/ βGP thermogels were morphological characterized by SEM measurements in order to check their porosity. Figure 4 shows an adequate and homogenous porosity for cell seeding and penetration for both thermogels, which was found to have an average pore diameter of 20 μm.
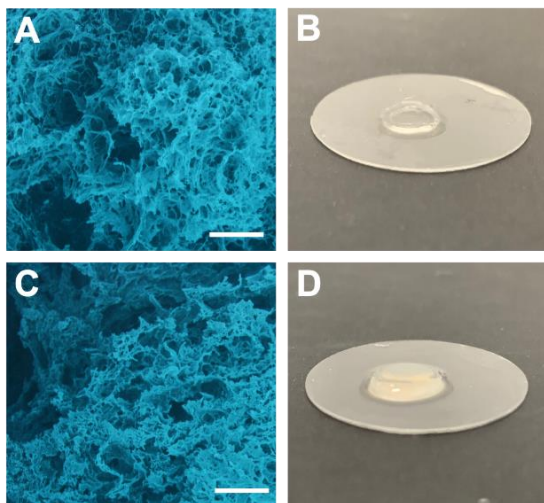

Fig 4: SEM images and CHI/ βGP thermogels: A-B) CHI (2.5%)- βGP (18% w/v); C-D) CHI (3%)- βGP (7% w/v). Scale bar 50 μm.

D. 3D neuronal networks characterization

The immunocytochemistry characterization allowed us to obtained information on the viability, growth and morphology of 3D structure of neuronal networks after 24 days of culture (Fig. 5).
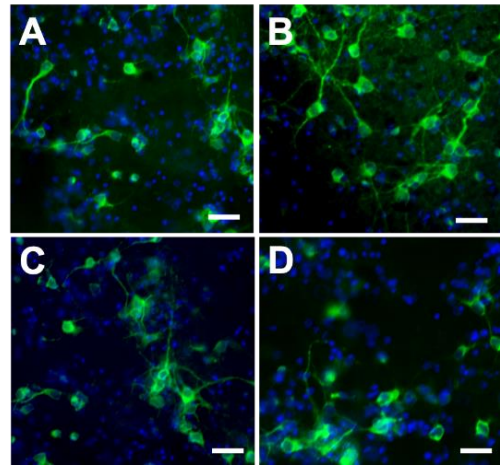

Fig 5: Optical images by using immunofluorescence technique. 3D primary neurons culture in A) CHI (2.5%)- βGP (18% w/v) and B) CHI (3%)- βGP (7% w/v). 3D h-iNeurons culture in C) CHI (2.5%)- βGP (18% w/v) and D) CHI (3%)- βGP (7% w/v). Scale bar 20 μm.

In all tested CHI/ βGP thermogels, cells were homogenously distributed within the whole scaffold volume. For both type of cells (animal and human derived), neuron cells present a spherical soma, similar to that one found in brain tissue [25,227].

IV. CONCLUSION

In this work, two different formulations of CHI/ βGP thermogels were fabricated and characterized. The preliminary results showed that both formulations are suitable for neuronal cell encapsulations, being able to sustain the viability and the growth of the two cultured cell populations, animal and human derived. In particular, the injectability tests showed that 3% CHI/ βGP formulation is potentially usable for minimally invasive *in vivo* applications and may thus represents alternative ink for 3D bioprinter.

V. ACKNOWLEDGMENTS

REFERENCES

[1] DeVolder, R., & Kong, H. J. (2012). Hydrogels for in vivo-like three-dimensional cellular studies. Wiley Interdisciplinary Reviews: Systems Biology and Medicine, 4(4), 351-365.
[2] DeVolder, R., & Kong, H. J. (2012). Hydrogels for in vivo-like three-dimensional cellular studies. Wiley Interdisciplinary Reviews: Systems Biology and Medicine, 4(4), 351-365.
[3] Nicodemus, G. D., & Bryant, S. J. (2008). Cell encapsulation in biodegradable hydrogels for tissue engineering applications. Tissue Engineering Part B: Reviews, 14(2), 149-165.
[4] Caliari, S. R., & Burdick, J. A. (2016). A practical guide to hydrogels for cell culture. Nature methods, 13(5), 405.
[5] Tibbitt, M. W., & Anseth, K. S. (2009). Hydrogels as extracellular matrix mimics for 3D cell culture. Biotechnology and bioengineering, 103(4), 655-663.

[6] Bryant, S. J., & Vernerey, F. J. (2018). Programmable hydrogels for cell encapsulation and neo-tissue growth to enable personalized tissue engineering. Advanced healthcare materials, 7(1), 1700605.

[7] Zhang, L., Li, K., Xiao, W., Zheng, L., Xiao, Y., Fan, H., & Zhang, X. (2011). Preparation of collagen–chondroitin sulfate–hyaluronic acid hybrid hydrogel scaffolds and cell compatibility in vitro. Carbohydrate polymers, 84(1), 118-125.

[8] Ferreira, A. M., Gentile, P., Chiono, V., & Ciardelli, G. (2012). Collagen for bone tissue regeneration. Acta biomaterialia, 8(9), 3191-3200.

[9] Burdick, J. A., & Prestwich, G. D. (2011). Hyaluronic acid hydrogels for biomedical applications. Advanced materials, 23(12), H41-H56.

[10] Hughes, C. S., Postovit, L. M., & Lajoie, G. A. (2010). Matrigel: a complex protein mixture required for optimal growth of cell culture. Proteomics, 10(9), 1886-1890.

[11] Unagolla, J. M., & Jayasuriya, A. C. (2019). Hydrogel-based 3D bioprinting: A comprehensive review on cell-laden hydrogels, bioink formulations, and future perspectives. Applied Materials Today, 100479.

[12] Aregueta-Robles, U. A., Martens, P. J., Poole-Warren, L. A., & Green, R. A. (2019). Tissue engineered hydrogels supporting 3D neural networks. Acta biomaterialia, 95, 269-284.

[13] Nichol, J. W., Koshy, S. T., Bae, H., Hwang, C. M., Yamanlar, S., & Khademhosseini, A. (2010). Cell-laden microengineered gelatin methacrylate hydrogels. Biomaterials, 31(21), 5536-5544.

[14] Zimmermann, J. A., & Schaffer, D. V. (2019). Engineering biomaterials to control the neural differentiation of stem cells. Brain research bulletin.

[15] Choi, G., & Cha, H. J. (2019). Recent advances in the development of nature-derived photocrosslinkable biomaterials for 3D printing in tissue engineering. Biomaterials Research, 23(1), 18.

[16] Tedesco, M. T., Di Lisa, D., Massobrio, P., Colistra, N., Pesce, M., Catelani, T., ... & Pastorino, L. (2018). Soft chitosan microbeads scaffold for 3D functional neuronal networks. Biomaterials, 156, 159-171.

[17] Dash, M., Chiellini, F., Ottenbrite, R. M., & Chiellini, E. (2011). Chitosan—A versatile semi-synthetic polymer in biomedical applications. Progress in polymer science, 36(8), 981-1014.

[18] I.Y. Kim, S.J. Seo, H.S. Moon, M.K. Yoo, I.Y. Park, B.C. Kim, et al., "Chitosan and its derivatives for tissue engineering applications", Biotechnol. Adv. 26 (2008).

[19] C. Shi, Y. Zhu, X. Ran, M. Wang, Y. Su, T. Cheng, "Therapeutic potential of chitosan and its derivatives in regenerative medicine", J. Surg. Res. 133 (2006) 185e192.

[20] A. Chenite, C. Chaput, D. Wang, C. Combes, M.D. Buschmann, C.D. Hoemann, et al.,"Novel injectable neutral solutions of chitosan form biodegradable gels in situ", Biomaterials 21 (2000) 2155e2161.

[21] Zhou, H. Y., Jiang, L. J., Cao, P. P., Li, J. B., & Chen, X. G. (2015). Glycerophosphate-based chitosan thermosensitive hydrogels and their biomedical applications. Carbohydrate polymers, 117, 524-536

[22] Qian, R.Q., & Glanville, R.W. (2005). Methods for purifying chitosan. US Patent, 6896809.

[23] Frega, M., Linda, K., Keller, J.M. et al. "*Neuronal network dysfunction in a model for Kleefstra syndrome mediated by enhanced NMDAR signalling*". Nat Commun 10, 4928 (2019).

[24] Frega, M., et al. "*Rapid Neuronal Differentiation of Induced Pluripotent Stem Cells for Measuring Network Activity on Micro-electrode Arrays*". J. Vis. Exp. (119), e54900, doi:10.3791/54900 (2017).

[25] Niemczyk B, Sajkiewicz P, Kolbuk D. "*Injectable hydrogels as novel materials for central nervous system regeneration.*" J Neural Eng. 2018;15(5):051002.

[26] A.J. Engler, et al., Matrix elasticity directs stem cell lineage specification, Cell 126 (4) (2006) 677e689.

[27] Cullen, D.K., et al.," *Neural tissue engineering and biohybridized microsystems for neurobiological investigation in vitro (Part 1)*". Crit Rev Biomed Eng, 2011. 39(3): p. 201-40.

Linear Regression Models to Improve the Estimation of Insulin Boluses in Type 1 Diabetes Therapy

G. Noaro[1], G. Cappon[1], S. Del Favero[1], G. Sparacino[1], and A. Facchinetti[1]

[1]*Department of Information Engineering, University of Padova*

Abstract—**In type 1 diabetes (T1D) management, blood glucose (BG) concentration is maintained in a safe range by administering suitable doses of exogenous insulin to counteract the lack of endogenous production. A critical task is the estimation of the meal insulin bolus (MIB) to compensate the postprandial glycemic excursion. The standard formula (SF) used for such a calculation could produce suboptimal estimations, i.e. critical hypo/hyperglycemic episodes, since it does not account for information on glucose dynamics. In this work, we investigate new linear regression models to improve the estimation of MIB, accounting for the glucose rate-of-change (ROC) provided in real-time by continuous glucose monitoring (CGM) sensor, a new key device used in T1D therapy.**

Three candidate MIB models based on multiple linear regression (MLR) and least absolute shrinkage and selection operator (LASSO) were developed. The models proposed were assessed leveraging a simulated environment in different mealtime scenarios and compared to SF in terms of glycemic outcome.

All the three tested models significantly improved the glycemic control with respect to SF. *In silico*, the new models reduced the error in MIB estimation from 1.45 U of SF to about 0.86 U, as well as hypoglycemia incidence (from 44.41% of SF to about 36%).

The new linear regression models has shown to be effective in improving MIB calculation, especially if accounting for CGM-ROC and easy-to-measure features. In particular, in this work, we developed models based on MLR and LASSO, which outperform SF and can be potentially applied in T1D therapy.

Keywords—**Continuous glucose monitoring, insulin therapy, glycemic control, hypoglycemia**

I. INTRODUCTION

Type 1 diabetes (T1D) is a chronic and metabolic disease characterized by elevated blood glucose (BG) levels, that occurs when the insulin-producing pancreatic β-cells become dysfunctional. Thus, in T1D management, blood glucose (BG) concentration is maintained in a safe range (70-180 mg/dL) by injecting insulin endogenously. One of the most critical task is the estimation of meal-time insulin doses to compensate the postprandial glycemic excursion. Traditionally, a standard formula (SF) [1] is used for such a purpose:

$$MIB_{SF} = \frac{CHO}{CR} + \frac{G_c - G_t}{CF} - IOB \qquad (1)$$

which takes into account meal carbohydrates (CHO), two therapy parameters tuned by the clinician (the insulin to CHO ratio - CR - and the correction factor - CF -) [2], the current BG concentration at meal-time (G_c), the BG concentration desired

at the end of the meal (G_t), and the insulin on board (IOB) [3]. We recently proved that the SF can under/overestimate the optimal meal-bolus dose in many situations [4], leading to critical hyper/hypoglycemic episodes during and after the meal. One of the main reasons of this suboptimality is that SF does not take into account information of glucose dynamics, e.g., if the BG is rising up or falling down at meal time. Nowadays, such an information on BG rate-of-change (ROC) is provided in real-time by continuous glucose monitoring (CGM) sensors [5], [6], i.e., new devices that allow measuring the glucose concentration almost continuously (e.g., every 5 minutes) for up to 10 days. Recently, several methods have been proposed in the literature aimed at correcting SF dosage according to ROC detected by CGM. Some of these approaches have strictly empirical derivation [7]–[9], whereas others leverage machine-learning methodologies [10]. However, a recent in silico assessment of these methods showed that none of them performs better than the others for all BG and ROC conditions at mealtime, calling for more effective and possibly personalized MIB calculation methods [4].

The aim of this work is to develop three models based on multiple linear regression (MLR) and least absolute shrinkage and selection operator (LASSO) for meal insulin bolus (MIB) calculation, accounting for CGM-ROC and other easily accessible features. In order to assess their ability to improve the glycemic control during and after the meal with respect to the SF, we leveraged a simulation environment. A simulated framework, indeed, has many advantages, for instance the possibility to obtain multiple meal scenarios maintaining identical initial conditions, a situation which is impossible to replicate in clinical trials. Moreover, the insulin dosage can be tested without exposing the real subject to any risk.

II. SIMULATED DATASET

We designed a simulation environment to obtain data of 100 virtual patients in single-meal and noise-free scenarios, using the UVa/Padova T1D Simulator [2]. In particular, the design consisted of different meal conditions in terms of preprandial ROC, BG and meal amounts. This resulted in the creation of 162 initial conditions: 9 different ROC values (from -2 to +2 mg/dL/min with a step equal to 0.5 mg/dL/min), 12 prandial BG values (from 70 to 180 mg/dL with a step equal to 10 mg/dL) and 15 meal amounts (from 10 to 150 g of
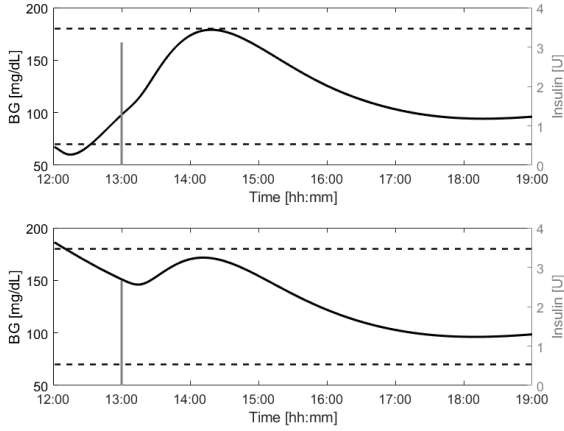
Fig. 1: Two representative simulated scenarios for a virtual subject considering a meal of 50 g. Upper panel shows a 7-hour BG curve with BG equal to 100 mg/dL and ROC equal to +1 mg/dL/min at mealtime and the respective MIB_{OPT} of 3.10 U. Lower panel shows a 7-hour BG curve with BG equal to 150 mg/dL and ROC equal to -0.5 mg/dL/min at mealtime and the respective MIB_{OPT} of 2.65 U.

CHO with step equal to 10 g) for each virtual subject. The respective optimal bolus dose (MIB_{OPT}) of each record was derived by minimizing the blood glucose risk index (BGRI) [11] evaluated in the postprandial time window, to quantify the risk of hypo- and hyperglycemia in this time frame.

In Fig. 1 two representative scenarios are depicted in terms of BG excursion and MIB_{OPT}. The upper panel shows an example with mealtime condition of BG = 100 mg/dL, ROC = +1 mg/dL/min, and CHO = 50 g. In the lower panel an example with mealtime BG = 150 mg/dL, ROC = -0.5 mg/dL/min and CHO = 50 g is represented. Note that, in both scenarios, MIB_{OPT} allows a proper glycemic control, maintaining the BG within the euglycemic range.

Finally, we extracted 10 features from each condition, in particular we chose variables which compose the SF (CHO, CR, CF, G_t, G_c, IOB), basal insulin (I_b), body weight (BW), and ROC. We would like to highlight that all the extracted features are easily accessible in daily life; this is important to ensure the applicability and usability of the new model by a T1D individual. Moreover, the final dataset was divided into training and testing set, including 80 subjects in the training and 20 subjects in the testing set. Then, due to different measurement units among features, variables were standardized, thus removing the mean and scaling to unit variance.

III. NEW LINEAR MODELS FOR MIB CALCULATION

For this work, we applied multiple linear regression (MLR) and least absolute shrinkage and selection operator (LASSO) regression to target the MIB_{OPT}, since linearity leads to an interpretable description of how the inputs affect the output. As a matter of fact, model interpretability is a desirable feature for our purpose, because it could facilitate acceptability by clinicians and allows to understand the role of each variable in the computation of the MIB.

A. MLR model

The first developed model is based on MLR and has the following form:

$$\hat{\boldsymbol{y}} = \hat{\alpha}_0 + \sum_{j=1}^{p} \boldsymbol{x_j} \cdot \hat{\alpha}_j \tag{2}$$

where $\boldsymbol{y}$ is the target variable, i.e. MIB_{OPT}, $\boldsymbol{x_j}$ is the j-th feature, α_j the coefficient related to the j-th feature, α_0 is the model intercept and p represents the number of features. Parameters $\hat{\alpha}_j$ are estimated through the least squares estimation method [12], which chooses the vector $\hat{\boldsymbol{\alpha}}$ of coefficients that minimizes the residual sum of squares (RSS):

$$\hat{\boldsymbol{\alpha}} = \underset{\boldsymbol{\alpha}}{\operatorname{argmin}} \, RSS(\boldsymbol{\alpha}) \tag{3}$$

where

$$RSS(\boldsymbol{\alpha}) = \sum_{i=1}^{N} (y_i - \hat{y}_i)^2 \tag{4}$$

and y_i is the i-th observation of MIB_{OPT}, $\hat{y}_i$ the corresponding model prediction.

B. LASSO models

Then, we applied a shrinkage method to our dataset, in particular LASSO regression. LASSO coefficients are estimated by minimizing eq. (4) with the addition of the absolute value of the coefficients magnitude as a penalty term:

$$\hat{\boldsymbol{\alpha}} = \underset{\boldsymbol{\alpha}}{\operatorname{argmin}} \{ RSS(\boldsymbol{\alpha}) + \lambda \sum_{j=1}^{p} |\alpha_j| \} \tag{5}$$

where $\lambda \geq 0$ is a parameter controlling the amount of shrinkage, set through an exhaustive grid search with cross-validation in the training set. LASSO regression was chosen since it also performs both variable selection and regularization [12], thus allowing to investigate if features, which are less significant than others, could be discarded. Moreover, due to the intrinsic nonlinearity of glucose-insulin system, we also explored the application of a second feature set, which includes the quadratic transformations of the input variables. Hence, two LASSO models were trained, the first one on the original feature set described in II, the second one with the addition of their quadratic value, hereafter named as LASSO and LASSO_Q respectively.

IV. ASSESSMENT CRITERIA

First, we evaluated, on the simulated test set, the quality of the estimates and the model goodness of fit, computing the root mean square error (RMSE) and the coefficient of determination (R^2) for MIB_{OPT}, SF, MLR, LASSO and LASSO_Q.

Then, using the UVa/Padova T1D Simulator we tested in terms of glycemic control the MIB estimates of each model, by evaluating the BG pattern in the 6-hour postprandial time frame. Three metrics were used for this assessment, i.e. the BGRI, previously introduced in Section II, the percentage of time spent in hyperglycemia (T_{Hyper} %) and in hypoglycemia
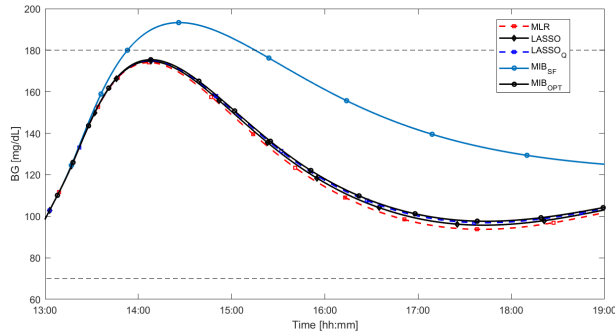
Fig. 2: Representative example of BG curves during postprandial time window for different methods of insulin bolus computation and different mealtime conditions. The prandial ROC is positive (1.5 mg/dL/min), starting BG=100 mg/dL and meal CHO is 30 g. The calculated MIB doses are MIB_{OPT}=2.80 U, MIB_{SF}=0.72 U, MIB_{MLR}=3.01 U, MIB_{LASSO}=2.90 U , MIB_{LASSO_Q}=2.84 U.

(T_{Hypo} %) [13]. In addition, the percentage of the incidence of hypoglycemic episodes (I_{Hypo}) was calculated.

Finally, to evaluate the statistical significance in terms of BGRI, T_{Hyper}, T_{Hypo} with respect to SF, Friedman's test was performed with 5% significance level. We chose the Friedman's test, i.e. the nonparametric equivalent of the classical balanced two-way ANOVA, to take into consideration that virtual subjects are repeated within the testing set (with same physiology, but different initial conditions), and thus adjust for possible row effects. In order to correct for multiple pairwise comparisons, we adjusted the p-values with the Bonferroni method.

V. RESULTS

A. Model evaluation

The aim of this first evaluation is assessing and quantifying, on the simulated testing set, whether the developed models are able to estimate MIB_{OPT} more accurately than SF. Table I reports the obtained results with regard to RMSE and R^2. In this terms, models MLR, LASSO, $LASSO_Q$ showed a better performance compared to the SF. Specifically, RMSE ranges between 0.87-0.86 U for the new models, considerably reducing the value of SF (1.45 U). Likewise, also R^2 improved, from 0.82 of SF to 0.91 of the proposed models.

The MLR and LASSO models were compared against SF also in terms of glycemic outcome. In Table II, the obtained results are reported. Considering the BGRI, SF resulted with the highest median risk (9.93), while the lowest median BGRI value was obtained by $LASSO_Q$ (9.08), that is close to the BGRI value of MIB_{OPT} (8.23). Regarding T_{Hypo}, median

TABLE I: Comparison of metrics for prediction accuracy and goodness of fit evaluation. Values related to SF, state-of-art methods and the models proposed are reported.

Metric	SF	MLR	LASSO	$LASSO_Q$
$RMSE$ [U]	1.45	0.87	0.87	0.86
R^2	0.82	0.91	0.91	0.91

TABLE II: Comparison of metrics assessing glycemic control for SF, state-of-the-art methodologies and the proposed models. Metrics related to MIB_{OPT} are reported as reference values. Median and interquartile range is reported for BGRI, T_{Hypo}, T_{Hyper}.

Metric	MIB_{OPT}	SF	MLR	LASSO	$LASSO_Q$
BGRI	8.23 (3.97-14.03)	9.93 (4.85-17.46)	9.10* (4.68-15.50)	9.09* (4.67-15.45)	9.08* (4.68-15.43)
T_{Hypo} %	0.00 (0.00-0.00)	0.00 (0.00-28.53)	0.00* (0.00-14.68)	0.00* (0.00-13.99)	0.00* (0.00-13.57)
T_{Hyper} %	29.92 (12.19-39.34)	29.09 (13.30-37.95)	29.92 (12.19-39.06)	29.92 (11.91-39.06)	29.92 (11.90-39.34)
I_{Hypo}%	24.24	44.41	36.28	36.15	35.93

[1]*Statistically significant compared to SF.

values resulted equal to 0 for all the methods, for this reason the metric I_{Hypo} was investigated, in order to quantify the impact of these methodologies on the shortcoming of hypoglycemia. Considering the 75th percentile of T_{Hypo} together with I_{Hypo} values, it can be stated that the magnitude and occurrence of hypoglycemic events was considerably reduced for the proposed models compared to SF. Best results were achieved by $LASSO_Q$ (75th percentile of T_{Hypo} equal to 13.57% and I_{Hypo} = 35.93%). As reported in Table II the improvement in terms of BGRI and T_{Hypo} given by MLR, LASSO and $LASSO_Q$ is statistically significant compared to SF. Regarding T_{Hyper}, no significant difference with SF was detected. Fig. 2 shows a representative postprandial BG curve following the administration of MIB computed through MIB_{OPT}, SF, MLR, LASSO, $LASSO_Q$. Note the occurrence of the hyperglycemic event after the application of SF, while the other methods approach an optimal glycemic control.

VI. CONCLUSION

In this work, we investigated if new insulin bolus calculation methods could be developed by leveraging linear regression techniques, CGM sensor data, and other easily accessible features. For this purpose, we developed three different models based on multiple linear regression (MLR) and least absolute shrinkage and selection operator (LASSO) for meal insulin bolus (MIB) calculation. By resorting a simulation framework *ad-hoc* designed for such a scope, we demonstrated that all three candidate models are able to better estimate the optimal MIB than the SF. We also proved that this ability translates into an improved glycemic control during and after the meal compared to SF, significantly reducing the time in hypoglycemia (T_{Hypo}), the global risk of hypo/hyperglycemia during meal-time (BGRI), and the incidence of hypoglycemic episodes (I_{Hypo}).

Future developments will include the impact of error sources, such as errors in patient behavior [14], carbohydrates miscalculations [15] and sensor measurements [16] [17] on the developed models, to test their robustness. Moreover, we will investigate the use of nonlinear regression models to take into account the nonlinear nature of the problem, and thus to further improve the glycemic control during the meal.

REFERENCES

[1] S. Schmidt and K. Nørgaard, "Bolus Calculators," *J Diabetes Sci Technol*, vol. 8, no. 5, pp. 1035–1041, 2014.

[2] P. Davidson, H. Hebblewhite, R. Steed, and B. Bode, "Analysis of Guidelines for Basal-Bolus Insulin Dosing: Basal Insulin, Correction Factor, and Carbohydrate-to-Insulin Ratio," *Endocr Pract*, vol. 14, no. 9, pp. 1095–1101, 2008.

[3] T. M. Gross, D. Kayne, A. King, C. Rother, and S. Juth, "A Bolus Calculator Is an Effective Means of Controlling Postprandial Glycemia in Patients on Insulin Pump Therapy," *Diabetes Technol Ther*, vol. 5, no. 3, pp. 365–369, 2003.

[4] G. Cappon, F. Marturano, M. Vettoretti, A. Facchinetti, and G. Sparacino, "In Silico Assessment of Literature Insulin Bolus Calculation Methods Accounting for Glucose Rate of Change," *J Diabetes Sci Technol*, vol. 13, no. 1, pp. 103–110, 2018.

[5] G. Cappon, M. Vettoretti, G. Sparacino, and A. Facchinetti, "Continuous Glucose Monitoring Sensors for Diabetes Management: A Review of Technologies and Applications," *Diabetes Metab J*, vol. 43, p. 383–397, Aug 2019.

[6] D. De Salvo and B. Buckingham, "Continuous glucose monitoring: current use and future directions." *Curr Diab Rep*, vol. 13, no. 5, pp. 657–62, Oct 2013.

[7] B. Buckingham, D. Xing, S. Weinzimer, R. Fiallo-Scharer, C. Kollman, N. Mauras, E. Tsalikian, W. Tamborlane, T. Wysocki, K. Ruedy, and R. Beck, "Use of the DirecNet Applied Treatment Algorithm (DATA) for Diabetes Management with a Real-Time Continuous Glucose Monitor (the FreeStyle Navigator)," *Pediatr Diabetes*, vol. 9, pp. 142–147, Apr 2008.

[8] G. Scheiner, *Practical CGM: A Guide to Improving Outcomes Through Continuous Glucose Monitoring*. American Diabetes Association, 2015.

[9] R. Ziegler, S. von Sengbusch, J. Kröger, O. Schubert, P. Werkmeister, D. Deiss, and T. Siegmund, "Therapy Adjustments Based on Trend Arrows Using Continuous Glucose Monitoring Systems," *J Diabetes Sci Technol*, vol. 13, no. 4, pp. 763–773, 2019.

[10] G. Cappon, M. Vettoretti, F. Marturano, A. Facchinetti, and G. Sparacino, "A Neural-Network-Based Approach to Personalize Insulin Bolus Calculation Using Continuous Glucose Monitoring," *J Diabetes Sci Technol*, vol. 12, no. 2, pp. 265–272, 2018.

[11] C. Fabris, S. D. Patek, and M. D. Breton, "Are Risk Indices Derived From CGM Interchangeable With SMBG-Based Indices?" *J Diabetes Sci Technol*, vol. 10, no. 1, pp. 50–59, 2016.

[12] T. Hastie, R. Tibshirani, and J. H. Friedman, *The elements of statistical learning: data mining, inference, and prediction, 2nd Edition*, ser. Springer series in statistics. Springer, 2009.

[13] T. Danne, R. Nimri, T. Battelino, R. M. Bergenstal, K. L. Close, J. H. DeVries, S. Garg, L. Heinemann, I. Hirsch, S. A. Amiel, R. Beck, E. Bosi, B. Buckingham, C. Cobelli, E. Dassau, F. J. Doyle, S. Heller, R. Hovorka, W. Jia, T. Jones, O. Kordonouri, B. Kovatchev, A. Kowalski, L. Laffel, D. Maahs, H. R. Murphy, K. Nørgaard, C. G. Parkin, E. Renard, B. Saboo, M. Scharf, W. V. Tamborlane, S. A. Weinzimer, and M. Phillip, "International Consensus on Use of Continuous Glucose Monitoring," *Diabetes Care*, vol. 40, no. 12, pp. 1631–1640, 2017.

[14] M. Vettoretti, A. Facchinetti, G. Sparacino, and C. Cobelli, "Type-1 Diabetes Patient Decision Simulator for In Silico Testing Safety and Effectiveness of Insulin Treatments," *IEEE Trans on Biomed Eng*, vol. 65, no. 6, pp. 1281–1290, 2018.

[15] C. Roversi, M. Vettoretti, A. Facchinetti, S. Del Favero, and G. Sparacino, "Identification of factors influencing the carb-counting error in the type 1 diabetes management," in *2019 55th Annual European Association for the Study of Diabetes (EASD)*, vol. 62, no. Suppl 1, Sept 2019, p. S1–S600.

[16] A. Facchinetti, S. Del Favero, G. Sparacino, and C. Cobelli, "Model of glucose sensor error components: identification and assessment for new Dexcom G4 generation devices," *Med Biol Eng Comput*, vol. 53, Nov 2014.

[17] M. Vettoretti, C. Battocchio, G. Sparacino, and A. Facchinetti, "Development of an Error Model for a Factory-Calibrated Continuous Glucose Monitoring Sensor with 10-Day Lifetime," *Sensors*, vol. 19, p. 5320, Dec 2019.

A Heuristic-Sliding-Window-based RRT Path Planning for Endovascular Catheterization

Zhen Li[1,2], Alice Segato[1], Alberto Favaro[1], Jenny Dankelman[2] and Elena De Momi[1]

[1] *Department of Electronics, Information and Bioengineering, Politecnico di Milano, Milan, Italy*
[2] *Department of Biomechanical Engineering, Delft University of Technology, Delft, The Netherlands*
{*zhen.li, alice.segato, alberto.favaro, elena.demomi*}*@polimi.it*
{*Z.Li-13, j.dankelman*}*@tudelft.nl*

Abstract—Catheter interventions are often used in endovascular procedures to obviate complicated open surgical interventions. One of the major challenges relates to moving the catheter toward the required location with safety and accuracy. Due to the unpredictable tissue deformation associated with device insertion and the uncertainties of intra-operative sensing, a fast and robust path planning algorithm would be advantageous. Most of current methods are pre-operative planning, ignoring time costs. This paper aims at proposing a faster and robust path planning algorithm based on heuristics information. In this paper, a novel Heuristic-Sliding-Window-based Rapidly-exploring Random Trees (HSW-RRT) path planning algorithm is proposed for endovascular catheterization. This method keeps the catheter away from vascular edges in light of safety concerns by sampling along the centerline. Simulation results show the feasibility of this path planning method in 2D scenarios. Path solutions can be generated with similar performance and less time effort than RRT*.

Keywords—Path Planning, Flexible Catheter, Autonomous Endovascular Intervention

I. INTRODUCTION

In Peripheral Artery Disease (PAD), arteries become narrowed or blocked, usually as a result of atherosclerosis or plaque. Total occlusion of the superficial femoral artery is present in up to 50% of patients showing symptoms of PAD [1]. For treatment of it, the standard approach has been to access the contralateral common femoral artery.

Catheters are one of the most versatile and essential instruments used in endovascular interventions. For example, it can be used to cannulate the femoral arteries by pushing the plaque aside and placing a stent nearby to restore and maintain the blood circulation as shown in Fig. 1. One of the major challenges relates to moving the catheter toward the required location with accuracy and safety.

Due to the narrow, tortuous, slender and unstructured blood vessels, the path planning for autonomous endovascular interventions becomes complicated. Many of the path planning for endovascular interventions are graph-based methods, sampling tree nodes along the vascular centerlines, as in [3]–[12]. The isobars under the steady fluid condition are applied instead of centerlines in [13]. The Dijkstra, A*, breadth-first searching and other standard searching algorithms are able to find the optimal path, while the nonholonomic constraints are ignored and they are time consuming. Moreover, the application scenario
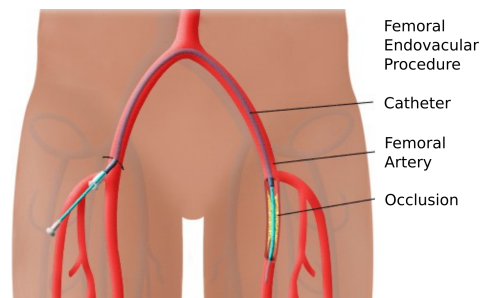

Fig. 1: Femoral endovascular procedure [2]

is limited to path planning in a static environment, ignoring the deformation of soft tissues during the clinical procedures. Learning based methods are also applied in endovascular navigation as in [14]–[18], while the data collection process for a specific application scenario is time consuming and the black box effect can not be ignored, which brings potential risks.

Sampling-based methods are developed well in mobile robots, and there is a lot of room for improvement on autonomous endovascular interventions. Probabilistic Roadmaps (PRM), Rapidly-exploring Random Trees (RRT) [19], [20], Fast Marching Trees (FMT) [21], Adaptive Fractal Trees (AFT) and their derivatives have attracted increasing attention recently. Nevertheless, in those papers they are pre-operative planning, ignoring the dynamic environments and real-time requirements. Due to the unpredictable tissue deformation associated with device insertion and the uncertainties of intra-operative sensing, a real-time path planning algorithm with high update frequency would be advantageous.

In this paper, a fast and robust path planning algorithm based on Rapidly-exploring Random Trees with a Heuristic Sliding Window is proposed for catheter interventions in endovascular procedures. (i) This method tries to keep the catheter away from vessel edges in light of safety concerns by sampling along the centerline. (ii) Instead of sampling in the overall search space, this method uses heuristics to improve the sampling efficiency. (iii) Considering the uncertainties of flexible robot model and deformations of soft tissues during the procedures, the propsoed path planning method allows faster path re-planning intra-operatively than RRT*. (iv) Sim-

ulation results in 2D scenarios show the feasibility of this path planning method. The path solutions are compared with that of RRT and RRT*, evaluating by time cost, path length and maximal curvature.

In this paper, the methodology is introduced in Sec. II, and the simulation results using different methods are discussed in Sec. III. Conclusions and future work are presented in Sec. IV.

II. METHODS

A. Search space

The original image in Fig. 2 is a 2D 294×220 digital subtraction angiography image from [22] with a virtual occlusion on the left side. It is segmented firstly via watershed algorithm and centerline is extracted via medial axis skeletonization.

Keeping away from vascular edges should be considered in light of safety concerns. If the search space is considered as the same as the collision free space inside blood vessels, the edge segment (red line in Fig. 3c) between 2 vertices sometimes is close to the vascular edges (orange contour). In that case, the catheter deployment can be dangerous as it can damage the deformable vessel tissue.

The image erosion and dilation are efficient and mature ways to shrink the free space, and they perform image convolution operations. Therefore, the path will locates in a search space which is smaller than the original collision free space, respectively the blue and orange zones in Fig. 2.

B. HSW-RRT

The Heuristic-Sliding-Window-based RRT (HSW-RRT) is a sampling-based path planning algorithm. The tree is constructed incrementally from samples drawn randomly from the search space. Instead of randomly sampling in overall search space, this method uses a heuristic sliding window to improve the sampling efficiency.

The heuristic sliding window is defined as a strip-shaped area, which is expanded from the centerline with an adaptive width as shown in Fig. 3a. In order to keep away from the vascular edges as far as possible, the window in this paper is limited to the centerline segment without strip width (i.e. the purple curve in Fig. 3a) and the window length is a user-defined parameter. This window is centered at the tree vertex (i.e. the blue point in Fig. 3a), which has the minimal cost function value as (1).

The function $cost\_to\_come$ returns the cumulative path length from the tree root to current node x. $cost\_to\_go$ indicates the cost to the goal location from current node x, and it can be represented by the Euclidean distance from x to the goal location.

$$
\begin{aligned}
f(x) &= cost\_to\_come(root, x) + h(x) \\
h(x) &= cost\_to\_go(x, goal)
\end{aligned}
\tag{1}
$$

Even if the samples are generated on the centerline, it does not mean that the connected edge between vertices strictly locates on the centerline as shown in Fig. 3b. In order to avoid getting stuck in a local minimum (i.e. keeping sampling locally around the vertex with minimal cost without exploring other
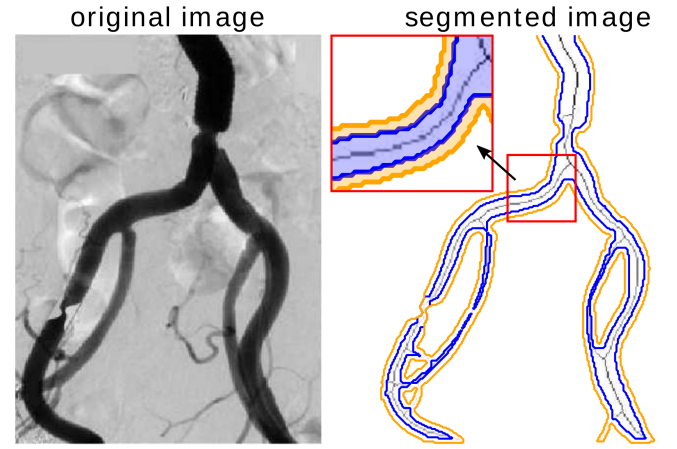

original image   segmented image

Fig. 2: Image segmentation and centerline extraction. The contour of segmented vessel is presented with orange line and the centerline is shown with greys heat map. The darker is the centerline color, the longer is the distance from vessel edges. The search space is defined as the zone within the blue contour.
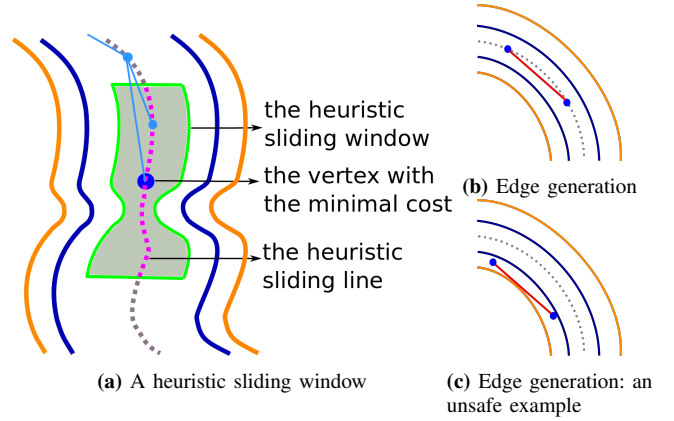

the heuristic sliding window

the vertex with the minimal cost

the heuristic sliding line

(a) A heuristic sliding window

(b) Edge generation

(c) Edge generation: an unsafe example

Fig. 3: HSW-RRT tree construction

possibilities), the sample should also be randomly generated in the overall centerline strip at a certain rate. For more details, see the pseudocode in Algorithm 1.

C. Path smoothing

The path solution obtained from HSW-RRT is a list of setpoints. The non-differentiable connections between line segments will exceed the robot manipulability. Path smoothing is required to meet robot's kinematics, i.e. the curvature of path should be bounded.

B-Spline is a spline function that has local support with respect to a given degree, smoothness, and domain partition. Given a knot sequence $t_0, ..., t_i, ..., t_m$, $m + 1$ B-splines with degree n can be defined by construction by means of the Cox–de Boor recursion formula as in (2).

$$
\begin{aligned}
b_{i,0}(x) &= \begin{cases} 1 & t_i \leq x < t_{i+1} \\ 0 & otherwise \end{cases} \\
b_{i,n}(x) &= \frac{x - t_i}{t_{i+n} - t_i} b_{i,n-1}(x) + \frac{t_{i+n+1} - x}{t_{i+n+1} - t_{i+1}} b_{i+1,n-1}(x)
\end{aligned}
\tag{2}
$$

The curvature at point (x, y) can be defined as (3). The maximal curvature of final path is evaluated as the smoothness

Algorithm 1 HSW-RRT
***
Input: search space X, initial and goal point x_{init}, x_{goal}
Output: path solution
Parameter: maximum edge length q, number of child vertices k, maximum number of samples n_{max}, resolution of points when checking collision, probability of checking solution, probability of sampling in overall free space p
***
 1: **procedure** HSW-RRT PATH SEARCHING
 2:     *initialization*(inputs and parameters)
 3:     *add_vertex*(x_{init})
 4:     *add_edge*(x_{init})
 5:     **while** true **do**
 6:         **for** i in q **do**
 7:             **for** j in $(1 : k)$ **do**
 8:                 **if** *random()* $< p$ **then**
 9:                     $x_{rand} \leftarrow random\_centerline()$
10:                 **else**
11:                     $x_{rand} \leftarrow random\_hsw(f_x)$
12:                 $x_{near} \leftarrow nearest\_vertex(x_{rand})$
13:                 $x_{new} \leftarrow new\_vertex(x_{rand}, x_{near}, \text{i})$
14:                 *add_vertex*(x_{new})
15:                 $L_x, L_c, f_x \leftarrow get\_nearby\_vertices(x_{new})$
         ▷ get the list of nearby vertices L_x with their cost-to-come L_c and the node with minimal cost function value f_x
16:                 *add_vertex*(x_{new})
17:                 *add_shortest_edge*(L_x, x_{new})
18:                 *rewire_tree*(L_x, x_{new})
19:                 $sol \leftarrow check\_solution()$
20:                 **if** *sol is true* **then return** path
         ▷ exit loop when finding a path or reaching n_{max}
***

in order to inspect the catheter nonholonomic constraints as index of performance.

$$curvature(x, y) = \frac{|\dot{x}\ddot{y} - \dot{y}\ddot{x}|}{(\dot{x}^2 + \dot{y}^2)^{\frac{3}{2}}} \quad (3)$$

III. RESULTS

The simulation is carried out in the PyCharm platform on a computer with Ubuntu system. This computer is equipped with an Intel (R) Core (TM) i5-8250U CPU @ 1.60 GHz 1.80 GHz processor and 8 GB RAM.

The simulation results of path planning via RRT, RRT* and HSW-RRT are shown in Fig. 4-7. The proposed method is also validated in another case as Fig. 7, which is a part of the vascular tree in the leg from [23]. The initial and goal location are the black and purple points, respectively. Blue line represents the tree expansion during the path searching procedure. Green line depicts the generated path after searching. And red line shows the final solution after path smoothing.

The performance evaluation of the proposed method is summarized in TABLE I, compared with traditional RRT series methods. The time cost, the path length, and the path maximal curvature are evaluated from 10 sets of start and goal states. The time cost is determined not only by the path planning
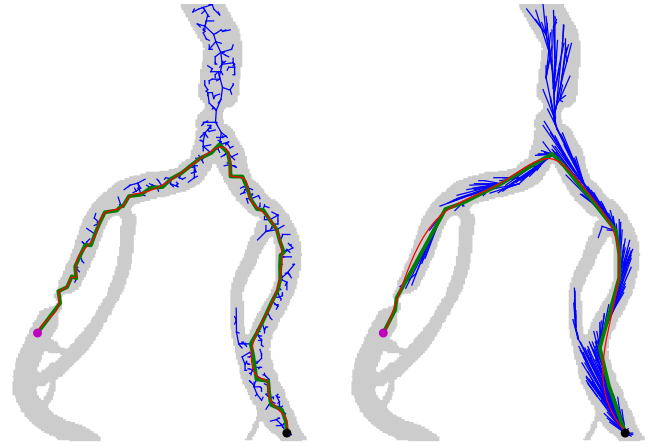

Fig. 4: The simulation result of RRT path planning

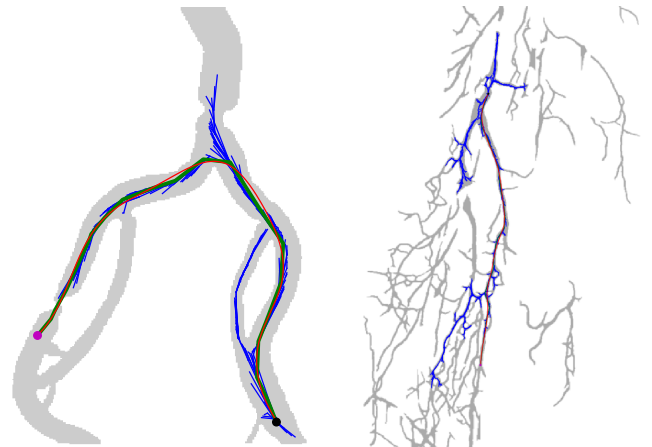
Fig. 5: The simulation result of RRT* path planning

Fig. 6: The simulation result of HSW-RRT path planning: case 1

Fig. 7: The simulation result of HSW-RRT: case 2 (from [23])

method, but also by the entry and the target points, i.e. the time cost varies upon different scenarios. The HSW-RRT generates a path solution with similar length and smoothness as RRT*, and takes less time effort than it. Even if HSW-RRT takes longer time than RRT, it's still worthwhile, considering the quality of path. If the femoral endovascular procedure takes from 45s to 25s [24], and the maximum bending angle is around $77°/cm$ (i.e. $0.086\ rad/px$ in Fig. 6), the path planning algorithm is reasonable. The catheter in [25] is designed with a maximum bending angle $61°/cm$, which means the path can be infeasible if the nonholonomic constraints are ignored during path planning.

TABLE I: The performance comparison.

Method	Time (ms)	Length of Path (px)	Maximal Curvature (rad/px)
RRT	300.2 ± 100.1	420.1 ± 22.1	0.902 ± 0.675
RRT*	4018.4 ± 1598.1	374.7 ± 6.8	0.070 ± 0.026
HSW-RRT	1598.2 ± 276.2	373.1 ± 9.9	0.086 ± 0.050

Note: 10 sets of start and goal locations are tested, which is $(283\pm4, 183\pm3)$ and $(218 \pm 3, 22 \pm 3)$, respectively.

IV. CONCLUSION

In this paper, a novel HSW-RRT method is proposed for endovascular catheterization. Instead of randomly sampling in the overall search space, this method uses a heuristic sliding window to improve the sampling efficiency. In order to avoid getting stuck in a local minimum, the sample should also be randomly generated in the overall centerline strip at a certain rate. Simulation results show the feasibility of this path planning method in 2D scenarios and the path solution can be generated around 1.6s for femoral endovascular catheterization. The HSW-RRT generates a path solution with similar length and smoothness as RRT*, and takes less time effort than it. Even though HSW-RRT takes longer time than RRT, it's still worthwhile, considering its reliability.

Later on, (i) the nonholonomic constraints should be expressed as bounded curvature, and controlled quantitatively via path smoothing or edge construction; (ii) the path planning will be implemented in 3D scenarios and the computational velocity will be improved; (iii) a re-planning algorithm based on initial path should be proposed when the deformation of environments is detected, taking the advantage of pre-operative path; (iv) if the full 3D model can not be reconstructed in real-time, vision servoing based control can be used for the intra-operative navigation of catheter by using 2D images, which will be investigated and implemented in the future.

REFERENCES

[1] L. L. Nadal, J. Cynamon, E. C. Lipsitz, and A. Bolia, "Subintimal angioplasty for chronic arterial occlusions," *Techniques in vascular and interventional radiology*, vol. 7, no. 1, pp. 16–22, 2004.

[2] AICD, "Cardiology patient eduction." [Online]. Available: www.aicdheart.com/patient_education/heart_HTML_scaleable/heart/fempop.htm

[3] B. Geiger, A. P. Kiraly, D. P. Naidich, and C. L. Novak, "Virtual bronchoscopy of peripheral nodules using arteries as surrogate pathways," in *Medical Imaging 2005: Physiology, Function, and Structure from Medical Images*, A. A. Amini and A. Manduca, Eds. SPIE, Apr. 2005.

[4] W. Sabra, M. Khouzam, A. Chanu, and S. Martel, "Use of 3d potential field and an enhanced breadth-first search algorithms for the path planning of microdevices propelled in the cardiovascular system," in *2005 IEEE Engineering in Medicine and Biology 27th Annual Conference*. IEEE, 2006, pp. 3916–3920.

[5] S. Schafer, V. Singh, K. R. Hoffmann, P. B. Noël, and J. Xu, "Planning image-guided endovascular interventions: guidewire simulation using shortest path algorithms," in *Medical Imaging 2007: Visualization and Image-Guided Procedures*, K. R. Cleary and M. I. Miga, Eds. SPIE, Mar. 2007.

[6] K. Ratnayaka, T. Rogers, W. H. Schenke, J. R. Mazal, M. Y. Chen, M. Sonmez, M. S. Hansen, O. Kocaturk, A. Z. Faranesh, and R. J. Lederman, "Magnetic resonance imaging–guided transcatheter cavopulmonary shunt," *JACC: Cardiovascular Interventions*, vol. 9, no. 9, pp. 959–970, May 2016.

[7] C. Sánchez, M. Diez-Ferrer, J. Bernal, F. J. Sánchez, A. Rosell, and D. Gil, "Navigation path retrieval from videobronchoscopy using bronchial branches," in *Clinical Image-Based Procedures. Translational Research in Medical Imaging*. Springer International Publishing, 2016, pp. 62–70.

[8] S. Martel, J.-B. Mathieu, O. Felfoul, A. Chanu, E. Aboussouan, S. Tamaz, P. Pouponneau, L. Yahia, G. Beaudoin, G. Soulez *et al.*, "Medical and technical protocol for automatic navigation of a wireless device in the carotid artery of a living swine using a standard clinical mri system," in *International Conference on Medical Image Computing and Computer-Assisted Intervention*. Springer, 2007, pp. 144–152.

[9] Y. Chang, X. Wang, Z. An, and H. Wang, "Robotic path planning using a* algorithm for automatic navigation in magnetic resonance angiography," in *2018 40th Annual International Conference of the IEEE Engineering in Medicine and Biology Society (EMBC)*. IEEE, 2018, pp. 734–737.

[10] Y. Xiao, W. Tan, Q. Zhou, and Y. Ji, "Pulmonary vascular segmentation algorithm based on fractional differential enhancement," in *International Conference on Mechatronics and Intelligent Robotics*. Springer, 2018, pp. 1262–1274.

[11] F. Yang, Y. Dai, J. Zhang, H. Sun, L. Cui, X. Yin, X. Gao, and L. Li, "Path planning of flexible ureteroscope based on ct image," in *2019 Chinese Control Conference (CCC)*. IEEE, 2019, pp. 4667–4672.

[12] K. Meng, Y. Jia, H. Yang, F. Niu, Y. Wang, and D. Sun, "Motion planning and robust control for the endovascular navigation of a microrobot," *IEEE Transactions on Industrial Informatics*, 2019.

[13] D. Huang, P. Tang, Y. Wang, L. Hejuan, W. Tang, and Y. Ding, "Computer-assisted path planning for minimally invasive vascular surgery," *Chinese Journal of Electronics*, vol. 27, no. 6, pp. 1241–1249, 2018.

[14] C. Tercero, S. Ikeda, T. Fukuda, F. Arai, M. Negoro, and I. Takahashi, "Catheter insertion reference trajectory construction method using photoelastic stress analysis for quantification ofRespect for TissueDuring endovascular surgery simulation," *International Journal of Optomechatronics*, vol. 5, no. 4, pp. 322–339, Oct. 2011.

[15] H. Rafii-Tari, J. Liu, S.-L. Lee, C. Bicknell, and G.-Z. Yang, "Learning-based modeling of endovascular navigation for collaborative robotic catheterization," in *Advanced Information Systems Engineering*. Springer Berlin Heidelberg, 2013, pp. 369–377.

[16] W. Chi, J. Liu, M. E. M. K. Abdelaziz, G. Dagnino, C. Riga, C. Bicknell, and G.-Z. Yang, "Trajectory optimization of robot-assisted endovascular catheterization with reinforcement learning," in *2018 IEEE/RSJ International Conference on Intelligent Robots and Systems (IROS)*. IEEE, Oct. 2018.

[17] W. Chi, J. Liu, H. Rafii-Tari, C. Riga, C. Bicknell, and G.-Z. Yang, "Learning-based endovascular navigation through the use of non-rigid registration for collaborative robotic catheterization," *International Journal of Computer Assisted Radiology and Surgery*, vol. 13, no. 6, pp. 855–864, Apr. 2018.

[18] X. Wang, Z. An, Y. Zhou, H. Wang, and Y. Chang, "Automating robot motion planning for magnetic resonance navigation using q-learning," in *2018 IEEE International Conference on Cyborg and Bionic Systems (CBS)*. IEEE, 2018, pp. 304–307.

[19] L. G. Torres, R. J. Webster, and R. Alterovitz, "Task-oriented design of concentric tube robots using mechanics-based models," in *2012 IEEE/RSJ International Conference on Intelligent Robots and Systems*. IEEE, 2012, pp. 4449–4455.

[20] C. Bergeles and P. E. Dupont, "Planning stable paths for concentric tube robots," in *2013 IEEE/RSJ International Conference on Intelligent Robots and Systems*. IEEE, 2013, pp. 3077–3082.

[21] K. Belharet, D. Folio, and A. Ferreira, "Simulation and planning of a magnetically actuated microrobot navigating in the arteries," *IEEE Transactions on Biomedical engineering*, vol. 60, no. 4, pp. 994–1001, 2012.

[22] Y. Yokoi, "Basics of angiography for peripheral artery disease," *Angiography and Endovascular Therapy for Peripheral Artery Disease*, p. 1, 2017.

[23] P. Bruno, P. Zaffino, S. Scaramuzzino, S. De Rosa, C. Indolfi, F. Calimeri, and M. F. Spadea, "Using cnns for designing and implementing an automatic vascular segmentation method of biomedical images," in *International Conference of the Italian Association for Artificial Intelligence*. Springer, 2018, pp. 60–70.

[24] H. Clogenson, "Mri-compatible endovascular instruments: Improved maneuverability during navigation," 2014.

[25] A. Ali, A. Sakes, E. A. Arkenbout, P. Henselmans, R. van Starkenburg, T. Szili-Torok, and P. Breedveld, "Catheter steering in interventional cardiology: Mechanical analysis and novel solution," *Proceedings of the Institution of Mechanical Engineers, Part H: Journal of Engineering in Medicine*, vol. 233, no. 12, pp. 1207–1218, 2019.

Estimation of the base of support during gait with an unobtrusive wearable system

R. Rossanigo[1], S. Bertuletti[2], M. Caruso[1], M. Knaflitz[1], U. Della Croce[2], and A. Cereatti[2]

[1] *Department of Electronics and Telecommunications, Politecnico di Torino*
[2] *Department of Biomedical Sciences, University of Sassari*

Abstract—**This study aimed at estimating the base of support (BoS) during gait with an unobtrusive wearable system. The BoS is the area identified by the points of contact of the body with the ground. During the double-support phase of gait both feet contribute to the BoS. The BoS is a measure of the subject's balance. The estimation of the BoS outdoors is still an open issue. The innovative hardware presented here is a combination of a magneto-inertial measurement unit (MIMU) and two infrared time of flight (IR-ToF) sensors. The methods implemented to estimate the BoS were tested on a healthy subject and validated with a stereo-photogrammetric system. The results suggest that the solution proposed may be an effective and low-cost tool for the estimate of the BoS during gait in outdoor conditions.**

Keywords—**out-of-lab gait analysis, MIMU, infrared time-of-flight sensors, base of support.**

I. INTRODUCTION

THERE is ample evidence that the base of support (BoS) and the step width (SW) are important parameters for the assessment of dynamic stability, balance control and risk of falling in healthy and pathological gait [1], [2]. In general, widening the BoS leads to an increase of stability as often observed in parkinsonian patients and in the elderly [3].

The BoS during walking can be defined as the area comprised by the outer edges of the feet in contact with the ground [4]. It is closely related to the SW, which is defined as the mediolateral distance between the feet [1].

In most studies assessing stability, BoS and SW were estimated from force-platforms and a stereo-photogrammetric (SP) system [1], [4]-[7]. Although these technologies provide accurate estimates, they restrict gait analysis to laboratory applications. Miniaturized magneto-inertial measurement units (MIMUs) have been proposed to analyse gait in real life, mostly in terms of body segments kinematics and of gait temporal and spatial parameters, such as stride time and stride length [8]-[11]. However, it is not possible to directly determine the relative position of two body segments in a common reference coordinate system using two MIMUs attached to them, as the physical quantities recorded by each MIMU are self-referenced [12]. This limitation makes MIMUs alone not suitable for estimating the BoS in real-world conditions. To overcome this limitation, the most straightforward solution is to integrate the MIMU system with additional sensors capable to provide distance measurements (i.e. inter-foot distance, IFD). There are few studies in the literature estimating IFD in out-of-lab conditions using ultrasound or infrared (IR) sensors. Weenk *et al.* [13] proposed a method to calculate the IFD using ultrasound sensors, requiring the instrumentation of both feet, using both an emitter and a receiver. Hung *et al.* [14] proposed to attach an IR LED to a foot and a camera to the other, a solution too bulky to be suitable for prolonged use. Methods based on light-intensity IR sensors as proposed by Trojaniello *et al.* [1] overcome the limit of the hardware distinction between emitter and receiver, however their performance is not stable as the environmental conditions change [16], [17]. Recently, Bertuletti *et al.* [17] proposed to integrate IR time-of-flight (ToF) sensors and a MIMU in a single wearable system (SWING). This technology, compared to the previous ones, allows to embed the transmitter and the receiver in the same chip, to reduce the size of the sensor, to increase the output data rate up to 50 Hz, lower power consumption (~2-5 mA) and to guarantee stable performance changing the environmental conditions [17]. The system was used for IFD estimation and step detection [18].

The goal of this work was to devise and preliminarily validate innovative methods based on the combined use of IR-ToF sensors and magneto-inertial technologies for the estimation of SW and BoS. Data acquired during straight walking of a healthy subject were compared to concurrent stereo-photogrammetric data, used as a gold standard.

II. MATERIAL AND METHODS

A. Experimental setup

The SWING system [19] was attached to the medial side of the right foot, identified as the instrumented foot (InFoot).

The MIMU (3D accelerometer range ±16 g, 3D gyroscope range ±2000 dps, 3D magnetometer range ±50 Gauss, output data rate 100 Hz) and the IR-ToF sensors (VL6180X, STMicroelectronics [20], measured distance range 0−200 mm, sampling frequency 50 Hz), were positioned as described by Bertuletti *et al.* [18].

The position of twenty retro-reflective markers attached to both feet (Fig. 1) were recorded by a 12-camera SP system (mod. Vero, Vicon, Oxford, UK).

Data were recorded while a healthy subject walked at a self-selected speed along a 5 m-walkway for 10 times with and without a flat screen applied to the medial side of the non-instrumented foot (Non-InFoot). To synchronize SWING data and SP data, the subject was asked to hit the InFoot on a force platform (electronically synchronized with the SP system) at the beginning and at the end of each acquisition.

Experiments conformed to the standards set in the Declaration of Helsinki.
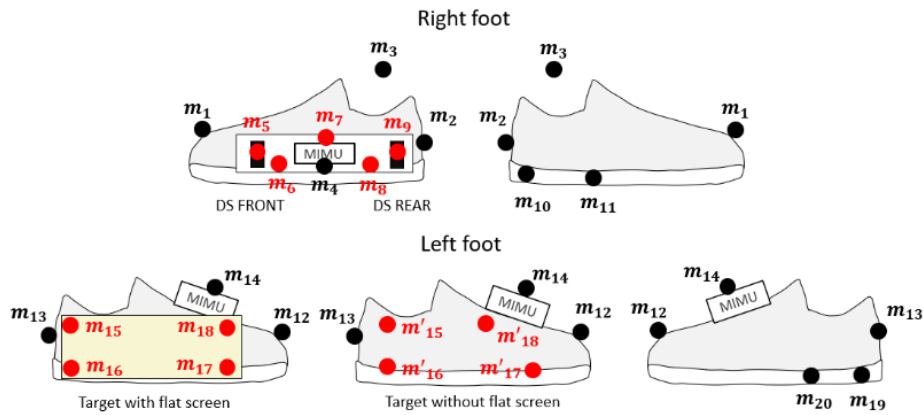
Fig. 1: Experimental setup. A rigid support with a MIMU and two IR-ToF sensors (DS REAR and DS FRONT) is attached to the medial side of the right foot. The MIMU attached to the left foot was used only to ensure that the Non-InFoot was stationary during the considered IR-ToF recordings. The black and red dots are the markers. The red markers are used only in the static acquisition for calibration purposes and removed during dynamic acquisitions not to interfere with the acquired movement. Their trajectories are reconstructed exploiting the rigidity of the three markers in the rear foot (m_2, m_{10}, m_{11} for the right foot and m_{13}, m_{19}, m_{20} for the left foot) . The first two illustrations of the left foot show the two tested setups with and without a screen attached to the medial side of the foot.

B. Data Analysis

The orientation of the InFoot was obtained using a sensor fusion algorithm based on the Madgwick's filter [21]. The displacement of the InFoot was obtained by double integrating the accelerations, after filtering [22] and gravity subtraction [9]. The integration interval was defined between two consecutive foot flat instants of the InFoot. To evaluate the foot flat instant a ZUPT detector based on the gyroscopic signals was applied [23]. To reduce drift, direct and reverse integration was implemented [22].

Once both orientation and position of the InFoot were determined in each instant of time, the position of the Non-InFoot with respect to a common coordinate system was obtained by following the procedure described below.

1. During the InFoot swing phase, IR-ToF readings provided the values of the distance between the IR-ToF sensors on the InFoot and the Non-InFoot surface.

2. The observed points on the Non-InFoot medial surface were all expressed in a global coordinate system (GCS), the InFoot (MIMU) coordinate system (in orange in Fig. 2) at the beginning of the swing (toe-off t_0 in Fig. 2).

3. The detected points of the Non-InFoot expressed in the GCS are fitted with a linear model, approximating the medial side of the Non-InFoot. The actual foot length is imposed to the linear model to define a segment approximating the medial edge of the Non-InFoot footprint.

C. SW and BoS estimation

The SW was estimated as the average of the recorded distances between the InFoot and the reconstructed Non-InFoot during the swing of a foot.

Reference values for SW were obtained based on marker trajectories, by computing the line passing through the IR-ToF
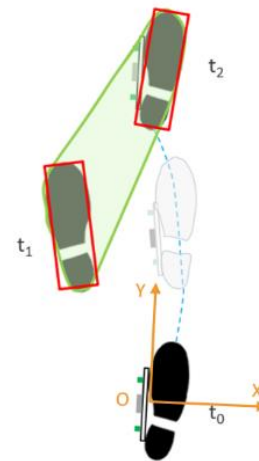

Fig. 2: Footprints from the beginning (t_0) to the end (t_2) of the swing phase of the InFoot. The BoS is considered between the Non-InFoot footprint in its stance phase (t_1) and the InFoot footprint in t_2. The red rectangles are the approximation of the footprints. The BoS is the green area. The light blue dotted line represents the right foot trajectory. The GCS is represented in orange.

sensors and perpendicular to the rigid support. The position of the IR-ToF sensors, the rigid support, as well as the medial side of the Non-InFoot (Fig. 1) were reconstructed by calibrating them during a static acquisition [24] and during dynamic acquisitions, knowing the position and orientation of both feet with respect to GCS, the trajectories of the markers were achieved.

The BoS was defined as the sum of the area of each footprint and the area between them during double support (Fig. 2). The footprints obtained with the SWING system were approximated with a rectangle with sides equal to the measured foot length and width, and the area between them is calculated with the Bretschneider formula for irregular quadrilaterals.

The gold standard values of the BoS were computed obtaining the feet length with the heel and toe marker, while the width of the footprint was imposed. The footprint medial vertices are linked to define the area between the feet.

Errors affecting the BoS estimation were characterized by the area error and the BoS location error (left/right shift). The latter is evaluated as the distance between the footprint centers calculated with the wearable system and with the SP system (Fig. 3). Fig. 4 shows a BoS area shifted forward and left with respect to the corresponding BoS obtained with the SP system. Thus, the footprint centers obtained with the wearable system do not coincide with those obtained with the SP system.

A descriptive statistic on both area errors and left/right shifts was computed considering the mean, standard deviation and 95% confidence interval, which is taken as descriptor of the measurement precision.

III. RESULTS

Errors affecting the estimates of both SW and BoS were computed with and without the presence of the screen on the medial side of the Non-InFoot.

A total of 92 SW values with the screen and 69 without were analysed, whereas a total of 20 BoS values both with and without the screen were analysed. Table I-IV illustrate the results.

When the screen is used the estimated Non-InFoot footprint is on average 55 mm far from its position obtained with the SP system as opposed to 62 mm when the screen is not used (Table III and IV). The InFoot position error is on average 67 mm with the screen and 92 mm without it (Table III and IV).

IV. DISCUSSION AND CONCLUSIONS

The study proposed and validated a method for estimating SW and BoS alternative to current methods used in gait analysis laboratories. Instrumenting a foot with a MIMU and two IR-ToF sensors was shown to be adequate to obtain valuable estimates of SW and BoS, in healthy gait.

The use of a screen applied to the medial side of the non-instrumented foot was shown to be beneficial for the estimate
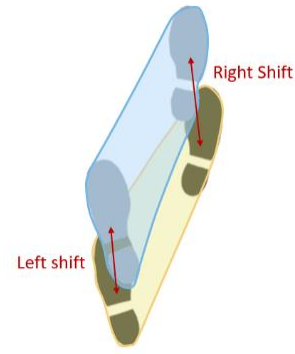

Fig. 3: BoS area obtained with wearable system (light blue) and with the SP system (yellow). If the position on the floor of the areas does not coincide, the Left and Right Shit are defined as the distance between the footprint centers.
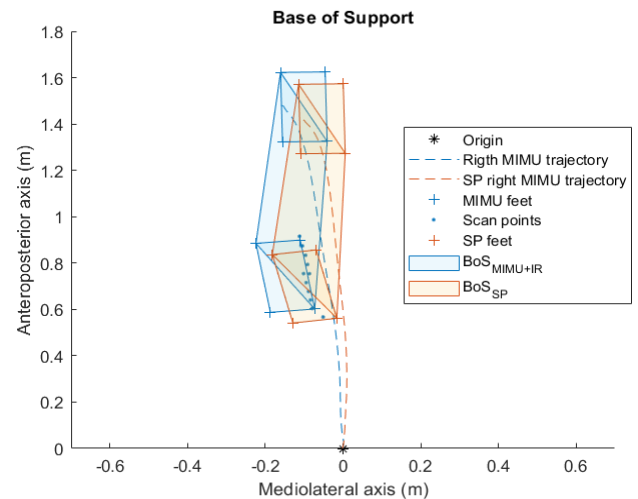

Fig. 4: A BoS obtained with the wearable system (light blue) and with the gold standard (yellow). The light blue dots ('scan points' in the legend) are the points of the Non-InFoot detected by the IR ToF sensors. It can be noticed that the resulting BoS is shifted forward and left..

TABLE I
SW VALUES AND ERRORS (WITH SCREEN)

Mean (mm)	Mean Error (mm)	Std Error (mm)	Percentage Error (%)	95% Confidence Interval Error (mm)
74	-23	21	23	(-27, -18)

TABLE II
SW VALUES AND ERRORS (WITHOUT SCREEN)

Mean (mm)	Mean Error (mm)	Std Error (mm)	Percentage Error (%)	95% Confidence Interval Error (mm)
56	-27	32	32	(-34, -19)

Table I and Table II: SW obtained results in terms of estimates and errors, calculated on 92 steps with the screen and on 69 steps without it. Negative values correspond to underestimation.

TABLE III
BoS ERRORS (WITH SCREEN)

Error Type	Mean	Std	95% Confidence interval
Area Error (mm^2)	-4100	6300	(-6900, 1300)
Percentage Area Error (%)	3.8	2.9	(2.5, 5.1)
Left shift (mm)	55	24	(45, 65)
Right shift (mm)	67	32	(53 81)

TABLE IV
BoS ERRORS (WITHOUT SCREEN)

Error Type	Mean	Std	95% Confidence Interval
Area Error (mm^2)	-12500	34500	(-27600, 2600)
Percentage Area Error (%)	10.1	19.8	(1.5, 18.8)
Left shift (mm)	62	27	(50, 74)
Right shift (mm)	94	46	(74, 114)

Table III and Table IV: BoS estimate errors calculated over 20 strides with and without the screen. Area error is the difference between the BoS area found with the wearable system and that found with the SP system. The left and right shifts are the distances between the footprint centers obtained with the wearable system and those obtained with the SP system. Negative values correspond to underestimation.

of both SW and BoS: 23% SW error with the screen vs 32% without it (Table I and II), 4% BoS area error with the screen vs 10% without it (Table III and IV). This is mainly due to the irregular surface of the Non-InFoot medial side. However, these preliminary results suggest that the experimental setup without the screen can be adopted for a greater comfort of the subject, considering that the SW errors differences between the two setups are not significant and that the 95% confidence intervals of SW and BoS errors overlap.

It was also observed that the IR-ToF sensors should not be positioned too close to the shoe sole to increase the chances of correctly recording signals even during swings characterized by a high clearance [18]. The maximum measured distance was set to 200 mm. This choice was a compromise resulting from two considerations: it had to be high enough to include cases of a significant external foot rotation, without compromising the output data rate [18].

The position estimation and the fitting of the non-instrumented foot are the most crucial sources of errors. In fact, the footprint position estimation is affected by an error both in the medio-lateral and the anteroposterior directions (Fig. 4). Besides the inaccuracy in fitting the distance data, the displacement estimation corrupts the footprint positioning due to some residual integration drift.

Future work should primarily focus on: *i)* improving the displacement estimation to enhance footprint positioning and *ii)* increasing the number of IFD values collected per stride to improve the reliability of the fitting of the distance data. This can be done either by using more than two IR-ToF sensors or by adopting a new technology that allows to estimate the IFD with an output data rate higher than 50 Hz.

Furthermore, methods' robustness should be tested on a larger number of subjects both healthy and with gait disorders.

REFERENCES

[1] E. Yiou, C. Teyssèdre, ''Comparison of base of support size during gait initiation using force-plate and motion-capture system: A Bland and Altman analysis'', *Journal of Biomechanics*, 49:4168–72, 2016.
[2] D. E. Krebs, D. Goldvasser, J. D. Lockert, L. G. Portney, K. M. Gill-Body, ''Is base of support greater in unsteady gait?'', *Physical Therapy*, vol. 82, February 2002.
[3] C. J. Hass, P. Malczak, J. Nocera, E. L. Stegemöller, A. Shukala, I. Malty, C.E. Jacobson, M. S. Okun, N. McFarland, ''Quantitative normative gait data in a large cohort of ambulatory persons with Parkinson's disease'', *PLoS ONE* 7(8): e42337, 2012. Available from: doi:10.1371/journal.pone.0042337
[4] V. Lugade, V. Lin, L. Chou, ''Center of mass and base of support interaction during gait'', *Gait & Posture*, 33: 406-411, 2011. Available from: doi:10.1016/j.gaitpost.2010.12.013
[5] T. Caderby, E. Yiou, N. Peyrot, M. Begon, G. Dalleau, ''Influence of gait speed on the control of mediolateral dynamic stability during gait initiation'', *Journal of Biomechanics,* 47(2):417–23, 2014. Available from: http://dx.doi.org/10.1016/j.jbiomech.2013.11.011
[6] T. Caderby, E. Yiou, N. Peyrot, B. Bonazzi, G. Dalleau, ''Gait Parameters Estimated Using Inertial Measurement Units: Detection of swing heel-off event in gait initiation using force-plate data'', *Gait & Posture*, 37(3):463–6, 2013. Available from: http://dx.doi.org/10.1016/j.gaitpost.2012.08.011
[7] M. Arvin, M. Mazaheri, M. J. M. Hoozemans, M. Pijnappels, B. J. Burger, S. M . P. Verschueren et al. , ''Effects of narrow base gait on mediolateral balance control in young and older adults'', *Journal of Biomechanics*, 49(7):1264–7, 2016. Available from: http://dx.doi.org/10.1016/j.jbiomech.2016.03.011
[8] D. Trojaniello, A. Cereatti, E. Pelosin, L. Avanzino, A. Mirelman, J. M. Hausdorff et al., ''Zero-Velocity Detection - An Algorithm Evaluation.Estimation of step-by-step spatiotemporal parameters of normal and impaired gait using shank-mounted magneto-inertial sensors: Application to elderly, hemiparetic, parkinsonian and choreic gait'', *Journal of NueroEngineering and Rehabilitation*, 11(1):152, 2014.
[9] B. Mariani, C. Hoskovec, S. Rochat, C. Büla, J. Penders, K. Aminian, ''3D gait assessment in young and elderly subjects using foot-worn inertial sensors'', *Journal of Biomechanics*, 43(15):2999–3006, 2010.
[10] A. Cereatti, D. Trojaniello, U. della Croce, ''Accurately measuring human movement using magneto-inertial sensors: techniques and challenges'', IEEE International Symposium on Inertial Sensors and Systems (ISISS), 2015.
[11] M. Bertoli, A. Cereatti, D. Trojaniello, L. Avanzino, A. Pelosin *et al.*, ''Estimation of spatio-temporal parameters of gait from magneto-inertial measurement units: multicenter validation among Parkinson, mildly cognitively impaired and healthy older adults'', *Biomedical Engineering Online*, 17(1), 58, 2018.
[12] A. M. Sabatini, ''Estimating three-dimensional orientation of human body parts by inertial/magnetic sensing'', *Sensors*, 11(2):1489–525, 2011.
[13] D. Weenk, D. Roetenberg, B. J. J. F Van Beijnum, H. J. Hermens, P. H. Veltink, ''Ambulatory estimation of relative foot positions by fusing ultrasound and inertial sensor data'', *IEEE Transactions on Neural Systems Rehabilitation Engineering*, 23(5):817–26, 2015.
[14] T. N. Hung, Y. S. Suh, ''Inertial sensor-based two feet motion tracking for gait analysis'', *Sensors*, 13, 5614-5629, 2013.
[15] D. Trojaniello, A. Cereatti, A. K. Bourke, K. Aminian, U. Della Croce, ''A waerable system for the measurement of the inter-foot distance during gait'', 20th IMEKO TC4 International Symposium and 18th International Workshop on ADC Modelling and Testing, 2014.
[16] T. Mohammad, ''Using Ultrasonic and Infrared Sensors for Distance Measurement'', *World Acad. Sci. Eng. Technol.*, 3, 267–272, 2009.
[17] S. Bertuletti, A. Cereatti, D. Comotti, M, Caldara, U. Della Croce, ''Static and dynamic accuracy of an innovative miniaturized wearable platform for short range distance measurements for human movement applications'', *Sensors*, 17:1492, 2017. Available from: doi:10.3390/s17071492
[18] S. Bertuletti, U. Della Croce, A. Cereatti, ''A wearable solution for accurate step detection based on the direct measurement of the inter-foot distance''. *Journal of Biomechanics*, 84:274–7, 2019. Available from: https://doi.org/10.1016/j.jbiomech.2018.12.039
[19] A. Cereatti, S. Bertuletti, M. Caldara, U. Della Croce, ''Sistema per l'analisi dell'attività motoria di una persona e relativo metodo'', Pat. 102017000003986, Italy, 2017.
[20] STMicroelectronics VL6180X. Available from: http://www.st.com/content/st_com/en/ products/imaging-and-photonics-solutions/proximity-sensors/vl6180x.html
[21] S. Madgwick, ''An efficient orientation filter for inertial and magneto-inertial sensor arrays'', Report x-io and University of Bristol, 2010.
[22] M. Zok, C. Mazzà, U. Della Croce, ''Total body centre of mass displacement estimated using ground reactions during transitory motor tasks: Application to step ascent'', *Medical Engineering and Physics*, 26(9 SPEC.ISS.):791–8, 2014.
[23] I. Skog, P. Händel, I. Skog, P. H. Andel, ''Zero-Velocity Detection — An Algorithm Evaluation'', IEEE Transcations on Biomedical Engineering, 2010.
[24] A. Cappozzo, F. Catani, U. Della Croce, A. Leardini, ''Position and orientation in space of bones during movement: anatomical frame definition and determination'', *Clinical Biomechanics*, vol. 10, no. 4, 171-178, 1995.

Correlation between hyper-acute EEG alterations and 7-Day NIHSS score in thrombolysis treated ischemic stroke patients

M. Ajčević[1], G. Furlanis[2], A. Miladinović[1], L. Stragapede[2], G. Silveri[1], P. Caruso[2], M. Naccarato[2], P. Manganotti[2] and A. Accardo[1]

[1] *Department of Engineering and Architecture, University of Trieste, Trieste, Italy*
[2] *Department of Medicine Surgery and Health Sciences, University of Trieste, Trieste, Italy*

Abstract—Early post-stroke prognosis is important for guiding treatment and rehabilitation strategies in order to improve recovery and minimize disability. Several demographic, clinical and neuroimaging factors were associated with functional outcome. Early prediction of post-stroke outcome is still challenging since there is large inter-subject variability. Thus, biomarkers that can add prognostic information are still needed.

This pilot study aimed to investigate the correlation between early stroke-related EEG changes, measured on bedside with wireless EEG device and short-term functional outcome, measured with 7-day National Institutes of Health Stroke Scale (NIHSS), in thrombolysis treated ischemic stroke patients.

Delta/alpha power ratio (ρ=0.67, p=0.031) and relative delta power (ρ=0.66, p=0.037) correlated directly with 7-day NIHSS, while relative alpha power (ρ =-0.69, p=0.028) correlated inversely with 7-day NIHSS.

In conclusion, in this preliminary study we assessed the correlation between EEG spectral parameters obtained in the pre-treatment hyper-acute phase and short-term functional outcome. These preliminary results highlight the value of hyper-acute EEG as a possible complementary tool in the evaluation of stroke severity and its potential role in the prediction of stroke-related outcome.

Keywords—EEG, Signal processing, Ischemic stroke, Outcome prediction.

I. INTRODUCTION

Despite advances in disease prevention, acute treatment and rehabilitation, ischemic stroke is still one of the principal causes of disability and mortality worldwide [1]. This neuroemergency condition is currently highly treatable using thrombectomy and intravenous thrombolysis to restore cerebral blood flow in selected patients [2]. Thrombolysis is widely adopted to facilitate reperfusion in patients with acute ischemic stroke, and its benefits are well established [2], [3], also in wake-up stroke patients [4].

Neuroimaging, together with clinical assessment, has been proving to play a key role in ischemic stroke diagnosis and it is of paramount importance for patients' eligibility for reperfusion therapy [5]-[9]. The National Institutes of Health Stroke Scale (NIHSS), consisting of 11 items to assess the main neurological functions, is the most adopted tool in the actual medical practice to evaluate neurologic impairment caused by stroke [10]. Early post-stroke short- and long-term prognostication is crucial for guiding the treatment and rehabilitation strategies in order to improve recovery and minimize the final disability [11]. Over the years, several demographic, clinical and neuroimaging factors were associated with functional outcome. Nevertheless, early prediction of outcome in ischemic stroke patients is still challenging because of large inter-subject variability [12]. Hence, biomarkers that can add prognostic information are still needed.

EEG is a non-invasive diagnostic technique, with a high temporal resolution, providing a rapid evaluation of instantaneous brain function. The reduction of cerebral blood flow in ischemic areas leads to alteration of brain electrical activity. These EEG changes are particularly characterized by increased power mainly in the delta frequency range and decreased in the alpha frequency range [13]. EEG alterations during in acute and post-acute phase of ischemic stroke and their predictive power have been widely studied in the past years [11], [14]-[17]. Nevertheless, there are only a few studies on EEG alterations in the earliest phase of ischemic stroke, performed within 4.5 hours from symptom onset [18], [19]. In addition, the correlation between EEG spectral parameters assessed in the pre-treatment hyper-acute phase and the functional outcome has not been studied yet.

In this preliminary study, we aimed to investigate the correlation between early stroke-related EEG changes, measured on bedside with wireless EEG device and short-term functional outcome measured with 7-day NIHSS in thrombolysis treated ischemic stroke patients.

II. MATERIALS AND METHODS

A. Study population and protocol

Ten acute ischemic stroke patients (4M/6F, age: median=80.5; range 59-89 years), admitted to the Stroke Unit of the Trieste University Hospital (Trieste, Italy), who underwent EEG recording at the bedside within 4.5 hours from stroke onset were included in this preliminary study. In the timespan between neuroimaging assessment and the beginning of reperfusion treatment, if the conditions were suitable in the emergency setting, EEG was acquired with a prewired headcap and wireless device. Previous stroke, hematic effusion, history of epileptic seizure, use of medication, such as neuroleptics or benzodiazepines, were exclusion criteria due to their effect on EEG assessment.

National Institutes of Health Stroke Scale (NIHSS) score assessment was performed at admission and on the 7th day or before in case of discharge (7-day NIHSS).

The included patients underwent thrombolysis treatment after fulfilment of eligibility criteria defined by the new

standardized protocol for diagnosis and treatment of acute stroke of the Trieste University Hospital introduced in March 2016. Patients eligible for thrombolysis were treated with intravenous recombinant tissue plasminogen activator - rtPA (0.9 mg/kg of body weight, maximum of 90 mg, infused over 60 minutes with 10% of the total dose administered as an initial intravenous bolus over 1 minute).

The research was conducted according to the principles of the Declaration of Helsinki and was approved by the regional ethics committee (Comitato Etico Regionale Unico FVG – CEUR - 115/2018). All participants released their informed consent.

B. EEG acquisition and processing

EEG signals were acquired at bedside within 4.5 h from stroke symptom onset, without delaying reperfusion treatment, by using 19 channel 10-20 Ag/AgCl electrodes wireless headset and Be Plus LTM amplifier @64 channels Wi-Fi (EBNeuro, Florence, Italy). All electrode impedances were kept below 5 kΩ. The sampling rate was set to 128 Hz. The off-line analysis was performed using in-house scripts developed in MATLAB (MathWorks Inc., Natick, MA). All recorded signals were digitally filtered with the 0.5–40 Hz 2nd order Butterworth bandpass filter. The first 60 s of the artefact-free EEG tracings were analyzed.

Power spectral density (PSD) was estimated for each channel using Welch's periodogram [20], averaged on 11 tracts of 10 s each, windowed with a Hann window, with 50% overlap. For each EEG channel band power values were calculated (delta: 1–4Hz; theta: 4–8Hz; alpha: 8–13Hz; beta: 13–30Hz). The relative powers for each spectral band were computed by normalizing with a total power across the 1–30 Hz range. Moreover, (delta+theta)/(alpha+beta) ratio DTABR and (delta/alpha ratio) DAR were calculated. Relative power for each band, DAR and DTABR parameters were averaged over all 19 scalp electrodes.

C. Statistical analysis

The Spearman correlation was used to determine the degree of correlation between 7-day NIHSS and quantitative indices extracted from the EEG. The Kruskal-Wallis test with post hoc Tukey test was performed to assess the differences among relative powers of frequency bands. A p-values <0.05 were considered statistically significant.

III. RESULTS

NIHSS at admission ranged from 3 to 23 (median: 12). CT assessment at admission showed the median ASPECT score of 9 (range 6–10). The median time between symptoms onset and hyper-acute EEG recording ranged from 85 to 265 min (median: 185 min). Median 7-day NIHSS was 0.5 (range 0-42).

Median and range values of quantitative indices, extracted from the EEG, as well as correlations with 7-day NIHSS, are reported in Table 1. The median relative delta, theta, alpha and beta powers were 0.37 (range 0.25–0.67), 0.18 (range 0.10–0.32), 0.16 (range 0.06–0.35) and 0.15 (range 0.06– 0.21), respectively. Relative theta band resulted significantly higher compared to other bands (p<0.01). The median DAR and

DTABR values were 2.86 (range 1.23–7.35) and 2.36 (range 1.16–4.66), respectively. 7-day NIHSS correlated significantly with DAR (ρ=0.67, p=0.031) and with relative delta power (ρ=0.66, p=0.037). In addition, a significant negative correlation was found between 7-day NIHSS and relative alpha power (ρ=-0.69, p=0.028).

TABLE I
CORRELATION BETWEEN EXTRACTED SPECTRAL PARAMETERS AND 7-DAY NIHSS

EEG spectral parameters	Median (range)	Spearman's ρ (p-value)	
Relative δ	0.37 (0.25–0.67)	0.66	(0.037)
Relative θ	0.18 (0.10–0.32)	-0.01	(0.987)
Relative α	0.16 (0.06–0.35)	-0.69	(0.028)
Relative β	0.15 (0.06– 0.21)	0.28	(0.437)
DAR	2.86 (1.23–7.35)	0.67	(0.031)
DTBAR	2.36 (1.16–4.66)	0.50	(0.141)

IV. DISCUSSION

The identification of individual factors modulating clinical recovery after a stroke is fundamental to personalize the therapeutic intervention to enhance the final functional outcome [11]. There is growing evidence regarding neurovascular coupling in acute ischemic stroke, and neurophysiological biomarkers seem increasingly relevant for predicting outcome [21]. The relation between EEG alterations in pre-treatment hyper-acute phase and clinical outcome has not been studied yet.

The main finding of this study is the identification of a significant correlation between stroke-related EEG alterations, during the earliest phase of ischemic stroke, <4.5h from symptom onset, and functional outcome measured with 7-day NIHSS in patients who underwent intravenous thrombolysis. In particular, DAR and relative delta power correlated directly, while alpha correlated inversely with 7-day NIHSS.

In the past, different demographic, clinical and neuroimaging patient-specific features were associated with the final disability. In the last decade, there is growing research interest towards investigating the predictive power EEG in stroke outcome. Several studies focused on the predictive power of acute and post-acute EEG alterations, reporting that the spectral parameters and ratios like relative delta power [14], [16], alpha power [11], [16], DAR [14], [16], [17] and DTABR [11], [16] are particularly informative for outcome prediction.

Performing an EEG recording in emergency departments can be difficult owing to space, training and complexity of the equipment. Portable wireless EEG devices with prewired headcap may solve these impeding factors [22] allowing the bedside acquisition in emergency settings [23], [24] and, therefore, can be used in hyperacute phase without compromising the treatment protocol.

Recent studies performed in the hyper-acute phase showed a significant correlation between increased delta activity and

hypoperfused area [17], as well as between neurological deficit at admission and DAR, DTABR, and relative alpha power [18]. Our preliminary study assessed the relation of EEG spectral parameters extracted in the pre-treatment hyper-acute phase and short-term functional outcome. These preliminary results obtained on the limited study sample should be confirmed in a larger study.

V. CONCLUSION

In conclusion, the results of this pilot study showed the significant correlation between early EEG spectral parameters: DAR, relative delta and power, measured in the pre-treatment phase and short-term clinical outcome in thrombolysis treated patients. These results highlight the value of hyper-acute EEG as a possible complementary tool in the evaluation of stroke severity and its potential role in the prediction of stroke-related outcome.

REFERENCES

[1] V.L. Feigin, B. Norrving, G.A. Mensah, "Global burden of stroke," *Circ Res*, vol.120, pp. 15–64, 2017.

[2] The National Institute of Neurological Disorders and Stroke rt-PA Stroke Study Group, "Tissue plasminogen activator for acute ischemic stroke," *N Engl J Med* vol. 333, pp. 1581–1587, 1995.

[3] V. Puetz, K. Barlinn, E. Bodechteil, B. Campbell, J. Linn, J. C. Gerber, "Imaging-based selection for revascularization in acute ischemic stroke," *Current opinion in neurology*, vol. 29, pp. 20-29, 2016. 4.

[4] G. Furlanis, M. Ajčević, A. B. Stella, et al., "Wake-up stroke: thrombolysis reduces ischemic lesion volume and neurological deficit," *Journal of Neurology*, vol. 267, pp. 666–673, 2020.

[5] P. Vilela, H. A. Rowley, "Brain ischemia: CT and MRI techniques in acute ischemic stroke," Eur J Radiol, vol. 96, pp. 162–172, 2017.

[6] G. Furlanis , M. Ajcevic , L. Stragapede , et al., "Ischemic Volume and Neurological Deficit: Correlation of Computed Tomography Perfusion with the National Institutes of Health Stroke Scale Score in Acute Ischemic Stroke," *J Stroke Cerebrovasc Dis*, vol. 27, pp. 2200–2207, 2018.

[7] P. Manganotti, G. Furlanis, M. Ajčević, et al., "CT perfusion and EEG patterns in patients with acute isolated aphasia in seizure-related stroke mimics," *Seizure - Eur J Epilepsy*, vol. 71, pp. 110–115, 2019.

[8] P. Caruso, M. Naccarato, G. Furlanis et al., "Wake-up stroke and CT perfusion: effectiveness and safety of reperfusion therapy," *Neurol Sci*, vol. 39: pp. 1705-1712, 2018.

[9] A. Granato, L. D'Acunto, M. Ajčević, et al., "A novel Computed Tomography Perfusion-based quantitative tool for evaluation of perfusional abnormalities in migrainous aura stroke mimic," *Neurol Sci*, 2020. Doi: https://doi.org/10.1007/s10072-020-04476-5.

[10] H.P. Adams, P. H. Davis, E. C. Leira, et al., "Baseline NIH stroke scale score strongly predicts outcome after stroke: a report of the trial of org 10172 in acute stroke treatment (TOAST)," *Neurology* vol. 53, pp. 126–131, 1999.

[11] C. Bentes, A. R. Peralta, P. Viana, et al., "Quantitative EEG and functional outcome following acute ischemic stroke," *Clinical Neurophysiology*, vol. 129, n. 8, pp. 1680-1687, 2018.

[12] C. Stinear, "Prediction of recovery of motor function after stroke," *Lancet Neurol*, vol. 9, pp. 1228–32, 2010.

[13] K. G. Jordan, "Emergency EEG and continuous EEG monitoring in acute ischemic stroke" *J Clin Neurophysiol,* vol. 21, pp. 341–352, 2004.

[14] S. P. Finnigan, S. E. Rose, M. Walsh, et al., "Correlation of quantitative EEG in acute ischemic stroke with 30-day NIHSS score. Comparison with diffusion and perfusion MRI," *Stroke*, vol. 35, pp. 899–903, 2004.

[15] S. P. Finnigan, S. E. Rose, M. Walsh, et al., "Quantitative EEG indices of sub-acute ischaemic stroke correlate with clinical outcomes," *Clinical Neurophysiology*, vol. 118, n. 11, pp. 2525-2532, 2007.

[16] R. V. Sheorajpanday, G. Nagels, A.J. Weeren et al., "Quantitative EEG in ischemic stroke: correlation with functional status after 6 months," *Clinical neurophysiology*, 122 (5), pp. 874-883, 2011.

[17] Finnigan, S., van Putten, M.J.: EEG in ischaemic stroke: quantitative EEG can uniquely inform (sub-) acute prognoses and clinical management. *Clin. Neurophysiol*, 124(1), 10–19 (2013)

[18] L. Stragapede, G. Furlanis, M. Ajcevic, et al., "Brain oscillatory activity and CT perfusion in hyper-acute ischemic stroke," *Journal of Clinical Neuroscience*, vol. 69, pp. 184-189, 2019.

[19] M. Ajčević, G. Furlanis, L. Stragapede et al., "Brain Oscillatory Activity and Neurological Deficit in Hyper-acute Ischemic Stroke: Correlation of EEG Changes with NIHSS," in *Proc Mediterranean Conference on Medical and Biological Engineering and Computing*, Coimbra, 2019, pp. 133-141, 2020. Doi: https://doi.org/10.1007/978-3-030-31635-8_16.

[20] P. Welch, "The use of fast fourier transform for the estimation of power spectra: a method based on time averaging over short, modified periodograms," *IEEE Trans. Audio Electroacoust*, vol. 15, n. 2, pp. 70–73, 1967.

[21] P. M. Rossini, C. Altamura, A. Ferretti, et al. "Does cerebrovascular disease affect the coupling between neuronal activity and local haemodynamics?," *Brain*, vol.127, pp.99–110, 2004.

[22] L. Murri L, S. Gori, R. Massetani, et al., "Evaluation of acute ischemic stroke using quantitative EEG: a comparison with conventional EEG and CT scan," *Neurophysiol Clin*, vol. 28, pp. 249–57, 1998.

[23] S. Debner, F. Minow, R. Emkes, et al., "How about taking a low-cost, small, and wireless EEG for a walk?," *Psychopathology*, vol. 49, n. 11, pp. 1617–21, 2012.

[24] W. D. Hairston, K. W. Whitaker, A. J. Ries, et al., "Usability of four commercially-oriented EEG systems," *J Neural Eng*, vol. 11, n. 4, 046018, 2014.

Transcatheter Aortic Valve with Embolic Filter: Experiments and Simulations

D. Carbonaro[1], C. Chiastra[1], U. Morbiducci[1] and A. Audenino[1]

[1] PoliTo^BIO^Med Lab, Department of Mechanical and Aerospace Engineering, Politecnico di Torino

Abstract— **Cerebrovascular events are one of the most critical complications following transcatheter aortic valve replacement. The majority of these events are associated to calcium debris generated by the stenotic valve manipulation. Embolic protection devices were accordingly designed to reduce the risk of these adverse events. Within this context, an innovative transcatheter aortic valve with embolic filter is proposed, which is temporarily released in the ascending aorta, and avoids severe regurgitation while treating the native valve before the replacement. Experimental tests and computational analyses were conducted on a prototype of the Nitinol frame of the device. The frame integrity throughout the clinical procedure was assessed, radial force curves were experimentally measured and used to calibrate a finite element model.**

Keywords—**Transcatheter aortic valve implantation, embolic protection device, Nitinol, finite element method.**

I. INTRODUCTION

TRANSCATHER aortic valve (TAV) implantation is the established therapy for patients with severe aortic stenosis and with major risks for open heart surgery [1]. Despite the recent procedural improvements and the last generation of TAV devices [2], several complications, including paravalvular leak, rhythm disturbances, tissue damage and cerebrovascular events are still associated with the treatment [3]. Cerebrovascular events are one of the most severe complications, with occurrence that ranges from 2.7% to 5.5% at 30 days after TAV replacement [4]. Several clinical studies indicated that the majority of these adverse events are related to calcium debris generated by the stenotic valve percutaneous treatment [5]. As a consequence, embolic protection devices have been developed to avoid the calcium debris to reach the cerebral vasculature [6]. Until now, two main types of embolic protection devices exist [7]: (1) filters, which capture the debris, and (2) deflectors, which direct the embolic material towards the descending aorta.

Within this context, a novel Transcatheter Valve with Antiembolic Filter (TVAF) [8] is proposed. The innovative device, temporarily deployed in the ascending aorta, is composed by an antiembolic filter sutured to a Nitinol frame, integrated with a prosthetic valve, that allows treating the native valve (if needed), avoiding severe regurgitation. In this work, biomechanical investigations were conducted on a prototype of the metallic frame, which was previously manufactured. Specifically, experimental tests were performed to assess the radial stiffness and structural integrity of the device and to calibrate a Finite Element (FE) model that will be used to support the device design phase.

II. MATERIAL AND METHODS

A. Trascatheter Valve with Antiembolic Filter

The proposed TVAF device is composed by (1) the Nitinol frame, (2) the antiembolic filter and (3) the prosthetic valve. Compatible with all TAV delivery systems, the device is temporarily released in the ascending aorta and avoids severe regurgitation while treating the stenotic valve before TAV implantation. Adequate anchoring and apposition are guaranteed by the self-expanding Nitinol frame. The preliminary design is showed in Fig. 1A, which has a major diameter of 30 mm (Fig. 1B) and a strut thickness equal to 0.4 mm. The filter, made of fabric, blocks and captures the calcific debris generated by the stenotic valve manipulation. Moreover, the prosthetic valve, sutured to the frame, allows treating the native valve, thus avoiding severe regurgitation before the TAV implantation. The self-expanding TVAF, enclosing the captured material, can be re-crimped multiple times in the delivery system before being extracted at the end of the procedure.

A prototype of the preliminary design of the Nitinol frame was previously manufactured and tested by Admedes GmbH (Pforzheim, Germany). Firstly, a Nitinol tube was laser cut, then expanded with a thermo-mandrel, going through various thermal cycles to define the super-elastic behavior of the material [9], and finally electropolishing was applied.
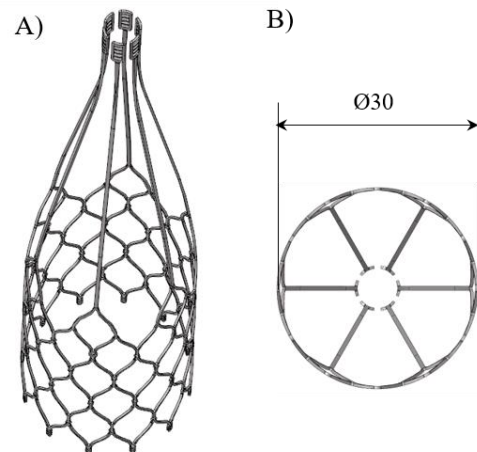

Fig. 1: A) CAD geometry of the preliminary design of the self-expanding Nitinol frame. B) Top view of the frame with indication of the major diameter.

B. Experimental tests

Within this study, biomechanical investigations were conducted on the Nitinol frame, omitting the structural influence of the filter and prosthetic valve and assuming that their stiffness is negligible compared to the frame [10]. Radial tests were conducted on the prototype frame with the RX650

(Machine Solutions Inc., Flagstaff, AZ, USA) radial force testing equipment, performing five crimping cycles with a minimum diameter of 6 mm and maintaining the temperature constant at 37 °C. Radial Resistive Force (RRF) and Chronic Outward Force (COF) [11] were measured as recommended by the FDA guidance [12]. Indeed, radial force exerted by the device can cause vascular injury if excessive or can result in malapposition, if too low. In order to assess the structural integrity of the frame it was conservatively accounted that the TVAF device can be crimped in the delivery sistem up to five times within the procedure. Moreover, crimping into a catheter of 6 mm of diameter was assumed to be the worst loading condition throughout the clinical procedure.

C. Computational analyses

A FE model that simulates the experimental radial procedure was implemented. The numerical model is made of two components: the TVAF frame and the crimping cylinder (Fig. 2A). A super-elastic material model [13] was assigned to the frame and the crimping machine was simplified as rigid cylinder [14]. In absence of material data and experiments on Nitinol samples, super-elastic material parameters were iteratively calibrated by fitting the simulated RRF and COF curves to the experimental data [15]. The upper part of the frame was neglected and only 1/12 of the frame was modelled (Fig. 2B), due to the circumferential symmetry, in order to achieve reliable results with acceptable computational costs.
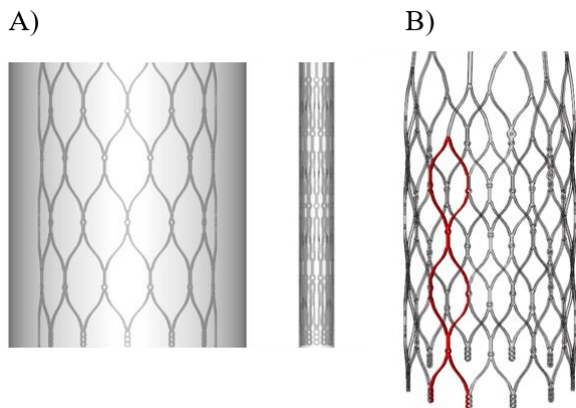
Fig. 2: A) Nitinol frame and crimping cylinder at the initial and final configuration of step 1. B) Finite element model of the frame in red.

A total of 357,472 C3D8R hexahedral elements with reduced integration were adopted to discretize the frame geometry [16] and the crimping cylinder was meshed with 32,864 SFM3D4R elements. Symmetry boundary conditions were applied at the extremities and one node at the bottom of each strut of the frame was constrained in axial direction. The FE simulation was performed on a complete crimping cycle and was divided in two steps. In the first step, radial displacements were assigned to the nodes of the cylinder, reducing the cylinder diameter from the initial value, greater than the major frame diameter, up to the value of 6 mm (Fig. 2A). Then, in the second step, radial displacements were assigned to the cylinder to retrieve it to the initial diameter. Contact between the frame and the cylinder was modelled with a pure master-slave contact algorithm, assuming a friction coefficient of 0.1 and hard-contact pressure-overclosure relationship. The non-linear analyses were performed using the FE implicit solver Abaqus Standard (Dassault Systèmes

Simulia Corp., Providence, RI, USA). The radial force, computed as the sum of the radial components of the generated contact forces, was measured for each iteration of the simulation, to obtain the RRF and COF curves.

III. RESULTS

Experimental tests assessed the frame structural integrity, showing no sign of failure after the performed crimping cycles.

RRF and COF curves are represented in grey for five crimping cycles in Fig. 3. A reduction of the major frame diameter and of the RRF and COF is observable throughout the cycles. Specifically, at the end of the first and fifth cycle a relative reduction of the 3% and 12% of the major frame diameter is observable, respectively. The decrease of the RRF and COF values with the number of cycles depends on the crimping diameter. In particular, the maximum exerted radial force of 59 N, when the crimping diameter is at the minimum value of 6 mm, remains nearly constant.

The simulated RRF and COF curves are fitted with good approximation to the first experimental cycle and are shown as black dotted lines in Fig. 2. Discrepancies are noticeable at the end the COF, due to the implemented material model, which does not represent inelastic deformations.
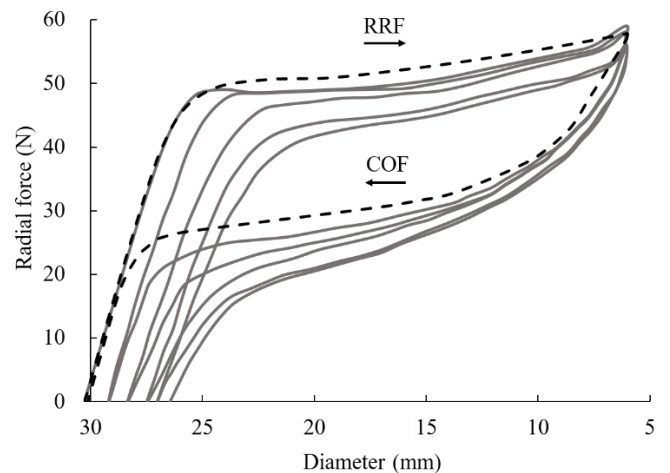

Fig. 3: Grey lines indicate experimental radial resistive and chronic outward forces curves for five cycles at 37°C. A reduction of the final frame diameter and of the computed radial force is observable throughout the five cycles. Black dotted lines represent the simulated curves of one crimping cycle.

Figure 4 shows the stress-strain curve of the calibrated material, with indication of the super-elastic material parameters, summarized in Table I.
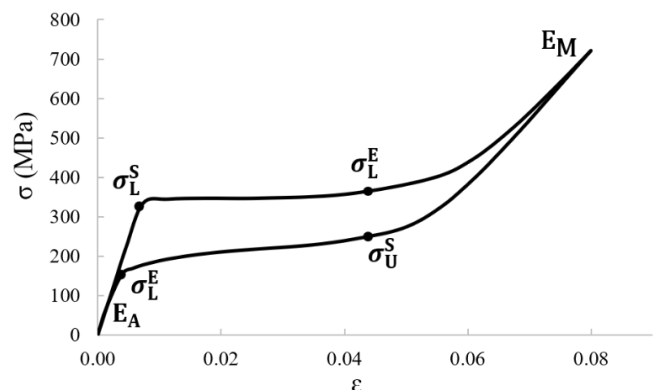

Fig. 4: Stress-strain curve of the calibrated super-elastic material with indication of the tuned super-elastic parameters.

TABLE I
TUNED NITINOL MATERIAL PARAMETERS

Parameters	Symbols	Values (MPa)
Austenite elastic modulus	E_A	45000
Martensite elastic modulus	E_M	19000
Start of transformation loading	σ_L^S	330
End of transformation loading	σ_L^E	345
Start of transformation unloading	σ_U^S	240
End of transformation unloading	σ_U^E	130

Super-elastic material parameters obtained through finite element model calibration.

No self-contact between the struts is observable at the minimum crimping diameter in Fig. 5. Maximum principal strain distribution shows a maximum value of 0.078, typically due to the struts bending [17].
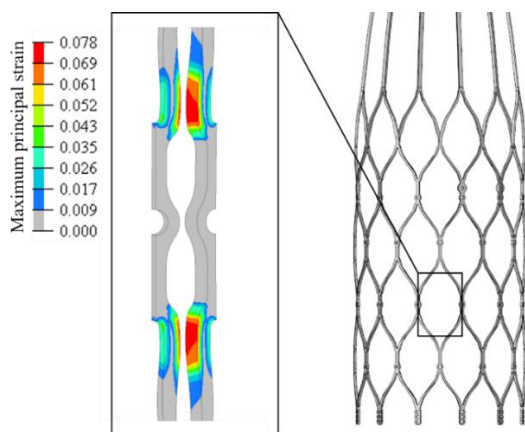
Fig. 5: Maximum principal strain at the minimum crimping diameter of 6 mm. Focus on the region of the frame with the highest values.

IV. DISCUSSION AND CONCLUSIONS

Preliminary experimental tests and numerical simulations were conducted within this study on the proposed TVAF device. The radial crimping test was performed on the prototype of the frame, obtaining RRF and COF curves for five crimping cycles. Then, the experimental procedure was numerically simulated and a FE model of the preliminary frame design was calibrated using the experimental data.

The experimental tests assessed the structural integrity of the frame and indicated a reduction of the major diameter and of the RRF and COF values throughout the crimping cycles. Specifically, those findings suggested that: (1) the reduction of the major frame diameter at the end of the first cycle should be taken into account by adequately oversizing the device with respect to the host tissue; (2) the decrease of the exerted radial force, which follows repeated crimping cycles, should be additionally accounted if the device is crimped multiple times into the catheter during the procedure; (3) permanent deformations of the material throughout the cycles were generated.

The numerical model was successfully calibrated using the experimental RRF and COF curves and material parameters were accordingly fitted. Differently from a previous study [18], the implemented material model was not capable to represent the inelastic deformations that were experimentally noticeable. Nevertheless, it should be noted that, at least during the first crimping cycle, the relative reduction of the frame major diameter was small enough to assume that this modelling limitation does not affect the validity of numerical analyses. Additionally, if further experimental tests on Nitinol samples were available, material parameter could be fitted using these data and the FE model could then be validated with radial tests [19].

Once the FE model is calibrated, numerical analyses can be used to predict the structural integrity and the radial curves of different designs, avoiding time and cost of the prototype manufacturing and testing. The computational model can provide useful information to investigate the interaction between the deployed device and the surrounding anatomy and to predict the clinical outcomes of the procedure. Moreover, the initial frame design can be optimized in terms of geometry and size of the struts, and guidelines on the manufacturing process can be addressed [20]. In this regard, computational modelling confirms to be a valuable tool in supporting the design phase and in characterizing the mechanical performance of the device.

REFERENCES

[1] B. E. Stähli, W. Maier, R. Corti, T. F. Lüscher, R. Jenni, and F. C. Tanner, "Aortic regurgitation after transcatheter aortic valve implantation: mechanisms and implications," *Cardiovascular Diagnosis and Therapy*, vol. 3, no. 1, p. 8, 2013.

[2] E. M. A. Wiegerinck, F. Van Kesteren, M. S. Van Mourik, M. M. Vis, and J. Baan Jr, "An up-to-date overview of the most recent transcatheter implantable aortic valve prostheses," *Expert Review of Medical Devices*, vol. 13, no. 1, pp. 31–45, January 2016.

[3] S. R. Kapadia *et al.*, "5-year outcomes of transcatheter aortic valve replacement compared with standard treatment for patients with inoperable aortic stenosis (PARTNER 1): a randomised controlled trial," *The Lancet*, vol. 385, no. 9986, pp. 2485–2491, June 2015.

[4] T. Gasior, N. Mangner, J. Bijoch, and W. Wojakowski, "Cerebral embolic protection systems for transcatheter aortic valve replacement," *J Interven Cardiol*, vol. 31, no. 6, pp. 891–898, Dec. 2018.

[5] G. Armijo, L. Nombela-Franco, and G. Tirado-Conte, "Cerebrovascular Events After Transcatheter Aortic Valve Implantation," *Front. Cardiovasc. Med.*, vol. 5, p. 104, July 2018.

[6] L. Nombela-Franco, G. Armijo, and G. Tirado-Conte, "Cerebral embolic protection devices during transcatheter aortic valve implantation: clinical versus silent embolism," *J. Thorac. Dis*, vol. 10, no. S30, pp. S3604–S3613, November 2018.

[7] H. Cubero-Gallego *et al.*, "Cerebral protection devices for transcatheter aortic valve replacement," *Ann. Transl. Med.*, vol. 7, no. 20, pp. 584–584, October 2019.

[8] E. Pasquino, F. Bonetti, S. Osta and F. Osta, "Transcatheter valve prosthesis for blood vesser," E.U. Patent 17171583.2, November 21, 2017.

[9] D. Stoeckel, A. Pelton, and T. Duerig, "Self-expanding nitinol stents: material and design considerations," *European Radiology*, vol. 14, no. 2, pp. 292–301, Feb. 2004.

[10] J. Bailey, N. Curzen, and N. W. Bressloff, "Assessing the impact of including leaflets in the simulation of TAVI deployment into a patient-specific aortic root," *Computer Methods in Biomechanics and Biomedical Engineering*, vol. 19, no. 7, pp. 733–744, May 2016.

[11] T. W. Duerig, D. E. Tolomeo, and M. Wholey, "An overview of superelastic stent design," *Minimally Invasive Therapy & Allied Technologies*, vol. 9, no. 3–4, pp. 235–246, January 2000.

[12] *Non-Clinical Engineering Tests and Recommended Labeling for Intravascular Stents and Associated Delivery Systems.* Guidance for Industry and FDA Staff, 1545, 2010.

[13] F. Auricchio and R. L. Taylor, "Shape-memory alloys: modelling and numerical simulations of the finite-strain superelastic behavior," *Computer Methods in Applied Mechanics and Engineering*, vol. 143, no. 1–2, pp. 175–194, April 1997.

[14] S. Tzamtzis, J. Viquerat, J. Yap, M. J. Mullen, and G. Burriesci, "Numerical analysis of the radial force produced by the Medtronic-CoreValve and Edwards-SAPIEN after transcatheter aortic valve implantation (TAVI)," *Medical Engineering & Physics*, vol. 35, no. 1, pp. 125–130, Jan. 2013.

[15] M. S. Cabrera, C. W. J. Oomens, and F. P. T. Baaijens, "Understanding the requirements of self-expandable stents for heart valve replacement: Radial force, hoop force and equilibrium," *Journal of the Mechanical Behavior of Biomedical Materials*, vol. 68, pp. 252–264, April 2017.

[16] A. Finotello, S. Morganti, and F. Auricchio, "Finite element analysis of TAVI: Impact of native aortic root computational modeling strategies on simulation outcomes," *Medical Engineering & Physics*, vol. 47, pp. 2–12, September 2017.

[17] L. Petrini *et al.*, "Simplified Multistage Computational Approach to Assess the Fatigue Behavior of a Niti Transcatheter Aortic Valve During In Vitro Tests: A Proof-of-Concept Study," *Journal of Medical Devices*, vol. 11, no. 2, p. 021009, Jun. 2017.

[18] L. Petrini, A. Bertini, F. Berti, G. Pennati, and F. Migliavacca, "The role of inelastic deformations in the mechanical response of endovascular shape memory alloy devices," *Proc Inst Mech Eng H*, vol. 231, no. 5, pp. 391–404, May 2017.

[19] N. Kelly *et al.*, "Comparison of computational modelling techniques for braided stent analysis," *Computer Methods in Biomechanics and Biomedical Engineering*, vol. 22, no. 16, pp. 1334–1344, December 2019.

[20] M. Conti, F. Auricchio, M. De Beule, and B. Verhegghe, "Numerical simulation of Nitinol peripheral stents: from laser-cutting to deployment in a patient specific anatomy," in *ESOMAT 2009 - 8th European Symposium on Martensitic Transformations*, pp. 06008-1-06008-6.

Assessment of Indoor Exposure Scenario by an 8x8 Planar Array Antenna at 3.7 GHz

M. Bonato[1,2], L. Dossi[1], E. Chiaramello[1], S. Fiocchi[1], S. Gallucci[1], G. Tognola[1], P. Ravazzani[1] and M. Parazzini[1]

[1] Institute of Electronics, Computer and Telecommunication Engineering, CNR, Milano, Italy
[2] Department of Electronics, Information and Bioengineering, Politecnico di Milano, Italy

Abstract—**The upcoming 5th generation networks will provide benefits and new services to the population, but will also drastically change the current RF-EMF exposure levels. The introduction of innovation technologies, (e.g. the use of mm-wave spectrum and the increments of the number of small cells and beamforming techniques coupled with MIMO antennas), underlined in fact the need of conducting promptly an adequate health risk exposure assessment. In the present paper, a specific case of future indoor exposure scenario is investigated, where it is simulated the presence of a 5G access point in a room. Specifically, the exposure levels of a human model due to an 8x8 indoor planar array antenna at 3.7 GHz are here analysed, following the ICNIRP guidelines.**

Keywords—**5G, RF-EMF exposure assessment, indoor scenario**

I. INTRODUCTION

IN the next future, innovative aspects and services will be introduced in the automotive, health and industry sectors, characterizing the new concept of future smart societies, smart cities and smart homes.

The upcoming 5th generation mobile networks (5G) based on wireless communications will in fact satisfy the new requirements of higher data-rate, higher capacity, higher traffic density, higher connection density and super high mobility, necessary to develop the concept of IoT [1].

As it was underlined in the last Releases of the standardization group 3GPP (3rd Generation Partnership Program), for developing this new network characteristics, it will be necessary the use of the mm-wave spectrum, ranging from 3 to 300 GHz, for wireless communication. The mm-waves guarantee the low latency and high data transmission rate, but they also suffer of very high path loss. For this reason, the number of small cells at base station (BS) will be incremented, coupled with methods of beamforming techniques for obtaining highly directional beams. This type of 5G networks configuration will be adopted not only at the outdoor BSs (positioned on the roof of high building) but also at radio units at lower height (e.g. on top of traffic lights) for the coverage in urban areas and in indoor scenario [2-4]. Therefore, all these innovations will drastically change the exposure conditions of a user to the RF EMF and for this reason the deployment of 5G networks is raising questions from the public in terms of exposure to RF EMF, with particular attention for more sensible subjects, like children neonates and fetuses. It is then evident the need of conduction promptly an exposure assessment to these new 5G networks [5]. In literature, different studies were conducted for evaluating the exposure levels both for uplink and downlink situations and also in

outdoor and indoor scenario [6-9]. The present work represented an effort to expand the knowledge about the future 5G exposure and was focused on an example of downlink exposure assessment by an 8x8 indoor planar array antenna at 3.7 GHz, for simulating the presence of a 5G access point in a room. The human exposure levels were evaluated following the exposure parameters indicated in the ICNIRP guidelines [10]. The frequency of 3.7 GHz was chosen according to the first 5G Italy launch, which will involve the use of 3.6-3.8 GHz frequency range [5]. Details of the exposure scenario assessment are described in the following paragraph.
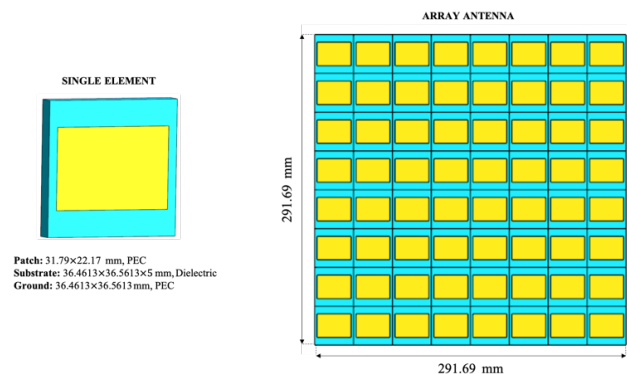
II. MATERIALS AND METHODS

Fig. 1: Sigle patch antenna and the complete 8x8 planar array antenna that was used as indoor BS.

A. Exposure Scenario

In Fig.1 it can be seen the model geometry of a single element and of an 8x8 indoor planar array antenna. Each single element of the antenna is composed by a simple patch antenna. The dimension of the three layers of the patch antenna are chosen in order to have a resonance of the antenna at 3.7 GHz. The ground and the patch elements are modelled by a PEC material, whereas the dielectric properties of the substrate element are $\varepsilon_r = 2.25$ and $\sigma = 0.0005 \, S/m$, according to data literature [11]. In total the dimensions of the array are around 29x29 cm, for a thickness of 0.5 cm. To assess the human exposure levels, it was used the Ella model, from the Virtual Family, which represent an average adult female human (age = 26 years old, height = $1.63 \, m$, mass = $57.3 \, kg$, BMI= $21.6 \, kg/m^2$). The model is placed at a distance of 50 cm between the antenna centre and the central point of the model head. Three different configurations were then examined: in the first the antenna is placed in front of the model head, in the second the antenna is placed back respect the model head, whereas in the last the antenna is placed lateral

respect the model head. The example of the frontal configuration is shown in Fig 2.
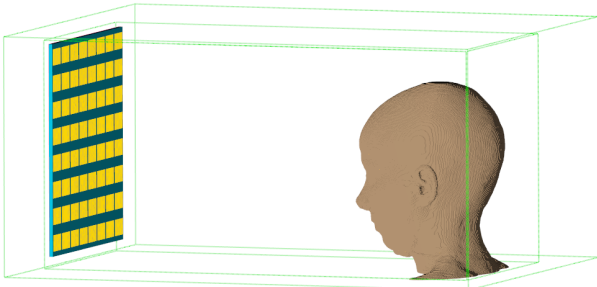
B. Computational Model

Fig. 2: Example of the indoor exposure scenario: here the 8x8 array antenna is placed in front of the head model.

For evaluating the exposure levels of the three different configurations, it was used the finite-difference time-domain (FDTD) method implemented in the platform Sim4Life. Each single element of the antenna was excited by a 3.7 GHz gaussian signal of 100 mW normalized input power. The phase shift between the elements was set to zero and all the antennas were excited simultaneously, in order to simulated the worst-case exposure scenario for all the three configurations. The domain of interest was limited to a box that included the head region area of the model, as it can be seen in Fig. 2. The dielectric proprieties of the tissues were chosen according to literature [12, 13]. For the boundaries of the simulations, it was applied an absorbing condition with perfectly matched layer (PML). At last, the model tissues were discretized by a mesh with a maximum step of 0.9 mm.

C. Exposure Assessment

The human exposure levels were evaluated for the three different configurations under examination. In particular, it was evaluated the specific absorption rate (SAR) obtained for the whole head normalized by 100 mW of input power in the 8x8 array antenna. Furthermore, whole-tissue SAR (SAR_{wt}) and SAR averaged on 10 g of tissue (SAR_{10g}) were evaluated for the head tissues.
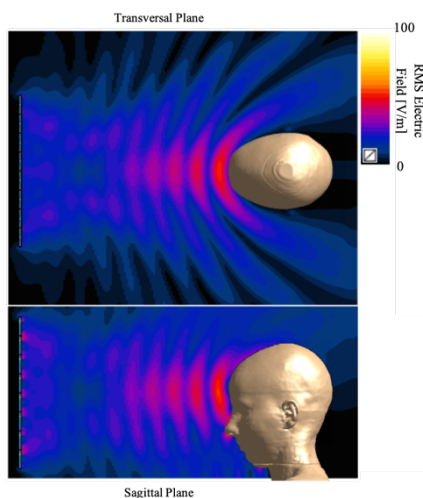
III. RESULTS

Fig. 3: Example of the distribution of E field generated by 8x8 planar array antenna at 3.7 GHz.

The present paragraph reports only some preliminary results obtained from the frontal configuration. In Fig.3 an example of the electric field values distributions obtained for the 8x8 array antenna are displayed, both in the transversal plane and in the sagittal plane. The values are normalized by an input power of 100 mW for the 8x8 array antenna. As it was expected the most exposed area was the frontal part of the head, in particular the nose and eyes areas, whereas in the back part of the head the electric field values were almost negligible.
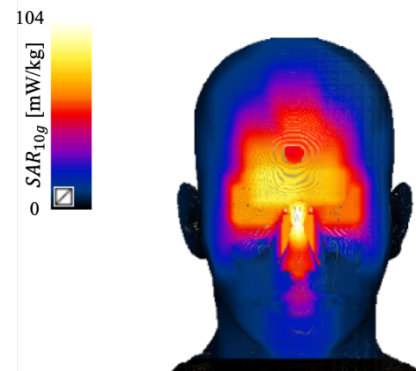

Fig. 4: Distribution of 10 g average SAR [mW/kg] induced by 8x8 planar array antenna on the Ella skin of the head for the frontal configurations.

Therefore, as it can be seen in Fig.4, the SAR_{10g} calculated for the skin tissue was characterized by higher values in the frontal region of the head, whereas the values were almost equal to zero in the back part. Furthermore, the SAR_{wt} for the whole head was equal to 5 mW/kg, whereas the maximum value of SAR_{10g} in the head was in the skin tissue, with a value equal to 104 mW/kg, lower than the ICNIRP limit of 2 W/kg for the average head and torso exposure. The SAR_{wt} presented peak higher values for the most superficial tissues (e.g. eyes tissues, skin, skull, and subcutaneous fat), whereas deeper tissues in the brain had almost negligible values of SAR_{wt}.

IV. CONCLUSION

This work represented a first attempt to evaluate the exposure levels in indoor scenario with the introduction of the 5G technology innovations. Next works will be focused to expand the knowledge about 5G exposure evaluating the exposure in different configuration settings and also introducing higher frequency ranges, that will be used in 5G networks (e.g. the 26 - 28 GHz frequency range). Future works will also involve the use of stochastic and machine learning techniques that will permit to consider the exposure variability of these new incoming scenarios [14, 15].

ACKNOWLEDGEMENT

REFERENCES

[1] J.G. Andrews, S. Buzzi, W. Choi, S.V. Hanly, A. Lozano, A.C. Soong, J.C. Zhang, "What will 5G be?". In *IEEE Journal on selected areas in communications*. 2014 Jun 3;32(6):1065-82.

[2] Boccardi F, Heath RW, Lozano A, Marzetta TL, Popovski P. Five disruptive technology directions for 5G. IEEE Communications Magazine. 2014 Feb 12;52(2):74-80.

[3] E. G. Larsson, O. Edfors, F. Tufvesson, T.L. Marzetta, "Massive MIMO for next generation wireless systems". IEEE communications magazine. 2014 Feb 12;52(2):186-95

[4] B. Ai, K. Guan, R. He, J. Li, G. Li, D. He, Z. Zhong K.M.S. and Huq, "On indoor millimeter wave massive MIMO channels: Measurement and simulation". In *IEEE journal on selected areas in communications*, 35(7), 2017, pp.1678-1690.

[5] Recommendations, ITU-T. K-Series. "5G technology and human exposure to RF EMF." (2017).

[6] P. Baracca, A.Weber, T. Wild, C. Grangeat, "A statistical approach for RF exposure compliance boundary assessment in massive MIMO systems". InWSA 2018; 22nd International ITG Workshop on Smart Antennas 2018 Mar 14 (pp. 1-6). VDE.

[7] C. Li, C. Xu, R. Wang, L. Yang, T. Wu, "Numerical evaluation of human exposure to 3.5-GHz electromagnetic field by considering the 3GPP-like channel features". Annals of Telecommunications. 2019 Feb 1;74(1-2):25-33.

[8] S. Shikhantsov, A. Thielens, G. Vermeeren, E. Tanghe, P. Demeester, L. Martens, G. Torfs, W. Joseph, "Hybrid ray-tracing/FDTD method for human exposure evaluation of a massive MIMO technology in an industrial indoor environment". IEEE Access. 2019 Feb 6;7:21020-31.

[9] D. Colombi, B. Thors, C. Törnevik, Q. Balzano, "RF energy absorption by biological tissues in close proximity to millimeter-wave 5G wireless equipment". IEEE Access. 2018 Jan 5;6:4974-81.

[10] International Commission on Non-Ionizing Radiation Protection, "ICNIRP guidelines for limiting exposure to time-varying electric, magnetic and electromagnetic fields (up to 300 GHz)", *Health Phys*, vol. 74, pp. 494–522, 1998.

[11] S. Shikhantsov, A. Thielens, G. Vermeeren, P. Demeester, L. Martens, G. Torfs, W. Joseph, "Statistical approach for human electromagnetic exposure assessment in future wireless atto-cell networks". *Radiation protection dosimetry*. 2019 May 1;183(3):326-31.

[12] C. Gabriel, S. Gabriel and Y.E. Corthout, "The dielectric properties of biological tissues: I. Literature survey," Physics in Medicine &Biology, 1996, 41(11), 2231.

[13] S. Gabriel, RW. Lau, and C. Gabriel, "The dielectric properties of biological tissues: II. Measurements in the frequency range 10 Hz to 20 GHz", *Phys Med Biol*, vol. 41, pp. 2251-2269, 1996.

[14] E. Chiaramello, S. Fiocchi, M. Parazzini, P. Ravazzani, J. Wiart, "Stochastic Dosimetry for Radio-Frequency Exposure Assessment in Realistic Scenarios". In Uncertainty Modeling for Engineering Applications 2019 (pp. 89-102). Springer, Cham.

[15] G. Tognola, M. Bonato, E. Chiaramello, S. Fiocchi, I. Magne, M. Souques, M. Parazzini, and P. Ravazzani, Use of Machine Learning in the analysis of indoor ELF MF exposure in children", *Int J Environ Res Public Health*, vol. 16, p. 1230-1243, 2019.

Blood glucose prediction from Flash Glucose Monitoring and Fitbit data:
a deep learning approach

P. Bosoni[1], M. Meccariello[1], V. Calcaterra[2,3], C. Larizza[1], L. Sacchi[1], and R. Bellazzi[1]

[1] Department of Electrical, Computer and Biomedical Engineering University of Pavia, 27100 Pavia, Italy
[2] Pediatric and Adolescent Unit, Department of Internal Medicine, University of Pavia, 27100 Pavia, Italy
[3] Pediatric Endocrinologic Unit, Department of Maternal and Children's Health, IRCCS Policlinico San Matteo, 27100 Pavia, Italy

Abstract—**The increasing adoption of wearable blood glucose (BG) monitoring devices is providing an important support in diabetes management. In the context of BG monitoring, lifestyle information can be crucial to better contextualize the glycemic profile, ultimately improving the personalized prediction of critical situations. Considering both univariate and multivariate scenarios, several methods have been proposed to develop personalized models for BG prediction. In this paper we present a multi-patient and multivariate deep learning approach for building a generalized model both to forecast the BG level and to detect adverse glycemic episodes in a short-time prediction horizon. The heart rate (HR) signal provided by Fitbit activity trackers is used together with BG measures collected with flash glucose monitoring systems. The proposed framework, based on Long-Short Term Memory (LSTM) artificial neural network, was evaluated on a clinical dataset of 17 young patients, threated at the IRCCS Policlinico San Matteo hospital in Pavia. Results suggest that a generalized model with good prediction performances can be developed and that exploiting HR information provided by Fitbit improves the accuracy of short-term glucose prediction.**

Keywords—**Blood glucose monitoring, Time series analysis, deep learning, data integration**

I. INTRODUCTION

Diabetes is actually on the rise across the globe. According to the 9th edition of the Diabetes Atlas presented by the International Diabetes Federation (IDF) in 2019, the number of adults living with diabetes has grown from 151 million to 463 million over the past 20 years [1]. Furthermore, without enough actions to address this serious health challenge, IDF estimates that there will be 578 million adults with diabetes by 2030, and 700 million by 2045 [1].

Diabetes in an umbrella term for a group of metabolic disorders characterized by an alteration in the patient's blood glucose (BG) levels, due to insulin deficiency or variable degrees of insulin resistance, that can lead to a number of serious and life-threatening complications [2]. Being a lifelong condition, one of the main aims of diabetes management is to obtain a near-normal glycemic control to reduce episodes of hypoglycemia (BG < 70 mg/dL) and hyperglycemia (BG > 180 mg/dL) [3], balancing interventions on diet, physical activity, lifestyle, and selecting the appropriate medications according to the patient's state.

The latest developments in BG monitoring technology have given a great support in the management of diabetes [4]. On the market there are several wearable devices that employ a subcutaneous sensor for measuring BG concentration. They provide patterns and trends to assist with decision making.

Continuous glucose monitoring (CGM) devices provide a real time information about the BG level, whereas flash glucose monitoring (FGM) devices require a scanner to periodically collect and read the BG values from a sensor. Even though CGM and FGM devices offer a real time snapshot of BG levels and allow using retrospective data to evaluate metabolic control between periodic clinical encounters, the accurate forecast of the BG level within a prediction horizon (PH) long enough to support decision-making still remains a challenge.

Starting from BG monitoring data, a number of data-driven methods have been proposed for BG prediction, ranging from autoregressive models to machine learning algorithms [5]-[6]. Considering the BG monitoring time-series as the only input, the minimum amount of historical data needed to make a forecasting with an acceptable accuracy was investigated, using a grid search on parameters such as observation window and sampling frequency of the BG time-series [7]. Interestingly, it is reported that a backward limit exists when considering historical data, since the prediction accuracy improves with an observation window of six hours regardless the model and the PH [7]. Moreover, given that the BG profile over the day is sensitive to multiple factors, also multivariate models have been considered [8].

Given the considerable amount of data made available by CGM and FGM devices, deep learning models have recently been successfully applied to BG predictions. A few works exploit artificial Neural Networks (NN) for BG forecasting, and most of these propose algorithms built to learn different patient-centric BG prediction models [9]-[12]. Personalized models solely based on a specific patient historical data are anyway not able to learn relationships that can be extended to a different subject. Thus, a general model built on a population of patients could be useful in real clinical scenarios, where the information for a new patient can be scarce at the beginning of the monitoring period.

In [13], a deep learning framework with one Long-Short Term Memory (LSTM) layer, one bidirectional LSTM layer and several fully connected layers was realized to generate patient-specific BG prediction models on a real patients' dataset, using CGM measurements. In [14], a multi-layer convolutional NN is implemented to learn a generalized model including also information on meals and insulin dosages recorded by the patients. The model is learnt on five real patients from the ABC4D clinical dataset, then tested on the rest of the subjects one by one, reaching acceptable

performance [15].

It is well known that BG is influenced by several factors, such as meals and therapy intake, but also lifestyle conditions such as workout and sleep. For this reason, considering the variables automatically collected by a generic smart band, e.g. heart rate (HR), activity and sleep data, seems promising [16].

In this paper, we introduce a multi-patient and multivariate deep learning approach to build a generalized model both to forecast the BG level and to predict hypoglycemia and hyperglycemia episodes in a short-time PH (15-30 minutes). We trained a LSTM-based algorithm on real diabetes pediatric patients, considering as input their BG and HR measurements, to test whether the combined use of these types of monitoring signals could improve predictions compared to the univariate scenario. The clinical dataset used to train the models was obtained from the AID-GM (Advanced Intelligent Distant— Glucose Monitoring) project [17]. In this project, a new platform to jointly collect and analyze BG monitoring and Fitbit [18] data was proposed and tested in a pilot study on a group of young patients treated at the Pediatric Diabetology outpatient service of the IRCCS Policlinico San Matteo hospital in Pavia, Italy. The study was approved by the Institutional Review Board (IRB) of the hospital.

II. METHODS

A. Model

Figure 1 shows the architecture of the proposed deep learning framework. The core of the model is represented by a LSTM layer, surrounded by a set of hidden layers. LSTM networks are a specific subclass of Recurrent Neural Network (RNN), and they were herein selected as they are particularly suitable for time-series forecasting. In fact, while the accuracy of RNN models tends to decline when the time-series becomes longer due to the vanishing or exploding gradient problems [19], LSTM can remember the previous data patterns over arbitrary time intervals, removing or adding information to a memory implemented as cells. This procedure is regulated by a gates structure that consists of an input gate, an output gate and a forget gate [19]. In addition, LSTM networks support multivariate inputs.
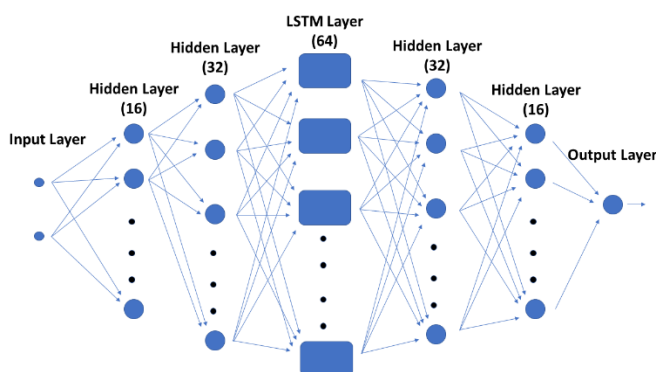

Fig. 1: The architecture of the proposed LSTM-based Neural Network

Besides the input layer for the multivariate time-series, the overall architecture of the proposed NN contains other six layers: hidden layer (16 neurons), hidden layer (32 neurons), LSTM layer with 64 LSTM cell, hidden layer (32 neurons),

hidden layer (16 neurons), and output layer (single neuron).

The architecture was implemented using the high-level neural network API Keras version 2.2.5 in Python 3.7.3 environment with TensorFlow backend [20]-[21]. A rectified linear unit (ReLU) activation function was used in all but the output layer, where we implemented a linear activation function. Weight matrices and bias vectors were randomly initialized at the beginning of the NN training procedure, and then updated using the Truncated Backward Propagation Trough Time method [22]. A RMSprop optimizer [23] with a learning rate of 0.001 was adopted to minimize Mean Absolute Error (MAE) as the cost function [24]. We considered 500 training epochs and a batch size of 96 points.

B. Dataset

In the AID-GM project, patients' BG profiles are collected using the Abbott FreeStyle Libre FGM system [25], which has been approved for use in pediatric patients [26], while HR profiles are collected with the Fitbit activity tracker. We have data from 17 patients, but not all were continuously using both the monitoring devices together. According to sensors sampling frequency, BG measurements are taken every 15 minutes, whereas HR measurements every minute.

Given the different sampling frequency, we first performed a timestamp alignment, by computing the mean of the HR values in the interval between two consecutive BG measurements. As a second step, we had to deal with missing data. The available time-series were divided in windows of 96 timestamps (24 hours), as the NN batch size, and the resulting subseries were discarded if the percentage of missing data was greater than 20%. As a result of this step, one patient was discarded for not meeting the data requirements. Linear interpolation was then performed to deal with the remaining missing data, using a bidirectional sliding window of 4 values.

The preprocessed dataset resulted into 47040 observations. This dataset was further divided into a training set with 12 randomly selected patients for developing a multi-patients and multivariate model, and a separate test set of 4 patients for evaluating its prediction performance.

C. Evaluation criteria

For the assessment of the proposed prediction models we considered some standard indicators widely used in the literature. The forecasting accuracy was evaluated both in analytical and clinical terms. For an analytical assessment, we used the Root-Mean Square Error (RMSE), which returns a quantitative measure of the forecast error on the same unit scale as the data, i.e. mg/dL. The RMSE, as reported in Eq. (1), is computed as the standard deviation of the residuals between the BG reference measurement y and the corresponding BG prediction $\hat{y}$, where N represents the time-series length.

$$RMSE = \sqrt{\sum_{i=1}^{N} \frac{(y(k)-\hat{y}(k|k-PH))^2}{N}} \qquad (1)$$

Since RMSE does not provide any information about the consequences of prediction errors on treatments decisions, in our evaluation we used also the Clarke Error Grid analysis (EGA) [27]. EGA is a non-parametric graphical method to interpret the mapping between the BG reference measurements and the corresponding BG predictions in terms

of severity of the potential harm caused by the prediction error.

The grid, shown in Figure 2, is divided into five zones. Zone A includes the area on both sides of the diagonal where the difference between reference and predicted BG values is less than 20%, leading to correct clinical decisions based on the prediction. In zone B, given a difference greater than 20%, the resulting clinical decision is not correct but at least uncritical. In zone C, BG prediction errors can lead to inappropriate treatment but without dangerous consequences for the patient, whereas in zone D the necessary corrections are not triggered, both in case of hypoglycemia and hyperglycemia. Prediction errors in zone E are the most dangerous because they lead to treat hypoglycemia instead of hyperglycemia and vice-versa.
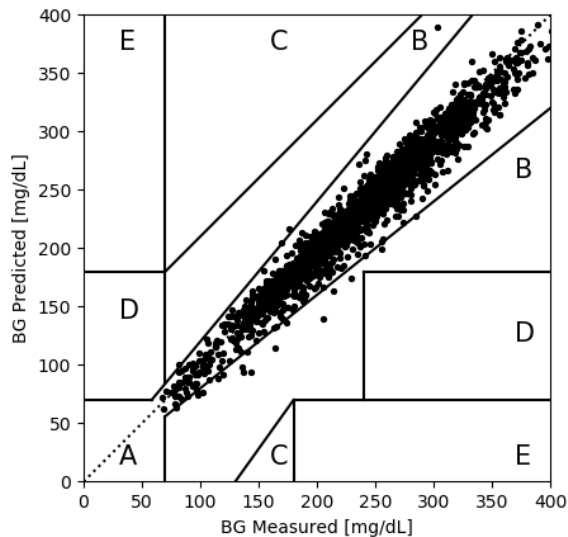
Fig. 2: LSTM Clarke Error Grid analysis for a test patient (PH=15 minutes)

To evaluate the capability of the proposed model to discriminate between adverse glycemic events, i.e. hypoglycemia and hyperglycemia episodes, and non-adverse glycemic events, we used the Matthews Correlation Coefficient (MCC). For hypoglycemia detection, we set a threshold of 70 mg/dL [3], labelling each BG measurement as hypoglycemic or non-hypoglycemic. The same operation was performed for hyperglycemia, considering a threshold of 180 mg/dL [3]. MCC provides a general overview of the classification performances, as stated in Eq. (2), and it is particularly suitable in case of unbalanced datasets, since it simultaneously takes into account true positives (TP), false negatives (FN), false positives (FP) and true negatives (TN) [28]. The MCC ranges in the interval [-1,1], from a complete disagreement to a total agreement between prediction and real observation.

$$MCC = \frac{(TP \times TN) - (FP \times FN)}{\sqrt{(TP+FP)(TP+FN)(TN+FP)(TN+FN)}} \quad (2)$$

III. RESULTS

Table I presents a comparison between the prediction errors in case of univariate and multivariate scenario within a 15 minutes PH. It is possible to notice that feeding the model with a combination of BG and HR measurements provides on average a lower prediction error, and consequently a greater accuracy. The same tendency can be observed within a 30

minutes PH, where the mean RMSE is 30.07 mg/dL for the multivariate model and 30.68 mg/dL for the univariate model. Interestingly, such values are comparable with those obtained by another generalized model trained on real diabetes patient [14].

TABLE I
RMSE OF BG PREDICTION (PH=15 MINUTES)

Patient	BG	BG-HR
14	19.07	18.80
15	14.70	14.16
16	16.57	16.63
17	21.75	20.30
Mean	18.02	17.47

In terms of clinical assessment, the Clarke Error Grid shown in Figure 2 displays that almost all points are in the zone of clinically correct decisions, with just a few points in zone B and no points in the dangerous area. Table II confirms a positive clinical assessment for all the other test patients, with less than 0.01% points outside zones A and B. Moreover, even within a 30 minutes PH, the percentage of points in zones C, D, and E sets on 0.01%.

TABLE II
CLARKE ERROR GRID IN PERCENTAGES (PH=15 MINUTES)

Patient	Zone A	Zone B	Zone C	Zone D	Zone E
14	0.92	0.07	<0.01	<0.01	<0.01
15	0.99	<0.01	0	0	0
16	0.95	0.05	0	<0.01	0
17	0.98	0.01	<0.01	<0.01	<0.01
Mean	0.96	0.03	<0.01	<0.01	<0.01

TABLE III
MCC PERFORMANCES (PH=15 MINUTES)

Patient	Hypoglycemia		Hyperglycemia	
	BG	BG-HR	BG	BG-HR
14	0,69	0.69	0.88	0.89
15	0.57	0.46	0.86	0.86
16	0.37	0.44	0.86	0.86
17	0.40	0.57	0.83	0.85
Mean	0.51	0.54	0.86	0.87

Table III presents the performance of the proposed model when used to predict the presence of an adverse glycemic event (hypoglycemia or hyperglycemia). As shown in the Table, whereas the performances in case of hyperglycemia prediction are satisfactory, MCC values are lower in case of hypoglycemia prediction. This can be due to the lower number of hypoglycemic events (3%) in the training data compared to

hyperglycemic events (33%). Nevertheless, even within a classification perspective, it is shown that the multivariate model performs slightly better than the model built with the BG time-series only.

IV. CONCLUSION

Given the considerable inter-patient and intra-patient variability in diabetes management, building a generalized model for accurate BG prediction represents a challenging task. Nevertheless, a generalized model results particularly useful in real clinical scenarios, where the information for a new patient can be limited.

In this paper we presented a multi-patient and multivariate deep learning approach to develop a generalized model for BG prediction and adverse glycemic episode detection. The forecasting framework is based on a LSTM layer, surrounded by a set of hidden layers. The model is trained on a set of real diabetes patients, considering temporal data provided by the Freestyle Libre FGM system and Fitbit activity tracker.

The resulting prediction performances are encouraging, and comparable with the literature. Considering the clinical assessment, the overall percentage of points within dangerous regions is negligible. The capability of the model to detect hyperglycemic episodes is satisfactory, while the prediction of hypoglycemia episodes can be improved. Interestingly, in both cases we showed that a combination of BG and HR measurements can help in BG forecasting, providing a higher accuracy compared the univariate scenario.

Future developments include an extension of the proposed model by integrating other life-style variables automatically collected by Fitbit, i.e. activity and sleep tracks. Moreover, a deeper architecture will be investigated, and a multinomial classification task will be implemented to discriminate between hypoglycemia, normoglycemia and hyperglycemia.

REFERENCES

[1] IDF Diabetes Atlas 9th edition. Available online: https://www.diabetesatlas.org/en/ (accessed on 30th January 2020).

[2] A. S. Fauci, S. L. Hauser, J. L. Jameson, D. L. Kasper, D. L. Longo, and J. Loscalzo, *Harrison's Manual of Medicine, 19e*. New York: McGraw-Hill Education LLC, 2016, ch. 173.

[3] L. Monnier, C. Colette, and D. R. Owens, "The application of simple metrics in the assessment of glycaemic variability," *Diabetes & Metabolism*, vol. 44, pp. 313-319, September 2018.

[4] Rodbard, D, "Continuous Glucose Monitoring: A Review of Successes, Challenges, and Opportunities," *Diabetes Technology & Therapeutics*, vol. 18, pp. S2-3-S2-13, January 2016.

[5] G. Sparacino, F. Zanderigo, S. Corazza, A. Maran, A. Facchinetti, and C. Cobelli, "Glucose concentration can be predicted ahead in time from continuous glucose monitoring sensor time-series," *IEEE Trans. Biomedical Engineering*, vol. 54, pp. 931-937, May 2007.

[6] T. Hamdi, J. Ben Ali, V. Di Costanzo, F. Fnaiech, E. Moreau, and J. -M. Ginoux, "Accurate prediction of continuous blood glucose based on support vector regression and differential evolution algorithm," *Biocybernetics and Biomedical Engineering*, vol. 38, pp. 362-372, February 2018.

[7] I. Rodríguez-Rodríguez, I. Chatzigiannakis, J. Rodríguez, M. Maranghi, M. Gentili, and M.-Á. Zamora-Izquierdo, "Utility of Big Data in Predicting Short-Term Blood Glucose Levels in Type 1 Diabetes Mellitus Through Machine Learning Techniques," *Sensors*, vol. 19, pp. 1-14, October 2019.

[8] S. Oviedo, J. Vehí, R. Calm, and J. Armengol, "A review of personalized blood glucose prediction strategies for T1DM patients," *International Journal for Numerical Methods in Biomedical Engineering*, vol. 33, pp. 1-21, June 2017.

[9] C. Pérez-Gandía, A. Facchinetti, G. Sparacino, C. Cobelli, E.J. Gómez, M. Rigla, A. de Leiva, and M.E. Hernando, "Artificial Neural Network Algorithm for Online Glucose Prediction from Continuous Glucose Monitoring," *Diabetes Technology & Therapeutics*, vol. 12, pp. 81-88, January 2010.

[10] S. Pappada, B.D. Cameron, P. M. Rosman, R. E. Bourey, T. J. Papadimos, W. Olorunto, and M. J. Borst, "Neural Network-Based Real-Time Prediction of Glucose in Patients with Insulin-Dependent Diabetes," *Diabetes Technology & Therapeutics*, vol. 13, pp. 135-141, February 2011.

[11] C. Zecchin, A. Facchinetti, G. Sparacino, G. De Nicolao, and C. Cobelli, "A new neural network approach for short-term glucose prediction using continuous glucose monitoring time-series and meal information," *in 2011 Proc. IEE EMBS Conf.*, pp. 5653-5656.

[12] T. Zhu, K. Li, P. Herrero, J. Chen, and P. Georgiou, "A deep learning algorithm for personalized blood glucose prediction," in *2018 Proc. Knowledge Discovery in Healthcare Data Inter. Workshop*, pp. 1-5.

[13] Q. Sun, M. V. Jankovic, L. Bally, and S. G. Mougiakakou, "Predicting Blood Glucose with an LSTM and Bi-LSTM Based Deep Neural Network," in *2018 Proc. NEUREL Conf.*, pp. 1-5.

[14] K. Li, C. Liu, T. Zhu, P. Herrero, and P. Georgiou, "GluNet: A Deep Learning Framework For Accurate Glucose Forecasting," *IEEE Journal of Biomedical and Health Informatics*, pp. 1-9, July 2019.

[15] M. Reddy, P. Pesl, M. Xenou, C. Toumazou, D. Johnston, P. Georgiou, H. Herrero, and N. Oliver, "Clinical Safety and Feasibility of the Advanced Bolus Calculator for Type 1 Diabetes Based on Case-Based Reasoning: A 6-Week Nonrandomized Single-Arm Pilot Study," *Diabetes Technology & Therapeutics*, vol. 18, pp. 487-493, August 2016.

[16] I. Rodríguez-Rodríguez, J.-V. Rodríguez, A. González-Vidal, and M.-Á Zamora, "Feature Selection for Blood Glucose Level Prediction in Type 1 Diabetes Mellitus by Using the Sequential Input Selection Algorithm (SISAL)," *Symmetry*, vol. 11, pp.1-17, September 2019.

[17] E. Salvi, P. Bosoni, V. Tibollo, L. Kruijver, V. Calcaterra, L. Sacchi, R. Bellazzi, and C. Larizza, "Patient-Generated Health Data Integration and Advanced Analytics for Diabetes Management: The AID-GM Platform", *Sensors*, vol. 20, p. 1-23, December 2019.

[18] Fitbit tracker. Available online: https://www.fitbit.com/us/home/ (accessed on 30th January 2020).

[19] S. Hochreiter and J. Schmidhuber, "Long Short-Term Memory", *Neural Computation*, vol. 9, pp. 1735-1780, November 1997.

[20] Keras functional API. Available online: https://keras.io/ (accessed on 30th January 2020).

[21] Tensorflow platform. Available online: https://www.tensorflow.org/ (accessed on 30th January 2020).

[22] P. Werbos, "Backpropagation through time: what does it do and how to do it," in *1990 Proc. IEEE*, pages 1550–1560.

[23] RMSprop implementation in Tensorflow. Available online: https://www.tensorflow.org/api_docs/python/tf/keras/optimizers/RMSprop (accessed on 30th January 2020).

[24] F. Chollet, *Deep Learning with Python*. New York: Manning Publications Co., 2018, ch. 7.

[25] FreeStyle Libre Continuous Glucose Monitoring System. Available online: https://www.freestylelibre.us/ (accessed on 30th January 2020).

[26] G.G. Massa, I. Gys, A. Op 't Eyndt, E. Bevilacqua, A. Wijnands, P. Declercq, and R. Zeevaert, "Evaluation of the FreeStyle® Libre Flash Glucose Monitoring System in Children and Adolescents with Type 1 Diabetes," *Hormone Research in Paediatrics*, vol. 89, pp. 189-199, April 2018.

[27] W. L. Clarke, "The Original Clarke Error Grid Analysis (EGA)," *Diabetes Technology & Therapeutics*, vol. 7, pp. 776-779, October 2005.

[28] D.M.W. Powers, "Evaluation: From Precision, Recall and F-Measure to ROC, Informedness, Markedness & Correlation," *Journal of Machine Learning Technologies*, vol. 2, pp. 37–63.

Comparison of the performances of six magneto-inertial sensor fusion filters for orientation estimation in movement analysis

M. Caruso[1], D. Laidig[2], A.M. Sabatini[3], M. Knaflitz[1], U. Della Croce[4], T. Seel[2], and A. Cereatti[4]

[1] Polito^BIO Med Lab – Biomedical Engineering Lab, Politecnico di Torino, Torino, Italy
[2] Control Systems Group, Technische Universität Berlin, Berlin, Germany
[3] The BioRobotics Institute and the Department of Excellence in Robotics & AI, Scuola Superiore Sant'Anna, Pisa, Italy
[4] Department of Biomedical Sciences, University of Sassari, Sassari, Italy

Abstract— **Magneto-Inertial technology is a promising alternative to optical stereophotogrammetry as it allows to measure the movement of subjects in real world conditions. Despite several sensor fusion filters for estimating the orientation have been published in the literature, there is still a lack of consensus about their accuracy. This work aims at evaluating the performance of six filters at three different rotation rates using an opto-electronic reference. To enable a "fair" comparison a tuning procedure for setting the proper parameter values for each algorithm was proposed. The procedure was designed to work without relying on any orientation reference. After tuning, all the filters performed reasonably (rms error < 6.5 deg). At slow, medium, and high rotation rates the lowest errors exhibited by the algorithms amounted to 2.5 deg, 2.7 deg, and 4.1 deg, respectively.**

Keywords— **gait analysis, wearable, MIMU, Kalman filter.**

I. INTRODUCTION

MAGNETO-inertial technology in the field of gait analysis is a promising tool for recording movement data in both indoor and outdoor conditions thus enabling to characterize subject motor performance under real world-conditions. Whereas optical stereo-photogrammetry (SP) represents the gold standard for human motion analysis, it is more suitable for assessing motor capacity (i.e. what a person can do in a standardized and controlled environment) rather than motor performance (i.e. the activity in real-world environment) [1]. A Magneto-Inertial Measurement Unit (MIMU) typically integrates an accelerometer, a gyroscope and a magnetometer. The relevant measures can be combined by means of sensor fusion algorithms [2] to estimate the 3-D orientation of the MIMU. The latter information is required for joint angle estimation, and to estimate linear velocity and displacement after gravity is removed from the accelerometer signals [2]. From a theoretical point of view, provided the initial conditions, the orientation can be estimated by time-integrating the angular velocity. However, the latter is corrupted by a non-constant bias whose integration leads to an orientation drift which grows unbounded over time [3]. The sensor fusion approach aims at compensating for such drift by exploiting the inclination and the Earth's magnetic north directions derived from the accelerometer and magnetometer

readings, respectively. However, these additional observations may not be sufficient to free the resulting orientation estimate from the drift. In fact, the inclination estimate is accurate only when the MIMU is stationary, since otherwise the accelerometer signals are the result of the combination of gravity and MIMU's acceleration. Moreover, the heading information estimated from the magnetometer output may be corrupted by ferromagnetic disturbances therefore limiting its indoor use. Finally, the electronic noise together with calibration errors and temperature sensitivity, further affect the reliability of the MIMU readings. To address the effects of all these sources of errors, several 3-D orientation estimation algorithms have been proposed in the last two decades. Most of the published algorithms are based on either Kalman (KF) or complementary (CF) filter approaches [4]. Despite the abundance of formulations in the literature, no definitive conclusions about the accuracy and the best performing algorithms have been reached yet [2]. This lack of consensus can be related to the high sensitivity of the performance of any sensor fusion filter to the specific set of parameters required and operating conditions [5]. This work aims at performing a direct comparison among the accuracy of six widely used sensor fusion algorithms applied to the recordings of motions performed at three rotation rates, using the orientation provided by a SP as a gold standard. The filters under analysis were the popular CFs proposed by Mahony, in 2008 [6] (MAH) and Madgwick in 2011 [7] (MAD), the recent CF proposed by Seel in 2017 [8] (SEL), the extended Kalman Filter by Sabatini in 2011 [3] (EKF), the KF newly integrated in the MATLAB software (MKF), and the proprietary Xsens filter (KF) integrated in the proprietary software (v1.7). This work was an extension of the one proposed in [9] having included the Mahony and Seel's filters in the analysis. To take into account the sensitivity of the sensor fusion filters to the specific set of parameters [5], a common strategy was designed for the selection of the suboptimal parameter values. This allowed a "fair" comparison among the algorithms. The proposed parameter optimization does not to require the knowledge of the ground-truth orientation, and can, therefore, be employed also when the gold standard is not available.

II. MATERIAL AND METHODS

A. Experimental set-up and protocol

Two MIMUs from Xsens (MTx, 100 samples/s) were carefully aligned on a manually squared off wooden board with seven passive markers as illustrated in Fig. 1. The three "blue" markers were used to define the SP local coordinate system, while the redundancy of the remaining makers was exploited to strengthen the orientation estimate obtained using the SVD technique [10]. Marker trajectories were acquired by a 12-camera SP (Vicon T20, 100 samples/s) to provide the gold-standard orientation. The local coordinate system of the two MIMUs (represented in green) was aligned to that of the SP by careful attachment. The force platform represented in Fig. 1 was used to synchronize the MIMUs and the SP system by means of a mechanical shock given by an operator at the beginning and at the end of each recording.
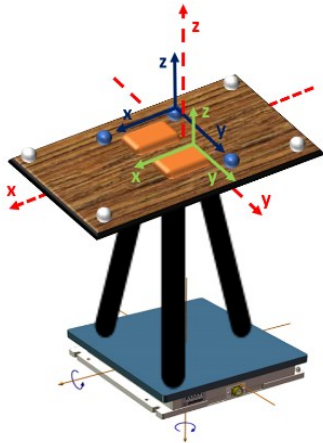
Fig. 1: The board with two MIMUs aligned (their axes are represented in green) was positioned on a tripod over a force platform. The SP local coordinate system is represented in blue. The board axes, represented in red, are assumed to be coincident to those of MIMUs and SP.

The board was first kept still and horizontal for one minute to allow the filter initialization, then a dynamic trial was recorded while the operator manually changed the board orientation in space. The movements involved rotations around each axis of the board at a time and then a free 3D rotation. The board was hit at the beginning and at the end for synchronization purposes. This protocol was executed at low (rms 120 dps for 70 seconds), medium (rms 260 dps for 45 seconds), and high rotation rate (rms 380 dps for 30 seconds). The rms values of the rotation rate were assessed in post processing.

B. Sensor fusion filters

All the considered algorithms used the quaternion representation of the 3-D orientation, known to be computationally convenient and singularity-free. A brief description of the algorithms is provided below.

MAD, MAH, SEL belong to the CF family in which the orientation obtained from the gyroscope readings is fused with that computed from accelerometer/magnetometer readings in the frequency domain according to their complementary spectral characteristics. The angular velocity is high-pass filtered before being integrated to reduce the effect of the slow-varying bias, while the accelerometer and magnetometer measurements are low-pass filtered to attenuate the high frequency noise. The sensor fusion process is governed by the value of the cut-off frequency which acts as a weighting factor. The value of the cut-off frequency must be the same for both low and high pass filters in order to preserve the whole band of the resulting orientation estimate and should be a trade-off [11]. One of the main characteristics of the CF, as opposed to KF, is that the fusion process does not consider any statistical description of the noise affecting the sensor readings. The MAD algorithm requires to set the value of the weighting factor β which if set to zero leads to an orientation computed from the gyroscope readings only, whereas larger values of β result in an orientation determined mainly from the accelerometer and magnetometer. The latter case is helpful in limiting the orientation drift but makes the orientation estimate more sensitive to the ferromagnetic disturbances and the body accelerations. The orientation quaternion representing the contribution of the accelerometer and magnetometer is computed by means of a gradient descent algorithm whose Jacobian Matrix is determined starting from the readings of these sensors.

MAH is also a CF which considers the discrepancy between the measured Earth's fixed vectors (gravity and magnetic field) and their estimates obtained using the orientation from the gyroscope. This discrepancy is then weighted by a parameter k_p and the result is subtracted from the angular velocity before the time integration.

SEL is a modular sensor fusion algorithm with independent accelerometer-based inclination corrections and magnetometer-based heading corrections. The magnetometer-based corrections are purely horizontal, which assures that magnetic disturbances cannot influence the inclination estimation. The algorithm is parameterized via two correction time constants for the inclination and heading disagreements, one optional bias estimation parameter and an adaptation factor that reduces the weight of the accelerometer readings during dynamic motions.

The algorithms EKF, MKF, and XKF belong to the family of the extended Kalman filters where the orientation is estimated within an optimization framework based on the statistical description of the different sources of noise. A general advantage of the KF consists in the possibility of tracking the disturbances (e.g. ferromagnetic interferences, body acceleration, gyroscope bias, etc.) by using the state vector augmentation technique. The EKF, as opposed to MKF and XKF, is based on the minimization of the uncertainty of the absolute orientation (KF direct formulations) rather than of the orientation error (KF indirect formulations). In the considered KF algorithms, the parameters to tune are related to the standard deviation (STDs) of the noise sensor readings. In particular, EKF allows to tune also the parameter related to the ferromagnetic disturbances modelled as a time-variant bias superimposed to the magnetometer readings. Both MKF and XKF augment their state vector also with the gyroscope biases and the acceleration errors (intended as the deviation from the gravity since the two contributions cannot be distinguished from the accelerometer output). It is worth highlighting that a higher state vector dimension does not necessarily grant better performances, since each state element is governed by its own

parameter to be tuned and, above all, a large dimension may create problems of system observability (when the output variables no longer contain all the information required to describe the system behavior) [12].

C. Adopted algorithm for parameter value definition

It has been demonstrated that the choice of the parameter values required by each sensor fusion algorithm strongly affects the orientation estimate accuracy [13]. The choice of the most suitable parameter values depends on both hardware characteristics [7] and experimental conditions such as kinematics characteristic of motor task [13] and severity of the ferromagnetic disturbances. Recent literature suggests that no well-established solutions for the identification of the parameter values have been found yet [5]. In general, the "appropriate" values are commonly chosen either following the suggestions provided by the authors in their original implementations for their specific data set or by minimizing the overall errors between the estimated orientation and the one provided by a gold standard [4]. The latter approach, also known as *trial and error*, is time-consuming and the results are case-specific. The original procedure proposed in this study aims at identifying the sub-optimal parameter values for each algorithm without relying on any reference data. It is, in itself, an original secondary outcome of this contribution since previous studies (e.g. [7], [11]) compared the algorithm accuracy by using the optimal parameter values (i.e. those which provided the lowest absolute errors) computed with the aid of the gold standard. The method exploits the principle that the orientation difference of two units aligned must be null during the recorded motion. For each algorithm, the parameter values were determined by minimizing the relative orientation difference between the two MIMUs mounted on the board. This optimization process was performed for each rotation rate condition. Preliminary results obtained in [14] have confirmed the hypothesis that the sub-optimal parameter values provide also low absolute errors (Fig 2). For MAD and MAH the tuned parameters were β and k_p, respectively (in MAH the additional k_i parameter was set to zero as default since the offset was removed from all the gyroscope signals before computing the orientation). SEL exposes four parameters, but the tuning was carried out only for two parameters for computational reasons, namely τ_{acc} and τ_{mag} which respectively govern the influence of the accelerometer and magnetometer readings on the final estimate. In EKF and MKF the tuning was limited to the sensors' STDs since they resulted to be the most influencing parameters based on results of a preliminary investigation. Parameter optimization was not possible for XKF due the parameters not being accessible in the proprietary software.
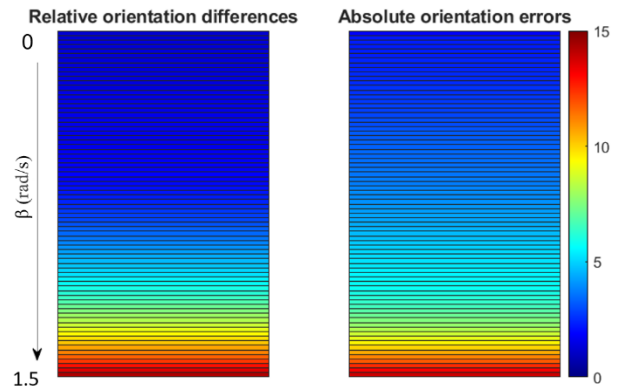

Fig 2: As an example, the relative differences and the absolute orientation errors (in degrees) as obtained by MAD at medium rate are reported using heatmaps. It can be observed that the β value which minimized the relative orientation differences provided also low absolute orientation errors.

D. Data processing and error computation

Each algorithm was implemented using the sub-optimal parameters as provided by the optimization procedure. For each MIMU, an estimate of the absolute orientation was obtained and compared with the reference (SP) to compute the absolute orientation errors. Errors from each MIMU were then averaged for the sake of conciseness. The estimated MIMU orientations as provided by SP and KF algorithms were both referred to the MIMU initial frame. The absolute orientation errors were evaluated only during the dynamic trial and expressed in terms of a single 3D rotation.

III. RESULTS AND DISCUSSION

The absolute orientation errors, for each rotation rate condition and averaged between the two MIMUs, are reported in TABLE I for each algorithm. The computation times demanded by the MATLAB implementation of the filters amounted to 0.53 s (MAD), 0.60 s (MAH), 1.70 s (SEL), 4.15 s (EKF), and 7.29 s (MKF) (Intel® Core™ i7-6500U CPU, dataset size = 25400 samples, clock frequency = 2.50 GHz).

TABLE I
ORIENTATION ERRORS AT THREE ROTATION RATES

(deg)	MAD	MAH	SEL	EKF	MKF	XKF
Slow	4.2	2.5	2.9	3.3	5.1	3.0
Medium	4.9	3.1	2.7	4.2	3.6	3.7
Fast	6.4	4.2	4.7	4.1	6.0	5.1

All the units are in degrees.

After parameters optimization, the errors of filters were similar showing differences between the maximum and minimum rms errors equal to 2.6 deg, 2.2 deg, and 2.3 deg for slow, medium and fast rotation rates, respectively. It is worth noting that for all filters but XKF, sub-optimal parameter values were separately tuned for each rotation rate condition. This can explain the overall good filters performances. One of the main evidences was that the performance of all algorithms decreased as the rotation rate increased, except for SEL and EKF whose accuracies were less sensitive to motion dynamics.

The lowest accuracy was found for MKF at slow condition (rms error equal to 5.1 deg), while MAH, SEL and XKF exhibited the smallest errors (difference lower than 0.5 deg are not considered as relevant, being of the same amplitude as the errors affecting the SP [4]). MAH and SEL resulted to be the best performing filters at medium rate, while MAD was the least accurate (4.9 deg). At high rotation rate MAH and EKF exhibited the smallest errors (4.1 deg). The good performances of MAH with respect to MAD, when optimal parameter were used (i.e. those provided by the optical reference), were already assessed by Ludwig *et al.*, in [15].

The findings of this study indicate that, when properly tuned, all the filters exhibited good performance. Furthermore, it shows that is not possible to identify a better performing family of filters between complementary and Kalman implementations, and this result is in line with the previous study of Bergamini *et al.* [4]. A key feature of this study was the implementation of the procedure for the definition of the sub-optimal parameter values, which allowed to perform a meaningful comparative evaluation. In summary, MAH and SEL were the best performing at slow and medium rate and together with EKF at high rate. However, the slightly higher accuracy of SEL with respect to MAH is associated to a longer execution time. MAH results to be more suitable for an implementation on low-power devices being three to twelve times faster than SEL and MKF, respectively. In addition, compared to SEL and MKF, MAH is the simplest filter to be employed since it requires the tuning of only two parameters. MKF with its eight parameters allows to better model the sources of error, which may have positive consequences on the filter accuracy. On the other hand, being the parameters mutually influenced, their tuning can be complicated, and the computation time required too high possibly making the algorithm not a suitable choice.

IV. CONCLUSION

The results of the comparison carried out in this paper suggested that, once sub-optimal values of the parameters of each algorithm are chosen, the accuracy of the algorithms under analysis was similar. The performances of the algorithms were similar independently from the mathematical approach on which they are based (CF or KF). These findings confirmed that the parameter values are the most critical factor [5]. When low-computational cost is a requirement, complementary filters should be preferred over the Kalman filters.

REFERENCES

[1] F. A. Storm, K. P. S. Nair, A. J. Clarke, J. M. Van der Meulen, and C. Mazzà, "Free-living and laboratory gait characteristics in patients with multiple sclerosis," *PLoS One*, vol. 13, no. 5, pp. 1–15, 2018.

[2] A. Cereatti, D. Trojaniello, and U. Della Croce, "Accurately measuring human movement using magneto-inertial sensors: Techniques and challenges," in *2nd IEEE International Symposium on Inertial Sensors and Systems, IEEE ISISS 2015 - Proceedings*, 2015, pp. 1–4.

[3] A. M. Sabatini, "Estimating three-dimensional orientation of human body parts by inertial/magnetic sensing," *Sensors*, vol. 11, no. 2, pp. 1489–1525, 2011.

[4] E. Bergamini, G. Ligorio, A. Summa, G. Vannozzi, A. Cappozzo, and A. M. Sabatini, "Estimating orientation using magnetic and inertial sensors and different sensor fusion approaches: Accuracy assessment in manual and locomotion tasks," *Sensors (Switzerland)*, vol. 14, no. 10, pp. 18625–18649, 2014.

[5] L. Ricci, F. Taffoni, and D. Formica, "On the orientation error of IMU: Investigating static and dynamic accuracy targeting human motion," *PLoS One*, vol. 11, no. 9, pp. 1–15, 2016.

[6] R. Mahony, T. Hamel, and J. M. Pflimlin, "Nonlinear complementary filters on the special orthogonal group," *IEEE Trans. Automat. Contr.*, vol. 53, no. 5, pp. 1203–1218, 2008.

[7] S. O. H. Madgwick, A. J. L. Harrison, and R. Vaidyanathan, "Estimation of IMU and MARG orientation using a gradient descent algorithm," *IEEE Int. Conf. Rehabil. Robot.*, vol. 2011, 2011.

[8] T. Seel and S. Ruppin, "Eliminating the Effect of Magnetic Disturbances on the Inclination Estimates of Inertial Sensors," *IFAC-PapersOnLine*, vol. 50, no. 1, pp. 8798–8803, 2017.

[9] M. Caruso, A. M. Sabatini, M. Knaflitz, M. Gazzoni, U. Della Croce, and A. Cereatti, "Accuracy of the Orientation Estimate Obtained Using Four Sensor Fusion Filters Applied to Recordings of Magneto-Inertial Sensors Moving at Three Rotation Rates," in *2019 41st Annual International Conference of the IEEE Engineering in Medicine and Biology Society (EMBC)*, 2019, pp. 2053–2058.

[10] A. Cappozzo, A. Cappello, U. D. Croce, and F. Pensalfini, "Surface-marker cluster design criteria for 3-d bone movement reconstruction," *IEEE Trans. Biomed. Eng.*, vol. 44, no. 12, pp. 1165–1174, 1997.

[11] R. G. Valenti, I. Dryanovski, and J. Xiao, "Keeping a good attitude: A quaternion-based orientation filter for IMUs and MARGs," *Sensors (Switzerland)*, vol. 15, no. 8, pp. 19302–19330, 2015.

[12] A. M. Sabatini, "Kalman-filter-based orientation determination using inertial/magnetic sensors: Observability analysis and performance evaluation," *Sensors*, vol. 11, no. 10, pp. 9182–9206, 2011.

[13] K. Lebel, P. Boissy, M. Hamel, and C. Duval, "Inertial measures of motion for clinical biomechanics: Comparative assessment of accuracy under controlled conditions - Changes in accuracy over time," *PLoS One*, vol. 10, no. 3, pp. 1–12, 2015.

[14] M. Caruso *et al.*, "Towards an automatic parameter setting for MIMU sensor fusion algorithms," *Gait Posture*, vol. 74, p. 8, 2019.

[15] S. A. Ludwig and K. D. Burnham, "Comparison of Euler Estimate using Extended Kalman Filter, Madgwick and Mahony on Quadcopter Flight Data," in *2018 International Conference on Unmanned Aircraft Systems, ICUAS 2018*, 2018, pp. 1236–1241.

A novel multi-sensor system for gait assessment in real-world conditions: preliminary results

F. Salis[1,2], S. Bertuletti[1,2], M. Caruso[3], T. Bonci[4], K. Scott[4], R. Rossanigo[1,2], U. Della Croce[1,2], C. Mazzà[4], A. Cereatti[1,2]

[1] *University of Sassari, Sassari, Italy*
[2] *IuC BoHNes, Sassari, Italy*
[3] *Politecnico di Torino, Torino, Italy*
[4]*Insigneo Institute and Department of Mechanical Engineering, University of Sheffield, Sheffield, UK*

Abstract— **Gait analysis is commonly performed in controlled environments. However, there is a growing interest in methods assessing motor performance in free-living conditions. Inertial measurement units (IMU) constitute a valid solution in the estimation of spatio-temporal gait parameters. However, performance of IMU-based methods is influenced by several factors and their validation in free-living conditions calls for a mobile gold standard as reference.**

To this end, the present study deals with the validation of a wearable multi-sensor system (INDIP) for digital gait assessment in free-living conditions. The INDIP integrates four magneto-inertial units, two distance sensors and two pressure insoles. Since its validation is on-going, preliminary outcomes obtained for two tasks from lab-based acquisitions on one healthy subject are presented and discussed. Results show low percentage errors (always <5%) and hopefully will be confirmed on more subjects and more complex tasks.

Keywords— **gait analysis, IMU, wearable sensors**

I. INTRODUCTION

A person's mobility is the result of the combination between their motor capacity (what they can do) and their motor performance (what they actually do), with the latter being strongly influenced by daily-life environments and behavioural choices. An accurate assessment of mobility hence calls for complementing a conventional one-time, laboratory assessment with continuous daily-living measures [1]-[4]. In this perspective, the use of a single inertial measurement unit (IMU) represents a low-cost and fully wearable solution to characterize gait in patients with motor impairments [5]. Methods for the estimation of clinically relevant spatio-temporal parameters generally rely on the analysis of signal morphology, the use of biomechanical models and/or machine learning techniques [6], [7]. However, the validity of these methods can be affected by several factors, including IMU location, characteristics, motor impairment severity, measurement environment, presence of obstacles/stairs, number of pauses, etc. Moreover, the use of inertial sensing alone does not allow to estimate some additional but yet important gait parameters such as step width and base of support.

A major obstacle in validating IMU-based methods in real-world conditions is the lack of gold standard measurement systems which allow for long-term monitoring based on minimally intrusive sensors. To respond to the abovementioned requirements, we designed and developed a wearable multi-sensor system (INDIP), which integrates magneto-inertial sensing technologies with infrared time-of-flight sensors and force sensitive resistor pressure insoles

[8],[9]. The INDIP system, by exploiting the complementary characteristic of the different sensors and data redundancy, is expected to provide the "best available" reference in out-of-lab gait analysis applications.

The INDIP validation and feasibility assessment entails two different phases: (i) lab-based acquisitions to compare INDIP performance with the stereo-photogrammetric (SP) system (gold standard) (ii) free-living activities acquisitions to evaluate usability and human factors.

In this preliminary study, we focused on the first validation phase by presenting results obtained in two motor tests of different complexity included in lab-based experimental protocol from one healthy subject.

II. MATERIALS AND METHODS

A. System Description – INDIP System

The INDIP system includes four magneto-IMU (fs=100 Hz), two plantar pressure insoles (PIs) (16 force resistive sensing elements, fs=100 Hz) and two time-of-flight distance sensors (DSs) (range=0.2 m, fs=50 Hz). Each DS provides distance readings by estimating the time that an electromagnetic wave (i.e. infrared ray) takes to travel a distance or, more properly, by measuring the phase shift between the emitted and the reflected signals. Each magneto-IMU includes a 3D accelerometer (full-scale up to ±16 g), a 3D gyroscope (full-scale up to ±2000 °/s) and a 3D magnetometer (full-scale up to ±50 Gauss). Data are processed by an ultra-low-power microcontroller (ARM® 32-bit Cortex®-M4 CPU) and stored in an on-board 128 MB flash storage for up to four hours of data logging. The system allows third-party devices to be synchronized via an external trigger. Multiple INDIP units can be synchronized via a BLE protocol (v. 4.1).

B. Experimental set-up

Validation experiments are currently in progress and will include 15 healthy participants recruited at both the University of Sassari (Italy) and the University of Sheffield (UK). The study was performed by following the principles outlined in the Helsinki Declaration. All participants signed the informed consent, approved by the ethics committee of the University of Sassari and Sheffield. For this preliminary study, we presented only the data acquired on a healthy adult female (height 1.70 m, EU shoe size 39). The subject was prepared by positioning the INDIP system and the markers for the SP system as

depicted in Fig.1. PIs were inserted in the shoes and feet magneto-IMU where positioned over the instep while lower back magneto-IMU was attached using an elastic belt. Wrist magneto-IMU was positioned on the non-dominant arm. To avoid mutual IR interferences, DSs were positioned asymmetrically (one just above the left ankle and the other about 3 cm higher on the right side), both pointing medially. Both magneto-IMU and DSs were attached using straps. PIs and DSs were connected to the magneto-IMU of the corresponding foot.

A total of 13 markers were used: four markers on the left foot, four markers on the right foot, four markers placed on a rigid cluster used as support for the lower back INDIP and one on the magneto-IMU on the wrist (Fig.1). Of the four markers on each foot, those on the heel and on the second metatarsal head are used in the algorithm, together with the four markers on the rigid cluster. Markers m_{LREF} and m_{RREF} are used to avoid confusion between right and left side in the labelling; m_{INDIP} is for additional checks. Marker trajectories were recorded using a 10-camera motion capture system (Vicon, MX T160, fs = 100 Hz). The SP and the INDIP system were synchronised using the above-mentioned external trigger.
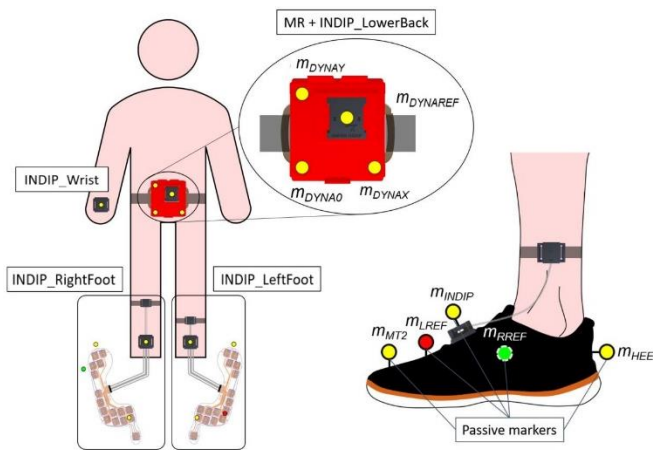
Fig. 1: INDIP system and markers positioning. The INDIP system includes INDIP_Wrist (wrist block), INDIP_RightFoot (right foot block), INDIP_LeftFoot (left foot block), INDIP_LowerBack (lower-back block).

C. Experimental protocol

The lab-based validation included several motor tests with an increasing level of complexity. For sake of brevity, we focused on two paradigmatic motor tests (Fig. 2), described below:

- Rectangle Test: the subject is asked to stand at the starting point and walk along the rectangular path identified with cones doing sharp 90° turnings and stopping at the end line.
- Hallway Test: the subject is asked to stand at the starting point and walk straight to the opposite end of the walkway while making sure of stepping up and down the step (height 20 cm). Once the participant reaches the cross (just after the step), he/she is asked to rest for 10 s before continuing. At the end of the walkway, he/she has to make a sharp U-turn and walk straight back along the walkway. Then, the participant stops at the cross for 10s once again and

completes the remaining walkway reaching the end point.

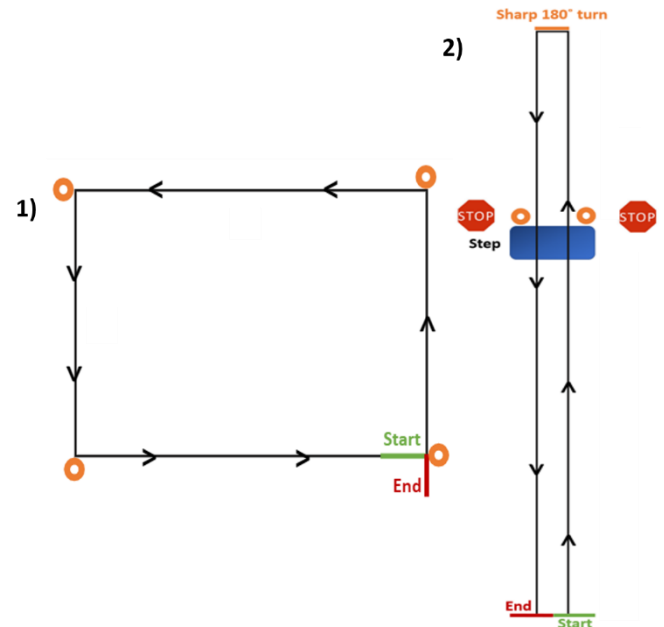The tasks were executed at comfortable self-selected speed.

Fig. 2: Representation of the tasks. 1) Rectangle Test; 2) Hallway Test

D. Data processing - INDIP

A preliminary calibration procedure was applied to each sensor according to [10],[11]. Each magneto-IMU underwent to a preliminary static spot check, 30 s long. A pre-processing procedure was applied for data synchronisation. The INDIP-based method exploits the redundancy proper to the multi-sensor platform for the estimation of the spatio-temporal parameters. The implemented algorithm consisted in the following steps:

(i) static/dynamic activity periods recognition is performed to keep only those portions in which there is movement. The subject is "active" if the acceleration of both lower-back and at least one foot is above a certain threshold [12],[13]

(ii) bilateral gait events detection at foot level from PIs signals. The strategy used to find initial contact (IC) and final contact (FC) events considers a sub-group of the PI sensing elements, called *neighbourhood*, looking at signals' morphology [14]. Candidate ICs correspond to rising edges in PI signals, while candidate FCs correspond to falling edges. Rising and falling edges are identified in signal's first derivative using peaks detection [9]. An IC/FC event is defined as the value in the middle of the candidate ICs/FCs obtained for each neighbourhood.

(iii) spatial description at foot level in terms of position and orientation. Starting from feet inertial data, a Madgwick filter is applied to compute orientation for each foot sensor. Then, velocity and displacement are obtained with a direct and reverse integration (DRI) approach [15].

(iv) strides detection and selection based on (ii, iii). Right and left strides are detected starting from the ICs. Selection is performed applying thresholds on some stride relevant parameters, including duration, length and height. At this

TABLE I
RECTANGLE TEST (NUMBER OF WBS = 1)

Parameters	WB 1		
	INDIP	SP	e%
Time location (s)	2.04 to 10.47	2.01 to 10.46	1.5, 0.1
Time duration (s)	8.43	8.45	-0.2
Path length (m)	8.44	8.30	1.7
Gait speed (m/s)	1	0.98	2
Number of strides	13 (7R, 6L)	13 (7R, 6L)	all
Number of turnings	3	3	all

Results obtained for the Rectangle Test

TABLE II
HALLWAY TEST (NUMBER OF WBS = 3)

Parameters	WB 1			WB 2			WB 3		
	INDIP	SP	e%	INDIP	SP	e%	INDIP	SP	e%
Time location (s)	2.24, 8.33	2.21, 8.35	1.36, -0.24	22.74, 27.9	22.58, 27.9	0.7, 0	42.5, 47.3	42.37, 47.4	0.4, -0.17
Time duration (s)	6.1	6.14	-0.8	5.16	5.33	-3.2	4.8	5	-4
Path length (m)	3.78	3.64	3.8	3.37	3.28	2.7	0.72	0.7	2.9
Gait speed (m/s)	0.62	0.6	3.3	0.65	0.62	4.8	3.45	3.48	-0.86
Number of strides	8 (4R, 4L)	8 (4R, 4L)	all	7 (4R, 3L)	7 (4R, 3L)	all	6 (3R, 3L)	6 (3R, 3L)	all
Number of turnings	0	0	all	1	1	all	0	0	all

Results obtained for the Hallway Test

stage, DSs are used as "stride counters" and give an additional information on the reliability of measure [16].
(v) walking bout (WB) detection and selection based on strides information. Right and left strides are combined to obtain WBs. Only WBs including a minimum of 2 right and 2 left strides are selected for the analysis.
(vi) estimation of spatio-temporal gait parameters for the identified WBs. For every test and each WB, the following information was extracted: time location (start and stop time instants (s)),duration (s), path length (m), gait speed (m/s), number of right and left strides, number of turnings. The accuracy of the INDIP-based method was assessed, for each WB parameter, as the difference between INDIP and SP estimates (obtained from marker-trajectories estimation) in terms of percentage errors.

III. RESULTS

The results obtained with the INDIP-based method and the percentage errors with respect to the gold standard for the Rectangle Test and the Hallway Test are shown in Table I and Table II, respectively.

IV. DISCUSSION

The setup of the validation protocol resulted to be feasible (no unexpected events during the experiment, system crashes, data loss or uncompleted trials) and acceptable for the subject (tasks easy to understand, comfortable technology).
In the Rectangle Test, both the INDIP-based method and the SP system detected a single WB. Extremely small percentage errors were achieved in the estimate of start and stop instants (e%=1.5% for the start, e%=0.1% for the stop), duration (e%= -0.2%), path length (e%= 1.7%) and gait speed (e%= 2.0%); the same number of strides and turnings was obtained with both methods (7R and 6L strides and 3 turnings).

For the Hallway Test, a total of three WBs were detected in both methods. Low percentage errors (<5%) were obtained for all the WBs. In the first WB, errors obtained were: 1.36% and -0.24% respectively for start and stop instant, -0.8% for time duration, 3.8 % for path length, 3.3% for gait speed. The same number of strides and turnings was detected with both INDIP and SP system (4R and 4L strides, no turnings). In the second WB, very low errors were obtained for start (0.7%) and stop (0%) instants, e%= -3.2% for duration, e%=2.7% for path length, e%=4.8% for gait speed. Also, in this case, both systems identified the same number of strides (4R and 3L) and turnings (one U-turn). About the third WB, 3R and 3L strides and no turnings were detected with both INDIP-based and SP-based methods. Percentage errors equal to 0.4% and -0.17% were respectively obtained for start and stop instant. Errors were low also for duration (-4%), path length (2.9%) and gait speed (-0.86%).
Gait initiation and termination phases (first and last step) were excluded by the comparison between the two methods.
It is interesting noting that, when the number of strides within a WB is higher, percentage errors are extremely low. This is what happens, for instance, in the Rectangle Test, were the total number of strides is 7 for the right foot and 6 for the left one. On the other side, when the number of strides is smaller, the difference between the outputs obtained from INDIP and SP is higher. This is expected as the gait speed computed over three strides is obviously highly variable. Despite this, the errors obtained are always below 5%.
The INDIP system is completely wearable, no differences are expected in usability and comfort moving from the lab to real world scenarios. Future algorithm improvements include the estimation of gait events also from feet inertial data to have a more accurate and complete information. Moreover, DS data can be used for the estimation of stride width and base of support. Hopefully, further increasing the INDIP-method robustness, these preliminary encouraging results will be

confirmed on more complex motor activities and more subjects.

V. CONCLUSION

A novel multi-sensor wearable system for the identification of WBs and the estimation of spatio-temporal parameters within them has been presented. Preliminary promising results suggest its potential use in prolonged daily-living measures. The same correct number of strides were found by both the INDIP-based and SP-based methods while the WBs where either a single continuous one (i.e. Rectangle Test) or different shorter ones (i.e. Hallway Test). A full validation of the INDIP-based method is on-going where a full experimental protocol with five different motor tasks is performed by 15 healthy subjects.

ACKNOWLEDGEMENT

REFERENCES

[1] O. Bock, *"Changes of locomotion in old age depend on task setting."* Gait & Posture, vol. 32, issue 4, pp. 645-649, October 2010.

[2] K. Donovan, *"Mobility beyond the clinic: the effect of environment on gait and its measurement in community-ambulant stroke survivors."* Clinical Rehabilitation, vol. 22, issue 6, pp. 556-563, June 2008.

[3] E. Giannouli, *"Mobility in old age: capacity is not performance,"* BioMed research international, 2016.

[4] I. Galperin, "*Associations between daily-living physical activity and laboratory-based assessments of motor severity in patients with falls and Parkinson's disease*." Parkinsonism & related disorders (2019).

[5] D. Trojaniello, *"Accuracy, sensitivity and robustness of five different methods for the estimation of gait temporal parameters using a single inertial sensor mounted on the lower trunk."* Gait & posture, vol. 40, issue 4, pp.487-492, 2014.

[6] M. Yuwono, *"Unsupervised nonparametric method for gait analysis using a waist-worn inertial sensor.",* Applied Soft Computing 14, pp. 72-80, 2014.

[7] R. C. González, *"Real-time gait event detection for normal subjects from lower trunk accelerations."* Gait & posture, vol. 31, issue 3, pp. 322-325, 2014.

[8] S. Bertuletti, *"Static and dynamic accuracy of an innovative miniaturized wearable platform for short range distance measurements for human movement applications.",* Sensors, vol. 17, issue 7, 2017.

[9] J. M. Hausdorff, *"Footswitch system for measurement of the temporal parameters of gait.",* Journal of biomechanics, vol. 28, issue 3, pp. 347-351, 1995.

[10] F. Ferraris, *"Calibration of three-axial rate gyros without angular velocity standards."* Sensors and Actuators A: Physical, vol. 42, issues 1-3, pp. 446-449, April 1994.

[11] D. Gebre-Egziabher, *"A non-linear, two-step estimation algorithm for calibrating solid-state strapdown magnetometers."* 8th International St. Petersburg Conference on Navigation Systems (IEEE/AIAA), 2001.

[12] G. M. Lyons, G. M., *"A description of an accelerometer-based mobility monitoring technique."* Medical engineering & physics, vol. 27, issue 6, pp. 497-504, July 2005.

[13] A. Hickey, *"Detecting free-living steps and walking bouts: validating an algorithm for macro gait analysis."* Physiological measurement, vol. 38, issue 1, N1-N15, 2017.

[14] M. Benocci, *"A wireless system for gait and posture analysis based on pressure insoles and Inertial Measurement Units."*, 2009 3rd International Conference on Pervasive Computing Technologies for Healthcare, pp. 1-6, IEEE, 2009.

[15] D. Trojaniello, *"Estimation of step-by-step spatio-temporal parameters of normal and impaired gait using shank-mounted magneto-inertial sensors: application to elderly, hemiparetic, parkinsonian and choreic gait."* Journal of Neuroengineering and rehabilitation, vol. 11, issue 1, p. 152, November 2014.

[16] S. Bertuletti, *"A wearable solution for accurate step detection based on the direct measurement of the inter-foot distance."* Journal of biomechanics, vol. 84, pp. 274-277, February 2019.

Use of an optimized automatic procedure for measuring the hydraulic permeability of articular cartilage

N. Giuliani[1], A.B. Lovati[2], M. Ferroni[1], L. Ferrari[1], L. Mangiavini[2], G.M. Perettti[2,3], and F. Boschetti[1]

[1] Dipartimento di Chimica, Materiali e Ingegneria Chimica, "Giulio Natta", Politecnico di Milano, Italy
[2] IRCCS Istituto Ortopedico Galeazzi, Milano, Italy
[3] Dipartimento di Scienze Biomediche per la Salute, Università degli Studi di Milano, Italy

Abstract— Permeability, *k*, is one of the main characteristics that allows cartilage to perform its functions. We developed an automatic procedure, based on LabVIEW, to directly measure the permeability of cartilage by use of a custom-made permeation setup. We compared the results with those obtained by standard indirect methods based on the poroelasticity theory and with numerical predictions, obtained by a mathematical model developed under Comsol Multiphysics. The preliminary results demonstrate the effectiveness of our automatic method to measure the hydraulic permeability of articular cartilage or any other soft tissue.

Keywords—Cartilage, osteoarthritis, permeability, poroelasticity

I. INTRODUCTION

THE articular cartilage is a thin layer of specialized connective tissue with viscoelastic and mechanical properties, which are especially important for preserving joints as they reduce friction between the moving articular surfaces, they also allow for better load distribution and provide impulsive loads absorption.

Permeability, *k*, is one of the main characteristics that allows cartilage to perform its functions adequately and can be defined as the ease with which a fluid passes through a porous medium. In healthy articular cartilage, the low value of this property (10^{-16} m^4/N·s) holds water inside the tissue, and this retained water is used to withstand most of the load to which the cartilage is subjected, thus preserving the ECM. This property also prevents synovial fluid from penetrating the cartilage tissue, ensuring adequate lubrication of the joints.

When the cartilage tissue undergoes degenerative processes like osteoarthritis (OA), an initial chondrocyte proliferation occurs, followed by an increase of water content and loss of proteoglycans and glycoproteins (GAG), which ultimately lead to breakage of the collagen fibers and result in superficial pitting. The gradual decrease of proteoglycans, responsible for the water content of the matrix, entails an increase of permeability with consequent loss of the normal functions of the healthy tissue.

II. MATERIALS AND METHODS

In this study we analysed 14 OA cartilage samples derived from 2 human femoral heads that had been removed during hip replacement surgery. The samples underwent direct and indirect measures (stress-relaxation test), as permeability can be directly measured, exploiting the Darcy equation, or it can be indirectly estimated, using theoretical models.

A. Set-up and optimized automatic procedure

Fig.1A represents our automated experimental set-up, used to facilitate the direct permeability measurement, composed by a custom made chamber (where the sample is housed, Fig. 1B), a volumetric pump (NE500, New Era Pump Systems, Inc., USA), to control the flow rate, a pressure transducer (IMP, Sensors One Ltd, UK), a digital camera (Dino-Lite, Taiwan) to measure the effective flow through the sample, and the control software developed within LabVIEW (National Instruments), to make the test procedure automatic.
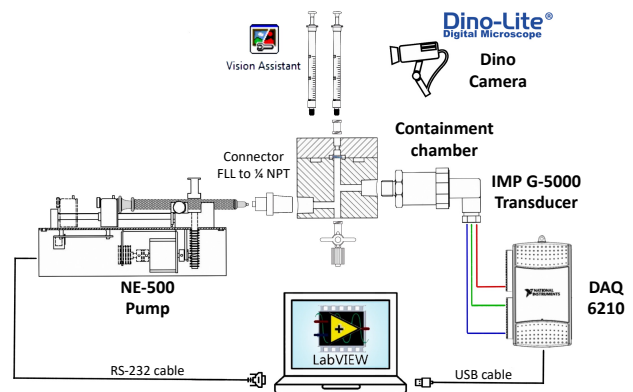

Fig. 1A: General scheme of the set-up that represents all of the components and their connections: the fundamental part is the control software which can acquire, through the DAQ acquisition card connected to the computer, the pressure signals measured by the transducer and control the syringe pump connected to the sample containment device; to estimate the effective flow rate through the sample, a video camera and two graduated capillaries are connected to the permeation chamber.

LabVIEW is a graphic programming environment that enables the design of clear, simple and intuitive interfaces and allows the direct control of the electronic instrumentation, such as the data acquisition hardware (DAQ), for the analysis and elaboration of signals.

Our program is able i) to control the volumetric pump, ii) to acquire, through the DAQ system, the pressure signals measured by the transducer and iii) to increase the flow rate value (input variable), when the signal pressure remains in a range previously defined by the user (Pressure stab. range±) during a specific amount of time (Stabilization time). The program can also record and automatically save the set parameters and the pressure values in an external Excel file at the end of the test, this feature allows the user to analyse and elaborate the output data at a later time to calculate the permeability sample.
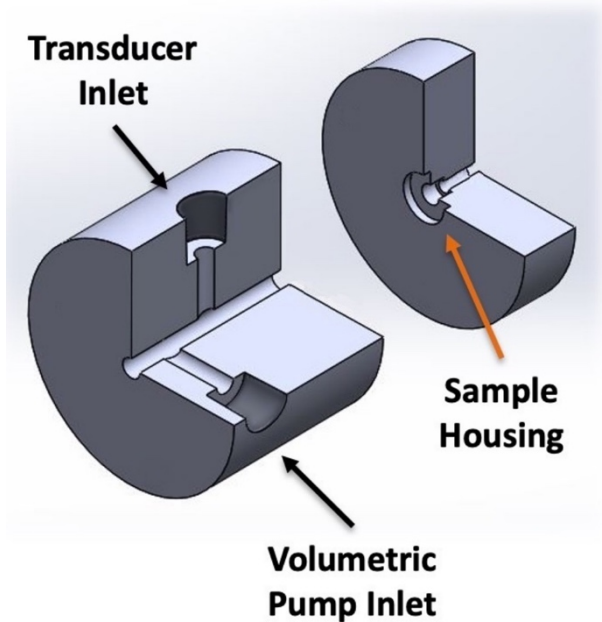
Fig. 1B: A detailed view of the custom permeation chamber composed by two axial cylinders. The sample housing is 12 mm in diameter whereas the area available for flow is 5 mm in diameter.

More useful functions performed by the implemented software are *a. Calibration of the pressure transducer* implemented directly into the control interface; *b. Storage of the runtime pressure values*, useful to obtain the pressure trend during the entire test and facilitate the data post-processing. Data are saved in real-time, based on a time-sampling chosen by the user; *c. Step independent flow rate increments*, this feature makes the test settings more versatile; *d. Maximum time step*, the purpose of this function is to limit the duration of the entire test, in fact, the excessive test length may cause pressure instability; *e. Pressure conversion* used to visualize the pressure value in the desired units of measurement; *f. Target Pressure*, whose purpose is to protect the pressure transducer and the analysed sample from damage: if the pressure value reaches the *Target Pressure* the test is instantly interrupted.

B. Direct permeability measurement

We performed 3-5 measurements for each sample, setting the flow rate (value range from 15 to 200 μL/hr) and measuring the pressure value when stabilized.

Permeability was computed as a function of the pressure gradient using Darcy equation from the parameters and the pressure values saved at the end of the test:

$$k = (A \cdot \Delta p) / (s \cdot Q) \qquad (1)$$

where A= passage area [m²]; s= thickness of sample [m].

C. Indirect permeability measurement

The central 5mm diameter of the samples tested for permeation were cut and subjected to indirect permeability measurements, via confined compression test in movement control (stress-relaxation test), with 5 deformation ramps. We interpolated the resulting experimental curve with the analytical solution extracted from Mow's linear biphasic model [1], thus obtaining the aggregate module H_A and the axial permeability value. The mean H_A value of each sample

was exploited to extract the deformation levels of the direct tests through the relation [2]:

$$\varepsilon = \Delta p / 2H_A \qquad (2)$$

this step allowed us to find the $k(\varepsilon)$ trend of both tests.

The experimental data were interpolated with a decreasing exponential according to Lai & Mow law [3]:

$$k = k_0 e^{M_0 \varepsilon} \qquad (3)$$

D. GAG evaluation

After the permeability measurements, for each sample the GAG and DNA contents were evaluate as described in [4]. Briefly, specimens were minced and digested in proteinase K (pH 7.6) (Sigma-Aldrich, Milan, Italy), then centrifuged and the supernatant was collected for analyses. DNA content was measured in the supernatant using a cell proliferation assay (CyQuant® kit – Life Technologies, Monza, Italy). The quantification of sGAG was performed using the 1,9-dimethylmethylene blue (DMMB) dye-binding assay (Sigma-Aldrich, Milan, Italy) and compared to a standard curve of chondroitin sulphate (Blyscan – Biocolor, Magenta, Italy). Briefly, the samples were incubated in 40 mM glycine/NaCl (pH 3.0) with 16 mg/mL DMMB at RT. The DNA and sGAG concentrations were determined by means of a spectrophotometer (Perkin Elmer Victor X3 microplate reader). Data from DNA and sGAG content analysis were normalised to the sample dry weights.

The mean value and standard deviation of H_A, k_0 for direct (k_{0darcy}) and indirect measurements (k_{0cc}) were calculated for each patient, to investigate the presence of a possible correlation between these parameters and the GAG content.

E. COMSOL Multiphysics simulations

Numerical simulations were performed under COMSOL Multiphysics 5.4 (COMSOL Inc., Burlington, MA, USA) to reproduce the conditions of the direct permeability test conducted on the cartilage tissue and design better experiments. In particular, the purpose of these simulations was to quantify the effect of several parameters on the stabilization time of the upstream pressure.

Time dependent studies were performed by means of the Poroelasticity module, as it combines a transient formulation of Darcy's law with a quasi-static formulation of Solid Mechanics, based on the resolution of Navier-Stokes equations, which together constitute a multiphysics coupling suitable to represent soft tissues.

Having to represent a cylindrical specimen, a two-dimensional axisymmetric model was created, which translates into a rectangular geometry, having dimensions equal to the thickness and radius of the sample (Fig. 2). Given the regularity of the implemented geometry, a mapped mesh consisting of square elements was created; moreover, since the variable of interest is more significant on the upper boundary, it was decided to build a finer mesh in the upper part of the geometry by creating a regular distribution of the elements in length with a ratio of 0.1 in thickness, as visible in Fig. 2.

Specifically, the steady state pressure of the upper side of the rectangle is the representative variable of the problem and the simulations were conducted varying the parameters of initial velocity v_0, permeability k, elastic module E and sample

thickness *s*. The values of the parameters were chosen on the basis of the experimental results obtained and are shown in Table 1.
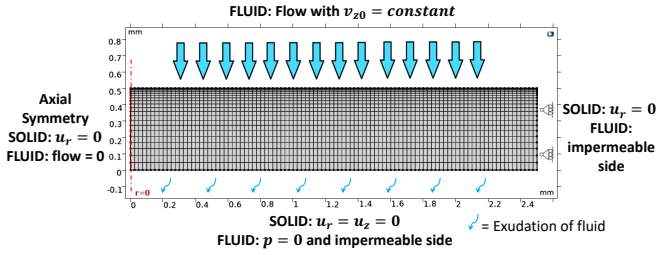

Fig. 2: Mesh and boundary conditions used in simulations.

TABLE I
SIMULATION PARAMETERS

Parameter	Values		
s [mm]	0.5	1	1.5
E [MPa]	0.1	0.3	0.6
v_0 [m/s]	2.83e-8	1.47e-7	2.83e-7
k [m²]	1e-17	1e-18	1e-19

Values used to perform parametric simulations.

III. RESULTS

A. Permeability Measurements

Pressure drops measured across the samples varied from 0.2 to 1 atm, depending on the sample physical and mechanical properties (k, s, E).

For each sample, the comparison graphs of direct and indirect permeability as a function of deformation were performed. Fig.3 shows one example of permeability trends where all points, i.e. those computed from the model and those derived from the experiments, were fitted by an exponential curve. For both tests, the permeability decreases with increasing deformation.

The average and SD values for indirect and direct k_0 and for H_A are conformed to the ones found in the literature [5]–[8] and they are summarized in Table 2.
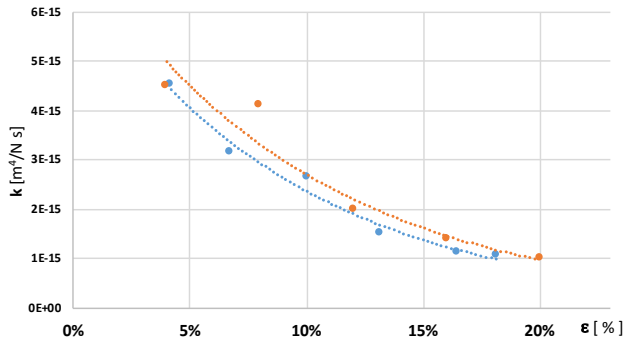
Fig. 3: Comparison between the direct and indirect test k(ε) curves for one of the tested cartilage samples. Blue dots and line: direct measurements (Darcy law); orange dots and line: indirect measurements (confined compression).

TABLE II
AVERAGE AND SD VALUES

Tissue	k_{0darcy} [m⁴/(N·s)]	k_{0cc} [m⁴/(N·s)]	H_A [MPa]
OA cartilage	0.36±1.8e-14	0.96±1.29e-13	0.36±0.25

Permeability values obtained by direct (k_{0darcy}) and indirect (k_{0cc}) test and aggregate modulus for analyzed cartilage.

In a few cases the two intrinsic permeability values differed by even by an order of magnitude, in general the indirect values where higher than the direct values. Causes of such differences can be attributed to intrinsic confined compression test errors [6], as the ideal boundary conditions do not coincide to the ones that occur during the effective test (gap between piston and chamber, imperfect sample dimensions). Moreover, the lengthy duration of the direct measurement test deteriorates the analysed sample, making it swell and then resulting in permeability increase measured indirectly.

B. GAG evaluation

As seen in literature, we found a mild positive correlation between GAG and H_A [7], [10] and a weak negative correlation between GAG and k_{0darcy} [10], [11]. Contrary to expectations, the relation between GAG and k_{0cc} resulted in a weakly positive correlation [7]. This phenomenon can be explained considering the sample swelling and the strong positive correlation between water content and permeability [12]–[14].

C. COMSOL Multiphysics simulations

The results of parametric simulations, summarized in Fig. 4, show that the stabilization time during permeation tests is strongly affected by the tissue parameters, while the test settings are irrelevant. In particular, the regime time is independent from the inflow velocity v_0, and it is instead non-linearly influenced by the permeability k, the elastic modulus E, and the sample thickness s. As shown in Fig. 4, the regime time decreases with the increase in permeability and elastic modulus, while increases with the increase of the sample thickness. These numerical results confirm how samples of soft tissues with low intrinsic permeability and stiffness typically show very high stabilization times.
Considering our proposed set of parameters, the permeability is the parameter that most influences the stabilization time: the latter decreases of two orders of magnitude when k increases from 1e-19 to 1e-17 m².

On the basis of these simulations, we believe it is inappropriate to maintain the same settings for different samples in the direct tests of permeability.

IV. CONCLUSION

The preliminary results demonstrate the effectiveness of our automatic method to directly measure OA cartilage permeability [7], [8]. A mild positive correlation between GAG e H_A and a weak negative correlation between GAG and k_0 for direct measurements [10], [11] was found in agreement with other authors [8], [10], [11], whereas GAG and k_0 for indirect measurements resulted in a weakly positive

correlation, probably because of sample swelling during permeation tests [12]–[14].

Finally, we hypothesised a new test protocol, which entails an inverted order of the test execution (contrary to what has been done in this preliminary study): if the confined compression test is carried out first, the direct permeability measure can be more robust without affecting the direct measurement test.

Fig. 4: Simulation results for 1.5 mm and 0.5 mm sample thickness. The time requested to reach a constant upstream pressure is calculated for different values of flow velocity (v_0), permeability (k), elastic modulus (E) and sample thickness (s).

This new executive order could give us two benefits: on one side, the measurement errors caused by the sample swelling and deterioration that occur during the direct permeability measurement test would be eliminated. On the other hand, the H_A value estimated from the indirect permeability measurement would allow us to determine the maximum pressure value that can be reached during the direct permeability tests, in order to guarantee the hypothesis of linearity required to apply Eq. 2.

This maximum pressure value can be entered into the direct test control software, under the voice Target Pressure, to ensure that the obtained result (i.e. k(Δp) and then k(ε)) satisfies the analytical model.

The setting of an efficient maximum time length of a single step (t max step) is extremely important: to do this, a numerical simulation should be run, using the parameters of the sample analyzed via a confined compression test to set the simulation, before the conduction of a direct measurement test.

Specifically, the model simulated using Comsol Multiphysics should have the same thickness of the analyzed sample, its elastic module E should be derived from Poisson ratio and the aggregate module H_A, while its permeability value (deducted from the indirect measure) may be decreased by 30% to take into account the confined compression test intrinsic errors [6].

In a future perspective, after the validation of the new execution order, this new test protocol could be used in combination with the optimized set-up to fulfil a wider range of applications, for example to compare the properties between healthy and pathological tissue or to complete the permeability study, analysing its trend also as a function of a constant pre-clamping deformation.

REFERENCES

[1]   V. C. Mow, S. C. Kuei, W. M. Lai, and C. G. Armstrong, "Biphasic creep and stress relaxation of articular cartilage in compression: Theory and experiments," *J. Biomech. Eng.*, vol. 102, no. 1, pp. 73–84, 1980.

[2]   B. Reynaud and T. M. Quinn, "Anisotropic hydraulic permeability in compressed articular cartilage," *J. Biomech.*, vol. 39, no. 1, pp. 131–137, 2006.

[3]   W. M. Lai and V. C. Mow, "Drag induced compression of articular cartilage during a permeation experiment.", *Biorheology*, vol. 17, pp. 111-123, 1980.

[4]   M. Bottagisio, A. F. Pellegata, F. Boschetti, M. Ferroni, M. Moretti, and A. B. Lovati, "A new strategy for the decellularisation of large equine tendons as biocompatible tendon substitutes," *Eur. Cells Mater.*, vol. 32, pp. 58–73, 2016.

[5]   K. A. Athanasiou, A. Agarwal, and F. J. Dzida, "Comparative study of the intrinsic mechanical properties of the human acetabular and femoral head cartilage," *J. Orthop. Res.*, vol. 12, no. 3, pp. 340–349, 1994.

[6]   F. Gervaso, G. Pennati, F. Boschetti, "Effect of geometrical mperfections in confined compression tests on parameter valuation of hydrated soft tissues", *J. Biomech.,* vol. 40, n. 13, pp. 3041-3044, 2007.

[7]   P. A. Rivers, M.P.Rosenwasser, V.C.Mow, R.J.Pawluk, J.Strauch, M.T.Sugalski, G.A.Ateshian, "Osteoarthritic changes in the biochemical composition of thumb carpometacarpal joint cartilage and correlation with biomechanical properties," *J. Hand Surg. Am.*, vol. 25, no. 5, pp. 889–898, 2000.

[8]   F. Boschetti and G. M. Peretti, "Tensile and compressive properties of healthy and osteoarthritic human articular cartilage," *Biorheology*, vol. 45, pp. 337–344, 2008.

[9]   C. T. Hung and V. C. Mow, "Chapter 3: Biomechanics of Articular Cartilage," in *Basic Biomechanics of the Musculoskeletal System*, 4th ed., Wolters Kluwer Health, 2012, pp. 60–101.

[10]   J. S. Wayne, K. A. Kraft, K. J. Shields, C. Yin, J. R. Owen, and D. G. Disler, "MR imaging of normal and matrix-depleted cartilage: Correlation with biomechanical function and biochemical composition," *Radiology*, vol. 228, no. 2, pp. 493–499, 2003.

[11]   J. Katta, T. Stapleton, E. Ingham, Z. M. Jin, and J. Fisher, "The effect of glycosaminoglycan depletion on the friction and deformation of articular cartilage," *Proc. Inst. Mech. Eng. Part H J. Eng. Med.*, vol. 222, no. 1, pp. 1–11, 2008.

[12]   C. G. Armstrong and V. C. Mow, "Variations in the intrinsic mechanical properties of human articular cartilage with age, degeneration, and water content," *J. Bone Jt. Surg. - Ser. A*, vol. 64, no. 1, pp. 88–94, 1982.

[13]   L. A. Setton, V. C. Mow, F. J. Müller, J. C. Pita, and D. S. Howell, "Mechanical Properties of Canine Articular Cartilage Are Significantly Altered Following Transection of the Anterior Cruciate Ligament," *J. Orthop. Res.*, vol. 12, no. 4, pp. 451–463, 1994.

[14]   K. L. Kleinhans and A. R. Jackson, "Hydraulic permeability of meniscus fibrocartilage measured via direct permeation: Effects of tissue anisotropy, water volume content, and compressive strain," *J. Biomech.*, vol. 72, pp. 215–221, 2018.

A patient-specific approach for the IDH risk evaluation in the early stage of Haemodialysis

G.Casagrande[1], M.L. Costantino[1]

[1] *Department of Chemistry, Materials and Chemical Engineering "Giulio Natta", Politecnico di Milano, MI, Italy*

Abstract— **Introduction: Intra-Dialysis Hypotension (IDH) occurs in 25-30% of the hemodialysis (HD) sessions. An open challenge is to find an index to quantify the risk of IDH onset, in the early stage of HD, for each specific patient. A similar index (J_i), defined as the weighted sum of influent parameters has been recently described by Vito et al. Aim of this work is its optimization, validation, and evaluation in a wider set of patients.**

Methods: The patients have been classified in Hypotension Prone (HP) and Hypotension Resistant (HR), using an updated criterion (IDH_D) to identify IDH episodes. The statistical analysis was repeated to verify, also using IDH-D, the pertinence of the already identified predictors. J_i accuracy was verified on the 1st dataset (70 patients - 450 sessions) and evaluated on a 2nd dataset (60 patients – 360 sessions). J_i higher than 1 suggests a risk of IDH onset. The effects of the different protocols adopted to manage IDH in the four involved Dialysis Units were also studied, identifying and evaluating a center-dependent risk threshold.

Results: J_i allows predicting the 77% of the IDH events when the threshold is set equal to 1. The use of center-specific thresholds allows slightly improving index specificity and sensitivity but does not substantially alter the results.

Conclusions: J_i allows a reliable prediction of IDH risk, for each specific patient, at the early stage of the HD sessions. It can allow HD prescription optimization when patient-specific longitudinal data were available

Keywords— **Haemodialysis, hypotension, patient-specific approach, artificial kidney**

I. INTRODUCTION

INTRA-Dialysis Hypotension (IDH) is one of the main haemodialysis related complications, affecting approximately 20-30% of the sessions [1-5] and its aetiology is multifactorial [2, 6-7]. IDH episodes are often associated with nausea, cramps and vomit implying discomfort for the patient, extra work for the clinicians and consequentially higher costs for the management of the treatment. Thus, one of the main questions in clinical practice is how to avoid or prevent IDH [11]. Several studies have been performed to identify predictors of IDH during the treatment, with some good results [4-5, 8, 10, 13-15], but one of the open challenges is to quantify the risk of IDH onset already in the early stages of the HD session, accounting also for the patient's peculiar reaction to treatment. To the authors' knowledge, the literature reports only one patient-specific index, which allows quantifying the risk to develop IDH during the incoming session, at the beginning of the session itself. This index, developed in the frame of DialysIS Project Interregional cross border cooperation action, has been developed based on the data gathered from two different clinical centres and preliminarily evaluated in terms of prediction accuracy [6]. The availability of new data

(recorded according to the same protocol) from two further centres which were involved in the same project, allowed the validation of the index and also the evaluation of the reliability of the previously proposed threshold.

II. MATERIALS AND METHODS

The current study is the development of the previous work [6], aimed to identify an IDH predictor (J_i index), to be evaluated at the beginning of each treatment i.

The accuracy of the index was evaluated both on the first dataset, acquired at the Nephrology and Dialysis Unit, Regional Hospital of Lugano, Switzerland and at the Nephrology and Dialysis Unit, A. Manzoni Hospital, Lecco, Italy, as well on the second set of data, acquired at the Nephrology and Dialysis Unit of Sant'Anna Hospital, Como, and of Ospedale di Circolo e Fondazione Macchi, Varese, Italy.

The possibility to optimize the J_i index performances identifying a centre-dependent risk threshold has been also studied.

A. Patient selection

According to the DialysIS project protocol, the enrolled patients were adults undergoing standard or alternative HD therapies. Inclusion criteria were: dialysis vintage elder than three months, artero-venous fistula as vascular access.

B. Data acquisition

The first dataset referred to 450 HD acquired from 70 subjects, 20 of which enrolled in Lugano and the other 50 in Lecco; 6-8 HD sessions for each patient were monitored.

The second dataset includes 360 sessions (6 sessions/patient) of 60 patients, 30 of which treated in Como and 30 in Varese.

The data were collected either from monitor sensors (clinical prescription, machine sensors data, blood pressure measurements), haemo-gas-analyser, and nurse surveys. Clinical history and registry data were also recorded for each subject [17]. Blood pressure was measured during HD, approximately every 15min, using a pressure sleeve on the contralateral arm.

C. The IDH_D criterion

During the Dialysis Project, a new criterion for the IDH identification was proposed and called IDH-D. This criterion, that is an improvement of the Santoro and Mancini criteria, tries to identify all the possible risky situations corresponding to unacceptable variations of arterial pressure, potentially correlated with long-term symptoms [14, 18]. It is defined as IDH any fall in SAP > 25% of SAP_0 associated with any

symptom classically related to IDH. Besides, it is classified as IDH any SAP<90mmHg, even without symptoms, for patients starting with SAP0 ≥100 mmHg. For patients starting with $SAP_0 < 100mmHg$, any fall in SAP >10% of SAP_0 if associated with symptoms or any fall in SAP>20% of SAP_0 even without symptoms are classified as IDH [6]. SAP_t is the Systolic Arterial Pressure evaluated at the t time instant during HD [16].

D. Check of the invariance of the influent parameters, when using IDH-D criterion

The identification of IDH events has been repeated on the first set of data using the IDH-D criterion, and the patients have been classified as Hypotension Prone (HP) or Resistant (HR), according to Vito et al. [6]. F-test and t-test analyses (p <0.05) have been repeated, to verify which of the registered parameters significantly differ between HR and HP patients.

E. J_i index definition

As in the previous work, Ji is defined as the weighted sum of the statistically influent parameters.

$$J_i = \frac{\alpha}{\overline{K}} * K_i^+ + \frac{\beta}{\overline{\Delta W}} * \Delta W_i + \frac{\gamma * \overline{MAP}}{MAP_i} + hp_i$$

where $\overline{K}, \overline{\Delta W}, and \overline{MAP}$ are respectively the cumulative mean values for the potassium concentration, the weight gain and mean arterial pressure of the patient at the beginning of the previously monitored sessions. Ki, ΔWi, MAPi are the same parameters, all evaluated at the beginning of the current session $_i$. Hpi is the hypotension proneness of each patient.

More in detail α, β γ are the coefficients, determined according to Vito et al, allowing weighting the influence of each term on the IDH onset during the current session [6]. Their calibration has been performed taking into account the incidence of the influencing parameters on the total number of hypotensive events registered on the whole population. The variations of the influencing parameters have been studied to define Basic Pre-Dialysis Conditions (BPDC) that can be related to the variation from the reference value of one or more other influencing parameters. A finite set of possible IDH causes (C_{ijk} cases), has been identified. Values of the weight coefficients have been determined for each patient considering the finite set of C_{ijk}. In this way a specific weight was assigned to each BPDC, taking into account the deviation of each parameter from the average condition.

The hypotension proneness (Hp$_i$) is defined as the number of the previous sessions characterized by IDH, for a specific patient. This parameter wants to quantify the effect of the patient-specific clinical history on the potential risk of IDH onset [6].

The first 3 sessions, recorded for each patient, have been used for the patient-specific parameter's weight calculation [6], then Ji index has been calculated for each one of the remaining sessions both belonging to the first and the second datasets. J_i threshold (J_{th}) was set to 1; $J_i > 1$ point at a session characterized by the risk of IDH onset [6].

The J_i index outputs have been compared with the real occurrence of IDH events during sessions usually managed by the clinicians. The sensitivity and the specificity of the J_i index (and their confidence interval) in the prediction of real IDH events have been thus assessed for each centre. An analysis of the Ji ability in the prediction of IDH in terms of True Positives (TP), True Negatives (TN), False Positives (FP) and False Negatives (FN) has been performed. The Positive and Negative Predictive Values (PPV and NPV respectively) have been also calculated.

The prevalence of IDH on the available data has been also evaluated in each one of the involved centres.

F. Centre dependent risk threshold

The effects of the specific protocols adopted to manage hypotension in the different centres have been studied analysing the distribution of the J_i values.

The idea to use a threshold equal to the 75th percentile (J_{th}=q75)) of the J_i values distribution, in each one of the involved centres has been explored. A second attempt has been done considering the centre-specific IDH prevalence (%IDHc); the threshold has been then set to the 1-%IDHc percentile (J_{th}=q(1-%IDH$_c$)). The sensitivity, specificity, TP, FP, TN, FN, PPV, NPV of the J_i index have been assessed by using the new thresholds.

III. RESULTS

A. Patients characteristics

The age of the enrolled patients (60.8% males) was equal to 67.2±13.1 years with a dialysis vintage of 73.9±82.1 months.

B. Index evaluation

The prevalence of IDH results to be 37.3% for Lugano, 9.4% for Como and Varese and 8% for Lecco.

Table III, section a. shows the performances of J_i on each involved centre, when the threshold is set to 1. Sensitivity, specificity, true and false positives and negatives, PPV, NPV, and % of predicted IDH, were determined by comparing J_i outputs in terms of IDH risk and real IDH occurrence.

The data acquired at Lugano and Lecco Dialysis Units were the ones statistically analysed to identify the influent parameters (84 and 82% of the IDHs respectively predicted); the data acquired at Como and Varese Dialysis Units were instead used to verify the applicability of the index in different centres (63 and 68% of IDHs respectively predicted).

C. Center-dependent risk thresholds

The ability of J_i to highlight IDH risk, when the new thresholds were used, is summarized in Table III, section b. and c.

The use of J_{th}=I75 decreases the FPs in 3 centres out of 4 but does not improve either sensitivity or specificity. The TP and the sensitivity in the Lugano result even worsened.

The use of J_{th}=I(1-%IDHc) brings to improved or stable sensitivity and allows improving specificity in 3 out of the 4 centres, with stable values in the other one. Average PPV and NPV slightly increase with the new thresholds, with no statistically significant differences.

TABLE III
J_i INDEX PERFORMANCES.

	Sens.	Spec.	TP	TN	FP	FN	PPV	NPV	Predicted IDH
a. Jth = 1									
Lugano, CH	0.84	0.52	16	33	30	3	34.8	52.3	16/19 (84%)
Lecco, I	0.82	0.84	9	107	20	2	31.0	84.3	9/11 (82%)
Como, I	0.63	0.77	5	56	17	3	22.7	76.7	5/8 (63%)
Varese, I	0.78	0.78	7	56	16	2	30.4	77.7	7/9 (78%)
b. Jth =I75									
Lugano, CH	0.53	0.84	10	53	10	9	50.0	84.1	10/19 (53%)
Lecco, I	0.82	0.80	9	102	25	2	26.5	80.3	9/11 (82%)
Como, I	0.63	0.79	5	58	15	3	25.0	79.5	5/8 (63%)
Varese, I	0.78	0.82	7	59	13	2	35.0	81.9	7/9 (78%)
c. Jth =I1-%IDHc									
Lugano, CH	0.89	0.52	17	24	39	2	30.4	38.1	17/19 (89%)
Lecco, I	0.82	0.91	9	115	12	2	42.9	90.6	9/11 (82%)
Como, I	0.78	0.78	4	58	15	4	21.1	79.5	4/8 (50%)
Varese, I	0.78	0.88	7	63	9	2	43.8	87.5	7/9 (78%)

True Positives (TP), True Negatives (TN), False Positives (FP) and False Negatives (FN) have been evaluated. The Positive and Negative Predictive Values (PPV and NPV respectively) have been also calculated.
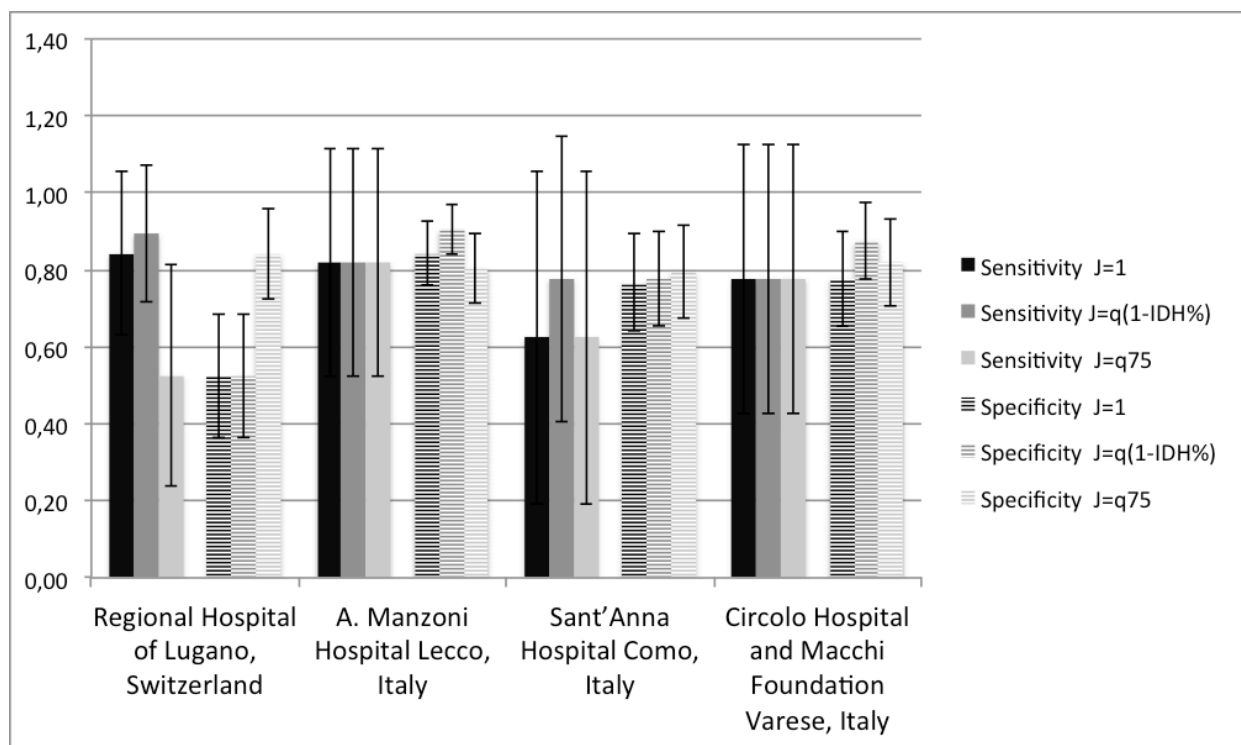
Fig. 1: Ji sensitivity and specificity for the different centres and thresholds. Error bars represent the Confidence Interval at 99%.

IV. DISCUSSION

J_i, when $Jt_h=1$, allows on average identifying the 77% of the hypotension's, since the early stage of each session. Figure 1 shows that J_i sensitivity and specificity result always around 70-80%, independently from the inter-centre variability. In the literature, screening tests characterized by similar performances were accepted for pathologies, whose prevalence is under 30%, like IDH [19-21].

The use of a unique threshold ($Jt_h=1$) does not lead to the same performances in different centres. This dependency can be statistically explained by the existence of a relationship among the prediction of a clinical test and the prevalence of the investigated pathology (here IDH) [19, 21-22]. The different prevalence can be on its turn explained either by the not homogeneous patient characteristics or by the different protocols used to manage IDH in the different centres.

Even if the visual analysis of Fig.1 suggests the use of centre dependent thresholds, the proposed algorithms to identify these thresholds did not lead to a significant improvement of the results.

The study of the SAP trends in those sessions, characterized by IDH onset in the presence of very low initial J_i has been thus performed. All of these sessions were characterized by $100 \leq SAP_0 \leq 120$ mmHg and pointed out IDHs correspond to

single measurements of $SAP_t<90mmHg$. Taking into account that automatic pressure sleeve measurements are characterized by not negligible errors, sometimes consistently higher than 5mmHg, more likely in elderly or diabetic patients [23] and that the error increases when $SAP<90mmHg$, in the considered range, where the maximum pathological SAP variation is 30mmHg, the measurements errors can be relevant. A more precise matching between J_i prediction and IDH identification during HD will, therefore, be obtained by using more precise pressure sensors.

Standing the absence of alternative reliable methods (gold standard) to evaluate the risk of IDH onset since the early stage of the HD treatment, the proposed index, based on easily measurable data, could be useful as a first screening for the clinician and the nurses that could benefit by the in-advance knowledge of the session-specific patient risk to develop IDH.

The only limit to the J_i use is that its calculation requires the preventive collection of data related to at least 3 sessions, to identify the patient-specific weights of the index, thus implying the availability of a relevant database in the centre. This limit could be overcome with the automation of the data recording process and the integration of data acquired from different devices, as the on-going healthcare digital transformation encourages [17].

V. CONCLUSION

The prediction of IDH events during HD is complex to be addressed, due to the multifactorial causes of the phenomenon. J_i index offers a patient-specific solution to this problem [6], allowing a feasible evaluation of the patient's pre-dialysis conditions.

This work also proposed an evaluation of the J_i index performances; average sensitivity and specificity of the prediction are respectively 77 % and 73% when $J_{th}=1$. These results can surely be improved but, from the clinical point of view, given the absence of other indexes, J_i provides a reliable prediction of IDH risk onset, for each specific patient, already at the early stage of the HD sessions. Based on it, clinicians and nurses could tailor HD prescription and improving treatment outcomes, mainly when, as the on-going healthcare digital transformation encourages, patient-specific longitudinal clinical data were available.

ACKNOWLEDGMENT

REFERENCES

[1] Palmer BF, Henrich WL. Recent advances in the Prevention and Management of Intradilaystic Hypotension. J Am Soc Nephrol. 2008; 19:8-11.

[2] Sands JJ, Usvyat LA, Sullivan T, et al. Intradialytic hypotension: Frequency, sources of variation and correlation with clinical outcome. Hemodialysis International. 2014; 18: 415–422.

[3] Morfin JA, Fluck RJ, Weinhandl ED, et al. Intensive Hemodialysis and Treatment Complications and Tolerability. Am J Kidney Dis. 2016; 68(5S1): S43-S50.

[4] Daugirdas JT. Pathophysiology of dialysis hypotension: an update. Am J Kidney Dis. 2001; 38(4S4): S11-17.

[5] Zhou YL, Liu HL, Duan XF, ET AL. Impact of sodium and ultrafiltration profiling on haemodialysis-related hypotension. Nephrol Dial Transplant. 2006; 21:3231–37.

[6] Vito D, Casagrande G, Cappoli G, et al. A predictive index of intra-dialysis IDH A statistical clinical data mining approach. IJSERM. 2015; 2(2):53-57.

[7] Santos SFF, Peixoto A, Perazella MA. How Should We Manage Adverse Intradialytic Blood Pressure Changes? Advances in Chronic Kidney Disease. 2012; 19(3): 158-165.

[8] Solem K, Olde B, Sörnmo L. Prediction of intradialytic hypotension using photoplethysmography. IEEE Trans Biomed Eng. 2010; 57(7): 1611–9.

[9] Casagrande G, Teatini U, Romei Longhena G, et al. A new method to evaluate patient characteristic response to ultrafiltration during hemodialysis. IJAO. 2007; 30(5): 377-384.

[10] Sörnmo L, Sandberg F, Gil E, et al. Noninvasive techniques for prevention of intradialytic hypotension. IEEE Rev Biomed Eng. 2012; 5:45–59.

[11] Schreiber MJ Jr. Clinical dilemmas in dialysis: managing the hypotensive patient. Setting the stage. Am J Kidney Dis. 2001; 38(4): S1-S10.

[12] Tislér A, Akócsi K, Borbás B, et al. The effect of frequent or occasional dialysis-associated hypotension on survival of patients on maintenance haemodialysis. NDT. 2003; 18: 2601–2605.

[13] Davenport A. Using dialysis machine technology to reduce intradialytic hypotension. Hemodial Int. 2011; 15(S1): S37–42.

[14] Mancini E, Mambelli E, Irpinia M, et al. Prevention of dialysis hypotension episodes using fuzzy logic control system. NDT. 2007; 22(5): 1420–7.

[15] Yamanaka N, Aoyama T, Ikeda N, et al. Characteristics of heart rate variability entropy and blood pressure during hemodialysis in patients with end-stage renal disease. Hemodial Int. 2005;9: 303–8.

[16] DialysIS Project (cross border cooperation program INTERREG IT-CH 2007-2013) Website. Hypotension working group final report. http://www.dialysis-project.eu/partnership/. Accessed the 2016-01-16.

[17] Vito D, Casagrande G, Bianchi C, Costantino ML. An interoperable common storage system for shared dialysis clinical data. IEEE Explore. 2016; https://doi.org/10.1109/EMBSISC.2016.7508626.

[18] Santoro A, Mancini E, Basile C. et al. Blood volume controlled hemodialysis in hypotension-prone patients: A randomized, multicenter controlled trial. Kidney Int, 2002; 62:1034–1045.

[19] Gatling W, Knight C, Hill RD. Screening for Early Diabetic Nephropathy: Which Sample to Detect Microalbuminuria? Diabetic Medicine. 1985; 2(6): 451-55.

[20] Sullivan L. The role of probability. Boston University School of Public Health. Online resources: http://sphweb.bumc.bu.edu/otlt/MPH-Modules/BS/BS704_Probability. Accessed November 12, 2016.

[21] Maxim LD, Niebo R, Utell MJ. Screening tests: a review with examples. Inhal Toxicol. 2014; 26(13): 811–828.

[22] Parikh R, Mathai A, Parikh S, ET AL. Understanding and using sensitivity, specificity and predictive values. Indian J Ophthalmol. 2008; 56(1): 45–50.

[23] Pickering TG, Hall JE, Appel LJ, et al. Recommendations for Blood Pressure Measurement in Humans and Experimental Animals Part 1. Circulation. 2005; 111: 697-716.

IoT ink pen for the ecological study of age-related changes in handwriting

D. Di Febbo[1], F. Lunardini[1], M. Malavolti[1], A. Pedrocchi[1], N. A. Borghese[2] and S. Ferrante[1]

[1] NEuroengineering And Medical Robotics Laboratory, Politecnico di Milano, Italy
[2] Applied Intelligent Systems Laboratory, Università degli Studi di Milano, Italy

Abstract—**Handwriting has been discovered to be subject to changes with age and pathologies and some quantitative indicators of the writing gesture have been studied as biomarkers for the diagnosis of age-related disorders. Their monitoring during daily-life could provide preventive alert of physical/cognitive degradation, but current technologies are not well-suited to this aim. In this study, we propose a novel technology for the ecological monitoring of handwriting, consisting in an instrumented traditional ink pen. As preliminary study, we acquired writing gesture data from healthy young and older adults, from which we extracted useful indicators. Our analysis showed statistical between-group differences in both handwriting and tremor indicators, such as for the in air-on sheet ratio, dimensionless jerk, modal frequency, approximate entropy and degree of determinism. Furthermore, the mean writing force and the approximate entropy were found to be correlated with the elders' age, confirming previous literature. These results successfully show the effectiveness of our novel device in detecting age-related changes in handwriting.**

Keywords—**Internet of Things, E-health, Handwriting analysis, Ageing.**

I. INTRODUCTION

Handwriting is a learned fine motor skill that involves both higher and lower cognitive functions, as well as feedback mechanisms [1]. Because of its complexity, some dynamic features of handwriting, such as the writing pressure [2], speed [3], jerk [2] and frequency components of the gestures (such as tremor [4]) undergo changes with the progress of age and/or with the presence of neurodegenerative pathologies (such as Parkinson's Disease (PD) and Essential Tremor (ET)) [5]. The possibility to use handwriting for detecting age-related pathologies and cognitive decline has been successfully investigated [3, 4 and 5]; in this framework, we can leverage the fact that handwriting is a common daily-life activity for the elder population, and thus its home-based monitoring may be well suited for the early detection of age-related physical and cognitive degeneration. However, transparency is a must-have feature for such ecologic monitoring system to be accepted, especially among the elder population which might be not tech-accustomed. Currently, the technologies employed to extract the informative features from the writing activity mainly consisted in electronic pens and tablets (e.g.: CTL460 Bamboo Pen® Tablet and the Wacom Tablet® UltraPAdA4), used to record the tip trajectory and the writing kinematics, and they rely on predefined writing protocols, such as sentences and fixed drawing patterns. In some studies, instead, ad-hoc devices have been proposed in the diagnosis of certain pathologies. For example, the *Manus platform* by Manus Neurodynamica (https://www.manusneuro.com/) is a tool for the support of the early diagnosis of Parkinson's Disease (PD) in clinical environments. The platform is composed by an electronic pen and a digital screen, and the clinical assessment requires the patient to perform standardized drawings and writing. However, such types of methods and technologies were designed for diagnostic purpose in research or clinical settings, therefore they are not well-suited for a daily-life use in unsupervised environments, since they lack of ecological validity.

Differently, in our study, we developed a novel technology more appropriate for a natural and uncontrolled scenario, where the subject can write on a common piece of paper. We designed an ink pen instrumented with an inertial measurement unit (IMU) and a pressure sensor to collect inertial information and the normal force applied to the tip during the writing activity. To respect the principle of transparent monitoring, we programmed the pen to autonomously record the signal when used; in addition, the backhand software automatically downloads the acquired data and then computes relevant handwriting and tremor indicators. Here, as a preliminary study, we computed the handwriting indicators from the pen data acquired from a population of young adults, and a population of elders. Results were then compared to characterize possible age-related variations of such measurements. The current work presents the technical features of the instrumented pen, the data acquisition protocol we used to collect data from young and older adults, the description of the handwriting indicators and the results of the comparison between the two groups of young adults and elders.

II. METHODS

A. The instrumented ink pen

The pen is shown in Figure 1. It includes an ultra-low power Cortex™ 32bit CPU (STM32L476), BlueNRG-MS single-mode network processor, an integrated flash to store 1MB of code and data and a Bluetooth Low Energy 4.0 (BLE) module.

Figure 1. A rendered image of the ink pen and its internal components.

The sensors are 3D linear accelerometers and gyroscopes (LSM6DSM iNEMO® 6DoF), and a miniaturized load cell (FC8E by Forsentek) with a diameter of 1.6 mm and a capacity of 50 N to measure the force exerted on the tip. All the electronics is included in the two PCB boards inserted in the top half of the pen. The battery is a special Li-Ion PIN-Type of Panasonic and it is recharged through an audio jack that can be connected to the cap. A LED is placed in the terminal part of the pen to indicate the device operating status. Ad-hoc designed plastic parts were 3D-printed to fix the electronic components inside the device. As for the firmware, it is programmed with the aim of autonomously acquiring and storing sensor data, without requiring particular actions from the user. It includes four states: *stand-by*; *active*; *recording*; *charging*. In the *stand-by* state, the pen is in battery saving mode and requires a slight touch to be awakened. In the *active* state, the pen is ready to record data if continuously moved for 15 additional seconds, otherwise it goes back to the stand-by state. In the *recording*, signals are stored onboard while the pen is moved or used to write. When the pen is left stationary for 15 seconds, the state turns into *stand-by* mode. Whenever the pen is connected to the charger, the status turns into *charging*. Every recoding is stored in a separate file and a third-party software is programmed to daily access the pen via BLE, download the files in csv format, erase the memory, compute relevant handwriting and tremor indicators, and load them into an indexed database (mongoDB®).

B. Acquisition protocol of the handwriting data

Handwriting data were acquired by emulating a daily life writing activity. Participants were asked to execute a simple protocol using the instrumented pen consisting in two tasks:

1. Writing a 5-item grocery list, in block letters (*List*).
2. Writing 7 lines of text using the italic font (*Text*).

No specifications on the size, speed and content of writing were imposed. A total number of 10 young (7 males and 3 females, age 27 ± 1.9 years) and 10 older (6 males and 7 females, age 70.6 ± 3 years) adults were recruited. The Ethical Committee of the Politecnico di Milano approved the study protocol n. 10/2018.

C. Definition and calculation of the handwriting indicators

We computed a set of handwriting indicators for each task performed by each subject. The handwriting indicators included time features, pressure features, acceleration features and tremor features. They were extracted from the following signals saved onboard, sampled at 50Hz: the 3-axis accelerometer time series [m/s^2] a_x, a_y and a_z, the 3-axis gyroscopes time series [rad/sec] ω_x, ω_y and ω_z, and the writing force signal (with non-scaled units), F_w. In the pre-processing stage, we unbiased the force signal (through off-set removal), de-trended and low pass filtered using a 4th order Butterworth with cut-off at 4Hz. The acceleration signals were high pass filtered with a 4th order Butterworth with cut-off at 0.75 Hz, to remove the DC component. Then, we segmented the time series into *strokes*, the writing segments, which were computed as the intervals in which the writing force signal was non-zero (*on-sheet* time). We defined the complementary non-writing segments as *in-air* time. The following indicators were calculated, for both writing tasks, using Matlab® R2017b.

In-air/on-sheet ratio, R_{io}. Computed as the ratio between the mean in-air time and the mean on-sheet time over the entire writing task. It is expected to increase with age and in presence of age-related pathologies [7].

Mean writing force, $\bar{F}$. Mean normal force applied to the pen tip within each single stroke, averaged over all strokes. Elders tend to have a weaker $\bar{F}$ than young adults and differences are even increased with pathologies [8].

Number of changes in acceleration, NCA. Computed as the number of local minima and maxima in the 3D acceleration within each single stroke, averaged over all strokes. *NCA* is related to the handwriting smoothness, which usually decreases with age [9].

Dimensionless jerk, J_d. Jerk is the time-derivative of acceleration and, when high, it indicates the occurrence of tremulous motor segments driven by rapid acceleration/deceleration [9]. Dimensionless jerk was obtained as in Eq. 1,

$$J_d = \frac{t_2-t_1}{v_{peak}^2} \int_{t_1}^{t_2} \dot{a}_x(t)^2 + \dot{a}_y(t)^2 + \dot{a}_z(t)^2 \, dt, \qquad (1)$$

where t_1 and t_2 were the initial and final stroke time instants respectively, and v_{peak} was the stroke peak velocity. It is computed for each single stroke and averaged over all strokes.

Modal frequency, f_{modal}. Derived from the frequency analysis of the acceleration signals below 15Hz. It measures the central tendency as the median frequency in a subject's handwriting and it has been observed to decrease with age [4]. Generally, it is possible to locate tremor components generated by particular dynamic conditions of the gesture in specific frequency bands. In particular, 7.5-12.5Hz components are usually found in pathological tremor [4].

Approximate entropy, ApEn. It measures the presence of repetitive patterns in the accelerometers data acquired during writing. Handwriting tremor time series show a chaotic behavior, but additive oscillation components, usually found in older and pathologic individuals (e.g. PD patients), increase the predictability, resulting in smaller values of *ApEn* [10].

Recurrent ratio, RR. Percentage quantity related to the self-similarity of a time series; it grows with the increase of predictability. Aging and pathological handwriting signals are expected to have larger values of *RR* [11].

Degree of determinism, DET. Percentage used to quantify the presence of deterministic fluctuations in the signal. As *RR*, the calculation is based on the Recurrence Quantification Analysis of a time series and it is expected to increase in presence of tremor [11].

D. Statistical analysis

We first assessed the homoscedastic properties of the indicators by applying a Lilliefors test of normality on each single indicator, inclusive of all the subjects. Since not all indicators resulted normally distributed, we adopted a nonparametric statistics. Thus, between-group (young vs elders) comparisons were carried out for each task separately, using the Mann-Whitney Test for unpaired samples.

In addition, for the elder group, we evaluated the statistical dependence between the rankings of the indicators and the subjects' age by computing the Spearman's rank correlation coefficient.

TABLE I
MANN-WHITNEY (YOUNG VS ELDERS)

Handwriting indicator	List				Text			
	Young (median IQR)		Elders (median IQR)	p-value	Young (median IQR)		Elders (median IQR)	p-value
R_{io}	0.54 0.24		0.51 0.11	0.48	**0.47 0.18**		**0.62 0.19**	**0.035**
$\bar{F}$	95.7 71.4		74.9 48.37	0.43	85.2 70.97		66.07 33.25	0.39
NCA	3 1		4 3	0.16	4 3		4 3	0.64
J_d	**8.41 6.06**		**48.81 78.54**	**0.006**	19.51 79.47		30.88 47.28	0.63
f_{modal} [Hz]	5.11 1.47		4.62 1.08	0.35	**5.12 0.66**		**4.69 0.79**	**0.028**
$ApEn$ [0-2]	0.98 0.18		0.96 0.12	0.52	**1.14 0.07**		**1.01 0.13**	**0.003**
RR [0-1]	0.46 0.21		0.43 0.19	1	0.34 0.12		0.44 0.20	0.16
DET [0-1]	0.77 0.21		0.84 0.10	0.63	**0.70 0.16**		**0.84 0.15**	**0.043**

Table I. Results of the Mann-Whitney test for the handwriting and tremor indicators between the young and elder groups.

Statistics was run using RStudio version 1.2.5033 (RStudio Inc., Boston, MA). Significance level was set at 5% for all tests.

III. RESULTS

Table I shows the median, inter-quartile-range (IQR) and the p-values of the Mann-Whitney test calculated for the comparison of the indicators between the young and the elder groups, in the two writing tests *List* and *Text*. The outcomes revealed that significant between-group differences emerged for dimensionless jerk (J_d) in the *List* task, and for in air-on sheet ratio (R_{io}), modal frequency (f_{modal}), approximate entropy ($ApEn$) and degree of determinism (DET) in the *Text*.

As for the correlation between indicators and age in the elder's group, Table II reports the Spearman's correlation coefficients (ρ). We observed a consistent positive statistical dependence (ρ=0.80) for mean writing force ($\bar{F}$), in the *Text* task, and a smaller but significant negative correlation ρ=-0.66) in the approximate entropy ($ApEn$), in the *List* task.

TABLE II
CORRELATIONS BETWEEN INDICATORS AND AGE IN ELDERS

Handwriting indicator	Task List ρ (p-value)	Task Text ρ (p-value)
R_{io}	0.22 (0.54)	0.20 (0.57)
$\bar{F}$	0.51 (0.12)	**0.80 (0.04)**
NCA	-0.05 (0.88)	0.23 (0.51)
J_d	-0.09 (0.79)	0.22 (0.53)
f_{modal} [Hz]	0.07 (0.83)	-0.46 (0.18)
$ApEn$ [0-2]	**-0.66 (0.03)**	-0.32 (0.35)
RR [0-1]	0.22 (0.51)	0.25 (0.48)
DET [0-1]	0.23 (0.54)	0.20 (0.57)

Table II. Spearman's correlation coefficients (ρ) between handwriting indicators and age in the elder group.

IV. DISCUSSION

In this study, we designed an instrumented ink pen for the ecological monitoring of handwriting. The pen was designed to extract useful monitoring information from the subject's daily-life writing activity in unsupervised environments (e.g.: home). Therefore, data acquisition and indicator extraction is completely autonomous. The pen integrated IMU and normal force on tip sensors, internal memory for saving data onboard and BLE connectivity to access the stored files and other functions. We embedded the pen in an Internet of Things (IoT) framework including a backhand software for the autonomous computation of the aging/pathology-related handwriting indicators and a cloud-based database to store them.

Two populations of healthy subjects, 10 young adults and 10 elders, were involved to acquire handwriting data and compute the indicators which has been previously studied in literature as biomarkers of age-related and pathological degradation. We avoided to impose the subjects to write predefined sentences or to draw fixed pattern, as we aimed at resembling a more natural condition as possible for the data acquisition. However, the proposed writing tasks differed in the font.

The statistical analysis confirmed that the value of some indicators actually changed with age, but results were task-dependent, since our outcomes showed that differences in handwriting were more significant in the *Text* task, where italic font was used. Such result may have been partly determined by the higher number of writing observations (strokes) available for the *Text* task, with respect to the *List* task. In particular, R_{io} appeared to increase in the elder group during *Text* writing. In accordance to previous studies [7], the percentage of in-air time during handwriting is increased with age since longer pause are waited in thinking instead of writing. Rosenblum et Al. [7] found the same trend, but different mean values for the R_{io} in young (31-45 years) and elder (61-75 years) subjects (1.41±0.55 and 1.71±0.52, respectively); the different mean value can be ascribed to the different alphabet, since the current work recruited Italian subjects, while in [7] the text was written in Hebrew. As for the *List*, R_{io} appeared not to substantially change between the two groups. According to literature, also the smoothness of the writing gesture decreases with age [9], as our result confirmed with a dimensionless jerk, J_d augmented for the elder group (8.41 young, 48.81 elders) while writing the *List*. The same trend of J_d emerged for the *Text*, although not significant. As for the tremor parameters during *Text* writing, f_{modal} and $ApEn$ were higher in the young group (5.12 young, 4.69 elders and 1.14 young, 1.01 elders, respectively), while DET was increased in the elder group (0.70 young, 0.84 elders). In agreement with previous researches, the time series related

to the handwriting in older subjects show a higher predictability, as the tremors components become stronger. Therefore, a higher entropy is found in the younger subjects handwriting [12], while a bigger degree of determinism is more likely to emerge in the elders' writing gesture [11]. Also f_{modal} has been previously shown to decrease with age [13]. Furthermore, the modal frequency was distant from the pathological-related range 7.5-12.5Hz in the healthy subjects involved in our study.

For what concerns the mean writing force ($\bar{F}$), the number of changes in acceleration (NCA) and the recurrence ratio (RR), they did not significantly differ between the two groups. However, they showed a trend in accordance with previous literature studies. For the elders, the writing force reached lower values, while the number of changes in acceleration and the recurrence ratio increased. That confirmed the loss of smoothness and the presence of more predictable patterns in the handwriting gesture with age.

Finally, we computed the correlation between the values of the handwriting indicators and the age of the 10 subject belonging to the elder group. The approximate entropy showed a negative correlation of ρ=-0.66, in *List*. That was an expected result since $ApEn$ tends to decrease with age. Also the mean writing force revealed a positive correlation of ρ=0.80 with age, in *Text*. Therefore, an opposite trend, with respect to the expected one, was found within the group of elder subjects. However, we used a limited number of samples (10) when computing the correlation.

V. CONCLUSION

To conclude, the present work shows the ability of this novel IoT technology to detect writing differences between population of healthy subjects of different age (young and older adults). Future work should increase the sample size to deepen the current findings. Further tests on healthy and non-healthy elder populations are the next steps toward the exploitation of such instrument in the ecological monitoring of age-related physical and cognitive decline. Indeed, we developed the IoT ink pen within the European MoveCare Project [14], which leverages home-based ICT with the aim of achieving ecological monitoring of age-related decline through quantitative measurements transparently recorded during common daily-life activities, to keep track of the user's frail status over time.

REFERENCES

[1] S. Planton, M. Jucla, F. E. Roux, J. F. Démonet. "The handwriting brain"; A meta-analysis of neuroimaging studies of motor versus orthographic processes", *Cortex*, vol. 49, pp. 2772–2787, 2013. doi: 10.1016/j.cortex.2013.05.011.

[2] Engel-Yeger, B., Hus, S. and Rosenblum, S., "Age effects on sensory-processing abilities and their impact on handwriting", *Canadian Journal of Occupational Therapy*, 79(5), pp. 264–274, 2012. doi: 10.2182/cjot.2012.79.5.2.

[3] Plamondon, R. et al. "The lognormal handwriter: Learning, performing, and declining", *Frontiers in Psychology*, vol. 4(DEC), pp. 1–14, 2013. doi: 10.3389/fpsyg.2013.00945

[4] Edwards, R. and Beuter, A. (1999) 'Indexes for identification of abnormal tremor using computer tremor evaluation systems', IEEE Transactions on Biomedical Engineering, 46(7), pp. 895–898. doi: 10.1109/10.771207.

[5] J. Walton, "Handwriting changes due to aging and Parkinson's syndrome", *Forensic Science International*, vol. 88, pp. 197–214, 1997.

[6] T.J. Heeren, A.M. Lagaay, W.C.A.V Beek, H.G.M. Rooymans, W. Hijmans. "Reference values for the Mini-Mental State Examination (MMSE) in Octo- and Nonagenarians" Journal of the American Geriatric Society. 30-10 pp. 1093-1096. 1990.

[7] Engel-Yeger, B., Hus, S. and Rosenblum, S., "Age effects on sensory-processing abilities and their impact on handwriting", *Canadian Journal of Occupational Therapy*, 79(5), pp. 264–274, 2012.

[8] Walton, J. "Handwriting changes due to aging and Parkinson's syndrome. Forensic Science International", 88(3), 197-214. 1997.

[9] Kholinne et Al. (2018). "The Dimensionless Squared Jerk: An Objective Parameter That Improves Assessment of Hand Motion Analysis during Simulated Shoulder Arthroscopy". BioMed Research International. 2018.

[10] Meigal, A. Y. et al. "Linear and nonlinear tremor acceleration characteristics in patients with Parkinson's disease". Physiological Measurement, 33(3), pp. 395–412. 2012.

[11] Hong, S. L., James, E. G. and Newell, K. M. "Coupling and Irregularity in the aging motor system: Tremor and movement", Neuroscience Letters, 433(2), pp. 119–124. 2007.

[12] Vaillancourt, et Al. "Regularity of Force Tremor in Parkinson's Disease". Official journal of the International Federation of Clinical Neurophysiology. 112. 1594-603. 2001.

[13] J. M. Hollerbach, "An Oscillation Theory of Handwriting". Biol. Cybern. 39, 139-156. 1981.

[14] Lunardini F, Luperto M, Romeo M, et al. "The MOVECARE Project: Home-based Monitoring of Frailty". Proceedings of the IEEE EMBS International Conference on Biomedical & Health Informatics (BHI); 2019 May; Chicago, USA; 2019

A simulation study on safety and efficacy of tFUS

M. Stefano[1], A. Scarpelli[1], F. Cordella[1] and L. Zollo[1]

[1] *Research Unit of Advanced Robotics and Human-Centred Technologies, Campus Bio-Medico University of Rome, Italy.*

Abstract—Transcranial Focused Ultrasound Stimulation (tFUS) is a non-invasive technique for brain stimulation, which has a better spatial resolution and depth penetration with respect to other non-invasive techniques. Computational analysis could be a useful tool to predict tFUS propagation in biological tissue in order to guarantee safety and efficacy of the stimulation.

This work aims at evaluating, by the means of a computational model, the maximum pressure and the average acoustic intensity generated by a pulsed tFUS stimulation waveform, whose duty cycle (DC) was modulated in the range from 100% to 40%. The main goal was to investigate the efficacy and the safety, respectively in terms of pressure and intensity, of the stimulus waveform when the DC is decreased. Moreover, the Full Width at Half Maximum (FWHM) intensity at the focus was observed.

The obtained results showed that the amount of average acoustic intensity decreased with the DC and the maximum pressure remains constant. Therefore, low value of DC permits to effectively and safely extend the stimulation duration. Moreover, the FWHM did not vary during DC modulation; hence, the spatial resolution of the focus remained unchanged. These results suggest that tFUS can be adopted to safely stimulate the somatosensory cortex, properly modulating the stimulus duration, in order to elicit different sensations in the human hand.

Keywords—transcranial focused ultrasound stimulation, computational model, sensory feedback, stimulation safety and efficacy

I. INTRODUCTION

Brain stimulation methods can be used to modulate cortical areas, for functional investigation of the brain and neurotherapeutics. The most used non-invasive techniques, such as Transcranial Magnetic Stimulation (TMS) and Transcranial Direct Current Stimulation (TDCS), can modulate the function of cortical areas without the need of a surgical intervention [1], [2], [3]. These techniques permit the stimulation of large cortical areas, on the order of centimeters, whereas the possibility of reaching deep cortical regions is very limited [4]. Therefore, as an alternative, other non-invasive techniques are being investigated to overcome this shortcoming.

Transcranial Focused Ultrasound Stimulation (tFUS) is a non-invasive method, for the stimulation of both the Central and the Peripheral Nervous System, that has a better spatial resolution and in-depth penetration with respect to other transcranial stimulation techniques, such as TDCS and TMS.

In fact, tFUS is a low energy technique delivering mechanical energy at high spatial resolution [5] that has been shown to be capable of modulating neural activity in mice [6], [7], rabbits [8] and monkeys [9]. Recent studies demonstrate that tFUS is also a safe and effective technique able to modulate human cortical activity [10], [11]. Ultrasonic neuromodulation on Central Nervous System can be applied on M1 cortex, Thalamus, V1 cortex, caudate region and posterior frontal cortex in humans [10], [11], [12], [13], [14]. More recently, the use of tFUS as non-invasive brain stimulation technique was proven to be able to elicit tactile sensations when applied on S1 and S2 cortex [5], [15], [16], [13], [17], [18]. It paves the way to its application in neuroprosthetics for restoring sensory feedback in amputee subjects.

Nevertheless, even if tFUS is a non-invasive method, attention needs to be paid to the power intensity applied on the target area. For instance, the temperature increases due to the acoustic intensity conveyed to the scalp could damage tissues if not kept below a safety threshold. Therefore, the signal intensity and the stimulation duration cannot overcome safety limits. It is evident that a preliminary study of tFUS outcome in simulation environment is extremely important. Computational models have been used to estimate power intensity and pressure profiles in biological tissues, considering anatomical variations between individuals [19], [20]. No studies have been performed to understand if the waveform modulation allows keeping the safety limits and the stimulation efficacy by reducing the stimulation intensity. Studies performed on other non-invasive stimulation techniques (such as transcutaneous electrical nerve stimulation, TENS), where the variation of the stimulation intensity (in terms of duration of the stimulation) can elicit different sensations in different hand areas [21], suggest that also with tFUS it is possible to vary the stimulation duration for eliciting different sensations. The main advantage of using tFUS with respect to other non-invasive stimulation approaches [22] relies in the possibility of achieving high selectivity stimulation and discrimination capabilities similar to invasive interfaces.

This work aims at investigating, by means of a computational model, if pulsed stimulation with a modulated waveform may be effective in terms of provided pressure and safe in terms of intensity. In other words, the scope is to ascertain whether it is possible to modulate the stimulation wave so that it has the same effectiveness, without affecting pressure, but with lower intensity and increased duration, with respect to stimulation waves typically adopted in literature.

II. METHODS

In this work, a 2D simplified human head model composed of a skull layer and brain tissue was considered. The ultra-

sound coupling medium was also modelled and the physical properties of each media were summarized in Table 1.

The propagation of the focused ultrasound was simulated in the 2D simplified human head model in order to investigate the maximum pressure amplitude, the mean intensity and the focus profile for different Duty Cycle (DC). The simulations were performed using a k-space pseudospectral method-based solver, i.e. k-Wave [23].

Simulations were performed on a computer with an Intel Core i7-8750H CPU at 2.20 GHz, 16GB RAM.

In Fig.1 the model is described. The transducer was modeled as an arc circle, 63.2 cm radius of curvature, based on a commercial ultrasound transducer, i.e. Sonic Concepts H-115 model. Two concentric circles modeled the brain and skull regions. Properties of the brain were assigned to the most inner region; whereas properties of skull were assigned to the ring area obtained from the outer circle (diameter of 77.5 mm) and the inner one (diameter of 72 mm). A 4 cm distance was considered between the arc circle and the outer circle of the skull layer. The properties of water were given to this domain. These properties are taken from [24].

Water, skull and brain were assumed to have different sound speed, density and attenuation coefficient.

A 20 cm × 20 cm simulation grid was considered to observe the focus profile in terms of maximum pressure amplitude (Pa) and average acoustic intensity (W/m²).
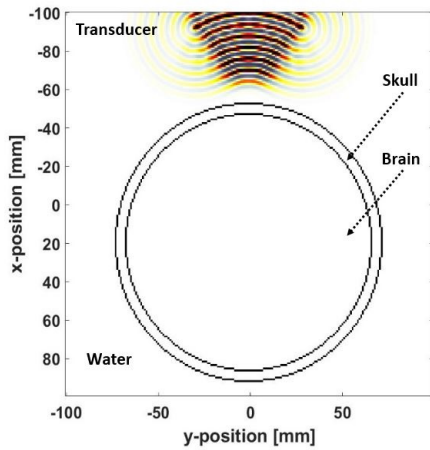
Fig. 1: The domain is composed of the transducer surface, the skull layer, the brain region and the water, which is the surrounding medium.

2D maps of coupling water, skull layer and brain were extracted for different values of the pulse duty cycle. Several simulations were performed varying the DC of the stimulus: it

	$c_s[m/s^2]$	ρ [kg/m³]	$\alpha_0[dB/MHz \cdot cm]$
Water [26]	1481	998	0.002
Skull [26]	2820	1732	7.75
Brain [27]	1500	1000	0.8

TABLE I: Media properties. c_s: sound velocity in medium; ρ: density of the medium; α_0: medium constant to evaluate the absorption coefficient

was varied from 100% to 40% with a step of 10%, tightening the step in the range from 50% to 40%.

To restrict the computation time, the total duration of the simulation was limited to 500 μs (DC of 100%) and the minimum duration of the pulse stimulus was fixed at 200 μs (DC of 40%), which was above the necessary duration t_{ss} (190 μs) to reach a steady-state. This value was obtained as follows

$$t_{ss} = \frac{\sqrt{s_x{}^2 + s_y{}^2}}{v_s} \qquad (1)$$

where s_x and s_y are the grid lengths in the x and y direction, respectively, and v_s is the minimum sound velocity in the medium evaluated between the considered media. The pulse stimulus was a sinusoidal waveform settled at a frequency of 250 kHz, which was the value used in tFUS experiments to somatosensory cortex stimulation on humans.

The amplitude of the sinusoidal waveform was fixed for all the simulations at 100 kPa. This value was determined during the free water simulation lasting 500 μs, in order to obtain a maximum average intensity under the safety threshold (3 W/cm² according to the IEC standard 60601-2-5 for physiotherapy US equipment).

For each DC value, two simulations were performed: one in free water and one with the coupling medium (water), skull and brain layers. Hence, it was possible to compare the behaviour of the beams in the two different domains in terms of maximum pressure and average acoustic intensity. The data extracted from the simulation were used to analyse the evolution of the maximum pressure and the average intensity in the focus modulating the DC of the pulse stimulus. Moreover, Full Width at Half Maximum (FWHM) of the average intensity profile on the focal plane was evaluated in order to observe the focal width, when DC was varied.

III. RESULTS

In the following section the behaviour of the maximum pressure and average intensity in water and in layered media obtained in simulation are described. Simulations were performed at eight different values of DC signal: 100%, 90%, 80%, 70%, 60%, 50%, 45% and 40%. A 100% DC and a 40% DC correspond to a stimulus duration of 500 μs and 200 μs, respectively.

The maximum pressure and the average acoustic intensity profile for a 100% DC in free water simulation are shown in Fig.2 (**a**) and Fig.3 (**b**) respectively. This simulation was performed varying the amplitude of the stimulus until the average acoustic intensity in the focus was about 3 W/cm². The obtained stimulus amplitude value was adopted for the remaining simulations.

In Fig.3 the maximum values of pressure and average intensity are reported for each stimulus DC for the free water and layered medium simulations.

FWHM of average intensity profile along y-axis was studied for the different simulations to observe the focal width at different value of the signal DC. The data extracted for each DC during the simulation in water and with the layered
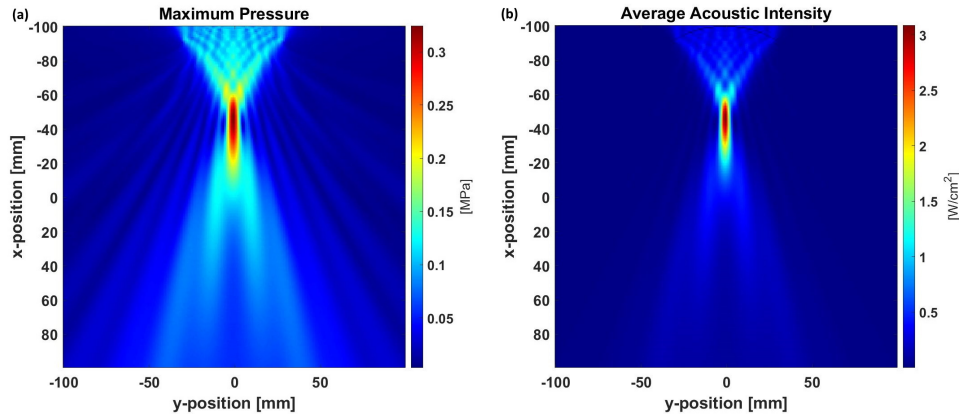
Fig. 2: 2D grid color map of maximum pressure (**a**) and average acoustic intensity (**b**) for a 100% DC stimulus obtained from the simulation in free water.
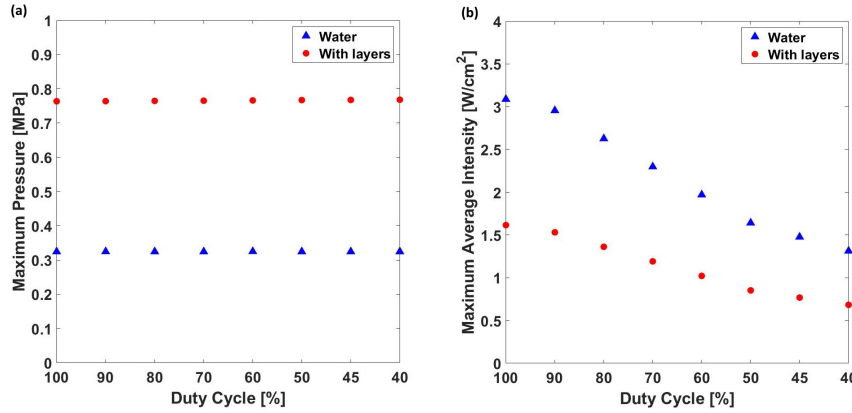

Fig. 3: Pressure and Maximum Average Intensity variation at different DC. (**a**) Maximum Pressure *vs* Duty Cycle in water and layered media; (**b**) Maximum Average Intensity *vs* Duty Cycle in water and layered media

medium, were fitted and shown in Fig.4, where the fitting using a Gaussian function of the average intensities can be observed.

IV. DISCUSSION

Maximum pressure amplitude and average intensity (Fig.2) were studied in free water at a 100% DC signal, to evaluate the maximum of average intensity in the focus according to the safety threshold. The corresponding stimulus amplitude was adopted in all the subsequent simulations. Comparing the maximum pressure amplitude color plot related to each stimulus DC for water and layered medium, it is possible to observe that the stimulation was effective since the value of maximum pressure was comparable with that of the steady-state.

Literature studies on the effects of the tFUS stimulus on the generation of action potentials in neuronal cells, hypothesized that the amplitude of an external pressure, i.e. the pressure stimulus coming from the transducer, and the stimulus duration can affect the generation of the action potentials [25]. This suggests that the pressure term can be seen as an index of stimulation efficacy.

Looking at the results shown in Fig.3 (**a**), it was evident that a decrease of the pulse stimulus DC did not affect the values of

the maximum pressure, meaning that the stimulation efficacy remained unchanged. Therefore, to deliver a signal that has a low value of DC, can be more safe and equally effective compared to stimulus signals that have higher DC values, Fig.3 (**b**). These results would lead to the possibility of increasing the stimulus duration, maintaining the safety and the efficacy of the stimulations.

The evaluation of the focal width could have been useful to verify that the stimulation occurred in a specific region of the considered tissue. From Fig.4, it is evident that the FWHM was almost the same for different values of signal DC. Therefore, to deliver a signal at low DC values do not affect the spatial resolution or selectivity of the stimulation.

V. CONCLUSION

In this work, a computational model was used to study the maximum pressure and average acoustic intensity occurring during tFUS stimulation. Two simulations on focused ultrasound in water and through a skull layer were performed to investigate the effect of focused ultrasound stimulation on biological tissues. In the free water simulation the entire domain was homogeneously modeled as water. For the layered simulation the medium was a simplified head model. They were developed to compare pressure and intensity at the focus
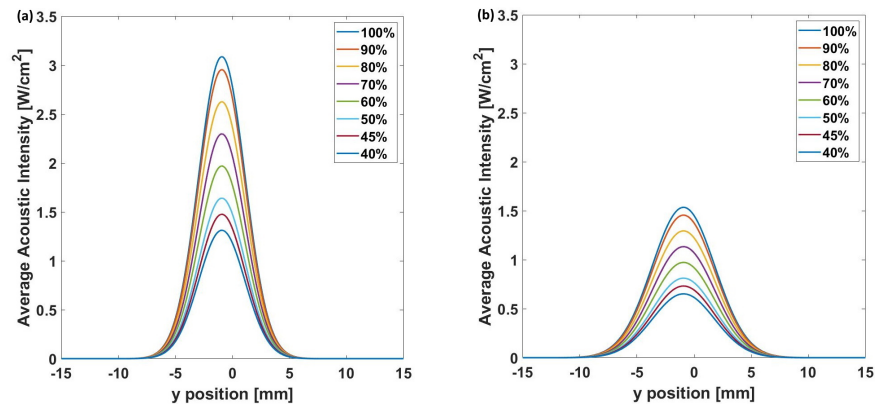
Fig. 4: Average Intensity profile on the focal plane *vs* y position in water and layered media for different values of DC. (**a**) Average Intensity *vs* y position in free water; (**b**) Average Intensity *vs* y position in layered medium

from both the simulations. A 2D simplified human head model was considered to guarantee low computational complexity and estimated simulation time.

Although in a preliminary computational framework, the obtained results demonstrated i) that a geometrical simplified human head model could be a useful tool for estimating the main values related to efficacy and safety of tFUS; ii) the possibility to investigate, from a theoretical point of view, how to modulate the stimulation waveform, with the aim to keep constant the efficacy and the safety of tFUS.

Future work will be devoted to improve the analysis of the effects of tFUS on the human head by increasing the model complexity and accounting more realistically for all the tissues of the human head. The obtained results could be confirmed by experimental validation starting from tissue-mimicking phantom materials before the tests on human subjects.

ACKNOWLEDGEMENT

REFERENCES

[1] F. Fregni et al. "Technonolgy insight: noninvasive brain stimulation in neurology-perspectives on the therapeutic potential of rTMS and tDCS", Nat. Clin. Pract. Neurol. 3, 383-393, 2007.

[2] M.S. George et al. "Noninvasive techniques for probing neurocircuitry and treating illness: vagus nerve stimulation (VNS), transcranial magnetic stimulation (TMS) and transcranial direct current stimulation (tDCS)", Neuropsychopharmacology 35, 301-316, 2010.

[3] K.E. Hoy et al. "Brain stimulation in psychiatry and its effects on cognition", Nat. Rev. Neurol. 6, 5, 267-275, 2010.

[4] C.K. Loo et al. "A review of the efficacy of transcranial magnetic stimulation (TMS) treatment for depression, and current and future strategies to optimize efficacy" J. Affect. Disord. 88, 255-267, 2005.

[5] W. Lee et al. "Simultaneous acoustic simulation of human primary and secondary somatosensory cortices using transcranial focused ultrasound", BMC Neurosci. 17-68, 2016.

[6] Y. Tufail et al. "Transcranial pulsed ultrasound stimulates intact brain circuits" Neuron, 66, 5, 681-694, 2010.

[7] R.L. King et al. "Effective parameters for ultrasound-induced in vivo neurostimulation" Ultrasound Med. Biol. 39, 2, 312-331, 2013.

[8] S.S. Yoo et al. "Focused ultrasound modulates region specific brain activity" Neuroimage 56, 3, 1267-1275, 2011.

[9] T. Deffieux et al. "Low intensity focused ultrasound modulates monkey visuomotor behavior", Curr. Biol. 23, 23, 2430-2433, 2013.

[10] W. Legon et al. "Neuromodulation with single-element transcranial focused ultrasound in human thalamus", Hum. Brain Mapp. 39, 1995–2006, 2018.

[11] W. Legon et al. "Transcranial focused ultrasound neuromodulation of the human primary motor cortex" Sci Rep 8, 10007, 2018.

[12] W. Lee et al. "Transcranial focused ultrasound stimulation of human primary visual cortex" Sci Rep 6, 34026, 2016.

[13] L. Ai et al. "Transcranial focused ultrasound for BOLD fMRI signal modulation in humans" Conf. Proc. IEEE Eng Med Biol Soc., 1758–1761, 2016.

[14] S. Hameroff et al. "Transcranial ultrasound (TUS) effects on mental states: A pilot study", Brain Stim.,6:409–415, 2013.

[15] W. Lee er al. "Image-guided transcranial focused ultrasound stimulates human primary somatosensory cortex", Sci Rep, 5, 88743, 2015.

[16] J. Mueller et al. "Transcranial focused ultrasound modulates intrinsic and evoked EEG dynamics", Brain Stim, 7:900–908, 2014.

[17] W. Legon et al. "Transcranial focused ultrasound modulates the activity of primary somatosensory cortex in humans", Nat. Neurosci., 17, 322–329, 2014.

[18] B. C. Gibson, et al. "Increased Excitability Induced in the Primary Motor Cortex by Transcranial Ultrasound Stimulation", Front Neurol., 9:1007, 2018.

[19] J. K. Mueller et al. "Computational exploration of wave propagation and heating from transcranial focused ultrasound for neuromodulation." J. of Neur. Eng. 13, 2016.

[20] J. K. Mueller, et al. "Numerical evaluation of the skull for human neuromodulation with transcranial focused ultrasound." J. of Neur. Eng. 14, 2017.

[21] Vargas, Luis, et al. "Merged Haptic Sensation in the Hand during Concurrent Non-Invasive Proximal Nerve Stimulation." 40th Annual Int. Conf. IEEE Eng. in Med. and Biol. Soc. 2018.

[22] C. Antfolk et al. "Sensory feedback in upper limb prosthetics" Expert Rev. of Med. Dev. 10, 1, 2013.

[23] B.E. Treeby et al. "Modeling nonlinear ultrasound propagation in heterogeneous media with power law absorption using a k-space pseudospectral method", J. Ac. Soc. Am., 131, 6, 4324-4336, 2012.

[24] E. Salkim et al. "Impact of neuroanatomical variations and electrode orientation on stimulus current in a deice for migraine: a computational study", J. Neur. Eng. 17, 2020.

[25] M. Plaksin et al. "Intramembrane cavitation as a predictive bio-piezoelectric mechanism for ultrasonic brain stimulation", Phys. Rev. X, 4, 1, 2014.

[26] B.E. Treeby, B.T Cox "Modeling power law absorption and dispersion in viscoelastic solids using a split-field and the fractional Laplacian", J. Acoust. Soc. Am. 136, 4, 2014.

[27] C. Baron et al. "Simulation of intracranial acoustic stimulation of intracranial acoustic fields in clinical trials of sonothrombolysis", Ultrasound in Med. Biol., 35, 7, 1148–1158, 2009.

Comparison of Parametric Linear Techniques for Glucose Prediction in Type-1 Diabetes

S. Faccioli[1], A. Facchinetti[1], G. Sparacino[1], and S. Del Favero[1]

[1] *Department of Information Engineering - DEI, University of Padova*

Abstract—*Objective:* **In this work, we considered the problem of predicting future values of glucose in type-1 diabetes subjects, exploiting information on injected insulin, carbohydrates intake and past glucose samples.**

Derivation of individualized predictors is crucial to cope with the wide inter- and intra-subject variability: in this direction, we explored different parametric linear black-box identification techniques to derive patient-tailored predictors.

Methods: **Different parameterizations (i.e., ARX, ARMAX, ARIMAX, and BoxJenkins), and different automatic strategies to choose individual-specific orders (parsimony criteria: AIC and BIC, and cross-validation) were considered. A model for each combination was identified using the mainstream technique in system identification, the Prediction Error Method, on 100 virtual subjects simulated with the UVA/Padova T1D Simulator.**

In order to find the best model class and order selection criterion, we computed Coefficient of Determination (COD) and Root Mean Square Error (RMSE) at different prediction horizons (PH), and compared the results using ANOVA.

Results: **Very similar performances were found for all perdition horizons, both between model classes, and between order selection criteria. For PH = 60 min, no statistically significant difference was found neither in terms of RMSE nor in terms of COD.**

Conclusion: **No significant difference was found neither between model classes, nor between order selection criteria.**

Keywords—**Individualized glucose prediction, linear models, black-box identification.**

I. INTRODUCTION

TYPE-1 DIABETES (T1D) is a disease in which the pancreas produces very little or no insulin - a hormone required for the body to use blood sugar or glucose (BG). T1D patients need to administer themselves insulin with external injections to keep their glucose in the safe range. Insufficient insulin administration causes high BG levels in the body, that could lead to several complications on the long term, but an overtreatment can lead conversely to hypoglycemia, i.e., with BG less than 70 mg/dL, that could represent an immediate threat for patient's life. Patients' experience plays a major role in this important challenge: they need to take decisions balancing the amount of insulin injection with BG levels and external disturbances such as meal intake or physical exercise.

Accurate predictions of future glucose levels would greatly improve T1D management: indeed, the design of effective algorithms, capable to forecast the presence of dangerously episodes, can give the user the opportunity to proactively and preventively act to avoid the event [1]. However, a very important challenge is the inter- and intra-subject variability: the glucose response to insulin and meal is different in every person and even in the same patient changes over time. This issue can be addressed by learning and updating patient-

specific models of the glucose-insulin dynamics [2]. Moreover, with these models, along with continuous glucose monitoring (CGM) data, we can use further additional information regarding external disturbances, such as insulin injection and meal consumption, that can improve the prediction accuracy [3].

The problem of individualization and adaptation to changes in order to obtain reliable BG predictors is an ongoing research topic, and broad attention has been put on this topic. For a systematic review on this, we refer interested reader to [4]–[7].

Data-driven techniques are particularly well suited for model customization on T1D subjects, and accurate predictors can be easily identified and individualized using these strategies. Although the real-patient model is nonlinear [8], various experiments, both in-silico and in-vivo, indicate that a linear approximation may capture the essential dynamic features [9]. We thus focused on a subclass of data-driven techniques, the linear black-box predictors: the input-output relation of the glucose-insulin system could thus be approximated by a parametrized linear data-driven model. This approach restricts the search of the system dynamics to a finite-dimensional set of functions parametrized by a parameters vector. In particular, parametric techniques have two different degrees of freedom: the model parametrization and the model order. Note that the choice of these degrees of freedom is crucial to obtain accurate predictors. Regarding the first degree, the class of the model, commonly used parametrizations are auto regressive with exogenous inputs (ARX), auto regressive moving average with exogenous inputs (ARMAX), auto regressive integrated moving average with exogenous inputs (ARIMAX), and Box-Jenkins (BJ). The other crucial choice that has to be addressed in the identification pipeline is then the model complexity, i.e., the number of parameters that have to be estimated (model order): this number need be wisely chosen using order selection criteria, for example parsimonious ones.

The aim of this work is to explore the impact on prediction of the degrees of freedom related to the parametric approach techniques. Using experimental data collected on a virtual population of 100 T1D individuals, we made a comparison between various system parametrizations, and various model-order selection criteria.

II. METHODS

A. Experimental data

The UVA/Padova T1D simulator captures inter-subject variability (the large differences in the physiology of different T1D individuals) by providing a population of $N = 100$ adults, whose physiological parameters are distributed to

replicate the variability observed in T1D people. In this paper, we use an updated version of the simulator [10], capable to account for variation and intra- subject variability (i.e., changes over time in a patient's physiology [11]).

1) *In-silico protocol:* For each subject, we simulated a 14-day protocol, with 3 meals per day, taking place with uniform probability in the intervals [06:30, 08:30] (breakfast), [12:00, 14:00] (lunch), and [19:30, 21:30] (dinner) with carbohydrates consumption uniformly distributed in [20, 60], [50, 90], and [50, 90] g, respectively. Throughout the day, insulin was administered to the patient by a PID closed-loop algorithm (basal insulin administration) with the aim to keep the patient BG in the nearly normal range. At each meal, the patient delivers himself an additional insulin dose (insulin bolus), proportional to the estimated carbohydrates amount. BG measurements and insulin data were available each $Ts = 5$ min, a typical sampling time for T1D devices. The measurement error of the CGM sensor is modeled as proposed in [12].

2) *Training and test partitioning:* For each of the 100 *in-silico* subjects, the final dataset consists in two different portions of approximately 2016 samples (i.e., 14 days). The first one was used as a training-set for estimating the prediction models, whereas the second one was solely used for assessing the final prediction performance.

B. Identification Techniques

Using parametric data-driven models, the glucose concentration measured by a CGM sensor, $g(k)$, can be represented by a linear combination of past CGM values ($g(k-1)$, $g(k-2)$, …), and present and past values of inputs, such as the carbohydrate intake ($m(k)$, $m(k-1)$, $m(k-2)$, …) and the insulin injections, ($i(k)$, $i(k-1)$, $i(k-2)$, …).

In the parametric model identification pipeline, the first choice that has to be taken is the model class; then, for a fixed parametrization, we have to decide the number of parameters that have to be estimated; finally, we need to estimate these unknown parameters.

Regarding the model class, with the ARX parametrization we can write the input-output relation of the glucose-insulin dynamics via polynomials using the back-shift operator q^{-1}, $q^{-1}[g(k)] = g(k-1)$, as follows:

$$A(q^{-1})g(k) = [B_1(q^{-1})\ B_2(q^{-1})] \begin{bmatrix} i(k - n_{k1}) \\ m(k - n_{k2}) \end{bmatrix} + e(k) \quad (1)$$

where $e(k)$ is white noise, whereas $A(q^{-1})$, $B_1(q^{-1})$, and $B_2(q^{-1})$ are polynomials in q^{-1} of orders n_a, n_{b1}, and n_{b2} respectively, defined as

$$A(q^{-1}) = 1 + a_1 q^{-1} + \cdots + a_{n_a} q^{-n_a},$$
$$B_1(q^{-1}) = b_{01} + b_{11} q^{-1} + \cdots + b_{n_{b1}1} q^{-n_{b1}}, \quad (2)$$
$$B_2(q^{-1}) = b_{02} + b_{12} q^{-1} + \cdots + b_{n_{b2}1} q^{-n_{b2}}.$$

The parameters $[n_{k1}\ n_{k2}]$ have been introduced to take into account the delay in the inputs action. The ARMAX parametrization, instead, considers a further polynomial of order n_c, $C(q^{-1}) = 1 + c_1 q^{-1} + \cdots + c_{n_c} q^{-n_c}$, that enters in

(1) by multiplying the error noise $e(k)$. The ARIMAX model structure is very similar to ARMAX, except that it contains d integrators in the noise source $e(k)$:

$$A(q^{-1})g(k) =$$
$$= [B_1(q^{-1})\ B_2(q^{-1})] \begin{bmatrix} i(k - n_{k1}) \\ m(k - n_{k2}) \end{bmatrix} + \frac{C(q^{-1})}{(1 - q^{-1})^d} e(k). \quad (3)$$

Finally, the more general BJ parametrization is defined as

$$g(k) = \left[\frac{B_1(q^{-1})}{F_1(q^{-1})}\ \frac{B_2(q^{-1})}{F_2(q^{-1})} \right] \begin{bmatrix} i(k - n_{k1}) \\ m(k - n_{k2}) \end{bmatrix} +$$
$$+ \frac{C(q^{-1})}{D(q^{-1})} e(k) \quad (4)$$

where $F_1(q^{-1})$, $F_2(q^{-1})$, and $D(q^{-1})$ are monic polynomials of orders n_{f1}, n_{f2}, and n_d respectively.

All the mentioned cases fit a general description

$$g(k) = [G_1(q^{-1}, \theta) G_2(q^{-1}, \theta)] \begin{bmatrix} i(k) \\ m(k) \end{bmatrix} +$$
$$+ H(q^{-1}, \theta) e(k) \quad (5)$$

where $G_1(q^{-1}, \theta)$, $G_2(q^{-1}, \theta)$, and $H(q^{-1}, \theta)$ are transfer functions parametrized in θ, a vector that corresponds to the coefficients of the polynomials.

Assuming that model complexity has been chosen, the unknown parameters θ can be identified with the following procedure, [13]: first, derive the 1-step ahead predictor associated with (5) as follows

$$\hat{g}(k|k - 1, \theta) =$$
$$= H^{-1}(q^{-1}, \theta)[G_1(q^{-1}, \theta) G_2(q^{-1}, \theta)] \begin{bmatrix} i(k) \\ m(k) \end{bmatrix} +$$
$$+ [1 - H^{-1}(q^{-1}, \theta)] g(k); \quad (6)$$

and then, according to the PEM approach, coefficients of the polynomials can be estimated minimizing the associated error:

$$\hat{\theta} = \underset{\theta}{\mathrm{argmin}} \sum_{1}^{N} (g(k) - \hat{g}(k|k - 1, \theta)). \quad (7)$$

For what it concerns the choice of model complexity we considered two options: one is using population order (PopOrd), i.e., to identify the same number of parameters in all subjects. The second option is to use well-known model complexity criteria to select the best patient-specific orders. In particular, we considered two well-known parsimonious criteria [13], i.e., the Akaike Information Criterion (AIC), and the Bayesian Information Criterion (BIC). Moreover, for this task we performed also a 7-fold Cross-Validation (CV). For each round of CV, we partitioned seven times the data into complementary subsets: 6 days of data were used to train the model, and the remaining day was used to assess the performance of that given number of parameters.

Note that exploring all possible orders combinations would have led to a computationally unfeasible analysis: for this reason, we forced all the polynomials orders to be equal, e.g., $n_a = n_{b1} = n_{b2}$ in the ARX parametrization, and so on. We tested orders ranging from 1 to 20 for ARX, ARMAX and ARIMAX parametrizations, whereas from 1 to 15 using BJ

models. Regarding the delays, we fixed the meal and insulin input's delay to physiological values, i.e., $n_{k1} = 9$ step and $n_{k2} = 3$ step. For the ARIMAX parametrization, we fixed the number of integrators d to 1.

C. Performance metrics

To assess the prediction accuracy of the identified models, we compared the prediction of future CGM values against its actual measurements $g(k)$ on the test-sets. Different prediction horizons (PH) were considered.

In details, let us denote with $\hat{g}(k|k - PH)$ the PH-step ahead prediction of a model, i.e., the prediction obtained by using past glucose values up to time $k - PH$, and inputs up to time k. The two signals, $g(k)$ and $\hat{g}(k|k - PH)$, were compared using two different metrics, namely root mean squared error (RMSE), and coefficient of determination (COD), commonly used in system identification [14], [15].

$$RMSE(PH) = \frac{1}{\sqrt{N}} \|g(k) - \hat{g}(k|k - PH)\|_2 \qquad (11)$$

where by $\|x(k)\|_2$ we denote the ℓ_2 norm of the signal $x(k)$, namely $\sqrt{\sum_1^N x(k)^2}$, N being the number of samples of the experiment. The COD is defined as

$$COD(PH) = 100 \left(1 - \frac{\|g(k) - \hat{g}(k|k - PH)\|_2^2}{\|g(k) - \bar{g}(k)\|_2^2} \right) \qquad (12)$$

where $\bar{g}(k)$ is the sample mean of the glucose signal.

To detect a difference in the accuracy metrics among the different model classes or complexity criteria an analysis of variance (ANOVA) was performed.

III. RESULTS

Fig. 1 and 2 show, for different parametric predictors, the prediction's RMSE: the median and interquartile range (IQR) over the population is plotted as a function of PH. Using the same complexity criterion (CV), in Fig. 1 a comparison of the different parametrizations under study is presented, showing that all these parametric linear approaches have very similar performance. Nevertheless, a marginal improvement is reached using the ARMAX parametrization. Fig. 2 shows that the model-order selection criteria have very similar accuracy too. Let us note that models identified using population orders (PopOrd) have larger variability, and slightly worse performance. Overall, an increase in the PH leads to a deterioration in the prediction accuracy for all given models.

Table I and II report, respectively, the 60-min prediction's COD and RMSE, for all combinations of model classes and complexity criteria. No statistically significant difference can be found: indeed, regarding the COD we obtained a *p-value* of about 0.13 and 0.29 among model classes and complexity criterion, respectively, whereas for the RMSE we got a *p-value* of 0.23 and 0.15, respectively.

Fig. 3 and 4 report the boxplots of the COD and the ΔCOD for each patient for PH = 60 min, for models with fixed selection criterion or model class, respectively. The difference of all parametric approaches is, on average, always similar to

zero, meaning that there is no significant difference between model classes or model-order selection criteria.
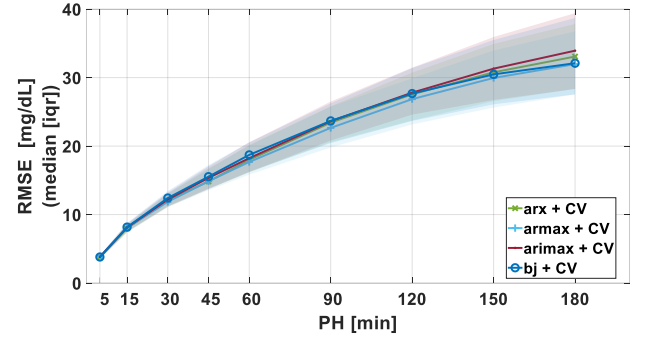
Fig. 1: RMSE over the population as a function of PH, for the different model classes, with fixed complexity criterion (CV)
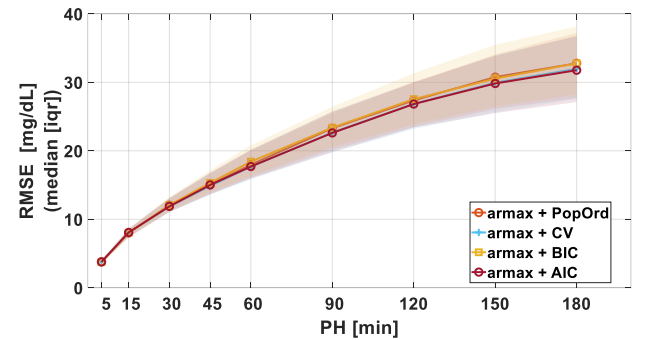
Fig. 2: RMSE over the population as a function of PH, for the different model-order selection criteria, with fixed parametrization (ARMAX)
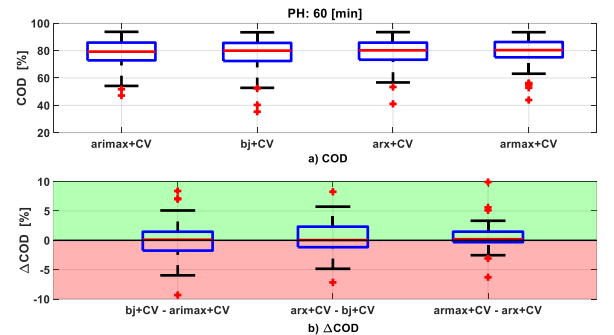
Fig. 3: Boxplot of COD and ΔCOD (per patient) for different model classes, using the same model-order selection criterion (CV)
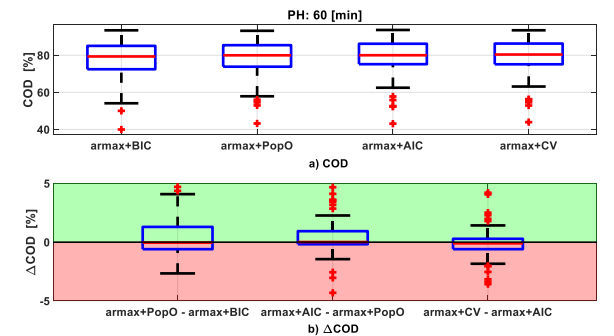

Fig. 4: Boxplot of COD and ΔCOD (per patient) for different complexity criteria, using the same model parametrization (ARMAX)

TABLE I

60-min COD	PopOrd	CV	BIC	AIC	p-value
ARX	79 [72.4, 84.8]	80.2 [73.3, 85.8]	79.4 [72.2, 87.1]	78.6 [71.7, 83.9]	
ARMAX	80 [73.8, 85.4]	80.4 [75.1, 86.3]	79.3 [72.4, 85.1]	80 [75.2, 86.2]	0.13
ARIMAX	80.1 [72.8, 85.8]	79.3 [72.9, 85.9]	78.9 [70.3, 84.4]	80.2 [74.3, 85.9]	
BJ	78 [70.8, 84.9]	80 [72.4, 85.6]	78.3 [72.4, 85.1]	80.1 [74, 85.8]	
p-value	0.29				

Comparison of different complexity criteria and different parametrizations. Median [IQR] prediction performance as COD for PH = 60 min

TABLE II

60-min RMSE	PopOrd	CV	BIC	AIC	p-value
ARX	18 [16.2, 20.2]	18 [16.2, 20.2]	18 [15.4, 20.1]	18.9 [16.5, 20.9]	
ARMAX	17.7 [15.8, 20.1]	17.7 [15.8, 20.1]	18.4 [16.3, 20.8]	17.7 [15.9, 20.2]	0.23
ARIMAX	18.2 [16.2, 20.5]	18.2 [16.2, 20.5]	18.9 [16.3, 21.5]	18 [16, 20.4]	
BJ	18.7 [16.2, 20.5]	18.7 [16.2, 20.5]	18.6 [16.7, 20.9]	18.1 [15.9, 20.1]	
p-value	0.15				

Comparison of different complexity criteria and different parametrizations. Median [IQR] prediction performance as RMSE for PH = 60 min

IV. CONCLUSION

In this paper, we considered the problem of predicting future values of glucose given injected insulin, carbohydrate intake, and CGM measured glucose. To deal with the large inter- and intra-subject variability, we derived individualized linear parametric predictors based on black-box models: we implemented different techniques on virtual-patient data, in order to compare the degrees of freedom, i.e., the model parametrization and the order selection criterion.

Results showed that no significant difference could be found neither between model classes, nor between order selection criteria. Prediction accuracy achieved with the methods tested in this work, do not differ from those of [7], that found a 60-min RMSE ranging from 18.9 mg/dL to 25.7 mg/dL on simulated data using a non-linear back-box approach (recursive neural network). In another contribution by our group [16], we considered the problem of BG prediction using CGM data only, also based on linear black-box models. The methods in [16] achieved RMSE of about ~20 mg/dL with PH=30 min on real data, whereas for the same PH we obtained a RMSE of about ~12 mg/dL. A word of caution is due: including inputs is expected to improve prediction, but a direct comparison of the RMSE achieved in the two contributions could be misleading, since in [16] the methods were tested on a more challenging dataset based on real data.

A systematic review of the many contributions on glucose prediction techniques goes beyond the scope of this paper and the interested reader can refer to [4]–[7].

ACKNOWLEDGEMENT

REFERENCES

[1] K. Turksoy, E. S. Bayrak, L. Quinn, E. Littlejohn, D. Rollins, and A. Cinar, "Hypoglycemia early alarm systems based on multivariable models," *Ind. Eng. Chem. Res.*, vol. 52, no. 35, pp. 12329–12336, 2013.

[2] M. Messori, C. Toffanin, S. Del Favero, G. De Nicolao, C. Cobelli, and L. Magni, "Model individualization for artificial pancreas," *Comput. Methods Programs Biomed.*, pp. 1–9, 2016.

[3] C. Zecchin, A. Facchinetti, G. Sparacino, and C. Cobelli, "How much is short-term glucose prediction in type 1 diabetes improved by adding insulin delivery and meal content information to CGM data? A proof-of-concept study," *J. Diabetes Sci. Technol.*, vol. 10, no. 5, pp. 1149–1160, 2016.

[4] S. Oviedo, J. Vehí, R. Calm, and J. Armengol, "A review of personalized blood glucose prediction strategies for T1DM patients," *Int. j. numer. method. biomed. eng.*, vol. 33, no. 6, pp. 1–21, 2017.

[5] J. I. Hidalgo, J. M. Colmenar, G. Kronberger, S. M. Winkler, O. Garnica, and J. Lanchares, "Data Based Prediction of Blood Glucose Concentrations Using Evolutionary Methods," *J. Med. Syst.*, vol. 41, no. 9, 2017.

[6] J. Xie and Q. Wang, "Benchmarking machine learning algorithms on blood glucose prediction for Type 1 Diabetes in comparison with classical time-series models," *IEEE Trans. Biomed. Eng.*, p. Epub ahead of print, 2020.

[7] P. G. Kezhi Li, John Daniels, Chengyuan Liu, Pau Herrero, "Convolutional Recurrent Neural Networks for Glucose Prediction," *IEEE J. Biomed. Heal. Informatics*, pp. 1–10, 2019.

[8] C. Dalla Man, R. A. Rizza, and C. Cobelli, "Meal simulation model of glucose-insulin system," *Annu. Int. Conf. IEEE Eng. Med. Biol. - Proc.*, vol. 54, no. 10, pp. 307–310, 2006.

[9] M. Messori, M. Ellis, C. Cobelli, P. D. Christofides, and L. Magni, "Improved postprandial glucose control with a customized Model Predictive Controller," *Proc. Am. Control Conf.*, pp. 5108–5115, 2015.

[10] C. Toffanin, R. Visentin, M. Messori, F. Di Palma, L. Magni, and C. Cobelli, "Toward a Run-to-Run Adaptive Artificial Pancreas: In Silico Results," *IEEE Trans. Biomed. Eng.*, vol. 65, no. 3, pp. 479–488, 2018.

[11] R. Visentin, C. Dalla Man, Y. C. Kudva, A. Basu, and C. Cobelli, "Circadian variability of insulin sensitivity: Physiological input for in silico artificial pancreas," *Diabetes Technol. Ther.*, vol. 17, no. 1, pp. 1–7, 2015.

[12] A. Facchinetti, S. Del Favero, G. Sparacino, J. R. Castle, W. K. Ward, and C. Cobelli, "Modeling the glucose sensor error," *IEEE Trans. Biomed. Eng.*, vol. 61, no. 3, pp. 620–629, 2014.

[13] L. Ljung, *System identification - Theory for the user*. 1987.

[14] D. A. Finan, C. C. Palerm, F. J. I. Doyle, and D. E. Seborg, "Effect of Input Excitation on the Quality of Empirical Dynamic Models for Type 1 Diabetes," *AIChE J.*, vol. 55, no. 5, pp. 1135–1146, 2009.

[15] A. Facchinetti, G. Sparacino, E. Trifoglio, and C. Cobelli, "A New Index to Optimally Design and Compare Continuous Glucose Monitoring Glucose Prediction Algorithms," *Diabetes Technol. Ther.*, vol. 13, no. 2, pp. 111–119, 2011.

[16] F. Prendin, S. Del Favero, G. Sparacino, and A. Facchinetti, "Personalized Linear Data-Driven Algorithms for Real-Time Glucose Forecasting in Type 1 Diabetes," in *Proc. of the Italian National Bioengineering Group (GNB 2020+1)*, 2020.

A markerless gait analysis protocol based on a single RGB-Depth camera: sensitivity to background changes

D. Balta[1], M. Salvi[1], F. Molinari[1], G. Paolini[2], G. Figari[2], U. Della Croce[3] and A. Cereatti[3]

[1] Department of Electronics and Telecommunications, Politecnico di Torino, Torino, Italy
[2] GPEM srl, Alghero, Italy
[3] Department of Biomedical Sciences, University of Sassari, Sassari, Italy

Abstract— **This work presents a two-dimensional markerless clinical gait analysis protocol to estimate the sagittal lower limb joint kinematics based on markerless recordings from a single RGB-Depth camera. The influence of different experimental setup conditions (presence/absence of a green coloured background) on the accuracy of this proposed method was also evaluated. The proposed protocol includes a subject separation from the background, the definition of a multi-segmental model of the lower limb and the estimation of the relative joint kinematics. The segmentation algorithm performance was assessed by computing the similarity between the computer-obtained segmentations and the corresponding manual tracings (ground-truth). The estimated joint angles were compared with those obtained using a reference optoelectronic marker-based clinical protocol. The offset between the mean waveforms and the RMS value of the waveforms difference after removing their offset were computed. The segmentation accuracy is higher than 0.9 in both the experimental setup conditions. There is a little worsening (2.2%) when the segmentation is computed without the green background, but it does not affect the accuracy of the estimated kinematics since the RMSD values are lower or equal to those obtained with the green background.**

Keywords—markerless, gait analysis, lower limb joint kinematics, RGB-D camera.

I. INTRODUCTION

MARKER-BASED opto-electronic stereo-photogrammetric technology represents the gold standard for clinical gait analysis assessments but its use is limited due to high set-up and operational costs. The use of markerless (ML) methods based on low-cost RGB camera integrated with depth sensing devices (RGB-D) is a promising alternative to marker-based (MB) systems due to their affordability, and the simple setup of the subject under analysis [1]. However, the validity of ML methods for biomechanical and clinical applications is still an open issue and it requires further efforts [2]. ML methods will facilitate the development of a new generation of low-cost movement analysis systems.

The proposed protocol includes a subject separation from the background, the definition of a multi-segmental model of the lower limb and the estimation of the relative joint kinematics. The image segmentation is a key component in several ML gait analysis systems. The state of the art introduces the need of a controlled environment including a coloured and uniform background since it standardises the experimental scenario [1],[3],[4]. However, it complicates the experimental setup conditions by increasing the number of required tools and the installation time.

The accuracy associated to ML protocols may vary due to different experimental setup conditions e.g. lights and background.

Therefore, the aim of this study is to evaluate the feasibility of estimating the lower limb joint kinematics using a ML approach without the need a uniform and colored background.

A. Experimental setup

Experiments were conducted on an informed and consenting healthy subject in a gait analysis laboratory equipped with a 9-camera MB Vicon system (f_s=120 Hz). ML data were acquired using one RGB-D camera (Intel RealSense D435, fs=30 fps). The camera was positioned laterally to the walkway (2.5 m from the walkway and 5 m away from the background). Two additional LED lamps were used (40 W each). The subject wore ankle socks of different colors (red and blue) and underwear. A set of 20 retroreflective markers were attached to the body according to the Davis protocol [5] (Fig. 1).

In the first experimental session, a large green sheet was used to obtain a uniform background. The experimental protocol consisted in: *(i)* static acquisition of the background, *(ii)* two static acquisitions (left and right side) of the subject in upright standing posture (duration 3s), *(iii)* three gait trials per side at self-selected speed. During the second experimental session, the background was removed, and the experiment protocol repeated.
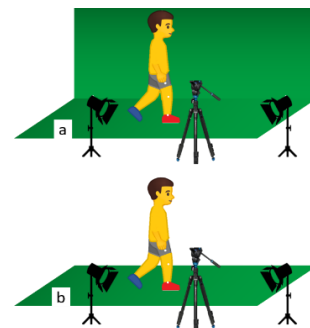

Fig. 1: a) experimental setup with the green background, b) experimental setup without the green background.

B. Method description

The proposed ML gait analysis protocol consisted in three main parts: subject segmentation, model definition and joint centre trajectories estimation (Fig. 2).
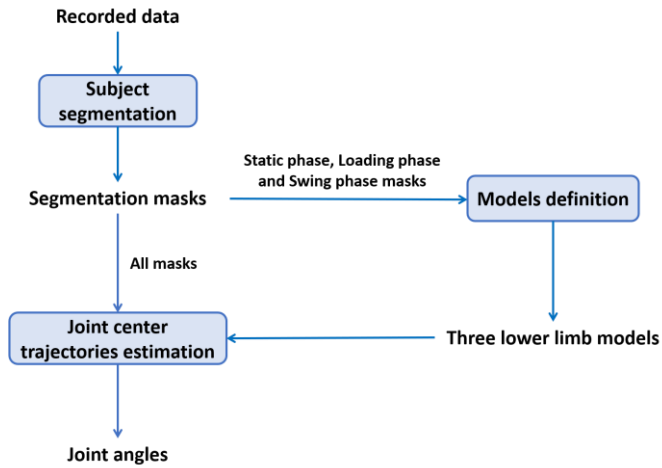
Fig. 2: Block-diagram of the proposed gait analysis protocol

a) Subject segmentation

Firstly, depth data was used to define the depth range within which the subject moves. The image region falling outside this range was removed and only the resulting image is kept for further analysis (this processing was applied to all the recorded frames). Then, for each RGB frame (static and dynamic acquisitions) an image subtraction operation was performed by using the background image. A rectangular region of interest (*ROI*) containing the subject was defined to remove the remaining pixels belonging to the background (Fig. *3*).
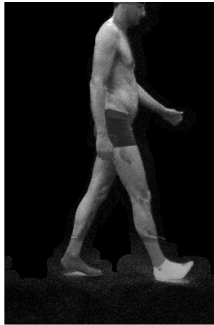
Fig. 3: A rectangular region of interest containing the subject.

A modified version of the algorithm proposed in [6] was implemented to automatically obtain a threshold to separate the subject from the image background. This algorithm is based on the computation of the progressive weighted mean curve (PWM_{CURVE}) calculated from the histogram of the image *ROI* [6]. Relevant information about the grayscale distribution of the image can be extracted by using the PWM_{CURVE}. In particular, if there are significant color variations in the grayscale image, consequently there are changes of concavity in the PWM_{CURVE} [6]. All the inflection points of the curve are calculated since they may be potential threshold values for performing the subject segmentation. Since there is only one subject in the image, the final threshold value *Th* corresponds to the intensity value of the first inflection point. The final segmentation *S* (Fig. 4a) is obtained as follows:

$$S_{x,y} = \begin{cases} 0, & if \ p_{x,y} \leq Th \\ 1, & if \ p_{x,y} > Th \end{cases} \qquad (5)$$

As feet segmentation is generally poor due to the presence of shadows/reflections on the floor, feet segmentation is performed directly in RGB image through colour filters (Fig.

4b). The upper body segmentation is then connected with the feet segmentation (Fig. 4b) obtained with color filter and the final result of the automated segmentation is shown in Fig. 4c.
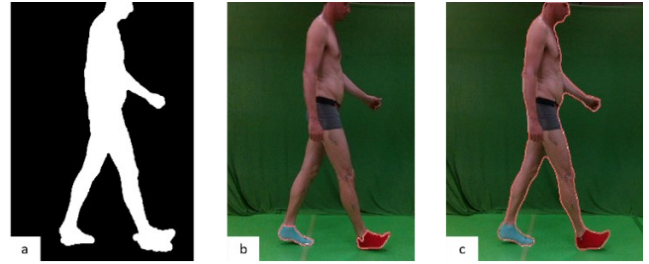
Fig. 4: a) Segmentation mask *S*, b) feet segmentation through colour filters c) final segmentation mask.

b) Multi-segmental model definition

The multi-segmental kinematic model is composed of three body segments (foot, shank and thigh) connected by three hinges representing the ankle joint over the lateral malleolus (LM), the knee joint over the lateral epicondyle (LE) and the hip joint over the great trochanter (GT) (Fig. 5). Since the distance of the walking subject from the RGB-D camera changes, subject rotations out of the sagittal plane, soft tissue artefacts [7] and parallax effects modify size and shape of the RGB image of all body segments across acquisition frames. To compensate for these artefacts, three distinct subject-specific lower limb models are defined and implemented to estimate the lower limb joint angles. The models are defined from the RGB images recorded during (*i*) the static upright standing, (*ii*) the loading phase and (*iii*) swing phase of gait cycle. For each of these reference images, a multiple anatomical calibration [7] of LM, LE and GT was manually performed by an expert operator with a mouse click. After the identification of the anatomical landmarks, the lower limb segments (foot, shank and thigh) are identified on each of the three reference images. The foot model is defined as the posterior portion of the foot contour, including the LM and it is extracted from the segmented image through a color filter. Depth image information is used to separate the lower limbs to allow the identification of shank and thigh models. The foreground shank is identified by computing the histogram of the depth values. The foreground shank is identified as the region of points characterized by the lowest depth values (being closer to the camera) and by the largest area (highest frequency in the histogram) since the shank in the foreground may partially cover the contralateral shank. For these reasons, a range of depth values around the highest peak of the histogram is identified by considering a heuristic threshold on the distance between the two overlapped shanks to isolate the foreground shank. A similar procedure is applied for the identification of the thigh in foreground. The resulting lower limb models are shown in Fig. 5.
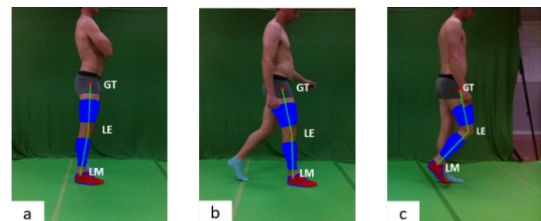

Fig. 5: Participant-specific lower limb model during a) static upright standing, b) loading phase, c) swing phase.

c) *Lower limb joint center trajectories estimation*

Joint center trajectories are tracked over the gait cycle. For each frame, the position of the LM is reconstructed by minimizing the distance between the segmented foot and the foot model using an iterative closest point (ICP) [8] technique. To reconstruct the position of the LE, firstly the portion of interest of the shank is extracted from the segmented image and the distance between the segmented shank and the shank model is minimized using the ICP technique. A similar procedure is employed to reconstruct the position of the GT. Once the trajectories of the LM, LE and GT are reconstructed during the entire gait cycle, the ankle joint angle is determined as the angle between LM-TOE segment and the LM-LE segment, the knee joint angle is determined as the angle between the LM-LE segment and LE-GT segment. Not having identified the pelvis, a pseudo-hip joint angle is determined as the angle between the LE-GT and vertical axis. The above-mentioned procedure is repeated for each model, thus producing three different joint angles patterns. To reduce soft tissue deformation and parallax errors ([7],[9]) the three kinematic curves are then combined into a single curve by linearly weighting each model contribution based on the percentage of the gait cycle.

C. *Data analysis*

The accuracy of subject segmentation is validated by comparing the automatic masks with those obtained by an expert operator based on the Jaccard Index (JI). JI is a statistic measurement for evaluating the similarity of two masks and it is defined as follows:

$$JI = \frac{M \cap A}{M \cup A} \qquad (5)$$

where M is the manual mask and A is the automatic one.
The accuracy of the estimate lower limb joint kinematics is assessed in terms of: (1) mean value difference between the mean curve measured by the MB system and that obtained from the ML method (*Offset*); (2) root mean square difference between the two mean waveforms after removing their relevant mean values (RMSD).

II. RESULTS

A. *Subject segmentation*

The mean and standard deviation of the JI in both experimental setup conditions are shown in TABLE I

TABLE I
MEAN AND STANDARD DEVIATION OF THE JI

WITH BACKGROUND	WITHOUT BACKGROUND
0.929 ± 0.010	0.909 ± 0.019

B. *Two-dimensional joint kinematics estimation*

The mean and standard deviation of the offsets of the lower limb joint kinematics in both experimental setup conditions are shown in TABLE II.

TABLE III shows the mean and standard deviation of the RMSD values between the two mean waveforms after removing their relevant mean values in both experimental setup conditions. Lower limb joint kinematics obtained from the MB protocol and from ML one for three trials without their offsets in both experimental setup conditions are shown in Fig.6.
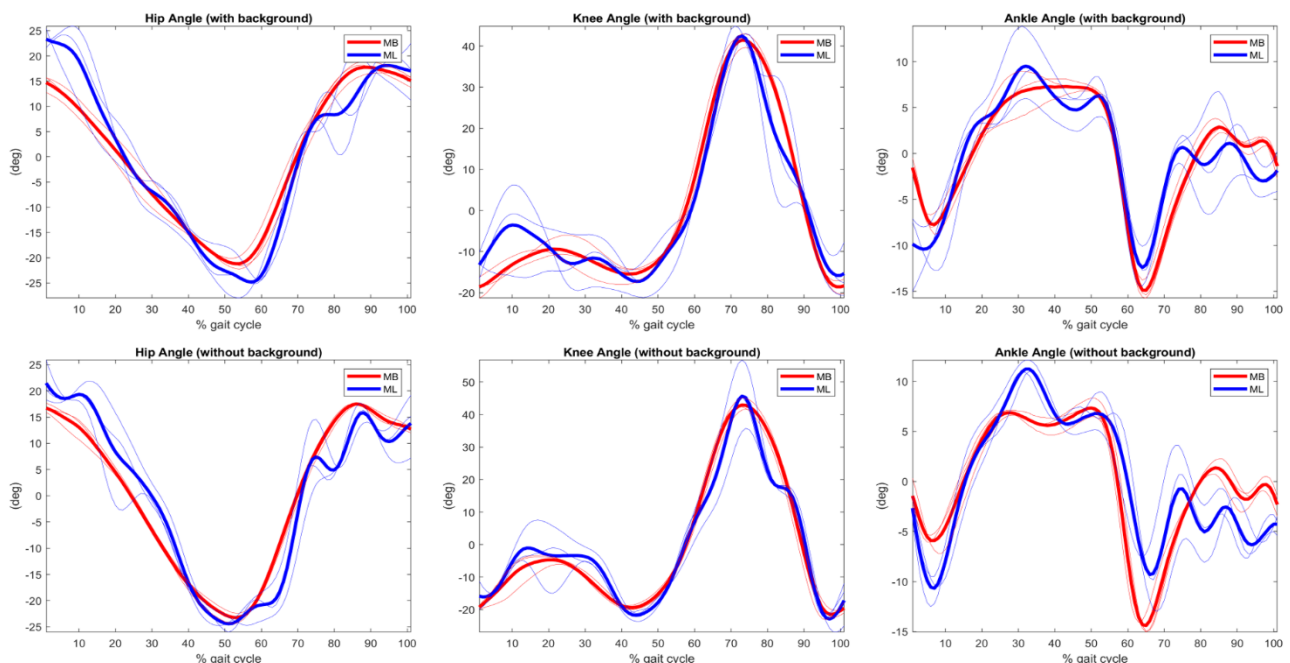

Fig. 6: Lower limb joint kinematics obtained from the MB (red lines) and from ML (blue lines) for three trials without their offsets with (first row) and without (second row) the green background. The red line in bold is the mean curve of the three trials obtained from the MB system and the blue line in bold is the mean curve obtained from the ML method.

TABLE II
THE MEAN AND STANDARD DEVIATION OF THE OFFSET FOR THE HIP, KNEE AND ANKLE KINEMATICS

(deg)	WITH BACKGROUND	WITHOUT BACKGROUND
Hip	$16.9° \pm 4.5°$	$12.4° \pm 3.5°$
Knee	$5.4° \pm 3.3°$	$2.7° \pm 2.4°$
Ankle	$10.9° \pm 2.7°$	$13.5° \pm 2.9°$

All the units are in degrees.

TABLE III
THE MEAN AND STANDARD DEVIATION OF THE RMSD FOR THE HIP, KNEE AND ANKLE KINEMATICS

(deg)	WITH BACKGROUND	WITHOUT BACKGROUND
Hip	$5.5° \pm 1.5°$	$4.5° \pm 1.3°$
Knee	$6.8° \pm 1.0°$	$5.1° \pm 2.1°$
Ankle	$3.3° \pm 0.3°$	$3.0° \pm 0.3°$

All the units are in degrees.

III. DISCUSSION

The proposed ML protocol has the potential to become a useful tool in clinical environments since it does not need the application of markers on the skin. Furthermore, it requires limited manual intervention to identify few anatomical landmarks, exclusively at the beginning of data processing. The segmentation algorithm, included in the proposed ML method, incorporates a fully automatic thresholding method based on the analysis of the image histogram. This solution appeared to be robust to variable image backgrounds in contrast to other algorithms proposed in literature (e.g. [1], [3],[4]) in which a homogeneous coloured background is required. In fact, as reflected by the JI, the ML method performs slightly worse when the background is removed (JI=0.929 and JI=0.909 with and without the green background respectively). As shown in Fig. 7, when removing the green background, the segmentation mask can be critical when the skin colour is very similar to the background colour.

The offset observed between the MB and ML joint kinematics estimates is somehow expected as the anatomical axes are different. Interestingly, the method performance, in terms of RMSD, after the removal of the green background, are similar and slightly smaller (RMSD=5.5° vs 4.5° for the hip, RMSD=6.8° vs 5.1° for the knee, RMSD=3.3° vs 3.0° for the ankle, with and without the green background respectively).

This suggests that small errors in segmenting the subject (only 2.2%) do not remarkably affect the accuracy of the estimated kinematics since the majority of the subject is correctly segmented (Fig. 7).
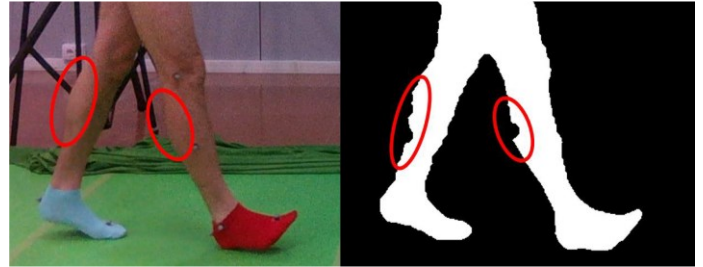
Fig. 7: The red lines represent the segmentation inaccuracies in the body regions which have a similar color to background.

IV. CONCLUSION

A preliminary validation demonstrated the possibility of conducting a markerless gait analysis acquisition without the need of a homogeneous coloured background by simplifying the experimental setup in favour of both system transportability and installation time. Future studies will be devoted to validating the proposed protocol on a large number of subjects.

REFERENCES

[1] A. Castelli, G. Paolini, A. Cereatti, and U. Della Croce, "A 2D markerless gait analysis methodology: Validation on healthy subjects," *Comput. Math. Methods Med.*, vol. 2015, 2015.

[2] L. Mündermann, S. Corazza, and T. P. Andriacchi, "The evolution of methods for the capture of human movement leading to markerless motion capture for biomechanical applications," *J. Neuroeng. Rehabil.*, vol. 3, 2006.

[3] E. Pantzar-Castilla *et al.*, "Knee joint sagittal plane movement in cerebral palsy: a comparative study of 2-dimensional markerless video and 3-dimensional gait analysis," *Acta Orthop.*, vol. 89, no. 6, pp. 656–661, 2018.

[4] I. Cocchi *et al.*, "A 2D markerless gait analysis protocol to estimate the sagittal joint kinematics of children with cerebral palsy," *2019 IEEE 23rd Int. Symp. Consum. Technol. ISCT 2019*, vol. c, pp. 192–196, 2019.

[5] R. B. Davis, S. Ounpuu, D. Tyburski, and J. R. Gage, "Davis_1991.pdf," *Human Movement Science*, vol. 10. pp. 575–597, 1991.

[6] M. Salvi and F. Molinari, "Multi-tissue and multi-scale approach for nuclei segmentation in H&E stained images," *Biomed. Eng. Online*, vol. 17, no. 1, pp. 1–13, 2018.

[7] A. Cappello, A. Cappozzo, P. F. La Palombara, L. Lucchetti, and A. Leardini, "Multiple anatomical landmark calibration for optimal bone pose estimation," *Hum. Mov. Sci.*, vol. 16, no. 2–3, pp. 259–274, 1997.

[8] P. J. Besl and N. D. McKay, "A Method for Registration of 3-D Shapes," in *IEEE Transactions on Pattern Analysis and Machine Intelligence*, 1992, vol. 14, no. 2, pp. 239–256.

[9] A. Cereatti, D. Trojaniello, and U. Della Croce, "Accurately measuring human movement using magneto-inertial sensors: Techniques and challenges," *2nd IEEE Int. Symp. Inert. Sensors Syst. IEEE ISISS 2015 - Proc.*, pp. 1–4, 2015.

Quantification and reduction of crosstalk in surface electromyogram by inverse modelling

L. Mesin[1]

[1] *Mathematical Biology & Physiology, Dept. Electronics and Telecommunications, Politecnico di Torino, Turin, Italy*

Abstract—**Crosstalk in surface electromyogram (EMG) is the signal recorded over a target muscle, but produced by a nearby one. It can limit the applications of surface EMG in many fields. The problem has been studied for long, but no standard method has been obtained to quantify or remove it, either than using a selective detection system, which however reduces also the representativeness of the data from the target muscle. Here, an inverse modelling method is proposed. The target and crosstalk EMG are approximately estimated, thus allowing both to quantify and to remove crosstalk. Simulation tests are shown considering nearby surface muscles investigated by arrays of electrodes placed over them in transverse direction with respect to the fibres. The proposed method reduces the effect of crosstalk: for example, considering the raw and processed data (respectively) over the muscle of interest, the mean error in root mean squared amplitude estimation is 7.6 and 2.6%, the maximum error in mean frequency estimation (from longitudinal single differential channels) is 2.6 and 0.8 Hz, the median error in conduction velocity estimation (from epochs of 250 ms, 3 monopolar channels aligned to the muscle fibres) is 2.41 and 0.52 m/s.**
Keywords—**Surface EMG, Crosstalk, Inverse Problem.**

I. INTRODUCTION

Surface electromyogram (EMG) has a relatively large pick-up volume. Thus it has the advantage of recording a large amount of information (from a large region, so that surface EMG represents the activity of a great portion of a target muscle). However, there is the problem of discriminating the sources of all this information. For example, some of the recorded signal may be produced by a muscle located nearby the target one. Such a contribution is called crosstalk. It may hinder the study of the target muscle, as documented in different applications: muscle coordination [1], prosthetic control [2], gait analysis [3], ergonomics for task evaluation [4] and reflexes [5] (other examples can be found in recent reviews [6][7]).

Many simulated [8][9] and experimental [6][10] studies have been devoted to address crosstalk. They allowed to investigate its biophysical origin. Surface EMG reflects the generation, propagation and extinction of the current flowing across the membranes of muscle fibres and triggering their contraction. The propagation of this current source provides a near field potential, whereas the effects of generation and extinction decay more slowly with distance. Thus, a motor unit (MU) action potential (MUAP) has a different waveform when it is recorded close or far to the location of the MU (as when it belongs to the target and crosstalk muscles, respectively). Moreover, crosstalk, being generated by a muscle farther

than the target one, is mainly constituted by generation and extinction effects. This is the reason why the first attempts to quantify crosstalk by cross-correlation failed [11]. Moreover, generation and extinction effects have a sharper shapes than propagating components, but they are more selectively filtered by the volume conductor when they are recorded from a large distance, so that the frequency contents of the EMG from target and crosstalk muscles are overlying and cannot be simply discriminated or separated by temporal filtering.

Thus, the main idea to reduce crosstalk in applications is to use selective spatial filters, which reduce the detection volume and hence also the effect of crosstalk [12][13]. However, the optimal configuration of the filter depends on the specific tissues [8][9], so that a fixed optimal filter could not be found, but it should be estimated by adapting to the specific condition [14]. Moreover, by reducing the detection volume, also the signal from the target muscle is largely discarded, reducing the representativeness of the recorded data [15]. Indeed, different portions of a muscle can behave differently [16], so that it is important to retain most signal from the target muscle, without reducing the detection volume, which would discard part of it.

In this paper, a method to quantify and reduce crosstalk is introduced. It is based on inverse modelling, which allows to estimate the signals produced by the target and the crosstalk muscles. This information is used to estimate the EMG produced by each muscle, to quantify crosstalk and to reduce the bias in estimating EMG indexes (reflecting amplitude, spectral content and conduction velocity - CV) of the two muscles.

II. METHODS

A. Inverse modelling algorithm

Surface EMG is the potential recorded over the skin reflecting the activity of bioelectric sources embedded in conducting tissues. The signal recorded during voluntary contractions can be simulated solving an electrostatic problem [17][18], with Poisson equation relating the bioelectric source (i.e., the cause) and the potential distribution in the tissue, thus, in particular, over the skin surface (i.e., the effect). Identifying the position of the sources from the recorded EMG is an inverse problem, as it requires to go in the opposite direction with respect to causality (so that the source is estimated from the potential, which means that the cause is computed knowing its effect). This problem was studied extensively in the field of surface electroencephalogram (EEG) [19][20]. Some studies

have also been proposed in the field of surface EMG (see [21] and quoted references). Most of these methods have a high computational cost, as they either require to decompose the interference EMG into constituent MUAPs or to apply intensive simulations by the finite elements method (FEM).

In this paper, the low cost alternative proposed in [21] is considered. It fits the data as a linear combination of a set of waveforms, each representing the activity of a portion of the muscle. A real-time implementation is possible. The method assumes the following model

$$b\left(x,t\right) = \sum_{n=1}^{N_R}\sum_{k=1}^{N_\tau} X_{n,k} a_n\left(x, t - \tau_{nk}\right) \tag{1}$$

where $b\left(x,t\right)$ is the recorded EMG, x is the space variable (indicating the position of the recording channels), t is the time variable, τ_{nk} is a delay (N_τ is the number of considered delays) and $a_n(x,t)$ are N_R basis waveforms representing the EMG response to a bioelectric source in a specific location. The unknowns are the coefficients $\{X_{n,k}\}$. If the coefficient $X_{n,k}$ is positive, it indicates that there is an activity from the nth region at a delay τ_{nk}.

Equation (1) can be rewritten in matrix form

$$AX = b, \tag{2}$$

where the basis waveforms are the columns of the matrix A and the vectors b and X include the measurements and the unknowns, respectively. The matrix A is not square in general, so that it cannot be inverted to find the unknowns. Moreover, as the measurements include noise and only few basis waveforms are considered, the two members of equation (2) can be considered only approximately equal. Thus, the problem was solved in the least mean squared sense after introducing Tikonov regularization to improve stability to noise

$$\min_X \|AX - b\|^2 + \alpha\|X\|^2 \tag{3}$$

where the first term is the residual norm (measuring the error in data fitting) and the second is the solution norm, imposing the energy of the solution to be small (hindering the selection of an oscillating solution, reflecting large phase cancellations). The solution was imposed not to show large oscillations by properly choosing the penalization parameter α which was set to be one thousandth of the maximum eigenvalue of the matrix $A^T A$. The problem has the following analytical solution

$$X = (A^T A + \alpha I)^{-1} A^T b \tag{4}$$

This expression can have unphysical negative values. In [21], the solution X was imposed to be positive by iteratively removing the negative values and projecting in the direction of the steepest descent of the squared error functional. Here, in order to get an optimal estimation of the signal from the target and crosstalk muscles, the positivity constraint was removed, allowing that the distribution could be even negative (thus, obtaining phase cancellations that allowed to improve the fit of the data).

B. Tests in simulation

The performances of the algorithm were tested on simulated surface EMGs. A cylindrical volume conductor model was used, including the following layers: bone (radius 20 mm, conductivity 0.02 mS/m), muscle (24 mm thick, transverse and longitudinal conductivities of 0.09 and 0.4 S/m), fat (5 mm thick, conductivity 0.04 S/m) and skin (1 mm thick, conductivity 0.022 S/m). Single fibre action potentials (SFAP) were simulated from a superficial portion of the muscle tissue, including two muscles. The location of the IZ and fibre ends were chosen randomly (uniform distribution with a range of 10 mm), so that the average location of the IZ was in the centre and the fibres had average lengths of 140 mm. Monopolar potentials were recorded by three parallel linear arrays of 16 electrodes (indicated in Figure 1A). They had 5 mm of inter-electrode distance, they were placed transverse to the fibres and were 10 mm distant from each other. The central array was at 35 mm from the IZ.

The centres of 400 MUs were randomly chosen, uniformly distributed in the cross-section of two muscles (referred to as M1 and M2 in the following; see Figure 1A and 1B). MU dimensions (i.e., the number of fibres belonging to them) were chosen varying exponentially between 15 and 300 [22]. Given the centre and the number of fibres N_b of a MU, the N_b fibres closest to the centre were selected and their SFAPs were summed-up to generate the MUAP.

For each muscle, interference EMGs were simulated as in [22] and summed to generate data including the contributions of both target and crosstalk muscles. A portion of simulated data is shown in Figure 1C, considering the total signal and those generated by either of the two muscles.

The inverse modelling algorithm included 90 basis functions, which were SFAPs obtained by the simulator considering fibres distributed in the muscle tissue with angle between $\pm 45^o$ (5° step, removing the angle of 0°) and depth between 1 and 9 mm (2 mm step).

C. Performance evaluation

Given the simulated and estimated EMGs from the two muscles, the following performance indexes were used to test the proposed algorithm.

- Accuracy of the estimation of the signals from the two muscles, measured in terms of the percentage mean squared error with respect to the average energy of the data (averaging across all channels and time samples).
- Quantification of crosstalk. The percentage root mean squared (RMS) amplitude of the surface EMG from the two muscles were computed considering either the simulated or the estimated signals.
- Possibility of reducing a bias in the estimation of the mean frequency (MNF) of the target muscle. MNF was estimated from the sample spectrum of longitudinal single differential (SD) channels. The EMG used for MNF estimation was either the raw signal (which is the sum of the contributions from the target and the crosstalk muscles), or the contribution of the simulated/estimated
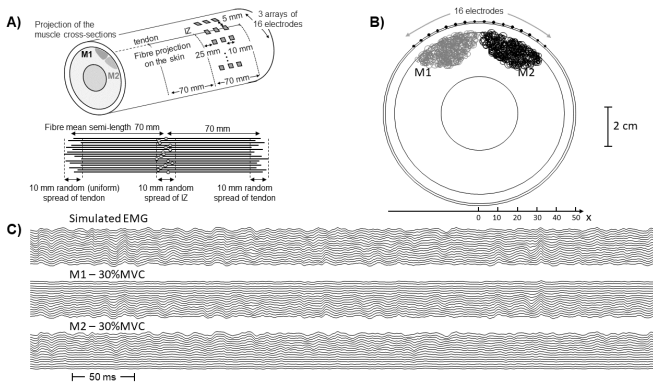
Fig. 1: Description of the simulation model. A) Cylindrical volume conductor (including bone, muscle, fat and skin layers) used for the simulations. Two muscles (M1 and M2) were simulated. Monopolar signals were acquired from a grid of electrodes of 16 rows and 3 columns (transverse and parallel to the muscle fibres, respectively). B) Cross-section of the volume conductor with indication of the location and dimension of the motor units (400 for each muscle). C) Example of simulated monopolar signal, showing the raw EMG and the contribution of each of the two muscles recorded by a linear array in the transverse direction with respect to the muscle fibres.

muscle. In practice, we are interested in estimating the correct MNF from the target muscle, which is the one under the detection channel (i.e., M1 for channels 1-8 and M2 for channels 9-16, in the transverse direction).

- Possibility of reducing the bias in CV estimation. The three monopolar signals aligned to the muscle fibres were used to estimate CV by a multi-channel spectral matching algorithm applied to epochs of duration 250 ms. The reference CV was estimated from the simulated signals from each muscle considering the channels placed over it. The performance of the inverse modelling approach was measured as the mean absolute difference between the reference CV and the one obtained using the original signal after removing the estimated crosstalk.

III. RESULTS

Some preliminary tests of the performances mentioned above are here shown. Specifically, Figures 2 and 3 indicate the accuracy in estimating the signals from the target and crosstalk muscles, the possibility of quantifying crosstalk (in terms of percentage RMS amplitude of the two muscles) and the reduction of bias in MNF and CV estimation.

Figure 2 shows an example of EMG processing on a signal including contributions of the two muscles at 50% of their MVC. The percentage RMSs of the two muscles (both simulated and estimated signals considered) are shown in 2A as functions of the transverse position. This indicates the possibility of quantifying the contributions of the target and crosstalk muscle and of compensating for a bias in amplitude estimation from the target muscle. The estimation of MNF is shown in 2B. Notice that an about constant value is obtained using the raw EMG, as the contributions of the two muscles are not discriminated. Some mistake is found in estimating

MNF of the signal from the muscle under the detection point in the region in which the two muscles are close (between channels 6 and 11). This mistake is removed considering the processed signal. Portions of signals are shown in 2C. Notice that the error in estimating the contribution from a muscle is lower when the detection channel is close to such a muscle and far from the other, and vice versa. This property justifies the problems in estimating RMS and MNF of the contribution from a muscle far from it, shown in 2A and 2B.

Figure 3 shows an example of estimation of CV of the target muscle (i.e., the one under the considered electrodes). Some portions of signals from the central channels are shown in 3A: notice that some MUAPs are visible in all channels, but they should be considered either as signal or as crosstalk. For example, the MUAPs indicated with a rectangle and an ellipse are visible in all channels, but they are produced by M1 and M2, respectively. The ability of the algorithm to discriminate the contributions of the two muscles improves far from the region in which they are close (as shown in 3B). Indeed, the channels number 8 and 9 are only 2.5 mm from the plane separating the two muscles (indicated by $x = 0$ in Figure 1B), so that part of the signal could be misinterpreted as a contribution of both muscles. This hampers the estimation of CV from those channels when using the proposed algorithm to remove crosstalk. Consider also that in such channels the contribution of crosstalk is mainly constituted by propagating components of MUAPs generated by MUs close to the electrodes. On the other hand, most crosstalk found in the other channels is due to non-propagating components (related to generation and extinction of action potentials). The removal of such a contribution is very important to reduce CV estimation bias.

IV. DISCUSSION

Crosstalk in surface EMG is an important problem which limits the reliability of many applications [1][2][3][4][5][6]. Different approaches have been proposed to measure, quantify and reduce it. However, no standard methodology is accepted and researchers usually rely on selective spatial filters, which face crosstalk by reducing the detection volume, thus focusing only on sources placed close to the detection point, which could be not representative of the overall activity of the target muscle.

In this work, a different method is proposed: estimating the contributions of the target and crosstalk muscles. This would in principle allow to quantify and to remove crosstalk. Hence, EMG descriptors, like amplitude, central frequency and CV, could be estimated more reliably, removing the bias induced by crosstalk. However, estimating the contributions of the different muscles is an unstable inverse problem. The signals are approximated using a limited number of sources (in this work, 90 sources were used to approximate the activity of 800 MUs). Moreover, close sources generate similar MUAPs which are difficult to discriminate. Finally, for all waveforms used by the inverse model, a CV equal to 4 m/s was considered. Additional problems, like additive noise or
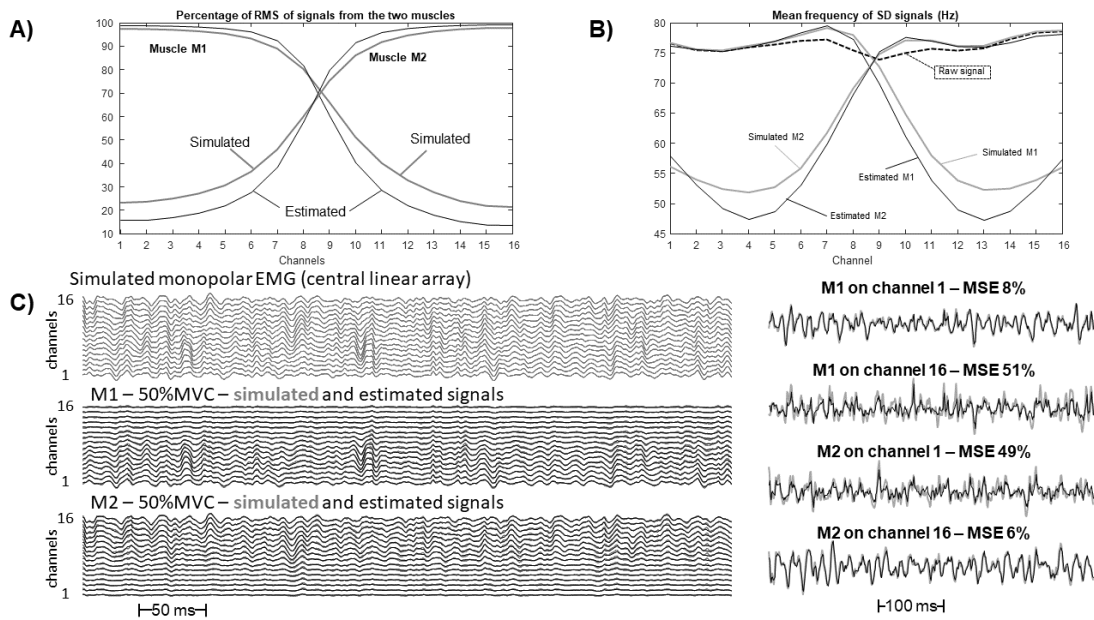
Fig. 2: Example of signal processing to estimate the contributions of the two muscles. A) Quantification of muscle crosstalk, in terms of the percentage of RMS of signals from the two muscles (central linear array in transverse direction). The mean error in estimating the percentage RMS of the muscle under the detection point (i.e., M1 for channels 1-8, M2 for channels 9-16) is 7.6% for the raw data and 2.6% for the processed signals (highly significant difference indicated by Wilcoxon signed rank test). B) Removal of the bias in the estimation of the mean frequency from single differential channels, estimated longitudinal to the muscle fibres (considering the first two electrodes closest to the innervation zone): the mean frequency obtained from the raw signal is compared to those obtained considering the simulated and estimated contributions from the two muscles. Mean error in estimating the mean frequency of the muscle under the detection point decreases from 4.4 to 2.1 Hz, after processing (with peak errors decreasing from 2.6 to 0.8 Hz, in the points close to the separation between the two muscles). C) Example of simulated monopolar signal, showing the raw EMG and the simulated and estimated contributions of each of the two muscles (central linear array in the transverse direction). Magnifications of the first and last channels are considered on the right, indicating the mean squared error (MSE) of the estimation of the contributions of each muscles.
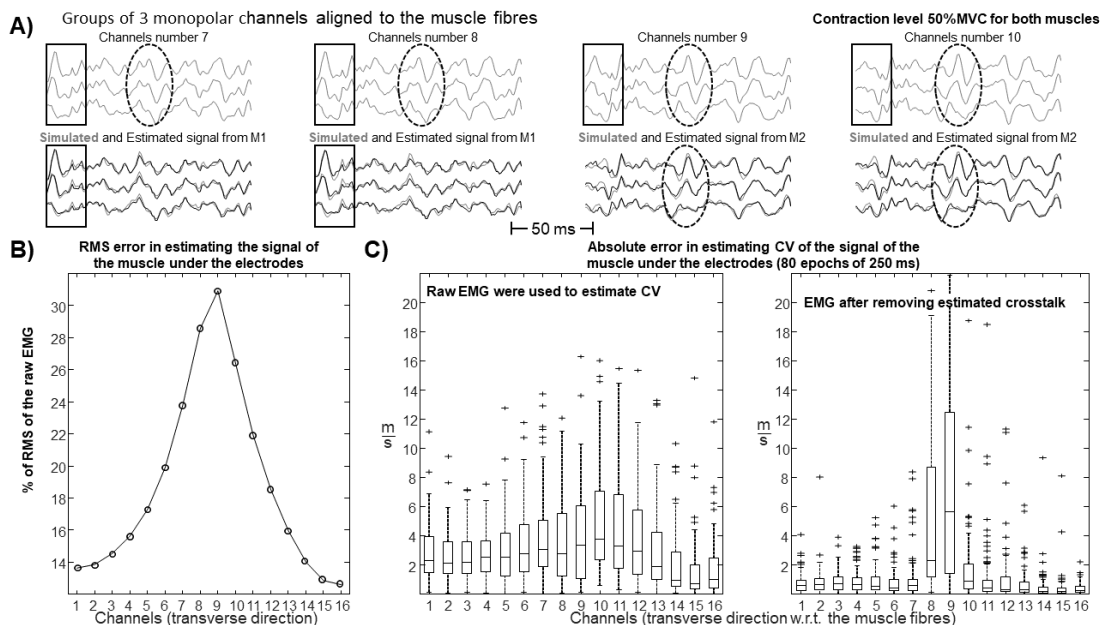
Fig. 3: Example of estimation of muscle fibre conduction velocity (CV) from either the raw EMG or the signals obtained after removing the contributions of the crosstalk muscles (i.e., the simulated/estimated signal of M2 was removed from channels 1-8, that of M1 from channels 9-16). A) Examples of data from channels close to the line of separation of the two muscles. B) RMS error in estimating the signal from the muscle under the channels normalized with respect to the raw signal. C) Absolute error in estimating CV of the signal of the muscle under the electrodes, considering either the raw EMG or the one obtained after removing the estimated crosstalk (median errors are 2.4 and 0.5 m/s for the raw and processed data, respectively; highly significant differences indicated by Wilcoxon signed rank test).

differences between the volume conductor used to simulate the basis waveforms and the EMG data, were neglected, as the algorithm was found to be stable in detecting the transverse location of the sources [21] (and hence, to discriminate the two muscles, which is of interest here).

Despite the objective difficulty of solving the problem, the proposed algorithm has provided reliable results, allowing to improve the estimation of RMS amplitude, MNF and CV (from electrodes which are at least about 10 mm distant from the crosstalk muscle). Only representative simulations are shown here, but additional tests with interference EMGs from both muscles with contraction levels in the range 10-100% MVC indicated that crosstalk may be reliably estimated in many conditions of practical interest. Specifically, the best estimations are obtained when the two muscles have similar force levels. For example, if the contribution of a muscle is not lower than the 30% of the other, the average error in quantifying the RMS due to crosstalk is lower than 10% and the estimations of MNF and CV of the target muscle have lower average errors than when using the raw data. In the opposite case, in which a muscle provides a much weaker contraction than the other, it produces a crosstalk which is difficult to estimate by the proposed algorithm (but it is also quite small, so that its effects are negligible).

REFERENCES

[1] F. Hug, "Can muscle coordination be precisely studied by surface electromyography?," J Electromyogr Kinesiol, vol. 21, pp. 1–12, 2011.

[2] N. Jiang, K.B. Englehart, P.A. Parker, "Extracting simultaneous and proportional neural control information for multiple-DOF prostheses from the surface electromyographic signal," IEEE Trans Biomed Eng, vol. 56, pp. 1070-80, 2009

[3] K. Mitchell Barr, A.L. Miller, K.B. Chapin, "Surface electromyography does not accurately reflect rectus femoris activity during gait: Impact of speed and crouch on vasti-to-rectus crosstalk," Gait & Posture, vol. 32, pp. 363-8, 2010.

[4] Yong-Ku Kong, M.S. Hallbeck, Myung-Chul Jung, "Crosstalk effect on surface electromyogram of the forearm flexors during a static grip task," J Electromyogr Kinesiol, vol. 20, pp. 1223-9, 2010

[5] R.A. Mezzarane, A.F. Kohn, "A method to estimate EMG crosstalk between two muscles based on the silent period following an H-reflex," Med Eng Phys, vol. 31, pp. 1331-6, 2009.

[6] I. Talib, K. Sundaraj, C.K. Lam, J. Hussain, M.A. Ali, "A review on crosstalk in myographic signals," Eur J Appl Physiol., vol. 119(1), pp. 9-28, 2019. Review.

[7] L. Mesin, "Crosstalk in surface electromyogram: literature review and some insights," Phys Eng Sci Med., 2020.

[8] L. Mesin, "Simulation of surface EMG signals for a multilayer volume conductor with a superficial bone or blood vessel," IEEE Trans Biomed Eng., vol. 55, pp. 1647-57, 2008.

[9] L. Mesin, S. Smith, S. Hugo, S. Viljoen, T. Hanekom, "Effect of spatial filtering on crosstalk reduction in surface EMG recordings," Med Eng Phys, vol. 31, pp. 374-83, 2009.

[10] I. Campanini, A. Merlo, P. Degola, R. Merletti, G. Vezzosi, D. Farina, "Effect of electrode location on EMG signal envelope in leg muscles during gait," J Electromyogr Kinesiol, vol. 17, pp. 515-26, 2007.

[11] M.M. Lowery, N.S. Stoykov, T.A. Kuiken, "A simulation study to examine the use of cross-correlation as an estimate of surface EMG cross talk," Journal of Applied Physiology, vol. 94, pp. 1324-34, 2003.

[12] D. Farina, L. Arendt-Nielsen, R. Merletti, B. Indino, T. Graven-Nielsen, "Selectivity of spatial filters for surface EMG detection from the tibialis anterior muscle," IEEE Trans. Biomed. Eng., vol. 50, pp. 354-64, 2003.

[13] C.J. De Luca, M. Kuznetsov, L. Donald Gilmore, S.H. Roy, "Interelectrode spacing of surface EMG sensors: Reduction of crosstalk contamination during voluntary contractions," J Biomechanics, vol. 45, pp. 555-61, 2012.

[14] L. Mesin, "Optimal spatio-temporal filter for the reduction of cross-talk in surface electromyogram," J Neural Eng., vol. 15(1), 016013, 2018.

[15] T.M. Vieira, A. Botter, S. Muceli, D. Farina, "Specificity of surface EMG recordings for gastrocnemius during upright standing," Sci Rep., vol. 7(1), 13300, 2017.

[16] A. Gallina, A. Botter, "Spatial localization of electromyographic amplitude distributions associated to the activation of dorsal forearm muscles," Front Physiol., vol. 4, 367, 2013.

[17] L. Mesin, "Volume conductor models in surface electromyography: Computational techniques, Comput. Biol. Med., vol. 43, pp. 942-52, 2013.

[18] L. Mesin, R. Merletti, "Distribution of electrical stimulation current in a planar multilayer anisotropic tissue," IEEE Trans Biomed Eng., vol. 55(2 Pt 1), pp. 660-70, 2008.

[19] C.M. Michel, M.M. Murray, G. Lantz, S. Gonzalez, L. Spinelli, R.G. de Peralta, "EEG source imaging," Clinical neurophysiology, 115:2195-222, 2004.

[20] M.A. Lopes, L. Junges, L. Tait, J.R. Terry, E. Abela, M.P. Richardson, M. Goodfellow, "Computational modelling in source space from scalp EEG to inform presurgical evaluation of epilepsy," Clin Neurophysiol., vol. 131(1), pp. 225-234, 2020.

[21] L. Mesin, "Real time identification of active regions in muscles from high density surface electromyogram," Comput Biol Med., vol. 56, pp. 37-50, 2015.

[22] A.J. Fuglevand, D.A. Winter, A.E. Patla, "Models of recruitment and rate coding organization in motor-unit pools," J. Neurophysiol., vol. 70, pp. 24702488, 1993.

Combining autoencoder and artificial neural network for classifying colorectal cancer stages

A. Brunetti[1,2], M. Caputo[1], T.M. Marvulli[1], G.D. Cascarano[1,2],
N. Altini[1], S. De Summa[3], and V. Bevilacqua[1,2]

[1] *Department of Electrical and Information Engineering, Polytechnic University of Bari, Bari, Italy*
[2] *Apulian Bioengineering srl, Via delle Violette 14, Modugno (BA), Italy*
[3] *Molecular Diagnostics and Pharmacogenetics Unit, IRCSS Istituto Tumori Giovanni Paolo II, Bari, Italy*

Abstract — **The genomics era produced a large amount of molecular data. Many efforts have been made in the last decade to sequence as many types of tumours as possible. The Genome Data Commons (GDC) is the largest repository of cancer molecular and clinical data. To date, the challenge is to use them to improve tumour classification and therapeutic approaches. Bioinformatics and data science became even more important to the aim to develop algorithms for translating genomic data into clinical practice. Colorectal cancer (CRC) is one of the deadliest malignancies in the world and, despite the therapeutic advances, much more is far from being known to better address patients.**

In the present study, we aimed to classify CRC tumour stages through gene expression data. Autoencoder and ANN are combined in a CRC grades classification framework based on gene expression. After performing differential expression analysis, we evaluated different strategies for features reduction. Since the autoencoder allowed to transform the feature space from 3213 genes to 64 features, it was used as input to an ANN. The robustness of the designed classifier was evaluated training and testing the ANN 250 times, randomly splitting data into training (80 %) and test (20 %) sets.

Results are reported as mean accuracy, sensitivity and specificity, showing about 84 % for accuracy, 89 % for sensitivity and 78 % of specificity.

In conclusion, the proposed approach could be useful in the molecular classification based on transcriptomic data of the pathological stages of CRC.

Keywords—**Autoencoder, Artificial Neural Network, Feature Reduction, Gene Expression, Colorectal Cancer.**

I. INTRODUCTION

COLORECTAL cancer (CRC) is the second leading cause of deaths due to cancer in the United States [1]. Adenocarcinomas included almost 95 % of all CRC subtypes (adenocarcinomas, carcinoid tumours, gastrointestinal stromal tumours, lymphomas and sarcomas). The pathologic stage of this malignancy results from the combination of clinical staging (physical exams, biopsies and imaging) and surgery information. American Joint Committee on Cancer (AJCC) developed the most used staging system, also called TNM system, which recapitulates the state of the primary tumour (T), of the regional lymph nodes (N) and metastasis (M) [2]. Stages range from I to IV, with increasing aggressiveness.

In the genomic era, the chance to identify genes, and thus biological mechanisms, able to discriminate pathological stages of CRC is still challenging for the improvement of the prognostic value of the pathological staging [3]. However, a large amount of molecular data is available to date. In particular, in 2006 National Cancer Institute and the National Human Genome Research Institute has begun a three-year pilot project on three cancer types (glioblastoma multiforme, lung, and ovarian cancer) bringing together several disciplines and institution in a cancer genomics program, called The Cancer Genome Atlas (TCGA). To date, TCGA produced over 2,5 petabytes of data, including 33 tumour types with multilayered data, namely mutational status, transcriptomic, CNV and methylation data and clinical information. Thus, the TCGA data portal (https://portal.gdc.cancer.gov/) is an authoritative source for cancer scientist to perform data mining. Recently, Huo *et al.* [4] were not able to identify a clear pattern of gene expression which could discriminate the four stages of CRCs, performing PCA of the differentially expressed genes between the four stages in the TCGA dataset.

In this work, we address the staging of colon cancer by combining a non-linear method for reducing the number of features, namely an autoencoder, with an Artificial Neural Network (ANN) for the final classification of the tumour.

II. MATERIALS AND METHODS

A. Data collection

The dataset is publicly available and can be downloaded from the GDC portal (Genomic Data Commons) web site. The GDC Data Portal is a robust-data-driven platform that allows cancer researches and bioinformaticians to search and download cancer data for analysis. The dataset was downloaded through GDC API (Application Programming Interface); setting different parameters, it is possible to return the result of a search or details about a specific entity. The GDC API uses JSON and standard HTTP methods. Communicating with the GDC API involves making requests to API endpoints which represent specific API functionality.

For this work, was used a Python application using a POST request following the GDC API User's Guide. For clinical data were used endpoints "cases", to find all files related to a specific case, and "files" to find all files with specific characteristics. To retrieve data, we filtered on "primary_site" = "Colon" and "project.program.name" = "TCGA". For gene data, we added the "files.data_type" = "Gene Espression Quantification" and "files.analysis.workflow_type" = " HTSeq – Counts" filters.

The dataset contained information of about 458 patients. Clinical data included information about age at diagnose, days to last follow-up, primary diagnosis, prior malignancy, site of resection or biopsy, tissue or organ of origin and tumour stage. Instead, gene data included 60483 gene expression level, including genes and their transcripts.

B. Data processing

Gene expression levels are organised in a count matrix whose rows represent genomic features, denoted by Ensembl Gene ID, and columns represent samples, denoted by Patient Case ID. The elements in this matrix for the statistical analysis are counts discrete non-negative integers for each gene in each sample.

For this analysis, patients were split according to the tumour stage in two classes: "low" for patients with tumour stage I or II, and "high" for patients with tumour stage III or IV.

The differential expression analysis of RNA-Seq data consists of normalising the raw counts and performing statistical tests to reject or accept the null hypothesis that two groups of samples show no significant difference in gene expression. The read count in RNA-Seq data has been found to be linear to the abundance of transcripts. However, the read count for a given gene depends not only on the expression level of the gene but also on the total number of reads sequenced and length of the gene transcript.

The normalisation technique used consists of computing the effective library size by considering a factor for each sample. By dividing each sample's counts by the corresponding size factors, we bring all the count values to a common scale, making them comparable. To estimate the size factors, we considered the median of the ratios of observed counts to those of a pseudo-reference sample, whose counts can be obtained by considering the geometric mean of each gene across all samples [5].

Then, to transform the observed counts to a common scale, the observed counts in each sample were divided by the corresponding size factor.

In order to better characterise the data, the mean and the dispersion of normalised counts were considered. Then, was examined the difference in gene expression between the two conditions by calculating the Fold Change for each gene, namely the ratio between the counts in the "high" group over the counts in the "low" group.

To determine if gene expressions in the two conditions were statistically different, namely reject the null hypothesis that the two data samples come from distributions with equal means, we used the "*nbintest*" (Negative Binomial Distribution") function from the "Bioinformatics Toolbox" included in MATLAB (release 2019b) [6].
The '*VarianceLink*' criterion used, namely the linkage type between the variance and mean, was "*Local Regression*" since the dataset had more than 1000 rows and was overdispersed. The results are shown in Fig. 1. The output of the test includes a vector of *p*-values. A *p*-value indicates the probability that a change in expression as strong as the one observed would occur under the null hypothesis, namely the conditions have no effect on gene expression.

Considering the obtained *p*-values, we observed an enrichment of low values (due to differentially expressed genes), whereas the others were uniformly spread (due to non-differentially expressed genes).

Then, we filtered out those genes with relatively low count to observe a more uniform spread of non-significant *p*-values across the range [0,1].
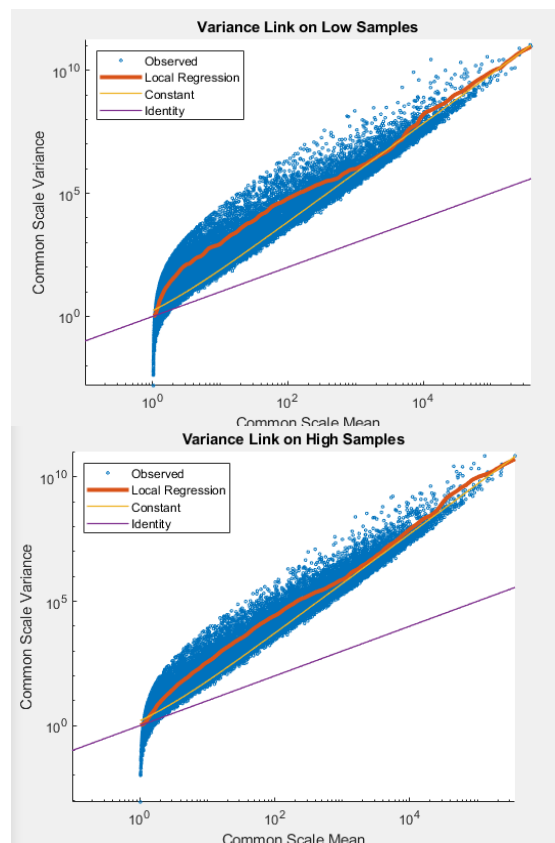

Fig. 1. Plot of Variance Link of two classes

Finally, to derive the significant genes, we used the MATLAB function "*mafdr*" (*Microarray False Discovery Rate*), which returns a positive false discovery rate for each feature. In this case, the Benjamini-Hochberg, a linear step-up procedure that provides an adjustment of the *p*-values, was used, so the probability of observing at least one significant result due to chance remains below the desired significance level [7]. The obtained results are reported in Fig. 2. The threshold for this analysis was set to 0.1, equivalent to consider 10 % of false positives as acceptable, identifying the genes that are significantly expressed by considering all the genes with adjusted *p*-values below this threshold.
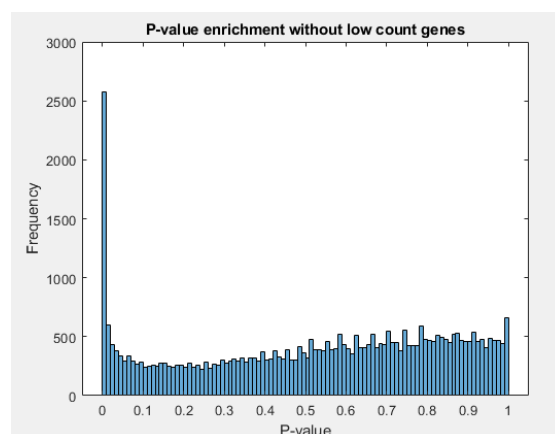

Fig. 2. Histogram after filtered of genes with relatively low counts

Through this analysis, we obtained 3123 genes which resulted relevant for the classification of the two classes of "high" and "low" patients.

C. Features extraction

After the data processing phase, 3213 genes revealed to be differentially expressed respect to the tumour stage. Before any feature processing, the dataset was normalised with z-score normalisation technique.

In order to reduce the number of features, we investigated a linear approach based on Principal Component Analysis (PCA). Analysing the cumulative explained variance of the transformed feature space, reported in Fig. 3, and considering those components accounting at least 90 % of the variance, we obtained a reduced dataset constituted by 295 features.
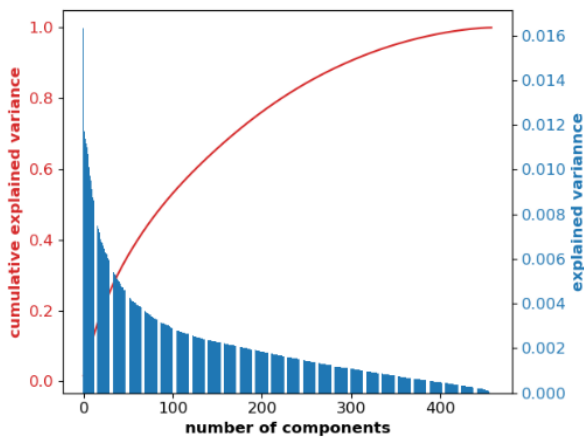
Fig. 3. PCA explained variance representation. Bar plot shows the explained variance for each component; Line plot, instead, shows the cumulative explained variance.

Since after PCA the number of features was still high, in order to further reduce the features space, a non-linear method for transforming the features was investigated. In this work, we designed and developed a stacked autoencoder in order to use data from the encoded layer as the new representation of the feature space.

Autoencoders are Artificial Neural Networks whose aim is to copy their inputs to their outputs, by creating a latent and compressed features space representation [8]. Several tasks involving the biomedical signal analysis make use of autoencoders, or Deep Learning strategies in general [9]. Autoencoders are trained by an unsupervised algorithm and use the backpropagation algorithm for weights updating in order to minimise a cost function.

From a topological point of view, a stacked autoencoder consists of multiple layers of neurons where the output of each hidden layer is connected to the input of the successive hidden layer (Fig. 4). According to this approach, the representation coming from the "Encoded Layer" was used as input in the subsequent step for discriminating between low and high levels of the tumour.

In this work, the encoder of the stacked autoencoder was constituted by an input layer with 3213 neurons, three hidden layers, with 2000, 1000 and 500 neurons respectively, and one encoded layer with 64 neurons. The decoder topology is obtained by reversing the hidden layers of the encoder. For all the layers, the hyperbolic tangent function was used.
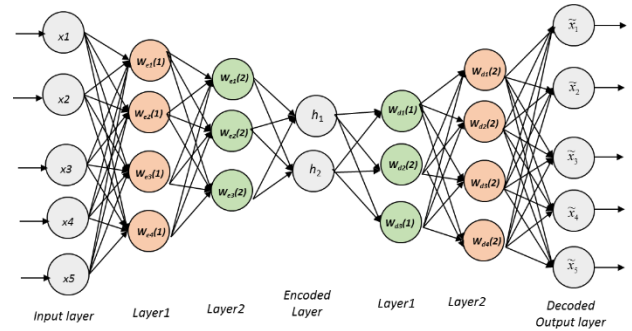
Fig. 4. Representation of an autoencoder

D. Classification

To perform the classification, we used an Artificial Neural Network processing the dataset reduced to 64 features. Specifically, the dataset was constituted of 458 samples, 354 were labelled as "low", whereas "104" as high.

Since data were unbalanced between the considered classes, the Adaptive Synthetic (ADASYN) sampling approach was performed for over-sampling the minority class [10], namely the "high" class; thus, the final dataset contained 346 samples labelled as "high".

The ANN architecture was fully-connected, constituted by 2 hidden layers with 16 and 8 neurons, respectively. The hyperbolic tangent function was used for all the neurons in the hidden layers. The output layer, instead, included 2 neurons characterised by the softmax function. The training algorithm was ADAM (Adaptive Moment estimation) [11], whereas the cost function was the Cross-Entropy loss, computed for two classes.

The performances of the ANN classifier were evaluated considering the Accuracy (Eq. 1), Sensitivity (Eq. 2) and Specificity (Eq. 3), considering Positive (P) a sample labelled as "high", Negative (N) a sample labelled as "low", and True Positives (TP), True Negatives (TN), False Positives (FP) and False Negatives (FN) according to the Confusion Matrix reported in Table I.

$$Accuracy = \frac{TP + TN}{TP + TN + FP + FN} \quad (1)$$

$$Sensitivity = \frac{TP}{TP + FN} \quad (2)$$

$$Specificity = \frac{TN}{TN + FP} \quad (3)$$

TABLE I
CONFUSION MATRIX FOR EVALUATING THE CLASSIFICATION APPROACH

		True Condition	
		Positive	*Negative*
Predicted	*Positive*	TP	FP
Condition	*Negative*	FN	TN

In order to evaluate the robustness of the implemented approach, the ANN model was trained and tested 250 times, randomly splitting the dataset into a training set (80 % of the samples) and test set (the remaining 20 %). At each iteration, also the synthetic samples were randomly generated to balance the number of samples for the two classes.

III. RESULTS

Results are reported in terms of mean values of Accuracy, Sensitivity and Specificity. Table II and Table III report the obtained Confusion Matrices for the training and test sets, respectively. The matrices contain the normalised mean values (± standard deviation) for TP, TN, FP and FN.

TABLE II
NORMALISED CONFUSION MATRIX OBTAINED FOR THE TRAINING SET

		True Condition	
		Positive	*Negative*
Predicted	*Positive*	0.494 ± 0.011	0.002 ± 0.006
Condition	*Negative*	0.001 ± 0.004	0.503 ± 0.011

TABLE III
NORMALISED CONFUSION MATRIX OBTAINED FOR THE TEST SET

		True Condition	
		Positive	*Negative*
Predicted	*Positive*	0.440 ± 0.041	0.111 ± 0.031
Condition	*Negative*	0.053 ± 0.023	0.396 ± 0.042

Fig. 5 and Fig. 6 show the Receiving Operating Characteristic (ROC) curve for the training and test set, respectively. Based on the reported confusion matrices, the Accuracy, Sensitivity and Specificity on the test set are 0.836, 0.893 and 0.781, respectively, showing good classification performance. Regarding the Area Under the Curve (AUC), instead, the obtained values for the test set (AUC = 0.89 ± 0.03) revealed the robustness of the implemented classifier, regardless of the dataset permutation used for training or test.
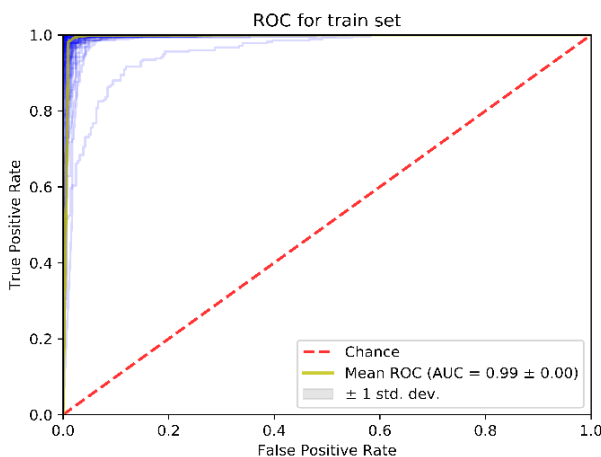
Fig. 5. ROC curve for the training set
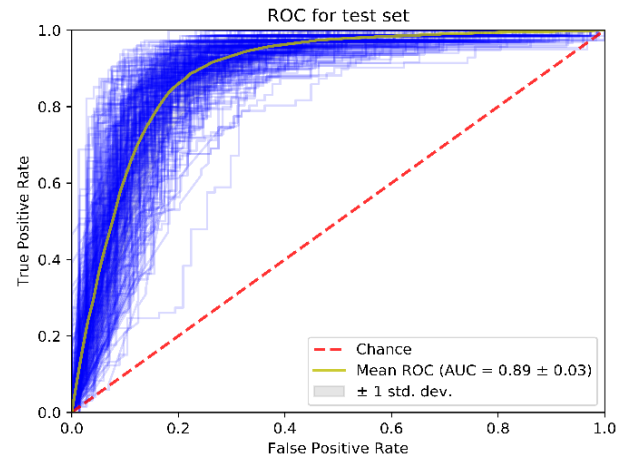
Fig. 6. ROC curve for the test set

IV. CONCLUSION

The results of the present paper showed how it could be possible to discriminate early and late stages CRC samples through transcriptomic data. Clinically speaking, this approach grants the possibility to identify patients that have to be treated with neo-adjuvant or adjuvant chemotherapeutic regimen. Notably, through this method, pathological staging could be performed from biopsies. More interestingly, the analytical framework presented in this paper should be considered in other case studies, not only CRC or more generally tumours. Indeed, the field of application of such a method is open to any biological question regarding molecular-based classifications.

REFERENCES

[1] "Cancer Statistics, 2017. - PubMed - NCBI." .
[2] "AJCC Cancer Staging Manual 7th edition criteria for colon cancer: do the complex modifications improve prognostic assessment? - PubMed - NCBI." .
[3] "The Eighth Edition AJCC Cancer Staging Manual: Continuing to build a bridge from a population-based to a more 'personalized' approach to cancer sta... - PubMed - NCBI." .
[4] T. Huo, R. Canepa, A. Sura, F. Modave, and Y. Gong, "Colorectal cancer stages transcriptome analysis," *PLoS One*, vol. 12, no. 11, Nov. 2017.
[5] S. Anders and W. Huber, "Differential expression analysis for sequence count data," *Genome Biol.*, 2010.
[6] J. C. Marioni, C. E. Mason, S. M. Mane, M. Stephens, and Y. Gilad, "RNA-seq: An assessment of technical reproducibility and comparison with gene expression arrays," *Genome Res.*, 2008.
[7] Y. Benjamini and Y. Hochberg, "Controlling the False Discovery Rate: A Practical and Powerful Approach to Multiple Testing," *J. R. Stat. Soc. Ser. B*, 1995.
[8] J. Schmidhuber, "Deep learning in neural networks: An overview," *Neural Networks*, vol. 61, pp. 85–117, Jan. 2015.
[9] D. Buongiorno, G. D. Cascarano, A. Brunetti, I. De Feudis, and V. Bevilacqua, "A Survey on Deep Learning in Electromyographic Signal Analysis," in *Lecture Notes in Computer Science (including subseries Lecture Notes in Artificial Intelligence and Lecture Notes in Bioinformatics)*, 2019.
[10] H. He, Y. Bai, E. A. Garcia, and S. Li, "ADASYN: Adaptive synthetic sampling approach for imbalanced learning," in *Proceedings of the International Joint Conference on Neural Networks*, 2008.
[11] D. P. Kingma and J. Ba, "Adam: A Method for Stochastic Optimization," *CoRR*, vol. abs/1412.6, 2014.

Development of a compliance-matching biohybrid vascular graft through an integrated approach.

E. Pederzani[1], A. Caimi[1], M. Pezzotta[1], A. Caldiroli[1], M. Lupacchini[1], M. Tironi[2], F. Sangalli[2], M. Figliuzzi[2], N. Azzollini[2], S. Fiori[2], F.G. Greco[3], E. Votta[1], G.B. Fiore[1], A. Remuzzi[4], S.A. Riboldi[3], M. Soncini[1], A. Redaelli[1]

[1] Department of Electronics, Information and Bioengineering, Politecnico di Milano, Italy
[2] Istituto di Ricerche Farmacologiche Mario Negri - IRCCS, Italy
[3] Bioengineering Laboratories S.r.l., Italy
[4] Università degli Studi di Bergamo, Italy

Abstract - The aim of this work is to evaluate the effects of compliance mismatch on vascular prosthesis failures. For this reason, we carried out a preliminary *in vitro* characterization of rat vessels and of compliance-tuned grafts. After this first experimental assessment, synthetic grafts are being implanted *in vivo* in order to evaluate the effects of compliance-matching and compliance-mismatching on the outcome of grafting. In parallel to the implant in the animal model, *in silico* characterization of graft-vessel interactions is performed, whose outputs (wall stresses and shear stresses) will be correlated with the outcomes of *in vivo* experiments in terms of vessel's response.

Keywords - Arteriovenous fistula, arteriovenous graft, Silkothane®, vascular prosthesis, haemodialysis.

I. Introduction

Patients undergoing chronic haemodialysis, 2.2 million patients worldwide, need a vascular access to connect the vascular system to an external dialysis equipment [1]. However, clinically available options for long-term haemodialysis accesses suffer from several drawbacks and are associated to high failure rates. One of the major causes of failure of synthetic grafts seems to be the compliance mismatch between the synthetic graft and the native vessel [2]. Innovative biohybrid arteriovenous grafts have been fabricated with tunable compliance to approach deformability observed *in vivo*. The grafts are three-layered tubular structures composed by inner and outer layers of electrospun silk fibroin and a core layer of Silkothane®, a blend of silk fibroin and polyurethane [3].
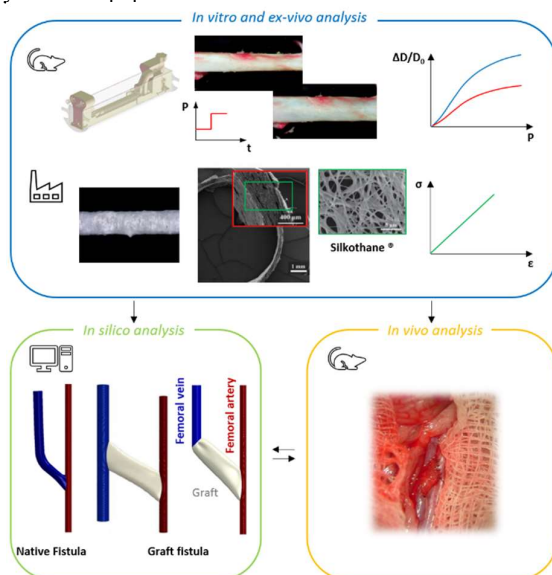
In this work, we developed an integrated workflow in order to couple synergistically *in-vitro*, *in-silico* and *in-vivo* approaches for the development of a strategy for the design of a compliance matching synthetic prosthesis (Figure 1). In order to study the effect of the graft-vessel compliance on the durability of the arteriovenous fistula (AVF), a comprehensive investigation of the possible damaging factors of the AVF integrity must be performed in an animal model (rat). Nevertheless, due to the lack of data available in literature for rat's abdominal aorta and vena cava, the *in-vitro* approach aims at developing an *ad-hoc* acquisition protocol and strategy to assess the biomechanics and the geometrical features of the native vessels and fabricated biohybrid grafts. Once detected, these values are used as input data for the *in-silico* analysis, in which different methodologies were exploited in order to virtually evaluate and predict the impact of the graft on the hemodynamics and on the biomechanical response of the entire arteriovenous graft (AVG) system. Finally, *in-vivo* strategy aims at assessing the durability of the AVG with the brand new biohybrid device, highlighting the effect of the compliance mismatch between the vessel and the graft and benefit of using more compliant grafts, and providing the data for the validation of the *in-silico* results and strategy.

II. Methods

A. Compliance measurements

We designed two systems for compliance measurements based on our previous experiences [4]-[5]: one optimized for tests in stationary conditions and the second one for dynamic evaluation.

A.1. Stationary System

First, we designed and prototyped an *ad hoc* versatile and compact device for stationary compliance measurements able to host native rat vessels and synthetic grafts of small caliber (Figure 2). The entire system is compatible with microscope and micro-CT experiments and compliant with the standards required for vascular grafts tests (temperature control, imposed pressure accuracy, image acquisition and analysis).

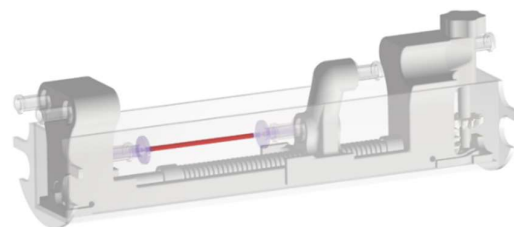Figure 1 Schematic representation of the proposed workflow.

Figure 2 Device for the stationary compliance measurements.

The sample holder manufactured by 3D printing technique (Ultimaker 3) in polylactic acid is inserted in a transparent external reservoir serving the fluidic circuit and keeping the sample wet. The sample holder is provided with two inlet and two outlet channels for the intraluminal and the extraluminal recirculation of the fluid. In order to obtain a complete fluid mixing to guarantee uniform temperature, the extraluminal inlet and outlet consist of six small channels. The holder allows the sample pretension by moving the sliding shoe on the right (Figure 2) using the knob, which acts on the worm screw under the sample by means of two bevel gear (2 mm every 360° of rotation of the knob).This system was used for testing native vessels from rats and biohybrid grafts of small caliber. Native tissue samples (abdominal aorta and vena cava) were harvested from 8-10 weeks MWF rats of 300 g.

Biohybrid grafts of small caliber were fabricated by electrospinning, using regenerated Bombyx mori silk fibroin (Innovhub) and the aromatic polycarbonate-urethane Carbothane™ AC-4075A (Lubrizol). Electrospinning parameters were optimized from [3] in order to obtain grafts with diameters around 1.5 mm and wall thickness of 0.15-0.3 mm. Three-layered conduits were generated by subsequently depositing on a rotating cylindrical collector (1.5 mm in diameter, 1000-2400 rpm rotational speed) three solutions: (i) a solution of silk fibroin 7% w/v in formic acid; (ii) a blend of 1% w/v silk fibroin and 3% w/v Carbothane™ in formic acid and dichloromethane (3:2 volume ratio) – referred to as Silkothane® in the text; (iii) a 7% w/v solution of silk fibroin in formic acid. Following washing and crystallization in ethanol/demineralized water solutions, removal of the meshes from the collector and vacuum drying at room temperature (4 h, 15 torr), Silkothane® grafts were sterilized by means of ethylene oxide, and stored at room temperature in dry conditions. Three respective percentages of SF and PU, namely SF25PU75, SF50PU50 and SF75PU25, were used to produce three-layered samples to better highlight the influence of each component on the composite material.

Compliance measurements were performed under a stereo microscope (Nikon SMZ1000) equipped with a digital camera (5MP USB 2.0 Color CMOS C-Mount Microscope MU500) for the external diameter and thickness measurements. The thickness of the vessel is estimated from cross section images made at the ends of the vascular samples. Some preliminary tests were carried out also within micro-CT system, characterized by an isotropic resolution with a pixel spacing and slice thickness equal to 8.9 μm (Bruker) allowing measurements of the luminal deformations (on going tests). It was necessary to optimize the solution used as a contrast medium to avoid extravasation; a satisfactory result is obtained by using iohexol with 8% gelatin. Experiments were carried out at 37°C, the samples were pressurized from 0 to 150 mmHg with 10 mmHg increments (the pump's supply voltage is increased monitoring the pressure sensor until the desired pressure value is reached), acquiring a digital image at each pressure value or 3D reconstructions, in micro-CT.

An ad-hoc semi-automatic tool was developed in Matlab (Mathworks, Natick, USA), to measure the distribution of vessel diameters throughout the acquired volume, from 3D micro-CT and from 2D stereo-microscopic imaging data. After the extrapolation of the centerline of the vessel, the images of the cross-sections were extracted and binarized to discriminate the region of interest and to extract the profile of the studied

structure. In order to avoid localized irregularities, due to imaging artifacts, the contour was fitted with spline and 4th order Fourier function.

A.2. Dynamic System
In parallel, we have developed a versatile device for dynamic compliance measurements to host both small and medium caliber vessels/grafts.

Figure 3 Device for the dynamic compliance measurements.

The dynamic system (Figure 3) was conceived in order to perform experiments in accordance with the specifications of the vascular graft tests regulation (ISO 7198:2016). The design of the fluidic circuit for medium recirculation follows the same strategy of the stationary system, except for the possibility to close completely the sample holder chamber with an additional transparent cover for running tests under extraluminal pressure conditions. The geometry and the size of the fluidic channels are optimized to allow the pressure measurements of the sample in dynamic conditions. A cable gland is integrated in the device to fix the sample connector in the position associated with the desired tension state (0.294 – 0.588 N), as required by the regulation. An Arduino-based electronic interface enabling the pressurization of the graft was developed to implement the dynamic regime: it allows to digitally reproduce a sinusoidal waveform variation of the voltage that supplies the pump and, at the same time, reading the pressure signal inside the sample by the use of a pressure sensor.

Fourteen grafts with different percentages of Silkothane® compositions layer (SF25PU75, SF50PU50 and SF75PU25) were tested within dynamic system, using a high-speed camera Phantom® Miro™ (640x480, 200fps) to record high-speed videos of the pressurized samples, which were subsequently elaborated to extract diameter's values.

B. In silico analysis
B.1. Vessel Characteristics
Since the impossibility to perform the AVF between the cava vein and the abdominal aorta in the rat, due to huge problem of the hemodynamics of the inferior part of the body, it has been planned to perform the *in-vivo* AVF in the femoral position, i.e. between the femoral artery (FA) and the femoral vein (FV). Nevertheless, the very tiny dimensions of the femoral vessels (less than 100 μm for the thickness) make the *in-vitro* measurements impractical; hence the *in-vitro* data extracted from cava veins and abdominal aortas were used.

The mechanical characteristics, i.e. Young Modulus (E), of the FA and FV, were reported in Table 1. Concerning the arterial side, E was calculated in the pressure range between 80-110 mmHg. While, for the venous side, two different moduli were defined according to two different pressure working regimes, since, after the anastomosis, the rat FV blood pressure rises from 10 mmHg (i.e., average venous pressure) to the arterial pressure regime [6]. Hence, in the proposed numerical model two different mechanical working conditions were defined.

The first one to take into account the arterialization process, while the second one to represent the hypertensive scenario experienced by the femoral vein after the surgical connection.

TABLE 1

	E [MPa]	ν [-]	Density [g/cm3]
FV (arterialization)	0.3	0.4[a]	1.10[c]
FV (post-arterialization)	1.4	0.4[a]	1.10[c]
FA	0.8	0.4[b]	1.10[c]

[a-b]FV and FA Poisson Ratios according to [7] and [8]
[c]Material density according to [9] for the vein and the artery.

The geometrical characteristics of the FV and AV of the rat (average weight of 300g) were extracted from the literature and reported in Table 2.

TABLE 2

	Diameter [mm]	Thickness [mm]
FV	0.75[a]	0.06[c]
FA	0.52[b]	0.06[d]

[a-c] Diameter and thickness of the FV according to [10] and [11]
[b-d] Diameter and thickness of the AV according to [12] and [13]

Regarding the biohybrid graft composed of Silkothane® the crucial information where reported in Table3.

TABLE 3

Diameter [mm]	1.5[a]
Thickness [mm]	0.1[a]
E [MPa]	4.0[b]
ν [-]	0.4[c]
Density [g/cm3]	0.42[b]

[a] Diameter and Thickness were obtained as described in the section A of the methods
[b] Mechanical properties according to [3]
[c] Silkelastograft Poisson's ratio according to [3]

B.2. Simulation set up

Three different cases were studied. In addition to the native AVF, two different arteriovenous graft (AVG) geometries were considered, i.e. the Y and Z configuration: the first case the graft is anastomosed end-to-end to the vein and end-to-side to the artery (Y AVG); the second case, the graft is anastomosed end-to-side for both compartment (Z AVG).

The three fluid-structure interaction (FSI) models of the different cases were developed through a protocol composed of different steps (Figure 4). The undeformed geometry of the vessels and the graft were created in ANSYS Design Modeler (v.17.2, ANSYS, Inc, Canonsburg, PA), following the geometrical features reported in Table 2 and 3, while the mechanical properties of the different parts were assigned according to the data reported in Table 1 and 3 (Figure 4a-4b). To mimic the final configuration of the fistula, the anastomoses were reproduced through structural finite element (FE) simulation, exploiting Abaqus/Explicit v.6.14 (Dassault Systèmes, Vèlizy-Villacoublay, France). The extremities of the vessel/graft were displacement driven towards the junction points derived through an *ad-hoc* Matlab code (Figure 4c). The sutured walls were imported in MeshMixer (Autodesk, Inc) to create the volume of the fluid domain which was coupled to the structural one in ANSYS Workbench v.17.2. Subsequently, a preliminary FSI simulation was performed to reproduce the vein arterialization process by applying a velocity ramp (i.e., 0÷7 cm/s) and pressure ramp (10÷80mmHg) on the fluid domain inlet and outlet, respectively (Figure 4d). In the case of the Z-AVG configuration, the venous inlet was considered as a constant

mass-flow rate inlet. Since it was demonstrated that numerical instabilities can be established from the coupling between FSI approach and lumped parameter model [14], auxiliary CFD simulations, performed in ANSYS Fluent v.17.2, were performed to compute the outlet pressure waveforms to be included into the final FSI model (Figure 4e). In order to obtain pressure information pertaining to the whole cardiac cycle, which ranges from 80 to 100mmHg, three-element RCR Windkessel systems were implemented and applied to all the outlets of the fluid volume of the different configurations.

Once the arterialized configurations were obtained and the outlet pressures were computed, the final comprehensive FSI simulations were run (Figure 4f). In order to consider, the mechanical behavior of the vein at high pressure regime, the Young modulus of FV was changed as reported in Table1.
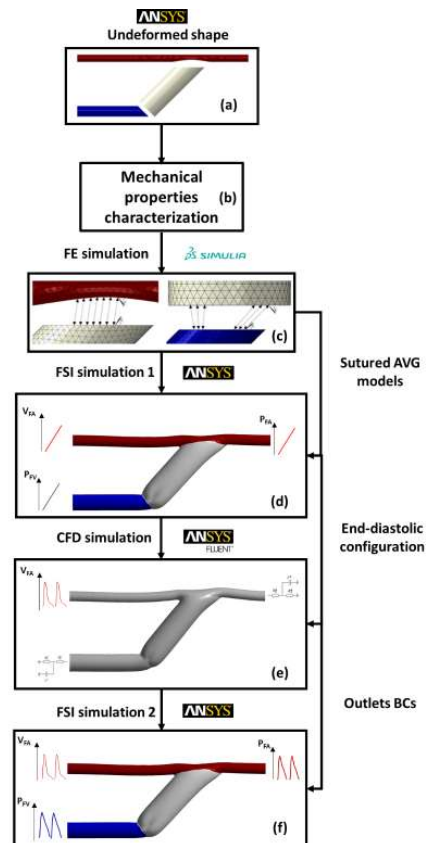

Figure 4 Workflow to perform FSI simulations.

III. RESULTS AND DISCUSSION

A. In vitro compliance measurements

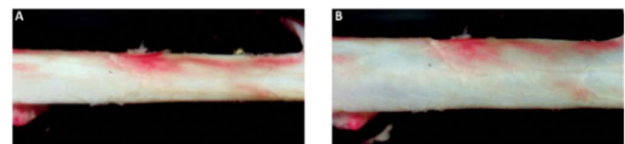Several tests were carried out on native rat vessels (Fig. 5-6).

Figure 5 (A) abdominal aorta at 0 mmHg; (B) abdominal aorta at 150 mmHg.

Abdominal aortas (n=9) from rats showed compliance values of 30.2±4.9, 14.7±1.5, 7.4±1.5%1/100 mmHg in hypo- normo- and hyper-tension ranges, respectively. Vena cava (n=7) showed compliance values of 54.5±33.3 and 32.9±16.9% 1/100 mmHg in 20-30 and 30-40 mmHg ranges.
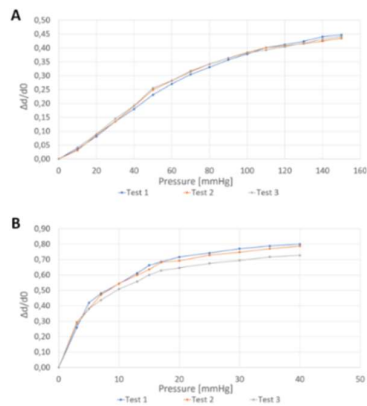
Figure 6 Normalized deformation *vs.* pressure for (A) aorta (B) vena cava.

Tests on the biohybrid grafts showed compliance values of about 2%, significantly lower than native tissues, but higher than traditional synthetic grafts. Even if the biohybrid scaffold does not resemble the native vessel compliance, a first *in vivo* implant in arterio-venous configuration was performed, as pilot test of further *in vivo* study; it was successful with a three-month follow-up denoting lumen patency and implant feasibility.

B. In silico results

The impact of the presence of the graft in the arteriovenous fistula was assessed from a mechanical and fluid-dynamical point of view (Figure 7-8).
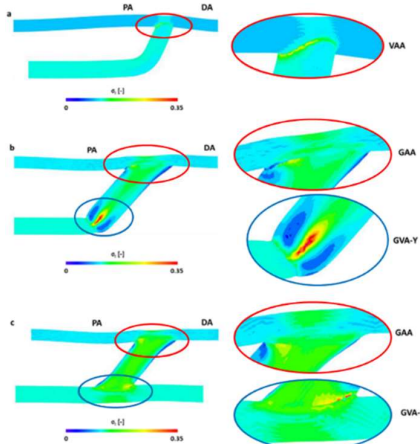
Figure 7 Maximum principal stress (σI) contours in the different configurations: (a) AVF, (b) Y-AVG, (c) Z-AVG. Zoom on the anastomoses (right). PA: proximal artery; DA: distal artery; VAA: vein-to-artery anastomosis; GAA: graft-to-artery end-to-side anastomosis; GVA-Y graft-to-vein end-end anastomosis GVA-Z: graft-to-vein end-to-side anastomosis.

The stress experienced by the system in the AVG is higher than the one experienced by the AVF (Figure 7). The Maximum principal stress (σ_I) achieved in the AVG, i.e. 0.278 MPa, is higher than the one calculated in the AVF, i.e. 0.181 MPa. The different stiffness of the synthetic graft compared to the vessels ones leads to a different mechanical response at the level of the anastomosis with the development of a high stress region. Parallel to the mechanical behavior, the fluid-dynamics changes between the configurations, not in term of velocity magnitude, but in terms of velocity pattern (Figure 8). In the AVG configurations the hemodynamics is visibly disturbed due to the presence of two wide recirculation regions. It can be noted how the flow entering the anastomoses from the proximal artery (PA) has a significant change in direction and

impinges on the opposite wall, creating swirling structures and secondary flows. In the AVF configuration disturbed flows can be detected, at the intradox region of the vein proximal to the artery.
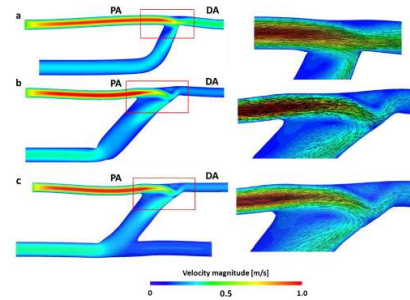
Figure 8 Fluid-dynamical results (left) in the Y AVF (a) and in the Y and Z AVG configurations (b-c) at the systolic peak. Velocity vector (right) corresponding to the vein-to-artery (a) and to graft-to-artery (b, c) end-to-side anastomoses. PA: proximal artery; DA: distal artery.

IV. CONCLUSION

The first experimental results demonstrate a fair possibility of modulating the compliance of the biohybrid graft produced varying the composition ratio; although further optimization manufacturing process is required. The on-going *in vivo* study, jointly with the results provided by the *in silico* tests, will provide a preliminary picture of the impact that compliance mismatch has in the prosthetic failure of these first implantations.

REFERENCES

[1] Radakovic D et al., A multilayered electrospun graft as vascular access for hemodialysis. PLoS One. 2017;12(10)
[2] Remuzzi A et al., Transitional Flow in the Venous Side of Patient-Specific Arteriovenous Fistulae for Hemodialysis. Ann. Biomed. Eng. 2016; 44(8):2388-401
[3] van Uden S. et al., A novel hybrid silk-fibroin/polyurethane three-layered vascular graft: towards in situ tissue-engineered vascular accesses for haemodialysis. Biomed Mater. 2019; 14(2), 025007.
[4] Piola M. et al., A compact and automated ex-vivo vessel culture system for the pulsatile pressure conditioning of human saphenous veins. JTERM 2016; 10(3): E204-E215.
[5] Piola M. et al., Full Mimicking of Coronary Hemodynamics for Ex-Vivo Stimulation of Human Saphenous Veins. Ann. of Biomed. Eng. 2017; 45(4): 884-897.
[6] Takase S. et al., Venous hypertension, inflammation and valve remodelling, Eur. J. Vasc. Endovasc. Surg. 2004; 28(5), 484-493.
[7] Weizsäcker H.W. et al., Passive elastic properties of the rat abdominal vena cava, Eur. J. Physiol. 1998; 412, 147–154.
[8] Weizsäcker H.W. et al., Passive elastic properties of the rat aorta, Biomedlzinische Tech. 1990; 35, 224–234.
[9] Caimi A. et al., Prediction of stenting related adverse events through patient-specific finite element modelling. J. Biomech. 2018; 79 135-146
[10] de Barros R.S.M. et al., Morphometric analysis of rat femoral vessels under a video magnification system, J. Vasc. Bras. 2017; 16(1), 73–76.
[11] Croatt A.J. et al., Characterization of a model of an arteriovenous fistula in the rat: The effect of L-NAME, Am. J. Pathol. 2018;176(5), 2530-2541.
[12] Kenwright D. et al., A Protocol for Improved Measurement of Arterial Flow Rate in Preclinical Ultrasound. Ultrasound Int. Open 2015; 1(2), E46–E52.
[13] Kasap M. et al., Morphometric analysis of dose-dependent effect of progesterone on experimental vasospasm-induced rat femoral arteries, Asian J. Neurosurg. 2018; 13(2), 271-276.
[14] de Villiers A.M. et al., A validated patient-specific FSI model for vascular access in haemodialysis, Biomechanics and Modeling in Mechanobiology. 2017; 17(2); 479-497

Correlation analysis of PRSA-based parameters during labor: a simulation study

M. Barbieri[1], T. Stampalija[1,2], M. W. Rivolta[3,*], and R. Sassi[3]

[1] *Unit of Fetal Medicine and Prenatal Diagnosis, IRCCS Burlo Garofolo, Trieste, Italy*
[2] *Dipartimento di Scienze mediche, chirurgiche e della salute, Università degli Studi di Trieste, Trieste, Italy*
[3] *Dipartimento di Informatica, Università degli Studi di Milano, Milan, Italy*
* Corresponding author: massimo.rivolta@unimi.it

Abstract—During labor, a fetus might suffer considerable stress due to uterine contractions (UCs). Based on results obtained on a near-term pregnant sheep model, UCs mimicked as complete umbilical cord occlusions (UCOs) significantly activate vagal response, making the fetal inter-beat time interval (FRR) to display a sawtooth-like shape, which can be modeled using a pair of exponential functions (for the growing and decaying fronts, respectively). In addition, acceleration and deceleration capacities (AC/DC) and deceleration reserve (DR) computed through Phase-Rectified Signal Averaging (PRSA) technique proved to be sensitive to acid/base balance (for a wide range of their parameters T and s). In this preliminary study, we used a mathematical model linking UCOs and FRR response to investigate, using synthetic series, whether AC, DC, and DR are correlated with the time constants of the exponential models. Also we verified how this relation is affected by different values of the parameter T (with $s = T$). We found that DC and DR were strongly correlated with the time constant describing the increase of FRR after the onsets of UCOs in the range $5 - 11$ (strongest correlation for DC was -0.87 at $T = 8$, while for DR -0.92 at $T = 10$, $p < 0.05$). AC was instead not significantly correlated with the decay time constant (likely to due the limited sample size available). This study motivates further investigations on PRSA related quantities and on the reasons behind their alterations during hypoxemia and metabolic acidosis.

Keywords—Fetal Heart Rate Variability (HRV) analysis, Labor, Phase-Rectified Signal Averaging (PRSA), Deceleration Reserve (DR)

I. INTRODUCTION

During labor, a fetus might suffer considerable stress due to uterine contractions (UCs) and head compression passing through the pelvic cavity, resulting in vagal stimulation and alterations of the fetal heart rate (FHR) [1]. The cardiotocography (CTG) is the most used monitoring system during labor to identify fetal compromise, and it is based on Doppler signal. However, CTG has some main limitations: 1) the low sampling frequency and the averaging process preclude finer analysis of FHR variability (FHRV); 2) although there is a strong association between some FHR patterns and the state of hypoxia/acidosis, overall CTG has low specificity and low positive predictive value to detect hypoxemia and/or metabolic acidosis; 3) finally, and of important clinical significance, CTG presents high intra and inter-observer variability and lack of quantitative assessment [2]. These limitations impact the rate of unnecessary interventions on one hand (cesarean sections or instrumental delivery), and lack of reduction of cerebral palsy and other labor-complications on the other side, representing, thus, an unresolved problem. The assessment of FHRV is the best available proxy of the autonomous nervous system (ANS) functional state. The nutrient deprivation and hypoxemia can pound on the ANS regulation of the cardiovascular system, affecting FHRV [3].

PRSA is a new methodology, proposed by Bauer *et al.* [4], capable of extracting quasi-periodic oscillations more resistant to non-stationarities, signal loss and artifacts. It provides two measures that quantify the average cardiac acceleration (AC) and deceleration (DC) capacity from a inter-beat time interval series (RR). This technique proved to be effective in the context of fetal monitoring when applied to CTG signals or fetal RR series (FRR). Our recent study [5] found that in fetal sheep exposed to repetitive umbilical cord occlusions (UCOs) - to mimic UCs - there is a high correlation between AC and DC and acid-base balance; particularly, AC and DC progressively increased during UCOs phases, suggesting an activation of ANS. AC and DC also achieved promising results in FHR monitoring, being capable to differentiate healthy fetuses and those with growth restriction [6], [7], [8].

Dissimilarities in AC and DC values arise when asymmetric increasing/decreasing trends appear in the signal, which is common during labor. Motivated by this consideration, we introduced the deceleration reserve (DR), a new and more predictive metric of measure for risk stratification during labor [9]. DR is given by the difference between DC and AC.

Regarding the mentioned animal model [5], we also found that at the beginning of each UCO, FRR increased progressively to quickly recover when pressure was released. Similarly, during an UC during labor, FRR increases analogously, as shown in Fig. 1(a). In [5], FRR response was modeled using an exponential model for both UCO and recover phases. These models were characterized by time constants, describing the speed of FRR adaptation (the higher the time constant is, the lower is the adaptation speed). Despite the remarkable results achieved by the aforementioned PRSA's parameters, it is not known yet what AC, DC, and DR actually measure. In this preliminary study, we hypothesized that AC, DC, and DR might estimate the time constants of the increasing and decreasing trends of heart rate response to UCO, and thus
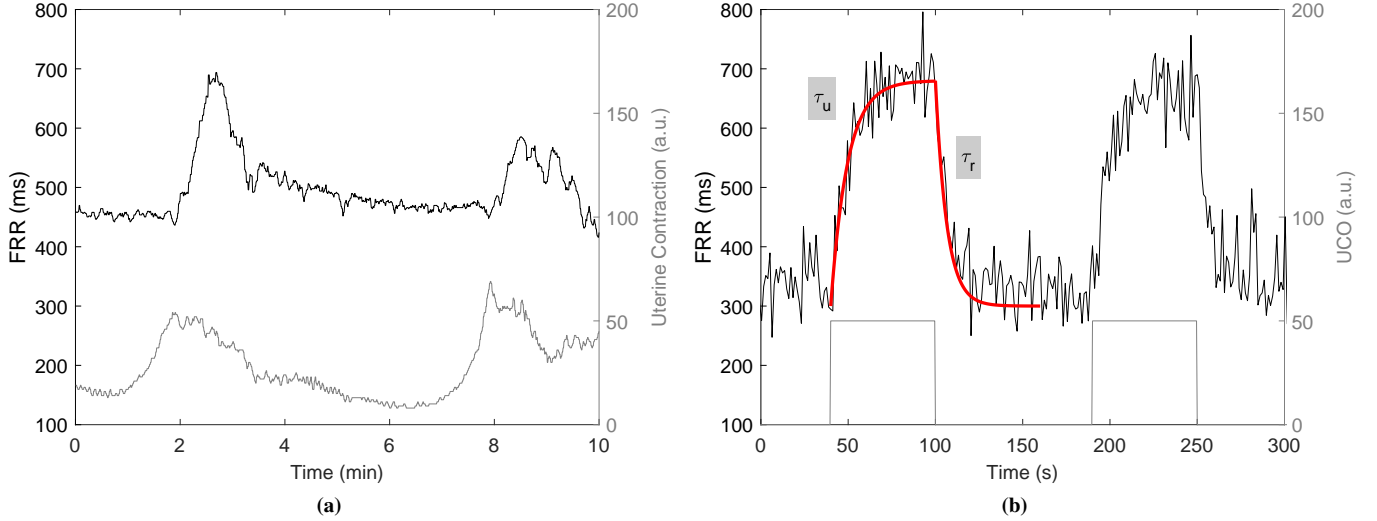
Fig. 1: Panel (a): Example of intrapartum human CTG-derived FRR series and its corresponding UC (light grey). Panel (b): Example of synthetic FRR series, UCO (light grey) and FRR response model (red).

characterize the response of the fetus to maternal contraction during labor.

II. METHODS

A. Background on PRSA and derived parameters

A complete description of the PRSA algorithm can be found in [4], [9]. Briefly, anchor points are first identified on the time series $x[k]$. Each time index k, where the sample $x[k]$ satisfies the condition

$$\frac{1}{T}\sum_{i=0}^{T-1}x[k+i] > \frac{1}{T}\sum_{i=1}^{T}x[k-i], \quad (1)$$

is inserted in the DC anchors' point list (for AC, the inequality sign must be flipped). Second, all the windows of $2L$ elements centered on each anchor point are aligned (anchor points are located at the $L+1$ sample) and then averaged, obtaining the PRSA series (a series of $2L$ elements).

From the PRSA series, AC and DC are then derived with

$$\text{DC (or AC)} = \sum_{i=1}^{s}\frac{\text{PRSA}[L+i]}{2s} - \sum_{i=0}^{s-1}\frac{\text{PRSA}[L-i]}{2s}. \quad (2)$$

DR is instead defined [9] as the sum of DC and AC (note that AC is a negative quantity for RR series).

B. The model

Synthetic FRR series were generated by adding White Gaussian Noise $w(t)$ to $y(t)$, the theoretical FRR response to the UCO $u(t)$, as in [10]. In particular, $y(t)$ was modeled with the following ordinary differential equation

$$\dot{y}(t) = -\tau_r^{-1}y(t) - (\tau_r^{-1} - \tau_u^{-1})u(t)y(t) + u(t), \quad (3)$$

where t is time, τ_u and τ_r the time constants of the growing and decreasing trends, respectively. When, $u(t)$ assumes only the values 0 or 1, the solution of (3) is the exponential function

$$y(t) = u(t)(1 - e^{-\frac{t}{\tau_u}}) + (1 - u(t))e^{-\frac{t}{\tau_r}}. \quad (4)$$

Finally, FRR is modelled with $x[k]$, which was built with

$$x[k] = 400y[k] + w[k] + 400, \quad (5)$$

where $y[k]$ and $w[k]$ are the discrete versions of $y(t)$ and $w(t)$, respectively. The variance of $w[n]$ was selected so that the signal-to-noise ratio was 10 db.

Fig. 1(b) shows a synthetic FRR signal and the corresponding UCO. The exponential model is superimposed.

C. The dataset

Seven 4-hour long FRR series were generated using the model described in sec. II-B. The UCO signal $u(t)$ was set to be a periodic square wave. In particular, 60 s of stimulation ($u(t) = 1$) followed by 90 s of rest ($u(t) = 0$) were repeated for the entire duration of the simulation.

Values of τ_u and τ_r were taken from [5], where the two time constants were estimated from an animal model of labor. Briefly, seven near-term pregnant sheep underwent to repetitive and complete UCOs. Occlusions were meant to mimic the fetal stress during the labor and lasted 60 s, then followed by a resting period of 90 s. The protocol ended when pH< 7.00 (measured through periodic blood samples) or up to 2 hours of stimulation. Fetuses were defined healthy prior the beginning of the stimulation protocol. Each UCO induced a heart rate deceleration resembling the time series reported in Fig. 1(b). From such time series, the two time constants τ_u and τ_r were estimated using a least square approach.

Given the fact the AC, DC, and DR are linearly dependent on the standard deviation of the input signal, we normalized the series to have unitary variance as in [9].

D. Statistical analysis

Correlation analysis was performed between AC vs τ_r, DC vs τ_u, and DR vs $\tau_u - \tau_r$, for T values in the range $1 - 50$, $s = T$, and $L = 50$. Correlations were considered statistically significant for p-values < 0.05.
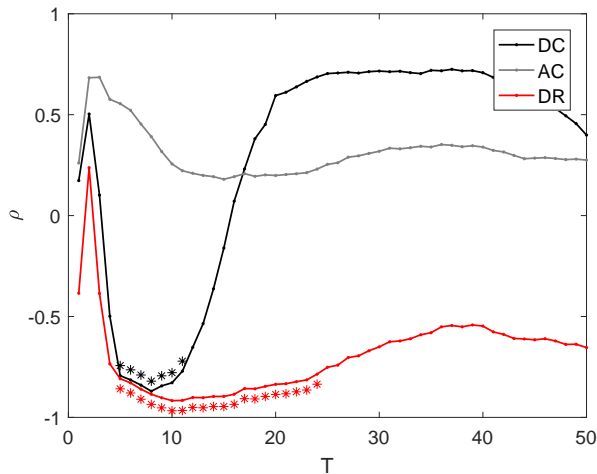
Fig. 2: Pearson's correlation coefficient ρ of AC vs τ_r, DC vs τ_u, and DR vs $\tau_u - \tau_r$. $*$ refers to statistically significant correlations ($p < 0.05$).

III. RESULTS

Figure 2(c) reports the Pearson's correlation coefficient ρ of the correlation analysis described in sec. II-D. We found that DC had a high statistically significant correlation with τ_u in the range $5 - 11$ of T ($s = T$), while DR had a larger span of significant correlations with $\tau_u - \tau_r$ in the range $5 - 24$. AC had no significant correlation with τ_r (likely due to the limited sample size).

IV. CONCLUSIONS

In this preliminary study, we determined that DC, DR, computed using PRSA were strongly correlated with the time constants of the FRR response to uterine contractions, for a wide range of T values.

Although the significant range for T we found was similar to the ones reported in [5], [6], further investigation is needed to determine the potential advantage of the use of these time constants in risk stratification along with PRSA's based parameters. The evaluation of the performance of these new metrics in identifying compromised fetuses during labor is still underway.

The main limitations of the study were two. First, the time constants available in the animal model were only seven, thus limiting the observation of further significant correlations (as in case of AC). Second, the sheep model comprised only normoxic fetuses. Extending the analysis to an hypoxic animal model might help in better guiding the selection of the T and s parameters, when DC or DR are used for risk stratification.

REFERENCES

[1] M. Y. Divon, Y. Muskat, L. D. Platt, and E. Paldi, "Increased beat-to-beat variability during uterine contractions: a common association in uncomplicated labor," *Am J Obstet Gynecol*, vol. 149, pp. 893–896, 1984.

[2] Z. Alfirevic, D. Devane, G. M. Gyte, and A. Cuthbert, "Continuous cardiotocography (CTG) as a form of electronic fetal monitoring (EFM) for fetal assessment during labour," *Cochrane Database Syst Rev*, vol. 2, p. CD006066, 02 2017.

[3] L. Bennet and A. J. Gunn, "The fetal heart rate response to hypoxia: insights from animal models," *Clin Perinatol*, vol. 36, no. 3, pp. 655–672, Sep 2009.

[4] A. Bauer, J. W. Kantelhardt, A. Bunde, P. Barthel, R. Schneider, M. Malik, and G. Schmidt, "Phase-rectified signal averaging detects quasi-periodicities in non-stationary data," *J Phys A*, vol. 364, pp. 423–434, 2006.

[5] M. W. Rivolta, T. Stampalija, D. Casati, B. S. Richardson, M. G. Ross, M. G. Frasch, A. Bauer, E. Ferrazzi, and R. Sassi, "Acceleration and Deceleration Capacity of Fetal Heart Rate in an In-Vivo Sheep Model," *PLoS ONE*, vol. 9, no. 8, p. e104193, 2014.

[6] T. Stampalija, D. Casati, M. Montico, R. Sassi, M. W. Rivolta, V. Maggi, A. Bauer, and E. Ferrazzi, "Parameters influence on acceleration and deceleration capacity based on trans-abdominal ECG in early fetal growth restriction at different gestational age epochs," *Eur. J. Obstet. Gynecol. Reprod. Biol.*, vol. 188, pp. 104–112, May 2015.

[7] S. Tagliaferri, A. Fanelli, G. Esposito, F. G. Esposito, G. Magenes, M. G. Signorini, M. Campanile, and P. Martinelli, "Evaluation of the Acceleration and Deceleration Phase-Rectified Slope to Detect and Improve IUGR Clinical Management," *Comput Math Methods Med*, vol. 2015, pp. 1–9, 2015.

[8] S. M. Lobmaier, N. Mensing van Charante, E. Ferrazzi, D. A. Giussani, C. J. Shaw, A. Müller, J. U. Ortiz, E. Ostermayer, B. Haller, F. Prefumo, T. Frusca, K. Hecher, B. Arabin, B. Thilaganathan, A. T. Papageorghiou, A. Bhide, P. Martinelli, J. J. Duvekot, J. van Eyck, G. H. Visser, G. Schmidt, W. Ganzevoort, C. C. Lees, K. T. Schneider, C. M. Bilardo, C. Brezinka, A. Diemert, J. B. Derks, D. Schlembach, T. Todros, A. Valcamonico, N. Marlow, and A. van Wassenaer-Leemhuis, "Phase-rectified signal averaging method to predict perinatal outcome in infants with very preterm fetal growth restriction- a secondary analysis of TRUFFLE-trial," *Am J Obstet Gynecol*, vol. 215, pp. 630.e1–630.e7, 2016.

[9] M. W. Rivolta, T. Stampalija, M. G. Frasch, and R. Sassi, "Theoretical value of deceleration capacity points to deceleration reserve of fetal heart rate," *IEEE Trans Biomed Eng*, vol. 95, 2019.

[10] M. W. Rivolta, T. Stampalija, D. Casati, E. Ferrazzi, A. Bauer, and R. Sassi, "A Methodological Assessment of Phase-Rectified Signal Averaging through Simulated Beat-to-Beat Interval Time Series," *Comput Cardiol*, vol. 41, pp. 601–604, 2014.

Falls and prostheses in patients with transfemoral amputation

P. Palumbo[1], S. Moscato[1], F. Caterini[1], A. Miccio[2], L. Casagli[2], A. Davalli[2], P. Randi[2], and L. Chiari[1,3]

[1] Department of Electrical, Electronic, and Information Engineering "Guglielmo Marconi", University of Bologna
[2] INAIL Prosthesis Centre, Budrio
[3] Health Sciences & Technologies CIRI, University of Bologna

Abstract—**The evidence about the clinical efficacy of lower limb prostheses, especially regarding fall risk, is scant. Here we present some findings from a retrospective study conducted on the archive of a large centre for prosthesis fitting and rehabilitation. Fall risk is analysed on transfemoral amputees in relation to their clinical profile and their prosthetic knees.**

Keywords—**Amputees, prostheses, falls, knees**

I. INTRODUCTION

Lower limb loss is a severe condition affecting about 300,000 persons in Italy. The estimated annual incidence of lower limb amputation is around 20 new cases per 100,000 inhabitants, with considerable differences from country to country. Among diabetic patients, the incidence is about 10 times higher than the general population. [1]–[4].

Patients with lower limb amputations suffer of mobility restrictions and increased risk of falling. More than half of this population fall at least once every year [5], [6]. The fall rate is even higher within rehabilitation hospital wards. Different intrinsic risk factors for falls have been identified so far, although generally on small populations. Above knee amputees have higher fall risk than below knee patients [7], [8].

Lower limb amputations may be due to several conditions: e.g. peripheral artery disease (PAD), diabetes, infections, cancer, trauma, or congenital conditions. As a result, patients with lower limb amputation show very heterogeneous clinical profiles and mobility levels. Similarly, the available prosthetic solutions are very different in terms of their design and price.

Little evidence is available on the role of the prosthetic components on fall risk, and their differential effect on patients with different clinical profiles and mobility levels [9].

The guidelines of the US Department of Veterans Affairs and US Department of Defense suggest (recommendation 15) to prescribe microprocessor-controlled knees (MPK) to decrease the risk of falling. This recommendation is graded as weak for [10]. The guidelines of the Scottish Physiotherapy Amputee Research Group [11] and the Dutch guidelines [12] do not give evidence-based indications on which prosthetic knee is more suitable for each class of patient.

Here we present preliminary results from a retrospective study that is being conducted on the archive of INAIL (Italian Institute for Insurance against Job Injuries) Prosthesis Centre, located in Budrio, Italy. The aim of this study is to get evidence on the clinical efficacy of different prosthetic knees for transfemoral amputees with different clinical profiles. Falls during the rehabilitation hospital stays (HS) at INAIL Prosthesis Centre have been chosen as the primary outcome.

II. METHODS

A. Data

Eligibility criteria were defined as follows: i) being a unilateral transfemoral amputee; ii) being 18 years or more; and iii) being an inpatient at INAIL Prosthesis Centre in the period 2011-2017. Written consent for data treatment for research purposes was searched for in paper-based medical records. Ethical approval was obtained by the Ethical Committee Area Vasta Emilia Centro (CE AVEC n 380/2018/OSS/AUSLBO).

Patients were assessed on different scales: the Barthel Index for functional independence [13], the Morse Scale for fall risk [14], the 10-meter Timed Walk Test (TWT) [15], the Locomotor Capability Index (LCI) [16], and the Amputee Mobility Predictor (AMP) [17] for balance and mobility. These scales are administered at hospital admission and discharge, except TWT and LCI that are administered when the patient is first able to walk outside the parallel bars and at hospital discharge. The Numerical Rating Scale (NRS) is used at hospital admission to measure pain at the stump, the phantom limb, the contralateral limb, and the back.

For each HS we also retrieved information on the length of stay, the type of HS (i.e. whether the patient was hospitalized for rehabilitation after a first prosthetic provision or a prosthetic renewal), the third payer (INAIL, the Italian Local Health Service (ASL), or patient out-of-pocket expense), and the goal of the rehabilitation (free walk, walk with one or two crutches, or with the walker). The goal of the rehabilitation is being extracted and classified from a field in the database filled with natural language sentences, testing hand-written rules based on string matching with Levenshtein distance and sequential neural networks. Drugs taken at home or during the HS are being mapped to ATC (Anatomical Therapeutic Chemical Classification System) codes [18] with the DrugBank database [19]. A comorbidity index is being computed on the basis of the information contained in the anamnestic fields of the electronic health records.

The prosthetic knee in use by each patient in each HS was determined by looking for the last prosthetic knee provided to the patient up to the current HS. We excluded prostheses for

bathing and, when two prosthetic knees were provided at the same HS, we retained the one of highest quality, considering the other as the back-up prosthesis. This algorithm for assigning prosthetic knees to HSs has been validated against 506 manually-checked knees (results not shown).

Data on the features of each prosthetic knee model were retrieved from the manufacturers' websites and the database of medical devices of the Italian Ministry of Health. Knee models were classified in four categories: 0 (locked), 1 (articulated, purely mechanic), 2 (with hydraulic or pneumatic control), and 3 (MPK).
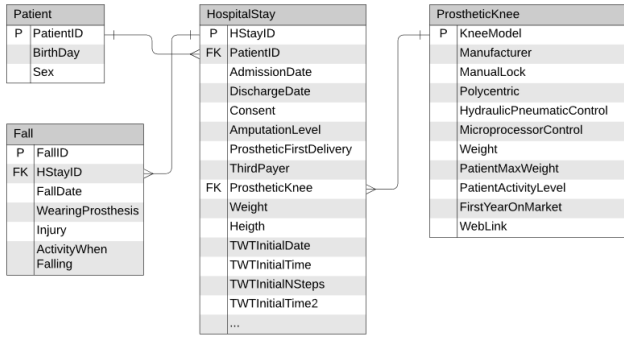
Fig. 1: Entity-relationship diagram of the dataset. P=primary key; FK=foreign key.

Data were organized as shown in Fig. 1. Data quality checks are being performed on accuracy, consistency, and completeness [20].

B. *Statistical models*

The association between HS features (x), features of the prosthesis worn during each HS (z), and number of falls occurred during each HS (y) were performed with mixed effect Poisson models, the number of falls being the dependent variable. Random effects were used to account for patients having multiple HSs.

The schematic approach for testing the marginal, conditional, and interaction effects of x and z features on falls (y) was borrowed from methodological literature on gene-environment analyses. More specifically, we chose a two-step procedure as follows [21].

Step 1. Each HS feature x is tested against falls in a univariate model shown in Eq. (1)

$$log(E[y_{ij}|x_{ij}]) = log(l_{ij}) + \beta_0 + \gamma_i + \beta_{mx}x_{ij} \qquad (1)$$

where x_{ij} is a HS feature of patient i in HS j, y_{ij} is the number of falls occurred during that HS, l_{ij} is the length of stay (expressed in number of days), γ_i is the random intercept for patient i, and β_{mx} is the marginal effect of feature x on falls.

Step 2. Each HS feature x whose marginal effect was found significant in step 1, was tested against falls within the model presented in Eq. (2)

$$log(E[y_{ij}|x_{ij}, z_{ij}]) = log(l_{ij}) + \beta_0 + \gamma_i + \beta_{cx}x_{ij} + \beta_{cz}z_{ij} + \beta_{xz}x_{ij}z_{ij} \qquad (2)$$

where z_{ij} is a feature of the prosthesis worn by subject i during hospital stay j, β_{cx} and β_{cz} are the conditional effects of x and z against falls, and β_{xy} is their interaction effect.

Inference on each marginal, conditional, and interaction effect ($\beta_{mx}, \beta_{cx}, \beta_{cz}, \beta_{xz}$) was performed with likelihood ratio tests. Significance was set with a threshold α=0.05. In case multiple models are fitted in step 2, corrections on p-values are needed to control type I errors.

Within the analyses presented in this paper, we have tested the effect of two HS features x, namely age (categorised in groups as shown in Fig. 3) and type of HS (first prosthetic provision or renewal), and one z feature, namely prosthesis category.

C. *Policy development and evaluation*

Upon completion of statistical tests, we plan to develop a model describing the current policy for prosthesis provision $P_0(z|x)$ (also known in some literature areas as "propensity score") [22], to suggest possible new policies $P_i(z|x)$, and to estimate their efficacy with respect to the outcome measures y [23].

III. RESULTS

A. *Descriptive statistics*

One-thousand-four-hundred-eighty-seven (1486) HSs, relative to 815 patients, have been included in the study (Fig. 2).
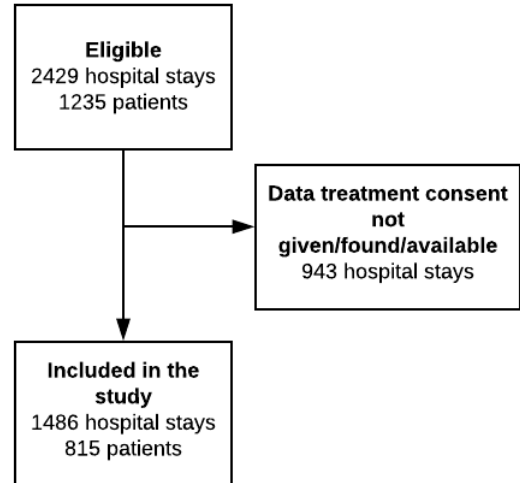

Fig. 2. Flowchart of patients and HSs being eligible and included in the study.

Most HSs were for prosthetic renewal rather than first prosthetic provision (78% vs 22%). Mean length of stay was 22 days, first provision HSs being longer (30 vs 19 days). Mean (standard deviation) age was 58.2 (14.7). Number of HSs for age group: 18-29 years: 59 (4.0%); 30-39 years: 116 (7.8%); 40-49 years: 271 (18.2%); 50-59 years: 343 (23.1%); 60-69 years: 329 (22.1%); 70-79 years: 295 (19.9%); 80 years or more: 73 (4.9%), During the rehabilitation, patients wore
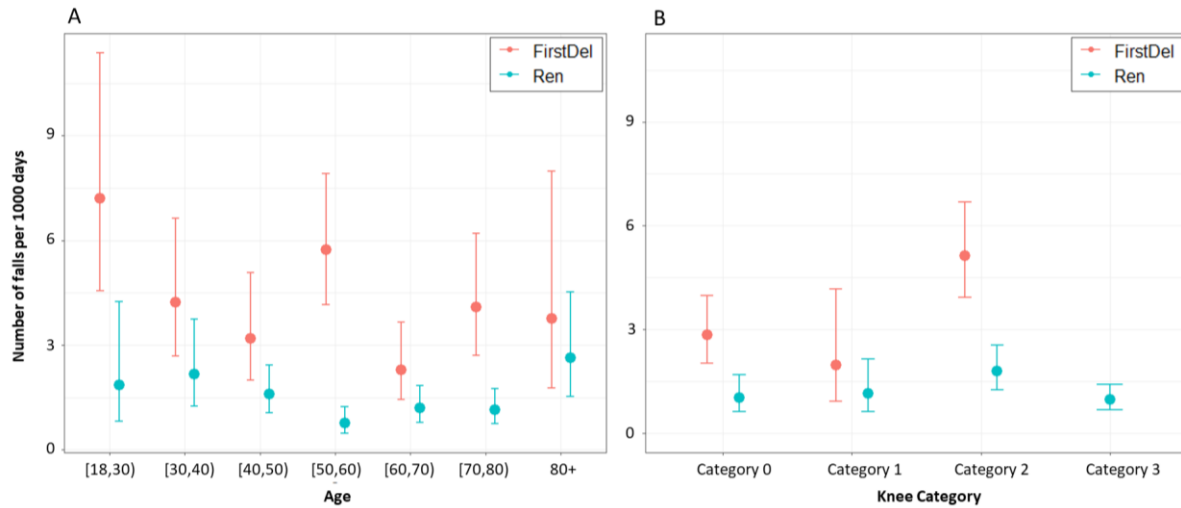
Fig. 3. Incidence rates (IR) for falls according to age group, type of HS (prosthetic first provision (FirstDel) or renewal (Ren)), and knee model category. IR are estimated with Poisson mixed effect models, fitted separately on first provisions and renewal HSs. Error bars correspond to ± 1 standard error on the Poisson model linear scale. IR for first provision HSs with knee category 3 is not estimated because of the low number of samples. The notation [a, b) used for age groups indicates an interval between a (included) and b (excluded).

54 different knee models, the number of HS for knee category (cat) being: cat. 0: 251 (17.4%), cat. 1: 113 (7.8%), cat. 2: 498 (34.5%), cat. 3: 583 (40.3%), cat. not available: 41.

Eighty-eight (88) patients experienced at least one fall during 94 HSs, for a total of 108 falls. The average fall incidence, as estimated from Poisson mixed effect models, is 2.3 (95% confidence interval 1.91-2.77) per 1000 days.

B. Association tests

The marginal effect of age on falls was not found significant (p=0.31) while the marginal effect of type of HS was found significant (p=0.0006), first prosthesis provision patients being at increased fall risk. Thus, the type of HS passed to step 2. Within the full model (Eq. 2), both the conditional effects of type of HS and prosthesis category were found significant (p=0.018 and p=0.038, respectively), while the interaction effect was not (p=0.83).

Fig. 3, panel A shows the incidence rates (IRs) for falls according to age group and type of HS (first prosthesis provision or renewal). Patients at their first prosthesis provision are at increased risk of falling. Panel B shows the IR for falls according to knee category and HS type. The IR for patient with knee category 3 at their first provision could not be estimated due to low number of samples.

IV. DISCUSSIONS

To the best of our knowledge, this is the first study assessing patient characteristics and prosthetic components (in particular, prosthetic knees) in relation to fall risk in patients with lower limb amputations.

Falls are of outmost concern, since they may lead to serious injuries, fear of falls, and mobility restrictions, thus limiting the patient functional independence. As such, they are considered sentinel events and are recorded in every hospital and rehabilitation centre. In the literature, proneness to falls is used to demonstrate the superiority of some technological prosthetic solutions and is often measured with *ad-hoc* laboratory platforms [24]. In the present study we have used real-world falls to evaluate the efficacy of commercially available knee prostheses.

Our preliminary results show that some features of the clinical course of a patient (e.g. receiving a prosthesis for the first time) and some prosthetic models do have a measurable effect on the patient fall risk. So far, the evidence on the effect of different prosthetic knees on fall risk has been scant and their prescription is much influenced by their cost, patient affordability and available public or insurance-based coverage plans rather than evidence of their clinical efficacy. Solid scientific knowledge can aid in establishing better clinical guidelines for prosthesis prescription and more rational and equitable choices for reimbursement plans.

Since the data for this study were taken from the archive of INAIL Prosthesis Centre, which is particularly devoted to care of workers injured at their workplace, most amputations are due to trauma. We know that this is not the case in the general population [3] and this bias has to be considered in further analyses addressing population estimations.

Having performed the analyses on only two personal features (age and type of HS) is a limitation of this study. As future developments, we are going to include: i) the Medicare Functional Classification K levels, as derived from AMP, since they have become a *de facto* standard for patient stratification; ii) a comorbidity index able to describe the clinical profile of the patient; iii) information on third payers available for medical expenditures, since they are know to greatly influence prosthetic prescription; iv) the Morse Scale, which is used to assess fall risk in hospitals; and v) the main acknowledged risk factors for falls in geriatric populations, including specific drug classes, comorbidities, and history of falls. We further plan to consider more outcomes besides falls, including TWT and AMP at hospital discharge. Finally, more methods will be applied to estimate the differential effect of the prostheses on patients with different clinical profiles [25].

A prospective longitudinal study is ongoing in two rehabilitation centres. In addition to the aforementioned clinical scales, patients' static and dynamic balance is evaluated by means of wearable sensors, force platforms and pressure insoles. Physical activity is monitored at home with

wearable actigraph units and falls are ascertained for 12 months after hospital discharge with phone interviews. We aim to set up a protocol that is comprehensive of the different domains affecting balance and is lean enough to be applied in a vast network of rehabilitation centres.

V. CONCLUSION

Some features related to the clinical course of lower limb amputees and their prosthetic components affect patient fall risk. More evidence on these intrinsic and prosthesis-related risk factors will aid in establishing better prescription criteria for prosthesis provision.

ACKNOWLEDGEMENT

REFERENCES

[1] P. Varma, M. G. Stineman, and T. R. Dillingham, "Epidemiology of Limb Loss," *Phys. Med. Rehabil. Clin. N. Am.*, vol. 25, no. 1, pp. 1–8, Feb. 2014.

[2] F. L. Lombardo, M. Maggini, A. De Bellis, G. Seghieri, and R. Anichini, "Lower Extremity Amputations in Persons with and without Diabetes in Italy: 2001–2010," *PLoS One*, vol. 9, no. 1, p. e86405, Jan. 2014.

[3] M. Spoden, U. Nimptsch, and T. Mansky, "Amputation rates of the lower limb by amputation level – observational study using German national hospital discharge data from 2005 to 2015," *BMC Health Serv. Res.*, vol. 19, no. 1, p. 8, Dec. 2019.

[4] M. Narres *et al.*, "Incidence of lower extremity amputations in the diabetic compared with the non-diabetic population: A systematic review.," *PLoS One*, vol. 12, no. 8, p. e0182081, 2017.

[5] W. C. Miller, M. Speechley, and B. Deathe, "The prevalence and risk factors of falling and fear of falling among lower extremity amputees.," *Arch. Phys. Med. Rehabil.*, vol. 82, no. 8, pp. 1031–7, Aug. 2001.

[6] C. Wong, S. Chihuri, and G. Li, "Risk of fall-related injury in people with lower limb amputations: A prospective cohort study," *J. Rehabil. Med.*, vol. 48, no. 1, pp. 80–85, Jan. 2016.

[7] S. W. Hunter, F. Batchelor, K. D. Hill, A.-M. Hill, S. Mackintosh, and M. Payne, "Risk Factors for Falls in People With a Lower Limb Amputation: A Systematic Review.," *PM R*, vol. 9, no. 2, pp. 170-180.e1, 2017.

[8] N. Steinberg, A. Gottlieb, I. Siev-Ner, and M. Plotnik, "Fall incidence and associated risk factors among people with a lower limb amputation during various stages of recovery – a systematic review," *Disabil. Rehabil.*, vol. 0, no. 0, pp. 1–10, 2018.

[9] E. M. Balk *et al.*, *Lower Limb Prostheses: Measurement Instruments, Comparison of Component Effects by Subgroups, and Long-Term Outcomes*. Agency for Healthcare Research and Quality (US), 2018.

[10] US Department of Veterans Affairs and US Department of Defense, "VA / DoD clinical practice guideline for rehabilitation of individuals with lower limb amputation," 2017.

[11] L. Brady, B. Carse, D. Morrison, A. Morton, N. Porteous, and H. Scott, "WestMARC Knee Guide for the Prosthetic Multidisciplinary Team 2017," 2017.

[12] J. Geertzen *et al.*, "Dutch evidence-based guidelines for amputation and prosthetics of the lower extremity: Rehabilitation process and prosthetics. Part 2," *Prosthet. Orthot. Int.*, vol. 39, no. 5, pp. 361–371, Oct. 2015.

[13] F. I. Mahoney and D. W. Barthel, "Functional evaluation: The Barthel index," *Md. State Med. J.*, vol. 14, pp. 61–5, Feb. 1965.

[14] J. M. Morse, C. Black, K. Oberle, and P. Donahue, "A prospective study to identify the fall-prone patient," *Soc. Sci. Med.*, vol. 28, no. 1, pp. 81–86, Jan. 1989.

[15] D. Datta, R. Ariyaratnam, and S. Hilton, "Timed walking test — an all-embracing outcome measure for lower-limb amputees?," *Clin. Rehabil.*, vol. 10, no. 3, pp. 227–232, Aug. 1996.

[16] C. Gauthier-Gagnon and M. C. Grisé, "Prosthetic profile of the amputee questionnaire: validity and reliability.," *Arch. Phys. Med. Rehabil.*, vol. 75, no. 12, pp. 1309–14, Dec. 1994.

[17] R. S. Gailey *et al.*, "The Amputee Mobility Predictor: An instrument to assess determinants of the lower-limb amputee's ability to ambulate," *Arch. Phys. Med. Rehabil.*, vol. 83, no. 5, pp. 613–627, 2002.

[18] "WHOCC - ATC/DDD Index." [Online]. Available: https://www.whocc.no/atc_ddd_index/. [Accessed: 31-Jan-2020].

[19] D. S. Wishart *et al.*, "DrugBank 5.0: A major update to the DrugBank database for 2018," *Nucleic Acids Res.*, vol. 46, no. D1, pp. D1074–D1082, Jan. 2018.

[20] "ISO/IEC 25012:2008 Software engineering — Software product Quality Requirements and Evaluation (SQuaRE) — Data quality model." .

[21] C. E. Murcray, J. P. Lewinger, D. V. Conti, D. C. Thomas, and W. J. Gauderman, "Sample size requirements to detect gene-environment interactions in genome-wide association studies," *Genet. Epidemiol.*, vol. 35, no. 3, pp. 201–210, Apr. 2011.

[22] P. R. Rosenbaum and D. B. Rubin, "The central role of the propensity score in observational studies for causal effects," *Biometrika*, vol. 70, no. 1, pp. 41–55, 1983.

[23] F. Ricci, L. Rokach, and B. Shapira, Eds., *Recommender systems handbook*, Second Edi. New York: Springer, 2015.

[24] F. M. Petrini *et al.*, "Enhancing functional abilities and cognitive integration of the lower limb prosthesis," *Sci. Transl. Med.*, vol. 11, no. 512, p. eaav8939, 2019.

[25] S. Athey and G. Imbens, "Recursive Partitioning for Heterogeneous Causal Effects," *Proc. Natl. Acad. Sci.*, vol. 113, no. 27, pp. 7353–7360, 2016.

Design and validation of a novel low cost-bicompartmental platform for cell and tissue cultures

L.P. Coppadoro[1], C. Foglieni[2], G. B. Fiore[1], M. Soncini[1]

[1] *Dipartimento di Elettronica, Informazione e Bioingegneria, Politecnico di Milano, Milano, Italy*
[2] *Cardiovascular Research Area, IRCCS San Raffaele Scientific Institute, Milano, Italy*

Abstract - In vitro **cell/tissue culture represents a widespread methodology for pathophysiology studies with good cost/benefit ratio. We have developed and are validating a novel system, that allows compartmentalized cultures and co-cultures, real time visualization of the culture growth, and recover/reuse of the biological material, based on conventional and low-cost rapid prototyping clean room-free technologies**

Keywords— **cell cultures, laser cutting, bicompartmental, immunofluorescence, live imaging.**

I. INTRODUCTION

Understanding the dynamic mechanisms at the base of perturbation of physiological homeostasis, leading to pathological conditions in the human body is not trivial and requires increasing the knowledge of how cells behave and interact. Modeling of a physiopathological status of cell-cell and cell-extracellular matrix interactions, and of tissue barrier functions under controlled conditions could be pivotal for the development of more effective drugs or tailored/regenerative medicine approaches. For these purposes numerous two-dimensional cell culture systems have been exploited in recent years. Even if these models have created an important dataset of information, they did not recapitulate the actual three dimensional (3D), highly complex microenvironment of *in-vivo* cells.

In fact, most cells change their phenotype and functions depending on the culture conditions, including the type of culture system, limiting the direct results translatability to human pathophysiology. Among the parameters affecting cells behavior, a crucial role is played by the chemo-electro-mechanical stimuli encountered in situ by cells, that have to be taken in account in order to reproduce key aspects of the complex human physiological microenvironment (Figure 1).

To mimic pathophysiological environments, numerous organ-on-a-chip systems were developed, combining fluid dynamics at the millimeter-micrometer scale and tissue engineering. However, most of these technologies have been mainly addressed in academia with polydimethylsiloxane (PDMS) devices manufactured using soft lithography techniques. The requirement for clean rooms and specialized skills has inhibited the large-scale accessibility and scalability of these technologies, limiting their commercial diffusion [1].

In the last years some low-cost, conventional technology-based alternatives, such as paper microfluidics, 3D-printed microfluidics, injection-molded blocks microfluidics and acrylic microfluidics have been proposed. In particular, laser cutting of plastics and double-sided tape could be considered as a valid alternative to PDMS-based systems, thanks to the good reproducibility and rapid, easy-to-handle production processes [2].

In this work, we developed an acrylic- and tape-based platform, i.e. using poly methyl methacrylate (PMMA), and double-sided tape, that enables compartmentalized *in-vitro* cultures and co-cultures, real time visualization of the culture growth in living cells, and recover/reuse of the biological samples for subsequent conditioning or analysis. A specific focus on the user-friendliness of the device in compliance with biologist's need was applied.
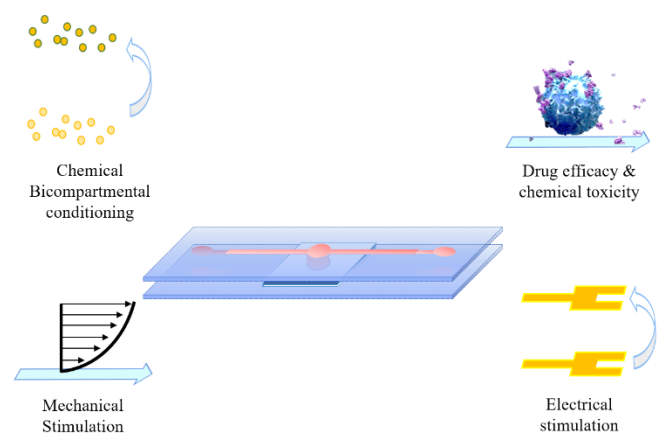

Fig. 1: Scheme of the required stimuli to recreate a correct physiopathological microenvironment in (fictitious) acrylic/tape-based culture system.

II. MATERIALS AND METHODS

Laser cutting (Versa Laser V2.30 ULS) and milling (Roland Modela MDX 40) technologies have been used to develop a novel system suitable to house a porous membrane and perform bi-compartmental cultures (Figure 2).
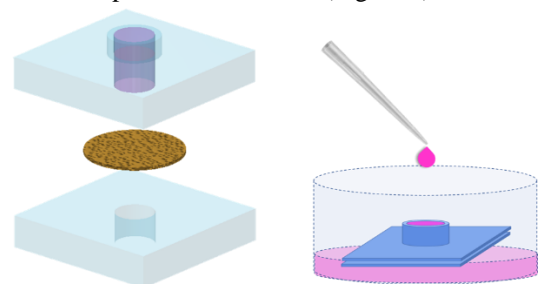

Fig. 2: Representative model of the static bi-compartmental culture system. Membranes are housed inside the platform and positioned in a petri dish.

The design process consists on the creation of a computer-aided design (CAD, Adobe Illustrator™) file, to guide the tip

of the laser cutter. A proper selection of the feature colors of the sketch allows to create complex drawings and to temporize the laser engraving.

It is also possible to select the laser power and the speed of the laser spot, depending on the material, its thickness and the required depth of cut, to obtain the correct layout of the device.

Three commercially available membranes Whatmann Cyclopore® (pore size = 3µm), Whatmann Nucleopore® (pore size = 3µm, NP3) and Whatmann Nucleopore® (pore size = 5µm, PVP-free, NP5) were chemically treated to eliminate toxic components such as polyvinilpirrolidone and increase the transparency, then housed and tested in the system. Membrane mounting procedure was optimized in order to have a well-tensioned membrane into the chamber.

To biologically validate the system, two different cell types have been tested: Caco-2, a human cell line recognized as a model of colonic epithelium (ATCC®HTB-37™, $4x10^4$ cells/system, with a culture surface equal to a 96-well plate), and primary human osteoblasts isolated from bone fragments obtained by orthopedic patients ($4x10^4$ cells/system).

In the first phase of the biological validation of the system, static cultures of Caco-2 cells were seeded on different membranes and run till confluence, to compare the suitability of the three membrane types. Cultures on Transwell® inserts (pore size = 3µm) were run in parallel and used as golden standard for bi-compartmental cell culture. Cells were cultured in sterile conditions using Dulbecco's Modified Eagle Medium (DMEM) with 10% FCS, 1% Pen-Strep, 5%Gentamicine, in a 37°C, 5%CO_2 standard incubator [3]. Presence of adherent/living cells were monitored by labeling with Acridine Orange, a nucleic acid-selective fluorescent cationic dye, at day 5, 7, 9, 11 [4]. At day 13 the confluent cells fixed in 0.8% paraformaldehyde solution were stained by DAPI (nuclei), and human epithelial antigen (HEA, a human transmembrane glycoprotein) or Junction Adhesion Molecule (JAM, a marker of tight junctions, belonging to immunoglobulin subfamily) antibodies. Cell density (number/field at 40x objective in 3 fields/membrane, 2 replicates/membrane type) and differentiation were analyzed on fluorescence and confocal microscopy images by FiJi and Volocity software. Each experimental condition was run in triplicate in at least two different experiments. This set of experiments lead to choose the Whatmann Nucleopore® (5µm, PVP-free) as preferred membrane, comparable to Transwell® for the subsequent experiments.

In the second validation phase, primary human osteoblast-like cells were seeded in the system with Whatmann Nucleopore® (5µm, PVP-free) membranes. Cells were cultured in Iscove's Modified Dubecco's Medium with 10% FCS, 100 U/ml penicillin, 100 µg/ml streptomycin, 50 U/ml mycostatin, and 0.25 µg/ml amphotericin B). Cells were monitored by Acridine Orange labeling at day 5 and 8. At day 15 the confluent cells were fixed in paraformaldehyde, then stained by DAPI (nuclei) and anti-Osterix (a transcription factor sp7 driving osteoblast differentiation) antibody. Cell differentiation was verified by fluorescence microscopy analysis.

III. RESULTS

We obtained confluent monolayers both with Caco-2 cells and human osteoblasts. In the first set of experiments the cell density was about $4x10^3$ cells/mm² over both Whatmann Nucleopore® (pore size = 3µm) and Whatmann Nucleopore® (pore size = 5µm, PVP-free), comparably with that determined over Transwell® inserts, while over Whatmann Cyclopore® (pore size = 3µm) the cells did not adhere properly (Figure 3). No relevant membrane crossing by cells was observed using Nucleopore® membranes
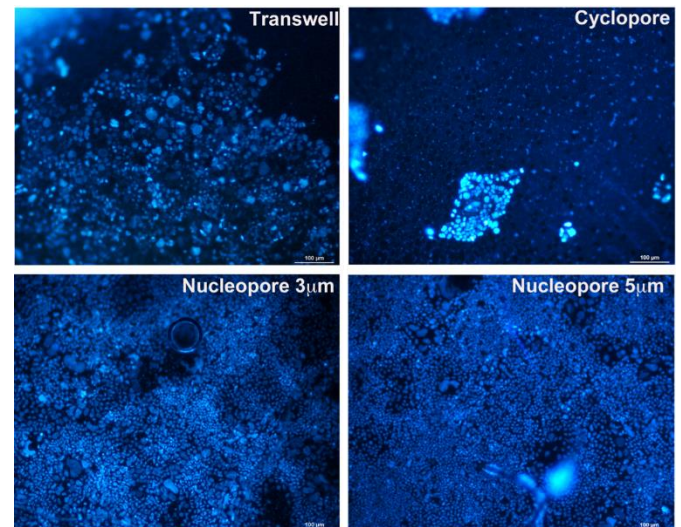

Fig. 3: Representative fluorescence images of Caco-2 cells distribution on the four different membranes: Transwell, Cyclopore, Nucleopore of 3µm pores Nucleopore of 5µm pores. Nuclear labeling with DAPI showing the distribution of cells over NP3 and NP5 is presented. Notice the improvement over Nucleopore vs. Transwell, our golden standard and the different pattern over Cyclopore. Detachment of overgrowth cells from Cyclopore, but not from Nucleopore was observed. Images obtained at 40x objective magnification.

The Acridine Orange (AO) label allowed to verify the absence of membrane toxicity along time and helped in establishing when the cells reach confluence and the culture has to be concluded. In Figure 4 it is possible to observe fluorescence images of living Caco-2 cells labeled nucleic acids at day 11. Again, over Whatmann Cyclopore the cells did not adhere properly.
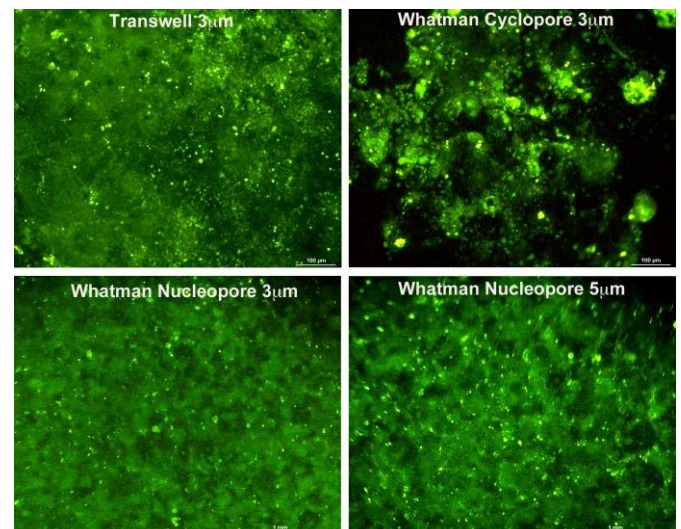

Fig. 4:Representative fluorescence images of living Caco-2 cells cultured in the system over different membranes and labeled with AO at day 11.

Caco-2 polarization was observed by confocal microscopy analysis over all whole membrane retrieved from the system, as presence of expressed JAM at the apical side and of HEA at the basal side, respectively (Figure 5).
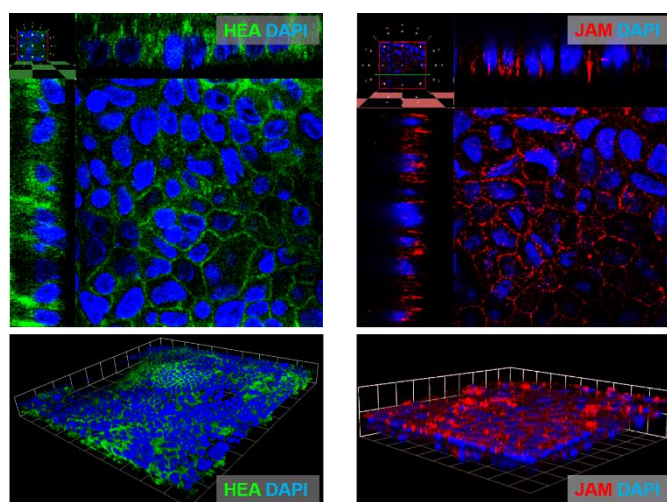

Fig. 5: Upper panels: confocal image cross sections of Caco-2 cell monolayer labeled with HEA and DAPI (left), and JAM and DAPI (right), demonstrating cell polarization. Lower panels: 3D renderings of Z-stacks from Caco-2 monolayer stained with the same antibodies confirming the correct HEA and JAM spatial distribution.

In the second set of experiments the proliferation and differentiation of human primary osteoblasts were monitored. AO confirmed the presence of confluent monolayers of osteoblast-like cells over Whatmann Nucleopore® (Figure 6), and the nuclear localization of Osterix indicated their differentiation to osteoblasts (Figure 7) [5].
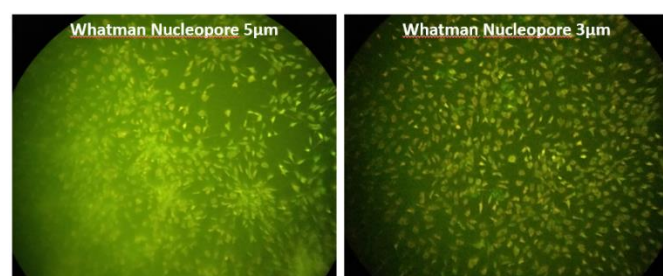
Fig. 6: Representative fluorescence images of living human primary osteoblasts cultured in the system over different membranes (NP3 and NP5) and labeled with AO at day 5.

Osteoblasts differentiation was observed in all samples.
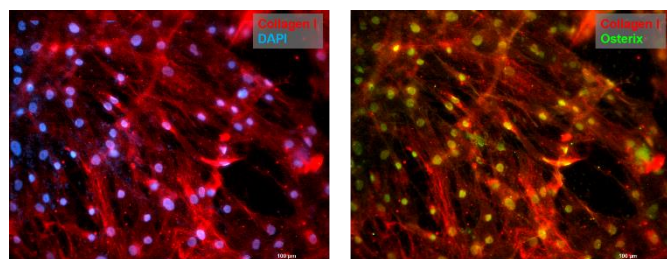
Fig. 7: Representative fluorescence images of primary human osteoblasts stained with Collagen I and DAPI (left), and Osterix and DAPI (right) showing the merge of different channels in the same field. Osterix localization into nuclei is compatible with osteoblast differentiation.

IV. CONCLUSION

The optimization of production protocols for the devices fabrication and membrane treatments led to a high repeatable, biocompatible and scalable system, that showed a good compatibility with living cells as Caco-2 cell line and primary human osteoblasts. We performed static cultures comparable with those on Transwell® inserts. The features of our novel system enable easy to handle and controlled cultures. In perspective, we will test co-cultures with direct contact of different kind of cells within our system, and we will upgrade the system to subject cells to dynamic (Low or Normal Shear Stress) stimulations, in single and in co-culture conditions.

REFERENCES

[1] D. I. Walsh, "Enabling Microfluidics: from Clean Rooms to Makerspaces", in *Trends Biotechnol.*, vol. 35, no. 5, pp. 383–392, 2017.
[2] Y. Ren, "Reconfigurable Acrylic-tape Hybrid Microfluidics," *Sci. Rep.*, vol. 9, no. 1, pp. 1–10, 2019.
[3] M. Cavarelli, "R5 HIV-1 envelope attracts dendritic cells to cross the human intestinal epithelium and sample luminal virions via engagement of the CCR5," *EMBO Mol. Med.*, vol. 5, no. 5, pp. 776–794, 2013.
[4] A. M. Amado, "Acridine orange interaction with DNA: Effect of ionic strength," *Biochim. Biophys. Acta - Gen. Subj.*, 2017.
[5] Y. Cao, "Osterix, a transcription factor for osteoblast differentiation, mediates antitumor activity in murine osteosarcoma," *Cancer Res.*, 2005

Analysis of heart rate variability as evaluation method for the risk of sepsis in the low-weight preterm infant

Fabio Tarricone[1], Viviana Bernocco[1], Domenico Buongiorno [1,2], Antonio Brunetti[1,2], Antonella D'Orazio[1], Antonio Del Vecchio[3], Vitoantonio Bevilacqua[1,2] and Flavia Petrillo[3]

[1] Department of Electrical and Information Engineering, Polytechnic University of Bari, Bari, Italy
[2] Apulian Bioengineering s.r.l., Via delle Violette 14, Modugno (BA), Italy
[3] Department of Women's and Children's Health, Neonatal Intensive Care Unit, Di Venere Hospital, Bari, Italy,

Abstract—**Neonatal sepsis is a clinical syndrome characterized by systemic signs of infection and the concomitant positivity of blood culture to the presence of pathogenic microorganism. This pathology particularly affects the neonates in intensive care, especially if they are preterm and low weight, with an incidence varying between 1 and 40% according to the onset (early or late). Prompt diagnostic and therapeutic interventions could reduce the high percentage of mortality that characterizes this pathology especially in the premature and low weight neonates. The main goal of this study was to investigate whether the HeRO Duet, an automatic and non-invasive device designed to early diagnose neonatal sepsis, can be an effective aid to support the clinician in making early diagnosis of sepsis.**

Keywords—**Neonatal Sepsi, HeRO duet, HeRo Score.**

I. INTRODUCTION

Sepsis is a clinical syndrome characterized by systemic signs of infection and the concomitant positivity of blood culture to the presence of pathogenic microorganism. The sepsis is divided into two main categories: early-onset sepsis and late-onset sepsis according to the period of onset that can be within the first 72 hours of life or after, respectively [1]. This pathology particularly affects infants in neonatal intensive care unit (NICU), especially if they are preterm and low weight, with an incidence ranging between 1% and 40% varying according to the onset period. The overall mortality rate of early-onset sepsis is between 3% and 40%, whereas such values decrease to 2% and 20% in the case of late-onset sepsis. Mortality rate peaks of up to 50% may be observed for premature and low-weight infants in NICU.

The most performed clinical investigations used to diagnose sepsis in NICU are blood culture, PCR (Polymerase Chain Reaction), complete blood count, C-reactive protein, interleukin and procalcitonin counts [2]. After an accurate evaluation of the above-mentioned diagnostic methods, it is worth noting that many of them do not allow for a timely intervention due to the amount of time required to receive the test result and the high blood concentration variability of many substances that are present in case of sepsis [3]. Furthermore, microbiological tests are characterized by a low sensitivity. Hence, there is the need for more appropriate tests that should be highly sensitive, predictive and fast to be performed.

The presented study has been conducted in collaboration with the clinicians of the Di Venere Hospital's NICU and consisted in investigating the diagnostic predictivity ability of sepsis the HeRo index computed by the innovative HeRo duet device (https://www.heroscore.com/).

II. METHODS AND MATERIALS

A. Patients

The study was conducted from February 2019 to January 2020 and involved eleven premature neonates (gestational age between 23 and 32 weeks – weight between 600 and 1600 gr.). All babies were at high risk of contracting sespi because of the hospitalization in the NICU, the prematurity and the low weight.

B. The HeRO duet device

The HeRO duet is a medical device that has been designed to non-invasively predict neonatal sepsis and works by getting data from a generic device used to monitor vital functions. In this study we used the Dräger C500 monitor (www.draeger.com). Through the acquisitions performed by the monitor device, the HeRO duet can acquire and analyse the electrocardiogram signal in order to compute the heart rate variability based on R-R interval duration. A complex model based on the observations of the heart rate variability is then used to generate the HeRO index that represents a factor associated with the increased risk of sepsis [4]. The HeRO index computation procedure is described within the HeRO duet manual [5].

The HeRo duet produces a new HeRO index value every hour considering the heart rate measured during the previous twelve hours. The risk of contracting sepsis is classified as [5]:

- low if the score is lower than 1;
- intermediate if the score ranges between 1 and 2;
- high if the score is higher than 2.

It is worth mentioning that patients featuring a high HeRO score are six times likely to contract sepsis than patients with a low HeRO score value [7].

C. Observation, Decision Making and Comparison

The HeRO index has been collected, acquired and analysed for a period that lasted from 10 to 30 days according to the degree of risk that considers several factors such as: positive obstetric anamnesis of rupture of membranes, positioning of central catheters and mechanical ventilation.

With the aim at better supporting the neonatologists, a graphical user interface (GUI) has been developed. The implemented GUI helps the clinical staff to view and analyze both the HeRo score and other clinical indices.

During the observation period, the HeRO index was continually checked by clinicians. A patient was considered as positive based on the HeRO score whether the relative value was higher than 2 for two consecutive hours.

The results of the test based on the HeRO score were then compared with the gold standard that was determined analyzing both the results of classical diagnostic tests and the clinical symptoms.
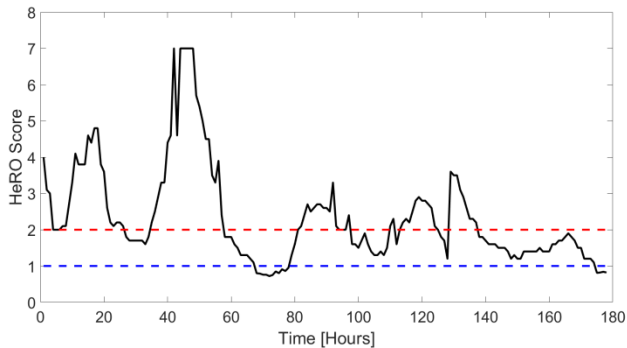
Fig. 1. HeRO score acquired by a patient with sepsis diagnosed as positive.
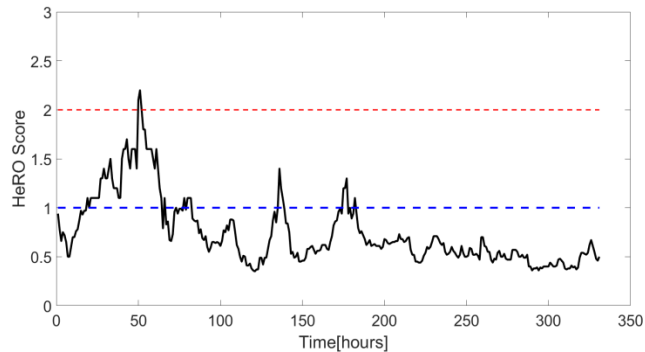
Fig. 2. HeRO score acquired by a patient without sepsis diagnosed as positive.
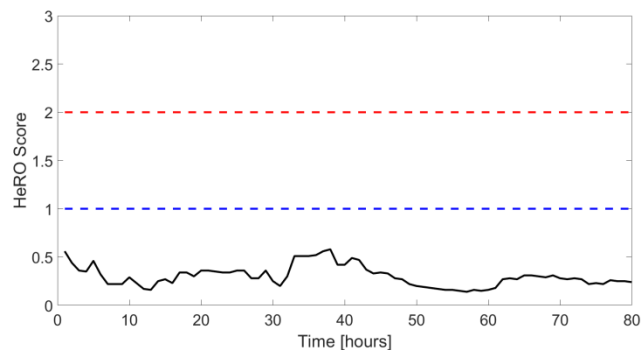
Fig. 3. HeRO score acquired by a patient without sepsis diagnosed as negative.

III. RESULTS

The predictive power of the test based on the HeRO score has been evaluated using the common metrics used for a classical binary classifier, with Positive and Negative classes. In detail, we computed and reported the confusion matrix (see Table 1), the accuracy (see Eq. 1), the specificity (see Eq. 2) and the sensitivity (see Eq. 3), where TP, TN, FP and FN stand for true positive, true negative, false positive and false negative, respectively.

Table 1. Confusion Matrix for performance evaluation of a generic binary classifier.

		True Condition	
		Positive	Negative
Predicted Condition	Positive	TP	FP
	Negative	FN	TN

$$Accuracy = \frac{TP+TN}{TP+TN+FP+FN} \qquad (1)$$

$$Specificity = \frac{TN}{TN+FP} \qquad (2)$$

$$Sensitivity = \frac{TP}{TP+FN} \qquad (3)$$

Table 2. Confusion Matrix of the sespis diagnostic test based on the HeRo score.

		True Condition	
		Positive	Negative
Predicted Condition	Positive	3	3
	Negative	0	5

The Table 2 reports the confusion matrix of the sepsis diagnostic test based on the HeRO score. Among the eleven patients involved in the study, the test was able to predict the presence of sepsis in the 100% of cases (three cases) that were considered positive according to the classical diagnostic tests (infection indices and blood culture). Figure 1 reports the HeRO score of a true positive case. The test was able to classify as negative five out of eight neonates without sepsis. Figure 3 shows the HeRO score of a true negative case. Three neonates without sepsis were wrongly diagnosed with sepsis. Figure 2 depicts the HeRO score of a false positive case. The values of the performance indices are reported below:

- accuracy is equal to 72.2 %
- sensitivity is equal to 100 %
- specificity is equal to 62.5 %

IV. DICUSSIONS

The observed promising results confirmed the efficacy of the HeRO score in predicting neonatal sepsis. This evidence means that the HeRO device can support clinicians in timely intervening on the patients. On a cohort of eleven premature low-weight neonates, the test based on the HeRO score has achieved sensitivity equal to 100% and a specificity equal to 62.5 %. All the neonates that contracted the sepsis were classified as positive. This feature might enable clinicians to start an antibiotic therapy several hours before the positive evidence of sepsis produced by classical tests. As reported by the HeRO manufacturer, the positivity to the HeRO test might allow for a sepsis diagnosis up to 24 hours before the evidence of clinical signs and/or the positivity to other

diagnostic tests [5]. In these cases, the clinician could timely request for laboratory tests and/or give higher attention to minimal clinical signs of sepsis with the aim at promptly starting the antibiotic therapy. A not-promptly diagnosis and therapy might cause an increase of the morbidity and mortality rates because of the prematurity and low-weight [6].

Three patients out of eight were wrongly diagnosed as positive for sepsis. However, it is worth mentioning that the manufacturer of the HeRO device reports a list of clinical situations and/or pharmacological therapies that might influence the HeRO score. As example, the release of cytokines could influence the heart rate variability thus causing an increase of the HeRO score. Such situation will generate a false positive case. In fact, also in this study, it has been important to not take decisions on the only basis of the HeRo score. Indeed, a comparison among the HeRO score, the classical diagnostic test results and conditions of the patients has been crucial to make a promptly and accurate diagnosis.

V. CONCLUSIONS

The neonatal sepsis is an invasive infection (usually a bacterial infection) that occurs during the neonatal period. A promptly diagnosis of sepsis is crucial for treating the neonate with the correct therapy. A big gap in the clinical settings is the absence of devices that allow for the monitoring of the sepsis thus enabling to get a promptly diagnostic result.

In this study we investigated the ability of the HeRO scored, produced by the HeRO device, to predict the diagnosis of sepsis. The observed promising results confirmed the efficacy of the HeRO score. As already known in literature, the data acquired in this study have also confirmed the high risk of nosocomial infections in late-onset sepsis. In fact, the pathology has repeatedly manifested in neonates that needed a central venous catheter, or CVC (especially if it was necessary for a period longer that 7-10 days) thus confirming the high risk of sepsis due to the positioning of CVC in premature and low-weight neonates.

Concluding, the obtained results evidenced that the HeRO device can support clinicians in timely intervening on the patients. However, the study has included only eleven patients, then future studies are necessary to confirm the obtained results on a larger cohort of neonates.

REFERENCES

[1] Camacho-Gonzalez, A., Spearman, P. W., & Stoll, B. J. (2013). Neonatal infectious diseases: evaluation of neonatal sepsis. Pediatric clinics of North America, 60(2), 367–389. doi:10.1016/j.pcl.2012.12.003
[2] Meem, M., Modak, J. K., Mortuza, R., Morshed, M., Islam, M. S., & Saha, S. K. (2011). Biomarkers for diagnosis of neonatal infections: A systematic analysis of their potential as a point-of-care diagnostics. Journal of global health, 1(2), 201.
[3] Caserta, M. T. (2015). Neonatal sepsis. Merck Manual, available: http://www. merckmanuals. com/professional/pediatrics/infections-in-neonates/neonatal-sepsis (accessed 12/05/16).

[4] Griffin, M. P., Lake, D. E., O'Shea, T. M., & Moorman, J. R. (2007). Heart rate characteristics and clinical signs in neonatal sepsis. Pediatric research, 61(2), 222-227.
[5] HeRO duet Version 3.1 System Manual
[6] Philip, A. G., & Hewitt, J. R. (1980). Early diagnosis of neonatal sepsis. Pediatrics, 65(5), 1036-1041.
[7] Griffin, M. P., Lake, D. E., Bissonette, E. A., Harrell, F. E., O'Shea, T. M., & Moorman, J. R. (2005). Heart rate characteristics: novel physiomarkers to predict neonatal infection and death. Pediatrics, 116(5), 1070-1074.

The eccentric phase of countermovement jump: comparing motion capture and inertial sensors

L. Truppa[1,2], M. Guaitolini[1,2], C. Castagna[3,4] and A. Mannini[1,2,5]

[1] The BioRobotics Institute, Scuola Superiore Sant'Anna, Pisa, Italy
[2] Department of Excellence in Robotics & AI, Scuola Superiore Sant'Anna, Pisa, Italy
[3] Università di Tor Vergata, School of Sport and Exercise Sciences, Rome, Italy
[4] Italian Football Federation (FIGC) Technical Dep., Football Training and Biomechanics Laboratory, Coverciano, Italy
[5] IRCCS Fondazione don Carlo Gnocchi, Firenze, Italy

Abstract—**Countermovement jump (CMJ) is a well-established practice in sports used to monitor both the fatigue in athletes and its supercompensation due to a periodic training path. It is primarily used to measure the lower-body power and has become one of the most frequently used performance tests by coaches, especially in football [1-2]. Currently, the most exploited technologies for CMJ performance monitoring are optical motion capture and force platforms, which are characterized by a high accuracy, but they result expensive, cumbersome and require a dedicated facility. In this framework, this study aims to measure eighteen biomechanical and kinematic parameters of the eccentric phase of CMJ by using several wearable magneto-inertial measurement units (MIMU) and an optoelectronic system as the ground truth. Eight semi-professional football referees performed a series of five jumps after a warm-up phase with four MIMUs and twelve reflective markers on their body. Parameters have been extracted from the four best jumps. The statistical analysis on the parameters show no significant differences between MIMUs and optical motion capture, confirming the former as a robust technology for performance assessment of the eccentric phase of CMJ.**

Keywords—**Countermovement jump, inertial measurement unit, MIMU, stereophotogrammetry, optical motion capture.**

I. INTRODUCTION

UNDERSTANDING the efficacy of a training program has a key role in sports; indeed, defining the correct training strategy results essential to optimize the performance and minimize the risk of injury. In the common practice, different kind of tests are exploited to assess athletes' biomechanical potentiality: i) postural analysis [3], ii) anthropometric assessment (*i.e.*, bending test) [4], iii) aerobic tests (*i.e.*, Yo-Yo intermittent recovery test) [5], iv) acceleration tests [6], v) coordination tests [7] and vi) force tests (*i.e.*, countermovement jump, squat jump) [2]. In particular, countermovement jump (CMJ) is made up of a single maximal vertical jump from a standing position and it evaluates the athlete's explosive power. This test has been frequently used to measure the athlete's lower-body power and biomechanical ability, becoming a cornerstone test for coaches and sport scientist [8].

CMJ performance has been evaluated by exploiting several technologies: contact mats [9], force platforms [10], optical motion capture systems (OMC) [11], video analysis and magneto-inertial measurements units (MIMUs) [3]. Among them, OMC is considered as the "gold standard" for human motion analysis [12]. Although the first four technologies are characterized by a high accuracy, they require a controlled environment, turning out to be impractical and not compatible with the athlete's sport routine.

On the other hand, MIMUs are very versatile, inexpensive and small-in-size sensors. They can be used in uncontrolled environments too (enabling the possibility to test methods directly on the playground) but they are, in general terms, less accurate for kinematic estimation compared to optoelectronic methods. For this reason, they require a particular care about computational strategies to extract reliable information from them [13-14-2].

Building on this, this work focuses on the kinematic and mechanical characterization of the eccentric phase of the jump, in which muscles exert a greater force and the variation in the biomechanical/kinematic parameters could be more significant, resulting in a more efficient analysis of the performance [15]. We compared two types of instrumentation that have been already tested for the study of CMJ: OMC and MIMUs. Previous works already targeted the validation of inertial sensors using OMC in jump tasks; however, most efforts are limited to the detection of the jump event and its height [13-2] or to joint kinematics [16].

II. MATERIALS AND METHODS

A. Participants

Eight semi-professional football referees (Sezione Associazione Italiana Arbitri di Firenze, Firenze, Italy. Age: 22.9±3.9 years, height: 179.9±7.6 cm, weight: 75.3±8.7 kg, years of previous training: 12.9±4.9 years) have been involved in tests. Athletes, in accordance with Helsinki protocol, signed an informed consent form and filled out a questionnaire to take part to the tests. No subject had a record of cardiovascular/respiratory disease and evidence of neuromuscular diseases.

B. Experimental procedures

The acquisition protocol was conducted in a controlled environment (*e.g.*, Italian Football Federation gymnasium in Coverciano, FI, Italy). After a 10 minutes warm-up phase of jogging on treadmill, MIMUs and optical markers were placed on the participant body and the athlete performed one series of 5 CMJs separated by a 10 seconds of rest time each. OMC was used as reference technology to validate MIMUs in the estimation of a set of 18 eccentric biomechanical and kinematic parameters. In particular, the firsts could be divided into four main groups:
i) Displacement parameters.The mean displacement of the centre of mass during the eccentric phase is analysed. Indeed, monitor the mean position of the barycentre

could be useful to quantify the jump loading level.

ii) Power and energy parameters. Parameters in this group allow to quantify the lower-limb explosive ability, resulting in extremely important indicators for performance assessment. The analysis of the literature identified the following parameters [1,17-18]: minimum and maximum relative power exerted, mean relative power over time, maximum power velocity (MPV), mean and minimum relative energy,

iii) Velocity parameters [17-18]. This group is useful to understand how easily the athlete performs the exercise. Minimum and mean velocity, velocity at negative power peak (VNPP), velocity at positive power peak (VPPP), area under the force-velocity curve were analysed.

iv) Time parameters [17-18]. They allow to pinpoint specific events in time during the execution of the exercise (*i.e.*, when the maximum power is exerted or how long the athlete stays in contact with the ground). Therefore, negative power peak time (NPPT), positive power peak time (PPPT), contact time (CT) were reported in this study.

Since the main muscles involved in vertical jump are hip and knee flexors/extensors, the knee and hip mean flex-extension angular velocities and their range of motion (ROM) were considered as indicative kinematic parameters. Similarly to distance parameters, ROMs could give useful information about the loading ability of the athlete, while angular velocities could be quantifiers of the difficulty encountered by the athlete during the exercise.

All parameters were estimated from the best four jumps of the relative series and then averaged on each participant.

C. Measurements

Data were acquired using an OMC (Vicon Bonita, Oxford, UK. Acquisition frequency: 100 Hz) consisting of eight infrared cameras arranged in such a way as to completely track the jump and four MIMUs (TuringSense, Santa Clara, CA, USA. Acquisition frequency: 100 Hz). Each MIMU was mounted on a 3D-printed plastic support together with three reflective markers needed to acquire reference data from the OMC. These four supports were placed on the right foot, shank, thigh and pelvis by using elastic bands (Figure 1). No specific biomechanical model were adopted to place the markers and compute the results. Indeed, as in can be seen from Figure 1, three reflective markers were applied on the plastic support to form a L-shape, allowing to define a OMC local frame by the means of Gram-Schmidt process. Since most of CMJ outputs refer to the human body centre of gravity, the pelvis sensor was placed in correspondence of the fifth lumbar vertebra (L5), which represents a reasonable approximation of the human centre of mass.

Two kinds of parameters were considered: biomechanical, which are referred to the centre of mass of the athletes' body, and kinematic, related to the lower-limb articular chain (Table 1). Biomechanical parameters were estimated by processing on Matlab (Mathworks, Natick, Massachusetts, United States) the measures of acceleration (MIMU) and the position of the reflective markers (OMC) of the plastic support placed on the fifth lumbar vertebra. Main formulas are shown in Table I. In

particular, the set of 18 parameters to analyse the CMJ were obtained from the velocity and acceleration at the centre of mass and from the knee and hip flex-extension angle. Concerning the kinematic parameters, output quaternions of the MIMUs were considered while reference quaternion from optoelectronic data were computed through the Gram-Schmidt process. Once defined the orientations of each segment, the quaternions associated to the lower limb joints were estimated as the product between the distal segment quaternion and the conjugate of the proximal one as reported in the expression (1). Finally, joint cardan angles were obtained from the joint quaternion.

$$q_{joint} = (q_{distal\ segment}) \otimes (q_{proximal\ segment})^{-1} \quad (1)$$
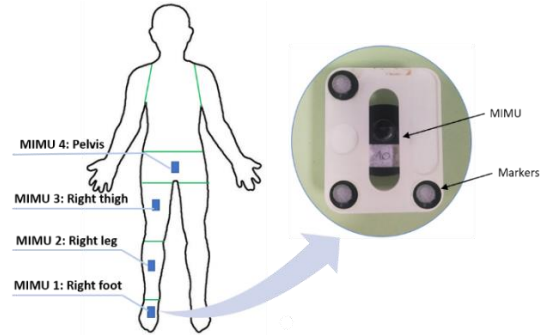

Fig. 1: Disposition of the IMUs on the body segments, a MIMU with its 3D-printed plastic support to host OMC markers.

TABLE I
MAIN FORMULA USED FOR PARAMETERS ESTIMATION

Physical quantities	OMC	MIMU
Measured quantity	x_{OMC}	a_{MIMU}
Velocity	$v(t) = \dfrac{d}{dt} x_{OMC}$	$v(t) = \int a_{MIMU} * dt$
Relative power	$\dfrac{W(t)}{m} = \dfrac{d^2}{dt^2} x_{OMC}(t) * v(t)$	$\dfrac{W(t)}{m} = a_{MIMU} * v(t)$
Mean relative power over time	$(\dfrac{U(t)}{m})_{mean} = \dfrac{\frac{U(t)}{m}}{t_{ecc}}$	
Mean power velocity	$(v_u)_{mean} = mean(\dfrac{d}{dt} \dfrac{U(t)}{m})$	
Relative energy	$\dfrac{U(t)}{m} = \int \dfrac{W(t)}{m} * dt$	
Distance	$x(t) = x_{OMC}$	$x(t) = \int \int a_{MIMU} * dt^2$
Angular velocities	$w_{FlexExt} = \dfrac{d}{dt} \theta_{FlexExt}$	

D. Statistical analysis

The Kolmogorov-Smirnov test was used to verify the non-normality of the parameters distribution. Once it has been confirmed that all the parameters belonged to non-gaussian populations, the comparison between MIMUs and OMC estimations was carried out by a Wilcoxon Rank Sum test. In addition, the Intraclass Correlation Coefficients (ICC) together with the Bland-Altman plot and limits of agreement (LA, estimated as in (2)) were estimated for each parameter to further verify the similarity between the two methods.

$$LA = 1.96 * \sigma(par_{IMU} - par_{OMC}) \quad (2)$$

Where par_{IMU} and par_{OMC} are generic IMU and OMC parameters respectively and σ is standard deviation.

The physical quantities from which the parameters were extracted (velocity and acceleration at the centre of mass and knee and hip angle) were reconstructed for both measurement methods and then compared by evaluating their root mean square errors (RMSEs) and the Spearman's correlation coefficient.

III. RESULTS AND DISCUSSION

Kolmogorov-Smirnov test rejected the null hypothesis that parameters came from a standard normal distribution while the Wilcoxon tests were not able in identifying statistically significant differences between MIMU and OMC estimations. Table II reports the values of the biomechanical and kinematic parameters (median and interquartile range (IQR)) together with the Wilcoxon test significance level.

TABLE II
BIOMECHANICAL AND KINEMATIC PARAMETERS

Parameters	OMC Median (IQR)	MIMU Median (IQR)	Wilcoxon test (p-value)	ICC
Mean distance (m)	-1.23 (0.44)	-1.27 (0.40)	0.80	0.99
Minimum power (W)	-3.26 (0.64)	-3.49 (1.16)	0.57	0.92
Maximum power (W)	4.29 (2.04)	4.30 (1.70)	1	0.93
Mean power over time ($W * dt^{-1}$)	0.20 (0.20)	0.20 (0.20)	0.95	0.98
MPV (W$* dt^{-1}$)	-16.0 (7.48)	-16.7 (7.18)	0.88	0.96
Mean energy (J)	-2.23 (1.14)	-2.38 (1.42)	0.72	0.94
Minimum energy (J)	-4.93 (2.32)	-5.24 (2.28)	0.64	0.94
Minimum velocity ($m * s^{-1}$)	-0.98 (0.22)	-1.01 (0.26)	0.80	0.95
Mean velocity ($m * s^{-1}$)	-0.55 (0.14)	-0.57 (0.16)	0.72	0.95
VNPP ($m * s^{-1}$)	-0.76 (0.14)	-0.77 (0.18)	0.72	0.94
VPPP ($m * s^{-1}$)	-0.66 (0.14)	-0.66 (0.18)	0.88	0.95
AFV ($N * m * s^{-1}$)	-11.6 (4.40)	-11.5 (3.62)	0.95	0.95
NPPT (ms)	-19.7 (5.12)	-19.7 (5.56)	0.94	0.93
PPPT (ms)	-43.9 (14.6)	-43.5 (13.7)	0.98	0.99
Knee ROM (°)	107.8 (23.6)	106.7 (23.6)	0.80	0.98
Knee mean angular velocity (°/sec)	113.5 (29.8)	113.1 (31.2)	1	0.98
Hip ROM (°)	95.2 (15.6)	96.1 (17.2)	0.88	0.99
Hip mean angular velocity (°/sec)	108.9 (17.0)	109.3 (13.4)	0.96	0.97

The time evolution in CMJ eccentric phase of knee flex-extension, center of mass acceleration and velocity obtained across participants for OMC and MIMU were compared (Figure 2a, Figure 3a, Figure 4a, Figure 5a). The agreement between the two methods in such estimations is confirmed by the RMSE and Spearman's correlation coefficient (Table 3).

Results shows a significant agreement between the two methods. In particular, the Bland-Altman plots of the parameters estimated with the two different technologies (Figure 2b, Figure 3b, Figure 4b, Figure 5b), their low LA and the excellent values of ICCs confirm the results of the Wilcoxon test that did not identified any significant difference between the two experimental setups.

Thus, results agree with previous studies that considered inertial sensors as a reliable source for joint angles estimation during jump [16], complementing this information with a set of 15 additional parameters extracted from acceleration and velocity of the (approximated) body center of mass.

TABLE III
RMSE AND CORRELATION COEFFICIENTS BETWEEN IMU AND OMC ESTIMATES

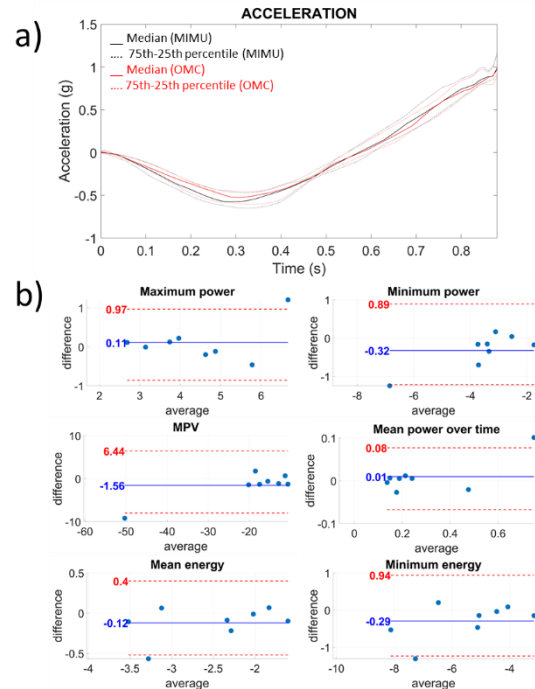|	RMSEs Median (IQR)	Spearman's correlation coefficient (p-value)
Acceleration (g)	0.04 (0.04)	0.998 (<0.001)
Velocity ($m * s^{-1}$)	0.05 (0.04)	0.999 (<0.001)
Knee flex-ext. angle (°)	2.19 (0.68)	0.999 (<0.001)
Hip flex-ext. angle (°)	3.45 (1.98)	0.999 (<0.001)

Fig. 2: a) Acceleration traces during the eccentrix phase of the jump, b) Bland-Altman plots of the parameters estimated from acceleration (IMU against OMC) with the corresponding LAs (in red) .
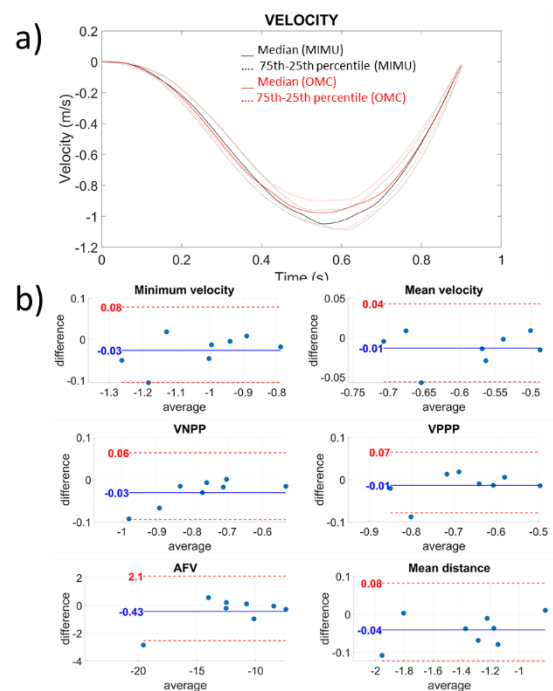

Fig. 3: a) Velocity traces during the eccentrix phase of the jump, b) Bland-

Altman plots of the parameters estimated from velocity (IMU against OMC) with the corresponding LAs (in red) .
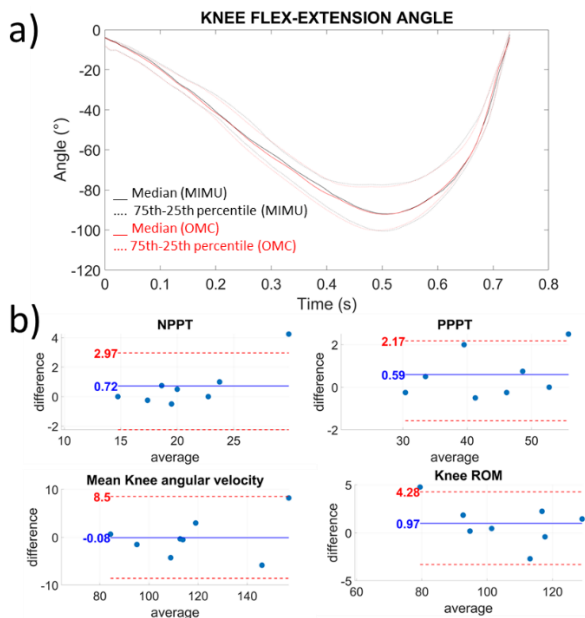

Fig. 4: a) Knee flex-extension angle traces during the eccentrix phase of the jump, b) Bland-Altman plots of the parameters estimated from knee angle (IMU against OMC) with the corresponding LAs (in red) .
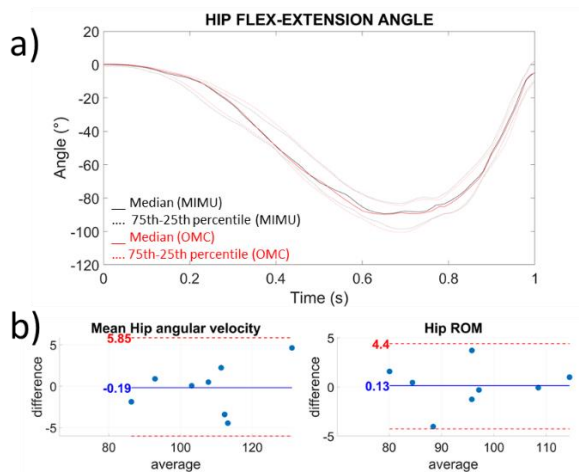

Fig. 4: a) Hip flex-extension angle traces during the eccentrix phase of the jump, b) Bland-Altman plots of the parameters estimated from hip angle (IMU against OMC) with the corresponding LAs (in red) .

IV. CONCLUSION

Results confirm our hypothesis: parameters to describe CMJ can be extracted by means of magneto-inertial sensors, without introducing significant errors. This work paves the way to new tests that can be conducted directly on the playground, taking advantage of the characteristic of wearable sensors that enables an ecological evaluation of the athletic gesture.

ACKNOWLEDGEMENT

REFERENCES

[1] Claudino, João Gustavo, et al. "The countermovement jump to monitor neuromuscular status: A meta-analysis." Journal of science and medicine in sport 20.4 (2017): 397-402.W.-K. Chen, *Linear Networks and Systems* (Book style).   Belmont, CA: Wadsworth, 1993, pp. 123–135.

[2] Picerno, Pietro, Valentina Camomilla, and Laura Capranica. "Countermovement jump performance assessment using a wearable 3D inertial measurement unit." Journal of sports sciences 29.2 (2011): 139-146M. Young, *The Techincal Writers Handbook*. Mill Valley, CA: University Science, 1989.

[3] Singla, Deepika, and Zubia Veqar. "Methods of postural assessment used for sports persons." Journal of clinical and diagnostic research: JCDR 8.4 (2014): LE01.

[4] Tsolakis, Charilaos, and George Vagenas. "Anthropometric, physiological and performance characteristics of elite and sub-elite fencers." Journal of Human Kinetics 23 (2010): 89-95.

[5] Bangsbo, Jens, F. Marcello Iaia, and Peter Krustrup. "The Yo-Yo intermittent recovery test." Sports medicine 38.1 (2008): 37-51.

[6] Lockie, Robert G., et al. "Reliability and validity of a new test of change-of-direction speed for field-based sports: The change-of-direction and acceleration test (CODAT)." Journal of sports science & medicine 12.1 (2013): 88.

[7] Dorcus, Roy M. "Performances of Athletes in Coördination Tests." Journal of Comparative Psychology 3.6 (1923): 475.

[8] Milosevic, Bojan, and Elisabetta Farella. "Wearable inertial sensor for jump performance analysis." Proceedings of the 2015 workshop on Wearable Systems and Applications. 2015

[9] Dias, Jonathan Ache, et al. "Validity of two methods for estimation of vertical jump height." The Journal of Strength & Conditioning Research 25.7 (2011): 2034-2039.W. D. Doyle, "Magnetization reversal in films with biaxial anisotropy," in *1987 Proc. INTERMAG Conf.*, pp. 2.2-1–2.2-6.

[10] Chavda, Shyam, et al. "Force-time characteristics of the countermovement jump: Analyzing the curve in Excel." Strength & Conditioning Journal 40.2 (2018): 67-77.J. P. Wilkinson, "Nonlinear resonant circuit devices (Patent style)," U.S. Patent 3 624 12, July 16, 1990.

[11] Aboodarda, Saied Jalal, et al. "Enhanced performance with elastic resistance during the eccentric phase of a countermovement jump." International journal of sports physiology and performance 8.2 (2013): 181-187.

[12] Schall Jr, Mark C., et al. "Accuracy and repeatability of an inertial measurement unit system for field-based occupational studies." Ergonomics 59.4 (2016): 591-602.

[13] MacDonald, Kerry, et al. "Validation of an inertial measurement unit for the measurement of jump count and height." Physical Therapy in Sport 25 (2017): 15-19.

[14] Bergamini, Elena, et al. "Estimating orientation using magnetic and inertial sensors and different sensor fusion approaches: Accuracy assessment in manual and locomotion tasks." Sensors 14.10 (2014): 18625-18649.

[15] Bosco, C., et al. "Neuromuscular function and mechanical efficiency of human leg extensor muscles during jumping exercises." Acta Physiologica Scandinavica 114.4 (1982): 543-550.

[16] Teufl, Wolfgang, et al. "Validity of inertial sensor based 3D joint kinematics of static and dynamic sport and physiotherapy specific movements." PloS one 14.2 (2019).

[17] R. J. Gathercole, T. Stellingwerff, and B. C. Sporer, "Effect of acute fatigue and training adaptation on countermovement jump performance in elite snowboard cross athletes," J. Strength Cond. Res., vol. 29, no. 1, pp. 37–46, 2015.

[18] R. Gathercole, B. Sporer, T. Stellingwerff, and G. Sleivert, "Alternative Countermovement-Jump Analysis to Quantify Acute Neuromuscular Fatigue Pilot study investigating the effects of a short-term low FODMAP diet in healthy runners with persistent exercise-associated GI symptoms View project," Int J Sport. Physiol Perform, vol. 10, pp. 84–92, 2015.

Evaluation of robotic endoscopic neurosurgery through kinematic analysis of a simulated surgery

S. E. Ovur[1], E. De Momi[1], E. K. Siena[1], A. Wynn[2,3], L. Lucangeli[4], A. De Benedictis[5], C.E. Marras[5], G. Ferrigno[1], and V. Camomilla[2].

[1] *Department of Electronics, Information and Bioengineering, Politecnico di Milano, Italy*
[2]*Interuniversity Centre of Bioengineering of the Human Neuromusculoskeletal System, University of Rome Foro Italico, Italy*
[3] *Department of Mechanical Engineering, University of Bath, Bath, UK*
[4]*University of Rome "RomaTre", Italy*
[5]*Dipartimento di Neuroscienze e Neuroriabilitazione Ospedale Pediatrico Bambino Gesù I.R.C.C.S., Roma, Italy*

Abstract— **Robots have been introduced in the surgical routine to improve intervention safety and accuracy. Several attempts have been made in the literature to analyze the gesture of the surgeon to provide a quantitative measure of its efficacy and effectiveness. The study describes the research design to characterize robotic brain surgery in comparison to free-hand surgery during a simulated surgery on a 3D printed phantom. The idea is to use outcome measures both targeting result and user actions (such as fluidity, lack of uncertainties, number of attempts) to monitor the training process of robotic surgery in comparison to free-hand surgery in surgeons not acquainted with the robot. Preliminary results are presented on movement fluidity, showing that robotic brain surgery provides smoother trajectories than free-hand brain surgery.**

Keywords—**Brain neurosurgery, motion analysis, surgeon training.**

I. INTRODUCTION

SURGICAL ROBOTS improves the precision and safety of surgical interventions. In neurosurgery, robots have been mainly used for stereotactic procedures [1], when the surgical instruments have to be precisely aligned with respect to the patient, as pre-operatively planned in the medical images reference space. Since the early 1960s, robotic technology has evolved, starting from its first use in the industrial sector to its use within the medical and surgical practice starting from first attempts in the 80s. Over the next decades, the use of medical robots has rapidly expanded to several specific fields, such as soft-tissue, urological, orthopedic, general laparoscopic, and cardiac surgeries.

Robotic assistance was developed in neurosurgical procedures to improve the feasibility and effectiveness of several procedures that require a high level of accuracy and safety, such as biopsy, neuroendoscopy, radiosurgery, neuromodulation treatments, and other stereotactic procedures [2]. Recently, more sophisticated systems have been proposed for other complex treatments, such as brain tumor removal, deep electrode placement for stereo-electroencephalography (SEEG) recording, laser ablation in medically intractable epilepsy, and other functional approaches. In this context, robotic technology is continuously improving. The main goal of this technology is to enhance the surgeon's skills so that he or she can perform microsurgical manipulations, minimally invasive access procedures, accurate stereotactic approaches, and image-guided procedures. In particular, three possible surgeon-robot interaction modalities have been described, depending on whether the robot performs specific preplanned

motions under the supervision of the surgeon (supervisory-controlled system), if the surgeon directly controls the robotic manipulator through a haptic interface (telesurgical system), or if the robot and surgeon jointly control the surgical instrument (shared-control system).

Moreover, robot-guided methods are of increased specific interest in pediatric neurosurgery. In fact, many brain diseases that occur during childhood, such as hydrocephalus, epilepsy, tumors, and movement and behavioral disorders, often constitute a particular challenge for neurosurgeons. Developing structures are more vulnerable to injury than the structures in adults, especially with regard to small and deep targets. Consequently, neurosurgical management requires careful preoperative planning and high intraoperative precision to correctly identify and reach the surgical target without damaging surrounding neurovascular structures.

Endoscopic procedures are usually performed by two techniques (free-hand and rigid, articulated support). These techniques show some limitations. The free-hand technique is strongly related to the operator experience and is hindered in long-lasting procedures (over 60 minutes) due to the surgeon's fatigue that could impair the accuracy of the procedure. The technique supported by the rigid, articulated arm helps in long procedures but reduces the accuracy of the movements. The limits mentioned above should be overcome by the new neuronavigation tools supported by a robotic arm with a suitable number of degrees of freedom. The neuronavigation systems equipped with robotic support (used for clinical purposes) have 5 to 6 degrees of freedom; the same number of the human upper limb (six) composed of the following joints: shoulder, elbow, and wrist. These systems also include different velocity control and movement modality (axial, isocentric, and free) that allow several surgeries to be performed, including neuroendoscopy. Among the robotic systems currently used, the Robotized Stereotactic Assistant (ROSA, Medtech) [3] is a recently developed image-guided device that guides spatial positioning and orientation of neurosurgical instruments according to a planned trajectory.

The main goal of neurosurgical procedures is to obtain the desired outcome thanks to the gesture accuracy, keeping it compatible with surgeon's dexterity and ergonomics. Most of the time, the brain anatomy is complex and the surgical corridors are small or distorted by the disease. Consequently, a system composed of neuronavigation and robotic platform allows the surgeon to optimize the postoperative result, while

minimizing the surgical fatigue. In fact, the availability of a robotic system enables the surgeon to improve the quality of the movements reducing tremor and numbers of attempts to reach the target, particularly in endoscopic procedure which often deals with eloquent structures (e.g. fornix, mammillary bodies, hypothalamus) involved in neuropsychological functions and behaviors.

The effectiveness of robot-assisted interventions has been proven [4]. Endoscopic procedures performed in free-hand modality or supported by a mechanical holder allow a different movement than those assisted by a robotic system. As a matter of fact, it seems that operator movements, carried out by robotic assistance, are more linear and accurate than those performed by free-hand modality. So far, the first aim of the project is to characterize the accuracy of robotic brain surgery in comparison to free-hand using targeting result and user actions (fluidity, lack of uncertainties, number of attempts, etc.) as outcome measures. In parallel, the project will define the learning ability, learning mechanisms, strength and pitfalls of the learning curve of robot-inexperienced surgeons. Monitor of the training process of robotic surgery in comparison to free-hand surgery in surgeons not using robots will be studied as a future development.

II. METHODS

A. Experimental protocol

In our observational study, a simulated surgery was performed on a phantom using both robotic- and free-hand-surgery. Neurosurgeons participating in the study were divided into two groups, both with at least three years of experience of endoscopic brain surgery:

1) *Expert in robotic surgery (RS)*: with at least three years of experience of robot-assisted endoscopic brain surgery
2) *Non-expert in RS (NRS)*.

The following steps were followed:
1. characterize the accuracy of robotic brain surgery in comparison to free-hand surgery
Three neurosurgeons familiar with the use of robot-assisted endoscopic brain surgery (thereinafter: robot surgeons group) act as a study group for this aim (they have 8.3±4y of experience with the robot; 12.7±7y endoscopy experience in general; 73.7±10kg; 1.80±0.11m). Accuracy parameters obtained from the simulated surgery (fluidity, lack of uncertainties, number of attempts, etc.) are computed for robot-patient registration procedures (laser pointer and camera-based) and the robotic- and free-hand-surgery. For the surgery sessions, the outcome measures are compared across conditions (robotic- and free-hand- surgery).
2. monitor the training process of robotic surgery in comparison to free-hand surgery in NRS
Five neurosurgeons who had never performed robot-assisted endoscopic brain surgery (thereinafter: non-robot surgeon group) act as a study group for this aim (13.4±5.9y endoscopy experience in general; 71.8±17.4kg; 1.75±0.11m). Accuracy parameters obtained from the simulated surgery (fluidity, lack of uncertainties, number of attempts, etc.) are computed for the robot registration procedures and the robotic- and free-hand-surgery. For the surgery sessions, the outcome measures are

compared across conditions (robotic- and free-hand- surgery) and across surgeon groups (robot and non-robot surgeons).

Each surgery included the following tasks based on a bespoke 3D printed phantom containing details derived from the real images of a patient (Figure 1):
- *approach:* approaching to the surgery area (image-guided, i.e. relying on neuronavigation screen. Trajectory correspond to the part of the dashed red lines in fig. 1 outside the ventricle)
- *reachA:* reaching the posterior are of the ventricles (endoscope guided)
- *line:* following a circular line simulating a surgical action on the ventricular surface (Monro foramen rim)
- *moveAB:* move a small object from the right fornix close to the foramen of Monro (hole A) and the lateral part of the right frontal horn close to the caudate head with the higher diameter (hole B)
- *tunnel:* get to the end of a cave cylinder (2mm diameter, 4mm length simulating crossing the Monro foramen)
- *reachB:* return back to hole B
- *moveBA:* move the small object back from hole B to A
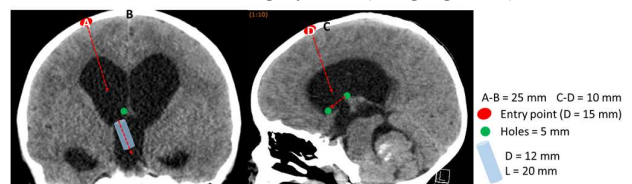- *exit:* exit from the surgery area (image-guided)

Fig. 1: Images of a real patient used for approach and exiting (when in the real surgery the endoscope is blinded by the brain parenchyma). All measures are in millimeters. Geometrical features (gray tube and green holes (cups)) have been replicated in the 3D printed phantom.
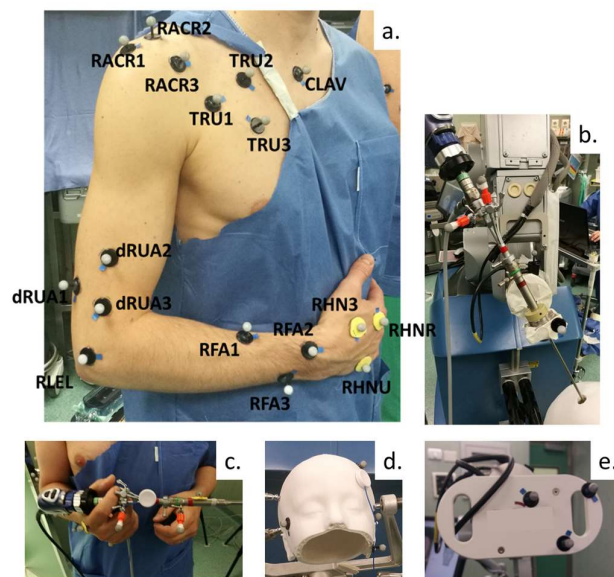

Fig. 2: Markers belonging to technical clusters are depicted for: a. shoulder (RACR1, RACR2, RACR3); distal upper arm (dRUA1, dRUA2, dRUA3); distal forearm (RFA1, RFA2, RFA3); hand second and fifth metacarpal head, fifth metacarpal head (RHN3, RHNU, RHNR); trunk (TRU1, TRU2, TRU3); b. free-hand probe; c. robotic-probe; d. phantom head; and e. laser-pointer for robot-patient registration. Five anatomical landmarks (C7, spinous process of the 7th cervical vertebra; LEL and MEL, lateral and medial elbow epicondyles; RS and US, radius and ulna styloid.) were calibrated with a rod equipped with markers. For two landmarks, a marker was also permanently acquired during the tasks (CLAV, on the clavicular notch; LEL on the lateral elbow epicondyle).
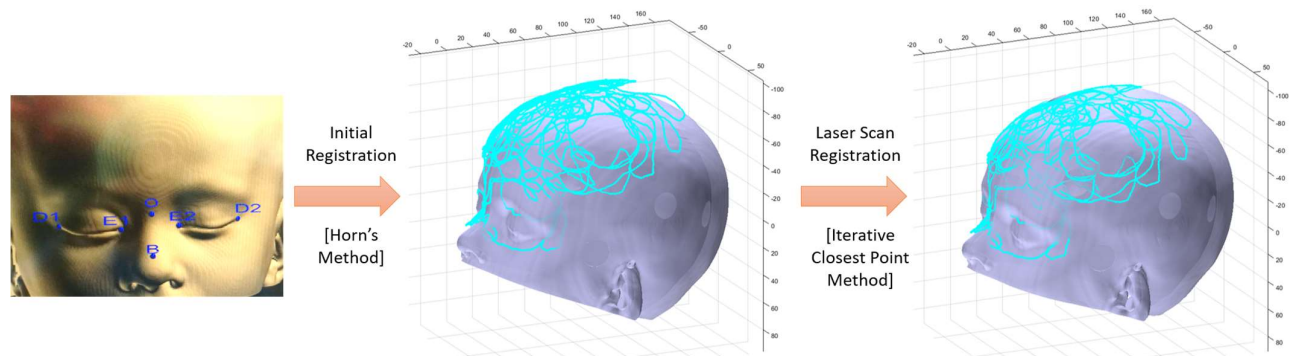
Fig. 3: Registration steps of the experimental setup from the robot frame to the CAD model of the skull. On the left, the six initial points used for the first estimation of registration are visualized. In the center results of one initial registration are reported (RMSE=4.7 [mm]) and, on the right, final registration results by using ICP method (RMSE=1.37 [mm]).

Acquisitions were performed at "Ospedale Pediatrico Bambin Gesù" in Rome, Italy. The Ethical Committee of the hospital approved the study.

B. Experimental setup

Passive optical markers were positioned to acquire the kinematics of trunk, operating upper limb, and tip probe, on the surgeon, free-hand and robotic-probe, phantom head, and laser-pointer (Fig. 2). The 15 technical and two anatomical markers placed onto the surgeons followed a model developed for overhead tasks [5-7] (Fig. 2a). The tip of the two endoscopic probes and six anatomical landmarks (ALs: C7, spinous process of the 7th cervical vertebra; LEL and MEL, lateral and medial elbow epicondyles; RS and US, radius and ulna styloids), were calibrated using a calibrated rod carrying three markers. Three segments (trunk, upper arm, and forearm) were considered as connected by six DoF shoulder and elbow joints. The shoulder joint centre was estimated using a regression equation [5]. Marker data were recorded with a four camera motion capture system (Bonita, Vicon Motion Systems Ltd, Oxford, UK) and software (Vicon Nexus V2.7).

C. Registration

In order to evaluate the acquired data, a CAD model of the head has been 3D printed. This model needs to be registered to the printed skull attached to the robot frame. Registration is performed in two stages. Initially, coarse registration accomplished by roughly measuring with the calibrated rod already mentioned pre-determined points on the skull for both printed and CAD skull models. Then, the registration is completed by using the acquired scan of the skull carried out with the mentioned calibrated rod.

In Fig. 3, initial points taken from the skull are visualized on the left. After that, the Horn's Method [8] is applied with those initial calibration points. Resulting registration is given in the center of Fig. 3. Where the cyan-colored line shows the head scan of the experimental skull setup and gray color represent registered CAD model. After that, this head scan is used to obtain a better registration by using the Iterative Closest Point (ICP) method [9]. Resulting registration is visualized in Fig. 3.

D. Performance metrics and data analysis

To quantify the quality of the motion in terms of lack of uncertainties and smoothness, the spectral arc length measure [10] was computed on the speed trajectories of the endoscopic probe tip as obtained from probe markers, after filtering by a Butterworth filter of the 10th order, with a 10Hz cut-off frequency. Default parameters (e.g. Max. Cutoff Frequency = 10 Hz) were used. Shapiro-Wilk test was used to test for normal distribution and a Wilcoxon test was used to compare the two different tasks (freehand and robot-assisted surgery).

III. RESULTS

A. CAD-Skull registration

Preliminary results show less than 2 mm accuracy in the registration of the 3D printed model with the CAD consistent with the patient images. As an example, in Fig. 3 the residual error with initial calibration by using Horn's method resulted as 4.7 mm root mean square error (RMSE), and after the application of ICP resulted as 1.37 mm RMSE. Considering the ten calibrations performed during experiments, median and 75th percentile were found as 8.13 mm and 8.82 mm respectively after the Horn's calibration, while they were
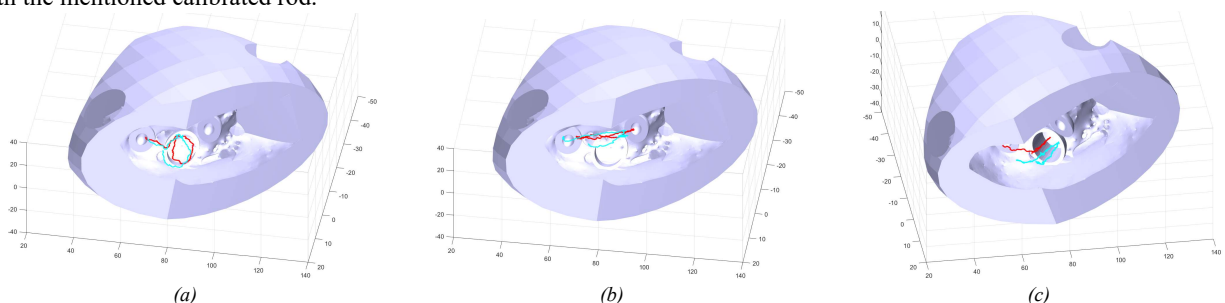

Fig. 4: Performed tasks are visualized during the robotic surgery (paths with cyan color) and free-hand surgery (paths with red color) during (a) drawing a circle - *line*, (b) moving from hole A to hole B – *moveAB* - and (c) moving along the *tunnel*.

decreased to 1.56 mm and 1.77 mm after the final calibration with ICP.

B. Preliminary Results on Data

In Fig. 4 (a), (b) and (c), three main tasks performed inside the skull are visualized for both robotic- and free-hand-surgery during the tasks of: 'drawing a circle', 'moving from hole A to hole B' and 'moving along the tunnel', respectively. The cyan-colored path shows the data acquired from the free-hand surgery and a red-colored path shows the data acquired during the robotic surgery.

The median of the Spectral arc length of the speed of the endoscope tip computed for RS and NRS with inter-quartile range (IQR) is reported in the Table below:

TASK	FREE HAND				ROBOT ASSISTED			
	RS		NRS		RS		NRS	
	median	IQR	median	IQR	median	IQR	median	IQR
Approach	-3.8	4.7	-4.2	2.2	-4.7	8.2	-2.4	0.2
Exit	-5.1	2.4	-3.5	4.2	-2.3	1.1	-4.1	1.3
Line	-4.7	3.0	-9.6	2.6	-5.1	0.9	-5.3	4.0
Move A	-9.1	1.3	-11.2	3.2	-6.5	4.0	-7.5	2.0
Move B	-9.3	4.0	-7.4	3.0	-10.5	16.0	-6.0	3.5
Reach A	-3.8	0.5	-3.7	2.5	-2.6	0.5	-3.0	0.6
Reach B	-5.3	2.4	-4.2	0.7	-4.0	2.3	-3.3	1.0
Tunnel	-7.5	2.0	-8.1	2.7	-3.2	2.4	-3.2	1.9

Figure 5 shows Boxplots of the spectral arc length of the speed for the two surgeon groups (RS and NRS) under the two conditions (freehand and robot).
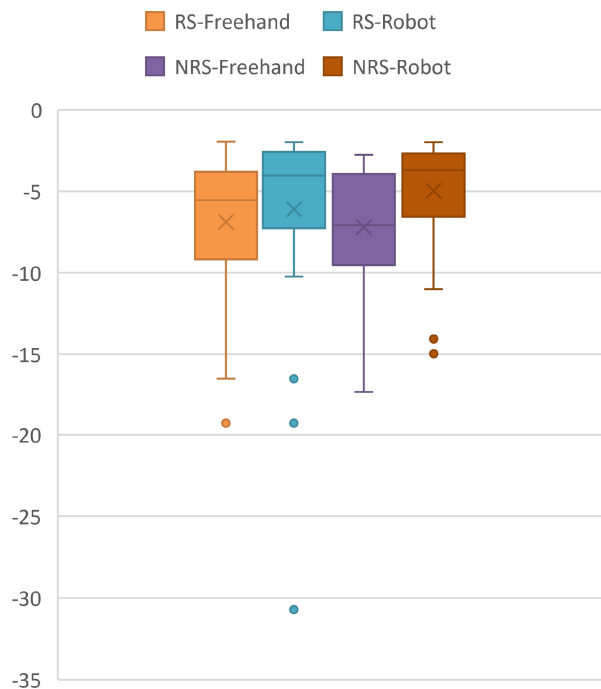

Fig. 5: Boxplots of the spectral arc length of the speed for the two surgeon groups (RS and NRS) and under the two conditions (freehand and robot-assisted).

According to Wilcoxon test, a significant difference (p<0.05) was confirmed between the robotic and free-hand surgeries without distinction between RS and NRS groups, pointing out the effect of the use of the robot on the movement fluidity. No difference was plausible between the two groups (RS and NRS) within the two conditions 'RS-NRS freehand': p=0.738 and 'RS-NRS' robotic surgery: p=0.733).

IV. CONCLUSION

This paper showed the feasibility of a method designed to assess the brain neurosurgery ability by using a Motion capture system and a bespoke head phantom and images set. Preliminary data processing shows that robotic surgery ensures smoother trajectories during the designed study case. No learning effect was studied in this paper. This will be done in future papers. Eventually, a real effect of the robot on the fluidity of the movement has been pointed out, even in non-robot surgeon despite lack of specific training. Furthermore, the developed phantom with its set of images set represents a good training device for either surgeon expert and non-expert with the robotic approach.

REFERENCES

[1] C. Faria, W. Erlhagen, M. Rito, … & E. Bicho, "Review of robotic technology for stereotactic neurosurgery." *IEEE reviews in biomedical engineering*, vol. 8, pp. 125-137, 2015.
[2] A. De Benedictis, A. Trezza, A. Carai, ... & P. Amante, "Robot-assisted procedures in pediatric neurosurgery." *Neurosurgical focus*, vol. 42(5), E7, 2017.
[3] M. Lefranc and J. Peltier. "Evaluation of the ROSA™ Spine robot for minimally invasive surgical procedures." *Expert review of medical devices*, vol. 13(10), 899-906, 2016.
[4] J. Heemskerk, D. E. de Hoog, W. G. van Gemert, C. … & N. D. Bouvy, "Robot-assisted vs. conventional laparoscopic rectopexy for rectal prolapse: a comparative study on costs and time." *Diseases of the colon & rectum*, vol. 50(11), pp. 1825-1830, 2007.
[5] A. C., Campbell, D. G., Lloyd, J. A., Alderson, B. C. Elliott, "MRI development and validation of two new predictive methods of glenohumeral joint centre location identification and comparison with established techniques." *Journal of Biomechanics*, vol. 42(10), pp. 1527–1532, 2009.
[6] A. Chin, D. G. Lloyd, J. A. Alderson, B. C. Elliott and P. Mills, "A marker-based mean finite helical axis model to determine elbow rotation axes and kinematics in vivo." *Journal of Applied Biomechanics*, vol. 26(3), 305–315, 2010.
[7] D. Wells, C. Donnelly, B. Elliott, K. Middleton, J. Alderson, "The inter-tester repeatability of a model for analysing elbow flexion-extension during overhead sporting movements." *Medical & Biological Engineering & Computing*, pp. 1 –8, 2018.
[8] B. K. Horn, "Closed-form solution of absolute orientation using unit quaternions." *Josa a*, vol. 4(4),P pp:.. 629-642, 1987.
[9] P. J., Besl, and N. D. McKay IV, "Method for registration of 3-D shapes." In Sensor fusion IV: control paradigms and data structures. Vol. 1611. *International Society for Optics and Photonics*, 1992.
[10] S. Balasubramanian, A. Melendez-Calderon, and E. Burdet, "A robust and sensitive metric for quantifying movement smoothness." *IEEE transactions on biomedical engineering*, vol. 59(8), 2126-2136, 2011.

Development of a novel bioreactor for the generation of controlled hydrodynamic stimuli on vascular planar tissue samples

Elia Pederzani[1], Lorenzo P. Coppadoro[1], Aldo J.S. Roldan[1], Chiara Foglieni[2], Monica Soncini[1], Gianfranco B. Fiore[1]

[1] Department of Electronics, Information and Bioengineering, Politecnico di Milano, Italy
[2] San Raffaele Hospital IRCCS, Milano Italy

Abstract - **The complex phenomena and interactions that occur within the vascular tissue during the evolution of atherosclerotic pathology are still not fully understood today. Most of the *in vitro* studies examine the phenomenon using endothelial layers, thus not being able to evaluate the development of an atherosclerotic plaque between intima and media tunica. Furthermore, the stress conditions are often far from the real stress state observed *in vivo*. For this reason, we have developed a device that not only allows to accommodate samples of vascular tissue, but which also offers the possibility of applying a wide range of shear stress patterns under strictly controlled conditions. Such a device is able to recapitulate atherogenic or atheroprotective stimuli thus paving the way for physiopathological studies aimed at unravelling the role of shear stress patterns on cells response in reliable tissue models.**

Keywords - **dynamic culture system, multidirectional wall shear stress, atherogenic solicitation.**

I. Introduction

Atherosclerosis is a chronic-degenerative pathological phenomenon that affects the arterial cardiovascular system. The evolution of the disease is due to the formation and progressive growth of a plaque of lipid nature, called atheroma, which progresses in the sub-endothelial tissue of the vessel [1]. In the most advanced stages of the pathology, the plaque reaches such dimensions as to partially occlude the vessel, thus causing a stenosis, and furthermore, it is susceptible to rupture that causes the release of dangerous agglomerates into the bloodstream that can cause thrombi.

In literature, one of the pro-pathological risk factors is the influence of blood flow on mechanotransduction mechanisms of endothelial cells [2]. In fact, the cells are extremely sensitive to tangential stresses occurring in the vessel wall (wall shear stress, WSS), which are correlated with local fluid dynamics. It is known that the arterial districts, where atherosclerotic plaques are most frequently found, are those with disturbed fluid dynamics. Indeed, the alteration of WSS is considered the trigger of endothelium's permeabilization and consequent lipids' diffusion within the intima tunica [3]. An in-depth literature analysis has allowed us to identify three main numerical indexes:

$$TAWSS = \frac{1}{T}\int_0^T |\vec{\tau}_w|\, dt \qquad (1)$$

$$OSI = \frac{1}{2}\left(1 - \frac{\left|\int_0^T \vec{\tau}_w dt\right|}{\int_0^T |\vec{\tau}_w| dt}\right) \qquad (2)$$

$$transWSS = \frac{1}{T}\int_0^T \left|\vec{\tau}_w\left(\vec{n} \times \frac{\int_0^T \vec{\tau}_w dt}{\left|\int_0^T \vec{\tau}_w dt\right|}\right)\right| dt \qquad (3)$$

where, T is cardiac cycle [s], $\vec{\tau}_w$ is WSS, $\vec{n}$ is the perpendicular vector to the vessel's endothelium.

The combined use of these indexes lets us to perform an accurate and complete characterization of the disturbed flow and to discriminate between atherogenic and atheroprotective conditions [4]. Despite this, the relationship between the hydrodynamic stress felt by endothelial cells and its effects on inflammation and mechanotransduction mechanisms has not yet been clearly established.

In this scenario, we have developed a novel device that allows to host human vascular tissue samples of not negligible thickness, and to apply multidirectional, complex and variable over time WSS patterns by reproducing the numerical values identified for the indexes described above. Furthermore, for its use in biological Labs, the device must have all the general requirements for cell and tissue culture bioreactors: biocompatibility of materials, sterility maintenance, to be compliant with good laboratory practices, low priming volume. The developed device enables the possibility to investigate the effects of specific WSS patterns on vascular cells behaviour.

II. Culture system

The strategy chosen for the bioreactor design is to apply a constant flow rate while the sample rotates with a specific motion function. In this way it is possible to reproduce the complex WSS multidirectional nature felt by endothelial cells *in vivo*. The designed bioreactor consists of two main elements: the vascular sample housing (dark grey, green, red Fig. *1*) and the parallel plates flow chamber (light grey, Fig. 1). The sample is placed in an *ad hoc* designed cartridge to be inserted in the housing system consisting of a ferrule coupled with a threaded element ("piston", green element Fig. 1), which includes also hydraulic channels for feeding the sample's adventitial side, and is secured to possible leakage with a silicone gasket. Once assembled, the housing system is placed in the parallel plate flow chamber (light grey, Figure. 1). The flow channel has a rectangular section and is sized to keep the required flow rate relatively low (under 100 mL/min) and avoiding edge effects on the exposed endothelium area. The channel is connected to the external

circuit using Luer-Lock® connectors and placed in continuity with a distributor at the inlet and with a collector at the outlet of the channel; the connectors are designed to avoid possible areas of fluid stagnation. Thanks to the presence of two gears (blue, Fig. 1) it is possible to transfer the rotary motion of a stepper motor to the entire housing system and consequently to the hosted biological sample. The motor's movement and the pump actuating the fluidic circuit are controlled by an Arduino-based electronic interface, enabling also the setting of the fluidynamic parameters (stress frequency, TAWSS, OSI, transWSS).
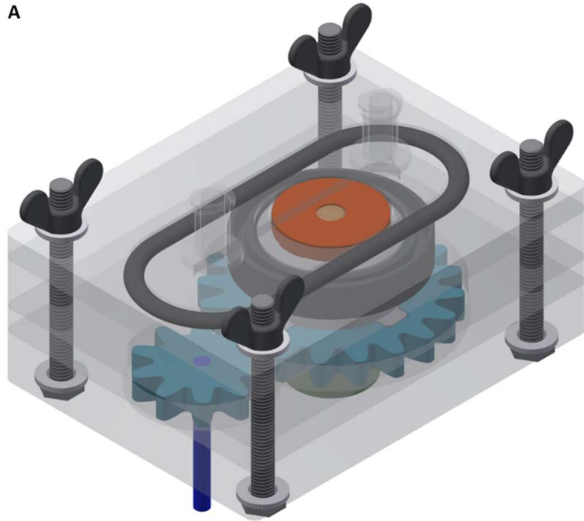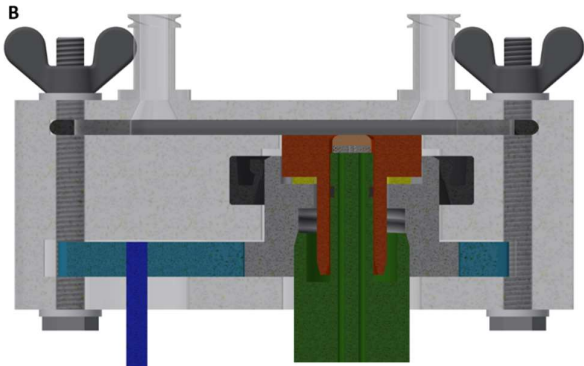
Fig. 1 (A) Assembled bioreactor; (B) sectional view on the middle longitudinal plane of the bioreactor.

In order to minimize the risk of tissue damage during sample handling and sample mounting within the bioreactor we have also devised specific procedures and realized auxiliary accessories. The steps for assembly the bioreactor are articulated in three main phases and must be carried out by the operator inside the laminar flow hood: first phase is aimed at punching the tissue sample; second phase is functional to correct assembly of the housing; third phase involves the assembly of the flow chamber with inside the housing. Fig. *2* shows all the steps to be performed. At the end of the procedure, the bioreactor is placed inside an incubator connecting it with the hydraulic circuit and coupling the stepper motor's shaft with the device's smaller gear. The correct alignment of the endothelium with the flow chamber bottom is essential to stimulate the sample with the desired WSS. The alignment is made possible by the joint use

of a distance sensor to detect the position of the sample with respect to a reference plane and the threated piston adjusting the sample position.
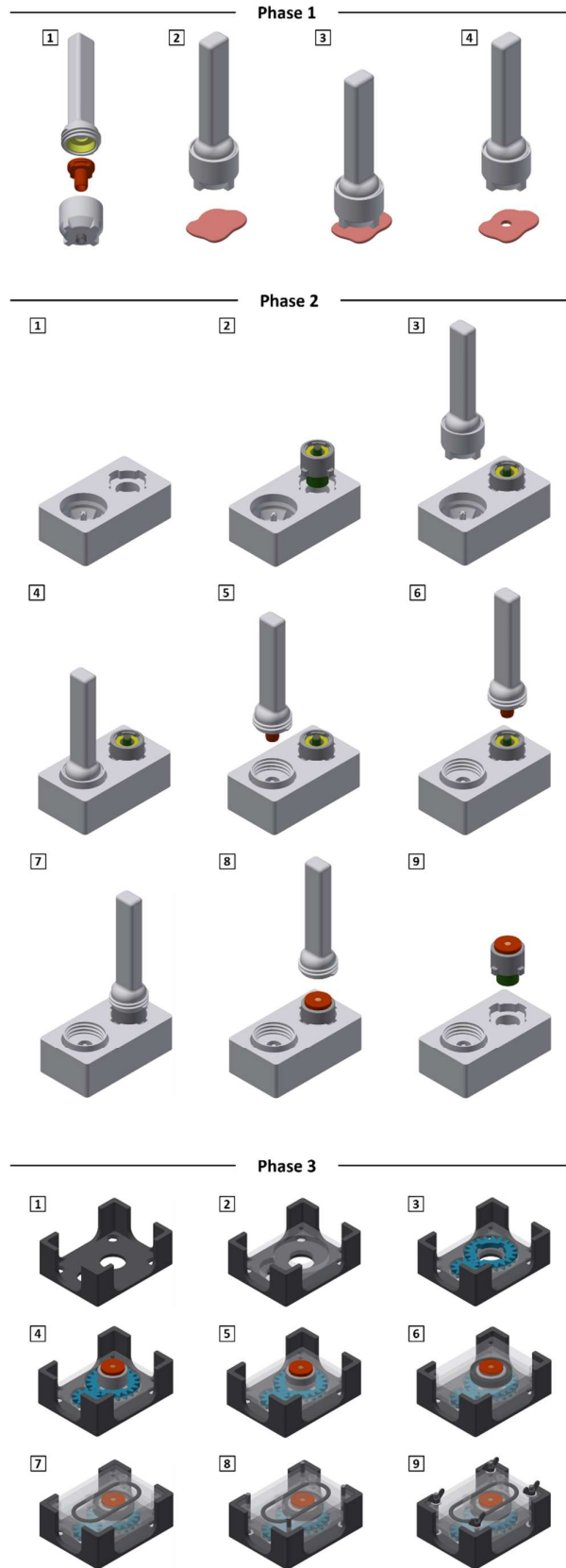

Fig. 2 Schematic of the steps to be performed during each assembly phase.

III. RESULTS AND DISCUSSION

Up to now, the device has been successfully verified by performing the first bench tests: *in silico* simulations, characterization of the endothelium surface position detection system and water tightness tests.

A. Fluidynamics simulation

In order to apply the desired WSS on the sample's endothelium, the required flow rate is estimated through Eq. (4) [5].

$$\vec{Q} = \vec{\tau}_w \frac{\pi^3 wh}{48\mu} \frac{\left[1 - \sum_{n,odd}^{\infty} \frac{1}{n^5} \frac{192\,h}{\pi^5\,w} \tanh\left(n\pi\frac{w}{2h}\right)\right]}{\sum_{n,odd}^{\infty} \frac{1}{n^3}\left[1 - \frac{\cosh\left(n\pi\frac{x}{h}\right)}{\cosh\left(n\pi\frac{w}{2h}\right)}\right]\frac{n\pi}{h}} \tag{4}$$

where μ is the dynamic viscosity of the fluid [Pa·s], w and h are width and the height of the channel [m], y it is the spatial coordinate in which to evaluate WSS $\left(-\frac{1}{2}w \le x \le \frac{1}{2}w\right)$.

The analytical result is used as flow rate input for the fluidynamic simulations using COMSOL Multiphysics® finite element simulation software. Analysing the simulation results (Fig. 3 and Fig. 4), the shear stress is uniformly distributed along the entire channel and the endothelium exposed area is not affected by edge effects (sample diameter of 5 mm). Furthermore, we can consider the flow flatly developed after about 7 mm. The graphics of Fig. 4 show a good solicitation accuracy: 5% less than the target WSS value. Therefore, Eq. (4) will be used in the electronic interface to set the flow rate necessary to obtain TAWSS value set by the operator.
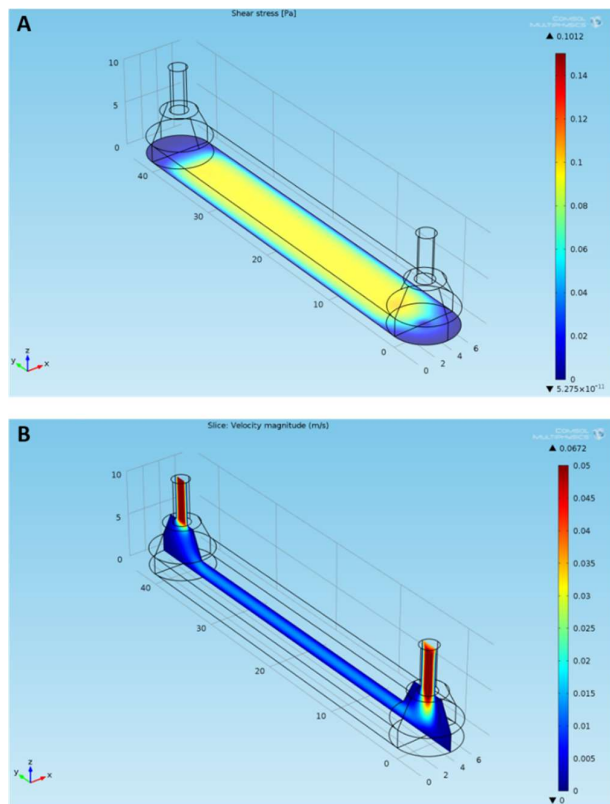

Fig. 3 Atherogenic condition ($TAWSS = 0.1\ Pa$): (A) color map of shear stress acting on the bottom of the channel; (B) color map of the fluid velocity module in the channel symmetry plane.
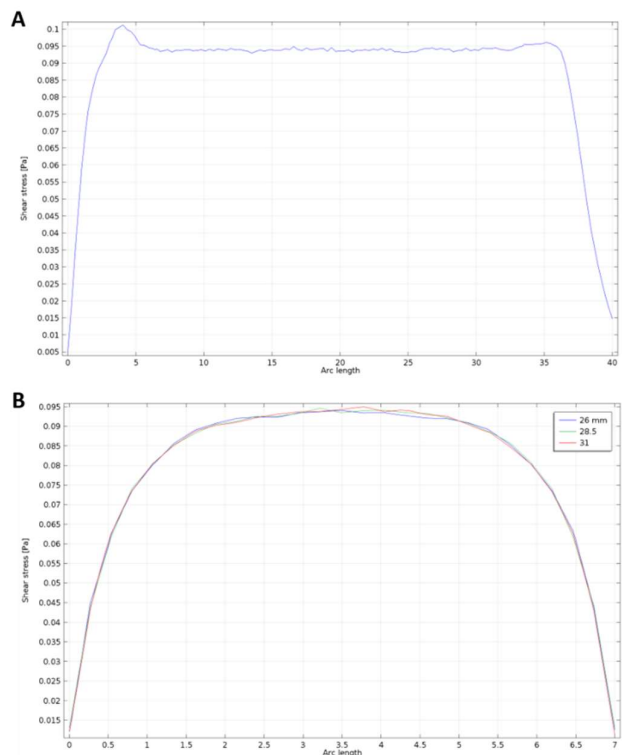

Fig. 4 Atherogenic condition ($TAWSS = 0.1\ Pa$): (A) trend of the shear stress modulus as a function of the canal length along the center line; (B) shear stress modulus as a function of the channel width along 3 different sections at 26 mm, 28.5 mm (sample center) and 31 mm from the inlet.

B. Characterization of the sample position detection system

In order to verify the effectiveness of the sample position detection system previously described in providing a precise numerical value that allows accurate positioning of the sample by adjusting the thrust exerted by the piston, an ad hoc validation apparatus has been set and used (Figure 5).
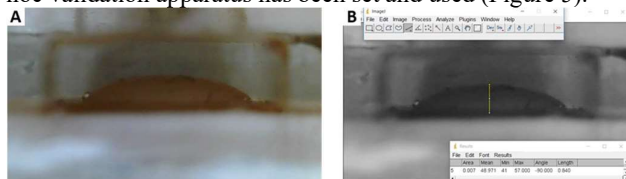

Fig. 5 (A) Original photograph; (B) image processed by ImageJ.

The average detection sensitivity of the detection system is approximately 300 mV/mm and the signal-to-noise ratio is approximately $SNR \cong 50$.

C. Hydraulic seal assessment

Based on the hydraulic characteristics of the system and the circuit, it can be estimated that the internal pressure will not exceed 20 mmHg under normal operating conditions. Therefore, in order to ensure safety of the sample within the culture system with respect to possible overpressure events due to any abnormal hydraulic situations, three watertight tests are carried out, pressurizing the bioreactor in a range from -300 mmHg up to 780 mmHg (with 50 mmHg increments) using distilled water as a filling fluid. In each of the three tests, there is no evidence of fluid leakage. Furthermore, a prolonged leak test is carried out, pressurizing the device at 100 mmHg, a pressure value higher than the typical values occurring in working conditions, and

evaluating any leaks each day for five days; even in this case no fluid losses are observed. Finally, a further five-days long seal test is performed at 100 mmHg, using culture medium (Dulbecco's Modified Eagle Medium) with 10% of Foetal Bovine Serum and placing the bioreactor inside a thermostat bath set at 37°C. Also, in this test the maintenance of the hydraulic seal is verified.

IV. CONCLUSION

The prototyped device represents an innovative device with respect to the current state of the art enabling the possibility to investigate the WSS effects, no longer on a cellular layer, but also on vascular tissue samples. The next steps of the project are: i) verification of the sterility maintenance of the device; ii) preliminary experiments with aorta patches to verify effects of different solicitation's pattern on the endothelium; iii) implementing a feedback loop system for the sample adjustment. In perspective we will exploit this device to examine the complex mechanobiological interactions that occur in the sub-endothelial tissue in the early stage of the atherosclerosis pathology evolution.

REFERENCES

[1] P. Libby, "Mechanisms of Acute Coronary Syndromes and Their Implications for Therapy," 2013.

[2] K. S. Cunningham and A. I. Gotlieb, "The role of shear stress in the pathogenesis of atherosclerosis," *Lab. Investig.*, vol. 85, no. 1, pp. 9–23, 2005.

[3] M. A. Gimbrone Jr and G. García-Cardeña, "Vascular endothelium , hemodynamics , and the pathobiology of atherosclerosis," *Cardiovasc. Pathol.*, vol. 22, no. 1, pp. 9–15, 2013.

[4] V. Peiffer, S. J. Sherwin, and P. D. Weinberg, "Computation in the rabbit aorta of a new metric - the transverse wall shear stress - to quantify the multidirectional character of disturbed blood flow," *J. Biomech.*, vol. 46, no. 15, pp. 2651–2658, 2013.

[5] H. Bruus, *Theoretical Microfluidics*, First. Oxford University Press, 2008.

Versatile perfusion and electrical stimulation bioreactor for bone tissue engineering

D. Massai[1], S. Gabetti[1], G. Putame[1], I. Armando[1], E. Fiume[2], A. Sanginario[3], D. Carbonaro[1],
F. Baino[2], A.L. Audenino[1], E. Verné[2], C. Bignardi[1]

[1] PolitoBIOMed Lab, Department of Mechanical and Aerospace Engineering, Politecnico di Torino, Italy
[2] Department of Applied Science and Technology, Politecnico di Torino, Italy
[3] Department of Electronics and Telecommunications, Politecnico di Torino, Italy

Abstract— In this study, we developed a versatile innovative bioreactor that allows combining biomimetic direct perfusion and tunable electrical stimulation, to be used for cell seeding or perfusion culture in bone tissue engineering applications. Fast, flexible and low-cost 3D printing technologies were used for manufacturing the bioreactor components. Preliminary tests validated the bioreactor in terms of ease of use, versatility, and functionality.

Keywords— Perfusion bioreactor, Electrical stimulation, Bone tissue engineering, 3D printing manufacturing.

I. INTRODUCTION

NOWADAYS, due to the aging of the population, the need for bone replacement is dramatically increasing worldwide together with the challenging clinical management of bone fractures [1]. In this scenario, bone tissue engineering (BTE) is rapidly evolving as a promising strategy for healing damaged bone tissue. In detail, by combining bone-forming cells, three-dimensional (3D) porous scaffolds, and physiological chemico-physical signals mimicking the *in vivo* environment of bone tissue [2]-[4], BTE aims to generate *in vitro* functional bone tissue substitutes containing mature and differentiated cells. However, reaching homogeneous cell distribution, guaranteeing efficient nutrient transport and waste removal, and providing biomimetic physical signals throughout thick 3D bone-like structures is challenging *in vitro*, particularly in static culture [5].

Bioreactors are culture devices appositely designed to cope with these limitations, enabling cell/tissue culture in a dynamic 3D environment, under user-defined physical stimuli (e.g., stretching, compression, electrical pulse, and fluid shear stress), and under monitored and controlled conditions [6]-[12]. In particular, a number of BTE studies demonstrated that perfusion bioreactors, providing continuous medium flow through the cultured constructs, guarantee beneficial mass transport during both cell seeding and 3D tissue culture [13], [14]. Moreover, flow-induced shear stress was shown to play a key role in proliferation and differentiation of osteoblasts and in promoting bone mineralization [15]. Other BTE studies demonstrated that electrical stimulation, successfully used for decades in clinical practice to stimulate bone healing, influences the behavior and/or function of bone-forming stem cells [16]. Inspired by these studies, we developed a versatile innovative bioreactor that, for the first time, combines biomimetic perfusion and tunable electrical stimulation, to be used for BTE cell seeding and tissue culture. Fast and flexible 3D printing technologies, i.e., stereolitography and fused deposition modeling (FDM), were used for bioreactor

manufacturing [17]. To investigate the electric field developing within the culture chamber and to define the optimal electrode configuration, a computational analysis was performed. Lastly, for validating the bioreactor functionality, preliminary perfusion tests were carried out using a glass-ceramic scaffold with foam-like 3D architecture.

II. MATERIALS AND METHODS

A. Bioreactor

Specific requirements guided the bioreactor design. In detail, the bioreactor should provide direct perfusion of the 3D cultured constructs, for guaranteeing homogeneous cell distribution during cell seeding procedure, and efficient nutrient transport and waste removal during tissue cultivation. Moreover, the device should allow delivering tunable and combinable physical stimuli, i.e., flow-induced shear stress and electrical stimulation. Customization and modularity requirements came from the need to guarantee versatility, to enable seeding and culturing of cylindrical constructs of different sizes. Lastly, the bioreactor should be compact to be placed on a standard incubator shelf and compatible with Good Laboratory Practices (GLP), thus it should be easy to use and to clean with standard tools and techniques available in a biological laboratory, with all materials in contact with culture medium and/or cells selected to be biocompatible and autoclavable. To satisfy these requirements, the proposed bioreactor is currently composed of: 1) a culture chamber, for housing the constructs; 2) a perfusion system, for guaranteeing continuous direct perfusion.

In detail, the culture chamber (outer diameter = 54 mm, height = 57 mm, priming volume ~ 10 ml) consists of two hollow cylindrical parts, which can be easily screwed together, presenting one medium inlet and one outlet, respectively. Four different toroidal silicone holders (outer diameter = 24 mm, inner diameter = 7-10 mm, height = 15 mm) were molded for housing press-fitted cylindrical scaffolds with different diameters (7-10 mm) and heights (1-15 mm), to be inserted within the culture chamber for direct perfusion (Fig. 1A). Two stainless steel circular planar electrodes are screwed at the bottom and top of the culture chamber, aligned with the medium inlet and outlet respectively (Fig. 1B), for delivering electrical stimulation when externally connected to an electrical stimulator. Lastly, silicone O-rings assure the culture chamber sealing.

The culture chamber is part of a closed-loop perfusion system, composed of gas-permeable tubing (platinum-cured

silicone, Masterflex), a peristaltic pump (REGLO Analog MS-4/6, Ismatec), a medium reservoir, stopcocks for medium sampling/replacement, and injection sites upstream and downstream the culture chamber for cell/solution injection. This system can be used for cell seeding, exploiting the injection sites and imposing a bidirectional flow (flow rate = 0.1-1 ml/min), or for perfusion culture, adopting unidirectional flow (flow rate = 0.5-3 ml/min).

The bioreactor culture chamber and the holder moulds were designed using the commercial computer aided design (CAD) software Solidworks 2017 (Dassault Systemes). The culture chamber (DentalSG resin, FormLabs) was 3D printed by stereolitography (Form 3, FormLabs). The molds (ABS plus-P430, Stratasys) were manufactured by FDM printing (uPrint SE Plus, Stratasys), and the holders were produced by pouring silicone (Sylgard 184, Dow Corning) into the molds. To define the optimal electrode configuration in terms of shape and position, a computational analysis described in the following was carried out.
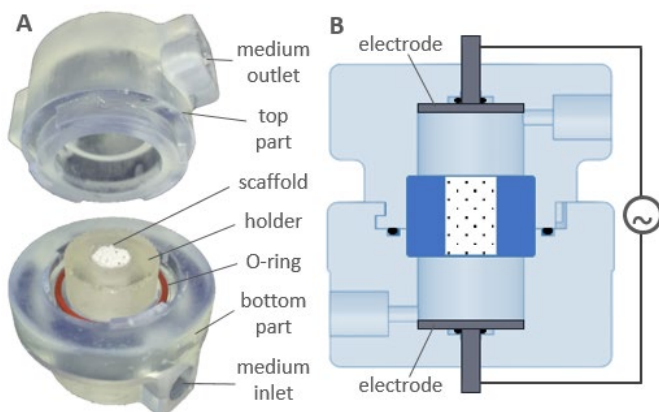

Fig. 1: A) Picture of the open culture chamber, housing an explanatory scaffold inserted press-fit in the holder; B) Section view of the culture chamber, with the circular planar electrode configuration.

B. Computational analysis

Using a commercial finite element analysis software (COMSOL Multiphysics) and adopting different electrode configurations, simulations of the electric field developing within the culture chamber were performed. In detail, three different configurations were considered: ring-shaped electrodes placed on the holder flat surfaces (RE); plate-shaped electrodes embedded in the silicone holder (PE); circular planar electrodes placed at the bottom and top of the culture chamber (CE). The 3D geometry was modelled as five different homogeneous sub-domains (the culture chamber, the holder, the scaffold, the culture medium volume, and the electrodes), and specific electrical properties were assigned to each of them. Stationary simulations were carried out imposing a voltage ranging from 0.5 to 15 V (step = 0.5 V) between the electrodes.

C. Preliminary tests

Tests on the bioreactor system were performed in-house for proving ease of assembling/coupling, watertightness, versatility, and reliability. In particular, for watertightness assessment, the system was tested in different configurations (culture chamber with O-ring, culture chamber with O-ring and holder, culture chamber with O-ring, holder and scaffold) using demineralized water and imposing five different flow rates (1 ml/min, 5 ml/min, 10 ml/min, 20 ml/min, 52 ml/min) for at least 1 h. As explanatory scaffold, a cylindrical silicate glass-ceramic scaffold [18], [19], produced by sponge replication and exhibiting a bone-like trabecular architecture (diameter = 10 mm, height = 10 mm, macropore size within 100-500 μm), was press-fitted within the 10 mm-diameter holder.

III. RESULTS AND DISCUSSION

A. Bioreactor

Preliminary tests confirmed the bioreactor ease of use, watertightness, versatility, and reliability. In particular, the correct screwing and coupling between the two parts of the culture chamber was proved, together with the holding and sealing performance of the holders. The watertightness was verified, with no leakage for all configurations and imposed flow rates. The preliminary tests confirmed that, in the current bioreactor configuration, the culture medium enters from the bottom of the culture chamber, passes through the construct guaranteeing direct perfusion, and goes out from the top, following an S-shaped path that allows avoiding stagnation/recirculation regions and air bubbles.

B. Computational analysis

The simulations provided a full description of the 3D pattern of the electric field and current density through the sub-domains, particularly in the scaffold region where cells will be seeded and cultured (Fig.2).
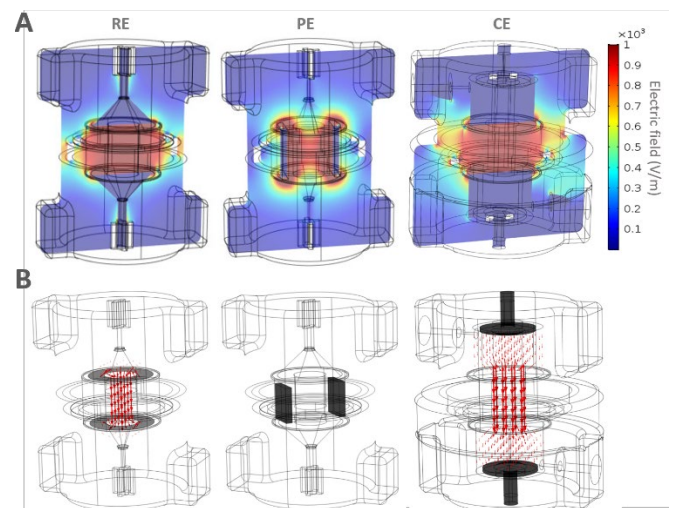

Fig. 2: A) Contour plots of electric field magnitude for the RE, PE, and CE configurations; B) Vector diagrams of the current density (red arrows) simulated for the RE, PE, and CE configurations.

Explanatory results, obtained imposing 15 V between the electrodes, showed that both RE and CE electrode configurations provide uniform distributions of electric field (Fig. 2A) and current density (Fig.2B) throughout the scaffold. Differently, the PE configuration is characterized by a heterogeneous electric field distribution through the scaffold. In detail, along the axial direction of the scaffold, the electric

field values increase towards the scaffold center, while in the radial direction the electric field values are the highest near the electrodes (Fig. 2A). Further, because in PE configuration the electrodes are embedded in the silicone holder, this latter insulates the electrodes and thus the current density is null (Fig. 2B). Since RE and CE configurations are comparable in terms of provided electrical stimuli, for ease of assembling we decided to adopt the CE configuration, which allows to easily connect the electrode pins to an external stimulator.

IV. CONCLUSION

Besides guaranteeing ease of use, versatility, and reliability, the developed bioreactor provides for the first time an *in vitro* 3D culture environment in which perfusion and electrical stimulation can be combined for resolving mass transport limitations and for mimicking the *in vivo* environment of bone tissue. The adopted in-house design and manufacturing procedures provided customization freedom, strict design-to-prototype timing, and low-cost and rapid production. In the current configuration, the bioreactor can be used for both cell seeding and direct perfusion culture. In the next future, it will be equipped with a dedicated electrical stimulator, and BTE constructs will be cultured under individual or combined dynamic conditions (i.e., perfusion and/or electrical stimulation) for investigating the effects of shear stress and electrical stimuli on bone tissue formation and maturation. In parallel, fluid dynamic computational analyses combined with microcomputed tomography of scaffolds [20] and mature constructs [21] will be performed, focusing particularly on shear stress distributions. This will enable to correlate the adopted flow rate, the induced shear stresses, the imposed electrical stimulation and the biological outcomes, helping to reduce the number of time-consuming and expensive trial-and-error experiments and ultimately providing a comprehensive characterization of the physical and biological processes developing within the bioreactor.

REFERENCES

[1] A. R. Amini, C. T. Laurencin, and S. P. Nukavarapu, "Bone tissue engineering: recent advances and challenges", *Critical reviews in biomedical engineering*, vol. 40 (5), pp. 363-408, 2012.

[2] F. Baino, E. Fiume, J. Barberi, S. Kargozar, J. Marchi, et al., "Processing methods for making porous bioactive glass-based scaffolds – A state-of-the-art review", *International Journal of Applied Ceramic Technology,* vol. 16, pp. 1762-1796, 2019.

[3] S. Kargozar, M. Mozafari, S. Hamzehlou, P. Brouki Milan, H.W. Kim, et al., "Bone tissue engineering using human cells: a comprehensive review on recent trends, current prospects, and recommendations", *Applied Science*, vol. 9, p. 174, 2019.

[4] E. Fiume, G. Serino, C. Bignardi, E. Vernè, and F. Baino, "Bread-derived bioactive porous scaffolds: an innovative and sustainable approach to bone tissue engineering", *Molecules*, vol. 24(16), p. 2954, 2019.

[5] Y. Martin, and P. Vermette, "Bioreactors for tissue mass culture: design, characterization, and recent advances", *Biomaterials*, vol. 26(35), pp. 7481-7503, 2005.

[6] I. Martin, D. Wendt, and M. Heberer, "The role of bioreactors in tissue engineering", *Trends in Biotechnology*, vol. 22(2), pp. 80-86, 2004.

[7] N. Plunkett and F. J. O'Brien, "Bioreactors in tissue engineering", *Studies in Health Technology and Information*, vol. 152, pp. 152-214, 2010.

[8] J. Hambor, "Bioreactor design and bioprocess control for industrialized cell processing", *Bioprocess International*, vol. 10, pp. 22-33, 2012.

[9] D. Massai, G. Cerino, D. Gallo, F. Pennella, M. Deriu et al., "Bioreactors as engineering support to treat cardiac muscle and vascular disease", *Journal of Healthcare Engineering*, vol. 4(3), pp. 329-370, 2013.

[10] C. Kropp, D. Massai, and R. Zweigerdt, "Progress and challenges in large-scale expansion of human pluripotent stem cells", *Process Biochemistry*, vol. 59, pp. 244-254, 2017.

[11] A. Pavesi, M. Soncini, A. Zamperone, S. Pietronave, E. Medico et al., "Electrical conditioning of adipose-derived stem cells in a multi-chamber culture platform", *Biotechnology and bioengineering*, vol. 111(7), pp. 1452-1463, 2014.

[12] D. Massai, G. Isu, D. Madeddu, G. Cerino, A. Falco et al., "A versatile bioreactor for dynamic suspension cell culture. Application to the culture of cancer cell spheroids", *PLoS One*, vol. 11(5), Article ID e0154610, 2016.

[13] G. Cerino, E. Gaudiello, T. Grussenmeyer, L. Melly, D. Massai, et al., "Three dimensional multi-cellular muscle-like tissue engineering in perfusion-based bioreactors", *Biotechnology and bioengineering*, 113(1), 226–236, 2016.

[14] J. Schmid, S. Schwarz, R. Meier-Staude, S. Sudhop, H. Clausen-Schaumann, et al., "A perfusion bioreactor system for cell seeding and oxygen-controlled cultivation of three-dimensional cell cultures", *Tissue Engineering. Part C Methods*, vol. 24(10), pp. 585–595, 2018.

[15] B. Carpentier, P. Layrolle, and C. Legallais, "Bioreactors for bone tissue engineering", *The International Journal of Artificial Organs*, 34(3), 259–270, 2011.

[16] L. Leppik, M. B. Bhavsar, K. Oliveira, M. Eischen-Loges, S. Mobini, et al., "Construction and use of an electrical stimulation chamber for enhancing osteogenic differentiation in mesenchymal stem/stromal cells in vitro", *Journal of visualized experiments: JoVE*, vol. 143, 10.3791/59127, 2019.

[17] G. Putame, M. Terzini, D. Carbonaro, G. Pisani, G. Serino, et al., "Application of 3D printing technology for design and manufacturing of customized components for a mechanical stretching bioreactor", *Journal of Healthcare Engineering*, 3957931, 2019.

[18] E. Fiume, E. Verné, F. Baino, "Crystallization behavior of SiO2-P2O5-CaO-MgO-Na2O-K2O bioactive glass powder", *Biomedical Glasses*, vol. 5, pp. 46-52, 2019.

[19] E. Fiume, D. Tulyaganov, G. Ubertalli, E. Verné. F. Baino, "Dolomite-foamed bioactive silicate scaffolds for bone tissue repair", Materials, vol. 13, pp. 628, 2020.

[20] D. Massai, F. Pennella, P. Gentile, D. Gallo, G. Ciardelli, et al., "Image-based three-dimensional analysis to characterize the texture of porous scaffolds", *BioMed research international*, 161437, 2014.

[21] G. Falvo D'Urso Labate, F. Baino, M. Terzini, A. Audenino, C. Vitale-Brovarone, et al., "Bone structural similarity score: A multiparametric tool to match properties of biomimetic bone substitutes with their target tissues," *Journal of Applied Biomaterials & Functional Materials*, vol. 14, no. 3, 2016.

Application of deer hearts for *ex-vivo* modelling of mitral valve pathology – preliminary results

M. Jaworek[1,2], E. Maroncelli[1,2], F. Lucherini[1,2], G. Gelpi[2,3], C. Romagnoni[2,3], R. Rosa[2,3], C. Manenti[1],
C. Antona[2,3], G.B. Fiore[1,2] and R. Vismara[1,2]

[1] Department of Electronics, Information and Bioengineering, Politecnico di Milano, Milan, Italy
[2] ForcardioLab – Fondazione per la Ricerca in Cardiochirurgia ONLUS, Milan, Italy
[3] Cardiovascular Department, 'Luigi Sacco' General Hospital, Milan, Italy

Abstract — **Functional mitral regurgitation (FMR) has high prevalence (2.5% in general population), its surgical treatment is considered challenging and the number of inoperable patients will be increasing due to population aging. Transcatheter treatments represent new therapeutic options for high risk patients, however realistic preclinical tests reproducing peculiarities of the pathology are needed to accelerate their development. In this work, applicability of deer hearts for FMR simulation in an *ex-vivo* setup was evaluated. Mitral valves (MVs) from 15 samples were harvested and their anatomy was preliminary assessed and compared with human and porcine hearts. Further, 5 deer hearts were tested under steady flow conditions and underwent a dilatation protocol to induce the pathology (constant intraventricular pressurization under 150 mmHg for 60 minutes). The evaluation was based on retrograde flow measurement, 3D volumetric echocardiographic images analysis and fiberscopic direct visualization. The dilatation protocol induced incremental increase of retrograde flow through MV throughout the time of the test. The MV geometry at post-dilatation reproduced the principal characteristics associated with FMR observed clinically and featured annulus dilation, MV leaflets malcoaptation and tenting. The FMR model housing deer hearts is promising for future application in realistic preclinical assessment of MV transcatheter therapies.**

Keywords — **experimental cardiovascular biomechanics, heart valves, functional mitral regurgitation, ex-vivo.**

I. INTRODUCTION

MITRAL valve (MV) physiological functioning is granted by a proper interaction between mitral annulus (MA), MV leaflets, chordae tendineae and papillary muscles (PMs). Functional mitral regurgitation (FMR) is a pathology which is secondary to ischemia or cardiomyopathy and is characterized by concomitant MA dilation and PMs displacement due to left ventricular dilation [1]. FMR prevalence is high (2.5% in general population), surgical MV correction is considered challenging and 49% of patients are denied the surgery mostly due to advanced age or comorbidities [2]. Moreover, the number of inoperable patients is expected to be increasing as the world population is aging.

Emerging transcatheter approaches could offer a therapeutic solution for the patients with high surgical risks [3]. These procedures are echocardiography-guided, and the devices interact closely with various anatomical structures (annulus, leaflets, atrium, ventricle or coronary sinus). The development of new minimally invasive therapies can be assisted by preclinical testing on bench models which should feature realistic FMR pathology reproduction, anatomical similarity and compatibility with echocardiography.

The last two are satisfied by bench simulators housing excised hearts (e.g. porcine) [4]. However, the ongoing challenge is reproduction of valvular pathologies in these experimental platforms. Heretofore FMR was simulated using human post-transplant hearts [5] which have limited availability. Recently, our group induced FMR in porcine hearts by implanting dilation devices at annulus and papillary muscle level [6]. Although this model was well controllable, its practical application was limited due to fixed mechanical constrains and space occupancy (e.g. unfeasible to perform annuloplasty, complex to record echo-images). Up to date there are no *in-vitro* or *ex-vivo* preclinical models which reproduce complete FMR mechanism and could be applied for transcatheter therapies assessment.

In this work, we evaluated the applicability of deer hearts for FMR simulation in an *ex-vivo* setup. We describe a protocol to induce the pathological conditions and its hemodynamic and echocardiographic assessment.

II. MATERIAL AND METHODS

A. Deer heart anatomical assessment

Frozen deer heart samples were collected from abattoirs from northern Italy. Deer age varied between 6 months to 10 years. The MVs from 15 samples were harvested and their anatomy was preliminary assessed and compared with human and porcine MVs [7], as there is no literature data concerning deer MV morphology. The following parameters of anterior and posterior leaflets were evaluated: thickness, height, length, area, tendinous chords number and length (Fig. 1).
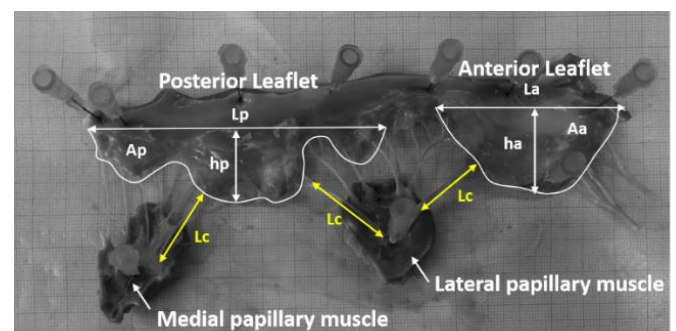

Fig. 1: Anatomical assessment of mitral valve of deer hearts. ha=anterior leaflet height, hp=posterior leaflet height, La=anterior leaflet length, Lp=posterior leaflet length, Aa=anterior leaflet area, Ap=posterior leaflet area, ta=anterior leaflet thickness, tp=posterior leaflet thickness, Ncl=number of lateral papillary muscle tendinous chordae, Ncm=number of medial papillary muscle tendinous chordae, Lcl=length of lateral papillary muscle tendinous chordae, Lcm=length of medial papillary muscle tendinous chordae.

III. RESULTS

A. Anatomical assessment

Deer MVs were morphologically similar to human ones (Fig. 1). They had two leaflets connected by chordae tendinea to two papillary muscles. The posterior leaflet had three well-defined scallops and anterior leaflet did not feature any indentations, as in humans. While swine MV, the most often used animal model for *ex-vivo* testing, has multiple scallops on posterior and anterior leaflet. Quantitative assessment (Tab.1) showed that most of the confronted parameters were on average higher comparing to human and porcine MVs and had higher variability. The widespread among deer MV data was related to wide age range of the analysed donors, however a linear correlation was found between excised deer hearts samples weight and MV leaflets area (R^2=0.62 and R^2=0.72 for anterior and posterior leaflet area, respectively). Hence, deer MV anatomy could be considered suitable for *ex-vivo* modelling, once preliminarily selected based on age (younger) or heart weight (<800 g).

B. Experimental setup and dilatation protocol

5 heart samples were tested under steady flow conditions with controllable intraventricular pressure setting in a setup shown in Fig. 2. Each sample was immersed in a saline solution tank. The aortic valve leaflets were removed and a centrifugal pump, connected via aorta, induced closing of the MV and potentially retrograde flow through the MV. The circuit was closed by connecting the inflow of the centrifugal pump with the water tank. The evaluation was based on retrograde flow measurement, 3D volumetric echocardiographic images registration and fiberscopic direct visualization under intraventricular pressure set to 100mmHg (corresponding to mean difference between ventricular and atrial pressure during systole).

TABLE I

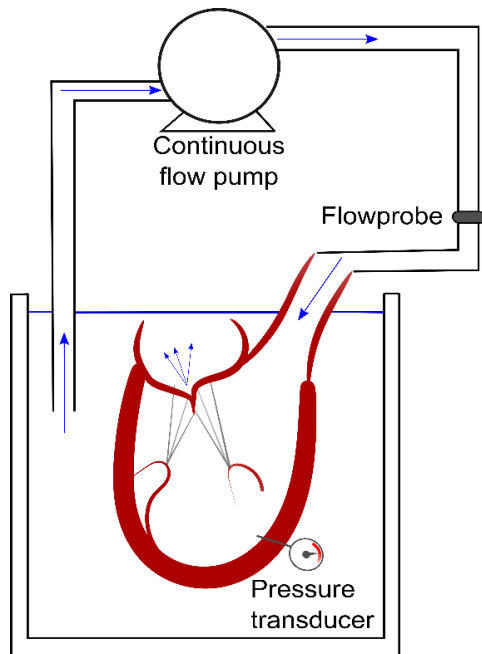| Parameter	Human [8]	Porcine [8]	Deer
ha, cm	2.0 ± 0.2	2.0 ± 0.4	2.5 ± 0.4
hp, cm	1.2 ± 0.1	1.2 ± 0.2	1.3 ± 0.4
La, cm	3.2 ± 0.4	3.2 ± 0.4	5.0 ± 0.9
Lp, cm	6.7 ± 0.8	7.4 ± 0.7	9.2 ± 1.5
Aa, cm^2	5.2 ± 1.1	6.7 ± 1.1	8.0 ± 2.1
Ap, cm^2	3.6 ± 0.7	8.1 ± 0.6	7.7 ± 2.4
ta, mm	0.3 ± 0.6	0.5 ± 0.1	0.5 ± 0.1
tp, mm	0.3 ± 0.5	0.5 ± 0.1	0.5 ± 0.1
Ncl	6.1 ± 0.2	6.7 ± 0.2	6.4 ± 1.1
Ncm	5.6 ± 0.2	5.8 ± 0.2	5.8 ± 1.0
Lcl, cm	1.7 ± 0.3	1.8 ± 0.2	2.6 ± 0.4
Lcm, cm	1.6 ± 0.2	1.6 ± 0.2	2.2 ± 0.4

Fig. 2: Mock circulation loop housing deer heart used for characterization of the model (intraventricular pressure set to 100 mmHg) and to perform dilatation protocol (intraventricular pressure set to 150 mmHg for 60 minutes).

Quantitative comparison of MV leaflets parameters between deer model, porcine model and human. ha=anterior leaflet height, hp=posterior leaflet height, La=anterior leaflet length, Lp=posterior leaflet length, Aa=anterior leaflet area, Ap=posterior leaflet area, ta=anterior leaflet thickness, tp=posterior leaflet thickness, Ncl=number of lateral papillary muscle tendinous chordae, Ncm=number of medial papillary muscle tendinous chordae, Lcl=length of lateral papillary muscle tendinous chordae, Lcm=length of medial papillary muscle tendinous chordae.

After recording baseline conditions, the samples underwent dilatation protocol aiming to induce pathological FMR conditions. The protocol, developed based on preliminary experimental activities, foresaw 60 minutes pressurization of the samples under constant intraventricular pressure of 150 mmHg. The progress of the dilatation was monitored every 10 minutes (by temporarily reducing the intraventricular pressure to 100mmHg) and after completing of the protocol.

The following morphological parameters were measured from 3D echocardiography: antero-posterior distance (A-P), medio-lateral distance (M-L, measured in orthogonal plane to A-P), maximal tenting height (THmax, the perpendicular distance between annular plane and the coaptation point between two leaflets. The maximum value of TH was determined rotating one of the long axis planes around the orthogonal MV short axis) and left ventricular diameter (LVd, the distance between ventricular walls perpendicular to A-P measured below MV).

B. Pathological model

At baseline MVs did not presented typical characteristics of FMR as assessed by experienced surgeons based on qualitative assessment from fiberscope and echocardiography imaging. The dilation protocol induced changes in geometrical configuration of MV apparatus which resulted in leaflets

malcoaptation and tenting. Representative fiberscopic and echocardiographic image are shown in Fig. 3.
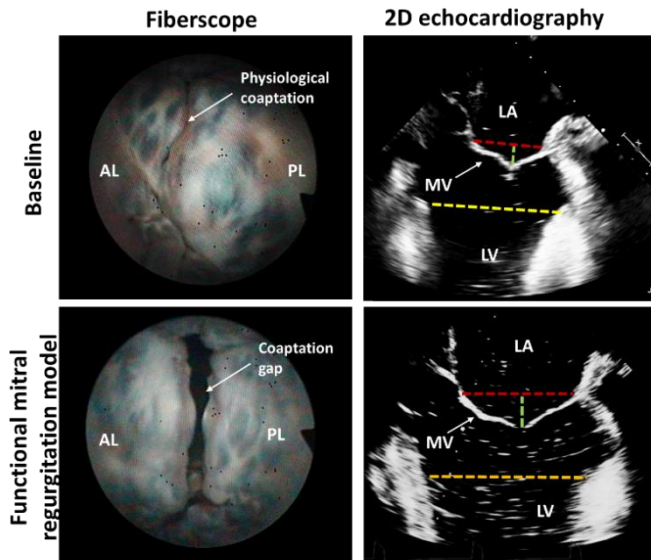

Fig. 3: Representative images of mitral valve (MV) from fiberscope (atrial view) and echocardiography (2D antero-posterior plane) at baseline and after dilatation protocol (functional mitral regurgitation model). AL=anterior leaflet, PL=posterior leaflet, LA=left atrium, LV=left ventricle. Red line indicates antero-posterior distance, green line – tenting height and yellow line – left ventricular diameter.

Table 2 reports the overall change between the quantitative parameters while Fig. 4 shows the change of retrograde flow through MV over time during the dilatation protocol for all tested samples. On average, retrograde flow increased with statistical significance (p=0.03) by the factor of 2.5 between the beginning and the end of dilatation protocol and the outcome was comparable with literature data [5].

The changes in valve morphology were graphically indicated by dashed lines on Fig. 3. The MV annulus enlarged as the principal diameters, A-P and M-L, increased by 25% (p=0.007) and 11% (p=0.001), respectively. Moreover, the LVd increased by 18% (p=0.02) inducing the displacement of papillary muscle causing the MV leaflets tenting as also confirmed by THmax increase by 59% (p=0.007).

High anatomical variability at baseline (wild animals, wide age range) could have contributed to the observed data spread and sample-to-sample differences in the quantitative assessment.

TABLE II

Parameter	Baseline	FMR model	p-value
$RF, \frac{l}{min}$	0.7 ± 0.4	2.7 ± 1.3	0.03
AP, mm	30.8 ± 4.1	38.5 ± 5.9	0.007
ML, mm	53.3 ± 5.1	59.3 ± 5.3	0.001
TH_{max}, mm	7.4 ± 1.7	11.7 ± 2.5	0.007
LV_d, mm	68.4 ± 4.6	80.5 ± 11.0	0.02

Quantitative assessment of the baseline and functional mitral regurgitation model (FMR). RF=retrograde flow, AP=antero-posterior distance, ML=medio-lateral distance, THmax=maximal tenting height, LVd – left ventricular diameter.
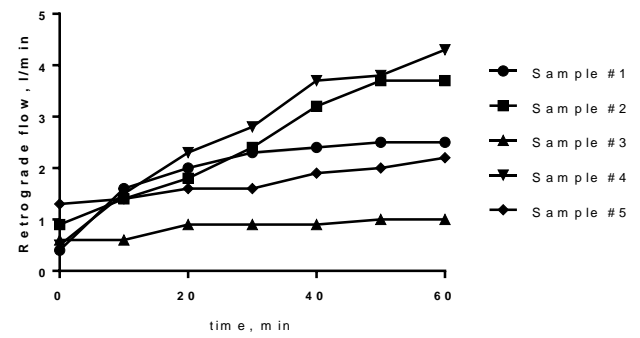

Fig. 4: The change of retrograde flow through mitral valve during the dilatation protocol for tested samples of deer hearts.

IV. CONCLUSION

Preliminary assessment of deer hearts in an *ex-vivo* setup suggested that dilatation under elevated constant pressure could constitute a simple and efficient way in obtaining a reproducible and realistic experimental pathological FMR model. This model features the principal characteristics of the FMR observed clinically including lack of coaptation, dilated annulus and ventricle, tethering of MV leaflets. This model could be applied in the future for realistic preclinical assessment of variety of transcatheter MV therapies (replacement with a prosthetic valve or repair by direct or indirect annuloplasty, leaflets grasping, papillary muscle approximation or ventricular reshaping) potentially contributing to their accelerated development.

V. ACKNOWLEDGMENTS

VI. REFERENCES

[1] S. He, A. Fontaine, A.Schwammenthal , et al. "Integrated Mechanism for Functional Mitral Regurgitation" *Circulation*, vol. 96, pp. 1826-1836, 1997
[2] M. Mirabel, B. Iung, G. Baron et al. "What are the characteristics of patients with severe, symptomatic, mitral regurgitation who are denied surgery?" *European Heart Journal*, vol. 28, pp. 1358–1365, 2007
[3] H.C. Herrmann and F. Maisano "Transcatheter therapy of mitral regurgitation", *Circulation*, vol. 130, pp. 1712-1722, 2014
[4] A.M. Leopaldi, R. Vismara, S. van Tuijl et al. "A novel passive left heart platform for device testing and research", *Medical Engineering and Physics*, vol. 37, pp. 361–366, 2015
[5] K. Fukamachi, M. Inoue, K. Doi, et al." Reduction of Mitral Regurgitation Using the Coapsys Device: A Novel Ex Vivo Method Using Excised Recipients Hearts" *ASAIO Journal*, vol. 51, pp. 82–84, 2005
[6] M. Jaworek, F. Lucherini, C. Romagnoni, et al. "Modelling of Lesions Associated with Functional Mitral Regurgitation in an Ex Vivo Platform" *Annals of Biomedical Engineering*, vol. 45, pp.2324-2334, Jul 2017
[7] K. Kunzelman, R.C. Eberhart and E. D. Verrier "Anatomical basis for mitral valve modelling" *Journal of Heart Valve Disease*, vol. 3, pp. 491-496, Sep 1994

Connectivity in Parkinson's disease patients with cognitive impairment: a simultaneous PET/MRI study

E. Silvestri[1,2], A. Antonini[2,3], M. Castellaro[1,2], R. Biundo[4], D. Cecchin[2,5], A. Bertoldo[1,2]

[1] Department of Information Engineering, University of Padua, Italy
[2] Padova Neuroscience Center, University of Padua, Italy
[3] Department of Neuroscience, University of Padua, Italy
[4] IRCCS San Camillo Hospital, Venice, Italy
[5] Department of Medicine, Unit of Nuclear Medicine, University of Padua, Italy

Abstract— In this study we investigated the interaction between β-amyloid cortical deposition and resting state functional connectivity in patients with Parkinson's disease and concurrent cognitive impairment. A simultaneous multimodal PET/MRI study has been performed. Cortical and subcortical amyloid burden was assessed by means of the ^{18}F-Flutemetamol tracer. Functional connectivity was analysed in terms both of structure and distribution, and of graph theory measures. The results showed a significant relationship between the increase in amyloid deposition and the changes in resting state functional connectivity in regions belonging from attention network. Albeit referred to a limited dataset, these findings suggest that the cortical amyloid burden plays an important role in the cognitive decline of Parkinson's disease patients and that the networks most affected are the attentive ones.

Keywords—PDD, amyloid load, dementia, resting state functional connectivity.

I. Introduction

DIAGNOSIS of Parkinson's disease (PD) relies on the presence of specific motor symptoms such as bradykinesia, resting tremor, and rigidity [1]. Along with these symptoms, patients with PD also develop either mild cognitive impairment or frank dementia [2]. The reported prevalence of dementia in PD rises with disease duration and averages at around 40% [3]. The cognitive decline is typically characterized by impairment of short-term recall, attention, visuospatial and executive functions such as decision making [4]. Multiple pathological processes have been linked to dementia in PD: degeneration of basal forebrain cholinergic nuclei, frontal-subcortical circuit deafferentation due to degeneration of brainstem dopaminergic neurons, diffuse cortical Lewy bodies associated with α-synuclein, and Alzheimer-like lesions with fibrillary β-amyloid (Aβ) plaques [5]. Among these, the presence of Aβ is one of the most studied in the last few years [4], since according to recent studies it might be related to the severity of the cognitive pathology [3][2]. Moreover, it can be non-invasively assessed by means of positron emission tomography (PET), using Aβ highly sensitive tracers [2][4][8]. Besides these pathophysiological studies, functional studies were carried out to investigate how brain networks, that underpin the deteriorated cognitive functions, are altered by pathology. In particular, resting state functional connectivity has proven to be a useful technique to probe these changes [1][6][7].

Since the presence of high amyloid load in Alzheimer's disease (AD) has been related to alterations in connectivity [8], and that dementia associated with Parkinson's disease when Aβ load is present has similar characteristics to AD, in this study we investigated the relationship between amyloid burden and brain connectivity changes. Simultaneous PET/MRI acquisitions were employed to acquire time matched amyloid load and resting state functional connectivity (rs-fMRI). The Aβ deposition was quantified using the recent ^{18}F-Flutemetamol tracer, one of the three currently Food and Drug Administration-approved ^{18}F-labelled amyloid PET imaging agents [9]. Functional brain connectivity was estimated from resting-state functional magnetic resonance images (rs-fMRI) and analysed by means of graph theory measures.

II. Materials and Methods

The study involved twelve patients (8 men; mean age 67.25y, range [57-77y]) affected by Parkinson's disease with different degree of cognitive decline, recruited at the Parkinson and Movement Disorders Unit, IRCCS (Istituto di Ricovero e Cura a Carattere Scientifico) San Camillo Hospital, Venice, Italy. The protocol for the experiments obtained the approval of the ethical committee of the University Hospital of Padova. Patients had given written informed consent before scans and cognitive evaluation. PD diagnosis was made according to the UK brain Bank criteria [10] and Lewy Body Disease was excluded according to international consensus criteria [11]. To determine their cognitive status, patients underwent an extended cognitive assessment which included Montreal Cognitive Assessment (MoCA) and Mini Mental State Examination (MMSE) [12]. A patient was assigned to the PDD or MCI group on the basis of a global evaluation of the cognitive tests by an expert neuropsychologist (Dr R.B.). In addition, patients were divided by an expert nuclear physician (Prof. D.C.) in two groups based on their pattern of β-amyloid neuritic plaque density. The ^{18}F-Flutemetamol PET patient's images were employed. According to FDA recommendation, patients were marked as amyloid positive (Aβ-Pos) when images exhibited an altered pattern of tracer uptake with white (WM) and grey matter (GM) boundaries difficult to disentangle, or as amyloid negative (Aβ-Neg) when in their images the white-grey matter intensity ratio was preserved.

Two patients were discarded because they did not complete the PET/MRI exam and two were discarded due to excessive head motion during the acquisition. The characteristics of the two final groups used in this study are reported in Table I.

	Aβ - Pos (N=3)	Aβ - Neg (N=5)
Age	70 ± 7 y	67 ± 8 y
Disease duration	6.7 ± 4.0 y	12.7 ± 6.7 y
Cognitive State	PDD	MCI
MMSE$_c$	20.2 ± 4.6	24.3 ± 1.8
MoCA$_c$	14 ± 2	21 ± 4

PDD = Parkinson's disease with dementia; *MCI* = Mild cognitive impaired; *MMSE$_c$* = Mini Mental State Examination; *MoCA$_c$* = Montreal Cognitive Assessment; $_c$ = corrected for education and age (according to the normative reference of the tests present in the literature (calibrated in Italian)).

A. PET/MRI acquisition protocol

Images were acquired at the Nuclear Medicine Unit, Department of Medicine–University Hospital of Padova, on a Siemens Biograph mMR (Siemens Medical Solutions USA, Inc.) equipped with a 16-channels head-neck coil.

Concerning PET imaging, as in [13], 90 minutes after the tracer administration, a 20-minutes PET list mode acquisition was performed. An average dose of 180MBq (range: 165–196MBq, according to the body mass index) of ^{18}F-Flutemetamol was administered to each patient. PET static images were reconstructed offline using the Siemens e7-tool for Biograph mMR. The image reconstruction pipeline included correction for scatter, dead time, attenuation (due to head and radio-frequency coil), tracer decay and normalization. Reconstruction was performed with Poisson ordered subset expectation maximization (3 iterations and 21 subsets). Patient's head attenuation map was estimated from the patient relevant Ultra-Short Time Echo (UTE) MR images as in [14].

The MR brain imaging protocol included the following sequences: UTE (TR/TE1/TE2 11.9/0.07/2.46ms, 1.6x1.6x1.6mm³); T1(T1w) Magnetization-Prepared Rapid Gradient-Echo (TR/TE 2400/3.2ms, 1x1x1mm³); 15min rs-fMRI: Echo-planar Imaging (GRAPPA 2, SMS (CMRR, R014) 2, TR/TE 1100/30ms, FA 63°, 3x3x3mm³, anterior-posterior (AP) phase encoding direction, 800 dynamic scans); two fMRI geometrically matched spin echo (SE) EPI (GRAPPA 2, SMS 2, AP and posterior-anterior (PA) phase encoding direction).

B. PET data analysis

Analyses were performed at the region of interest (ROI) level. ROIs were defined according to the Gordon atlas [15] for the cortical GM and according to the MICCAI2012 atlas (http://www.neuromorphometrics.com/2012_MICCAI_Chall enge_Data.html) for the deep GM nuclei. The choice of the two atlases is compromise between the good segmentation of the subcortical nuclei, provided by the MICCAI2012 atlas, and the refined functional segmentation for the study of the resting state networks (RSNs), provided by the Gordon atlas.

The Standard Uptake Volume Ratio (SUVR) was employed to quantify the Aβ load. The cerebellum GM was used as reference [16]. For each patient the SUVR was computed at the voxel level and the mean SUVR was extracted for each ROI. Finally, the average SUVR was computed for each ROI and each group.

C. MRI data analysis

Structural and functional images were processed using a combination of the following software: Advanced Normalization Tools software (ANTs) [17], FMRIB Software Library (FSL) [18], and Connectome Workbench [19].

The structural images were corrected for bias field inhomogeneities [20] and, following the pipeline in [21], automatically parcelled using the two above mentioned atlases. The parcellation included the 333 Gordon's ROIs, that can be grouped in the following resting state networks (RSN): Visual (VIS), Retrosplenial-Temporal (RSTN), Sensory-Motor hand (SMH), Sensory-Motor mouth (SMM), Auditory (AUD), Cingulo-Opercularis (CON), Ventral Attention (VAN), Salience (SAL), Cingulo-Parietal (CPN), Dorsal Attention (DAN), Fronto-Parietal (FPN), Default Mode Network (DMN). The MICCAI2012 selected subcortical ROI that were included in the final parcellation were the left and right accumbens, caudate and pallidum nuclei, the left and right thalami and the left and right hemispheres cerebellum grey matter. The resting state acquisition of each patient was pre-processed in the individual space. Functional images were corrected for slice timing, readout distortion [22], and head motion. The rs-fMRI volumes were realigned to the single-band volume using an affine transform and the estimated parameters were exploited to compute the patient's head framewise displacement (FD) [23]. Each subject T1w image was linearly registered to the rs-fMRI. To remove remaining source of noise, WM, cerebrospinal fluid (CSF), 6 rigid-body motion parameters along with their derivatives were regressed out from each voxel of the motion-corrected rs-fMRI [24]. The WM and CSF signals were computed as in [25]. Finally, images were high pass filtered (cut-off frequency 1/128 Hz).

FC matrices computation: The time course of each ROI was extracted by averaging the time courses of all the voxels inside the ROI. Before computing FC matrices as zero-lag cross-correlation between each pair of ROIs time courses, time points related to fMRI volumes highly corrupted by motion were identified using the FD and discarded [26]. The FD threshold was set to 0.4 [23]. FC matrices were z-Fisher transformed to allow further statistical comparisons and averaged over the two groups.

Graph theory analysis: Graph-related adjacency and weighted matrices has been obtained from the Aβ-Pos and Aβ-Neg average FC matrices removing weak and non-significant links. At this aim a sparsity threshold approach was applied to the two groups' average FC with a connection density of 0.2 [27]. Global and local graph measures were employed to summarize the graph properties. In particular, node degree (Deg), node strength (Str), betweenness centrality (BC), clustering coefficient (CC) and local efficiency (EL) were implemented as defined in [28].

D. Statistical Analysis

The two groups were separately tested for significant differences in SUVR and functional connectivity. Then we checked for significant relationship among alteration in connectivity and Aβ neuritic plaque density.

Aβ load: To evaluate whether there was a significant difference in Aβ burden between the two groups at the whole

brain level, the median and dispersion of the group mean SUVR of all the ROIs were compared respectively with the Wilcoxon rank sum and Ansari-Bradley tests. The two tests were implemented in a permutation test framework with 20.000 permutations.

Functional connectivity: The two mean FC of the Aβ-Pos and Aβ-Neg groups were compared both in terms of FC weight distribution and in terms of matrix structure. To assess differences in median and dispersion of the distributions, the Wilcoxon rank sum and Ansari-Bradley statistics were implemented in a permutation test framework with 20.000 iterations. The Krzanowski test [29] was employed to investigate differences FC matrices structure. Since we hypothesised that differences between the groups could have been restricted to single specific RSNs, we further compared the structure of the FC matrices restricted to that RSNs and the distribution of intrinsic and extrinsic connections for each single network as in [30]. Intrinsic and extrinsic connections refer respectively to the set of links between all the nodes belonging to a specific network and set of the links of all the nodes among that specific network with the rest of nodes. Finally, differences in Deg, Str, BC, CC, and EL both at the whole brain level and at the RSN level were evaluated by means of Wilcoxon rank sum test.

Functional-pathophysiological integration: To investigate whether there is a relationship between the changes in FC graph metrics and the increase of β-amyloid load a correlation analysis has been performed. The changes were computed at the ROI level as difference between the feature values of Aβ-Pos and Aβ-Neg groups and the analysis was restricted to RSNs where Aβ load and graph measures resulted to significantly differ.

In all tests the significance value was set at 0.05 and the false discovery rate [31] was employed to correct for multiple comparison.

III. RESULTS

Based on the clinical assessment, 3 patients resulted in having an altered amyloid load pattern (Aβ-Pos group) and 5 in having a preserved WM-GM intensity ratio pattern (Aβ-Neg group). Concerning demographic information, a significant difference among the two group has been found only in the MMSE and MoCA values.

The whole brain SUVR between the two groups was significantly different both in median and in dispersion (p-value $<10^{-6}$ and p-value 0.025). The average SUVR values in Aβ-Pos and in Aβ-Neg group were respectively 1.64±0.26a.u. and 1.28±0.17a.u. SUVR relative changes ranged from -0.08 a.u. to 0.71a.u.

The FC distribution significantly differs between the two groups at whole brain level and for the following RSNs (intrinsic FC): VAN (0.062±0.053 Aβ-Pos, 0.076±0.049 Aβ-Neg), DAN (0.098±0.070 Aβ-Pos, 0.110±0.060 Aβ-Neg) and FPN (0.098±0.054 Aβ-Pos, 0.110±0.050 Aβ-Neg), with a p-value $<10^{-6}$ in all cases. Moreover, the same networks and the DMN resulted to significantly differ in the extrinsic FC (p-value $<10^{-6}$ in all cases), with a decrease in FC in the Aβ-Pos group. DAN, FPN and VAN intrinsic FC matrices as well as

distributions are shown in Figure 1. No statistical difference was found in FC and RSNs structure between the two groups.
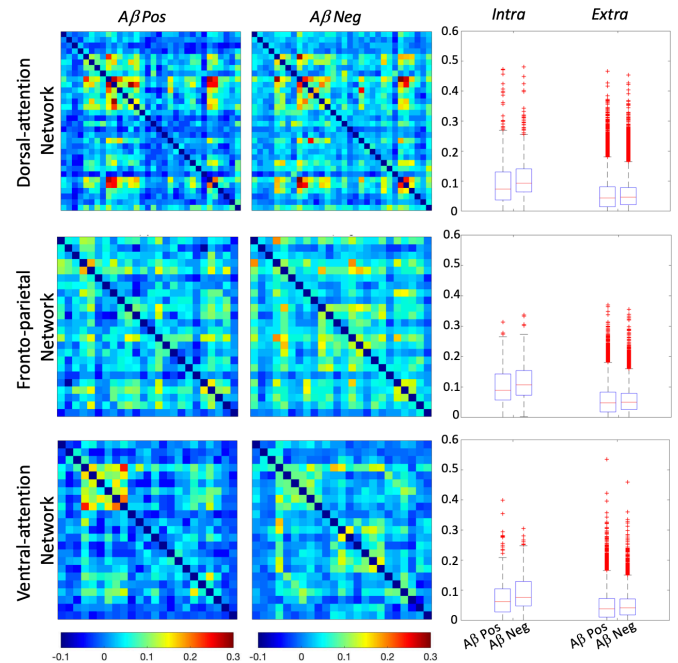

Fig. 1: Resting state networks resulted to be significantly different in intrinsic and extrinsic connections between the two groups. The matrices on the two panels on the left represent the average intrinsic functional connectivity values respectively of Aβ-Pos and Aβ-Neg patients. On the right panel: boxplot of connection weights (intrinsic on the left side and extrinsic on the right-hand side).

Concerning graph theory measures, differences were found in BC and EL at whole brain level (p-value $<10^{-6}$ in both cases). Albeit not significant after multiple comparisons correction, DMN, VAN, DAN and FPN and DMN differ between the two groups in Deg (p-value 0.022, 0.014, 0.031, 0.012 respectively), BC (p-value 0.038, 0.026, 0.013, 0.043), CC (p-value 0.018, 0.007, 0.019, 0.049) and EL (p-value 0.004, 0.037, 0.046, 0.032).

Correlation analysis between functional network measures and Aβ deposition was performed on VAN, FPN, DAN and DMN. A positive significant correlation (p<0.05, not corrected for multiple comparisons) between the changes in Str, CC and EL and the increase in amyloid load in Aβ-Pos has been found in the ventral attention network. The obtained Pearson's correlation values were respectively 0.46 (p-value 0.016), 0.47 (p-value 0.012) and 0.50 (p-value 0.009). A scatterplot of the ROI-wise correlation analysis for Str, CC and EL in the VAN is depicted in Figure2.

IV. CONCLUSIONS

The multimodal integration of features of pathophysiology (SUVR) and connectivity (graph metrics) is a promising tool to detect the interplay between neurodegenerative processes and cognitive functions. Our analyses focused on FC and how this could be related to amyloid burden. PDD patients have been found to have a preserved FC structure, but a decrease in functional connectivity in attention-related network when compared with Aβ-Neg group, which is in line with recent studies [32][33]. In addition, in PDD patients, as in AD [8], changes in attention network's global and local properties are linked to GM Aβ burden. These findings suggest that amyloid
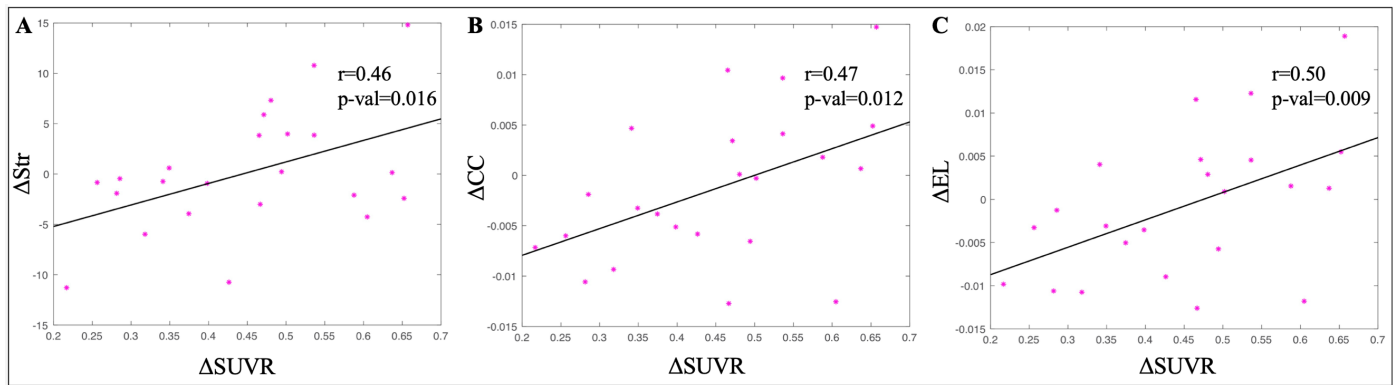
Fig. 2: Scatterplot of ROI-wise changes in SUVR (ΔSUVR) versus changes in FC-derived graph measures obtained in the Ventral Attention Network. Panel A, B, C represent respectively changes in node strength (ΔST), clustering coefficient (ΔCC) and local efficiency (ΔEL). The black line in each scatterplot depicts the linear fit of the data.

could contribute to cognitive disfunction in PD patients and that the attentive networks seem to be the most involved. The major limitation of the study is related to the number of the subjects thus further studies on a larger dataset are required to confirm these results.

REFERENCES

[1] R. Biundo, L. Weis, and A. Antonini, "Cognitive decline in Parkinson's disease: the complex picture," *npj Park. Dis.*, vol. 2, no. 1, p. 16018, 2016.

[2] P. Edison *et al.*, "Amyloid load in Parkinson's disease dementia and Lewy body dementia measured with [11C]PIB positron emission tomography," *J. Neurol. Neurosurg. Psychiatry*, vol. 79, no. 12, pp. 1331–1338, 2008.

[3] D. J. Brooks, "Imaging amyloid in Parkinson's disease dementia and dementia with Lewy bodies with positron emission tomography," *Mov. Disord.*, vol. 24, no. SUPPL. 2, pp. 742–747, 2009.

[4] D. Aarsland *et al.*, "Cognitive decline in Parkinson disease," *Nat. Rev. Neurol.*, vol. 13, no. 4, pp. 217–231, 2017.

[5] S. Gomperts *et al.*, "Amyloid is linked to cognitive decline in patients with Parkinson disease without dementia.," *Neurology*, vol. 80, no. 1, pp. 85-91 7p, 2013.

[6] L. R. Peraza *et al.*, "Resting state in Parkinson's disease dementia and dementia with Lewy bodies: Commonalities and differences," *Int. J. Geriatr. Psychiatry*, vol. 30, no. 11, pp. 1135–1146, 2015.

[7] J. Gratwicke, M. Jahanshahi, and T. Foltynie, "Parkinson's disease dementia: A neural networks perspective," *Brain*, vol. 138, no. 6, pp. 1454–1476, 2015.

[8] Y. Zhou, F. Yu, and T. Q. Duong, "White matter lesion load is associated with resting state functional MRI activity and amyloid PET but not FDG in mild cognitive impairment and early Alzheimer's disease patients.," *J. Magn. Reson. Imaging*, vol. 41, no. 1, pp. 102–9, Jan. 2015.

[9] V. P. Reddy, "Chapter 7 - Organofluorine Compounds as Positron Emission Tomography Tracers," in *Organofluorine Compounds in Biology and Medicine*, V. P. Reddy, Ed. Amsterdam: Elsevier, 2015, pp. 201–240.

[10] D. J. Gelb, E. Oliver, and S. Gilman, "Diagnostic Criteria for Parkinson Disease," *Arch. Neurol.*, vol. 56, no. 1, p. 33, 1999.

[11] I. G. McKeith *et al.*, "Diagnosis and management of dementia with Lewy bodies: Third report of the DLB consortium," *Neurology*, vol. 65, no. 12, pp. 1863–1872, 2005.

[12] R. Biundo *et al.*, "MMSE and MoCA in Parkinson's disease and dementia with Lewy bodies: a multicenter 1-year follow-up study," *J. Neural Transm.*, vol. 123, no. 4, pp. 431–438, 2016.

[13] N. Nelissen *et al.*, "Phase 1 Study of the Pittsburgh Compound B Derivative 18F-Flutemetamol in Healthy Volunteers and Patients with Probable Alzheimer's Disease," *J. Nucl. Med.*, vol. 50, no. 8, pp. 1251–1259, 2009.

[14] C. Catana *et al.*, "Towards Implementing an MR-based PET Attenuation Correction Method for Neurological Studies on the MR-PET Brain Prototype," vol. 51, no. 9, pp. 1431–1438, 2010.

[15] E. M. Gordon, T. O. Laumann, B. Adeyemo, J. F. Huckins, W. M. Kelley, and S. E. Petersen, "Generation and Evaluation of a Cortical Area Parcellation from Resting-State Correlations," *Cereb. Cortex*, vol. 26, no. 1, pp. 288–303, 2016.

[16] V. Leinonen *et al.*, "Diagnostic effectiveness of quantitative [18F]flutemetamol PET imaging for detection of fibrillar amyloid β using

cortical biopsy histopathology as the standard of truth in subjects with idiopathic normal pressure hydrocephalus," *Acta Neuropathol. Commun.*, vol. 2, no. 1, p. 46, 2014.

[17] B. B. Avants, N. J. Tustison, G. Song, P. A. Cook, A. Klein, and J. C. Gee, "A reproducible evaluation of ANTs similarity metric performance in brain image registration," *Neuroimage*, vol. 54, no. 3, pp. 2033–2044, 2011.

[18] S. M. Smith *et al.*, "Advances in functional and structural MR image analysis and implementation as FSL," *Neuroimage*, vol. 23, no. SUPPL. 1, pp. S208–S219, 2004.

[19] D. S. Marcus *et al.*, "Informatics and Data Mining Tools and Strategies for the Human Connectome Project," *Front. Neuroinform.*, vol. 5, no. June, pp. 1–12, 2011.

[20] N. J. Tustison *et al.*, "N4ITK: Improved N3 bias correction," *IEEE Trans. Med. Imaging*, vol. 29, no. 6, pp. 1310–1320, 2010.

[21] M. F. Glasser *et al.*, "The minimal preprocessing pipelines for the Human Connectome Project," *Neuroimage*, vol. 80, pp. 105–124, 2013.

[22] J. L. R. Andersson and S. N. Sotiropoulos, "An integrated approach to correction for off-resonance effects and subject movement in diffusion MR imaging," *Neuroimage*, vol. 125, pp. 1063–1078, 2016.

[23] J. D. Power, K. A. Barnes, A. Z. Snyder, B. L. Schlaggar, and S. E. Petersen, "Spurious but systematic correlations in functional connectivity MRI networks arise from subject motion," *Neuroimage*, vol. 59, no. 3, pp. 2142–2154, 2012.

[24] H. J. Jo *et al.*, "Effective preprocessing procedures virtually eliminate distance-dependent motion artifacts in resting state FMRI," *J. Appl. Math.*, vol. 2013, 2013.

[25] Y. Behzadi, K. Restom, J. Liau, and T. T. Liu, "A component based noise correction method (CompCor) for BOLD and perfusion based fMRI," *Neuroimage*, vol. 37, no. 1, pp. 90–101, 2007.

[26] J. D. Power, A. Mitra, T. O. Laumann, A. Z. Snyder, B. L. Schlaggar, and S. E. Petersen, "Methods to detect, characterize, and remove motion artifact in resting state fMRI," *Neuroimage*, vol. 84, pp. 320–341, 2014.

[27] M. P. van den Heuvel, S. C. de Lange, A. Zalesky, C. Seguin, B. T. T. Yeo, and R. Schmidt, "Proportional thresholding in resting-state fMRI functional connectivity networks and consequences for patient-control connectome studies: Issues and recommendations," *Neuroimage*, vol. 152, no. February, pp. 437–449, 2017.

[28] M. Rubinov and O. Sporns, "Complex network measures of brain connectivity: Uses and interpretations," *Neuroimage*, vol. 52, no. 3, pp. 1059–1069, 2010.

[29] W. J. Krzanowski, "Permutational tests for correlation matrices," *Stat. Comput.*, vol. 3, no. 1, pp. 37–44, 1993.

[30] M. R. Brier *et al.*, "Loss of Intranetwork and Internetwork Resting State Functional Connections with Alzheimer's Disease Progression," *J. Neurosci.*, vol. 32, no. 26, pp. 8890–8899, 2012.

[31] Y. Benjamini and Y. Hochberg, "Controlling the false discovery rate: a practical and powerful approach to multiple testing," *Journal of the Royal Statistical Society B*, vol. 57, no. 1. pp. 289–300, 1995.

[32] A. Abós *et al.*, "Discriminating cognitive status in Parkinson's disease through functional connectomics and machine learning," *Sci. Rep.*, vol. 7, no. March, pp. 1–13, 2017.

[33] R. Lopes *et al.*, "Cognitive phenotypes in parkinson's disease differ in terms of brain-network organization and connectivity," *Hum. Brain Mapp.*, vol. 38, no. 3, pp. 1604–1621, 2017.

Does a medical device nomenclature suitable for all purposes exist? Twenty years of Italian experience with the CND and its adoption in EUDAMED at European level

M. Franzò[1,4], F. D'Agostino[2], C. Chierchia[2], K. Cucchiara[2], E. Carrani[1], L. Sampaolo[5], E. Stella[3], M. Torre[1] and M. Asaro[2]

[1] Scientific secretariat of the Presidency, Italian National Institute of Health, Rome (Italy)
[2] Regione Autonoma Friuli Venezia Giulia – European Medical Device Nomenclature implementation working group, Trieste (Italy)
[3] Italian Ministry of Health, Rome (Italy)
,[4] Department of Mechanical Engineering, La Sapienza University of Rome, Rome (Italy)
[5] National Centre for Disease Prevention and Health Promotion - Italian National Institute of Health, Rome, Italy

Abstract— **There are many purposes for using a nomenclature of medical devices.**

The Italian CND is a free public available nomenclature, arises from a comparison with existing nomenclatures and is structured to allow a connection with other systems.

Since 2007 the CND is used, in the Italian database, for regulatory affairs in order to register and classify homogeneously medical devices from a technical and economics point of view; in 2019 the CND has been adopted from European Commission as official nomenclature.

It is not possible to think that a nomenclature can meet all needs. However, it is possible to guarantee the interoperability of different classification systems by adopting a single hierarchical nomenclature as a common basis from which to develop different "subclassifications" for different purposes.

Aim of this paper is to present the Italian experience in the development of the national medical device nomenclature and its extension to the European level.

Keywords— **Medical Device legislation, European Union, classification, nomenclature**

I. INTRODUCTION

ADVANCES in medical device (MD) technology have been dramatic in recent years resulting in both an increased number of medical devices (estimated to be approximately 500,000 different devices in Europe) and an increase in the invasiveness and critical function which devices perform [1].

According to the World Health organization, at present, there is no common standard name for each type of medical device, an inconsistency that causes confusion between the various types of devices, affects traceability and has an adverse impact on health care delivery [2]. Globalization of the medical device market and trading across economic borders requires prioritization of regulatory convergence which should be accompanied by a common and consistent language with which to communicate device information [3]. To describe and identify these medical devices in an unambiguous manner, there is a need for a common method [4]. A standardized classification and nomenclature of medical devices will serve as a common language for recording and reporting medical devices across the whole health system at all levels of health care for a whole range of uses. Standardization of nomenclature is also essential for defining and naming innovative technologies, classifying the devices for regulatory approval (registration) and for streamlining procurement of these products (2 OMS).

The advent of the European directives, initiated a new era, where national and indeed international bodies were given the opportunity to cooperate and harmonize their efforts in achieving the one thing that they all needed, namely, a standardized method of identifying the products placed in the global market. Many nomenclature systems (CNMD, EDMA, ISO 9999, JFMDA, NKKN, UMDNS), all built upon different structures, and used locally or nationally for diverse purposes and with unusual approaches, were chosen to develop the Global Medical Device Nomenclature (GMDN) [4].

On 19th April 2010, the EU Commission adopted the decision of establishing the European Databank on Medical Devices (Eudamed). The aim of the European databank for medical devices was to strengthen market surveillance by providing competent authorities with fast access to information on manufacturers and authorised representatives, devices and certificates and to vigilance data, to share information on clinical investigation data, as well as to contribute to a uniform application of those Directives, in particular in relation to registration requirements [5]. With the New Regulation on Medical Devices, Eudamed was formally established and the Commission was recommended to ensure that an internationally recognised medical devices nomenclature is available free of charge to manufacturers and other natural or legal persons required by this Regulation to use that nomenclature [6].

On 4th March 2019, the EU Commission adopted the Italian National Nomenclature of Medical Devices (Classificazione Nazionale dei Dispositivi medici, CND) as a base for the development of the European Medical Device Nomenclature (EMDN) to support the activity of the future European database of medical devices EUDAMED [7].

The aim of this paper is to present the Italian experience in the development of the Italian national medical device nomenclature and its further extension to the European level.

II. METHOD

Since 90's, Italy started to define a nomenclature that allow to classified biomedical technologies in a standard way (CIVAB): even through, this nomenclature did not include all the world of medical devices.

In the 00's, in according to the UE directives, the competent office decided to create a wider nomenclature including most of the medical devices placed on the market. Following which, was made a benchmarking with the other existing nomenclatures in the medical field [8] (Table I):

- **UNITED NATIONS COMMON CODING SYSTEM (UNCCS)**: designed for the identification of both goods and services and used in supplies and tenders; 6 characters hierarchical coding system.
- **CIVAB**: was made from a project related to biomedical technologies with aim of developing a standard coding to support the purchase, management and maintenance of biomedical equipment; the coding is associated with an alphanumeric speaking code (3 class characters, 3 manufacturer characters, 2 model characters).
- **UNIVERSAL STANDARD PRODUCTS AND SERVICES CLASSIFICATION (UNSPSC)**: multi-sector standard, evolution of the UNCCS, for classification of products and services, for achieving company-wide visibility of spend analysis, as well as, enabling procurement to deliver on cost-effectiveness demands and allowing full exploitation of electronic commerce capabilities; 8 characters hierarchical coding.
- **UNIVERSAL MEDICAL DEVICE NOMENCLATURE SYSTEM (UMDNS)**: used in applications ranging from hospital inventory and work-order controls to national agency medical device regulatory systems and from e-commerce and procurement to medical device databases; facilitates identifying, transferring, and communicating data about medical devices; not hierarchical 5 numeric codes nomenclature.
- **EUROPEAN DIAGNOSTIC MANUFACTURERS ASSOCIATION'S IN-VITRO DIAGNOSTIC PRODUCT CLASSIFICATION (EDMA)**: used to code in vitro diagnostic medical devise, grouping reagents and instrumentation (accessories); represents the interests of IVD'S european manufacturers for the purpose to support the collection and analysis of market statistics; now is called as GIVD classification; 4 characters hierarchical classification.
- **GLOBAL MEDICAL DEVICE NOMENCLATURE (GMDN)**: it provides a nomenclature used for the exchange of information of medical devices; the list of terms is updated through member modification requests; not hierarchical 5-digit list of numeric codes.

TABLE I
OTHER EXISTING NOMENCLATURES IN THE MEDICAL FIELD IN THE 00'S

Nomenclature	CIVAB, UMDNS GMDN
Classification	UNCCS, UNSPSC, EDMA

The Italian Financial Law 2003, among other things, established that medical devices should be classified in uniform classes and sub classes with an indication of the reference price. It has been giving the responsibility for this classification to the National Commission for Medical Devices (CUD), technical advisory body of the Ministry of Health.

The first version of the Classificazione Nazionale dei Dispositivi Medici (CND) was defined by the CUD in July 2005 and approved with the Ministerial Decree of 22 September 2005 [9].

Subsequently, the Italian Financial law of 2006 involved the State - Regions Conference, [10] for the approval of the national nomenclature.

The new CND version, was established by Italian Ministry of Health Decree of 20 February 2007. Since that date the CND became the official nomenclature of products identified as medical devices in accordance with European Legislation and national transposition standards [11] and valid at National level.

TABLE II
SEQUENCE OF MINISTERIAL DECREES THAT INTRODUCED THE
NEW VERSIONS OF THE CND

CND Version	Ministerial Decree
1	22 September 2005
2	20 February 2007
3	13 March 2008
4	12 February 2010
5	7 October 2011
6	29 July 2013
7	8 June 2016
8	13 March 2018

The construction, the maintenance and the updates of the CND have been based on the following three fundamental principles [12]:

A. **Participative approach:** The medical device sector is very complex and heterogeneous, that's the reason why, it requires highly differentiated and qualified expertise in the field of MD. Besides, it has become necessary, for a reliable nomenclature for medical devices, the contribution of a broad participation of all stakeholders (economic operators and healthcare professional).

B. **Qualified validation of proposals:** Nomenclature proposals are technically validated to establish the actual need considering:
   - other existing nomenclature systems available also at international level
   - consumption and expense information
   - assessment with sector experts from the different disciplines

C. **Formal adoption and free public availability**

The nomenclature has an alpha-numeric structure which is developed in a multi-level hierarchical tree and it clusters medical devices in three main levels:

- **Category:** the first hierarchical level. There are 22 categories identified by a letter and each ones includes devices for anatomical district (8), functional use (9) and other criteria (5).
- **Group:** the second hierarchical level. There are 146 anatomical/function groups, identified by a two-digit numbers from 01 to 99 for each category.
- **Type:** the third hierarchical level. There are, if necessary, until 5 levels of detail which one identified by a two-digit numbers.

Each medical device is classified by an alphanumeric code made of a letter referring to the "Category", a couple of numbers referring to the "Group" and a series of other couples of numbers referring to the "Type" to a maximum of 7 levels (Figure 1).
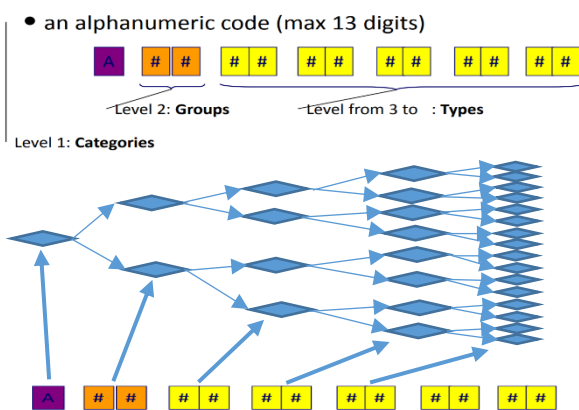

Figure 1: Representation of the CND structure

The nomenclature covers the whole panorama of medical devices, not only biomedical equipment (Z category) and in vitro diagnostic devices (W category).

The CND nomenclature is one of the tools used for the governance of the medical device sector characterized by extremely high complexity and fragmentation. It aims to support the improvement of patient safety and the quality of health systems by enabling information to be communicated in a standardized manner.

It allows more effectively monitoring the consumption and use of devices, a better evaluation of accidents and to obtain a reference prices for homogeneous classes of medical devices making the purchasing processes more transparent by the national health system.

The CND is used in:
- marketing activities
- vigilance and market surveillance
- analysis and definition of economic planning policies

The CND system, which represents the basis of the Italian information system for the registration of medical devices, constitutes an official, freely and available reference to all stakeholders: being a hierarchical nomenclature and therefore not very flexible to changes, specific items have been inserted to code the equipment accessories (hardware "80", software "82", consumables "85") and devices that cannot be included in a specific type (other "99").

Although the shallow depth of the nomenclature levels, the periodic updates allow the creation of new branches with the possibility of including devices that were previously in the item "99".

A device with multiple functionalities could create ambiguity in the coding and make the choice fall on more terminal item: in this case, multiple choice is not possible and it is necessary to refer to the main intended use.

III. DISCUSSION

There are basically two different approaches for medical devices "categorisation": nomenclatures (NOM) and a classifications (CLA). NOM give more detailed and specific information on the single element. The granularity of the information of each term of a NOM is not predefined. On the other hand, the granularity of a CLA is intrinsically related to its hierarchical structure. In choosing between the two approaches, a tradeoff must be considered: NOMs tend to describe DMs in more detail but do not allow easy management of large amounts of information, on the other hand, CLAs are more rigid and less flexible in describing DMs but allow for easier management of the information, due to a hierarchical structure that brings together and organizes the articles provided.

The choice in the construction of the CND was oriented on the second approach in consideration of the huge number of devices on the market (millions of different MDs) and related information that was intended to manage. It was decided to lose in descriptive precision to privilege the ability to organize and manage information in a simple and easily understandable way at all levels of the health system. For devices that are not complex in terms of technical and functional characteristics, classifying in a single terminal branch is quite easy; for devices with more complex technical characteristics and / or more functionalities, making a univocal classification and in a terminal branch could be more complicated.

IV. CONCLUSION

For its features, the CND has been adopted by the European Commission as official nomenclature for the future databank EUDAMED and will be reviewed, updated and renamed as European Medical Devices Nomenclature (EMDN).

The revision of the current CND with other existent nomenclatures will ensure that the new EMDN will be articulated in a way comparable with the other systems.

The experience of the Italian database of medical devices shows that the CND allows the classification of DMs for regulatory purposes and for monitoring expenditure, however it cannot be said that it is in itself usable for any purpose (for example, in the experience of the Italian Arthroprosthesis Registry, the CND is supported by further elements that allow to technically characterize the DMs of interest). The CND (and EMDN at European level) constitute a "classification root" from which specific systems can be developed for particular purposes and ensure interoperability between them.

REFERENCES

[1] T. Melvin, M. Torre, "New medical device regulations: the regulator's view" *Efort Open Reviews*, vol. 4, pp 140-145, 2019.

[2] *World Health Organization*. "Standardization of medical devices nomenclature: International classification, coding and nomenclature of medical devices. Executive board 145th session 30April 2019" [Online] Available:
https://apps.who.int/gb/ebwha/pdf_files/EB145/B145_3-en.pdf

[3] J. White and G. Carolan-Rees, "Current state of medical device nomenclature and taxonomy systems in the UK: spotlight on GMDN and SNOMED CT.", *JRSM Short Rep.*, vol. 4, pp. 1-7, 2013.

[4] K. Anand, SK. Saini, BK. Singh and C. Veermaram, "Global Medical Device Nomenclature: The Concept for Reducing Device-Related Medical Errors". *J Young Pharm.*, vol. 2, pp. 403–409, 2010.

[5] (Journal Online) (2010, April, 23) Title. *Official Journal of the European Union* "Commission Decision of 19 April 2010 on the European Databank on Medical Devices (EUDAMED). L 102/45"

[6] (Official communication) Regulation (EU) 2017/745 of the European Parliament and of the Council of 5 April 2017 on medical devices, amending Directive 2001/83/EC, Regulation (EC) No 178/2002 and Regulation (EC) No 1223/2009 and repealing Council Directives 90/385/EEC and 93/42/EEC (Text with EEA relevance).

[7] (Official communication of the European Commission) "The CND nomenclature will be made available in the future EUDAMED" [Online] Available:
https://ec.europa.eu/docsroom/documents/34264/attachments/1/translat ions/en/renditions/native.

[8] (European project) Final report "Sistemi di controllo del mercato e della gestione dei dispositivi medici in Europa: problematiche e prospettive per lo sviluppo di banche dati europee."
Sottoprogetto A: "Adozione di standard comuni per la nomenclatura e la codifica dei dispositivi medici nei paesi dell'unione europea ed il sistema di classificazione GMDN di EUDAMED: struttura ed estensione del Global Medical Device Nomenclature".

[9] (Official communication) (Rome, 2005, September, 22) Ministerial Decree of 22 September 2005 - Approvazione della Classificazione Nazionale dei dispositivi medici (CND).

[10] C. Giuricin "Classificazione nazionale dei dispositivi medici (C.N.D.) struttura e finalità" in 2007 Proc. CNDM.

[11] (Official communication) (Rome, 2007, February, 20) Ministerial Decree of 20 February 2007 - Approvazione della Classificazione Nazionale dei dispositivi medici (CND).

[12] M. Asaro, "CND: History and structure" in Brussels 4 October 2019 EMDN working group Conf.

Resting State Networks spatio-spectral fingerprints: the Default Mode Network case study

I. Mazzonetto[1], E. Ambrosini[2,3], A. Vallesi[2,4,5] and A. Bertoldo[1,5]

[1] Department of Information Engineering, University of Padova, Padova, Italy.
[2] Department of Neuroscience, University of Padova, Padova, Italy.
[3] Department of General Psychology, University of Padova, Padova, Italy.
[4] Neuroscience Research Unit, IRCCS San Camillo Hospital, Venice, Italy.
[5] Padova Neuroscience Center, University of Padova, Padova, Italy.

Abstract—**The resting state functional magnetic resonance imaging (fMRI) approach has allowed to investigate the large-scale organization of processing systems in the human brain, revealing that it can be viewed as an integrative network of functionally interacting regions. However, to date, the neuronal basis of the fMRI signal dynamics at rest are not fully understood, weakening the fMRI capability to explain brain activity. In this scenario, the integration with information derived from electroencephalography (EEG) is very useful, since conversely from fMRI, EEG represents a direct measure of neuronal activity. EEG-fMRI resting state studies investigating the correlation between fMRI signals and corresponding global EEG spectral characteristics in single spectral bands have provided a certain degree of inconsistency in the results. This may be due to the fact that the distinct functional networks involve more than a single frequency band, and therefore analysis of simultaneous EEG/fMRI data should consider the whole frequency spectrum. A couple of studies have been performed in this direction but they did not investigate the impact of the scalp distribution of EEG spectral metrics. To overcome this gap, this study aims to identify the spatio-spectral fingerprints of distinct networks by using an analytical approach that takes into account the interplay between the different EEG frequency bands and the corresponding topographic distribution within each network. This approach was applied to four sub-components of the Default Mode Network (DMN), revealing for the first time the distinctive subcomponent-specific spatial-frequency patterns of correlation between the fMRI signal and EEG rhythm.**

Keywords—**EEG-fMRI integration, Default Mode Network**

I. INTRODUCTION

BRAIN'S spontaneous activity, as measured with fMRI-derived BOLD signal during resting state condition, has been shown to be organized into multiple, highly specific functional networks, the so-called resting state networks (RSNs). A number of reliable RSNs characterized by functional specificity have been described, such as, the visual, somatomotor, dorsal and ventral attention, default, cognitive control, limbic, and auditory network. Perhaps, the most studied RSNs is the default-mode network (DMN). DMN is composed by brain regions that have not previously been documented as a "proper functional system" (as opposed to, for example, the motor or visual system [1]) and that show a decrease of their neural activity during the execution of a task [2]. Interestingly, several studies have suggested that the DMN can be fractionated into distinct sub-networks specifically related to tasks requiring self-referential thought (preferentially engaging dorsal medial prefrontal cortex, MFPC), or specifically related to "pure" (i.e., non self-referential) resting state (preferentially engaging precuneus), or related to both mental states (engaging ventral MPFC and posterior cingulate cortex) [3], [4].

To date the neuronal basis of the low-frequency fluctuations of the BOLD signal are not fully understood. Contributing to this open issue is the fact that BOLD signal is an indirect measure of neuronal activity related to hemodynamic [5]. By contrast, electroencephalography (EEG) is a direct measure of neuronal activity. Therefore, the combination of EEG and fMRI can yield insights that are not accessible to one modality alone. The first EEG-fMRI studies investigated the BOLD correlates of spontaneous fluctuations in alpha activity [6], [7], [8]. However, there is a certain degree of inconsistency in the results from these and other EEG-fMRI studies investigating the correlation between BOLD signals and corresponding global EEG spectral characteristics in single spectral bands, such as the theta, alpha, and beta ones [6], [7], [9], [10], [11], [12]. This can be explained by the fact that a specific cerebral rhythm is not associated with just one functional network [13]. Moreover, using single (at the spatial level) EEG spectral metrics, such as the power averaged over all scalp channels [13] or extracted by single of few channels [8], [6], causes the loss of spatial specificity of electrical oscillations, a source of information about EEG spectral activity that is essential to appreciate its functional meaning [14]. Therefore, for data integration, the scalp distribution of EEG spectral metrics derived from the whole frequency spectrum should be considered. In [14], the author tried to tackle this issue, by assessing the topographic association of EEG spectral dynamics and RSNs fluctuations by means of the statistical approaches called EEG covariance mapping [15] and topographic ANOVA. However, these statistical tests compared the entire scalp distributions and could not identify neither the scalp regions that specifically determined the pattern of observed results nor the interplay between the different frequency bands in driving the observed results. The aim of the present study is to define a data-driven method that allows to take into account the interplay between different EEG frequency bands (i.e., to compare their specific patterns of correlations with RSN activity) and the corresponding topographic distribution within each RSN, as well as to compare the specific RSN-related topographic association of EEG spectral dynamics and BOLD fluctuations to identify specific spatio-spectral fingerprints of distinct RSNs. This method was applied to the subnetworks composing the DMN in order to identify even the subtle differences in the specific spatio-spectral correlates of related sub-RSNs.

II. METHOD

A. Simultaneous EEG/fMRI acquisition

Twenty-two healthy young volounteers took part in the experiment. Data from two participants were discarded

because of excessive head movements. Therefore, the results are reported for 20 participants (12 female; mean age: 23 years; age range: 20 – 28 years). The study was approved by the Bioethical Committee of the Azienda Ospedaliera di Padova and was conducted in accordance with the guidelines of the Declaration of Helsinki. Structural and functional images were acquired using a 3T Ingenia Philips whole body scanner (Philips Medical Systems, Best, The Netherlands) equipped with a 32-channel head-coil, at the Neuroradiology Unit of the University Hospital of Padova, Italy.

Functional data were obtained using a whole head T2∗-weighted echo-planar image sequences (repetition time, TR: 2000 ms; echo time, TE: 35 ms; voxel size: 2.4 × 2.4 × 4.8 mm). The functional acquisition lasted 400 s. During this time, subjects were asked to lie inside the scanner, to move as little as possible, and to keep their eyes open. After functional session, a T1-weighted anatomical image (TR/TE: 8.1/3.7; voxel size: 0.49 × 0.49 × 1 mm) was acquired.

The EEG signal was recorded using an MR-compatible system (Brain Products, Munich, DE), connected to 64 sintered Ag/AgCl ring electrodes and mounted on an elastic cap (BrainCap MR) according to the extended 10–20 system. Electrocardiographic (ECG) signal was acquired by means of an electrode placed in the middle of participants' back, approximately 4 cm left to the spine. Channels FCz and AFz served as online reference and ground, respectively. The EEG signal was band-pass filtered online between 0.016 and 250 Hz and digitized at a sampling rate of 5 kHz.

B. Preprocessing

Functional data were slice-timing corrected and rigidly realigned to the first volume. To quantify participants' head movements during the acquisition, framewise displacement (FD) was calculated for each participant [16]. Subjects with mean FD above two standard deviations (SD) from the sample mean (0.09 mm, SD = 0.02 mm) were excluded. To perform normalization, an affine transformation from the first volume of the functional data to the anatomical image was combined with a non-linear transformation from the anatomical image to the standard Montreal Neurological Institute template and applied to all volumes. Functional images were temporally filtered with a high-pass filter with cut-off frequency equal to

0.01 Hz and spatially smoothed using a Gaussian kernel with a full-width at half-maximum of 4 mm. The aforementioned preprocessing steps were performed with FSL [17]. The fMRI data were then decomposed into 50 functional networks using a group-level spatial Independent Component Analysis (ICA) as implemented in the GIFT toolbox (http://mialab.mrn.org/software/gift/). The number of components was taken as the mean of the estimated components for each subject using the minimum description length criterion. The Infomax ICA algorithm was run 10 times in ICASSO to identify the most stable components across all iterations. RSNs were selected by visual inspection based on previous literatures [18], [19] and back-reconstructed through dual regression. The sub-networks composing DMN were identified based on their spatial distribution and similarities in BOLD time courses and labelled according to [3]. Similarity was evaluated by performing an agglomerative hierarchical cluster analysis using the Ward's linkage method [20] based on the Euclidean distance metric.

The EEG data preprocessing was performed using EEGLAB 13.6.5 [21] and Matlab R2016b (The MathWorks, Natick, MA). The gradient and ballistocardiographic artifacts were removed using the fMRIB plugin [22]. Data were then bandpass filtered with a zero-phase Hamming windowed sinc FIR filter (cut-off: 0.5 and 48.5 Hz, bandwidth = 1 Hz) and downsampled to 250 Hz. After bad channels detection, the MRI artifact residuals, ocular movements and muscular activity were removed by means of Independent Component Analysis based on fast fixed-point ICA algorithm (http://research.ics.aalto.fi/ica/fastica/). Removed channels were then interpolated and data were re-referenced to the average of all electrodes.

C. EEG/fMRI integration

EEG data were segmented into epochs of 2000 ms, according to the TR of fMRI acquisition, and power spectrum was computed for each of them using a Welch's overlapped segment averaging estimator to obtain a 0.5 Hz resolution (250-points Hamming window, 500-points discrete Fourier transform, 125 points of overlap). From the absolute power spectrum, relative power for the delta (1-3.5 Hz), theta (4-7 Hz), alpha (7.5–12.5 Hz), beta (13–24 Hz) and gamma (24.5-
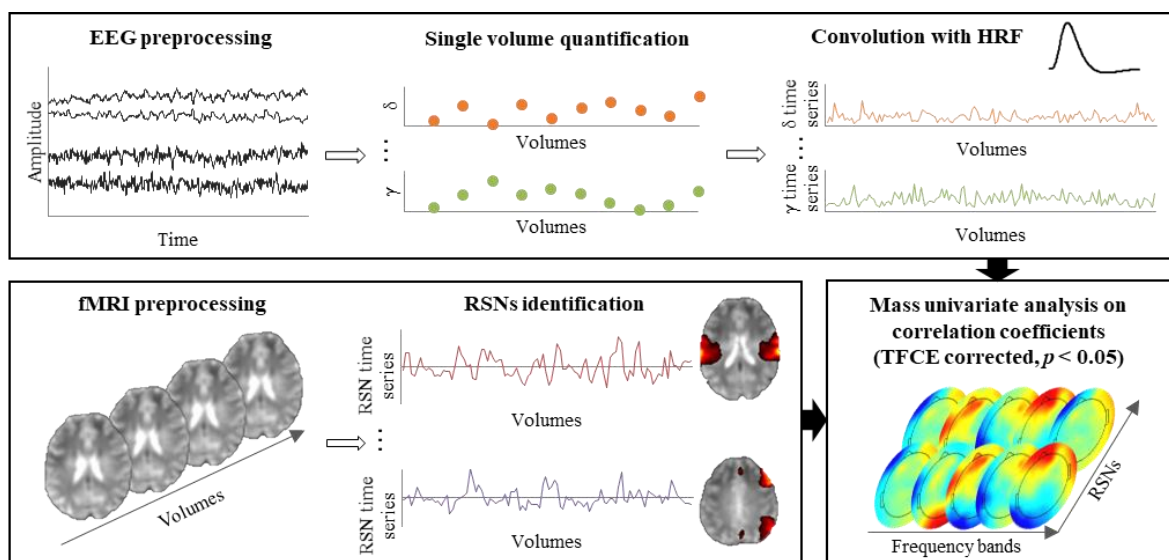

Fig. 1: A flow diagram summarizing the different stages of the analysis.

45 Hz) bands were calculated. For each specific rhythm, relative powers along the epochs were concatenated and the resulting time series was convolved with the canonical hemodynamic response function [13]. To analyze the correspondence between neuronal rhythms and RSNs, for each subject and channel, the RSNs average signals of the subnetworks obtained by clustering were correlated to the different band-power time series.

To detect specific inter-band topographical patterns of significant EEG-fMRI relationship, for each network the Fisher-transformed correlation coefficients were analyzed over the sensor space by means of mass-univariate analysis (ANOVA) with the five bands as factor. In order to assess the differences in how a resting state network correlated with the five frequency bands, post hoc pairwise t-tests were performed. Finally, to investigate the presence of specific spatio-spectral fingerprints of distinct RSNs, a further mass univariate ANOVA in sensor-frequency space with the networks of interest as a factor was performed.

The main stages of the analysis were illustrated in Fig 1.

III.   RESULTS

The four subnetworks composing the DMN were displayed in Fig.2: regions of "Self+Rest" network were involved in both self-reference and rest processes; regions of "Self" network were preferentially engaged during explicit self-reference process; regions of "Rest" and "Rest2" were more related to purely rest process. In Fig. 2, for each subnetwork of the DMN, the scalp topography displayed the result of the ANOVA analysis. Electrodes with significant inter-band differences (TFCE corrected, $p < 0.05$) in the correlation with the fMRI signal were showed as black dots. For each spatio-spectral cluster, post-hoc analyses were performed on the electrode with the maximum effect, marked in the scalp topography with a larger dot. When distinct clusters were not clearly identifiable, electrodes where the effect was maximal were taken as representative. For these electrodes, the across-subject mean values of the correlations between the time course of the network and the different band power time series were plotted in the graphs of the Fig. 2.

All sub-networks displayed significant positive correlation (TFCE corrected, $p < 0.5$) with the alpha band time series in the posterior electrodes, as found in [13] and [14]. Significant negative correlations were found between theta band and "Self+Rest", "Self" and "Rest2" networks in both anterior and posterior electrodes in accordance with [12], [14] and [23]. Despite these across-the-board correlations, this approach highlighted the presence of distinctive subcomponent-specific spatial-frequency patterns. As regard Self+Rest network, the scalp topography showed that significant (TFCE corrected, $p < 0.05$) band-dependent correlation differences were grouped into two distinct clusters: one cluster was located over central-frontal electrodes, the other one over an extended bilateral occipito-temporo-parietal region, with a clear right lateralization of the magnitude of the effect. Post-hoc analyses revealed that mean network correlation with alpha band significantly differed (TFCE corrected, $p < 0.05$) from the correlation with theta band in Fz and with all other bands in P6. Network "Self" showed significant (TFCE corrected, $p < 0.05$) band-dependent correlation differences over most of the scalp. Significant differences in the EEG-fMRI correlations were found between delta and gamma, delta and alpha, theta and alpha both in F1 and P4 (TFCE corrected, $p < 0.05$). ANOVA analysis on the correlations of network "Rest" revealed a significant band-dependent correlation differences mainly in the posterior electrodes (TFCE corrected, $p < 0.05$). The significant cluster also include temporal, left central-frontal and right frontal electrodes. The post-hoc tests results disclosed significant differences between alpha-fMRI correlations and delta- and theta-fMRI correlations in both F1 and P6 (TFCE corrected, $p < 0.05$). Other significant differences were found between delta and gamma in F1 and between delta and beta in P6 (TFCE corrected, $p < 0.05$). As regard ANOVA results related to network "Rest2": significant electrodes (TFCE corrected, $p < 0.05$) could be divided into two clusters, a smaller one over mid-left frontal electrodes and a more widespread one in the right centro-temporo-parietal regions. Specifically, significant differences between correlations with alpha and theta were found in both F1 and P4 (TFCE corrected, $p < 0.05$), whereas significant differences between alpha and both delta and beta were only identified in P4 (TFCE corrected, $p < 0.05$). The results described above reflect the inter-band differences in the topographical distribution of EEG power-fMRI relationship for each subcomponent of the Default Mode Network taken separately. To find out whether these EEG-fMRI correlation patterns were
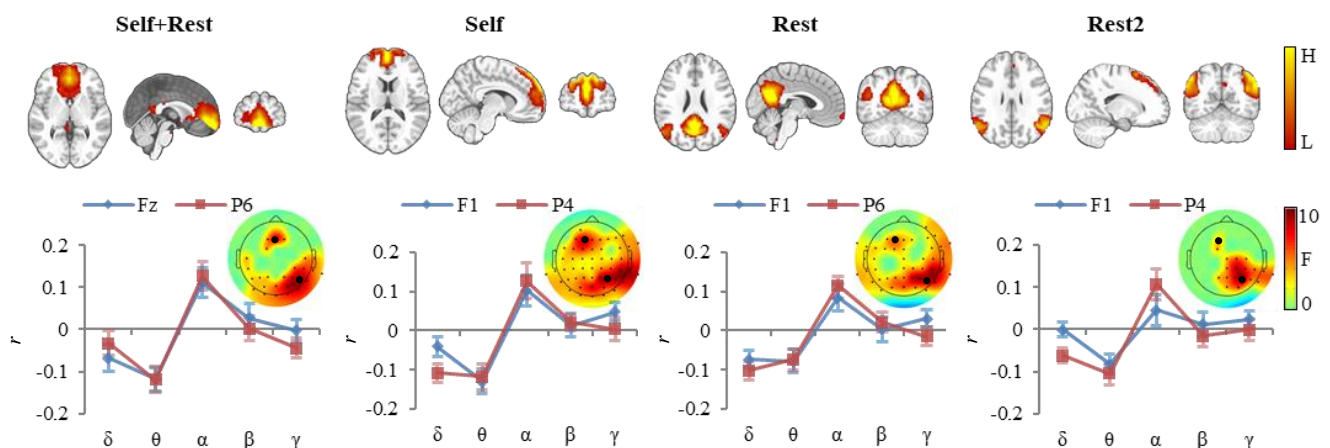

Fig. 2: Results of the analysis aimed at investigating the spatial distribution of correlations between the activity of the different subnetworks of the DMN and the EEG rhythms. Black dots on the scalp topographies highlight electrodes in which a significant effect was found (TFCE corrected, $p < 0.05$). The two biggest dots show the electrodes with maximal effect.

component-specific or rather general features of the DMN, a mass univariate ANOVA in sensor x frequency space was performed with the four networks as a factor. As shown in the first column of Fig. 3, the analysis revealed several spatio-spectral clusters of significant inter-networks differences in the EEG-fMRI correlations. A first cluster was visible over the occipital electrodes, which involved mainly theta and gamma bands; a second cluster was located over the right temporo-frontal electrodes and involved bands from delta to alpha; a third small cluster was present in the right parietal region of the scalp and involved the delta band; finally, a one-channel cluster was found over Cz for the theta band. Notably, concerning the spectral dimension, none of the clusters involved the high-frequency bands (beta and gamma bands). In the second column of Fig. 3, the mean correlations between network fMRI signals and delta, theta and alpha bands, measured in a representative electrode of the two most widespread clusters, were plotted as function of the different networks. In Oz electrode, positive correlations with alpha as well as negative correlations with theta distinguished the two RSNs involved in self-related processes (Self+Rest and Self networks) from Rest and Rest2. In F2 electrode, belonging to the lateralized frontal cluster, positive correlation with alpha identified Self+Rest, Rest and Self networks with respect to Rest2, whereas negative correlation with theta discerned between the self-related and the rest-related subcomponents. In this scalp site, thus, each subcomponent of the DMN could be distinguished from the other ones, based on the combination of their correlation with alpha and theta bands.
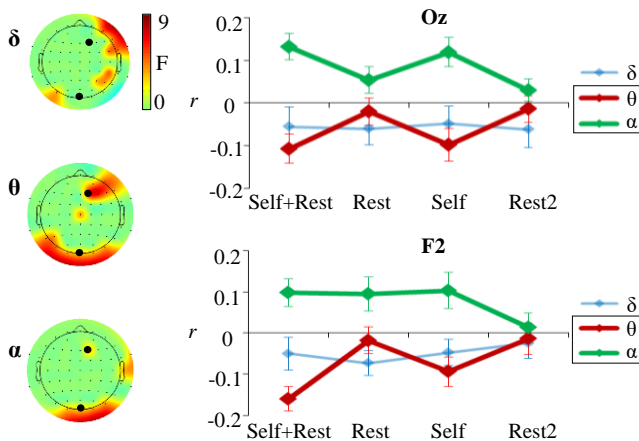

Fig. 3: Results of the analysis aimed at investigating specific spatio-spectral patterns that were significantly different across the subcomponents of the DMN.

IV. CONCLUSION

The present results extend previous findings by identifying the specific scalp regions showing: 1) significant inter-band differences in EEG-fMRI correlations within each-specific sub-RSN, and, importantly, 2) significant differences in patterns of EEG-fMRI correlations over different frequency bands across different sub-RSNs, representing specific spatio-spectral fingerprints of those RSNs. This approach seems to be able to identify even the more subtle differences exhibited by these four related sub-RSNs in their specific EEG-derived spatio-spectral fingerprints. Thus, it could be fruitfully applied to identify the more marked differences among the main RSNs.

REFERENCES

[1] S. M. Smith et al., "Correspondence of the brain's functional architecture during activation and rest", Proc Natl Acad Sci U S A, vol. 106, no. 31, pp. 13040-5, 2009.
[2] M. E. Raichle et al., "A default mode of brain function", Proc Natl Acad Sci U S A, vol. 98, no. 2, pp. 676-82, 2001.
[3] S. Whitfield-Gabrieli et al., "Associations and dissociations between default and self-reference networks in the human brain", Neuroimage, vol. 55, no. 1, pp. 225-32, 2011.
[4] J. R. Andrews-Hanna, J. S. Reidler, J. Sepulcre, R. Poulin, and R. L. Buckner, "Functional-anatomic fractionation of the brain's default network", Neuron, vol. 65, no. 4, pp. 550-62, 2010.
[5] S. Ogawa et al., "Intrinsic signal changes accompanying sensory stimulation: functional brain mapping with magnetic resonance imaging", Proc Natl Acad Sci U S A, vol. 89, no. 13, pp. 5951-5, 1992.
[6] H. Laufs et al., "EEG-correlated fMRI of human alpha activity", Neuroimage, vol. 19, no. 4, pp. 1463-76, 2003.
[7] H. Laufs et al., "Electroencephalographic signatures of attentional and cognitive default modes in spontaneous brain activity fluctuations at rest", Proc Natl Acad Sci U S A, vol. 100, no. 19, pp. 11053-8, 2003.
[8] R. I. Goldman, J. M. Stern, J. Engel, and M. S. Cohen, "Simultaneous EEG and fMRI of the alpha rhythm", Neuroreport, vol. 13, no. 18, pp. 2487-92, 2002.
[9] M. Moosmann et al., "Correlates of alpha rhythm in functional magnetic resonance imaging and near infrared spectroscopy", Neuroimage, vol. 20, no. 1, pp. 145-58, 2003.
[10] B. Feige et al., "Cortical and subcortical correlates of electroencephalographic alpha rhythm modulation", J Neurophysiol, vol. 93, no. 5, pp. 2864-72, 2005.
[11] S. I. Goncalves et al., "Correlating the alpha rhythm to BOLD using simultaneous EEG/fMRI: inter-subject variability", Neuroimage, vol. 30, no. 1, pp. 203-13, 2006.
[12] R. Scheeringa et al., "Frontal theta EEG activity correlates negatively with the default mode network in resting state", Int J Psychophysiol, vol. 67, no. 3, pp. 242-51, 2008.
[13] D. Mantini, M. G. Perrucci, C. Del Gratta, G. L. Romani, and M. Corbetta, "Electrophysiological signatures of resting state networks in the human brain", Proc Natl Acad Sci U S A, vol. 104, no. 32, pp. 13170-5, 2007.
[14] K. Jann, M. Kottlow, T. Dierks, C. Boesch, and T. Koenig, "Topographic electrophysiological signatures of FMRI Resting State Networks", PLoS One, vol. 5, no. 9, p. e12945, 2010.
[15] T. Koenig, L. Melie-Garcia, M. Stein, W. Strik, and C. Lehmann, "Establishing correlations of scalp field maps with other experimental variables using covariance analysis and resampling methods", Clin Neurophysiol, vol. 119, no. 6, pp. 1262-70, 2008.
[16] J. D. Power, K. A. Barnes, A. Z. Snyder, B. L. Schlaggar, and S. E. Petersen, "Spurious but systematic correlations in functional connectivity MRI networks arise from subject motion", Neuroimage, vol. 59, no. 3, pp. 2142-54, 2012.
[17] S. M. Smith et al., "Advances in functional and structural MR image analysis and implementation as FSL", Neuroimage, vol. 23 Suppl 1, pp. S208-19, 2004.
[18] C. F. Beckmann, M. DeLuca, J. T. Devlin, and S. M. Smith, "Investigations into resting-state connectivity using independent component analysis", Philos Trans R Soc Lond B Biol Sci, vol. 360, no. 1457, pp. 1001-13, 2005.
[19] E. A. Allen et al., "Tracking whole-brain connectivity dynamics in the resting state", Cereb Cortex, vol. 24, no. 3, pp. 663-76, 2014.
[20] J. H. Ward, "Hierarchical grouping to optimize an objective function", Journal of the American statistical association, vol. 58, pp. 236-244, 1963.
[21] Delorme and S. Makeig, "EEGLAB: an open source toolbox for analysis of single-trial EEG dynamics including independent component analysis", J Neurosci Methods, vol. 134, no. 1, pp. 9-21, 2004.
[22] R. K. Niazy, C. F. Beckmann, G. D. Iannetti, J. M. Brady, and S. M. Smith, "Removal of FMRI environment artifacts from EEG data using optimal basis sets", Neuroimage, vol. 28, no. 3, pp. 720-37, 2005.
[23] T.P. White et al., "Theta power during encoding predicts subsequent-memory performance and default mode network deactivation", Human Brain Mapping, vol. 34, pp. 2929-2943, 2013.

Improving the assessment of vascular complexity in peripheral artery occlusive disease

P. Bruno[1], P. Zaffino[2,*], F. Calimeri[1], S. Scaramuzzino[3], C. Indolfi[4], S. De Rosa[4], M.F. Spadea[2]

[1] University of Calabria, Department of Mathematics and Computer Science, Italy

[2] Magna Graecia University of Catanzaro, Department of Experimental and Clinical Medicine, Italy

[3] ASL AL di Alessandria, SC Tecnico, Tecnologie Biomediche ed ICT, Italy

[4] Magna Graecia University of Catanzaro, Department of Medical and Surgical Sciences, Division of Cardiology, Italy

* Corresponding author, p.zaffino@unicz.it

Abstract—In this work we propose a method to improve the visual assessment of vascular complexity in cine-angiography images from patients affected by peripheral artery occlusive disease (PAOD); in particular, we aim at evaluating the inter-clinician variability when scoring vascular complexity over "raw" and "processed" cine-angiography videos. The proposed workflow consists of 2 main steps: (i) conversion of the cine-angiographies to single static images with a broader field of view (FOV), and (ii) automatic segmentation of the vascular trees. In order to accomplish steps (i) and (ii) we make use of approaches based on machine-learning and deep-learning, respectively. We assessed the method on 20 cine-angiography acquisitions and asked three experienced interventional cardiologists to visually examine and then score the vascular complexity on cine-angiography (video), static image (grayscale) and segmented image (segmented). The inter-class correlation coefficient (ICC) was computed as inter-observer agreement metric and to account for possible systematic error, that depends on the experience of the raters. Absolute agreement was higher over the segmented image ($ICC = 0.956$) compared to the video ($ICC = 0.761$) and the grayscale image ($ICC = 0.918$). The 95% confidence level was statistically in favour of the segmented image; systematic error among raters was found. Results suggest that extracting the vascular tree from cine-angiography can substantially improve the reliability of visual assessment of vascular complexity in PAOD. Next steps will consist of the identification of a quantitative index as complexity score, in order to both speed up the clinical workflow and reduce the subjective error.

Keywords — Computer-Aided Diagnosis, Cine-Angiography, Vascular Complexity, Deep Learning, Machine Learning

I. Introduction

Peripheral Arterial Occlusive Disease (PAOD) is a common pathological condition where narrowed arteries reduce blood flow to the limb; the human body automatically tries to compensate the occlusions by angiogenesis, which is the formation of new blood vessels. Assessing the new collateral vascular network in patients with PAOD has a significant impact on both therapeutic decisions and on prognostic estimation. The evaluation of collateral growth is typically performed by physicians by visually inspecting cine-angiographies and giving a qualitative score of vessel branching complexity. Obtaining a cine-angiography (from a patient leg) currently requires to inject the patient with a radiopaque contrast mean and move the C-arm (or the patient couch) in order to film the whole leg. This procedure, however, presents several issues:

- each single frame of cine-angiographiy has a small field of view (FOV); this means that visual assessment is often limited to the portion of the vessel tree visible in the image;

- cine-angiograpy is a 2-D projective image and the contrast of vessels is jeopardized by the presence of catheters, surgical tools, screws and other anatomical structures, especially bones;

- the acquisition method (i.e., moving the C-arm or the patient couch) reduces the quality of images that are typically characterized by various lighting effects and motion blur, or generates overlapped frames due to irregular C-arm movements.

Because of the limitations mentioned above, it is clear that the assessment of vascular complexity in PAOD is highly dependent on the experience of the physician and that inter-observer variability is very high. Ideally, it would be good to segment the entire vascular tree from the images and present the extracted structure for the evaluation of ramification.

Tracking and segmenting vascular structures are crucial tasks in many medical applications, and several methods have been proposed [1], [2], [3], [4], [5], [6], [7] in literature. However, the segmentation on cine-angiography image frames is not trivial, because of the presence of several image artifacts and background noise. Our group recently proposed a method to automatically segment the vascular tree from cine-angiography images [8], in order to improve the clinical interpretation of the complexity of vascular collaterals in PAOD patients. The method consists of 2 steps: (i) a machine learning approach is used to build a static image with lager FOV (stiched image), starting from different image frames extracted from cine-angiography, and (ii) an adaptation of U-Net fully deep convolutional neural network (DCNN) architecture is employed to segment the vascular tree from the stitched image. In this work we assess the clinical impact of the proposed strategy by measuring and comparing the inter-observer variability in case of: (i) cine-agiography, (ii)
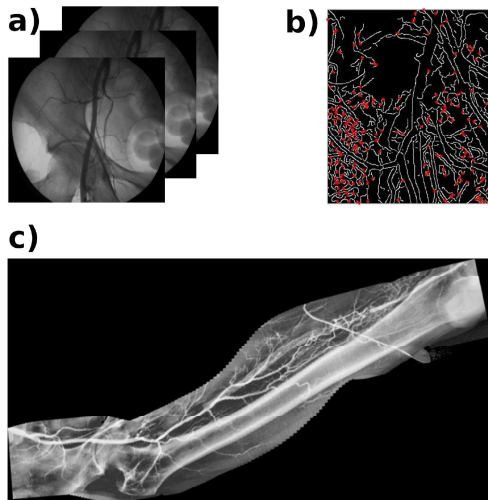
Fig. 1: Exemplary images from from cine-angiography to grayscale image. In panel a the original 2D frames over time are shown. Panel b depicts the points of interest detected by feature extraction algorithms. In panel c the stitching result is presented.

Fig. 2: Workflow of the architecture, which takes in input grayscale image and corresponding ground truth and returns segmentantion label.

TABLE I: Confusion matrix for vessel classification.

	Vessel present	Vessel absent
Vessel detected	True Positive (TP)	False Positive (FP)
Vessel not detected	False Negative (FN)	True Negative (TN)

stitched cine-angiography, and (iii) segmented image, in the following referred to as *video*, *grayscale* and *segmented*, respectively. We assess the method by means of a proper analysis executed on the images of 20 patients with PAOD. Our hypothesis is that presenting only the vascular tree for visual judgement would reduce the inter-observer variability.

II. MATERIALS AND METHODS

In the following we summarize the main steps needed to obtain grayscale and segmented image, respectively, as described in [8]. Then, we describe the datased used in this study and the inter-observer variability analysis.

A. Cineangiography stitching

Image stitching procedure was implemented and applied to cine-agiography image frames in order to obtain a single image with a wider FOV. Therefore, each cine-angiography, which is composed by a variable number of frames (i.e. range of $50 - 250$), was transformed from a 2D-overtime to a pure 2D image. The stitching procedure was based on identifying corresponding features (fiducial points) on 2 consecutive frames. To maximize the number of the features, each image underwent the following pre-processing steps:
In Fig. 1 the steps for the generation of the grayscale image are shown.

B. Vessel segmentation by deep learning

In order to perform vessel segmentation, we exploited the U-net model described in [8] and [9], i.e. a fully convolutional network with symmetrical structure, composed of a contracting and an up-sampling part. All layers used Rectified Linear Unit (ReLU), except for the last layer, where softmax was used in order to select the best scoring category. Dropout of 0.5 and batch normalization were used to address the overfitting
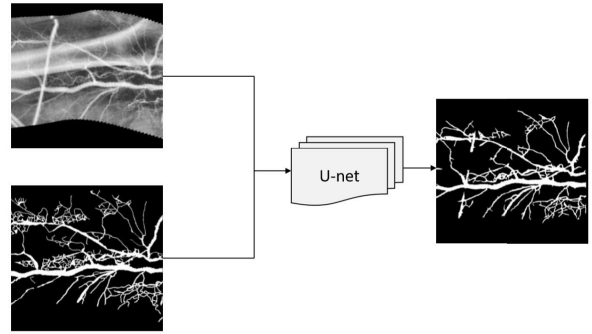
problem and improve learning. The network was implemented in TensorFlow [10] using the Keras wrapper and trained for 800 epochs, using the Adadelta [11] optimizer with default parameters, categorical cross-entropy as loss function, learning rate 10^{-5} and batch size 32.

All experiments have been performed on a machine equipped with a 12 x86_64 Intel(R) Core(TM) CPUs @ 3.50GHz, running Linux Debian 7 and using CUDA compilation tools, release 7.5, $V7.5.17$ NVIDIA Corporation $GM204$ on GeForce GTX 970. In Fig. 2 the overall structure used to perform binary segmentation is shown.

C. Data

The proposed approach was tested on a dataset including 20 cine-angiographies acquired at the Interventional Cardiology Units of Magna Graecia University Hospital (Catanzaro, Italy) and at Federico II University Hospital (Naples, Italy); patients have previously given explicit informed consent to the use of their anonymized data for research purpose. For each cine-angiography, a stitched image was generated according to Sec. II-A; the resulting images represent the entire ilio-femoral district for each patients.

The Ground Truth (GT) segmentations for the input images were manually drawn by an expert clinician on grayscale image. The network model was trained and evaluated using 4-fold cross-validation; folds are split into disjoint sets of patients such that training set is the 80% of the entire dataset and testing is the 20%; in particular, the 20% of the training set is used as validation set in order to monitor the training process and prevent overfitting.

D. Data analysis

The accuracy of image segmentation was assessed by the Receiver Operating Characteristic (ROC) analysis.

Modality	ICC	Lower Boud	Upper Boud
Video	0.76	0.24	0.92
Grayscale	0.92	0.75	0.97
Segmented	0.96	0.91	0.98

TABLE II: $ICC(A, k)$ (two way random model) computed for the three investigated modalities (averaged measures). Lower and upper bound represent the 95% confidence interval.

Taking into account Table I, image pixels were labelled as TP, TN, FP and FN. ROC curve is a plot of true positive fractions ($S_e = \frac{TP}{TP+FN}$) versus false positive fractions ($S_p = 1 - \frac{TN}{TN+FP}$) by varying the threshold on the probability map. The Area Under the Curve (AUC) of ROC was assumed as a metric to evaluate the accuracy of pixel classification, being the range 0 to 1 bad to excellent prediction.

In order to account for inter-observer variability, 3 experienced interventional cardiologists were asked to judge the complexity of the vascular tree by looking at the i) video, ii) grayscale image and iii) segmented image. In particular, the clinicians' evaluation was performed on the test set. The score ranged from 1 to 10, meaning from less to most complex vascularization. Inter-observer variability was calculated for each of the 3 cases by applying the inter-class correlation coefficient (ICC) analysis [12]. ICC is a widely used index in test-retest, intra-rater and inter-rater reliability analyses. It can be defined in different forms, up to 10, depending on the: 1) model (1-way random effects, 2-way random effects, or 2-way fixed effects), 2) the type (single rater/measurement or the mean of k raters/measurements), and 3) he definition of relationship considered to be important (consistency or absolute agreement) [12]. In choosing the proper ICC, we adopted the two-way random model, as described in [13]. We built a matrix nxk, with n number of scored images for each modality and k, number of observers. Given MS_R the mean square for rows, MS_C the mean square for columns and MS_E the residual mean, we computed the absolute agreement among raters as:

$$ICC(A, k) = \frac{MS_R - MS_E}{MS_R + \frac{MS_C - MS_E}{n}} \quad (1)$$

and the degree of consistency among raters as:

$$ICC(C, k) = \frac{MS_R - MS_E}{MS_R} \quad (2)$$

This latter was chosen to separate possible systematic error. Both indexes were estimated at 95% confidence level. ICC index varies between 0 to 1 with 0 meaning no-agreement and 1 perfect agreement. Statistical analysis was performed by using IBM SPSS statistics software v26 (IBM Corp. in Armonk, NY).

III. RESULTS

The $mean \pm std$ of AUC was 0.986 ± 0.006 with a min-max range of $0.974 - 0997$, where std is the standard deviation. In particular, it is important to know that a high AUC values
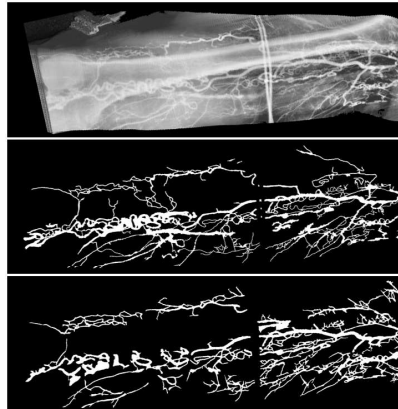

Fig. 3: Worst case result obtained in terms of automatic segmentation. From top to botton stitched image, GT and automatic segmentation.

Modality	ICC	Lower Boud	Upper Boud
Video	0.89	0.77	0.95
Grayscale	0.95	0.89	0.98
Segmented	0.96	0.91	0.98

TABLE III: $ICC(C, k)$ (two way random model) computed for the three investigated modalities (averaged measures). Lower and upper bound represent the 95% confidence interval.

is translated into very good segmentation. Figure 3 shows the worst case in terms of automatic segmentation together with the stitched image and the GT. The presence of cables and artifacts reduced the accuracy of the segmentation which, however, was very good for the purpose of the use.

Table II and Table III reports the $ICC(A, k)$ and $ICC(C, k)$ respectively, for the three image modalities. In terms of absolute agreement we can notice that $ICC(A, k)$ is maximum on the segmented image and lower on the video. This support our hypothesis that i) a full FOV image and ii) the extraction of the vascular tree help the raters to agree in their judgement. The 95% confidence level shows the spread of the variability, being very large for the video. No differences between grayscale and segmented image was revealed by $ICC(C, k)$, although it is still slightly evident the improvement of full FOV vs. video.

IV. DISCUSSION

In this work we proposed and validated a method to reduce the the inter-observer variability in visual scoring the vascular complexity of patients with PAOD. The method is potentially of relevant impact, as vascular angiogenesis is highly correlated with diagnostic and prognostic evaluation, and wrong assessment can lead to wrong clinical decision. In designing our methodology we tried to solve several limitations that are currently present in current clinic procedures, in particular:

- the visualization of the entire detected anatomical district. To this aim, we proposed a machine learning based procedure to optimally stitch each image frame of the

cine-angiography and generate a full FOV gray scale image.

- The enhancement of the vascular tree vs. other anatomical structures and surgical tools. The role of the contrast mean, in fact, is limited by the presence of other high density objects in the scene. One solution might be to acquire a subtractive angiography but this would extend the time required for the exam, the radiation dose received by the patient and it would be prone to motion artifacts. Another solution could rely on the use of a tomographic volume of the district to remove the unwanted structures as in [14]. To solve this issue, we proposed vessel segmentation based on deep learning. We originally tried traditional methods proposed in literature for this task, as the Frangi's filter [1]. However, given the complexity of the image, only a deep learning approach was able to reach a very high accuracy of the segmentation. Indeed, deep learning algorithms proved to be able to achieve notable results in image segmentation tasks [15], [16], [17], [18]

The inter-observer analysis we performed was based on the computation of the ICC. The interpretation of ICC value is a nontrivial task, because there are different forms of ICC which give different values and can lead to wrong conclusions [12]. In our case, we made the following assumptions: (i) the model is two-way random, because both images and raters are randomly selected by a population of possible images and raters and the raters scored all images; (ii) since we were interested to the reliability of 3 observers and not of single rater, we computed ICC for averaged measurements; (iii) finally, in choosing the type of ICC we computed both accuracy ($ICC(A, k)$) and consistency ($ICC(C, k)$). By looking at Eq. 1 and Eq. 2 one can notice that while $ICC(A, k)$ accounts for variability intra-rater, $ICC(C, k)$ does not. This means that rates might be highly correlated among them but they can statistically present a systematic error in over- or under-scoring the image. In fact, by looking at the results we can say that the inter-observer variability is always higher in case of video based assessment and that scoring the grayscale image decrease the variability but present a systematic error ($ICC(C, k) > ICC(A, k)$). The segmented image provide the lowest inter-observer variability, with a very narrow confidence interval and wipes out the systematic error.

V. CONCLUSION

Our hypothesis about the possibility to improve the visual assessment of the vascular tree in PAOD by means of the vessel tree segmentation is confirmed. Future work will focus on providing a quantitative metric for scoring the vascular complexity and design an artificial intelligence framework to classify the diagnosis and the prognosis of PAOD patients based on images and clinical data.

REFERENCES

[1] A. F. Frangi, W. J. Niessen, K. L. Vincken, and M. A. Viergever, "Multiscale vessel enhancement filtering," in *International conference on medical image computing and computer-assisted intervention*, pp. 130–137, Springer, 1998.

[2] M. Niemeijer, J. Staal, B. van Ginneken, M. Loog, and M. D. Abramoff, "Comparative study of retinal vessel segmentation methods on a new publicly available database," in *Medical imaging 2004: image processing*, vol. 5370, pp. 648–656, International Society for Optics and Photonics, 2004.

[3] H. Fu, Y. Xu, S. Lin, D. W. K. Wong, and J. Liu, "Deepvessel: Retinal vessel segmentation via deep learning and conditional random field," in *International conference on medical image computing and computer-assisted intervention*, pp. 132–139, Springer, 2016.

[4] D. Scorza, S. Moccia, G. De Luca, L. Plaino, F. Cardinale, L. S. Mattos, L. Kabongo, and E. De Momi, "Safe electrode trajectory planning in seeg via mip-based vessel segmentation," in *Medical Imaging 2017: Image-Guided Procedures, Robotic Interventions, and Modeling*, vol. 10135, p. 101352C, International Society for Optics and Photonics, 2017.

[5] S. Moccia, S. Foti, A. Routray, F. Prudente, A. Perin, R. F. Sekula, L. S. Mattos, J. R. Balzer, W. Fellows-Mayle, E. De Momi, et al., "Toward improving safety in neurosurgery with an active handheld instrument," *Annals of biomedical engineering*, vol. 46, no. 10, pp. 1450–1464, 2018.

[6] S. Moccia, E. De Momi, S. El Hadji, and L. S. Mattos, "Blood vessel segmentation algorithms—review of methods, datasets and evaluation metrics," *Computer methods and programs in biomedicine*, vol. 158, pp. 71–91, 2018.

[7] P. Zaffino, G. Pernelle, A. Mastmeyer, A. Mehrtash, H. Zhang, R. Kikinis, T. Kapur, and M. F. Spadea, "Fully automatic catheter segmentation in mri with 3d convolutional neural networks: application to mri-guided gynecologic brachytherapy," *Physics in Medicine & Biology*, vol. 64, no. 16, p. 165008, 2019.

[8] P. Bruno, P. Zaffino, S. Scaramuzzino, S. De Rosa, C. Indolfi, F. Calimeri, and M. F. Spadea, "Using cnns for designing and implementing an automatic vascular segmentation method of biomedical images," in *International Conference of the Italian Association for Artificial Intelligence*, pp. 60–70, Springer, 2018.

[9] P. Bruno, P. Zaffino, S. Scaramuzzino, S. De Rosa, C. Indolfi, F. Calimeri, and M. F. Spadea, "Segmentation of vessel tree from cine-angiography images for intraoperative clinical evaluation.," in *RiCeRcA@ AI* IA*, 2018.

[10] M. Abadi, P. Barham, J. Chen, Z. Chen, A. Davis, J. Dean, M. Devin, S. Ghemawat, G. Irving, M. Isard, et al., "Tensorflow: A system for large-scale machine learning," in *12th {USENIX} Symposium on Operating Systems Design and Implementation ({OSDI} 16)*, pp. 265–283, 2016.

[11] M. D. Zeiler, "Adadelta: an adaptive learning rate method," *arXiv preprint arXiv:1212.5701*, 2012.

[12] K. O. McGraw and S. P. Wong, "Forming inferences about some intraclass correlation coefficients.," *Psychological methods*, vol. 1, no. 1, p. 30, 1996.

[13] T. K. Koo and M. Y. Li, "A guideline of selecting and reporting intraclass correlation coefficients for reliability research," *Journal of chiropractic medicine*, vol. 15, no. 2, pp. 155–163, 2016.

[14] M. F. Spadea, A. Fassi, P. Zaffino, M. Riboldi, G. Baroni, N. Depauw, and J. Seco, "Contrast-enhanced proton radiography for patient set-up by using x-ray ct prior knowledge," *International Journal of Radiation Oncology* Biology* Physics*, vol. 90, no. 3, pp. 628–636, 2014.

[15] P. Zaffino, D. Ciardo, P. Raudaschl, K. Fritscher, R. Ricotti, D. Alterio, G. Marvaso, C. Fodor, G. Baroni, F. Amato, et al., "Multi atlas based segmentation: should we prefer the best atlas group over the group of best atlases?," *Physics in Medicine & Biology*, vol. 63, no. 12, p. 12NT01, 2018.

[16] E. Tappeiner, S. Pröll, M. Hönig, P. F. Raudaschl, P. Zaffino, M. F. Spadea, G. C. Sharp, R. Schubert, and K. Fritscher, "Multi-organ segmentation of the head and neck area: an efficient hierarchical neural networks approach," *International journal of computer assisted radiology and surgery*, vol. 14, no. 5, pp. 745–754, 2019.

[17] F. Milletari, N. Navab, and S.-A. Ahmadi, "V-net: Fully convolutional neural networks for volumetric medical image segmentation," in *2016 Fourth International Conference on 3D Vision (3DV)*, pp. 565–571, IEEE, 2016.

[18] K. Fritscher, P. Raudaschl, P. Zaffino, M. F. Spadea, G. C. Sharp, and R. Schubert, "Deep neural networks for fast segmentation of 3d medical images," in *International Conference on Medical Image Computing and Computer-Assisted Intervention*, pp. 158–165, Springer, 2016.

Comparison of different CNNs for breast tumor classification from ultrasound images

Jorge F. Lazo[1], Sara Moccia[2,3], Emanuele Frontoni[3] and Elena de Momi[1]

[1] *Department of Electronics, Information and Bioengineering*, Politecnico di Milano, Milan, Italy
[2] *Department of Advanced Robotics, Istituto Italiano di Tecnologia, Genoa, Italy*
[3] *Department of Information Engineering, Università Politecnica delle Marche, Ancona, Italy*

Abstract—Breast cancer is one of the deadliest cancer world-wide. A timely detection could reduce mortality rates. In the clinical routine, classifying benign and malignant tumors from ultrasound (US) imaging is a crucial but challenging task. An automated method, which can deal with the variability of data is therefore needed. In this paper, we compared different Convolutional Neural Networks (CNNs) and transfer learning methods for the task of automated breast tumor classification. The architectures investigated in this study were VGG-16 and Inception V3. Two different training strategies were investigated: the first one was using pretrained models as feature extractors and the second one was to fine tune the pretrained models. A total of 947 images were used, 587 corresponded to US images of benign tumors and 360 with malignant tumors. 678 images were used for the training and validation process, while 269 images were used for testing the models. Accuracy and Area Under the receiver operation characteristic Curve (AUC) were used as performance metrics. The best performance was obtained by fine tuning VGG-16, with an accuracy of 0.919 and an AUC of 0.934. The obtained results open the opportunity to further investigation with a view of improving cancer detection.

Keywords—Convolutional Neural Network, Transfer Learning, Deep Learning, Breast Tumors, Ultrasound Images.

I. INTRODUCTION

Breast cancer is the most common cancer in women [1]. Cancer screening is performed via Breast Ultrasound (BUS) imaging and mammography. BUS is recommended in a large variety of cases, such as women under the age of 30 and/or in case of pregnancy. Cancer diagnosis is performed in the clinical practice by clinicians through visual BUS-image analysis. However, it is well known that BUS image acquisition and analysis are highly dependent on the clinician level of expertise [2].

Computer-aided diagnosis (CAD) systems for BUS image analysis have recently shown to be able to tackle the variability associated with both breast anatomy and BUS images, becoming a suitable tool to improve diagnosis accuracy [3].

In the last few years, deep-learning (DL) approaches, and more specifically convolutional neural networks (CNNs), have become the standard in research for BUS-image analysis [4]. However, there are still open challenges that need to be addressed. Among them, the necessity of relying on a large and annotated BUS dataset for CNN training [4]. A possible solution to attenuate this issue could be to exploit transfer learning and fine tuning. These kind of approaches has already been applied in other studies and imaging modalities present-

ing promising results as reported in [5], [6], [7]. However, even transfer learning seems to be the way of proceeding, there are different techniques to perform this method, and to our knowledge, there is no study in the comparison of this strategies applied to this kind of data.

In this paper we explore the use of pre-trained existing models and two different training strategies with the aim of determining which of these strategies and model is more suitable for the task of breast tumor classification. The paper is organized as follows: Sec. II reviews the state of the art in automated tumor classification methods, Sec. III delve into the methodology explaining the architectures and transfer learning techniques used. In Sec. V information about the dataset used and details about the training is provided. In Sec. IV the results are presented and discussed. Finally, Sec. VI, concludes this paper discussing results and proposing future improvements.

II. DEEP LEARNING IN BUS IMAGE ANALYSIS

In the last few years, DL methods and specifically CNNs have become the state of the art for image analysis tasks. The application of DL in the analysis of medical US images involves different specific tasks, such as classification, segmentation, detection, registration, as well as the development of new methodologies for image-guided interventions.

In the specific case of tumor classification, different extensions and variations of DL approaches have been developed. In [8] the authors propose the use of different CNNs for locating regions of interest (ROIs) corresponding to lesions. In [9], CNNs are used as feature extractors and the features obtained are classified with a Support Vector Machine (SVM). In [10] an architecture based on AlexNet is proposed, and its performance is compared with some pretrained models, using a small custom-built dataset. In [11], a method based on the use of Generative Adversarial Networks (GANs) for data augmentation is proposed, later the authors compare the performance of this network in the task of generating synthetic data, using pretrained models, in this case VGG16, Inception, ResNet and NasNet. A further step is taken in [12], where the authors propose the use of ensembles to develop a better and more comprehensive generalized model. Their model is based in the use of VGG16-like architectures as well as different versions of ResNet and DenseNet. In [13] a modification to the GoogLeNet architecture is proposed, this network is an early version of Inception V3 and it is composed by a main

branch and two auxiliary classifiers, specifically they suggest to remove the auxiliary classifiers from the main branch of the network. In [14] they compare different pre-trained models but only using fine-tuning. In this study they compare the CNNs ResNet50, InceptionV3, and Xception.

III. PROPOSED METHODS

In this work, we investigated two different transfer learning techniques: (i) fine tuning and (ii) using pretrained CNNs as feature extractor. Each of these methods were tested using two different CNN architectures:

A. CNN architectures

- VGG-16 is a 16-layer CNN model which has a sequential architecture consisting of 13 convolutional layers and 5 max-pooling layers [15]. The architecture starts with a convolutional layer with 64 kernels. This number is doubled after each pooling operation until it reaches 512. The pooling layer is placed after selected convolutional layers in order to reduce dimension in the activation maps and hence of the subsequent convolution layers. This in general reduces the number of parameters that the CNN needs to learn. The convolutional kernel size of all the convolutional layers in this model is 3x3. The model ends with three fully-connected (FC) layers with 64 neurons each, which perform the classification.
- Inception V3 [16] uses an architectural block called inception module, which consists of convolutional kernels with different sizes (1x1, 3x3 and 5x5) that are connected in parallel (Fig. 1). The use of different kernel sizes allows the identification of image features at different scales. Furthermore, Inception V3 uses not just one classifier but two, the second one is an auxiliary classifier which is used as regularizer. One of the main advantages of this model is that it is composed of about 23 million of parameters even it has 42 layers, therefore the computational cost for training this network is also less than the one needed to retrain VGG-16. However, given its more complex topology it is also harder to retrain.

B. Transfer learning

As introduced in Sec. I, training a CNN model from scratch requires a large number of computational resources as well as a fair amount of labeled data. It also often requires a considerable amount of time, even using several graphics processing units (GPUs).

Transfer learning allows making the training process more efficient by using a model that has already been trained on a different dataset. There are different ways to perform transfer learning, in this work fine tuning and feature extraction techniques were explored. The first one refers to re-adjust the weights of the new distribution of the new training data, i.e. to tune the weights of the CNN by training it on the new dataset for few epochs and with a low learning rate. Usually, only the weights in the last layers are retrained. In this work, both
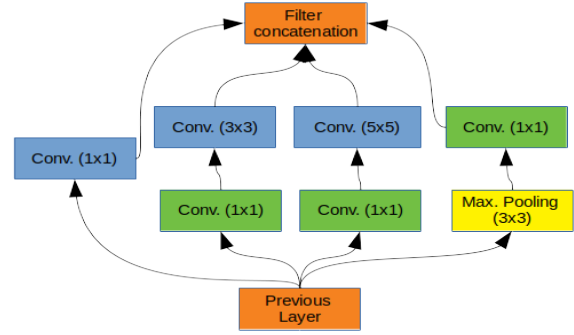

Fig. 1: Diagram of the inception module. The module is composed by several convolutional kernels of size 1x1, 3x3 and 5x5 connected in parallel. The 1x1 kernels placed before the 3x3 and 5x5 is used to reduce the dimensionality of the feature map. The output of each of the branches is finally concatenated before getting into the next stage.
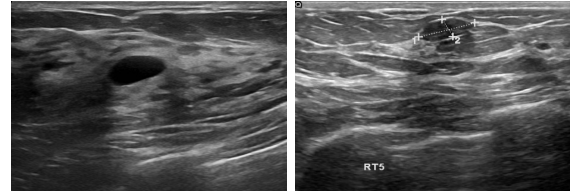

Fig. 2: Samples of two images from the BUSI dataset. Image with a benign tumor (left) and with a malignant tumor (right).

VGG 16 and Inception V3 were pretrained on ImageNet[1], a dataset which has more than 14 million images belonging to 1000 classes. The second method, feature extraction, refers to use the whole network as a feature identifier, and then making use of the high level features, obtained from the network, in another classifier.

The fine-tuning strategy was performed by replacing the last fully connected layer composed by 2 neurons (one for the benign and the other for the malignant class), and then fine-tune different number of layers in the network. The layers chosen to be fine-tuned were the very last one up to the last 3 layers of each network.

In the case of the feature extraction method, an additional classifier was added and trained, this was composed by a Global Average Pooling Layer, a Fully connected layer with a Rectified Linear Unit (*ReLU*) activation function. Finally, a fully connected layer with *softmax* activation function and 2 neurons.

IV. RESULTS

A. Dataset

The data used for this work came from two public available datasets collected by the groups of Rodriguez et al.[2] and Fahmy et al.[3] The first dataset consists of 250 breast tumor

TABLE I: Comparison of the obtained results with VGG-16 and Inception V3 with different training methods each one. The numbers highlighted in black correspond to the model and method that obtained the highest scores in terms of *ACC* and *AUC*.

Model	trainable parameters	ACC	AUC
Feature extraction			
VGG-16	512,512	0.862	0.791
Inception V3	1,311,744	0.713	0.623
Fine-tuning			
VGG-16	1,054,722	**0.919**	**0.934**
Inception V3	2,388,539	0.756	0.783

images (100 benign and 150 malignant) with an average size of 100x75 pixels. The second one consists of 963 images of an average image size of 500x500 pixels, in this dataset 487 images correspond to images with benign tumors, 210 with malignant tumors and 266 images with any tumor at all. For this project only the images with benign and malignant tumors were used.

Hence, the dataset used in this work consisted of 537 and 360 with benign and malignant tumors, respectively. The whole dataset was shuffled randomly, and then split, in a stratified fashion, in two subsets, with 630 images for training and validation, and 269 for testing. A sample of benign and malignant BUS images is shown in Fig. 2.

During the training of the networks, mini-batch gradient descent method was applied and Adam optimization algorithm. At the moment of creating the training batches the images were reshaped "on the fly" to match the size of the input of each network, 224x224 pixels in the case of VGG-16 and 299x299 pixels for the case of Inception V3.

B. Training settings

Training was performed with an initial learning rate of 0.001. The size of the output for the added fully connected (FC) layer was 1024 and 512 for Inception V3 and VGG-16 respectively. The mini-batch size used was of 50 images.

The experiments were carried out on an Nvidia GPU GTX 1660 using Keras with TensorFlow backend.

C. Performance Metrics

To evaluate the proposed CNNs, the area (AUC) under the Receiver Operating Characteristic (ROC) curve was computed. The accuracy (ACC), was computed as follows:

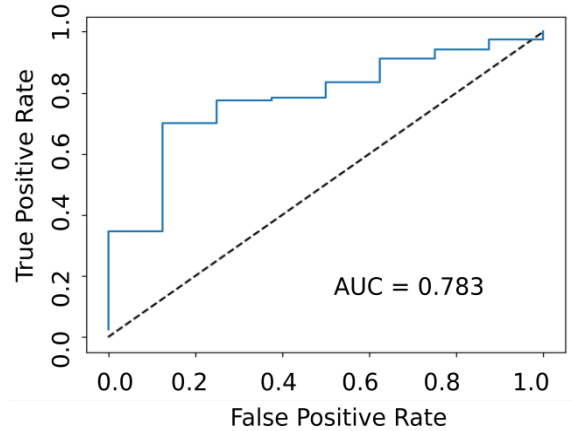$$ACC = \frac{TP + TN}{TP + FP + FN + TN} \qquad (1)$$

where TP and TN are the amount of malignant BUS images correctly classified, respectively, and FN and FP are the amount of malignant BUS images missclassified.

V. RESULTS AND DISCUSSION

The obtained ROC curves for VGG-16 and Inception V3 using the fine-tuning are shown in Fig. 3, a summary of the
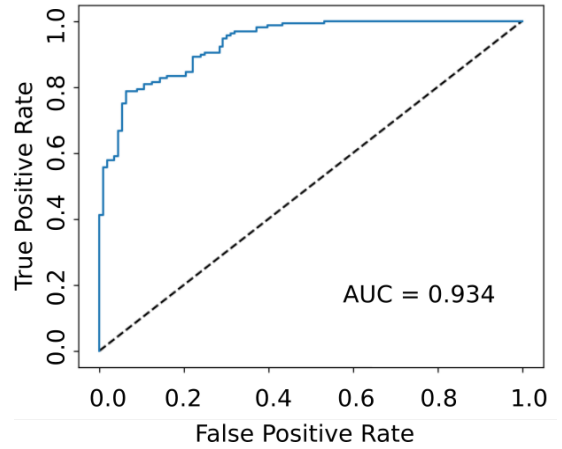
(a)

(b)

Fig. 3: Receiver operating characteristics (ROC) curves for the 2 different models tested using fine-tuning: (a) VGG-16, (b) Inception V3.

results obtained with each network and each training method is presented in Table I. Fine tuning worked better, and the model which performed better was VGG-16 in both cases. However, the difference between these two tranfer learning methods is smaller with Inception V3. In the case of the ACC, the difference is only of 0.046 while the difference of the AUC is 0.16. Using fine tuning on VGG-16, the values of ACC = 0.919 and AUC = 0.934 were obtained.

Inception V3 only reaches the values of 0.756 and 0.783, respectively in the test dataset. However, during the training, it reaches accuracy values over 0.93 and AUC of 0.89 which implies that the model is over-fitting. Normalization techniques, such as Dropout and L_2 normalization, may help to reduce the over-fitting issue and improve its performance in the testing stage [17]. A deep exploration of the hyperparameters choice such as the batch size, the learning rate, the number of layers to be retrained (for the case of fine tuning), the size of the fully connected layers and number of layers (for the case of feature extraction) and the use of normalization methods is needed to be carried out. As is it possible to see from the sample
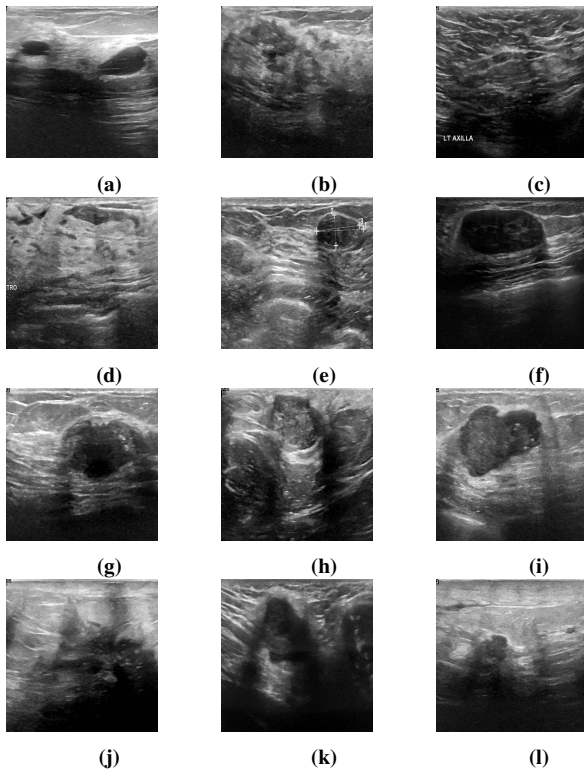
Fig. 4: Sample of results obtained by using fine tuning and VGG-16 architecture. (a)-(c) images with benign tumors missclassified as malign, (d)-(f) images with benign tumors correctly classified, (g)-(i) images with malign tumors missclassified as benign, (j)-(l) images with malign tumors correctly classified.

of results show in Fig. 4 the variability of the content in the images affects the predictions made by the network. This may could be tackled by using different data augmentation methods which can generalize the variability of this kind of data.

VI. CONCLUSION

In this paper, we explored the application of CNN for the task of tumor classification using BUS images. We trained two pretrained models in two different ways: using the existing models as feature extractors and fine tuning them. We observed that for this case fine tuning achieved better results and in general the architecture VGG-16 performed better in the test dataset. The best value obtained for accuracy was 0.919 with an AUC of 0.934. In the case of Inception V3 the values obtained were considerably lower, 0.756 and 0.783 respectively, but its performance during the training was better, reaching an accuracy value of 0.93. The results obtained using fine tuning are in the same range as the one of the state of the art, but we can state that fine tuning is the strategy to go and which should be developed further. Further normalization methods will be needed in order to avoid over-fitting as it seems to be the case. Future work includes the use of data augmentation, the testing of different and novel architectures which have claimed to be more robust against perspective transformations, spatial orientation, scale changes, etc. such as

Capsule Networks and the exploration of image segmentation with other architectures.

REFERENCES

[1] R. L. Siegel, K. D. Miller, and A. Jemal, "Cancer statistics," *A Cancer Journal for Clinicians*, vol. 69, no. 1, pp. 7–34, 2019.

[2] I. WIDELY, "Variability in the interpretation of screening mammograms by us radiologists," *Arch Intern Med*, vol. 156, pp. 209–213, 1996.

[3] M. Xian, Y. Zhang, H. Cheng, F. Xu, B. Zhang, and J. Ding, "Automatic breast ultrasound image segmentation: A survey," *Pattern Recognition*, vol. 79, pp. 340 – 355, 2018.

[4] S. Liu, Y. Wang, X. Yang, B. Lei, L. Liu, S. X. Li, D. Ni, and T. Wang, "Deep learning in medical ultrasound analysis: A review," *Engineering*, vol. 5, no. 2, pp. 261 – 275, 2019.

[5] H. Shin, H. R. Roth, M. Gao, L. Lu, Z. Xu, I. Nogues, J. Yao, D. Mollura, and R. M. Summers, "Deep convolutional neural networks for computer-aided detection: Cnn architectures, dataset characteristics and transfer learning," *IEEE Transactions on Medical Imaging*, vol. 35, no. 5, pp. 1285–1298, May 2016.

[6] M. C. Fiorentino, S. Moccia, E. Cipolletta, E. Filippucci, and E. Frontoni, "A learning approach for informative-frame selection in us rheumatology images," in *International Conference on Image Analysis and Processing*. Springer, 2019, pp. 228–236.

[7] F. Calimeri, A. Marzullo, C. Stamile, and G. Terracina, "Optic disc detection using fine tuned convolutional neural networks," in *2th International Conference on Signal-Image Technology & Internet-Based Systems*. IEEE, 2016, pp. 69–75.

[8] M. H. Yap, G. Pons, J. Martí, S. Ganau, M. Sentís, R. Zwiggelaar, A. K. Davison, and R. Martí, "Automated breast ultrasound lesions detection using convolutional neural networks," *IEEE journal of biomedical and health informatics*, vol. 22, no. 4, pp. 1218–1226, 2017.

[9] I. Bakkouri and K. Afdel, "Breast tumor classification based on deep convolutional neural networks," in *International Conference on Advanced Technologies for Signal and Image Processing*. IEEE, 2017, pp. 1–6.

[10] B. Zeimarani, M. G. F. Costa, N. Z. Nurani, and C. F. F. Costa Filho, "A novel breast tumor classification in ultrasound images, using deep convolutional neural network," in *XXVI Brazilian Congress on Biomedical Engineering*, R. Costa-Felix, J. C. Machado, and A. V. Alvarenga, Eds. Singapore: Springer Singapore, 2019, pp. 89–94.

[11] W. Al-Dhabyani, M. Gomaa, H. Khaled, and F. Aly, "Deep learning approaches for data augmentation and classification of breast masses using ultrasound images," *International Journal of Advanced Computer Science and Applications*, vol. 10, no. 5, 2019.

[12] W. K. Moon, Y.-W. Lee, H.-H. Ke, S. H. Lee, C.-S. Huang, and R.-F. Chang, "Computer-aided diagnosis of breast ultrasound images using ensemble learning from convolutional neural networks," *Computer Methods and Programs in Biomedicine*, vol. 190, p. 105361, 2020.

[13] S. Han, H.-K. Kang, J.-Y. Jeong, M.-H. Park, W. Kim, W.-C. Bang, and Y.-K. Seong, "A deep learning framework for supporting the classification of breast lesions in ultrasound images," *Physics in Medicine & Biology*, vol. 62, no. 19, p. 7714, 2017.

[14] T. Xiao, L. Liu, K. Li, W. Qin, S. Yu, and Z. Li, "Comparison of transferred deep neural networks in ultrasonic breast masses discrimination," *BioMed research international*, vol. 2018, 2018.

[15] K. Simonyan and A. Zisserman, "Very deep convolutional networks for large-scale image recognition," *arXiv preprint arXiv:1409.1556*, 2014.

[16] C. Szegedy, V. Vanhoucke, S. Ioffe, J. Shlens, and Z. Wojna, "Rethinking the inception architecture for computer vision," in *IEEE Conference on Computer Vision and Pattern Recognition*, 2016, pp. 2818–2826.

[17] E. Phaisangittisagul, "An analysis of the regularization between l2 and dropout in single hidden layer neural network," in *7th International Conference on Intelligent Systems, Modelling and Simulation (ISMS)*, Jan 2016, pp. 174–179.

Integration of 3D Action Observation Therapy and Rehabilitation Exercises in Mixed Reality: A Feasibility Study on Post-Stroke Patients

S. E. Lenzi[1,2,*], P. Mosna[2,*], S. Lazzarini[3], M. Gobbo[4], M. Angelini[2], R. Buraschi[3],
S. Negrini[3,4], M. Fabbri Destro[1], P. Avanzini[1], G. Rizzolatti[1], N.F. Lopomo[2]

[1] Istituto di Neuroscienze, Consiglio Nazionale delle Ricerche, Parma, Italy
[2] Dipartimento di Ingegneria dell'Informazione, Università degli Studi di Brescia, Brescia, Italy
[3] Centro di Riabilitazione "E. Spalenza – Don Gnocchi", IRCCS Fondazione Don Carlo Gnocchi ONLUS, Rovato, Italy
[4] Dipartimento di Scienze Cliniche e Sperimentali, Università degli Studi di Brescia, Brescia, Italy
* equal contribution

Abstract— **Action Observation Treatment (AOT) represents a novel top-down rehabilitative approach, based on the exploitation of the mirror neuron system, which aims to restore motor function in patients with functional impairments, through an observation-execution matching. Actually, in a typical AOT session, the patient is first required to observe a video with a recorded action and then perform the same task. This method presents a great potential in magnifying the efficacy of standard rehabilitative therapies. The main goal of this paper was to report the design and development of an innovative rehabilitation system exploiting AOT through the integration of 3D immersive video display and the realization of rehabilitation exercises in a Mixed Reality (MR) environment; the system included, for each exercise, different levels of difficulty, that are all customizable to the patient's characteristics. The system was preliminary tested in a feasibility study focused on the rehabilitation of upper limb in post-stroke patients. Overall usability was assessed and several metrics bases on kinematic data acquired with wearable sensors were also explored, thus to monitor the advances and automatize the choice of the difficulty level through the rehabilitation session. First person 3D immersive display was highly tolerated by the subjects with no critical events registered; furthermore, MR approach demonstrated to be very suitable, safety and well-accepted by the patients, with a good level of engagement. These preliminary findings provided evidence about the feasibility of the proposed approach and the efficacy of the system in the clinical context.**

Keywords—**Rehabilitation, Action Observation Treatment, 3D Video, Mixed Reality, Motion Tracking, Post-Stroke Patients.**

I. INTRODUCTION

THERE is wide evidence in scientific literature that the observation of an action can produce in the observer an activation of specific regions of the brain, that underpins the planning of the execution of the same action, at cerebral level. At the basis of this phenomenon there is the Mirror Neurons System (MNS) [1]. In a human subject, the MNS is indeed dedicated to understand the aim of an action performed by someone else, by mapping a sensor information into the internal motor system. From these physiological evidences, scientists suggested the possibility to administer repeated observations of actions to ease the learning (or even re-learning) of specific motor skills. In this perspective, Action Observation Therapy (AOT) represents a novel top-down rehabilitation method that is based on this paradigm and was widely demonstrated to improve rehabilitation efficacy. In a standard AOT session, the patient is required to observe a specific object-directed task and, afterward, to execute what he observed. Literature reported that patients who underwent this therapy – considered as an additional treatment, complementary to the standard physical and rehabilitative medicine approaches - obtained quicker advancements and objective improvements of their impaired motor skills, when compared with the mere application of standard rehabilitation methods. In particular AOT reported promising results in both neurological patients [2] and non-neurological ones [3], including also the treatment of orthopaedic cases [4].

AOT should be correctly administered to maximize the resonance of the MNS. In this context, MNS response can be influenced by the modality in which the visual stimulus is presented; literature reported that MNS discharge is in fact dependent on specific visual features of the action stimuli. Monocular cues were demonstrated to be insufficient for the perception of a body, that deforms or whose spatial configuration changes in time. Therefore, stereopsis can be considered of the utmost importance for the correct interpretation of shapes and kinematics of moving segments during the observation of actions [5]. Thus, the use of 3D videos during the action-observation phase should be recommended, since they inherently epitomize the potential advantage of video-recorded stimuli (i.e. invariant reproducibility of the movements) with the "realness" of the visual experience.

In order to improve AOT efficacy, further challenges are related to the execution phase. In this stage the patients have in fact to repeatedly reproduce the action that they observed. Boredom should be avoided, and engagement should be encouraged, thus to maximize the rehabilitation effectiveness. In this perspective, several approaches have been proposed, so far. Virtual Reality (VR) resulted to be extremely promising, since it can integrate multisensory stimuli in a realistic environment, gives the possibility to adapt and enhance intensity of the task-oriented training, increases motivation (through, for instance, game-based solutions), and gives the possibility to monitor patients advancements [6].

However, VR presented also several drawbacks – even in healthy subjects - such as discomfort, isolation and dizziness. In the last years – thanks, above all, to the gaming consumer market - a novel approach entered into the "game", and it seems to be able to overcome the main VR-related issues: the Mixed Reality (MR). In the rehabilitation context, MR presents undoubted advantages ensured by pass-through cameras or "see-through" overlaying capability [7], such as: 1)

patients can see the real environment, thus isolation is avoided and interaction with the clinical staff is performed as usual; 2) patients can see also their own limbs, thus embodiment is "native" and the interfacing with the virtual objects can be maintained natural. Therefore, MR allows for natural gestures in an ecological environment in which the patient can train, following specific protocols.

Starting from these analyses, we hypothesized that combining a novel AOT approach, based on 3D immersive display, with a training phase performed in MR, could facilitate the whole rehabilitation process. Therefore, the main goal of this work was to report the design and feasibility study of an integrated system able to provide both 3D display and training execution in MR. Furthermore, the system combined also a wearable motion tracking system, able to provide information about several metrics, related to the patient's performance throughout the rehabilitation sessions. Without loss of generality, the system was decline for upper-limb analysis and tested on post-stroke patients.

II. MATERIALS AND METHODS

A. System Overview

The system was specifically designed to provide an integrated solution (hardware + software) to assists both physicians and patients during the rehabilitation phase. From the physician's perspective, the system was thought to support the planning of the rehabilitation session (i.e. type of exercise and level of difficulty) and track the metrics related to the patient's performance over time. From the patient's side, the system was designed to realize a threefold task: 1) providing immersive 3D action observation, 2) supporting the execution of training exercises in MR and 3) tracking the movements performed by the subject.

The used patient-side technologies were chosen to integrate several functions, including 3D display, MR interaction and tracking of the patient's movements.
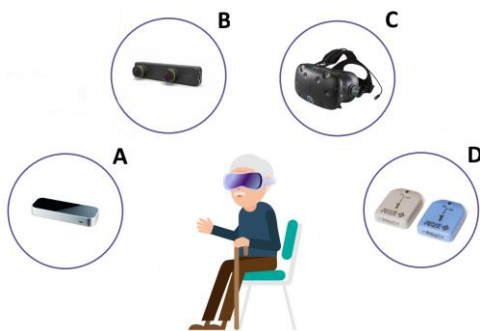

Figure 1. Patient-side technological components: A) Leap sensor (Leap Motion, USA), B) Zed Mini camera (Stereolabs Inc, USA), C) HTC Vive VR headset (HTC, Taiwan), D) Wavetrack (Cometa Systems, Italy).

For the feasibility study, as reported in figure 1, we integrated:

- Leap sensor (Leap Motion, USA) for tracking hands and fingers, used both to acquire the patient's movements and to ensure interaction with the virtual objects;
- Zed Mini camera (Stereolabs Inc, USA) as pass-through and overlaying function;
- HTC Vive VR headset (HTC, Taiwan) for 3D displaying both AOT videos and virtual objects;

- Wavetrack (Cometa Systems, Italy) for tracking patient's upper limb movements.

All these devices were synchronized via the implemented software framework.

Concerning high-level interfacing design, the user interfaces were thought to allow physician to interact with the integrated system by means of a common PC, thus to plan the details of the rehabilitation session, including the type of exercise, duration of the action observation, duration of the exercise and the level of difficulty. Several further information is required by the system in order to manage patient's data, considering also the type of pathology (e.g. name, surname, sex, date of birthday, impaired limb, etc) and the required training. The interface lets the user start the session and monitor both the action observation and the execution of the exercise through a video that shows the same view observed by the patient. During patient's activity, the user can track also the score realized by the patient (depending on the tasks) and further parameters are collected (such as execution time, rate of success, etc.).

Physician-side PC and patient-side PC communicate by using web-socket, a network protocol (Figure 2), which allows for a full duplex data and messaging channel, thus to maintain those PCs in separated zones and requiring only a physical or wireless network connection. This key architectural point allows for the separation between the user console and the rehabilitation platform. This design choice was due to the possibility of implementing the system also for telerehabilitation purposes.
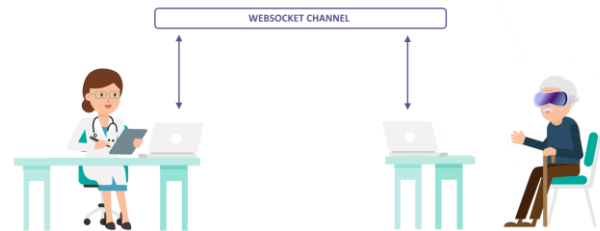

Figure 2. Schematic representation of the system components at high level. On the left side the physician is able to plan the rehabilitation session; on the right side the patient realizes 3D action observation and training in MR. In this specific setting PCs are connected via a network protocol (WebSocket channel).

The user interface was design also to allow for technical action, such as the configuration of the wearables (i.e. number of sensors, identifiers and their position) and their calibration. From the patient-side the interface is only visual (projected into the headset) and allow for the 3D video visualization and to perform rehabilitation exercises in MR, with projection of the virtual objects on the real environment. During the execution phase, patient's movements are acquired, and several events are also recorded, including for this specific application: object-created, grasp-begin, grasp-end, target-reached, contact and hover. More details about the specific tasks implemented in the feasibility study are hereinafter reported.

From the development point of view, the full suite was realized by using C# (user interface and script) and Unity 3D (visualization and interaction) and interfacing each technology by exploiting specific external libraries (e.g. Leap Motion

SDK and ZED SDK). The SW suite was designed specifically including 5 components (i.e. Management console, Unity code, Motion data acquisition, Event framework and Message framework), which allow for the management of the whole system.

B. Experimental Protocol

A first pilot study was conducted in order to assess system feasibility and usability. The study was specifically realized on sub-acute post-stroke patients (3-6 months after ischemic and haemorrhagic ictus) with partially limited motor function (upper limb Fugl-Meyer scale score between 20-60). All the involved patients signed specific informed consent. The study was approved by the Ethical Committee of the clinical center, where the experiments were performed (Prot. 09_13/02/19). The system was thence specifically designed to allow the rehabilitation of the upper limb.

The experimental session started with patient preparation and task explanation. In the preparation phase, 4 inertial sensors were placed on the subject's body (i.e. trunk, arm, forearm, hand) and a sensors-to-segment static calibration was performed; then the subject adopted a safety position on the chair following the instruction of the clinician; then, the head-mounted display was positioned on the patient's head (Figure 3). The preparation and explanation phase had a duration of about 20 minutes.
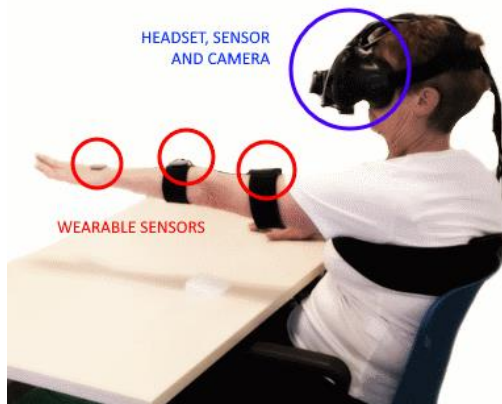

Figure 3. Example of the setup used in the experimental sessions.

Then the training session started. Each execution phase was preceded by the action observation phase. Both action observation and training phase lasted 2 minutes. Each task was executed once for each experimental session. The training phase had an overall duration of about 20 minutes. The overall duration of the experimental session was of about 36 minutes. The number of AOT session were set to 10. For this preliminary study, in agreement with the clinical staff, 4 different exercises were proposed: 1) reaching; 2) reaching and grasp; 3) goalkeeper; 4) occupational task. Accordingly, both the 3D AO videos and the tasks in MR were prepared.

C. 3D Action Observation

Stimuli for the AO phase were recorded using a 180° stereoscopic camera (LucidVR, Lucid Creative). The camera recorded videos with a record rate of up to 120 Mbps, and the resolution is 180°x180° of FoV (Field of View) with a 4k-30 fps/eye that records videos in FULL HD format with 1080 pixels per eye. Videos were recorded putting the camera on a tripod and regulating the camera height so that the lens was positioned right at the eye level of the subject performing the

action. An example of the obtained perspective is given in figure 4.

Figure 4. Example of acquired 3D action observation stimulus.

The video has been recorded in the same environment in which the task would be executed by the subjects in order to augment the sense of engagement and embodiment. Every recorded video shows the same movements required for the execution of the tasks. A video for each difficulty level (from 0 to 5) has been recorded. Two different subjects were recorded: a male (25 years old) and a female (27 years old). For each subject, two different videos were recorded for each limb side (right and left).

D. Rehabilitation in Mixed Reality

According to the identified exercises, the system was designed to allow for the realization of these specific tasks. In particular, the reaching task was realized by creating a virtual target in defined positions of the space in front of the patient (figure 5.A).
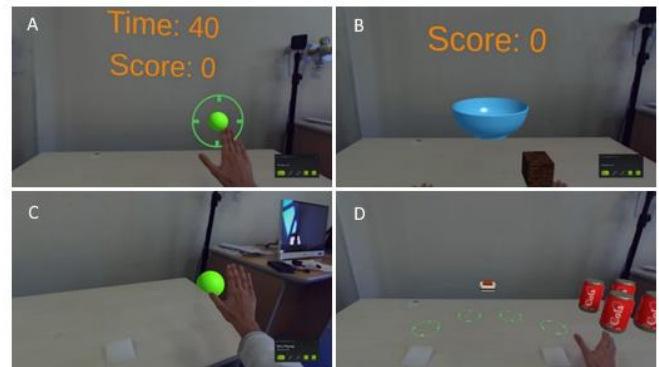

Figure 5. Tasks realized in Mixed Reality (MR): A) Reaching task; B) Reaching and Grasping; C) Goalkeeper; D) Occupational tasks.

The reaching and grasping task was designed by introducing a virtual object (e.g. a cube, a sphere, a dodecahedron) at the level of the table, which had to be grasped and put in a virtual bow, placed exactly in front of the patients (Figure 5.B). The goalkeeper required to stop with the hand a ball moving at different speeds towards the patients (Figure 5.C). The occupational exercise, in this case, required to move several cans from a starting position towards locations identified by visible targets, laying at the table level (Figure 5.D).

E. Data Analysis and Metrics

Both clinicians and patients were supposed to be enrolled in the usability assessment. For each identified task, open questions about critical events and execution difficulty were asked. Furthermore, the System Usability Scale (SUS) - a 10-questions Likert-like questionnaire - was adopted and submitted to the clinical staff; qualitative feedbacks from the patients were also collected. Further variables were then

chosen to complete the usability analysis, including: Completion Rate (CR), Error-free rate (EFR) and Time on Task (TT). Furthermore, several kinematic variables were chosen to analyse motion quality and the improvements obtained by subjects during the rehabilitation process. In particular, the following metrics were selected:

- Hand max reaching velocity (HMRV);
- % Cycle Hand Max Velocity (CHMV%);
- Mean Spectral Arc Length (SPARC) [8].
- Mean Reach Path Ratio (MRPR) [9];
- Tip Max Distance (TMD);
- Mean Interaction Time (MIT);
- Mean Resolution Time (MRT).

Joint angles kinematics were also estimated from wearable sensors.

III. RESULTS

For the feasibility study, two patients and one physiotherapist were involved. For the end user, the SUS score was 70, thus attested a good level of system usability. In general, the clinician reported a good opinion about the system (i.e. easy to use, effective, although it is reported the need for a technical support and few features could be improved). The user did not report any critical or non-critical error in tasks completion, nor general issues related to the realization of each step within the procedure. Few specific remarks were related technical issues (i.e. detection of hand-object interaction and object "shadowing"). One of the patients involved (Patient 1, 65 years old woman) participated to the usability analysis; she did not report any motion sickness problems and the tasks were all completed without any critical errors. No fatigue insurgence was reported, for during all the training sessions.

Examples of the metrics used in the assessment of patients' performance is reported in figure 6 and figure 7.
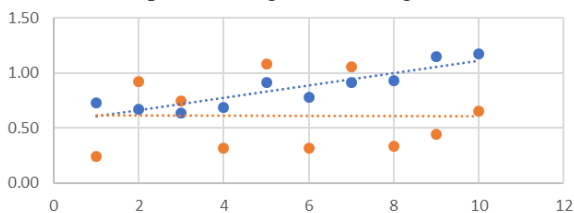

Figure 6. Hand max reaching velocity during the reaching tasks with respect to the session (from 1 to 10). Blue dots for patient 1; orange dots for patient 2.
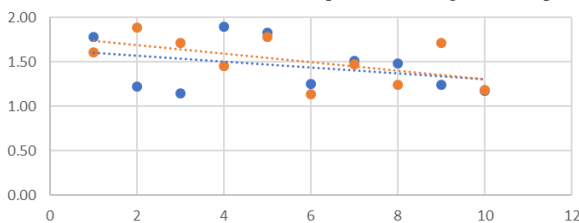

Figure 7. Mean reach path ration during the goalkeeper tasks with respect to the session (from 1 to 10). Blue dots for patient 1; orange dots for patient 2.

Patient 1 demonstrated an increasing performance in both the required tasks during the progress of the sessions. On the other hand, patient 2 (50 years old, male) reported an improvement in the goalkeeper as well, but a stable outcome in the reaching task.

IV. DISCUSSION

Preliminary results about the usability seem to suggest that the developed system was easy to use and effective in the realization of the rehabilitation sessions. Furthermore, questionnaires showed that the user tasks were well designed. This perspective is promising when considering the possibility of introducing this system within a clinical context. However, few technological issues were present (i.e. match between the position of the virtual hand and the real hand, shadowing of the objects, etc.). A clearer perspective of the overall system performance will be obtained by increasing the overall number of the involved users. From the patient's point of view, the system provided an optimal level of engagement, without critical issues. Furthermore, the system was able to monitor the advances reached by each patient during the training sessions, highlighting specific behaviour due to both the increasing performance and the level of pathology. The proposed parameters represent optimal metrics to be used, not only in tracking the progresses of the patients, but also to automatically adapt the level of difficulty of the exercises.

V. CONCLUSION

This work showed a promising methodology for motor rehabilitation, integrating 3D action observation and task execution in MR. Scientific literature supported this approach, underling the possibility of magnifying the efficacy of the standard rehabilitation treatment. Results obtained from this feasibility study were good, although some technical issues should be fixed and improved. Nevertheless, this work can be intended as a first step in the realization of an effective approach that can improve functional recovery.

REFERENCES

[1] G. Rizzolatti, "The mirror neuron system and its function in humans," Anat. Embryol. (Berl)., vol. 210, no. 5–6, pp. 419–421, 2005.
[2] A. Nuara, P. Avanzini, G. Rizzolatti, and M. Fabbri-Destro, "Efficacy of a home-based platform for child-to-child interaction on hand motor function in unilateral cerebral palsy," Dev. Med. Child Neurol., pp. 1–9, 2019.
[3] M. Bassolino, M. Campanella, M. Bove, T. Pozzo, and L. Fadiga, "Training the motor cortex by observing the actions of others during immobilization," Cereb. Cortex, vol. 24, no. 12, pp. 3268–3276, 2014.
[4] J. H. Villafañe, M. Isgrò, M. Borsatti, P. Berjano, C. Pirali, and S. Negrini, "Effects of action observation treatment in recovery after total knee replacement: A prospective clinical trial," Clin. Rehabil., vol. 31, no. 3, pp. 361–368, 2017.
[5] S. Ferri, K. Pauwels, G. Rizzolatti, and G. A. Orban, "Stereoscopically Observing Manipulative Actions," no. August, pp. 3591–3610, 2016.
[6] S. Ahn and S. Hwang, "Virtual rehabilitation of upper extremity function and independence for stoke: A meta-analysis," J. Exerc. Rehabil., vol. 15, no. 3, pp. 358–369, 2019.
[7] L. Chen, T. Day, W. Tang, and N. W. John, "Recent Developments and Future Challenges in Medical Mixed Reality," pp. 1–13, 2017.
[8] S. Balasubramanian, "On the analysis of movement smoothness," J. Neuroeng. Rehabil., pp. 1–11, 2015.
[9] S. L. Dejong, S. Y. Schaefer, and C. E. Lang, "Need for Speed : Better Movement Quality During Faster Task Performance After Stroke," 2012.

Predicting the Onset of Chronic Obstructive Pulmonary Disease in the English Longitudinal Study of Ageing

M. Vettoretti[1], A. Facchinetti[1], and B. Di Camillo[1]

[1] Department of Information Engineering, University of Padova, Padova, Italy

Abstract—Chronic obstructive pulmonary disease (COPD) is a chronic lung disease estimated to be responsible of about 5% of all deaths worldwide. The identification of subjects at risk of developing COPD is important to reduce its global burden, as early interventions on modifiable risk factors (e.g. smoking) can delay or even prevent the decline of lung function. A few models to predict risk of COPD onset in the general population were developed, which included a small set of risk factors. The aim of this work is to develop a new predictive model of COPD onset, testing the predictive ability of a variety of variables, including socio-economic and lifestyle factors, wellbeing status, respiratory symptoms, medical history, lung function measurements and blood test biomarkers. The model was developed by applying logistic regression to a training set (n=2897) extracted from the English Longitudinal Study of Ageing. Most important variables for COPD prediction were selected by least absolute shrinkage and selection operator regularization. The analysis showed that variables not considered by the literature models, such as physical activity, depression, marital status, self-reported health, fibrinogen, C-reactive protein and cholesterol can be important predictors of COPD onset. The derived model presented good discrimination and calibration performance on an independent test set (n=724), with area under the receiver-operating characteristic curve equal to 0.81 and expected-to-observed event ratio equal to 0.93. Future works include an external validation of the model, the use of different modelling techniques (e.g. survival models) and the application of variable ranking methods.

Keywords—COPD, predictive models, logistic regression, chronic lung disease, preventive medicine.

I. INTRODUCTION

CHRONIC obstructive pulmonary disease (COPD) is a category of chronic lung diseases characterized by persistent limitation in lung airflow, including chronic bronchitis and emphysema. Symptoms of COPD include dyspnea, chronic cough and excessive sputum or mucus production. Such symptoms can precede the development of airflow limitation by many years, although not all people with respiratory symptoms develop COPD. The onset of COPD is a gradual process and it usually occurs in over forty years old people. According to the Global Burden of Disease Study, 251 million people suffered from COPD in 2015, which was estimated to be responsible for 5% of all deaths worldwide [1]. Diagnosis of COPD requires a repeatable measure of lung function performed by spirometry. Specifically, COPD is diagnosed when both pre- and post-bronchodilator values of FEV1/FVC are below the lower limit of normality (LLN) [2].

The major risk factor for COPD is smoking. Other risk factors were found to be associated with COPD development, like asthma, family history of COPD, socio-economic status, respiratory symptoms, indoor and outdoor air pollution. Early interventions in people at risk of developing COPD, such as lifestyle changes, can slow the decline in lung function and post-pone or prevent the development of COPD [3].

Although many risk models to predict exacerbations in COPD patients exist, only few models were proposed for the prediction of COPD onset. A recent review identified four studies on prediction of COPD onset, of which only two were performed on the general population [4]. The study by Higgins et al. [5] used logistic regression to derive a risk index for COPD, including age, sex, smoking and lung function measurements, but the discrimination ability of such risk index was not assessed. The study by Kotz et al. [6] used sex-specific Cox proportional hazard models to predict COPD diagnosis in a large database collected from 239 Scottish general practices. Only four variables were considered as candidate predictors, i.e. age, smoking, level of deprivation and history of asthma, which were all included in the final model. The final model presented good discrimination ability on a 10-year prediction horizon with an area under the receiver-operating characteristic curve equal to 0.83 for males and 0.85 for females. Another study recently proposed a mixed-effect regression model to predict lung function decline in a cohort of American adults [7]. However, it is important to note, that the outcome of this study was airflow limitation defined as pre-bronchodilator FEV1/FVC value below LNN, which does not necessarily imply a COPD diagnosis.

To summarize, few models to predict future COPD onset were proposed and such models include only a small number of pre-selected variables. The aim of our work is to investigate the role in COPD prediction of a large set of variables, including lifestyle, wellbeing, and socio-economic factors, as well as information on medical history, measurements of lung function, and blood test biomarkers. For this purpose, a new predictive model of COPD onset, based on multiple logistic regression and least absolute shrinkage and selection operator (LASSO), was developed and validated using the data collected in the English Longitudinal Study of Ageing.

II. DATASET AND VARIABLES

A. The English Longitudinal Study of Ageing

The English Longitudinal Study of Ageing (ELSA) is an ongoing study of health, social, wellbeing and economic circumstances in the English population aged 50 and older, funded by the U.S. National Institute of Ageing and a consortium of UK Government departments [8]. The sample mostly included whites (about 98% of the sample).

Participants have a face-to-face interview every 2 years and a clinical examination every 4 years. Currently, the study includes 8 waves of data collection covering a period of 15 years (2002-2017). At waves 3-6, and 7, new participants entered the study to maintain the size of the sample.

B. Selection of subjects for this study

Since the clinical examinations were performed only in waves 2, 4, 6 and 8, we assigned to each subject a baseline wave among waves 2, 4 and 6 (not wave 8 because no follow-up would be available). Specifically, subjects that entered the study in wave 1 were assigned baseline wave 2 (n=9,432), subjects that entered in waves 3/4 were assigned baseline wave 4 (n=4,357), and subjects recruited in waves 5/6 were assigned baseline wave 6 (n=1,557).

We then selected the subjects who i) were free of COPD at the baseline wave, ii) had the clinical examination at the baseline wave, and iii) had information on COPD diagnosis in a period of 12 years after the baseline. COPD diagnosis was determined according to the subject's answer to the question Q1:"Has a doctor ever told you that you have chronic lung disease such as chronic bronchitis or emphysema?". Then, a binary variable to indicate incident COPD was created as follows. Subjects answering "yes" to Q1 at any time during the 12-year follow-up period were assigned class "1". Subjects answering "no" at all follow-up interviews, including the one occurring 12 years after the baseline, were assigned class "0".

The selected sample included 3,621 subjects of whom 451 developed COPD during the 12-year observation period after the baseline.

C. Selection of variables for this study

Potential predictive variables for COPD development were selected from the set of variables collected at the ELSA baseline visits. In total, 33 variables were selected which can be divided into 10 categories: demographics, socio-economic, lifestyle, physical measures, wellbeing, home environment, respiratory symptoms, medical history, lung function, blood test biomarkers. The entire variable list is reported in Table I.

In particular, economic deprivation was measured by question Q2:"How often you find you have too little money to spend on what you feel you and your household's needs are?", whose possible answers ("never", "rarely", "sometimes", "often", "most of the time") were coded with integers between 1 and 5. Variable "alcohol drinking" was built as an ordinal variable with 3 levels, i.e. no alcohol drinking, moderate and frequent. Frequent drinkers were defined as women drinking more than 7 standard drinks per week and men drinking more than 14 standard drinks per week, according to the guideline of the NIH National Institute on Alcohol Abuse and Alcoholism. Depression was measured by a reduced version of the Center for Epidemiologic Studies Depression Scale that includes 8 items. The derived score is an integer going from 1 to 8, with higher values representing a major presence of depression symptoms. Life expectation was coded as a number between 0 and 100, representing the self-reported probability of living to 75 if the respondent is under 65, to 80 if the respondent is aged 66 to 69, to 85 if the respondent is aged 70 to 74 etc. Self-reported health status was measured on a 5-level

scale ranging between excellent and poor. The house problem score was defined as the number of problems in the living accommodation reported by respondents. The possible problems were: shortage of space, noise from neighbours, noise from streets, not enough light, pollution, damp, water infiltration, condensation problem, problems with electrical wiring or plumbing, general rot and decay, insects mice or rats, too cold in winter. The variable "solid fuel at home" was defined as use of solid fuel, e.g. coal or wood, at home for heating, cooking or other purposes. Finally, regarding lung function, the variable ΔFEV1/FVC was defined as the difference between the subject's FEV1/FVC ratio and the LLN which was calculated for each subject using the equations proposed by the European Respiratory Society Global Lung Function Initiative [9], which allows to calculate personalized LNN values depending on subject's age, sex, height, ethnicity.

TABLE I
VARIABLES SELECTED FOR MODEL DEVELOPMENT

Category	Variable	Values
Demographics	Sex	0=females, 1=males
	Age	Continuous [years]
	Marital status	0=married, living as married 1=separated, widowed 2=never married
Socio-economic	Education	0=grade 11 or less 1=high school 2=bachelor degree 3=graduate school
	Economic deprivation	Integers, range 1-5
Lifestyle	Ever smoked	0 = no, 1 = yes
	Cigarettes/day	Integers, range 0+
	Alcohol drinking	0=never 1=moderate 2=frequent
	Frequency of moderate or vigorous physical activity	0 = hardly ever or never 1 = 1-3 times per month 2 = once/week 3 = >once/week
Physical measures	Body mass index	Continuous [kg/m^2]
	Heart rate	Continuous [beats/min]
Wellbeing	Depression score	Integers, range 1-8
	Life expectation	Integers, range 1-100
	Self-reported poor health	Integers, range 1-5
Home environment	House problem score	Integers, range 1-12
	Solid fuel at home	0 = no, 1 = yes
Respiratory symptoms	Severe chest pain	0 = no, 1 = yes
	Phlegm in the morning	0 = no, 1 = yes
	Shortness of breath when walking	0 = no, 1 = yes
	Attack of wheezing or whistling	0 = no, 1 = yes
	Wake up at night with shortness of breath	0 = no, 1 = yes
Medical history	Asthma	0 = no, 1 = yes
	Hypertension	0 = no, 1 = yes
	Diabetes	0 = no, 1 = yes
Lung function	FEV1	Continuous [L]
	ΔFEV1/FVC	Continuous [unitless]
	Peak flow	Continuous [L/min]

	Ferritin	Continuous [ng/mL]
	Hemoglobin	Continuous [g/dL]
Blood test biomarkers	*Fibrinogen*	Continuous [g/L]
	Triglycerides	Continuous [mg/dL]
	Total cholesterol	Continuous [mg/dL]
	C-reactive protein	Continuous [mg/L]

III. MODEL DEVELOPMENT AND VALIDATION

A. Model development

Selected data were randomly split into a training set, containing 80% of selected subjects, and a test set, containing the remaining 20% of subjects, stratifying by COPD incidence. The training set was used for model development, while the test set was used for final model assessment. Missing values in the candidate predictive variables were imputed by the k Nearest Neighbour algorithm (k=5), using only the training set data for imputation. All the variables were normalized to their maximum value in the training set. Then, a logistic regression model was fitted by maximum-likelihood to predict the 12-year incidence of COPD, using as variables all those selected in Section II.C (Table I). Logistic regression model is described by the following equation:

$$\log\left(\frac{p}{1-p}\right) = \beta_0 + \beta_1 x_1 + \cdots + \beta_n x_n \qquad (1)$$

where p is the probability of COPD diagnosis during follow-up, $x_1,..,x_n$ are the subject's variables, $\beta_1,… \beta_n$ the related coefficients and β_0 the intercept of the model. Significance of model coefficients is tested by the Wald test with 5% significance level.

In order to identify the most important predictive variables of COPD, remove from the model redundant terms and reduce risk of overfitting, the logistic regression model is also identified by applying the LASSO regularization in which model parameters are estimated penalizing large values of the model coefficients and the smaller in absolute value coefficients are set to zero. The regularization parameter λ is chosen by maximizing the discrimination ability of the model, measured by the area under the receiver-operating characteristic curve, in a bootstrap validation performed on the training set. Specifically, a grid of possible λ values going from 0.001 to 0.1 with step 0.001 was defined. Then, 100 sets were generated by bootstrap resampling on the training set. For each bootstrap set, the LASSO model was trained for all the values of λ, and its discrimination performance was assessed in the out-of-bag sample. The value of λ that maximises the average discrimination performance on the 100 out-of-bag samples was chosen as optimal value λ_{OPT}. Finally, the LASSO model with λ_{OPT} is trained on the entire training set.

B. Performance metrics

Performance of the full and the LASSO model were assessed on the test set in terms of discrimination and calibration. Discrimination is the ability of the model to correctly rank the subjects according to their risk of COPD onset. Discrimination was assessed by the receiver-operating characteristic (ROC) curve (sensitivity vs. 1-specificity) and the area under the ROC curve (AU-ROC). The AU-ROC varies between 0 and 1, with

0.5 corresponding to a random assignment of the scores, and 1 representing the perfect score.

Calibration represents the ability of the model to correctly predict the incidence of COPD during the follow-up period. Model calibration was graphically assessed by calibration plot (predicted vs. observed event probability). Calibration was also quantitatively assessed by the expected-to-observed event ratio (E/O), i.e. the ratio between the expected number of events and the number of observed events. Values of E/O close to 1 indicate that the model has good calibration, whereas values significantly higher/lower than 1 indicate that the model tends to over/underestimate the event probability.

95% confidence intervals for AU-ROC and E/O were built by computing the metrics on the 100 out-of-bag samples generated as described in Section III.A.

TABLE II
COEFFICIENTS OF THE FULL MODEL AND THE LASSO MODEL

Variable	Coefficient Full model	P-value	Coefficient LASSO model
Intercept	-0.1373	0.8466	-0.6545
Male sex	0.9863	<0.0001	0.6571
Age	-0.4486	0.2899	-
Education level	0.0279	0.8982	-
Marital status, class 1	0.3149	0.0469	0.1545
Marital status, class 2	0.3265	0.3151	-
Ever smoked	0.8414	<0.0001	0.7005
Cigarettes/day	0.8525	0.0378	0.8228
Alcohol drinking	-0.1353	0.6176	-
Body mass index	-1.0323	0.0609	-0.5069
Heart rate	0.2799	0.6743	-
Depression score	0.1215	0.6738	0.0509
Life expectation	-0.2197	0.4324	-0.0824
Self-rep. poor health	1.1050	0.0003	1.0035
House problem score	0.1890	0.7728	-
Solid fuel at home	0.0170	0.9432	-
Economic deprivation	0.3530	0.1550	0.2795
Physical activity	-0.7042	0.0002	-0.5691
Chest pain	-0.1147	0.6021	-
Phlegm in the morning	0.2297	0.1550	0.1953
Short breath walking	0.5326	0.0007	0.4282
Attack of wheezing	0.6861	<0.0001	0.6629
Short breath night	-0.0813	0.7360	-
Asthma	0.3702	0.0431	0.2563
Hypertension	-0.2720	0.0642	-0.0989
Diabetes	-0.0191	0.9421	-
FEV1	-3.4609	<0.0001	-2.6997
ΔFEV1/FVC	-2.3179	<0.0001	-2.2822
Peak flow	-2.3752	0.0008	-1.7541
Ferratin	0.0796	0.9341	-
Hemoglobin	0.2264	0.7253	-
Fibrinogen	2.286	0.0043	2.1004
Triglycerides	-1.2223	0.3783	-
Total cholesterol	-0.9432	0.1307	-0.4862
C-reactive protein	1.3959	0.2480	1.0411

IV. RESULTS

The training set and the test set included 2897 and 724

subjects, respectively, of whom 361 developed COPD in the training set, 90 developed COPD in the test set.

In Table II, the coefficients estimated for the full model and the corresponding p-values are reported. Variables that resulted to significantly increase risk of COPD (5% significance level) were: male sex, being separated, divorced or widowed, smoking, number of cigarettes per day, a low self-reported health status, shortness of breath when walking, attacks of wheezing, previous asthma and high levels of fibrinogen, a biomarker found to be strongly associated with COPD [10]. Factors associated with a decrease of COPD risk were: physical activity and high values of FEV1, ΔFEV1/FVC and peak flow. The final LASSO model (Table II) included, in addition to these variables, body mass index, life expectation, hypertension and total cholesterol, which were negatively associated with COPD onset, and depression score, economic deprivation, morning phlegm and C-reactive protein, which were positively associated with COPD onset.

As visible in Table III, both on the training set (bootstrap validation) and on the test set the full model and the LASSO model perform well in terms of discrimination (AU-ROC>0.80) and calibration (E/O very close to 1). The ROC curve and the calibration plot obtained on the test set are reported in Fig. 1. This representation evidences slightly better performance of the LASSO model in terms of discrimination and a better calibration of the full model for the highest decile of predicted risks (largest data point in the calibration point).

TABLE III
PERFORMANCE OF THE IDENTIFIED MODELS

Model	Bootstrap validation on the training set		Test set	
	AU-ROC	E/O	AU-ROC	E/O
Full	0.83 [0.80-0.86]	1.01 [0.89-1.15]	0.81	0.92
LASSO	0.83 [0.80-0.86]	1.00 [0.89-1.14]	0.81	0.93

V. CONCLUSION

We developed a new model for COPD onset prediction, investigating the predictive ability of a variety of variables. Our analysis showed that variables related to lifestyle, wellbeing, socio-economic factors and blood test biomarkers, which were not considered by literature COPD models, can in fact have an important role in COPD risk prediction. The developed model was validated on an independent test set and presented good discrimination and calibration performance. Future works include an external validation of the developed model, the use of different modelling techniques (e.g. survival models) and the application of methods to rank the variables according to their predictive ability.
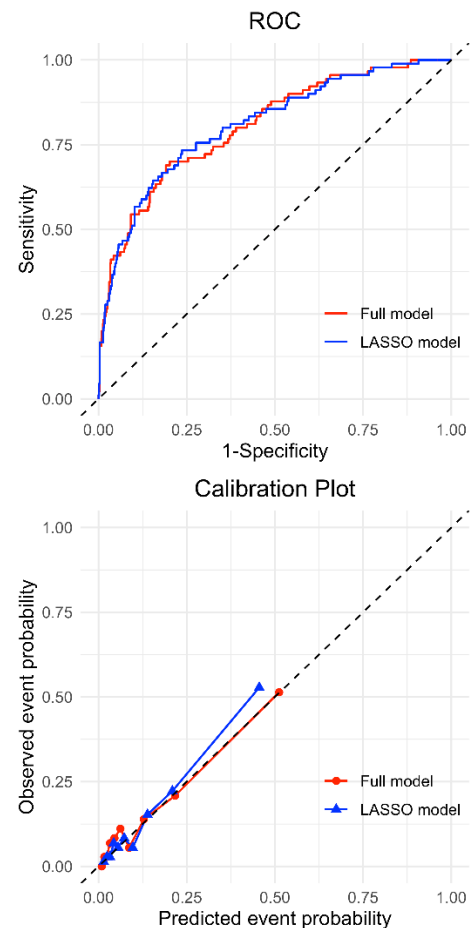
ACKNOWLEDGEMENT

Fig. 1: Top panel: ROC curve on the test set for the full model (red) and the LASSO model (blue). Bottom panel: Calibration plot on the test set for the full model (red) and the LASSO model (blue).

REFERENCES

[1] GBD 2015 Chronic Respiratory Disease Collaborators, "Global, regional, and national deaths, prevalence, disability-adjusted life years, and years lived with disability for chronic obstructive pulmonary disease and asthma, 1990-2015: a systematic analysis for the Global Burden of Disease Study 2015", *Lancet Respir Med*, vol. 5, pp. 691-706, Sep 2017.
[2] Global Initiative for Chronic Obstructive Lung Disease, "Global Strategy for the Diagnosis, Management and Prevention of Chronic Obstructive Pulmonary Disease", 2020 [Online]. Available: https://goldcopd.org/wp-content/uploads/2019/12/GOLD-2020-FINAL-ver1.2-03Dec19_WMV.pdf [accessed on Feb 3rd 2020].
[3] S.I. Rennard, M.B. Drummond, "Early chronic obstructive pulmonary disease: definition, assessment, and prevention", *Lancet*, vol. 385, pp. 1778-1788, May 2015.
[4] M. C. Matheson, "Prediction models for the development of COPD: a systematic review" *Int J Chron Obstruct Pulmon Dis,* vol. 13, pp. 1927-1935, Jun 2018.
[5] M.W. Higgins et al., "An index of risk for obstructive airways disease", *Am Rev Respir Dis*, vol. 125, pp. 144-151, 1982.
[6] D. Kotz, C.R. Simpson, W. Viechtbauer, O.C.P. van Schayck, A. Sheikh, "Development and validation of a model to predict 10-year risk of general-practitioner-recorded COPD", *NPJ Prim Care Respir Med*, vol. 24, pp. 14011, May 2014.
[7] W. Chen et al., "An individualized prediction model for long-term lung function trajectory and risk of COPD in the general population", *Chest*, pii: S0012-3692(19)33868-1, Sep 2019 [Epub ahead of print].
[8] A. Steptoe, E. Breeze, J. Banks, J. Nazroo, "Cohort profile: the English longitudinal study of ageing", *Int J Epidemiol* vol. 42, pp. 1640-1648, 2013.
[9] P.H. Quanjer et al., "Multi-ethnic reference values for spirometry for the 3-95-yr age range: the global lung function 2012 equations", Eur Respir J, vol. 40, pp. 1324-43, Dec 2012.
[10] A. Duvoix et al., "Blood fibrinogen as a biomarker of chronic obstructive pulmonary disease", Thorax, vol. 68, pp.670-676, Jul 2013.

Thrombogenicity of cardiovascular devices: mutual and relative effect of biomaterial and shear stress

S. Bozzi[1], F. Vercellino[1], Filippo Consolo[2], Yana Roka Moiia[3], Tatiana Mercarini[1], Marvin Slepian[3] and A. Redaelli[1]

[1] Department of Electronics, Information and Bioengineering, Politecnico di Milano, Milan, Italy
[2] Coagulation Service and Thrombosis Research Unit, San Raffaele Scientific Institute, Milan, Italy
[3] Department of Medicine and Biomedical Engineering, College of Medicine, University of Arizona, Tucson, Arizona, USA

Abstract—**Supra-physiologic levels of shear stress and blood contact with artificial material are considered the main causes of the thrombogenicity of cardiovascular devices, such as prosthetic heart valves and ventricular assist devices. To investigate the mutual and relative role of these factors in platelet activation a set of experiments was performed consisting in the evaluation of platelet activation in samples of isolated platelets exposed to different levels of shear stress and different materials. The results showed that 1) platelet activation by mechanical stimuli exhibits a dose-time-response, which depends on the material in contact with the platelets, 2) biomaterials have a different thrombogenic potential, being polyethylene the least thrombogenic among the ones investigated and 3) the contact with an artificial material and the mechanical stimulation have approximately the same effect on platelet activation.**

Keywords—**Cardiovascular devices, platelet activation, shear stress, biomaterial**

I. Introduction

Thrombosis is a potentially fatal complication for patients with cardiovascular devices such as prosthetic heart valves and ventricular assist devices [1-2]. Thromboembolic events are known to be due mainly to the combination of two factors, concurring in platelet activation and subsequent thrombus formation: the supra-physiologic levels of shear stress and the interaction between platelets and the surface of the implanted material . A number of studies have investigated the effect of the mechanical stimulus and of the contact with artificial materials on platelet activation [3-7]. However, the mutual and relative role of these factors is currently unclear. The present work presents a preliminary study to provide new insights into the relative role of shear stress and biomaterial interaction in platelet activation.

II. Methods

Blood was drawn from healthy adult volunteers into acid-citrate dextrose (ACD-A) and centrifuged to obtain platelet-rich plasma (PRP). PRP was gel-filtrated through chromatography columns to obtain gel-filtered platelets. After gel-filtration, the GFP sample was diluted with Hepes Tyroides buffer up to a concentration of 20.000 plts/μl.

Platelets were exposed to three different shear stress levels (500, 750 and 1000 dyne/cm^2) for different durations (10, 20 and 30 minutes). The stimulation was performed through a forth and back movement imposed with a syringe pump (Hamilton PSD/8 Precision Syringe Pump) within tubings of different materials (Fig. 1).

Five materials have been studied: Ethylene tetrafluoroethylene (ETFE), Polyethylene (PE), Polyether ether ketone (PEEK), Polytetrafluoroethylene (PTFE) and coated glass (with Sigmacote siliconizing reagent). Glass was also investigated as a positive control. For each combination of shear stress, exposure time and materials five experiments were performed (N = 5, n = 10). After stimulation, the platelet activation was evaluated using the Platelet Activation State (PAS) assay, which is a specific assay for the evaluation of shear-mediated platelet activation [8]. The PAS was also evaluated before the experiments ("no stim", negative control) and after pump filling ("0 min") to evaluate the effect of the filling operation on platelet activation.
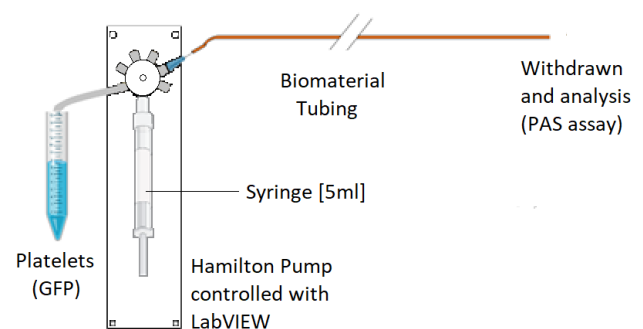

Fig. 1: Schematic representation of the experimental setup for platelet stimulation at different levels of shear stress and in contact with different artificial materials.

The PAS assay consists in incubating GFP samples with 200 nM acetylated prothrombin (Ac-FIIa) and 100 pM factor Xa for 10 minutes at 37°C. Due to acetylation, the generated thrombin is inactive on fibrinogen and has no positive feedback on platelets, resulting in a linear correlation between the thrombin production rate and the actual level of platelet activation. PAS values obtained by the assay are normalized against the activity of fully activated platelets and therefore expressed as a fraction of the maximum thrombin-generating capacity.

Normal distribution of data was tested with Shapiro-Wilk normality test. In intra-biomaterials comparisons, the Brown-Forsythe and Welch analysis of variance (ANOVA) test was used for normally distributed data. Conversely, non-parametric Kruskal-Wallis one-way ANOVA test was performed. In inter-biomaterials, data were analyzed by the two-way ANOVA test.

III. RESULTS AND DISCUSSION

A. Time effect

Fig. 3 shows the effect of the stimulation duration on platelet activation in different biomaterials and for different shear stresses. It is evident that for all the materials the platelet activation state increases with time, even if differences did not reach statistical significance. It can also be noticed that for a given material the increment of platelet activation over time increases with increasing mechanical stimulation. These results are confirmed by a number of studies, showing that platelet respond to mechanical stimuli with a consistent dose and time response [9-10].
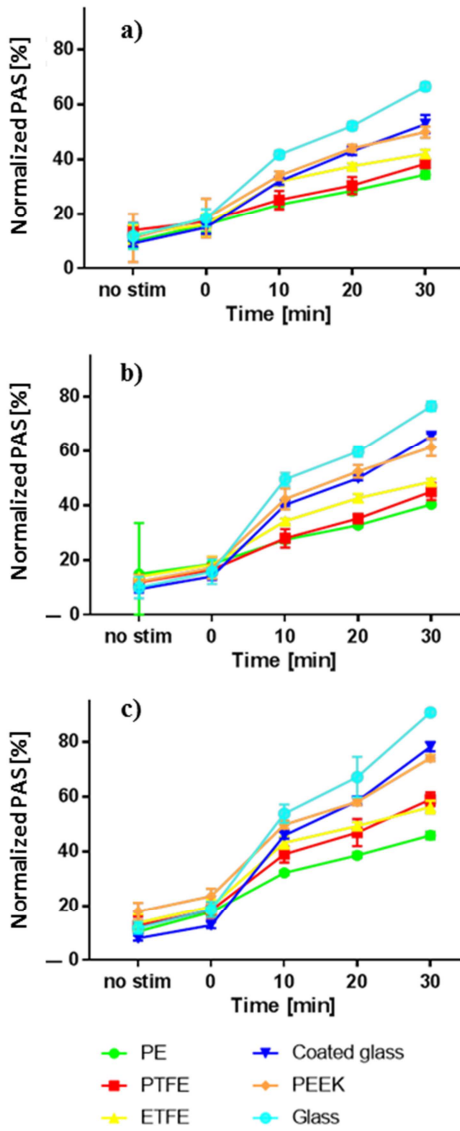
Fig. 3: Platelet activation state (PAS) as function of stimulation time for different biomaterials and different shear stresses: a) 500 dyne/cm^2, b) 750 dyne/cm^2 and c) 1000 dyne/cm^2.

B. Shear stress effect

The effect of shear stress on platelet activation was investigated separately for each biomaterial. Fig 4 shows the PAS as a function of shear stress and stimulation time in all the studied materials.
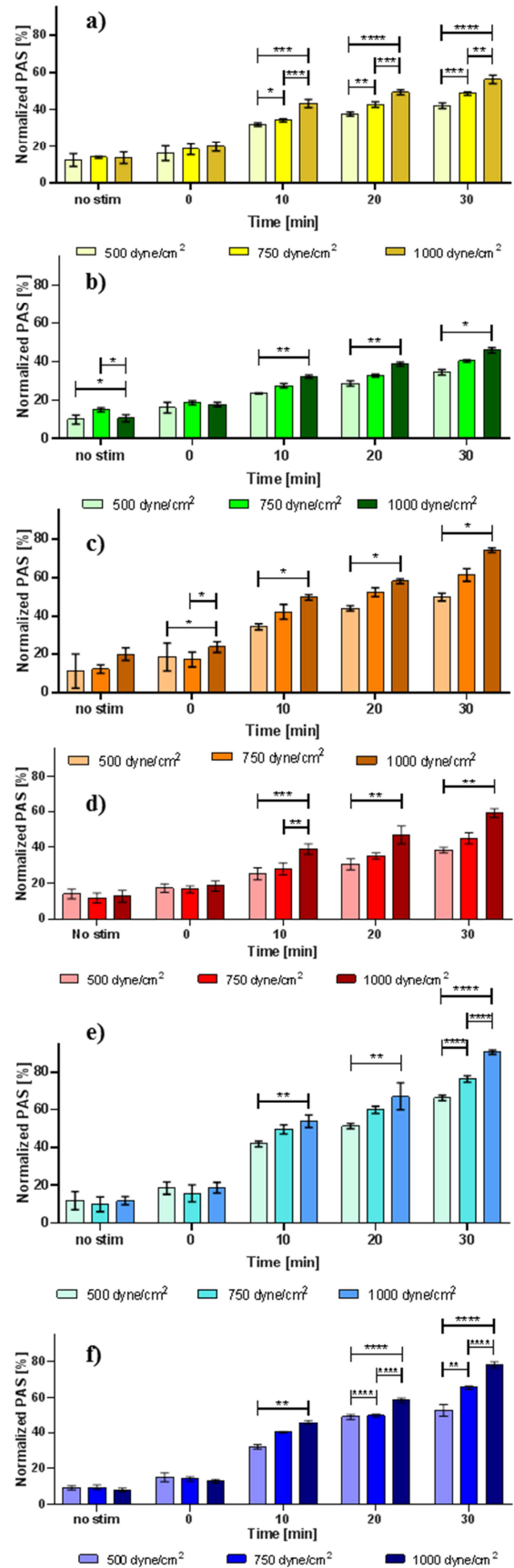
Fig. 4: Platelet activation state (PAS) as function of shear stress at different stimulation times, for each biomaterial: a), ETFE, b) PE, c) PEEK, d) PTFE, e) Coated glass and f) glass.

Results show that PAS increases with increasing mechanical stimuli as already observed in many works [10-12]. Analyzing separately each material in more details, four different trends can be recognized: blood in contact with ETFE is strongly affected by the shear stress level, with significant differences in platelet activation between all the studied stimulation intensities (500, 750 and 1000 dyne/cm^2). In presence of PE and PEEK, the effect of the mechanical stimulus is lower and significant changes in PAS can only be observed between 500 and 1000 dyne/cm^2. In PTFE tubings the shear stress level induces significant differences in platelet activation mostly at the beginning of the stimulation (i.e. at 10 minutes). Finally, when blood is in contact with coated glass or glass the platelet activation state is affected by the intensity of the mechanical stimulus only after a given period of time (20 minutes for coated glass and 30 minutes for glass).

C. Biomaterial effect

The effect of the contact with an artificial material is shown in Fig 5. When compared at a given shear stress and exposure time, the materials presented statistical differences in almost all the cases. This allows a classification in terms of thrombogenic potential. Glass resulted to be the most thrombogenic material while PE was responsible of the lowest platelet activation. PEEK and coated glass showed almost the same behavior and were the most thrombogenic after glass. The ranking of PTFE and ETFE varied depending on the exposure time and shear stress level, but in most of the cases PTFE was less thrombogenic than ETFE. Considering all the experiments, the following ranking of the materials can be made (from the least to the most thrombogenic): PE, PTFE, ETFE, PEEK, coated glass and finally glass.

D. Combined effect of shear stress and biomaterial

The relative and mutual effect of shear stress and material contact was evaluated considering only biomaterial used in the cardiovascular filed (i.e. excluding coated glass and glass). The results showed that the interaction between the two variables has a negligible contribution, accounting for less than 4% of the total variance (Table 1). The contribution of shear stress ranged between 36% and 43% while the contribution of the biomaterial surface contact varied from 48% to 59%, depending on the duration of the stimulation. The effect of the material was always higher but the differences were not significant, so it can be concluded that mechanical stress and artificial material contact have the same effect on platelet activation.

TABLE I

Time	Interaction	Material	Shear Stress
10 min	3.1%	48%	42%
20 min	2.0%	59%	36%
30 min	3.9%	50%	43%

Percentage of total variance explained by shear stress, material contact and their interaction (two-way ANOVA test)
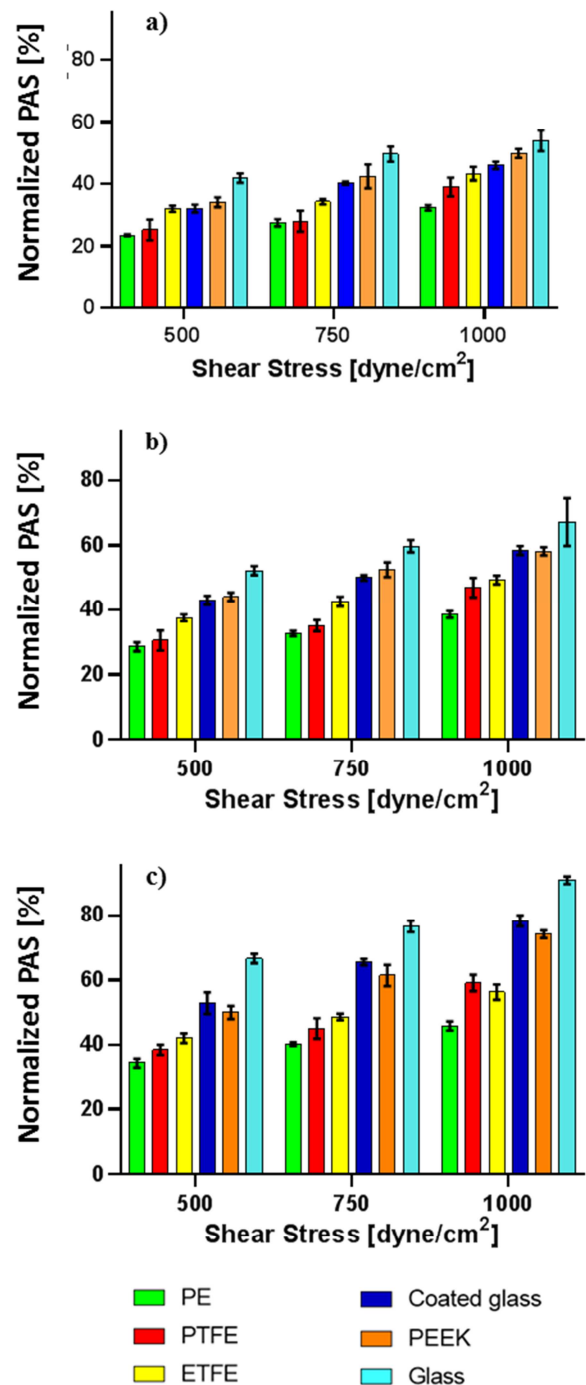

Fig. 5: Platelet activation state (PAS) as function of shear stress for each biomaterial, at different stimulation times: a) 10 minutes, b) 20 minutes and c) 30 minutes.

IV. CONCLUSIONS

In this work we presented the results of a set of experiments aimed at investigating the effect of shear stress and biomaterial interaction in platelet activation. The main goal was to provide deeper insights into the relative and mutual role of the two main causes of thrombotic complications in cardiovascular devices.

The results of the study have demonstrated that: (1) platelet activation increases with the exposure time to a mechanical

stimulus and the amplitude of the increase depends on the shear stress level, being higher for higher shear stress values, (2) the intensity of the mechanical stimulation has a strong effect on platelet activation, (3) biomaterials have a different thrombogenic potential: PE is the least thrombogenic followed by PTFE, ETFE, PEEK, (4) the contact with an artificial material and the mechanical stimulus have approximately the same effect on platelet activation, independently on the exposure time to the mechanical stimulation.

Further studies will investigate the effect of a preliminary exposure to an artificial material followed by a mechanical stimulation and, conversely, the effect of a mechanical stimulus followed by the contact with a biomaterial surface.

REFERENCES

[1]   E. Wilkins, *European Cardiovascular Disease Statistics*. Network, Brussels, 2017.

[2]   E.G. Butchart, A. Ionescu, N. Payne, J. Giddings, G.L. Grunkemeier and A.G. Fraser, "A new scoring system to determine thromboembolic risk after heart valve replacement", *Circulation* vol. 108, pp. 68–74, 2003.

[3]   V. Tarzia, E. Buratto, G. Bortolussi, M. Gallo, J. Bejko, R. Bianco et al., "Hemorrhage and thrombosis with different LVAD technologies: a matter of flow?", *Ann Cardiothorac Surg*, vol. 3, pp. 582-584, 2014.

[4]   W. Yin, Y. Alemu, K. Affeld, J. Jesty and D. Bluestein, "Flow-induced platelet activation in bileaflet and monoleaflet mechanical heart valves", *Ann Biomed Eng*, vol. 32, pp. 1058–1066, 2004.

[5]   C. H. Gemmell, "Flow cytometric evaluation of material-induced platelet and complement activation", *J. Biomater. Sci. Polym.*, vol. 11, pp. 1197–1210, 2000.

[6]   G. Girdhar and D. Bluestein, "Biological effects of dynamic shear stress in cardiovascular pathologies and devices". *Expert Rev Med Devices*, vol. 5, pp. 167–181, 2008.

[7]   A. Ask, D. Holt and L. Smith, "In vivo comparison study of FDA-approved surface-modifying additives and poly-2methoxyethylacrylate circuit surfaces coatings during cardiopulmonary bypass" *J. Extra Corpor. Technol.*, vol. 38, pp. 27–32, 2006.

[8]   J. Jesty and D. Bluestein, "Acetylated prothrombin as a substrate in the measurement of the procoagulant activity of platelets: elimination of the feedback activation of platelets by thrombin", *Anal Biochem*, vol. 272, pp. 64–70, 1999.

[9]   J. Sheriff, P. Tran, M. Hutchinson, T. DeCook, M.J. Slepian et al., "Repetitive hypershear activates and sensitizes platelets in a dose-dependent manner", *Artif Organs*, vol. 40, pp. 586–95, 2016.

[10] F. Consolo, J. Sheriff, S. Gorla, N. Magri, D. Bluestein, F. Pappalardo, M.J. Slepian, G.B. Fiore, A. Redaelli, "High frequency components of hemodynamic shear stress profiles are a major determinant of shear-mediated platelet activation in therapeutic blood recirculating devices", *Sci Rep*, vol. 7, 2017.

[11] M.J. Slepian, J. Sheriff, M. Hutchinson, P. Tran, N. Bajaj, J.G. Garcia, S. Scott Saavedra and D. Bluestein, "Shear-mediated platelet activation in the free flow: perspectives on the emerging spectrum of cell mechanobiological mechanisms mediating cardiovascular implant thrombosis", *J Biomech*, vol. 50, pp. 20-25, 2017.

[12] F. Consolo, L. Valerio, S. Brizzola, P. Rota, G. Marazzato, V. Vincoli, S. Reggiani, A. Redaelli and G. Fiore, "On the Use of the Platelet Activity State Assay for the In Vitro Quantification of Platelet activation in blood recirculating devices for extracorporeal Circulation", *Artif. Organs*, vol. 40, pp. 971–980, 2016.

Gellan gum-based hydrogels as injectable materials for cartilage tissue engineering

L. Riacci[1], L. Vannozzi[1,2], L. Garcia-Hevia[1,2] and L. Ricotti[1,2]

[1] The BioRobotics Institute, Scuola Superiore Sant'Anna, Piazza Martiri della Libertà 33, 56127, Pisa, Italy
[2] Department of Excellence in Robotics & AI, Scuola Superiore Sant'Anna, Piazza Martiri della Libertà 33, 56127, Pisa, Italy.

Abstract— Recently, new tissue engineering approaches are being developed as an alternative to traditional treatments for cartilage repair. Materials in the form of hydrogels are particularly attractive as owing to their biocompatibility, degradability, and ability to homogeneously mix with stem cells and bioactive molecules. Hydrogels can be injectable, thus to easily fill defects with different shapes, thus repairing the articular cartilage in a minimally invasive way.

This manuscript reports the analysis of gellan gum-based hydrogels as injectable materials for the *in situ* delivery of chondrocytes for the treatment of cartilage defects. Gellan gum and methacrylated gellan gum were prepared and analyzed through rheometry, to assess their suitability for being injected with chondrocytes. Then, one selected formulation was further characterized in terms of mechanical properties, analyzing the influence of light exposure. Finally, preliminary biological tests with chondrocytes were performed to analyze the interaction with the material.

Keywords—gellan gum, chondrocytes, cartilage tissue engineering, photocrosslinking.

I. INTRODUCTION

Cartilage is a specialized form of connective tissue, which is formed by an extracellular matrix (ECM) composition allowing the tissue to bear mechanical stresses without permanent distortion. Its role is crucial for body movements, as well as for the protection of bones at joints. It can be found in hip, elbow, shoulder and knee joints, where it is also named as articular cartilage (AC). It provides a low-friction gliding surface for articulation, supporting shock-absorption, wear-resistance, and lubrication [1]. AC is an anisotropic tissue with a total thickness in the range 2-4 mm, organized into four different zones, which vary in terms of density, ECM composition and activity of chondrocytes. The chondrocytes are the active biological component and the critical player that maintains the ECM balance within the cartilage. Chondrocytes can sense and respond to the different mechanical stimuli, contributing to the biomechanics of cartilage [2].

The cartilage has a minimal ability to heal itself because it lacks a vascular network. Furthermore, the chondrocytes' low proliferation and migration rate also make the complete regeneration of a defect challenging to accomplish. Hence, traumatic joint injuries, abnormal joint loading, and degenerative joint diseases can all cause severe defects in AC tissue. Regardless of the cause, cartilage injuries can be divided into two groups: chondral defects and osteochondral ones [3]. Chondral defects only affect the AC layer and do not extend to the underlying subchondral bone. Differently, osteochondral lesions affect both cartilage and the subchondral bone. In the last case, both blood cells and mesenchymal progenitor cells may promote the regeneration process, but usually, weaker fibrous cartilage is formed [4]. In general, the cartilage repair process may depend on the defect depth and size [5]. Other essential factors are the age and the intensity of the trauma.

The treatment of cartilage defects divides into non-surgical and in surgical approaches [6]. Non-surgical one are applied to mild to moderate cases. They are based on non-pharmacological therapy (*e.g.* physical therapy and weight loss), pharmacological therapy (*e.g.* analgesics and opioids) and intra-articular injections of viscosupplements (*e.g.* hyaluronic acid) or platelet-rich plasma (PRP). Such treatments can temporarily relieve the pain but they are not able to reverse the cartilage damage [7]. On the other hand, surgical approaches are indicated for moderate to severe cases. Surgical treatments can also be divided into cell-based and non-cell reconstructive therapies [8]. Non-cell reconstructive therapies involve arthroscopic chondroplasty, microfracture, mosaicplasty/osteochondral grafts and, as the ultimate option, knee replacement. Instead, cell-based therapies involve the injection of stem cells or the autologous chondrocyte implantation (ACI) procedure. The current therapies are quite effective in reducing the pain and replacing the AC function up to a certain degree [9]. However, practical solutions for the regeneration of this tissue have not been found, yet.

The aim of cartilage tissue engineering (CTE) is to regenerate functional tissue using cells and scaffolds to replace the defected cartilage. To this aim, features such as biocompatibility, permeability to nutrients and surface properties allowing the integration with the surrounding tissue are critical requirements for the scaffold design [1]. Biomaterials used in CTE can be classified into natural or synthetic ones or decellularized matrices. Natural polymers have inherent features that endow them with several advantages over synthetic polymers such as: bioactivity, a composition similar to the tissue they are replacing and susceptibility to cell-triggered proteolytic degradation. They can be further classified into protein-based materials, such as collagen, gelatin and fibrin, and carbohydrate-based materials, such as gellan gum, alginate, hyaluronic acid, and chitosan [10]. However, natural polymers possess disadvantages such as: low mechanical properties, the difficulty of processing and possible immunogenc problems [11]. On the other hand, synthetic polymers are easier to synthesize, they can be tailorable from a chemical and mechanical viewpoint, and normally have a lower cost. Many synthetic biopolymers are used for CTE, such as poly (glycolic acid), poly (lactic acid), biodegradable polyurethanes, and poly (ethylene glycol) [12].

However, the main drawbacks involve the low cell adhesiveness, proliferation and differentiation, thus the need to be treated for positively interacting with the cells and the surrounding tissue. Decellularized ECM is another route to be pursued for substituting the cartilage. It is grounded on the removal of cellular components by physical stress and/or chemical or enzymatic agents. These processes preserve the natural bioactive cues that are naturally present in the ECM (*e.g.* composition, anatomical architecture and mechanical integrity) [13]. However, the decellularization of the ECM is still challenging and needs a source of tissue to be used, which can raise immunogenic issues.

As mentioned, a scaffold made from a natural materials is normally affected by low mechanical properties. The improvement of mechanical properties by increasing the crosslinking density (*e.g.* by chemical crosslinking with photoinitiators) must trade with the viability of the cells within the scaffold. Among the natural materials, gellan gum (GG) represents an attractive candidate to be explored within the CTE field [14]. GG is a linear, anionic and high molecular weight polysaccharide (about 500 kDa). It is water-soluble and exhibits a temperature-dependent behavior (sol/gel in the temperature range of 35-40 °C). GG has a structure similar to the glycosaminoglycans of the native cartilage (*e.g.* choindroitin sulphate and hyaluronian), since both have glucuronic acid in their repetitive unit. On the other hand, GG has various limitations (*e.g.* mechanical weakness, poor stability in physiological fluids), which can be improved by reacting with methacrylic anhydride (MA) to make the material photoresponsive (methacrylated gellan gum, GGMA), thus favoring a chemical crosslinking.

In this paper, we report the analysis of GG-based hydrogels as injectable materials for the *in situ* delivery of chondrocytes for the reconstruction of AC defects.

II. MATERIALS AND METHODS

A. Preparation of Gellan Gum

Gellan Gum (GG, Gelzan, Sigma Aldrich) was dissolved at a concentration of 1 and 2 % wt. in deionized water (d-H_2O) while stirring for 30 min at 80 °C. Then, the solutions were filtered using a filter with a nominal diameter of 0.20 µm.

B. Gellan Gum methacrylation

The methacrylation of GG was carried out by following the procedure reported in [15]. Briefly, GG was dissolved (1% wt. in d-H_2O) with a magnetic stirrer at 75 ° C for 1 h. The solution was then cooled to 60 °C and 8.5 mL of MA per 100 mL of solution were slowly added. The solution reacted for 6 h at a controlled pH range (8 - 9.5). Then, the solution was centrifuged (3500 rpm for 3 min) at 30 °C to remove the unreacted MA, and the supernatant diluted (1:2) with d-H_2O preheated at 40 °C. The solution was dialyzed (membrane cut-off: 12-14 kDa) at 60 °C for 5 days. Once dialysis was complete, the solution was quickly frozen in liquid nitrogen and stored at -80 °C. Finally, aliquots were lyophilized for 3 days to obtain the gellan gum metahcrylated (GGMA) powder.

C. Preparation of Methacrylated Gellan Gum

GGMA was dissolved at a concentration of 1 and 2 % wt. in d-H_2O, in a bath at 37 ° C for about 1 h, then filtered using a filter with a nominal diameter of 0.20 µm.

For the formation of a crosslinked hydrogel (Fig. 1), the lithium phenyl-2,4,6-trimethylbenzoylphosphinate (LAP) photoinitiator was added to the solution at a concentration of 0.05% wt. Hydrogels were prepared by adding 200 µL of the solution within a polydimethylsiloxane (PDMS) mold in a cylindrical cavity (diameter: 10 mm, height: 2 mm). The solution was photocrosslinked with UV light (wavelength: 365 nm, nominal power: 200 W) at an intensity of 5 mW/cm^2 for 30 s. Once formed, the hydrogel underwent to LED and halogen visible light for 15 min, at an intensity of 19,000 lux (this accounted for the additional exposure that the hydrogels would receive in the surgical scenario, due to the arhtorscopic tool light).
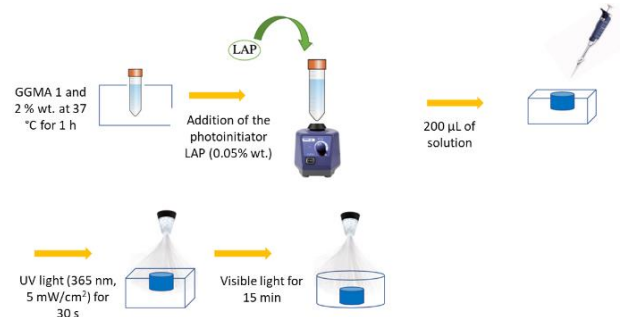

Fig. 1: Representation of the main phases involving the crosslinking of the GGMA hydrogels.

D. Rheometric tests

Rheometric tests were carried out with a rheometer (Anton Paar MCR 302), using a parallel plate setup covered by a heated Peltier hood. Tests were performed on both GG and GGMA at concentrations of 1% and 2% wt. by loading 400 µL of solution between the two plates at a distance of 1 mm. Two tests were performed: (1) viscosity analysis as a function of temperature (from 20 °C to 50 °C), at a speed of 2 °C/min and a shear rate of 100 s^{-1}; (2) shear stress as a function of shear rate (from 0.01 to 1000 s^{-1}) at a temperature of 37 °C. Starting from the rheological tests, the consistency index (K) and the flow behavior index (n) were calculated through the linear interpolation of the logarithmic values of the viscosity graph, as a function of the shear rate at a fixed temperature (37 °C), following the Ostwald-de Waele's constitutive law for non-Newtonian fluids [16]:

$$\log(\eta) = (n - 1)\log(\gamma) + \log(K) \qquad (1)$$

The maximum shear stress in a syringe can be calculated as:

$$\tau = -KR[Q\left(\frac{3n+1}{n}\right)R^{-\frac{3n+1}{n}}]^n \qquad (2)$$

E. Injectability tests

Injectability tests were performed by compressing a syringe piston loaded with the hydrogel. The syringe (1 mL) was equipped with different needle sizes (20G and 22G, length: 3.8 cm), and pushed using a speed of 2.5 mm/s, compatible with the real clinical application. The injection was performed both in air and within a phosphate buffer solution (PBS), simulating possible surgical scenarios.

F. Mechanical characterization

Uniaxial compression tests were performed using a traction test machine (Instron 2444), applying a compression rate of 1

mm/s. Before the mechanical characterization, the samples were kept in PBS at 37 °C for 24 h. The compressive Young's modulus (E) was calculated from the linear region of the strain-stress curve (initial 10% of the linear region) as follows:

$$E = \sigma * \varepsilon \qquad (3)$$

where σ is the stress and ε is the strain.

G. Cell embedding and viability assay

Human chondrocytes (Cell applications, Inc) were used as a cell model. For the experiment with the hydrogel, a small cell pellet (density: 400,000 cells/sample) was mixed with the hydrogel previously placed in a bath at 37 °C for about 10 min. Subsequently, LAP was added at a concentration of 0.05% wt., and 200 μL of the hydrogel solution were poured inside the PDMS mold, previously sterilized with ethanol and UV light for 30 min. The photocrosslinking was performed for 30 s at 5 mW/cm^2, afterwards the culture medium was slowly added to submerge the hydrogel. Then, the sample was exposed for 15 min to visible light through a LED light. The hydrogels were placed in the incubator, and the culture medium was renewed every 3 days.

A Live/Dead test was performed after 7 days to evaluate the chondrocyte viability within the hydrogel. The hydrogel was manually cross-sectioned, placed on a slide, and visualized with a fluorescence microscope equipped with FICT and TRITC filters.

H. Statistical analysis

Young's modulus and injection force data were statistically analyzed with one-way ANOVA and Tukey's post-test (GraphPad Prism v6) and reported as mean ± standard deviation. In all statistical tests, the significance threshold was set to * =p <0.05, ** = p < 0.01.

III. RESULTS

A. Injectability analysis

The rheological behavior may significantly influence hydrogel injectability. The viscosity of the different formulations is shown in Fig. 2.
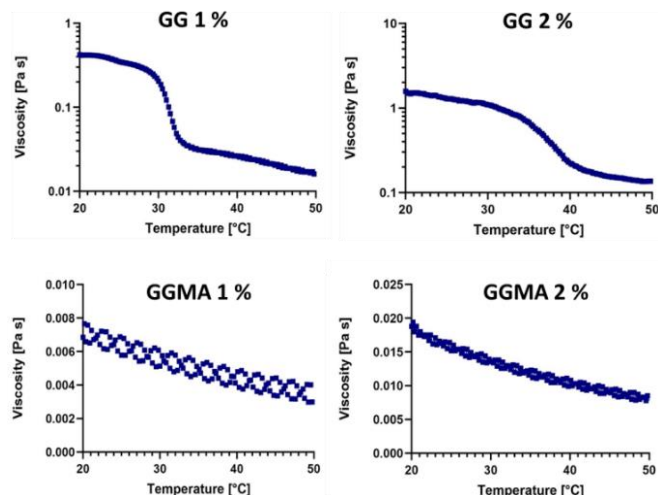

Fig. 2: Viscosity vs. temperature of GG (1 and 2 % wt.) and GGMA (1 and 2 % wt.).

As visible in the graphs, GG presented a gelation point (30-40 °C) that is dependent on the concentration of the solution, while GGMA did not show such a feature. Furthermore, the viscosity resulted higher for the higher polysaccharide

concentration. Since they are non-Newtonian fluids, the hydrogels may undergo shear-thinning: indeed, their viscosity decreased upon increasing the applied shear stress. Fig. 3 shows the viscosity against the shear rate for the analyzed materials, highlighting the K and n values extrapolated by the interpolation of such curves (equation 1).
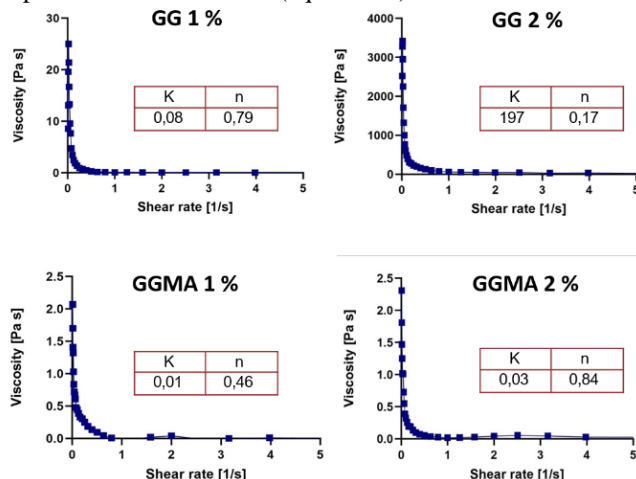

Fig. 3: Viscosity vs. shear rate of GG (1 and 2 % wt.) and GGMA (1 and 2 % wt.). K and n values are reported for each formulation.

The K and n values for GGMA resulted lower with respect to the GG ones, at the same concentration. The shear stress values, derived from equation 2, are reported in Table 1.

TABLE I. SHEAR STRESS VALUES DEPENDING ON THE NEEDLE DIAMETER

Material formulation	20G	22G
GG – 1 % wt.	0.86 Pa	1.42 Pa
GG – 2 % wt.	376 Pa	419 Pa
GGMA – 1 % wt.	0.06 Pa	0.08 Pa
GGMA – 2 % wt.	0.43 Pa	0.74 Pa

Given these results, we focused our attention on GGMA 2% wt. for the following experiments because of the lower shear stress applied to cells and the higher stability in physiological fluids than GG. In addition, 2 % GGMA showed highly favorable biological performance [17].

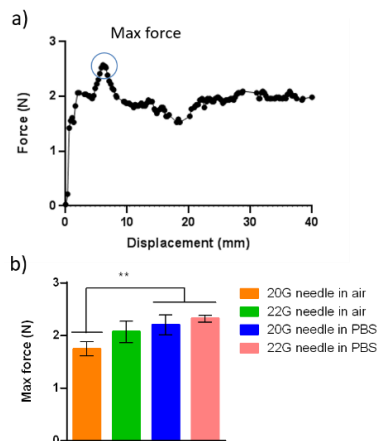Fig. 4 reports the analysis of the injection force for 2% GGMA.

Fig. 4: a) Representative graph of an injection force profile for GGMA (2% wt.), and b) comparison between the maximum injection forces for different needle sizes and experimental conditons (injection in air and in PBS).

It can be observed that the maximum force needed to inject the material is higher within a physiological fluid, while there

is not such a difference when varying the needle size. Such a force value (about 2 N) is compatible with the injection of cells [18].

B. Hydrogel photocrosslinking and mechanical properties

The combination of the photoinitiator LAP and the UV wavelength of 365 nm satisfied the requirement of rapid crosslinking of GGMA (2% wt.) (30 s), making it compatible with a minimally invasive surgical scenario (multiple cartilage defects could be rapidly treated in a single operation). Halogen and LED lights are widely used as illumination means in surgical procedures. We tested their influence on photosensitive GGMA hydrogels, after achieving a full crosslinking through 30 s of UV light (Fig. 5).
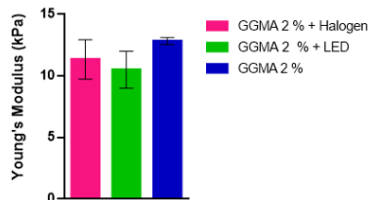
Fig. 5: Young's modulus of GGMA hydrogels exposed to visible light by means of halogen and LED sources, compared with a control (absence of visible light after UV crosslinking).

The 2% GMMA hydrogels, after UV crosslinking, were featured by an average compressive modulus of 12.8 kPa; the application of both visible lights after UV crosslinking did not influence their mechanical behavior in a significant way. Thus, we demonstrated that the adopted solution would not be influenced by an arthroscopic illumination during the surgical procedure.

C. Analysis of cell viability

Fig. 6 shows cross-section images of a GGMA hydrogel with embedded chondrocytes after 7 days.
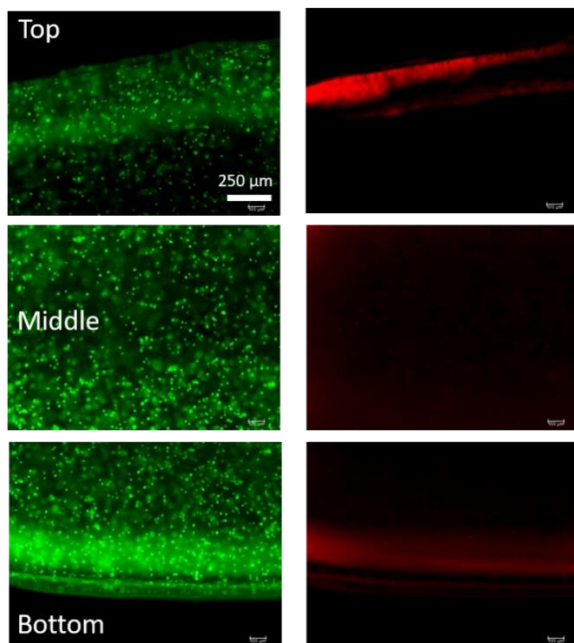

Fig. 6: Fluorescence images, obtained through the Live/Dead assay, of a cross-section of the 2% GMMA hydrogel embedding human chondrocytes. Live cells are colored in green, dead/necrotic cells are colored in red.

The images show the presence of viable cells after 7 days of culture, demonstrating that 2% GGMA hydrogels crosslinked by UV are able to effectively encapsulate chondrocytes for long-term applications in the CTE field.

IV. Conclusion

The manuscript reports a preliminary analysis of gellan gum-based hydrogels as injectable materials for CTE. GGMA resulted more promising than GG in minimally invasive application scenarios, due to its crosslinkability and *in situ* localization ability, through UV light. 2% GMMA safely encapsulated human chondrocytes. Future efforts will aim to analyze the long-term degradation behavior of this material, the ability to produce a suitable ECM and the possibility to host stem cells.

References

[1] A. J. Sophia Fox, A. Bedi, and S. A. Rodeo, "The basic science of articular cartilage: Structure, composition, and function," *Sports Health*, vol. 1, pp. 461–468, 2009.

[2] T. Aigner and J. Stöve, "Collagens - Major component of the physiological cartilage matrix, major target of cartilage degeneration, major tool in cartilage repair," *Adv. Drug Deliv. Rev.*, vol. 55, pp. 1569–1593, 2003.

[3] J. A. Buckwalter, "Articular cartilage injuries" *Clin. Orthop. Relat. Res.*, vol. 402, pp. 21–37, 2002.

[4] L. Zhang, J. Hu, and K. A. Athanasiou, "The Role of Tissue Engineering in Articular Cartilage Repair and Regeneration," *Crit. Rev. Biomed. Eng.*, vol. 37, pp. 1–57, 2009.

[5] A. M. Bhosale and J. B. Richardson, "Articular cartilage: structure, injuries and review of management," *Br. Med. Bull.*, vol. 87, pp. 77–95, 2008.

[6] B. Mollon, R. Kandel, J. Chahal, and J. Theodoropoulos, "The clinical status of cartilage tissue regeneration in humans," *Osteoarthr. Cartil.*, vol. 21, pp. 1824–1833, 2013.

[7] M. Ondrésik et al., "Management of knee osteoarthritis. Current status and future trends," *Biotechnol. Bioeng.*, vol. 114, pp. 717–739, 2017.

[8] C. Vinatier and J. Guicheux, "Cartilage tissue engineering: From biomaterials and stem cells to osteoarthritis treatments," *Ann. Phys. Rehabil. Med.*, vol. 59, pp. 139-144, 2016.

[9] A. R. Armiento, M. J. Stoddart, M. Alini, and D. Eglin, "Biomaterials for articular cartilage tissue engineering: Learning from biology," *Acta Biomater.*, vol. 65, pp. 1–20, 2018.

[10] L. S. Nair and C. T. Laurencin, "Biodegradable polymers as biomaterials," *Prog. Polym. Sci.*, vol. 32, pp. 762–798, 2007.

[11] S. Bhatia, "Natural polymers vs synthetic polymer," *Natural Polymer Drug Delivery Systems.* Springer, Cham, 2016. 95-118.

[12] S. Camarero-Espinosa, B. Rothen-Rutishauser, E. J. Foster, and C. Weder, "Articular cartilage: From formation to tissue engineering," *Biomater. Sci.*, vol. 4, pp. 734–767, 2016.

[13] K. E. M. Benders et al., "Extracellular matrix scaffolds for cartilage and bone regeneration," *Trends Biotechnol.*, vol. 31, pp. 169–176, 2013.

[14] J. T. Oliveira et al., "Gellan gum: a new biomaterial for cartilage tissue engineering applications," *J. Biomed. Mater. Res. A*, vol. 93, pp. 852-863, 2010.

[15] D. F. Coutinho et al., "Modified Gellan Gum hydrogels with tunable physical and mechanical properties," *Biomaterials*, vol. 31, pp. 7494-7502, 2010.

[16] A. Allmendinger et al., "Rheological characterization and injection forces of concentrated protein formulations: an alternative predictive model for non-Newtonian solutions," *Eur. J. Pharm Biopharm.*, vol. 87, pp. 318-328, 2014.

[17] C. A. Vilela et al., "In vitro and in vivo performance of methacrylated gellan gum hydrogel formulations for cartilage repair," *J. Biomed. Mater. Res. A*, vol. 106, pp. 1987-1996, 2018.

[18] M. H. Chen et al., "Methods to assess shear-thinning hydrogels for application as injectable biomaterials," ACS Biomater. Sci. Eng., vol. 3, pp. 3146-3160, 2017.

Modeling Intraperitoneal Insulin Kinetics in Patients with Type 1 Diabetes

F. Moret[1], M. Schiavon[1], C. Cobelli[1], and C. Dalla Man[1]

[1] Department of Information Engineering, University of Padova, Padova, Italy

Abstract—**Nowadays, standard insulin therapy in type 1 diabetes (T1D) is based on exogenous insulin administration through the subcutaneous (SC) tissue. Despite recent advances in insulin formulations, the appearance of insulin in plasma after SC administration still presents some issues limiting optimal glucose control, especially the delay and the large inter/intra-subject variability in its absorption. This paved the way for exploring new routes of exogenous insulin administration. Several studies have recently shown that intraperitoneal (IP) insulin administration, despite its higher invasiveness in comparison with the SC one, could represent a valid alternative option. However, to the best of our knowledge, a mathematical model describing absorption and distribution of insulin after IP administration is still lacking. Here, the aim is to fill his gap.**

Eight patients with T1D treated by implanted IP pump were studied in hospitalized settings for a total of 72 hours. During the experiment, frequent blood samples were drawn for plasma insulin concentration measurements. Four candidate models were tested. Model comparison and selection was performed based on model ability to predict the data, parameter precisions and parsimony criteria.

The most parsimonious model was represented by a linear two-compartment absorption model from the IP space coupled with a two-compartment model of whole-body insulin kinetics, with hepatic insulin extraction driven by glucose concentration in plasma.

The proposed model was able to accurately describe most of the data and provided precise parameter estimates. Future developments will account for possible nonlinear relationships between IP insulin dosing and kinetics observed in clinical data.

Keywords—**Model modeling, parameter estimation, insulin delivery, intraperitoneal route, type 1 diabetes, artificial pancreas.**

I. INTRODUCTION

TYPE 1 diabetes (T1D) is an autoimmune disease characterized by the destruction of the insulin-secreting pancreatic beta cells, leading to chronic hyperglycemia [1]. A 24/7 management of this disease is needed to keep glucose in the target range (70 – 180 mg/dL) and prevent diabetes-related long- and short-term complications [2].

The standard therapy of T1D consists in exogenous insulin administration through a basal-bolus strategy: basal insulin is administered to keep glycemia within the normal range between meals and overnight, while boluses are injected before and after meals to prevent post-prandial hyperglycemic events. This is usually obtained via the subcutaneous (SC) route, implemented through the use of insulin pens (Multiple Daily Injection, MDI) or the more recent insulin pump (Continuous Subcutaneous Insulin Infusion, CSII) devices. However, while SC insulin delivery is convenient and minimally invasive, it is well-known that insulin appearance in plasma after SC administration is still suboptimal, mainly due to the delay and large inter-/intra- subject variability in its absorption [3].

To partially overcome these issues, a new way of exogenous insulin administration has been recently proposed, i.e. the Intraperitoneal (IP) route. Two main approaches for IP insulin delivery have been developed: implantable pumps (Medtronic Minimed, Northridge, CA, USA) and the DiaPort system (Roche Diagnostics, Mannheim, Germany). The first one consists in a pump implanted in the abdomen, which delivers insulin via a catheter towards the liver; while the second one consists in a flexible catheter placed in the peritoneal space with a small titanium port–body implanted into the SC tissue. Despite the higher invasiveness of IP vs. SC devices, these raised great interest in the community thanks to their ability to mimic more closely the physiological conditions occurring in healthy subjects. In fact, the IP insulin delivery allows to include a first liver pass, thus restoring the portal-periphery insulin gradient and avoiding peripheral overinsulinization usually occurring with SC insulin delivery [4],[5]. As a result, this allow to improve glycemic control and thus patients satisfaction than standard therapies [6],[7],[8],[9],[10]. Finally, this technology might be successfully incorporated in an implantable artificial pancreas.

However, to the best of our knowledge, a mathematical model of IP insulin absorption and kinetics is still lacking. A better understanding of this process would be useful to help patients to properly adjust IP insulin therapy to improve glucose control. Moreover, a model of IP insulin absorption would be also an important component of in silico platforms, e.g. [11],[12],[13],[14], to develop and test new open- and closed-loop insulin treatment strategies [16]. Here, we aim to develop a mathematical model of IP insulin absorption and kinetics from data of patients with T1D treated by implanted IP pumps.

II. DATABASE & METHODS

A. Database

Eight patients with T1D treated by implanted IP pump infusing U-400 regular insulin and monitored by a subcutaneous continuous glucose monitoring (CGM) sensor were studied in a hospitalized setting [15]. The study protocol was approved on 11 September 2007 by the regional ethics committee Comité de Protection des Personnes Sud Mediterranée IV, France. After patient's admission and glucose sensor calibration (14 h), the study consisted of two randomized consecutive phases:

- OPEN-LOOP (CONTROL) PHASE: patients were studied for 24 h (one day with 3 meals) with IP insulin pump programmed

based on patients' standard basal-bolus insulin therapy.
- CLOSED-LOOP PHASE: patients were studied for 48 h (2 days with 3 meals per day) with the IP insulin pump manually programmed by the patient to deliver 30% of meal insulin bolus approximatively 15 minutes before meal time, while the basal insulin infusion was automatically modulated by a Proportional–Integral–Derivative (PID) algorithm driven by the SC glucose sensor (CGM).

B. Model of intraperitoneal insulin kinetics

A two-compartment linear model was developed to describe the absorption of IP insulin:

$$\begin{cases} \dot{I}_{q_1}(t) = -k_d \cdot I_{q_1}(t) + inf(t) & I_{q_1}(0) = Inf(0)/k_d \\ \dot{I}_{q_2}(t) = -k_a \cdot I_{q_2}(t) + k_d \cdot I_{q_1}(t) & I_{q_2}(0) = Inf(0)/k_a \\ Ra_I(t) = k_a \cdot I_{q_2}(t) \end{cases} \quad (1)$$

where I_{q_1} and I_{q_2} (mU) are the insulin masses in the first and second IP compartment, respectively; inf (mU/min) the insulin infusion rate from the IP pump; k_d (min^{-1}) the rate of distribution between the two IP compartments; k_a (min^{-1}) the rate of absorption from the IP, and Ra_I the rate of IP insulin appearance in the whole-body insulin kinetics model.

This model has been coupled with the two-compartment model of whole-body insulin kinetics currently implemented in the UVA/Padova T1D simulator [12]:

$$\begin{cases} \dot{I}_p(t) = -(m_2 + m_4) \cdot I_p(t) + m_1 \cdot I_l(t) & I_p(0) = I_{pb} \\ \dot{I}_l(t) = -(m_1 + m_3(t)) \cdot I_l(t) + m_2 \cdot I_p(t) + Ra_I(t) & I_l(0) = I_{lb} \\ I(t) = \frac{I_p(t)}{V_I} \end{cases} \quad (2)$$

where I_p and I_l (mU) are the insulin masses in plasma and liver, respectively; V_I (L) is the volume of insulin distribution; I (mU/L) is the plasma insulin concentration; m_2 is the rate of hepatic plasma flow [17]; m_1 is the rate of insulin distribution from liver to plasma (min^{-1}); m_4 is the rate of insulin degradation in plasma (min^{-1}) and m_3 is the rate of insulin degradation in the liver (min^{-1}) given by:

$$m_3(t) = \frac{HE(t) \cdot m_1}{1 - HE(t)} \quad (3)$$

where HE represents the hepatic insulin extraction. In addition, the post-hepatic insulin clearance CL (L/min) was obtained as a combination of model parameters as:

$$CL = \frac{((m_1 + m_3(0))(m_2 + m_4) - m_1 m_2)}{(m_1 + m_3(0))} \cdot V_I \quad (4)$$

Thus, using (3), we can obtain:

$$m_4 = \frac{CL}{V_I} - HE_b \cdot m_2 \quad (5)$$

In this work, four models of HE were tested [18]:
- Model I: HE is assumed to be constant and fixed to 0.6 [12], [19].

- Model II: HE is regulated by glucose concentration in plasma:

$$HE = -a_G \cdot G(t) + a_{0G} \quad (6)$$

where a_G (dL/mg/min) represents the control of glucose on HE and a_{0G} (dimensionless) is obtained from the steady-state constraint

$$a_{0G} = HE_b + a_G \cdot G_b \quad (7)$$

with G_b the glucose concentration at basal state.

- Model III: HE is regulated by insulin mass in the liver compartment (I_l):

$$HE = -a_I \cdot I_l(t) + a_{0I} \quad (8)$$

where a_I (L/mU/min) represents the control of hepatic insulin on HE and a_{0I} (dimensionless) is obtained from the steady-state constraint

$$a_{0I} = HE_b + a_I \cdot I_{lb} \quad (9)$$

with I_{lb} the insulin mass in the liver at basal state.

- Model IV: HE is regulated by both plasma glucose concentration and insulin mass in the liver compartment (I_l) as

$$HE = -a_G \cdot G(t) - a_I \cdot I_l(t) + a_{0GI} \quad (10)$$

where a_G and a_I were already defined previously and a_{0GI} (dimensionless) is obtained from the steady-state constraint

$$a_{0GI} = HE_b + a_I \cdot I_b + a_G \cdot G_b \quad (11)$$

C. Model Identification

All models were tested for *a priori* identifiability [17] using the software DAISY [23]. All models resulted *a priori* identifiable once m_2 is assumed to be known (fixed to 0.268 min^{-1} [20]) and, without loss of generality, $k_d \geq k_a$ since these two parameters are interchangeable.

All models were numerically identified on plasma insulin concentration data of both the open-loop and closed-loop phase with a Bayesian Maximum a Posteriori (MAP) estimator. Specifically, depending upon model, a priori information on the parameters related to the insulin kinetics, V_I, m_1, CL and HE_b [12][19] have been used to help numerical identifiability. In addition, to assess intra-subject variability in the IP insulin absorption parameters, k_a and k_d were allowed to assume different values during the main meals intervals (breakfast, lunch and dinner) during the day. Measurement error on plasma insulin data was assumed to be uncorrelated, Gaussian, with zero mean and known standard deviation [21].

Model identifications and statistical analysis were carried out by using Matlab® (R2019b) and the *ode45* solver implemented in Matlab® was used to integrate the model differential equations.

D. Model selection

The best model is selected based on standard criteria: randomness of residuals (Runs test), precision of parameter estimates (expressed as coefficient of variation, CV %) and model parsimony (Akaike Information Criterion corrected for finite sample sizes, AICc) [22].

E. Statistical analysis

Model parameters are presented as mean±SD. Paired two-samples comparison was done by paired t-test and ANOVA was used for multiple comparison. Significance level was set at *p=0.05* for all the statistical tests.

III. RESULTS

In Fig. 1, insulin data vs. model predictions in a representative subject in the open loop phase (upper panel), together with the predicted profiles of hepatic insulin extraction (lower panel), are shown. Al models are able, on average, to predict the data in the open-loop phase.
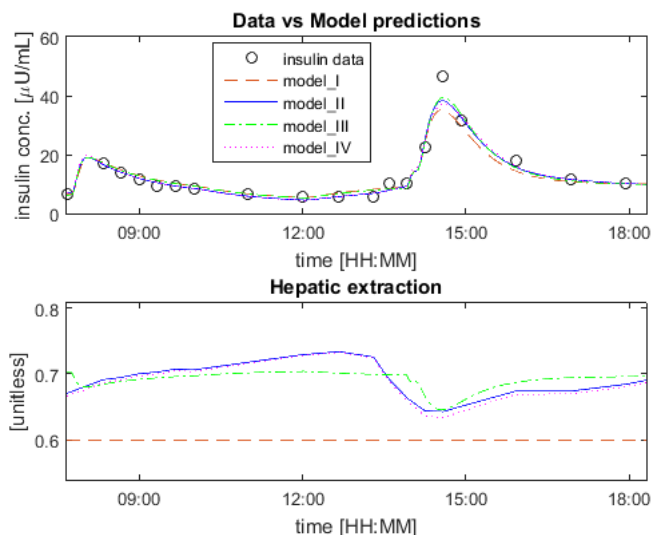

Fig. 1: Open-loop phase. <u>Upper panel</u>: plasma insulin data vs. model predictions in a representative subject; <u>lower panel</u>: model-predicted hepatic insulin extraction (*HE*).

This was true also for most of the subjects/intervals in the closed-loop (Fig. 2). However, with respect to the open-loop data, model performances slightly degraded in the closed-loop one. In particular, in some subjects/intervals, very fast variations in IP insulin absorption and/or kinetics were observed. In such cases, all the tested models were not able to well predict the data.

Model comparisons are summarized in Table I. The percentage of subjects who passed the Runs test was higher for Model II and Model IV. Model parameters resulted, on

median, estimated with a satisfactory precision among subjects. Finally, AICc was the lowest in Model II. Therefore, taking together all the criteria, Model II is selected as the best model to describe insulin data after IP infusion.
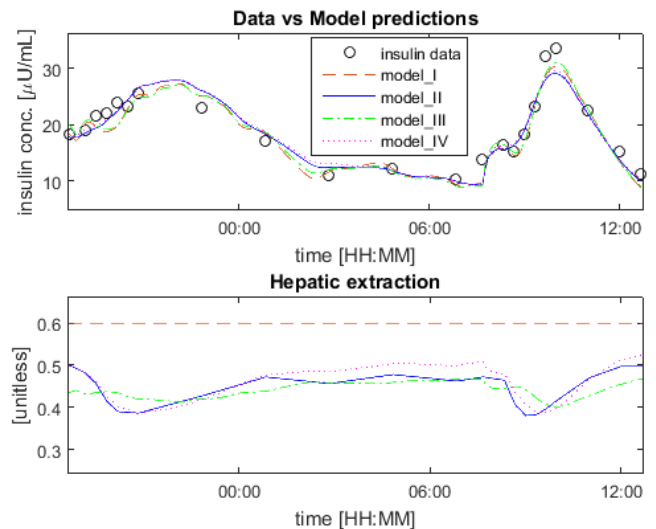

Fig. 2: Closed-loop phase. <u>Upper panel</u>: plasma insulin data vs. model predictions in a representative subject; <u>lower panel</u>: model-predicted hepatic insulin extraction (*HE*).

Once the best Model has been selected, one could use its parameter estimates to answer some questions: is there a circadian pattern in IP absorption? To answer these questions, we applied one-way ANOVA to compare parameters k_d and k_a obtained with Model II at breakfast vs. lunch vs. dinner during open- and closed-loop phase. We found that, the absorption parameters were not significantly different among the main meals. As a result, during the open-loop phase, k_d and k_a were equal to 0.144±0.092 min^{-1} and 0.031±0.016 min^{-1} respectively, while during the closed-loop phase they were 0.169±0.093 min^{-1} and 0.013±0.008 min^{-1}, respectively. Interestingly, k_a resulted significantly higher in the open-loop vs. closed-loop phase data (p<10^{-3}), while this was not the case for k_d. This result may suggest a possible nonlinear relationship between IP insulin absorption and insulin dosing which needs to be further investigated.

TABLE I
SUMMARY RESULTS OF MODEL COMPARISON

MODEL	RESIDUAL INDEPENDENCE (*)	PRECISION OF PARAMETER ESTIMATES (**)	AICc (***)
I	75%	17% [11%, 23%]	771 [555, 935]
II	88%	19% [13%, 25%]	723 [542, 997]
III	75%	17% [13%, 25%]	890 [540, 1302]
IV	88%	20% [13%, 25%]	804 [570, 960]

* Percentage of random cases assessed by Runs test.
** Median [25th, 75th] percentile of all parameters CV among subjects.
*** Median [25th, 75th] percentile of AICc values.

Conversely, ANOVA did not highlight any difference in insulin kinetics parameters when comparing open- vs. closed-loop phase. This can be partially due to the use of the Bayesian estimator. In fact, despite the estimated kinetics parameters showed an appropriate inter-subject variability, on average, they did not deviate significantly from the prior information [12][19].

IV. CONCLUSION

In this work, a battery of models describing IP insulin absorption and kinetics were proposed. In particular, IP insulin absorption was modeled as two-compartment linear model which was coupled with a two-compartment model describing whole-body insulin kinetics [12] including different descriptions of hepatic insulin extraction.

The selected model represents the best trade-off between the ability to predict the data with the minimum number of precisely estimated parameters. It is composed by a linear two-compartment IP absorption model coupled with a two-compartment model of insulin kinetics with hepatic insulin extraction driven by glucose concentration in plasma. In particular, the model well predicted insulin data in most of the subjects/intervals. Noteworthy, in a few cases of the closed-loop phase data, some particular patterns in insulin appearance after IP administration were observed leading to the inability of the model to well predict the data in these few cases. However, such a difference was partially expected since, by protocol, the pattern of insulin dosing between open- vs. closed-loop data was very different.

Future work will include the incorporation of nonlinear relationships between IP insulin dosing and kinetics.

V. ACKNOWLEDGMENTS

REFERENCES

[1] P. R. van Dijk, S. J. Logtenberg, R. O. Gans, H. J. Bilo, and N. Kleefstra, "Intraperitoneal insulin infusion: treatment option for type 1 diabetes resulting in beneficial endocrine effects beyond glycaemia," *Clinical Endocrinology,* vol. 81, pp. 488–497, 2014.

[2] World Health Organization (1999). Definition, diagnosis and classification of diabetes mellitus and its complications: report of a WHO consultation. Part 1, Diagnosis and classification of diabetes mellitus. World Health Organization. Available: https://apps.who.int/iris/handle/10665/66040

[3] M. Schiavon, C. Dalla Man, and C. Cobelli, "Modeling subcutaneous absorption of fast-acting insulin in type 1 diabetes," *IEEE Transactions on Biomedical Engineering,* vol. 65, no. 9, pp. 2019-2086, 2018.

[4] J.L. Selam, R.N. Bergman, D. Raccah, N. Jean-Didier, J. Lonzano, and M.A. Charles, "Determination of portal insulin absorption from peritoneum via novel nonisotopic method," *Diabetes,* vol. 39, no. 11, pp. 1361-1365, 1990.

[5] D.M. Nathan, F.L. Dunn, J. Bruch, C. McKitrick, M. Larkin, et al., "Postprandial insulin profiles with implantable pump therapy may explain decreased frequency of severe hypoglycemia, compared with intensive subcutaneous regimens, in insulin-dependent diabetes mellitus patients," *The AmericaJournal of Medicine,* vol. 100, pp. 412-417, 1996.

[6] M. J. Haardt, J. L. Selam, G. Slama, J. P. Bethoux, C. Dorange, et al., "A cost–benefit comparison of intensive diabetes management with implantable pumps versus multiple subcutaneous injections in patients with type I diabetes," *Diabetes Care,* vol. 17, pp. 847–851, 1994.

[7] J. L. Selam, D. Raccah, N. Jean–Didier, J. L. Lozano, K. Waxman, et al., "Randomized comparison of metabolic control achieved by intraperitoneal insulin infusion with implantable pumps versus intensive subcutaneous insulin therapy in type I diabetic patients," *Diabetes Care,* vol. 15, pp. 53–58, 1992.

[8] P. R. van Dijk, S. J. Logtenberg, K. H. Groenier, R. O. Gans, N. Kleefstra, et al. "Continuous intraperitoneal insulin infusion in type 1 diabetes: a 6–year post-trial follow–up," *BMC endocrine disorders,* vol. 14, no. 30, pp. 1–7, 2014.

[9] P. R van Dijk, K. H. Groenier, J. H. DeVries, R. O. Gans, N. Kleefstra, et al., "Continuous intraperitoneal insulin infusion versus subcutaneous insulin therapy in the treatment of type 1 diabetes: effects on glycemic variability," *Diabetes technology & therapeutics,* vol. 17, pp. 379–384, 2015.

[10] E. Dassau, E. Renard, J. Place, A. Farret, M. J. Pelletier, et al., "Intraperitoneal insulin delivery provides superior glycaemic regulation to subcutaneous insulin delivery in model predictive control-based fully-automated artificial pancreas in patients with type 1 diabetes: a pilot study," *Diabetes, Obesity and Metabolism,* vol. 19, pp. 1698–1705, 2017.

[11] B.P. Kovatchev, M. Breton, C. Dalla Man, and C. Cobelli, "In silico preclinical trials: a proof of concept in closed-loop control of type 1 diabetes", *J Diabetes Sci Tech,* vol. 3, no. 1, pp. 44-55, 2009.

[12] R. Visentin, E. Campos-Náñez, M. Schiavon, D. Lv, M. Vettoretti, et al., "The UVA/PADOVA type 1 diabetes simulator goes from single meal to single day," *Journal of Diabetes Science and Technology,* vol. 12, pp. 273–281, 2018.

[13] R. Hovorka, F. Shojaee-Moradie, P. V. Caroll, L.J. Chassin, I. J. Gowrie, et al., "Partitioning glucose distribution/transport, disposal, and endogenous production during IVGTT," *Am J Physiol Endocrinol Metab*, vol. 282, pp. E992-E1007, May. 2002.

[14] E.D. Lehmann, C. Tarin, J. Bondia, E. Teufel, and T. Deutsch, "Development of AIDA v4.3b Diabetes Simulator: technical upgrade to support incorporation of insulin lispro, aspart, and glargine insulin analogues," *Journal of Electrical and Computer Engineering*, vol. 2011, pp. 1-17, 2011.

[15] E. Renard, J. Place, M. Cantwell, H. Chevassus, and C. C. Palerm, "Closed–Loop insulin delivery using a subcutaneous glucose sensor and intraperitoneal insulin delivery," *Diabetes Care,* vol. 33, pp. 121–127, 2010.

[16] A. J. Barnes, and R. W. Jones, "PID-based glucose control using intra-peritoneal insulin infusion: an in silico study," *14th IEEE Conference on Industrial Electronics and Applications (ICIEA)*, XI'an, China, pp. 1057-1062, 2019.

[17] C. Cobelli, E. R. Carson, *Introduction to Modeling of Metabolic in Physiology and Medicine*, San Diego, CA: Academic Press, 2008.

[18] F. Piccinini, C. Dalla Man, A. Vella, and C. Cobelli, "A model for the estimation of hepatic insulin extraction after a meal," *IEEE Transactions on Biomedical Engineering,* vol. 63, pp. 1925–1932, 2016.

[19] C. Dalla Man, F. Micheletto, D. Lv, M. Breton, B. Kovatchev, et al., "The UVA/PADOVA type 1 diabetes simulator: new features," *Journal of Diabetes Science and Technology,* vol. 8, pp. 26–34, 2014.

[20] R. S. Sherwin, K. J. Kramer, J. D. Tobin, P. A. Insel, J. E. Liljenquist, et al., (1974, May). A model of the kinetics of insulin in man. The J. Clin. Investigation, vol. 53, no. 5, pp. 1481–1492, 1974.

[21] G. Toffolo, M. Campioni, R. Basu, R.A. Rizza, and C. Cobelli, "A minimal model of insulin secretion and kinetics to assess hepatic insulin extraction," *American Journal of Physiology–Endocrinology and Metabolism,* vol. 290, pp. 169–176, 2006.

[22] K. P. Burnham, and D. R. Anderson, "Multimodel inference: understanding AIC and BIC in model selection," *Sociological Methods & Research*, vol. 33, no. 2, pp. 261-304, 2004.

[23] G. Bellu, M.P. Saccomani, S. Audoly, L. D'Angiò, "DAISY: A new software tool to test global identifiability of biological and physiological systems", *Computer Methods and Programs in Biomedicine*, vol. 88, no. 1, pp. 52-61, 2007.

The influence of turbulence modelling on thrombosis in cardiovascular devices

S. Bozzi[1], D. Dominissini[1], A. Redaelli[1] and G. Passoni[1]

[1] *Department Electronics, Information and Bioengineering, Politecnico di Milano, Milano, Italy*

Abstract—**Numerical models for platelet activation assessment (PAS) are based on the Navier-Stokes (NS) equations coupled with a biomechanical model for platelets. The non-linear structure of the flow/platelet model equations implies that the eulerian and lagrangian solutions are significantly influenced by the turbulence model used in the NS equations. Reynolds averaged Navier-Stokes equation (RANS) have been extensively used – and still are - for hemodynamic simulations, while Large Eddy Simulation (LES) and Direct Numerical Simulation (DNS) to a lesser extent. The effect of the turbulent model on the blood motion has been only partially investigated, while the influence on the PAS is still unexplored. Different turbulence models are compared here both in terms flow variables and PAS around and past a bi-leaflet mechanical heart valve (BMHV). A measure of the PAS anomalies is obtained and some explanations thereof are given with respect to the structure of turbulence models considered.**

Keywords— **RANS, turbulence models, lagrangian integration, platelet activation.**

I. INTRODUCTION

COMPUTATIONAL fluid dynamics (CFD) has been largely adopted as a simulation tool for fluid mechanics in cardiovascular devices, like mechanical heart valves (MHVs). Numerical simulations helped researchers and physicians in understanding the cyclic laminar-turbulent-laminar flow transient due to cardiac forcing [1]-[3]. The systolic acceleration rapidly opens the aortic valve and the flow through it is primarily laminar, characterized by large-scale coherent structures. Differently, after the systolic peak, these flow structures rapidly break-up past the leaflets thus dissipating energy by means of intermittent intense shear stresses.

In prosthetic heart valves the onset non-physiological shear stresses results in pathological platelet activation and the related thrombus formation [4]. Exaggerated shear stresses, with respect to the physiological state, has been recognized as a triggering condition for platelet activation and aggregation, since many years [5]. Hence, patients with MHVs need lifelong therapies with anticoagulants to limit thromboembolic risk [6].

Platelet activation can be assessed coupling CFD models with a biomechanical model which links the eulerian flow variables (shear stresses), with the platelet activation state (PAS) [7]-[9]. The PAS model consists in the Lagrangian integration - along platelet trajectories - of a stress norm by non-linear kernel functions which are very sensitive to the eulerian field variables. The so-called direct numerical simulation (DNS) - i.e. the numerical integration of the Navier-Stokes equation up to the dissipative scales – give an accurate representation [1, 10] of the turbulent flows without any extra model. Conversely this approach is rather demanding from a computational viewpoint. This is why "cheaper" options like the Reynolds averaged numerical simulations (RANS) are still in use for high Reynold number flows in complex geometries. Albeit dated back in the past century, RANS closures are essentially based on empirical relations whose parameters are far away from being general and need specific calibrations. Due to this lack of generality, the shear stresses strongly depend on the turbulent closure, hence it is crucial to ascertain how the turbulence model affects the PAS of a cardiovascular device. The influence of the turbulent model on the largest flow structures has received some attention in the past [11], while their effects on PAS has not yet been investigated.

Here we quantify the effects of different turbulence models on the flow field at a bileaflet mechanical heart valve (BMHV) and on the lagrangian mapping of platelet activation. Four numerical experiments have been conducted: a direct numerical simulation (DNS), a large eddy simulation (LES) and two Reynolds-averaged Navier-Stokes simulations (SST k - ω and RSM or Reynolds Stress Model). All solutions are compared in terms of Eulerian variables, like the velocity in the proximity of the valve, and Lagrangian quantities as the stress accumulation, the stress rate and the PAS.

II. MATERIALS AND METHODS

THE geometrical model of the valve was generated by ANSYS® SpaceClaim 18.2, on the basis of an existing CAD of the BMHV (Figure 1b) by Sorin (now LivaNova, cardiac Surgery Units). The two leaflets have been assumed stationary, at the maximum opening since the valve stays in this configuration for a considerable time window around the systolic peak [12]. The BMHV was placed between two cylindrical pipes (diameter D=22 mm). The entry length was extended by 2D, while the cylindrical domain past the valve was extruded by 5D (Figure 1a).

The fluid domain has been meshed differently for the four models. All the RANS runs are based on the same mesh, with a spatial discretization of the order of the Taylor microscale and a boundary layer with y+ = 1 (Figure 1c) accuracy. DNS and LES have been solved using a characteristic mesh size of 8 η and 16 η, respectively, where η is the Kolmogorov microscale. The total number of elements resulted in $3.3 \cdot 10^6$ cells for RANS, $9.3 \cdot 10^6$ for LES and $5.4 \cdot 10^7$ for DNS. No previous DNS simulation [1] [5-6] used more than 10^7 cells.
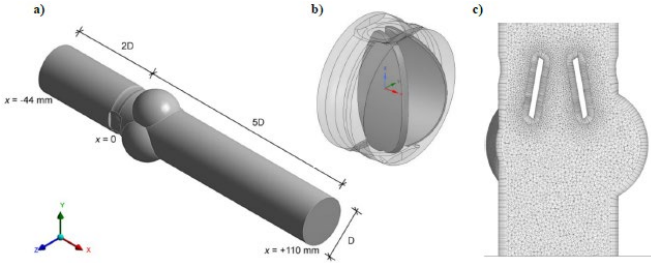
Fig. 1: Computational domain (a), Sorin bicarbon valve (b) and mesh for RANS simulation (c)

The flow field through the BMHV was obtained by integrating the 3D, unsteady, incompressible continuity and momentum equations. An incompressible and Newtonian fluid with density 1060 kg m-3 and dynamic viscosity 0.035 Pa s was used to model the blood. The numerical simulations have been performed by ANSYS® Fluent 18.2, with a SIMPLE algorithm for pressure-velocity coupling, a 2nd order scheme for space discretization and a 1st order implicit formulation for the time marching algorithm. A fully developed profile was imposed at the inlet and while a zero pressure at the outlet. The time window of each simulation has been set to 290 ms, i.e. the systolic phase.

Spherical particles (about 10^4, diameter of 3 µm) have been injected into the domain, with a concentric areal density at $t = 112$ ms, on a cross-plane, one diameter upstream the leaflets. A discrete particle model (DPM) has been adopted for lagrangian tracking of the "platelets" and at each time step the stress tensor components have been stored for each particle, and their position as well. The nine components of the stress tensor τ_{ij} were combined into a single scalar norm σ, the scalar stress [13], as in Eq. (1).

$$\sigma = \left(\frac{1}{12}\left(\tau_{ii} - \tau_{jj}\right)^2 + \frac{1}{2}\tau_{ij}^2\right)^{1/2} \qquad (1)$$

The platelet activation state (PAS), for one transit through the valve only, has been assessed by integration of the ordinary differential equation along each platelet trajectory [8], as in Eq. (2).

$$\frac{dPAS(t)}{dt} = (S + F + G)\big(1 - PAS(t)\big) \qquad (2)$$

S, F and G are given function of the "scalar stress" and stand for platelets sensitization (S), exponential contribution of the local stress (F) and of the stress rate (G), respectively. All formal details are given in [8].

III. RESULTS AND DISCUSSION

THE CFD models have been compared in terms of Eulerian velocity and scalar stress fields at three characteristic instants of the systolic phase: the time of maximum acceleration (A), the peak (P) and the time of maximum deceleration (D). During the acceleration phase, the flow remains essentially laminar, hence all the turbulence models give very similar solutions. Differently, at the systolic peak the flow pattern

downstream the valve exhibit complex and smaller structures that the more accurate LES and DNS only are able to capture. Looking at the velocity magnitude (Figure 2 top), it is evident how the velocity structure upstream the valve is very similar for all the simulations. On the contrary downstream the valve the velocity patterns are quite diverse for RANS, LES and DNS. High shear are evident downstream the leaflets and in the sinuses (Figure 2 bottom). The SST k - model produces exaggerated scalar stress, as resulting from an unrealistic turbulent viscosity (one order of magnitude larger than the physical one) close to the valve.
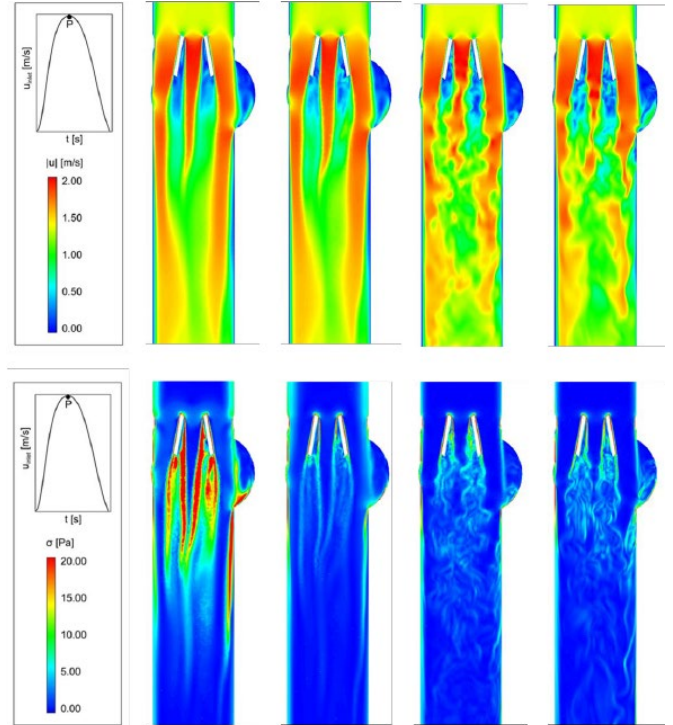

Fig. 2: Contours of velocity magnitude (top panel) and scalar stress contours (bottom panel) at the peak phase (P). From left to right: SST k-ω, RSM, LES, DNS.

The statistical quantiles for the PAS distributions of the four numerical experiments (Figure 3) indicate that the SST k-ω model apparently perform better than RSM and even LES. This anomalous results can be understood recalling that the turbulent viscosity in the SST k-ω model is amplified so that even a small fluid velocity can result in a very large shear stress. Hence the agreement with DNS is a mere coincidence, or a statistical outlier, rather than a proof of consistency and/or predictability of the SST k-ω turbulence closure.

Assuming DNS as the reference numerical experiment, as done in [1] and described more in detail in [10], it is evident that the PAS calculation may differ considerably when using more conventional RANS turbulence closures. Namely the differences may be more than 50% with RSM, while 18 % with LES.
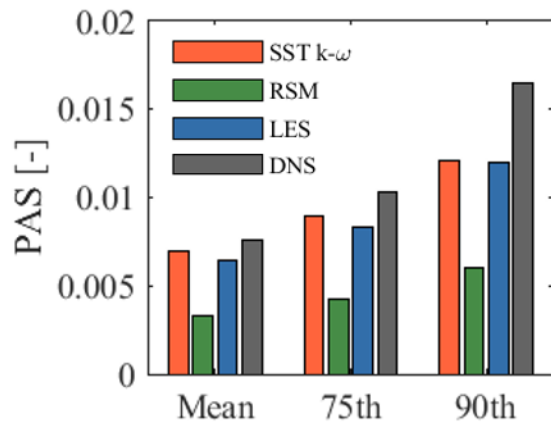
Fig. 3: Quantiles of PAS distribution for the different models.

IV. CONCLUSIONS

PLATELET activation state (PAS) assessment may vary up to 50% when adopting RANS based turbulence closures, compared to the more realistic DNS. DNS and, to an acceptable approximation, LES should be preferred when computing shear stress along particle trajectories and when along them a non-linear kernel is integrated to calculate the PAS. In this respect new lagrangian formulations for turbulent closures should be envisaged, when DNS or LES are unfeasible faster calculations.

REFERENCES

[1] L. Dasi, L. Ge, H. Simon, F. Sotiropoulos, P. Yoganathan, *"Vorticity dynamics of a bileaflet mechanical heart valve in an axisymmetric aorta"*, Phys. Fluids, Vol. 19, pp. 067105, 2007.

[2] M. De Tullio, A. Cristallo, E. Balaras, R. Verzicco, *"Direct numerical simulation of the pulsatile flow through an aortic bileaflet mechanical heart valve,"* J. Fluid Mech., Vol 622, pp. 259-290, 2009.

[3] F. Sotiropoulos, C. Aidun, I. Borazjani, R. MacMeccan, *"Fluid mechanics of heart valves and their replacements,"* Ann. Rev. Fluid Mech., Vol. 48, pp 259-283, 2016.

[4] A. Yoganathan, K. Chandran, F. Sotiropoulos, *"Flow in prosthetic heart valves: state-of-the-art and future directions",* Ann. Biomed. Eng., Vol. 33, pp. 1689-1694, 2005.

[5] Z. Ruggeri, J. Orje, R. Habermann, A. Federici, A. Reiniger, *"Activation-independent platelet adhesion and aggregation under elevated shear stress,"* Blood, Vol. 108(6), pp. 1903-1910, 2006.

[6] J. Peura, M. Colvin-Adams, G. Francis, K. Grady, T. Hoffman, M. Jessup et al., *"Recommendations for the use of a mechanical circulatory support: Device strategies and patient selection: A scientific statement from the American heart association,"* Circulation, Vol 126(12), pp. 2648-2667, 2012.

[7] M. Nobili, J, Sheriff, U. Morbiducci, A. Redaelli, "Platelet activation due to hemodynamic shear stress: damage accumulation model and comparison to in vitro measurements."*ASAIO J*, vol. 54(1), pp. 64-72, 2008.

[8] J. Soares, J. Sheriff, D. Bluestein, "A novel mathematical model of activation and sensitization of platelets subjected to dynamic stress histories", *Biomech. Model. Mechanobiol.*, Vol 12, pp. 1127-1141, 2013.

[9] F. Consolo, J. Sheriff, S. Gorla, N. Magri, D. Bluestein, F. Pappalardo, M. J. Slepian, G. B. Fiore, A. Redaelli, "High frequency components of hemodynamic shear stress profiles are a major determinant of shear mediated platelet activation in therapeutic blood circulating devices," *Sci. Reports*, Vol. 7(1) pp. 4994, 2017.

[10] P. Moin, K. Mahesh, *"Direct Numerical Simulation: A Tool in Turbulent Research,"* Ann. Rev. Fluid Mech., Vol. 30, pp 539-578, 1998.

[11] A. Pal, K. Anupindi, Y. Delorme, N. Ghaisas, D. A. Shetty, S. H. Frankel, "Large Eddy Simulation of transitional flow in a idealized stenotic blood vessel: evaluation of subgrid scale models," J. Biomed. Eng., Vol. 136, pp. 071009.

[12] T. Le, F. Sotiropoulos, "Fluid structure interaction of an aortic heart valve prosthesis driven by an animated left ventricle." J. Comp. Physics, Vol. 244, pp. 41-62, 2013.

[13] M.M. Faghih, M.K. Sharp, *"Extending the Power-Law Hemolysis Model to Complex Flows,"* J. Biomed. Eng., Vol. 138, pp 124504, 2016.

Stretchable polymer-based biopotential electrodes for unobtrusive EMG detection

A. Spanu, A. Bonfiglio, and D. Pani

Abstract—**Thanks to the recent technological advances, the goal of effectively integrating imperceptible and ubiquitous electronics onto standard garments and clothes has lately become a more realistic scenario. Modern wearable electronics can in fact provide unique solutions for the integration of devices such as biochemical sensors and electrodes for the unobtrusive monitoring of biopotentials. However, despite the numerous proposed approaches, the challenge of integrating electronics onto stretchable textiles still represents an open research issue.**

In order to overcome this issue, in this work we propose a simple method for the fabrication of polymer-based electrodes that can be screen-printed directly onto commercial stretchable fabrics. Our sensorized arm sleeve allowed to reliably detect the muscular activity of the forearm with performance comparable to that of commercial gelled Ag/AgCl electrodes, thus making the proposed approach suitable for biomedical applications such as prosthesis control, sport and fitness, rehabilitation, and long-term electrophysiological monitoring.

I. INTRODUCTION

In the past decade, wearable electronics has evolved tremendously, and nowadays several approaches to the integration of electrodes and electronics into fabrics have been successfully explored [1][5]. However, the challenge of obtaining stretchable sensorized garments that can reliably monitor biomedical parameters such as electromyographic (EMG) and electrocardiographic (ECG) signals still represents an open research issue. Amongst the different materials that have been recently studied for textile applications, PEDOT:PSS is undoubtedly the most interesting one. In fact, thanks to its relatively high conductivity (both ionic and electronic [6]), transparency, and good processability, PEDOT:PSS turned out to be a very good material for body/electrode interfaces, particularly for sEMG [7] and ECG [8]-[10] monitoring. This polymer can be deposited using several low-cost and large area solution-based fabrication techniques, such as ink-jet printing, spray coating, electrospinning, electrodeposition, dip coating, and screen printing. The combination of the interesting properties of this material, together with fabrication approaches that are compatible with those typical of the textile industry, make PEDOT:PSS-based textile electrodes a very effective and convenient alternative to standard commercial Ag/AgCl electrodes in terms of comfort and unobtrusiveness. Unfortunately, the recent literature demonstrated the intrinsic fragility of screen-printed textile electrodes to mechanical stress induced by the stretch of the fabric [11]. In this work we expressly addressed this problem by providing a solution that revealed its effectiveness in surface EMG detection on the forearm using a sensorised commercial elastic sleeve.

II. MATERIALS AND METHODS

The formulation of the developed PEDOT:PSS-based ink is (in volume): ⅓ Ethylene Glycol and ⅔ PEDOT: PSS (PH 1000 by Clevios™). Additionally, the addition of GOPS (3-GlycidylOxyPropyltrimethoxySilane) provided cross-linking features to the solution, which was carefully mixed, sonicated and annealed at 70 °C for 20 minutes.

The obtained PEDOT:PSS ink has been used for the fabrication of two couples of electrodes, which have been

Figure 1. Sensorized polyester stretchable arm sleeve for sEMG applications.

screen-printed onto a stretchable and breathable 100% polyester commercial arm sleeve and carefully positioned in order to target the *brachioradialis* (BR) and the *flexor carpi ulnaris* (FCU) muscles. Before the screen printing, the printing region was pre-stretched in order to reproduce the operating conditions (i.e., the mechanical stress that the fabric usually undergoes when the garment is worn), thus ensuring the retainment of their electrical properties during its use. After a final bake at 70 °C, each electrode is contacted with a 2-ply conductive steel thread and connected to a snap button, as shown in Fig. 1.

In order to assess the electrode characteristics, a small pilot trial was performed on four healthy male subjects between 24 and 40 years old in normal psychophysical conditions. The surface EMG signals were recorded with an MP45 Data Acquisition System (Biopac System, Inc., CA, USA). The subjects were shaved on the interested part of the forearm and their skin was gently abraded with Nuprep gel (Weaver and Company, Colorado, USA) to reduce the contact impedance. In order to have a reference for the performance of the textile electrodes, disposable gelled Ag/AgCl electrodes (CDES000024 by Spes Medica Srl, Genoa, Italy) were applied distally on the BR. The textile electrodes were finally wetted with a drop of saline solution to improve the skin/electrode interface.

During the recording session, the subject under test was asked to stay in a comfortable sitting position, with the dominant arm at rest while keeping in the open arm an isometric hand dynamometer (SS25LB, Biopac System, Inc., CA, USA). The force signal was recorded by the Biopac device along with the signals from the BR (both textile and Ag/AgCl electrodes) in the first part of the experimental session, and from the BR and the FCU during the second part. The subject
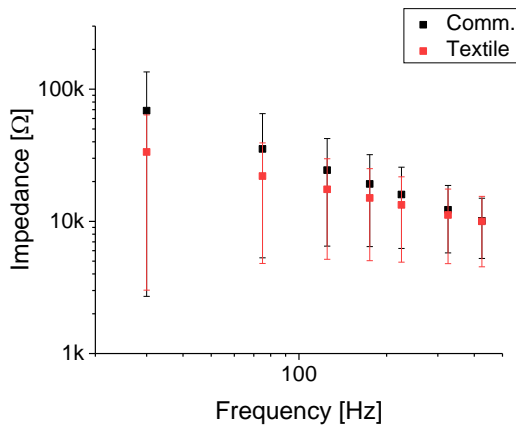
Figure 2. Skin contact impedance spectrum of a couple of electrodes applied on the forearm on the BR muscle. Mean values over four subjects. Error bars represent one standard deviation.

was then asked to exert the maximum voluntary contraction (MVC) by squeezing the hand dynamometer, keeping the power grip for about 10 seconds. Then, after other ten seconds of rest where the intrinsic electrode noise was recorded (no voluntary contractions), a series of ten repetitions of 2-second squeezing and 4-second of complete rest was performed.

Table 1. RMS values of the signal baseline (below 20 Hz) and in-band (between 20 and 400 Hz) for the four subjects.

Subject	RMS baseline [mV] Tex/Comm	RMS in-band [µV] Tex/Comm
#1	6.65/1.58	9.5/7.5
#2	15.7/7.42	2.7/ 2.8
#3	1.03/ 0.06	11.0/12.0
#4	0.2/ 0.22	14.2/8.2

Finally, the subject was asked to perform wrist flexion-extensions, the typical movement implemented for the basic control of hand prostheses in transradial amputees.

Comparisons between the two electrode technologies involved the analysis of the root mean square (RMS) noise amplitude, the skin contact impedance and the Pearson's correlation coefficient between the parts of the signals representing active muscle contractions. The skin contact impedance was measured in the range 30-425 Hz with an Agilent 4285A LCR meter. The noise amplitude was evaluated both in-band (20-400 Hz) and at low frequencies, where textile electrodes are more prone to introduce movement artefacts because of the limited adherence to the skin.

The raw EMG signal was band-pass filtered between 20 and 400 Hz through a cascade of two 2nd order Butterworth filters [12], applied bidirectionally to obtain a null phase shift. When needed, the envelope was extracted by a sliding window RMS, with a window lasting 200 ms [13].

All the processing was performed by using Matlab 2018b (The MathWorks, Inc., MA, USA).

III. EXPERIMENTAL RESULTS

The analysis of the skin contact impedance is shown in Fig. 2. Surprisingly, it revealed better performance of the textile electrodes compare to the Ag/AgCl ones, although this does not reflects the signal performance difference, being the textile electrodes more prone to suffer from baseline wandering artifacts. The RMS values of the signal baseline and in-band obtained for all the participants to the experiment are shown in Table 1.

In order to evaluate the similarities between the textile electrodes and the Ag/AgCl commercial ones, a correlation

Table 2. Pearson's correlation coefficient ρ (mean and standard deviation).

Subject	ρ (µ±σ)
#1	0.87±0.09
#2	0.97±0.04
#3	0.85±0.07
#4	0.80±0.10

analysis of the envelopes has been performed. Using the clench force to delineate the signal (using a threshold equal to 5% of the MVC force), the onset and end of all the repetitions of the ten squeeze repetitions were identified and used for the EMG segmentation on the BR for both the textile and the commercial electrode. The normalized Pearson's correlation coefficient between the two was then computed and reported in Table 2, revealing a good agreement between the two technologies. An example of both the raw and the filtered signals, as well as the envelopes and the clench force, is shown for the textile and the commercial electrodes, respectively in Fig. 3 and Fig. 4.

As a preliminary demonstration of the feasibility of our approach for specific applications, such as prostheses control, the EMG activity of the BR and the FCU muscles was evaluated during a simple wrist flexion-extension movement [14][15]. As shown in Fig. 5, the action of the two antagonist muscles is clearly detectable so that the recognition of flexion and extension does not requires a complicated threshold
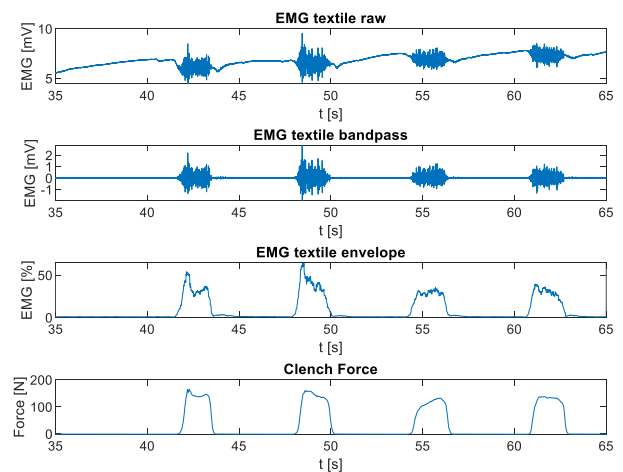

Figure 3. Textile electrodes characterization. From top to bottom: raw signals, band-passed signals, RMS envelope, and clench force (BR).

computation in order to properly work, making this solution of

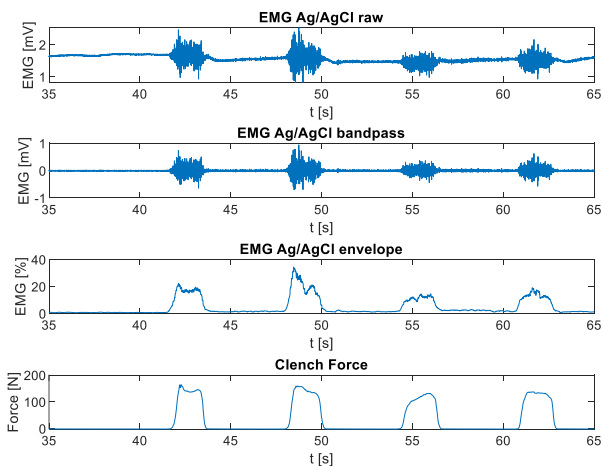great impact in terms of unobtrusiveness and comfort for the patient.

Figure 4. Ag/AgCl commercial electrodes characterization. From top to bottom: raw signals, band-passed signals, RMS envelope, and clench force (BR).

IV. CONCLUSION

We here proposed an interesting and versatile approach for the monitoring of biopotentials, which can represent a step forward with respect to standard Ag/AgCl electrodes for a less obtrusive and more comfortable EMG monitoring. A simple way to screen print PEDOT:PSS-based electrodes onto stretchable fabric has been presented and the effectiveness of the obtained textile electrodes has been demonstrated using a sensorized arm sleeve specifically designed for the monitoring of two different muscles in the forearm. Performance-wise, the electrodes showed comparable amplitude and good similarity when compared to commercial gelled electrodes in terms of
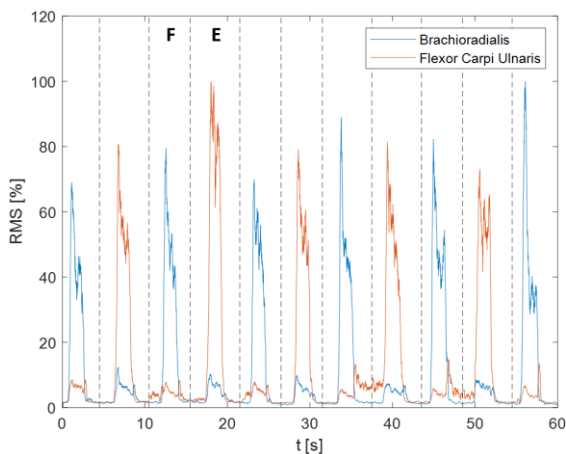

Figure 5. EMG activity of the BR and the FCU during the wrist flexion-extension movement. The two phases, i. e. flexion (F) and extension (E), are clearly detectable.

waveform profile, thus making the proposed approach suitable for several applications such as rehabilitation, prosthesis control, and fitness.

REFERENCES

[1] Marozas, Vaidotas, et al. "A comparison of conductive textile-based and silver/silver chloride gel electrodes in exercise electrocardiogram recordings." Journal of electrocardiology 44.2 (2011): 189-194.

[2] Weder, Markus, et al. "Embroidered electrode with silver/titanium coating for long-term ECG monitoring." Sensors 15.1 (2015): 1750-1759.

[3] Paul, Gordon, et al. "Novel active electrodes for ECG monitoring on woven textiles fabricated by screen and stencil printing." Sensors and Actuators A: Physical 221 (2015): 60-66.

[4] Shu, Lin, et al. "In-shoe plantar pressure measurement and analysis system based on fabric pressure sensing array." IEEE Transactions on information technology in biomedicine 14.3 (2010): 767-775.

[5] Paul, Gordon, et al. "The development of screen printed conductive networks on textiles for biopotential monitoring applications." Sensors and Actuators A: Physical 206 (2014): 35-41.

[6] Berggren, Magnus, and George G. Malliaras. "How conducting polymer electrodes operate." Science 364.6437 (2019): 233-234.

[7] Pani, D., et al. "Validation of Polymer-Based Screen-Printed Textile Electrodes for Surface EMG Detection." IEEE Transactions on Neural Systems and Rehabilitation Engineering 27.7 (2019): 1370-1377.

[8] Pani, Danilo, et al. "Fully textile, PEDOT: PSS based electrodes for wearable ECG monitoring systems." IEEE Transactions on Biomedical Engineering 63.3 (2015): 540-549.

[9] Sinha, Sneh K., et al. "Screen-printed PEDOT: PSS electrodes on commercial finished textiles for electrocardiography." ACS applied materials & interfaces 9.43 (2017): 37524-37528.

[10] Achilli Andrea, Annalisa Bonfiglio, and Danilo Pani. "Design and characterization of screen-printed textile electrodes for ECG monitoring." IEEE Sensors Journal 18.10 (2018): 4097-4107.

[11] Pani, Danilo, Andrea Achilli, and Annalisa Bonfiglio. "Survey on textile electrode technologies for electrocardiographic (ECG) monitoring, from metal wires to polymers." Advanced Materials Technologies 3.10 (2018): 1800008.

[12] De Luca, Carlo J., et al. "Filtering the surface EMG signal: Movement artifact and baseline noise contamination." Journal of biomechanics 43.8 (2010): 1573-1579.

[13] Celadon, Nicolò, et al. "Proportional estimation of finger movements from high-density surface electromyography." *Journal of neuroengineering and rehabilitation* 13.1 (2016): 73.

[14] Momen, Kaveh, Sridhar Krishnan, and Tom Chau. "Real-time classification of forearm electromyographic signals corresponding to user-selected intentional movements for multifunction prosthesis control." IEEE Transactions on Neural Systems and Rehabilitation Engineering 15.4 (2007): 535-542.

[15] Li, Guanglin, et al. "Performance of electromyography recorded using textile electrodes in classifying arm movements." 2011 Annual International Conference of the IEEE Engineering in Medicine and Biology Society. IEEE, 2011.

DoMoMEA: a home neuromotor telerehabilitation system for stroke patients

A. Zedda[1,2], E. Gusai[1], M. Caruso[3], S. Bertuletti[4], S. Spanu[1], G. Baldazzi[1,2], G. K. Masciavè[1], A. Pibiri[5], M. Monticone[5], A. Cereatti[3], L. Raffo[1] and D. Pani[1]

[1] *Department of Electrical and Electronic Engineering, University of Cagliari, Cagliari, Italy*
[2] *Department of Informatics, Bioengineering, Robotics and Systems Engineering, University of Genova, Genova, Italy*
[3] *Department of Electronics and Telecommunications, Politecnico di Torino, Torino, Italy*
[4] *Department of Biomedical Sciences, Bioengineering Unit, University of Sassari, Sassari, Italy*
[5] *Department of Medical Sciences and Public Health, University of Cagliari, Cagliari, Italy*

Abstract— **Patients who survived brain stroke events are followed up for immediate hospital neurorehabilitation. In normal clinical practice, after hospital discharge, they are recommended to continue rehabilitation treatment in the extra-clinical environment. One of the main problems that affect patients autonomously following neurorehabilitation activities is the lack of compliance. The reasons for compliance deficiency are manifold, but patients suffer most from the absence of medical monitoring. Moreover, the repetitiveness of traditional rehabilitation tasks can produce a reduced patient engagement possibly leading to drop out from the protocol.**

The DoMoMEA telerehabilitation system aims at providing a solution to these problems, by presenting a possibility to quantitively monitor the rehabilitation progress of stroke patients from remote, through a store-and-forward communication paradigm. A specific rehabilitation protocol composed of measurable exercises was conceived and an Android-based platform interfacing low-cost magneto-inertial measurement units and pressure sensors was developed. Installation-free web applications support all the telehealth features exposed by the system. A clinical trial with 40 patients will start as soon as the COVID-19 restrictions will allow it.

Keywords—**Telerehabilitation, neurorehabilitation, exergame, stroke.**

I. INTRODUCTION

STROKE is one of the primary clinical conditions and the leading cause of disabilities among the adult population all over the world, with about 15 million cases every year. In Italy, stroke represents the third cause of death, after cardiovascular disease and neoplasia, and the main cause of neuromotor disability. Around 200,000 stroke events occur every year, with 80% of new episodes and 20% of relapse. The stroke prevalence rate is significantly higher in the elderly population (75%), progressively increasing with age (over 65 years old), and slightly higher in men (7.4%) than in women (5.9%). Within one year since the acute event, one-third of stroke survivors experience a high degree of disability and become totally dependent from a caregiver. [1]

The consequences of a stroke event can be observed also in society, because of the loss of work for several stroke survivors and the huge costs for the National Health Service (NHS). Lack of clinical personnel, logistical and economic resources deficiencies as well as social and geographical factors are the main problems the NHS has to face in order to ensure equal and fair access to healthcare services to all the citizens [2]. In

fact, rehabilitation is the most effective treatment for post-stroke patients and has a primary role in the neuromotor deficit recovery and perceived disability reduction, especially within 6-8 months from the onset of the acute event. A poor provision of care, associated with a reduced number of sessions or an early unprotected discharge from the care center, can compromise the full recovery of patients' motor abilities.

Telerehabilitation could offer a valuable solution to solve the problem of providing high levels of care to a large number of patients at a low cost. Compared to standard care, home-based stroke rehabilitation demonstrated to be more cost-effective [3] by still allowing a control over the patient's progress. Different telemonitoring approaches have been proposed so far, but mainly we can identify those exploiting orthoses [4] and those based on free-body exercises [5]. The former can be applied to treat moderate to severe impairments but are usually bulky and expensive. Conversely, the latter are suited only in mild to moderate impairment, being unable to assist the patient's movement, but can be implemented with low-cost technologies to reconstruct the body movements such as depth cameras [6] or magneto-inertial sensors [7]. Beyond the effectiveness and efficiency of the proposed solutions in the short term, patient's engagement is important for the compliance in the long term. The exergaming approach is known to have a significant motivational component in post-stroke rehabilitation [8].

The DoMoMEA project (sites.unica.it/domomea-project) aims at providing a novel solution for the telerehabilitation of stroke patients with mild impairment. The project, which involves a cluster of eleven SME and BE in the fields of health services provision and ICT, was funded by Sardegna Ricerche with POR FESR 2014/2020 funds. Regions like Sardinia, characterized by low population density, embody the perfect condition for the experimentation of telerehabilitation services. In fact, such systems can help overcoming the limits of the conventional rehabilitation approaches while ensuring to everyone an equal access to medical treatments regardless their economic conditions and even if patients live in rural areas. The DoMoMEA advantage over previous research projects is the portability of the solution, which can be easily defined an m-health system and can be operated without any constraint is space and time without expensive computer platforms. In this work, the main characteristics of the project
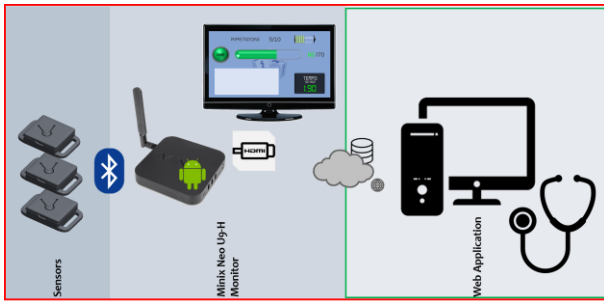
Figure 1. The DoMoMEA system architecture: the red canvas encloses the patient's domain, with the sensors connected via Bluetooth to an Android device showing the user interface. Data are collected locally, stored and forwarded through the Internet to a remote server. The clinical staff's domain (enclosed in the green canvas) is represented by a simple web application, exporting the data with different levels of details.

are presented, along with the current level of development, which is almost at its end. The clinical trial, originally expected to start in March 2020, has been delayed by the COVID-19 pandemic and will start as soon as the containment measures will be released.

II. METHODS

DoMoMEA is the acronym for Home neuromotor telerehabilitation for stroke patients with a mild impairment through advanced electronic devices. The main purpose of the DoMoMEA project is to provide patients with a low-cost dedicate system for the delivery of a personalized neurorehabilitation protocol in their home, with telemonitoring features. During the execution of the exercises, the patient's movements are measured to extract all the relevant clinical parameters needed to assess the quality of the exercise and the patient's progress by exploiting a store-and-forward telemedicine approach. Moreover, real-time visual and auditory feedbacks are provided through the Unity 3D interface running on the patient's Android device.

A. DoMoMEA rehabilitation protocol

A complete neurorehabilitation protocol, composed of technically measurable exercises designed for post-stroke patients, has been defined. Following the current guidelines, the protocol features repetitive functional and task-oriented exercises. In order to guarantee the effectiveness of the rehabilitation, the functional exercises have been accurately selected based on specific characteristics, including specificity (recovery of basic and advanced neuromotor skills) and transferability of the motor task (context where the subjects perform their actions). Moreover, the provision to patients of appropriate feedback about the performed action enriches the rehabilitation with an additional element of neuromotor control. All the exercises included in the protocol respond to well-defined principles:

1) repetitive contractions, both eccentric and concentric, of specific muscle groups;
2) muscle-strengthening exercises to improve muscle strength and intersegmental proprioceptive control;
3) task-oriented exercises of specific daily actions combining motor tasks with cognitive tasks.

Overall, fifteen different exercises were designed and programmed to systematically train the subjects' upper and lower limbs and trunk, up to the threshold of moderate fatigue, paying attention to their intensity, duration, frequency and safety.

The exercises were divided into five groups:

1) joint recovery and muscle strengthening of the upper and lower limbs,
2) joint recovery and muscle strengthening of the trunk,
3) proprioceptive and balance exercises,
4) functional recovery of the upper limb,
5) functional walk.

B. The DoMoMEA rehabilitation system

Figure 1 presents a pictorial representation of the DoMoMEA system architecture. At the patient's home, the system exploits:

- an Android device, possibly a TV-box connected to a TV,
- internet facilities,
- magneto-Inertial Measurement Units (MIMU),
- thin-film pressure sensors.

All the sensors communicate with the Android device through a Bluetooth classic connection. The system exploits up to seven low-cost 9-axis MIMUs (by 221e, Italy), used to measure the acceleration and angular velocity of the body segment of interest along with the local magnetic field. An on-board sensor fusion algorithm provides the orientation of each MIMU, needed to reduce the computational load in real-time streaming processing. The measured signals are further processed and fused together to provide the biomechanical variables of clinical interest such as the joint angles. From them, it is possible to estimate the execution time, the range of motion and execution errors. The system also features force sensitive resistors (by 221e, Italy), to monitor the plantar pressure and the pressure in some contact points during specific exercises. A custom digital acquisition module was designed to stream the sensor data to the Android device by exploiting a Bluetooth classic connection.

The Android device features a custom Unity 3D interface providing serious feedback to the patient on the biomechanical variables involved in each exercise or by using them to control an exergame, by exploiting a gamification approach. In the first case, angles, times, warnings and suggestions are put on video, helping the patient in correcting wrong movements and achieving good performance. In the second case, the patient is engaged in simple videogames without a quantitatively accurate measurement of the specific ability to train (e.g., a specific ROM increase). In this case, the patients are invited to achieve better performance by a score, defined by algorithms expressly conceived in to provide feedback on timing and biomechanical variables at the same time.

On the Android device, data from the exercises are temporally stored to be forwarded to a remote server at the earliest opportunity. Thanks to the adoption of a store-and-forward approach based on the transmission of synthetic reports (raw data are also logged for research purposes only), the amount of data to be transmitted and stored is reduced, relaxing the requirements on the Internet connection speed and

Figure 3. Example of serious interface. MIMUs are encircled in red.

Figure 2. Example of an interface for exergame.

allowing to serve also isolated places not served by broadband Internet connections. Store-and-forward technologies have important potentials:

1. flexibility: the patients can carry out the proposed neuromotor rehabilitation at any time of the day; the clinician can access the data from any position at any time of the day, easily analyzing the time series of the individual;

2. scalability: the system summarizes the results of each rehabilitation session in a few objective and measurable parameters, allowing the rehabilitation team to access information on the progress of the rehabilitation and on the detail of the execution of the individual exercises quickly to serve a larger population of patients;

3. measurability: compared to video conferencing systems, very common in the telerehabilitation field, the system allows accessing numerical data of known accuracy, improving objectivity;

4. reduced infrastructural requirements: the summary of the sessions is compact so that it can be sent also through mobile internet connections for people living in rural areas;

5. transportability: being free from fixed network connections, the system can follow the patients wherever they go, without requiring any installation. The choice of the Android operating system further enhances this mobility aspect.

C. The telerehabilitation infrastructure

The telemedicine framework for the DoMoMEA project was developed using the Django framework and PostgreSQL. Django is a framework based on Python. Thanks to Django, in conjunction with Nginx and Gunicorn, is now possible to interact with the PostgreSQL database, which will contain all the patients' data for each day of exercise. The server has been set-up using the GARR service and it is currently active.

In order to support the personalization of the therapy based on the patient's motor skills, through a web application it is possible to customize the safety limits and goals for the specific patients and to update their device from remote by means of a configuration file that will be automatically downloaded by the Android device as soon as it connects to the server to upload new data. From this perspective, DoMoMEA is highly customizable, in the sense that for each patient and for each exercise the game tries to set the right difficulty of the challenge. The same web application can be

used to read the patients' data and perform trend analyses.

Some automatic controls over the data are carried out by the server itself and if suspicious data are present on the database, the doctor is immediately and automatically warned by the server through system-generated e-mail.

III. THE CLINICAL TRIAL

The DoMoMEA system implements a specific rehabilitation protocol. While preliminary tests are already being performed on healthy subjects, the telerehabilitation features will be tested on the field by a pilot randomized and controlled trial involving 40 patients with mild motor impairment, divided into two arms: with or without the device. The rehabilitation protocol, following the CONSORT principles, will last for 8 weeks, 5 days/week, and two groups in the experimental arm will be defined: 10 subjects using the exergames and 10 using serious interface showing only the mechanical parameter of interest. Inclusion criteria will be: age (40-75), first cerebral stroke affecting the left side of the brain (within 6 months from the acute event) and autonomy in walking. Exclusion criteria will be: cognitive impairment (MMSE < 24), cardiac instability, respiratory instability, neurodegenerative disorders, systemic diseases. The clinical experimenter will be blinded but not the therapists, for obvious reasons. Outcome measurements will include the Motricity Index, Trunk Control Test, Barthel Index, Short-Form Health Survey-36 items, Global Perceived Effect, etc. The assessments will be performed at the beginning and end of treatment and after three months (follow up). Usability and acceptability will be also assessed through validated tools.

IV. CONCLUSION

The ongoing functional tests performed on healthy subjects are demonstrating the features, qualities and limits of the developed system. The clinical trial, originally foreseen for March 2020, have been delayed by the COVID-19 pandemic. Unfortunately, the availability of the DoMoMEA system could have been particularly useful in similar circumstances, when the fragile patients must stay at home and could perform their rehabilitation in their own home. The trial is currently ready to start, as soon as the restrictions imposed by the COVID-19 pandemic will enable to have safe interactions between the researchers and the enrolled patients.

With its scientific and industrial partnership, the DoMoMEA project aims at introducing a shift in the

neurorehabilitation of stroke patients with mild impairment, to support their recovery process in the cheapest and more comfortable way, without compromises in the provided assistance level. Remarkably, the system design can be easily adapted to different motor rehabilitation needs and extended to include cognitive rehabilitation. The availability of this system will allow novel and hitherto impossible studies, since commercial solutions are limited and closed. The DoMoMEA team is willing to collaborate with scientific and technological partners for further developments of this powerful tool.

REFERENCES

[1] S. S. Virani *et al.*, "Heart Disease and Stroke Statistics-2020 Update: A Report From the American Heart Association.," *Circulation*, p. CIR0000000000000757, Jan. 2020.

[2] G. Fattore *et al.*, "The social and economic burden of stroke survivors in Italy: a prospective, incidence-based, multi-centre cost of illness study," *BMC Neurol.*, vol. 12, no. 1, p. 137, Jan. 2012.

[3] R. S. Rasmussen *et al.*, "Stroke rehabilitation at home before and after discharge reduced disability and improved quality of life: a randomised controlled trial.," *Clin. Rehabil.*, vol. 30, no. 3, pp. 225–36, Mar. 2016.

[4] J. H. Jung, D. B. Valencia, C. Rodriguez-De-Pablo, T. Keller, and J. C. Perry, "Development of a powered mobile module for the ArmAssist home-based telerehabilitation platform," in *IEEE International Conference on Rehabilitation Robotics*, 2013.

[5] D. Kairy *et al.*, "Maximizing post-stroke upper limb rehabilitation using a novel telerehabilitation interactive virtual reality system in the patient's home: Study protocol of a randomized clinical trial," *Contemp. Clin. Trials*, vol. 47, pp. 49–53, Mar. 2016.

[6] S. Ponte, S. Gabrielli, J. Jonsdottir, M. Morando, and S. Dellepiane, "Monitoring game-based motor rehabilitation of patients at home for better plans of care and quality of life," in *Proceedings of the Annual International Conference of the IEEE Engineering in Medicine and Biology Society, EMBS*, 2015, vol. 2015-November, pp. 3941–3944.

[7] N. Byl, W. Zhang, S. Coo, and M. Tomizuka, "Clinical impact of gait training enhanced with visual kinematic biofeedback: Patients with Parkinson's disease and patients stable post stroke," *Neuropsychologia*, vol. 79, pp. 332–343, Jan. 2015.

[8] K. R. Lohse, C. G. E. Hilderman, K. L. Cheung, S. Tatla, and H. F. M. Van Der Loos, "Virtual reality therapy for adults post-stroke: A systematic review and meta-analysis exploring virtual environments and commercial games in therapy," *PLoS One*, vol. 9, no. 3, Mar. 2014.

[9] L. A. Simpson, J. J. Eng, and M. Chan, "H-GRASP: the feasibility of an upper limb home exercise program monitored by phone for individuals post stroke," *Disabil. Rehabil.*, vol. 39, no. 9, pp. 874–882, Apr. 2017.

Internal fixation of femur fractures: a new wireless electromechanical dynamization system

G. Dichio[1,3], G. Putame[1,3], M. Terzini[1,3], S. Cannata[2,3], P. Costa[4], E.G. Pasero[2,3] and A.L. Audenino[1,3]

[1] *Department of Mechanical and Aerospace Engineering, Politecnico di Torino, Turin, Italy* [2] *Department of Electronics and Telecommunications, Politecnico di Torino, Turin, Italy,* [3] *Polito[BIO]Med Lab, Politecnico di Torino, Turin, Italy,* [4] *Intrauma S.p.A., Rivoli, Italy*

Abstract – **Dynamization of fracture fixation is an important strategy to reduce the time of recovery for a patient. The principal aim of this treatment is to stimulate the proliferation of callus in the early phase of recovery and to accelerate the new bone formation. External stabilization is a gold standard technique for this type of treatment, but internal fixation has recently gained increasing attention. In this framework, the here introduced dynamization system has been developed for the treatment of polytraumatized patients, who would benefit from the fast recovery guaranteed by a minimally invasive technique and by the elimination of the need for re-intervention. Indeed, thanks to an innovative concept, an electromechanical wireless system has been developed in order to accomplish in a simple outpatient intervention the unlocking of the axial load from static to dynamic mode.**

Keywords – **plate dynamization, wireless systems, femur fractures, internal fixation**

I. INTRODUCTION

FRACTURES of the lower limbs, including the long bones Tibia and Femur, represent approximately the 28.5% of total body fractures, which is estimated to be equivalent of about 300,000 cases per year in the only United States. These injuries can be frequent in all age groups and are the consequence of traumatic events occurred in the context of road accidents or falls from high heights. Furthermore, those so-called "high energy" trauma can occur as isolated lesions or associated with other lesions in poly-traumatized patients.

The main purpose of the fracture treatment with a medical device is to ensure stable support to the bone during the healing phase, and to allow the patient to walk as soon as possible. To reduce even more the time of recovering, a new concept of axial dynamization has been recently investigated in the treatment of long bone fractures [1]. Axial dynamization is a condition of fracture stabilization in which the fixation allows unrestricted axial loading by muscle contraction and physiologic weight bearing, whilst bending and rotational loading remain controlled [2]. The effect of dynamization on fracture healing are both the stimulation of the proliferation of the periosteal callus in the early phase and second the acceleration of the remodelling and hypertrophy response of normal bone cells late in the healing phase [3].

External fixation has been in the past an ideal means of applying axial dynamization, since a telescoping frame mechanism can be used to control rotational and bending forces yet allowing free axial compression of the fracture when physiologically loaded. External fixation still remains the best choice for the initial stabilization of fractures with severe soft tissue injuries and poly-traumatized patients [4].

Nevertheless, for long bone fractures the best choice is internal stabilization, which is based on the following principle of internal fixation: (1) stabilization with inter-fragmentary compression by means of screws and/or plates, which guarantees absolute stability and brings bone to direct healing; (2) the immobilization of a fracture with nailing or with a bridge plate, which provides a less rigid fixation, and provides for the consolidation of the bones with indirect healing through the formation of the callus [5]. In particular, the bridge plate technique is indicated in comminute long bone fractures affecting the proximal or distal growth area, since the intervention can be done with a minimally invasive technique using a percutaneous approach, despite reduction with closed manoeuvres remains still an important problem [6].

Following those principles, the new device here presented allows for an initial implantation of the device in "static" mode and a subsequent unlocking of a sliding support, in a completely non-invasive mode. Indeed, thanks to a wireless activation, the two device components mutual sliding can be un-locked during a simple outpatient intervention, thus allowing dynamic sliding and early healing. In this way, it will be possible to treat complex cases of poly-traumatized patients with major lower limb problems in a single session, without having to provide for further surgery.

II. MATERIALS AND METHODS

A. Plate design

Unlike the dynamic bridge plates currently on the market, in which the release is carried out by activating a screw during a second surgery, the here proposed bridge plate replaces the screw connecting the two mutually sliding parts with a electromechanical (EM) mechanism, able to dynamize the plate in a completely non-invasive way.

Following a standard CAD process, the plate physical structure has been iteratively modelled and dimensioned in order to resist the standard physiological loads. For the structural project requirements, all the geometries have been simulated using traditional FEA procedure, in order to accomplish a predefined structural rigidity of the final design.

Furthermore, to study the influence of the friction, as well as the geometry of the unlocking mechanism, a simplified multi-body model has been created and simulated too, representative of the main study parameters.

B. Design requirements

In addition to structural requirements, other important design input for the physical realization of device were related to the geometry size and integration of preselected electrical components. Those are, in order of importance:

- The final concept must have only one free degree of freedom, while the others needs to be "locked", i.e. supported by the metallic structure;
- The final dimension of the device should be on the order of a standard femoral plate, which are near to 210 x 25 x 10 mm considering length x width x height;
- The unlocking force needs to be minimal, since the device is intended to be implanted into the body, and the mechanical power is limited by the small dimension of the possible actuation system.
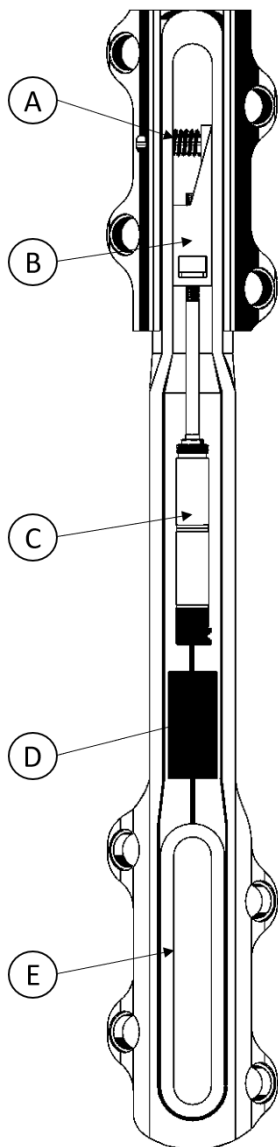
Fig. 1: Detail of the internal actuation system of the plate: A. pin; B. wedge-shape block; C. brush motor; D. receiver circuit; E. receiver coil.

III. RESULTS AND DISCUSSION

A. The unlocking mechanism

Following the design requirements, the unlocking mechanism has been developed consisting of two perfectly complementary metallic parts, designed and sized so that they can relatively slide (Fig. 1, part A-B).

Moving in order with respect to the configuration shown, the first part (the pin - denoted by A) was conceived as a prismatic base with a triangular shape and a semi-circular extension.

The angle of the pin base was initially presumed from the theoretical friction coefficient of the surfaces in contact, as will be detailed in the next section. The section of the semi-circular extension was defined thanks to structural calculations as an ellipse whose larger radius is equal to 3.5 mm, in order to guarantee his structural resistance especially in the initial phase of loading, when the plate is in "static" mode. The function of the pin is ensuring the initial locking between the two mutually sliding parts of the plate, ensuring the structural resistance of the construct when is locked, as shown in Figure 2. To facilitate the pin release and minimize the forces involved, the pin is wrapped by a preloaded spring, which when released moves the pin inside the plate, thus un-locking the system.
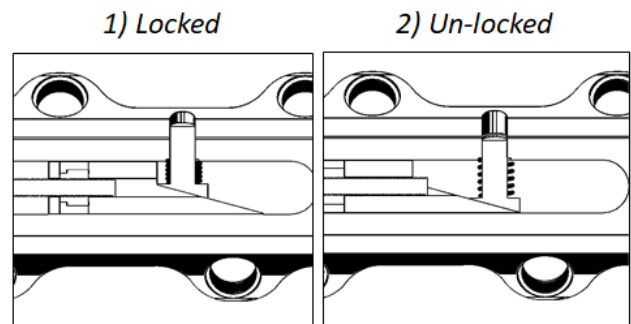

Fig. 2: Detail of the locking mechanism in the locked (1) and un-locked (2) configurations.

The second of the two parts (the wedge-shape block - denoted by B) was conceived as a rectangular block with a terminal part of triangular shape. The angle of inclination is the same of the pin base, in order to perfectly slide each other. It has also a central hole used for the passage of the worm screw, and a recess used to host the nut of the EM actuation system.

B. Angle optimization

For the correct sizing of the unlocking mechanism components, the main parameter is the angle of friction at which the preload of the spring is exactly balanced by the resistance of the plane (the component of horizontal force due to friction). This angle depends on several parameters, but the most important are, by literature, the pair of materials in contact, the surface finishing conditions, and the presence of lubrication. So, it can be strictly related to the physical process that has been selected to produce the components but can also be determined by the presence of different materials or lubricant interposed between the two surfaces. In order to

study his influence on the axial force acting on the motor, a simple multi-body system has been developed taking into account the main physical and geometrical parameters of the systems, which are also highlighted in the following expression:

$$Fa = Fn * \mu = Kp * \cos(\varphi) * tg(\varphi) = Kp * sen(\varphi) = Fp \quad (1)$$

Where: *Fa* is the friction force parallel to the plane; *Fn* is the component of the force, normal to the plane; μ is the friction coefficient between the surfaces; *Fp* is the component of the force, parallel to the plane; *Kp* is the spring preload and φ is the inclination angle of the pre-defined geometry.

As shown in equation (1), the selection of an angle of inclination exactly equal to the friction angle, i.e μ=tg(φ), transform the relation in an identity, since *Fa* will be exactly equal to *Fp*. In this condition, the initial force resultant on the block will be zero.

In our case, since we want to obtain a relative sliding of the un-locking mechanism with the application of a very small force, it is important to choose an angle of inclination as close as much to the theoretical friction angle between those two surfaces, or at least over dimension it of a small quantity in order to have a positive force instead of negative one.

A lists of the standard friction coefficients used to simulate the contact problem into the multi-body model is shown in Table 1.

TABLE I
MATERIAL FRICTION PROPERTIES

Materials	μ_s: static coefficient	μ_d: dynamic coefficient
Greasy aluminum – Dry steel	0,30	0,20
Greasy aluminum – Greasy steel	0,23	0,16
Greasy steel – Dry/Greasy steel	0,23	0,16
Acrylic – Dry/Greasy steel	0,20	0,15
Nylon – Dry/ Greasy aluminum	0,10	0,06
Nylon – Acrylic	0,10	0,06
Nylon – Nylon	0,10	0,06

Principal friction coefficient usually utilized for multi-body modelling of contact problems.

Because the physical value can slightly differ from the values obtained by theoretical equations, due to possible tolerances of the physical process, an experimental testing on the unlocking mechanism is fundamental.

C. Electromechanical actuation

For the actuation of the wedge-shape block, a preassembled motor reduction system has been selected (Fig. 1- part C).

This is composed of a three sub-block which are: (1) a DC motor; (2) a planetary gear's reduction mechanism, which

can have from 1 to 5 stages of reduction depending on the outer torque and velocity we need; (3) a metric screw drive, which can have different lengths and nuts, depending on the application and efficiency needed.

Taking into account the design constraints, the following combination was selected:

- RE6 DC motor, Φ 6mm, precious metal brushes, 0.3 W of nominal Power, and 4.5 V of nominal tension;
- GP6S screw driver, Φ 6mm, composed of a Planetary gearhead with 3 or 4 stages of reduction, and a metric lead screw with standard length of 45 mm.

The main advantages of brush motors are their relative cheapness with respect to the brushless ones, the simplicity of the regulators that must pilot them and the prompt response to commands at low revs and when stationary.

Fig. 3: The metal brush motor with the 4 stages gear reduction system and the preselected screw drive in the assembled configuration.

D. Electrical power supply

In order to supply power to the motor, an inductive power transfer system has been conceived, consisting of two magnetically coupled coils. The voltage supply – namely 4.5 V - is applied to the transmitting coil and the related power is transferred to the receiver side (Fig. 1 – part E), to which a supercapacitor is connected. The charge stored into the supercapacitor is then used to supply power to the electric motor, which will start to rotate, thus making the pin retract.
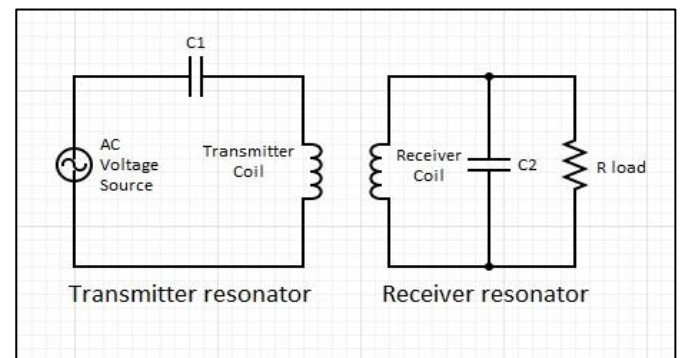

Fig. 4: Schematic of simplified circuit.

The equivalent circuit can be depicted as shown in Figure 4, where C1 and C2 capacitors are deployed in order to implement a resonating system, thus maximizing the power transfer. A different view of the same topology is shown in Figure 5, highlighting resistive losses in both sides of the system, as well as the supercapacitor (indicated as C_{sup}) [7].
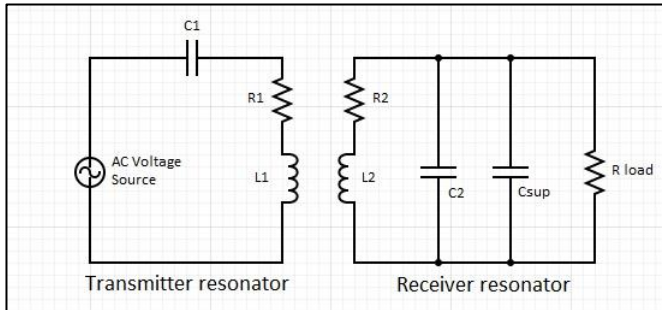
Fig. 5: Inductive power transfer circuit with supercapacitor.

The fundamental electrical components needed for the implementation of the physical circuit are:

- 1 transmitter coil;
- 1 receiver coil;
- 1 supercapacitor;
- 2 capacitors to set the resonance condition;
- 1 voltage supply for the transmitter side.

One of the main design constraints to consider must be the size and geometry of the receiver coil, which should be small enough to be hosted on the plate, yet big enough to receive enough power to supply the motor. For this reason, a Printed Circuit Coil (PCC) like the one shown in the Figure 6 could be used. Moreover, additional components might be necessary to convert voltages from DC to AC on the transmitter side – and vice versa on the receiver side – making the power transfer to work in a proper manner.
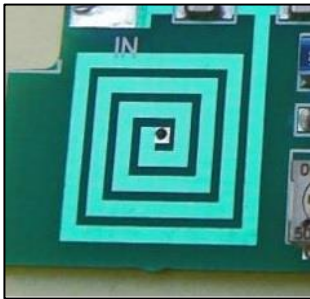

Fig. 6: Printed Circuit Coil.

Finally, for a safe feedback to the medical doctor, might be also worth to take into account a feedback element able to sense if the pin has completed its motion – e.g. a switch that closes at the pin motion end.

IV. CONCLUSION

The dynamization system here presented resulted feasible in all the technical aspects, both from the electrical and from the mechanical point of view. An electromechanical unlocking mechanism has been developed which, by using the transfer of energy from the outside to the inside of the body by means of two inductors, allows the recharging of a super-capacitor whose energy is used to activate a DC motor. The motor, directly connected to a motion reduction mechanism, manages to axially move a wedge-shaped block which activates the retraction of the pin. The next step of this work will be the physical realization of the components and the testing of the critical parts, in order to verify the fulfilment of all the predefined design requirements.

REFERENCES

[1] E. Egger, F. Gottsauner-Wolf, et.al., "Effect of axial dynamization on bone healing", *The journal of trauma*, vol. 34, no. 2.
[2] T. Yamaji, K. Ando, et al., "The effect of micromovement on callus formation", *Journal of Orthopaedic Science*, (2001) 6:571-575;
[3] M. Foxworthy and R.M. Pringle, "Dynamization timing and its effect on bone healing when using the Orthofix Dynamic Axial Fixator", *Injuty vol.* 26, no. 2, pp. 117-119, 1995;
[4] L.E. Claes, H-J. Wilke, et. Al., "Effect of dynamization on gap healing of diaphyseal fractures under external fixation", *Clinical Biomechanics*, vol 10, n.5, pp. 227-234, 1995;
[5] C. Sommers, T. Ruedi, "Fissazione interna delle fratture", *Tecniche chirurgiche in ortopedia e traumatologia*, 01-01-210.
[6] S. Larsson, W. Kim, et. Al, "Effect of early axial dynamization on tibial bone healing", *Clinical orthopaedics and related research*, n. 388, pp. 240-251;
[7] Y. B. Fadel, S. Ktata et al., "A Modified Wireless Power Transfer System for Medical Implants", *Energies* 12(10):1890, May 2019;

Human papillomavirus early promoter: Sensitivity analysis and biological behaviour

A. Giaretta[1]

[1] *Department of Information Engineering, University of Padova, Padova*

Abstract— **A minimal mathematical model of Human Papillomavirus early promoter (*EP*) transcriptional regulation was recently developed, able to predict the main features of *HPV* gene regulation at the beginning of the infection.**

A sensitivity analysis is performed to characterize the transcriptional regulation of the major *E2* viral regulator. Some biological insights were also obtained by studying the model dynamical response.

Sensitivity analysis indicates some key parameters for both a monostable and a bistable behaviour of the system and helped elucidating other key parameters for the only model bistability. In silico simulations showed and suggested interesting responses that could be associated with the viral latency.

Keywords—**mathematical modelling, *HPV*, early promoter, sensitivity analysis.**

I. INTRODUCTION

HUMAN papillomaviruses (*HPVs*) can induce benign lesions but also severe lesions such as invasive cervical cancer. In the past decades the understanding of the *HPV* molecular biology was amazingly increased but we still have to understand a huge amount of molecular mechanisms that control the viral infection. Mathematical models can help understanding still elusive mechanisms and for this reason we have recently published some works about the *HPV* regulation [1-6].

Of primary importance is the understanding of the early promoter (*EP*) regulation that controls the beginning of the infection. We have recently published a minimal model of such promoter [5]. The aim of this study is to extend such work by performing a sensitivity analysis to characterize the influence of model parameters under different biological conditions. A second aim is to present some dynamical behaviours having a potential biological interest.

II. METHODS

A. Model

The *EP* controls the synthesis of the *mE2 mRNA* which encodes for the *E2* protein. This latter forms *DE2* homodimers that are the major feedback regulators of the *EP* transcriptional control. When *DE2* is in low concentration the system works in open loop and *mE2* is controlled by a basal transcriptional synthesis. When *DE2* is in higher concentration it acts as a positive feedback regulator, while when *DE2* is in high concentrations it acts as a negative feedback regulator. The main mechanisms are depicted in Fig. 1.

B. Model equations

We recall model differential equations from our previous work [3]:

$$m\dot{E}2 = S(DE2) - \delta_{mE2}\,mE2 \tag{1}$$

$$\dot{E}2 = k_{E2}\,mE2 - \delta_{E2}\,E2 - 2k_f E2^2 + 2k_r DE2 \tag{2}$$

$$D\dot{E}2 = k_f\,E2^2 - (k_r + \delta_{DE2})\,DE2 \tag{3}$$

Where *S(DE2)* is the transcriptional synthesis which is modelled as in [5]:

$$S(DE2) = \frac{s_2\,C\,DE2^2 + s_1\,B\,DE2 + s_0\,A}{C\,DE2^2 + B\,DE2 + A} \tag{4}$$

Where s_0 accounts for the basal synthesis rate and s_1 and s_2 account for the positive and negative feedback synthesis rates, respectively. *A* is the basal transcription propensity, while *B* and *C* are the positive and negative feedback strengths, respectively. Further details can be found in [5].

The meaning of the other model parameters is given in Table I.

C. Sensitivity Analysis

Following classical definitions [7], the effect of parameter perturbation on the variable of interest (*Y* in the present case) can be described by its first-order partial derivatives, namely:

$$S_i(t) = \frac{\partial Y(t; \boldsymbol{p})}{\partial p_i}\,\frac{p_i}{Y(t)} \tag{5}$$

where $S_i(t)$ is the sensitivity of *Y* at time *t* with respect of the perturbation of the p_i parameter and $\boldsymbol{p} = [p_1,\ldots,p_N]$ is the vector containing the model parameters.

Being a function of time, sensitivity analysis allows one to measure both the extent to which a single parameter affects the system behavior and when it happens. However, in order to facilitate the ranking of model parameters based on their influence on model output, it is convenient to define some indices. A consolidated metric is the overall sensitivity to parameter p_i over the entire simulation interval $[t_1, t_2]$:

$$S_i^{tot} = \frac{1}{t_2 - t_1} \int_{t_1}^{t_2} S_i(t)\,dt \tag{6}$$

D. Implementation

We consider two parameter sets. One defined in Table I where the system exhibits a bistable behaviour as in [5], and

Fig.1 Early promoter (*EP*) regulatory core. *mE2* transcript is produced by the *EP*. *mE2* is converted into *E2* protein. This latter forms a homodimer, *DE2*, which induces a positive feedback on the *EP* when *DE2* is in low concentration and becomes a negative feedback when *DE2* is in high concentration.

TABLE I

Parameters	Description	Value [parameter region]	Unit of measure	Reference
s_0	mE2 basal transcription synthesis rate	5e-2	[CN min^{-1}]	Calibrated to be consistent with [5]
s_1	mE2 positive feedback synthesis rate	4.52	[CN min^{-1}]	Calibrated to be consistent with [5]
s_2	mE2 negative feedback synthesis rate	3.8e-2	[CN min^{-1}]	Calibrated to be consistent with [5]
A	Propensity to perform a basal transcription	2e-3	[min^{-2}]	Inferred from [5]
B	Strength of the positive feedback, as function of DE2, on the EP	3e-4	[CN^{-1} min^{-2}]	Inferred from [5]
C	Strength of the negative feedback, as function of DE2, on the EP	1.9e-7	[CN^{-2} min^{-2}]	Inferred from [5]
k_{E2}	E2 translation rate	1e-2	[min^{-1}]	Calibrated to satisfy the CN range [5]
k_f	DE2 heterodimer association forward rate	3.7e-5	[CN^{-1} min^{-1}]	Assumed
k_r	DE2 heterodimer dissociation backward rate	3.6e-2	[min^{-1}]	Assumed
δ_{mE2}	mE2 degradation rate	5.6e-2	[min^{-1}]	[5]
δ_{E2}	E2 degradation rate	3.4e-3	[min^{-1}]	[5]
δ_{DE2}	DE2 degradation rate	5.1e-4	[min^{-1}]	Assumed to satisfy the biological constraint $\delta_{E2} \gg \delta_{DE2}$ [5]

the other one by changing the parameter s_1 = 1e-3 in order to have a monostable behaviour of the system.

Model simulations are implemented in MATLAB. We used the indirect method [7] to implement the sensitivities (eq. 5), which makes use of the finite difference approximation:

$$S_i(t) = \frac{Y(t; p_1,..,p_i + \Delta p_i,..,p_N) - Y(t; \boldsymbol{p})}{\Delta p_i} \frac{p_i}{Y(t)} \quad (7)$$

where Δp_i is the parameter perturbation. A 1% parameter increment was considered, that is $\Delta p_i/p_i = 0.01$. All calculations were performed in MATLAB (Math Works, Natick, MA).

III. RESULTS

The overall sensitivity analysis patterns of the mE2, E2 and DE2 state variables are shown in Fig.2, under the two parameter space conditions (i.e., monostability and bistability). In both the explored conditions, the major sensitive parameters are the basal transcription synthesis and the degradation of the mE2 transcript for mE2. For E2 protein and DE2 homodimer it is also important the degradation of the E2 protein but interestingly the degradation of the homodimer is not a sensitive parameter. In the case of bistability the formation/dissociation dimer parameters, the positive feedback synthesis rate, as well as the positive and negative feedback strengths become quite sensitive parameters. It is interesting to notice that the basal transcription synthesis rate, and the mE2 and E2 degradation rates induce an amplifying effect on all the state variables, being the sensitivity absolute value higher than 1. This happens also for the formation/dissociation DE2 rates for the DE2 homodimer state variable. This indicates that a 1% perturbation in a single model parameter induces an amplified effect on the overall pattern of the model state variables. Sensitivity analysis also allows to measure when each parameter contributes to the model dynamics. For this model all the parameters behave in a similar manner. They tend to affect the three state variables at the beginning of the infection and anyway in the first stages. For the sake of clarity, we show the response of the DE2 homodimer (which is qualitatively good to appreciate) in response to the variation of the basal and positive feedback synthesis rates (s_0 and s_1). We can observe how the s_0 basal

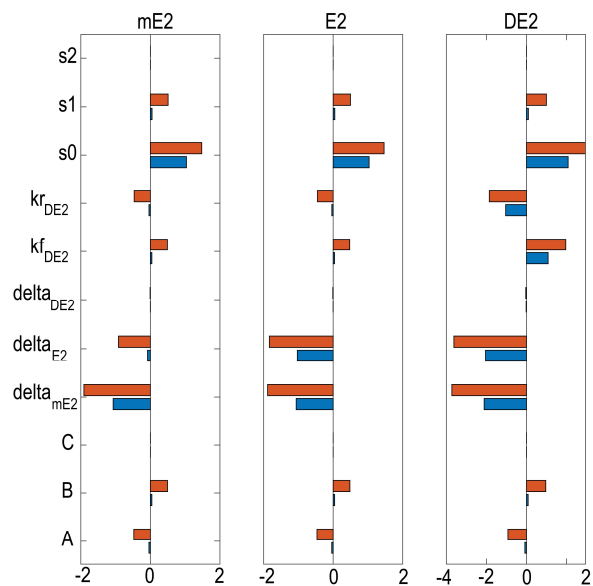
Fig.2 Overall sensitivity analysis, related to the model parameters, for the mE2 mRNA, E2 protein and DE2 homodimer monostability (blue bars) and bistability (orange bars).
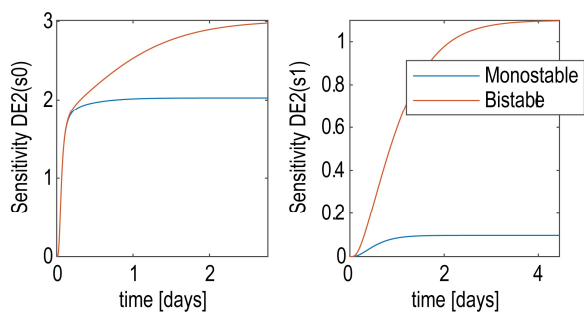

Fig.3 Sensitivity analysis during time evolution of DE2 homodimer under a 1% perturbation of s0 and s1 and under the monostable and bistable conditions.

transcription synthesis rate induces a very fast change at the very beginning of the infection for both the monostable and the bistable behavior. It also induces a change in DE2 (and the other variables) also for several days in the case of bistability (Fig. 3).

We also investigate some biological behaviors of the system

that weren't shown in [5]. We show a possible model trajectory of the system under the bistability condition where for the low copy number (*CN*) equilibria is of around 5 *CN* and the high *CN* equilibria (when the virus is active) is of around 70 *CN*. We finally show another interesting biological result where by modulating the positive feedback strength the system undergoes a ghost saddle node bifurcation [8] and the system can exhibit delays of different amplitude before converging to the high *CN* equilibria, hence before the virus becomes active and replicative [3].
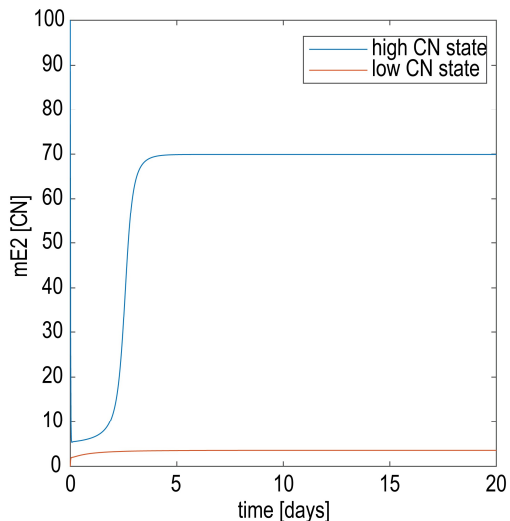

Fig.4 *mE2 mRNA* model trajectories under the bistable behavior.
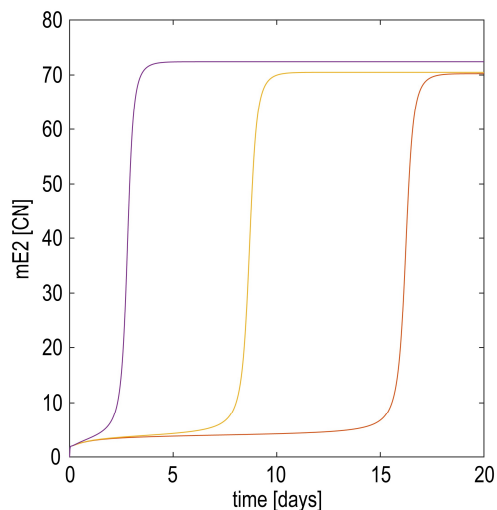

Fig.3 System response to different strengths (*B*) of the positive feedback. The lower (and more close to the bistability) *B* the higher the delay to reach the high copy number steady state.

IV. CONCLUSION

In this work we have extended a recent published work [3] about a minimal model of the *HPV EP* transcriptional regulation by performing a local sensitivity analysis. We have shown how the system is more sensitive to the molecular degradations of the viral products, to the basal transcription synthesis and, even if in a minor extent, to the association/dissociation rate of the *DE2* feedback regulator. We have also shown how the model becomes more sensitive

to crucial bifurcation parameters, such as the feedback strengths and the feedback synthesis rates (as shown in [3]) when the model working point is associated with a bistable behaviour. This is an interesting result because it allows to identify the systems sensitivity to crucial parameters that could drive the viral latency behaviour through the bistability [3].

We have also shown how the model, under a bistable behaviour, can exhibit a high *CN* (associated with the viral active replication) or a very low *CN* that could be associated with a latent response to the immune evasion. Moreover, we have found how the positive feedback strength (*B*) can induce very strong delay in the system response before reaching the active replication regimen. This is of great interest under a biological perspective since it is known the existence of *DE2* co-regulators (e.g., *p300*) that can strongly amplify the positive feedback response of the *EP* [5]. This is obtained by modifying the *DE2* affinity to the *DNA*, in other words by changing the positive feedback strength.

This work represents a starting point for a future global sensitivity analysis [9] in order to capture possible interactions between parameters whose jointly variation is associated with the bistability.

REFERENCES

1. Giaretta A, Di Camillo B, Barzon L, Toffolo GM. Modeling HPV Early Promoter Regulation. Conf Proc IEEE Eng Med Biol Soc. 2015;2015:6493–6.
2. Giaretta A, Toffolo GM. Modeling HPV Late Promoter Regulation. Conf Proc IEEE Eng Med Biol Soc. 2018;2386–9.
3. Giaretta A. Stochastic Modeling of the Co-Regulation between Early and E8 Promoters in Human Papillomavirus. ConfProc IEEE Eng MEd Biol Soc. 2018;8:5026–9.
4. Giaretta A, Toffolo GM. Sensitivity Analysis of a Model of Human Papillomavirus Late Promoter Regulation. 2019 41st Annu Int Conf IEEE Eng Med Biol Soc. 2019;(2):2913–6.
5. Giaretta A. Human Papillomavirus Early Promoter Regulatory Core as a Bistable Switch. 2019 41st Annu Int Conf IEEE Eng Med Biol Soc. 2019;2925–8.
6. Giaretta A, Toffolo GM, Elston TC. Stochastic modeling of human papillomavirusearly promoter gene regulation. J Theor Biol. 2020;486:110057. Available from: https://doi.org/10.1016/j.jtbi.2019.110057
7. Perumal TM, Gunawan R. Understanding dynamics using sensitivity analysis : caveat and solution. BMC Syst Biol. 2011;5(1):41. Available from: http://www.biomedcentral.com/1752-0509/5/41
8. Steven H S. Nonlinear Dynamics And Chaos: With Applications To Physics, Biology, Chemistry, And Engineering. Westview Press. 2015;
9. Saltelli A, Ratto M, Andres T, Campolongo F, Cariboni J, Gatelli D, et al. Global sensitivity analysis - the primer. Chichester: John Wiley & Sons; 2008.

Experimental validation of an e-textile t-shirt for ECG monitoring

F. Amitrano[1,2], A. Coccia[1,2], L. Donisi[1,3], A. Biancardi[1], G. Pagano[1] and G. D'Addio[1]

[1] ICS Maugeri SPA SB, Institute of Care and Scientific Research, Telese Terme (BN) and Bari, Italy

[2] Department of Information Technologies and Electrical Engineering, University of Naples 'Federico II', Naples, Italy

[3] Department of Advanced Biomedical Sciences, University of Naples 'Federico II', Naples, Italy

Abstract— **This paper describes a comparative analysis of a new wearable system based on E-Textile electrodes for non-invasive daylong monitoring of electrocardiogram (ECG). The proposed wearable device, named SWEET Shirt, is capable of measuring electrocardiogram signal through an instrumented T-shirt that uses E-Textile sensors sewn directly onto the fabric, making the system non-invasive for the user. SWEET Shirt measurements have been validated by comparing a subset of ECG-derived parameters to that granted by a standard Holter ECG used in clinical environment. ECG data have been simultaneously collected from the two devices used in the study on two male subjects, in short-term (2 hours) and long-term (24 hours) registrations. Passing-Bablok regression and Bland-Altman plots have been used to assess benchmarking. Statistical analysis pointed out great reliability in short-term measurement, while in long-term registration the great number of artefacts aroused in the signal does not allow very reliable measurements.**

Keywords—**e-textile, electrocardiography, benchmarking, signal processing.**

I. Introduction

OVER the past few years, there has been an incredible development of the smart textile industry, which has brought to an exponential increase of e-textile sensors for wearable applications [1], [2]. Electronic-Textiles (ET) are intelligent fabrics characterized by the integration of electro-active elements and micro-sensors in common garments. ET fabrics can detect, respond and adapt to the environment they meet, while maintaining their typical wearability and comfort. ETs are the elements that enable the development of wearable electronic devices. The increasing awareness in ET performances and advantages is leading to the use of ET wearable devices also in healthcare field, as a tool for patient monitoring.

ET wearable devices show several advantages with respect to the standard devices. They are comfortable, usually low cost and easy-to-use. This allows the use of these device at home, enabling patient monitoring for long time, and removing the influence of the clinical environment on patient's performance.

The above-mentioned features validate the increasing interest of healthcare industry in ET wearable devices of the last few years. However, while the great potential in the development of innovative ET medical devices is underlined, it is always useful to remember that they must guarantee reliable performance in line with accepted medical standards. The need to ensure a certain degree of comfort can affect the results offered by ET devices. The level of ET technology achieved so far, cannot yet guarantee performances comparable to that offered by laboratory equipment, which takes advantage of the absence of structural constraints to achieve very high levels performances. It is therefore essential that new systems entering the world of clinical monitoring, and in general in the medical field, must be tested in advance to verify their reliability [3],[4]. Among other diffused health applications, gait analysis [5],[6] and electrocardiogram (ECG) monitoring using wearable sensors have aroused great interest, showing great application perspectives. SWEET-Shirt is a new wearable system, based on ET technology, that allows the acquisition and transmission of ECG signal, with purposes related to remote health care monitoring. Aim of this study is to verify ECG measurement achieved with SWEET Shirt, in comparison to that granted by a standard Holter ECG used in clinical environment.

II. Materials and Methods

A. SWEET Shirt

SWEET Shirt is a wearable t-shirt made of an e-textile unit, a sensorized t-shirt, and an electronic portable unit that allows data transmission. This system allows the acquisition of ECG signal, and the wireless transmission to a platform that guarantees their usability for the physicians. The measurement of these vital biosignals and their subsequent processing for feature extraction, leads to a collection of real-time gathered physiological parameters, which can give an overall estimation of the user's health condition at any given time [7].

E-textile sensors are connected to the electronic unit by textile threads sewn directly onto the knitted fabric. The fabric connecting threads terminate metal buttons to which the electronics unit is then connected. This unit, powered by rechargeable batteries, incorporates conditioning and transmission circuits and it is housed in a plastic case located in a chest pocket (Fig. 1).

B. Holter Medilog® FD5

A 3-channel digital Holter recorder (Oxford Medilog FD5) was used to acquire subject's ECG signal (Fig. 2). The device uses three, five or seven electrodes and works at a sampling rate of 8000 Hz, with a resolution of 15.5 bits. The device is also equipped with a button that the patient can operate in case of chest pain or other relevant symptoms.

An integrated data acquisition card allows the analogue-to-digital conversion of ECG signal. Signal processing is then provided by a dedicated software. A report is finally generated which summarizes the result of the examination in a schematic and discursive form.

Fig. 1: SWEET Shirt device for ECG monitoring.

Fig. 2: ECG Holter Medilog Darwin.

C. Study Population

Two male subjects were involved in the study: a pathological subject with heart disease (aged 68) and a non-pathological subject (aged 25). Informed consent was provided to all participants by ensuring both the ethical purpose of the research and the total degree of safety of the wearable system under study that has no conductive element in contact with the skin or radiation effects of any kind.

D. Experimental Setup

ECG data have been simultaneously collected from the two devices used in the study. The seven electrodes used from the ECG Holter Recorder have been placed on subject's thorax as shown in Fig.3, in order to avoid overlapping with SWEET Shirt ET electrodes. Subjects have been then asked to wear SWEET Shirt. Finally, data acquisition was started simultaneously on the two devices. During the acquisition time, subjects were free to perform their every-day activities.

ECG data have been collected on short-term and long-term acquisitions. Short-term acquisitions have been performed on both pathological and non-pathological subjects, lasting 2 hours each, while only non-pathological subject has been monitored 24 hours long in long-term acquisition.

E. Data Processing

ECG signals have been digital processed to obtain synthetical parameters. Holter ECG signal has been automatically processed through the commercial software provided with the hardware.

SWEET Shirt ECG signal has been processed using a custom-made set of algorithms, developed using Matlab. The first step of processing has been made to assess the tachogram, which represents the series of RR intervals identified in ECG signal. The following parts of the algorithm are organized in three section, each one regarding a different kind of data analysis: the first one provides the analysis of Heart Rate Variability (HRV) in time domain, the second section contains HRV analysis in frequency domain and the last section has been developed to provide non-linear analysis on ECG signal. We focused on HRV and non-linear analysis as they are tools widely used in scientific research to better characterize ECG assessment [8],[9]. In this study three main parameters have been chosen to undergo the statistical analysis: Standard Deviation of Normal-to-Normal intervals (SDNN), the ratio between Low Frequency and High Frequency components of tachogram power spectrum (LF/HF Ratio) and the Higuchi Fractal Dimension assessed on the tachogram signal.

All the parameters have been assessed on successive time windows of tachogram signal. In short-time acquisitions, time windows width has been set to 5 minutes, while in long term analysis time windows width has been set to 1 hour, both yielding to a set of 24 measures.

F. Statistical Analysis

Statistical analysis has been performed to assess the reliability of the new ET based device, SWEET Shirt. All the parameters derived from SWEET Shirt ECG signal processing have been compared to the ones evaluated by the Holter software. The agreement between the two systems has been investigated by means of Passing-Bablok (PB) regression and Bland-Altman (BA) analysis.

In 1983 Passing and Bablok proposed a new regression method for testing the agreement of two sets of measurement achieved by different systems. This method overcomes the limitation of the ordinary least square regression model as it is based on robust, non-parametric model [10]. PB regression is not sensitive towards outliers and it assumes imprecision in both measurement methods and that errors in both methods have same distribution, not necessarily normal. The requirements for PB regression are: continuously distributed measurements and linear relationship between methods [11].

BA analysis is a graphical method used to compare two measurement systems. It is provided by plotting the differences between the two measurements against their averages, considered to be the best estimation for the real value of the measuring object. If the differences are randomly distributed around the zero-value axis, no proportional nor systematic error is underlined by the analysis. Quantitative assessment is given through the bias, as the mean of the differences, and the limits of agreement (LoA) assessed as the bias ±1.96 times standard deviation of the differences [12],[13]. If the differences between methods do not have a normal and/or symmetric distribution, limits of agreement are considered to be between the 2.5% and 97.5% percentiles. Significant statistical errors are said to be present if the confidence interval does not contain zero value.
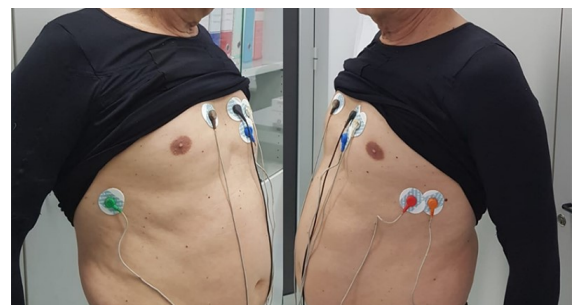

Fig. 3: ECG Holter electrodes placement.

PB regression have been performed using Matlab, while BA analysis has been performed using GraphPad Prism.

III. RESULTS AND DISCUSSION

In Table I results of PB regression are reported for non-pathological (above) and pathological (below) subjects. For each of the three analysed parameters, slope and offset, with their 95% Confidence Interval (CI), are given. In all provided results, slope values are close to 1 and their CIs always include 1. Similarly, the offset values are close to 0 in all analyses, with CIs always including 0 values.

Table II contains BA quantitative results and Fig.4 shows the BA plots of the analysed parameters. In the short-term registration for the non-pathological volunteer, the values of bias are very close to 0, and both bias CIs and LoA have low width, always including 0 value. In long term registration bias values are higher, and both CIs and LoA include zero value but they have large widths, pointing out low reliability for these measurements. In short term registration for pathological subject bias values for SDNN and LF/HF Ratio are higher than the ones evaluated for non-pathological volunteer, but much lower than the ones assessed in long term registration. The bias assessed for Higuchi Fractal Dimension is higher than the corresponding of other acquisitions, and its CI does not include 0 value. BA plots show random distribution for all the

evaluated parameters, except for the Higuchi Fractal Dimension in pathological volunteer. In this case it is clear that data are distributed below the line of zero, pointing out a systematic error in the measurement, which can be removed by adding the assessed bias to the values measured by the new proposed system.

In conclusion we can affirm that the measurements provided by SWEET Shirt on short term registration for non-pathological subject are very reliable, while great uncertainty is pointed out in measurements of long-term registration. The causes of these results can be attributed to the low adherence offered by the ET electrodes inside SWEET Shirt. In long-term registration the activities executed by the subject during the 24 hours cause a great number of artefacts. The ECG signal from SWEET Shirt is clearly visible in just 36.49% of the registration time, while the signal from the holter recorder is clear from artefacts in 84.86% of the whole time.

IV. CONCLUSION

The aim of this study is to assess the reliability of a new system for ECG monitoring based on ET technology. Results achieved with the statistical analysis point out that great reliability in measurements is achieved when the ET electrodes of the new proposed device are well-fixed on subject's skin. In long-term registration the great number of artefacts aroused in

TABLE I
PASSING BABLOK REGRESSION

	Non-Pathological Subject							
	Short Term Registration				Long Term Registration			
	Slope	95% CI	Offset	95% CI	Slope	95% CI	Offset	95% CI
SDNN	1.00	0.993 to 1.01	0	-0.454 to 0.430	0.986	0.692 to 1.21	3.30	-9.27 to 20.3
LF/HF Ratio	1.00	0.974 to 1.04	-0.00740	-0.0506 to 0.0273	0.907	0.695 to 1.23	0.224	-0.319 to 0.642
Higuchi Fractal Dimension	1.00	0.977 to 1.03	-0.00610	-0.0554 to 0.0435	0.850	0.661 to 1.13	0.247	-0.230 to 0.575
	Pathological Subject							
	Short Term Registration							
	Slope		95% CI		Offset		95% CI	
SDNN	0.932		0.597 to 1.39		0.692		-8.86 to 7.02	
LF/HF Ratio	0.919		0.618 to 1.39		-0.409		-1.50 to 0.358	
Higuchi Fractal Dimension	1.33		0.807 to 2.28		-0.500		-2.09 to 0.396	

TABLE II
BLAND ALTMAN ANALYSIS

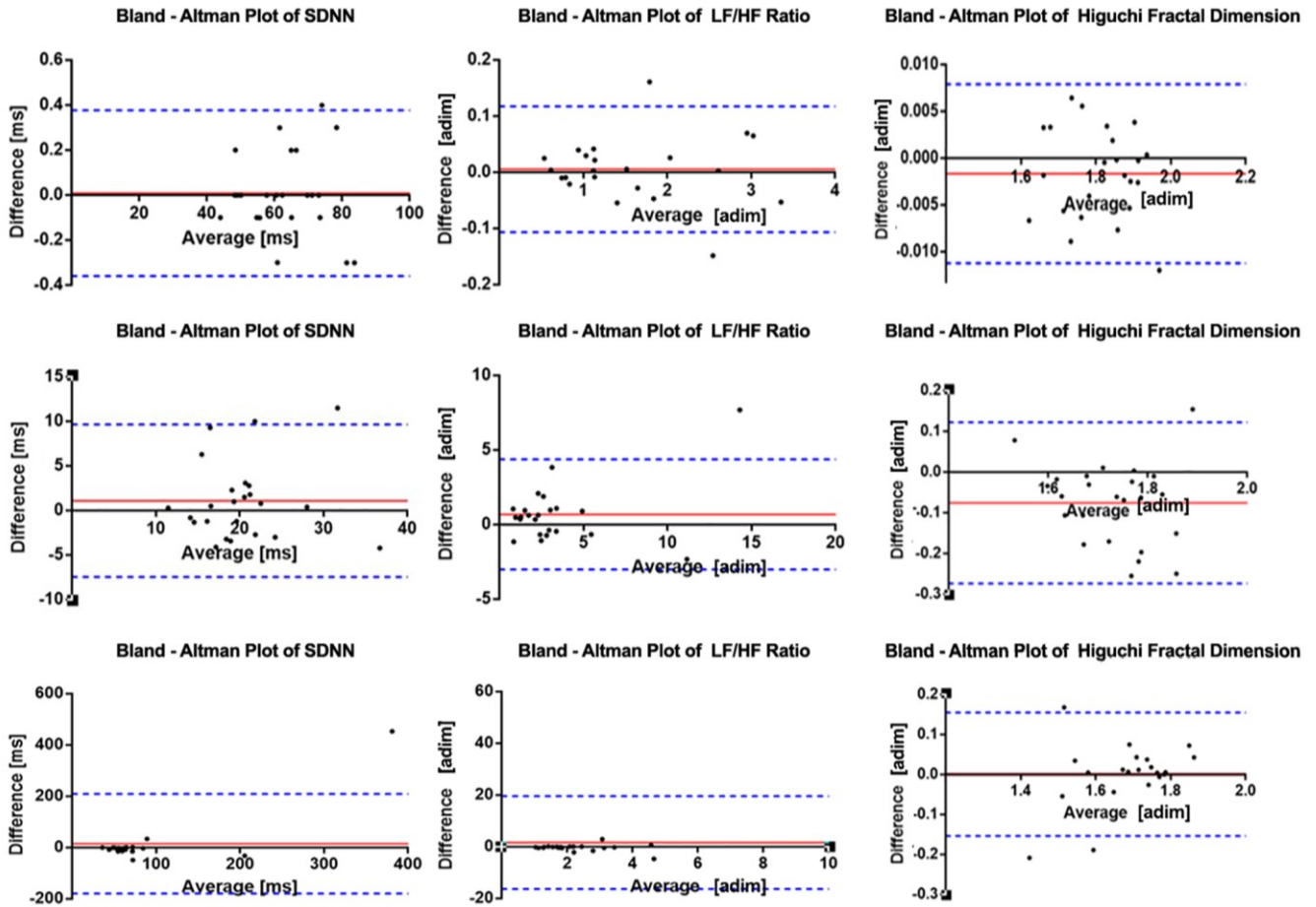|	Non-Pathological Subject					
	Short Term Registration			Long Term Registration		
	Bias	95% CI	LoA	Bias	95% CI	LoA
SDNN [ms]	0.00870	-0.0713 to 0.0887	-0.360 to 0.377	15.2	-27.9 to 58.3	-179 to 209
LF/HF Ratio [adim]	0.00539	-0.0189 to 0.0297	-0.107 to 0.117	1.64	-2.35 to 5.62	-16.3 to 19.6
Higuchi Fractal Dimension [adim]	-0.00165	-0.00372 to 0.000424	-0.0112 to 0.00791	0.000831	-0.0335 to 0.0351	-0.154 to 0.155
	Pathological Subject					
	Short Term Registration					
	Bias		95% CI		LoA	
SDNN [ms]	1.10		-0.711 to 2.92		-7.44 to 9.65	
LF/HF Ratio [adim]	0.684		-0.101 to 1.47		-3.01 to 4.38	
Higuchi Fractal Dimension [adim]	-0.0756		-0.118 to -0.0336		-0.273 to 0.122	

Fig. 4: Bland-Altman plots of the parameters in short-term registration for non-pathological volunteer (first row); in short-term registration for pathological subject (second row) and in long-term registration for non-pathological volunteer (last row). Red lines represent bias, blue dashed lines represent LoA.

the signal does not allow very reliable measurements. This means that the principal problem is linked to electrodes adhesion on skin, which should be improved to have better performance.

V. ACKNOWLEDGEMENT

REFERENCES

[1] Pani D, Achilli A, Bonfiglio A. Survey on Textile Electrode Technologies for Electrocardiographic (ECG) Monitoring, from Metal Wires to Polymers. Advanced Materials Technologies. 2018;1800008.

[2] Castano, L. M., & Flatau, A. B. (2014). Smart fabric sensors and e-textile technologies: a review. Smart Materials and Structures, 23(5), 053001.

[3] D'Addio, G., Donisi, L., Pagano, G., Improta, G., Biancardi, A., & Cesarelli, M. (2019, July). Agreement between Opal and G-Walk Wearable Inertial Systems in Gait Analysis on Normal and Pathological Subjects. In 2019 41st Annual International Conference of the IEEE Engineering in Medicine and Biology Society (EMBC) (pp. 3286-3289). IEEE.

[4] Donisi, L., D'Addio, G., Pagano, G., Coccia, A., & Cesarelli, M. (2019). Study of Agreement between two Wereable Inertial Systems for Gait Analysis based on a different sensor placement: G-Walk System and Opal System. Gait & Posture, 74, 14.

[5] D'Addio, G., Evangelista, S., Donisi, L., Biancardi, A., Andreozzi, E., Pagano, G., ... & Cesarelli, M. (2019, July). Development of a Prototype E-Textile Sock. In 2019 41st Annual International Conference of the IEEE Engineering in Medicine and Biology Society (EMBC) (pp. 17498-1752). IEEE. DOI 10.1109/EMBC.2019.8856739

[6] D'Addio, G., Iuppariello, L., Bifulco, P., Lanzillo, B., Pappone, N., & Cesarelli, M. (2017). Validity and reliability of textile system Sensoria for posturographic measurements. Giornale italiano di medicina del lavoro ed ergonomia, 39(4), 278-284.

[7] Pantelopoulos, A., & Bourbakis, N. G. (2009). A survey on wearable sensor-based systems for health monitoring and prognosis. IEEE Transactions on Systems, Man, and Cybernetics, Part C (Applications and Reviews), 40(1), 1-12.

[8] Accardo, A., Cusenza, M., De, A. F., Fornasa, E., & D'Addio, G. (2012). Ultradian rhythms during day and night in normal and COPD subjects. Studies in health technology and informatics, 180, 1120-1122.

[9] Cusenza, M., Accardo, A., D'Addio, G., & Corbi, G. (2010, September). Relationship between fractal dimension and power-law exponent of heart rate variability in normal and heart failure subjects. In 2010 Computing in Cardiology (pp. 935-938). IEEE.

[10] Passing, H., & Bablok, W. (1983). A new biometrical procedure for testing the equality of measurements from two different analytical methods. Application of linear regression procedures for method comparison studies in clinical chemistry, Part I. Clinical Chemistry and Laboratory Medicine, 21(11), 709-720.

[11] Bablok, W., & Passing, H. (1985). Application of statistical procedures in analytical instrument testing. Journal of Analytical Methods in Chemistry, 7(2), 74-79.

[12] Weinfurt, P. (2010). Biomedical Technology Assessment: The 3Q Method. *Synthesis Lectures on Biomedical Engineering*, *5*(1), 1-101.

[13] Vidali, M., Tronchin, M., & Dittadi, R. (2016). Protocol for the comparison of two laboratory methods. *BIOCHIMICA CLINICA*, *40*(2), 129-142.

Benchmarking between a Sensorized E-textile Sock for Remote Monitoring and a Stereophotogrammetric System

L. Donisi[1,2], A. Coccia[2,3], F. Amitrano[2,3], C. Ricciardi[1], G. Cesarelli[4,5] and G. D'Addio[2]

[1] *Department of Advanced Biomedical Sciences, University of Naples Federico II, Naples, Italy*
[2] *Bioengineering Unit, ICS Maugeri SPA SB Institute of Care and Scientific Research, Telese Terme (BN), Italy*
[3] *Department of Information Technology and Electrical Engineering, University of Naples Federico II, Naples, Italy*
[4] *Department of Chemical, Materials and Production Engineering, University of Naples Federico II, Naples, Italy*
[5] *Center for Advanced Biomaterials for Healthcare, Italian Institute of Technology, Naples, Italy*

Abstract—Despite a significant growth of interest for e-textile wearable devices in the contest of remote monitoring, there is still a lack of knowledge about the agreement between them and their related gold standard. Aim of this study is to investigate the agreement between a sensorized e-textile sock namely SWEET Sock and the stereophotogrammetry considered the "gold standard" in the context of gait analysis. Twenty-nine free walk acquisitions of three healthy subjects instrumented by both systems were recorded. The study of agreement was performed through different statistical approaches: Paired t-test, Bland-Altman Analysis and Passing-Bablok regression. The result showed that there was not a perfect agreement about each spatiotemporal parameter analysed between the two systems. This result should be taken in correct account before using the two different systems in an interchangeable way, for example to evaluate the patients' rehabilitation outcome in terms of spatiotemporal parameters.

Keywords—Wearable devices, e-textile, agreement, benchmarking.

I. INTRODUCTION

Thecnolgy today plays an increasingly central role in all fields of medicine such as the rehabilitation medicine. In recent years the continuous advances in miniaturization of electronic devices, as well as in mobile and remote computing, have promoted a significant growth of interest for wearable technology widely used in the gait analysis to monitor quantitatively motion [1]-[3]. The concept of wearable corresponds to a device that is always connected to a person (which can be transported constantly), comfortable and easy to store and use, and that is unobtrusive like clothing [4]; then they are cheap, washable and easily customizable [5]. The interest of the healthcare industry for wearable systems stems from the need to monitor patients for long periods of time. This occurs when medical doctors want to monitor patients whose chronic condition includes the risk of sudden acute events. The main advantage of wearable technologies is the possibility to use them at home and so the capability to monitor patients' parameters in a remote way. Statistical studies showing a growth in the use of wearable technology suggest that soon wearable systems will be part of routine clinical evaluations [6]. In the wide panorama of wearable technology, gait analysis using wearable sensors has made important progress and shown good application prospects. The fusion of gait analysis technology and remote medical systems, whereby gait analysis results can be transmitted to a centralized medical location and processed by trained medical personnel, will be an interesting developing trend. Once these two developments are achieved, gait analysis using wearable sensors will be widely performed in daily environments, various clinical occasions, and other possible applications to monitor physical activity, playing an important role as medical assistance tool [7].

The purpose of this paper is to validate the performances of SWEET Sock, a prototype sensorized e-textile sock, carrying out a study of agreement between the sock and a gold standard Stereophotogrammetric System: SMART-DX 700 by BTS Bioengineering.

II. MATERIALS AND METHODS

A. E-textile Sock

An E-textile Sock named SWEET Sock was analyzed in the present study [8]. SWEET Sock is a sensorized sock in e-textile, integrated into a m-Health system. The device allows the acquisition of plantar pressures and accelerometric signals deriving from the motion of the lower limbs. The detected biosignals are acquired through a LilyPad Arduino microcontroller and transmitted, through Simblee BLE technology, to a custom-made mobile app. Data are afterwards uploaded, through a mobile app, on a web server. Here a custom made MATLAB GUI platform, developed for digital signal processing, allows to compute the main kinematic and spatiotemporal parameters related to posturography and gait.

B. Stereophotogrammetry

Stereophotogrammetry is considered the gold standard in the gait analysis field. SMART-DX 700 by BTS Bioengineering was used in the present study as reference.

SMART-DX 700 System is composed of 6 infrared digital cameras; it comes with the following hardware features: a sensor resolution of 1.5 megapixel, an acquisition frequency at maximum resolution of 250 fps, a maximum acquisition frequency of 1000 fps and an accuracy less than 0.1 mm. Hardware communicates with a PC workstation running SMART Clinic Software able to store and compute parameters related to kinematic (spatiotemporal parameters, joint angles) and dynamic (forces exchanged).

C. Experimental Session

The experimental sessions provided simultaneous recordings of the lower limbs' accelerometric signals computed by SWEET Sock and SMART-DX 700 measurement systems. Twenty-nine free walking acquisition on three healthy subjects were recorded. The test subject was equipped with both systems: 2 E-textile SWEET Sock and 22 passive retro-reflective markers placed at specific points of reference on the body according DEVIS protocol as shown in Fig. 1. Benchmarking study was performed by comparing the spatiotemporal parameters' values computed by SWEET Sock system with the corresponding ones computed by SMART-DX 700 stereophotogrammetric system. In particular for SWEET Sock, spatiotemporal parameters were computed through specific algorithm developed in MATLAB environment by authors, from acquired accelerometric signals; while for the SMART-DX 700 system the corresponding spatiotemporal parameters were retrieved from the reports generated by SMART CLINIC software. The following spatiotemporal parameters computed by both systems were considered for the benchmarking analysis: Gait Cycle Time (s): duration of a complete gait cycle; Stride Velocity (m/s): walking speed; Step Length (m): distance between two consecutive right-left foot falls at the moments of initial contacts; Cadence (steps/minute): stepping rate; Stance Time (s): average time of a gait cycle that either foot is on the ground; Swing Time (s): average time of a gait cycle that either foot is off the ground.

Fig. 1 : Subject instrumented by both systems

D. Statistical Analysis

Agreement between measurements computed by the two systems: SWEET Sock and SMART-DX 700 was investigated by Bland-Altman Analysis, Passing-Bablok regression and two tailed Paired t test; the latter in its parametric or non-parametric form (by Wilcoxon matched pairs signed-rank test) in according to D'Agostino-Pearson omnibus normality test result. Passing-Bablok regression analysis allows to evaluate the constant systematic error (intercept of regression line) and the proportional systematic error (slope of regression line) according if their related 95% confidence limits include or not 0 value for the intercept and 1 for the slope [9],[10]. Bland-Altman plot describes the bias and the standard deviation respectively as the average and the standard deviation of the differences between the measures computed by two different measurement methods, allowing to calculate the limits of agreement, calculated as the bias ±

1.96 times its standard deviation [11]–[13] and studying the absence of a significant statistical error, depending if the confidence limits of the bias contain or not 0 value [10]. Finally Paired t-test was used to reject the null hypothesis that there is no difference between the two devices in mean values [14], through the calculation of the p-value; a two-tail test was used and the nominal alpha level was set to 0.5.

III. RESULTS

Table I, Table II and Table III show the results obtained using the three different statistical approaches used to assess the agreement between the two systems for gait analysis: SWEET Sock and SMART-DX 700.

Fig. 1 and Fig. 2 show the Bland-Altman plot and the scatter plot with the Passing-Bablok regression line.

TABLE I
PAIRED T-TEST ANALYSIS

Parameter	SMART-DX	SWEET Sock
Gait Cycle Time (s)	1.05±0.04	1.03±0.03***
Stance Time (s)	0.61±0.02	0.53±0.02****
Swing Time (s)	0.44±0.03	0.50±0.01****
Stride Velocity (m/s)	1.38±0.10	1.29±0.19***
Cadence (steps/minute)	115.20±4.80	116.40±3.07*
Step Length(m)	0.72±0.05	0.64±0.10****

*p<0.5**p<0.01***p<0.001****p<0.0001 at ANOVA test

TABLE II
BLAND-ALTMAN ANALYSIS

Parameter	bias	95% bias confidence interval	Limits of agreement
Gait Cycle Time (s)	0.02	[0.01 ÷ 0.02]	-0.02; 0.06
Stance Time (s)	0.08	[0.07 ÷ 0.08]	0.05; 0.10
Swing Time (s)	-0.06	[-0.07 ÷ -0.06]	-0.10; -0.02
Stride Velocity (m/s)	0.09	[0.01 ÷ 0.17]	-0.34; 0.52
Cadence (steps/minute)	-1.15	[-2.08 ÷ -0.22]	-5.10; 3.69
Step Length(m)	0.07	[0.03÷ 0.11]	-0.13; 0.28

TABLE III
PASSING-BABLOK REGRESSION ANALYSIS

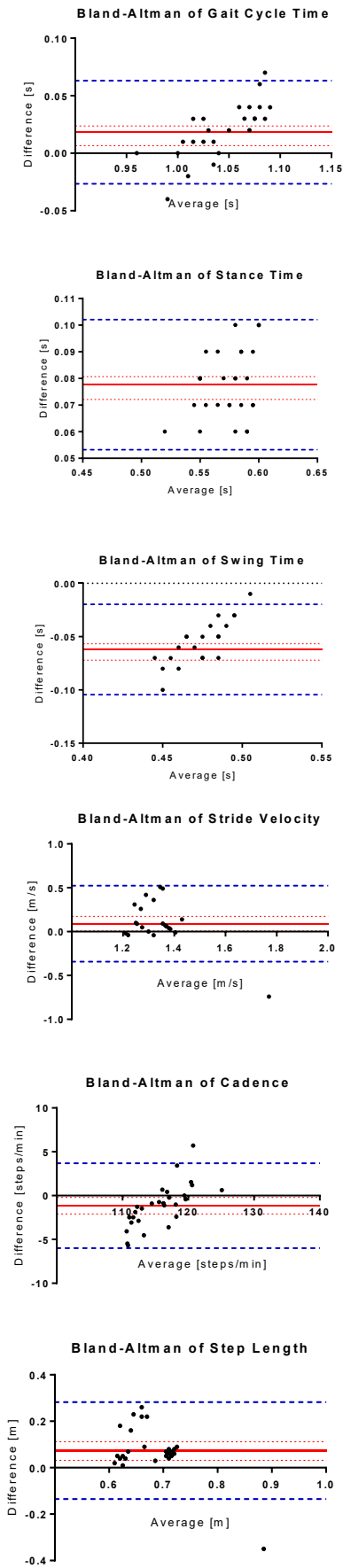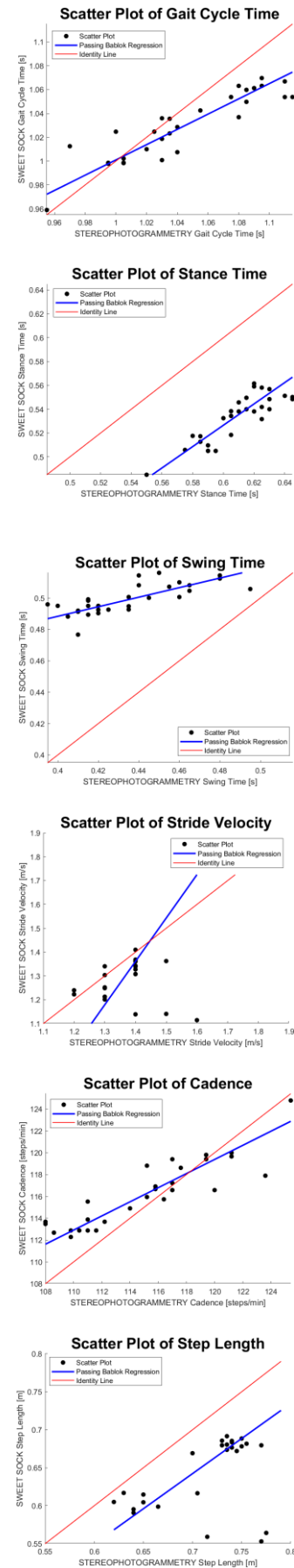| Parameter	Slope and its 95% confidence interval	Offset and its 95% confidence interval
Gait Cycle Time (s)	0.64 [0.49 ÷ 0.75]	0.36 [0.24 ÷ 0.52]
Stance Time (s)	0.90 [0.69 ÷ 1.13]	-0.01 [-0.15 ÷ 0.11]
Swing Time (s)	0.30 [0.21 ÷ 0.40]	0.37 [0.32 ÷ 0.41]
Stride Velocity (m/s)	1.82 [0.91 ÷ ∞]	-1.18 [-∞ ÷ 0.07]
Cadence (steps/minute)	0.65 [0.50 ÷ 0.76]	41.76 [29.14 ÷ 58.45]
Step Length (m)	0.92 [0.64 ÷ 2.40]	-0.01 [-1.09 ÷ 0.20]

Fig.1 : Bland-Altman Plots

Fig. 2 : Scatter Plots with Passing-Bablok regression line

IV. CONCLUSION

Results described in the above tables and plots allow to highlight the following findings for each spatiotemporal parameter.

Gait Cycle Time parameter showed a non-agreement because of a constant systematic error (eliminable through zeroing of bias) and a proportional systematic error. The Bland-Altman plot showed that the vast majority of the points were over the line of zero, this means that SWEET Sock underestimated this parameter compared to SMART-DX 700.

Stance Time parameter showed a non-agreement for the presence of a constant systematic error (eliminable), in fact a bias even if close to zero was present

Swing Time parameter showed a non-agreement for the presence of a constant systematic error and of a proportional systematic error that led SWEET Sock to overestimate this parameter compared to SMART-DX 700.

Stride Velocity parameter showed a non-agreement because of a constant systematic error (eliminable) and so a good potential agreement after zeroing of the bias.

Cadence parameter showed a non-agreement for the presence of a constant systematic error and of a proportional systematic error. A bias equal to -1.15 and a greater distribution of the point over the line of identity in the Bland-Altman plot (Fig. 1) led to the conclusion that SWEET Sock overestimated this parameter.

Finally Step Length parameter showed a non-agreement too. Paired t-test showed an overall greater value for the parameter computed by SMART-DX, so in this case SWEET Sock underestimated this parameter compared to SMART-DX 700.

Results showed a not perfect agreement between the two measurement systems on each motion parameter analysed in the study. Although we had quite contained errors, an interchangeable use of the two systems is not recommended. We had two different types of errors: a constant systematic error (easily eliminated by zero bias by means of a simple subtraction operation from initial data) and a proportional systematic error. However, the clinical impact of a statistically significant systematic error should be interpreted on the basis of established acceptability criteria. It is possible in fact that relatively small proportional or constant systematic errors, although statistically significant, they do not preclude the use of a given method. In conclusion, you can consider possible to combine the parameters' values computed by SWEET Sock system with those computed by the reference gold standard Stereophotogrammetry, providing that it takes into accounts the errors made by SWEET Sock on each parameter considered.

ACKNOWLEDGEMENT

REFERENCES

[1] D'Addio, G., Donisi, L., Pagano, G., Improta, G., Biancardi, A., & Cesarelli, M. (2019, July). Agreement between Opal and G-Walk Wearable Inertial Systems in Gait Analysis on Normal and Pathological Subjects. In *2019 41st Annual International Conference of the IEEE Engineering in Medicine and Biology Society (EMBC)* (pp. 3286-3289). IEEE. **DOI:** 10.1109/EMBC.2019.8857841

[2] D'Addio, G., Donisi, L., Mercogliano, L., Cesarelli, G., Bifulco, P., & Cesarelli, M. (2019, September). Potential Biomechanical Overload on Skeletal Muscle Structures in Students During Walk with Backpack. In *Mediterranean Conference on Medical and Biological Engineering and Computing* (pp. 262-266). Springer, Cham. https://doi.org/10.1007/978-3-030-31635-8_31

[3] D'Addio, G., Iuppariello, L., Bifulco, P., Lanzillo, B., Pappone, N., & Cesarelli, M. (2017). Validity and reliability of textile system Sensoria for posturographic measurements. *Giornale italiano di medicina del lavoro ed ergonomia*, *39*(4), 278-284.

[4] Engin, M., Demirel, A., Engin, E. Z., & Fedakar, M. (2005). Recent developments and trends in biomedical sensors. *Measurement*, *37*(2), 173-188.

[5] DeRossi, D., & Lymberis, A. (2005). Guest editorial new generation of smart wearable health systems and applications. *IEEE transactions on information technology in biomedicine*, *9*(3), 293-294.

[6] Bonato, P. (2003). Wearable sensors/systems and their impact on biomedical engineering. *IEEE Engineering in Medicine and Biology Magazine*, *22*(3), 18-20.

[7] Mathie, M. J., Coster, A. C., Lovell, N. H., & Celler, B. G. (2004). Accelerometry: providing an integrated, practical method for long-term, ambulatory monitoring of human movement. *Physiological measurement*, *25*(2), R1.

[8] D'Addio, G., Evangelista, S., Donisi, L., Biancardi, A., Andreozzi, E., Pagano, G., ... & Cesarelli, M. (2019, July). Development of a Prototype E-Textile Sock. In *2019 41st Annual International Conference of the IEEE Engineering in Medicine and Biology Society (EMBC)* (pp. 17498-1752). IEEE. **DOI:** 10.1109/EMBC.2019.8856739

[9] Passing, H., & Bablok, W. (1983). A new biometrical procedure for testing the equality of measurements from two different analytical methods. Application of linear regression procedures for method comparison studies in clinical chemistry, Part I. *Clinical Chemistry and Laboratory Medicine*, *21*(11), 709-720.

[10] Sotgia, S., Zinellu, A., Pinna, G. A., Deiana, L., & Carru, C. (2008). A new general regression-based approach for method comparison studies. *Clinical chemistry and laboratory medicine*, *46*(7), 1046-1049.

[11] Bland, J. M., & Altman, D. (1986). Statistical methods for assessing agreement between two methods of clinical measurement. *The lancet*, *327*(8476), 307-310.

[12] Altman, D. G., & Bland, J. M. (1983). Measurement in medicine: the analysis of method comparison studies. *Journal of the Royal Statistical Society: Series D (The Statistician)*, *32*(3), 307-317.

[13] Bland, J. M., & Altman, D. G. (1999). Measuring agreement in method comparison studies. *Statistical methods in medical research*, *8*(2), 135-160.

[14] Blair, R. C., & Cole, S. R. (2002). Two-sided equivalence testing of the difference between two means. *Journal of Modern Applied Statistical Methods*, *1*(1), 18.